Natural Stone, Weathering Phenomena, Conservation Strategies and Case Studies

edited by S. Siegesmund, T. Weiss and A. Vollbrecht

Geological Society
Special Publication
No. 205

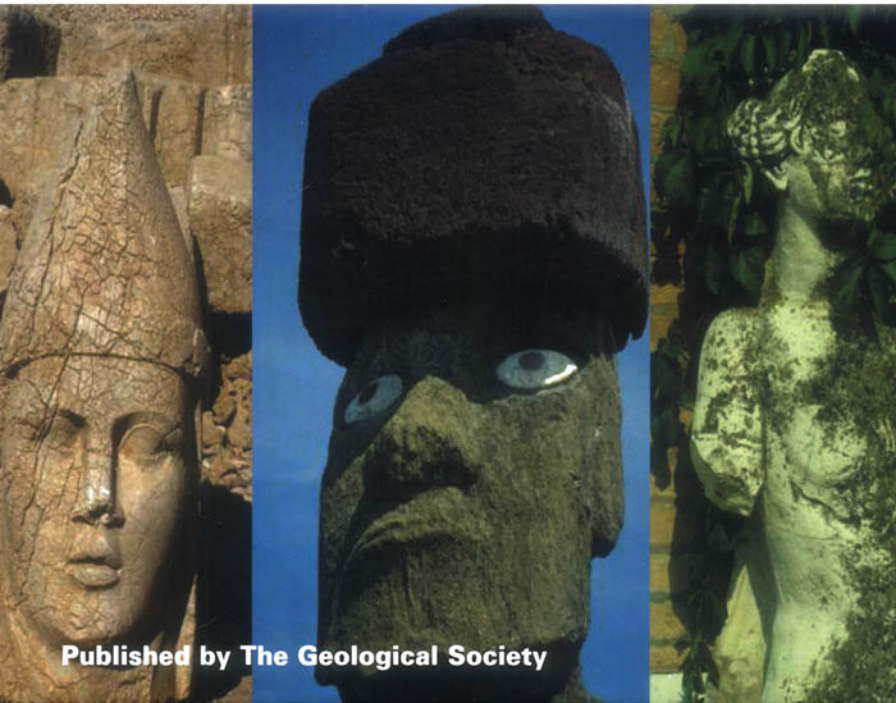

Published by The Geological Society

Natural Stone, Weathering Phenomena, Conservation Strategies and Case Studies

Geological Society Special Publications
Society Book Editors
A. J. FLEET (CHIEF EDITOR)
P. DOYLE
F. J. GREGORY
J. S. GRIFFITHS
A. J. HARTLEY
R. E. HOLDSWORTH
A. C. MORTON
N. S. ROBINS
M. S. STOKER
J. P. TURNER

Reviewing procedures

The Society makes every effort to ensure that the scientific and production quality of its books matches that of its journals. Since 1997, all book proposals have been refereed by specialist reviewers as well as by the Society's Books Editorial Committee. If the referees identify weaknesses in the proposal, these must be addressed before the proposal is accepted.

Once the book is accepted, the Society has a team of Book Editors (listed above) who ensure that the volume editors follow strict guidelines on refereeing and quality control. We insist that individual papers can only be accepted after satisfactory review by two independent referees. The questions on the review forms are similar to those for *Journal of the Geological Society.* The referees' forms and comments must be available to the Society's Book Editors on request.

Although many of the books result from meetings, the editors are expected to commission papers that were not presented at the meeting to ensure that the book provides a balanced coverage of the subject. Being accepted for presentation at the meeting does not guarantee inclusion in the book.

Geological Society Special Publications are included in the ISI Science Citation Index, but they do not have an impact factor, the latter being applicable only to journals.

More information about submitting a proposal and producing a Special Publication can be found on the Society's web site: www.geolsoc.org.uk.

It is recommended that reference to all or part of this book should be made in one of the following ways:

SIEGESMUND, S., WEISS, T. & VOLLBRECHT, A. (eds) 2002. *Natural Stone, Weathering Phenomena, Conservation Strategies and Case Studies*. Geological Society, London, Special Publications, **205**.

ONDRASINA, J., KIRCHNER, D. & SIEGESMUND, S. 2002. Freeze–thaw cycles and their influence on marble deterioration: a long-term experiment. *In*: SIEGESMUND, S., WEISS, T. & VOLLBRECHT, A. (eds) *Natural Stone, Weathering Phenomena, Conservation Strategies and Case Studies*. Geological Society, London, Special Publications, **205**, 9–18.

GEOLOGICAL SOCIETY SPECIAL PUBLICATION NO. 205

Natural Stone, Weathering Phenomena, Conservation Strategies and Case Studies

EDITED BY

S. SIEGESMUND, T. WEISS AND A. VOLLBRECHT
University of Göttingen, Germany

2002
Published by
The Geological Society
London

THE GEOLOGICAL SOCIETY

The Geological Society of London (GSL) was founded in 1807. It is the oldest national geological society in the world and the largest in Europe. It was incorporated under Royal Charter in 1825 and is Registered Charity 210161.

The Society is the UK national learned and professional society for geology with a worldwide Fellowship (FGS) of 9000. The Society has the power to confer Chartered status on suitably qualified Fellows, and about 2000 of the Fellowship carry the title (CGeol). Chartered Geologists may also obtain the equivalent European title, European Geologist (EurGeol). One fifth of the Society's fellowship resides outside the UK. To find out more about the Society, log on to www.geolsoc.org.uk.

The Geological Society Publishing House (Bath, UK) produces the Society's international journals and books, and acts as European distributor for selected publications of the American Association of Petroleum Geologists (AAPG), the American Geological Institute (AGI), the Indonesian Petroleum Association (IPA), the Geological Society of America (GSA), the Society for Sedimentary Geology (SEPM) and the Geologists' Association (GA). Joint marketing agreements ensure that GSL Fellows may purchase these societies' publications at a discount. The Society's online bookshop (accessible from www.geolsoc.org.uk) offers secure book purchasing with your credit or debit card.

To find out about joining the Society and benefiting from substantial discounts on publications of GSL and other societies worldwide, consult www.geolsoc.org.uk, or contact the Fellowship Department at: The Geological Society, Burlington House, Piccadilly, London W1J 0BG: Tel. +44 (0)20 7434 9944; Fax +44 (0)20 7439 8975; Email: enquiries@geolsoc.org.uk.

For information about the Society's meetings, consult *Events* on www.geolsoc.org.uk. To find out more about the Society's Corporate Affiliates Scheme, write to enquiries@geolsoc.org.uk.

Published by The Geological Society from:
The Geological Society Publishing House
Unit 7, Brassmill Enterprise Centre
Brassmill Lane
Bath BA1 3JN,
UK

(*Orders*: Tel. +44 (0)1225 445046
Fax +44 (0)1225 442836)
Online bookshop: http://bookshop.geolsoc.org.uk

The publishers make no representation, express or implied, with regard to the accuracy of the information contained in this book and cannot accept any legal responsibility for any errors or omissions that may be made.

© The Geological Society of London 2002. All rights reserved. No reproduction, copy or transmission of this publication may be made without written permission. No paragraph of this publication may be reproduced, copied or transmitted save with the provisions of the Copyright Licensing Agency, 90 Tottenham Court Road, London W1P 9HE. Users registered with the Copyright Clearance Center, 27 Congress Street, Salem, MA 01970, USA: the item-fee code for this publication is 0305–8719/02/$15.00.

British Library Cataloguing in Publication Data
A catalogue record for this book is available from the British Library.

ISBN 1–86239–123–8

Typeset by Type Study, Scarborough, UK
Printed by Cambrian Printers, Aberystwyth, UK.

Distributors

USA
AAPG Bookstore
PO Box 979
Tulsa
OK 74101–0979
USA
Orders: Tel. +1 918 584-2555
Fax +1 918 560-2652
E-mail bookstore@aapg.org

India
Affiliated East–West Press PVT Ltd
G-1/16 Ansari Road, Daryaganj,
New Delhi 110 002
India
Orders: Tel. +91 11 327-9113
Fax +91 11 326-0538
E-mail affiliat@nda.vsnl.net.in

Japan
Kanda Book Trading Co.
Cityhouse Tama 204
Tsurumaki 1-3-10
Tama-shi
Tokyo 206–0034
Japan
Orders: Tel. +81 (0)423 57-7650
Fax +81 (0)423 57-7651

Contents

Preface vii

SIEGESMUND, S., WEISS, T. & VOLLBRECHT, A. Natural stone, weathering phenomena, conservation strategies and case studies: introduction 1

Weathering of natural building stones

ONDRASINA, J., KIRCHNER, D. & SIEGESMUND, S. Freeze–thaw cycles and their influence on marble deterioration: a long-term experiment 9

THOMACHOT, C. & JEANNETTE, D. Evolution of the petrophysical properties of two types of Alsatian sandstone subjected to simulated freeze–thaw conditions 19

CASSAR, J. Deterioration of the Globigerina Limestone of the Maltese Islands 33

Weathering processes

DOEHNE, E. Salt weathering: a selective review 51

ZEISIG, A., SIEGESMUND, S. & WEISS, T. Thermal expansion and its control on the durability of marbles 65

MALAGA-STARZEC, K., LINDQVIST, J. E. & SCHOUENBORG, B. Experimental study on the variation in porosity of marble as a function of temperature 81

WEISS, T., SIEGESMUND, S. & FULLER, E. R. Thermal stresses and microcracking in calcite and dolomite marbles via finite element modelling 89

Fabric dependence of physical properties

WEBER, J. & LEPPER, J. Depositional environment and diagenesis as controlling factors for petro-physical properties and weathering resistance of siliciclastic dimension stones: integrative case study on the 'Wesersandstein' (northern Germany, Middle Buntsandstein) 103

STROHMEYER, D. & SIEGESMUND, S. Anisotropic technical properties of building stones and their development due to fabric changes 115

SIEGESMUND, S., VOLLBRECHT, A. & HULKA, C. The anisotropy of itacolumite flexibility 137

WEISS, T., RASOLOFOSAON, P. N. J. & SIEGESMUND, S. Ultrasonic wave velocities as a diagnostic tool for the quality assessment of marble 149

MIDDENDORF, B. Physico-mechanical and microstructural characteristics of historic and restoration mortars based on gypsum: current knowledge and perspective 165

Biodeterioration

POHL, W. & SCHNEIDER, J. Impact of endolithic biofilms on carbonate rock surfaces 177

SCHIAVON, N. Biodeterioration of calcareous and granite building stones in urban environments 195

HOPPERT, M., BERKER, R., FLIES, C., KÄMPER, M., POHL, W., SCHNEIDER, J. & STRÖBEL, S. Biofilms and their extracellular environment on geomaterial: methods for investigation down to nanometer scale 207

Quality assessment and conservation of stones

FITZNER, B., HEINRICHS, K. & LA BOUCHARDIERE, D. Limestone weathering on historical monuments in Cairo, Egypt 217

ALVAREZ DE BUERGO, M. & FORT GONZÁLEZ, R. Characterizing the construction materials of a historic building and evaluating possible presevation treatments for restoration purposes 241

RUEDRICH, J., WEISS, T. & SIEGESMUND, S. Thermal behaviour of weathered and consolidated marbles 255

MATIAS, J. M. S. & ALVES, C. A. S. The influence of petrographic, architectural and environmental factors in decay patterns and durability of granite stones in Braga monuments (NW Portugal) 273

MICHALSKI, S., GÖTZE, J., SIEDEL, H., MAGNUS, M. & HEIMANN, R. B. Investigations into provenance and properties of ancient building sandstones of the Zittau/Görlitz region (Upper Lusatia, Eastern Saxony, Germay) 283

KOCH, A. & SIEGESMUND, S. Bowing of marble panels: on-site damage analysis from the Oeconomicum Building at Göttingen (Germany) 299

SAHLIN, T., STIGH, J. & SCHOUENBORG, B. Bending strength properties of untreated and impregnated igneous, sedimentary and metamorphic dimension stones of different thickness 315

Environmental conditions

LEFÈVRE, R. A. & AUSSET, P. Atmospheric pollution and building materials: stone and glass 329

SMITH, B. J., TURKINGTON, A. V., WARKE, P. A., BASHEER, P. A. M., MCALISTER, J. J., MENEELY, J. & CURRAN, J. M. Modelling the rapid retreat of building sandstones: a case study from a polluted maritime environment 347

TÖRÖK, Á. Oolitic limestone in a polluted atmospheric environment in Budapest: weathering phenomena and alterations in physical properties 363

FASSINA, V., FAVARO, M. & NACCARI, A. Principal decay patterns on Venetian monuments 381

CHAROLA, A. E. & WARE, R. Acid deposition and the deterioration of stone: a brief review of a broad topic 393

VILES, H. A. Implications of future climate change for stone deterioration 407

KLEMM, W. & SIEDEL, H. Evaluation of the origin of sulphate compounds in building stone by sulphur isotope ratio 419

SCHAFER, M. & STIEGER, M. A rapid method for the determination of cation exchange capacities of sandstones: preliminary data 431

Index 441

Preface

The safeguard of our cultural heritage in the modern world requires the application of many different theoretical, experimental and empirical resources provided by the geoscience, chemistry, material science, biology and construction engineering. The past decades have seen an unprecedented level of research activity in this area. Most of the results are published as extended abstracts in conference proceedings and are usually difficult to access, especially for the international community. As such, we have edited the present volume with the intention of providing an integrated approach to the study of the deterioration of geomaterials rather than to focus on individual facets of the discipline. The production of this volume was inspired by international workshops held in Göttingen (Germany), Strasbourg (France) and Prague (Czech Republic). The editors gratefully ackowledge B. Fitzner for the cover photos and the following colleagues for their reviews: G. Alessandrini, G. Ashall, S.A. Bortz, D. Boscence, P. Brimblecombe, F. J. Brosch, St. Brüggerhoff, B. Budelmann, L. Burlini, H. Burkhardt, D. Camuffo, J. Cassar, T. Le Champion, A. E. Charola, E. Doehne, A. Ehling, E. Evenson, V. Fassina, L. Fiora, B. Fitzner, R. Gaupp, S. Golubic, A. S. Goudie, G. Grassegger, W. D. Grimm, S. Grunert, P. Hackspacher, K. Heinrichs, K. Helming, M. Hoppert, J. Hoefs, W. Klemm, R. Koch, K. Kraus, L. Lazzarini, A. Jornet, J. Kulenkampff, K. Knorr, R. A. Lefèvre, U. Lindborg, R. Löfvendahl, P. Ludwig, K. Malaga, P. Marini, D. Meischner, P. W. Mirwald, D. Mottershead, H. Pape, G. Poli, T. Popp, M. Prasad, A. Putnis, A. Rohatsch, H. Ruppert, B. Sabbioni, H. Schaeben, J. Schneider, J. Schön, J. Schröder, H. Siedel, B. Silva, B. Smith, R. Snethlage, E. Stadlbauer, M. Steiger, A. Török, V. Vergès-Belmin, H. Viles, P. Warke, T. Warscheid, H.R. Wenk, E. Winkler, G. Wheeler, T. Yates, M. Young, A. Zang, F. Zezza.

Siegfried Siegesmund
Thomas Norbert Weiss
Axel Vollbrecht

This page intentionally left blank

Natural stone, weathering phenomena, conservation strategies and case studies: introduction

SIEGFRIED SIEGESMUND, THOMAS WEISS & AXEL VOLLBRECHT
Geowissenschaftliches Zentrum Göttingen, Strukturgeologie und Geodynamik, Universität Göttingen, Goldschmidtstr. 03, 37077 Göttingen, Germany

The weathering of historical buildings, as well as that of any monument or sculpture using natural stone (or man-made porous inorganic materials) is a problem identified since antiquity. Although much of the observed world-wide destruction of these monuments can be ascribed to war and vandalism, many other factors can contribute significantly to their deterioration. These threaten the preservation of the current inventory of historically, artistically or culturally valuable buildings and monuments. Furthermore, a drastic increase in deterioration has been observed on these structures during the past century. This prompted Winkler (1973) to make a pessimistic prediction, that at the end of the last millennium these structures would largely be destroyed because of predominantly anthropogenic environmental influences. Fortunately, this has proven not to be the case.

There is a general belief that natural building stones are durable, and not for nothing does the Bible refer to the Rock of Ages. However, all rocks will weather and eventually turn to dust. If rocks are cut and used in buildings, the chance of deterioration increases because other factors come into play. To understand the complex interaction that the stone in a building suffers with its near environment, (i.e., the building, and the macro environment, the local climate and atmospheric conditions), requires an interdisciplinary approach with the work of geologists, mineralogists, material scientists, physicists, chemists, biologists, architects and art historians.

Although most historical buildings use natural stone as the main construction material, other materials, such as mortars for masonry or rendering and ceramic roof tiles, to name a few, may interact as well with the building stones. These materials, if not chosen correctly can also be a source of eventual deterioration.

What characterizes natural stones, geomaterials, apart from the chemico-mineralogical composition and texture, is their very heterogeneous and anisotropic fabric. This originates from a varying, polyphase formation (e.g. crystallization from a melt, sedimentation, diagenesis, metamorphism and deformation) over long geological time periods, i.e. millions of years. The particular rock fabric determines the variability in the observed weathering and deterioration patterns and processes. To find an appropriate approach for reducing these deterioration processes, cutting-edge research is needed to elucidate the actual mechanisms. Knowledge of the properties of geomaterials, of their weathering processes and of subsequent material changes is a basic requirement to understand the complex mechanisms involved in producing the eventual deterioration.

All geomaterials at the Earth's surface, exposed as a natural outcrop or in a building, are subject to the destructive physical, chemical and biological aspects of weathering. Moreover, when they are part of a building, anthropogenic influences will increase significantly – after all the building is a result of that influence – affecting both material properties, for example thickness of the cut block will influence its mechanical resistance, and the weathering processes. These cannot be viewed as independent processes since complex interactions operate between them.

Physical weathering is caused specifically by freeze-thaw processes, salt weathering as well as hygric, thermal and wet-dry cycling. As a result of these processes, the stone undergoes a progressive fragmentation along preferred anisotropic surfaces, for example, intra- and intercrystalline microcracks, cleavage planes, twin lamellae and joints etc.

Chemical weathering can essentially be understood as resulting from the reactions that are induced on mineral constituents of the stone by water, carbon dioxide and oxygen from the air. This chemical disintegration largely takes place at the sub-microscopic level, and therefore exposed stone surfaces containing complex systems of pores, fracture surfaces and grain boundaries provide the surfaces where these chemical reactions can occur.

The most significant single environmental factor is the presence of moisture on and in the stone. Not only can water induce some chemical

From: SIEGESMUND, S., WEISS, T. & VOLLBRECHT, A. 2002. *Natural Stone, Weathering Phenomena, Conservation Strategies and Case Studies*. Geological Society, London, Special Publications, **205**, 1–7.
0305-8719/02/$15.00 © The Geological Society of London 2002.

reactions, but under thermal cycling it can cause physical damage through freeze-thaw, hygric cycling and controls salt crystallization when soluble salts are present. Furthermore, it is a necessary component for biological colonization. Microorganisms in turn will generate acids and chelating agents that can corrode and attack the minerals present in the stone.

Anthropogenic influences begin already during the quarrying process. Rocks are then subjected to the effects of the actual quarrying techniques as well as the resulting changes of environment. These can be very significant for the material properties and weathering processes that the stone will eventually show once it is included in the masonry. An anthropogenic influence will also affect changes in the environment by air pollution from industry or car exhausts. These, in general, acid pollutants were the main cause of some of the most dramatic deterioration observed during the mid-twentieth century and served to call world wide attention to the need for preservation of this stone-made cultural heritage.

Natural stone conservation in conjunction with restoration is an old theme. Already in Roman times the principle that regular stone or building maintenance is necessary was recognized, especially if long-term preservation of the building was desired. Also, traditional conservation measures were essentially based on protecting the building stones from water. For this purpose, either specific construction measures, such as coverings or canopies to prevent water from direct contact with the water were used, or sacrificial coatings or protective treatments were applied.

The protection of our architectural heritage has both cultural and historical importance, as well as a substantial economic and ecological value. Large sums of money are being spent world-wide on measures for the preservation of monuments and historical buildings. The economic and ecological commitment to the preservation of monuments and historical buildings requires, however, a prudent handling of the appropriate funds. This demands an optimization of damage analysis procedures and damage process controls as well as the development of monitoring and early warning systems for damage prevention. Therefore, the goal needs to be the implementation of permanent preservation measures, which requires long-term maintenance. This is ultimately controlled by the limited economic resources and the increased number of cultural assets that are recognized as of value to be preserved.

The process of uncontrolled building construction appears to be over – at least in the western world. The demands for resource protection on the already existing inventory of buildings leads to the situation where more and more architects have to deal with question of how to handle the older inventory of historic buildings and even monuments rather than design of new construction. Awareness of the importance of the safeguarding of our architectural heritage has increased significantly and it is hoped that it will lead eventually to a means of achieving a sustainable, long-term preservation.

The present volume combines review articles with reports on recent progress in our research field. The first section of papers is dedicated to weathering of natural building stones.

Weathering of natural building stones

Weathering is the natural way of stone decay into smaller particles. Weathering is a slow, continuous process that affects all substances exposed to the atmosphere, especially marble. As well as chemical weathering mechanical weathering causes stones to lose their strength. There are several causes of mechanical weathering. Changes in temperature and freeze thaw successions are some examples. Expansion and contraction in the stone texture is the result of variations in temperature. Frost action, as discussed by **Ondrasina, Kirchner & Siegesmund**, occurs when water enters tiny cracks in the stone and freezes at lower temperatures. When the ice expands it will weaken the stone fabric after a period of time. Much of our marble looks just as fresh today as on the day it was installed. In some areas, however, the marble has badly deteriorated. This deterioration occurs in areas where the marble is repeatedly wetted. The mechanism for these proceedings will be discussed in this paper.

But temperature changes are also important for other rock types. Alsatian monuments are built with two types of Buntsandstein sandstone (**Thomachot & Jeannette**). Their different pore structures cause them to have mixed petrophysical properties and occasion a different response to frost. To understand these differences, frost simulations where absorption/drying periods are not allowed, have been carried out. These experiments have demonstrated the importance of wetting/drying periods in changing the porous network, which can then lead to material damage. It seems that most of the damage, usually attributed to frost action, cannot be imputed to ice formation. Wetting–drying cycles accentuated by freezing, are probably the main cause of stone weathering.

The evident differences in weathering between the Soll and Franka stone types of the Globerigina Limestone Formation are related to the mineralogy, geochemistry and porosity of these building stones by **Cassar**. The weathering of the more marly rocks depends mainly on exposure to atmospheric conditions especially in the near-shore environment. The weathering process of Globigerina Limestone in general, and Franka in particular, has been explained as a sequence of steps, from formation of a thick and compact superficial crust, to the loss of this crust and to the initiation of alveolar weathering. No crust forms in the Soll type, and severe deterioration occurs here at an early stage in the weathering process.

Weathering processes

A special weathering factor is salt weathering, since it may be caused both naturally and anthropogenically. A literature review on the effects of salt weathering is provided by **Doehne**. Salts have long been known to damage porous materials, mainly through the production of physical stress resulting from the crystallisation of salts in pores. Salts can also damage stone through a range of other mechanisms, such as differential thermal expansion, osmotic swelling of clays, and enhanced wet/dry cycling due to deliquescent salts. The review combines views from geomorphology, environmental science, geotechnical and material science, geochemistry and conservation.

The magnitude and dynamics of thermally induced weathering are addressed in the paper by **Zeisig, Siegesmund & Weiss**. They give a unique compilation of thermal degradation in marble. Different types of commercially used marbles composed of calcite and/or dolomite are investigated by thermal expansion measurements. The marbles do not only vary in composition but also in texture, grain shape and grain size. Special emphasis is placed on the magnitude and directional dependence of thermal degradation and its correlation with fabric observations. The basic outcome is that all fabric parameters have to be considered for the assessment and understanding of the proneness to weathering of a marble.

The current condition of many building facades and historical monuments clearly reveals that they are not immune to the impact of weathering and associated deterioration. The effect of thermal stress on porosity change for two types of marble has been investigated by **Malaga-Starzec, Lindqvist and Schouenbourg**. The results indicate that inter-granular decohesion starts already between 40°C and 50°C. This temperature is easily reached on building surfaces in most European countries during summer time. Damage diagnosis of natural stone based on investigations of porosity changes could diminish not only aesthetical but also economical problems.

The assessment of the intensity of rock degradation is one of the most important aims for preservation and conservation purposes. Ultrasonic wave velocities are frequently used for a non-destructive diagnosis of marble deterioration. The paper by **Weiss, Rasolofosaon & Siegesmund** gives a quantitative determination of the reduction of ultrasonic wave velocities as a function of pre-existing and thermally induced microcracks with special emphasis on anisotropy. Thermally induced microcracks lower ultrasonic wave velocities significantly and a correlation with the microfabric of marble is evident. Thus, ultrasonic wave velocities have been proven to be an efficient tool for the non-destructive determination of marble degradation.

Fabric dependence of physical properties

Rock fabric determines significantly the properties of different building stones. A new integrative approach presented by **Weber & Lepper** deals with the complex interrelations between the geological background on the one hand and specific dimension stone properties on the other hand: Weathering resistance and petrophysical properties of siliciclastic dimension stones are governed by depositional environment (type of fluvial architecture) and diagenesis (quartz cement and clay matrix contents). This is evidenced by two contrary examples of historical exterior use (former monastery churches). For the actual use of siliciclastic dimension stones, these relevant aspects should be considered.

This approach is valid for sedimentary rocks, while comparable correlations can be observed for metamorphic rocks. Every natural building stone represents an anisotropic and heterogeneous system. Degree and type of a fabric anisotropy may vary and are characterized by grain shape preferred orientations, microcrack systems and preferred orientations of the rock-forming minerals (here referred to as texture). The fabric dependence of mechanical rock properties like compressive, tensile and abrasive strength and their development due to an increasing mylonitic deformation is discussed by **Strohmeyer & Siegesmund**. With regard to mica bearing rocks as investigated in this study

the mica texture is the most prominent factor influencing the mechanical behaviour.

Particular fabric properties may even lead to very unconventional material properties. Itacolumites are very special rocks due to their high flexibility. The flexibility is mainly related to a penetrative network of open grain boundaries that enable a limited body rotation of individual quartz grains (**Siegesmund, Vollbrecht & Hulka**). Continuous layers of white mica display deformation features indicative of shear along its layer-parallel cleavage planes. As demonstrated by simple bending experiments, flexibility is a highly anisotropic phenomenon. Solution along grain boundaries, volumetric strain by thermal contraction of quartz and bulk extension are processes discussed for the origin of the extreme values of secondary grain boundary porosity.

Computer simulations may help to understand observations and the processes behind them. Natural building stones like marbles are in general heterogeneous and anisotropic materials. Up to now there has been a lack of knowledge on the effect of different fabric and material properties on marble degradation. Thus, an alternative approach to simulate and understand marble weathering is presented in the paper of **Weiss, Siegesmund & Fuller**. A finite element analysis of marble degradation reveals that besides different single crystal properties of calcite and dolomite, the main rock forming minerals in marble, the texture has an important effect on marble weathering. Since identical microstructures are used for the modelling, the effect of single crystal properties and the texture could be quantified. Scattering in the stress distributions, finally leading to microcracking, due to different textures is larger than the difference between calcite and dolomite marbles without textural changes.

Not only the rock itself but connecting materials may be the source of deterioration or places subjected to degradation. The use of calcium sulphate based mortars has a very long tradition and was used at the Pyramid of Cheops, Towers of Jericho as well as on sacred buildings in Germany. **Middendorf** discusses the difficulties for restoration and conservation of those historic buildings since the information about composition including the admixtures and additives used are missing. He presents results on studies of historic calcium sulphate based mortars which will form the basis to develop mortars for restoration purposes. His focus is on the improvement of the water resistance of calcium sulphate based restoration mortars. The increase of water resistance can be achieved by chemical additives or hydraulic and/or latent hydraulic admixtures.

Biodeterioration

A number of different papers address biodeterioration. This effect is ubiquitous and widely not considered in past times. The colonisation by endolithic microorganisms such as cyanobacteria, chlorophycaceae, fungi and lichens on natural carbonate rock surfaces as well as carbonate building stones is discussed by **Pohl & Schneider**. Under a residual and protective carbonate rock layer (150 to 300μm beneath the surface) photobiontic microorganisms occupy more then 60% of the dissolved rock volume. Deeper beneath the substrate an initially dense, then progressively diminishing hyphal network of mycobionts develops. On natural carbonate rock surfaces no grain loss or exfoliation was observed as is often found on silicate rocks. After an initial material loss underneath the carbonate surfaces, a more protective rather than destructive impact of endolithic biofilms on carbonate rock substrates is suggested.

The importance of biodeterioration for granitic and calcareous building stones is outlined in the paper by **Schiavon**. He concludes that the combined effect of physical degradation by lichen hyphae, penetrating in a rock, and chemical attack by organic acid with associated growth of inorganic salts leads to accelerated weathering. Different types of weathering patinas are observed which are clearly associated with fungal and bacterial activities. They lead to extensive corrosion and dissolution of mineral surfaces beneath them. As it is the case with soiling patinas from air pollution, the biological patinas observed by **Schiavon** never form a protective layer on the stone surface and, thus, their careful removal is always suggested.

Basically all types of building material are colonizable by microorganisms. Often, surfaces are covered with a rigid layer composed of microbial cells and extracellular biopolymers (biofilm). Biodeterioration of building material is determined by the metabolic activities of the cells as well as the impact of the extracellular biopolymers. In order to elucidate the mechanisms of biodeterioration, preparation techniques have been designed by **Hoppert, Kämper, Pohl, Flies, Berker, Ströbel & Schneider** to preserve the cellular and extracellular structures of the biofilm down to the micrometer scale.

Quality assessment and conservation of stones

Systematic descriptions of damage szenarios and their quantification are required to assess the degree of degradation on a monument. Phenomenological observations may, therefore, be combined with laboratory analyses. Studies on weathering of building stones were carried out by **Fitzner, Heinrichs & La Bouchardiere** comprising laboratory analysis and in situ investigations, the latter including detailed survey of weathering forms, registration and evaluation of weathering forms by means of monument mapping and in situ measurements. For historical monuments made from limestones in the centre of Cairo the weathering forms, weathering products and weathering profiles show a clear correlation between the damage and salt loading of the limestones as a consequence of air pollution and rising humidity. The deterioration characteristics of many historical stone monuments in Cairo is alarming and needs a control like rising humidity, desalination, cleaning, stone repair, fixation or consolidation of loose stone material, structural reinforcements and stone replacement.

Comprehensive knowledge about the situation on-site is indispensable for an appropriate conservation strategy. Before attempting any restoration project on monuments and historic buildings, characterization of the stone must be carried out, and the causes of stone deterioration need to be established in order to eliminate or mitigate them effectively. The assessment of the efficiency and durability of some preservation treatments with water-repellent effects is discussed by **Alvarez de Buergo & Fort** on the basis of a two-year project carried out at the Palace of Nuevo Baztán, a state-designated historic monument built in the early eighteenth century in Madrid, Central Spain, whose façades are mainly built in limestone. Two siloxane-based products were ultimately determined to be the most effective on the basis of chromatic variables, water vapour permeability, water-stone contact angle, SEM observations and durability (artificial ageing tests).

Due to the frequent utilization of marble as a building and monumental stone, its conservation and preservation is an important challenge in the saving of our cultural heritage. The change of thermoelastic behaviour of marble upon consolidation is discussed by **Ruedrich, Weiss & Siegesmund**. Based on the comparison of weathered and consolidated marbles, the influence of the rock fabric and the stone consolidant on thermal weathering of marbles is considered. For the directional dependence and intensity of marble weathering, the texture, the grain boundary geometry and the preferred grain boundary orientation are of crucial importance. The different properties of consolidants, like their adhesion properties and their glass transition temperatures significantly affect the thermoelastic behaviour of marbles.

Stone decay processes are controlled by multiple factors inherent to the rocks (and their natural heterogeneity and variability) and related to the surrounding environment. The theoretical and laboratory modelling of these processes is hindered by the complex interactions between these diverse factors. **Matias & Alves** try to cast light in these relationships and the influence of diverse factors by the study of decay patterns (established from detailed observation of stone decay features and their distribution) in thirty-nine monuments built with granitic stones.

Extensive conservation and reconstruction effort of historical buildings and cultural monuments has led to an increasing demand for detailed information on the ancient stone material. Knowledge about provenance and technical properties of building material is required to evaluate weathering processes and successfully preserve and reconstruct historical buildings. The results of a case study on ancient building sandstones from the Görlitz/Zittau area in Eastern Germany by **Michalsky, Götze, Siedel & Heimann** show that it is possible to assign unequivocally historically used material to specific sandstone occurrences. A combination of macroscopic rock description, thin section and CL microscopy coupled with image analysis, scanning electron microscopy, and analysis of technical parameters (e.g., Hg porosimetry, total water uptake) is very useful for this purpose.

Particular emphasis may be placed also on recent architecture and its problems. The use of natural stone panels or cladding material for building facades has led to some durability problems, especially with marble slabs. The most spectacular phenomenon is the bowing of marble panels. The influence of intrinsic and extrinsic parameters is discussed by **Koch & Siegesmund** on the basis of a detailed study performed on the Oeconomicum Building at the University of Goettingen. Particularly, rock fabric is detected as a key parameter contributing to the deterioration of marble and the final degree of bowing. Rock fabric controls the mechanical and physical properties such as porosity, permeability, Young's modulus and thermal expansion.

Mechanical properties are important when using rocks as building materials. **Sahlin, Stigh & Schouenbourg** discuss the bending strength properties of eight different rock types. Conventional dimension stone tiles are normally untreated and at least 10 mm thick. However, a production method has been developed that makes it possible to produce dimension stone tiles only 4 mm thick without high amounts of waste material. The tiles are impregnated with a mixture of potassium-based waterglass, water, colloidal silica, and Berol 048 (non-ionic surfactant), using a repeated cycling between vacuum and atmospheric pressure.

Environmental conditions

A number of papers address the importance of the environment for stone alteration. Study of the decay of stone and glass by atmospheric pollution carried out by LISA in Europe since the early 1980s is reviewed by **Lefèvre & Ausset**. The authors make a nice explanation of two different types of gypsum development, i.e., above and below the surface. The quantification of the effects of atmospheric pollution on stone raises the question, whether the SO_2 contents in stone can be directly related to quantifiable damage rates. A significant advance particularly in theory regarding the modelling of alteration of building materials is presented based on the UN-ECE-ICP "Materials" study and an attempt made to map SO_2 and potential damage.

The decay dynamics of sandstones in a polluted maritime environment was investigated by **Smith, Turkington, Warke, Basheer, McAlister, Meneely & Curran**. Visible decay is triggered by the delamination of surface layers associated with the near-surface accumulation of chloride and sulphate salts, particularly gypsum. These simulation studies show that after the initial state of weathering the continuous salt weathering and rapid loss of surface material are of critical importance to understand the subsequent decay pathway and control the conservation strategies.

The continental climate and severe air pollution causes major damage to 'sensitive' stones such as limestones. In a study of buildings in Budapest **Török** has demonstrated that the interaction of atmospheric pollutants and oolitic limestone leads to the formation of weathering crusts. A range of black and white crusts are described including their mineralogical composition and physical properties. The increased values of surface strength and decreased water absorption are described in detail with models of crust formation. The rate of crust strengthening and mineralization is controlled by wind/rain exposure and pollution concentration.

The mechanisms of gypsum formation and accumulation on Venetian monuments are reported by **Fassina, Favaro & Naccari**. The different forms of decay (white washing, dirt accumulation and dirt wetting) were used for a simplified model controlled by the degree in sulphation. The most extensive sulphate formation occurs in the black dendrite-shaped crust restricted to the interface between the white washing areas and the sheltered ones. Gypsum formation strongly depends on the mineralogical composition and the rock fabric. In compact limestones gypsum appears only at the surface while in marbles these effects are more penetrative.

An important point in the elucidation of deterioration mechanisms is the correlation between the deterioration factor dose and the resulting damage. The role of acid deposition in the deterioration of stone is discussed in the overview by **Charola & Ware**. Specifically, dry and wet deposition are considered along with their resulting deterioration mechanisms. Key factors in this process are dry deposition of gaseous pollutants, the nature of the stone, including structure and porosity, and the presence of surface moisture as moderated by time of wetness.

The global climate has, over geological time, experienced great change over a range of time span. The implication of future climate changes for stone deterioration over the next 100 years is discussed by **Viles**. Based on a range of scenarios of future emissions of greenhouse gases, and on a range of climatic models the global average temperature and sea level are projected to rise over the twenty-first century. The complex interaction of chemical, physical and biological weathering processes on stone decay may change for example in Mid-Europe due to much more warmer and wetter winters and warmer and drier summers.

The formation of sulphate salts caused by direct attack of polluted air and rain water on the stone surface is a main factor for its deterioration in monuments. In some cases the sources of sulphur could be more complex involving building material or ground water, soil etc. **Klemm & Siedel** demonstrate the use of the sulphur isotope ratio in sulphate salts as a fingerprint to evaluate the influence of potential sulphur sources. The dominant role of anthropogenic factors was found as well as the locally differing situation in an industrial region of Central Europe.

The cation exchange capacities of sandstones

(CEC) have been studied by **Schäfer & Steiger**. Clay minerals occuring as very small particles in sandstones are the most likely single contributor to the cation exchange capacities. For weathered sandstones significantly different cation exchange capacities were observed along profiles close to the exposed surface. Even after a relatively short exposure time in a heavily polluted atmosphere the CEC in the weathering zone is only about half of the value compared with the unweathered ones.

We gratefully acknowledge constructive comments on the final version by H. Viles and A.E. Charola.

References

WINKLER, E. M. 1973. *Stone: Properties, Durability in Man's Environment*. Springer, New York.

This page intentionally left blank

Freeze–thaw cycles and their influence on marble deterioration: a long-term experiment

JOSEF ONDRASINA[1], DIRK KIRCHNER[2] & SIEGFRIED SIEGESMUND[1]
[1]*Göttinger Zentrum Geowissenschaften, Goldschmidtstrasse 3, 37077 Göttingen, Germany (e-mail: ssieges@gwdg.de)*
[2]*Deutsches Bergbau-Museum, Herner Strasse 45, 44787 Bochum, Germany*

Abstract: The deterioration of three marbles (Palissandro, Sterzing and Carrara) differing in composition and rock fabric has been studied using measurements of the thermal dilatation in the temperature range from –40°C up to 60°C. A long-term freeze–thaw experiment was performed to characterize the frost weathering via Young's modulus. The results show that the combined effect of heating and cooling under dry and water-saturated conditions significantly influences the material properties. The thermal dilatation and its anisotropy can be explained by the crystallographic preferred orientation of calcite and dolomite as well as with the thermal expansion behaviour of these minerals. The residual strain, i.e. the permanent length change, after thermal treatment is different for the investigated samples and less pronounced for the dolomitic marble from Palissandro. The hygric expansion is of only minor importance and weak in the phlogopite-bearing Palissandro sample within the direction parallel to the foliation.

Fresh and artificially weathered marbles were exposed to 204 freeze–thaw cycles. The Young's modulus for the Carrara marble decreases from 55 GPa to 28 GPa while the porosity increases from 0.25% to 0.62%. The effect on the Palissandro and the calcitic Sterzing marbles is less pronounced while the artificially weathered ones clearly exhibit a drastic reduction in Young's modulus.

The progressive loss in strength is caused by progressive microfracturing or the loss of cohesion along grain boundaries due to the crystallization pressure of ice growth. The experimental data along with existing theoretical models lead to the conclusion that the physical weathering of marble is influenced by cooling and heating under mid-European climatic conditions.

Marble is a very unique material. It was used throughout history as an ornamental stone and is still being used in the same fashion today. Without exaggeration, a large part of the cultural heritage of humanity has been influenced by the use of marble as a material for artistic endeavors and major construction purposes. The weathering phenomena of marble as well as for other building stones are poorly understood and are still under discussion. The chemical weathering of marbles by superficial dissolution is a simple process when considering the attacks of acid rain or biofilms (for example Grimm 1999). More recently, the effects of cracking by internal stresses, thermal cracking and moisture expansion are being debated in the literature (e.g. Winkler 1997). The combined action of the physical weathering processes often discussed as the initial deterioration of crystalline marbles may be controlled by wetting and drying, insolation, salt crystallization, thermal expansion, frost cracking, etc. The thermal expansion by heating–cooling cycles between 20°C and 80°C (see Sage 1988; Widhalm *et al.* 1996; Siegesmund *et al.* 2000) shows that a limited number of temperature changes lead to a residual strain, i.e. a permanent length change. Frost cracking occurs when water freezes due to a 9% volume expansion. Powers & Helmuth (1953) discussed the growth of segregation ice with water migrating to freezing centres as the control for frost damage. Such crystallizations in porous rocks are of considerable interest in a wide variety of geological environments and are basic to the understanding of near-surface fluid–rock interaction. In contrast, salt crystallization in building stones is well known to cause damage due to the force of crystallization associated with growing crystals. Surprisingly, the effect of frost-induced degradation of marbles is widely overlooked. The amount of freeze–thaw cycles in Germany may differ between six and around 80 per year depending on environmental conditions, exposure and the building physics (see discussion in Grimm 1999).

In this paper we explore the combined action of heating–cooling cycles on marbles. Different marbles were selected to investigate the thermal

From: SIEGESMUND, S., WEISS, T. & VOLLBRECHT, A. 2002. *Natural Stone, Weathering Phenomena, Conservation Strategies and Case Studies*. Geological Society, London, Special Publications, **205**, 9–18.
0305-8719/02/$15.00 © The Geological Society of London 2002.

expansion in the temperature range from –40°C up to 60°C in order to get an estimate on the residual strain under dry and water-saturated conditions. Moreover, the same marble types and their artificially weathered equivalents were exposed to 204 freeze–thaw cycles. To quantify the amount of deterioration the Young's moduli were measured after every fifth cycle. The rock physical properties were also combined with the mineralogical and fabric data to improve their directional dependence.

Methods of investigation

For the petrophysical investigations of each sample thin sections were cut and prepared from homogeneous blocks with respect to the visible macroscopic fabric elements (foliation and lineation). The reference system is illustrated in Figure 1. The mineral composition was determined by using the X-ray diffraction method. The lattice preferred orientation (i.e. texture) was determined by neutron diffraction measurements (Ullemeyer *et al.* 1998; Siegesmund *et al.* 1994; Brockmeyer 1994). The most significant advantage of neutrons compared with X-rays is their low absorption in matter, i.e. the method allows the analysis of relatively large sample volumes, specifically the analysis of coarse-grained specimens (for details see Siegesmund *et al.* 2000).

Different kinds of petrophysical measurements were carried out. To quantify the total porosity, the buoyancy weighting method was used. The thermal expansion measurements were performed by using a dilatometer (type DIL 801S). The sample size corresponds to a prism of 15 mm diameter and 50 mm length. Calibration of the dilatometer was done using borosilicate glass and the final displacement was better than 1 μm. In order to simulate temperature changes comparable to those expected under natural conditions, temperature ranges between –40°C and 60°C with a heating rate of 1°C/min were used. A computer-controlled feed of liquid nitrogen was used to cool the samples. This experimental setup, furthermore, leads to an improved method for ascertaining the effects of water-saturated and dry conditions on freeze–thaw cycles. Additionally, the hygric expansion for all samples was measured at room temperature.

The long-term freeze–thaw cycle has been carried out according to DIN 52104 standard. The characterization of the weathering by freeze–thaw cycles on the marble samples was enhanced by the Young's modulus. The modulus of elasticity or Young's modulus (E) is based on the relationship between stress and strain, i.e. expressed as the ratio of the stress to rate of strain (statistically measured Young's modulus). However, it is also possible to determine Young's modulus non-destructively by using dynamic measurements of the ultrasonic wave velocities. The dynamic modulus is based on the determination of the compressional (Vp) and shear wave velocities as well as the densities. In the laboratory we measured the rod waves, which requires a fixed geometry of the samples. This experimental approach correlates with a one-dimensional state of stress.

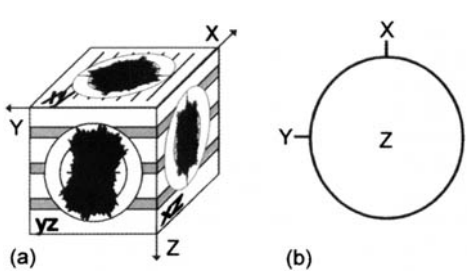

Fig. 1. Reference system of sample orientation. (**a**) Schematic cube with foliation (XY-plane) and lineation (X-direction) with a given grain boundary orientation illustrating a shape fabric, and (**b**) projection of the X-, Y- and Z-axis of the sample cube in the Schmidt net, lower hemisphere.

Results

Microfabrics of the samples

The investigated marbles from Palissandro (P1), Sterzing (ST) and Carrara (C2) show complex fabric elements. They differ in composition and grain size. Palissandro is a dolomitic marble which is composed of dolomite, calcite, phlogopite and minor quartz. The pronounced foliation and lineation are macroscopically visible by the compositional banding, formed by the light and dark brownish layers ranging in thickness up to 6 mm. More rarely, elongated, lens-shaped quartz aggregates of 1–2 mm thickness can be observed within the foliation. The lineation is represented by elongated dolomite grains. The average grain size of this fine-grained marble is about 120 μm. In the XZ- and YZ-section the dolomite is characterized by a marked grain-flattening shape fabric (Fig. 2 P1 and Fig. 3) with all signs of intracrystalline deformations, i.e. undulose extinction, twins and subgrain formation. Grain boundary migration has caused some coalescence into even longer grains. In some more coarse-grained domains a weakly

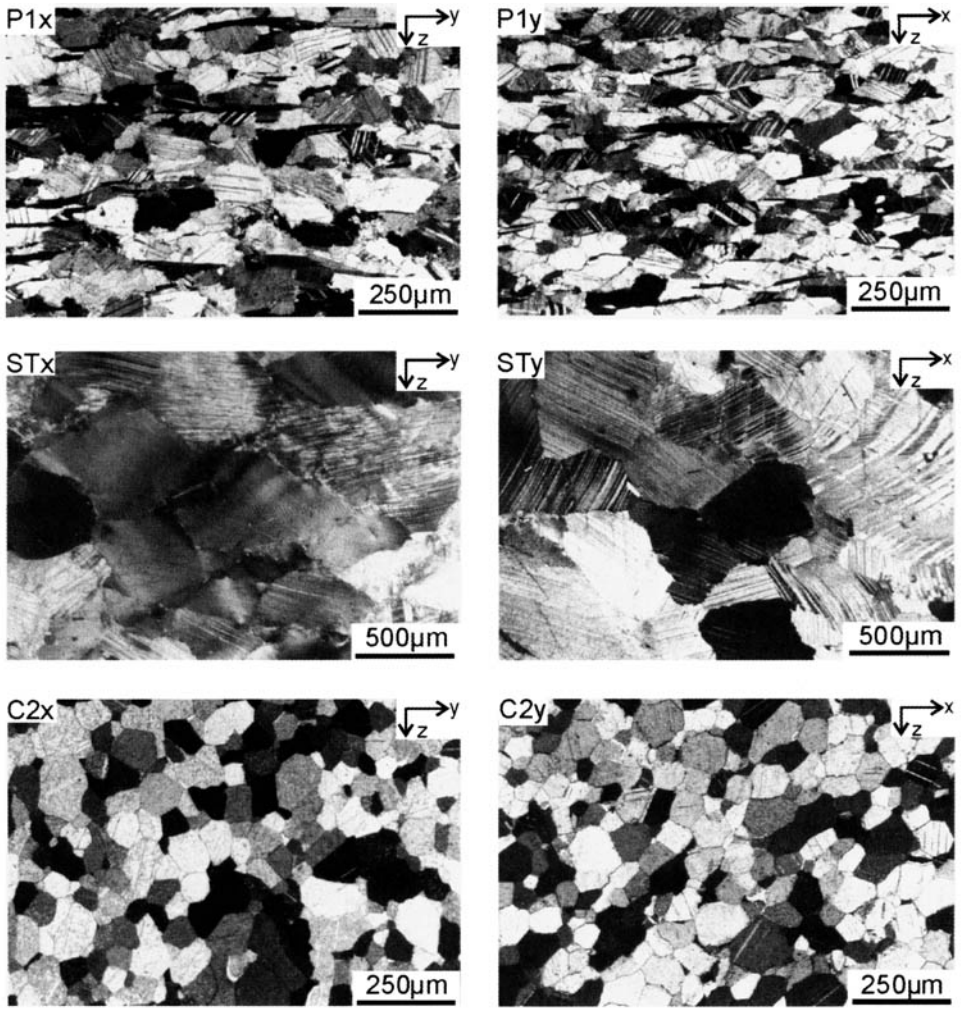

Fig. 2. Photomicrographs of the investigated marbles Palissandro (P1), Sterzing (ST) and Carrara (C2). The photomicrographs are obtained from two sections parallel to the YZ-plane (X-direction) and parallel to the XZ-plane (Y-direction).

developed core and mantle structure is observed. The aspect ratio of the phlogopite reaches up to 20:1. Intracrystalline deformation microstructures such as bending and kinking are also observed.

The Sterzing marble is calcitic in composition with a lesser amount of dolomite and muscovite, light grey and weakly foliated (Fig. 2 ST and Fig. 3). The grain size is up to 2.5 mm with an average of about 1.1 mm. Twinning is more frequent and the grains show undulose extinction, deformation bands, bent twin lamellae and seldom subgrain formation. The grain boundaries are irregular, forming an inequigranular–interlobate structure.

The Carrara sample C2 is white, fine-grained and contains very thin greyish veins which are folded. Planar fabrics like a metamorphic banding or foliation are difficult to discern. The average grain size is around 140 μm. The grain boundaries are straight and regular. Twins and open cleavage planes can be observed (Fig. 2 C2 and Fig. 3).

Texture

Based on the neutron texture measurements a quantitative texture analysis was carried out by means of the iterative series expansion method

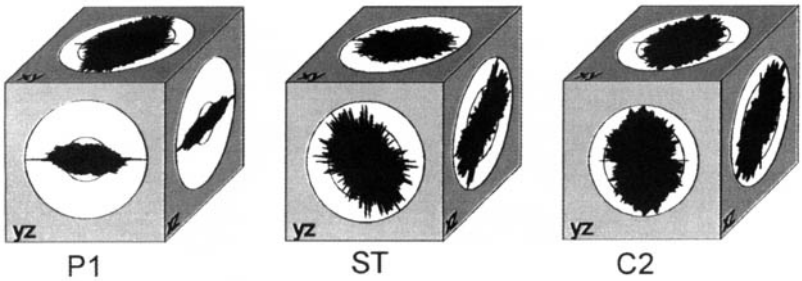

Fig. 3. Shape preferred orientation given as the grain boundary orientation with respect to the sample coordinates parallel to the XZ-, YZ- and XY-plane.

(Dahms & Bunge 1988). In this method, the texture is completely described by the coefficients C of spherical harmonical functions. The main advantage is that from this information all pole figures of any lattice direction can be calculated by simple geometrical operations. The (001) pole figures for calcite (C2, ST) and dolomite (P1) show a large variation in the orientation pattern, intensity distribution and with respect to the reference coordinate system. The c-axis pole figure in P1 exhibits an intensity maximum subparallel to Z (normal to the foliation) with a weakly elongated density distribution within the XZ-plane (Fig. 4). In dolomite crystallography, the (110) poles are arranged on a great circle around the (001) pole density maximum, i.e. along the primitive circle (XY-plane). The Sterzing marble is indicated by a moderate girdle-like shape of the intensity distribution weakly asymmetric to the XZ-plane (Fig. 4). The highest intensity can be observed approximately parallel to the Z-direction. The a-axes are arranged along the primitive circle with a maximum concentration subparallel to Y and a minimum within X. C2 shows a much weaker lattice preferred orientation with a broader elongated maximum distribution around 30° off to the X-direction. Consequently, the a-axis distribution is also arranged along a broad great circle (Fig. 4f).

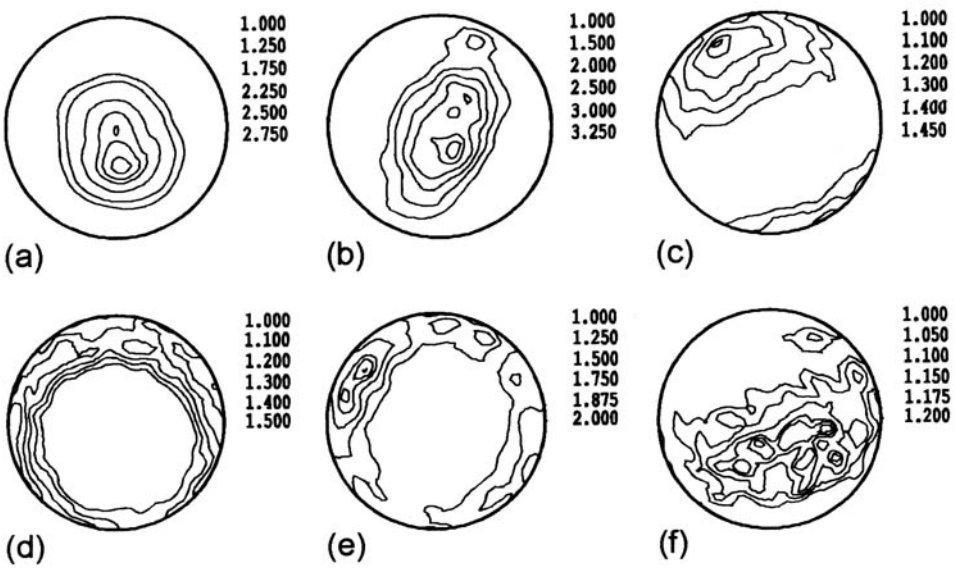

Fig. 4. Calcite and dolomite texture of the investigated Palissandro marble (**a**, **d**), Sterzing marble (**b**, **e**) and Carrara marble (**c**, **f**). Pole figures are given for the c-axes (a, b, c) and a-axes (d, e, f) (lower hemisphere, stereographic projections).

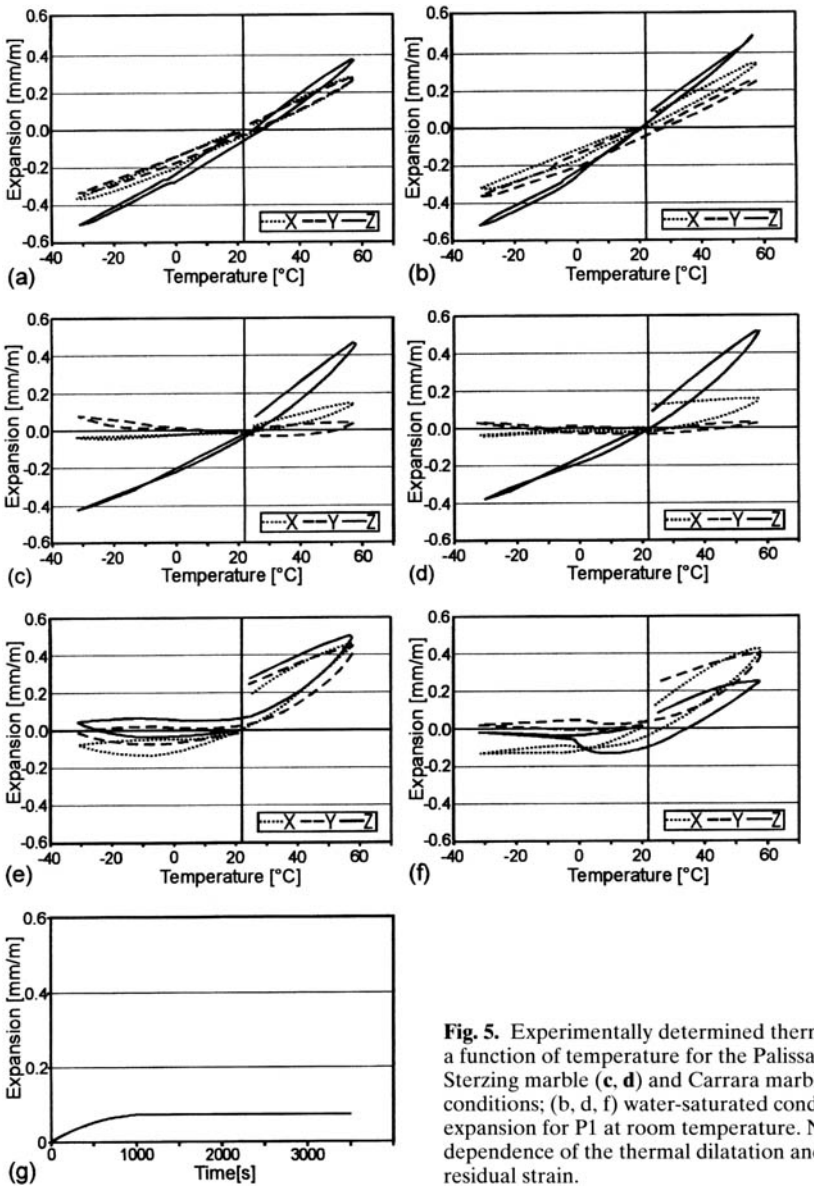

Fig. 5. Experimentally determined thermal dilatation (a–f) as a function of temperature for the Palissandro marble (**a**, **b**, **g**), Sterzing marble (**c**, **d**) and Carrara marble (**e**, **f**): (a, c, e) dry conditions; (b, d, f) water-saturated conditions; (g) hygric expansion for P1 at room temperature. Note the directional dependence of the thermal dilatation and the amount of residual strain.

Thermal expansion as a function of temperature

The thermal expansion (millimetres/metre) expresses the relative length change of a polycrystalline sample (Grüneisen 1926). The connection to the temperature is non-linear, i.e. the thermal expansion coefficient α which describes the specific length change ($10^{-6}K^{-1}$) depends on the considered temperature interval. For the investigated samples the thermal dilatation experiments were carried out in the temperature range between –40°C and 60°C. The cooling as well as the heating rate was 1°C/min. Figure 5 illustrates the effect of cooling and heating on the thermal expansion and its directional dependence. The Palissandro marble (Fig. 5a) contracts while cooling and shows a pronounced expansion when heating up to 60°C. The Y- and X-direction exhibits a comparable behaviour as a function of temperature. A slightly higher influence of the temperature is

observed along the Z-direction, i.e. perpendicular to the macroscopic foliation. However, in all cases a residual strain or a permanent length change is more or less lacking. The same experimental run was also done under water-saturated conditions (Fig. 5b). Compared to the dry conditions the contraction and expansion behaviour with temperature is more pronounced as well as its directional dependence. Additionally, the hygric expansion under room temperature was measured. Among all samples only P1 shows a significant length change within the Z-direction (Fig. 5g).

The Sterzing marble (Fig. 5c) shows a different behaviour. Again the Z-direction is most sensitive to cooling and heating. The Y-direction shows an expansion up to –35°C and contracts under temperatures above 0°C, while parallel to X the length change during cooling is more or less zero. In contrast to P1 a residual strain is observed along the X- and Z-direction. The water-saturated data are more or less comparable with the findings under dry conditions, although the directional dependence and the residual strain are much higher (Fig. 5d).

The Carrara marble (C2) exhibits a very weak length change while cooling (Fig. 5e). Only in the Z-direction does it expand at lower temperature, whereas the effect of cooling is less important although a small residual strain after cooling is evident. At the heating cycle up to 60°C a weak directional dependence of the thermal expansion can be recognized. More important is the observation that after cooling to room temperature the residual strain is also anisotropic and up to 0.3 mm/m at maximum. The material properties at water-saturated conditions are given only for the Z-direction. From Figure 5f it can be observed that the length changes with decreasing temperature are quite different for dry and water-saturated conditions. After cooling below 0°C a residual strain is noticed, while the permanent length change is significantly different after heating.

Long-term freeze–thaw cycles

The effect of frost action on stone deterioration is well known since Kieslinger (1930). In order to constrain the effect of freezing water a long-term study was established. The prismatic samples (40 mm × 40 mm × 160 mm) were deposited in a climate chamber for at least 6 hours at –20°C. After each cooling the samples were stored for 2 hours in a water bath at a constant temperature of 20°C. In total, 204 cycles were carried out within a 14 month period. In addition to the fresh marble samples a second set of the same marble type was artificially weathered in such a way that the samples were heated up to 200°C with a heating rate of 1°C/min. Afterwards they cooled down to room temperature very slowly. To characterize the state of deterioration the Young's modulus or the ultrasound wave velocities were measured. In order to constrain quantitatively the influence of freezing and thawing on the marbles the Young's modulus was measured after each fifth cycle. The basic assumption for the assessment of the state of deterioration of a building stone on the basis of ultrasonic measurements is that a decrease in the velocity is correlated with a certain stage of deterioration, i.e. a loss in strength.

The effect of weathering by freeze–thaw cycles on the Carrara, Sterzing and Palissandro marbles is shown in Figure 6. A pronounced difference is observable between the fresh and artificially weathered marbles. The highest decrease of the Young's modulus from fresh to the artificially weathered ones can be observed for C2, where the value changes from 55 GPa (Vp = 4.9 km/s) to less than 10 GPa (Vp = 1.8 km/s), while for P1 the reduction is less pronounced (Vp changes from 6.6 km/s to 5.8 km/s). After five to seven cycles a first remarkable loss occurs in the Young's modulus (see Fig. 6). Furthermore, a second pronounced decrease in the Young's modulus of around 5–10 GPa is seen after 100–115 cycles especially for the fresh samples. The Young's modulus decreases continuously during the experimental run and is at a maximum for C2 where a reduction in strength of up to 50% must be recognized. The increase of the Young's modulus for the artificially weathered C2 sample is due to the water content in the pore spaces since water has a higher velocity compared to air.

Discussion and conclusion

The effects of weathering on marble range from a superficial disintegration to a complete loss of cohesion along grain boundaries due to dilatancy, i.e. the total decay of the material. The thermal expansion coefficient α expresses the volume change of a material as a function of temperature. The anisotropy of the thermal expansion coefficient α of calcite and dolomite is characterized by axial symmetry with the symmetry axis parallel to the crystallographic c-axis. The single crystal data published by Kleber (1983) for calcite are extremely anisotropic: $\alpha_{11} = 26 \times 10^{-6}K^{-1}$ parallel and $\alpha_{22} = \alpha_{33} = -6 \times 10^{-6}K^{-1}$ perpendicular to the crystallographic c-axis, while dolomite shows values of $\alpha_{11} = 25.8 \times 10^{-6}K^{-1}$ parallel and $\alpha_{22} = \alpha_{33} = 6.2 \times 10^{-6}K^{-1}$

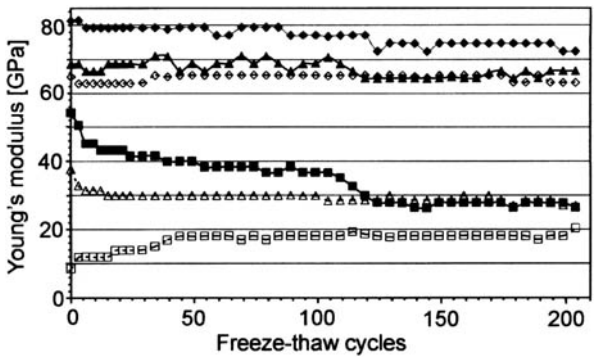

Fig. 6. The Young's modulus of P1 (rhombohedrons), ST (triangles) and C2 (squares) as a function of 204 freeze–thaw cycles. The filled symbols represent the fresh marbles, whereas the open symbols represent the artificially weathered equivalents.

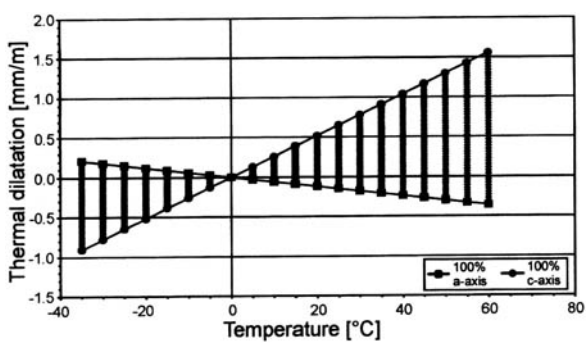

Fig. 7. The thermal dilatation versus temperature for the calcite single crystal given for the range between –35°C and 60°C, assuming a linear relationship). Note the change of contraction and expansion of the c-axes and a-axes during cooling and heating.

perpendicular to the c-axis (Markgraf & Reeder 1985). Consequently, when cooled, calcite crystals contract along the c-axis, but expand along the a-axes while the opposite behaviour occurs when heated. These relationships are illustrated in Figure 7 assuming a linear relationship. The effects are less dominant for dolomite.

For the samples P1, C1 and ST the thermal properties are quite different (Fig. 5). The directional dependence of each sample has to be discussed with respect to the lattice preferred orientation. The thermal expansion for a monomineralic rock has to be between an isotropic situation (random orientation of all crystals), and a situation of maximum anisotropy where all crystals have the same crystallographic orientation which corresponds to the single crystal anisotropy (see Fig. 7). All the possible anisotropies are between these two end members and are controlled by the texture. To explain this relationship in more detail Figures 4, 5 and 7 must be combined. The Sterzing marble contracts parallel to the Z-direction and expands along the Y, while X is of intermediate nature in the temperature range from room temperature down to –35°C. These effects can be easily explained if we recall that parallel to Z a maximum concentration of the c-axes can be observed which is the direction of maximum expansion in the single crystal. Consequently, the largest length changes occur parallel to Z, i.e. contraction from 0°C down to –35°C and expansion above 0°C. In contrast, along Y an opposite material behaviour is observed. Subparallel to Y lies the maximum intensity of the a-axis maximum corresponding to the minimum dilatation of the single crystal. Therefore, an expansion along the Y-direction must occur below 0°C and a contraction in the temperature range above zero. This behaviour is strongly dependent on the texture strength. The thermal expansion versus temperature relationship for C2 and P1 is comparable and should not be explained in detail.

In summary, the experimental results presented in this paper fit the observations reported in the literature. For example, Sage (1988) documented, for thermal expansion by heating–cooling between 20°C and 80°C, that often after a limited number of temperature changes the residual strain will be more or less constant. The highest residual strain, i. e. the formation of microfractures, is observed after the first heating–cooling event (see Sage 1988; Widhalm *et al.* 1996; Siegesmund *et al.* 2000). Rüdrich *et al.* 2001 documented for a variety of marbles that the dilatation of a 1 m slab at a temperature interval of ΔT = 40°C would be between –0.1 mm and 1.0 mm which is strongly controlled by the fabric. This observation is in agreement with the findings of Battaglia *et al.* (1993), that for the temperature range between 20°C and 50°C a residual strain can be observed. For dolomitic marbles the amount of temperature-induced deterioration is less significant, which is probably due to the single crystal data of dolomite (the thermal expansion and strength).

Grelk (pers. comm.) clearly documented for a temperature interval of 20°C up to 80°C that if water is present, the length change may increase after each cycle. For Palissandro, only under water-saturated conditions is a very weak permanent length change observable. The hygric expansion parallel to Z is very small and within the limits of the method's measuring accuracy. Sandstones or tuffs exhibit a 10 to 500 times higher swelling or shrinking compared with Palissandro (Felix 1983). Thermal expansion behaviour under water-saturated conditions produces a somewhat higher residual strain which would point to hygric expansion. Winkler (1997) correlated these effects with ordered water through capillary condensation. Poschlod (1990) also found that for Carrara marble exposed to different moisture contents a stepwise drying produces a small permanent length change. The process of such stone decay is not yet fully understood.

The above-mentioned initial stages of deterioration processes may be superimposed by frost-thaw events. The processes taking place during freezing and thawing will be discussed in more detail in connection with the experimental results of the long-term investigation. The average Young's modulus of 57 marbles (see Gebrande 1982) has a value of 70.28 GPa with an 80% confidence. The relationship between the observed experimental data and behaviour during the weathering cycles can be best explained by considering the single crystal properties. The Young's modulus of calcite and dolomite crystals based on the elastic constants (Dandekar 1968) has values of 84 GPa and 119 GPa, respectively. These average values represent an elastically isotropic material, which holds not true for both minerals and most marbles, since they behave elastically anisotropically. Calcite and dolomite for example show an extreme anisotropy for the P-wave velocities of around 26%. However, a first rough estimation on the weathering behaviour can be obtained, if the marbles are considered to be a quasi-isotropic material.

Sample P1 shows the highest *E*-value of the fresh and weathered conditions which is easily explained by its dolomite content. In contrast, both calcite marbles exhibit a less pronounced Young's modulus, whereas the Carrara marble is highly sensitive to the freeze–thaw cycles.

The deterioration of rocks during freezing depends on the pore size distribution, the relative humidity, the water saturation and the possible presence of salts (Jerwood *et al.* 1990). The effect of pore size on crystallization was demonstrated by Briggs (1953). Fitzner (1988) found for sandstone that during freezing the pore size distribution increases. In the case of marbles the porosity is mostly less than 1%. For example, Rüdrich *et al.* (2001) discovered a porosity of 2.5% with a maximum pore radius in the range from 0.56 μm to 5.6 μm for weathered Carrara marble, whereas in the unweathered marble a porosity of 0.51% was measured with a pore radius between 0.03 μm and 0.10 μm. To understand the factors governing the formation of larger pores it is important to improve the ice growth hypothesis from experimental and theoretical findings. Numerical simulations from Walder & Hallett (1985) have been used to calculate the breakdown of marble by the growth of ice within cracks. The calculations indicate that sustained freezing is most effective in producing crack growth when temperature ranges from –4°C to –15°C if ample water is available. At higher temperatures the crystallization pressure would not be high enough to produce significant crack growth and at lower temperatures the migration of water is strongly inhibited. Under optimum conditions, at –22°C, the expansion of frozen water would produce a theoretical pressure of 207 MPa against the walls in a closed system (Bland & Rolls 1998); this pressure is much higher than the tensile strength of marbles. The crack growth versus ice pressure modelling of Walder & Hallett (1985) presents ice pressures at a maximum of about 7 MPa at –5°C, while Bland & Rolls (1998) reported from laboratory measurements a value of about 20 MPa. This may also be one reason why Carrara

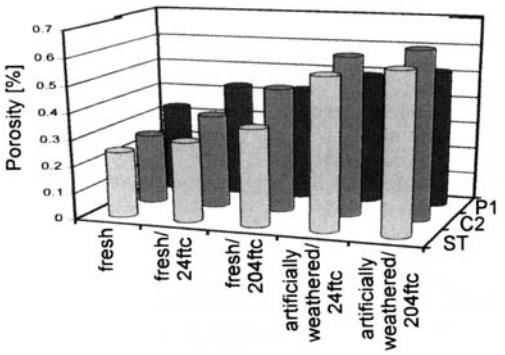

Fig. 8. Changes in porosity while freezing and thawing for P1, ST and C2 versus weathering for the fresh state, after 24 and 204 freeze–thaw cycles (ftc) as well as for the artificially weathered material.

marble shows the most significant loss in Young's modulus correlated with an increasing porosity (Fig. 8). Following these results, the question arises as to what happens in smaller pores under non-water-saturated conditions. According to Ozawa (1997), ice cannot crystallize in small pores of around 1 μm, but instead the supercooled water will migrate into a more open system. However, the frost cracking depends on the environmental conditions (for example the cooling rate), on the crack size, the elastic moduli, grain size and pore shape. The grain size and grain-boundary geometry of the Carrara marble (straight grain boundaries) should support crack formation as compared to the Palissandro and Sterzing marbles, with their more curved and interlocked grain boundaries. The injection of blue resin into the open pore volume of the weathered Carrara marble clearly shows that the open grain boundaries, but also the twins and cleavage planes, are decorated (Fig. 9). Furthermore, the grain boundaries in the highly weathered examples are interconnected to intergranular microcracks, i.e. the formation of a progressive network is being developed.

S. S. thanks the Deutsche Forschungsgemeinschaft for the Heisenberg fellowship (Si 438/10-1, 2), the contract Si 438/13-1 and the BMBF. We are very grateful to the Deutsche Bergbau-Museum for all their support and also for the long-term stay of J. O. Reviews of the manuscript by W.-D. Grimm and A. Jornet are gratefully acknowledged.

References

BATTAGLIA, S., FRANZINI, M. & MANGO, F. 1993. High sensitivity apparatus for measuring linear thermal expansion: preliminary results on the response of marbles. *Il Nuovo Cimento*, **16**, 453–461.

BLAND, W. & ROLLS, D. 1998. *Weathering*. Arnold, London.

BRIGGS, E. K. 1953. The supercooling of water. *Proceedings of the Physical Society (London)*, **66B**, 688–694.

BROCKMEYER, H. G. 1994. Application of neutron diffraction to measure preferred orientations of geological materials. *In*: BUNGE, H. J., SIEGESMUND, S., SKROTZKI, W. & WEBER, K. (eds) *Textures of Geological Materials*. DGM Informationsgesellschaft, Oberursel, 327–344.

DAHMS, M. & BUNGE, H.-J. 1988. The iterative series expansion method for quantitative texture analysis. I. General outline. *Journal of Applied Crystallography*, **22**, 439–447.

DANDEKAR, D. P. 1968. Variation in the elastic constants of calcite with pressure. *Physical Reviews*, **172**, 873–877.

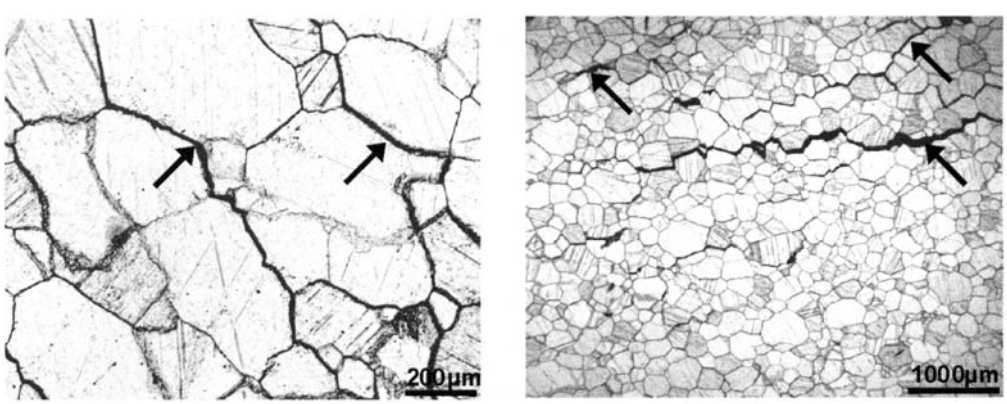

Fig. 9. Microphotographs of the weathered Carrara marble after the long-term freeze–thaw cycles. The residual porosity is shown by the blue resin injected into the samples.

DIN 52104. Prüfen von Naturstein 'Frost-Tau-Wechsel-Versuch' Verfahren. Beuth Verlag, Berlin.

FELIX, C. 1983. Sandstone linear swelling due to isothermal water sorption. *Material Science and Restoration. International Conference September 1983*, Esslingen/Germany. Edition Lack + Chemie, 305–310.

FITZNER, B. 1988. Porosity properties of naturally or artifically weathered sandstones. *In*: Ciabach, J. (ed) *VIth International Congress on Deterioration and Conservation of stone*, Torun, 236–245.

GEBRANDE, H. 1982. Elasticity and inelasticity. *In*: Angenheister, G. (ed.) Landolt-Börnstein, *Physikalische Eigenschaften der Gesteine*, Band 1b, Springer, Berlin, 1–98.

GRIMM, W.-D. 1999. Beobachtungen und Überlegungen zur Verformung von Marmorobjekten durch Gefügeauflockerung. *Zeitschrift der Deutschen Geologischen Gesellschaft*, **150**, 195–236.

GRÜNEISEN, E. 1926. Zustand des festen Körpers. *In*: Geiger, H. & Scheel, K. (eds) *Thermische Eigenschaften der Stoffe*. Handbuch der Physik, Bd. 10, Berlin.

JERWOOD, L. C., ROBINSON, D. A. & WILLIAMS, B. R. G. 1990. Experimental frost and salt weathering of chalk-II. *Earth Surface Processes and Landforms*, **15**, 699–708.

KIESLINGER, A. 1930. Das Volumen des Eises. *Geologie und Bauwesen*, **2**, 199–207.

KLEBER, W. 1983. *Einführung in die Kristallographie*. Berlin.

MARKGRAF, S. A. & REEDER, R. 1985. High-temperature structure refinements of calcite and magnesite. *American Mineralogist*, **70**, 590–600.

OZAWA, H. 1997. Thermodynamics of frost heaving: a thermodynamic proposition for dynamic phenomena. *Physical Review*, **E56**, 2811–2816.

POSCHLOD, K. 1990. Das Wasser im Porenraum kristalliner Naturwerksteine und sein Einfluss auf die Verwitterung. *Münchener geowissenschaftliche Abhandlungen, Reihe B, Allgemeine und Angewandte Geologie*, **7**, 1–61.

POWERS, T. W. & HELMUTH, R. A. 1953. Theory of volume changes in hardened Portland cement paste during freezing. *Highway Research Board Proceedings*, **32**, 285–297.

RÜDRICH, J., WEISS, T. & SIEGESMUND, S. 2001. Deterioration characteristics of marbles from the Marmorpalais Potsdam (Germany): a compilation. *Zeitschrift der Deutschen Geologischen Gesellschaft*, **152**, 637–664.

SAGE, I. D. 1988. Thermal cracking of marble. *In*: Marinos, P. G. & Koukis, G. C. (eds) *Engineering Geology of Ancient Works, Monuments and Historical Sites*. Balkema, Rotterdam, 1013–1018.

SIEGESMUND, S., HELMING, K. & KRUSE, R. 1994. Complete texture analysis of a deformed amphibolite: comparison between neutron diffraction and U-stage data. *Journal of Structural Geology*, **16**, 131–142.

SIEGESMUND, S., ULLEMEYER, K., WEISS, T. & TSCHEGG, E. 2000. Physical weathering of marbles caused by ansiotropic thermal expansion. *International Journal of Earth Sciences*, **89**, 170–182.

ULLEMEYER, K., SPALTHOFF, P., HEINITZ, J., ISAKOV, N. N., NIKITIN, A. N. & WEBER, K. 1998. The SKAT texture diffractometer at the pulsed reactor IBR-2 at Dubna: experimental layout and first measurements. *Nuclear Instrument Methods Physical Research*, **A 412**, 80–88.

WALDER, J. & HALLETT, B. 1985. A theoretical model of the fracture of rock during freezing. *Geological Society of American Bulletin*, **96**, 336–346.

WIDHALM, C., TSCHEGG, E. & EPPENSTEINER, W. 1996. Anisotropic thermal expansion causes deformation of marble cladding. *Journal of Performance and Construction*, **10**, 5–10.

WINKLER, E. 1997. *Stone in Architecture*. Springer, Berlin.

Evolution of the petrophysical properties of two types of Alsatian sandstone subjected to simulated freeze–thaw conditions

C. THOMACHOT & D. JEANNETTE

Centre de Géochimie de la Surface, EOST, 1 rue Blessig 67084 Strasbourg Cedex, France (e-mail: celine@illite.u-strasbg.fr)

Abstract: Stone monuments in Alsace (eastern France) are built with two types of Buntsandstein sandstone (Lower Triassic). Their different pore structures cause them to have mixed petrophysical properties and occasion a different response to frost. To understand these differences, frost simulation experiments have been carried out on samples of both stones. Four series of 30 freeze–thaw cycles were reproduced on samples maintained at constant saturation, either total or partial, without drying or rewetting. Macroscopic and microscopic change due to frost was observed by scanning electronic microscope, by mercury porosimetry and P-wave velocity measurements. Change of tensile strength and capillary kinetics was also assessed before and after each series. Results demonstrate that frost action increases heterogeneity of the porous network particularly in the initially more heterogeneous sandstone. When saturation is partial, no macroscopic cracking occurs and capillary absorption decreases. When saturation is total, macroscopic cracking prevails over microscopic heterogeneity and capillary absorption increases. Control tests have also been carried out to evaluate the effects induced by absorption–drying cycles without frost, and dilation experiments have been added to assess freeze–thaw action on dilation of sandstones. The results of all these experiments demonstrate that frost plays a less decisive part in the weathering mechanisms of stones than wetting–drying.

Water freezing in a porous medium is led by both water properties (volume change, plasticity, etc.) and porous network complexity.

In theory, water freezes at 0°C under atmospheric pressure; this is an exothermic reaction. In practice, water generally freezes below 0°C and can stay liquid at negative temperatures: this phenomenon is called supercooling. Important parameters are the presence of freezing nuclei (Lliboutry 1964; Chahal & Miller 1965), water salinity (Powers & Helmuth 1953) but also pore radius (Fagerlund 1971), which is a proper characteristic of the medium. Because a porous medium can have different pore radii, water can freeze progressively during a temperature drop below 0°C, and a ratio of unfrozen water can stay at the end. These phenomena, working together with ice volume expansion, can lead to several stress-creating processes in the porous medium: the growth of hydraulic pressures (Powers 1956; Litvan 1978; Powers & Helmuth 1953) or capillary pressures (Everett 1961).

The nature of porous media (porosity structures, transfer and mechanical properties), the way they are saturated (totally, partially, water supplied during the freezing), and freezing conditions (T_{min}, dT/dt, freezing duration) drive the congealing process and by consequence the growth of stresses (Hirschwald 1912). Cracking occurs when stresses override the medium rupture resistance. At a macroscopic scale, frost action is responsible for all shivering, flaking and gelidisjunction, which are often created by combinations of the processes previously explained (Letavernier 1984).

Gelivity scales result from experimental measurement and are seldom reliable. Indeed, they are based on one particular protocol. This protocol may be different from natural conditions (total saturation, test-tubes lying in water, drying periods between freezing–defreezing cycles, etc.) and it often emphasizes one factor (temperature decreasing speed, fixed minimum temperature, number of freezing–defreezing cycles, etc.). Moreover, these scales are most often based on the study of a particular rock group (especially calcareous rocks: Lautridou & Ozouf 1978, 1982; Letavernier 1984; Remy 1993). Different methods of resistance evaluation are used (visual criterion, granulometric criterion, mercury porosimetry, transfer and mechanical properties, etc.). Comparing the results from different authors would mean in fact comparing the protocols, the characteristics of the tested rocks and the damage measurement techniques. This would be difficult. However, by reading the literature, one can

From: SIEGESMUND, S., WEISS, T. & VOLLBRECHT, A. 2002. *Natural Stone, Weathering Phenomena, Conservation Strategies and Case Studies*. Geological Society, London, Special Publications, **205**, 19–32.
0305-8719/02/$15.00 © The Geological Society of London 2002.

choose the experimental conditions for a given parameter to test.

One goal of this study is to better understand freezing processes and to evaluate the freezing resistance of Vosgien sandstone and millstone grit. These rocks are usually used on stone monuments in Alsace and especially Strasbourg's cathedral. On the lowest parts of the cathedral, where there are quiet conditions, millstone grit seems to be more frost-cleft than Vosgien sandstone; on the higher parts, near the spire, Vosgien sandstone, which has recently been installed during restoration works, seems to damage faster with unset grains at the surface. To study how these two rocks resist freezing, one has to precisely characterize their porosity structure, their transfer properties and their mechanical properties. Freezing conditions and damage evaluation methods are chosen so as to emphasize one particular parameter or process. In this study, the evolution of rocks under freezing–defreezing cycles is evaluated mainly by using the following methods: mercury porosimetry, capillary inhibition and dilation. One can also use water porosimetry, traction resistance, acoustic wave propagation and environmental microscopy.

Materials

The Vosgien sandstone and the Meules sandstone used in Alsatian buildings have similar mineralogical compositions but mixed petrophysical properties. Their response to weathering, especially to frost action, is different. So the initial aim of this study was to show the importance and demonstrate the role of the pore structure in controlling weathering of the two stone types.

Simulation studies were devised to reflect natural frost conditions in Alsace. These utilized two saturation degrees:

- partial saturation simulating the maximum natural conditions found on blocks from a building and involving saturation by capillary absorption N_{cap};
- total saturation simulating extreme saturation conditions in which all connected pores are filled with water under vacuum (total saturation N_t).

Saturation degrees were maintained during successive freeze–thaw cycles by placing samples in nylon water-proof bags. The characteristics of these experiments therefore differed from the natural conditions in which stone can either dry by evaporation or be recharged by capillary absorption during the freezing process. This reflected one of the aims of the study which was to demonstrate the part of frost in modifying the porous network of stone without any water exchange with the outside. With this aim in view, other test blocks were subjected to cyclic capillary absorption–drying without frost. Also dilation caused by freeze–thaw cycles at partial saturation was compared to dilation due to absorption–drying.

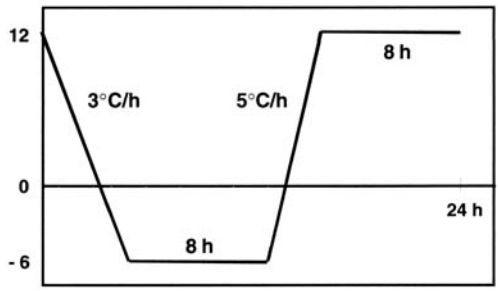

Fig. 1. Freeze–thaw cycle used during experiments.

Frost experiments

Freeze–thaw cycles were generated in a programmable LMS cold room. Temperature was measured by a four-channel thermometer with 0.5 cm copper-constantan thermocouples. Two packs of eight $7 \times 7 \times 7$ cm^3 samples of both sandstones were isolated in a water-proof sheath to maintain saturation during experiments: one pack at capillary saturation (N_{cap}) and the other one at total saturation under vacuum (N_t). Experimental samples were subjected to 24 h freeze–thaw cycles ranging from +12°C to –6°C (Fig.1). During all experiments, bedding was vertical. Before and after each series of 30 cycles, samples were dried so that capillary absorption could be measured to assess the effect of freeze–thaw on capillary kinetics. Thus, during experiments, which included three series of 30 freeze–thaw cycles, samples were dried then saturated only four times, before and after each series: the first time to measure the initial capillary properties and the three other times to evaluate the effects of each freeze–thaw series.

Control tests without freeze–thaw action were made on two blocks of both sandstones to evaluate any change of capillary transfer induced exclusively by wetting and drying. These blocks were subjected to four cycles of wetting by capillary absorption and drying. Variations of the capillary kinetics were subtracted from the capillary variations measured after frost series.

Analytical methods

Visual inspection

Damage to the two sandstones was first evaluated macroscopically with the naked eye then at the end of all the experiments microscopically by means of a Jeol scanning microscope (JSM 840 SEM).

Porosimetry methods

Water porosimetry under vacuum (N_t) was assessed before and after frost series (NF B 10–503 1973).

Mercury injection porosimetry was measured before and after frost by means of a Micromeretics Pore Sizer 9320, on cylindrical samples specially designed to be tested by this analytical method.

This method quantifies the pore access distribution of the rock as well as the microscopic change of the porous network due to frost action. It also determines the pore threshold which allows the biggest part of the porous network to be filled. On a porosimetry curve, the pore threshold is at the intersection of the two tangents at the top of the curve (Katz & Thompson 1986).

Measurement of transfer properties (absorption, drying and permeability)

To measure capillary absorption, the bottom of the samples is placed in water in a tub where relative humidity (R.H.) is constant and kept at nearly 100% to avoid drying (NF B 10–502 1980). The weight increase per surface unit and the capillary height are plotted over the square root of time, according to the Washburn law. The first curve is characterized by a two-part progression: at the beginning of the experiment, the weight increase curve is linear and corresponds to the progressive filling of the interconnected pores. The slope of this curve is called the A coefficient (g cm^{-2} h$^{-1/2}$) and is relative to the weight increase of the sample. At the top of this first linear part, the value is that of free porosity (N_{cap}). Next to this point, saturation of the porous network is slower with a weaker incline. This corresponds to the filling of the trapped porosity by diffusion of air through water. There is more or less trapped porosity. Its proportion depends on the pore distribution and on the nature of fluids used: when wetting fluid, moved by capillary pressure, reaches a widening pore, pressure declines and filling becomes very slow. If a finer capillary bypasses it or if there is a microporous sheet coating it, it is trapped and remains filled with air (Bousquié 1979; Fig. 2).

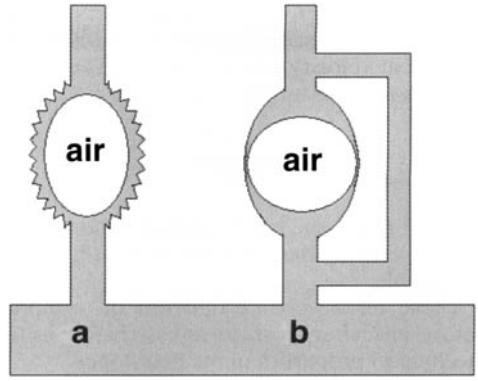

Fig. 2. Trapping mechanisms of macropore with air during capillary absorption (Bousquié 1979): (a) rugosity or (b) bypassing.

The slope of the second curve, relative to the migration of the wet zone, corresponds to the B coefficient (cm h$^{-1/2}$).

To complete the petrophysical data and to understand better the effects of frost action, drying kinetics and water permeability were also measured. In evaporation experiments, saturated samples are isolated, except for one face, in a water-proof sheath. Then they are put to dry in a tub where relative humidity is controlled by brine (Acheson 1963; Schlünder 1963). The drying curve is obtained by plotting water loss per surface unit over time. This is equivalent to porosity desaturation. In this case, water permeability was measured by a constant-head permeameter on totally saturated samples of 2 cm height and 2 cm diameter, along the bedding or perpendicular to it.

Measurement of mechanical properties

P-wave velocity of blocks was measured perpendicular to and along the bedding, before and after frost. Samples of 7 cm cubes were placed in between transducers of 3 cm diameter at 500 kHz. A 200 N force was applied to maintain contact between the sample and the transducers (NF B 10–505 1973). In a porous material, P-wave velocity varies according to the heterogeneity distribution of pores. Porosity increase usually induces velocity decrease (Gregory 1976) as the propagation of waves is checked by air. This interrelation is valid for materials of identical mineralogy.

Tensile strength of the sandstones was determined by Brazilian tests. Samples of 1 cm height

and 2 cm diameter were positioned vertically on their edges and subjected to a load whose displacement velocity was 10^{-1} μm s^{-1}. The tensile strength (σ_t) is given by the relationship:

$$\sigma_t = -\frac{2F}{\pi d h}$$

where F (N) is the breaking force, and d and h are respectively the diameter and the height of the sample.

These tests were carried out on samples, before and after frost, to assess change in the mechanical properties of the two stones.

Dilation

In addition, dilation experiments were carried out on other cylindrical samples of 4 cm diameter and 7 cm length with vertical and horizontal bedding. Degree of saturation was only partial as it was technically impossible to achieve successively dilation by total saturation and freeze–thaw cycles. Also, the objective of these particular experiments was focused on natural weather conditions.

The samples were placed on a steel bracket with a displacement transducer on top of it. Before freezing, samples were subjected to capillary absorption at 12°C and water dilation was measured as well as the migration of the capillary fringe (B coefficient). At the beginning of freeze–thaw cycles, samples were saturated by capillary absorption (N_{cap}).Then water was removed from the tub. Drying began when the freeze–thaw cycles started. After some cycles, temperature was maintained constant at 12°C and drying continued.

Petrography and pore structure of Buntsandstein sandstone

Monuments in Alsace, and especially Strasbourg's cathedral, are typically built of two types of Buntsandstein sandstone (Lower Triassic; Mader 1985): a thinly bedded variety of 23.5 % total porosity, rich in clay minerals, known as the Meules sandstone; and a coarser variety, less rich in clay, with 18% total porosity, known as the Vosgien sandstone.

The Vosgien sandstone is composed of 80% quartz grains. These are usually massive, ovoid and average 200 μm in length. The grains are cemented by light overgrowths. Although elongated, the grains do not lie in beds, and this is visible by microscope. On average, clay minerals, strained by iron oxides, represent 4% of the weight of the rock. They form a thick coating which lines the biggest intergranular spacings. Viewed by microscope, thin sections impregnated with coloured resins (Zinszner & Meynot 1982) show intergranular spaces subdivided into irregular large pores which can be as long as 300 μm (Fig. 3a). Although sometimes isolated, these pores are generally linked by narrow throats filled with clayey concentrations. These represent a macroporosity which is likely to be trapped during capillary absorption (Mertz 1991). In contrast, micropores cannot be individually identified under a microscope. They concentrate in clayey zones, with altered feldspars, in reduced pore interconnections near the contact points between grains, and they are almost all associated with the clayey coating which lines the largest pores. Thus, the porous network of this sandstone observed under the microscope is highly heterogeneous because of the contrasts between the large intergranular pores and the number of microporous zones.

Bedding within the Meules sandstone is visible macroscopically. In thin sections it comprises higher (6 to 7%) clayey concentrations. Quartz and feldspar grains of this stone are on average 60 μm long. They are angular and lie parallel to the bedding. The largest pores are 10 to 40 μm long and their distribution varies in relation to the petrographical composition (Fig. 3b). A clay matrix forms aggregates which provide cohesion between grains. In spite of macroscopic heterogeneity caused by bedding, microporosity associated with the clay matrix controls connectivity of the pore network so that on the whole the pore structure is homogeneous.

Scanning electronic microscope observations of sandstone samples before and after freeze–thaw cycles show microscopic change in the pore structure, particularly that of the Vosgien sandstone. Microporosity due to clay coating and quartz overgrowth is removed by frost action (Fig. 4). The network after freeze–thaw has more rounded mineral grains and a higher macroporosity. On the other hand, the Meules pore structure before and after frost shows little difference (Fig. 4). Clay minerals form aggregates which are slightly less numerous after freeze–thaw. Aggregates are more difficult to remove than coating and widening due to frost action shown by mercury porosimetry is too weak to be observed by SEM.

Evolution of the petrophysical properties

Porosity

After three series of 30 cycles, neither of the sandstones, tested at capillary saturation, showed macroscopic change and the values of

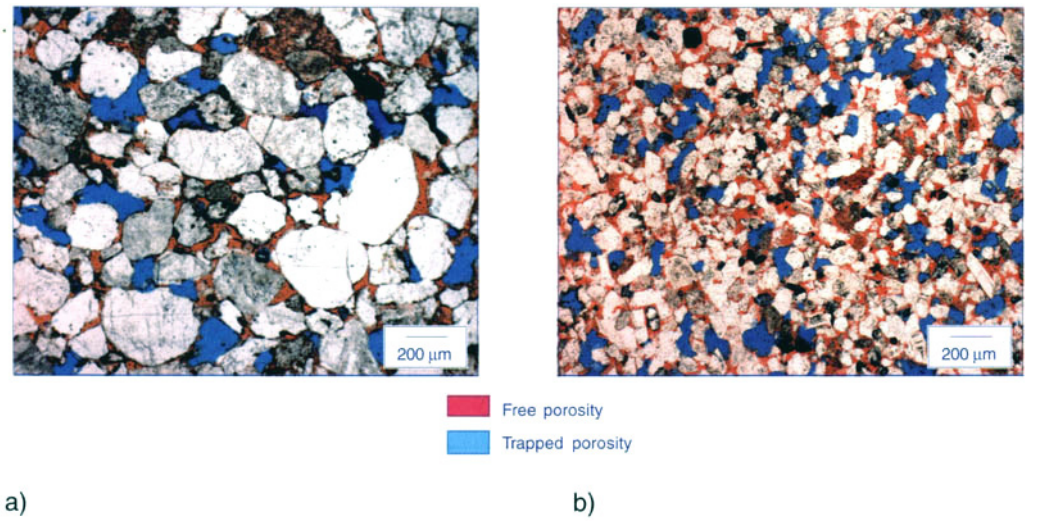

Fig. 3. Same-scale coloured thin sections of the Vosgien sandstone (**a**) and the Meules sandstone (**b**): red resin occupies the free porosity and the blue one, the trapped porosity.

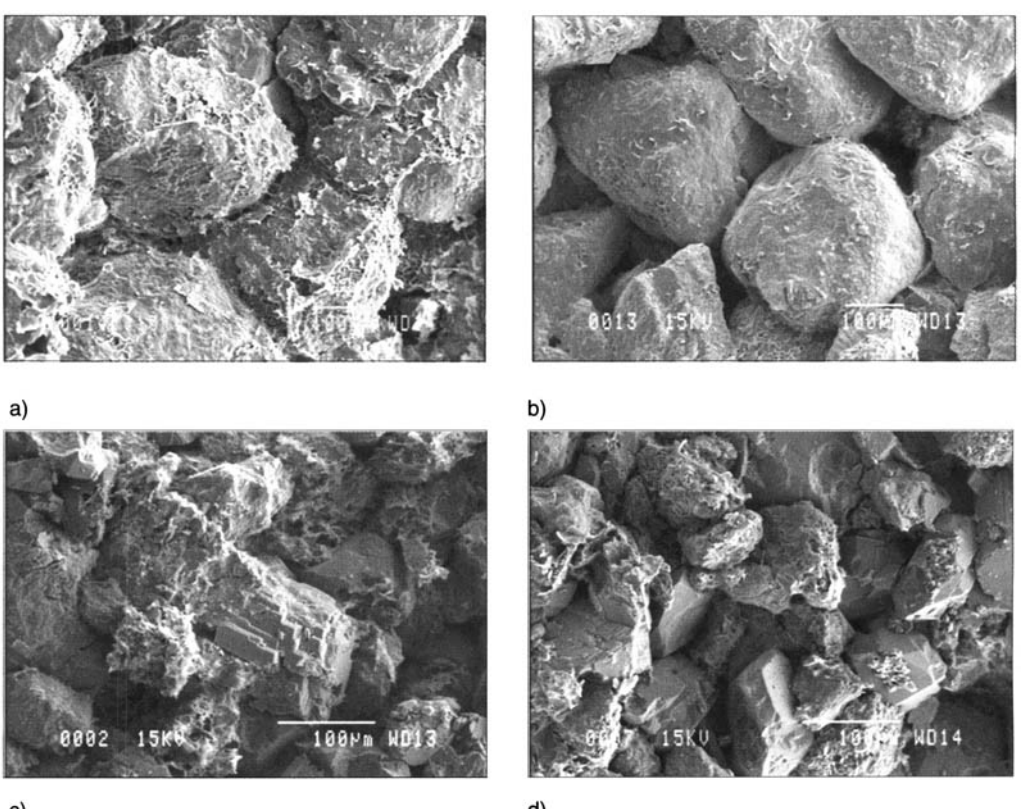

Fig. 4. SEM images of Vosgien sandstone, before (**a**) and after (**b**) 30 freeze–thaw cycles; SEM images of Meules sandstone, before (**c**) and after (**d**) 30 freeze–thaw cycles.

Table 1. *Characteristics of the porosity of the Vosgien sandstone and the Meules sandstone, before and after frost series on different types of saturation*

	Vosgien sandstone			Meules sandstone		
	Before frost	After frost at capillary saturation	After frost at total saturation	Before frost	After frost at capillary saturation	After frost at total saturation
Total porosity, N_t (%)	18	18	18.9	23.5	23.5	24.1
Free porosity, N_{cap} (%)	11.5	11.6	12.1	14.5	14.6	14.8
Trapped porosity, $N_p = N_t - N_{cap}$ (%)	6.5	6.4	6.8	9	8.9	9.3
Degree of partial saturation by capillary absorption S (= N_{cap}/N_t (%)	64	64	64	62	62	61
Mercury porosity (%)	17.4	18.8	18.8	20.8	22.4	22.5
Mercury pore threshold *Ra* (μm)	6	10.6	10.5	4.7	6	6
Invaded volume at *Ra* (%)	46.2	49.3	50.0	61.4	63.3	63.3

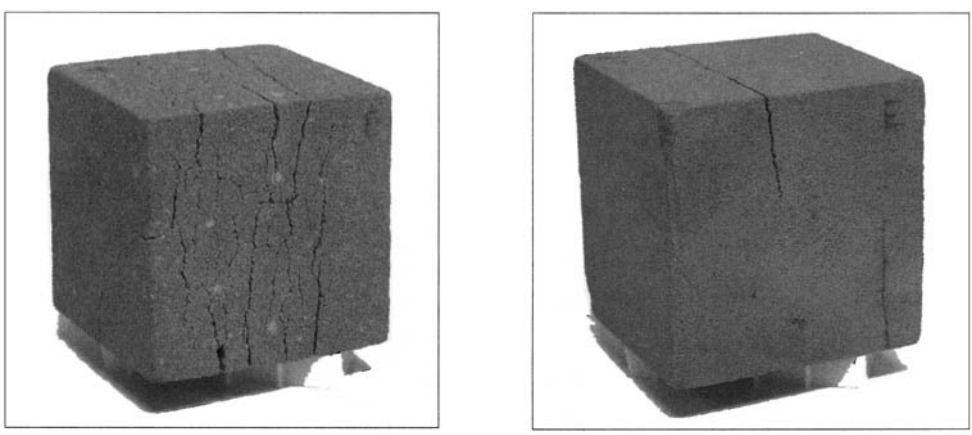

a) b)

Fig. 5. Fractured blocks of Vosgien sandstone (**a**) and Meules sandstone (**b**) after three series of 30 freeze–thaw cycles.

their total porosity remained unchanged (Table 1). In contrast, both sandstones tested at total saturation fractured early in the cycle progression. Porosity increased, rising after 3 × 30 cycles from 18 and 23.5% total porosity to 18.9 and 24.1%, for the Vosgien and the Meules sandstones, respectively. In the case of Vosgien sandstone, cracking occurred on the tenth cycle of the first series and developed during the following series. Cracks were numerous and ramified and accompanied by grain loss (Fig. 5a). There were a lot of cracks at the end of the experiments on blocks subjected to more than 3 × 2 cycles. In the case of Meules sandstone, cracking occurred on the sixth cycle of the first series, but developed very little during the following series. There was only one thin crack and there was no grain loss. At the end of the experiments, only blocks subjected to more than 3 × 6 freeze–thaw cycles had just a thin crack (Fig. 5b).

In both cases and with both saturations, the degree of partial saturation by capillary absorption ($S = N_{cap}/N_t$) after freeze–thaw experiments remained unchanged (Table 1).

Mercury porosimetry confirmed the larger porosity and the larger homogeneity of the Meules sandstone compared to Vosgien sandstone. Indeed, the volume of mercury injected at the pore threshold of Meules sandstone was 61.4% whereas it was only 46.2% for Vosgien sandstone (Table 1).

In both cases and with both saturations,

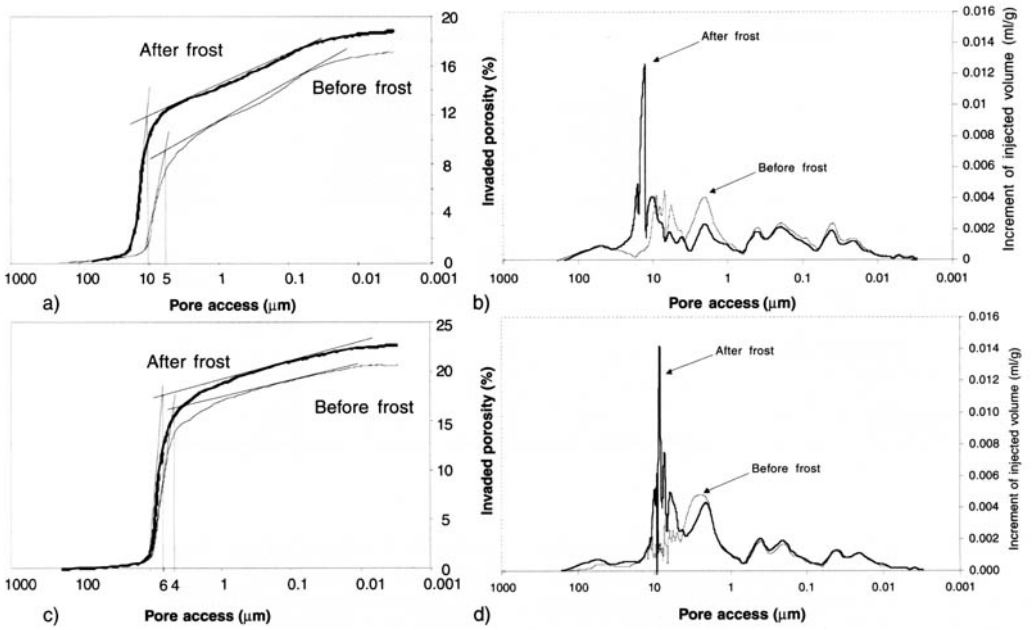

Fig. 6. Mercury porosimetry curves of the Vosgien sandstone (**a**, **b**) and the Meules sandstone (**c**, **d**) before and after 30 freeze–thaw cycles.

Table 2. *P-wave velocity and tensile strength of the Vosgien and the Meules sandstone, before and after frost series on two types of saturation*

	Vosgien sandstone			Meules sandstone		
	Before frost	After frost at capillary saturation	After frost at total saturation	Before frost	After frost at capillary saturation	After frost at total saturation
P wave velocity (m s^{-1})						
// to stratification	2690	2580	< 2050	2370	2380	1670
⊥ to stratification	2730	2610	< 680	2170	2180	1240
Tensile strength (MPa)						
// to stratification	2.1	–	1.3	2.4	–	1.6

mercury porosity increased with the number of frost–thaw cycles (Fig. 6). Change due to frost was perceptible thanks to this method. It was not perceptible when it was measured on bigger samples by water porosimetry under vacuum. Mercury measurements showed that on the Vosgien sandstone especially, the percentage of the finest accesses to pores (<2 μm) decreased slightly because of frost, whereas the largest accesses to pores increased. The pore threshold increased from 6 to 10 μm (Fig. 6a and b). The development of large pores, the size of which reached 80 μm, testifies to the formation of a fracture network whose largest cracks can be observed macroscopically. On the Meules sandstone, frost induces small modifications of the pore network: the small increase in total mercury porosity is due to an increase in macroporosity as well as to a displacement of the pore threshold toward larger pore access (Fig. 6c and d).

Mechanical properties

P-wave velocity measurements made before exposure to freeze–thaw showed greater homogeneity in the Vosgien sandstone (Table 2).

Table 3. *Transfer properties of the Vosgien sandstone and the Meules sandstone*

	Vosgien sandstone			Meules sandstone		
	Before frost	After frost at capillary saturation	After frost at total saturation	Before frost	After frost at capillary saturation	After frost at total saturation
Capillary transfer kinetics (// stratification)						
A (g cm^{-2} $h^{-1/2}$)	0.15	0.09	2.54	1.35	1.25	1.55
B (cm $h^{-1/2}$)	1.46	1.00	10.01	9.01	8.87	8.73
Drying kinetics at 33% R.H.						
F1 (g cm^{-2})	–0.015	–	–	–0.009	–	–
Water permeability Kw (mD)						
// stratification	2.3	–	–	124.3	–	–
⊥ stratification	0.4			92.4		

Indeed, velocities were approximately equal on parallel and perpendicular planes. In comparison, P-wave velocities for the Meules sandstone were weaker perpendicular to bedding.

Change due to freeze–thaw attenuates P-wave velocity. The fact that these sandstones have similar mineralogical compositions means that freeze–thaw accentuates heterogeneity. If any, changes were too small to be perceptible by this method on the samples tested at capillary saturation. But on the samples tested at total saturation, changes were perceptible and proportionately more important perpendicular to bedding, especially on Vosgien sandstone: this orientation is perpendicular to the common fracture planes. The tensile strength measurements confirmed these changes (Table 2).

Transfer properties

Different pore structures (homogeneity, mercury threshold, permeability, etc.) give the two sandstones mixed petrophysical properties (Table 3). In particular, Meules sandstone has faster capillary transfer kinetics (A ≈ 1.35 g cm^{-2} $h^{-1/2}$; B ≈ 9.01 cm $h^{-1/2}$) and less fast drying kinetics (–0.009 g cm^{-2} at 33% R.H.) than Vosgien sandstone (A ≈ 0.15 g cm^{-2} $h^{-1/2}$; B ≈ 1.46 cm $h^{-1/2}$, –0.016 g cm^{-2} at 33% R.H.) (Fig. 7). For both sandstones, water permeability is always more important parallel to bedding (Table 3). Water permeability of Meules sandstone is more important by two orders of magnitude than the water permeability of Vosgien sandstone whatever the orientation of the bedding (Table 3).

On the control samples, only subjected to four cycles of capillary absorption/drying, A and B capillary coefficients measured during the first cycle ('Before frost' values, Table 3) decrease to 0.14 and 1.08 g cm^{-2} $h^{-1/2}$ for the A coefficient, 1.10 and 8.53 cm $h^{-1/2}$ for the B coefficient respectively for Vosgien and Meules sandstones. These variations are subtracted from capillary variations recorded after frost series.

On Vosgien sandstone tested at capillary saturation where no macroscopic cracking occurred, capillary transfers globally decreased with the number of frost series (Fig. 8a). After four series, capillary coefficients were A ≈ 0.09 g cm^{-2} $h^{-1/2}$ and B ≈ 1.00 cm $h^{-1/2}$. This decrease means that heterogeneity of the porous network increased and it confirmed mercury porosimetry measurements. It showed that heterogeneity increase was more with frost than with absorption-drying only. On Vosgien sandstone tested at total saturation, there were numerous macroscopic cracks and as their number increased along with the number of freeze–thaw cycles, capillary transfers increased too (Fig. 8b). After four series, the capillary coefficients were A ≈ 2.54 g cm^{-2} $h^{-1/2}$; B ≈ 10.01 cm $h^{-1/2}$. Cracks formed preferential channels and this increased capillary kinetics.

On Meules sandstone tested at capillary saturation, no macroscopic cracking occurred and capillary transfers decreased with the number of frost series (Fig. 8c). After four series, capillary coefficients were A ≈ 1.25 g cm^{-2} $h^{-1/2}$ and B ≈ 8.87 cm $h^{-1/2}$. On Meules sandstone tested at total saturation, there were few cracks and capillary transfers did not vary much (Fig. 8d, Table 3). After four series, the capillary coefficients were A ≈ 1.55 g cm^{-2} $h^{-1/2}$ and B ≈ 8.73 cm $h^{-1/2}$. Compared to Vosgien sandstone, Meules sandstone had high initial capillary coefficients so that capillary transfer variations were less

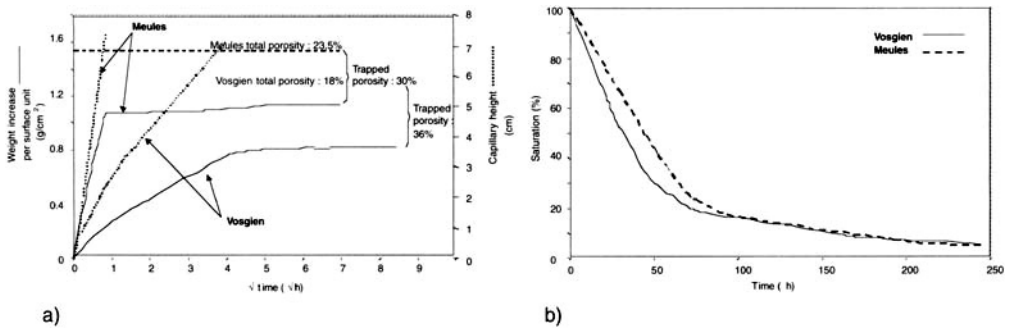

Fig. 7. (**a**) Capillary absorption kinetics of the Vosgien sandstone and the Meules sandstone; (**b**) drying kinetics of the Vosgien sandstone and the Meules sandstone.

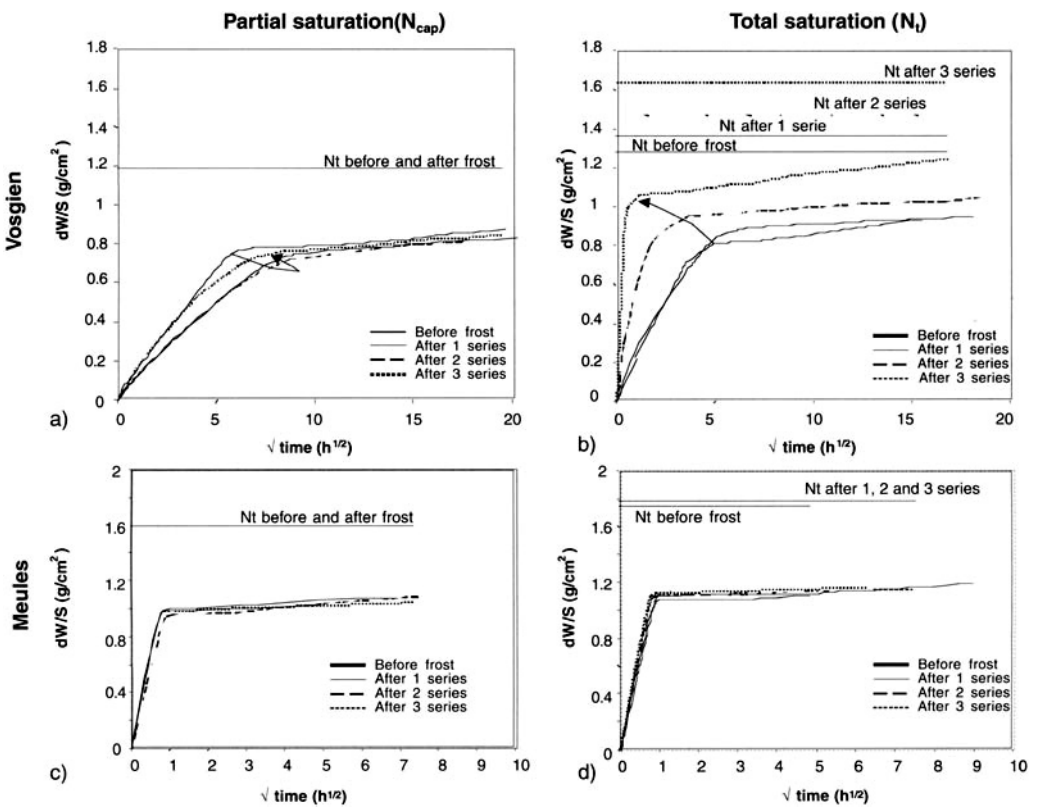

Fig. 8. Variations of capillary transfers of the Vosgien and the Meules sandstones subjected to series of freeze–thaw cycles at different saturation.

significant and visible on the curves. Its better transfer properties do not depend on a more important macroporosity and pore threshold. They can only be in relation to the better homogeneity of the porous network. Transfer of unfrozen water is facilitated and so is ice extrusion toward trapped pores or outside the sample.

Dilation and hydration phenomena

Water dilation before freezing

In Vosgien sandstone, bedding is not really marked and the B coefficients of the capillary fringe migration in both orientations of the bedding are not significantly different (1.26 and 1.14 cm $h^{-1/2}$). That is why differences noticed were insignificant between the maximal water dilations in the two orientations (3.0 and 3.9 μm cm^{-1}).

In Meules sandstone, bedding is more marked and the differences between the B coefficients of the capillary fringe migration in both orientations are more perceptible (9.64 and 5.26 cm $h^{-1/2}$). This justifies the great difference between the values of maximal water dilation depending on the orientation of bedding (0.7 and 3.2 μm cm^{-1}).

The water dilation is in relation to the orientation of bedding. Dilation is all the more important as B is weak.

Dilation under freezing

At capillary saturation (N_{cap}), freeze–thaw did not induce a higher dilation than the maximum water dilation whatever the sandstone or the orientation of the bedding. Total dilation indicated dilation of the most sensitive layer.

When bedding was vertical, drying was quick and dilation variations due to frost were weaker than those due to water dilation.

When bedding was horizontal (Fig. 9b and d), drying was slower and the resulting dilation was the added dilations of all the beds. Anisotropy was also underlined by the values of the B coefficients. There was no dilation during the freezing process but a slight retraction as temperature decreased. When dilation was measured perpendicular to bedding (Fig. 9a and c), retraction was perceptively significant below –6°C (Fig. 10a). This was not the case when dilation was measured parallel to bedding (Fig. 10b). The retraction below –6°C was due to the cumulative effect of ice contraction at constant temperature (Thomas 1938; Blachère 1975) and of migration of unfrozen water from the finest pores towards the largest (Prick *et al.* 1993). At the end of the experiments, no residual dilation was measured.

Discussion

At capillary saturation, no dilation was observed during the freezing process and there was no macroscopic change on the samples even though microscopic changes were measured by mercury porosimetry. This confirmed the reservations of a few authors about frost mechanisms in the weathering of stones (Hamès *et al.* 1987; Prick *et al.* 1993). Freeze–thaw experiments were carried out without water exchange with the outside. Test controls showed that simple absorption–drying cycles decreased capillary transfer and modified pore structures. However, these changes were smaller than those introduced by freeze–thaw cycles after absorption and did not cause macroscopic cracking even after 90 freeze–thaw cycles. With the same experimental conditions on German sandstone, Weiss (1992), noticed no cracking even after 250 freeze–thaw cycles. Frost accentuates heterogeneity of the pore structures but is not sufficient to cause cracks on capillary saturation.

Summary and conclusions

Freeze–thaw on the two sandstones decreased microporosity and increased macroporosity. In spite of the pore threshold increase and the largest size of the macropores, the largest dispersion of the pore access accentuated heterogeneity of the porous network, especially in Vosgien sandstone.

In Vosgien sandstone tested under partial saturation, water of menisci froze but could extrude toward the trapped macropores. No macroscopic cracking occurred as shown by observation and measurement of P-wave velocity. However, macroporosity widening shown by the mercury porosimetry and decrease of the capillary absorption coefficients, indicated a greater heterogeneity as it was more difficult to soak larger trapped pores because of the little pore access. At total saturation, ice extrusion outside the samples was hindered by heterogeneity of the porous network and there were numerous cracks which prevailed over microscopic heterogeneity. These cracks in their turn increased total porosity, decreased P-wave velocity and generated a large and well connected network which helped capillary absorption of the samples.

Given the homogeneity of the Meules sandstone, frost action led to a slightly more heterogeneous network. In partially saturated Meules sandstone, ice extrusion was possible in the macropore and no macroscopic cracking occurred. But heterogeneity caused by frost was too insignificant to change capillary absorption. In totally saturated Meules sandstone, ice extrusion outside the sample was facilitated by the homogeneous porous network, and produced just a few localized cracks which slightly increased absorption.

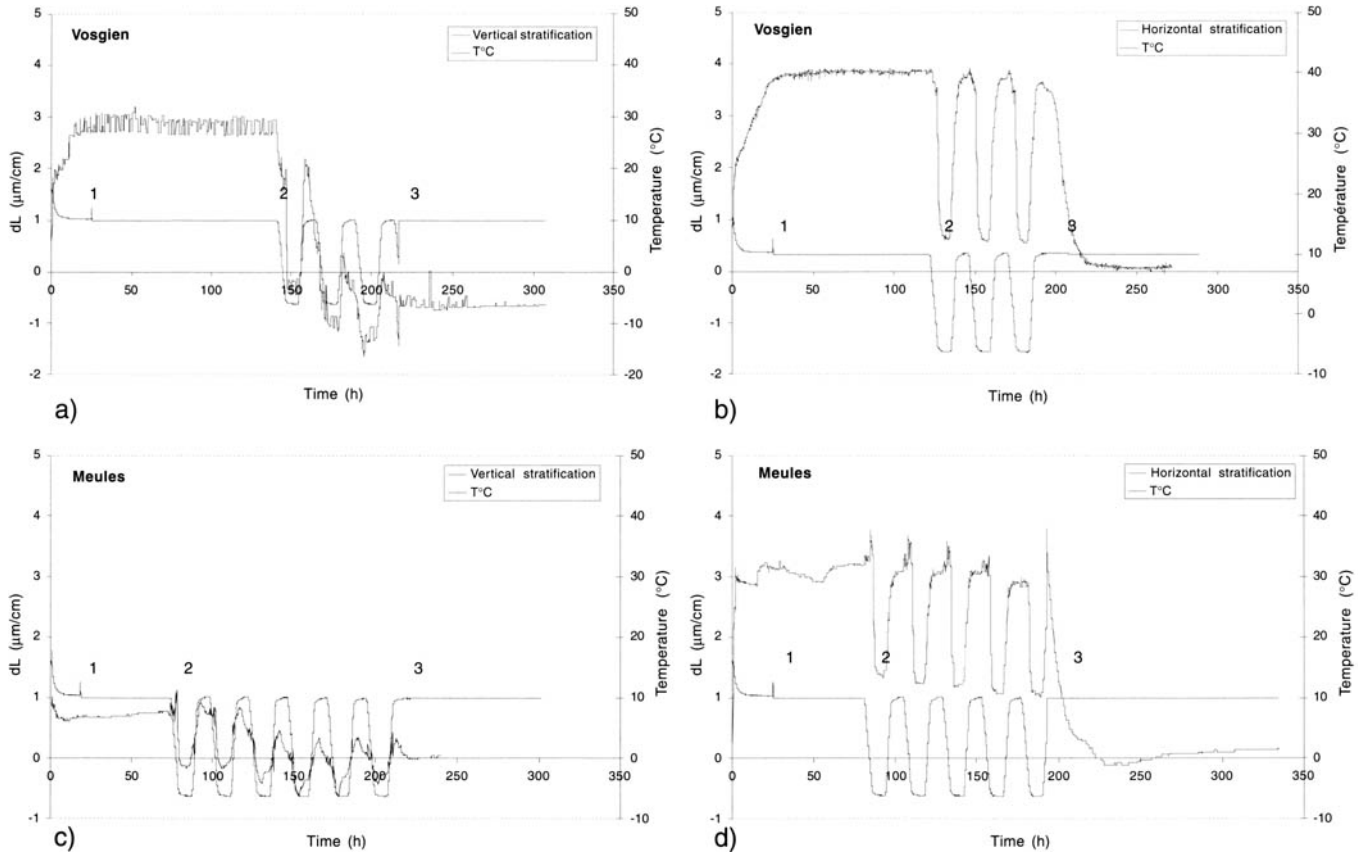

Fig. 9. Dilation curves of the Vosgien and the Meules sandstone subjected to a capillary absorption at constant temperature and to drying during 24 h freeze–thaw cycles along two orientations of stratification.

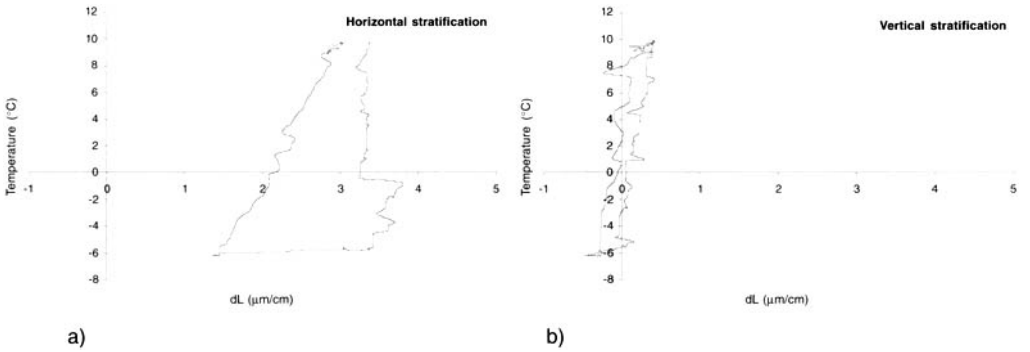

Fig. 10. Dilation variations during a freeze–thaw cycle: (**a**) perpendicular to stratification; (**b**) parallel to stratification.

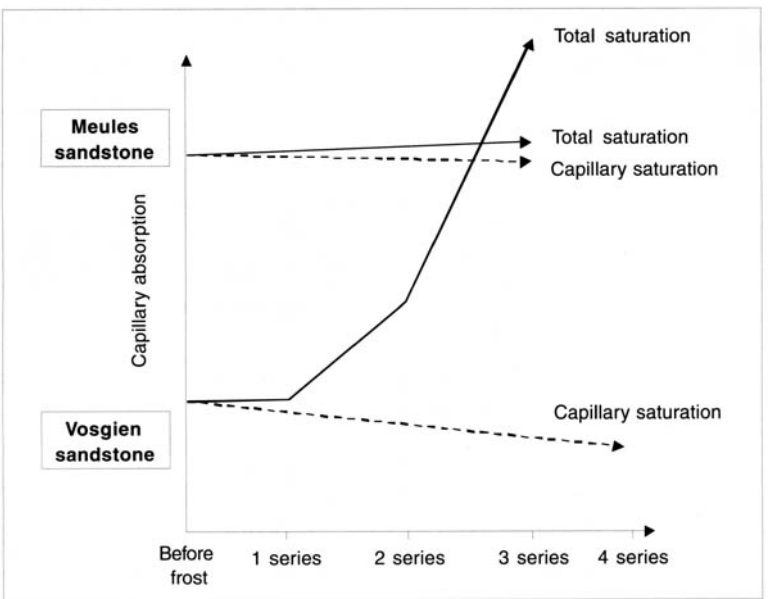

Fig. 11. Schematic evolution of the capillary transfer of the Vosgien and the Meules sandstones.

The diagram in Figure 11 summarizes the different capillary evolutions of these two sandstones after a series of frost–thaw cycles: Meules sandstone has fast initial capillary absorption which is not modified by frost action whatever the saturation of the samples; Vosgien sandstone has poor initial capillary absorption which is modified more significantly by frost action especially when samples are totally saturated.

The results of these experiments cannot be transposed to natural conditions because building sandstones are subjected simultaneously to absorption–drying and freeze–thaw cycles. The specific conditions of this experimental method have focused only on the freeze–thaw process and this can explain the lack of cracking of the blocks tested at partial saturation. Lack of cracking also concurs to the opinion of a few authors who think that wetting–drying cycles play a more important part than ice in stone weathering (Dunn & Hudec 1972; Fahey & Dagesse 1984; Pissart & Lautridou 1984; Hamès *et al.* 1987; Weiss 1992).

In the same conditions of exposure, Meules

sandstone, which is characterized by fast capillary absorption and slow drying, becomes more saturated than Vosgien sandstone, characterized by slow capillary absorption and fast drying. Different capillary and drying transfers in the two sandstones are not taken into account in these experimental conditions while in natural conditions they may play a major role. They can explain why, in natural conditions and contrary to the experiments, the Vosgien sandstone of Alsatian buildings does not present cracks attributable to frost while the Meules sandstone is subjected to important cracking during frost periods.

The results have demonstrated the importance of wetting–drying periods in changing the porous network which can then lead to material damage. It seems that most of the damage usually attributed to frost action cannot be imputed to ice formation. Wetting–drying cycles, accentuated by freezing, are probably the main cause of stone weathering.

This is EOST Contribution No. 2002-301-UMR 7517. We would like to thank J.-D. Bernard, M. Darot and T. Reuschlé of the Institut de physique du globe of Strasbourg for allowing us to measure the mechanical properties of sandstone samples at the laboratory of rock mechanics. We also wish to thank L'Oeuvre-Notre-Dame for presenting us with the cold room and for granting us access to the cathedral building site in view of the observations to be made there for our study. Thanks to Arlette and Mathieu.

References

ACHESON, D. T. 1963. Vapor pressure of saturated aqueous salt solutions. *In*: *Humidity and Moisture*. Rheinhold. New York, **3**, 521–530.

BLACHÈRE, J. R. 1975. Le gel de l'eau dans les matériaux poreux. *VIème Congrès international FFEN*, Le Havre, 296–303.

BOUSQUIE, P. 1979. *Texture et porosité de roches calcaires*. Thesis, l'Université Paris VI et Ecole des Mines de Paris.

CHAHAL, R. S. AND MILLER, R. D. 1965. Supercooling of water in glass capillaries. *British Journal of Applied Physics*, **16**, 231–239.

DUNN, J. R. & HUDEC, P. P. 1972. Frost and sorption effects in argillaceous rocks. Frost action in soils. *Highway Research Record* (Highway Research Board), **393**, 65–78.

EVERETT, D. H. 1961. The thermodynamics of frost damage to porous solids. *Transactions of the Faraday Society*, **57**, 1541–1551.

FAGERLUND, G. 1971. Degré critique de saturation: un outil pour l'estimation de la résistance au gel des matériaux de construction. *Matériaux et Constructions RILEM*, **4**(23), 271–283.

FAHEY, B. D. & DAGESSE, D. F. 1984. An experimental study of the effect of humidity and temperature variations on the granular disintegration of argillaceous carbonate rocks in cold climates. *Arctic and Alpine Research*, **16**, 291–298.

GREGORY, A. R. 1976. Fluid saturation effects on dynamic elastic properties of sedimentary rocks. *Geophysics*, **41**, 895–921.

HAMÈS, V. LAUTRIDOU, J. P. OZER A. & PISSART A. 1987. Variations dilaométriques de roches soumises à des cycles "humidification-séchage". *Géographie Physique et Quaternaire*, **XLI**(3), 345–354.

HIRSCHWALD, J. 1912. *Handbuch der bautechnischen Gesteinsprüfung*. Berlin Borntraeger.

KATZ, A. J. & THOMPSON, A. H. 1986. Quantitative prediction of permeability in porous rock. *Physical Review*, **34**(7), 8179–8181.

LAUTRIDOU, J. P. & OZOUF, J. C. 1978. Relation entre la gélivité et les propriétés pétrophysiques des roches calcaires. *Colloque Internationnal de l'UNESCO/RILEM sur l'Altération et la Protection des Monuments en Pierre*, Paris, 3.3 report.

LAUTRIDOU, J. P. & OZOUF, J. C. 1982. Experimental frost shattering: 15 years of research at the Centre de Géomorphologie du CNRS. *Progress in Physical Geography*, **6**(2), 215–232.

LETAVERNIER, G. 1984. *La gélivité des roches calcaires, relation avec la morphologie du milieu poreux*. Thesis l'Université de Caen, France.

LITVAN, G. G. 1978. Freeze–thaw durability of porous building materials. *In*: *Durability of Building Materials and Components*. Special Technical Publication STP 691, American Society for Testing and Materials, 455–463.

LLIBOUTRY, L. 1964. *Traité de glaciologie*. Masson, Paris.

MADER, D. 1985. Aspects of fluvial sedimentation in the Lower Triassic Buntsandstein of Europe. *Lecture Notes in Earth Sciences*, **4**, Springer, Berlin.

MERTZ, J. D. 1991. *Structures de porosité et propriétés de transport dans les grès*. Sciences géologiques, no. **90**. PhD Thesis, University Louis Pasteur, Strasbourg.

NF B 10–502. 1980. *Pierres calcaires: mesure de l'absorption d'eau par capillarité*. AFNOR.

NF B 10–503. 1973. *Mesures de la porosité, de la masses volumique réelle et de la masse volumique apparente*.

NF B 10–505. 1973. *Pierres calcaires: mesure de la propagation du son (ondes longitudinales)*. AFNOR.

PISSART, A. & LAUTRIDOU, J.-P. 1984. Variations de longueur de cylinders de Pierre de Caen (calcaire bathonien) sous l'effet de séchage et d'humidification. *Zeitschrift für Geomorphologie*, suppl. **49**, 111–116.

POWERS, T. C. 1956. Résistance au gel du béton jeune. *Colloque RILEM "Bétonnage en hiver"*, Cophenague.

POWERS, T. C. & HELMUTH, R. A. 1953. Theory of volume changes in hardened Portland cement paste during freezing, *Proceedings of Highway Research Board*, **32**, 285–297.

PRICK, A. PISSART, A. & OZOUF J-C. 1993. Variations dilatométriques de cylindres de roches calcaires subissant des cycles de gel-dégel. *Permafrost and Periglacial Processes*, **4**, 1–15.

REMY, J. M. 1993. *Influence de la structure du milieu poreux carbonaté sur les transferts d'eau et les changements de phase eau-glace. Application à la durabilité au gel de roches calcaires de Lorraine.* PhD Thesis, l'Institut National Polytechnique de Lorraine, France.

SCHLÜNDER, E. U. 1963. A simple procedure for measurement of vapor pressure over aqueous salt solutions. *In*: *Humidity and Moisture*. Rheinhold, New York, **3**, 535–544.

THOMAS, W. N. 1938. *Experiments on the freezing of certain buildings materials*. Department of Scientific and Industrial Research (Great Britain), Building Research Station, Technical Paper **17**.

WEISS, G. 1992. Die Eis- und Salzkristallisation im Porenaum von Sandsteinen und ihre Auswirkungen auf das Gefüge unter besonderer Berücksichtigung gesteinsspezifischer Parameter. *Münchner Geowissenschaftiche Abhandlungen*, B, **9**.

ZINSZNER, B. & MEYNOT, C. 1982. Visualisation des propriétés capillaires des roches réservoirs. *Revue de l'Institut Français du Pétrole*, **37**, 337–361.

Deterioration of the Globigerina Limestone of the Maltese Islands

JOANN CASSAR

Institute for Masonry and Construction Research, University of Malta, Msida MSD06, Malta (e-mail: joann.cassar@um.edu.mt)

Abstract: The Globigerina Limestone occurs as two types of building stone: the resistant 'franka' and the easily weathering 'soll'. Research on both fresh and weathered samples has led to an understanding of the main differences in these two types of stone. The causes and mechanisms of deterioration have also been established. 'Franka' and 'soll' differ in geochemical and mineralogical composition and in physical properties. The 'soll' is richer in the non-carbonate fraction, which occludes some of the pore space, resulting in a lower overall porosity and a higher proportion of small pores. The ambient local environment, heavily loaded with sea salt, particularly sodium chloride and sulphates, readily induces deterioration in 'soll', whereas 'franka' tends to resist better in this aggressive environment. The weathering process of Globigerina Limestone in general has been explained as a sequence of steps, from the formation of a thick and compact superficial crust, to the loss of this crust, to the initiation of alveolar weathering. Understanding the deterioration mechanisms of Globigerina Limestone permits criteria for proper conservation treatment to be established.

The Maltese Islands, consisting of two main islands, Malta and Gozo, as well as a small number of islets, are rich in built heritage. Monuments built of the local limestone range from unique prehistoric, megalithic temples (Fig. 1) to Baroque palaces (Fig. 2), churches and fortifications. Many of these monuments are of international importance and are included in the UNESCO World Heritage List. These include the prehistoric temples of Hagar Qim, Mnajdra, Tarxien and Ggantija (amongst others) and the fortified city of Valletta, the capital city of Malta. Most monuments and vernacular architecture are built of the local Globigerina Limestone, one of the few natural resources of the islands. The Upper and Lower Coralline Limestone formations were also used for building in the past, but to a much lesser extent. In the prehistoric temples of Malta and Gozo, the outer wall is usually built of Coralline Limestone, as for example in the Mnajdra and Ggantija temples. The outside of the Citadel of Gozo is mostly built of Ghajn Melel Member of the Upper Coralline Limestone (Table 1). The Gebel Imbark Member was also used in the decoration of facades in Valletta. However, it is the Globigerina Limestone that has been largely used for building in the Maltese Islands. This stone is even today a keystone of the local economy. It can be described as a typical 'soft limestone', very easy to carve and shape. It forms part of the large family of Oligo-Miocene 'soft limestones' which are widely distributed in the Mediterranean area.

Even casual observation shows great variability in weathering properties of this stone. This can be attributed to the interaction of its intrinsic properties with external conditions. The building stone obtained from the Globigerina Limestone Formation is fairly homogeneous in texture and colour. Stone that appears different in the quarry is traditionally not used for building. However, within the Globigerina Limestone, Maltese stone workers have long distinguished two varieties. 'Franka' (or freestone) is the generic name, whereas 'soll' (sometimes written as 'sol') is the name ascribed to building stone that weathers easily. Layers of 'franka' and 'soll' can also be seen in abandoned, exposed quarry faces (Fig. 3). Thus, 'franka' will withstand exposure well, mellowing into a honey-coloured stone with a resistant surface often colonized by multi-coloured lichens, as seen in some areas of the megalithic buildings erected during the fourth millennium BC (Fig. 4). On the other hand, 'soll' blocks deteriorate and powder away after a few decades and often show varying degrees of alveolar (or honeycomb) weathering, losing much of their original thickness in the process (Fig. 5).

In addition to intrinsic properties, external environmental conditions have an important role to play in the deterioration of building stone. It has been known for millennia that areas close to the sea are likely to be severely affected by salt weathering. This fact was mentioned by Marcus Vitruvius Pollio in the first century BC and continues to be discussed and debated even

From: SIEGESMUND, S., WEISS, T. & VOLLBRECHT, A. 2002. *Natural Stone, Weathering Phenomena, Conservation Strategies and Case Studies*. Geological Society, London, Special Publications, **205**, 33–49.
0305-8719/02/$15.00 © The Geological Society of London 2002.

Fig. 1. Prehistoric megalithic temple complex of Hagar Qim, built entirely of Globigerina Limestone. One of a series of free-standing constructions in the Maltese Islands, the earliest surviving structures built by man.

Fig. 2. One of the imposing Baroque buildings of Valletta, built of Globigerina Limestone.

Table 1. *Lithostratigraphical subdivisions on the Maltese Islands (Oil Exploration Directorate 1993)*

Formation/Member	Thickness (m)	Lithologies
Upper Coralline Limestone Formation		
Gebel Imbark Member	4–25	Hard pale grey carbonates with sparse faunas. Deposits now restricted to erosional outliers and synclinal cores.
Tal-Pitkal Member	30–50	Pale grey and brownish-grey coarse grained wackestones and packstones containing significant coralline algae, mollusc and echinoid bioclasts
Mtarfa Member	12–16	Massive to thickly bedded carbonate mudstones and wackestones, yellow in their lower levels and unconformable upon Greensand in western outcrops. Carbonates become white and chalky in the upper two-thirds of eastern outcrops.
Ghajn Melel Member	0–13	Massive bedded dark to pale brown foraminiferal packstones containing glauconite occur above a basal upper Coralline Limestone erosion surface in western Malta.
Greensand Formation	0–11	Friable, brown to greenish glauconite-rich sands occur above a marked erosion surface truncating the Blue Clay Formation.
Blue Clay Formation	15–75	Medium grey and soft, pelagic marls, typically with well developed pale bands rich in planktonic foraminifera but lower clay content.
Globigerina Limestone Formation		
Upper Globigerina Limestone Member	8–26	A tripartite, fine-grained planktonic foraminiferal limestone sequence comprising a lower cream-coloured wackestone, a central pale grey marl and an upper pale cream-coloured wackestone
Middle Globigerina Limestone Member	15–38	A planktonic foraminifera-rich sequence of massive, white, soft carbonate mudstones locally passing into pale-grey marly mudstones.
Lower Globigerina Limestone Member	0–80	Pale cream to yellow planktonic foraminiferal packstones rapidly becoming wackestones above the base.
Lower Coralline Limestone Formation		
Il-Mara Member	0–20	Tabular beds of pale-cream to pale-grey carbonate mudstones, wackestones and packstones in 1 to 2 m thick units.
Xlendi Member	0–22	Planar to cross-stratified, coarse-grained limestones (packstones) with abundant coralline algal fragments.
Attard Member	10–15	Grey limestones (wackestones and packstones) are typical throughout Malta.
Maghlaq Member	>38	Massive bedded, pale yellowish grey carbonate mudstones are dominant, benthonic foraminifera alone are frequent.

in recent years (Goudie & Viles 1997). The physical and chemical properties of stone will then determine the degree and type of salt-induced deterioration it undergoes.

This paper is an overview of research carried out from 1982 to date on the composition and properties of Globigerina Limestone and studies on its deterioration. This paper illustrates differences in geochemical, mineralogical, petrographical and physical properties of 'franka' and 'soll' types of Globigerina Limestone, which give rise to variations in durability. These results, combined with data on the types and concentrations of soluble salts present in weathered stone, which salts originate primarily from the sea, have led to the establishment of a weathering model for Globigerina Limestone.

Geological context

The Maltese Islands consist of only 316 km^2 of exposed land, lying 93 km due south of the

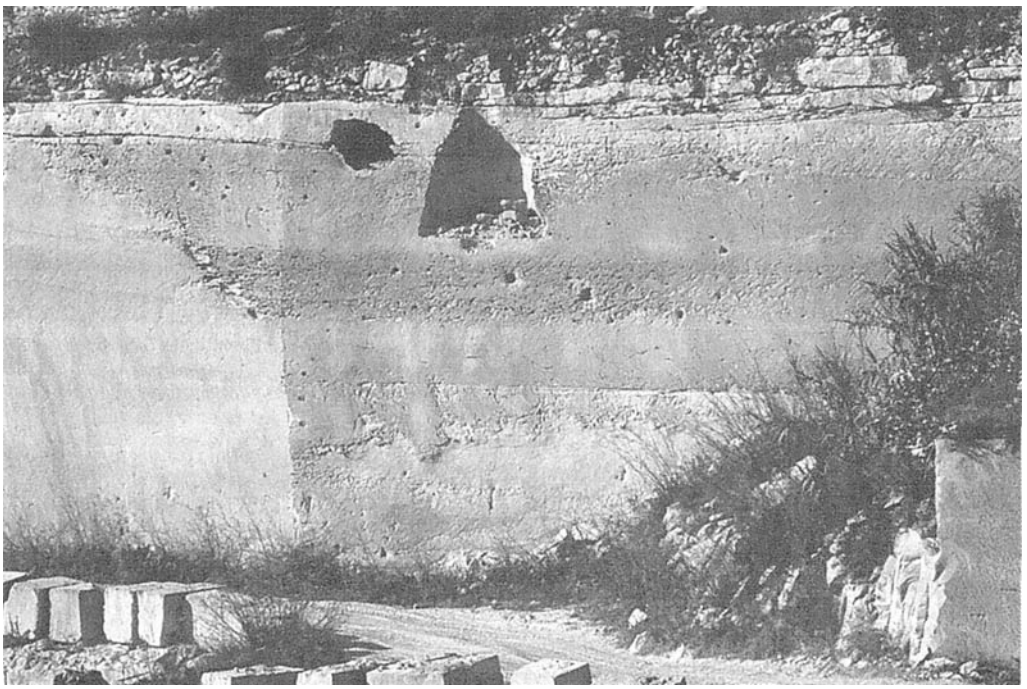

Fig. 3. Layers of 'franka' and 'soll', easily distinguished by their different weathering character, in an abandoned quarry face.

Ragusa Peninsula of Sicily on the southern end of the Pelagian shelf. The islands are characterized by Mesozoic sediments ranging from pure to marly carbonates, formed in shallow waters (0–150 m) on a stable near-horizontal platform. This region has seen continuous carbonate sedimentation since the Triassic. The outcropping succession is Oligo-Miocene in age and is made up of a series of limestones and associated marls and, more rarely, dolomitic limestones and dolomites, as well as sporadic Quaternary deposits (Pedley 1978).

There are five main formations in the Maltese Islands: Upper Coralline Limestone, Greensand, Blue Clay, Globigerina Limestone and Lower Coralline Limestone (Table 1).

The Globigerina Limestone Formation crops out mainly in the central and southern parts of the main island of Malta, and in the western part of the smaller island of Gozo. It is thick-bedded at outcrop. Sections where bioturbation is concentrated are common (Figs 6 and 7). This formation is divided into three members by two continuous phosphorite-rich horizons, which are usually about 50 cm thick. The three members thus formed are: the Upper, Middle and Lower Globigerina Limestone. The Lower Globigerina facies is the main material employed in building. It is composed primarily of massive, pale cream to yellow, globigerinid-rich biomicritic limestones and partially marly limestones. Macrofossils are abundant only locally and consist of molluscs, echinoderms, bryozoa and various pteropod species.

Within the Lower Globigerina Limestone, 'franka' and 'soll' types usually occur in layers, which vary in thickness. The first written reference to 'soll' was made by C.H. Colson, who called it *'saul'* (Murray 1890). He described the quarries at 'Ta Daul' (now known as 'Tad-Dawl', in Mqabba), as consisting of different layers. The author mentions 'a layer of darker stone that will not stand exposure called 'Saul'.' In 1958, an unpublished report on Maltese stone by the Building Research Establishment mentions 'soll' stone as sometimes occurring in otherwise good quality strata. Though the authors state that this stone type is referred to in published work as being darker than 'franka' and hence easily identified, it is argued that less durable stones could originate from occasional poor seams in a quarry, which would be difficult to identify in advance. Much research, primarily by staff and students at the University of Malta, has

Fig. 4. Two well preserved Globigerina Limestone megaliths in the Hagar Qim temple complex, showing extensive lichen growth on the sound surfaces.

been carried out on 'franka' and 'soll' types from 1982 to date, aimed at filling in this void – that of identifying, and subsequently characterizing, these two stone types.

Research programmes

Four research programmes on Globigerina Limestone have been carried out by various researchers (Table 2). Samples were obtained from boreholes, fresh and abandoned quarry faces, archaeological sites and a historical building. The great majority of these sites are located in and around Siggiewi/Mqabba/Qrendi in Malta (Fig. 8); this is also the main quarry area of the Maltese Islands. In addition, continuous environmental monitoring took place in the village of Siggiewi over a period of 15 months, including the sampling and analysis of marine aerosol and total particle (dust) deposition.

Research programme 1

The geochemical, mineralogical and petrographical characterization of the Lower Globigerina Limestone of the Maltese Islands (Cassar 1999) included the analyses of 122 samples taken from cores obtained from three boreholes (B1, B2 and B3) located in the main Mqabba/Tal-Handaq quarry area (Fig. 8).

Of these samples, 109 samples were Lower Globigerina Limestone. A subset consisted of 90

Fig. 5. Pronounced deterioration, including alveolar weathering (honeycombing), of Globigerina Limestone in a Valletta building.

samples that were visibly similar, being homogeneous in colour and texture, considered to be representative of the commonly used building stone.

This research programme was also aimed at the identification and geochemical characterization of the 'franka' and 'soll' types within the Lower Globigerina Limestone, as well as mineralogical and petrographical studies. Geochemical analyses were carried out by X-ray fluorescence (XRF) and atomic absorption spectrometry (AAS), mineralogical identification by X-ray diffraction (XRD) and petrographical studies by polarizing microscope (Cassar 1999). XRF was carried out using a Philips PW 1480 spectrometer. Conditions employed for major elements were those recommended by Franzini & Leoni (1972). The concentrations of elements were obtained from calibration curves, using 15 international carbonate standards (Cassar 1999). The errors associated with each element were calculated and ranged from 4% for TiO_2 and Fe_2O_3, to 7% for Al_2O_3, to 10% for SiO_2, to 11% for K_2O. AAS was carried out using a Perkin Elmer 303 AAS, with an air-acetylene flame. The error recorded here was on average 3%. XRD was carried out utilizing a Philips PW 2233/20 X-ray diffractometer; the 2θ angular range was 2° to 42°. The relative proportions of the minerals present were estimated by measuring the relative peak heights. Knowing the approximate concentration of calcite, as $CaCO_3$, from calcimetric analysis, allowed the concentration of the non-carbonate fraction to be fairly accurately known. This was then used to estimate the concentrations of the non-calcite minerals, following the relative heights of the remaining peaks. Calcimetric determinations were carried out utilizing a Dietrich-Frühling calcimeter. The volume of CO_2 evolved was determined following treatment of a weighed, dry powdered sample with HCl. The errors for these measurements were calculated as a maximum of 4% in the 70–90% range, the range of $CaCO_3$ concentrations of interest in this work.

Samples from two abandoned quarry faces in an active quarry in Mqabba were also analysed. These 23 samples were identified in the field by their weathering forms. The exposed surfaces were in all cases removed before the analyses (Vella *et al.* 1997; Cassar 1999). Subsequently, this research was extended to include 28 fresh samples obtained from active quarry faces, the

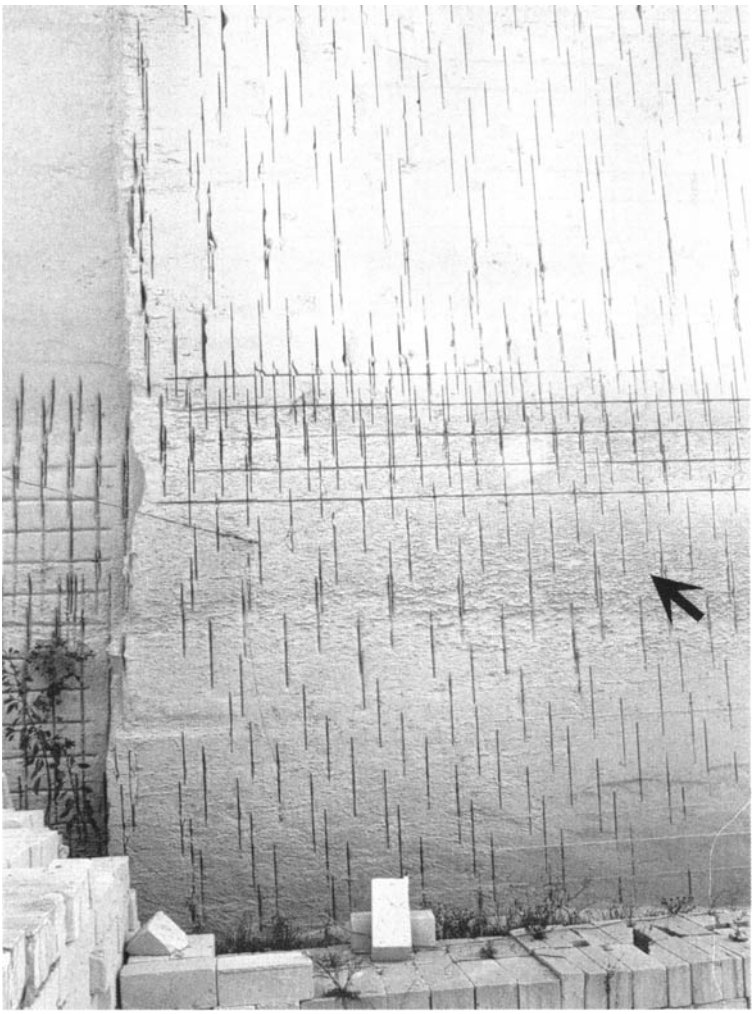

Fig. 6. View of a recently abandoned quarry face, showing a layer (arrow) where bioturbation is evident.

'franka' and 'soll' types being visually identified by quarry owners (Cassar 1999).

Research programme 2

Total porosity of fresh quarry samples was investigated by helium pycnometry, and pore size distributions by mercury intrusion porosimetry. The pycnometer used was a Quantachrome helium gas pycnometer; core samples with diameter:length ratio of 1:1 were prepared. The estimated error for these measurements was *c.* 1%. A Quantachrome Porosimeter, series As-33, with Quantachrome Poro2pc software was used for pore size distribution measurements. The procedure used was based on NORMAL 4/80 (1980). The estimated error of the results is *c.* 1%. The first work was carried out in 1993 by an undergraduate student (P. Farrugia) at the Faculty of Architecture and Civil Engineering of the University of Malta. Here 12 samples visually identified by quarry owners as 'franka' or 'soll' were tested (Table 2). Later, similar work was carried out on 14 samples from the same quarry area by Fitzner *et al.* (1995, 1996).

Research programme 3

This research programme included the study of 70 samples from the prehistoric temples of Hagar Qim and Tarxien in Malta and Ggantija in Gozo (Fig. 8) and included dry cores as well as

Fig. 7. A closer view of bioturbation in weathered Globigerina Limestone. The length of the large trace is approximately 6 cm.

surface chippings. Both badly weathered and sound megaliths were sampled, the precise location being chosen primarily on the basis of archaeological and conservation considerations. Mineralogical analyses were carried out and physical properties (porosity, pore size distribution and water absorption characteristics) were determined. Soluble salts present were also identified by wet chemical methods (Vannucci *et al.* 1994).

Table 2. *Summary of sampling campaigns and types of analyses carried out*

Sampling and analyses	Location	Researcher	Year of publication	No. of samples	Analyses				
					Geochemical	Mineralogical	Petrographical	Physical	Soluble salts
Fresh samples									
Boreholes	Mqabba/Tal-Handaq	Cassar	This study	90	x	x	x		
Quarries	Mqabba/Qrendi/Kirkop	Cassar	This study	28	x				
	Naxxar/Siggiewi/Kirkop Qrendi/Mqabba	Farrugia	This study	12				x	
	Mqabba/Siggiewi/Naxxar	Fitzner *et al.*	1995, 1996	14		x	x	x	
Weathered samples									
Quarries	Mqabba	Vella *et al.*	1997	23	x				
Prehistoric temples	Qrendi, Tarxien, Gozo	Vannucci *et al.*	1994	70		x		x	x
Historical building	Siggiewi	Fassina *et al.*	1996	47					x
Air sampling									
nternal/external	Siggiewi	Torfs *et al.*	1996	80					x

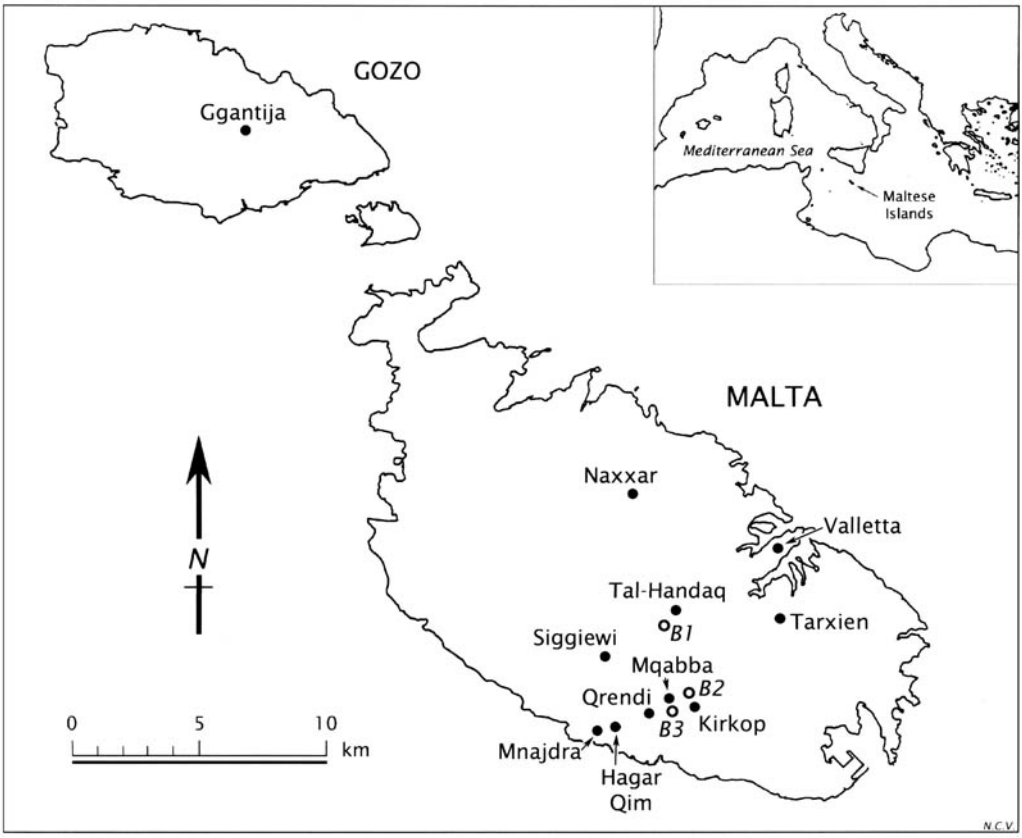

Fig. 8. Map of the Maltese Islands, showing the main quarry areas, as well as locations of buildings sampled for study purposes. B1, B2 and B3 are the three boreholes sampled.

Research programme 4

A separate research programme concerned the seventeenth century church of Santa Marija Ta' Cwerra in the village of Siggiewi (Fig. 9). A total of 47 samples were obtained from inside the church by dry drilling different walls at various heights and to different depths. These, as well as samples of efflorescence, were subjected to soluble salt analyses, both chemical, by ion chromatography (IC) and mineralogical, by XRD (Fassina *et al.* 1996). Ion chromatography was used for Cl^-, NO_3^- and SO_4^{2-} determinations, using a Dionex 4000i instrument. Estimated uncertainty is 5%.

This research programme also involved 15 months of continuous environmental monitoring, both internally and externally, as well as air and total particulate deposition sampling and analyses. Environmental monitoring was carried out from April 1994 to June 1995. Internal sensors measured hourly values for air temperature, relative humidity and wall temperature, while external sensors measured air temperature and relative humidity. Wind speed and direction and solar radiation were also monitored. Particulate deposition on the roof was collected every week from March 1994 to December 1995; about 80 samples were collected. Outdoor aerosols were also collected weekly during the same period. Analyses of the particulate deposition were carried out using IC, AAS and atomic emission spectrometry (AES), whereas aerosols were analysed by energy dispersive X-ray fluorescence (EDXRF) and IC/AAS/AES (Torfs *et al.* 1996). For EDXRF, a Tracor Spectrace 5000 instrument was used, having a Si(Li) detector and a Rh target. The X-ray spectra were analysed using AXIL software. Accuracy is in the range of 5%. For AES, the instrument used was a Perkin Elmer 3030 spectrometer. The average relative standard deviations for real samples are usually about 1 to 10%.

Fig. 9. The seventeenth century church of Santa Marija Ta' Cwerra, in the village of Siggiewi.

Table 3. *Geochemical data for Lower Globigerina Limestone*

	Na_2O	MgO	Al_2O_3	SiO_2	K_2O	P_2O_5	CaO	TiO_2	MnO	Fe_2O_3
Minimum (%)	0.00	0.30	0.40	1.8	0.04	0.10	44.49	0.03	0.00	0.26
Maximum (%)	0.19	1.08	2.90	9.4	0.47	0.71	52.87	0.20	0.02	1.64
Mean (%)	0.04	0.71	1.18	4.0	0.19	0.21	49.71	0.08	0.01	0.66

Data are for 90 samples obtained from boreholes and unclassified with respect to 'soll' or 'franka' (Cassar 1999)

Results

Unweathered samples

General data. The geochemical profile of fresh, homogeneous Lower Globigerina Limestone is given in Table 3. Within the non-carbonate fraction, SiO_2 is present in highest concentrations, reaching a maximum of 9.4%, followed by Al_2O_3 with concentrations up to 2.9%, and Fe_2O_3, with up to 1.64% (Cassar 1999).

Mineralogical data relevant to the same samples are given in Table 4. The main minerals occurring in the insoluble residue are phyllosilicates (up to 12%) and quartz (up to 8%), confirming the high Si and Al values obtained by geochemical analysis. K-feldspars occur up to concentrations of 1%, and there are occasional plagioclases and apatite (Cassar 1999).

Porosity studies on unweathered Globigerina Limestone reveal that it has a high total porosity, which varies considerably with both location and depth of sampling. Values obtained by different researchers range from 32% up to 41%. Pore size distributions are discussed in the following sections.

'Franka' and 'soll' types. Results for 'franka' and 'soll' samples from both fresh and abandoned quarry faces show a distinct difference in

Table 4. *Main mineralogical composition of Lower Globigerina Limestone*

	Q%	K-F%	P	Ph%	Ap	D	C% (calcim.)	IR% (diff.)
Ranges	tr. – 8	0 – 1	0 – tr.	1 – 12	0 – +	0 – tr.?	86 – 99	1 – 14

Data are for 90 samples obtained from boreholes (Cassar 1999)
Key: Q, quartz; K-F, potassium feldspars; P, plagioclases; Ph, phyllosilicates; Ap, apatite; D, dolomite; C, calcite; calcim., calcimetry; IR, insoluble residue; diff., by difference; tr., traces; +/++, presence in amounts as indicated by the number of plus signs; ?, an uncertain result

Table 5. *Preliminary geochemical data for 'franka' and 'soll' limestone types, including results of t-test for statistical significance*

	Type	N	Mean	Std. Deviation	t	Significance (2-tailed)
Al_2O_3	soll	25	1.34	0.61	5.44	0.000
	franka	26	0.65	0.19		
SiO_2	soll	25	4.79	1.8	5.72	0.000
	franka	26	2.57	0.79		
K_2O	soll	25	0.20	0.085	5.05	0.000
	franka	26	0.10	0.048		
TiO_2	soll	25	0.11	0.052	4.85	0.000
	franka	26	0.053	0.017		
Fe_2O_3	soll	25	0.75	0.28	5.4	0.000
	franka	26	0.43	0.12		

Data are for samples obtained from fresh and abandoned quarry faces (Cassar 1999).
Independent samples test; t-test for equality of means; 95% confidence interval

the composition of the non-carbonate fraction of the two types of Globigerina Limestone. The elements that particularly distinguish 'franka' from 'soll' limestone are Al_2O_3, SiO_2, K_2O, TiO_2 and Fe_2O_3 (Cassar 1999). Preliminary data are given in Table 5.

Mineralogical studies on the two stone types correlated the mineral phases associated with the geochemical differences. 'Soll' is thus generally richer in quartz (8%) and phyllosilicates (12%) than 'franka'. In 'franka' stone, quartz occurs to a maximum of 2% and phyllosilicates to a maximum of 3% (Cassar 1999). This would appear to contradict the conclusions drawn by Fitzner *et al.* (1996) who stated that a correlation between mineral composition and different stone qualities could not be recognized.

Thin sections of both 'franka' and 'soll' samples were observed microscopically. It was seen that the pore spaces of the 'franka' are both inter- and intra-granular, with the fossil chambers generally being empty. On the other hand, the 'soll' pores are primarily inter-granular, with parts of the fossil chambers often being filled.

Porosity measurements on 'franka' and 'soll' samples have to date been rather limited. Two studies undertaken, one by the University of Malta (1993) and one by Fitzner *et al.* (1995, 1996) show 'soll' limestone to have a lower overall porosity than 'franka'. The first study found an average total porosity of 32.2% for 'soll' samples compared with an average of 38.3% for 'franka' samples. The range of values for 'soll' samples was 31.9% to 32.7%; for 'franka' samples the range of values obtained was of 38.2% to 38.5%. In the second study,

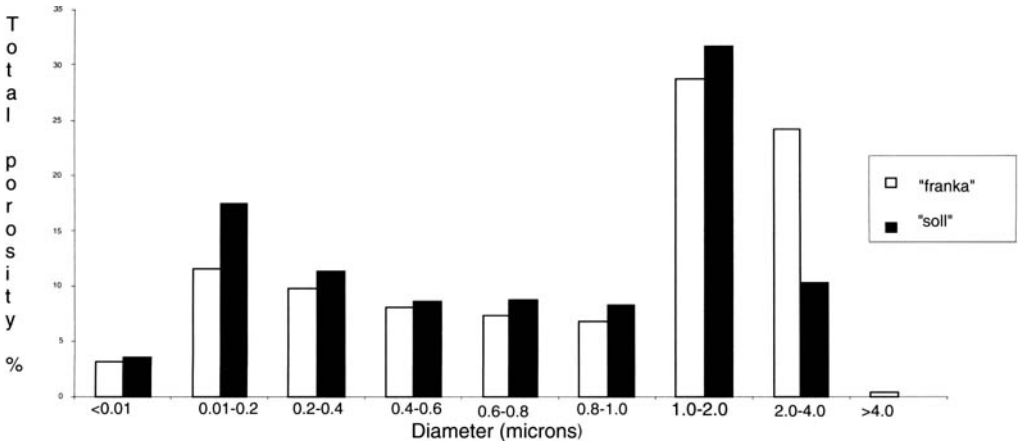

Fig. 10. Pore size distributions for two 'franka' and 'soll' samples taken from the same quarry in Mqabba.

samples of 'bad quality' ('soll') and 'good quality' ('franka') samples were analysed. Reported total porosity values for representative samples of each were 33% and 34.8% respectively (Fitzner *et al.* 1996). The samples were obtained from different quarries, at different depths, but in the same general quarry area (Table 2).

Pore size distributions within 'franka' and 'soll' types also vary. Both studies found that whereas 'franka' limestone has a greater proportion of large pores, 'soll' has more small and very small pores. An example of two samples, one 'franka' and one 'soll', both taken from the same quarry in Mqabba, at different depths, is given in Figure 10. Although these results are highly indicative, further work is currently being planned.

Weathered samples

General data. Soluble salt analyses of weathered Globigerina Limestone from the prehistoric temples of Hagar Qim, Tarxien and Ggantija show high concentrations of chlorides, sulphates and nitrates, compared with unweathered samples. Values obtained include chlorides in concentrations of up to 1.2% in surface samples (maximum in a sample from Tarxien) and up to 1.1% in the substrate (maximum in a sample from Ggantija) (Vannucci *et al.* 1994). Sulphates attain a maximum of 0.8% in samples from Tarxien. Nitrate concentrations of over 200 ppm (samples from all sites) and in one case over 700 ppm (sample from Hagar Qim) occur.

In the church of Ta' Cwerra, high concentrations of soluble salts also occur. Here it was possible to observe the distribution of salts within the walls. Sulphates are mainly concentrated in the lower parts of the walls; chlorides and nitrates appear mainly in higher areas (Fassina *et al.* 1996). Chlorides achieve a maximum concentration of 1.35% at 250 cm height and 0–5 cm depth; nitrate levels reach a maximum of 0.88% at the same height and depth, whereas sulphates reach a value of 0.24% at 0.5 m height and 0–5 cm depth. The concentration of Na^+ is in the range of 3.8% to 42.5%, depending on the location. The lowest concentrations were found in samples of badly deteriorated stone taken externally from the south wall; the sample with the overall highest concentration was also obtained externally form the south wall, this time from the depth of alveolar weathering. Other samples with moderately high Na^+ concentrations were obtained from efflorescence inside the church; here concentrations ranged from 16.0% to 21.9%. Concentrations of ions are expressed in weight per cent of the dissolved mass of sample.

Mineralogical analysis of weathered Globigerina Limestone samples has confirmed the presence of new mineral phases not detected in unweathered samples. Halite occurs in samples from all three temple sites and in the church of Ta' Cwerra. Other minerals include small amounts of sylvite, thenardite, gypsum, mirabilite and trona (Fassina *et al.* 1996). Possible sources of these salts include marine aerosol and air pollution. A primarily marine origin was confirmed by data obtained by analysing air and total deposition samples from Siggiewi. A different situation occurs in the

Fig. 11. View of one apse of the Tarxien prehistoric temples where extensive restoration work using Portland cement was carried out in the 1950s. All of the elements seen in this figure have been capped and/or coated with cement, whereas the large statue is a copy in cement of a stone original, now located in the National Museum of Archaeology.

Tarxien temples (Fig. 11); here one of the main sources is Portland cement that was used on a large scale in restoration works, including the capping of many megaliths, carried out in the 1950s. Microanalysis in fact confirmed the presence of sodium sulphate in fragments and core samples taken from Globigerina Limestone blocks that had in the past been capped with cement.

Porosity studies on weathered Globigerina Limestone from the prehistoric temple sites showed that total porosity generally varies between 19% and 52% (compared to 32–41% for unweathered stone). One exceptionally low value of 7.6% was also obtained. Low porosities usually occur in superficial crusts whereas higher porosities occur in internal samples (Vannucci *et al.* 1994). In a few samples, however, the surface layer is more porous than the substrate. Pore size distribution studies of weathered samples show that in some crusts there is an inversion in pore size distribution, with very small pores being found in the outer layer, the absolute maximum occurring at <0.2 μm (Vannucci *et al.* 1994). On the other hand, results to date have shown that in unweathered stone, both 'franka' and 'soll', maximum concentrations of pores occur between 1 and 4 μm (Fig. 10).

Differences in water absorption behaviour between crust and substrate are also evident. The absorption capacity by weight is a low 9% in crusts and a high 25% in substrates. The saturation index for the crusts is again usually less than that for the substrate, once again confirming the greater density of the outer crust. Values as low as 52% for crusts and as high as 97% for substrates occur; the saturation index for unweathered quarry samples is on average 89% (Vannucci *et al.* 1994).

Microscopic observations. In thin section, different samples of weathered Globigerina Limestone from the temple sites show the presence of a compact outer layer in various stages of formation (Vannucci *et al.* 1994). Secondary calcite gradually occludes the superficial pores, forming a compact crust over a more porous substrate, the latter often having irregular, intercommunicating voids. Other samples show an even more compact crust, about 1 cm thick,

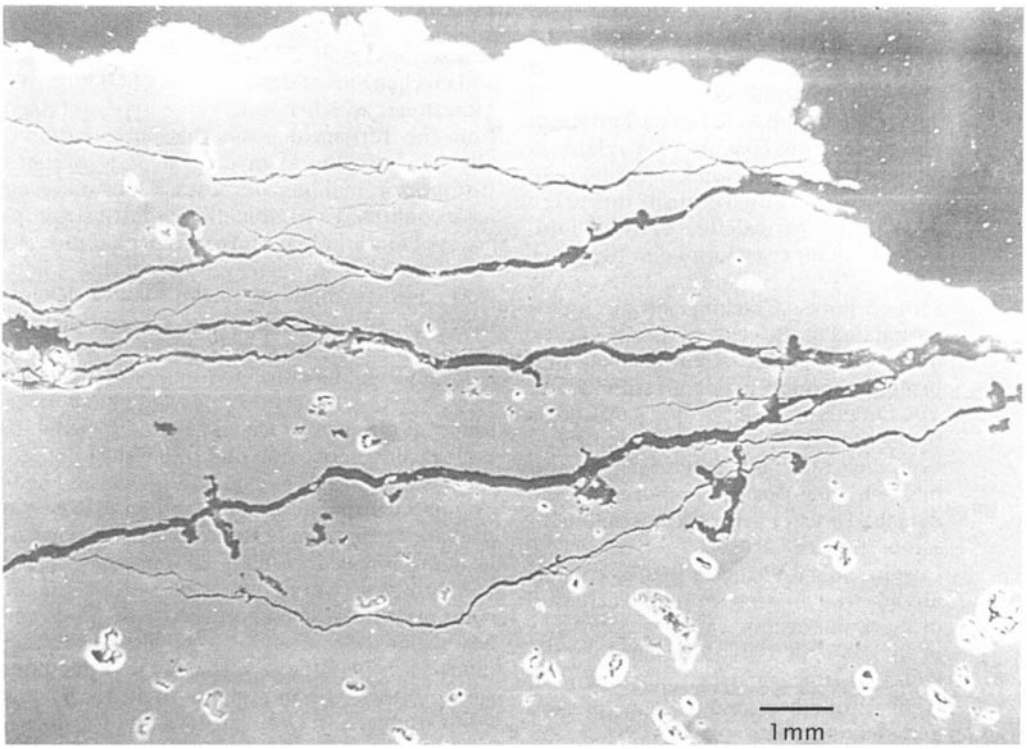

Fig. 12. Photomicrograph of part of a compact external crust, obtained from the Tarxien temples, which is intersected by a series of micro-cracks parallel to the external surface. These cracks have probably been caused by salts.

intersected by a series of micro-cracks parallel to the external surface (Fig. 12). These cracks are assumed to be original, and not due to thin section preparation, as embedded samples were used. SEM observations show the crusts to have compact external as well as internal surfaces. The external part of the crust is sometimes encrusted with halite. In some samples, on the other hand, the SEM shows surfaces virtually powdering away, probably where the crust has fallen off. This confirms porosity data which sometimes show surface layers to be more porous than the substrate.

Air sampling data. The major ions detected in total particulate deposition at Ta' Cwerra church are Na^+, Mg^+ and Cl^- and the most abundant elements in the aerosols are Ca, Na, Cl and S. As Na, Cl and S are mainly sea-derived elements, deterioration on the church walls is explained as being mainly influenced by the marine environment, although the village of Siggiewi is some kilometres away from the sea (Fig. 8). Ca, on the other hand, originates from the limestone itself. Relating the results of these analyses with the analyses of soluble salts from stone samples taken from the built environment, it is confirmed that the main source of soluble salts is the sea; anthropogenic emissions are considered to be of secondary importance (Torfs *et al.* 1996).

Deterioration processes: causes and mechanisms

Combining all available data, the weathering processes on Globigerina Limestone can be explained as a sequence of steps, as defined separately by Vannucci *et al.* (1994) and Fitzner *et al.* (1996). Here, these two weathering models are combined as follows.

1. Formation of a thick and compact surface crust due to reprecipitation of calcite originally dissolved from within the stone by absorbed water containing varying amounts of soluble salts. This

incipient crust can be called a 'protocrust' and is usually 1–2 cm thick.

2. Recurring cycles of dissolution and precipitation result in the formation of 'layers' of crust parallel to the surface of the stone. This consists of a relatively compact 'core', a weak intermediate zone with a very high porosity due to the dissolution of calcite, and a hard, compact outer crust formed by the deposition of reprecipitated calcite in the surface pores. Cracking, lifting and/or partial loss of the crust generally occurs, due to mechanical stress such as that brought about by salt crystallization. The underlying deteriorated substrate is thus exposed. This reveals loss of cohesion, corrosion and powdering. It also has a high porosity compared to the detached crust. Further accumulation of salt occurs.
3. Loss of the crust exposes a surface that is already much deteriorated. Increased evaporation occurs where the crust has been lost. Salt crystallization near the stone's surface causes detachment of stone through granular disintegration and 'flaking'. This phase is often followed by initiation of the process of alveolization (honeycombing). This depends on the number, orientation and size of the sedimentary structures (bioturbation) present. Due to this type of deterioration, a new crust is not able to form.
4. Further salt crystallization results in further loss of stone. Alveoli increase in depth. The rest of the crust loses contact with the substrate and falls off with adhering stone. The alveoli join up. Salt accumulation and detachment of stone material continue.
5. The final phase of alveolar weathering occurs. The receded stone surface gives rise to so-called 'back weathering', which may increase in depth by further detachment of stone material.

This is the general model for weathering of 'franka'. In the case of 'soll', the loss of large fragments of stone generally occurs at an early stage, and so no crust has time to form. Thus, one distinct difference between these two stone types is that the 'soll' tends to show severe deterioration even at low salt concentrations, whereas 'franka' will tend to resist better, at least low salt concentrations.

Conclusion

Our studies resulted in a definition of the causes and mechanisms of deterioration of Globigerina Limestone, which is one stone type obtained from the Tertiary deposits that have traditionally been exploited in central and southern Europe for building purposes. Data obtained have confirmed a combination of intrinsic properties of this lithology and external conditions to be responsible for decay. Globigerina Limestone used for building in the Maltese Islands occurs in two types: the 'franka' which usually weathers well and the 'soll' which deteriorates badly, even in the same environment. These two types of Globigerina Limestone have been found to differ in geochemical, and hence mineralogical, composition and in physical properties. As regards environmental causes, salts originating from the sea are considered to be the primary cause of deterioration. This is particularly pronounced in the 'soll' limestone, which has a lower overall porosity, with a higher concentration of small pores. As 'soll' limestone has higher concentrations of phyllosilicates and quartz, it is hypothesized that some of the pore space in this type of stone is occluded by this non-carbonate fraction. In fact, optical microscopy shows the 'soll' pores to be primarily intergranular, with parts of the fossil chambers often being filled. The pore spaces of the 'franka' are both inter- and intra-granular, with the fossil chambers generally being empty.

These findings also provide information on the sedimentary environment within which these two stone types formed. The Globigerina Limestone formation is known to have been deposited in waters <100 m deep (Pratt *et al.* 1991). In this low energy environment, clay minerals accumulated due to the absence of currents at this depth. The formation of the 'soll' member probably corresponds to periods of deposition of greater quantities of clastic material or to a slowing down of carbonate sedimentation. This then probably led to a reduction both in total porosity and in pore size.

When material with a high concentration of small and very small pores is placed in an environment that contains high concentrations of soluble salts, it cannot resist the periodic cycles of solution and recrystallization for long. Deterioration soon follows. Rossi Manaresi and Tucci (1991), working on various types of stone, including biocalcarenites from southern Italy (Puglia) and Sicily, concluded that high crystallization pressure attained when a stone with a large percentage of small pores (<1 μm) is contaminated with soluble salts, will lead to

salt-induced decay. Kozlowski *et al.* (1990), working on coarse- and fine-grained limestone, found that the coarser variety, with a higher percentage of large pores, is more resistant to damage than the fine-grained type, with a higher percentage of small pores.

Understanding the deterioration mechanisms of Globigerina Limestone, as discussed here, allows criteria for proper conservation treatment to be established. This must necessarily include the elimination, or at least the drastic reduction, of soluble salts within the material, and the prevention of recontamination. Unless this is carried out effectively, any subsequent treatment of the stone is bound to fail.

The author would like to acknowledge the work on Globigerina Limestone by student P. Farrugia of the Faculty of Architecture and Civil Engineering of the University of Malta, carried out during 1993. Some of the porosity data quoted in this study were the result of Farrugia's work. The author thanks G. Debono of the Oil Exploration Department, Malta, for his useful comments and A. Buhagiar of the University of Malta for his help with the statistics. Special thanks are also due to the late S. Vannucci, Professor of Applied Geology at the Department of Earth Sciences, University of Florence, Italy, for his help and advice throughout the years of research on Globigerina Limestone. This paper is dedicated to his memory.

References

CASSAR, J. 1999. *Geochemical and mineralogical characterization of the Lower Globigerina Limestone of the Maltese Islands with special reference to the 'soll' facies*. PhD Thesis, University of Malta.

FASSINA, V., MIGNUCCI, A., NACCARI, A., STEVAN, A., CASSAR, J. & TORPIANO, A. 1996. Investigation on the moisture and salt migration in the wall masonry and on the presence of salt efflorescence on stone surface in the Church of Sta. Marija Ta' Cwerra at Siggiewi, Malta. *In*: ZEZZA, F. (ed.) *Origin, Mechanisms and Effects of Salt on Degradation of Monuments in Marine and Continental Environments*. Proceedings, European Commission Research Workshop on Protection and Conservation of the European Cultural Heritage, Bari, Italy. Research Report No. 4, 291–308.

FITZNER, B., HEINRICHS, K. & VOLKER, M. 1995. Stone deterioration of monuments in Malta. *In*: Pancella, R. (ed.) *Preservation and Restoration of Cultural Heritage*. Proceedings, Laboratoire de Conservation de la Pierre Congress, Montreux, 89–100.

FITZNER, B., HEINRICHS, K. & VOLKER, M. 1996. Model for salt weathering at Maltese Globigerina Limestones. *In*: ZEZZA, F. (ed.) *Origin, Mechanisms and Effects of Salt on Degradation of Monuments in Marine and Continental Environments*. Proceedings, European Commission Research Workshop on Protection and Conservation of the European Cultural Heritage, Bari, Italy. Research Report No. 4, 331–344.

FRANZINI, M. & LEONI, L. 1972. A full matrix correction in X-Ray fluorescence analysis of rock samples. *Atti Societa' Toscana Scienze Naturali*, Memorie, Serie A, 79, 7–22.

GOUDIE, A. & VILES, H. 1997. *Salt Weathering Hazards*. John Wiley, Chichester.

KOZLOWSKI, R., MAGIERA, J., WEBER, J. & HABER, J. 1990. Decay and conservation of Pińczów porous limestone. I. Lithology and weathering. *Studies in Conservation*, **35**, 205–221.

MURRAY, J. 1890. The Maltese Islands, with special reference to their geological structure. *Scottish Geographical Magazine*, **6**, 449–488.

NORMAL 4/80. 1980. Distribuzione del volume dei pori in funzione del loro diametro. *Raccomandazioni NORMAL*, Centro Stampa ICR, Rome.

OIL EXPLORATION DIRECTORATE. 1993. *Geological map of the Maltese Islands*. Office of the Prime Minister, Malta.

PEDLEY, H. M. 1978. *A new lithostratigraphical and palaeoenvironmental interpretation for the Coralline Limestone formations (Miocene) of the Maltese Islands*. Overseas Geology and Mineral Resources, **54**, Institute of Geological Sciences, London.

PRATT, S., PEDLEY, M. & BOSENCE, D. 1991. The Globigerina Limestone Formation of Gozo: pelagic limestones, phosphorites and extensional tectonics. *In*: BOSENCE, D. (ed.) *Field Guide to the Cenozoic Platform Carbonates of the Maltese Islands*. Field Guide No. 22, British Sedimentological Research Group.

ROSSI MANARESI, R. & TUCCI, A. 1991. Pore structure and the disruptive or cementing effect of salt crystallisation in various types of stone. *Studies in Conservation*, **36**, 53–58.

TORFS, K., VAN GRIEKEN, R. & CASSAR, J. 1996. Environmental effects on deterioration of monuments: case study of the Church of Sta. Marija Ta' Cwerra, Malta. *In*: ZEZZA, F. (ed.) *Origin, Mechanisms and Effects of Salt on Degradation of Monuments in Marine and Continental Environments*. Proceedings, European Commission Research Workshop on Protection and Conservation of the European Cultural Heritage, Bari, Italy. Research Report No. 4, 441–451.

VANNUCCI, S., ALESSANDRINI, G., CASSAR, J., TAMPONE, G. & VANNUCCI, M. L. 1994. The prehistoric, megalithic temples of the Maltese Islands: causes and processes of deterioration of Globigerina Limestone. *In*: FASSINA, V., OTT, H. & ZEZZA, F. (eds) *Conservation of Monuments in the Mediterranean Basin*. Proceedings of the 3rd International Symposium, Venice, Italy, 555–565.

VELLA, A. J., TESTA, S. & ZAMMIT, C. 1997. Geochemistry of the soll facies of the Lower Globigerina Limestone Formation, Malta. *Xjenza*, Malta Chamber of Scientists, **2**, 27–33.

VITRUVIUS POLLIO, MARCUS. First century BC. *Vitruvius: The Ten Books on Architecture*. [Translated in 1960 by Morris Hicky Morgan. Dover Publications, New York].

This page intentionally left blank

Salt weathering: a selective review

ERIC DOEHNE

The Getty Conservation Institute, 1200 Getty Center Drive, Suite 700, Los Angeles, CA 90049-1684, USA (e-mail: edoehne@getty.edu)

Abstract: The past decade has seen a growing scientific interest in the still poorly understood subject of salt weathering, a phenomenon with significant cultural and economic consequences. This interest has led to an increase in research results and growing clarification of the roles salts play in weathering and decay. The development of improved mitigation methods to reduce the decay of building materials by salts has been a slow process, often arising from the analysis of unique field situations and otherwise dependent on simplified laboratory experiments and computer modelling. Collecting, reviewing, synthesizing and disseminating the existing data on salt weathering is a difficult task. The size and scope of the topic are mirrored in the diverse disciplines that have historically contributed to understanding the action of salts in porous materials and mitigation methods. Nevertheless, an appreciation of existing, even contradictory, data is an important tool for increasing understanding. There are now over 1800 research articles on the topic of salt weathering originating from several disciplines, as well as over 6000 references on the general problems of building material decay. In order to navigate such a vast collection of data and knowledge, this article describes the multidisciplinary nature of the study of salt damage to porous building materials, provides a framework for considering the complexity of salt damage, and serves as a selective literature survey largely focused on recent work and those articles with relevance for conservation.

'In time, and with water, everything changes'
(Leonardo da Vinci)

Over the past ten years, there has been increasing scientific interest in building material decay phenomena, especially the incompletely understood subject of salt weathering. The reaction of salts with moisture in rock outcrops produces an intriguing array of weathering forms such as tafoni, honeycombs and pedestal rocks, as well as abundant rock debris (Goudie & Day 1980; Mustoe 1982; Smith 1994). Salt weathering of building materials can be equally destructive (Haynes *et al.* 1996). Salt weathering is widely recognized as one of the primary agents in the deterioration of historical architecture, structures in archaeological sites, and archaeological objects (Schaffer 1932; Lewin 1982). Understanding and finding ways to reduce damage caused by salts holds great significance for the conservation of material cultural heritage (Torraca 1982; Amoroso & Fassina 1983; Goudie & Viles 1997). Moreover, damage to modern concrete building foundations caused by salts has recently been the subject of litigation leading to multi-million dollar settlements and judgments (Haynes 2002; Kasdan *et al.* 2002). Salt weathering is indisputably a process with profound cultural and economic consequences.

Salts have long been known to damage porous materials (Herodotus 420 BC; Luquer 1895) through the production of physical stress resulting from the crystallization of salts in pores (Taber 1916; Jutson 1918). Salts can damage stone and other building materials through a range of other mechanisms as well, such as differential thermal expansion, osmotic swelling of clays, hydration pressure, and enhanced wet/dry cycling caused by deliquescent salts (Smith 1994). A 1997 book by Goudie & Viles summarizing salt weathering hazards raised awareness of the problem and broadened the field of investigation in recent years. Despite this, many unresolved issues related to salt weathering remain, ranging from the details of the damage mechanisms (Flatt 2002) to the interactions between substrate, environment and salt type (Charola 2000), and the expression of this process in the landscape (Smith *et al.* 2000) and in building stone (Kuchitsu *et al.* 2000; Schwarz *et al.* 2000).

This article is intended to describe the multidisciplinary nature of the study of salt damage to porous building materials; communicate the complexity of salt weathering and discuss open questions; and serve as a limited literature survey largely focused on recent work and those articles with relevance for conservation.

From: SIEGESMUND, S., WEISS, T. & VOLLBRECHT, A. 2002. *Natural Stone, Weathering Phenomena, Conservation Strategies and Case Studies*. Geological Society, London, Special Publications, **205**, 51–64.
0305-8719/02/$15.00 © The Geological Society of London 2002.

Background

The majority of the published literature on salt weathering originates from a collection of distinct disciplines, each responsible for specific contributions: geomorphology, environmental science, geotechnical and materials science, geochemistry, and, lastly, conservation, perhaps the most multidisciplinary of the fields. There is a rich literature in geomorphology on salt weathering phenomena, particularly that published by scientists from the United Kingdom (Smith 1994; Goudie & Viles 1997). Environmental scientists have studied the important role of salts in atmospheric aerosols and their fallout (Pósfai *et al.* 1995; Torfs & Van Grieken 1997). The geotechnical field has dealt with expansive sulphate soils, or salt heave (Xiaozu *et al.* 1999), concrete decay from salt crystallization (Haynes *et al.* 1996; Mehta 2000; Haynes 2002), and testing of building materials using standardized salt crystallization tests such as ASTM aggregate sound test C88–90 (ASTM 1997), and RILEM PEM/25 (RILEM 1980). Materials scientists have provided useful insights on the fundamental mechanisms of salt attack (McMahon *et al.* 1992; Scherer 2000). In the geochemical literature, the concepts of pressure solution, force of crystallization, and displacive growth are important to understanding that salt attack is a part of a larger set of interrelated behaviours (Carstens 1986; Maliva & Siever 1988; Minguez & Elorza 1994). Finally, the conservation literature is vast and especially rich in case studies and documentation of methods of mitigating salt damage (Schwarz & Roesch 1993; Young 1995; Siedel 1996; Charola *et al.* 1998; Price 2000; Unruh 2001). Nevertheless, the conservation literature on salts can be difficult to survey, since many articles are published in conference proceedings (Price 1996). Two recent summaries of the literature illustrate the breadth of applicable research: an overview of the role of salts in the deterioration of porous materials by Charola (2000) and a discussion of salts and crusts by Steiger (2002).

Following these recent efforts, this paper presents a current survey of the multidisciplinary contributions to the field of salts and building deterioration. A large bibliography of research articles on salts and building deterioration phenomena was assembled in order to facilitate the integration of these related researches. Some observations based on this survey are discussed below, and an associated selected bibliography can be obtained from the Society Library or the British Library Document Supply Centre, Boston Spa, Wetherby, West Yorkshire LS23 7BQ, UK as Supplementary Publication No. SUP18182 (4 pages). It is also available online at www.geolsoc.org.uk/SUP18182.

A recitation of the sometimes significant, sometimes subtle, differences in terminology and definitions employed in the literature of salt weathering reveals the multidisciplinary nature of the scientific literature. The same basic phenomena are variously described in different disciplines and countries as salt attack, salt damage, salt crystallization, haloclastisme (French), and salzsprengung (German). Less common terms include salt burst, salt exudation, haloclasty, salt decay, salt crystallization pressure, crystal wedging, salt fretting, and salt heave in soils.

In the geomorphology literature, the terms 'honeycomb weathering', 'alveolar weathering', and the less common descriptors 'stone lattice', 'stone lace', and 'fretting' (Mustoe 1982), reference a characteristic form of salt weathering in stone defined by irregular cavities in otherwise regular rock surfaces, although in recent publications those terms are increasingly discarded in favour of the term 'tafoni' for cavities large and small. Substantial research has been performed by geomorphologists on tafoni (singular: tafone), a term that normally refers to pits and caverns in rock faces resulting from extensive salt weathering of stone in salt-rich and desert environments (Kirchner 1996; Turkington 1998). Tafoni also occur in humid temperate environments; however, it is not yet clear that salt weathering plays a role in the formation of tafoni in this type of climate (Mikulas 2001).

In the conservation literature, the term 'rising damp' is widely used to characterize salt weathering, but in Australia this process of moisture and salts mobilized by capillarity and deliquescence is regionally referred to as 'salt damp' (Young 1995). Many buildings and sites are also affected by salt-rich aerosols, which may accumulate and be mobilized by 'falling damp' or 'penetrating damp'.

In the concrete literature, the terms 'salt attack' and 'sulphate attack' are sometimes incorrectly used interchangeably (Mehta 2000), and recent authors have proposed the terms 'physical salt attack' or 'salt hydration distress' as distinct from the chemical reaction of salts with concrete (Haynes *et al.* 1996; Hime *et al.* 2001; Haynes 2002). Stone conservators typically use the terms 'desalting', 'salt extraction', or 'desalination', referring to salt reduction methods using immersion, intermittent washing, poulticing or compress treatments.

Given the variety of terms used and the

diversity of disciplines researching the topic of salt weathering, it seems clear that at least some of the apparent contradiction in the literature is merely the result of differences in terminology (Hime *et al.* 2001).

Salt damage: dealing with complexity

Two major difficulties encountered by those investigating salt weathering are the multiple variables involved and the fact that the physiochemical reactions of greatest importance occur along thin, nanometre-scale films inside a porous solid. Such interactions are inherently difficult to study in situ and in tempo, further inhibiting understanding of the degree of interaction between possible variables. To aid understanding of the variables, it is useful to classify them as properties of the substrate, solution, salt type, or environment (Fig. 1). The properties interact in specific ways determined by thermodynamic equilibria and kinetic factors to produce a range of salt behaviours.

It is important to note that not all salt behaviours result in deterioration. For example, the production of surface efflorescence is often impressive and highly visible, but generally results in little damage. Likewise, salt creep can move salts over the surface of materials but, as the name implies, is a surficial process. Salts such as magnesium sulphate can actually bind together (i.e. cement) previously fractured material.

Understanding the properties that contribute to a particular weathering effect, and differentiating between benign and damaging salt behaviours, allows the investigator to focus on the latter. Typical damage behaviours or processes for salts can include surface scaling, deep cracking, expansion, granular disintegration, surface powdering and microcracking. For particular damage mechanisms, such as crystallization pressure, the degree of damage (sometimes measured as the damage factor, damage function or dose-response function) is often attributable to specific properties and can be the single most important metric (Viles 1997). For example, in the case of sodium sulphate crystallization, the degree of supersaturation and the location of crystallization appear to be the keys to understanding the degree of damage (Rodriguez-Navarro & Doehne 1999*a*). In turn, there are a few important properties and kinetic factors, such as the evaporation rate, that largely control how much damage results from this mechanism (Fig. 1).

By focusing on the nature (i.e. moment, location and type) and, especially, the degree of salt damage, the field of variables, or properties, directly responsible can be narrowed considerably and investigators can begin to answer the questions most relevant to specific damage types. Why are certain types of stone much more vulnerable than other types to salt damage (Goudie 1999*b*)? Why are certain salts much more damaging than other salts (Hoffmann & Grassegger 1995; Aires-Barros & Mauricio 1997; Rodriguez-Navarro & Doehne 1999*a*)? Is damage caused mostly by relatively rare environmental events (rapid cooling) or cumulative everyday stresses (humidity cycling)? What are the long-term effects of various conservation treatments, such as desalination or consolidation, on salt damage? How can desalination and preventive conservation efforts be enhanced? Can general agreement be achieved regarding the fundamental mechanisms of salt weathering? What are the appropriate equations to use in calculating crystallization pressure (Duttlinger & Knöfel 1993; La Iglesia *et al.* 1997; Benavente *et al.* 1999; Scherer 1999; Charola 2000)? Can the large number of laboratory simulation studies of salt weathering be reconciled with field data and explained using existing theories? Can salt weathering forms such as tafoni be accurately modelled using existing knowledge? How do the behaviours of water, salts, and substrate compare at the important mesopore scale (2–50 nm) versus the macro-scale (Brown 2001; Hochella 2002)? These complex questions, together with such basic questions as how the hydration of salts progresses and how crystallization pressures are sustained in situ, are still in need of study (Charola & Weber 1992; Doehne 1994; Steiger *et al.* 2000). Nevertheless, the research performed in recent years and surveyed herein has significantly advanced overall understanding of the damage caused by salt weathering processes.

Deterioration due to salts: theory and laboratory observations

Several important advances in salt damage arising from theoretical and laboratory research have application for the conservation field and deserve highlighting. The research summarized here addresses the precise nature of the relationship between salt stress and material pore size; how supersaturated solutions develop and are maintained; the contradictory behaviour of the common salts halite and gypsum in the field as opposed to the laboratory; and the important role of humidity cycling in salt crystallization.

George Scherer (1999, 2000) has recently advanced the theoretical framework for understanding stress caused by the crystallization of

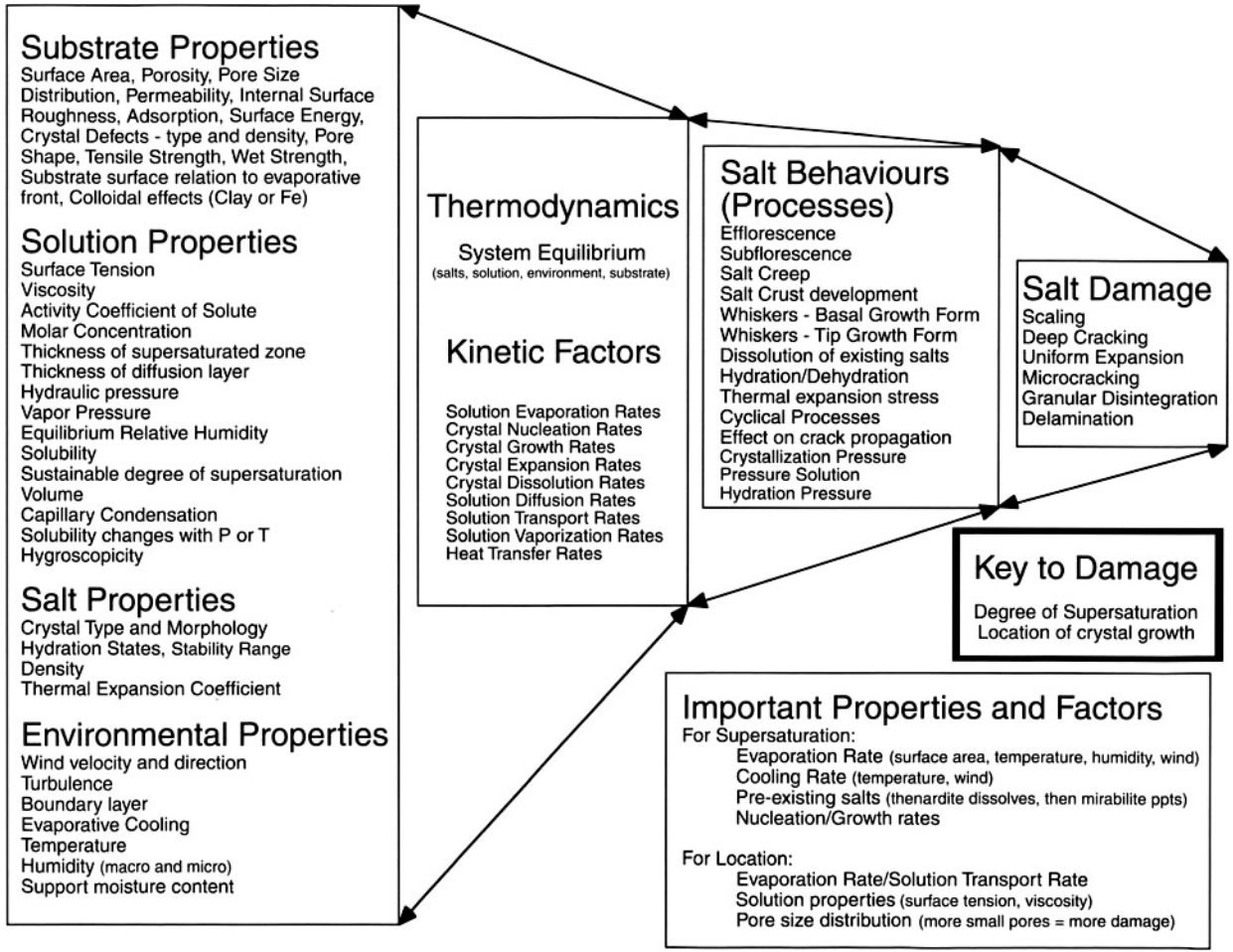

Fig. 1. Diagram of properties, factors and behaviours in the salt crystallization process.

salts in pores. This research helps explain why salt crystallization may not damage certain materials: in some cases, the local stress field is not large enough to propagate critical flaws in the material. While stones with large pores tend to fare better than those with abundant small pores, Scherer's work points out that large pores effectively behave like small pores when filled with salt. Scherer (1999) finds that the maximum pressure salt crystallization can achieve is highly dependent on pore size, predicting that most of the damage occurs when salt growth migrates from larger to smaller pores in the size range of 4 nm to 50 nm. Scherer's work clarifies the visual model of how salts growing on the nanometre-scale thin film between salt and stone can result in stresses that exceed the strength of most porous building materials. Putnis & Mauthe (2001) have noted that halite cementation in porous sandstone reinforces the observation that larger pores fill before smaller pores, confirming that fluids in small pores can better maintain the higher supersaturation.

It has long been known that the solution must be supersaturated, in order for salt crystallization to damage porous materials (Goudie & Viles 1997). What has been unclear until recently is how, in a material with abundant nucleation sites, such a supersaturated solution was created and maintained. Crystallization can be characterized as needing a driving force, such as a supersaturated solution, to create and sustain it. The generally accepted kinetic pathways to produce such a solution or mode of supersaturation generation are rapid cooling, for salts with a strong solubility dependence on temperature, and rapid evaporation for the remainder of salts (Rodriguez-Navarro *et al.* 1999). A third reaction pathway was first noted by Chatterji & Jensen (1989), more recently by Doehne *et al.* (2001), and in detail by Flatt (2002). This pathway is the presence of fine-grained pre-existing salts that dissolve rapidly to produce a supersaturated solution, such as is caused by the wetting of thenardite, leading to the rapid precipitation of mirabilite from solution, as observed in the environmental scanning electron microscope SEM (Doehne 1994; Rodriguez-Navarro & Doehne 1999*a*).

Another unresolved conundrum is the contrast between severity of damage in the field caused by halite and gypsum (Kirchner 1996), two of the most common salts, as compared to their relatively benign behaviour in the laboratory (Smith & McGreevy 1988; Goudie & Viles 1997; Robinson & Williams 2000). Understanding gypsum's behaviour is especially important to stone conservation in view of the common occurrence in the field of 'black crust' containing abundant gypsum, a product of the reaction of regional sulphate air pollution with building stone (Verges-Belmin 1994; Wittenburg & Dannecker 1994). Despite the ongoing reduction of sulphate air pollution over the past 20 years, the rate of loss of carbonate stone surface has not slowed proportionally at sites such as St Paul's Cathedral in London. This discrepancy has been attributed to salt crystallization damage from pre-existing gypsum (Trudgill *et al.* 1991).

Gypsum also plays a significant role in the typical problems of masonry buildings near the sea. Salt weathering related to sodium chloride and gypsum from sea spray salts and soil capillary waters is addressed in a recent case study documenting the decay history of the site of Civil Palaces in Alicante, Spain (Louis *et al.* 2001). The desalination of porous building materials typically results in the non-proportional removal of salts (Bromblet & Verges-Belmin 1996). If gypsum is present, the removal of hygroscopic salts may decrease its mobility since the solubility of gypsum is significantly increased by the presence of sodium chloride and other salts (Robinson & Williams 2000).

Other open questions pertaining to salt damage of porous materials are the role of the range of humidity cycling, the potential presence of damage thresholds, and the degree to which damage over the long term can be reduced by decreasing humidity fluctuations. Experiments on ceramic tiles loaded with NaCl, Na_2SO_4 and $CaSO_4.2H_2O$ and simulating the humidity cycles (43–55% relative humidity (RH) and 0–11% RH) of museum display cases (Nunberg & Charola 2001) over the course of six months found that measurable deterioration of the tiles had taken place. This ran contrary to expectations that no damage would occur in a closed environment with limited humidity cycling well below the deliquescence point of the salt (equilibrium relative humidity or RHeq). The discovery of damage suggests that while environmental control significantly reduces the rate of damage, additional research is needed to understand the limits of environmental control and how the damage was produced. In this example, the mode of solution supersaturation is not clear. However, the filling of larger pores with salt and the creation of smaller pores may play a role, as might capillary condensation of water in fine pores combined with limited humidity cycling exerted over time (Rucker *et al.* 2000). The results of Nunberg & Charola (2001) suggests that environmental control may provide less protection than previously believed (Price 2000).

The standard salt crystallization tests (ASTM and RILEM) for building materials, where sample blocks are repeatedly immersed in saturated solutions of sodium sulphate and then dried, are widely used to estimate resistance to frost damage and general durability (Price 1978; Marschner 1979). Nevertheless, there has been some controversy over the applicability of the tests, given the severity of the test and the sometimes inconsistent results (Sheftick 1989; Hunt 1994). Recent research has addressed this problem from two directions: examining the way the test actually operates (Rodriguez-Navarro *et al.* 2000*a*) and proposing new standard test methods which more closely simulate typical conditions (Benavente *et al.* 2001). The assumption of many researchers has been that the damage from this test occurred due to the hydration of sodium sulphate. More recent work suggests that direct crystallization of thenardite (Na_2SO_4) may occur (Rodriguez-Navarro *et al.* 2000*a*) in addition to rapid mirabilite ($Na_2SO_4.10H_2O$) crystallization during immersion (Doehne *et al.* 2001; Flatt 2002). Goudie (1999*a*) found that salt crystallization tests of limestone were poor predictors of frost resistance. Efforts to discover parameters that correlate with building stone durability continue, with emphasis on those that can be measured more easily than salt crystallization resistance (Moh'd *et al.* 1996; Ordonez *et al.* 1997; Nicholson 2001).

New methods for studying salt weathering

An important turning point in the advancement of salt weathering studies has been the development of methods that provide data on material behaviour in situ and in tempo, such as ultrasonic field testing (Goudie 1999*b*; Simon & Lind 1999), acoustic emission (Storch & Tur 1991; Grossi *et al.* 1997), time-lapse and environmental scanning electron microscopy (ESEM) (Doehne 1997; Rodriguez-Navarro & Doehne 1999*b*), and three-dimensional imaging methods such as nuclear magnetic resonance (NMR) (Rucker *et al.* 2000) and micro-computer tomography scanning (Degryse *et al.* 2001). Such methods add the third and fourth (time) dimensions to previous studies and aid in separating the effects of salts from other decay phenomena. For example, Pel (2000) found that the absorption of a concentrated NaCl solution in calcium-silicate brick, as seen when using NMR, revealed a sharp wetting front. Unexpectedly, the sodium was clearly seen to lag behind the moisture profile. Little sodium, if any, was observed near the wetting front, an apparent result of the interaction of sodium ions with the pore surface. In tests of 21 limestones using non-destructive methods, Goudie (1999*b*) noted that even durable stones which showed no visible decay after salt crystallization tests were found to have suffered significant decreases in their modulus of elasticity values, indicating loss of strength. Limestone durability was generally found to correlate with high values of modulus of elasticity, lower water absorption capacities, high densities and low salt uptakes.

Deterioration due to salts: field observations

A wide range of important field observations of decay to porous building materials over several decades has been summarized by Arnold and colleagues (Arnold & Küng 1985; Arnold & Zehnder 1985, 1988, 1991). These observations clearly establish the strong relationship between the rate of salt decay and the environmental conditions. Arnold and co-workers discuss the morphology of the salt crystals and its relationship to the support moisture content. With a relatively dry substrate with a slow evaporation rate, the crystals take on an acicular form; when more moisture is present, a salt crust may form (Arnold & Küng 1985; Arnold & Zehnder 1985). Subsequent observations of climate and salt behaviour in six churches over the course of five years showed that 'hygroscopic salts crystallize periodically according to the variations of relative humidity and to a much lesser extent of temperature. Within continuously heated rooms crystallization and decay are related to variations in relative humidity caused primarily by the heating and subordinately by natural variations of the outside climate. In non heated rooms seasonal variations of temperature also induce periodic crystallization'. (Arnold & Zehnder 1988). Arnold and co-workers also documented the fractionated pattern of salts in walls with rising damp, dividing the wall into four zones in vertical succession differentiated by degrees of damage and salt content. The lowest zone was perpetually damp with salts remaining in solution, succeeded by the zone of greatest damage and, finally, the uppermost zone marking the limit of rising moisture caused by deliquescent salts. The highest salt content does not always correspond to the greatest damage, since ion mixtures that are strongly hygroscopic will not crystallize under normal conditions. The sources of the salts are attributed by Arnold to the extensive use of cement-based mortars and concrete in large restoration programmes over the past 50 years, as well as salts from air pollution and rising damp. Soluble salts

from cement-based mortars and concrete are still today an important cause of decay to historic building materials, despite efforts to improve cement quality and reduce the overall use of these materials (Moropoulou 2000).

A brief review of other more recent field observations on salt weathering is considered next. Some useful insights into rates of salt weathering have recently been gained through the measurement of tafone depth using rock surfaces with a range of known ages (Matsukura & Matsuoka 1991; Sunamura 1996; Norwick & Dexter 2002). Tafoni are cavities or pits in otherwise homogeneous rock surfaces. The current consensus appears to confirm the salt weathering origin of most tafoni (Pye & Mottershead 1995; Mikulas 2001; Norwick & Dexter 2002). For tafoni that have developed over the last century, linear recession rates are estimated at 0.6 to 5.2 mm/year (Sunamura 1996). Tafone depth was also found to develop twice as fast as the width of the pit, providing additional confirmation for the salt weathering origins of tafoni. More recent analysis has shown that while there is significant scatter in the depth measurements, it appears that the weathering rate is actually non-linear, with a time lag followed by rapid recession and then a much slower rate of loss as the tafoni age. This pattern generates a sigmoidal or 'S-shaped' curve, a typical example of which is given by the following equation:

$$D = b1 + e^{(b2+(b3/t))} \quad (1)$$

where D is the depth of the tafone, t is the age of the surface and $b1$, $b2$, and $b3$ are constants solved for mathematically (Norwick & Dexter 2002).

A speculative explanation for the non-linearity suggests that the rate of loss is first limited by low salt concentrations, then becomes dominated by a positive feedback loop with an increasing rate of damage related to increasing salt concentration, followed by a negative feedback loop as the scale of the tafoni reaches a point where it apparently no longer allows efficient salt weathering (Norwick & Dexter 2002). This non-linear pattern is typical for many other natural weathering processes (Goudie 1995). Such non-linearity may help explain why salt weathering rates measured in laboratory settings have been much more rapid than those typically found in field studies. While erosion rate data from the study of stone structures for conservation are surprisingly uncommon, such patterns of low rates of decay, followed by a rapid increase have been noted by Charola (2000) and Snethlage *et al.* (1996). The fact that field salt weathering rates are typically non-linear and may show a low initial rate of loss suggests that stone conservators should interpret short-term observations of overall stability of vulnerable structures, such as wall paintings, with caution.

One of the advantages marble possesses for resisting salt damage is its minimal porosity and tendency not to have a strong capillary suction (which can lead to rising damp). However, recent studies of the marble monuments at the archaeological site of Delos, Greece, have shown that salts deposited from atmospheric aerosols are responsible for damage of marble sculpture (Jeannette 2000; Chabas & Jeannette 2001). Additionally, recent work on soil chemistry in Hawaii using strontium isotope data has found that about 50% of the calcium in soil samples from a coastal location originated from salt spray, not soil mineral weathering as expected (Whipkey *et al.* 2000). This suggests that salt spray has a strong effect on the local environment, perhaps dependent on overall wind and storm patterns.

An extensive survey and analysis of bedrock in the Valley of the Kings, Luxor, Egypt, recently resulted in warnings concerning the hazards to ancient tombs from swelling clays and salts activated by moisture from the exhalations of tourists as well as flash floods (Wüst & McLane 2000; Wüst & Schlüchter 2000). Expansion from hydration of anhydrite and crystallization cycling of abundant sodium chloride were cited as important decay mechanisms in important royal tomb sites, such as Seti I, which have seen a rapid increase in stone loss since their opening by archaeologists.

Warke & Smith (2000) suggest that 'Salt weathering is a threshold phenomenon where decay is manifest only when a stress/strength threshold is crossed'. This conclusion is based on the analysis of two similar sandstone blocks, one sound and one damaged, with similar salt content and distribution. They found that NaCl was deeper and more mobile in the stone (6 cm) than expected from surface damage (2 cm). A strong correlation of decay rate with environmental variation has recently been documented by Cantón *et al.* (2001). In a range of experiments the weathering rate of a calcareous mudstone was found to most closely follow the number of wetting/drying cycles. Some useful cautionary notes on the real world distribution of salts in sandstone can be found in Turkington & Smith (2000). The researchers concluded that 'The widely held perception that urban environments are 'dry' with shallow surface wetting of

building stone does not appear to hold true for certain building stone'.

Salt weathering is traditionally associated with coastal and desert environments (Theoulakis & Moropoulou 1999); however, regions with a tropical monsoon climate may also be affected by salt weathering due to the strong contrast between the rainy and dry seasons. Two recent examples are the famous temples at Angkor in Cambodia (Uchida *et al.* 2000) and the brick monuments in Ayutthaya, Thailand (Kuchitsu *et al.* 2000). At Angkor, one of the main causes of deterioration was identified as crystallization pressure from gypsum and phosphate minerals growing between exfoliated layers of sandstone. The sulphur and phosphate are derived from rain water leaching of bat guano, which subsequently moves into the stone through rising damp (Uchida *et al.* 2000). At Ayutthaya, gypsum efflorescence is found in the rainy season, with more soluble salts such as thenardite appearing in the dry season. Most damage occurs at the beginning of the dry season to brick surfaces, and Kuchitsu *et al.* (2000) propose methods to reduce water impregnation of the bricks in the rainy season as a conservation measure.

Interrelationship between salt weathering and other decay mechanisms

With an understanding of the properties necessary for a particular salt damage mechanism to be activated, it is possible to contemplate modifying those properties to better understand the damage mechanism and to develop preventive conservation measures. Changing a parameter such as surface tension using surface active agents was recently found to have a strong effect on damage from sodium sulphate crystallization since it directly affects where salts crystallize (Rodriguez-Navarro *et al.* 2000*b*). The authors speculated that biologically produced surfactants might have a similar effect. Two articles have subsequently found that the presence of bacteria, associated biofilms, and biopolymers greatly increases the damage caused by salts (May *et al.* 2000; Papida *et al.* 2001).

The relationship between salts and frost weathering was explored recently by Williams & Robinson (2001). The authors extended the range of salts known to intensify frost weathering (potassium and ammonium alums) and confirmed the significance of halite in the process. Williams & Robinson (2001) show that the degree of damage to stone varied greatly depending on the combinations of salts involved. While most salts contributed to damage proportionally when used in combination, some salt mixtures caused intensified damage out of proportion to the component salts. The topic of salt mixtures and their effect on salt damage and other decay mechanisms is complex since the behaviour of the mixture cannot be predicted from single salt data (Steiger & Dannecker 1995; Steiger 1996; Steiger & Zeunert 1996). However, the use of computer models such as the semi-empirical ion interaction model of Pitzer provides an important predictive tool for studying most field situations where salt mixtures are the rule (Clegg & Brimblecombe 2000; Steiger *et al.* 2000).

Dragovich (1997) studied the weathering of marble tombstones near Sydney, Australia, and was surprised to measure a low weathering rate (540 μm/100 years). The seaward-facing sides of the marble blocks, which were exposed to greater salt input, unexpectedly weathered more slowly than the landward side. This suggests that even in coastal environments salt weathering is only one aspect of the full weathering process.

Prevention, mitigation, and treatment options

Avoiding damp is a fundamental principle for maintaining any structure where porous materials are used (Ashurst & Ashurst 1988). The most important mitigation method is prevention, through the physical separation of building materials from soil moisture and salts with the traditional 'damp-proof course.' This is typically an impermeable barrier such as plastic (current structures), glazed brick, bitumen, or other material. The service life of the plastic sheeting used in modern concrete slab construction is not well known. In existing salt-laden structures, salts can be removed through poulticing and in some cases the affected masonry may be replaced. However, in the past few decades, the cost of such replacement has led to increasing use of chemical damp-proof courses in the form of injected siloxane. Below, a range of treatment options and research into the reduction of salt damage is discussed.

Salts tend to cause damage in building materials when activated by a change in humidity, temperature or the presence of liquid water. If the composition of the salts is known, then calculating the stability range (relative humidity and temperature) for the salts allows establishment of the appropriate conditions for minimizing damage due to a change of state. Establishing

such controlled conditions should substantially extend the life of the material. An important new report by Price (2000) documents the development of an expert system to provide such information and is an extremely useful repository of detailed thermodynamic and kinetic information concerning individual salts, salt mixtures, and their calculated and actual behaviour. Other researchers have also explored this approach (Aires-Barros & Mauricio 1997). Unfortunately, controlled environments for stone objects and structures tend to be the exception rather than the rule, and field experience suggests that damage tends to occur whenever significant concentrations of salts are present in porous masonry (A. Arnold, personal communication).

The practice of poulticing salts using highly absorbent materials such as clays or wood pulp has long been employed by stone conservators to remove salts from important wall paintings and carved stone. Study of the effectiveness of these methods has shown that, while chloride and nitrate are readily removed, sulphate removal is more difficult. Artificial anionic clays (hydrotalcites) are recommended for enhanced extraction of the less soluble gypsum (Vicente & Vicente-Tavera 2001). Vicente (2001) also noted the loss of extraction efficiency under conditions of high humidity. Simon *et al.* (1996) found that a new high porosity compress render was generally more effective at removing salts than a traditional sacrificial lime plaster, although the introduction of water to the surface during the treatment increased nitrate concentrations higher up on the wall. Siedel (1996) also noted the difficulty of controlling desalination, achieving results that were 'contradictory and sometimes even undesirable on large monuments.'

Two desalination methods (total immersion and intermittent washings) were studied recently for their potential for use in the removal of salts from ceramic tiles by Freedland & Charola (2001). The authors found that for more soluble salts, such as NaCl, repeated washings were more effective, while long-term immersion was more efficient for less soluble salts such as gypsum as well as for sodium sulphate in ceramic tiles with fine pores. Based on a substantial body of experimental work, Charola *et al.* (2001) have developed a reproducible method to calculate the salt remaining in an object after desalination.

An interesting effort to move sodium chloride from a brick vault into an adsorbing mortar above the vault used differential humidity to mobilize the salts (Larsen & Bøllingtoft 1999; Larsen 2001). With a low relative humidity above the vault and a moist environment (below the deliquescence point of the salts), it was found that the kinetics for NaCl movement solely attributable to humidity are slow, and that NaCl most readily moves into the mortar (from damaged bricks) when liquid water is present.

A newly proposed approach mitigating salt weathering is the reduction of the interfacial energy between the salt and the stone using a specially selected non-swelling polymer with the appropriate surface properties (Scherer *et al.* 2001). By placing such a barrier between the pore walls and salts, it is anticipated that greater surface energy compatibility may be achieved and the salts should stop growing when they come in contact with the polymer.

Long experience with salt weathering of building foundations in Adelaide, Australia, a region with a Mediterranean climate and salt-rich soil, has resulted in a host of practical methods for mitigating this damage (Blackburn & Hutton 1980; Young 1995). Young found that decay is most commonly found at the base of walls, where solutions migrating from local salt-rich soils damage masonry, mostly in cases where a damp-proof course is either lacking, has been damaged or was bridged by later masonry. The most effective treatment is replacement of the salt-laden stone and reinstallation of a damp-proof course. The high cost of this treatment limits its use to severe cases or situations where sufficient funding is readily available. The most common treatment is injection of waterproofing agents (siloxane) to provide a chemical damp-proof course and desalination of the salt-laden masonry. The longevity of these treatments remains uncertain, with some failures attributed to problems with desalination or incomplete injection. Saline soils are an increasing regional problem in south and southeast Australia, and salt weathering of heritage structures in this region has begun to mount (Spennemann 2001).

Planetary salt weathering

Salt weathering is a global phenomenon, present in Antarctica as well as Death Valley. This diversity has been appreciated by geologists and planetary scientists, who have suggested that salt weathering mechanisms may help explain unusual features on Mars (Malin 1974). Photographs from Mars taken at the Pathfinder landing site reveal features remarkably similar to honeycomb weathering structures on Earth (Rodriguez-Navarro 1998). McCord *et al.* (2001) found that under conditions typically found on the Jovian moon Europa, magnesium sulphate

could remain hydrated on a geological time scale.

Summary and future work

As of this writing, there are over 1800 references in the scientific literature on the topic of salt weathering of porous materials and over 6000 references addressing general problems of building material decay. Many of these articles describe unique case studies that may be difficult to interpret or apply to other situations. In order to navigate this vast collection of data and knowledge borne of disparate disciplines, this article serves as an organizing framework to consider the complexity of salt damage, presents an overview of multidisciplinary research and open questions on this topic, and provides a limited literature survey largely focused on recent work and those articles with relevance for conservation. The research surveyed here has clearly advanced our understanding of the damage caused by salt weathering processes, and raises important questions for the conservation of material heritage. Future investigation into salt weathering should include more quantitative measurements of field weathering rates and laboratory studies using methods such as three-dimensional imaging to further illuminate the relationships between salt weathering mechanisms and the properties of solution, substrate and environment, and to contribute to a better understanding of the action and kinetics of salt mixtures in weathering stone. Finally, improving methods to prevent and mitigate salt weathering of building materials clearly deserves more effort and attention.

The author is indebted to M. Steiger and A. Putnis for their comments and critical reviews, which greatly improved the manuscript. This paper was supported by the Getty Conservation Institute under the research project entitled 'Salt Damage.' Also, the support of A. de Tagle, S. Simon, W. Ginell, and J. M. Teutonico is acknowledged. K. Zehnder generously contributed many useful references. The full building materials decay bibliography is available from the author.

References

AIRES-BARROS, L. & MAURICIO, A. 1997. Transition frequencies of evaporitic minerals on monuments stone decay. *In*: MOROPOULOU, A., ZEZZA, F., KOLLIAS, E. & PAPACHRISTODOULOU, I. (eds) *4th International Symposium on the Conservation of Monuments in the Mediterranean*. Texniko Enimeahthpio, Rhodes, Greece, 33–51.

AMOROSO, G. G. & FASSINA, V. 1983. *Stone Decay and Conservation: Atmospheric Pollution, Cleaning, Consolidation and Protection*. Materials Science Monographs, **11**, Elsevier, Amsterdam.

ARNOLD, A. & KÜNG, A. 1985. Crystallization and habits of salt efflorescences on walls. Part I: Methods of investigation and habits. *In*: FÉLIX, G. (ed.) *5th International Congress on Deterioration and Conservation of Stone*, Lausanne, 1985. Presses Polytechniques Romandes, Lausanne, 255–267.

ARNOLD, A. & ZEHNDER, K. 1985. Crystallization and habits of salt efflorescences on walls. Part II: Conditions of crystallization. *In*: FÉLIX, G. (ed.) *5th International Congress on the Deterioration and Conservation of Stone*, Lausanne, 1985. Presses Polytechniques Romandes, Lausanne, 269–277.

ARNOLD, A. & ZEHNDER, K. 1988. Decay of stony materials by salts in humid atmosphere. *In*: CIABACH, J. (ed.) *Proceedings of the 6th International Congress on Deterioration and Conservation of Stone*. Nicholas Copernicus University, Torun, Poland, 138–148.

ARNOLD, A. & ZEHNDER, K. 1991. Monitoring wall paintings affected by soluble salts. *The Conservation of Wall Paintings*. Proceedings of a symposium organized by the Courtauld Institute of Art and the Getty Conservation Institute, London, July 13–16, 1987. Getty Conservation Institute, Marina del Rey, 103–135.

ASHURST, J. & ASHURST, N. 1988. *Practical Building Conservation*. Gower Technical Press, Aldershot.

ASTM, 1997. *ASTM C88–90, Standard test method for soundness of aggregate by use of sodium sulphate or magnesium sulphate*. Annual Book of ASTM Standards 4.2. ASTM, 37–42.

BENAVENTE, D., GARCIA DEL CURA, M. A. *et al.* 1999. Thermodynamic modelling of changes induced by salt pressure crystallization in porous media of stone. *Journal of Crystal Growth*, **204**, 168–178.

BENAVENTE, D., ORDÓÑEZ, S. *et al.* 2001. Quantification of salt weathering in porous stones using an experimental continous partial immersion method. *Engineering Geology*, **59**, 313–325.

BLACKBURN, G. & HUTTON, J. T. 1980. Soil conditions and the occurrence of salt damp in buildings of metropolitan Adelaide. *Australian Geographer*, **14**, 360–365.

BROMBLET, P. & VERGES-BELMIN, V. 1996. L'élimination des sulphates sur la statuaire calcaire de plein air: une habitude discutable [The removal of sulphates from calcareous stone outdoor statuary: a questionable practice]. *Le dessalement des matériaux Poreux*. 7es journées d'études de la SFIIC, Poitiers, 9–10 mai 1996. SFIIC, Champs-sur-Marne, 55–63.

BROWN, G. E. J. 2001. How minerals react with water. *Science*, **294**, 67–70.

CANTÓN, Y., PINI, R. *et al.* 2001. Weathering of a gypsum-calcareous mudstone under semi-arid environment at Tabernas, SE Spain: Laboratory and field-based experimental approaches. *Catena*, **44**, 111–132.

CARSTENS, H. 1986. Displacive growth of authigenic pyrite. *Journal of Sedimentary Petrology*, **56**, 252–257.

CHABAS, A. & JEANNETTE, D. 2001. Weathering of marbles and granites in marine environment:

Petrophysical properties and special role of atmospheric salts. *Environmental Geology*, **40**, 359–368.

CHAROLA, A. E. 2000. Salts in the deterioration of porous materials: An overview. *Journal of the American Institute for Conservation*, **39**, 327–343.

CHAROLA, A. E., FREEDLAND, J. *et al.* 2001. Salts in ceramic bodies IV: considerations on desalination. *Internationale Zeitschrift für Bauinstandsetzen und Baudenkmalpflege*, **7**, 161.

CHAROLA, A. E., HENRIQUES, F. M. A. *et al.* 1998. The Tower of Belem exterior conservation project. *Internationale Zeitschrift für Bauinstandsetzen 4. Jahrgang*, **4**, 587–610.

CHAROLA, A. E. & WEBER, J. 1992. The hydration–dehydration mechanism of sodium sulphate. *In*: RODRIGUES, J. D., HENRIQUES, F. & JEREMISAS, F. T. (eds) *7th International Congress on Deterioration and Conservation of Stone*, Lisbon Portugal, 15–18 June 1992, Proceedings. Laboratorio Nacional de Engenharia Civil, Lisbon, 581–590.

CHATTERJI, S. & JENSEN, A. D. 1989. Efflorescences and breakdown of building materials. *Nordic Concrete Research*, **8**, 56–61.

CLEGG, S. L. & BRIMBLECOMBE, P. 2000. Pitzer model of electrolyte solutions. *In*: Price, C. A. (ed.) *An expert chemical model for determining the environmental conditions needed to prevent salt damage in porous materials*. European Commission Research Report 11, Protection and Conservation of European Cultural Heritage. Archetype Publications, London, 13–18.

DEGRYSE, P., GEET, M. V. *et al.* 2001. Microfocus computer tomography as a qualitative approach to frost damage in modern restoration mortars. *Internationale Zeitschrift für Bauinstandsetzen und Baudenkmalpflege*, **7**, 47.

DOEHNE, E. 1994. In situ dynamics of sodium sulphate hydration and dehydration in stone pores: Observations at high magnification using the environmental scanning electron microscope. *In*: FASSINA, V., OTT, H. & ZEZZA, F. (eds) *The Conservation of Monuments in the Mediterranean Basin*. Proceedings of the 3rd International Symposium, Venice, 1994 (La conservazione dei monumenti nel bacino del Mediterraneo Atti del 3o Simposio Internazionale, Venezia, 1994). Soprintendenza di Beni Artistici e Storici di Venezia, 143–150.

DOEHNE, E. 1997. ESEM development and application in cultural heritage conservation. *In*: GAI, P. L. (ed.) *In-Situ Microscopy in Materials Research: Leading International Research in Electron and Scanning Probe Microscopies*. Kluwer, Dordrecht, 45–62.

DOEHNE, E., SELWITZ, C. *et al.* 2001. Damage to monuments from the crystallization of mirabilite, thenardite and halite: mechanisms, environment, and preventive possibilities. *Eleventh Annual V. M. Goldschmidt Conference*. Geochemical Society.

DRAGOVICH, D. 1997. Weathering of marble tombstones in a near-coastal environment, Australia. *In*: MARINOS, P. G. (ed.) *Engineering Geology and the Environment*. Balkema, Rotterdam 3129–3134.

DUTTLINGER, W. & KNÖFEL, D. 1993. Salzkristallisation und Salzschadensmechanismen, Jahresberichte aus dem Forschungsprogramm 'Steinzerfall – Steinkonservierung,' Band 3 – 1991. *Ein Förderprojekt des Bundesministers für Forschung und Technologie*. Verlag Ernst & Sohn, Berlin, 197–213.

FLATT, R. J. 2002. Salt damage in porous materials: How high supersaturations are generated. *Journal of Crystal Growth*, **242**, 435–454.

FREEDLAND, J. & CHAROLA, A. E. 2001. Salts in ceramic bodies III: An experimental study on desalination. *Internationale Zeitschrift für Bauinstandsetzen und Baudenkmalpflege*, **7**, 147.

GOUDIE, A. 1995. *The Changing Earth: Rates of Geomorphological Processes*. Blackwell, Oxford.

GOUDIE, A. S. 1999*a*. A comparison of the relative resistance of limestones to frost and salt weathering. *Permafrost and Periglacial Processes*, **10**, 309–316.

GOUDIE, A. S. 1999*b*. Experimental salt weathering of limestones in relation to rock properties. *Earth Surface Processes and Landforms*, **24**, 715–724.

GOUDIE, A. S. & DAY, M. J. 1980. Disintegration of fan sediments in Death Valley, California, by salt weathering. *Physical Geography*, **1**, 126–137.

GOUDIE, A.S. & VILES, H. 1997. *Salt Weathering Hazards*. John Wiley, Chichester.

GROSSI, C. M., ESBERT, R. M. *et al.* 1997. Acoustic emission monitoring to study sodium sulphate crystallization in monumental porous carbonate stones. *Studies in Conservation*, **42**, 115–125.

HAYNES, H. 2002. Sulphate attack on concrete: Discrepancy between laboratory and field experience. *Concrete International*, **24**(July).

HAYNES, H., O'NEILL, R. *et al.*, 1996. Concrete deterioration from physical attack by salts. *Concrete International*, **18**, 63–68.

HERODOTUS, 420 BC. History: 'I observed . . . that salt exuded from the soil to such an extent as even to injure the pyramids'. **2.12 (Book 2)**.

HIME, W. G., MARTINEK, R. A. *et al.* 2001. Salt Hydration Distress. *Concrete International*, **23**, 43–50.

HOCHELLA, M. F., JR. 2002. There's plenty of room at the bottom: Nanoscience in geochemistry. *Geochemica et Cosmochimica Acta*, **66**, 735–743.

HOFFMANN, L. & GRASSEGGER, G. 1995. Salzsprengeffekte an Naturbausteinen mit verschiedenen umweltrelevanten Salzen, Umwelteinflüsse erfassen, simulieren, bewerten. 24. *Jahrestagung der GUS der FhG. 22.–24. März 1995*, Pfinztal/Karlsruhe, 23–13.

HUNT, B. 1994. There's no alternative. *Stone Industries*, **5**(February), 37–39.

JEANNETTE, D. 2000. Originalite des mecanismes d'alteration sur les vestiges archeologiques de Delos (Cyclades, Greece) Delos (Cyclades, Greece). *Comptes Rendus de l'Academie de Sciences – Serie IIa: Sciences de la Terre et des Planetes*, **330**, 683–688.

JUTSON, J. T. 1918. The influence of salts in rock weathering in sub-arid Western Australia. *Royal Society of Victoria, Proceedings*, **30**, 165–172.

KASDAN, SIMONDS *et al.* 2002. *Sulphate Attack to Concrete.* http://www.kasdansimonds.com/sulphate_attack.html http://www.kasdansimonds.com/news2.html.

KIRCHNER, G. 1996. Cavernous weathering in the Basin and Range area, southwestern USA and northwestern Mexico. *Zeitschrift für Geomorphologie*, Supplement **106**, 73–97.

KUCHITSU, N., ISHIZAKI, T. *et al.* 2000. Salt weathering of the brick monuments in Ayutthaya, Thailand. *Engineering Geology*, **55**, 91–99.

LA IGLESIA, A., GONZALEZ, V. *et al.* 1997. Salt crystallization in porous construction materials I. Estimation of crystallization pressure. *Journal of Crystal Growth*, **177**, 111–118.

LARSEN, P. K. 2001. The development and testing of a salt extracting mortar. *Internationale Zeitschrift für Bauinstandsetzen und Baudenkmalpflege*, **7**, 79.

LARSEN, P. K. & BØLLINGTOFT, P. 1999. Desalination of a painted brick vault in Kirkerup Church. *Preprints, 12th Triennial Meeting, ICOM Committee for Conservation*, 29 August–3 September. ICOM, Lyon, 473–477.

LEWIN, S. Z. 1982. The mechanism of masonry decay through crystallization. *In*: *Conservation of Historic Stone Buildings and Monuments*. National Academy of Sciences, Washington, DC, 120–144.

LOUIS, M., DEL CURA, M. A. G. *et al.* 2001. The civil palaces in Gravina Street, Alicante: building stones and salt weathering. *Materiales de Construcción*, **51**, 23–37.

LUQUER, L. M. 1895. The relative effects of frost and sulphates of soda efflorescence tests on building stones. *American Society of Civil Engineers – Transactions*, **33**, 235–247 and 247–256.

MALIN, M. C. 1974. Salt weathering on Mars. *Journal of Geophysical Research*, **79**, 3888–3894.

MALIVA, R. G. & SIEVER, R. 1988. Diagenetic replacement controlled by force of crystallization. *Geology*, **16**, 688–691.

MARSCHNER, H. 1979. Application of salt crystallisation test to impregnated stones. *Research in Archaeology and Conservation*, 70–77.

MATSUKURA, Y. & MATSUOKA, N. 1991. Rates of tafoni weathering on uplifted shore platforms in Nojima-Zaki, Boso Peninsula, Japan. *Earth Surface Processes and Landforms*, **16**, 51–56.

MAY, E., PAPIDA, S. *et al.* 2000. Comparative studies of microbial communities on stone monuments in temperate and semi-arid climates. *In*: CIFERRI, O., TIANO, P. & MASTROMEI, G. (eds) *Of Microbes and Art: the role of microbial communities in the degradation and protection of cultural heritage Part 1. Ecology of microbial communities developing on art works*. Kluwer/Plenum, New York.

MCCORD, T. B., SIEGER, M. T. *et al.* 2001. Thermal and radiation stability of the hydrated salt minerals epsomite, mirabilite, and natron under Europa environmental conditions. *Journal of Geophysical Research E: Planets*, **106**, 3311–3319.

MCMAHON, D. J., SANDBERG, P. *et al.* 1992. Deterioration mechanisms of sodium sulphate. *In*: RODRIGUES, J. D., HENRIQUES, F. & JEREMISAS, F. T. (eds) *7th International Congress on Deterioration and Conservation of Stone*, Lisbon, Portugal, 15–18 June 1992, Proceedings. Laboratorio Nacional de Engenharia Civil, Lisbon, 705–714.

MEHTA, P. K. 2000. Sulphate attack on concrete: Separating myths from reality. *Concrete International*, **22**, 57–61.

MIKULAS, R. 2001. Gravity and oriented pressure as factors controlling 'honeycomb weathering' of the Creataceous castellated sandstones (northern Bohemia, Czech Republic). *Bulletin of the Czech Geological Survey*, **76**, 217–226.

MINGUEZ, J. M. & ELORZA, J. 1994. Diagenetic volume-for-volume replacement – force of crystallization and depression of dissolution. *Mineralogical Magazine*, **58**, 135–142.

MOH'D, B. K., HOWARTH, R. J. *et al.* 1996. Rapid prediction of Building Research Establishment limestone durability class from porosity and saturation. *Quarterly Journal of Engineering Geology*, **29**, 285–297.

MOROPOULOU, A. 2000. Reverse engineering to discover traditional technologies: a proper approach for compatible restoration mortars. *PACT (Athens, Greece)*, **58**, 81–107.

MUSTOE, G. E. 1982. The origin of honeycomb weathering. *Geological Society of America Bulletin*, **93**, 108–115.

NICHOLSON, D. T. 2001. Pore properties as indicators of breakdown mechanisms in experimentally weathered limestones. *Earth Surface Processes and Landforms*, **26**, 819–838.

NORWICK, S. A. & DEXTER, L. R. 2002. Rates of development of tafoni in the Moenkopi and Kaibab formations in Meteor Crater and on the Colorado Plateau, northeastern Arizona. *Earth Surface Processes and Landforms*, **27**, 11–26.

NUNBERG, S. & CHAROLA, A. E. 2001. Salts in ceramic bodies II: Deterioration due to minimal changes in relative humidity. *Internationale Zeitschrift für Bauinstandsetzen und Baudenkmalpflege*, **7**, 131.

ORDONEZ, S., FORT, R. *et al.* 1997. Pore size distribution and the durability of a porous limestone. *Quarterly Journal of Engineering Geology*, **30**, 221–230.

PAPIDA, S., MURPHY, W. *et al.* 2001. Enhancement of physical weathering of building stones by microbial populations. *International Biodeterioration and Biodegradation*, **46**, 305–317.

PEL, L., KOPINGA, K. *et al.* 2000. Saline absorption in calciumsilicate brick observed by NMR-scanning. *Journal of Physics D: Applied Physics*, **33**.

PÓSFAI, M., ANDERSON, J. R. *et al.* 1995. Compositional variations of sea-salt-mode aerosol particles form the North Atlantic. *Journal of Geophysical Research*, **100**, 23,063–23,074.

PRICE, C. A. 1978. The use of sodium sulphate crystallisation test for determining the weathering resistance of untreated stone. Deterioration and protection of stone monuments, International Symposium, Paris, June 5–9 1978. Unesco-Rilem, Paris.

PRICE, C. A. 1996. *Stone Conservation. An Overview of Current Research*. Getty Conservation Institute, Los Angeles.

PRICE, C. A. 2000. *An expert chemical model for determining the environmental conditions needed to prevent salt damage in porous materials*. European Commission Research Report 11, Protection and Conservation of European Cultural Heritage. Archetype Publications, London.

PUTNIS, A. & MAUTHE, G. 2001. The effect of pore size on cementation in porous rocks, *Geofluids*, 37–41.

PYE, K. & MOTTERSHEAD, D. N. 1995. Honeycomb weathering of Carboniferous sandstone in a sea wall at Weston-super-Mare, UK. *Quarterly Journal of Engineering Geology*, **28**, 333–347.

RILEM, 1980. Recommandations provisoires/Tentative Recommendations. (RILEM) Commission 25-PEM. Protection et erosion des monuments: Essais recommandés pour mesurer l'altération des pierres et évaluer l'efficacité des méthodes de traitement. *Matériaux et Constructions*, **13**, 175–253.

ROBINSON, D.A. & WILLIAMS, R. B. G. 2000. Experimental weathering of sandstone by combinations of salts. *Earth Surface Processes and Landforms*, **25**, 1309–1315.

RODRIGUEZ-NAVARRO, C. 1998. Evidence of honeycomb weathering on Mars. *Geophysical Research Letters*, **25**, 3249–3252.

RODRIGUEZ-NAVARRO, C. & DOEHNE, E. 1999*a*. Salt weathering: influence of evaporation rate, supersaturation and crystallization pattern. *Earth Surface Processes and Landforms*, **24**, 191–209.

RODRIGUEZ-NAVARRO, C. & DOEHNE, E. 1999*b*. Time-lapse video and ESEM: Integrated tools for understanding processes in situ. *American Laboratory*, 28–35.

RODRIGUEZ-NAVARRO, C., DOEHNE, E. *et al.* 1999. Origins of honeycomb weathering: The role of salts and wind. *Bulletin of The Geological Society of America*, **111**, 1250–1255.

RODRIGUEZ-NAVARRO, C., DOEHNE, E. *et al.* 2000*a*. How does sodium sulphate crystallize? Implications for the decay and testing of building materials. *Cement and Concrete Research*, **30**, 1527–1534.

RODRIGUEZ-NAVARRO, C., DOEHNE, E. *et al.* 2000*b*. Influencing crystallization damage in porous materials through the use of surfactants: Experimental results using sodium dodecyl sulphate and cetyldimethylbenzylammonium chloride. *Langmuir*, **16**, 947–954.

RUCKER, P., HOLM, A. *et al.* 2000. Determination of moisture and salt content distributions by combining NMR and gamma ray measurements. *Materialsweek – Munich*, September.

SCHAFFER, R. J. 1932. *The Weathering of Natural Building Stones*. Special Report No.18, Building Research Establishment, Garston.

SCHERER, G. W. 1999. Crystallization in pores. *Cement and Concrete Research*, **29**, 1347–1358.

SCHERER, G. W. 2000. Stress from crystallization of salt in pores. *9th International Congress on Deterioration and Conservation of Stone*, Venice, 19–24 June, 187–194.

SCHERER, G. W., FLATT, R. *et al.* 2001. Materials science research for the conservation of sculpture and monuments. *Materials Research Society Bulletin*, **26**, 44–50.

SCHWARZ, H. J. & ROESCH, H. 1993. Damage to frescoes caused by sulphate-bearing salts: where does the sulphate come from? *Studies in Conservation*, **38**, 224–230.

SCHWARZ, H. J., GERVAIS, A. *et al.* 2000. Natural stone conservation in St. Michaelis Cloister, Hildesheim. *Proceedings of the 6th International Congress on Applied Mineralogy ICAM 2000*. Rotterdam, Germany, S.1031–1038.

SHEFTICK, 1989. Na_2SO_4 Soundness Test Evaluation. *Cement, Concrete and Aggregates*, **11**, 73–79.

SIEDEL, H. 1996. Experiences from desalting of tuffstone and sandstone monuments by compresses. *Le dessalement des matériaux poreux*, 7es journées d'études de la SFIIC, Poitiers, 9–10 mai 1996. SFIIC, Champs-sur-Marne, 191–198.

SIMON, S. & LIND, A.-M. 1999. Decay of limestone blocks in the block fields of Karnak Temple (Egypt): non-destructive damage analysis and control of consolidation treatments. *ICOM Committee for Conservation, Triennial meeting* (12th), Lyon, 29 August – 3 September 1999, Preprints, Vol. 2, 743–749.

SIMON, S., HERM, C. *et al.* 1996. Desalination and control of salt transport phenomena: Experiences with compress renderings in the ring crypt of St. Emmeram, Regensburg. *Le dessalement des matériaux poreux*, 7es journées d'études de la SFIIC, Poitiers, 9 – 10 mai 1996. SFIIC, Champs-sur-Marne, 147–159.

SMITH, B. J. 1994. Weathering processes and forms. *In*: ABRAHAMS, A. D. & PARSONS, A. J. (eds) *Geomorphology of Desert Environments*. Routledge Chapman & Hall, London, 39–63.

SMITH, B. J. & MCGREEVY, J. P. 1988. Contour scaling of a sandstone by salt weathering under simulated hot desert conditions. *Earth Surface Processes and Landforms*, **13**, 697–705.

SMITH, B. J., WARKE, P. A. *et al.* 2000. Limestone weathering in contemporary arid environments: A case study from southern Tunisia. *Earth Surface Processes and Landforms*, **25**, 1343–1354.

SNETHLAGE, R., WENDLER, E. *et al.* (eds) 1996. Tenside im Gesteinsschutz-Bisherige resultate mit einem neuen Konzept zur Erhaltung von Denkmilern aus Naturstein. *Natursteinkonservierun in der Denkmalpflege*. Ernst & Sohn, Berlin, 127–146.

SPENNEMANN, D. H. R. 2001. The creeping disaster: dryland and urban salinity and its impact on heritage. *Cultural Resource Management*, **24**, 22–25.

STEIGER, M. 1996. Distribution of salt mixtures in a sandstone monument: Sources, transport and crystallization properties. *In*: ZEZZA, F. (ed.) *EC Research Workshop on Origin, Mechanisms and Effects of Salts on Degradation of Monuments in Marine and Continental Environments*. European Commission, Protection and Conservation of the European Cultural Heritage, Research Report 4, Bari, 241–246.

STEIGER, M. 2002. Salts and crusts. *In*: BRIMBLECOMBE, P. (ed.) *The Effects of Air Pollution on the Built Environment*. Air Pollution Reviews, Imperial College, London.

STEIGER, M. & DANNECKER, W. 1995. Hygroskopische Eegenschaften und Kristallisationsvergalten von Salzgemischen. *Jahresberichte aus dem Forschungsprogramm Steinzerfall Steinkonservierung*. Ernst und Sohn, Berlin, 115–128.

STEIGER, M. & ZEUNERT, A. 1996. Crystallization properties of salt mixtures: comparison of experimental results and model calculations. *In*: RIEDERER, J. (ed.) *Proceedings of the 8th International Congress on Deterioration and Conservation of Stone*, Berlin, 30 Sept.–4 Oct. 1996. Möller Druck, Berlin, 535–544.

STEIGER, M., BEYER, R. *et al.* 2000. Data compilation and experimental determinations. *In*: PRICE, C. A. (ed.) *An expert chemical model for determining the environmental conditions needed to prevent salt damage in porous materials*. European Commission Research Report 11, Protection and Conservation of European Cultural Heritage, Archetype Publications, London, 19–37.

STORCH, W. & TUR, P. 1991. Untersuchung einiger Schädigungsvorgänge an Natursteinen mittels Schallemissionsanalyse, Jahresberichte Steinzerfall – Steinkonservierung 1989. *Ein Förderprojekt des Bundesministers für Forschung und Technologie*, 189–195.

SUNAMURA, T. 1996. A physical model for the rate of coastal tafoni development. *Journal of Geology*, **104**, 741–748.

TABER, S. 1916. The growth of crystals under external pressure. *American Journal of Science*, **41**, 532–556.

THEOULAKIS, P. & MOROPOULOU, A. 1999. Salt crystal growth as weathering mechanism of porous stone on historic masonry. *Journal of Porous Materials*, **6**, 345–358.

TORFS, K. & VAN GRIEKEN, R. 1997. Chemical relations between atmospheric aerosols, deposition and stone decay layers on historic buildings at the Mediterranean coast. *Atmospheric Environment*, **31**, 2179–2192.

TORRACA, G. 1982. Porous building materials. *Materials Science for Architectural Conservation* (2nd edn). ICCROM, International Centre for the Study of the Preservation and Restoration of Cultural Property, Rome.

TRUDGILL, S. T., VILES, H. A. *et al.* 1991. Trends in stone weathering and atmospheric pollution at St Paul's Cathedral, London, 1980–1990. *Atmospheric Environment, Part A*, **25A**, 2851–2853.

TURKINGTON, A. V. 1998. Cavernous weathering in sandstone: Lessons to be learned from natural exposure. *Quarterly Journal of Engineering Geology*, **31**, 375–383.

TURKINGTON, A. V. & SMITH, B. J. 2000. Observations of three-dimensional salt distribution in building sandstone. *Earth Surface Processes and Landforms*, **25**, 1317–1332.

UCHIDA, E., NAKAGAWA, T. *et al.*, 2000. Deterioration of stone materials in the Angkor monuments, Cambodia. *Engineering Geology*, **55**, 101–112.

UNRUH, J. 2001. A revised endpoint for ceramics desalination at the archaeological site of Gordion, Turkey. *Studies in Conservation*, **46**, 81–93.

VERGES-BELMIN, V. 1994. Pseudomorphism of gypsum after calcite, a new textural feature accounting for the marble sulphation mechanism. *Atmospheric Environment*, **28**, 295–304.

VICENTE, M. A. & VICENTE-TAVERA, S. 2001. Clay poultices in salt extraction from ornamental stones: a statistical approach. *Clays & Clay Minerals*, **49**, 227–235.

VILES, H. A. 1997. Group report: what is the state of our knowledge of the mechanisms of deterioration and how good are our estimates of rates of deterioration? *In*: BAER, N. S. & SNETHLAGE, R. (eds) *Saving our Architectural Heritage. The Conservation of Historic Stone Structures*. Report of the Dahlem Workshop, Berlin, March 3–8, 1996. John Wiley, New York, 95–112.

WARKE, P. A. & SMITH, B. J. 2000. Salt distribution in clay-rich weathered sandstone. *Earth Surface Processes and Landforms*, **25**, 1333–1342.

WHIPKEY, C. E., STEWART, B. W. *et al.* 2000. The importance of sea spray to the cation budget of a coastal Hawaiian soil: A strontium isotope approach. *Chemical Geology*, **168**, 37–48.

WILLIAMS, R. B. G. & ROBINSON, D. A. 2001. Experimental frost weathering of sandstone by various combinations of salts. *Earth Surface Processes and Landforms*, **26**, 811–818.

WITTENBURG, C. & DANNECKER, W. 1994. Salt enrichment in building stones by deposition of sulfur and nitrogen containing species from urban atmospheres. *In*: FASINA, V., OTT, H. & ZEZZA, F. (eds) *The Conservation of Monuments in the Mediteranean Basin*. Proceedings of the Third International Symposium, Venice, 1994. Soprintendenza di Beni Artistici e Storici di Venezia, 179–183.

WÜST, R. A. J. & MCLANE, J. 2000. Rock deterioration in the Royal Tomb of Seti I, Valley of the Kings, Luxor, Egypt. *Engineering Geology*, **58**, 163–190.

WÜST, R. A. J. & SCHLÜCHTER, C. 2000. The origin of soluble salts in rocks of the Thebes mountains, Egypt: The damage potential to ancient Egyptian wall art. *Journal of Archaeological Science*, **27**, 1161–1172.

XIAOZU, X., JIACHENG, W. *et al.* 1999. *Mechanisms of Frost Heave and Salt Expansion of Soils*. Science Press, Beijing/New York.

YOUNG, D. 1995. *Rising Damp and Salt Attack*. State Heritage Branch, Department of Environmental and Natural Resources, Adelaide. http://www.environment.sa.gov.au/heritage/pub_desc.html#rising_damp

Thermal expansion and its control on the durability of marbles

ANNETTE ZEISIG, SIEGFRIED SIEGESMUND & THOMAS WEISS
Geowissenschaftliches Zentrum der Universität Göttingen, Goldschmidtstrasse 3,37077 Göttingen, Germany (e-mail: tweiss@gwdg.de)

Abstract: Marbles as ornamental stones as well as in their natural environments show complex weathering phenomena. The physical weathering of marbles due to thermal treatment is often discussed as the initial stage of deterioration. Eighteen different well-known marble types were selected to quantify experimentally the effect of heating and cooling within the temperature range of 20°C to 85°C while three different ramps at 40°C, 60°C and 85°C were performed. The marbles differ in composition from calcitic to dolomitic as well as in their fabrics. The average grain size varies from 50 μm up to 3 mm, while the grain boundary geometry differs from a granoblastic foam structure to those with weakly inequigranular-amoeboid structure. The lattice preferred orientations are also highly different in c-axis and a-axis distributions. With respect to the heating and cooling cycles three distinct groups of marbles can be distinguished: Type I is characterized by an isotropic thermal expansion (α) and large isotropic residual strain (permanent length changes); Type II exhibits an anisotopic α and no or small isotropic residual strains; while Type III shows an anisotropic α and anisotropic residual strain. Most samples show deteriorations due to thermal treatment, which cannot be uniformly explained without taking into account the rock fabrics. The magnitude and directional dependence of the thermal expansion is mainly controlled by the lattice and shape preferred orientation. The composition, grain size, grain boundary geometry and pre-existing microcracks modify in a more complex way the progressive loss of cohesion due to dilatancy caused by the anisotropic thermal expansion.

Over the last few decades, many field and laboratory studies have shown that marble shows a very special weathering behaviour and, moreover, the important mechanisms of rock decay in a range of environments are still under discussion (Fig. 1).

The high reactivity of calcite and dolomite in humid environments is well known. Solution, precipitation, alteration and corrosional phenomena, including stress-induced ones, represent the largest variety of chemical and biological action (Lasaga & Blum 1986; Watson & Brenan 1987; MacInnis & Brantley 1992; Schwarz *et al.* 1991*a*, *b*; Simon & Snethlage 1993).

The progressive loss of cohesion along grain boundaries is often discussed as an initial stage of marble decay caused by physical weathering. Kessler (1919) found that repeated heating and cooling may lead to permanent length changes, and therefore to changes in the microfabric. These observations were confirmed by many researchers. Rosenholtz & Smith (1949), Zezza *et al.* (1985), Grimm & Schwarz (1985), Sage (1988), Watson & Brenan (1987), Grimm (1999). Thomasen & Ewert (1984), Monk (1985), Bortz *et al.* (1988), Poschlod (1990) and Winkler (1996) all concluded that a variation in moisture content controls decay in marbles. Poschlod (1990) found a maximum value of 100 μm/m for the hygric expansion of Carrara marble, while Grimm (1999) reported length changes up to 1 mm/m. The highly anisotropic thermal expansion of calcite, and the less pronounced expansion in dolomite, is frequently discussed as the main driving force of marble deterioration. Rosenholtz & Smith (1949), Sage (1988), Franzini (1995) and Widhalm *et al.* (1996) reported length changes of 1 mm/m due to heating and cooling. Thermally treated marbles, which do not return to the initial length change after cooling, can show a residual stress even as a result of very small temperature changes between 20 and 50°C (Battaglia *et al.* 1993). Widhalm *et al.* (1996), Tschegg *et al.* (1999) and, more quantitatively, Siegesmund *et al.* (2000*a*, *b*) show that the rock fabric has a significant influence on the distinct differences in weathering of marbles, although they are of nearly identical compositions. The rock fabric includes the grain size, grain boundary geometry, shape preferred orientation, lattice preferred orientation (here referred to as texture) and pre-existing microcracks.

To demonstrate the importance of rock fabrics on physical weathering due to thermal expansion, a large collection of marbles was selected. The marbles differ in composition,

From: SIEGESMUND, S., WEISS, T. & VOLLBRECHT, A. 2002. *Natural Stone, Weathering Phenomena, Conservation Strategies and Case Studies.* Geological Society, London, Special Publications, **205**, 65–80.
0305-8719/02/$15.00 © The Geological Society of London 2002.

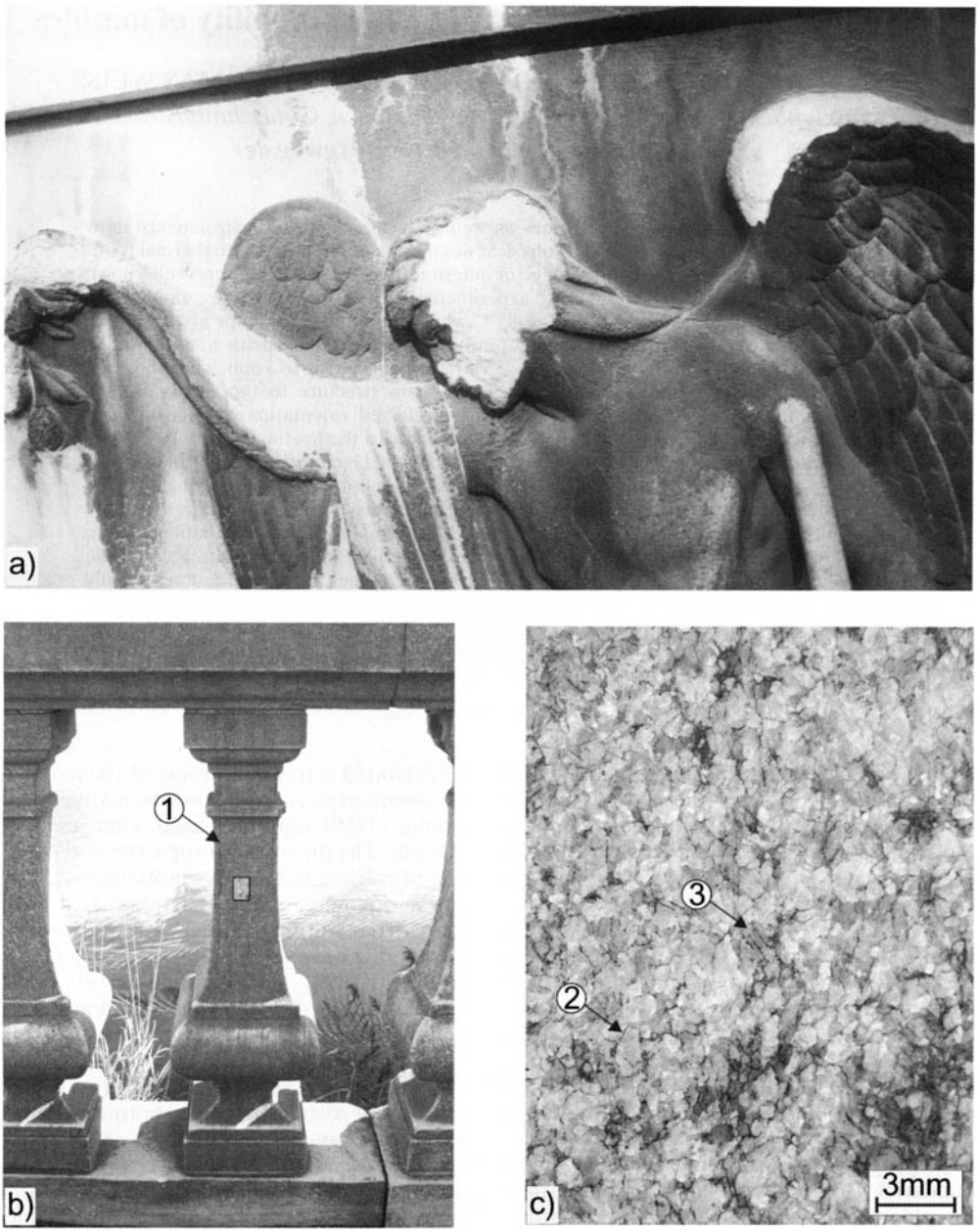

Fig. 1. Weathering of marble. (**a**) A relief at the Südfriedhof in Munich showing granular disintegration, backweathering and loss of relief structure. (**b**) Baluster from the Marmorpalais in Potsdam, rock type Grosskkunzendorf marble. A vertical foliation acts as a preferred zone of weakness leading to penetrating fractures (1). (**c**) Detail from (b): a certain amount of degradation is visible by microbial fouling preferentially along the grain boundaries (2) but also along intragranular (3) planes (e.g. cleavage planes).

grain size, shape fabrics and texture. Based on texture analyses of calcite and dolomite, the directional dependence of thermal dilatation was modelled and quantitatively compared with the experimental data. Emphasis is placed on the extent to which each fabric element in the polycrystalline marble controls the residual strain to characterize the effect of stone decay.

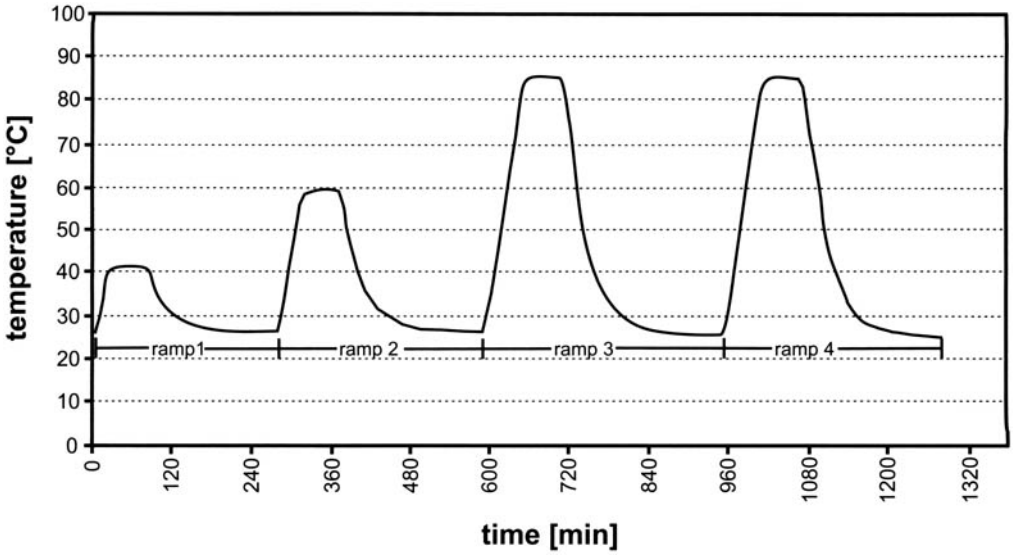

Fig. 2. Temperature pattern of the ramps performed in the thermal dilatation measurements. Heating was performed at a rate of 1°C/min. The destination temperatures are 40°C (ramp 1), 60°C (ramp 2) and 85°C (ramps 3 and 4).

Experimental

Thermal expansion measurements were performed by using a triple dilatometer (for details see Widhalm *et al.* 1996). The sample size corresponds to a cuboid of 10 × 10 × 50 mm. Calibration of the dilatometer was done using quartz glass, and the final displacement resolution was better than 1 μm. Due to a sample length of 50 mm a final residual strain of about 0.02 mm/m could be resolved. This setup allows the simultaneous measurement of the thermal expansion anisotropy of three specimens at identical experimental conditions. Thermal dilatation is a property which can be described by a second rank tensor. To quantify an arbitrary orientation of a second rank tensor, measurements in six independent directions were performed (see Siegesmund *et al.* 2000*b*).

In order to simulate temperature changes comparable to those observed under natural conditions for building or ornamental stones, the upper temperature limit was fixed at 85°C. Heating was performed with a velocity of 1°C/min to ensure thermal equilibration of the specimen. Thermal degradation may occur at significantly lower temperatures than 85°C. Thus, different ramps were driven in the thermal dilatation measurements (Fig. 2). The first ramp was up to about 40°C. After reaching the destination temperature, this temperature was kept stable until the continuous expansion of the sample vanished. Then, the specimen was cooled to room temperature. The same sequence was applied for the second ramp (60°C) and third ramp (85°C). Generally it was observed that the slope of the curves was small in ramps 2 and 3 until the end of the previous ramp was reached. Then, the slope increased significantly. The last ramp up to 85°C was repeated to investigate whether the samples are continuously degraded or the residual strain is only a phenomenon observed for one-off heating to a certain destination temperature. Different units are used for the description of thermal expansion and residual strain. The thermal dilatation coefficient α is calculated as the ratio between the length change of the sample Δl and the original sample length l multiplied by the temperature interval ΔT in kelvin ($\alpha = \Delta l/(l \times \Delta T)$). The corresponding unit is 10^{-6} K^{-1}. In contrast, the residual strain ε (in mm/m) is defined as the ratio between the length change of the sample Δl and the original sample length l. Thus, values for the residual strain can only be directly compared within the same ramp.

For the texture measurements neutron diffraction was applied. The analysis was carried out at the time-of-flight (TOF) neutron diffractometer NSHR, which is located at the pulsed reactor IBR-2 of the Frank Laboratory for Neutron Physics in Dubna, Russia (for the

Table 1. *Fabric of the marbles investigated*

Marble	Abbr.	Fabric	Grain size	SPO	Comp.	mrd	TD-type
Carrara	C1	inequigranular-polygonal	200 μm (50–100 μm)	+	cc	1.42	I
Carrara	C2	inequigranular-polygonal	300 μm (100–200 μm)	+	cc	1.46	I
Diamant	D1	equigranular-interlobate	2–3 mm	+	cc	2.96	III
Arabella	GA	equigranular-polygonal	100 μm	–	do	1.33	I
Grosskunzendorf	GK	equigranular-interlobate	1.5 mm	–	cc	2.35	II
Gitano	GT	seriate-polygonal	50 μm	0	cc	2.47	II
Thassos	GTH	equigranular-interlobate	1.75 mm	+	do	7.00	II
Volakas	GV	inequigranular-polygonal	75–100 μm	+	cc	2.58	III
Lasa	LA1	inequigranular-interlobate	1 mm	+	cc	2.19	III
Lasa	LA2	inequigranular-interlobate	1 mm	+	cc	1.57	III
Palisandro	P1	equigranular-interlobate	300 μm	+	do	2.85	II
Rosa Estremoz	RE	equigranular-polygonal	1.5 mm	+	cc	1.59	III
Soelk	SK1	inequigranular-interlobate	1.25 mm	+	cc	2.94	III
Soelk	SK2	inequigranular-interlobate	1.5 mm	+	cc	3.06	III
Sterzing	ST	inequigranular-interlobate	2.6 mm	+	cc	3.42	III
Wachau	W1	seriate-interlobate	1 mm (250–500 μm)	–	cc	2.09	III
Wachau	W2	seriate-interlobate	1–1.5 mm (500 mm)	–	cc	2.38	III

The commercial name and the abbreviation (abbr.) used in the present study are shown as well as the general fabric, grain size, shape preferred orientation (SPO) composition (comp.: cc, calcitic; do, dolomitic), c-axis maximum in multiples of random distribution (mrd) and thermal dilatation type (TD-type). For marbles with different grain sizes, the second grain size is given in parentheses.

experimental setup see Ullemeyer *et al.* 1998). Based on the neutron diffraction measurements quantitative texture analysis was carried out by means of the iterative series expansion method (Dahms & Bunge 1989). In this method, the texture is described by the coefficients C of spherical harmonic functions. From the C coefficients, anisotropic physical rock properties like elastic wave velocities or thermal dilatation may be easily modelled by averaging the single crystal properties over all observed orientations (e.g. Siegesmund & Dahms 1994). Thus, it is reasonable to assume that the intrinsic properties of a polycrystal are between the maximum and the minimum value of the single crystal. To evaluate the tensorial properties for a second-order quantity of a textured rock the Voigt, Reuss or Hill averaging techniques can be applied (Voigt 1928; Reuss 1929). In this study the Voigt approximation was used. However, the existence and the effect of pre-existing microcracks and grain boundaries is not considered in this model calculation.

The shape preferred orientation was quantified by a semi-automated image analysis method (Duyster 1991). Hand drawn images of grain boundaries of representative cross-sections with respect to the sample coordinate system are scanned and vectorized to determine quantified shape parameters. The quantified shape fabric parameters are given as the characteristic grain boundary orientation plotted in a rose diagram parallel to the three orthogonal sections (Fig. 3).

Rock samples, microfabrics and texture

Eighteen different commercial types of marble have been investigated. They are from Italy (Carrara, Lasa, Sterzing), Greece (Diamant, Arabella, Gitano, Thassos, Volakas, Palisandro), Portugal (Rosa Estremoz), Poland (Grosskunzendorf) and Austria (Soelk, Wachau) and have been widely used as building stones in the past as well as at present. Mineralogically all samples belong to calcitic and dolomitic marbles (Arabella, Thassos and Palisandro) with quartz, biotite, muscovite, phlogopite and ore minerals as accessory phases. The most important characteristics of the fabric elements are summarized in Table 1.

The average grain size, which was calculated from microscopical observations or from the digitized images of the grain boundaries, ranges from 50 μm (Gitano) up to 3 mm (Diamant). All samples are also characterized by a large variation in the shape fabric. The grain boundary orientation given for the xy-, xz- and yz-planes may differ from a more or less random distribution to a distinct planar or linear shape fabric. An example for a random distribution is the Arabella marble, while most of the other marbles (e.g. Soelk, Thassos and Carrara) exhibit a shape preferred orientation (Fig. 3). A more detailed discussion of the fabric is given for

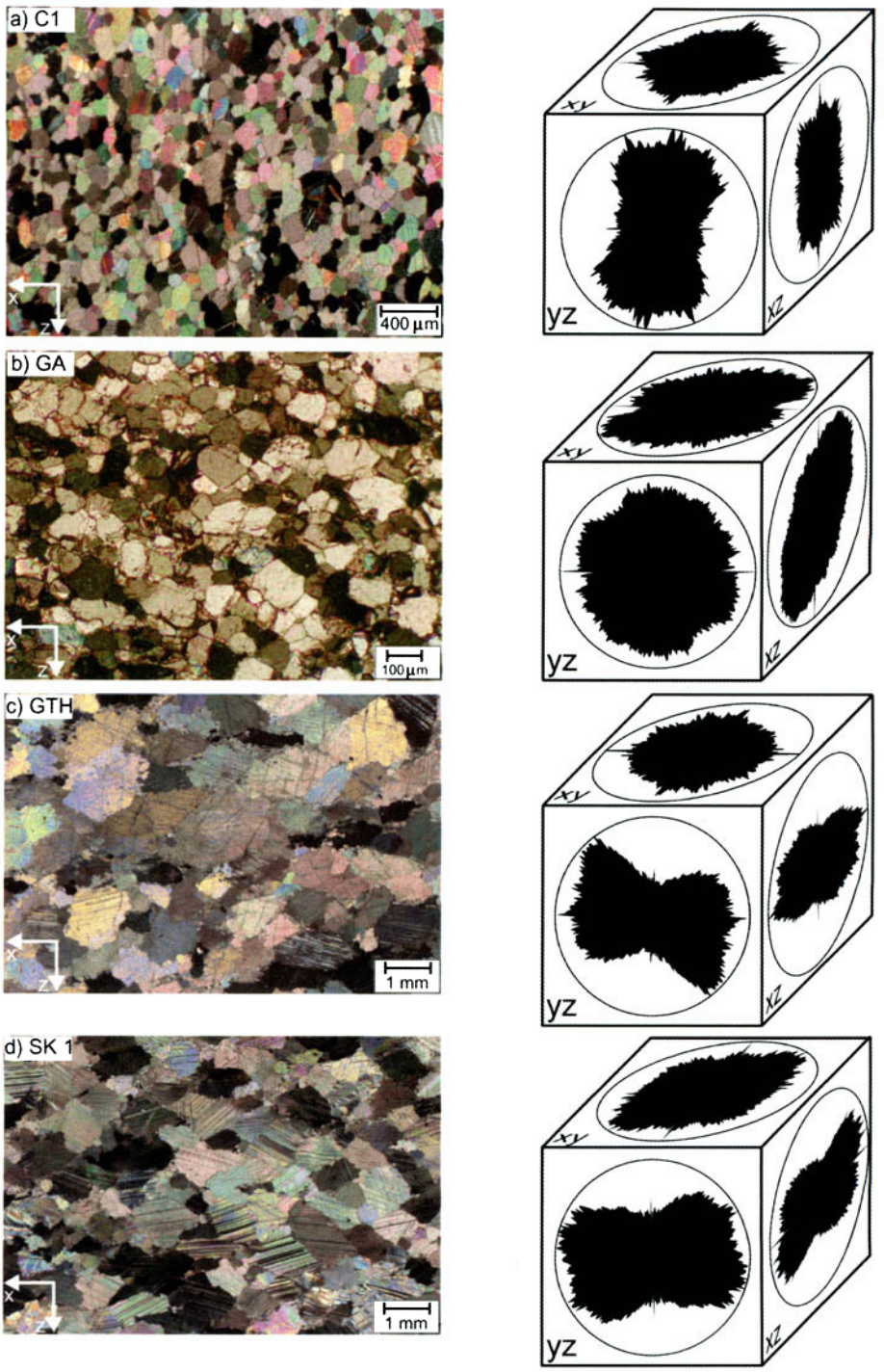

Fig. 3. Microfabric of the marbles investigated: (**a**) Carrara marble (C1), (**b**) Arabella marble (GA), (**c**) Thassos marble (GTH) and (**d**) Soelk marble (SK1). The microfabric is shown in the xz-section of the structural reference frame (left column); the preferred orientation of grain boundaries is shown for all mutually perpendicular planes (right column).

Thassos, Arabella, Soelk and Carrara marbles because they exhibit remarkable differences in the thermal dilatation behaviour. The shape of the grain aggregates can generally be classified between equigranular-polygonal and inequigranular-polygonal in the sense of Moore (1970).

Since a dolomitic composition may have an influence on the durability of marbles, dolomitic and calcitic marbles were compared. Carrara (calcite) and Arabella (dolomite) are fine grained marbles with more or less straight grain boundaries (foam structure). In contrast, Thassos and Soelk are more coarse grained, while the grain boundaries can be characterized as equigranular-interlobate and inequigranular-interlobate. The much higher irregularity of the lobate grain boundaries is clearly shown in Figure 3. Thassos and Soelk exhibit two sets of conjugate planar fabrics with an opening angle of around 50°, which are slightly asymmetrically disposed to the foliation. These fabrics can be easily observed in thin sections and in the corresponding grain boundary surfaces (see Fig. 3). In summary, the grain boundary geometry or the grain interlocking for all marbles ranges between equigranular-polygonal (Rosa Estremoz) up to seriate-interlobate (Gitano) with a slight tendency to be inequigranular-amoeboid (Wachau). This implies that the metamorphic and deformation history over geologically long time spans that control the development of the rock fabrics was quite different for the samples with different fabric types. Recrystallization processes, for instance, may control the grain size and the configuration of grain boundaries. The evidence for grain boundary migration recrystallization is the presence of highly irregular grain boundaries. The driving force is the difference in the dislocation density resulting in a bulging of the grain boundaries into crystals with the higher dislocation density (Gottstein & Mecking 1985). In other cases, subgrain recrystallization may lead to an equilibrium fabric of polygonal crystals with interfacial angles of approximately 120° (Carrara or Arabella). From the mechanical point of view it seems to be clear that a decrease in grain boundary energy is correlated with the decrease in strength of a polycrystalline material.

Besides other processes (for a review see Skrotzki 1994) deformation may be responsible for the development of a lattice preferred orientation (here referred to as texture) which also has a significant influence on physical properties and their directional dependence (e.g. Siegesmund & Dahms 1994; Kocks *et al.* 2000). All samples were analysed with respect to their textures. Leiss & Ullemeyer (1999) discussed the fundamental texture types of calcite and dolomite which are found in nature. In summary, they can be described by a rotating single crystal with the c-axis or a-axis as the rotation axis, respectively. These c-axis and a-axis fibre types can combine to form intermediate texture types. The c-axis and a-axis pole figures for Thassos, Arabella, Soelk and Carrara are illustrated in Figure 4a–d. Usually a single c-axis maximum, which is in most cases elongated to an oval-shaped pattern, can be observed. According to the calcite crystallography the a-axis poles are arranged on a great circle around the c-axis pole density maximum. The maximum pole density is highly variable. The maximum of the c-axis distributions varies from 1.4 mrd (Carrara) to 7.0 mrd (Thassos) (mrd = multiples of random distribution). The latter maximum of (001) indicates a strong texture and, consequently, a pronounced anisotropy of the physical properties must be expected. In order to characterize the textures of all 18 samples, the tensor shape T calculated from the pole figure tensor is applied to describe the different c-axis concentrations (Jelinek 1981). It varies from 1 (perfectly planar) to –1 (perfectly linear). The shape factor T calculated from the pole figure tensor characterizes the texture differences very well. It covers the range from $T = -0.859$ (Wachau) to $T = 0.881$ (Rosa Estremoz) indicating a well-pronounced cluster-like and a moderate girdle-like shape of the intensity distribution as the extreme cases (Fig. 5). Extremely planar c-axis distributions (i.e. complete gridles) are not observed. The maximum intensity, obtained from a simplified texture reproduction with $L = 2$ ranges from 1.4 to 7.0 (Table 1).

Results

Thermal expansion as a function of temperature

The thermal expansion coefficients α of all marbles investigated show a more or less pronounced directional dependence of α (Fig. 6). The directional dependence is weak for the C1 and GA marble and it is very pronounced for the GTH and SK1 marble (see Table 1 for abbreviations). However, it is not only the thermal dilatation coefficient that may be directionally dependent; the residual strain also can be a parameter which varies in magnitude and directional dependence (Fig. 6). On the basis of this extended experimental data set, the thermal

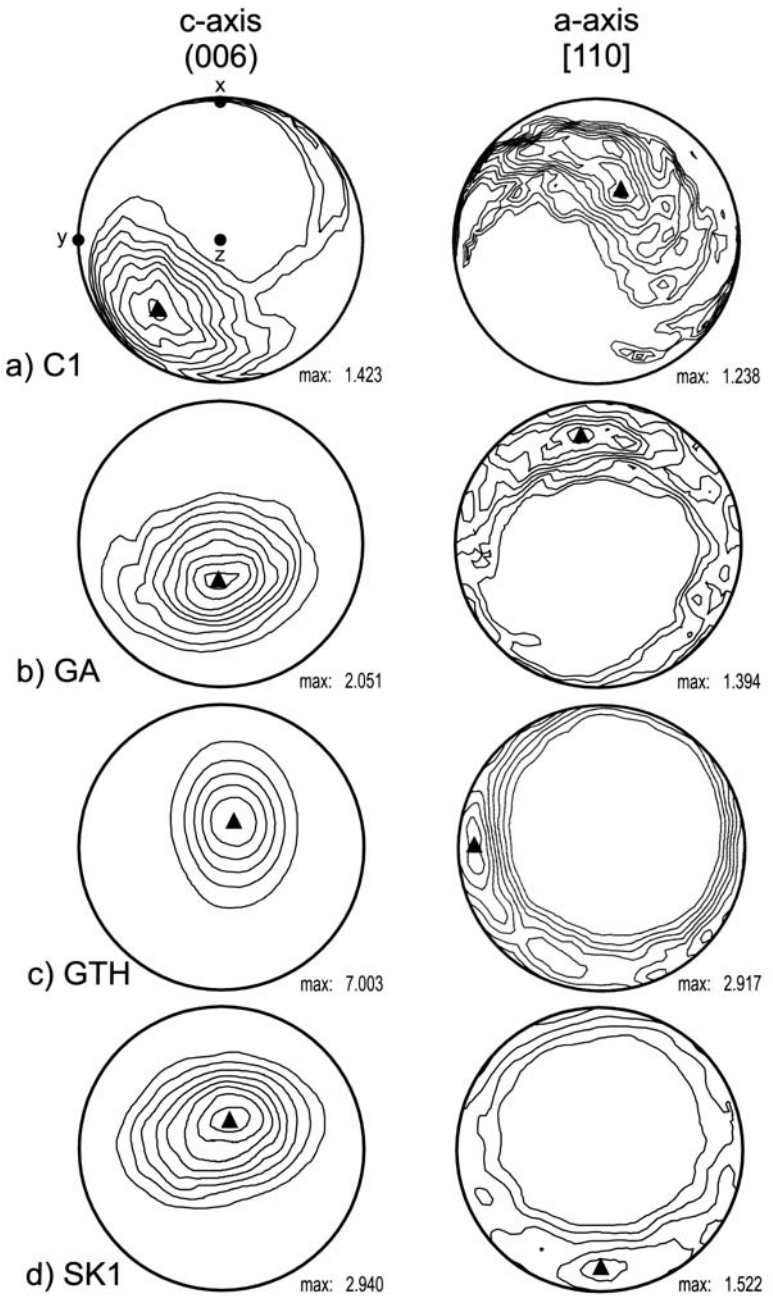

Fig. 4. Texture of the marbles investigated: (**a**) Carrara marble (C1), (**b**) Arabella marble (GA), (**c**) Thassos marble (GTH) and (**d**) Soelk marble (SK1). The c-axis (left column) and a-axis (right column) distributions are shown. The isolines are given as multiples of random distribution (mrd) varying between 1 mrd and the maximum intensity (max), which is marked with a triangle (equal area projection, lower hemisphere). The coordinates of the structural reference frame are shown in (a).

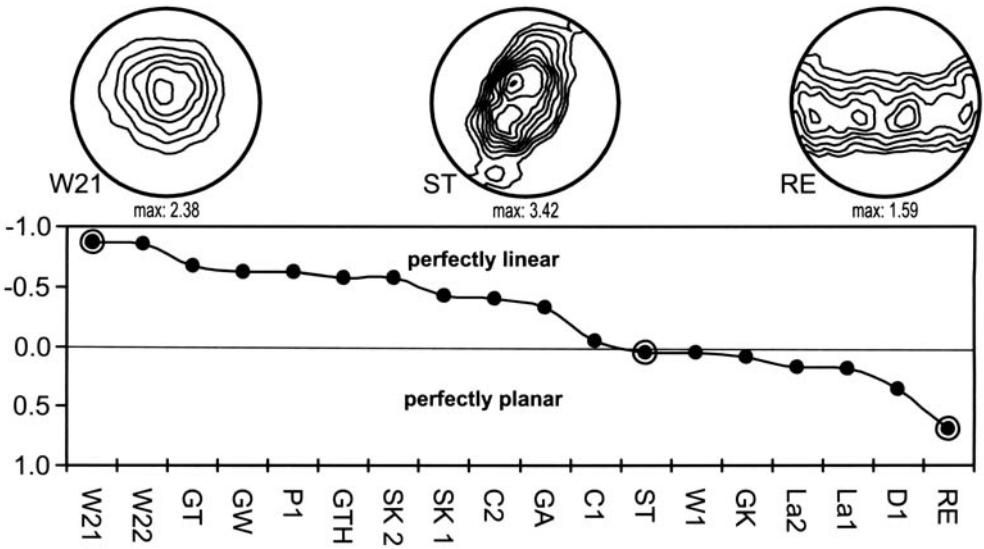

Fig. 5. Variation of texture patterns: the shape factor T as a function of marble type. Examples of pole figures for marbles with linear (W21), neutral (ST) and planar (RE) c-axis distributions are given at the top of the graph (isolines in mrd, equal area projection, lower hemisphere).

expansion versus temperature relationships can be classified into different groups. The samples TH, GA, SK1 and C1 are used as examples to illustrate this interdependence for the directions parallel to the x-, y- and z-direction. The different types can be summarized as follows:

Type I: isotropic α and large isotropic residual strain
Type II: anisotropic α and no or a small isotropic residual strain
Type III: anisotropic α and anisotropic residual strain

Type I. The curves for the Carrara marble clearly exhibit a weak directional dependence of both α and the residual strain. The magnitude of the residual strain is dependent on the destination temperature. The curves for the first, second and third ramp show a successive increase in residual strain. The final result is a permanent expansion of the sample of about 0.2 mm/m. This value corresponds to the summed contribution of all residual strains observed in the preceding ramps. The Arabella marble shows a similar behaviour, but a slightly smaller permanent expansion (about 0.1 mm/m).

Type II. The marble from Thassos is, according to its strong texture, very anisotropic but shows almost no residual strain. Thus, it may be regarded as a marble which is relatively resistant against thermal degradation. The curves show an almost linear thermal expansion and, due to an overlapping of the curves, the individual ramps are hard to discern. Subtypes of this behaviour (e.g. GT, P1) show a small isotropic residual strain.

Type III. The Soelk marble shows both a strong directional dependence of α and the residual strain. A larger residual strain is observed parallel to the z-direction than in the other directions. After the first ramp, the residual strain is very small. It increases significantly in the second and third ramp (see Fig. 6). This effect can best be seen when the z-direction is considered. After the fourth ramp no residual strain is observed. It can be concluded that a certain thermal degradation is monitored by a reinforced gradient of the curves after a certain temperature is reached, corresponding to an increase of α in this part of the curve. A clear directional dependence of the residual strain is also observed for the Wachau marble, but the magnitude is smaller for this marble.

In principle, all marbles investigated can be assigned to these types of thermal behaviour (see Table 1).

Determination of thermal degradation

The Soelk marble is used as an example to illustrate thermal degradation in detail (Fig. 6e, f).

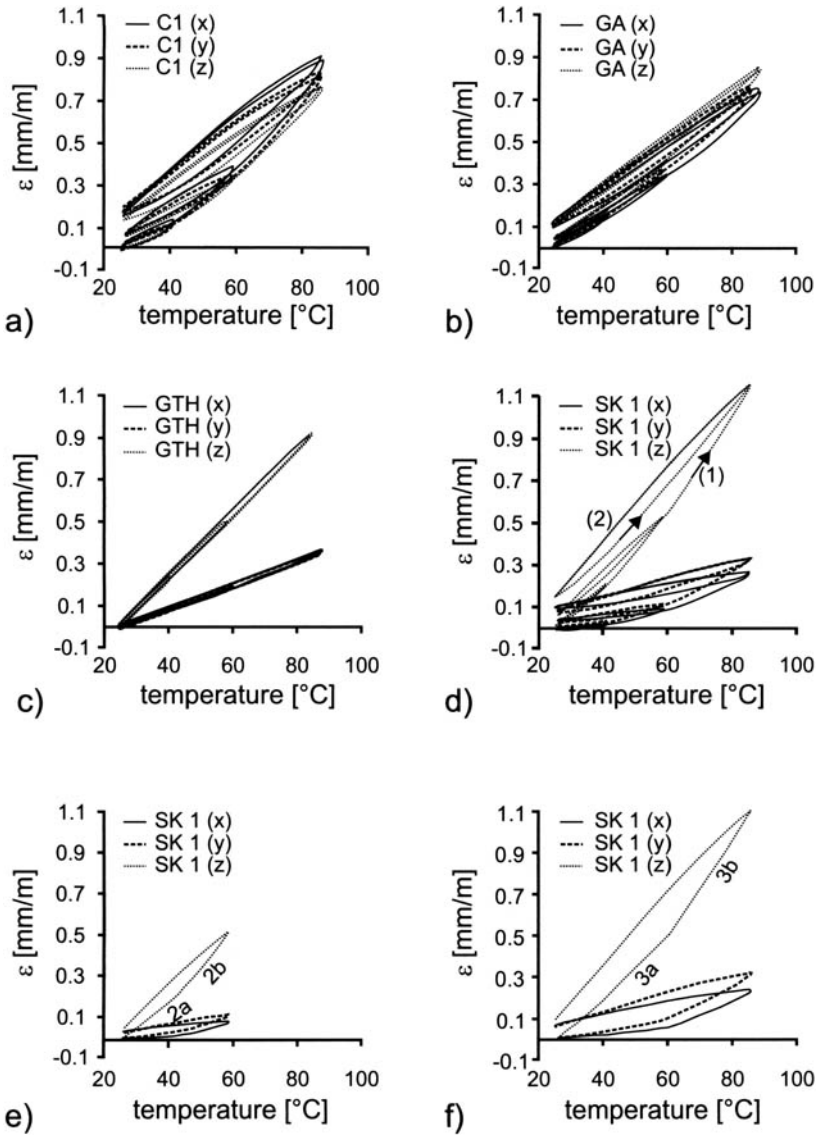

Fig. 6. Thermal dilatation (ε) as a function of temperature: (**a**) Carrara marble (C1), (**b**) Arabella marble (GA), (**c**) Thassos marble (GTH) and (**d**) Soelk marble (SK1). The curves give an overview on all the thermal cycles (ramps) investigated. The final residual strain corresponds to the total contribution of all temperature cycles. (**e** and **f**) Specific examples for the second (e) and third (f) ramps for the SK1 marble (x-, y-, z-direction). In (d) the expansion curves for ramp 3 (1) and ramp 4 (2) at increasing temperature are marked by arrows.

Therefore, the data obtained for the second and third ramp up to 60°C and 85°C, respectively, are used. In the second ramp (Fig. 6e), the curves exhibit a small slope until the temperature of the first ramp (40°C) is reached. In the second part of the curve, the slope increases. The same relationship applies for the third ramp, where an increase in the slope is observed at 60°C, i.e. at the destination temperature of ramp 2. An example for the increase in α associated with thermal microcracking can be given for the z-direction (i.e. maximum dilatation direction), where α increases from 13×10^{-6} (ramp 3a) to 22×10^{-6} (ramp 3b).

Buffering of pre-existing microcracks

It is not unequivocally true that a change in α is only associated with an increase in thermal degradation. The gradient in the first part of the curves can also be smaller when a buffering of pre-existing microcrack systems has to be considered (e.g. Leiss & Weiss 2000). That applies to marbles which are already degraded or which show, as a consequence of their complex geological history, pre-existing microcracks.

Direct evidence for the first cause can be drawn from the experimental data (Fig. 6d) of the Soelk marble using the fourth ramp. In the z-direction, the gradient of the curve is different in the first and second part of the curve, even if no residual strain is observed. Thus, there must be a buffering by pre-existing crack systems. The 'buffering effect' of the Soelk marble in this specific direction (z-direction) in the fourth ramp is relatively small compared to the strong thermal degradation of this marble observed in the previous ramps.

Initiation of thermal degradation

Since the starting temperature for a thermal degradation of marble is supposed to be a characteristic of the specific marble type, it is necessary to have a look at the behaviour of the marbles in the different ramps. For most of the marbles, a very weak residual strain is observed after the first ramp up to 40°C. The values are in the range of the detection limit, i.e. around 0.02 mm/m. In the second ramp up to 60°C the residual strain generally increases. While the C1, C2 and GK marbles reach a residual strain of about 0.05 mm/m, indicating a thermal degradation at relatively low temperatures, the other marbles show values between 0.01 and 0.04 mm/m. In the third ramp, almost all marbles show a residual strain larger than 0.05 mm/m. Exceptions are GT, GTH, P1, W1 and W2. Thus, the latter marbles seem to be rather stable in terms of thermal degradation. In the fourth ramp, the residual strain vanishes for all of the marbles, i.e. no further thermal degradation occurs. The residual strain is generally smaller than observed in the first ramp.

Anisotropy of the thermal dilatation: intrinsic

A compilation of all marbles investigated using the data from the third ramp gives an overview of the particular properties described above. The data of this ramp are used, since almost all marbles show a residual strain at this temperature level and a strong fabric-induced directional dependence of the dilatation coefficient α (Fig. 7). The variation of α is shown as a function of the first and second part of the curve. As mentioned above, the first part of the curve is supposed to be controlled by the intrinsic properties, while the second part of the curves show the interaction between intrinsic properties and thermal degradation. The latter factor may also show a directional dependence when a preferred direction of microcracking is observed.

The weakest variation of α calculated from ramp 3a is observed for the C2 marble, and a very strong directional dependence is observed for the Soelk marble. The α-values for the first part of ramp 3 vary in a wide range from almost zero (Lasa, Rosa Estremoz and Sterzing marbles) to a value of about 15×10^{-6} K^{-1} (Thassos marble). The equivalent expansion associated with an observed α for a 1 m marble slab can be directly determined from Figure 7b. These values have to be regarded as being close to the intrinsic properties, since only the parts of the curves before thermal degradation starts have been evaluated.

Anisotropy of the thermal dilatation: thermally degraded

The second part of the curves gives completely different information. In general, all α-values are higher than those of ramp 3a (Fig. 7a). This indicates that a certain amount of thermal degradation occurred. The GTH marble shows a very small difference in α between ramps 3a and 3b, while it is very pronounced for the C2 marble. For the RE marble, the anisotropy of the thermal dilatation is enlarged in ramp 3b giving evidence for a strong directional dependence of thermal degradation. For some marbles the variability of α at different sample directions is smaller (e.g. GT) or equal in ramps 3a and 3b indicating a uniform crack nucleation. The magnitude and directional dependence of the residual strain associated with the third ramp is shown in Figure 8.

Magnitude of thermal degradation

The residual strain of a sample is characteristic for the degradation of a marble as a consequence of thermal treatment. For a fabric-dependent comparison of thermal degradation, the residual strain associated with ramp 3 is used. This ramp shows a magnitude of residual strain which is clearly above the experimental

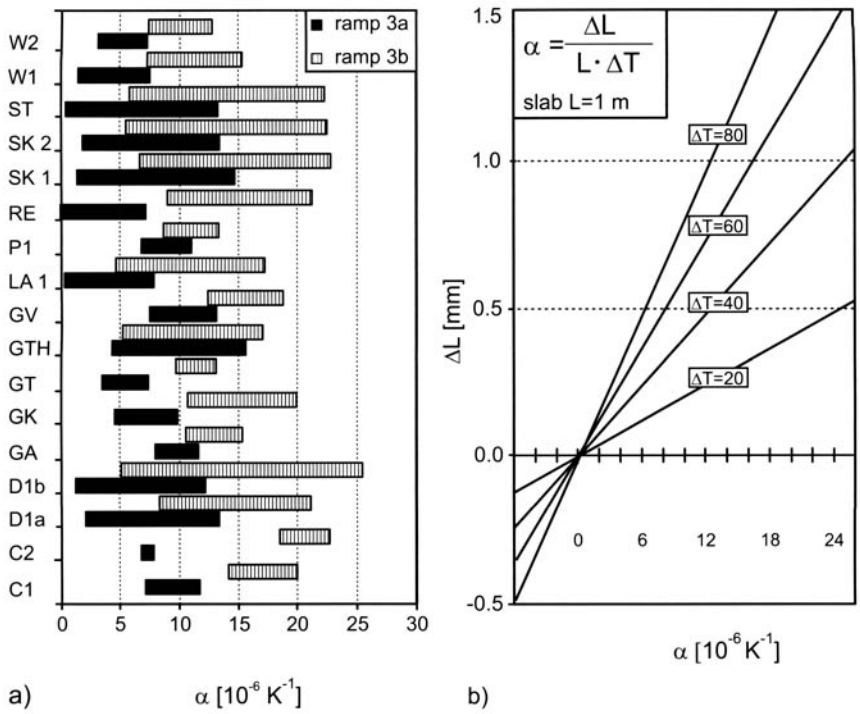

Fig. 7. Variation of the thermal dilatation coefficient as a function of marble type. (**a**) The coefficient of thermal expansion is shown for the first part of the curve (black) and the second part of the curve (hatched) according to the observations described in Figure 6f. (**b**) The expansion of a 1 m marble slab as a function of α for different temperature intervals is shown based on the given formula.

resolution. Thus, these values can be evaluated with a high degree of confidence.

Generally, the residual strain varies from almost zero (GTH) to around 0.2 mm/m for C2. Another extremely deteriorated specimen comparable to C2 is the RE marble, which shows a very high residual strain of about 0.15 mm/m. Two dolomite marbles (GTH, P1) show a very small proneness to thermal weathering. However, most of the marble types investigated are in the range of about 0.05 to 0.1 mm/m. All these values concur quite well with the observed increase of α as a consequence of thermal treatment (cf. Fig. 7).

There is clear evidence that the grain size does not significantly influence the residual strain, even if there is a slight tendency towards a higher residual strain for samples with small grain sizes (Fig. 8). This is even more surprising, since marbles with a larger grain size predominantly exhibit interlobate fabrics, while the finer grained marbles predominantly show polygonal fabrics. An exception is the RE marble with a polygonal fabric and a large grain size.

It can be summarized that a more or less pronounced directional dependence of the residual strain is a general property of all marbles investigated. The start, the magnitude and directional dependence of the residual strain cannot be simply assigned to one fabric property (e.g. the grain size). A combination of all fabric parameters must be considered to understand thermal degradation in marble.

Directional dependence of thermal degradation

In order to quantify the directional dependence of the residual strain, the Soelk marble is used as an example. There is a clear difference between both values (α and the residual strain) at different sample directions. The strong directional dependence of α is obvious considering the strong texture of this marble (see Fig. 4d). For ramp 3b, a strong increase of the slope indicates a certain thermal degradation. To check the relationship between texture-induced and

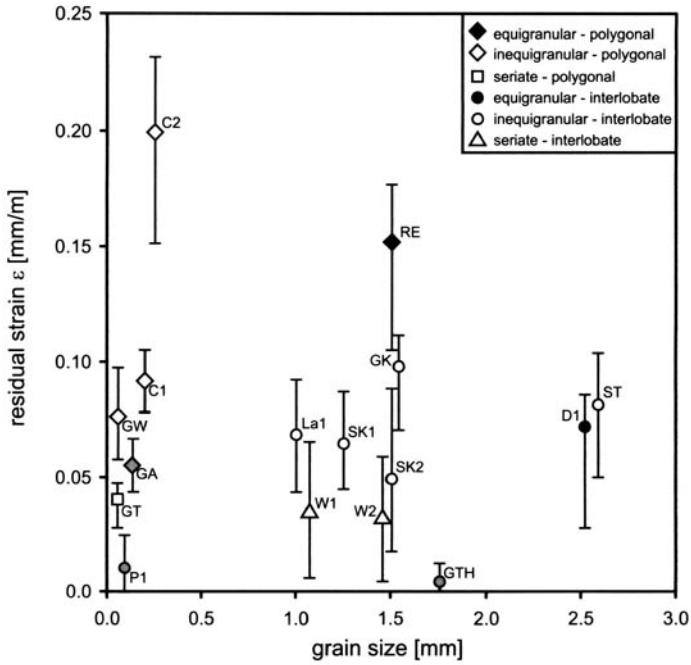

Fig. 8. Residual strain of different marbles as a function of grain size. The maximum and minimum values are given as error bars, the average is calculated from measurements at six independent sample directions. The different fabric types (polygonal, interlobate etc.) are indicated by symbols; dolomite marbles are marked by grey filled symbols.

grain-fabric-induced thermal dilatation the following approach was taken.

At first, the texture-based pole figure of α was calculated. The calculation of second rank tensorial properties like thermal expansion based on textures is described in detail in Siegesmund & Dahms (1994). The basic principle is that the single crystal properties are averaged over all measured orientations. It clearly shows a maximum of α for the z-direction and a minimum parallel to the x-direction (Fig. 9a). A very similar pole figure is obtained, when the almost linear slope of the curves is used for the calculation of the experimentally determined α (Fig. 9b). Therefore, experimental data have been used from six independent directions. The experimentally observed values agree quite well with the modelled ones. For ramp 3b an increase in the slope of the curves concurring with an increase in the dilatation coefficient α is observed, so the difference between α in ramps 3a and 3b can be used to determine the direction of preferred thermal degradation (Fig. 9c). It is obvious that for the Soelk marble the strongest degradation occurs parallel to the c-axis maximum, i.e. perpendicular to the z-direction of the structural reference frame. This can be explained by the observed shape anisotropy of this marble which shows a preferred orientation of grain boundaries perpendicular to the z-directions. A preferred alignment of frequently occurring twin-planes parallel to the foliation may also be of importance (see Fig. 3d) because coarse grained marbles may show a thermal degradation at inter- and intragranular planes while fine grained marbles are predominantly degraded along the grain boundaries (Ruedrich *et al.* 2002).

Intrinsic versus extrinsic anisotropy

A basic question for the comparison of thermal behaviour of the different marbles is whether the anisotropy of α, here referred to as $A = \alpha_{min} / \alpha_{max}$, observed in the experiments is closely linked to the texture. This effect can be best documented when the experimentally determined values (A_{exp}) are shown as a function of calculated (A_{mod}) data. Experimental values are shown for the first part (ramp 3a) and the second part (ramp 3b) of one thermal cycle. A low anisotropy in the graph is characterized

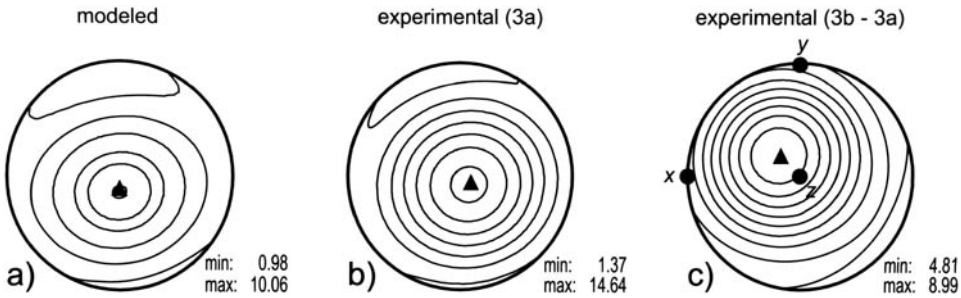

Fig. 9. Texture-induced and experimental dilatation. (**a**) Modelled distribution of the texture-based α; (**b**) directional dependence of the experimentally determined α from ramp 3a; (**c**) increase of α at ramp 3b.

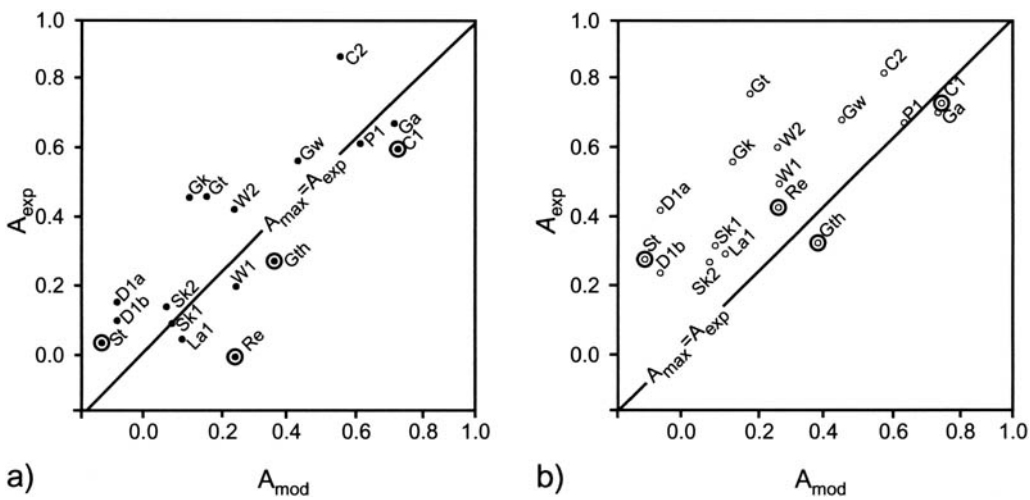

Fig. 10. Anisotropy of experimental thermal dilatation A_{exp} ($A = \alpha_{min}/\alpha_{max}$) as a function of the modelled thermal dilatation A_{mod}. (**a**) A_{exp} calculated from ramp 3a; (**b**) A_{exp} calculated from ramp 3b. The marble types which are described in the text are outlined.

by a value close to 1, while a pronounced anisotropy results in values smaller than 1. There is a general agreement between A_{exp} and A_{mod} (Fig. 10). Samples with a weakly calculated anisotropy exhibit a weak experimental anisotropy and vice versa, when the values calculated for the linear part of the experimental data are considered. The experimental values for the second part are more scattered, which can be taken as an indication that the thermal degradation of a particular marble is controlled not only by the texture but by the complete grain fabric. A few examples may illustrate this behaviour more explicitly (the examples are outlined in the graph). The C1 marble shows a weak anisotropy in both parts of the curve. This indicates that the thermal degradation is uniformly distributed over all orientations. The ST marble shows a stronger anisotropy in the first part of the ramp (Fig. 10a) than in the second part. Thus, the intrinsic anisotropy must be higher and the thermal degradation must be more uniform. The RE marble shows the opposite effect. A stronger anisotropy in the second part than in the first part of the ramp indicates strongly direction-dependent thermal degradation. The GTH marble shows a clear coincidence of the values in both diagrams. Thus, its thermal degradation must be very small or very uniform. This could be shown in Figure 8 for this marble. Consequently, the correlation between A_{exp} and A_{mod} can be used to visualize both the

anisotropy of the thermal dilatation coefficient and the change in α as a consequence of thermal degradation.

Discussion and conclusions

There are many factors supposed to influence thermal degradation of marble. The rock fabric, i.e. composition, grain size, grain shape anisotropy, grain boundary morphology and texture, significantly triggers the proneness to thermal weathering of a marble (e.g. Siegesmund *et al.* 2000*b*). The effect of the different fabric parameters can be summarized as follows.

(1) The modal composition is an important factor for the thermal properties of a marble, since the thermal expansion behaviour is at least partially controlled by the single crystal properties. Both calcite and dolomite show an extreme directional dependence of α at different crystallographic directions. Parallel to the c-axis, both minerals show an α value of about $26 \times 10^{-6}\,K^{-1}$. However, parallel to the a-axis calcite shows a negative α value of about $-6 \times 10^{-6}\,K^{-1}$ while the corresponding value for dolomite is about $6 \times 10^{-6}\,K^{-1}$. Thus, even strongly anisotropic dolomite marbles will not show any contraction with increasing temperature as shown for the GTH marble. Since the GA (dolomite) and C1 (calcite) marble show a similar thermal degradation, the residual strain is likely not to be controlled exclusively by the composition. However, other mechanical properties like compressive and tensile strength of calcite and dolomite marbles may vary significantly according to the different Young's modulus and shear modulus of these minerals (Bass 1995). Accessory minerals like mica may have more effect on other weathering processes (e.g. Ondrasina *et al.* 2002).

(2) The grain size cannot be the most important factor for marble degradation (see Fig. 7). Marbles with a large grain size exhibit the same magnitude of residual strain as marbles with a small grain size. A similar relationship was also proposed by Tschegg *et al.* (1999). This correlation applies even for extraordinarily deteriorated examples like C2 and RE. However, thermal degradation is a strongly direction-dependent parameter, and thus, its directional dependence must be taken into account.

(3) The grain shape anisotropy significantly triggers thermal degradation, as shown for the SK1 marble. This observation is supported by the observations of Ruedrich *et al.* (2002) for a weathered Prieborn marble (see also Siegesmund *et al.* 2000*b*). Thus, since grain boundary cracking is the most prominent factor for marble degradation, a substantial part of the observed directional dependence of residual strain must be attributed to shape fabrics.

(4) The grain boundary morphology, i.e. the irregularity of grain boundaries, does not play such an important role as was previously assessed. Marbles with interlobate fabrics as well as marbles with polygonal fabrics may show a residual strain after thermal treatment. An exception may be the WA marble, which shows amoeboid (i.e. highly irregular) grain boundaries leading to a very small residual strain. However, the large amount of mica and a clearly inequigranular grain size distribution may accommodate a certain amount of thermally induced stress that does not exceed the threshold of cohesion. Thus, further studies must be performed to quantify and localize a fabric-dependent deterioration.

(5) The texture clearly determines magnitude and directional dependence of α, since there is a general agreement between calculated (texture-based) and experimentally determined anisotropies. Thermal degradation changes this relation, i.e. the anisotropies increase or decrease according to a coincidence or contrariness of thermal degradation and intrinsic dilatation, respectively. A general observation is that the maximum of thermal degradation is closely linked to the c-axis maximum. A deviation in this behaviour can be traced back to shape preferred orientations oblique to the c-axis maximum. However, the individual grain-to-grain orientation may be of importance. Tschegg *et al.* (1999) found that large internal stresses, leading to thermal microcracking when the threshold of cohesion is exceeded, are caused by an almost random orientation of the grains. The specific relationship of this almost random orientation may also be valid for strongly textured marbles at certain sample directions. This could cause a directional dependence of thermal degradation even if no clear shape preferred orientation is observed. However, this assumption must be validated in the future by single grain texture measurements and model calculations.

(6) Pre-existing microcrack systems may be of importance as well. Siegesmund *et al.* (2000*b*) have shown that a change in the anisotropy patterns between modelled and experimentally determined values may be explained by pre-existing microcracks, resulting from a complex geological history.

In summary, it can be stated that there is a clear fabric dependence of residual strain after thermal treatment and, thus, of thermal degradation. Thermally induced microcracks lead to a

residual strain after heat treatment and, thus, to a deterioration of the rock's quality. However, the fabric cannot be reduced to one or a small number of parameters (e.g. only grain size, grain shape etc.). The thermal degradation of a marble is controlled by an interaction of all fabric parameters.

We gratefully acknowledge the help of E. Tschegg and K. Ullemeyer for their support with the experimental run of the thermal expansion measurements and the neutron texture measurements. The study was supported by the Deutsche Forschungsgemeinschaft with the grants Si 438/10-1, 2 (Heisenberg-Fellowship) and Si 438/13-1. We extend our thanks to the reviewers F. Zezza and H.R. Wenk for their constructive reviews which helped to improve the paper.

References

BASS, J. D. 1995. Elasticity of minerals, glasses, and melts. *In*: AHRENS, T. J. (ed.) *Handbook of Physical Constants*. American Geophysical Union, Washington, DC, 45–63.

BATTAGLIA, S., FRANZINI, M. & MANGO, F. 1993. High sensitivity apparatus for measuring thermal expansion: preliminary results on the response of marbles. *Il Nuovo Cimento*, **16**, 453–461.

BORTZ, S. A., ERLIN, B. & MONK, C. B., JR. 1988. Some field problems with thin veneer building stones. *In*: DONALDSON, B. (ed.) *New Stone Technology, Design, and Construction for Exterior Wall Systems*. American Society for Testing and Materials, Philadelphia, Special Technical Publication **996**, 11–31.

DAHMS, M. & BUNGE, H.-J. 1989. The iterative series-expansion method for quantitative texture analysis, I. General Outline. *Journal of Applied Crystallography*, **22**, 439–447.

DUYSTER, J. 1991. *Strukturgeologische Untersuchungen im Moldanubikum (Waldviertel, Oesterreich) und methodische Untersuchungen zur bildanalytischen Gefuegequantifizierung von Gneisen*. PhD Thesis, University of Goettingen.

FRANZINI, M. 1995. Stones in monument: natural and anthropogenic deterioration of marble artifacts. *European Journal of Mineralogy*, **7**, 735–743.

GRIMM, W. D. 1999. Beobachtungen und Ueberlegungen zur Verformung von Marmorobjekten durch Gefuegeauflockerung. *Zeitschrift der Deutschen Geologischen Gesellschaft*, **150**(2), 195–235.

GRIMM, W. D. & SCHWARZ, U. 1985. Naturwerksteine und ihre Verwitterung an Muenchener Bauten und Denkmaelern Ueberblick ueber eine Stadtkartierung. Bayerisches Landesamtes für Denkmalpflege, Muenchen (Lipp), Arbeitsheft **31**, 28–118.

GOTTSTEIN, G. & MECKING, H. 1985. Recrystallization. *In*: WENK, H.-R. (ed.) *Preferred Orientation in Deformed Metals and Rocks, an Introduction to Modern Texture Analysis*. Academic Press, Orlando, 183–214.

JELINEK, V. 1981. Characterization of the magnetic fabric of rocks. *Tectonophysics*, **79**, 63–67.

KESSLER, D. W. 1919. *Physical and chemical tests of the commercial marbles of the United States*. Technologic Papers of the Bureau of Standards, **123**, Government Printing Office, Washington DC.

KOCKS, U. F., TOMÉ, C. N. & WENK, H.-R. 2000. *Texture and Anisotropy. Preferred Orientations in Polycrystals and their Effect on Materials Properties*. Cambridge University Press.

LASAGA, A. C. & BLUM, A. E. 1986. Surface chemistry, etch pits and mineral-water reactions. *Geochimica et Cosmochimica Acta*, **50**(10), 2263–2379.

LEISS, B. & ULLEMEYER, K. 1999. Texture characterisation of carbonate rocks and some implications for the modeling of physical anisotropies, derived from idealized texture types. *Zeitschrift der Deutschen Geologischen Gesellschaft*, **150**(2), 259–274.

LEISS, B. & WEISS, T. 2000. Fabric anisotropy and its influence on physical weathering of different types of Carrara marbles. *Journal of Structural Geology*, **22**, 1737–1745.

MACINNIS, I. N. & BRANTLEY, S. L. 1992. The role of dislocations and surface morphology in calcite dissolution. *Geochimica et Cosmochimica Acta*, **56**(3), 1113–1126.

MONK, C. B., JR. 1985. The rational use of masonry. *Protocol of the Third North American Masonry Conference*. Construction Research Centre, Civic Engineering Department, University of Texas, 191–227.

MOORE, A. C. 1970. Descriptive terminology for the textures of rocks in granulite facies terrains. *Lithos*, **3**, 123–127

ONDRASINA, J., KIRCHNER, D., SIEGESMUND, S. 2002. Freeze–thaw cycles and their influence on marble deterioration: a long-term experiment. *In*: SIEGESMUND, S., WEISS, T. & VOLLBRECHT, A. (eds) *Natural Stone, Weathering Phenomena, Conservation Strategies and Case Studies*. Geological Society, London, Special Publications, **205**, 9–18.

POSCHLOD, K. 1990. Das Wasser im Porenraum kristalliner Naturwerksteine und sein Einfluss auf die Verwitterung. *Muenchner Geowissenschaftliche Abhandlungen*, **7**, 1–62.

ROSENHOLTZ, J. L.& SMITH, D. T. 1949. Linear thermal expansion of calcite, var. Iceland spar and Yule marble. *The American Mineralogist*, **34**, 846–854.

RUEDRICH, J., WEISS, T. & SIEGESMUND, S. 2002. Thermal behaviour of weathered and consolidated marbles. *In*: SIEGESMUND, S., WEISS, T. & VOLLBRECHT, A. (eds) *Natural Stone, Weathering Phenomena, Conservation Strategies and Case Studies*. Geological Society, London, Special Publications, **205**, 255–272.

REUSS, A. 1929. Berechnung der Fliessgrenze von Mischkristallen auf Grund der Plastizitaetsbedingung für Einkristalle. *Zeitschrift für Angewandte Mathematik und Mechanik*, **9**, 49–58.

SAGE, J. D. 1988. Thermal microfracturing of marble. *In*: MARINOS & KOUKIS (eds) *Engineering Geology of Ancient Works, Monuments and Historical Sites*. Balkema, Rotterdam, 1013–1018.

SCHWARZ, A., LEHLHORN, L., BOUÉ, A. & MANGELS, H. 1991*a*. Bewittertung von Natursteinen mit schadgashaltiger Luft, orientierende Simulationsversuche in einer Doppelklimakammer, Teil 1. *Bautenschutz und Bausanierung*, **14**, 85–97.

SCHWARZ, A., LEHLHORN, L., BOUÉ, A. & MANGELS, H. 1991*b*. Bewitterung von Natursteinen mit schadgashaltiger Luft, orientierende Simulationsversuche in einer Doppelklimakammer, Teil 2. *Bautenschutz und Bausanierung*, **14**, 108–110.

SIEGESMUND, S. & DAHMS, M. 1994. Fabric-controlled anisotropy of elastic, magnetic and thermal properties of rocks. *In*: BUNGE, H. J., SKROTZKI, W., SIEGESMUND, S. & WEBER, K. (eds) *Textures of Geological Materials,* Oberursel (DGM Informationsgesellschaft), 353–379.

SIEGESMUND, S., WEISS, T. & TSCHEGG, E. 2000*a*. Control of marble weathering by thermal expansion and rock fabrics. *19th International Congress on Deterioration and Conservation of Stone*, Venice. Elsevier, Amsterdam, 205–213.

SIEGESMUND, S., ULLEMEYER, K., WEISS, T. & TSCHEGG, E. 2000*b*. Physical weathering of marbles caused by thermal anisotropic expansion. *International Journal of Earth Science,* **89**, 170–182.

SIMON, S & SNETHLAGE, R. 1993. *The first stages of marble weathering, preliminary results after short-term exposure of nine month.* Forschungs-Bericht, (Eurocare-Euromarble EU 496), München (Bayrisches Landesamt für Denkmalpflege) **11/1993**, 37–44.

SKROTZKI, W. 1994. Mechanisms of texture development in rocks. *In*: Bunge, H. J., Skrotzki, W., Siegesmund, S. & Weber, K. (eds) *Textures of Geological Materials*. Oberursel (DGM Informationsgesellschaft), 147–164.

THOMASEN S. E. & EWART C. S. 1984. Durability of thin-set marble. *Third International Conference on Durability of Building Materials and Components*. American Society for Testing and Materials, 313–323.

TSCHEGG, E., WIDHALM, C. & EPPENSTEINER, W. 1999. Ursachen mangelnder Formbestaendigkeit von Marmorplatten. *Zeitschrift der Deutschen Geologischen Gesellschaft*,**150**(2), 283–297.

ULLEMEYER, K., SPALTHOFF, P. L., HEINITZ, J., ISAKOV, N. N., NIKTIN, A. N. & WEBER, K. 1998. The SKAT texture diffractometer at the pulsed reactor IBR-2 at Dubna: experimental layout and first measurements. *Nuclear Instruments & Methods in Physics Research*, **A412/1**, 80–88.

VOIGT, W. 1928. *Lehrbuch der Kristallphysik*. Teubner, Leipzig.

WATSON, B. E. & BRENAN, J. M. 1987. Fluids in the lithosphere; 1. Experimentally-determined wetting characteristics of $CO_2 - H_2O$ fluids and their implications for fluid transport, host-rock physical properties, and fluid inclusion formation. *Earth and Planetary Science Letters*, **85**(4), 497–515.

WIDHALM, C., TSCHEGG, E. & EPPENSTEINER, W. 1996. Anisotropic thermal expansion causes deformation of marble cladding. *Journal of Performance of Constructed Facilities*, **10**, 5–10.

WINKLER, E. M. 1996. Technical note: properties of marble as building veneer. *International Journal of Rock Mechanics, Mineral Science & Geomechanics*, **33**(2), 215–218.

ZEZZA, U., PREVIDE MASSARA, E., MASSA, V. & VENCHIARUTTI, D. 1985. Effect of Temperature on Intergranular Decohesion of the Marbles. *5th International Congress on Deterioration and Conservation of Stone*, Lausanne, Vol. 1, 131–140.

Experimental study on the variation in porosity of marble as a function of temperature

KATARINA MALAGA-STARZEC[1,2], JAN E. LINDQVIST[2] & BJÖRN SCHOUENBORG[2]

[1] *Department of Inorganic Chemistry, Göteborg University, SE-412 96 Göteborg, Sweden (e-mail: katarina.malaga@sp.se)*

[2] *Swedish National Testing and Research Institute, Building Technology, Building Materials, Brinellgatan 4, Box 857, S-501 15 Borås, Sweden*

Abstract: The current condition of many building claddings and historical monuments clearly reveals that they are not immune to weathering action due to daily or seasonal temperature changes. In this study, porosity changes by variation in temperature have been investigated for two marble types: one calcitic and one pure dolomitic. The samples were exposed to ascending temperatures from 40 to 200°C. The results indicate that intergranular decohesion starts between 40 and 50°C. Some significant differences in temperature response for these two marble types could be distinguished. The temperature range 40–60°C is easily reached on building surfaces in most European countries during the summer months. A better understanding of the effect that temperature has on the porosity of marble could be used to develop a methodology for assessing suitable conditioning of marble before testing as well as to suggest appropriate impregnation and/or surface treatments of buildings and outdoor sculptures.

The weathering of marble, clearly observed in many historical monuments, typically consists of the progressive breakdown of rock cohesion (granular decohesion) and manifests itself by increased porosity and sugaring of the surface. This problem has recently received increased attention since natural stone claddings on some famous buildings such as the Amoco building in Chicago and Finlandia House in Helsinki started to bow and had to be replaced (Jornet & Ruck 2000). This type of failure is commonly visible some ten to fifteen years after the completion of the building. In some cases the phenomenon has been observed after only one year. Among the many possible causes of marble decay, temperature fluctuations play an important role. There have been many studies (Kessler 1919; Sage 1988; Tschegg *et al.* 1999; Royer-Carfagni 1999; Siegesmund *et al.* 2000) describing the temperature expansion of marble as well as that of other stone types. From these it has been demonstrated that as the temperature increases the rate of expansion increases. For different types of marble, at ordinary temperatures, the range appears to be between one-quarter and two-thirds that of steel (Kessler 1919). Thermal stress resulting from changes in the temperature of ambient air can be sufficient to produce microfractures between the mineral grains of a rock. This can happen even in temperate climates because of anisotropy and differences in the rates of thermal expansion among the minerals. Marble consists of calcite and/or dolomite. Calcite exhibits linear thermal expansion parallel to the *c* axis but contracts perpendicular to the *c* axis; whereas in dolomite, both the *c* and *a* axes expand, though at different rates. These phenomena may cause the intercrystalline bonds to fracture resulting in a loss of strength as well as permanent expansion. An important feature is that the fracturing is irreversible and thereafter, the porosity and volume will increase (Turner *et al.* 1954).

The quantification of porosity is not commonly used in the characterization of marble, although its importance was long ago identified (Pittman 1971). According to Anselmetti *et al.* (1998), the combination of microporosity and macroporosity data can explain the physical properties of the stone material. The strength of a porous material decreases with increasing porosity but is also controlled by the size and spatial distribution of the pores. Water transport is particularly important and appears to be mainly controlled by the macropores in highly permeable materials and by the amount of intrinsic microporosity in the less permeable. Pore size and pore size distribution influence the internal surface area per unit material volume and this in turn determines the amount of

From: SIEGESMUND, S., WEISS, T. & VOLLBRECHT, A. 2002. *Natural Stone, Weathering Phenomena, Conservation Strategies and Case Studies.* Geological Society, London, Special Publications, **205**, 81–88.
0305-8719/02/$15.00 © The Geological Society of London 2002.

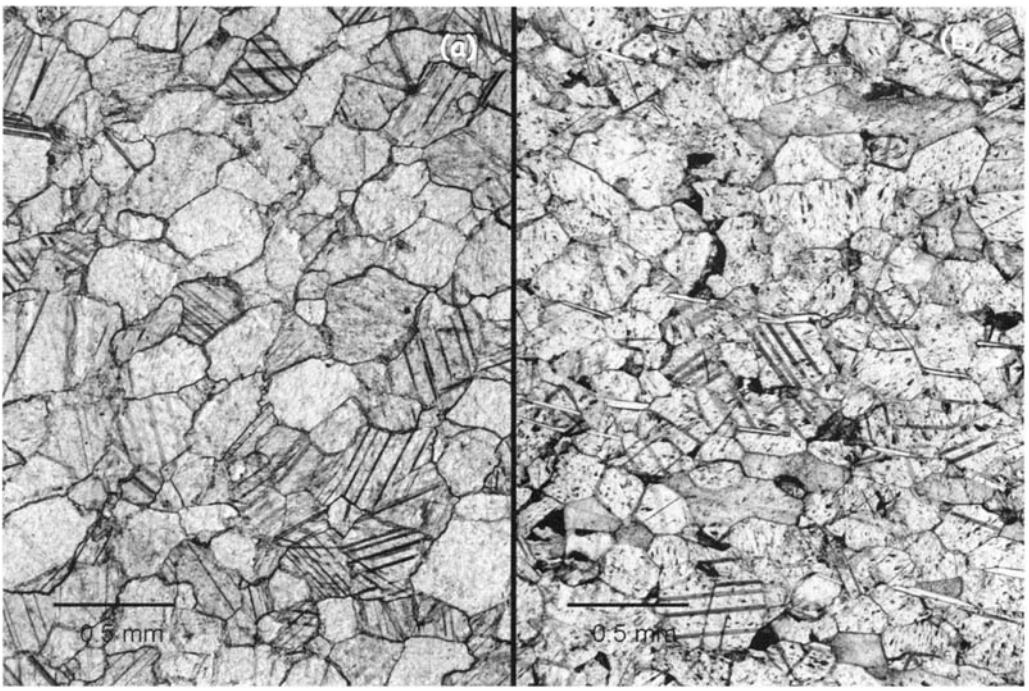

Fig. 1. Photomicrographs of polished thin sections of (**a**) the calcitic and (**b**) the dolomitic marbles. The images are taken using differential interference contrast in reflected light.

absorbed water, the freeze–thaw properties as well as salt crystallization durability of the material.

It appears that a study of porosity can provide valuable information in order to determine what properties make some marble types more susceptible to disintegration than others. In order to determine how heating to various temperatures initiates changes in the porosity, samples of calcitic marble and dolomitic marble were analysed by gas adsorption.

Experimental

Materials

Two different types of marble were used in the study, one from Italy and one from Sweden. The samples were fresh, each of them sawn from a big block directly from the quarry. The Italian marble specimen (Fig. 1a) is almost pure calcitic (>99%) and the average grain size is 0.46 mm. There is no preferred orientation of the minerals. The Swedish marble specimen (Fig. 1b) is dolomitic (93%) and contains some phlogopite (4%) and tremolite (3%). The average grain size is 0.43 mm. The mineral grains have a clear preferred orientation. Both materials are characterized by a very low porosity. Despite a similar mean grain size, the grain size distribution differs between the two marble types as can be seen in Figure 2. The grain size distribution has been determined by linear-traverse measurements. The 30 randomly orientated traverses, each 1.8 mm long, have been measured on the thin sections. The transformation of chord lengths into a grain size has been done in accordance with Åkesson (2001).

Testing procedure and sample preparation

For investigation of the surface area, average pore size and pore size distribution, the gas adsorption technique was used in this study (TriStar 3000 Analyser, Micromeritics). For sample preparation and heat conditioning a compact degassing unit was used (SmartPrep, Micromeritics). Both units were computer controlled and all calculations were performed by using Win3000 software. The TriStar 3000 Analyser uses multipoint analysis (in this case eight points for BET surface area for the relative pressure P/P_0 = 0.06–0.2, and 55 points for pore size distribution for P/P_0 = 0.14–0.995) for each sample.

The surface area was calculated by the BET

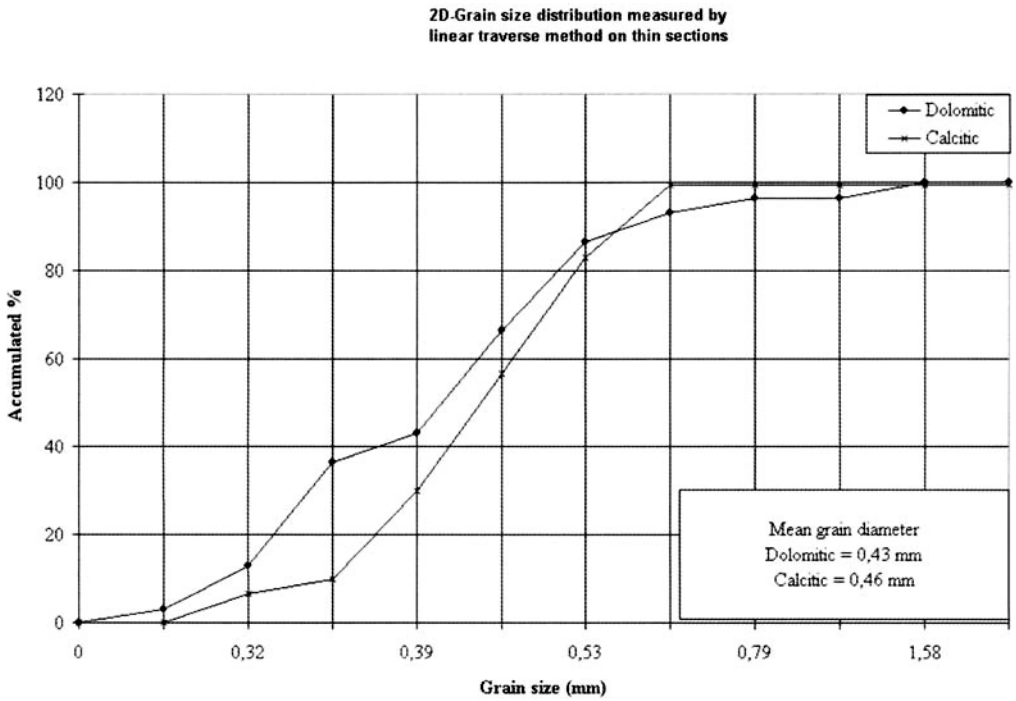

Fig. 2. Grain size distribution as determined by linear-traverse method.

(Brunauer, Emmett and Teller) method, the average pore diameter by analysis of the adsorption isotherm (4V/A by BET) and the pore size distribution by applying the BJH (Barrett, Joyner and Halenda) method with the Halsey equation (Webb & Clyde 1997). The pore size model is expressed in terms of the diameter of the opening, assuming the pores to be cylindrical.

The BET method is based on the assumption that the forces active in the condensation of gases are also responsible for the binding energy in multimolecular adsorption. The surface area of a solid occupied by single adsorbed molecule lacks uniformity, primarily because the area depends on the structure of the solid surface. The TriStar 3000 Analyser uses 16.2 $Å^2$ for the area occupied by a nitrogen molecule at liquid nitrogen temperature and the thickness of a nitrogen monolayer is taken to be 3.54 Å. The calculation method assumes that at 99.5% relative pressure all pores are filled.

The marble samples were crushed and sieved to 2–4 mm test specimens. About 7 g were used for one part sample and analysis. Prior to the adsorption of nitrogen, the samples were treated by a combination of heat and flowing inert gas. The purpose of degassing was to remove previously adsorbed molecules (e.g. water) from surfaces and pores. In order to ensure that all samples were free of impurities, all of them were weighted until constant weight was established (the difference between two consecutive measurements was less than 1%). The temperatures chosen for the heat treatment were 40, 50, 60, 70, 80, 100 and 200°C. The selection of temperatures between 40 and 80°C was intended to imitate the conditions that could be found on natural stone claddings outdoors (Perrier 1996). The two higher temperatures were used for observation of the stone materials under extreme conditions. The time of heat treatment varied from one (100 and 200°C) to five days (40–80°C), depending on time required for the samples to dry. For each temperature, three to six samples were used.

After the degassing and heat treatment, three samples were moved simultaneously to the TriStar 3000 Analyser and mounted into the closed system. Prior to the analysis a leak test was performed in order to detect if any further degassing of the sample was necessary or if any leakage or instability of the system were occurring. The analysis was done under a constant cool temperature achieved by immersing samples in liquid nitrogen. An adsorptive gas in

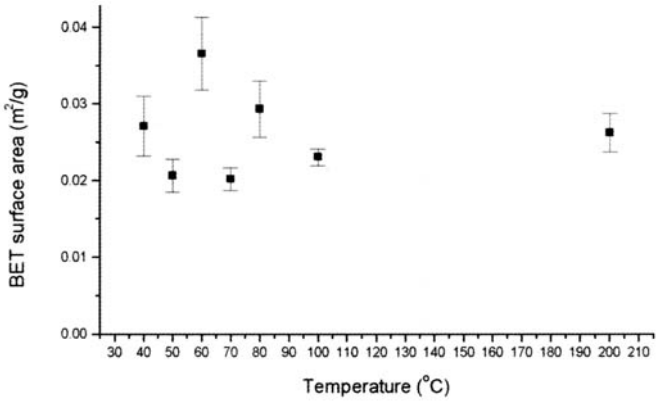

Fig. 3. Variation of the BET surface area for the calcitic marble due to temperature changes.

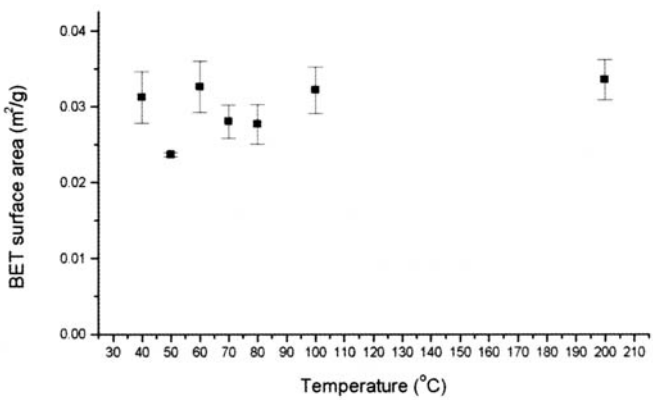

Fig. 4. Variation of the BET surface area for the dolomitic marble due to temperature changes.

the form of pure nitrogen was used. The analysis of the shape of the isotherms yielded information about the surface and internal pore characteristics of the material. Assuming that negligible microporosity (<2 nm) occurred in the samples, only pores with diameter of 2–200 nm were analysed.

Results

The effects induced by heat treatment of the calcitic and dolomitic marbles are illustrated in Figures 3–6. The BET surface area (multipoint) and mean pore size are presented as mean values with standard deviation.

Figure 3 displays the results of the BET surface area for the calcitic marble and Figure 4 the dolomitic marble. Both curves follow the same trend, though with different amplitudes. The BET surface area for both marbles decreases between 40 and 50°C and thereafter starts to increase. This increase is especially pronounced for the calcitic marble where the value increases by almost 40% at 60°C compared to the initial one. The dolomitic marble, at the same temperature, gains almost its original BET surface area. At about 70°C, the BET surface area of both materials decreases. Again, for the calcitic marble this change is much more evident. The two marble types behave differently between 70 and 100°C. The calcitic marble increases its BET surface area up to 80°C and decreases down to 100°C while the dolomitic marble shows a slight decrease at 80°C and an increase thereafter. From 100 to 200°C the BET surface area increases for both marble types.

The average pore size values of the calcitic and dolomitic marble are presented in Figures 5 and 6. Here again, the calcitic marble shows a higher variation of the mean pore size due to changes in temperature compared to the dolomitic marble. The lowest values are observed for temperatures of 60 and 80°C for

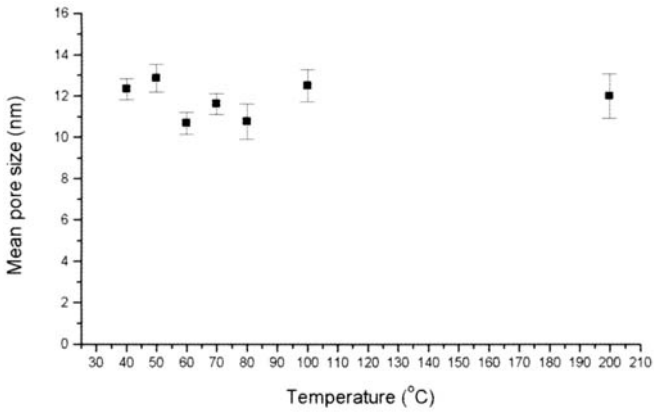

Fig. 5. Average pore size for different temperatures calculated for the calcitic marble.

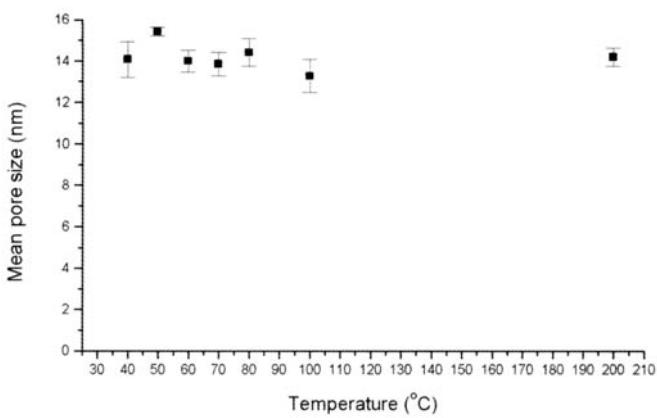

Fig. 6. Average pore size for different temperatures calculated for the dolomitic marble.

the calcitic marble and 60, 70 and 100°C for the dolomitic marble. The highest values in the mean pore size are reached at 50°C for both marbles.

Qualitative analysis of the heat-treated samples using fluorescence microscopy shows that the porosity is concentrated around the grain boundaries. This method shows fluorescent light from the pores that have been filled with fluorescent dye. Open cracks were most pronounced for the marbles exposed to 80°C (Fig. 7).

Discussion

This study showed that exposure to thermal stress of the investigated marble types, excluding other factors such as humidity, resulted in changes in the values of BET surface area and mean pore size. The variation in the standard deviation indicated a relatively high spread of data for the calcitic sample. As this spread was larger than the precision of the measurements it could be assumed that it was associated with inhomogeneity of the calcitic samples.

The range of pore sizes detected by gas adsorption is from 2 nm to 200 nm. The pore size distribution versus area is plotted in a diagram with three pore size classes: 2–10, 10–100, and 100–200 nm. The smallest pore size class, 2–10 nm, is chosen to assess if any variation in the smallest pore range occurs, which would indicate initial cracking of the material.

The pore size distribution curves indicate that intergranular decohesion may already be active between 40 and 50°C (Figs 8 and 9) where the BET surface area (Figs 3 and 4) decreases for both the calcitic and dolomitic marble. The decrease/increase in the BET surface area could be explained by thermal expansion/contraction of the mineral crystals. Thermal stress produces tensile strain within the material, which leads to

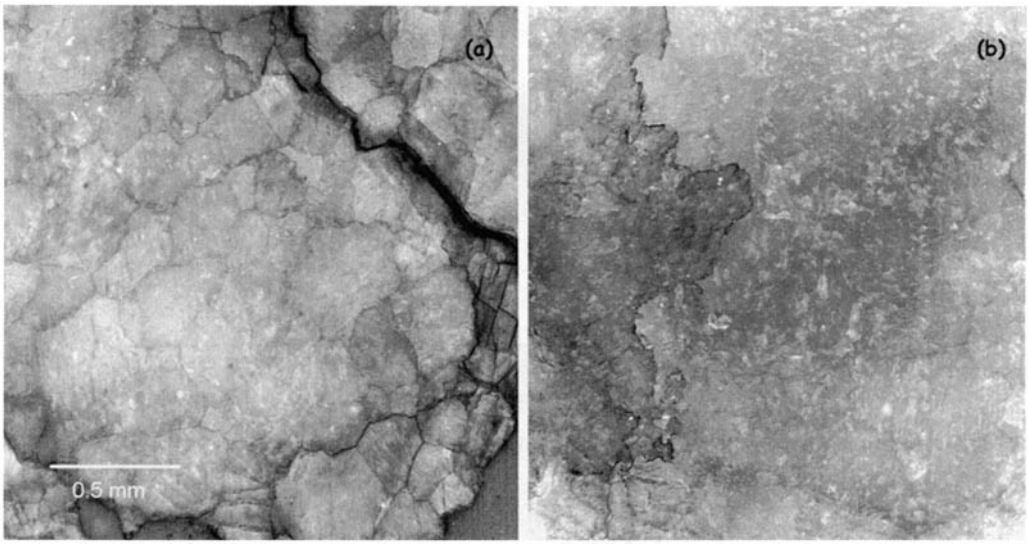

Fig. 7. Photomicrographs (negative images) of polished thin sections of (**a**) the calcitic and (**b**) the dolomitic marbles. The images are taken using fluorescence in reflected light.

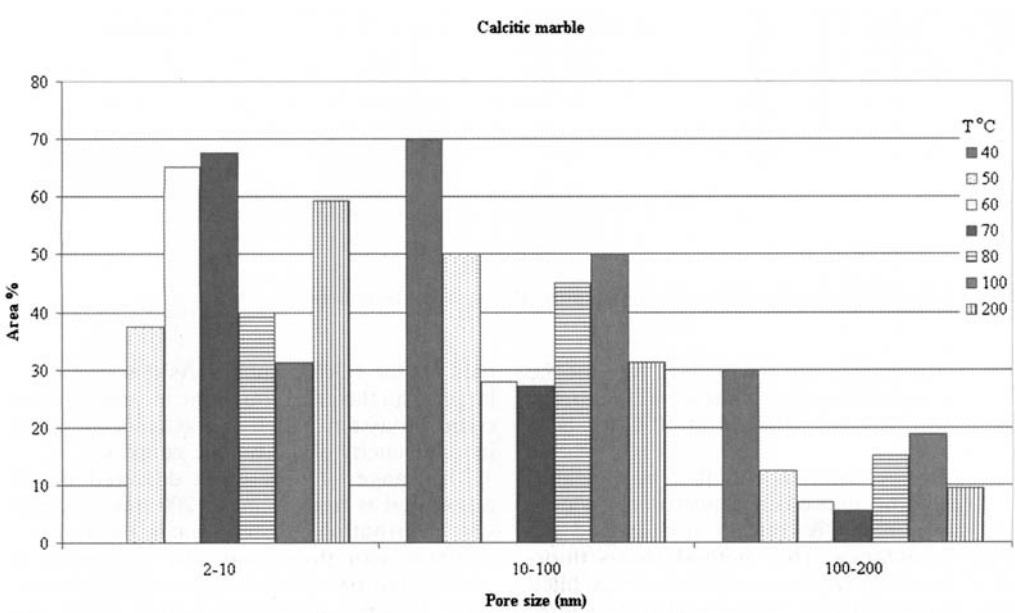

Fig. 8. Pore size distribution versus occupied area established for the calcitic marble.

fracture when reaching a critical level. Figure 7 shows that the initial cracking of the materials could support this hypothesis. The fracturing is probably generated at the surface of the marble and extends over relatively small dimensions. In this investigation this phenomenon is especially noticeable for the calcitic marble. Compared to the dolomitic marble, the calcitic marble has a larger area consisting of the smallest pores in all of the experiments. This means that the initial cracking of the dolomitic marble is delayed compared to the calcitic marble. The larger BET surface area and mean pore size for the dolomitic marble, plus its dolomitic content,

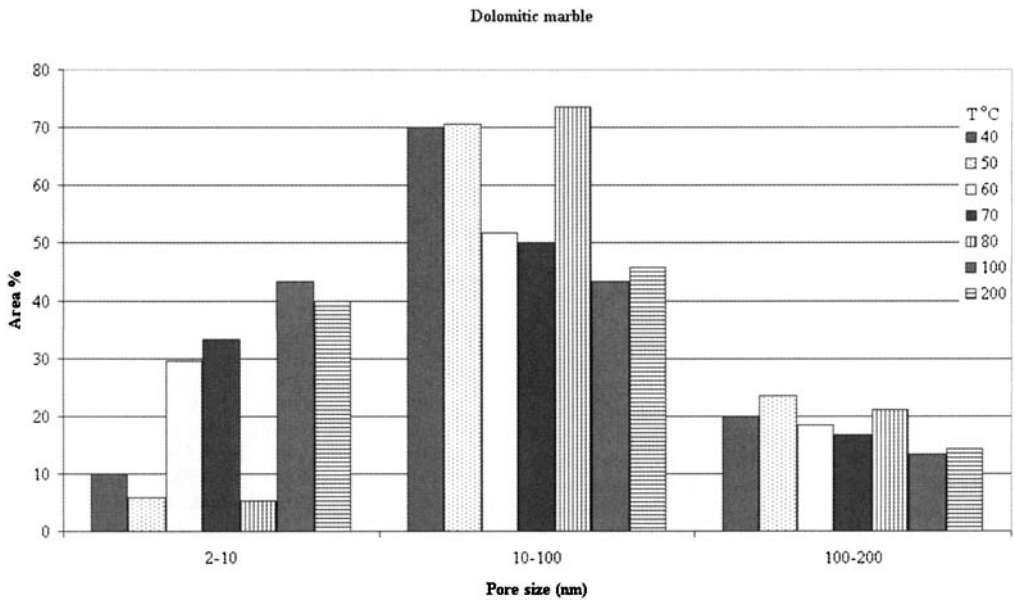

Fig. 9. Pore size distribution versus occupied area established for the dolomitic marble.

could have a mitigating effect on the generation of microfractures compared to the calcitic marble.

The observed changes have to be evaluated further since they may also be influenced by other factors such as the mineralogy (clay minerals if present), fabric, different stages in the sample preparation (e.g. crushing), influence of liquid nitrogen on material behaviour during the analysis, or incomplete drying of the material. The pore size distributions presented in this study are limited to the range of 2–200 nm. In order to have a more general picture of the porosity variation due to temperature changes, further studies, such as microscopy and/or porosimetry, are therefore needed. A comparison between additional types of marble frequently used for building cladding could give more information about significant factors influencing microfracturing of the stone material. Different methods of pre-conditioning the test specimens should also be investigated.

Conclusions

The temperature range 40–70°C is easily reached on building facades in most European countries during the summer months. The results of this study suggest that the process of intergranular decohesion starts between 40 and 50°C for some marble types. The analysed calcitic marble is more susceptible to temperature changes than the dolomitic marble. The resultant changes of the BET surface area and the mean pore size are quite variable depending upon several factors, such as original pore structure, the crystallographic and mineralogical characteristics of the marble types and, as in this study, the temperature variation.

A porosity change in carbonate rock samples is of considerable importance in rock mechanics and rock weathering. The differential thermal expansion/contraction associated with different mineralogical and textural properties of the materials may explain part of the bowing process of facade claddings. In addition, the findings provide essential information that should be used when conditioning all marble stones for further testing. If intergranular decohesion occurs at temperatures as low as 40–50°C this has to be taken into account when drying test specimens for all standardized tests.

An understanding of the role of temperature on marble porosity could be used to develop a methodology for assessing suitable pretreatments for the marble slabs and to suggest suitable surface treatments of weathered facade claddings and outdoor sculptures. Research should therefore be focused on pore structural changes related to the progress of degradation and the use of pore structural measurements to assess and predict the effectiveness of selected impregnation materials in use with materials of appropriate mineralogy and texture.

This work was financially supported by the KK Foundation and the Swedish National Testing and Research Institute.

References

ÅKESSON, U. 2001. *Numerical description of rock texture by using image analysis and quatitative microscopy*. Licentiate thesis, Earth Sciences Centre, Gothenburgh University, **A73**.

ANSELMETTI, F. S., LUTHI, S. & EBERLI, G. P. 1998. Quantitative characterization of carbonate pore system by digital image analysis. *AAPG Bulletin*, **82**, 1815–1836.

JORNET, A. & RUCK, P. 2000. Bowing of Carrara marble slabs: A case study. *In*: CALVI, G. & ZEZZA, U. (eds) *Proceedings of the International Congress. Quarry – Laboratory – Monument*. International Congress, Pavia, Italy, **1**, 355–360.

KESSLER, D. W. 1919. *Physical and Chemical Tests on the Commercial Marbles of the United States*. Technologic Papers of the Bureau of Standards, **123**, Government Printing Office, Washington.

PERRIER, R. 1996. *Mesure de la dècohèsion thermique des marbres par l'attènuacion des vibrations en flexion*. TechniPierre, **96**, Institut Scientifique de Service Public, France.

PITTMAN, E. D. 1971. Microporosity in carbonate rocks. *AAPG Bulletin*, **55**, 1873–1881.

ROYER-CARFAGNI, G. F. 1999. On the thermal degradation of marble. *International Journal of Rock Mechanics and Mining Sciences*, **36**, 119–126.

SAGE, J. D. 1988. Thermal microfracturing of marble. *In*: MARINOS & KOUKIS (eds) *Engineering Geology of Ancient Work, Monuments and Historical Sites*. Balkerna, Rotterdam, 1013–1018.

SIEGESMUND, S., WEISS, T. & TSCHEGG, E. K. 2000. Control of marble weathering by thermal expansion and rock fabrics. *Proceedings of the 9th International Congress on Deterioration and Conservation of Stone*. Venice, Italy.

TSCHEGG, K., E., WIDHALM, C. & EPPENSTEINER, W. 1999. Ursachen mangelnder Formbeständigkeit von Marmorplatten. *Zeitschrift der Deutscher Geologischer Gesellschaft*, **150(2)**, 283–297.

TURNER, F. J., GRIGGS D. T. & HEARD, H. 1954. Experimental deformation of calcite crystals. *Bulletin of Geological Society of America*, **65**, 883–934.

WEBB, P. A. & CLYDE, O. 1997. *Analytical Methods in Fine Particle Technology*. Micrometitics Instrument Corporation, USA.

Thermal stresses and microcracking in calcite and dolomite marbles via finite element modelling

THOMAS WEISS[1], SIEGFRIED SIEGESMUND[1] & EDWIN R. FULLER JR[2]

[1] *Geowissenschaftliches Zentrum der Universität Göttingen, Goldschmidtstrasse 3, 37077 Göttingen, Germany (e-mail: tweiss@gwdg.de and ssieges@gwdg.de)*

[2] *National Institute of Standards and Technology, 100 Bureau Drive, Gaithersburg, Maryland 20899-8520, USA (e-mail: edwin.fuller@nist.gov)*

Abstract: Microstructure-based finite element simulations were used to study the thermo-mechanical behaviour of calcite and dolomite marbles. For a given mineral microstructure, thermal stresses and elastic strain energy varied with the single-crystal elastic constants and coefficients of thermal expansion. Moreover, they were a strong function of crystallographic texture. Given the same morphological microstructure and crystallographic texture, calcite had larger thermal stresses and elastic strain energy than dolomite. Hence, calcite has an earlier onset of microcracking upon either heating or cooling, and has a greater extent of microcracking at a given temperature differential. However, the variation in thermal stresses and microcracking propensity for either mineral with different randomly assigned textures was greater than the variations between the two minerals. The measured bulk thermal expansion anisotropy suggested that the random representations had some degree of texture. Simulations using the actual texture of the real microstructure, as determined by electron-backscattered diffraction, showed the largest degree of bulk thermal expansion anisotropy, the smallest strain energy, and hence the smallest amount of thermal microcracking. Microstructure-based finite element simulations are considered an excellent tool for elucidating myriad influences of microstructure and physical properties on the thermal degradation of marbles and other rocks.

Natural building stones are frequently used as constructive and decorative materials in both the interior and exterior of buildings, as well as for sculptures (Fig. 1). Marbles, in particular, are preferred for such applications due to their bright, white colour and translucence. However, utilization of marble frequently causes severe problems with time. In such cases, the result is a deterioration of the rock's microfabric, finally leading to a complete structural degradation of the material in the form of granular disintegration (Figs 1d, 2). Deterioration phenomena associated with this degradation are bowing of facade claddings, nucleation and growth of microcracks on massive structural parts and a loss of relief structure.

Microcrack nucleation and growth, as a consequence of thermal stresses, are considered the initial processes in marble degradation (e.g. Siegesmund *et al.* 2000). Initially, marbles exhibit a very low porosity of approximately 0.2%. During degradation, microcrack density increases, thereby providing pathways for subsequent chemical and biological attacks.

Marbles are relatively simple materials composed of calcite ($CaCO_3$) and/or dolomite ($CaMg(CO_3)_2$) as the main rock-forming minerals. Numerous experimental studies indicate that various microstructural parameters (such as grain size, grain morphology, global and local texture, and single-crystal properties of the constituents) are primary factors influencing thermal degradation of marble (Siegesmund *et al.* 2000). However, a clear and concise determination of the influence of these various factors has not been achieved at present, since all stones are very heterogeneous and stochastic materials. This heterogeneity and randomness mean that most of the properties vary between different marble types, and indeed, even within the same marble type, thus making direct comparisons difficult. Accordingly, the present investigation takes another approach. An object-oriented finite element method (OOF), developed at the National Institute of Standards and Technology (USA), is used to determine physical properties and microcracking behaviour based on the material microstructure (Langer *et al.* 2001). This method allows determination of thermal stresses (as well as many other physical properties) in a sample microstructure as a

From: SIEGESMUND, S., WEISS, T. & VOLLBRECHT, A. 2002. *Natural Stone, Weathering Phenomena, Conservation Strategies and Case Studies.* Geological Society, London, Special Publications, **205**, 89–102.
0305-8719/02/$15.00 © The Geological Society of London 2002.

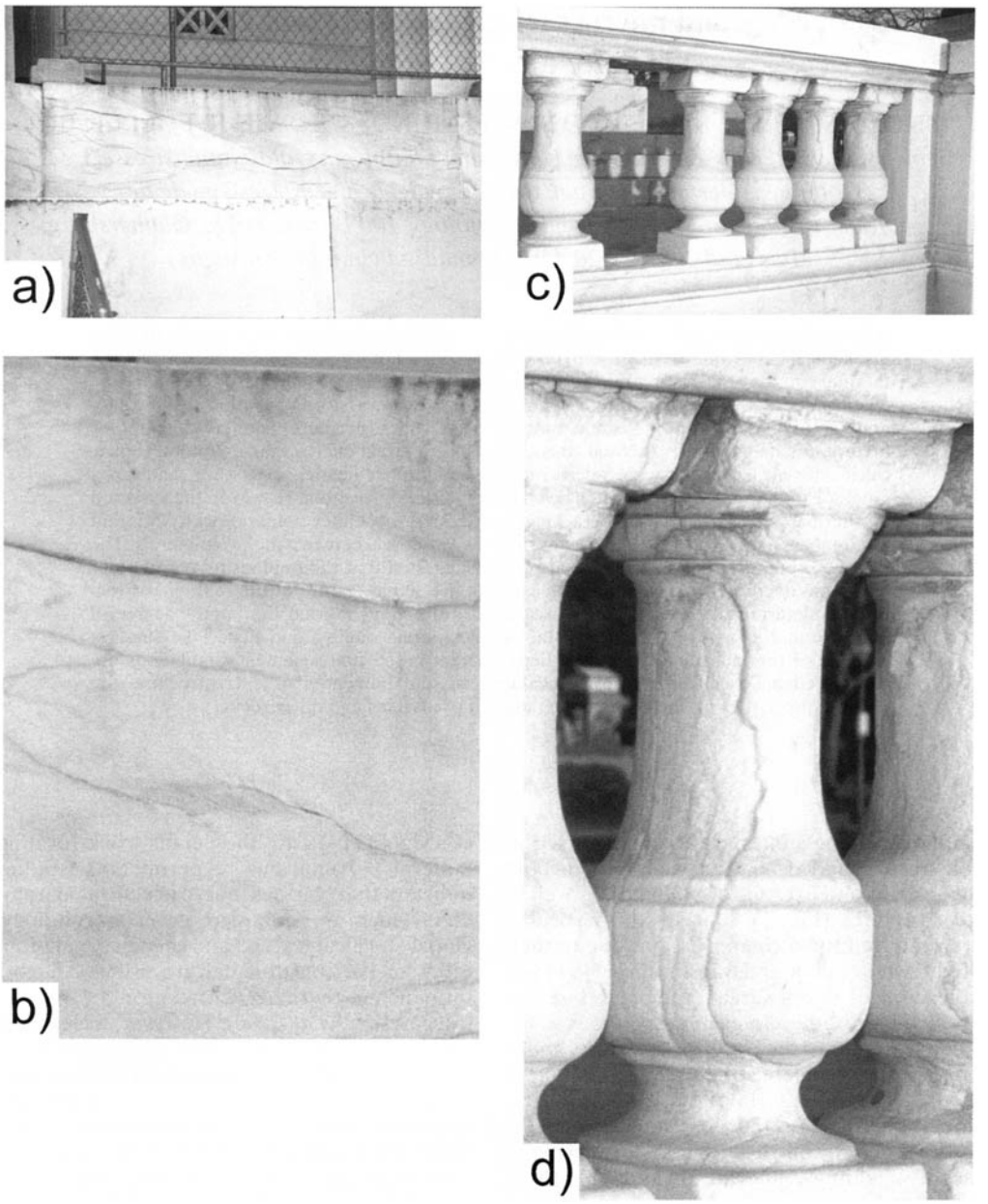

Fig. 1. Degradation of marble at the macroscopic scale: (**a**) fractures in the stairway of the Lincoln Memorial (Washington, DC, USA); (**b**) detail from (a) showing fractures parallel and oblique to the foliation; (**c**) granular disintegration leading to loss of material and relief structure at a baluster of the Capitol stairways (Washington, DC, USA); (**d**) detail from (c).

consequence of heating or cooling. The advantage of this method is that variations in physical behaviour can be achieved by systematically changing one or more parameters while monitoring the response from the microstructure.

Experiments and simulations

Microstructure

The basic OOF concept is that a specific microstructure is used as the input for subsequent

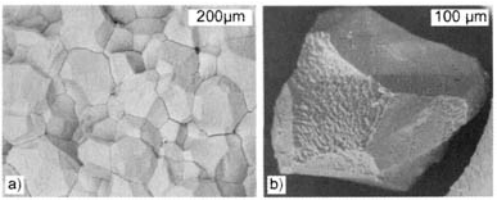

Fig. 2. Thermal degradation of marble at the microscopic scale: (**a**) SEM image of the fractured surface of a marble showing a predominantly intergranular fracture surface and extensive intergranular microcracking; (**b**) an individual marble grain resulting from total separation along the grain boundaries, so-called granular disintegration.

simulations of material behaviour. In the present study, a microstructure of a dolomitic marble from Sivec (the Former Yugoslav Republic of Macedonia) was used. Crystallographic orientations of the various grains in the microstructure (average grain size of *c.* 200 μm) were determined by orientation imaging microscopy using electron-backscattered diffraction (EBSD). Single-crystal orientations were measured on a 5 μm spaced regular grid using the stage-scan mode on an electronic microscope (Schmidt & Olesen 1989; Olesen & Schmidt 1990). These single-crystal orientations are specified by three Euler angles (Bunge 1985) that are associated with a spatial coordinate in the X-Y orientation imaging grid. The result is an orientation image map, from which, after noise reduction and digital processing, a microstructural image was determined. Each single grain orientation is represented by a colour code (Fig. 3). This data set provides information on the realistic texture of the microstructure under investigation. To study finite element meshing effects, both a high (Fig. 3a) and a low (Fig. 3b) resolution image were used (see discussion below).

Image processing

The basis for microstructure-based finite element modelling is a microstructure given as a bitmap (or pixel map) graphical image. As the first step, all pixels associated with a specific grain must be determined. This process is complicated by the noise in the EBSD image. However, it is done by several different methods that are based on the definition of a specific range in pixel colours: for example, a burning algorithm, where neighbouring pixels to a selected pixel are selected only if they are within a specified colour range, and so forth. After each grain is fully identified, the pixels that define it are associated with a certain group of pixels. In our case, the individual grains are numbered and each grain represents a group of pixels. This allows individual assignment of specific properties to a specific grain. Once the assignment of the grains is done, grain boundaries with a given thickness can be defined as the outermost shells of pixels surrounding each grain. In the present study, a shrinking algorithm in OOF was used to define a single outermost shell of pixels for each grain. These grain boundaries are then assigned to different (grain boundary) pixel groups.

Material properties

The next step in developing the finite element model is the assignment of elastic, thermal, and fracture properties to each grains and its associated grain boundaries. A grain boundary between two grains is assumed to be composed of two parts, each having the same elastic and thermal properties of the host grain, as well as its crystallographic orientation, but a reduced fracture surface energy, as described below. Elastic properties of a grain are described by the single-crystal elastic constant tensor (C_{ij}) in the crystal coordinate system and the crystallographic orientation. The single-crystal elastic constant tensors for the rock-forming minerals (here calcite and dolomite) are given in Table 1. Both minerals have trigonal symmetry of $\bar{3}2/m$ and $\bar{3}$, respectively. Thermal properties of a grain are given by the coefficient of thermal expansion tensor (α_i) and the crystallographic orientation. The thermal expansion tensors for calcite and dolomite are given in Table 2.

Finally, the fracture surface energy that is required to form a new surface (via either a transgranular cleavage crack or an intergranular grain-boundary crack) is needed for the modelling. Since there are no known values for either calcite or dolomite (much less the tensor properties of this parameter), we assumed that the fracture surface energy (γ_{xtal}) for each grain is isotropic and that it has the same value for both calcite and dolomite. Fracture surface energies of crystals are typically of order 0.3–1.1 J m^{-2} (Becher & Freiman 1978; White *et al.* 1988). Accordingly, a value of γ_{xtal} = 0.5 J m^{-2} was used. The fracture resistance energy of the grain boundaries (γ_{ig}) was also assumed to be isotropic but at a reduced value of 40% of the crystal fracture surface energy, i.e. γ_{ig} = 0.2 J m^{-2} (e.g. Sridhar *et al.* 1994; Zimmermann *et al.* 2001). The actual input value of the fracture surface energy in OOF depends on the units of length and stress that are used for

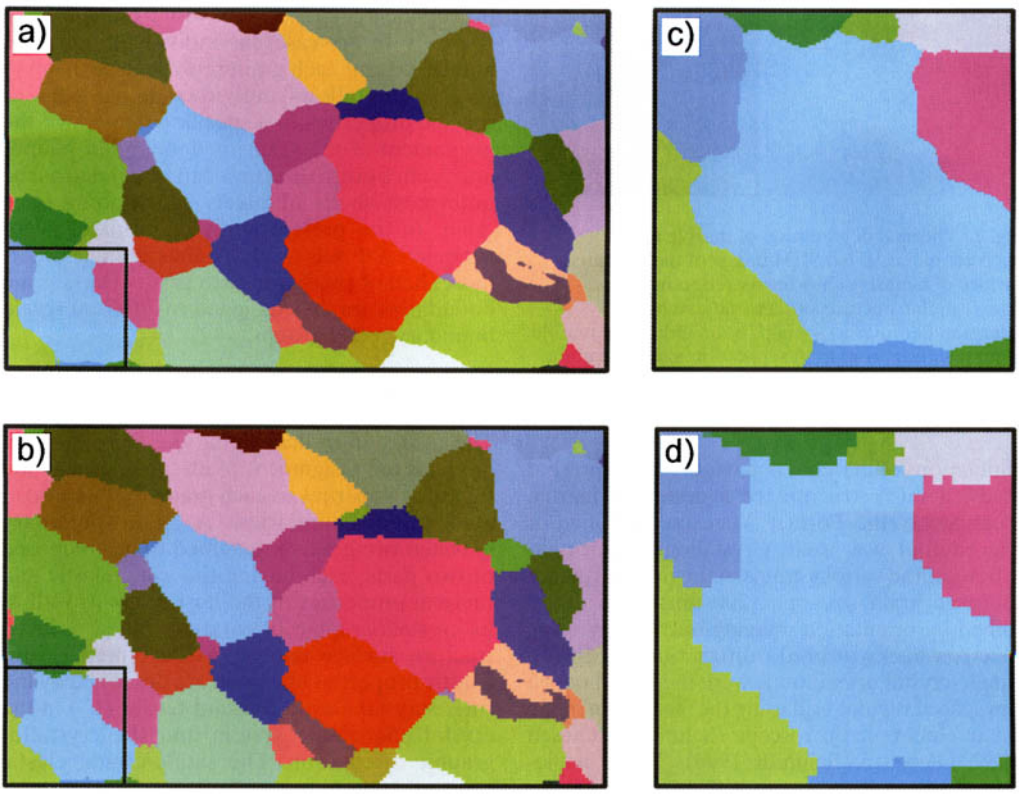

Fig. 3. Microstructure of the Sivec dolomite marble used for the finite element modelling: (**a**) the high-resolution (740 × 442 pixels) image used for the adaptive meshing, showing the relatively smooth grain boundaries; (**b**) the low-resolution (185 × 110 pixels) image used for the simple meshing; the width of both images is 2 mm; (**c** and **d**) magnified regions of (a) and (b), respectively. Note the differences in grain-boundary contours.

Table 1. *Elastic constants (in GPa) for calcite and dolomite (Bass 1995)*

	C_{11}	C_{33}	C_{44}	C_{12}	C_{13}	C_{14}	C_{15}
Calcite	144	84	33.5	53.9	51.1	−20.5	–
Dolomite	205	113	39.8	71	57.4	−19.5	13.7

Table 2. *Coefficients of thermal expansion (in 10^{-6} K^{-1}) for calcite (Kleber 1959) and dolomite (Reeder and Markgraf 1986)*

	$\alpha_{\perp c} = \alpha_1$	$\alpha_{\parallel c} = \alpha_3$
Calcite	−6	26
Dolomite	6	26

the microstructure and elastic constants, respectively. In the present investigation, the width of the micrograph is 2000 μm and the elastic constants are in GPa. Accordingly, values for γ_{xtal} and γ_{ig} must be given in kJ m^{-2} = GPa μm. Fracture is implemented in OOF by reducing the directional elastic moduli, both the tensile and shear moduli, across the fracture plane by a multiplicative factor (e.g. Carter *et al.* 1998; Zimmermann *et al.* 2001). Multiplicative factors (or knockdown values, k_1 and k_2) for reducing the tensile and shear elastic moduli

across the fracture plane were chosen to be $k_1 = 1 \times 10^{-6}$ and $k_2 = 2 \times 10^{-6}$, respectively.

Three-dimensional crystal orientations are given via three Euler angles. However, the definition used in OOF is different from that used by the texture community (e.g. Bunge 1985). The OOF input Euler angles (α, β, γ) are related to those of Bunge ($\varphi_1, \Theta, \varphi_2$) by the relations:

$$\alpha = \Theta$$
$$\beta = \mathrm{mod}[(90 - \varphi_2), 360]$$
$$\gamma = \mathrm{mod}[(270 - \varphi_1), 360]$$

where the *mod* or *modulo* function returns the remainder of a number, n, after it is divided by a divisor, d, i.e.

$$\mathrm{mod}[n,d] = n - d^*\mathrm{int}[n/d]$$

and the *int* function rounds a number down to the nearest integer. Although three-dimensional elastic, thermal, and crystallographic orientations can be specified in OOF, the thermo-elasticity computation itself is via a two-dimensional finite element code. Accordingly, all simulations are performed in a plane-stress approximation.

The mesh

After assigning materials properties to the grains and grain boundaries, a finite element mesh is created, which is based on the microstructure and material contrast therein (Fig. 4). There are principally two different methods to create a mesh for a given microstructure in OOF: simple meshing and adaptive meshing. Simple meshing gives a regular mesh based on the pixel resolution of the image, whereas adaptive meshing allows refinement of the mesh to specific details of the microstructure and a coarser mesh elsewhere. This means in our case that grains and grain boundaries can have different mesh densities. Both methods have advantages and disadvantages, as discussed here. Since the resolution of the microstructure is 740×442 pixels, a simple mesh in OOF would give a finite element mesh of 654 160 elements. This extremely large simple mesh would have required more computer resources than were available to solve. Thus, we used an image with a reduced resolution image of 185×110 pixels (see Fig. 3b) to generate models based on a simple mesh.

A number of different adaptive meshes were created in order to investigate the influence of the reduced mesh resolutions. If the mesh is relatively coarse, the accuracy of reproducing the grain-boundary geometry is different from that of a fine mesh (Fig. 4). The mesh with the smallest number of elements is characterized by a coarse grid in the interior of the grains and a fine grid on the grain boundaries. It consists of about 20 000 elements (Fig. 4a). A refinement of the interfaces (here grain boundaries) results in a mesh with a larger number of elements, 52 000 (Fig. 4b). A homogeneous distribution of nodes and elements was achieved by a more or less regular but adaptive mesh consisting of 40 000 elements (Fig. 4c). Since the grain boundaries are relatively stair-stepped in this model, a finer adaptive mesh was created consisting of 80 000 elements (Fig. 4d). Reproduction of the grain boundaries is relatively good for this model. An even finer uniform but adaptive mesh generated the mesh with the highest resolution consisting of 160 000 elements (not shown).

A simple mesh based on the low-resolution image is shown in Figure 4e. It consists of 40 700 elements and has a very similar node or element density as the equivalent adaptive mesh shown in Figure 4c (see Fig. 4f). To estimate the influence of mesh resolution, the total elastic strain energy for a temperature change of +100°C was calculated for the same simulation at different mesh resolutions.

Texture effects

The occurrence of thermal stresses at grain boundaries, exceeding the threshold of grain-boundary adhesion, is attributed to the strong anisotropy in the thermal expansion coefficient for the different crystallographic directions. There exist many studies for ceramic materials revealing that in principle the magnitude of the thermal stresses at grain boundaries between adjacent grains is proportional to the maximum difference in the thermal expansion coefficient (e.g. Clarke 1964; Evans 1978; Clarke 1980; Fu and Evans 1985; Tvergaard and Hutchinson 1988). When the grains have the same orientation, no stresses are generated. However, in polycrystalline materials the effective magnitude and orientation of thermally induced stresses will depend on the interaction between all grains.

In order to simulate different sample conditions we used the following approach. Three randomly textured samples, denoted here as RAN1, RAN2, and RAN3, were generated by choosing crystallographic orientations for all the grains in the microstructure from equidensity orientation space (Bunge 1985). This is equivalent to choosing the Euler angle α from a

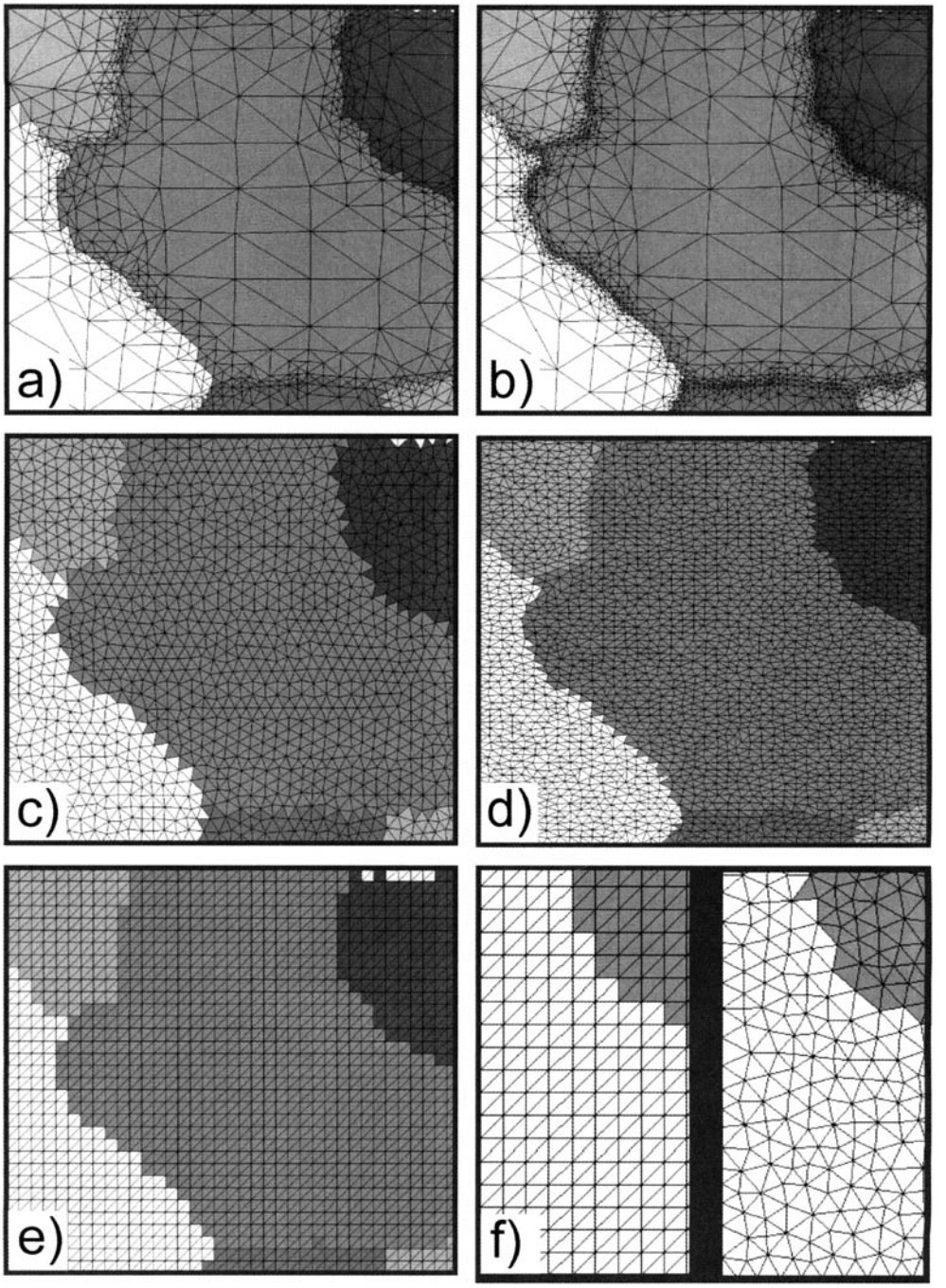

Fig. 4. Different types of adaptive and simple meshes used for the finite element simulations, showing only a small region (see Fig. 3c or d) of the complete mesh: (**a**) a non-uniform adaptive mesh with 20 522 elements; (**b**) an adaptive mesh with further grain-boundary refinement of (a), and 52 508 elements; (**c**) a homogeneous adaptive mesh with 40 700 elements; (**d**) a homogeneous adaptive mesh with 80 000 elements; (**e**) a simple mesh with 40 700 elements; (**f**) magnified regions from (c) and (e). The high-resolution microstructural image (740 × 442 pixels) was used for the meshes in (a–d) and the low-resolution image (185 × 110 pixels) was used for the mesh in (e). See text for details.

uniform distribution of $\cos(\alpha)$ in $(-1, 1)$ and the Euler angles β and γ from a uniform distribution in $(0, 2\pi)$. A fourth texture, denoted as REAL, was that of the actual microstructure. It was created by using the actual crystallographic orientations of the grains as determined from the EBSD measurements. In all cases, the same morphological microstructure was used.

Finite element simulations

Finally, finite element simulations were performed to characterize the thermoelastic behaviour of marble with and without microcracking. Since only a small fraction of the marble microstructure (i.e. 59 grains) was used for the modelling, it was necessary to impose boundary conditions to simulate the behaviour of the surrounding marble on this microstructure. To this objective, all sides were required to remain straight. An alternative approximation would have been to allow all sides to be free. One simulation was done with the latter boundary conditions. As mentioned before, all simulations were a plane-stress approximation.

Stresses, total elastic energy, and average coefficient of thermal expansion were measured on heating and cooling the sample by 100°C. It was assumed that the initial microstructure is in a stress-free state. These simulations were performed with and without allowing fracturing to occur. Fracture is implemented in this model by assuming that the elastic strain energy of an individual element is converted to fracture surface energy. The element is then 'mutated' by 'softening' or reducing the elastic constant tensor normal to the proposed crack plane (the maximum principal stress direction) in both tension and shear (see, for example, Carter *et al.* 1998; Vedula *et al.* 2001; Zimmermann *et al.* 2001). Allowing elements to mutate by changing their properties is a history-dependent process. Accordingly, simulations where microcracking was allowed were performed in 1°C increments, once it occurred.

Results

Thermal stresses

To elucidate the influence of the finite element mesh on simulated residual stress values, the total elastic strain energy in the microstructure was evaluated for both a calcite and a dolomite marble with random texture RAN1 upon heating by 100°C. No microcracking was allowed in these simulations. Values for the total elastic strain energy (U) are in the range of $U_{cc} = 200 \pm 2$ μJ for the calcite marble simulations and $U_{do} = 114 \pm 1$ μJ for the dolomite marble simulations (see Table 3). Since the variation in total elastic energy calculated for the different mesh resolutions is quite small we can exclude a mesh effect, except possibly for microcrack initiation as discussed below. This holds true even for the simple mesh generated based on the low-resolution image (Table 3).

Material properties, however, have an important influence on the stress magnitude and distribution throughout the sample. For instance, given the same morphological grain microstructure and the same texture, the total strain energy for calcite is substantially greater than that of dolomite. The ratio between them, (U_{cc}/U_{do}), however, is constant, and when averaged over the various mesh simulations, has a value of 1.76 ± 0.00. The difference between calcite and dolomite can be explained by the differences in the single-crystal elastic constants (C_{ij}) and the thermal expansion anisotropy ($\Delta\alpha = \alpha_3 - \alpha_1$) for these two minerals. From simple arguments one expects U to scale as $C_{ij} \cdot [\Delta\alpha\Delta T]^2$ for a given temperature differential (ΔT), so that elastic strain energy increases with elastic

Table 3. *Total elastic strain energy (in μJ) as a function of mesh resolution (RAN1 texture)*

No. of elements	Mesh type	Calcite	Dolomite	U_{cc}/U_{do}†
20 522	adaptive	202	115	1.76
40 700	adaptive	202	115	1.76
52 508	adaptive	200	113	1.76
80 000	adaptive	200	113	1.76
160 000	adaptive	198	113	1.76
40 700	simple	202	115	1.76
mean*		200	114	1.76
std dev.*		002	001	0.00

* The average value (mean) of all meshes and the standard deviation (std dev.) are also given
† Elastic strain energy U for calcite (U_{cc}) and dolomite (U_{do}).

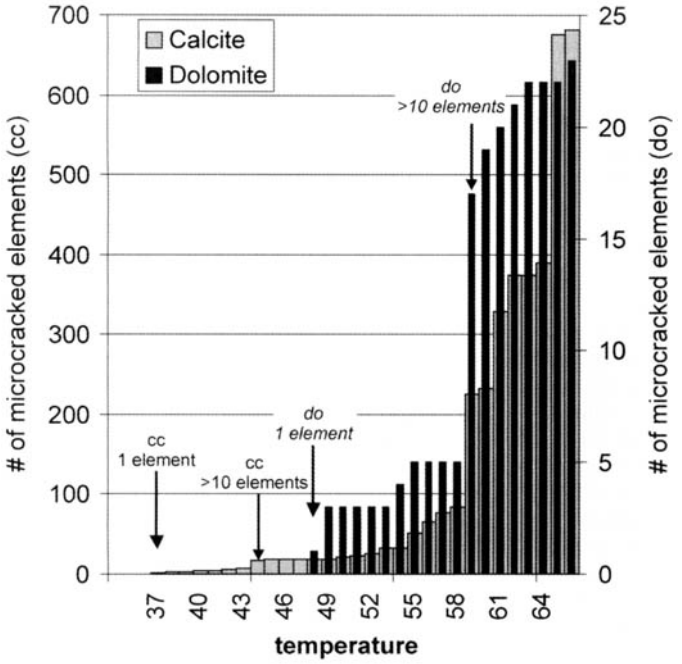

Fig. 5. Accumulative distribution of fractured elements for microcracking simulations of calcite (cc) and dolomite (do) marbles with randomly assigned crystallographic texture (RAN1). Arrows mark the first microcracking (mutating) of one and more than ten elements for both calcite and dolomite, respectively. Note the different scales for calcite and dolomite.

constants (high stiffness) and thermal expansion anisotropy (as well as with the temperature differential). While dolomite is stiffer than calcite (see Table 1), calcite has a substantially greater thermal expansion anisotropy (see Table 2), to give it the higher elastic strain energy. To illustrate this phenomenon further, simulations were performed for two hypothetical materials, one with the elasticity of dolomite, but the thermal expansion anisotropy of calcite, and another with the elasticity of calcite, but the thermal expansion anisotropy of dolomite. The former material gives large residual stresses with total elastic strain energy of 310 μJ, whereas the latter material gives low residual stresses with total elastic strain energy of only 84 μJ. The elastic strain energies for the real minerals, calcite and dolomite, are situated between these two extremes at 200 μJ and 114 μJ, respectively.

Onset of thermal degradation

As elastic strain energy supplies the fracture surface energy for microcrack formation and propagation: the greater the elastic strain energy the greater the propensity for microcracking. Accordingly, upon heating calcite marble is predicted to microcrack at a lower temperature than dolomite marble (Fig. 5) and to have more extensive microcracking at a given temperature (Figs 5 and 6). Upon heating the microstructure with RAN1 texture in 1°C increments, the onset temperature for thermal microcracking (i.e. the temperature when the first elements mutate, or fracture) occurs at 37°C for the calcite marble, while the dolomite marble does not show signs of microcracking until 48°C (marked by the arrows in Fig. 5). However, these onset temperatures might be a local phenomenon associated with the failure of isolated, non-representative elements. Accordingly, perhaps a better measure for the onset microcracking temperature is the temperature when a more significant number of elements (e.g. more than 10) begin to fracture. This onset temperature occurs at 44°C for calcite and 59°C for dolomite (see Fig. 5). Simple phenomenological models for spontaneous microcracking (e.g. Kuszyk & Bradt 1973; Cleveland & Bradt 1978; Evans 1978; Case *et al.* 1980; Clarke 1980; Davidge 1981; Tvergaard & Hutchinson 1988) can be formulated to show that microcracking initiates at a critical value of the elastic strain energy (for a given average grain size and fracture surface energy). Thus, one expects the ratio of the onset microcracking temperatures for dolomite to calcite to scale as the inverse square root of the elastic strain energy ratio without microcracking:

$$\frac{\Delta T_{\mathrm{do}}}{\Delta T_{\mathrm{cc}}} = \sqrt{\frac{U_{\mathrm{cc}}}{U_{\mathrm{do}}}} = \sqrt{1.76} = 1.33$$

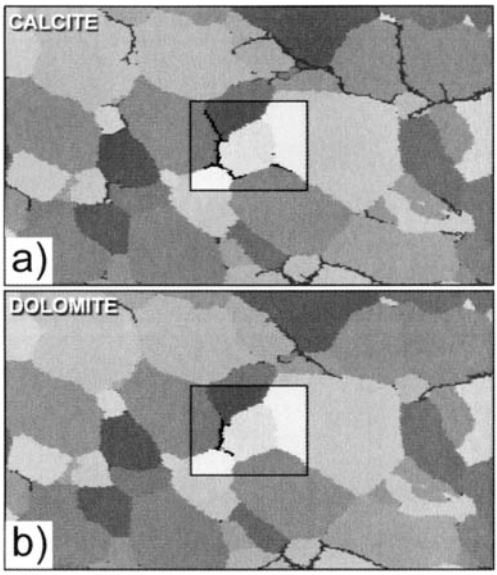

Fig. 6. Simulations of thermal microcracking in (**a**) calcite and (**b**) dolomite marble after heating in 1°C increments by a total temperature differential of ΔT = 100°C. The width of the images is 2 mm. Crystallographic texture is randomly assigned (texture RAN1). The rectangular boxes accentuate a useful area of comparison in the central region of the images.

This is in excellent agreement with the simulation results:

$$\frac{\Delta T_{do}}{\Delta T_{cc}} = \frac{59°C}{44°C} = 1.34$$

The observed initiation location for almost all microcracking was at grain triple-junctions. See several indications in Figures 6 and 7.

Effect of temperature and texture

At a given temperature, the amount of microcracking is quite different for the two types of marble. For example, upon heating to 66°C (see Fig. 5), the number of fractured elements for calcite marble is 681, while only 23 elements failed in the dolomite marble. This difference can be seen qualitatively in the simulations that were heated to 100°C (Fig. 6). Nonetheless, despite the differences in the degree of microcracking between calcite and dolomite marbles the patterns are quite similar (Fig. 6). This is a manifestation of the microstructural morphology and crystallographic texture.

Although crystallographic texture was not a principal variable in the current study, much information regarding its influence can be gleaned from these simulations. All the simulated crystallographic textures used in the present studies (RAN1, RAN2, RAN3) were randomly chosen from equidensity orientation space (Bunge 1985). Considering just simulations for calcite marble, microcrack patterns associated with heating to 100°C in 1°C increments are shown for the three random textures in Figure 7a, b and c, respectively. Microcrack patterns associated with cooling to −100°C in 1°C increments are shown for these random textures in Figure 7d, e and f, respectively. All simulations display a combination of intergranular and transgranular microcracking. However, a predominance of intergranular (grain-boundary) cracking is observed. Additionally, the microcrack patterns that form on heating (Fig. 7a, b and c) are diametrical to those that form on cooling (Fig. 7d, e and f). Cracks that formed on heating do not form on cooling, and vice versa.

These results for calcite were quantified further by calculating the *bulk* coefficient of thermal expansion in both the x-direction (α_x) and y-direction (α_y) for the various simulations. Note that this is an *average* thermal expansion coefficient for the entire 100°C temperature interval; differential thermal expansion coefficients will be considered in future studies. These simulations included not only those shown in Figure 7a, b and c with microcracking, but also the corresponding simulations without microcracking. Additionally, simulations with and without microcracking were preformed for the crystallographic texture of the actual microstructure (REAL). In all cases the microstructure was heated to a temperature differential of +100°C, and in 1°C increments when microcracking was permitted. Results for the uncracked microstructure are given in Table 4 and those of the corresponding microcracked microstructure in Table 5. The thermal expansion coefficients for the cracked samples are significantly greater due to microcracking. There is also a large degree of anisotropy in the bulk thermal expansion coefficients. Since the x- and y-directions are statistically equivalent (except possibly for the REAL texture of the actual microstructure), this anisotropy reflects the actual crystallographic texture in these *representations* of random texture. That is, each sample is based on a random distribution, but this does not preclude that any one representation is textured. The data for RAN1 and RAN3 texture suggest a preferred orientation of the c-axes in the x-direction; data for the REAL texture suggest a higher c-axis concentration in the y-direction; and data for RAN2

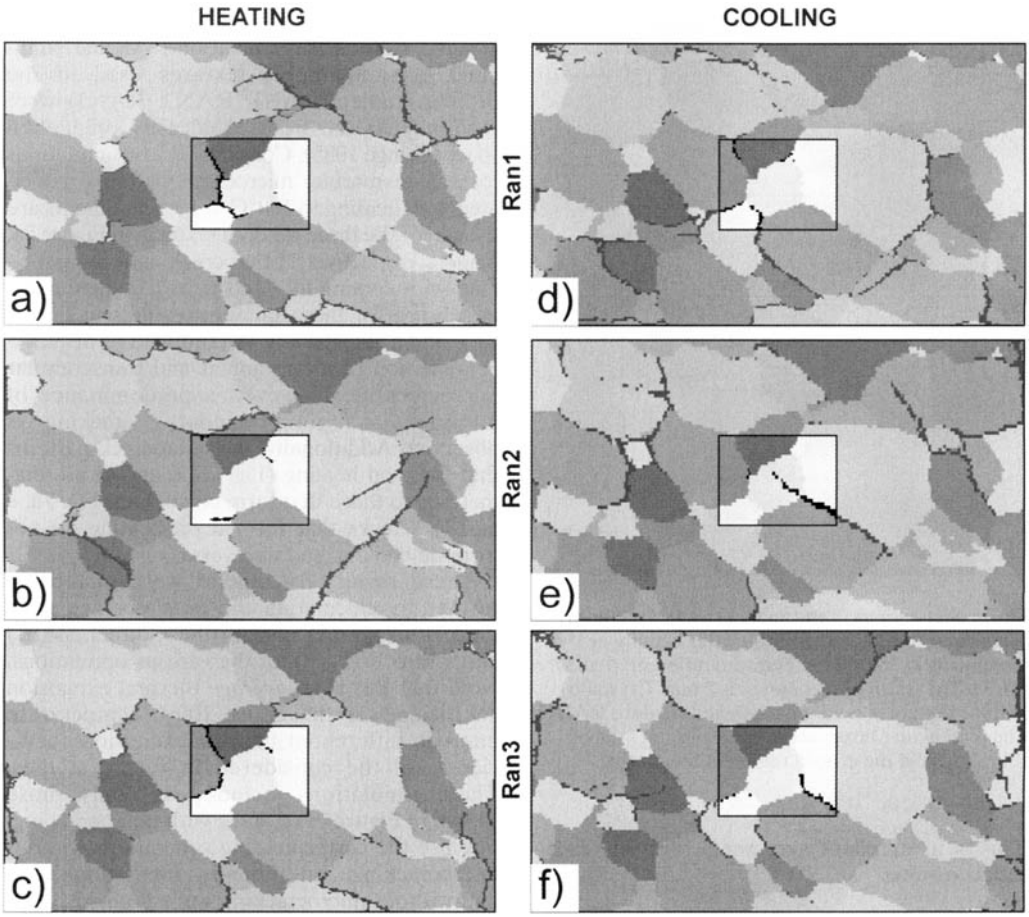

Fig. 7. Simulations of thermal microcracking in calcite on heating and cooling in 1°C increments to 100°C as a function of crystallographic texture (the width of the images is 2 mm). Simulations (**a**), (**b**) and (**c**) represent the microcracking that occurred in three different realizations (RAN1, RAN2 and RAN3, respectively) of random texture for the same micrograph (i.e. the same grain morphology) upon heating by $\Delta T = 100°C$. Simulations (**d**), (**e**) and (**f**) represent the microcracking that occurred for the same three different realizations (RAN1, RAN2 and RAN3, respectively) upon cooling by $\Delta T = -100°C$. The rectangular boxes accentuate a useful area of comparison in the central region of the images.

suggest an untextured sample. Preliminary pole figures for these 59 grains were generated, but no obvious texture was apparent. This is clearly an area for further investigation.

The possible presence of texture is also suggested by the large differences in elastic strain energy for the different simulations (see Table 4): the greater the bulk thermal expansion anisotropy (i.e. the lower the value of $A_\alpha = \alpha_{min}/\alpha_{max}$), the lower the elastic strain energy. Indeed, this effect is much greater than the differences between calcite and dolomite, which resulted from the crystalline elastic stiffness and thermal expansion anisotropy.

Comparing the elastic strain energy in Table 5 to the corresponding simulation in Table 4 shows the degree of stress relief due to micro-cracking. When microcracking is allowed, the elastic strain energy is significantly lower in the cracked sample (Table 5) than in the uncracked sample (Table 4). However, this reduction in elastic strain energy is smaller when the bulk thermal expansion anisotropy is larger (small A_α) and the total elastic strain energy is smaller. This observation suggests that the extent of microcracking is less in these cases. Again, this is an area for further investigations.

Table 4. *Average thermal expansion coefficients (α_x and α_y), its anisotropy (A_α), and the total elastic strain energy U of calcite as a function of texture without cracking*

	α_x (10^{-6} K^{-1})	α_y (10^{-6} K^{-1})	A_α*	U (μJ)
RAN1	6.13	3.20	0.52	200
RAN2	4.62	4.67	0.99	224
RAN3	7.18	2.17	0.30	189
REAL	0.65	5.78	0.11	97

* The A_α values are calculated as $A_\alpha = \alpha_{min}/\alpha_{max}$.

Table 5. *Average thermal expansion coefficients (α_x and α_y), its anisotropy (A_α), and the total elastic strain energy U of calcite as a function of texture with cracking*

	α_x (10^{-6} K^{-1})	α_y (10^{-6} K^{-1})	A_α*	U (μJ)
RAN1	8.46	7.21	0.85	104
RAN2	8.19	7.93	0.97	120
RAN3	11.00	2.76	0.25	112
REAL	1.63	6.46	0.25	72

* The A_α values are calculated as $A_\alpha = \alpha_{min}/\alpha_{max}$.

Discussion and conclusions

The thermomechanical behaviour of calcite and dolomite marbles, as elucidated by microstructural simulations, showed varied and different responses to thermal treatment. Both onset and magnitude of thermal microcracking vary for these minerals, when assumed to have exactly the same microstructure and texture, being greater for calcite. Thus, finite element modelling indicates that dolomite marbles may be more resistant against thermal weathering than calcite marbles. However, variations due to different textures significantly affect the distribution of thermal stresses within the marbles, and indeed, may be the more important variable in determining marble durability. There is a strong inverse correlation between thermal stresses and degree of texture, since higher elastic strain energies are associated with weakly textured marbles, and vice versa. When the actual (measured) texture for the real microstructure is considered, the total elastic strain energy of both calcite and dolomite is reduced by about 50% (see Table 5 for specific values for calcite). Thus, the actual texture in this case leads to much lower stresses than those within a sample of randomly chosen texture (on average). Further investigations, e.g. with intentionally textured microstructures, are needed to quantify this phenomenon. Additionally, investigations of the interactions between specific grain-to-grain orientations with bulk-averaged properties, as in the studies of Fu & Evans (1985), may be particularly enlightening.

Thermal microcracking leads to a stress relief with a simple interpretation that elastic strain energy is converted to fracture surface energy. However, this does not explain either microcrack initiation or extent. Simple phenomenological models (e.g. Kuszyk & Bradt 1973; Cleveland & Bradt 1978; Davidge 1981) relate spontaneous microcrack initiation to a critical value of the elastic strain energy multiplied by the average grain size divided by the fracture surface energy. As seen above, this describes well the different microcrack initiation temperatures for calcite and dolomite marbles with the same microstructure. However, more local microcracking criteria might provide more insight into the microcrack initiation and growth processes. Such approaches, usually fracture mechanics based (e.g. Evans 1978; Tvergaard & Hutchinson 1988), assume that microcracks initiate at microstructural defects on the grain boundaries and at triple-grain junctions. Initiation of microcracks at grain boundaries and triple-grain junctions was generally observed in the present simulations. The propensity for high elastic strain energy density at grain boundaries and at triple-grain junctions is illustrated in the uncracked microstructure of Figure 8a. After microcracking, most of this elastic strain energy is converted to fracture surface energy (see Fig. 8b). However, several high strain energy density elements are still associated with crack tips. To illustrate the general reduction in strain energy, the elastic energy densities in grain number 35 (see dotted line in Fig. 8a) show a significant reduction after

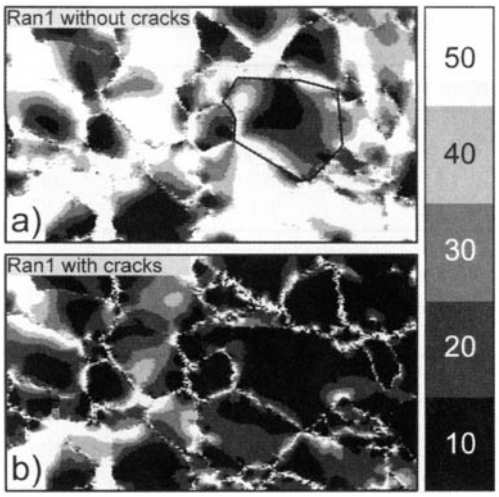

Fig. 8. Elastic strain energy density distribution in a simulation sample that (**a**) prohibits and (**b**) allows microcracking during heating (RAN1 texture, ΔT = 100°C, sample width = 2 mm). The colour scale in increasing strain energy density is from black to white. The elastic strain energy density as a function of element number for grain 35, which is outlined by a dotted line, is given in Figure 9.

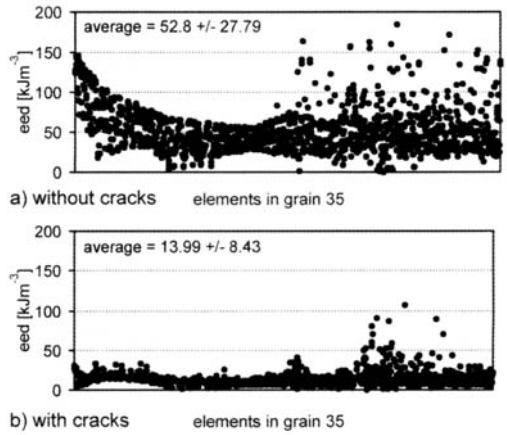

Fig. 9. Elastic strain energy density (eed) as a function of element number for elements in grain 35 of the simulation sample that (**a**) prohibits and (**b**) allows microcracking during heating (RAN1 texture, ΔT = 100°C; see Fig. 8). The element number sequence (monotonically increasing) is the same for both graphs, but has no significance.

thermal cracking (Fig. 9). The average value is reduced from 52.8 to 14.0 kJ m^{-3}.

Regarding the microstructural finite element simulation approach and the parameters used therein, the following considerations are pertinent and germane.

Different types of meshes (i.e. adaptive or simple meshes with varying resolutions) do not cause any significant differences in thermally induced stress distributions. While the very small adaptive meshes with sparse-node density and correspondingly large element size within the grains (see Fig. 4a) are not suitable for microcrack simulations (due to the *fracturing* of large elements), they are very fast and accurate for stress and strain energy simulations. Utilization of an intermediate mesh with 80 000 elements gave a good compromise between accuracy and processing performance for all the thermomechanical behaviours studied here.

All simulation experiments performed here, except one, were performed using the same boundary conditions, namely, all sides were free, but required to remain straight. For the one exception, all boundaries were totally free. In any finite size simulation, boundary conditions can have an important influence on the thermomechanical behaviour. This is expected to be particularly valid for simulations of fracture behaviour. In the current simulations, many microcracks and fractures originated and propagated near the edge of the microstructure (see Fig. 7). This is no doubt a result of the constraint that the microstructure edges remain straight. The one simulation with free boundary conditions (i.e. no requirement for the edges to remain straight) showed almost no fracturing at the outer edge of the microstructure. Both conditions are approximations to the actual behaviour of this small piece of microstructure when embedded in the full microstructure. Thus, neither boundary condition is more *correct* than the other. Nonetheless, it remains to assess the influence of various boundary conditions and to determine which boundary conditions tend to bound physical behaviour.

Simulations and theoretical calculations generally require physical properties data as inputs. Occasionally, certain approximations are required or make the simulations more elucidating. Our first assumption is related to the thermal expansion coefficients. Reported values of thermal expansion coefficients for various minerals vary from author to author. We used values for calcite (Kleber 1959) and dolomite (Reeder & Markgraf 1986) that only differ in the sign of thermal expansion coefficient perpendicular to the crystallographic c-axis, namely, $\alpha_1 = \alpha_{\perp c}$. This allows a simple evaluation of whether contraction (i.e. negative

coefficient of expansion) or expansion of the grains perpendicular to the c-axis with increasing temperature has a major effect on thermal degradation. Such a simple situation might provide much insight for investigations of the interactions between specific grain-to-grain orientations with bulk-averaged properties, as those of Fu & Evans (1985).

The second assumption regarding physical properties is related to the fracture surface energy. For both minerals, the same *isotropic* transgranular (cleavage) fracture surface energy (γ_{xtal}) was used. Additionally, the same ratio between γ_{xtal} and the intergranular (grain boundary) fracture surface energy (γ_{ig}) was assumed. Moreover, no anisotropy was assumed for either of these values. A recent analysis by White *et al.* (pers. comm.), which extends an analysis by Gilman (1960), suggest that the cleavage fracture surface energy (γ_{xtal}) is proportional to the Young's modulus across the cleavage plane multiplied by the interplanar spacing. This relation provides a simple estimate of the relative values for calcite and dolomite. However, at present this calculation has not been done. Different values of γ_{xtal} for the two minerals would no doubt influence their relative propensity for microcracking.

Transgranular fracture was frequently observed in the present simulations, even at relatively low temperatures. Since most marbles empirically exhibit granular disintegration, indicative of intergranular failure, this suggests that something is not quite correct. The most likely suspect is the relative ratio of γ_{ig} to γ_{xtal}, although grain boundary properties can clearly affect results (Saigal *et al.* 1998; Vedula *et al.* 2001). The value of 40% used in the present simulations is the same as that used by Sridhar *et al.* (1994) and Zimmermann *et al.* (2001). In the former case, this value was chosen because it was close to the ratio that gave an intergranular–transgranular fracture transition for a model without thermal expansion anisotropy strains (Yang *et al.* 1990). Accordingly, the actual ratio for calcite and dolomite is probably less than 40%. A systematic study could easily identify a threshold (with some stochastic scatter from various microstructures) below which fracture would always be intergranular. Our speculation is that it is not much less than 40%.

A final comment is made with regard to the fracture criterion that is implemented in these simulations. It is a local failure criterion, but probably not a realistic one, although it is based on conversion of local strain energy to elastically *soften* elements. Any assumed small defect, such as on a grain boundary or at a grain triple-junction, is surely subelement size. Thus, the microfracture mechanics for a different hierarchy of modelling needs to be embodied in these localized failure criterion of the OOF finite element analysis. Better criteria deserve much consideration and further research.

The authors gratefully acknowledge the assistance of and many helpful discussions with D. M. Saylor, M. R. Locatelli and S. A. Langer on various aspects of texture analyses and finite-element modelling, and are greatly appreciative to A. C. E. Reid and G. S. White for critical reviews of the manuscript and N. Østerby Olesen for help with the EBSD measurements. T. Weiss and S. Siegesmund were supported by the Deutsche Forschungsgemeinschaft with grants Si 438/10-1,2 (Heisenberg-Fellowship) and Si 438/13-1. T. Weiss is appreciative of the support in part of the Center for Theoretical and Computational Materials Science at the National Institute of Standards and Technology, Gaithersburg, MD, USA. E. R. Fuller Jr expresses his sincere appreciation to the Alexander von Humboldt foundation for their support.

References

BASS, J. D. 1995. Elasticity of minerals, glasses, and melts. *In*: AHRENS, T. J. (ed.) *Handbook of Physical Constants*. American Geophysical Union, Washington, DC, 45–63.

BECHER, P. F. & FREIMAN, S. W. 1978. Crack propagation in alkaline earth fluorides. *Journal of Applied Physics*, **49**, 3779–3783.

BUNGE, H. J. 1985. Representation of preferred orientations. *In*: *Preferred Orientation in Deformed Metals and Rocks: An Introduction to Modern Texture Analysis*. Academic Press, New York, 73–108.

CARTER, W. C., LANGER, S. A. & FULLER, E. R. JR. 1998. *The OOF manual: Version 1.0*. National Institute of Standards and Technology (NIST), NISTIR No. 6256. (Also available as Document No. PB99-118473INZ from National Technical Information Service, Springfield, VA, 22161, and on the Internet at http://www.ctcms.nist.gov/oof/)

CASE, E. D., SMYTH, J. R. & HUNTER, O. 1980. Grain-size dependence of microcrack initiation in brittle materials. *Journal of Material Science*, **15**, 149–153.

CLARKE, D. R. 1980. Microfracture in brittle solids resulting from anisotropic shape changes. *Acta Metallurgica*, **28**, 913–924.

CLARKE, F. J. P. 1964. Residual strain and the fracture stress-grain size relationship in brittle solids. *Acta Metallurgica*, **12**, 139–143.

CLEVELAND, J. J. & BRADT, R. C. 1978. Grain size/microcracking relations for pseudobrookite oxides. *Journal of The American Ceramic Society*, **61**, 478–481.

DAVIDGE, R. W. 1981. Cracking at grain boundaries in polycrystalline materials. *Acta Metallurgica*, **29**, 1695–1702.

EVANS, A. G. 1978. Microfracture from thermal expansion anisotropy – I. single phase systems. *Acta Metallurgica*, **26**, 1845–1853.

FU, Y. & EVANS, A. G. 1985. Some effects of microcracks on the mechanical properties of brittle solids – I. Stress, strain relations. *Acta Materialia*, **33**, 1515–1523.

GILMAN, J. J. 1960. Direct measurements of the surface engeries of crystals. *Journal of Applied Physics*, **31**, 2208–2218.

KLEBER, W. 1959. *Einführung in die Kristallographie*. VEB Verlag Technik, Berlin.

KUSZYK, J. A. & BRADT, R. C. 1973. Influence of grain size on effects of thermal expansion anisotropy in $MgTi_2O_5$. *Journal of The American Ceramic Society*, **56**, 420–423.

LANGER, S. A., FULLER, E. R. Jr. & CARTER, W. C. 2001. OOF: an image-based finite-element analysis of material microstructures. *Computing in Science and Engineering*, **3**, 15–23.

OLESEN, N. O. & SCHMIDT, N.-H. 1990. The SEM/ECP technique applied on quartz twinned crystals. *In*: KNIPE, R. J. & RUTTER, E. H. (eds) *Deformation Mechanisms, Rheology and Tectonics*. Geological Society, London, Special Publications, **54**, 369–373.

REEDER, R. & MARKGRAF, S. A. 1986. High temperature crystal chemistry of dolomite. *American Mineralogist*, **71**, 795–804.

SAIGAL, A., FULLER, E. R. Jr., LANGER, S. A., CARTER, W. C., ZIMMERMANN, M. H. & FABER, K. T. 1998. Effect of interface properties on microcracking of iron titanate. *Scripta Metallurgica et Materialia*, **38**, 1449–1453.

SCHMIDT, N.-H. & OLESEN, N. O. 1989. Computer-aided determination of crystal-lattice orientation from electron-channeling patterns in the SEM. *Canadian Mineralogists*, **27**, 15–22.

SIEGESMUND, S., ULLEMEYER, K., WEISS, T. & TSCHEGG, E. 2000. Physical weathering of marbles caused by thermal anisotropic expansion. *International Journal of Earth Science*, **89**, 170–182.

SRIDHAR, N., YANG, W., SROLOVITZ, D. J. & FULLER, E. R., Jr. 1994. Microstructural mechanics model of anisotropic-thermal-expansion-induced microcracking. *Journal of The American Ceramic Society*, **77**, 1123–1138.

TVERGAARD, V. & HUTCHINSON, J. W. 1988. Microcracking in ceramics induced by thermal expansion or elastic anisotropy. *Journal of The American Ceramic Society*, **71**, 157–166.

VEDULA, V. R., GLASS, S. J., SAYLOR, D. M., ROHRER, G. S., CARTER, W. C., LANGER, S. A. & FULLER, E. R. Jr. 2001. Residual stress predictions in polycrystalline alumina. *Journal of The American Ceramic Society*, **84**, 2947–2954.

WHITE, G. S., FREIMAN, S. W., FULLER, E. R. JR. & BAKER, T. L. 1988. Effects of crystal bonding on brittle fracture. *Journal of Material Research*, **3**, 491–497.

YANG, W. H., SROLOVITZ, D. J., HASSOLD, G. N. & ANDERSON, M. P. 1990. The effect of grain boundary cohesion on the fracture of brittle, polycrystalline materials. *In*: ANDERSON, M. P. and ROLLETT, A. D. (eds) *Simulation and Theory of Evolving Microstructures*. The Metallurgical Society, Warrendale, 277–284.

ZIMMERMANN, A., CARTER, W. C. & FULLER, E. R. Jr. 2001. Damage evolution during microcracking of brittle solids. *Acta Materialia*, **49**, 127–137.

Depositional environment and diagenesis as controlling factors for petro-physical properties and weathering resistance of siliciclastic dimension stones: integrative case study on the 'Wesersandstein' (northern Germany, Middle Buntsandstein)

JUTTA WEBER[1] & JOCHEN LEPPER[2]

[1] *Department of Geology, University of Cologne, Zülpicher Strasse 49a, D-50674 Köln, Germany (e-mail: weber.jutta@t-online.de)*

[2] *Niedersächsisches Landesamt für Bodenforschung, Stilleweg 2, D-30655 Hannover, Germany (e-mail: j.lepper@nlfb.de)*

Abstract: A case study on the 'Wesersandstein' (Middle Buntsandstein) indicates that weathering resistance and quality of dimension stones are functions of depositional environment, and of diagenetic alterations (eogenetic as well as mesogenetic) during geological history.

Two types of dimension stones, one deposited in a braided and the other in a meandering river system, were compared with respect to the fluvial architecture, the diagenetic modifications, the raw block prospectivity, and the petro-physical properties. The integrative synthesis of all these approaches indicates that depositional environment (type of fluvial architecture) and diagenesis (quartz cement and clay matrix contents) are the key processes which generally control the petro-physical properties and the weathering resistance of siliciclastic dimension stones. The highly quartz cemented 'Grauer Wesersandstein' with low clay matrix content, deposited as channel fill (braided river system), is characterized in general as a high quality dimension stone with very good petro-physical properties (e.g. high compressive strength, tensional strength, abrasion resistance, and freeze–thaw resistance) and high weathering resistance. In contrast to this, the 'Roter Wesersandstein', deposited as point bar and floodplain deposits of meandering rivers with low quartz cement and high clay matrix contents shows minor quality petro-physical properties (e.g. minor compressive strength, tensional strength, abrasion resistance, and freeze–thaw resistance) and weathering resistance.

This new integrative approach combines hitherto isolated studies on dimension stone quality. It shows the complex interrelations between the geological background on the one hand and specific dimension stone properties on the other hand.

The quality of dimension stones mainly corresponds to their resistance against destruction which is defined by standard petro-physical properties. These are density, porosity, water absorption, compressive strength, flexural strength, abrasion resistance, frost–thaw resistance (Smith 1999; and for the 'Wesersandstein' Lepper 2000). Controlling factors for these properties are: depositional environment (sedimentary architecture, petrographic composition); eodiagenesis and mesodiagenesis (compaction, cementation, mineral alteration); and geological and tectonic history (subsidence, uplift, exhumation, telogenetic effects).

The aim of this case study on the 'Wesersandstein' (Early Germanic Triassic, Middle Buntsandstein) known under the trade name 'Grauer Wesersandstein' (GWS, Grey Weser Sandstone) and 'Roter Wesersandstein' (RWS, Red Weser Sandstone), is an integrative characterization of the interrelation between depositional environment, diagenesis and dimension stone qualities.

Geological setting of the study area

The study area is situated in the northern part of Germany, the Weser uplands near Bad Karlshafen (Fig. 1). During Middle Buntsandstein times, various clastic sediments, including sandstones, siltstones and claystones, were deposited in a wide south to north trending river system, that followed the direction of the Hessian Depression. These clastic sediments were accumulated in a northward integrated subbasin, the Reinhardswald Trough, where the so-called Solling-Folge attains a maximum thickness of 120 m. The Solling-Folge includes

From: SIEGESMUND, S., WEISS, T. & VOLLBRECHT, A. 2002. *Natural Stone, Weathering Phenomena, Conservation Strategies and Case Studies*. Geological Society, London, Special Publications, **205**, 103–114.
0305-8719/02/$15.00 © The Geological Society of London 2002.

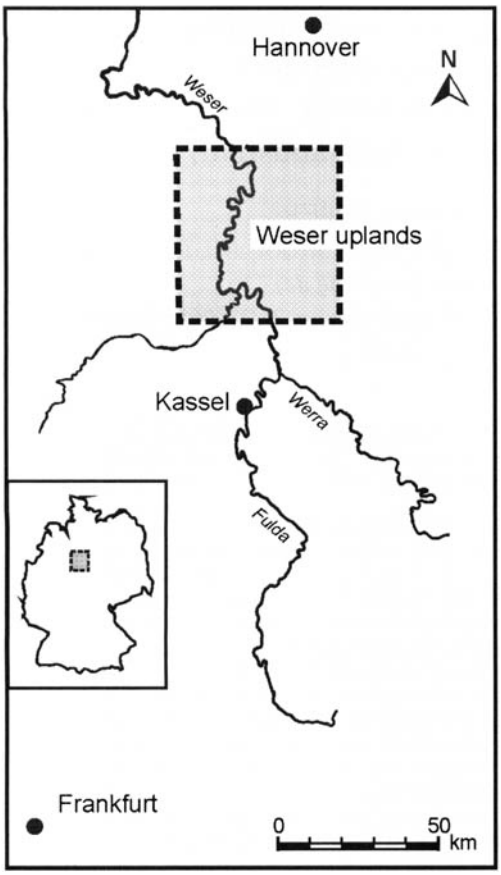

Fig. 1. Study area: Weser uplands, northwest Germany.

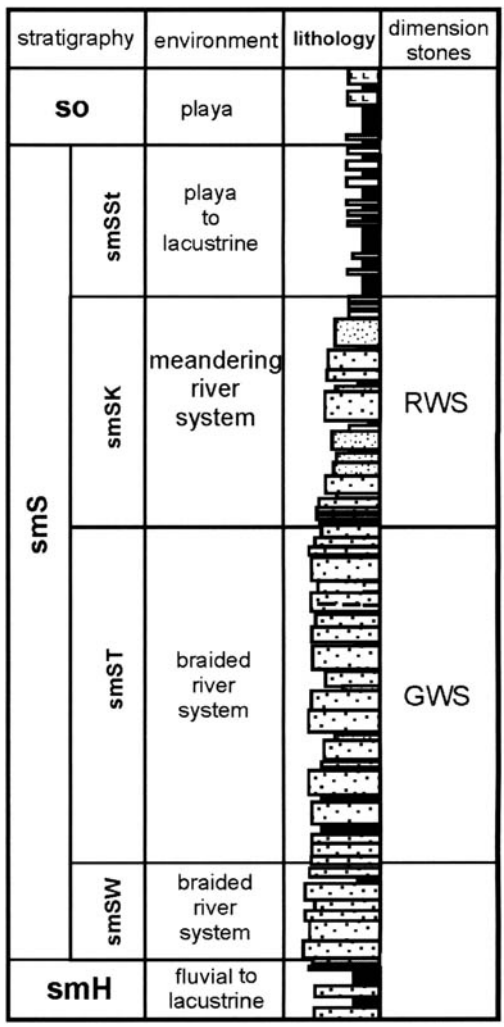

Fig. 2. Stratigraphic column of the Solling-Folge: environment, lithology and sections of dimension stone deposits. Stratigraphy: smH, Hardegsen-Folge; smS, Solling-Folge (smSW, Wilhelmshausen Beds, smST, Trendelburg Beds, smSK, Karlshafen Beds, smSST, Stammen Beds); so, Upper Buntsandstein. Lithology: L, evaporites; black, clay and siltstones, dots, sandstones (modified after Weber 2000 and Lepper & Röhling 1998).

two major sections (Trendelburg Beds and Karlshafen Beds, maximum thickness 90 m) with various dimension stone deposits (Fig. 2).

Depositional environment

The lower Solling-Folge is dominated by sandy braided rivers (Olsen 1988; Bindig 1991; Weber 2000). The fluvial architecture (Miall 1996) is composed of channels (CH) of different hierarchies (metres to decametres in width, decametres to a few hundreds of metres in length, and 0.3 to 2 m thick), downstream accretion (DA, several metres in width, a few decametres in length, and 0.5 to 1 m thick), laminated sandstones (LS, several decametres to hundreds of metres in lateral extent, and 0.3 to 3 m thick) with intercalated floodplain fines (FF, clay-siltstones), initial palaeosoils (calcretes) and heterogeneous crevasse splays (CS). Channel and downstream accretion sandstones show very good dimension stone quality and are exploited under the trade name 'Grauer Weser-sandstein' (GWS, Grey Weser Sandstone). The lithological trend from pure to clay and mica-rich sandstones reflects the transition from a braided to a meandering river system with lower water energy and therefore increasing mixed

load character of the deposits (Tietze 1982; Weber & Ricken 1998).

The upper Solling-Folge is characterized by clay-rich meandering river deposits comprising point bars with low inclination lateral accretion (LA), laminated sandstones (LS), floodplain fines (FF), crevasse splays (CS) and oxbow lakes (FF ox). Lateral accretion and laminated sandstones represent moderate to good quality dimension stones and are exploited under the trade name 'Roter Wesersandstein' (RWS, Red Weser Sandstone; Fig. 3, Table 1).

Sediment petrography

Sandstones of the lower Solling-Folge (sandy braided rivers) are predominantly medium grained and greyish coloured with high quartz cement contents (up to 18%). In river channel positions (fluvial architectural elements CH and DA) low clay mineral and mica contents and a grain-supported fabric prevail. The grain shape is subangular to subrounded, grain contacts are mostly point-shaped, elongated and subordinately concavo-convex. The main components are quartz (detrital and authigenic, 65–85%), feldspars (predominantly potassium feldspar, 15–28%), minor clay matrix (illite and kaolinite) and larger detrital mica grains (2–12%). In proximal floodplain positions (fluvial architectural element LS) the content of clay matrix and mica increases to 20–28%. Accordingly, sandstones of the lower Solling-Folge are predominantly classified as subarkoses (Folk 1974; Weber 2000; Fig. 4).

Sandstones of the upper Solling-Folge (fluvial architectural elements LA and LS), which were deposited in mixed load meandering river systems, are fine grained Red Beds and are classified as subarkosic wackes with moderate quartz cement content (2–8%). The main components are quartz (detrital and authigenic, 60–80%), feldspars (predominantly potassium feldspar, 15–25%), as well as clay matrix (illite, kaolinite and chlorite) and larger, detrital mica grains oriented parallel to bedding planes (up to >30%). Grain shape is subangular to subrounded, grain contacts are elongated to concavo-convex (Fig. 4, Table 1). Floodplain fines of both braided and meandering river systems with high clay matrix and mica contents are classified as clay-siltstones (Weber 2000).

Diagenesis

Diagenetic investigations were done by thin section analyses with a HC2-LM hot CL-microscope from Neuser (1997), with a beam current of 14 kV and cathode current of 15 $\mu A\ mm^{-2}$. The quantification of detrital and authigenic phases is based on point counting under transmitted light, crossed polars and cathodoluminescence with a total count of 2580 points per thin section (six photographs, each counted with 425 points, average values). Additionally, grain sizes and grain interrelationships were investigated by image analysis (VIDAS 25, Zeiss) and scanning electron microscopy (clay morphology).

The subarkoses and subarkosic wackes of the Solling-Folge were buried and modified by diagenetic processes, including mechanical compaction, cementation (predominantly quartz cement) and mineral alteration. Petrographic composition and fluvial architecture govern distinct diagenetic pathways (Fig. 5; Weber 2000).

Subarkoses of the lower Solling-Folge ('Grauer Wesersandstein') were compacted mechanically during the eogenetic stage from estimated initial porosities of approximately 40% down to an average intergranular volume (IGV) of 26% (Houseknecht 1988). Subsequently, grain rearrangement, minor chemical compaction, and minor quartz cementation (QC 1) led to IGVs of about 22%.

During the mesogenetic stage, two main quartz cementation phases, which can be distinguished by different cathodoluminescence colours, stabilized the grain framework (QC 2, dark brown luminescence and QC 3, dark blue luminescence). A total of 18% quartz cement is observed. Minor authigenic clay coatings (illite, kaolinite) and/or minor carbonate cements occur only subordinately in the remaining pore space that reaches volumes of about 5 to 10%.

Subarkosic wackes of the upper Solling-Folge ('Roter Wesersandstein'), which show estimated initial porosities of 60% (Houseknecht 1988), were compacted down to IGV values of approximately 13%, indicating a stronger effect of mechanical and chemical compaction. Quartz cementation (2–8%), which took place during the mesogenetic stage, is represented by only one phase. The remaining pore space of approximately 5 to 10% is partly faced with minor authigenic clays (illite, kaolinite and chlorite) and/or minor carbonate cements.

The authigenic clay minerals kaolinite and illite as the final phase result from feldspar alteration processes. Silica, which is also a product of feldspar alteration, is considered to be an important internal source for the observed grain framework stabilizing quartz cement of the 'Wesersandstein' (Weber 2000).

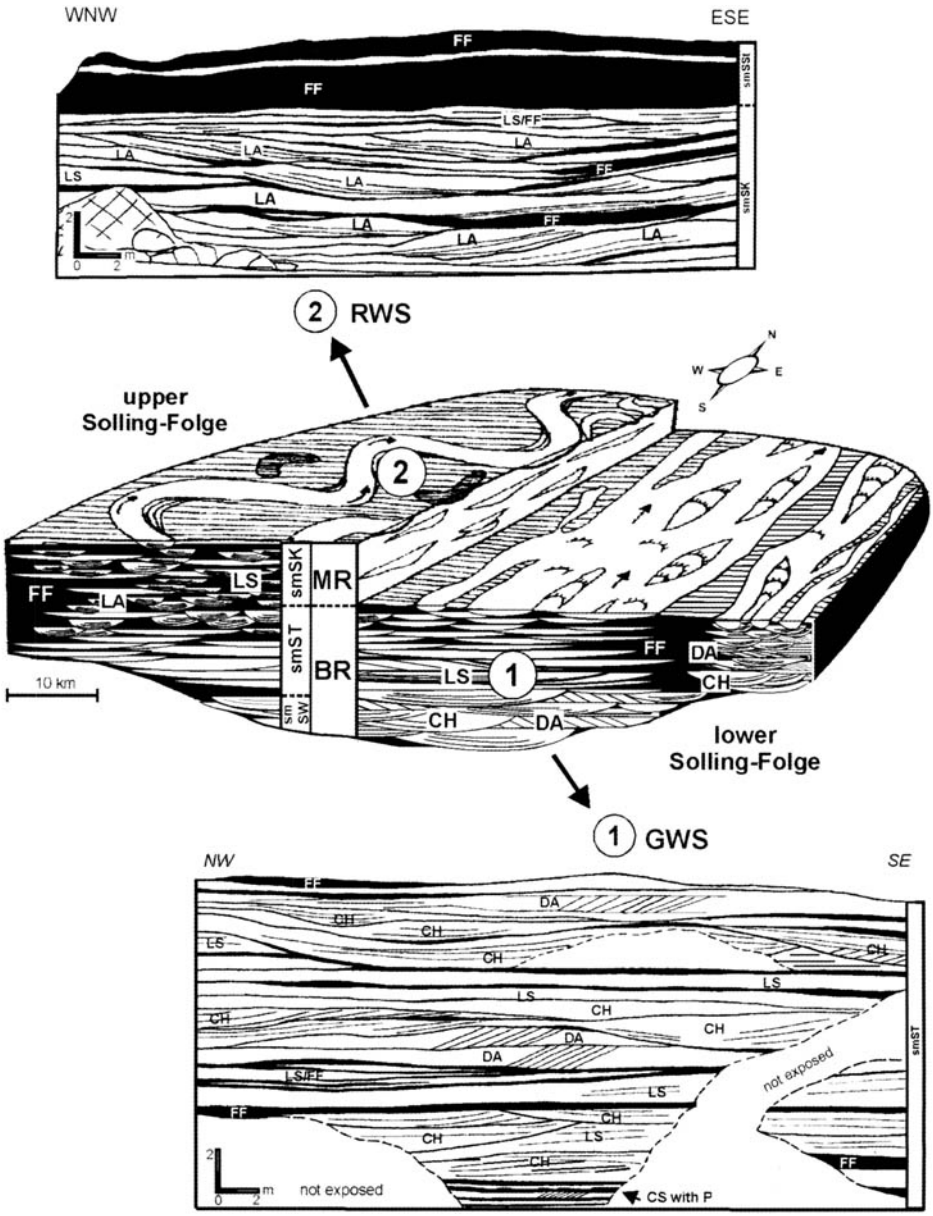

Fig. 3. Typical fluvial architectural elements of the Solling-Folge. Lower Solling-Folge: braided rivers (BR) with channels (CH), downstream accretion (DA), laminated sandstones (LS) and floodplain fines (FF). Upper Solling-Folge: meandering rivers (MR) with lateral accretion (LA), laminated sandstones (LS) and floodplain fines (FF). Fluvial architecture of specific exposures: (1) abandoned quarry Würgassen, Trendelburg Beds (smST) including the 'Grauer Wesersandstein', lower Solling-Folge; (2) Quarry Niemeyer, Karlshafen Beds (smSK) including the 'Roter Wesersandstein', upper Solling-Folge (modified after Weber 2000).

These distinctly different diagenetic pathways, which correspond to typical compaction–cementation features, cause specific dimension stone properties. Sensitive quality parameters are quartz cement and clay (predominantly primary clay matrix, minor authigenic clay minerals like illite, kaolinite and chlorite) and mica contents of the sandstones, which show an

Table 1. *Database for sediment petrography, fluvial architecture and diagenesis of the 'Wesersandstein'*

Sample	DQ	QC	F	CM	Mi + Lit	Car	FAE	Dimension stone
KH-01-2	56.4	4.6	15.5	16.4	2.3		LA	RWS
KH-02a-1	41.3	3.5	17	25.3	6.5		LS	RWS
KH-03-1	54.1	7.1	15.7	15.7	2.3		LA	RWS
KH-03-2	60.9	6.4	14.3	10.9	2.8		LA	RWS
KH-06-1	54.2	5.2	15.9	18.8	1.8		LA	RWS
KH-06-2	55.5	7.5	19.2	10.9	3		LA	RWS
KH-07-1	39.3	3.2	21.6	29	3.7		LS/FF	RWS
KH-09-1	50.3	6.4	17.2	21.4	2.4		LA	RWS
KH-09-2	52.9	3.2	16.6	20.9	1.3		LA	RWS
KH-11-1	46.4	7.3	18.2	19.5	2.6	0.3	LA	RWS
KH-18-1	46.6	2.1	18.5	23.2	3.8		LS	RWS
NB3-2-4	44.1	4.4	25.4	19	2.6		LS	RWS
NB3-3-2	50.5	2.9	10.6	28	1.4	0.2	LA	RWS
NB3-8-2	53.7	6.5	17.7	14.6	1		LA	RWS
NB3-10-1	45.4	2.1	26.8	20.7	1.7		LS	RWS
HE-1	51.2	8.4	12.5	19.4	0.9		LS	RWS
HE-2	50.5	10.1	12.9	17.2	1.8		LS	RWS
HE-3	55.9	11.9	8.6	16.2	1.3		LS	RWS
HE-1-2	53.5	12	14.6	9.7	2.8		LS	RWS
EC-1	62.7	14.4	13.2	1.2	1	4.7	CH	RWS
Wü1-05-1	53.2	12.1	24.2	6.2	0.2	–	CH	GWS
Wü1-05-3	50.4	15.3	24.4	6.3	1	–	CH	GWS
Wü1-07-1	52.4	8.6	16	11.7	–	–	CH	GWS
Wü1-07-2	57	15.6	15.1	2.3	0.4	–	CH	GWS
Wü1-07-3	51.6	16.3	20.2	5.7	0.5	0.3	CH	GWS
Wü1-07-5	46.6	12.6	23	13.6			CH	GWS
Wü1-07-7	52.4	12.2	17.9	6.7	1.7		CH	GWS
Wü1-07-9	52.8	13.5	19.5	9.4	0.3	–	CH	GWS
Wü1-14-1	57.8	18.3	15.4	4.6	–	–	CH	GWS
Wü1-14-2	59	16.6	15	4.8	–	0.9	CH	GWS
Wü1-14-3	54.3	17.8	16.7	5.4	–	-	CH	GWS
Wü1-14-6	55.4	12.5	19.2	8.2	–	0.4	CH	GWS
Wü1-14-10	58.1	12.5	15.4	8.7	0.9	–	CH	GWS
Wü1-16-3	48.2	10.2	19.3	16.8	0.7		LS	GWS
Wü1-20-1	51.3	15.4	18.7	7	–	–	DA	GWS
Wü1-22-1	42.8	13.2	26.4	14.7	0.4	0.6	LS	GWS
Wü1-22-3	41.3	13.2	29.1	14	0.8	–	LS	GWS
Wü1-26-1	51.9	13.2	16.7	11.6	1.6	0.5	LS	GWS
Wü1-26-3	51.7	13.1	20.5	9.4	0.5	0.5	LS	GWS
Wü1-27-1	50.7	7.3	19.4	18.5	0.2	0.5	LS	GWS
Wü1-27-2	36.7	3.6	26.2	28.5	1.2	0.8	LS	GWS
Wü1-29-1	53	15	19.4	6	0.7	0.2	LS	GWS
Wü1-29-4	54.7	6.5	18.1	14.2	1	0.4	LS	GWS
Wü1-31-1	49.2	13.6	22.9	10.4	0.9	0.2	LS	GWS
Wü1-31-2	53.1	5.5	19.9	14.7	1.1		LS	GWS
Wü1-33-2	55.9	9.4	18.2	6.7	0.3	1.4	DA	GWS

DQ, detrital quartz; QC, quartz cement; F, feldspar; CM, clay minerals; Mi + Lit, micas + lithoclasts; Car, carbonates; FAE, fluvial architectural element; GWS, 'Grauer Wesersandstein'; RWS, 'Roter Wesersandstein' (modified after Weber 2000)

inverse correlation (Fig. 6). Clay minerals are inhibitors for quartz cementation (Dewers & Ortolewa 1991), therefore the content of clay matrix in dimension stones controls quartz precipitation which is the major lithification process. High quartz cement content corresponds with low clay matrix and mica contents and is related to good dimension stone quality (subarkoses of the 'Grauer Wesersandstein'). In contrast to this, the comparably minor quality of dimension stones (subarkosic wackes of the 'Roter Wesersandstein') is caused by lower

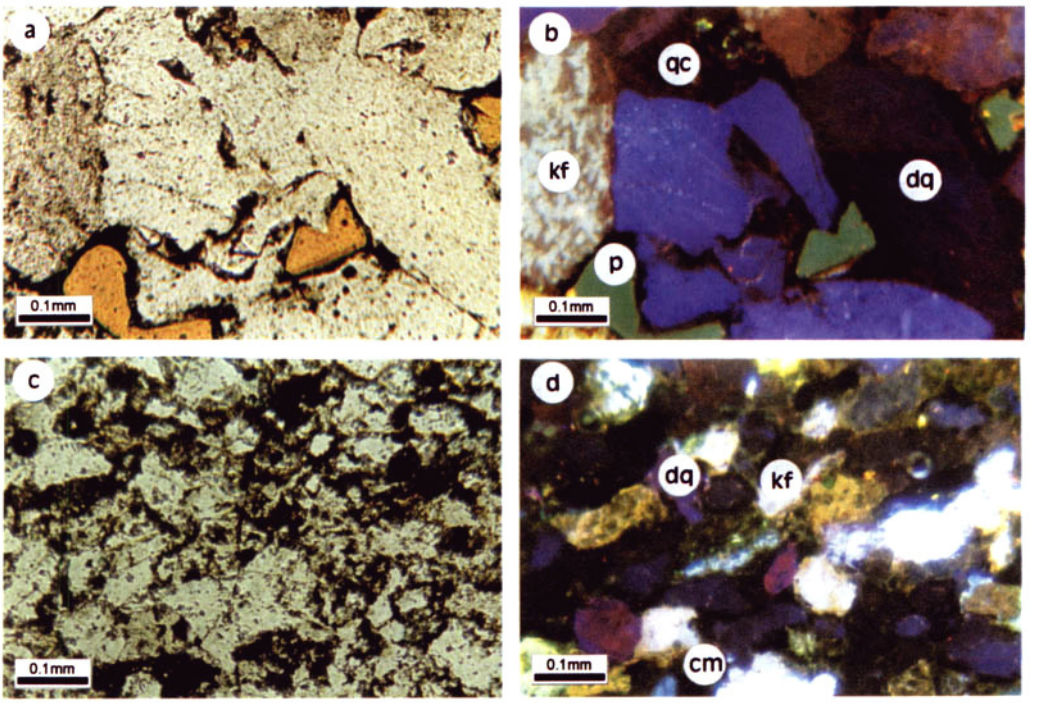

Fig. 4. Photomicrographs of the 'Grauer Wesersandstein' (**a**, **b**) and the 'Roter Wesersandstein' (**c**, **d**) in transmitted light (left side) and under cathodoluminescence (right side). Key: cm, clay minerals; dq, detrital quartz; kf, potassium feldspar; m, mica; p, pore space; qc, quartz cement.

quartz cement content, which corresponds to high clay matrix and mica contents. Koch & Siegesmund (2001) show also a distinct interrelation between high clay matrix content and reduced weathering resistance.

Fracture system analysis

The type and dimension of fracture systems control the size and the amount of extractable raw blocks. Depending on the processing equipment and the final products, a minimum raw block volume of 0.4 m^3 and, additionally, a minimum length of 0.4 m of all three sides is generally required (Singewald 1992; Weber *et al.* 2001). The quantity and size of raw blocks which match these conditions can be assessed by a three-dimensional fracture system analysis, a predominantly orthogonal fracture system provided.

The following potential fractures have to be considered: planes (bedding and cleavage) and joints; other discontinuities like faults; and veins, filled with calcite or quartz.

Raw block prospectivity

This parameter defines the percentage of extractable raw blocks in a deposit which suit the above-mentioned requirements. Accordingly, it represents an essential criterion for the economic evaluation of a deposit with respect to the yield of processable raw blocks (Fig. 7).

The raw block prospectivities of the 'Grauer Wesersandstein' and the 'Roter Wesersandstein' are given in Table 2. As evidenced by similar values of fracture spacing of the 'Grauer Wesersandstein' and 'Roter Wesersandstein' in the southern part of the study area, the raw block prospectivity is primarily controlled by tectonic effects. The additional importance of the sedimentary architecture is reflected by relatively high raw block prospectivities of the 'Roter Wesersandstein' in the northern part of the study area, which are attributed to extended channel dimensions. The best raw block prospectivities with respect to the sedimentary architecture are to be expected in the axis parts of channel systems with maximum extension of the sandbodies in all three dimensions.

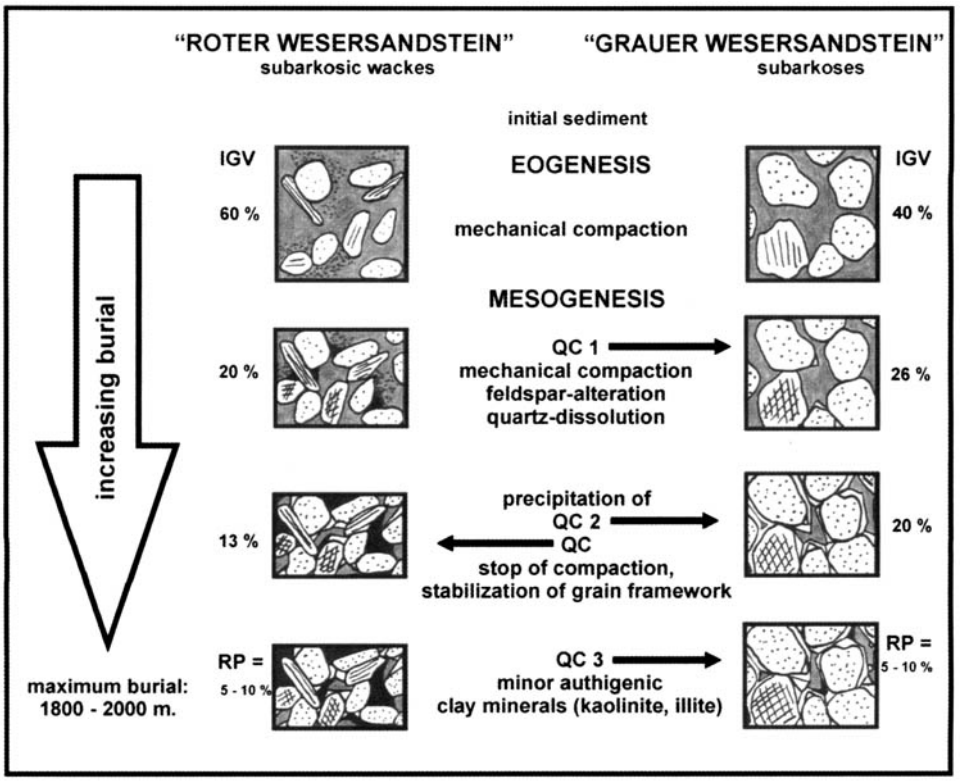

Fig. 5. Diagenetic history of the 'Wesersandstein' (modified after Weber 2000). Subarkoses ('Grauer Wesersandstein', GWS) are characterized by moderate mechanical compaction and minor quartz cementation (QC 1) during eogenesis, followed by mesogenetic polyphase quartz cementation (QC 2, QC 3), which stopped further compaction at moderate intergranular volumes (IGVs) of 15 to 22%. Subarkosic wackes ('Roter Wesersandstein', RWS) show higher compaction rates (IGV = 8 to 13%) and are cemented by only one quartz phase. IP, initial porosity; RP, remaining porosity.

Table 2. *Raw block prospectivity (see Fig. 7) of the 'Grauer Wesersandstein' (GWS) and the 'Roter Wesersandstein' (RWS)*

GWS	RWS (S)	RWS (N)
<3	<3	24
1.5	7	39
7	9	22
13	<1	26
		<2 (fault zone)

S, N, southern and northern parts of the study area, respectively (modified from Lepper 1997)

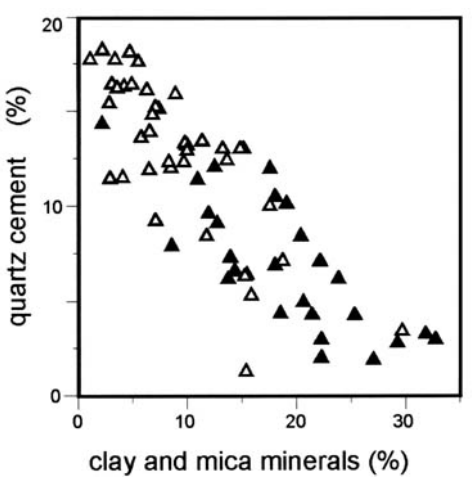

Fig. 6. Inverse relationship of quartz cement content to clay matrix and detrital mica contents. Open triangles: 'Grauer Wesersandstein' (GWS); black triangles: 'Roter Wesersandstein' (RWS).

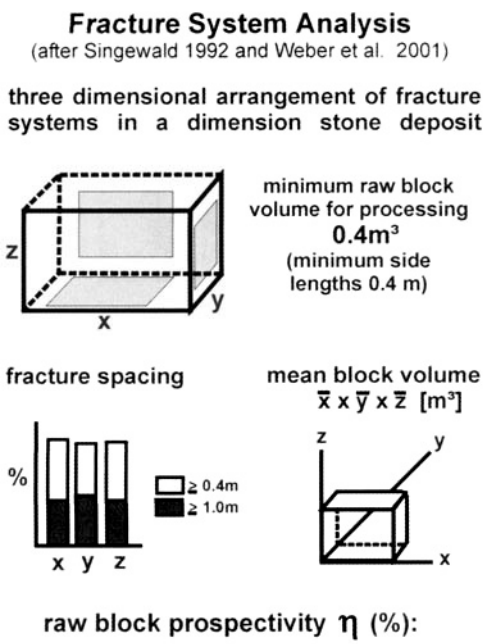

Fig. 7. Basic parameters for fracture system analysis (modified from Lepper & Weber 2001).

Table 3. Petro-physical parameters of the 'Grauer Wesersandstein' (GWS) and the 'Roter Wesersandstein' (RWS)

Petro-physical parameters	GWS	RWS
Density (g/cm³) DIN 52102 (D)	2.60–2.64	2.64–2.73
Porosity (%) DIN 52102 (11)	5.7–13.9	10.2–19.1
Water adsorption (g) DIN 52103 (VA)	3.0–9.2	8.2–25.8
Compressive strength (N/mm²) DIN 52105	66.7–212.8	36.7–121.1
Abrasion wear (cm³) DIN 52108	7.97–16.33	12.67–32.98
Flexural strength (N/mm²) DIN 52112	13.8–34.8	5.9–18.8
Frost–thaw resistance (mass %) DIN 52104 (1C)	0.03–0.32	0.03–0.31
Frost–salt resistance	0–1	0–4

Modified from Lepper (1997) and Lepper & Weber (2001). DIN, Deutsches Institut für Normung e.V.

Petro-physical properties

Petro-physical properties of dimension stones are measured by different national standards (e.g. American Society for Testing and Materials, British Standards Institution, Deutsches Institut für Normung (DIN), French National Standards, Italian National Standards; Smith 1999). These parameters reflect the resistance against destruction influences like weathering/freezing, compressional, tensional or irregular stress. Taking into account that fabric anisotropies (e.g. stratification, pore size and geometry) are the main controlling factors for the directional dependence of petro-physical properties, the testing methods and fabric should be documented (Koch & Siegesmund 2001).

A compilation of the most important petro-physical parameters (testing methods defined by DIN standards) of the 'Wesersandstein' is presented in Table 3. The petro-physical properties reveal a distinct correlation to depositional environment and diagenetic overprint. Generally very good petro-physical parameters (e.g. low water adsorption, high compressive strength, high tensional strength, high abrasion resistance, high freeze–thaw resistance) of the 'Grauer Wesersandstein' correspond to high quartz cement contents up to 18%, and, additionally, low clay matrix contents of approximately 10%.

Contrasting with this, the 'Roter Wesersandstein' with a distinctly higher clay matrix (up to 30%) and moderate quartz cement content up to 8%, is generally characterized by a minor quality of petro-physical properties (e.g. higher water adsorption, lower compressive strength, lower tensional strength, lower abrasion resistance, lower freeze–thaw resistance).

Accordingly, the petro-physical properties correspond primarily to the sensitive parameters *cementation* (type and amount of grain framework stabilizing phase), *clay matrix* (predominantly primary, minor authigenic) and detrital mica *contents* (parallel bedding planes).

These parameters are therefore considered as the most important indicators for good (high quartz cement content) or minor weathering resistance (high clay matrix and detrital mica content) of siliciclastic dimension stones, which

is also confirmed by the results of Koch & Siegesmund (2001).

Synthesis and conclusions

The quality of siliciclastic dimension stones is primarily conditioned by the following parameters: depositional environment, petrographic composition, diagenetic overprint, petro-physical properties and raw block prospectivity. This is evidenced by an integrative case study conducted on siliciclastic dimension stone deposits in northern Germany ('Grauer Wesersandstein' and 'Roter Wesersandstein').

The characterization of the 'Grauer Wesersandstein' (Fig. 8) is summarized below:

- fluvial deposits of a braided river system (fluvial architectural elements CH, DA, LS);
- subarkoses with high quartz cement content (up to 18%) and generally low clay matrix and detrital mica contents (up to 10%);
- medium to low raw block prospectivity;
- high quality petro-physical parameters (e.g. low water adsorption, high compressive strength, high tensional strength, high abrasion resistance, high freeze–thaw resistance);
- highly cemented channel (CH) and sandbar deposits (DA), used as building stone: e.g. hydraulically riven setts and sawn slabs for urban pavements and hard landscaping, hydraulically riven or manually split and dressed stones for facade cladding and hard landscaping, sawn facing stones with riven exterior view side, sawn massive stair steps and bollards (due to its mechanical resistance this sandstone is less used for carved sculptures);
- weathering resistance: generally very good (high quartz cement content and low clay matrix and detrital mica contents), reflected by high quality petro-physical parameters.

The former monastery Lippoldsberg (twelfth century) provides an example of the appropriate use of dimension stones in sensitive parts of the building. The profiled socle, the profiled portal frame, and the quoins are of 'Grauer Wesersandstein'. Due to their high quartz cement and low clay matrix and mica contents correlated with high quality petro-physical parameters these exposed channel sandstones (CH) generally are not affected by severe weathering damage (Fig. 9).

The characterization of the 'Roter Wesersandstein' (see Fig. 8) is summarized below:

- fluvial deposits of meandering rivers (fluvial architectural elements LA, LS);
- subarkosic wackes with moderate quartz cement content (up to 8%) and high clay matrix and detrital mica contents up to 30% (micas parallel to bedding planes);
- low to high raw block prospectivity (depending on the fluvial architecture);
- minor quality petro-physical parameters (e.g. higher water adsorption, lower compressive strength, lower tensional strength, lower abrasion resistance, lower freeze–thaw resistance);
- moderate cemented lateral accretion sandstones (LA), used as building material and ornamental stone: e.g. hydraulically riven setts and sawn slabs for urban pavements and hard landscaping, hydraulically riven or manually split and dressed stones for hard landscaping, sawn slabs for facade cladding, sawn massive stair steps and bollards, carved sculptures and cut dimension stones;
- minor cemented laminated sandstones (LS) with high clay and mica content, used as building material: e.g. manually split and dressed flagstones for urban pavements and hard landscaping, manually split and dressed thin flagstone slabs for roofing and facade cladding (produced only in historical times);
- weathering resistance: mediocre (moderate quartz cement content and high clay matrix and detrital mica contents) reflected by comparably minor quality petro-physical properties.

The former monastery Amelungsborn (twelfth to fourteenth century) is constructed of 'Roter Wesersandstein' (lateral accretion sandstones, LA, and laminated sandstones, LS). This lithofacies of dimension stones contains moderate amounts of quartz cement and high clay matrix and mica contents which correlate with comparably poor quality petro-physical parameters. In sensitive parts of the monastery (e.g. socle), they are affected by weathering and distinct loss of material (Fig. 10).

Dimension stones have been used for monuments and buildings for thousands of years. Their resistance against natural destructive influences (e.g. weathering, ground water, or

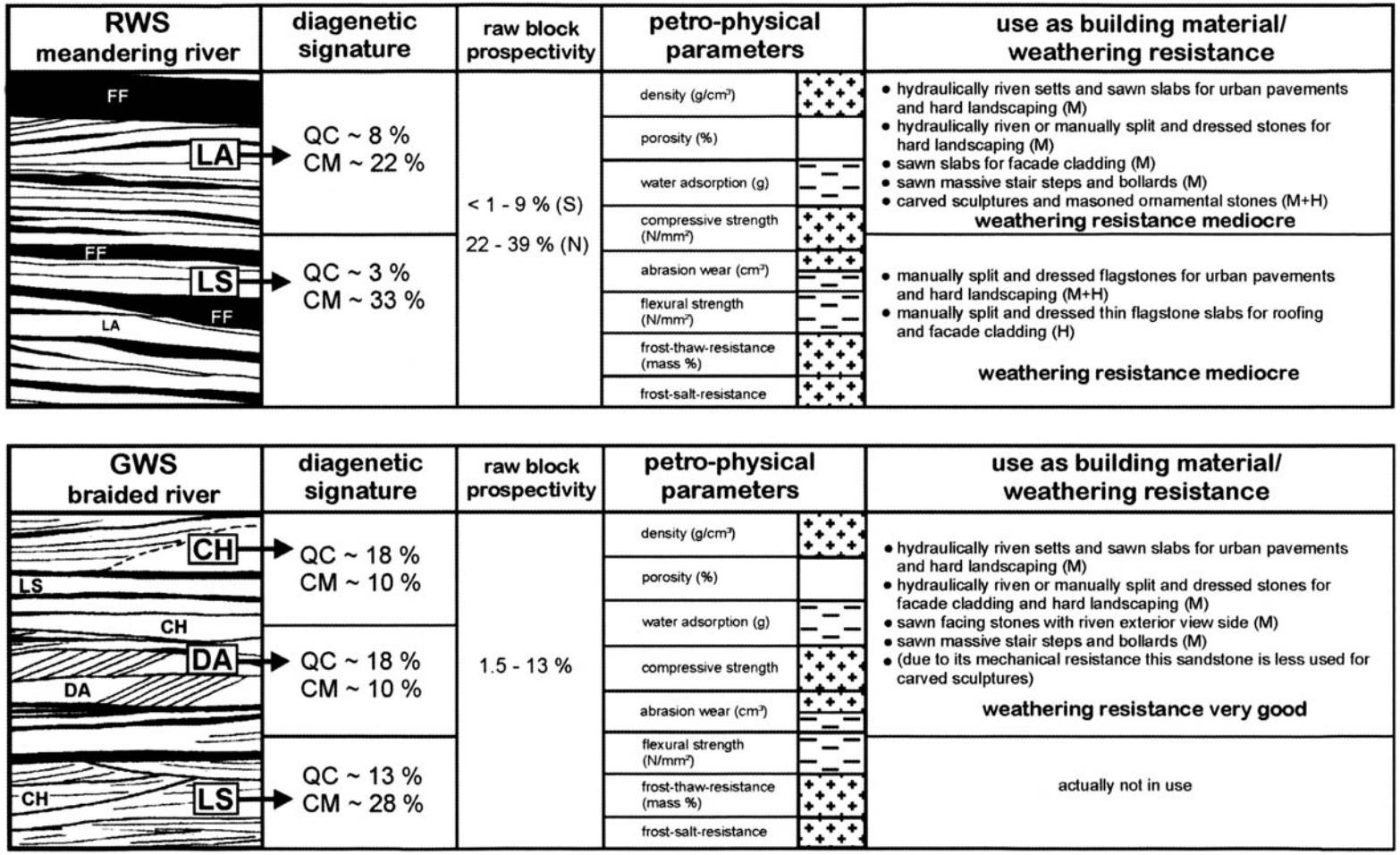

Fig. 8. Synthesis of the various methods and characterization of the dimension stone quality for the 'Grauer Wesersandstein' and the 'Roter Wesersandstein'. CM, clay minerals; QC, quartz cement. High quality petro-physical parameters correlate with high quartz cement content (+), minor quality petro-physical parameters with high clay matrix content (−). Medium quality petro-physical parameters are characterized by moderate contents of quartz cement and clay matrix (+,−). H, historical use; M, modern use; N, northern part of the study area; S, southern part of the study area.

Fig. 9. Former monastery Lippoldsberg (twelfth century). The profiled socle, the profiled portal frame, and the quoins are masoned of 'Grauer Wesersandstein'.

Fig. 10. Former monastery Amelungsborn (twelfth to fourteenth century). The 'Roter Wesersandstein' is affected by weathering and distinct loss of material, particularly in sensitive parts of the building.

salt efflorescence) predominantly depends on lithofacies, depositional environment and diagenesis.

The authors are grateful to S. Siegesmund for his invitation to contribute this paper. The manuscript benefited from constructive comments by R. Gaupp, R. Koch, and S. Siegesmund. J. Dehnhardt is thanked for his linguistic improvements.

References

BINDIG, M. 1991. *Räumliche und zeitliche Entwicklung der fluviatilen Environments der Solling-Folge (Buntsandstein, Germanische Trias)*. PhD Thesis, Darmstadt.

DEWERS, T. & ORTOLEWA, P. 1991. Influences of clay minerals on sandstone cementation and pressure solution. *Geology*, **19**, 1045–1048.

FOLK, R. L. 1974. *Petrology of Sedimentary Rocks*. Hemphill, Austin, Texas.

HOUSEKNECHT, D. 1988. Intergranular pressure solution in four quartzose sandstones. *Journal of Sedimentary Petrology*, **58**, 228–246.

KOCH, A. & SIEGESMUND, S. 2001. Gesteinstechnische Eigenschaften ausgewählter Bausandsteine. *Zeitschrift der Deutschen Geologischen Gesellschaft*, **152**(2–4), 681–700.

LEPPER, J. 1997. Naturwerksteine in Niedersachsen. *Zeitschrift für angewandte Geologie*, **43**(1), 3–10.

LEPPER, J. 2000. Der Wesersandstein – ein historisches Baumaterial. Vorkommen, materialkundliche Aspekte, Verwendung. *Berichte der Denkmalpflege in Niedersachsen*, **3/2000**, 129–132.

LEPPER, J. & RÖHLING, H.-G. 1998. Buntsandstein. *Hallesches Jahrbuch für Geowissenschaften*, Reihe **B6**, 27–34.

LEPPER. J. & WEBER, J. 2001. Integratives Bewertungskonzept für eine siliziklastische Naturwerkstein-Lagerstätte im Roten Wesersandstein bei Bad Karlshafen. *Zeitschrift für angewandte Geologie*, **47**(2), 79–86.

MIALL, A. D. 1996. *The Geology of Fluvial Deposits*. Springer, Berlin.

NEUSER, R. D. 1997. The present state of optical cathodoluminescence microscopy: developments and facilities at the Ruhr-University, Bochum. *Gaea heidelbergensis*, **3**, 253.

OLSEN, H. 1988. The architecture of a sandy braided-meandering river system: an example from the Lower Triassic Solling Formation (M. Buntsandstein) in W-Germany. *Geologische Rundschau*, **77**, 797–814.

SINGEWALD, C. 1992. *Naturwerkstein – Exploration und Gewinnung*. Steintechnisches Institut Mayen, Köln.

SMITH, M. R. (ed.) 1999. *Stone: Building Stone, Rock Fill and Armour Stone in Construction*. Geological Society, London, Engineering Geology Special Publications, **16**.

TIETZE, K. W. 1982. Zur Geometrie einiger Flüsse im Mittleren Buntsandstein (Trias). *Geologische Rundschau*, **71**, 813–828.

WEBER, J. 2000. Kieselsäurediagenese und gekoppelte Sedimentarchitektur – eine Beckenanalyse des Reinhardswald-Troges (Norddeutsches Becken, Solling-Folge, Mittlerer Buntsandstein). *Forum für Geologie und Paläontologie, Universität zu Köln*, **7/2000**, 3–165.

WEBER, J. & RICKEN, W. 1998. Fluvial architecture and silica diagenetic pattern of the Solling Folge (Reinhardswald trough, Solling area, NW Germany). *Zentralblatt für Geologie und Paläontologie* **I**(7–8), 747–767.

WEBER, J., DEHNHARDT, J. & LEPPER, J. 2001. Trennflächenanalyse zur Vorratsermittlung von Naturwerkstein-Lagerstätten. *Zeitschrift für angewandte Geologie*, **47**(2), 74–78.

Anisotropic technical properties of building stones and their development due to fabric changes

DANIEL STROHMEYER & SIEGFRIED SIEGESMUND
Geowissenschaftliches Zentrum Goettingen, Strukturgeologie & Geodynamik, Goldschmidtstrasse 3, 37077 Goettingen, Germany (e-mail: dstrohm@gwdg.de)

Abstract: Technical properties of building stones are of critical importance in applied geosciences such as engineering geology, and also with respect to construction or building physics. Among the many factors which control the technical properties, special importance is given to the rock fabrics influencing the anisotropy of these technical properties. To demonstrate this relationship a sequence of mylonitic rocks, i.e. metagranitoid progressively deformed to mylonite and ultramylonite, was selected. The mineralogical and chemical composition of the protolith and mylonite is nearly identical. All investigated parameters (tensile strength, compressive strength, abrasive strength, magnetic susceptibility and ultrasound wave velocities) are anisotropic and finally controlled by the mineralogical composition and the different fabric elements like microstructural features, the crystallographic and shape preferred orientations and the state of microcracking. The development of the rock fabric with mylonitization, in particular the preferred orientation of mica, seems to be most important for the directional dependence of rock physical properties, at least in mica-rich rocks. However, various sets of microcracks, the degree of grain size reduction, the intensity of the foliation and the compositional layering can significantly modify the results. The interaction of superimposing parameters for different technical properties does not allow any simple cross-correlation.

The properties of dimensional stones, i.e. polycrystalline aggregates, are influenced by the properties and volume fraction of the rock-forming minerals. The selection of building stones is usually done for aesthetic reasons; however, their technical properties are not taken into consideration, which must satisfy certain requirements based on building physics. The reference standards of each country or at the European scale dictate the necessary requirements. For example, the suitability of dimensional stones for ventilated facades requires measurement of the flexural strength and freeze–thaw tests. In the case of marble panels (see discussion in Koch & Siegesmund 2002) the spectacular phenomenon of bowing is not considered by current European standard (EN) testing. Bowing has also been reported from gravestones made from granite (Winkler 1994).

Without any doubt the tests most often used are those that quantify the mechanical quality of dimensional stones. In most stone certifications a value of the Young's modulus or of the strength is given without any further qualification. This is highly questionable, since commonly, most of the rocks are anisotropic when considering physical properties (Siegesmund 1996). The assumption of isotropy is only valid for rocks with a random distribution of minerals, microcracks, pores etc. An anisotropic fabric can be caused by the crystallographic preferred orientation (here referred to as texture) of rock-forming minerals together with their shape-controlled anisotropy and the preferred orientation of microcracks. In consequence, an anisotropic rock fabric can produce a pronounced dependence of technical and physical properties. This is very important, since building stones may often be cut in different directions to enhance decorative effects. Furthermore, such directions do not coincide with the determined highest strength values. The importance of direction-dependent strength values is valid, for example, for overhead floors, brackets, architraves, balconies and staircases.

To demonstrate the effect of anisotropic rock fabrics on the physical properties we selected a sequence of mylonitic rocks, i.e. a metagranitoid that was transformed by ductile deformation to an ultramylonite (three samples: Iv1, Iv1b, Iv2). A progressive mylonitization is usually characterized by a process of grain size reduction compared to the protolith resulting from crystal plastic processes. These processes produce another characteristic feature of a deformed rock, a crystallographic preferred orientation.

From: SIEGESMUND, S., WEISS, T. & VOLLBRECHT, A. 2002. *Natural Stone, Weathering Phenomena, Conservation Strategies and Case Studies*. Geological Society, London, Special Publications, **205**, 115–135.
0305-8719/02/$15.00 © The Geological Society of London 2002.

In these rocks different physical properties like compressive strength, tensile strength, elastic wave velocities, the magnetic susceptibility and the abrasion strength were measured. The anisotropic physical properties are discussed in terms of the rock fabrics and the mineralogical composition.

Experimental

Mineralogical and fabric investigations

The mineralogical composition was determined by electron microprobe (Jeol JXA 8900) element mapping and phase analysis of three mutually perpendicular thin sections. Pore radii distributions were measured by mercury porosimetry. The texture of muscovite was determined by universal stage measurements in three mutually perpendicular thin sections. The microcrack distribution was assessed qualitatively with the universal stage. Neutron diffraction measurements (Leiss & Ullemeyer 1999) were performed in Dubna, Russia, on cylindrical samples with a diameter and a length of 40 mm to examine the texture of quartz and albite. Additional information concerning the texture of phyllosilicates was done by measuring the anisotropy of the magnetic susceptibility (AMS) using a KLY-2 Kappabridge and computed using the ANISO 11 program developed by Jelinek (1977).

Rock mechanical tests

All mechanical testing was performed in three mutually perpendicular directions by using a class I universal testing machine manufactured by Walter & Bay (Switzerland). For the tensile/compression and abrasive test (Boehme method) the samples were cored parallel to the x-, y-, z-axis of the reference system (Fig. 1) and sawn perpendicular to the x-, y-, z-axis of the reference system (Boehme method), respectively. The tensile strength was determined indirectly by using the Brazilian test following the recommendations of DIN 22024; however, the loading rate was 30 N s^{-1}. The sample sizes were 40 mm in diameter with a length of 20 mm. To determine the compressive strength the uniaxial compression test (UCS) after DIN EN 1926 was used. The samples were 50 mm in diameter and length. The increase in load was 1000 N s^{-1}. The abrasive strength was assessed by using the Boehme test as described in DIN 52108. References are also given in DIN EN 1341/1342/1343. To minimize the experimental error, five to 18 specimens (Brazilian and UCS) and two to three specimens (Boehme method) were measured in each direction, respectively.

Ultrasonic wave velocities

To estimate the three-dimensional distribution of open microcracks compressional wave velocities (*Vp*) of water-saturated and dry spheres (50 mm in diameter) were measured in 192 directions. All data were plotted in pole figures using the Schmidt net lower hemisphere (Fig. 1). To display the crack-induced rock anisotropy difference diagrams were calculated (*Vp* water-saturated minus *Vp* dry). The resonant frequency of the transmitter was 1 MHz. The spatial dependence of P-wave velocities studied

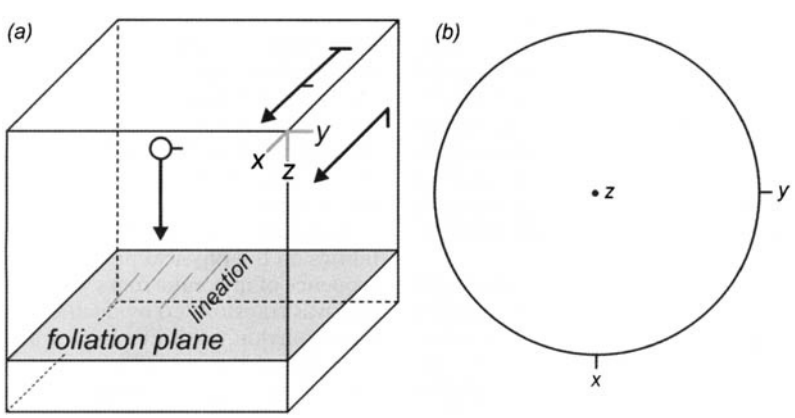

Fig. 1. (**a**) Marking system/reference system (arrows) used for delineation of the macroscopic visible foliation and lineation. (**b**) Depiction of pole figures and *Vp* pattern diagrams; Schmidt-net lower hemisphere; projection plane equal to foliation plane; z-axis vertical in the middle of the diagram.

on spherical samples allows the determination of velocities in a general triclinic body. If the spheres are investigated under dry and water-saturated conditions, material behaviour is highly influenced by pore fluid which can be used to diagnose the microcrack fabrics. The difference between the water-saturated and dry (air-filled) conditions is a powerful tool to quantify the open cracks via the *Vp* data. The effect of open cracks is reduced but not completely suppressed, because *Vp* compressibility of air is higher than that of water. The calculated ΔVp ($Vp_{saturated} - Vp_{dry}$) gives an idea about the crack-induced anisotropy (Schild *et al.* 2001). This method is comparable to the measurement of dry samples under various confining pressures as performed by Meglis *et al.* (1996), Duerrast *et al.* (1999) and Rasolofosoan *et al.* (2000). The *Vp* pattern of the water-saturated sample mainly shows the intrinsic anisotropy characterized by the preferred orientation of the rock-forming minerals, their single crystal anisotropy and their volume content (Siegesmund *et al.* 1993; Siegesmund 1996) and is dominated by highly anisotropic phyllosilicates. The trapped pore space cannot be water-saturated and contributes to the *Vp* anisotropy of the water-saturated specimen. Another factor is healed cracks which may form zones of anisotropy, but they do not affect the ultrasonic wave velocities. Hence, they may change due to an increasing degree of mylonitization without causing any changes concerning the ΔVp pattern.

In addition, ultrasonic wave velocity measurements were performed on cylindrical samples cored in three mutually perpendicular directions. Various confining pressures were applied from 2 to 400 MPa. The dimension of the samples was 30 mm in diameter and 35 mm in length. The running time of two mutually perpendicular shear waves and one compressional wave (resonant frequency 1 MHz) was simultaneously determined.

Rock samples and their fabrics

To investigate the fabric development of mylonites and its control on the mechanical and physical properties, a shear zone from the Sesia-Lanzo Zone (Italy) was chosen. Three samples were collected that are characterized by different degrees of mylonitization. The material was taken from the boundary and towards the centre of the shear zone. All samples show the same state of weathering. The more or less undeformed protolith (Iv1) is a metagranitoid overprinted under retrograde greenschist facies conditions. Iv1b and Iv2 are a mylonite and an ultramylonite, respectively. The mineralogical and chemical composition of all samples is nearly identical. Main constituents are plagioclase (albite), quartz and muscovite; garnet, K-feldspar, chlorite, clinozoisite/epidote are associated minerals and apatite and zircon occur as asseccories (Table 1). Macroscopically green coloured microcrystalline aggegates consist of chlorite, albite, garnet and sericite. Techmer (1996) considered these to be alterations originating from K-feldspar grains. The slight changes in the mineralogical composition within the shear zone are due to fluid–rock interactions. They are characterized by newly formed clinozoisite/epidote, muscovite and chlorite (Techmer 1996), while the clinozoisite/epidote content slightly increases towards the shear zone centre. Therefore, the subsidary changes in mineralogical composition should have no significant influence on the mechanical and physical rock properties.

The protolith (Iv1) exhibits an L-fabric. The elongated quartz crystals as well as the microcrystalline polyphase aggregates define a distinct lineation while a weakly developed macroscopic foliation can be deduced from slightly flattened quartz crystals. The mylonite (Iv1b) and the ultramylonite (Iv2) show all signs of an LS-fabric. The progressive and more narrow spaced foliation with increasing mylonitization is defined by the preferred orientation of minerals and grain boundaries as well as a distinct layering of quartz-, albite- and chlorite-clinozoisite/epidote-rich layers (Fig. 2).

The fabric development is accompanied by a distinct reduction in grain size. In Iv1 quartz as well as K-feldspar appears as large crystals with an average grain size of 1 to 3 mm. Recrystallized grains, subgrains and migrated grain boundaries are typical deformation features in quartz while K-feldspar usually shows brittle deformation. The green aggregates have a

Table 1. *Mineralogical composition Iv1, Iv1b, Iv2*

Mineral	Vol %*	Vol %†
plagioclase	27	29
quartz	35	26
muscovite	15	17
garnet	4	5
K-feldspar	5	5
chlorite	6	6
clinozoisite	6	10
minor comp.	2	2

* By electron microprobe element mapping and phase analysis

† Average from Techmer (1996)

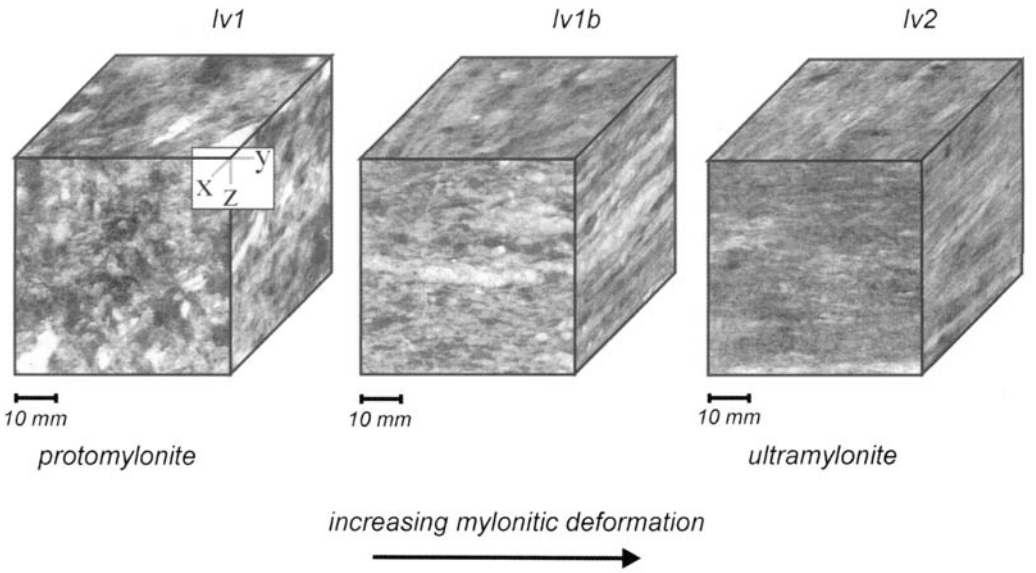

Fig. 2. Foliation development due to mylonitization. Scanned cubes. Dark layers are chlorite and clinozoisite/epidote enriched; bright layers are quartz and albite enriched.

diameter of 3–4 mm. Albite, chlorite and sericite as a part of these aggregates are fine-grained (about 1–2 μm). Within the rest of the material they show a grain size of 100–150 μm. As a result of the progressive mylonitic deformation Iv2 is dominated by an equigranular fabric with an intermediate grain size of 150–300 μm (Fig. 3). The occurrence of large quartz and feldspar grains decreases from Iv1 to Iv2. The microcrystalline aggregates suffer a strong flattening and are concentrated in distinct layers. The density of all the samples is 2.74 g cm^{-3} and the results of mercury porosimetry reveal a maximum of pore radii between 0.01 and 0.1 μm (Fig. 4).

Texture

From other research studies it is well known that the texture of the rock-forming minerals is a very important factor for physical and mechanical properties of the whole rock. The texture of muscovite as well as of quartz and albite were determined. The samples exhibit a pronounced quartz texture pattern; however, the intensity of the texture is low. Therefore the effect on the mechanical properties should be of minor importance. Albite has a weak texture (Fig. 5), and will therefore not be discussed in detail, whereas muscovite shows a pronounced texture. This associated with the high anisotropic properties and the mechanical weakness of the muscovite 001 plane leads to the assumption that muscovite controls the mechanical and physical properties (e.g. Shea & Kronenberg 1993; Siegesmund *et al.* 1995; Siegesmund 1996). The muscovite preferred orientation becomes stronger in the sample set with progressive mylonitization. Sample Iv1 reveals an approximately complete girdle distribution about the stretching lineation (x) with a maximum of (001) poles 30° inclined to the z-axis. Weakly developed girdles with a strong point maximum close to the foliation pole are evident in samples Iv1b and Iv2. The fabric symmetry becomes more oblate without reaching a perfect transversal isotropic pattern (Fig. 6a–c).

A well-established and frequently used method for the quantification of fabrics in a deformed rock is the determination of the anisotropy of the magnetic susceptibility (e.g. Hrouda 1982; Borradaile 1988; Siegesmund *et al.* 1995). In gneissic rocks, paramagnetic phyllosilicates with lattice-dependent magnetic properties are assumed to control the whole rock AMS which was quantitatively shown by Siegesmund *et al.* (1995). The only paramagnetic and anisotropic minerals in the Sesia-Lanzo mylonites are muscovite, chlorite and clinozoisite/epidote. The latter has only a weak anisotropy with respect to the magnetic properties, and may not have a great impact on the

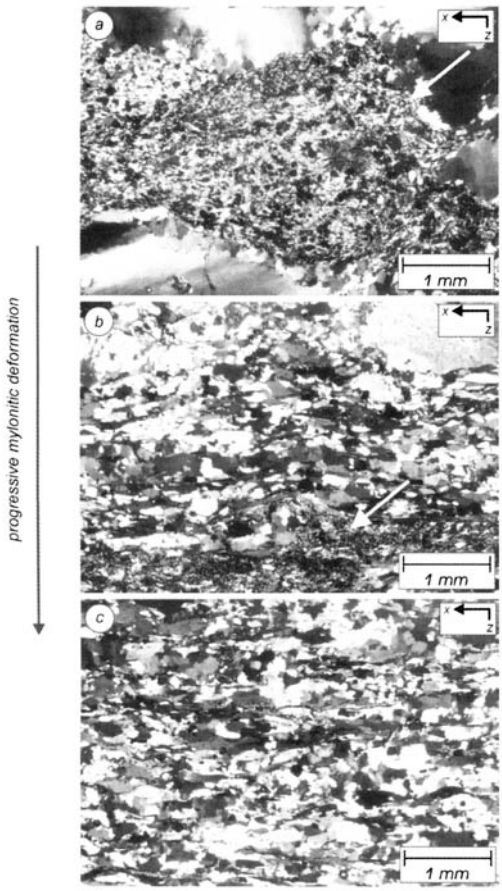

Fig. 3. Fabric development. Optical micrographs; crossed polarizers. Microcrystalline aggregates (see text) are marked by white arrows. (**a**) xz-plane of sample Iv1. (**b**) xz-plane of sample Iv1b. (**c**) xz-plane of Iv2.

Table 2. *Anisotropy of magnetic susceptibility data*

Sample	L	F	T	P	P'
Iv1	1.017	1.004	−0.635	1.021	1.023
Iv1b	1.027	1.050	0.335	1.079	1.080
Iv2	1.015	1.037	0.667	1.052	1.054

L, lineation factor after Balsey and Buddington (1960); F, foliation factor after Stacey *et al.* (1961); T, shape factor after Jelinek (1981); P, factor of anisotropy after Nagata (1961); P', factor of anisotropy after Jelinek (1981)

bulk rock magnetic susceptibility. Muscovite and chlorite, which are highly anisotropic, may influence the magnetic properties in the same way because of their similar magnetic behaviour (Borradaile 1987).

K_{max} of the AMS ellipsiod is aligned parallel to the stretching lineation (x), whereas K_{min} is subparallel to the maximum of muscovite (001) poles (for the AMS data see Table 2). K_{int} lies perpendicular to the lineation within the foliation. This holds true for all three samples (Fig. 6a–c) and mainly coincides with observations made by Juckenack (1990) and Siegesmund *et al.* (1995). The length of the half axes of the AMS ellipsoid increases from Iv1 to Iv2. The shape factor T (Jelinek 1981) covers the range from −0.635 corresponding to a more prolate AMS ellipsoid to a highly oblate AMS ellipsoid with values of 0.667 (Fig. 7).

Microcracks

The samples Iv1b and Iv2 display an approximately orthogonal microcrack pattern which is nearly orientated perpendicular to the axis of the reference system and parallel to the xy-, yz- and xz-planes, respectively. The microcrack pattern of Iv1 is comparable to that of the other two samples, however Iv1 is rotated 30° around the x-axis (Fig. 8a). The main features of the whole microcrack families are intragranular

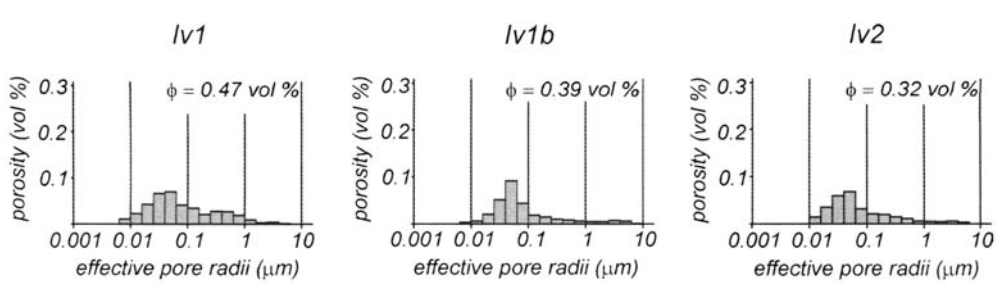

Fig. 4. Pore radii distribution. Φ is total porosity.

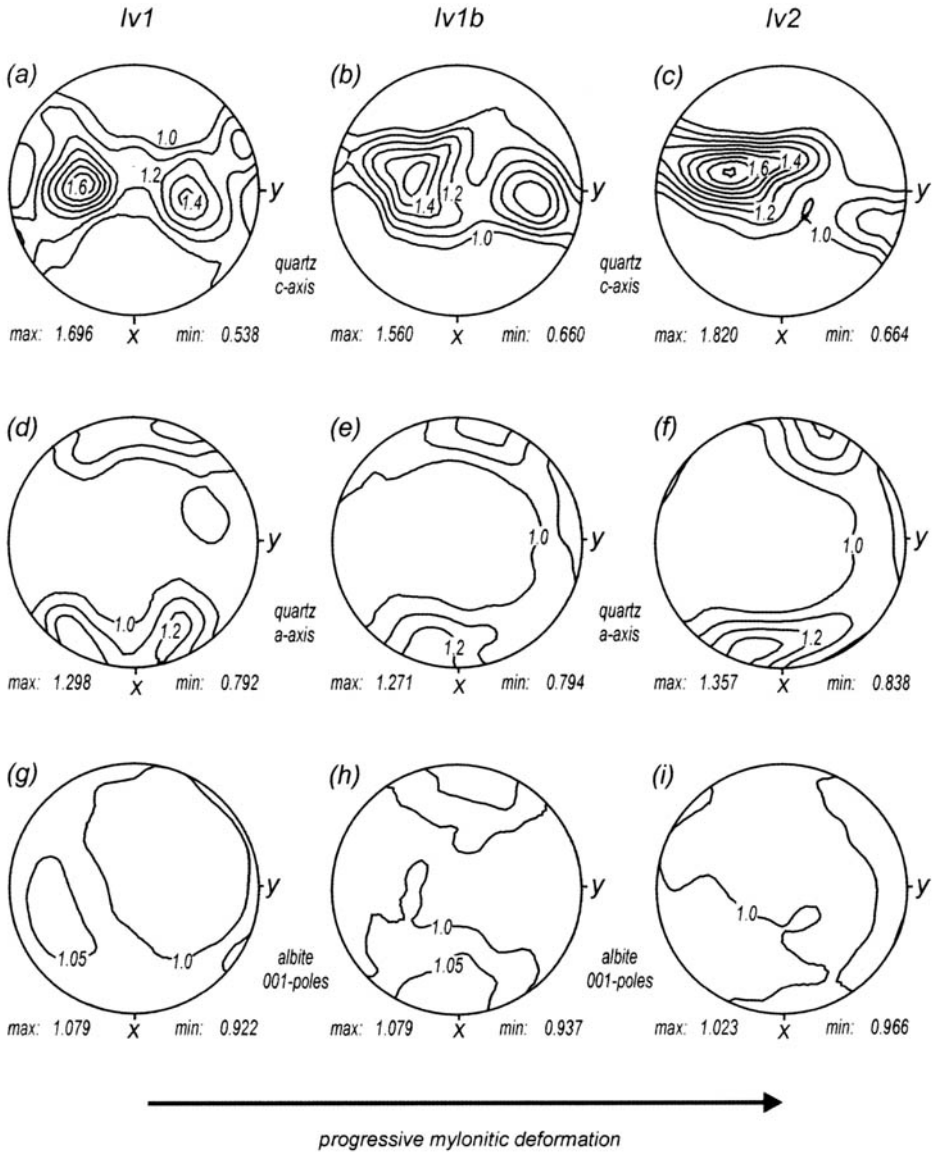

Fig. 5. Quartz and albite texture. Schmidt-net lower hemisphere; multiples of random distribution. (**a–c**) Distribution of quartz c-axis. (**d–f**) Distribution of quartz a-axis. (**g–i**) Distribution of albite (001) poles.

healed, open, mineralized and cleavage cracks (for nomenclature see Kranz 1983; Vollbrecht *et al.* 1994). The cleavage cracks frequently occur parallel to the (001) plane of muscovite and chlorite (Fig. 8b). Quartz accommodates a great amount of healed cracks decorated with secondary fluid inclusions, which occur most frequently parallel to the yz-plane (Fig. 8c). Open and mineralized cracks displaying a more irregular shape can also be observed in quartz but less often (Fig. 8d). K-feldspar, clinozoisite/epidote and garnet exhibit open and irregular-shaped microcracks (Fig. 8e). Progressive mylonitization causes changes in the microcrack system. The development of a stronger phyllosilicate texture leads to a more preferred orientation of (001) cleavage cracks from the protolith (Iv1) to the ultramylonite (Iv2). Dynamic recrystallization is another process that influences the microcracks in quartz and albite leading to a

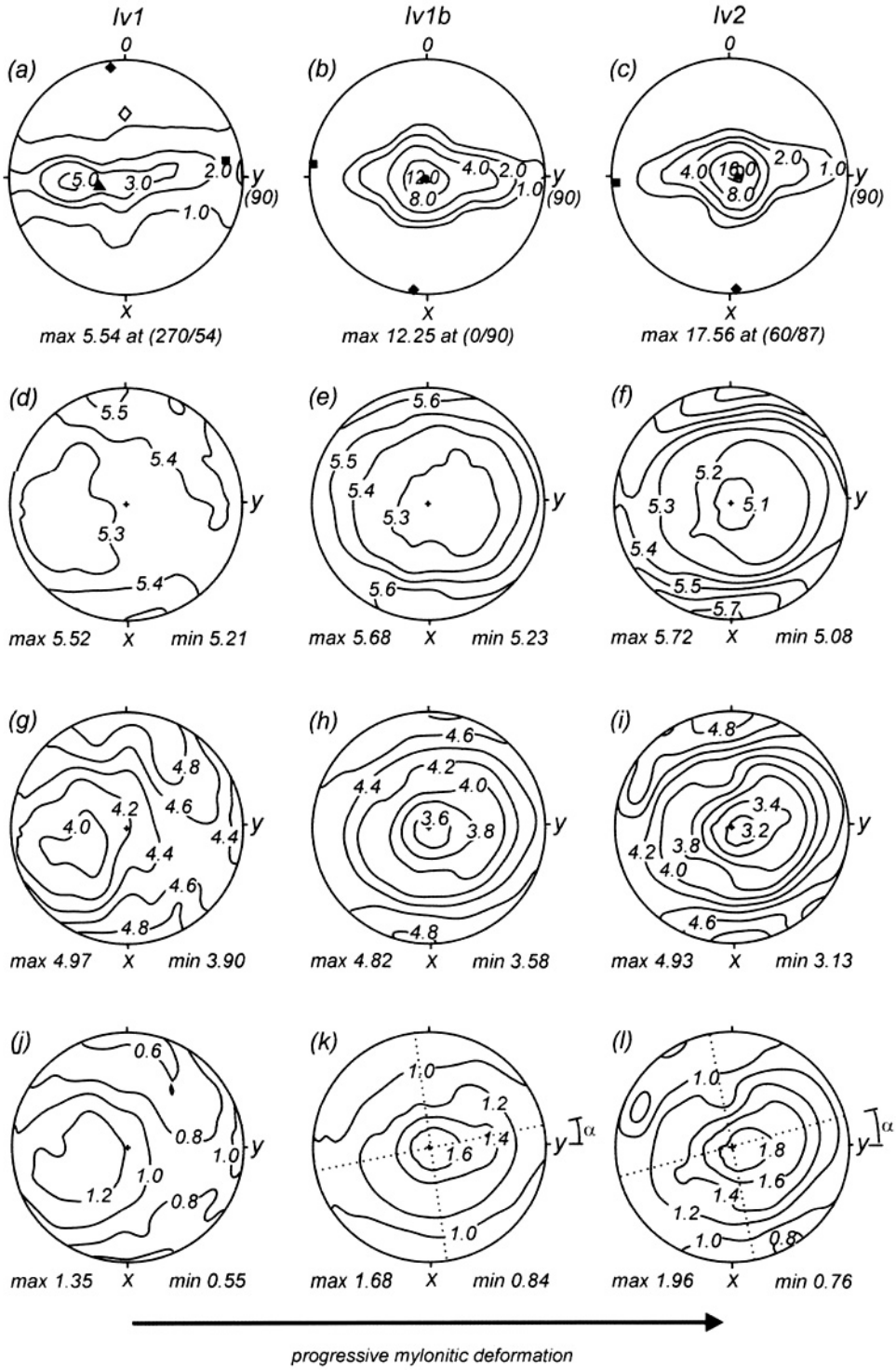

Fig. 6. Muscovite texture and compressional wave velocities. (**a–c**) Muscovite (001) poles in multiples of random distribution (220 grains per sample); main axis of AMS ellipsoid: K_{max} (rhombes); K_{int} (squares); K_{min} (triangles). (**d–f**) Vp (km s^{-1}) pattern of the water-saturated spherical specimens. (**g–i**) Vp (km s^{-1}) pattern of dry spherical samples. (**j–l**) Calculated ΔVp pattern (Vp of saturated sample minus Vp of dry sample); dotted lines show estimated maxima of planes of microcrack systems excluding the muscovite cleavage planes. Estimates of Vp experimental error are ± 50 m s^{-1}.

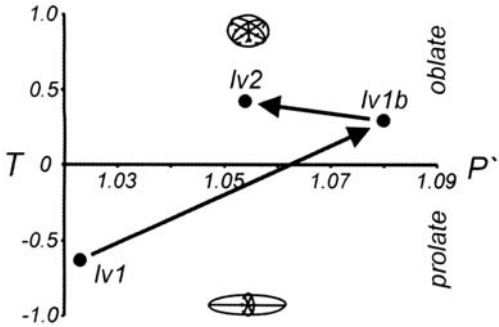

Fig. 7. P`–T diagram after Jelinek (1981).

reduction of pre-existing microcracks (Passchier & Trouw 1996). Furthermore the loss in grain size leads to shorter cracks (Iv1b, Iv2) in contrast to those described in Iv1. In summary, the mylonitic deformation accomplishes a concentration of (001) phyllosilicate cleavage cracks and a loss in healed and mineralized cracks in quartz and albite including smaller crack length. The cleavage cracks become more dominant from Iv1 to Iv2.

To quantify the different microcrack populations and their orientation the analyses of the compressional wave velocities can be applied (see Experimental section).

The maximum of open microcrack poles marked by the highest ΔVp in the diagram (Fig. 6j–l) coincides with the maximum of muscovite (001) poles. Hence, it can be concluded that muscovite cleavage cracks are the most dominant crack population. The contribution of other cracks to the ΔVp pattern is more complicated. The coincidence of the orthogonal microcrack pattern (see Fig. 8a) with the orthogonal Vp pattern (Fig. 6k–l) is probably a first indication. This cannot be explained by the muscovite texture alone (see Fig. 6a–c). The significantly higher Vp of the cylindrical specimen under a confining pressure of 400 MPa in comparison to the Vp of the water-saturated samples obtained along the same directions (Table 3) clearly documented that the crack porosity and the trapped pore space have their influence on the Vp pattern, respectively. The distribution of healed cracks within the sample set are interpreted as potential planes of mechanical weakness. However, they cannot be estimated by this approach.

Mechanical properties

Tensile strength

The tensile strength covers the range of 7.7 to 19.3 MPa (Table 4) for all investigated samples and directions (x-, y- and z-direction means direction of tensile forces is parallel to the x-, y- and z-axis of the reference system; see Fig. 1). In all samples the z-direction reveals the lowest and the x-direction the highest strength values, whereas the y-direction is intermediate (Fig. 9). With the mylonitization the anisotropy ([strength max. minus strength min.]/strength max.) of the tensile strength increases from 26% (Iv1) to 48% (Iv1b) and finally to 60% (Iv2). The x-direction becomes higher in strength, whereas the z-direction becomes less pronounced. The y-direction is more or less constant. During the indirect tensile strength

Table 3. *Ultrasonic wave velocities*

Sample*	Vp, 2 MPa† (km s^{-1})	Vp, 400 MPa† (km s^{-1})	Vp saturated‡ (km s^{-1})	Vp 400 MPa – Vp saturated (km s^{-1})
Iv1x	4.87	6.42	5.49	0.93
Iv1y	4.14	6.31	5.39	0.92
Iv1z	4.42	6.24	5.35	0.89
Iv1bx	5.11	6.67	5.66	1.01
Iv1by	4.65	6.30	5.53	0.77
Iv1bz	3.63	6.11	5.25	0.86
Iv2x	5.26	6.69	5.72	0.97
Iv2y	4.40	6.33	5.39	0.94
Iv2z	3.31	6.05	5.10	0.95

* x, y, z indicate velocities parallel to x, y or z axis
† Derived from measurements of dry cylindrical samples under a confining pressure
‡ Derived from measurements of water-saturated spherical samples

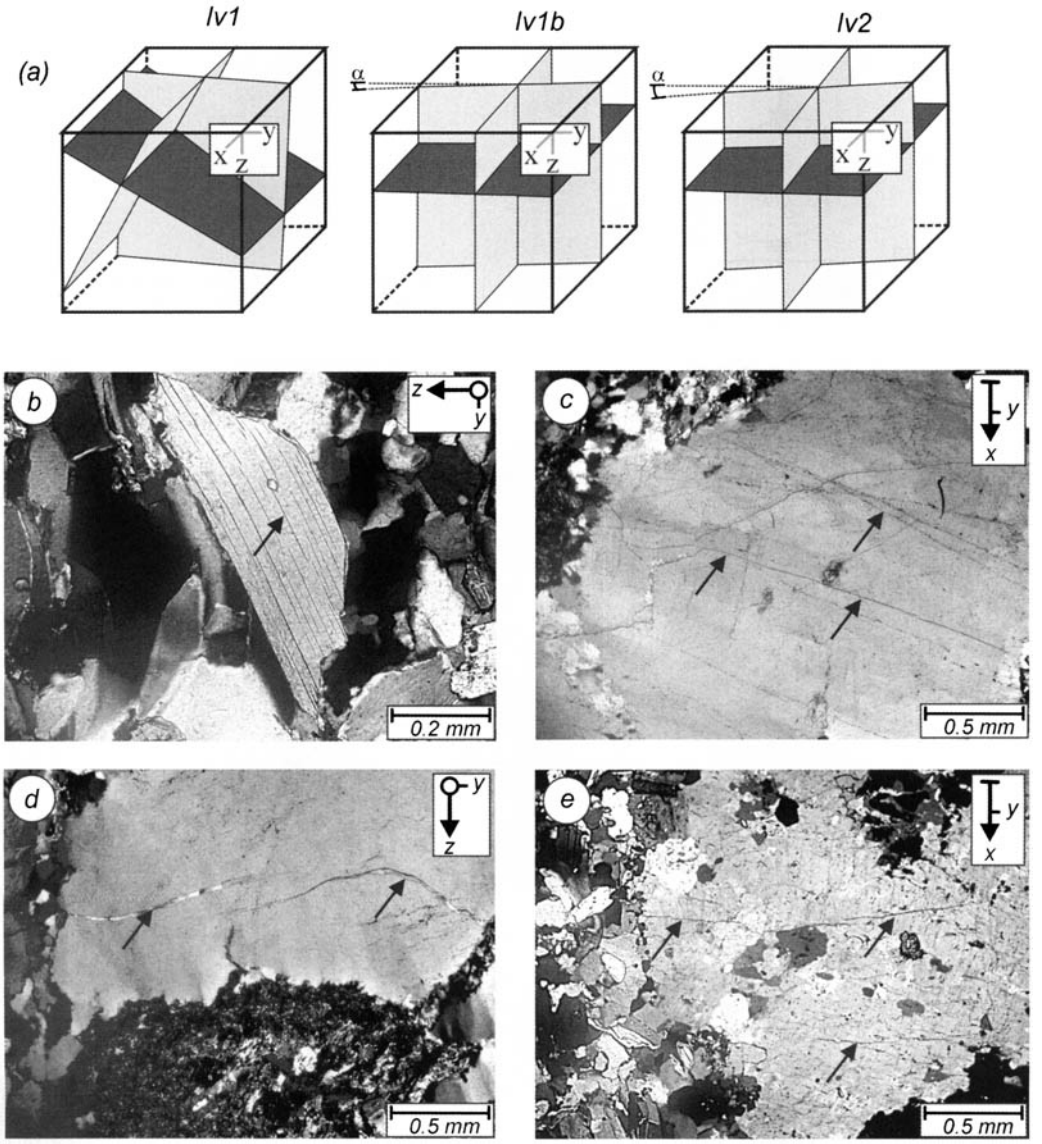

Fig. 8. Pre-existing microcracks. Optical micrographs; crossed polarizers (**a**) Orientation of microcrack systems in Iv1, Iv1b and Iv2; dark grey planes mark the preferred orientation of muscovite (001) cleavage planes. (**b**) Open cleavage cracks in muscovite; example marked by arrow (sample Iv1b). (**c**) Healed microcracks decorated with secondary fluid inclusions; examples marked by arrows (sample Iv1). (**d**) Mineralized microcracks in quartz marked by arrows (sample Iv1). (**e**) Open microcracks in K-feldspar; examples marked by arrows (sample Iv1b).

test (Brazilian test), the specimens fail if the stress exceeds the cohesion of the starting material (Nagaraj 1993). To investigate the fracture plane in more detail the scanning electron microscope was applied. In most cases the muscovite cleavage planes are the planes of weakness and often get activated during failure (Fig. 10a). In particular, the z-direction seems to be weak because of the strong muscovite texture causing a preferred orientation of (001) planes parallel to the xy-plane. Albite and K-feldspar also fail along their cleavage planes (Fig. 10b). Moreover, microcrack formations along interconnected microcrack networks can

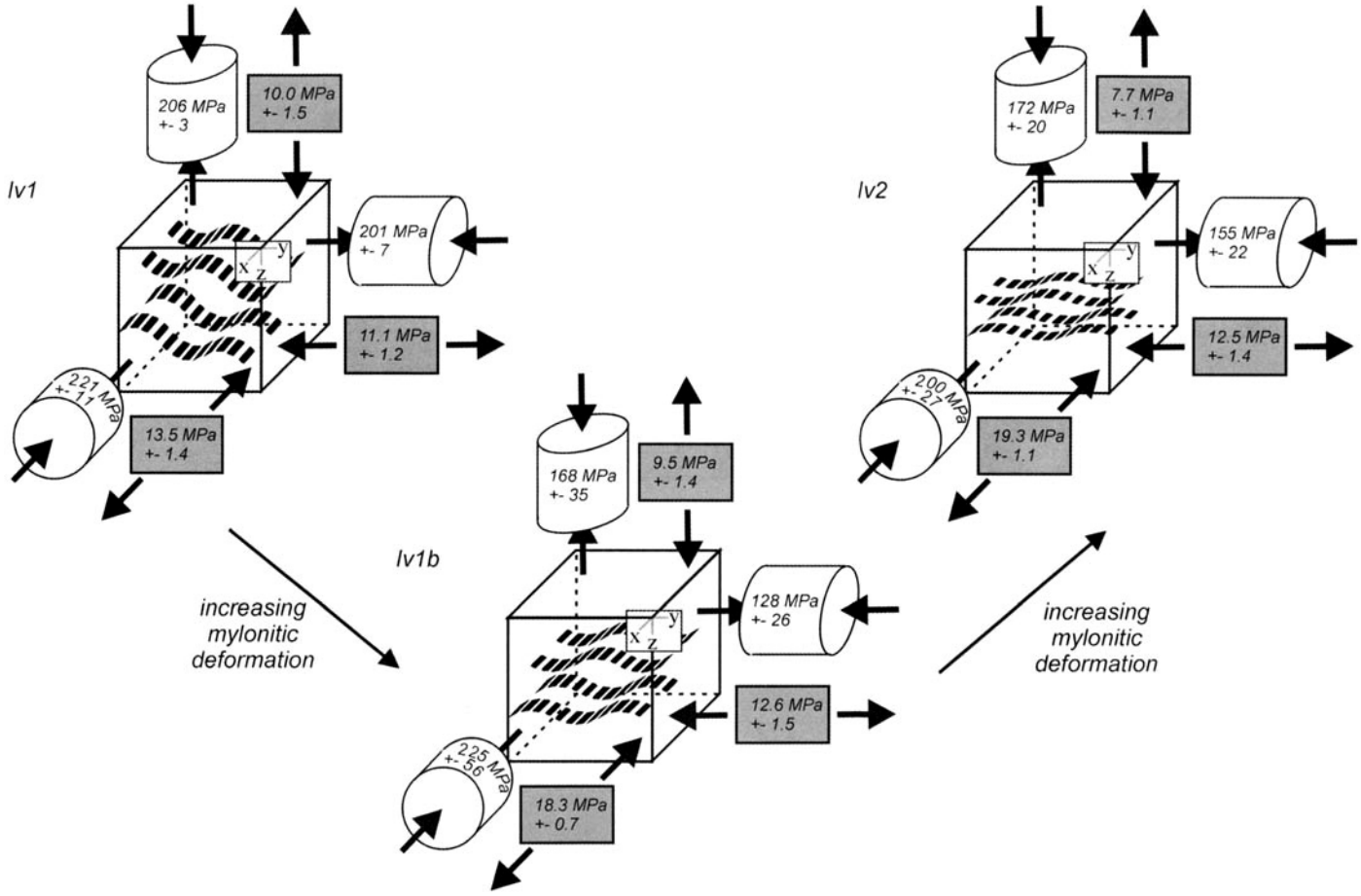

Fig. 9. Compressive and tensile strength. Tensile strength values and twice standard deviation within grey rectangles; compressive strength and twice standard deviation within cylinders; direction of compressive and tensile forces marked by arrows; schematic prefered orientation of muscovite marked by black bars inside the cubes.

Table 4. *Mechanical properties*

Sample*	Tensile strength† (MPa)	Number of measured samples	Compressive strength‡ (MPa)	Number of measured samples	Abrasive strength§ (cm^3)	Number of measured samples
Iv1x	13.5 (1.4)	6	221 (11)	5	7.36 (0.33)	2
Iv1y	11.1 (1.2)	5	201 (7)	5	7.58 (0.17)	2
Iv1z	10.0 (1.5)	8	206 (3)	5	8.58 (0.20)	3
Iv1bx	18.3 (0.7)	5	225 (56)	9	6.81 (0.21)	2
Iv1by	12.6 (1.5)	9	128 (26)	5	7.93 (0.30)	2
Iv1bz	9.5 (1.5)	18	168 (35)	5	8.87 (0.27)	2
Iv2x	19.3 (1.1)	6	200 (27)	7	6.40 (0.14)	3
Iv2y	12.5 (1.4)	17	155 (22)	5	7.91 (0.23)	3
Iv2z	7.7 (1.1)	14	172 (20)	8	9.14 (0.22)	2

* x, y, z indicate strength parallel to x, y, z axis or plane perpendicular to x, y, z axis (Boehme method)
† Determined by Brazilian test following the recommendations of DIN 22024; numbers in brackets are twice standard deviation
‡ Determined by uniaxial compression test following the recommendations of DIN EN 1926; numbers in brackets are twice standard deviation
§ Determined by Boehme test following the recommendations of DIN 52108; numbers in brackets are twice standard deviation

be clearly documented in Figure 10c,d. Grain boundaries are also zones of weakness (Fig. 10e). Less than 10% in total of the fracture surface is estimated as grain boundaries. The fracture zones are related to newly formed open and reactivated pre-existing, mineralized and healed cracks. The nucleation and propagation of mode-I (tensile) transgranular cracks favourably follow the cleavage planes of the rock-forming minerals.

Uniaxial compressive strength

The uniaxial compressive strength (UCS) ranges between 225 MPa and 128 MPa (Table 4) (x-, y- and z-direction means direction of load is parallel to x-, y- and z-axis of the reference system; see Fig. 1). Due to the progressive mylonitization among the sample set, the UCS values exhibit no distinct development (Fig. 9). Sample Iv1 is approximately isotropic (concerning the determined directions) whereas Iv1b is the most anisotropic one (43%). The x-direction in the case of Iv1b and Iv2 exhibits the highest (225 MPa and 200 MPa, respectively), whereas the y-direction shows the lowest UCS values (128 MPa and 155 MPa, respectively). The results of optical investigations reveal that in uniaxial compression tests, the cleavage planes of the rock-forming minerals and pre-existing microcracks were activated by propagation of mode-I (tensile) and mode-II (shear) crack pairs. The influence of open grain boundaries is of minor importance. The failure pattern varies significantly with regards to the progressive mylonitization. Most conspicuous is the x-direction. Iv1 samples exhibit a cone-shaped fracture plane, whereas Iv1b shows a roof-shaped appearance. The fracture pattern of Iv2 tends to be a roof-shaped form, but is not as distinct as in Iv1b and comprises kinking of the foliation (quartz-albite-enriched and chlorite-clinozoisite/epidote-enriched layers) and macroscopical splitting parallel to the foliation plane (Fig. 11a–d). The pattern of failure planes in the y- and z-direction are always roof-shaped but the geometrical form of the fracture planes becomes more distinct from Iv1 to Iv2. All fracture planes reveal a facet-like geometry and a certain bowed shape according to the shear stress distribution within the specimen (Fig. 12). Stress–strain diagrams are generated and displayed in Figure 13. The general behaviour of the samples is similar in all directions. Nevertheless, the data suggest that samples bearing high compressive strength values tend to show a steeper slope coinciding with a higher compression modulus (for example Iv1b, x-direction) and vice versa (for example Iv1b, y-direction).

Abrasive strength (Boehme method)

The Boehme values (known as abrasive strength) vary between 6.40 cm^3 and 9.14 cm^3 (Table 4). For the Boehme method the x-, y-, z-direction corresponds to the planes orientated perpendicular to the x, y, z-axis of the reference system (see Figs 1 and 14). Lower values are

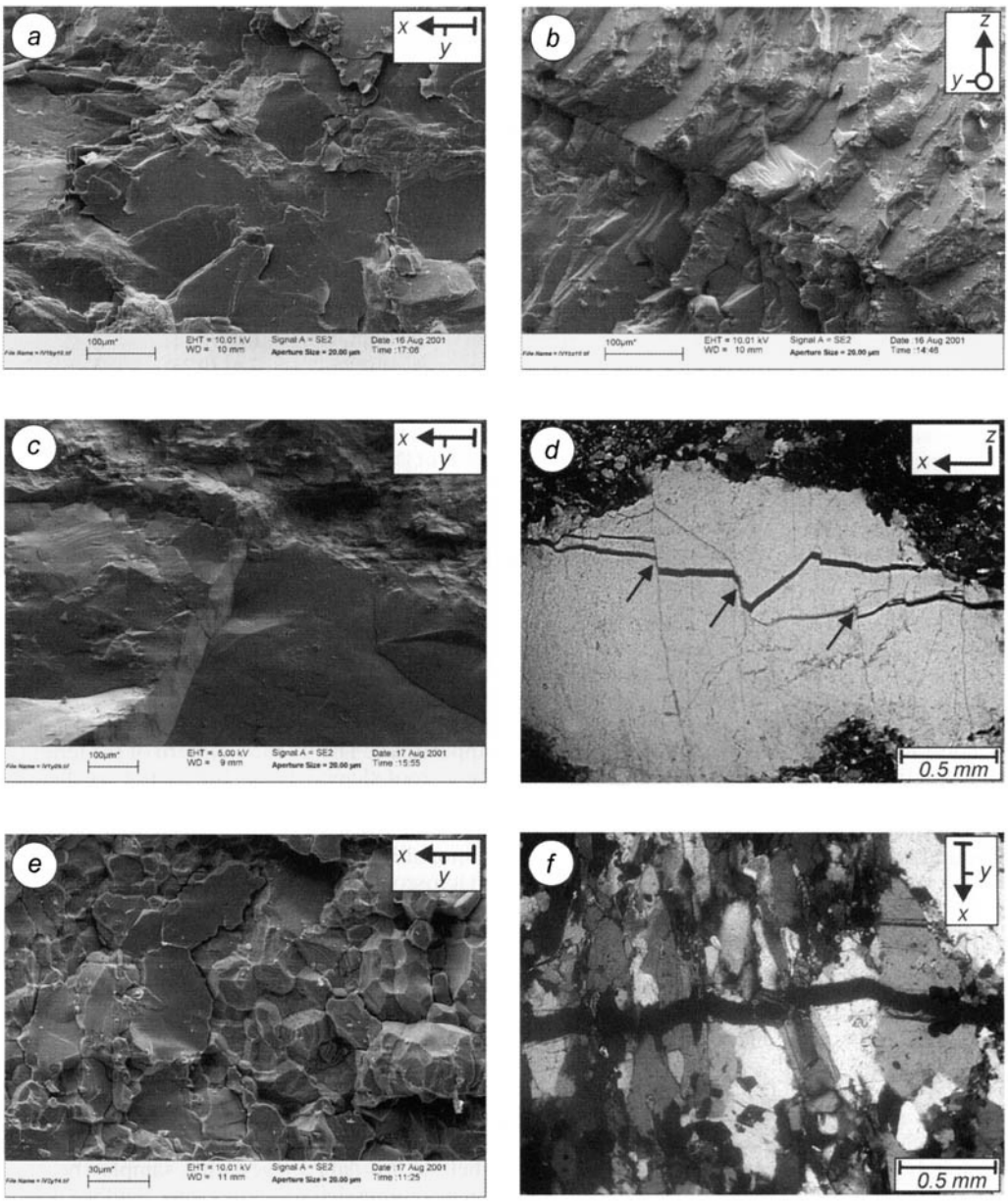

Fig. 10. Favourably activated planes in Brazilian test. Scanning electron micographs; secondary electrons (a–c, e) and optical micrographs; crossed polarizers (d, f). (**a**) Activated (001) plane in muscovite. (**b**) Fracture of K-feldspar (baveno-twin); (001) and (010) cleavage planes activated. (**c**) Activated healed microcrack in quartz. (**d**) Activated healed microcracks in quartz marked by arrows. (**e**) Fracture pattern in microcrystalline quartzitic area. (**f**) Fracture plane filled by resin in sample Iv1b.

attributed to high abrasive resistance and vice versa. The anisotropy of the individual samples increases from Iv1 (14%) to Iv2 (30%) (Fig. 14). The highest abrasive strength is observed for the x-direction while the z-direction is consistently lower. This holds true for all three samples. The increasing mylonitic deformation leads to a stronger x-direction and a weaker z-direction (Fig. 14). The y-direction is invariant. No indication of SiC (abrasive used in the

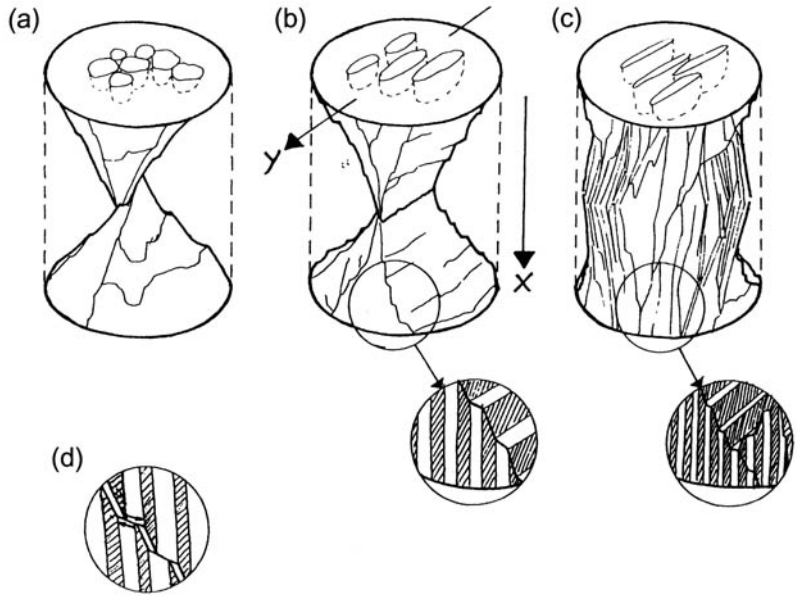

Fig. 11. Fracture pattern after uniaxial compression test. Samples cored and tested parallel to the x-direction. The x- and y-axes of the reference system are indicated in (b). (**a**) Iv1. (**b**) Iv1b. (**c**) Iv2. (**d**) Crack propagation during uniaxial compression test; arrows mark dislocation direction.

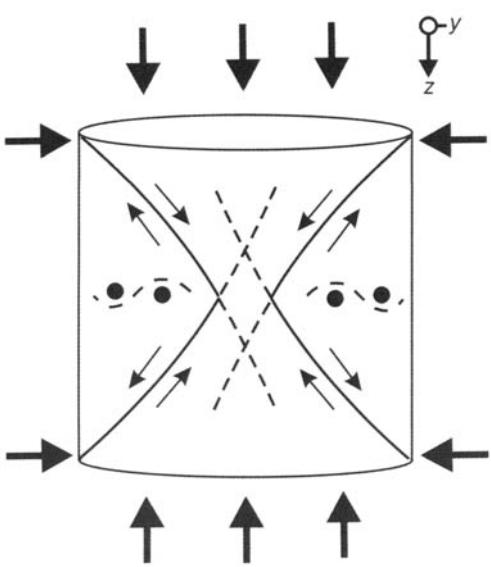

Fig. 12. Uniaxial compression test. Direction of sample load and forces at top and bottom of the sample (bold arrows); black lines mark planes of maximum shear stress; shear sense indicated by small arrows.

Boehme test) traces can be observed on the surfaces of the tested samples. The sample surfaces are rough and the abrasion seems to be controlled by mineral destruction processes. For the progressive abrasion muscovite basal planes (Fig. 15a,b), albite and K-feldspar cleavage planes as well as pre-existing microcracks were preferrentially activated (Fig. 15c,d). Therefore, abrasive strength does not only depend on the Mohr hardness of the rock-forming minerals, but on the abundance and interlocking of minerals and pre-existing microcracks and their preferred orientation. Activation of grain boundaries is of minor importance and is rarely observed in the tested samples.

Discussion

Until recently several attempts have been made to quantify the relation between rock fabric and mechanical properties. Howarth & Rowlands (1987) calculated a texture coefficient (TC) considering a wealth of fabric parameters like grain size, grain shape, packing density, porosity and degree of interlocking. However, the results suggest that the TC is only sufficient as a pre-predictive tool and does not provide precise results (Ersoy & Waller 1995; Azzoni *et al.* 1996). For example, in metamorphic rocks the predicted mechanical properties constrained by the TC do not show a good agreement with the experimental data (Brosch *et al.* 2000).

This study has focused on the fabric development in a progressively mylonitized sample set

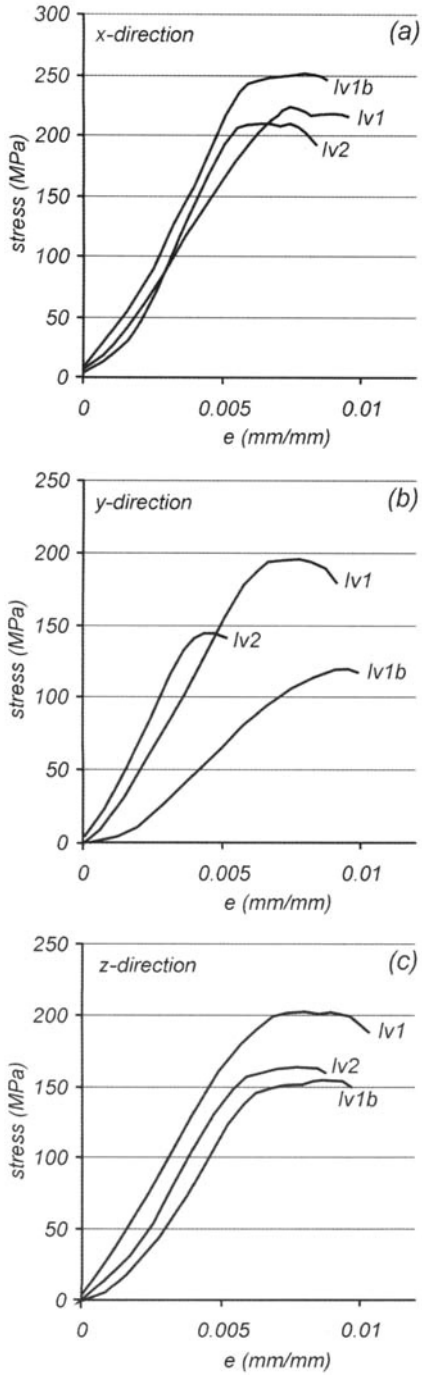

Fig. 13. Stress–strain curves derived by uniaxial compression test.

and its control of the physical and mechanical rock properties. The solid state behaviour of well-foliated rocks depends on the rheology and the volume content of the weakest mineral, forming continuous layers in favourable orientation (Jordan 1988; Handy 1990; Shea & Kronenberg 1992, 1993).

The phyllosilicates show a perfect cleavage parallel to their (001) plane and often exhibit a strong preferred orientation in metamorphic rocks. They are the weakest component in the rock with respect to their strength (as observed by Muegge 1898). They are assumed to control the rock strength (Gottschalk *et al.* 1990; Shea & Kronenberg 1993). Biotite and muscovite exhibit relatively low activation energies for dislocation of 82 kJ mol^{-1} (Kronenberg *et al.* 1990) and 47 kJ mol^{-1} (Mares & Kronenberg 1993), respectively, in comparison to stronger silicates like plagioclase with 237 kJ mol^{-1} (Shelton 1981; Tullis *et al.* 1991). The strong textures observed in phyllosilicates like muscovite and chlorite are accompanied by a high anisotropic mechanical behaviour (Kronenberg *et al.* 1990) which probably is responsible for the anisotropic mechanical rock properties.

Concerning the compressive strength the proportional number of mica grains aligned for sliding (parallel to (001) plane) and kinking has a great impact on the rock strength. High contents lead to relatively lower compressive strength values, but the volume content and the mica subfabric are important factors too. If the micas build interlayers a great amount of stress that occurs will get resolved on the (001) planes by sliding. This, coinciding with volume contents higher than 30%, leads to a ductile response (easy glide; Christoffersen & Kronenberg 1993). A more randomly preferred orientation and a dispersed arrangement of mica within a framework of other rock constituents like feldspar and quartz cause a more brittle response due to compressive forces. This includes crack nucleation and crack propagation of mode-I flaws within the brittle silicate framework due to mode-II crack (frictional sliding parallel to mica (001) planes) interaction (Segall & Pollard 1980; Gottschalk *et al.* 1990; Shea & Kronenberg 1993).

Considering the tensile strength, the volume percentage of phyllosilicates (001) planes orientated with angles near 90° to tensile forces is of great importance (Peck *et al.* 1985). High mica contents cause relatively lower resistance of rock to tensile fracture. However, other factors may contribute to rock strength. For example pre-existing sets of microcracks and the

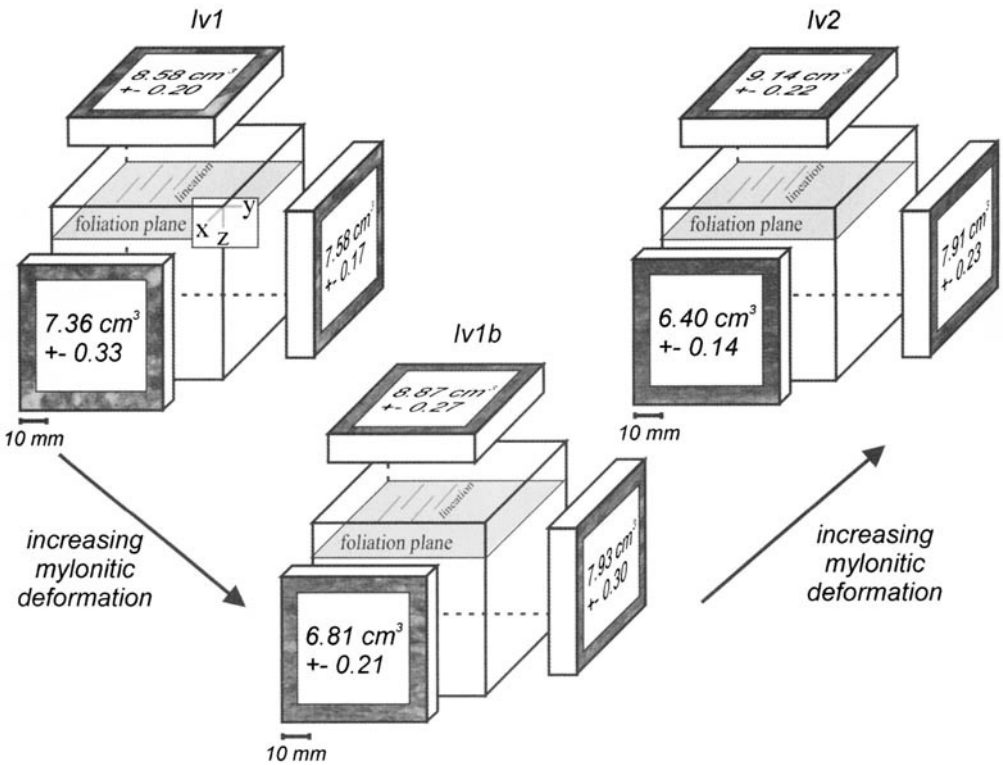

Fig. 14. Abrasive strength; given volumes indicate material loss.

feldspars with their perfect cleavage parallel to the (001) plane are assumed to influence the tensile and compressive strength values (Peck *et al.* 1985; Gottschalk *et al.* 1990; Li *et al.* 1998). Pre-existing microcracks in many cases follow crystallographic planes (Vollbrecht *et al.* 1999). Hence, microcracks in phyllosilicates tend to occur parallel to the (001) plane and intensify the effect of phyllosilicate texture.

Phyllosilicates dominate the physical and mechanical properties of a rock. Therefore, the strength data will be compared to the muscovite distribution pattern and the resulting symmetry of the AMS tensor. If indeed the tensile strength and abrasive strength of the examined rocks mainly depend on the muscovite texture, their development from a prolate (Iv1) to a more oblate fabric (Iv1b and Iv2) should cause similar symmetries of the mechanical properties. Due to the muscovite preferred orientation the x- and y-directions should become more alike and the z-direction should develop weaker abrasive and tensile strength values. The latter is observable among the sample set, whereas the x-direction shows increasing strength values due to the progressive mylonitization and the y-direction is approximately constant (Fig. 16a,b). Hence, the symmetry of strength values does not become oblate. This cannot be explained by the mica lattice preferred orientation alone. Therefore, other fabric elements should be responsible for the observed strength variations parallel to the x-direction. Pre-existing healed microcracks accommodated in the large quartz crystals of Iv1 were reduced due to dynamic recrystallization processes, and therefore are less frequent in Iv1b and Iv2. This may cause the relatively higher strength values in the x-direction and in the plane perpendicular to the x-direction (Boehme method), respectively. A decrease in the proportional number of microcracks perpendicular to the x-direction should cause a relatively lower ΔVp parallel to the x-direction (Fig. 6). This is not observable among the sample set, since ΔVp values are approximately constant parallel to the x-direction (Fig. 16c). However, reactivated healed microcracks may be responsible for the change of strength parameters. As shown in Figure 10c,d, these certain microcracks often become activated during the Brazilian test and

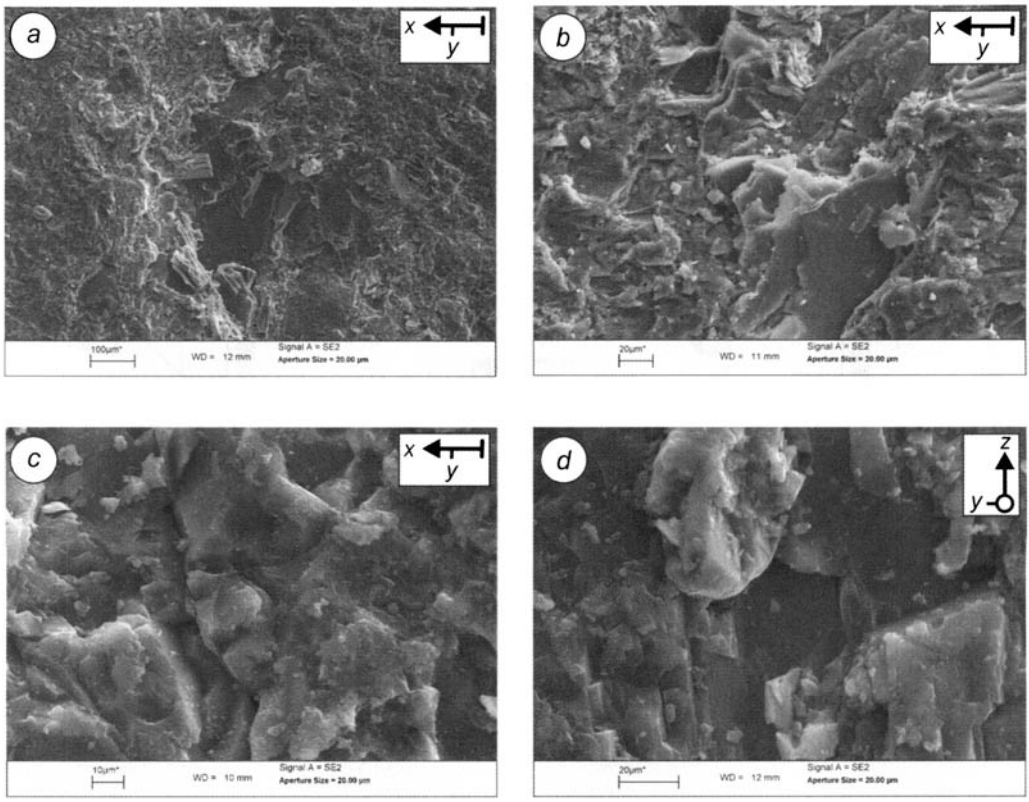

Fig. 15. Activated planes in Boehme test (abrasive test). Scanning electron micrographs; secondary electrons. (**a**, **b**) Activated (001) planes of muscovite. (**c**) Quartzitic area after the Boehme test. (**d**) Activated (001) and (010) planes in K-feldspar.

cause no significant changes in ΔVp pattern (see Experimental section).

Muscovite texture may to a great extent influence the tensile and abrasive strength values. This may be provided by a good direct correlation between the Vp_{sat} representing the intrinsic Vp and the strength values (Fig. 17a,b). However, a complete model predicting the rock strength and symmetry development due to fabric changes has to consider the distribution of microcracks and other parameters like grain size and development of any planar fabric, respectively.

The uniaxial compressive strength is an important and frequently used parameter to characterize the rock strength and has been investigated by several researchers. A few of these studies were performed to explain the rheology of the upper crust (e.g. Gottschalk *et al.* 1990; Shea & Kronenberg 1992, 1993) and others focused on geotechnical questions (e.g. Dearman *et al.* 1978; Koroneos *et al.* 1980; Schultz 1995; Duevel & Haimson 1997). In particular metamorphic rocks like gneisses show a strong directional dependency of compressive strength values. These rocks in many cases were assumed to be transversely isotropic with the foliation plane as an isotropic element. Even DIN EN 1926 recommends the determination of only two directions: the load perpendicular and parallel to any layering. Concerning the Sesia-Lanzo rocks the three measured directions reveal three varying compressive strength values in dependence of the fabric (Fig. 9).

The results of other investigations also exhibit varying compressive strength with respect to macroscopic fabric elements. Gottschalk *et al.* (1990) observed a maximum of compressive strength parallel to the macroscopic visible lineation. Brosch *et al.* (2000) found a maximum of UCS values perpendicular to the foliation plane, therefore perpendicular to the lineation. In the Sesia-Lanzo rocks the compressive

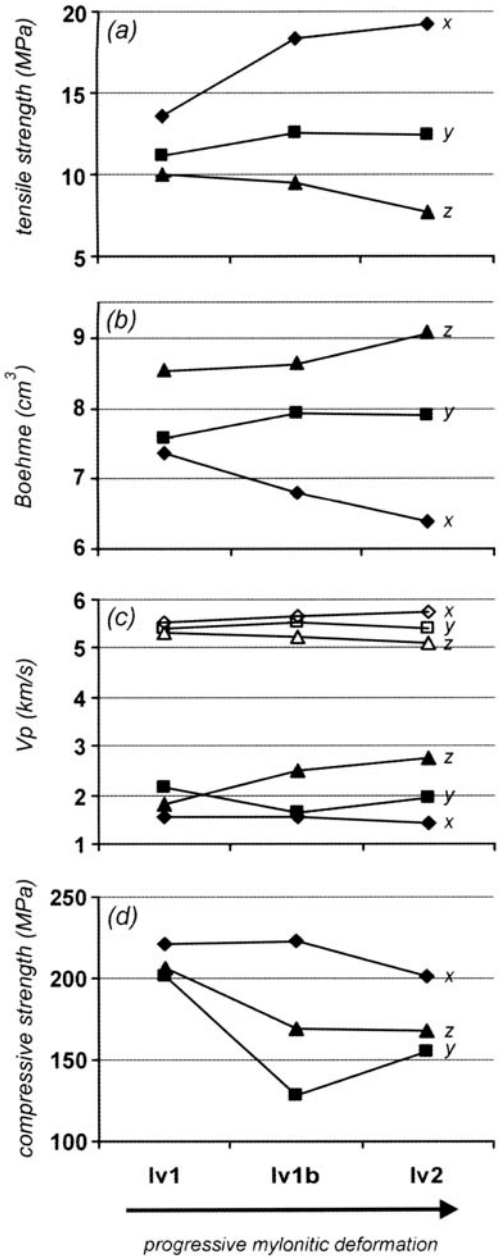

Fig. 16. Mechanical parameters and compressional wave velocities due to progressive mylonitization. The measured directions are indicated. (**a**) Tensile strength. (**b**) Abrasive strength (Boehme method); x-, y-, z-directions correspond to the planes perpendicular to the x-, y-, z-axes of the reference system. (**c**) Compressional wave velocities of water-saturated spherical samples (open symbols) and calculated ΔVp (bold symbols). (**d**) Compressive strength.

strength is highest in samples loaded parallel to the lineation. This holds true for the whole investigated sequence. When the development of mica texture is due to progressive mylonitization, the symmetry of compressive strength should be transformed from prolate to more oblate. The x-direction and the y-direction should reach similar values, whereas the z-direction is assumed to get the highest compressive strength. This is not valid in the case of the Sesia-Lanzo rocks (Fig. 16d). From Iv1b to Iv2 the predicted development is in part observable, but the prolate component remains dominant meaning the x-direction is the strongest direction. Between Iv1 and Iv1b the change of compressive strength does not fit to the model mentioned above. Instead of getting stronger the z-direction becomes weaker as well as the y-direction, whereas the x-direction is strongest and nearly constant (Fig. 9). This may be explained by the model of 'supply of planes of weakness' (planes of weakness defined as any plane of discontinuity within the rock sample; e.g. cleavage planes, foliation planes, layering, microcracks) and the particular stress localization during uniaxial compression. The diameter:length ratio of 1:1 as well as the interlocking of the ground sample and the ground loading plates of the universal testing machine cause 'quasi' triaxial conditions (Nagaraj 1993) and a particular location of shear stress among the specimen (Fig. 12). Slip planes may occur in angles of 18–45° to the direction of load (Stavrogin & Tarasov 2001). Hence, diameter:length ratios of 1:2 or even smaller may give different results. In DIN EN 1926 sample dimensions of 1:1 are recommended, with special emphasis on dimension stones. The orientation of planes of weakness at shallower angles with respect to shear stress influence the uniaxial compressive strength. If these planes are higher in concentration, a relatively lower compressive strength is expected and vice versa. The phyllosilicates and their texture have a great impact on the UCS values. The anisotropy within one sample (for example Iv1) can be explained by the influence of muscovite (001) planes and their related cleavage cracks orientated parallel to the planes of maximum shear stress.

Furthermore the layering, defined by quartz and albite, clinozoisite/epidote and chlorite layers, also controls the mechanical behaviour. A combination of mode-I (tensile) and mode-II (shear) cracks leads to a stepped geometry of the fracture plane (Stavrogin & Tarasov 2001) (Fig. 11a–d). The interlocking of both layers supported by the phyllosilicate content and distribution is also important. This is

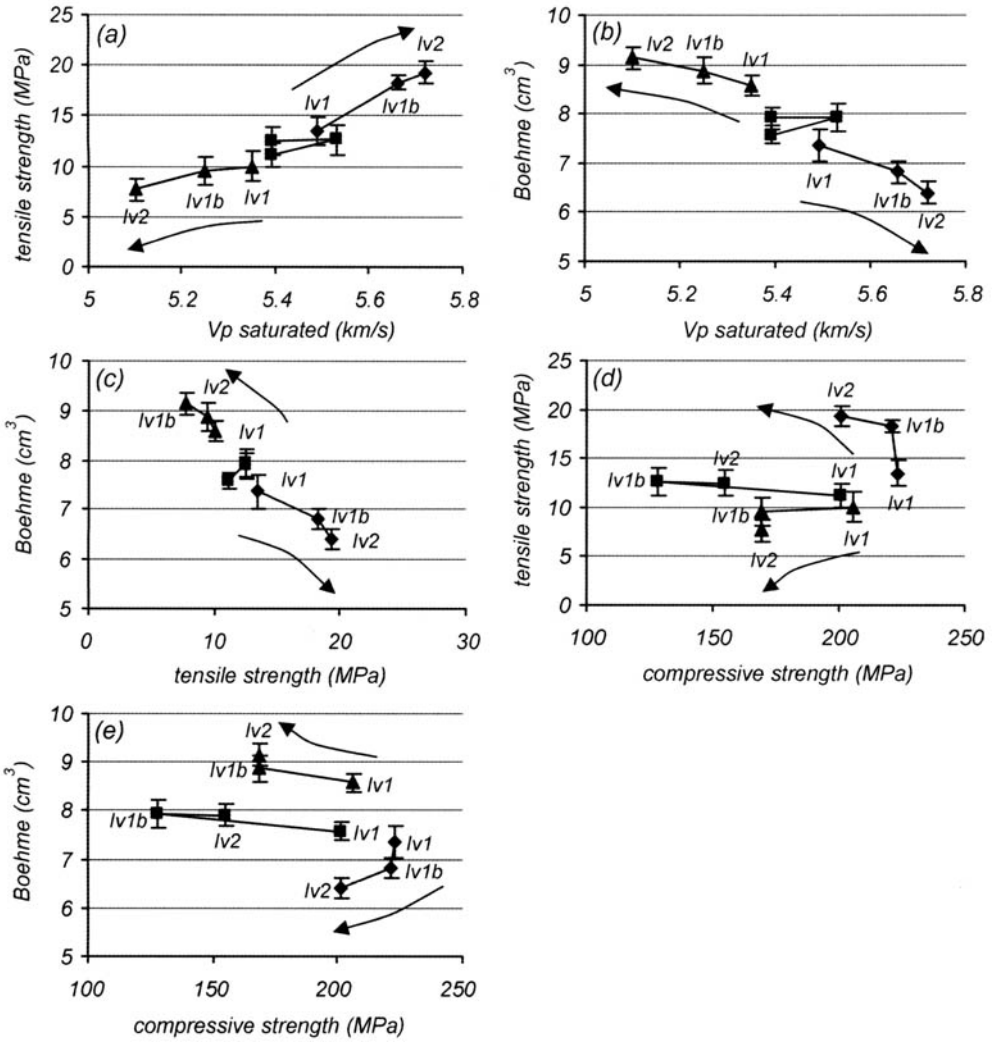

Fig. 17. Relations between mechanical and seismic parameters. The x-direction is marked by rhombes; y-direction marked by squares; z-direction marked by triangles; arrows display development of values due to progressive mylonitization. Experimental errors of compressive strength (d, e) see Table 4. For details see text.

clearly documented by the observed failure pattern of samples Iv1, Iv1b and Iv2 (Fig. 11a–c). For example in Iv2 loaded in the x-direction macroscopically visible mode-I cracks can be recognized. They do not occur in the samples Iv1 and Iv1b and can be explained by an improved fissility parallel to the foliation plane.

From Iv1 to Iv2 the increasing mylonitization leads to more narrowly spaced foliation, and therefore, should enhance the significantly lower strength in the y-direction.

Pre-existing microcracks accommodated by quartz and K-feldspar are not assumed to contribute greatly to compressive strength. In Iv1 the maxima of these microcrack systems (Fig. 8) are aligned to weaken the y- and z-direction of the load. Despite this fact, these directions exhibit the highest compressive strength values considering all samples.

In summary, the conditions during a uniaxial compression test are more complex than in the tensile strength test and Boehme method. The direction of the shear forces does not coincide with the direction of sample load. The interlocking of the sample and the testing machine

makes the stress location triaxial (Fig. 12). Hence, it is not possible to explain the development of UCS values due to progressive mylonitization in detail.

Conclusions

Tensile and abrasive strength mainly depend on the preferred orientation of phyllosilicates (e.g. muscovite) and their related microcracks. In detail other sets of microcracks like healed or mineralized cracks have to be taken into account. Consequently, the development of fabric, in particular of the phyllosilicate texture, causes changes concerning the tensile and abrasive strength. The tested specimens fractured by nucleation and propagation of mode-I cracks along cleavage planes of rock-forming minerals and pre-existing microcracks.

The development of compressive strength values cannot be explained adequately by changes of phyllosilicate texture. Other factors like grain size reduction, more closely spaced foliation, segregation in layers composed of quartz/albite or clinozoisite/epidote/chlorite and increasing fissility parallel to the foliation plane may influence the compressive strength. All these superimposed fabrics cause difficulties in discriminating the parameters (single fabric elements; planar or linear) which influence the rock strength. The quantity and spatial arrangement of discontinuities forming zones of weakness characterize the resistance of rock to compressive fracture.

Compressional wave velocity measurements on dry and water-saturated spheres are suitable for quantifying the crack-induced anisotropy in order to predict qualitatively the anisotropy of mechanical properties (Figs 6 and 17a,b).

Mechanical parameters which depend on similar failure processes (tensile and abrasive strength) exhibit a rather good direct correlation (Fig. 17c). Inspection of Figure 17d,e reveals that there are no distinct relations between the compressive strength on the one hand, and tensile and abrasive strength on the other hand. This may be caused by superimposing parameters and the fact that the direction of load does not coincide with the direction of maximum shear stress leading to sample failure due to uniaxial compression (see section on Uniaxial compressive strength). Moreover, the failure process during the compression test depends on the nucleation of mode-I and mode-II crack pairs (Fig. 11d) merged to form a macroscopic fracture plane in comparison to tensile and abrasive strength where only mode-I cracks occur.

The results of this study may be valid concerning the characterization of mechanical anisotropy of phyllosilicate-bearing rocks like gneisses and granites. For the purpose of applying these data to sedimentary rocks or rocks without any phyllosilicates further research work is necessary.

The authors thank the Bundesministerium für Bildung und Forschung (03DU0GO3-3) and the Deutsche Forschungsgemeinschaft (Heisenberg fellowship S. Siegesmund) for financial support of the recent research project. Furthermore, we would like to thank F. J. Brosch (University of Graz, Austria) and T. Popp (University of Kiel, Germany) for their constructive and helpful reviews. We are grateful to P. Machner and B. Middendorf (both from the University of Kassel) for their aid in performing the abrasive strength measurements. Thanks go to Klaus Ullemeyer and Peter Spalthoff (both University of Goettingen) for their help concerning the analysis of texture data.

References

AZZONI, A., BAILO, F., RONDENA, E. & ZANINETTI, A. 1996. Assessment of texture coefficient for different rock types and correlation with uniaxial compressive strength and rock weathering. *Rock Mechanics and Rock Engineering*, **29**, 39–46.

BALSLEY, J. R. & BUDDINGTON, A. F. 1960. Magnetic susceptibility anisotropy and fabric of some Adirondack Granites and Orthogneisses. *American Journal of Science*, **258-A**, 6–20.

BORRADAILE, G. J. 1987. Anisotropy of magnetic susceptibility; rock composition versus strain. *Tectonophysics*, **138**, 327–329.

BORRADAILE, G. J. 1988. Magnetic susceptibility, petrofabrics and strain. *Tectonophysics*, **156**, 1–20.

BROSCH, F. J., SCHACHNER, K., BLUEMEL, M. & FASCHING, A. 2000. Preliminary investigation results on fabrics and related mechanical properties of an anisotropic gneiss. *Journal of Structural Geology*, **22**, 1773–1787.

CHRISTOFFERSEN, R. & KRONENBERG, A. K. 1993. Dislocation interactions in experimentally deformed biotite. *In*: STEPHEN, H. K., SYLVESTER, A. G., TULLIS, J., WENK, H. R. & TREAGUS, S. H. (eds) Microstructures and rheology of rocks and rock-forming minerals; a collection of papers in honor of John Christie's 60th birthday. *Journal of Structural Geology*, **15**(9–10), 1077–1095.

DEARMAN, W. R., BAYNES, F. J. & IRFAN, T. Y. 1978. Engineering grading of weathered granite. *Engineering Geology*, **12**, 345–374.

DIN 22024, 1989. *Rohstoffuntersuchungen im Steinkohlenbergbau: Bestimmung der Spaltzugfestigkeit von Festgesteinen*. Beuth Verlag, Berlin.

DIN 52108, 1988. *Pruefung anorganischer nichtmetallischer Werkstoffe; Verschleißpruefung mit der Schleifscheibe nach Boehme*. Beuth Verlag, Berlin.

DIN EN 1341, 2000. *Platten aus Naturstein fuer Aussenbereiche: Anforderungen und Pruefverfahren*. Beuth Verlag, Berlin.

DIN EN 1342, 2000. *Pflastersteine aus Naturstein fuer Aussenbereiche: Anforderungen und Pruefverfahren*. Beuth Verlag, Berlin.

DIN EN 1343, 2000. *Bordsteine aus Naturstein fuer Aussenbereiche: Anforderungen und Pruefverfahren*. Beuth Verlag, Berlin.

DIN EN 1926, 1999. *Pruefverfahren fuer Naturstein: Bestimmung der Druckfestigkeit*. Beuth Verlag, Berlin.

DUERRAST, H., SIEGESMUND, S. & PRASAD, M. 1999. Die Schadensanalyse von Naturwerksteinen mittels Ultraschalldiagnostik: Moeglichkeiten und Grenzen. *Zeitschrift der deutschen Geologischen Gesellschaft*, **150**, 359–374.

DUEVEL, B. & HAIMSON, B. 1997. Mechanical characterization of pink Lac du Bonnet Granite; evidence of nonlinearity and anisotropy. *In*: KIM, K. (eds) ISRM international symposium, NY Rocks '97. *International Journal of Rock Mechanics and Mining Sciences and Geomechanics Abstracts*, **34**, 543.

ERSOY, A. & WALLER, M. D. 1995. Textural characterisation of rocks. *Engineering Geology*, **39**, 123–136.

GOTTSCHALK, R. R., KRONENBERG, A. K., RUSSELL, J. E. & HANDIN, J. 1990. Mechanical anisotropy of gneiss; failure criterion and textural sources of directional behavior. *Journal of Geophysical Research, B, Solid Earth and Planets*, **95**, 21,613–21,634.

HANDY, M. R. 1990. The solid-state flow of polymineralic rocks. *Journal of Geophysical Research, B, Solid Earth and Planets*, **95**, 8647–8661.

HOWARTH, D. F. & ROWLANDS, J. C. 1987. Quantitative assessment of rock texture and correlation with drillability and strength properties. *Rock Mechanics and Rock Engineering*, **20**, 57–85.

HROUDA, F. 1982. Magnetic anisotropy of rocks and its application in geology and geophysics. *Geophysical Surveys*, **5**, 37–82.

JELINEK, V. 1977. The statistical theory of measuring anisotropy of magnetic susceptibility of rocks and its application. *Geofyzika Brno*, **1**, 1–88.

JELINEK, V. 1981. Characterization of the magnetic fabric of rocks. *Tectonophysics*, **79**, T63–T67.

JORDAN, P. 1988. The rheology of polymineralic rocks; an approach. *In*: ZANKL, H., BELLIERE J., & PRASHNOWSKY, A. (eds) Detachment and shear. *Geologische Rundschau*, **77**(1), 285–294.

JUCKENACK, C. 1990. *Beitrag der Anisotropie der magnetischen Suszeptibilitaet (AMS) fuer Struktur- und Gefuegeuntersuchungen von Metamorphiten: Einzelbeispiele und regionale Anwendung im Spessart-Kristallin*. PhD Thesis, Georg- August-Universitaet Goettingen, Germany.

KOCH, A. & SIEGESMUND, S. 2002. Bowing of marble panels: on-site damage analysis from the Oeconomicum building at Goettingen (Germany). *In*: SIEGESMUND, S., WEISS, T. & VOLLBRECHT, A. (eds) *Natural Stone, Weathering Phenomena, Conservation Strategies and Case Studies*. Geological Society, London, Special Publications, **205**, 299–314.

KORONEOS, E. G., TASSOJANNOPOULOS, A. I. & DIAMANTOPOULOU, A. 1980. On the mechanical and physical properties of ten Hellenic marbles. *Engineering Geology*, **16**, 263–290.

KRANZ, R. L. 1983. Microcracks in rocks; a review. *In*: FRIEDMAN, M. & TOKSOEZ, M. N. (eds) Continental tectonics; structure, kinematics and dynamics. *Tectonophysics*, **100**(1–3), 449–480.

KRONENBERG, A. K., KIRBY, S. H. & PINKSTON, J. 1990. Basal slip and mechanical anisotropy of biotite. *Journal of Geophysical Research, B, Solid Earth and Planets*, **95**, 19,257–19,278.

LEISS, B. & ULLEMEYER, K. 1999. Texture characterisation of carbonate rocks and some implications for the modeling of physical anisotropies, derived from idealized texture types. *Zeitschrift der Deutschen Geologischen Gesellschaft*, **150**(2), 259–274.

LI, C., PRIKRYL, R. & NORDLUND, E. 1998. The stress-strain behaviour of rock material related to fracture under compression. *In*: PUSCH, R. (ed.) Computational methods in engineering geology. *Engineering Geology*, **49**(3–4), 293–302.

MARES, V. M. & KRONENBERG, A. K. 1993. Experimental deformation of muscovite. *In*: STEPHEN, H. K., SYLVESTER, A. G., TULLIS, J., WENK, H. R. & TREAGUS, S. H. (eds) Microstructures and rheology of rocks and rock-forming minerals; a collection of papers in honor of John Christie's 60th birthday. *Journal of Structural Geology*, **15**(9–10), 1061–1075.

MEGLIS, I. L., GREENFIELD, R. J., ENGELDER, T. & GRAHAM, E. K. 1996. Pressure dependence of velocity and attenuation and its relationship to crack closure in crystalline rocks. *Journal of Geophysical Research, B, Solid Earth and Planets*, **101**, 17,523–17,533.

MUEGGE, D. 1898. Ueber Translationen und verwandte Erscheinungen in Krystallen. *Neues Jahrbuch Mineral. Geol. Paleontol.*, **1**, 71–158.

NAGARAJ, T. S. 1993. *Principles of Testing Soils, Rocks and Concrete*. Elsevier, Amsterdam.

NAGATA, T. 1961. *Rock Magnetism*. Maruzen, Tokyo.

PASSCHIER, C. W. & TROUW, R. A. J. 1996. *Microtectonics*. Springer, Berlin.

PECK, L., BARTON, C. C. & GORDON, R. B. 1985. Microstructure and the resistance of rock to tensile fracture. *Journal of Geophysical Research. B*, **90**, 11,533–11,546.

RASOLOFOSAON, P. N. J., RABBEL, W., SIEGESMUND, S. & VOLLBRECHT, A. 2000. Characterization of crack distribution; fabric analysis versus ultrasonic inversion. *Geophysical Journal International*, **141**, 413–434.

SCHILD, M., SIEGESMUND, S., VOLLBRECHT, A. & MAZUREK, M. 2001. Characterization of granite matrix porosity and pore-space geometry by in situ and laboratory methods. *Geophysical Journal International*, **146**, 111–125.

SCHULTZ, R. A. 1995. Limits on strength and deformation properties of jointed basaltic rock masses. *Rock Mechanics and Rock Engineering*, **28**, 1–15.

SEGALL, P. & POLLARD, D. D. 1980. Mechanics of discontinuous faults. *Journal of Geophysical Research*, **85**, 4337–4350.

SHEA, W. T. & KRONENBERG, A. K. 1992. Rheology and deformation mechanisms of an isotropic mica schist. *Journal of Geophysical Research, B, Solid Earth and Planets*, **97**, 15,201–15,237.

SHEA, W.T. & KRONENBERG, A. K. 1993. Strength and anisotropy of foliated rocks with varied mica contents. *In*: STEPHEN, H. K., SYLVESTER, A. G., TULLIS, J., WENK, H. R. & TREAGUS, S. H. (eds) Microstructures and rheology of rocks and rock-forming minerals; a collection of papers in honor of John Christie's 60th birthday. *Journal of Structural Geology*, **15**(9–10), 1097–1121.

SHELTON, G. L. 1981. *Experimental deformation of single and polyphase crustal rocks at high temperatures and pressures*. PhD Thesis, Brown University.

SIEGESMUND, S. 1996. The significance of rock fabrics for the geological interpretation of geophysical anisotropies. *Geotektonische Forschungen*, **85**, 1–123.

SIEGESMUND, S., VOLLBRECHT, A. & PROS, Z. 1993. Fabric changes and their influence on P-wave velocity patterns; examples from a polyphase deformed orthogneiss. *Tectonophysics*, **225**, 477–492.

SIEGESMUND, S., ULLEMEYER, K. & DAHMS, M. 1995. Control of magnetic rock fabrics by mica preferred orientation; a quantitative approach. *Journal of Structural Geology*, **17**, 1601–1613.

STACEY, F. D., LOVERING, J. F. & PARRY, L. G. 1961. Thermomagnetic properties, natural magnetic moments and magnetic anisotropy of some chondritic meteorites. *Journal of Geophysical Research*, **66**, 1523–1534

STAVROGIN, A. N., TARASOV, B. G. 2001. *Experimental Physics and Rock Mechanics: Results of Laboratory Studies*. Balkema, Lisse.

TECHMER, K. S. 1996. Element mobilization in a ductile shear zone from the Sesia-Lanzo zone (northern Italy): a microstructural, petrographical and chemical study. *Zeitschrift für geologische Wissenschaften*, **24**(5/6), 699–713.

TULLIS, T. E., HOROWITZ, F. G. & TULLIS, J. 1991. Flow laws of polyphase aggregates from end-member flow laws. *Journal of Geophysical Research, B, Solid Earth and Planets*, **96**, 8081–8096.

VOLLBRECHT, A., DUERRAST, H., KRAUS, J. & WEBER, K. 1994. Paleostress directions deduced from microcrack fabrics in KTB core samples and granites from the surrounding area. *Scientific Drilling*, **4**(5–6), 233–241.

VOLLBRECHT, A., STIPP, M. & OLESEN, N. O. 1999. Crystallographic orientation of microcracks in quartz and inferred deformation processes; a study on gneisses from the German Continental Deep Drilling Project (KTB). *In*: SCHMID STEFAN, M., HEILBRONNER, R. & STUENITZ, H. (eds) Deformation mechanisms in nature and experiment. *Tectonophysics*, **303**(1–4), 279–297.

WINKLER, E. M. 1994. *Stone in Architecture: Properties and Durability*. Springer-Verlag, Berlin.

This page intentionally left blank

The anisotropy of itacolumite flexibility

SIEGFRIED SIEGESMUND, AXEL VOLLBRECHT & CAROLA HULKA
GZG, Strukturgeologie & Geodynamik, Goldschmidtstrasse 3, 37077 Göttingen, Germany

Abstract: Itacolumites are very special rocks due to their high flexibility. The investigated Brazilian itacolumites and associated non-flexible quartzites are of comparable composition but differ in their rock fabrics. The shape and size of quartz is mainly controlled by the mica fabric. Quartz textures and grain boundary migration features are indications for deformation at temperatures of about 500°C. The flexibility is mainly related to a penetrative network of open grain boundaries which enable a limited body rotation of individual quartz grains. Continuous layers of white mica display deformation features indicative of shear along the layer-parallel cleavage planes. As demonstrated by simple bending experiments, the flexibility is a highly anisotropic phenomenon which can be related to a directional dependence of grain shape fabrics and corresponding grain boundary pore spacing. According to quantitative estimates, the amount and anisotropy of bending can be explained by the rotation of separated quartz grains between layers of mica which act as flexural slip planes and are also responsible for the observed elastic rebound. Solution along grain boundaries, volumetric strain by thermal contraction of quartz and bulk extension are processes discussed for the origin of the extreme values of secondary grain boundary porosity.

Von Eschwege (1883) and Harder & Chamberlin (1915) were the first to describe itacolumites from Mt Itacolumito in Ouro Preto, Brazil (Minas Gerais State).

Bates & Jackson (1980) defined itacolumites as a 'micaceous sandstone' or a 'schistose quartzite' that contains interstitial, loosely interlocking grains of mica, chlorite and talc, and that exhibits flexibility when split into thin slabs. Itacolumites have been reported from Brazil, India, USA and France (for compilation of data see Suzuki & Shimizu 1993). The most spectacular feature of the itacolumites is their high flexibility. The origin of this abnormal mechanical behaviour is still under discussion. The term 'Itacolumite' commonly used for flexible quartzites is, however, misleading, since quartzites from the Itacolomi Group are non-flexible. The flexible quartzites of the area of Ouro Preto belong to the Moeda Formation of the Minas Supergroup and were designated as 'Ouro Preto Stone' by the Commision for Ornamental Rocks and Coating of the State of Minas Gerais (P. C. Hackspacher, pers. comm.).

Several authors (e.g. Mügge 1887; Ginsburg & Lucas 1949; Verma 1982) suggested that itacolumites originated from a near-surface fluid–rock interaction which may cause chemical weathering along grain boundaries. De Vries & Jugle (1968) and Dusseault (1980) assumed that the loss in cohesion along grain boundaries is due to thermal treatment. More recently, Suzuki *et al.* (1993) and Suzuki & Shimzu (1993) suggested that the flexibility of itacolumites is mainly controlled by the rock fabric. From acoustic emisson studies Suzuki *et al.* (1993) found that a large number of events, in particular those with a lower frequency, are the result of microcrack formation along the open grain boundaries. They developed, based on observations made by De Vries & Jugle (1968) and Sakanaka *et al.* (1989), a so-called 'jigsaw puzzle model' where a uniform distribution of narrow, interconnected voids between the rock-forming minerals allow a limited amount of flexibility.

The metaquartzites and associated itacolumites selected for this study belong to the Moeda Formation from the Minas Supergroup/Caraca Group of the Minas Gerais District (Brazil) and, in addition, from the Andrelandia Formation located 250 km to the SW of Minas Gerais. The Minas Supergroup (Lower Palaeoproterozoic platformal sediments) comprises a lower clastic unit (Caraca Group), an intermediate unit of chemical sediments with marbles and iron ores (Itabria Group) and an upper clastic unit (Piracicaba Group) composed of psammitic to pelitic metasediments together with dolomites and banded iron formations (Door 1969; Almeida *et al.* 1977; Baars & Rosiere 1994). Roeser (1977) and Herz (1978) defined greenschist facies metamorphism for almost the entire Minas Supergroup with an increase in metamorphic conditions up to amphibolite facies from the west to the east.

Microfabrics, textures, porosities and pore

From: SIEGESMUND, S., WEISS, T. & VOLLBRECHT, A. 2002. *Natural Stone, Weathering Phenomena, Conservation Strategies and Case Studies*. Geological Society, London, Special Publications, **205**, 137–147.
0305-8719/02/$15.00 © The Geological Society of London 2002.

geometries were investigated and simple bending tests were performed to gain a better knowledge about the parameters that may control the flexibility of the selected itacolumite samples. For this, data for highly flexible itacolumites were compared with those obtained for non-flexible quartzites from the same stratigraphic sequence.

Methods

The rock fabric was investigated by optical microscopy and scanning electron microscopy (SEM) in order to obtain detailed information about the bulk fabric geometry, deformation microstructures and the topography of grain boundaries.

A quantitative shape fabric analysis was carried out using a semi-automated image analysis system designed by Duyster (1991). Hand drawn images of grain boundaries as visible in three representative orthogonal thin sections (xz-, yz- and xy-plane, see below) were scanned and vectorized. The shape fabrics are given as rose diagrams of the grain boundary orientation and mean values of grain dimensions.

The quartz texture was analysed by X-ray diffraction in the backscattered mode (for details see Ullemeyer *et al.* 2000). Corrections due to changing geometrical conditions during the experimental run (absorption and defocusing effects) were performed. The incomplete pole figures were processed by mathematical algorithms (e.g. Dahms & Bunge 1989). The muscovite textures ((001) cleavage planes) were measured by conventional U-stage microscopy.

Porosity was determined by buoyancy weighting at room temperature while for the pore size distribution mercury porosimetry was used. The basic principle is that a higher pressure is required to press the mercury in narrow pores than in larger ones.

The reference system for all samples is defined by the macroscopic fabric elements (foliation, lineation). As usual, the fabric diagrams were plotted on a Schmidt net (lower hemisphere) with x oriented parallel to the lineation; the xy-plane is the foliation plane, and z is coaxial with the foliation pole.

Results

Macroscopic flexure bahaviour

The flexibility of the investigated itacolumites displays an anisotropic behaviour. This is demonstrated by simple loading experiments shown in Figure 1. Bars of thin itacolumite layers (27 × 4 × 0.8 cm) cut normal to the macroscopic foliation (xy-plane) and normal and parallel to the lineation (L, x) were fixed at the ends and subjected to a constant load (1 kg) at the centre. The bending of the bar cut normal to *L* is significantly stronger (0.9 cm) than for the bar cut parallel to L (0.7 cm). When the constant load is removed the strain recovers instantaneously, i.e. the itacolumite shows macroscopically a quasi-elastic behaviour. Additional loading experiments have not been performed because simple tests did not show any significant bending in other main directions.

Petrography and fabrics

The itacolumites are closely associated with non-flexible quartzites with comparable mineralogy. They are mainly composed of quartz (80–95 vol%) and muscovite (2–10 vol%) with kyanite, tourmaline, zircon, feldspars and ores being the main accessories.

Both the itacolumite (sample FM4) and the non-fexible quartzite display a distinct foliation which is mainly produced by alternating layers with different quartz/mica ratios. A macroscopic lineation is defined by elongated aggregates of fine-grained mica forming isolated domains on the foliation.

On the microscale, it is visible that within the quartz-rich layers the small flakes of white mica are randomly distributed with a strong shape preferred orientation parallel to the layering (Fig. 2a). The shape and size of the quartz grains is partly controlled by the distribution of the mica flakes, i.e. smaller grain size in mica-rich domains and straight grain boundaries parallel to the foliation in contact with mica. This points to a readjustment of quartz grain boundaries within a pre-existing mica fabric by grain boundary migration. Locally, this is also indicated by bulging of grain boundaries between mica flakes (Fig. 2b). As a whole, the quartz fabric may be described as equilibrated showing 120° triple junctions in mica-free domains. A slight elongation of individual grains parallel to the lineation is visible in the xz-sections (Fig. 2a, see also Fig. 4) as compared with the shape fabric in yz-sections (Fig. 2c). In the flexible itacolumite a high porosity along quartz grain boundaries is detectable by optical microscopy even at low magnification (Fig. 2d), in contrast to the non-flexible quartzite where the grain boundaries are mostly closed (Fig. 2e). SEM images reveal straight grain boundaries along these pores with a good fitting of opposite planes (Fig. 2f)

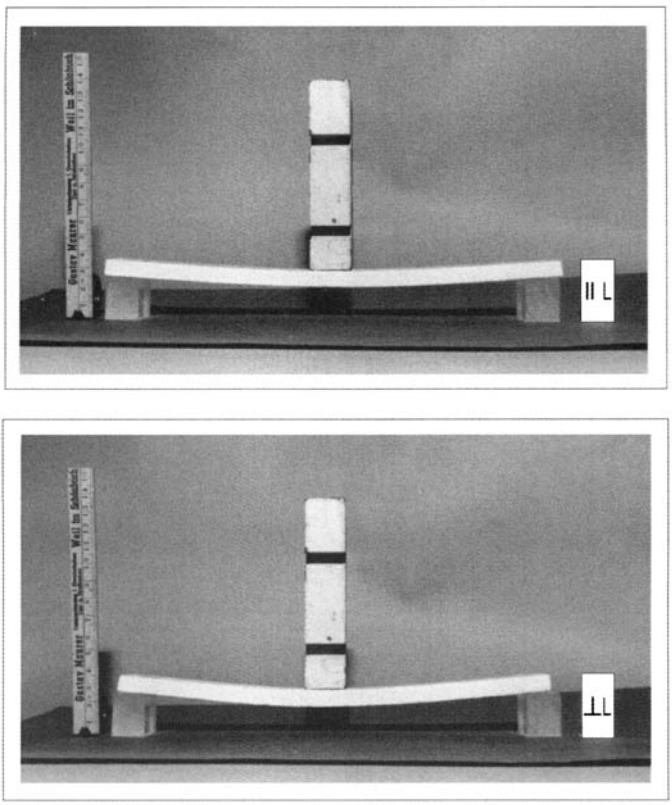

Fig. 1. Macroscopically visible anisotropy of flexibility within the foliation of the investigated itacolumite: (**a**) cross-section parallel to lineation and normal to foliation; (**b**) cross-section normal to lineation and normal to foliation.

suggesting that they mainly resulted from a mechanical opening rather than solution processes, though on the smaller scale etching structures are also observed (Fig. 2g). Systematic variation in shape on different grain boundaries indicates that etching was crystallographically controlled. Surprisingly, most of these etching structures are represented by positive forms rather than the well-known etch-pits. As a whole, this porosity must be of secondary origin post-dating the above-described grain boundary migration. On grain boundaries inclined at a low angle to the thin section surface, a high density of fluid inclusions can be observed (Fig. 2h). These inclusions may be sites of stress concentration leading to a mechanical weakening of grain boundaries and thus may have contributed to their opening. Similar fluid inclusions also exist within the non- flexible quartzite, where only a very limited number of grain boundaries is opened.

Besides the randomly distributed white mica flakes, a small amount of xenomorphic feldspars is detectable within the quartzitic layers (mainly microcline), with grain sizes comparable with those of quartz.

Within the thin continuous layers of white mica the individual flakes are significantly larger than in the quartzitic layers (Fig. 3a). Moreover, many flakes display deformation features which are indicative of shear along the cleavage planes. These are intercalations of very fine-grained material (Fig. 3b), which cannot be identified by optical microscopy, as well as drag and kink structures partly associated with a disintegration to tiny shreds (Fig. 3c). These structures may be attributed to macroscopic bending of itacolumite which is accomplished by flexural slip mainly affecting the mica layers. It is questionable, however, whether these structures were produced in the natural environment or during experimental deformation. A natural deformation is evident from comparable microveins parallel to mica cleavage planes filled with quartz (Fig. 3d). This extension

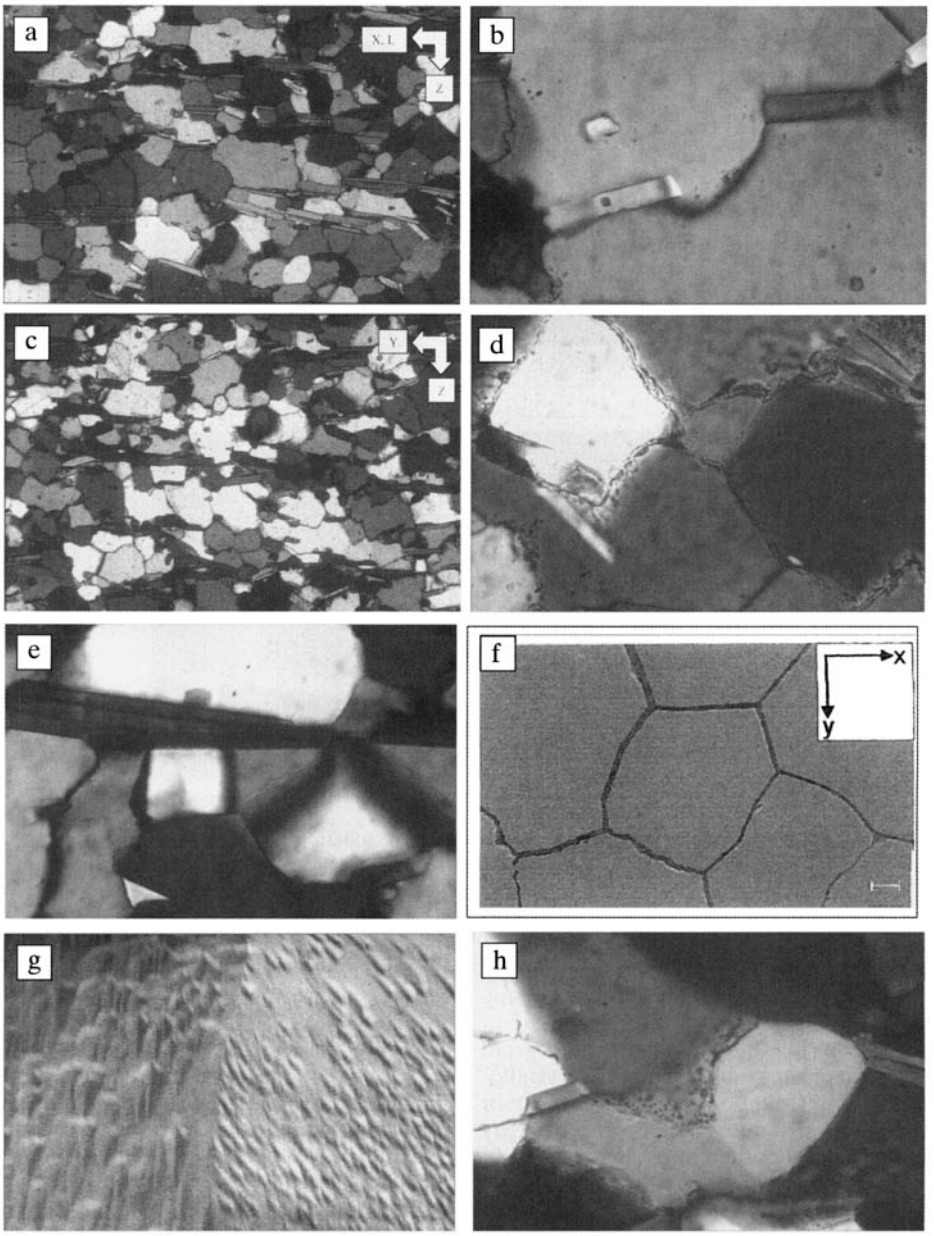

Fig. 2. Quartz fabrics. (**a**) Typical shape fabric in xz-section normal to the foliation and parallel to the lineation, (sample FM 4, itacolumite); a weak elongation of quartz grains parallel to the lineation (X, L) is visible; width of the image is 1.6 mm. (**b**) Bulging of quartz grain boundary between two mica flakes, indication of grain boundary migration (sample FM 2, non-flexible quartzite); width of the image is 0.25 mm. (**c**) Shape fabric of the same sample in yz-section normal to the foliation and lineation; as compared to the xz-section, there is no preferred elongation of quartz grains within the foliation; width of the image is 1.6 mm. (**d**) Open quartz grain boundaries in itacolumite (sample FM 4, itacolumite); width of the image is 0.25 mm. (**e**) Comparatively closed grain boundaries in non-flexible quartzite (sample FM 2); width of the image is 0.25 mm. (**f**) SEM image of open grain boundaries in itacolumite (sample FM 4, secondary electrons; scale bar: 2 μm). (**g**) SEM image (secondary electrons) showing natural etching features on quartz grain boundary in itacolumite (broken specimen); width of the image is 21 μm. (**h**) Fluid inclusions on grain boundaries (sample FM 2); width of the image is 0.25 mm. For further explanation see text.

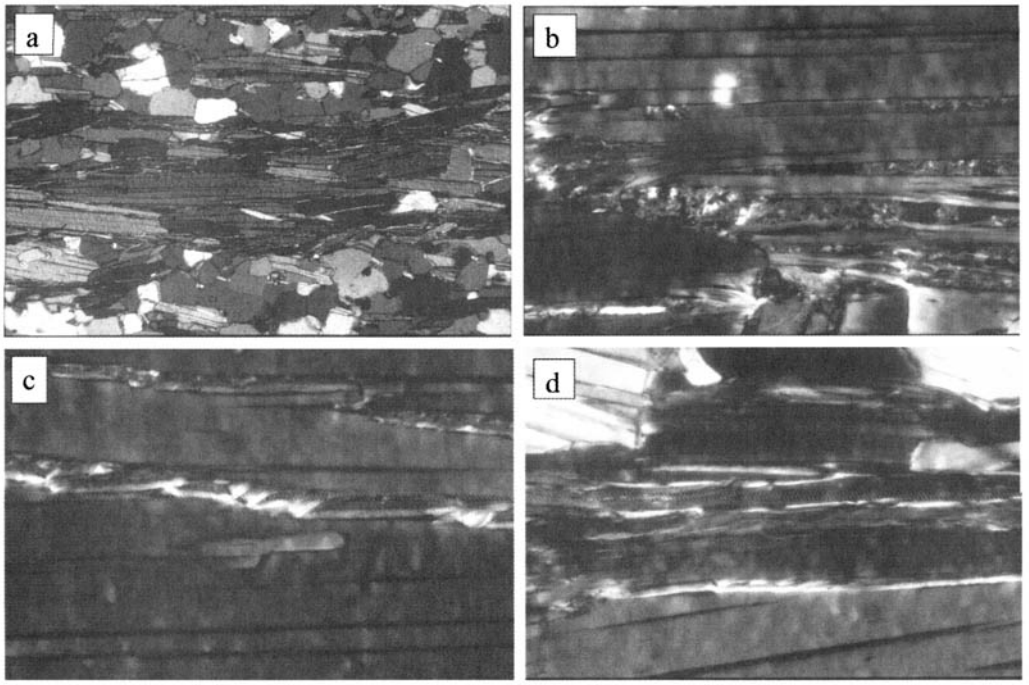

Fig. 3. Mica fabrics (sample FM 4, itacolumite). (**a**) Continuous layer of white mica; width of the image is 1.6 mm. (**b**) Fine layers of 'crushed material' between mica cleavage planes, width of the image is 0.25 mm. (**c**) Flexural bending of cleavage planes indicating sinistral shear; width of the image is 0.22 mm. (**d**) Microveins parallel to cleavage planes filled with quartz; width of the image is 0.25 mm. Features illustrated in (b), (c) and (d) are interpreted to be related to flexural bending. For further explanation see text.

normal to the cleavage planes can be related to the inner arc of bent layers of itacolumite where flexural slip is inhibited.

The quantified shape orientation distribution of quartz for samples CH6 (itacolumite) and FM 6 (quartzite) is given in Figure 4a–d based on the digitized images of grain and phase boundaries in three orthogonal sections (yz-, xz- and xy-plane). The evaluation of the grain boundary orientations reveals for both rock types different sets of planar fabrics with significant shape preferred orientation of quartz grains. In the flexible itacolumite (Fig. 4a,c) quartz grains show a distinct elongation parallel to x (lineation) and, in addition, parallel to z (normal to the layering). The latter direction, however, is mainly developed in certain fabric domains, especially in coarse grained areas (see Fig. 4a, yz-section) and to a lesser extent in contacts to mica. In the non-flexible quartzite (Fig. 4b,d) the x-parallel elongation is less pronounced. Here, the weak preferred orientation in z mainly results from the reorientation of quartz grain boundaries normal to mica flakes which are more frequent in this sample. For a rough evaluation of a quantitative model for the anisotropy of itacolumite flexibility (see below) the following data are of special interest: (1) the approximate mean aspect ratio of quartz grains in sections parallel (xz) and normal (yz) to the lineation, which are 1.9 and 1.7, respectively, and (2) the corresponding dimensions of quartz long axes measured parallel to the foliation which are 0.18 mm parallel to x and 0.16 mm parallel to y.

The amount of mercury incorporated in the pore space is measured as a function of pressure. The total mercury volume at a given pressure can be inverted in a volumetric number characterizing pores with a certain dimension. The effective porosity differs from 1.11 vol.% to 4.78 vol.% for the non-flexible quartzite and the itacolumite, respectively (Fig. 5). By using the buoyancy weighting a total porosity of around 8% was measured for the itacolumite. The pore size distribution of the non-flexible quartzite ranges from 0.01 to 10 μm with a maximum at around 0.5–0.7 μm. In contrast, the itacolumite has a significant maximum pore size above 1 μm while in total it covers the range between 0.1 and

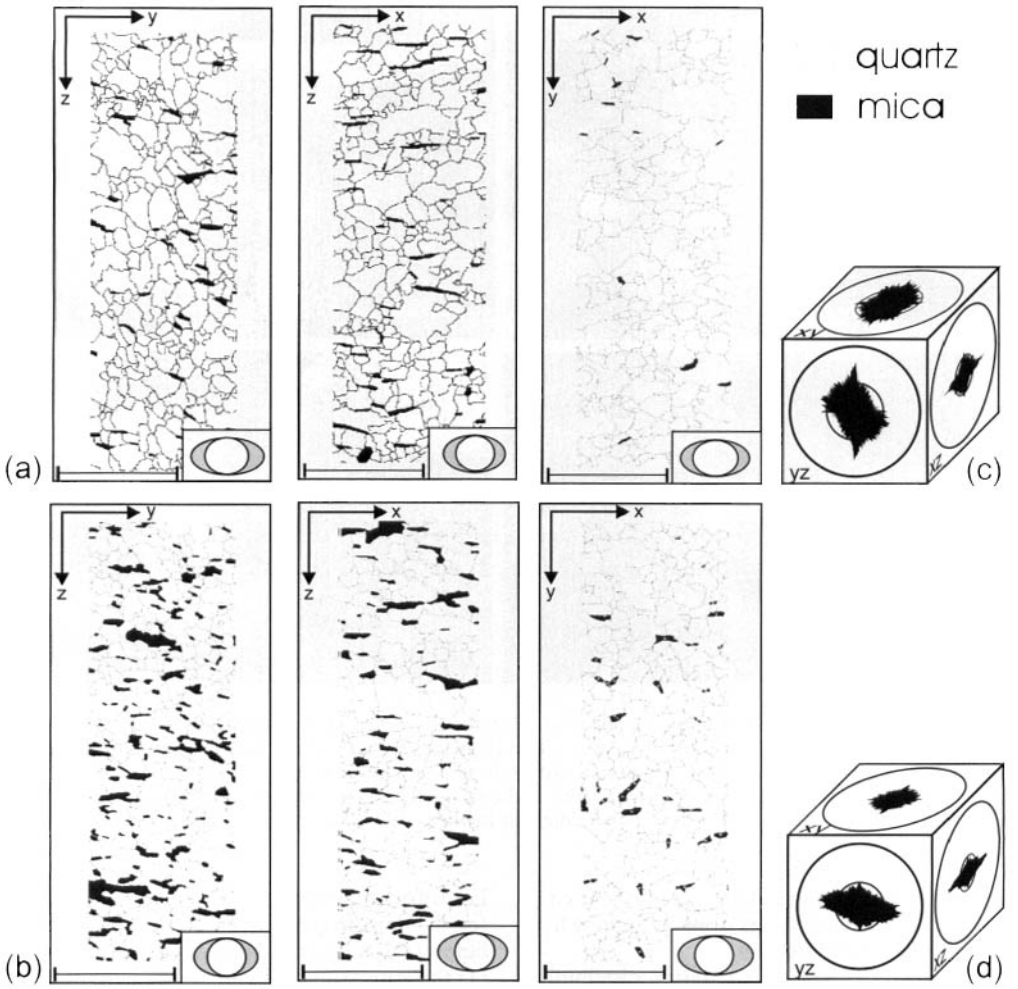

Fig. 4. Quantified quartz shape fabrics of (**a**) and (**c**) itacolumite and (**b**) and (**d**) non-flexible quartzite. (c and d) Orientation of grain boundaries measured in three orthogonal thin sections (xy, xz, yz). For further explanation see text. Scale bars are 1 mm.

10 μm. In summary, there is a significant change to larger pores, i.e. predominantly above 1 μm and therefore in the range of capillary pores.

Texture

The lattice preferred orientation of quartz and muscovite (Fig. 6) was measured to find whether the orientation pattern may be responsible for the loss of cohesion along the grain boundaries due to stress during thermal treatment. The texture is known as the main controlling factor for the mechanical and thermal properties of a rock (see for example Siegesmund *et al.* 2000). The thermal expansion of quartz is given by $\alpha_{11} = 9 \times 10^{-6}$ mm m^{-1} °C^{-1} and $\alpha_{22} = \alpha_{33} = 14 \times 10^{-6}$ mm m^{-1} °C^{-1} parallel to c- and a-axis (Kleber 1959) and may cause excessive internal thermal stresses during moderate heating. From room temperature to 100°C a length change of 0.08% parallel to the c-axis and 0.14% parallel to the a-axis is observed. This corresponds to a volume change of around 0.36% (Winkler 1997). Moreover, the Young's modulus parallel to and perpendicular to the crystallographic c-axis is highly anisotropic and yields values of around 95 GPa and 3 GPa, respectively. The latter were calculated from the compressional and shear wave velocities (V_s) by using the slower V_s value along the a-axes due to the

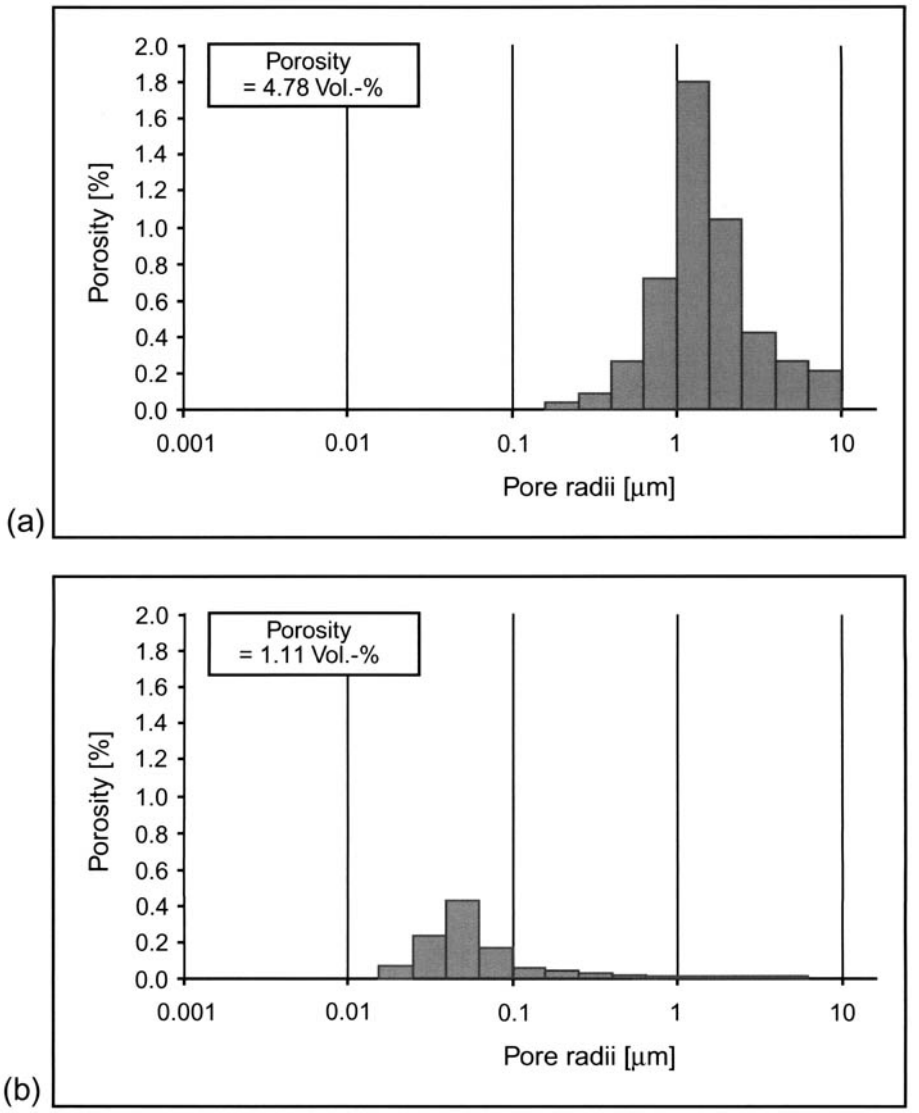

Fig. 5. Porosity and pore radius distribution of (**a**) itacolumite and (**b**) non-flexible quartzite. For further explanation see text.

pronounced shear wave splitting, according to the single crystal data given by McSkimin *et al.* (1965).

The quartz c-axis texture of the non-flexible quartzites (Fig. 6b) displays a single girdle pattern inclined to the foliation with several submaxima. According to the crystallography of quartz the a-axes are arranged along the primitive circle with three distinct maxima (Fig. 6b). Concerning the related processes of texture formation, the c-axis pattern allows for different interpretations. Assuming lattice rotation as the controlling mechanism, the submaximum close to the y-axis may be attributed to prism <a> glide as one of the active slip systems, which implies deformation at comparatively high temperatures (e.g. Hobbs 1985).

Within the itacolumite a relict single girdle c-axis distribution slightly inclined in a sinistral sense to s and L occurs (Fig. 6a). However, in contrast to the non-flexible quartzite, the pronounced maxima are close to the margin of

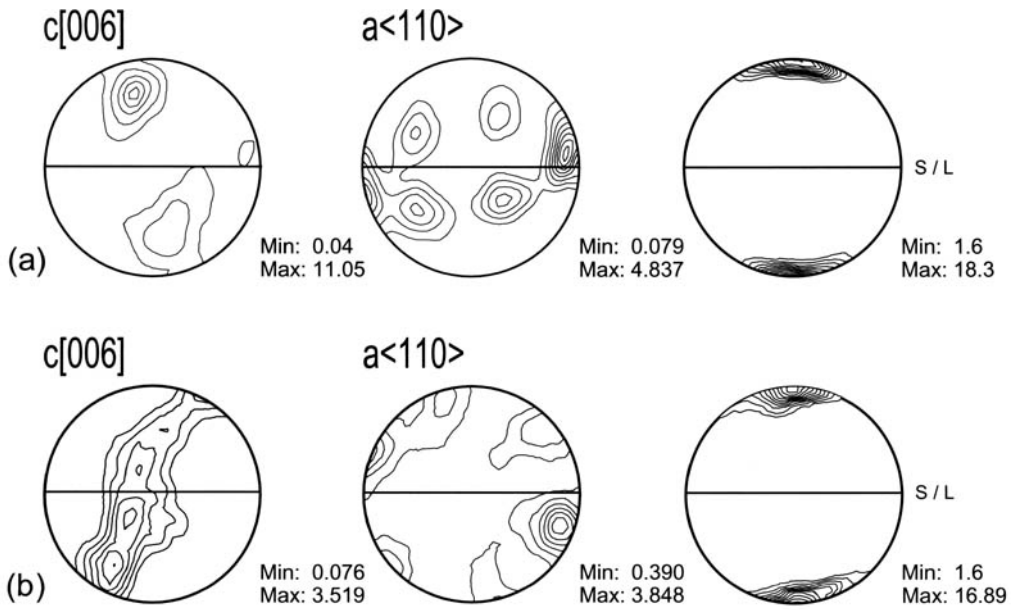

Fig. 6. Textures of quartz and white mica for (**a**) itacolumite and (**b**) non-flexible quartzite. For further explanation see text.

the diagram. The corresponding a-axis pole figure (Fig. 6a) displays a pronounced girdle close to the foliation (s). This texture pattern may be attributed to slip on basal planes at comparatively lower temperatures.

The weak elliptical shape of the (001)-pole maximum of muscovite around the foliation normal z for both samples (Fig. 6) shows that the cleavage planes are distinctly orientated parallel to the foliation with a slight rotation around the lineation. The orientation pattern of the muscovite in the non-flexible quartzite is slightly asymmetrical with respect to the reference system.

Interpretation

Geometrical model

The present geometrical model for the mechanical behaviour of itacolumite focuses on the observed anisotropy of itacolumite flexibility within the foliation plane (Fig. 7). As already suggested by other authors, the flexibility is basically related to the penetrative network of open grain boundaries which enable a certain amount of body rotation of individual grains. If this basic assumption is accepted, the anisotropy of flexibility could be related to a directional dependence either of the grain boundary pore spacing or the grain shapes. SEM observations have shown that the grain boundary pore space varies over a certain range but clear evidence of a directional dependence is missing. On the other hand, the shape fabric analyses show a distinct stretching of quartz grains parallel to the macroscopic lineation which is suggested to be the decisive parameter in the geometrical model illustrated in Figure 7.

For a clear illustration, the basic model contains several simplifications and exaggerations. It is assumed that within the yz-plane (normal to L) the grains are square shaped with grain boundary alignment parallel and normal to the foliation (Fig. 7a). In the xz-plane (parallel to L) the grains are elongated parallel to L by the factor 2 as compared to the yz-plane. This elongation of quartz grains enables a stronger bending around an axis parallel to the lineation (x) than around an axis normal to it (y) if a constant degree of rotation is assumed for individual grains. If the measured values of grain dimensions are applied to this model (see above), the observed differences in the degree of bending (9 and 7 mm, respectively) are in good accordance with the corresponding ratio of grain long axes (0.16 and 0.18 mm, respectively). If the corresponding angle of rotation

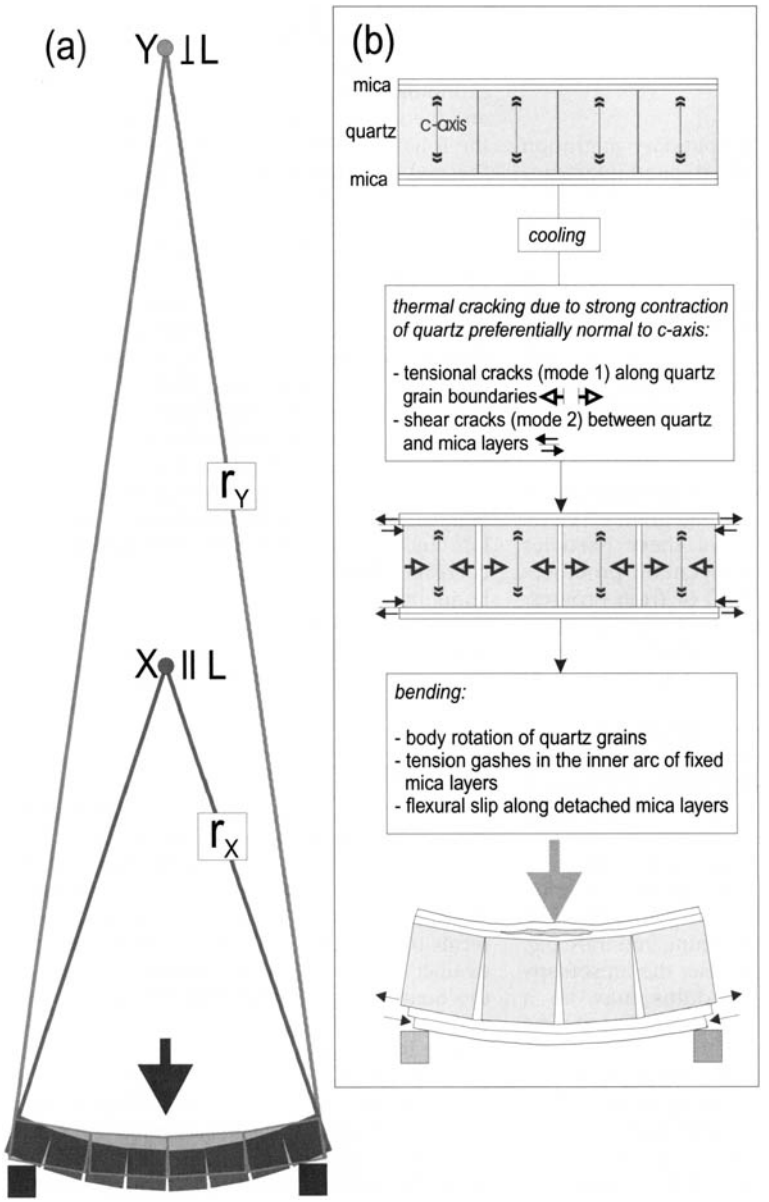

Fig. 7. (**a**) Geometrical model of anisotropic flexibility of the investigated itacolumite; X and Y are the axes of flexural bending; radii of curvature (r_X and r_Y) are related to the aspect ratios of individual grains (rectangles). (**b**) Schematic sketch of microstructural development.

between the edge of the bars and the centre of loading (3.8° and 3.0°, respectively) is related to the number of grain boundaries, the calculated rotation between neighbouring grains is in the range between 4×10^{-3} and 5×10^{-3} degrees which can be achieved without problem along the 1 μm wide grain boundary pores.

As illustrated in Figure 7b, this bending is associated with flexural slip which preferentially occurs within the mica-rich layers as indicated by different shear strain features (Fig. 3b,c) and the lack of comparable microstructures in the quartzitic fabric domains. Moreover, the elastic behaviour of the large mica flakes within theses layers (Fig. 3a) may be the main cause for the observed macroscopic elastic rebound of bent itacolumite. While in uncoupled mica layers bending of itacolumite leads to flexural slip, flexural bending in thicker coupled mica layers produces tension gashes parallel to cleavage planes and compressional structures like kink bands in the inner arc (Fig. 7b). Corresponding

extensional structures in the outer arc have not been observed.

Genetic aspects

Quartz textures and grain boundary migration features suggest that the investigated quartzites suffered temperatures of at least 500°C after deposition, in contrast to the samples studied by Dusseault (1980) for which a diagenetic origin of the final fabrics was suggested. In both cases, the grain boundary porosity which is responsible for the flexibility should be of secondary origin, and must have been produced after the peak temperatures. In general, three kinds of processes can contribute to a secondary porosity along grain boundaries.

1. Solution of second phase particles which were concentrated at the grain surfaces. The concentration of these particles may result from diagenetic processes (coating/cementation) or from progressive accumulation in front areas of migrating grain boundaries (former solid inclusions in the detrital quartz grains).
2. Volumetric strain by thermal contraction during cooling. If the quartzitic fabric domains are fixed by a comparatively rigid frame of less contracting mica layers, the contraction of individual quartz grains may lead to thermal cracking and opening of grain boundaries (for values of thermal expansion of rock-forming minerals; e.g. Devore 1969). Likewise, the anisotropy of the Young's modulus may be a driving force for microcracking during unloading.
3. Bulk extension of the quartzite in the brittle field by tectonic processes. As in case (2) grain boundaries my be opened as potential planes of weakness, especially if decorated by impurities, which is often the case in quartzites.

For the samples of this study, a complex origin of the grain boundary porosity is suggested. According to the morphology of the open grain boundaries, solution transfer seems to be of minor importance. On the other hand, the fitting of neighbouring open grain boundaries points to extensional cracking which could be associated with either a bulk volume increase (dilatancy) or a volumetric strain of quartz (thermoelastic contraction). A bulk tectonic extension, however, cannot explain the differences in grain boundary porosity between itacolumite and non-flexible quartzite. On the other hand, the quartz texture within the itacolumite is more pronounced than in the non-flexible quartzite and favours thermally induced cracks normal to the foliation (Fig. 7b), resulting from maximum thermal contraction normal to the c-axis, which are preferentially orientated at a high angle to the foliation. Grain boundary cracks with this orientation can be well related to the above-proposed model of free rotation of grains during flexural deformation. In contrast, the weaker quartz texture of the non-flexible quartzite with c-axes more evenly distributed along a girdle should result in a lower bulk frequency of cracks with a higher portion of cracks parallel to the foliation. This could be the main reason for the different mechanical properties of both rock types. Following this interpretation, the specific behaviour of the itacolumite can be attributed to late increments of ductile deformation and corresponding texture formation at lower temperatures. Another reason could be differences in the mechanical stability of grain boundaries due to different densities of impurities (fluid inclusion), which has not been investigated up to now.

Summary

Detailed fabric and texture analyses together with petrophysical measurements have been carried out on highly flexible itacolumites and non-flexible quartzites of the same lithostratigraphic unit. The data can be interpreted in terms of a geometrical model which relates the distinct anisotropy of itacolumite flexibility to the quartz shape fabric. The flexibility is basically attributed to rotation of quartz grains which is enabled by a high grain boundary porosity. The bending is associated with flexural slip along layers of white mica which are also responsible for the elastic rebound.

It is suggested that the main cause for the high grain boundary porosity is thermal cracking resulting from the high thermal contraction of quartz between the comparatively rigid layers of less contracting mica. The specific quartz texture of the itacolumite together with the anisotropy of thermal contraction of quartz favoured the formation of grain boundary cracks preferentially orientated normal to the foliation. These cracks are in a suitable orientation to enable grain rotation during the flexure of itacolumite. In contrast, the different quartz texture of the non-flexible quartzite is not suitable to produce a comparable amount of this crack type.

Cracking on grain boundaries may have been stimulated by a high concentration of fluid inclusions as potential loci of stress concentration.

The authors gratefully acknowledge the helpful comments by P. Hackspacher and L. Burlini. Thanks are due K. Ullemeyer who helped with the calculation of the quartz textures. S. S. thanks the German Science Foundation for a Heisenberg Fellowship and the BMBF for financial support. C. A. Rosiere and P. Hackspacher supplied the investigated samples. M. Axmann helped to edit the figures.

References

ALMEIDA, F. F. M., NEVES, B. B. B. & FUCK, R. A. 1977. Provincias Estruturais Brasileiras. *Atas Simpósio Geologia Nordeste*, **8**, 363–391.

BAARS, F. J. & ROSIERE, C. A. 1994. Geological map of the Quadrilatero Ferrifero. *In*: DE WITT, M. J. & ASWAL, L. A. (eds) *Greenstone Belts*. Oxford Monographs on Geology and Geophysics Series, Oxford University Press, 529–557.

BATES, R. L. & JACKSON, J. A. 1980. *Glossary of Geology*. American Geological Institute.

DAHMS, M. & BUNGE, H. J. 1989. The iterative series expansion method for quantitative texture analysis I. General comments. *Journal of Applied Crystallography*, **22**, 439–447.

DEVORE, G. W. 1969. Differential thermal contractions and compressibilities as a cause for mineral fracturing and annealing. *Contributions to Geology*, **8**, 21–36.

DE VRIES, R. C. & JUGLE, D. B. 1968. Structure-property relation in flexible sandstone. *Journal of the American Ceramic Society*, **51**, 387–390.

DOOR, J. N. 1969. *Physiographic, stratigraphic and structural development of the Quadril tero Ferrifero, Minas Gerail, Brasil*. United State Geological Survey, Washington, Professional Paper 641A.

DUSSEAULT, M. B. 1980. Itacolumites; the flexible sandstones. *Quarterly Journal of Engineering Geology*, **13**, 119–128.

DUYSTER, J. 1991. *Strukturgeologische Untersuchungen im Moldanubikum (Waldviertel, Österreich) und methodische Untersuchungen zur bildanalytischen Gefügequantifizierung von Gneisen*. PhD thesis, University of Göttingen.

GINSBURG, L. & LUCAS, G. 1949. Presence de quartzites elastiques dans les gres amoricains metamorphiques de Berrien (Finistere). *Comptes Rendus des Seances de L'academie des Sciences*, **228**, 1657–1658.

HARDER, E. C. & CHAMBERLIN, R. T. 1915. The Geology of Central Minas Gerais, Brazil. *Journal of Geology*, **23**, 385–424.

HERZ, N. 1978. *Metamorphic rocks of the Quadrilatero Ferrifero, Minas Gerais, Brazil*. United State Geological Survey, Washington, Professional Paper 641A.

HOBBS, B. E. 1985. The geological significance of microfabric analysis. *In*: WENK, H. (ed.) *Preferred Orientations in Deformed Metals and Rocks: an Introduction to Modern Texture Analysis*. Academic Press, Orlando, 463–484.

KLEBER, W. 1959. *Einführung in die Kristallographie*. VEB Verlag Technik, Berlin.

MCSKIMIN, H. J., ANDREATCH, P. & THURSTON, N. R. 1965. Elastic moduli of quartz versus hydrostatic pressures at 5 and −195.8 °C. *Journal of Applied Physics*, **36**, 1624–1632.

MÜGGE, O. 1887. Ueber « Gelenksandstein » aus der Umgegend von Dehli. *Neues Jahrbuch für Mineralogie, Geologie und Paläontologie*, **1**, 195–197.

ROESER, H. 1977. Strukturelle und texturelle Untersuchungen in der Eisenerzlagerstätte « Pico de Itabiro » bei Itabirito, Minas Gerais, Brasilien. *Clausthaler* geowissenschaftliche Dissertation **9**.

SAKANAKA, K., KAMEYAMA, T. & FUKUDA, K. 1989. Possibility of synthesis of flexible ceramics. *Journal of the National Institute of Chemical Engineers Japan*, **83**, 395–400.

SIEGESMUND, S., ULLEMEYER, K., WEISS, T. & TSCHEGG, E. K. 2000. Physical weathering of marbles caused by anisotropic thermal expansion. *International Journal of Earth Science*, **89**, 170–182.

SUZUKI, H. & SHIMIZU, D. 1993. Petrography of Indian, Brazilian and Appalachian itacolumites. *Journal of the Geological Society of Japan*, **99**, 391–401.

SUZUKI, H., YOKOYAMA, T. & NISHIHARA, H. 1993. Scanning electron microscope and acoustic emission studies of itacolumites. *Journal of the Geological Society of Japan*, **99**, 443–456.

ULLEMEYER, K., BRAUN, G., DAHMS, M., KRUHL, H. J., OLESEN, N. Ø. & SIEGESMUND, S. 2000. Texture analysis of a muscovite-bearing quartzite: a comparison of some currently used techniques. *Journal of Structural Geology*, **22**, 1541–1557.

VERMA, V. K. 1982. Flexibility in itacolumites from Brazil, India and United States. *Journal of the Indian Association Sedimentologists*, **3**, 19–28.

VON ESCHWEGE, M. 1823. Esquisse geognostique du Brasil. *Annales des Mines*, **8**, 410–413.

WINKLER, E. M. 1997. *Stone in Architecture*. Springer, Berlin.

This page intentionally left blank

Ultrasonic wave velocities as a diagnostic tool for the quality assessment of marble

T. WEISS[1], P. N. J. RASOLOFOSAON[2] & S. SIEGESMUND[1]

[1] *Geowissenschaftliches Zentrum der Georg-August-Universität Göttingen, Goldschmidtstrasse 3, D-37077 Göttingen, Germany (e-mail: tweiss@gwdg.de)*

[2] *Institut Français du Petrole, Geophysics Department, Rock Physics Laboratory, 1 et 4 avenue de Bois Preau, 92852 Rueil Malmaison Cedex, France*

Abstract: Marbles are frequently used as building stones even if they mostly show a limited durability. Thus, different marbles with different fabric types and states of preservation have been investigated in order to constrain the interaction between fabric, state of deterioration and ultrasonic wave velocities. Experimental data reveal that the state of preservation of a marble is clearly documented by ultrasonic wave velocities of compressional waves. For a maximum porosity of up to 1% velocities determined on dry samples range from about 1 km s^{-1} to over 6 km s^{-1}. Anisotropy of ultrasonic wave velocities is a common feature of marbles due to a lattice preferred orientation of the anisotropic rock-forming minerals calcite and dolomite. Pre-existing and thermally induced microcracks tend to increase this anisotropy. For Lasa marble, this increase can be explained by a coincidence of intrinsic anisotropy and the effect of pre-existing and thermally induced microcracks. For many marbles, velocities are reduced to at about 1 km s^{-1} as a consequence of thermal degradation due to only one heating cycle up to 100°C. Model calculations reveal that the velocity reduction is caused by cracks with an extremely small aspect ratio of about 0.005 or even less. The porosity associated with this very early stage of deterioration will not be increased significantly and thus, thermal degradation cannot be determined by other petrophysical measurements.

Sculptures and monuments made of marble are often subjected to strong degradation within a limited time span. The final stage of this weathering is frequently characterized by a granular disintegration of the marble, i.e. the cohesion between the grains is completely lost (Fig. 1). In the initial stage of weathering, thermally induced microcracks are thought to play an important role in degradation (Widhalm *et al.* 1996; Siegesmund *et al.* 2000). They are caused or enhanced by the strong directional dependence of the thermal dilatation coefficient α of calcite (Fig. 2). When the thermal stresses exceed the threshold of cohesion between adjacent grains microcracks are formed (e.g. Tschegg *et al.* 1999; Weiss *et al.* 2002).

To avoid the complete loss of some culturally and historically important buildings or monuments and the tremendous costs of conservation or replacement of degraded marbles, more elaborate methods to detect structural disintegration are required. For many years ultrasonic measurements have been used as a non-destructive tool for the quality assessment of marble and other building stones (Duerrast *et al.* 1999; Snethlage *et al.* 1999). The basic assumption is that a decrease in the velocity of compressional waves (Vp) is correlated with a certain stage of deterioration of a marble. A classification of the state of deterioration of Carrara marble and an empirically derived correlation function between Vp and porosity, presented by Köhler (1991), is shown in Table 1.

In order to understand the relationship between ultrasonic wave velocities, porosity and type of pore fluid in the present investigation the interaction between the microfabric and the ultrasonic wave velocities is re-evaluated using the Lasa marble as a particular example. A comprehensive compilation of the behaviour of different commercially used marble types is used to describe differences in the ultrasonic wave velocity diagnostics as a consequence of varying microfabric types and different degrees of weathering. Furthermore, selected marbles are thermally altered to constrain magnitude and directional dependence of thermal degradation. In our investigations we focus on compressional wave velocities since they are widely used for both on-site inspections and laboratory studies.

From: SIEGESMUND, S., WEISS, T. & VOLLBRECHT, A. 2002. *Natural Stone, Weathering Phenomena, Conservation Strategies and Case Studies.* Geological Society, London, Special Publications, **205**, 149–164.
0305-8719/02/$15.00 © The Geological Society of London 2002.

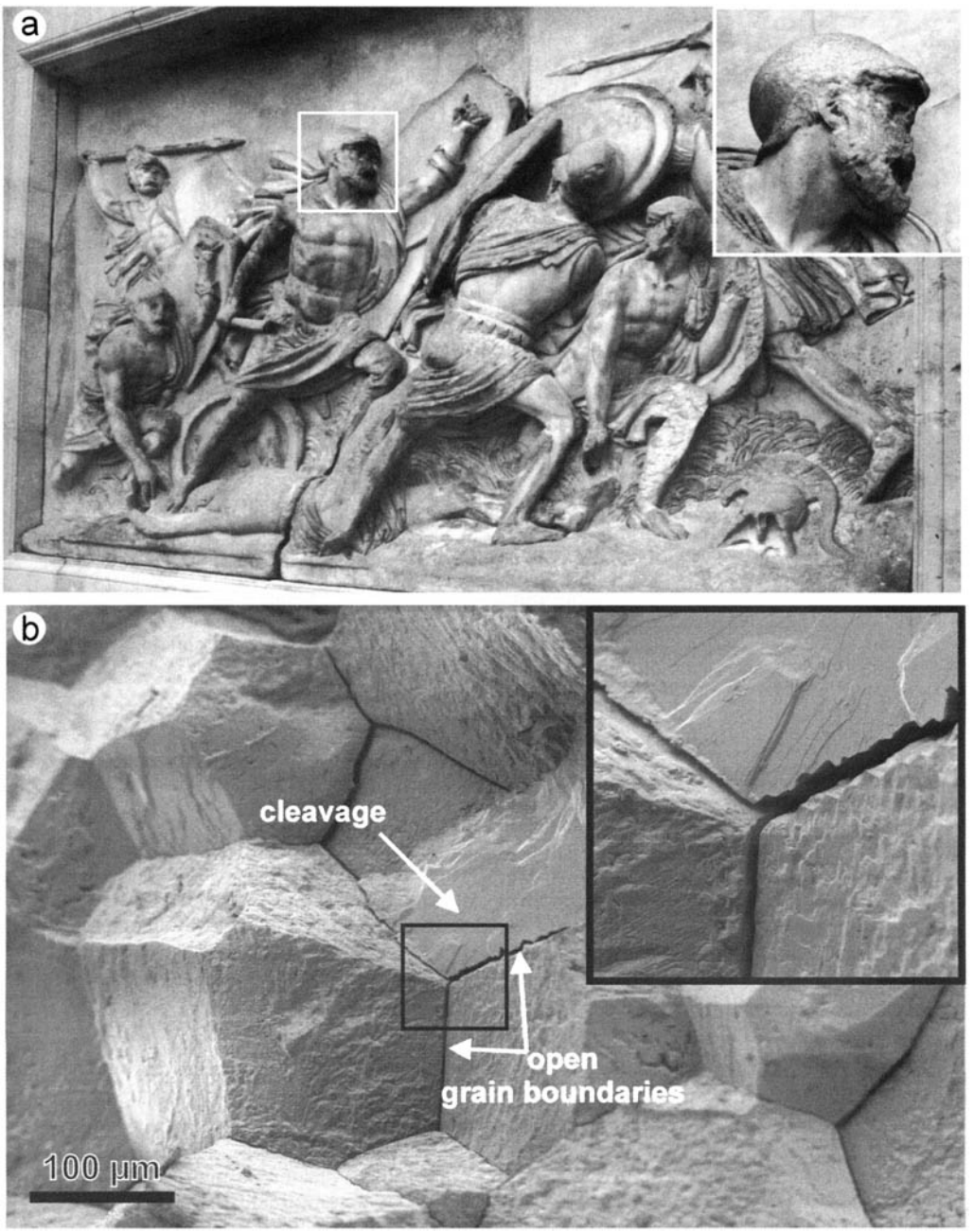

Fig. 1. Degradation of marble. (**a**) A relief from the Siegestor in Munich (Germany) showing granular disintegration; (**b**) SEM images of a fracture plane in Carrara marble showing decohesion along the grain boundaries and fractures along cleavage planes.

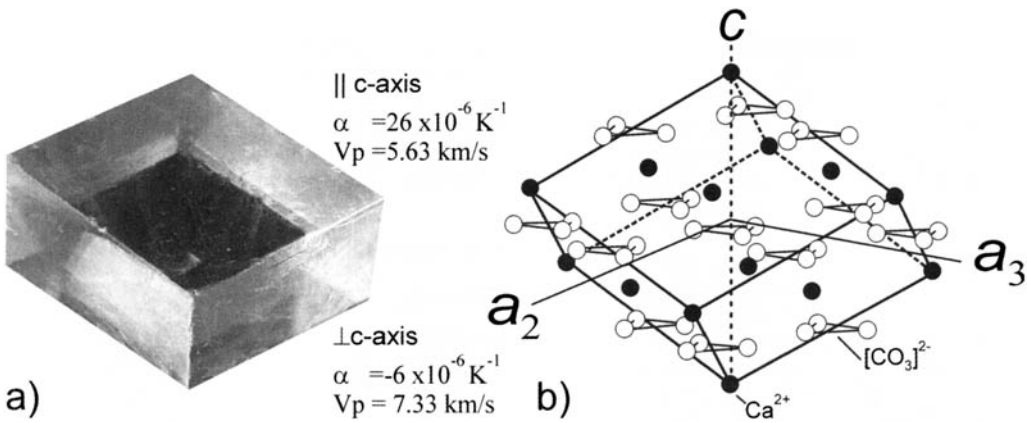

Fig. 2. Single crystal properties of calcite. (**a**) Calcite cleavage rhombohedron with the coefficients of thermal expansion (after Kleber 1959) and ultrasonic wave velocities (Dandekar 1968) parallel and perpendicular to the crystallographic c-axis; (**b**) calcite structure with respect to the calcite crystallography (c-axis and a-axes).

Table 1. *State of deterioration of Carrara marble based on ultrasonic velocity measurements (after Köhler 1991)*

Damage class	Vp (km s^{-1})	Condition
0	> 5.0	fresh
I	3.0–5.0	increasingly porous
II	2.0–3.0	granular disintegration
III	1.5–2.0	fragile
IV	< 1.5	crumbling rock

Fundamentals

Anisotropy of elastic properties

A more or less pronounced directional dependence of almost all petrophysical properties is observed for natural building stones (Siegesmund 1996). Thus, anisotropy is rather the rule than an exception and must be taken into account for all natural building stones. In particular marbles may show a pronounced anisotropy, even if their composition is relatively simple. It is caused by the strong single crystal anisotropy of calcite (Fig. 2) and/or dolomite, the main rock-forming minerals in marble, in combination with their lattice preferred orientation (here referred to as texture) and volume content. The intrinsic properties can be overprinted by extrinsic factors like pre-existing microcracks and porosity caused or enhanced by weathering.

The elastic wave propagation is different in porous and non-porous media (e.g. Bourbié *et al.* 1987). At first glance, marbles can be treated as non-porous materials since their initial porosity is mostly very small (Ruedrich *et al.* 2001). The interaction of anisotropic crystals leads to a more or less anisotropic behaviour of the bulk rock depending on the texture. With a given single crystal anisotropy, the bulk rock anisotropy may vary accordingly from almost random, for a rock with a weak texture, to strongly anisotropic, for a rock with a pronounced texture. When extrinsic parameters (e.g. pores, microcracks) are present, in particular ultrasonic wave velocity propagation is affected (Christensen 1965). The velocities of ultrasonic wave velocities (Vp) are mostly lowered, even if this phenomenon depends on the type of pore fluid (see discussion below).

Relationship between porosity and Vp

Even if the initial porosity of a marble is mostly very small, pre-existing microcracks have an important effect on physical properties (Weiss *et al.* 2001). They result from a complex geological history and may show a uniform distribution or a directional dependence. During weathering, the porosity increases and the resulting material has clearly to be treated as porous. This new porosity can be uniformly distributed or directionally dependent.

There are different theoretical approaches describing the elastic behaviour of cracked or porous materials. The main methods for computing the elastic properties of a heterogeneous material, i.e. a material containing minerals, cracks and different pore fluids, can be classified into the following overall categories.

The first category of methods ignores the geometry of the pore space. Associated methods just average some simple physical parameters like travel-time (Wyllie *et al.* 1956, 1958), stiffness (Voigt 1928) and compliance (Reuss 1929), even if there exist more sophisticated ones (Hashin-Strikman bounds; Hashin 1981). These methods either are applicable to restricted types of rocks (e.g. sedimentary rocks with average to large primary porosity) or give only rough estimates of the overall elastic parameters, especially when the rock exhibits compliant features (cracks, microfractures, etc.) and when its constituents have contrasted stiffnesses (e.g. mineral grains and saturating fluids).

Another category assumes specific geometries for the pores (spherical, ellipsoidal, disc-shaped etc.). One of the most commonly used and accepted method in this group is that of O'Connell & Budiansky (1974). The method, a self-consistent method, is predictive and determines the effect of each heterogeneity (pores, cracks, grains etc.) taking into account the presence of the surrounding heterogeneities and their interactions.

There also exist methods to quantify the effect (magnitude and directional dependence) of extrinsic parameters on ultrasonic wave propagation. Here we use the method proposed by Arts *et al.* (1996) and applied to natural rocks by Rasolofosaon *et al.* (2000). The method considers the elastic properties of the rock sample under various confining pressure conditions. With increasing confining pressure microcracks are closed. The difference between the elastic compliances of the rock under high and ambient pressure leads to a quantitative microcrack characterization, using mathematical derivation based on strict mechanical principles (Rasolofosaon *et al.* 2000). The same procedure can be used to determine the difference in compliance between a water-saturated and a dry sample or to quantify the effect of thermally induced microcracks. The inversion process provides the additional compliance, more precisely the normalized compliance, due to the presence of the cracks and its directional dependence. The normalized compliance is the ratio (in per cent) between the compliance of the cracks and the compliance of the rock matrix. Note that the compliance of the cracks is proportional to the crack density (number of cracks per unit length) multiplied by the compliance of a single crack. As a consequence, from a mechanical point of view, a few very compliant cracks and many weakly compliant cracks would have the same effect with this approach.

Experimental methods

Fabric-induced anisotropy

In order to understand a rock's behaviour it is essential to gather as much information as possible on the rock's structure, since there is a complex interaction between the rock fabric and petrophysical properties as compiled by Siegesmund (1996). Thus, qualitative and quantitative description of critical fabric parameters is indispensable. A qualitative fabric description is obtained by transmitted light microscopy using standard thin sections. Quantified fabric data are determined by digital image analysis giving information on grain size, grain size distributions, grain shape and shape preferred orientations. The amount of pre-existing microcracks is obtained by the measurement of microcracks using a universal stage. Since special emphasis is placed on the directional dependence of ultrasonic wave velocities, all investigations are carried out on at least three mutually perpendicular directions or sections. All data are related to an orthogonal reference system (x, y, z), defined with respect to macroscopic and microscopic features like lineation and foliation. In this coordinate frame, the xy-plane is the plane parallel to a foliation, the x-direction is the direction of the lineation. When no macroscopic fabric elements were found an arbitrary reference system is defined.

Determination of ultrasonic wave velocities

For the ultrasonic measurements spherical rock samples with a diameter of 50 mm and an accuracy of 0.02 mm have been prepared. Spherical samples allow the determination of an arbitrary anisotropy pattern. This becomes important when the symmetry of the anisotropy pattern is not associated with the reference coordinate system, i.e. when the maximum or minimum velocity does not coincide with the x-, y- or z-direction determined macroscopically.

Transient times of ultrasonic pulses (piezoceramic transducers, resonant frequency 0.5 MHz) were measured in 90 directions using the pulse transmission technique at ambient conditions

(Birch 1960). With a given diameter, the velocities of compressional waves (Vp) can be calculated. The measurements were performed at dry (Vp_{dry}) and completely water-saturated (Vp_{sat}) samples to simulate different sample conditions. Furthermore, specimens were heated up to 100°C to force thermal degradation after the samples had been measured at water-saturated and dry sample conditions. The heating was performed at a rate of about 1°C min^{-1} to ensure continuous thermal equilibration of the samples and comparability with other thermal degradation measurements (e.g. Zeisig *et al.* 2002).

At low confining pressures, velocities are the result of an intrinsic and extrinsic part. With increasing confining pressure, microcracks are closed and their reducing effect on the ultrasonic wave velocities vanishes. Thus, Vp measurements in the present study have also been performed under hydrostatic pressure. For these measurements, (i) spheres (50 mm diameter) and (ii) cylindrical samples (length and diameter 30 mm) have been used. Cylindrical samples give more accurate data on absolute velocity values, since the coupling of the transducers on the specimen surface is less problematic than on spherical samples. All specimens were orientated according to the x-, y- and z-direction of the structural reference frame. The porosity of the marbles was determined by buoyancy weighting of the spheres used for the ultrasonic measurements.

Results

Origin and microfabric of the marbles investigated

Marbles from different localities in Italy (Carrara and Lasa) and Poland (Kauffung, Prieborn, Grosskunzendorf) have been used for the investigations. Their fabric properties are shown in detail in Weiss *et al.* (1999; except Lasa marble) and are summarized in Table 2. Some of the specimens are directly from the quarry (fresh samples), while the weathered ones were previously used on buildings and had been replaced on-site. The different marbles cover a broad range of textures, microfabrics and weathering states (Weiss *et al.* 1999). All of the marbles, with the exception of the Kauffung marble, are more or less pure calcitic marbles. The Kauffung marble has dolomitic veins predominantly parallel to the macroscopically visible metamorphic foliation (Weiss *et al.* 1999). Some of the marbles show an equilibrated microstructure with straight grain boundaries (microstructural Type I). Others show serrated grain boundaries (Type II), or a bimodal grain size distribution with small recrystallized and large relict grains with irregular grain boundaries (Type III), or a microstructure with evidence for grain boundary migration (Type IV). Of course, the classification into four fabric types requires some simplification of the naturally very heterogeneous rock fabric. Thus, the prevailing presence of one of the above-mentioned fabric characteristics does not necessarily exclude the others.

Intrinsic versus extrinsic anisotropy

The Lasa marble may be used as a case study for the variations of ultrasonic velocities at different sample conditions in dependence on the rock fabric. The sample is directly from the quarry and, thus, comprises characteristics gathered from its geological and processing (quarrying) history. It exhibits a serrate microfabric (Type II, Fig. 3a–c) and a weak texture with c-axis (006) maximum of about 1.8 mrd and a-axis [110] maximum of 1.3 mrd (Fig. 3d,e) (mrd = multiples of random distribution). The c-axes show a slight girdle tendency (Fig. 3d).

The Vp_{min} at water-saturated condition parallels the maximum of the c-axis concentration and the Vp_{max} the maximum of the a-axis concentration, respectively (Fig. 4a). The velocities cover a range between 6.3 and 6.65 km s^{-1}. Evidently, orthogonal measurements along the x-, y- and z-direction would not monitor the total anisotropy in this case, since the Lasa marble shows a Vp_{max} and Vp_{min} at oblique angles in between the x-, y-, and z-direction.

The velocity pattern determined on the dry specimen is quite similar (Fig. 4b). However, the velocities are significantly reduced, possibly due to the presence of pre-existing microcracks. By comparing measurements at water-saturated and dry sample conditions it is evident that pre-existing cracks also show a correlation with the texture. The maximum difference between Vp_{sat} and Vp_{dry} (1.8 km s^{-1}) is found parallel to the z-direction, the minimum (1.25 km s^{-1}) at an intermediate angle between the x- and y-direction (Fig. 4c). An increase in the directional dependence of Vp due to microcracks is observed, since intrinsic Vp_{min} and the maximum velocity reduction due to cracks coincide. Vp_{sat} covers the range between 6.3 and 6.65 km s^{-1} while Vp_{dry} is in the range between 4.5 and 5.4 km s^{-1}. The calculation of the normalized compliance is based on the data determined on the water-saturated and dry

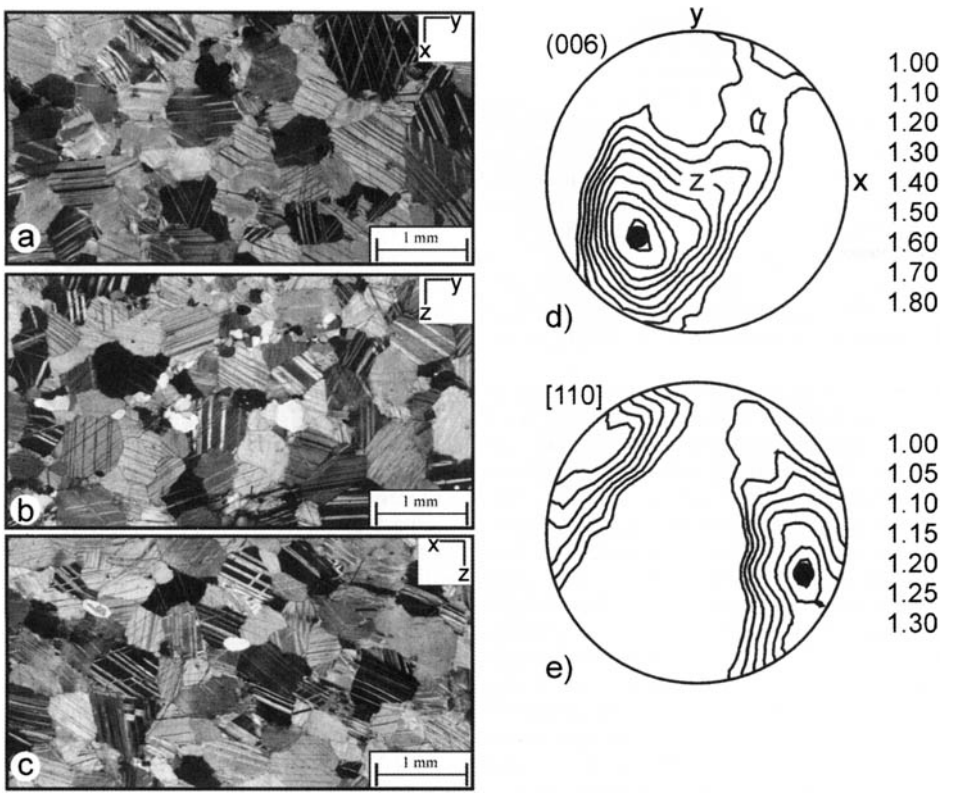

Fig. 3. Microfabric of the Lasa marble. (**a–c**) Microstructure (crossed polarizers); (**d**) c-axis (006) and (**e**) a-axis [110] pole figures (isolines in multiples of random distribution, mrd). The texture was measured by means of neutron diffraction. The reference coordinate system is indicated in c-axis pole figure; the maximum is indicated by a filled circle.

sample. It is a characteristic for pre-existing cracks, and the maximum value parallel to the z-direction (109%) is approximately twice as large as the corresponding minimum (Fig. 4c).

This effect can be understood when the microfabric is taken into account. The general shape preferred orientation of the calcite grains is weak (Fig. 5a, b). However, in the xz-section a weak shape anisotropy is observed (Fig. 5c). Grain boundaries show a preferred orientation parallel or slightly oblique to the foliation. Two sets of open microcracks, associated to e-twins (Fig. 5d) and cleavage planes (Fig. 5e), are observed for the Lasa marble. Both exhibit a maximum parallel to the z-direction, while the cleavage planes show a second maximum parallel to the x-direction (Fig. 5e). Thus, the coincidence of the aforementioned fabric properties may lead to the larger velocity difference between the water-saturated and dry sample condition parallel to the z-direction (see Fig. 4c).

Thermally-induced microcracks

After the measurement of the specimens under water-saturated and dry sample conditions, the samples were thermally treated by heating up to 100°C. All marbles except the Kauffung marble exhibit a pronounced velocity decrease of about 1 km s^{-1} as a consequence of thermal treatment (Table 2). Again the Lasa marble is used as a particular example. The directional dependence of newly generated cracks as a consequence of thermal treatment for this marble can be visualized when the pole figures for the dry and the thermally cracked sample condition are compared. Notice that the pole figures in Figures 4b and 6a represent the same measurement, while the pole figures in Figure 6b and e

Fig. 4. Ultrasonic wave velocities in Lasa marble before thermal alteration: (**a**) at water-saturated conditions; (**b**) at dry sample conditions; and (**c**) their difference pole figure. Normalized compliances are given as a maximum (circle), intermediate (square) and minimum (triangle) value and their positions are indicated in the difference pole figure. The velocity minimum is filled in black.

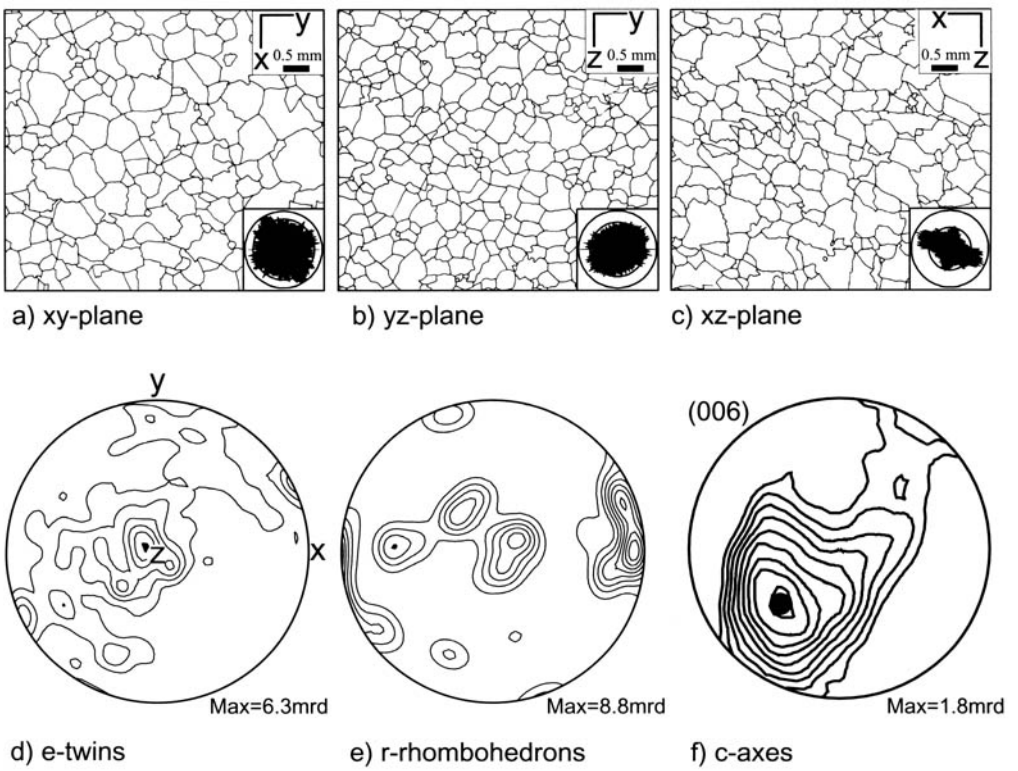

Fig. 5. Quantified fabric of Lasa marble. (**a–c**) Digitized images of the grain boundaries and their orientation (as rose diagrams) in respect to the reference coordinate system; (**d**) orientation diagram of open e-twins and (**e**) cleavage planes determined with a standard universal stage (the maximum is given in multiples of random distribution, contour interval is 1 mrd); (**f**) c-axis (006) texture, measured by neutron diffraction (contour interval is 0.1 mrd).

Table 2. *Summarized fabric properties and ultrasonic wave velocities of the investigated marbles*

Marble type	Sample condition	Approx. grain size (μm)	Micro-structure	Comp.	Φ (%)	Vp_{dry}			Vp_{sat}			Vp_{tcr}		
						Vp_{max} (km s^{-1})	Vp_{min} (km s^{-1})	A (%)	Vp_{max} (km s^{-1})	Vp_{min} (km s^{-1})	A (%)	Vp_{max} (km s^{-1})	Vp_{min} (km s^{-1})	A (%)
Lasa I	fresh	400	I/II	cc	0.43	5.10	4.42	13.30	6.48	6.19	4.46	–	–	–
Lasa II (LA)	fresh	400	II	cc	0.37	5.39	4.48	16.94	6.67	6.29	5.57	4.25	3.45	18.82
Lasa III	fresh	400	II	cc	0.38	5.39	4.61	14.62	6.50	6.09	6.35	4.60	3.64	20.87
Carrara I	fresh	95	III	cc	0.20	6.42	6.16	4.13	6.76	6.62	2.12	5.56	5.32	4.32
Carrara II (CA)	fresh	130	III	cc	0.14	6.53	6.41	6.26	6.83	6.61	3.26	5.48	5.08	7.30
Carrara III	fresh	150	I	cc	0.44	3.45	2.67	22.50	6.14	5.94	3.46	–	–	–
Carrara IV	weathered	140	I	cc	0.94	1.54	1.43	7.39	5.55	5.35	3.53	–	–	
Prieborn	weathered	150	I	cc	0.77	3.03	2.11	30.12	5.65	5.31	6.11	–	–	–
Kauffung I (KA)	fresh	80	III	cc/do	0.23	6.58	5.43	17.78	7.17	6.31	12.04	6.56	5.44	17.07
Kauffung II	weathered	80	III	cc/do	0.32	6.34	5.04	20.44	6.97	6.19	11.22	–	–	–
Kauffung III	weathered	80	III	cc/do	0.26	6.97	5.99	14.11	6.95	6.08	12.57	–	–	–
Kauffung IV	weathered	80	III	cc/do	0.27	6.72	5.84	13.05	7.00	6.19	12.57	–	–	–
Grosskunzendorf I (GK)	fresh	1500	IV	cc	0.31	5.05	4.37	13.59	6.83	6.48	5.18	4.20	3.64	13.33
Grosskunzendorf II	weathered	1500	IV	cc	0.46	4.59	3.63	20.81	6.42	6.10	5.09	–	–	–

Abbreviations: comp., composition; Φ, porosity; Vp_{dry}, Vp at dry sample conditions; Vp_{sat}, Vp at water-saturated sample conditions; Vp_{tcr}, Vp at thermally cracked sample conditions; A, anisotropy calculated as $A = ((Vp_{max} - Vp_{min})/Vp_{max}) \times 100$

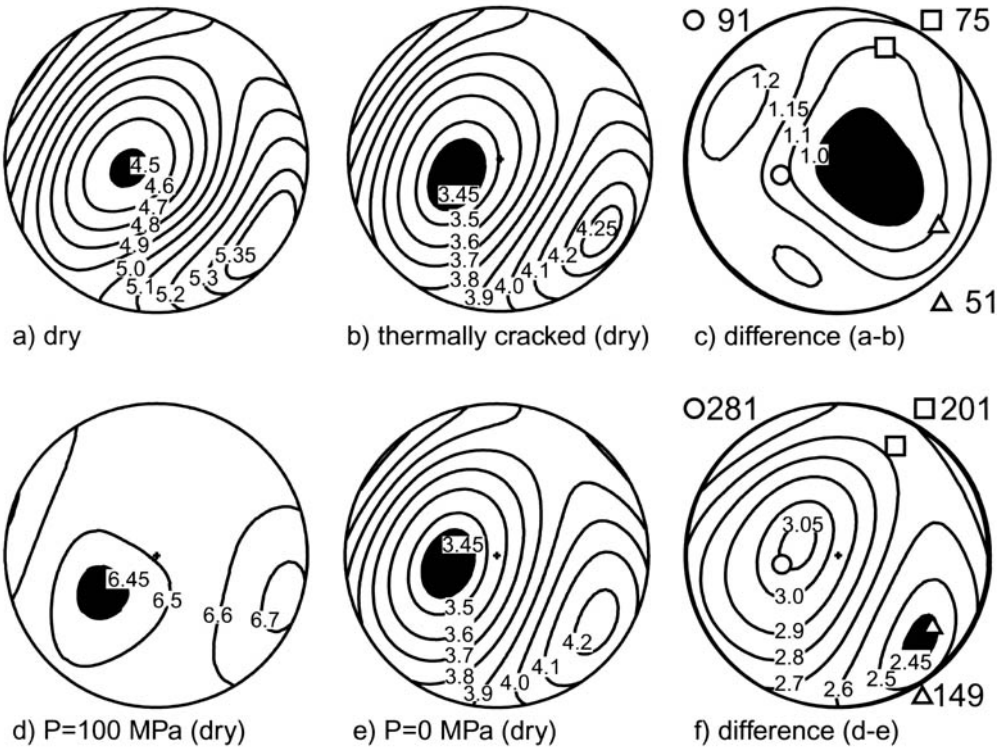

Fig. 6. Ultrasonic wave velocity measurements after thermal alteration: (**a**) at dry sample condition, (**b**) at dry but thermally cracked condition and (**c**) their difference pole figure. Measurements of the thermally altered sample; (**d**) at a confining pressure of 100 MPa, (**e**) at 0 MPa and (**f**) their difference pole figure. Velocity isolines are given in kilometres per second, the reference coordinates are the same as in Figure 3d.

are retrieved from a different experimental setup. A tremendous velocity reduction of about 1 km s^{-1} is observed after only one heating cycle up to 100°C (Fig. 6b,c). The associated difference pole figure exhibits a weak anisotropy which may explain a deviation in the pole figure pattern (compare Figs 4c and 6c). This observation indicates that the velocity reduction due to thermally induced cracks is generally more uniform. A more uniform distribution of thermally induced microcracks may be expected when grain boundary cracking is the predominant crack mechanism since the shape preferred orientation is very weak for this marble. Intergranular (grain boundary) cracking is the probable crack mechanism at these low temperatures (Fredrich & Wong 1986; Weiss *et al.* 2002). However, the directions of maximum, intermediate and minimum normalized compliance for the thermally cracked specimen still coincide with the directions of the pre-existing cracks (compare Figs 4c and 6c). Note that, after one heating cycle, the additional compliance due to thermally induced microcracks (here 91%) is in the same range as that of the pre-existing cracks. Thus, thermal degradation must be very efficient in reducing ultrasonic wave velocities.

Pressure dependence of Vp

The pressure-dependent measurements of the Lasa marble were performed on the thermally treated sample. At a confining pressure of 100 MPa (Fig. 6d) the pole figure is quite similar to the pole figure at water-saturated condition. This indicates that most of the crack porosity caused by pre-existing cracks is accessible and is stiffened by the presence of water. Thus, even the small porosity of 0.37% of the Lasa marble may be interconnected porosity. The corresponding pole figure at 0 MPa pressure (Fig. 6e) shows a good coincidence with the dry measurement shown in Figure 6b even if different

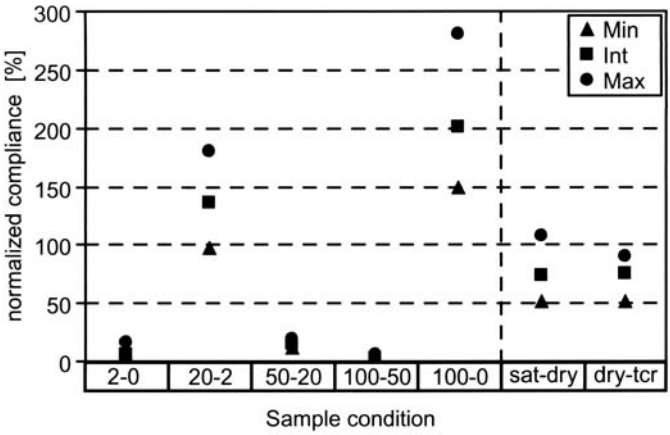

Fig. 7. Normalized compliance of the Lasa marble at different sample conditions (as indicated). The normalized compliances were calculated for incremental pressure intervals between 2 MPa and 0 MPa (2-0), 20 MPa and 2 MPa (20-2), 50 MPa and 20 MPa (50-20), 100 MPa and 50 MPa (100-50). The total value for the normalized compliance was determined from the measurement at 100 MPa and 0 MPa (100-0). Corresponding values for the difference between the water-saturated and dry sample conditions (sat-dry) and for the dry and dry but thermally cracked (dry-tcr) sample conditions are given additionally.

experimental setups were used. This may be taken as an indication that the velocity measurements using different experimental setups really give comparable data. The effect of both types of microcracks, pre-existing and thermally induced ones, can be derived from Figure 6f. The *Vp*-reduction is in the range from 2.45 to 3.05 km s^{-1} and the symmetry of the difference pole figure equals that observed in Figure 4c.

At a pressure of 100 MPa, all cracks are closed and the corresponding pole figure is characteristic for the intrinsic material properties of the Lasa marble. This is documented by the observation that the largest increase in *Vp* (i.e. a large value for the normalized compliance) is observed already at 20 MPa while it is significantly lower at the other incremental pressures (i.e. 50 MPa minus 20 MPa and 100 MPa minus 50 MPa). This means that even at a relatively small pressure of 20 MPa most of the cracks are already closed. Depending on the type of the porosity (i.e. flat cracks or round pores), a complete closure of microcracks may be reached at significantly higher confining pressures. The normalized compliance at 20 MPa is not entirely equivalent to the total amount of normalized compliance observed for the pressure difference between 100 MPa and 0 MPa (Fig. 7). Thus, an interaction of all microcracks and a reinforced effect of cracks on ultrasonic wave velocities must be expected.

A pressure-dependent increase of velocities is a general property of many marbles. Four principal types describing the interdependence between pore space and intrinsic anisotropy are shown in Figure 8. The velocities were determined on cylindrical samples cut along the x-, y- and z-direction of the structural reference frame. A strong and weak pressure-dependent increase in *Vp* can be observed for intrinsically isotropic (Fig. 8a, b) and anisotropic (Fig. 8c, d) marbles, respectively. Even marbles directly from the quarry in one region, as for example Carrara, can exhibit completely different properties (see Fig. 8a, b) as a consequence of their different fabrics (Barsotelli *et al.* 1998; Leiss & Weiss 2000). Changes in the composition (i.e. certain dolomite contents) are clearly monitored by higher ultrasonic wave velocities (Fig. 8c, d). All specimens with cracks show a strong increase of *Vp* within the first 100 MPa. Basically all calcitic marbles investigated exhibit an average velocity of about 6.7 km s^{-1} at a pressure of 200 MPa, regardless how small their Vp_{dry} may be.

Maximum velocity of water-saturated samples

The compilation of the behaviour of all marbles shown in Table 2 gives important information on the response of different marbles to water saturation. The maximum velocity of water-saturated samples (Vp_{sat}) tends to decrease with a decreasing velocity at dry (Vp_{dry}) sample conditions (Fig. 9a). The linear trend was

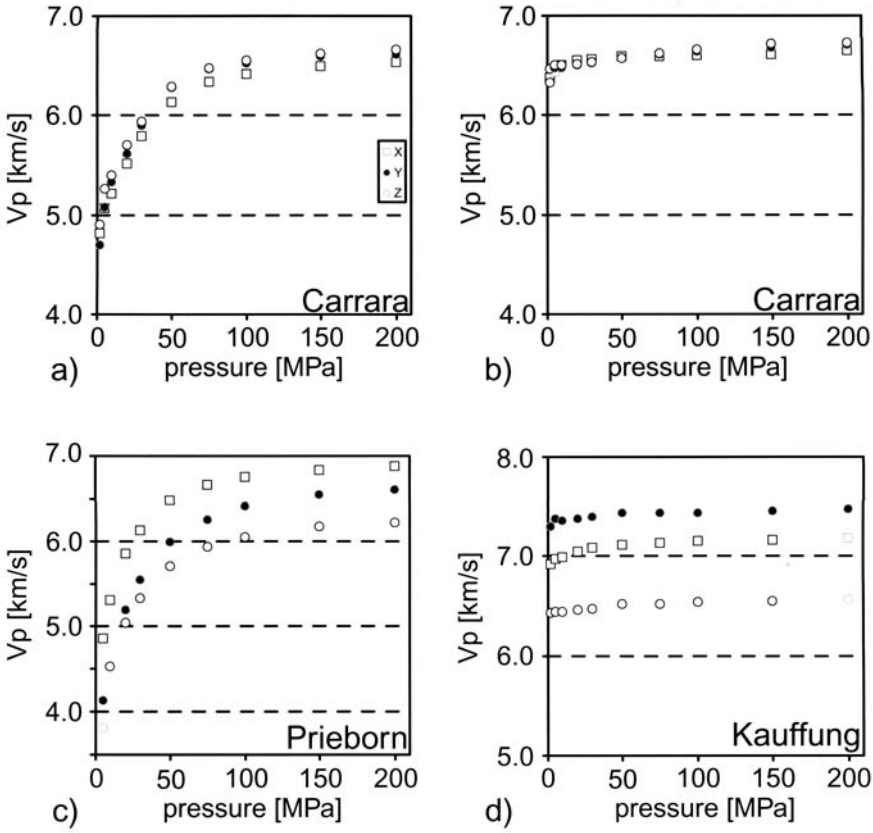

Fig. 8. Relationship between intrinsic and extrinsic anisotropy of different marbles. Relatively isotropic marbles with (**a**) a high and (**b**) a low amount of pre-existing microcracks. Anisotropic marbles with (**c**) a high and (**d**) a low amount of pre-existing microcracks. While marbles with pre-existing microcracks (a, c) show a distinct increase in *Vp* with increasing pressure, the *Vp* increase is very weak for non-cracked marbles (b, d). Note that for the first case the velocity increase with pressure vanishes at about 100 MPa indicating that most of the cracks are closed at this pressure interval. The dolomitic composition of the Kauffung marble (d) is clearly visible in higher velocities compared to the other calcite marbles.

calculated for all Vp_{max} and Vp_{min} and varies only slightly (see Fig. 9a). Some specific examples may be used to illustrate this effect. Example A (a strongly weathered Carrara marble with a porosity of 0.97%), shows a weak anisotropy (A) at both water-saturated and dry sample conditions (Fig. 9b); Vp_{dry} varies from 1.43 to 1.54 km s^{-1} (A = 7.1%) and Vp_{sat} from 5.35 to 5.55 km s^{-1} (A = 3.6%). In contrast, example B (a Prieborn marble with a porosity of 0.77%) shows a higher variation in velocities at dry sample conditions than at water-saturated sample conditions: Vp_{dry} varies from 2.11 to 3.03 km s^{-1} (A = 30.12%) and Vp_{sat} from 5.31 to 5.65 km s^{-1} (A = 6.11%). Both specimens show a similar microstructure with straight grain boundaries (polygonal fabric; Weiss *et al.* 1999) but remarkable differences in the behaviour of ultrasonic wave velocities.

All individual velocity directions, determined on one sample, follow the trend which was calculated for all marbles. This effect is also evident for example C (the fresh Lasa marble with a porosity of 0.37%), even if the velocities at dry sample conditions are significantly higher compared to example B. Most of the marbles rapidly leave the curve characterizing the coincidence of Vp_{sat} and Vp_{dry}. An exceptional example for a marble with a very small initial porosity and a very small degree of degradation is shown with example D. This specimen, a marble from Kauffung in Poland with a porosity of 0.23%, shows a coincidence of Vp_{dry} and Vp_{sat}. The anisotropy of Vp varies according to

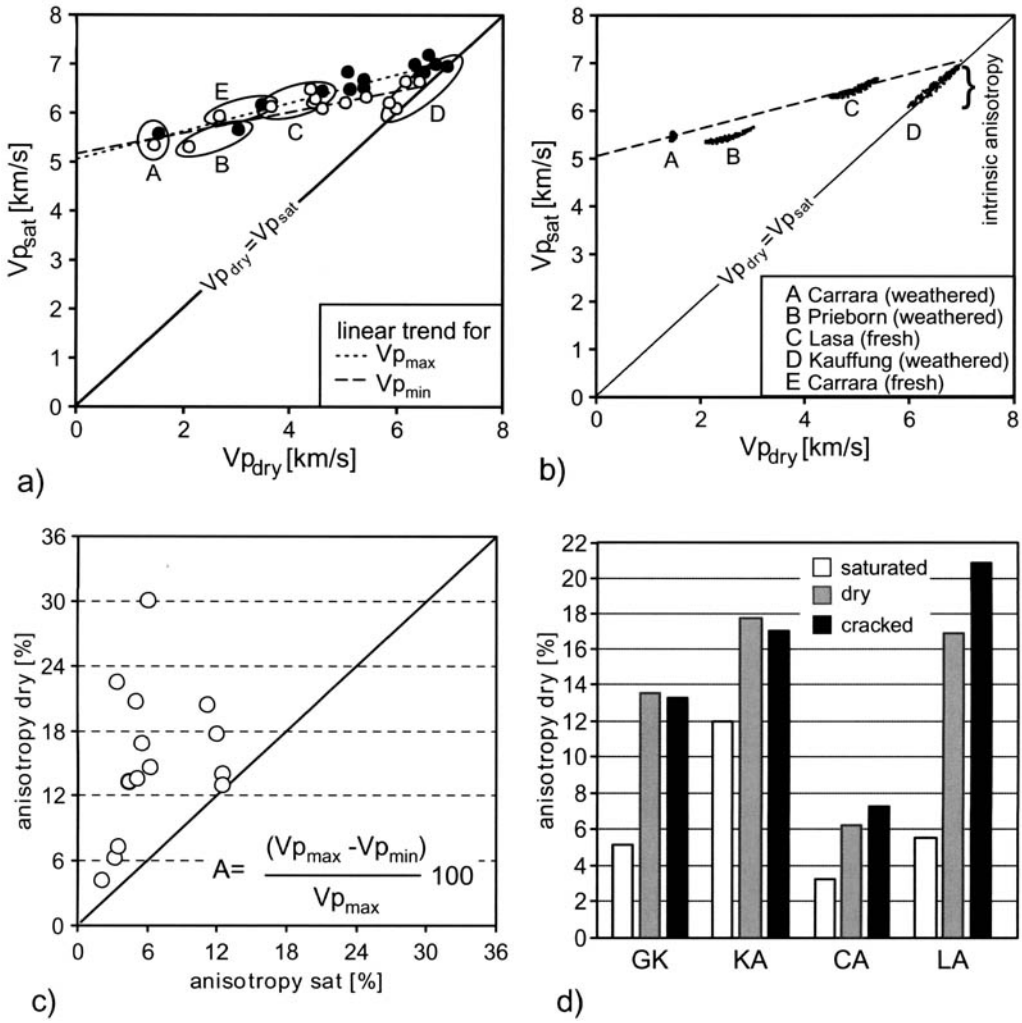

Fig. 9. Ultrasonic wave velocities in marbles. (**a**) Velocities at water-saturated sample conditions (Vp_{sat}) as a function of velocities at dry sample conditions (Vp_{dry}). Different specific examples (A–E, see (b) for description) described in the text are outlined. A linear trend has been calculated for all maximum (black circles) and minimum (white circles) Vp. (**b**) For selected examples all Vp data determined on spherical samples are shown for all measured directions. (**c**) Anisotropy (A) of the samples as a function of water-saturation. (**d**) Change in anisotropy due to thermal cracking (for abbreviations see Table 2).

the strong texture of this marble from 12.04% at water-saturated to 17.78% at dry sample conditions and only a small deviation from the curve ($Vp_{sat} = Vp_{dry}$) is observed (Weiss *et al.* 2001). Due to the strong anisotropy of this marble, a pronounced directional dependence of thermal dilatation has to be expected. Another marble with extraordinary properties is shown by example E. This Carrara marble is fresh from the quarry and has a porosity of 0.44%. However, Vp_{dry} is already very low covering the range between 2.67 and 3.45 km s^{-1} even if Vp_{sat} is relatively high (5.94 to 6.14 km s^{-1}). The anisotropy of this marble is relatively low at water-saturated sample conditions (3.46%) and very large at dry sample conditions (22.5%). Moreover, Ruedrich *et al.* (2001) have shown that this marble has, compared to other Carrara marbles, a higher propensity for thermal degradation.

Anisotropies in dry marbles may vary from 4% to 30% (Fig. 9c). When the marbles are

water-saturated, they cover a significantly smaller range between 3% and 12%. A thermal degradation may reinforce or reduce the anisotropy in marble leading to a higher (CA and LA) or lower (GK and KA) anisotropy of thermally cracked specimens calculated as percentages, respectively (Fig. 9d). However, these values have to be handled with care. A velocity difference of 1 km s^{-1} in a marble with Vp_{max} = 7.0 km s^{-1} and Vp_{min} = 6 km s^{-1} gives an anisotropy of A = 14.29% while the same velocity difference in a marble with Vp_{max} = 3.0 km s^{-1} and Vp_{min} = 2 km s^{-1} gives an anisotropy of A = 33.33%. If it is assumed that a homogeneously degraded marble shows an overall velocity reduction of 1 km s^{-1} at all sample directions its final anisotropy crucially depends on the initial (intrinsic) anisotropy. The final anisotropy may be larger even if there is a uniform degradation.

Model calculations

In order to find constraints for the magnitude and shape of the pore space in marble we modelled the velocity reduction as a function of crack geometry using the well known theoretical prediction of O'Connell & Budiansky (1974). The basic principle is that a given porosity is formed by certain types of ellipsoidal cracks. The crack geometry is only defined by the aspect ratio (i.e. the ratio between small and large axis of the ellipsoid) of the cracks. Spherical cracks have an aspect ratio of 1 and flat cracks of less than 1. The model calculations reveal that Vp strongly decreases as a function of porosity, as observed experimentally (Weiss *et al.* 2001). This can only be caused by extremely flat cracks with an aspect ratio of about 0.005 for dry samples (Fig. 10a). At water-saturated conditions the trend given by the experimental data is slightly steeper than the modelled one for an aspect ratio of 0.005 (Fig. 10b). From the model calculations it must be expected that largely deteriorated samples (i.e. samples showing a low velocity at dry sample conditions) show a reduced Vp even at water-saturated conditions. The model-based velocity reduction for a water-saturated and a dry specimen with an average Vp of 6.49 km s^{-1} is shown in Figure 10c. It is obvious that for both, water-saturated and dry specimens, the ultrasonic wave velocities should decrease with increasing porosity when the cracks have an aspect ratio of about 0.005. This presumption is supported by the experimental data (see Fig. 10a, b) showing a similar trend of Vp_{sat} versus Vp_{dry} (Fig. 10d).

Laboratory versus field studies

On-site investigations using ultrasonic wave velocity measurements may not be easy to perform. Elastic waves propagating in rocks containing heterogeneities are affected by attenuation. The result is a loss of energy at the transducer. In the laboratory signals with a central frequency of about 1 MHz are usually used on sample with a limited size of a few centimetres. On-site inspections proved that the central frequency must be significantly lower to obtain an interpretable signal at the receiver. The difference in the central frequency has an important effect on all derived petrophysical properties. Some typical values for the central frequencies of the transducers, the wavelengths, the resolution and the maximum transmission distance in marble, both in the laboratory and in the field, are listed in Table 3.

From a theoretical point of view it is evident that the highest transmission distance is obtained at lower frequencies. However, there is a link between the transducer size and the central wavelength for a maximum efficiency in the emission and the reception of the waves. Typically the optimum value of the product of the transducer diameter (in inches) and the central frequency (in MHz) is around 0.5. For instance, a laboratory transducer of 1000 kHz has a typical diameter of 0.5 inches. As a consequence, the smaller the frequency the larger the transducer size, which is a limiting factor in practice. In fact commercial transducers used in the field have a typical central frequency of about 50 kHz and a size of about one inch, instead of the ideal value of about 10 inches. In conclusion the values for the maximum transmission distance (see Table 3) correspond to measurements under optimum conditions which are mostly not encountered on-site. Consequently the maximum transmission distance expected in the field can be significantly lower. For detailed investigations it must be considered that the spatial resolution of two individual heterogeneities also varies with the central frequency. Thus, with a frequency of about 10 kHz, a clear differentiation between two objects with a displacement of a few centimetres will not be resolved.

Conclusions

Ultrasonic wave velocity measurements are a powerful and sensitive tool for the damage assessment of marble. Thus, they may be used in a very early stage of deterioration when the rocks are apparently still intact. Water

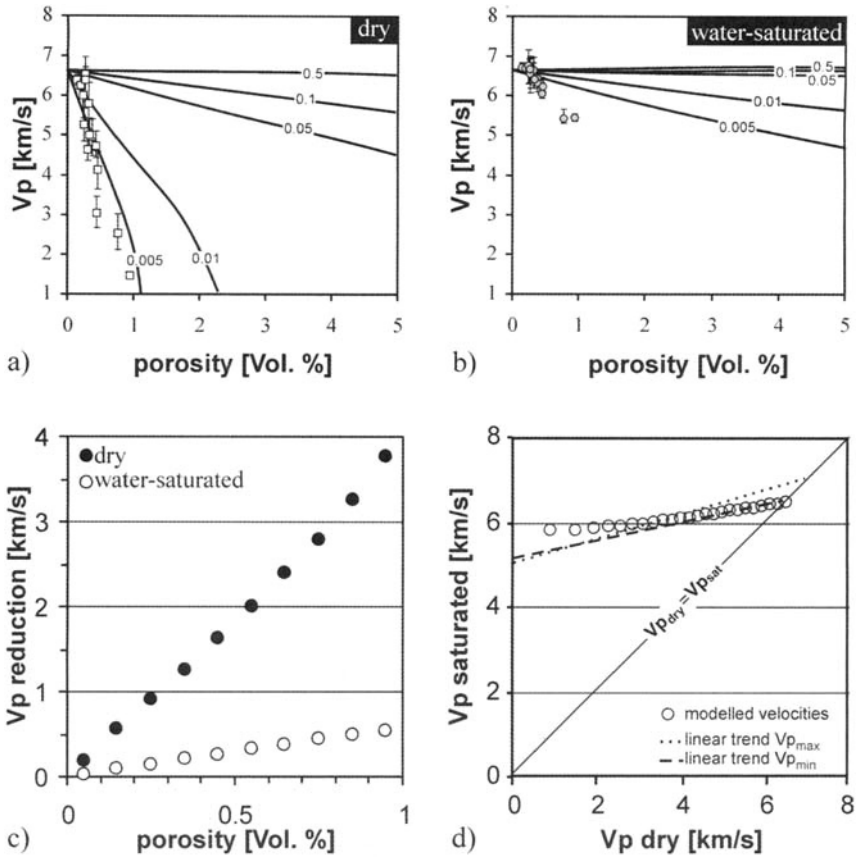

Fig. 10. Experimental versus modelled *Vp*. Velocity reduction due to microcracks with a certain aspect ratio (here 0.005, 0.01, 0.05, 0.1 and 0.5; black lines) for (**a**) dry sample conditions and (**b**) water-saturated sample conditions. Experimental data are given as average velocities (squares in (a) and circles in (b)) and their anisotropy as error bars. (**c**) Velocity reduction as a function of porosity according to the model of O'Connell & Budiansky (1974) for water-saturated and dry sample conditions and (**d**) the corresponding Vp_{sat} versus Vp_{dry} relationship. For comparison, the linear trend based on experimental data (see Fig. 9a) is given.

Table 3. *Frequency (f) dependence of some physical parameters of interest for on-site and laboratory measurements*

Physical parameter	Velocity	Field	Laboratory	
	(km s^{-1})	f = 10 kHz	f = 100 kHz	f = 1000 kHz
Wavelength	2	2 dm	2 cm	2 mm
	6	6 dm	6 cm	6 mm
Resolution	2	0.5 dm	0.5 cm	0.5 mm
	6	1.5 dm	1.5 cm	1.5 mm
Maximum transmission distance	2	20 dm	20 cm	20 mm
	6	60 dm	60 cm	60 mm

All physical parameters have been calculated for two different velocities in the material under investigation (2 and 6 km s^{-1}). The resolution parameter gives information on the maximum distance between two heterogeneities in a material which can be clearly discriminated. The maximum transmission distance is the transmission path through a sample allowing a detectable signal at the receiver position. All values are approximate.

saturation has an important influence on the magnitude and directional dependence of ultrasonic wave velocities. Hence, it is essential to gather sufficient information on the state of water saturation of an object under investigation, at least when it consists of marble.

The rock fabric determines both magnitude and directional dependence of thermal degradation. Therefore, a comprehensive knowledge of fabric properties of a marble under investigation is indispensable for a conclusive and extensive damage characterization. There exists no simple relationship between the microstructure (e.g. grain shape) and the texture (lattice preferred orientation) of marble. Thus, before using a marble on a building or as a replacement, it is essential to examine its fabric properties.

Anisotropy is the rule rather than the exception for many marbles used as natural building stones and, thus, has to be considered for conservation and reconstruction purposes as well as for on-site inspections. Anisotropy of ultrasonic wave velocities and thermal expansion are closely linked to each other. High ultrasonic wave velocities concur with small thermal expansion coefficients and small ultrasonic wave velocities with high thermal expansion coefficients. Thus, ultrasonic wave velocity measurements under water-saturated conditions give indications for intrinsic thermal expansion behaviour of a marble under investigation. This is a topic for further research for on-site application.

Enhanced understanding and quantification of the effect of thermal degradation can be achieved using theoretical models. Model calculations give important information on both the magnitude of thermal degradation and the type of thermal degradation (i.e. the possible pore geometry).

Future studies may lead to a link between short-term observations, as they are presented here, and their long-term development. The basic question to be solved is whether obvious differences in the velocity reduction due to thermally induced microcracks after only one heating cycle influence the long-term stability of marble and to what extent. When this relationship is understood, a prognosis of the lifetime of marbles may be established in advance, i.e. before utilization of a specific marble, by a simple ultrasonic screening test.

We gratefully acknowledge the constructive reviews of J. Schön and M. Prasad. This work was supported by the German Science Foundation (Grants Si 438/10-2 and Si 438/13-1). We appreciate the help with ultrasonic wave velocity measurements of M. Masson and helpful discussions with B. Zinszner and help with sampling from G. Molli.

References

ARTS, R. J., RASOLOFOSAON, P. N. J. & ZINSZNER, B. 1996. Experimental and theoretical tools for characterizing anisotropy due to mechanical defects in rocks under varying pore and confining pressures. *In*: FJAER, E., HOLT, R. M., RATHORE, J. S. (eds) *Seismic Anisotropy* (Proceedings of the 6th International Workshop on Seismic Anisotropy). Society of Exploration Geophysicists, Tulsa, 384–432.

BARSOTTELLI, M., FRATINI, F., GIORGETTI, G., MANGANELLI DEL FA, C. & MOLLI, G. 1998. Microfabric and alteration in Carrara marble: a preliminary study. *Science and Technology for Cultural Heritage*, **7**(2), 115–126.

BIRCH, F. 1960. The velocity of compressional waves in rocks up to 10 kilobars, Part I. *Journal of Geophysical Research*, **65**, 1083–1102.

BOURBIÉ, T., COUSSY, O. & ZINSZNER, B. 1987. *Acoustics of Porous Media*. Gulf, Houston.

CHRISTENSEN, N. I. 1965. Compressional wave velocities in metmorphic rocks at pressures up to 10 kilobars. *Journal of Geophysical Research*, **70**, 6147–6164.

DANDEKAR, D. P. 1968. Variation in the elastic constants of calcite with pressure. *AGU Transactions*, **49**, 323 S.

DUERRAST, H., SIEGESMUND, S. & PRASAD, M. 1999. Schadensanalyse von Naturwerksteinen mittels Ultraschalldiagnostik: Möglichkeiten und Grenzen. *Zeitschrift der deutschen geologischen Gesellschaft*, **150**(2), 359–374.

FREDRICH, J. T. & WONG, T. F. 1986. Micromechanics of thermally induced cracking in three crustal rocks. *Journal of Geophysical Research*, **91**(B12), 12743–12746.

HASHIN, Z. 1981. Analysis of Composite Materials – A Survey. *Journal of Applied Mechanics*, **50**, 481–505.

KLEBER, W. 1959. *Einführung in die Kristallographie*. VEB Verlag Technik, Berlin.

KÖHLER, W. 1991. Untersuchungen zu Verwitterungsvorgängen an Carrara-Marmor in Potsdam-Sanssouci. *In*: MÖLLER, H.-H. (ed.) *Steinschäden – Steinkonservierung*. Kolloq. im Rahmen des Kulturabkommens zw. der BRD und der DDR, Dresden, 2–6 Okt. 1989. Berichte zu Forschung und Praxis in der Denkmalpflege in Deutschland, 2, Hannover, 50–54.

LEISS, B. & WEISS, T. 2000. Fabric anisotropy and its influence on physical weathering of different types of Carrara marbles. *Journal of Structural Geology*, **22**, 1737–1745.

O'CONNELL, R. J. & BUDIANSKY, B. 1974. Seismic velocities in dry and saturated cracked solids. *Journal of Geophysical Research*, **79**(35), 5412–5426.

RASOLOFOSAON, P. N. J., RABBEL, W., SIEGESMUND, S. & VOLLBRECHT, A. 2000. Characterization of

crack distribution: fabric analysis versus ultrasonic inversion. *Geophysical Journal International*, **141**, 413–424.

REUSS, A. 1929. Berechnung der Fliessgrenze von Mischkristallen auf Grund der Plastizitatsbedingung für Einkristalle. *Zeitschrift für Angewandte Mathematik und Mechanik*, **9**, 49–58.

RUEDRICH, J., WEISS, T. & SIEGESMUND, S. 2001. Deterioration characteristics of marbles from the Marmorpalais Potsdam (Germany): a compilation. *Zeitschrift der deutschen geologischen Gesellschaft*, **152**(2–4), 637–663.

SIEGESMUND, S. 1996. The significance of rock fabrics for the geological interpretation of geophysical anisotropies. *Geotektonische Forschungen*, **85**, 1–123.

SIEGESMUND, S., ULLEMEYER, K., WEISS, T. &. TSCHEGG, E. K. 2000. Physical weathering of marbles caused by anisotropic thermal expansion. *International Journal of Earth Sciences*, **89**, 170–182.

SNETHLAGE, R., ETTL., H. & SATTLER, L. 1999. Ultraschallmessungen an PMMA-getränkten Marmorskulpturen. *Zeitschrift der deutschen geologischen Gesellschaft*, **150**(2), 387–396.

TSCHEGG, E. K., WIDHALM, C. & EPPENSTEINER, W. 1999. Ursachen mangelnder Formbeständigkeit von Marmorplatten. *Zeitschrift der deutschen geologischen Gesellschaft*, **150**(2), 283–297.

VOIGT, W. 1928. *Lehrbuch der Krystallphysik*. B. G. Teubner, Leipzig.

WEISS, T., LEISS, B., OPPERMANN, H. & SIEGESMUND, S. 1999. Microfabric of fresh and weathered marbles: Implications and consequences for the reconstruction of the Marmorpalais Potsdam. *Zeitschrift der deutschen geologischen Gesellschaft*, **150**(2), 313–332.

WEISS, T., RASOLOFOSAON, P. N. J. & SIEGESMUND, S. 2001. Thermal microcracking in Carrara Marble. *Zeitschrift der deutschen geologischen Gesellschaft*, **152**(2–4), 621–636.

WEISS, T., SIEGESMUND, S. & FULLER, E. 2002. Thermal stresses and microcracking in calcite and dolomite marbles quantified by finite element modelling. *In*: SIEGESMUND, S., WEISS, T. & VOLLBRECHT, A. (eds) *Natural Stone, Weathering Phenomena, Conservation Strategies and Case Studies*. Geological Society, London, Special Publications.

WIDHALM, C., TSCHEGG, E., EPPENSTEINER, W. 1996. Anisotropic thermal expansion causes deformation of marble cladding. *Journal of Performance of Constructed Facilities, ASCE*, **10**, 5–10.

WYLLIE, M. R. J., GREGORY, A. R. & GARDNER, L. W. 1956. Elastic wave velocities in heterogeneous and porous media. *Geophysics*, **21**, 41–70.

WYLLIE, M. R. J., GREGORY, A. R. & GARDNER, G. H. F. 1958. An experimental investigation of factors affecting elastic wave velocities in porous media. *Geophysics*, **23**, 459–493.

ZEISIG, A., SIEGESMUND, S. & WEISS, T. 2002. Thermal expansion and its control on the durability of marbles. *In*: SIEGESMUND, S., WEISS, T. & VOLLBRECHT, A. (eds) *Natural Stone, Weathering Phenomena, Conservation Strategies and Case Studies*. Geological Society, London, Special Publications, **205**, 65–80.

Physico-mechanical and microstructural characteristics of historic and restoration mortars based on gypsum: current knowledge and perspective

BERNHARD MIDDENDORF

University Kassel, Faculty of Civil Engineering, Department of Structural Materials, Moenchebergstrasse 7, D-34125 Kassel, Germany (e-mail: midden@uni-kassel.de)

Abstract: The use of gypsum based mortar can be traced back over 4500 years. In Germany, in the vicinity of natural gypsum outcrops, in addition to lime mortars, calcium sulphate based mortars were widely used for joints in exterior walls of sacred buildings. There are several medieval buildings with well-preserved calcium sulphate-based mortars. The high water solubility of gypsum ($CaSO_4 \bullet 2H_2O$) is a disadvantage that makes it difficult in general to handle calcium sulphate based building materials in areas exposed to weathering. Physico-mechanical as well as mineralogical investigations of historic calcium sulphate based mortars have shown that long-term weathered mortars have a much denser microstructure, larger average grain sizes, and a higher compressive strength than laboratory prepared mortars. Porosity models of these mortars will be presented which are helpful to prepare calcium sulphate based mortars with a higher water resistance for restoration purposes. The reason for the change of crystal size and morphology as well as of porosity and strength can be explained by crystallization and recrystallization processes of these calcium sulphate based mortars, as a consequence of long-term weathering. Since it is obvious that crystal size and its distribution have an enormous effect on the weathering resistance, the development of mortars with comparable structural properties is of present interest. In current use are chemical additives which modify the morphology and size of gypsum crystals of set mortars. Another possibility to influence the weathering resistance is the addition of hydraulic and/or latent hydraulic admixtures.

The use of calcium sulphate based mortar has a long tradition. Famous examples are the Pyramid of Cheops, Towers of Jericho and buildings in Pompeii. In Germany, there are three centres for the historic use of calcium sulphate based building materials which are located close to natural gypsum occurrences (Bad Segeberg/Lüneburg, Harz Mountains, Franconia).

A difficulty for the restoration and the conservation of monuments is the missing information about the composition of the historic mortars, including the additives used. After the first half of the nineteenth century, knowledge of the production, preparation and properties of different calcium sulphate based materials ran out of fashion when hydraulic binders like Portland cement were introduced (Steinbrecher 1992). Modern calcium sulphate based building materials are always designed for interior use, due to the special properties of this material. General advantages of calcium sulphate based building materials are low production costs, quick and controllable setting behaviour, good adhesion to plaster and simplicity of application. However, its high solubility in water (2.6 g l^{-1} at 20°C) and low wet compressive strength restrict its use to the interior of buildings (Russel 1960). Nevertheless, mineralogical investigations of historic joint mortars from different brick buildings in northern Germany and Italy have shown that gypsum–anhydrite mortars with a small amount of lime have also been used on the outside of sacred buildings (Cioni 1991; Middendorf & Knöfel 1998a,b). A great part of these joints and of the masonry is still well preserved. Also, in central Germany some monuments were built with natural stone and gypsum based mortars. According to Steinbrecher (1992) this durability is due to its composition – binder and aggregate made out of the same kind of substance – as well as to its preparation with extremely small quantities of water. A water/binder value of less than 0.4 and a bulk density of 2.0 g cm^{-3} is mentioned for a historic gypsum mortar. If so, the use of additives was absolutely necessary, otherwise workability could not be achieved.

The aim of this study is the characterization and assessment of microstructure of calcium sulphate based mortars. For this purpose historic and laboratory mixed mortars were compared. The former are mortar samples from

From: SIEGESMUND, S., WEISS, T. & VOLLBRECHT, A. 2002. *Natural Stone, Weathering Phenomena, Conservation Strategies and Case Studies*. Geological Society, London, Special Publications, **205**, 165–176.
0305-8719/02/$15.00 © The Geological Society of London 2002.

different sacred buildings in Germany. The laboratory mixed mortars were prepared using industrial products. The properties of set mortars were investigated using optical and scanning electron microscopy (SEM), mercury intrusion porosimetry (MIP), and X-ray diffraction (XRD). Additionally the compressive strength was determined. Using special software, the MIP results allow both pore structure visualization and calculation of the grain size distribution of the set calcium sulphate based mortars.

Results of the studies of historic calcium sulphate based mortars (Rüth 1932; Lucas 1986, 1992; Middendorf 1994; Werner 1986) will form the basis to the development of mortars for restoration purposes. The focus is on the improvement of the water resistance of calcium sulphate based restoration mortars and on the establishment of guidelines for the development and industrial production of these mortars.

Properties of historic and restoration mortars

A reconnaissance study of about 100 different mortars sampled from various historic brick masonry buildings in northern Germany and the Netherlands (Middendorf 1994) has shown that the mortars can be divided into three groups. Based on their compositions one can distinguish between lime, lime gypsum and gypsum lime mortars. The former types of mortars were used in profane buildings and, to a lesser extent, in sacred buildings. According to this study, the use of gypsum lime mortars is restricted to sacred buildings. The advantage of calcium sulphate based mortars are the favourable setting behaviour, in addition to higher initial and final compressive strengths. Therefore, this type of mortar possesses suitable characteristics for the construction of complex building parts. This might also be the explanation for the use of gypsum mortars in the construction of arches and vaults of numerous sacred buildings in Tuscany, Italy (Cioni 1991). On the other hand, lime mortar was used for the construction of the foundation masonry walls.

A comparison of the compositions of the different mortar types has shown that the content of aggregates decreases with increasing gypsum content. The presence of aggregates within the gypsum-rich mortars is most likely the result of impurities within the raw materials (Middendorf 1994). The detected amount of aggregate is extremely low and, owing to the given content, does not appear to have an effect on the mechanical mortar properties.

Figure 1 shows the correlation between mortar composition and compressive strength, according to the German standard DIN 18555-9. Before measurement the samples were stored for at least 7 days at 20°C and 65% relative humidity. This approach provides reproducible and comparable compressive strength measurements. The compressive strength of lime mortars varies between 4 and 10 MPa, while gypsum–lime mortars have an average compressive strength of 22 MPa. These results show that the higher the gypsum content of the mortar, the higher the compressive strength.

Petrographic microscopy and X-ray diffraction phase analyses have shown that historic gypsum mortars still contain small amounts of anhydrite but no relict hemihydrate as binder phase. The

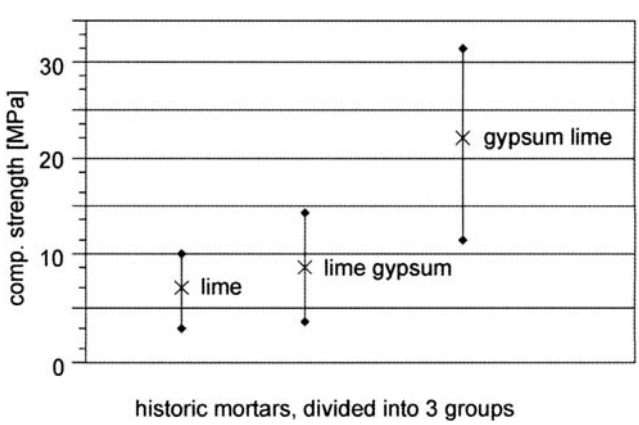

Fig. 1. Compressive strength (including standard deviation) of historic mortars.

presence of these small amounts of anhydrite indicates that high temperatures were reached during the manufacturing process. Given the fact that historic mortars had much more time to react, even anhydrite could be transformed to gypsum. However, for this reaction moisture is also needed which implies that, depending on the time and the availability of moisture, several solution and re-precipitation processes took place in historic mortars. This is also supported by studies of the microstructure using scanning electron microscopy. Historic gypsum mortars have a much denser microstructure than laboratory prepared restoration mortars based on calcium sulphate. These observations correspond well with the porosity of the set mortar and are in agreement with former studies (Middendorf & Budelmann 1995, 1998; Singh & Garg 1996). Figure 2b shows a SEM picture of a laboratory mixed mortar based on calcium sulphate hemihydrate. Idiomorphic crystals can be identified which are acicular parallel to the crystal c-axis. If one compares the microstructural observations with long-term weathered historic gypsum samples, one can observe that the gypsum crystals are not well shaped but rounded. The latter is a consequence of the penetration of water into the microstructure and of the dissolution and precipitation of the gypsum (Fig. 3). Taking the void space into account, it appears that this weathered historic sample must have a lower porosity than the laboratory mixed restoration sample.

In Figure 4 the microstructure of a commercially available gypsum based restoration mortar (Fig. 4a) and a historic mortar (Fig. 4b) are compared. From SEM photos it is obvious that there is a significant difference in crystal size and porosity. The gypsum crystals in the restoration mortars are much smaller than in historic mortars, because of less crystallization and recrystallization. In contrast, the microstructure of a long-term weathered historic mortar is built up with large and rounded crystals owing to accumulated crystallization processes.

It is well known that the water resistance and the compressive strength of calcium sulphate based mortars are functions of the porosity (Odler & Rößler 1989; Middendorf 1994). A low mortar porosity limits the water transport into the microstructure and, therefore, will provoke a higher water resistance. A dense microstructure with less porosity allows greater interlock and intergrowth of individual crystals and causes a higher compressive strength. This is confirmed by the results of this study (Fig. 1). The gypsum-rich mortars have both a lower total porosity and a higher compressive strength than lime-rich mortars. More detailed studies on the porosity (Fig. 5) have shown that the difference in total porosity is caused by the amount of capillary pores (10–10 000 nm), while the amount of both air voids and gel pores is similar. Compared to historic calcium sulphate based mortars, laboratory mixed calcium sulphate based restoration mortars have a much higher amount of capillary pores. The former have values in the range of 11 to 15 vol% while the values for the latter fall in the range of 20 to 35 vol%. These differences in porosity are best explained by alteration of the pristine microstructure of the historic mortars in countless wet–dry cycles during natural weathering. This caused dissolution and precipitation of gypsum. As a consequence, bigger gypsum crystals grow at the expense of smaller ones. This interpretation also corresponds with the results of the SEM investigations (Fig. 4).

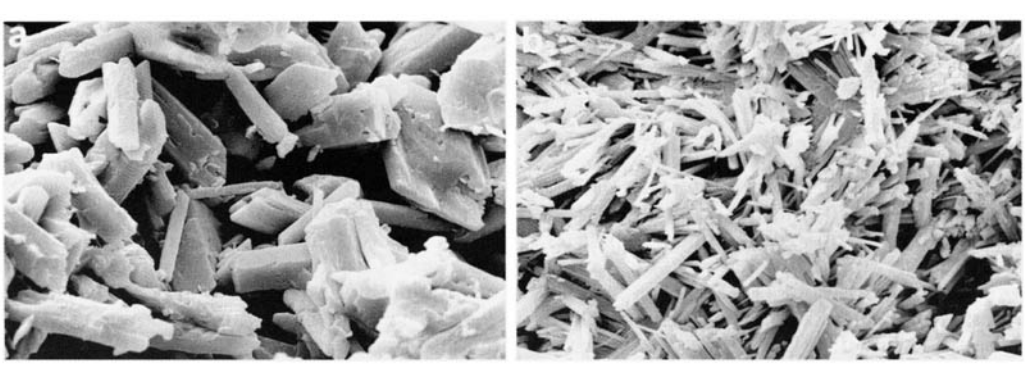

Fig. 2. Comparison of microstructures of gypsum-based building materials. SEM pictures, width 45 μm (each). (**a**) Gypsum with 0.1 wt% citric acid; (**b**) gypsum without admixtures.

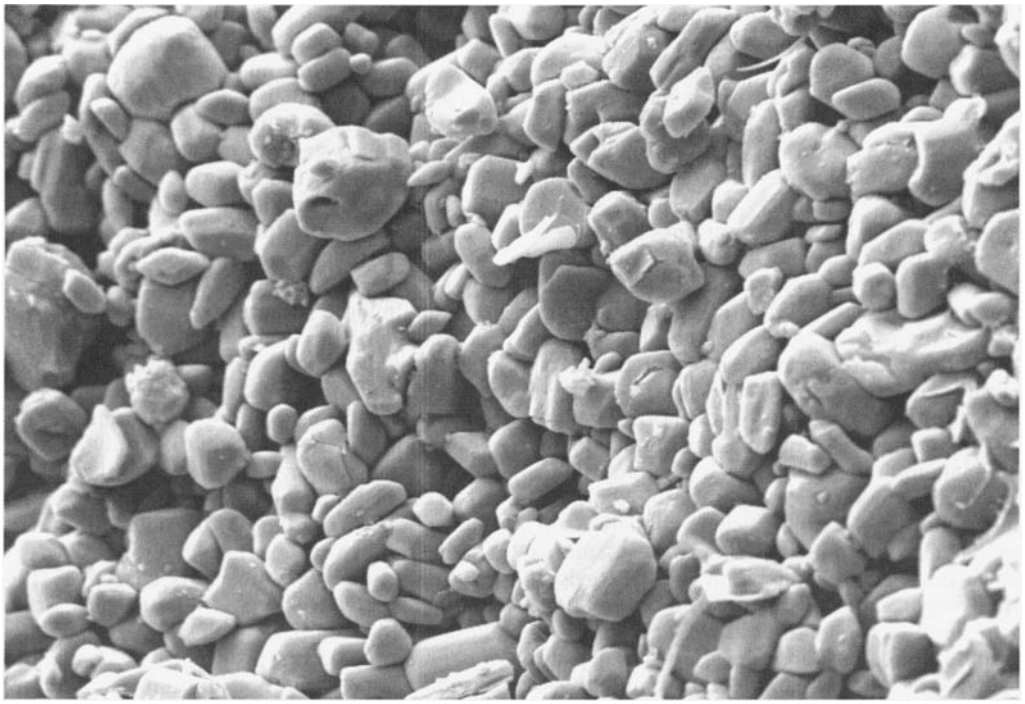

Fig. 3. SEM photos of a historic gypsum mortar. Width of picture 70 μm.

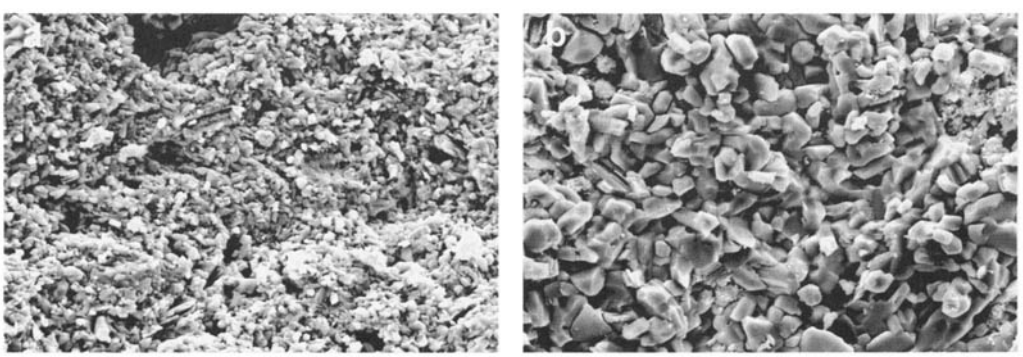

Fig. 4. SEM photos of the microstructures of a restoration (**a**) and a historic mortar (**b**). Width of pictures 145 μm (each).

Using the data of the MIP investigations, the pore structure of solid materials can be modelled. Figure 6 illustrates an example of computerized pore structure modelling. Here an externally applied historic gypsum mortar with a total porosity of 13 vol% is shown. The pores are calculated as cubes (grey) and the throats as cylinders (black). Figure 6a shows the calculation of random structure, whereas in Figure 6b: a view into the pore structure is presented. In Figure 7 a comparison of the modelled pore structures is presented. Figure 7a shows the result of a calculated pore structure of a historic gypsum mortar with a total porosity of 19.1 vol%. Figure 7b presents a calculated pore structure of a calcium sulphate based restoration mortar with a total porosity of 28.3 vol%. The latter has not only a lower porosity but also smaller pores.

In addition to the visualization of pore structures this modelling tool can be used to calculate microstructure related properties, like

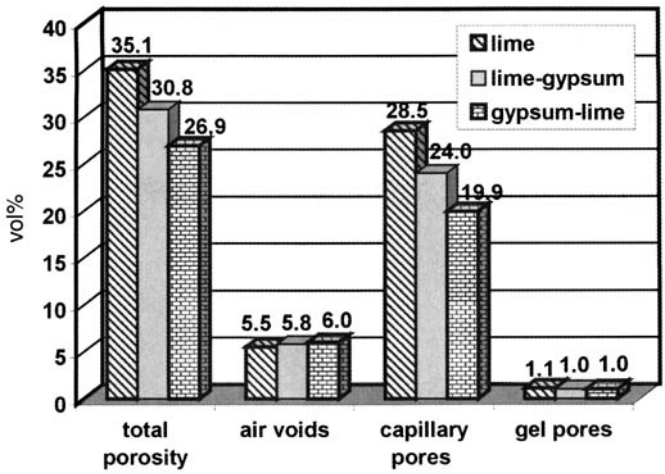

Fig. 5. Total porosity and pore size distribution of historic mortars.

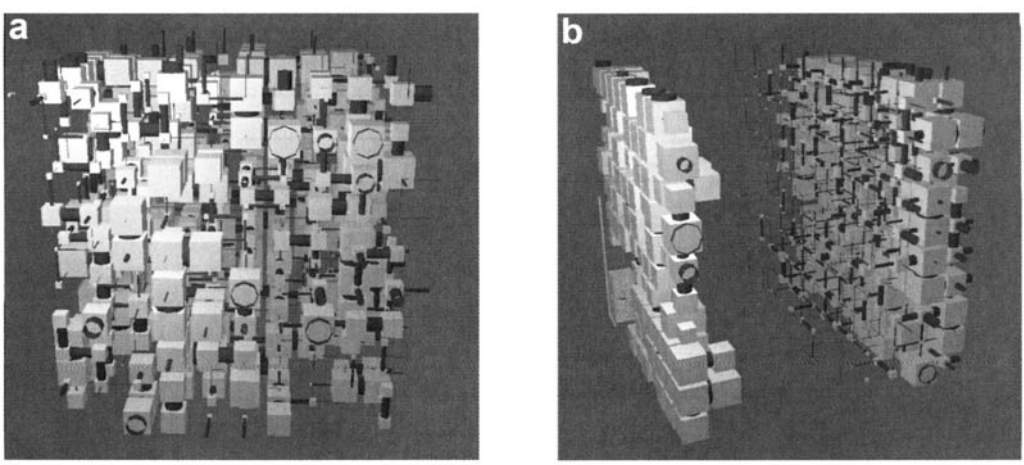

Fig. 6. Modelled pore structure of a historic gypsum mortar. Total porosity 13 vol%; length of cube approximately 2500 μm. (**a**) Random structure view; (**b**) vertical view.

capillary water suction and water and vapour permeabilities. By knowing the detailed pore structure, it is also possible to calculate the grain size distribution of the solid state materials. This kind of modelling allows the particle size distribution of mortars to be determined. For the investigations presented here such calculations have been done with the modelled pore structure data of Figure 7. The distribution results are shown in Figures 8 and 9. In Figure 8 the particle size distribution of the restoration mortar is depicted. There the x-axis represents the particle sizes from 0 to 200 μm. It can be observed that the particle size follows, in general, a Gaussian distribution in the above-mentioned range. The particle size distribution of the historic mortar is shown in Figure 9. It can easily be observed that the particle sizes are generally larger than for the restoration mortar. These modelled crystal size distributions support the results of the SEM investigations.

Summarizing it can be said that historic gypsum mortars have a much more dense microstructure combined with larger crystals. This enlarging of the crystals is the result of recrystallization and crystallization processes caused by wet–dry cycles which take place during long-term weathering.

The dense structure, combined with larger crystals, must be responsible for the obvious enhanced water resistance of historic calcium

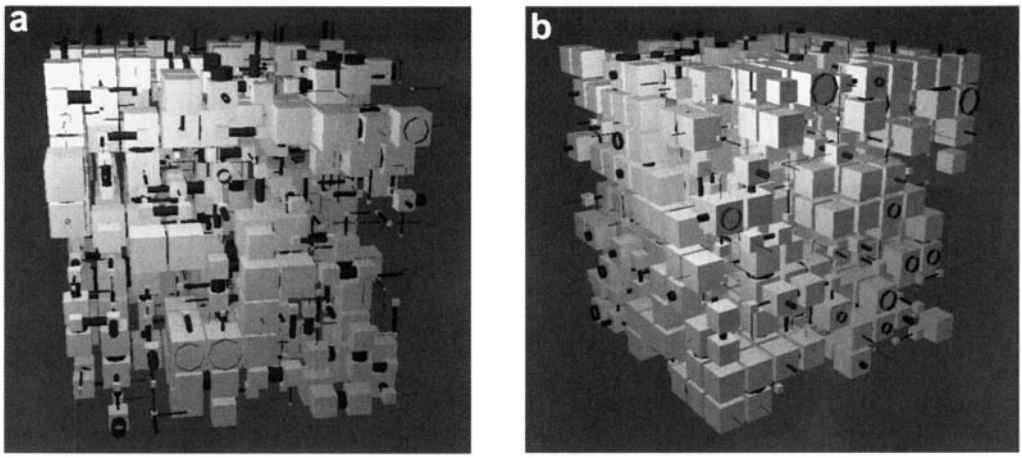

Fig. 7. Comparison of modelled pore structures. Length of cubes approximately 1000 μm. (**a**) Historic gypsum mortar, total porosity 19.1 vol%; (**b**) restoration mortar after 9 months of weathering, total porosity 28.3 vol%.

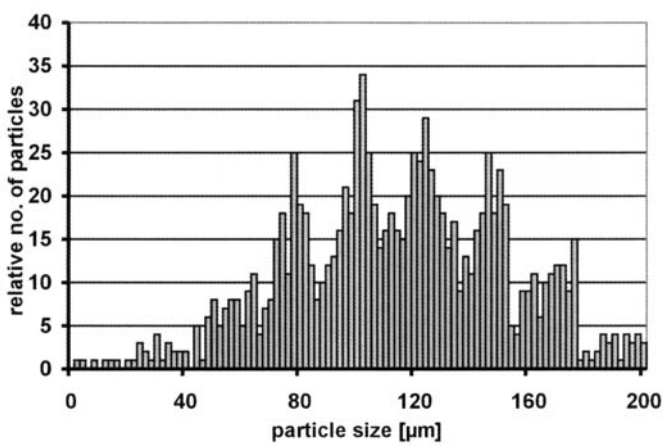

Fig. 8. Modelled particle size distribution of a restoration mortar based on gypsum (Fig. 4). The x-axis extends over the range 0 to 200 μm.

sulphate based mortars. This natural process is extremely slow. But for the development of water-resistant restoration mortars – based on calcium sulphate – special additives and admixtures can be investigated to enlarge the gypsum crystals in order to increase the density of the the microstructure from the beginning.

Water-resistant calcium sulphate based mortars in prospect

There are numerous publications and patents dealing with the increase of water resistance of calcium sulphate based building materials (e.g. Matyszweski *et al.* 1980; Steinbach & Rieder 1985; Balzer 1991; Sellers *et al.* 1991; Stanzinger *et al.* 1991; Gerhardinger *et al.* 1994; Middendorf 1994). There are several different approaches. One of them makes use of additives, in order to increase the resistance to the dissolving effect of water. These additives mostly have a water-proving and plasticizing effect and, moreover, improve the mechanical properties of the building materials. In Matyszweski *et al.* (1980) tests are described in which the addition of fine pulverized calcium lingosulphonate compounds, a macromolecular, hydrophilic and capillary active substance, reduces the water absorption capacity of gypsum based building materials to 1%. Other publications (Steinbach & Rieder 1985; Balzer 1991; Sellers *et al.* 1991; Stanzinger *et al.* 1991;

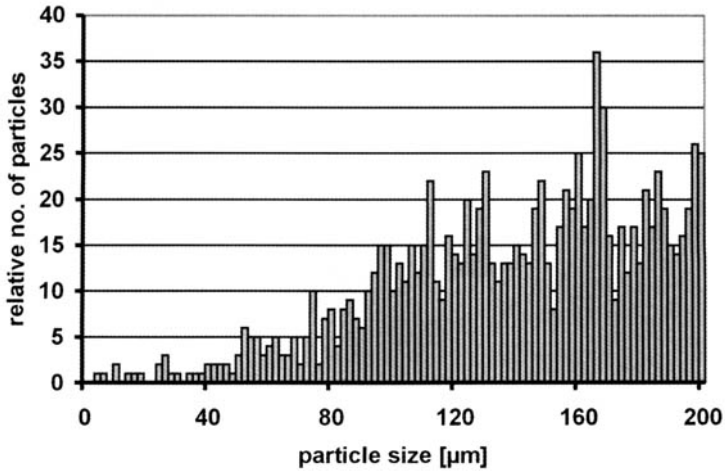

Fig. 9. Modelled particle size distribution of a historic gypsum mortar (Fig. 4). The x-axis extends over the range 0 to 200 µm.

Gerhardinger *et al.* 1994) describe polymethyl hydrogen siloxane, alkylhydrogen polysiloxane etc., which provide hydrophobing qualities to calcium sulphate based materials.

Another approach to increase the water resistance of calcium sulphate based building materials turns to hydraulic, latent hydraulic and pozzolanic admixtures. Apart from reactive microsilica (Balzer 1991; Middendorf 1994), cement rich in alumina (Kassautzki 1987) and low in aluminate content (Dondl 1972; Lelong 1972; Psader & Hermann 1987; Berneth *et al.* 1990), trass (Balzer 1991; Middendorf 1994), fly ash (Koschany *et al.* 1969; Singh & Garg 1992; Middendorf 1994) and granulated blast furnace slag sand (Koschany *et al.* 1969, Koslowski *et al.* 1988; Singh & Garg 1995) are also used. The strength of the microstructure is caused by the crystallization of calcium silicate-hydrate (CSH)- and calcium-aluminate-hydrate (CAH)-phases and partly by ettringite. Conclusive models for the explanation of the reaction mechanisms of an increased water resistance are only beginning to emerge.

In the following, some basic possibilities for increasing the water resistance of calcium sulphate based building materials, that have been investigated in our laboratories, will be discussed.

Structure modification with admixtures and/or additives

Additives influence the morphology and habit of growing gypsum crystals resulting in microstructures with reduced capillary porosity and increased water resistance. Adding citric acid as a setting retarder (Schmidt 1981; Koslowski 1983; Middendorf *et al.* 1992; Middendorf & Budelmann 1995) is common practice. Directly after mixing of the calcium sulphate based building material, already very small amounts of citric acid cause a selective adsorption of the calcium citrate on crystal nucleii and on the growing dihydrate crystals with inhibitory effects on the speed of crystal growth and on the development of dihydrate crystals (Koslowski 1983). Owing to partial blocking of crystal steps and crystal kinks, the number of growing dihydrate crystals is reduced, which results in a change of the morphology and the size of the crystals, as can also be seen from Figure 2. Using citric acid as a retarder produces gypsum based mortars with a higher water resistance (Middendorf 1994). According to current knowledge this is due to the reduction of the total surface of the gypsum crystals and to the preferred growth of less reactive crystal faces. If we know in detail the working mechanisms of additives on crystal growth, the microstructure of calcium sulphate based building materials could be nearly 'tailored' for every desired use. That would be real product design.

Another possibility to make the structure more dense, to decrease the capillary porosity and to increase the water resistance, is to put additional finely milled reaction-inert admixtures into the mixture (e.g. finely milled limestone). As an alternative one can also use microsilica. The latter has the advantage of its

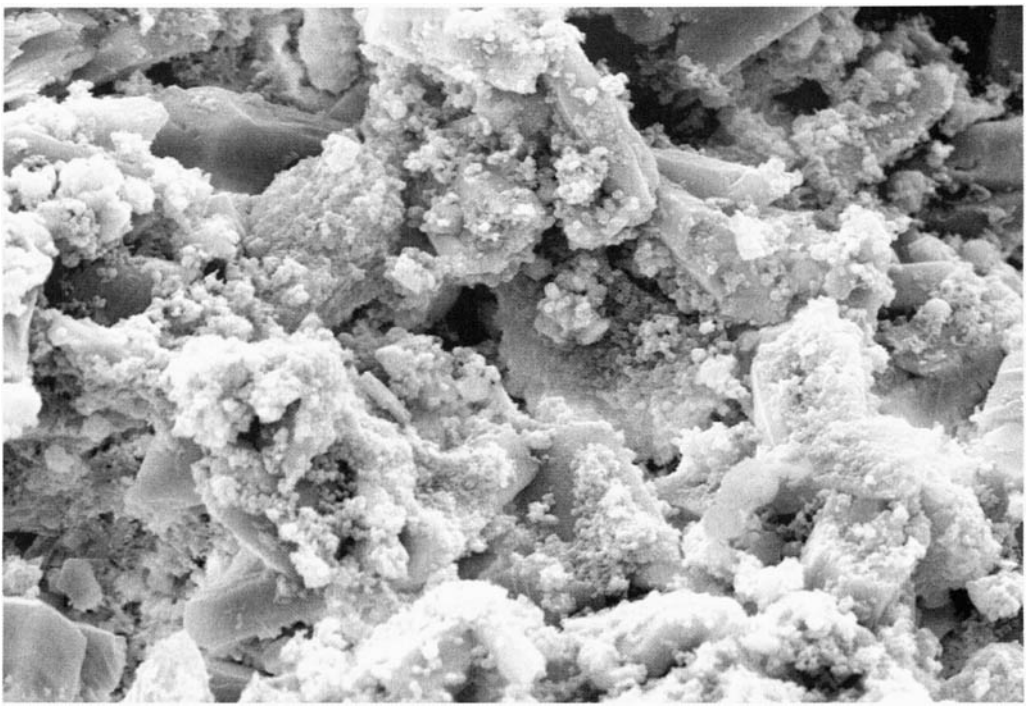

Fig. 10. SEM picture of a calcium sulphate based building material with added microsilica. The spandrils between the gypsum crystals are filled with microsilica, which results in a reduction of capillary porosity. Width of picture 45 μm.

additional pozzolanic reaction if defined amounts of calcium hydroxide are added to the binders containing calcium sulphate. Figure 10 shows an SEM picture of calcium sulphate based building material to which microsilica has been added; here the fine distribution of microsilica reducing porosity can be seen in the spandrils between the gypsum crystals.

Through combined addition of additives with similar effects and of pore-filling admixtures, a very dense calcium sulphate based building material, with a lower porosity, and with a high water resistance can be produced. Apart from high moisture resistance, this building material also has a high mechanical strength; however, it needs a long setting time which has to be considered when using it.

Defined development of water resistant phases by using hydraulic, latent-hydraulic and/or pozzolanic admixtures

Through defined addition of hydraulic and latent-hydraulic and/or pozzolanic admixtures, the growth of less water-soluble phases (e.g. CSH, CAH) having structure-reinforcing properties can be promoted. In publications and patents (Singh & Garg 1995; Middendorf & Budelmann 1998) water-resistant gypsum binders based on hemihydrate, finely milled blast furnace slag sand and small amounts of Portland cement (OPC) are described. During hydration, in addition to dihydrate, CSH- and CAH-phases and primary ettringites also develop from these mixtures which decreases the porosity and increases the strength. In Figure 11 such water-insoluble and structure-reinforcing newly developed phases can be seen.

Experiments with hydraulic (special cements) and pozzolanic admixtures can also result in the development of CSH- and CAH-phases and primarily developed ettringites, depending on the right dosage (Middendorf & Budelmann 1998). However, the reaction processes involved are not yet sufficiently known. The addition of such admixtures promises success, but with regard to controlled reaction processes it has to be further investigated.

Fig. 11. SEM scan of a calcium sulphate based building material with finely milled blast furnace slag sand. The arrows indicate the newly developed, water-insoluble and structure-reinforcing phases. Width of picture 45 μm.

Inherent passivation of surfaces through recrystallization processes

From preservation of brick monuments it is known that masonry made of gypsum mortar has shown resistance to weather attack, although dihydrate can be highly soluble in water. As the reproduction of historic building material is nearly impossible, because, normally, the recipes are not sufficiently known, nor are the original storage places available, it has been attempted to develop water-resistant calcium sulphate based mortar for exterior masonry, based on industrial building materials. Mortars from α-hemihydrate, β-hemihydrate and hydrated white lime as binders and limestone powder and fine quartz sand as aggregates correspond fairly well to demands, as has been confirmed by building investigations over many years (Middendorf *et al.* 1994; Middendorf 1994). Water resistance is developed because gypsum lime mortar can close pores and cracks by moisture through recrystallization processes. This can be called autogenous healing or an inherent passivation of the surface. As outlined in Figure 12, the gypsum lime mortar is partly dissolved by water but, owing to the amount of lime and aggregate, they are not considerably worn out. The biggest part of the gypsum, having been dissolved partly by water, is absorbed via capillary pores into the microstructure and precipitates there again. This process causes a reduction of both the amount of capillary pores and the total porosity resulting in decreasing water absorption capacity. Both calcite and aggregate have been enriched on the weathered joint surface, because they are less soluble than gypsum (Figure 13). In this way, the joint mortar shelters the gypsum-rich part of the inner joint. In this case gypsum lime mortars are no longer susceptible to moisture reduction of mechanical strength.

Summary

Compared to calcium sulphate based restoration mortars, historic gypsum mortars have a much more dense microstructure, combined with a higher average grain size of gypsum crystals. This is caused by recrystallization and crystallization processes induced by wet–dry cycles during the weathering processes. The dense

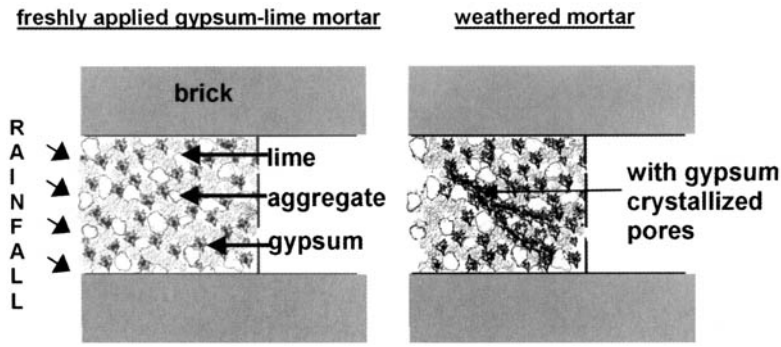

Fig. 12. Principle of the inherent passivation of gypsum lime mortars. The right-hand part of the figure illustrates the dissolution and reprecipitation of gypsum causing a denser microstructure.

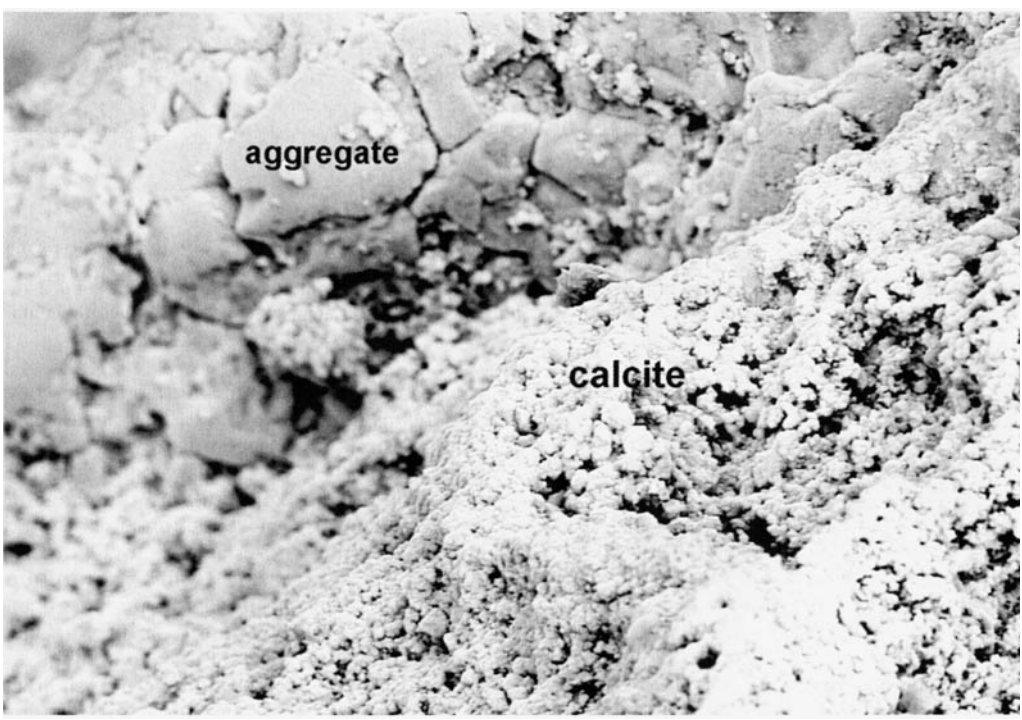

Fig. 13. SEM picture of a surface of a long-term weathered gypsum lime mortar. Only the phases calcite and aggregate can be observed on the surface. Width of the picture 200 μm.

structure, in combination with larger crystals, must be responsible for the high water resistance of historic calcium sulphate based mortars.

There are a number of approaches to increase the water resistance of calcium sulphate based mortars. One approach is the inherent surface passivation due to the use of complex gypsum lime mortars which provokes dissolution and precipitation of gypsum, causing a denser microstructure and finally a lower porosity. Additives also can influence the water resistance of gypsum based materials, since they affect the morphology of the gypsum crystals, the grain size distribution and the total porosity. Inert pulverized admixtures, such as microsilica, cause a blocking of the pore space which reduces capillary porosity. The latter diminishes the water absorption capacity and increases the

water resistance. Adding specific hydraulic, latent-hydraulic and/or pozzolanic admixtures to the calcium sulphate based mortars can initiate the growth of water-insoluble phases which, in turn, blocks pore space and strengthens the structure.

The results provide useful information on the development of water-resistant calcium sulphate based mortars for restoration purposes. A more fundamental study on the combined effect of additives and admixtures is necessary for a reproducible production of this type of mortar with tailored properties in water resistance that resemble historic mortars.

Constructive and thorough reviews by C. Vellmer greatly improved the original manuscript and helped to clarify thoughts. I am also grateful to M. Gehrke for laboratory support. Part of this work was funded by AiF and DFG research grants.

References

BALZER, M. 1991. *Untersuchungen zur Steigerung der Wasserfestigkeit von Gipsbindern*. PhD Thesis, Technical University Clausthal, Germany.

BERNETH, C.-P., POCH, W. & RUF, H. 1990. *Hydraulisches Bindemittel und seine Verwendung*. Europäische Patentanmeldung 0 427064 A2.

CIONI, P. 1991. Small thickness brick vaults in Tuscany: theirs characteristics and consolidation. *Proceedings of the 9th International Brick/Block Masonry Conference*, Berlin, Germany, Vol. 3, 1523–1530.

DONDL, V. 1972. *Verfahren zur Verbesserung von Mörtelmassen*. Patent-Offenlegungsschrift 2 222486.

GERHARDINGER, D., MAYER, H. & MITTERMEIER, J. 1994. *Verfahren zur wasserabweisenden Imprägnierung von Gips*. Patent-Offenlegungsschrift DE 44 19257 A1.

KASSAUTZKI, M. 1987. *Verfahren zur Herstellung eines Baustoffes und Bindemittels mit erhöhter Wasserbeständigkeit*. Patent-Offenlegungsschrift DE 37 43467 A1.

KOSCHANY, R., FIETSCH, G. & VOGT, H. 1969. *Verfahren zur Herstellung von Erzeugnissen aus CaSO4-Bindemitteln, alkalisch reagierenden Bindemitteln und Industrieanfallstoffen*. Patentschrift DE 79 948.

KOSLOWSKI, T. 1983. *Zitronensäure – Ein Verzögerer für Gips*. PhD Thesis, RWTH Aachen, Germany.

KOSLOWSKI, T., LUDWIG, U. & FRÖHLICH, A. 1988. *Verfahren zur Herstellung eines nach dem Anmachen mit Wasser schnellerstarrenden hydraulischen Bindemittels mit definierter Wasserfestigkeit der daraus hergestellten erhärteten Masse*. Patenschrift DE 38 43625 C2.

LELONG, B. 1972. *Schnellerhärtende Gussmischung auf Gipsbasis mit hoher Dichte und verlängerter Gießbarkeitsdauer*. Patent-Offenlegungsschrift 2 222490.

LUCAS, H. G. 1986. Gipsstein und Gipsmörtel als Baustoffe im alten Windsheim. *Der Stuckateur*, **8**, 27–32.

LUCAS, H. G. 1992. *Gips als historischer Außenbaustoff in der Windsheimer Bucht – Verbreitung, Gewinnung und Beständigkeit im Vergleich zu anderen Natursteinwerken*. PhD Thesis, RWTH Aachen, Germany.

MATYSZWESKI, T., BURDZINSKA, T. & SALADAJCZYK, A. 1980. Modifizierung der Eigenschaften des Chemiegipses mit Hilfe verschiedener Zusatzmittel. *TIZ-Fachberichte Rohstoff-Engineering*, **2**, 89–91.

MIDDENDORF, B. 1994. *Charakterisierung historischer Mörtel aus Ziegelmauerwerk und Entwicklung von wasserresistenten Fugenmörteln auf Gipsbasis*. PhD Thesis, University Siegen, Germany.

MIDDENDORF, B. & BUDELMANN, H. 1995. Effects of different additives on microstructural developments in gypsum based materials. *Proceedings of the Fifth Euroseminar on Microscopy Applied to Building Materials*, Leuven, Belgium, 40–49.

MIDDENDORF, B. & BUDELMANN, H. 1998. Evaluation and optimisation of calciumsulfate based flooring plaster with regards to water resistance. *Proceedings of the 20th International Conference on Cement Microscopy*, USA, 246–258.

MIDDENDORF, B. & KNÖFEL, D. 1998*a*. Gypsum and lime mortars of historic German brick buildings: analytical results as well as requirements for adapted restoration material. *In*: BAER, N. S. *et al.* (eds) *Conservation of Historic Brick Structures: Case Studies and Reports of Research*. Donhead Publishing, Dorset, England, 197–208.

MIDDENDORF, B. & KNÖFEL, D. 1998*b*. Characterisation of historic mortars from secular and religious buildings in Germany and the Netherlands. *In*: BAER, N. S. *et al.* (eds) *Conservation of Historic Brick Structures: Case Studies and Reports of Research*. Donhead Publishing, Dorset, England, 180– 196.

MIDDENDORF, B., BÖTTGER, K. G. & KNÖFEL, D. 1992. REM-Untersuchungen der Einflüsseverschiedener Verzögerer und Zusatzmittel auf die Bindemittelausbildung in Zement- bzw. *Gipsmörtelmischungen. Beiträge Elektronenmikroskopische Direktabbildungen von Oberflächen*, **25**, 215–222.

MIDDENDORF, B., ZÖLLER, A. & KNÖFEL, D. 1994. Gips-Kalk-Fugenmörtel für die Anwendung im Außenbereich historischer Ziegelgebäude. *12. Internationale Baustofftagung ibausil, Weimar*, Germany, Vol. 2, 31–40.

ODLER, I. & RÖßLER, M. 1989. Zusammenhänge zwischen Porengefüge und Festigkeit abgebundener Gipspasten, Teil II: Einfluss chemischer Zusätze. *Zement-Kalk-Gips*, **8**, 419–424.

PSADER, J. & HERMANN, G. 1987. *Verwendung von Gipsbaustoffen als Klebe-bzw. Verfugmasse*. Patent-Offenlegungsschrift DE 37 42913 A1.

RUSSEL, J. J. 1960. Einfluss des Festigkeitsgehaltes auf die Druckfestigkeit kleiner Gipswürfel. *Zement-Kalk-Gips*, **8**, 345–351.

RÜTH, G. 1932. Schäden, Schutz und Sicherungsmaßnahmen bei Bauten mit Gipsmörtel. *Der Bautenschutz*, **1 & 3**, 1932.

SCHMIDT, P. 1981. Die Anwendung von Citronensäure und deren Salze als Abbindeverzögerer für Gips – Eine Literaturübersicht. *Tonindustrie Zeitung*, **105**(1), 27–30.

SELLERS, D., ALTMANN, F. A. & RICHARDS, T. W. 1991. *Verfahren zur Herstellung eines wasserbeständigen Gipsgemisches*. Patent-Offenlegungsschrift DE 41 24892 A1.

SINGH, M. & GARG, M. 1992. Investigation of a durable gypsum binder for building materials. *Construction & Building Materials*, **6**, 52–56.

SINGH, M. & GARG, M. 1995. Activation of gypsum anhydrite-slag mixtures. *Cement and Concrete Research*, **25**, 332–338.

SINGH, M. & GARG, M. 1996. Relationship between mechanical properties and porosity of water-resistant gypsum binder. *Cement and Concrete Research*, **26**, 449–456.

STANZINGER, E., NEUNER, K.-H., WINTZHEIMER, E. & MARTIN, J. 1991. *Verfahren zur Herstellung von wasserabweisenden porösen Gipsformkörpern*. Patent-Offenlegungsschrift, DE 41 28424 A1.

STEINBACH, H.-H. & RIEDER, M. 1985. *Verfahren zur Herstellung wasserabweisender poröser Formkörper aus Gips*. European Patent 0 171018 B1.

STEINBRECHER, M. 1992. Gipsestrich und -mörtel: Alte Techniken wiederbeleben. *Bausubstanz*, **10**, 59–61.

WERNER, A. 1986. Sanierung von Kirchenbauten an der Elbe. *Bausubstanz*, **5**, 36–40.

WETHMAR, H. & BAIER, H. 1988. *Wasserfester Gips – Gipszement*. Patent-Offenlegungsschrift, DE 38 31671 A1.

Impact of endolithic biofilms on carbonate rock surfaces

WOLFHART POHL & JÜRGEN SCHNEIDER

Geowissenschaftliches Zentrum der Universität Göttingen Goldschmidtstrasse 3, D-37073 Göttingen, Germany (e-mail: jschnei@gwdg.de)

Abstract: Almost all natural carbonate rock surfaces as well as carbonate building stones are ubiquitously colonized by micro-organisms such as cyanobacteria, chlorophyceae, fungi and lichens. This colonization occurs endolithically, mostly euendolithically, through active penetration into the rock. Freshly exposed surfaces, such as in glacial forelands of the Dachstein Mountains (Austria) show mature, fully differentiated endolithic colonization after only 15 years of atmospheric exposure. After a time period of 100 to 150 years, coverage of carbonate rock surfaces by endolithic biofilms is almost complete.

Most endolithic biofilms (lichens) show similar internal architecture. Under a residual, protective carbonate rock layer are photobiontic micro-organisms. They occupy a well defined zone between 150 to 300 μm beneath the rock surface. In this zone up to 60% of the rock substrate is replaced by microbial biomass. Within the photobiontic layer a constant recycling of cells takes place, where bacteria act as decomposers. Deeper beneath the substrate develops an initially dense, then progressively thinning hyphal network of the mycobiont (i.e. a fungus).

Significant differences in amounts and distribution of biomass were observed and quantified which are regional and climatic, but also local and surface age-controlled. Temperature, irradiation and water availability are presumed to be the primary factors. Evidence for a biogenic mechanical surface destabilization (grain loss, desquamation, exfoliation) as observed on siliciclastic rocks, was not found on natural carbonate rock surfaces.

The 'life strategy' of endolithic biofilms is adapted to conserve their substrates. It commences with quick emplacement within the rock, initially causing some material loss. However, as soon as the endolithic biofilm is established, approaching an equilibrium with the climatic and ecological conditions, it behaves essentially conservatively: it does not continue with growth increments or habitat enlargement.

This adaptation of euendolithic biofilms has a generally *more protective* than destructive impact on their carbonate rock substrates. These observations are important for a better understanding of weathering and deterioration processes, applicable to protection policies and maintenance of cultural monuments.

Observations in natural environments are essential for a better understanding of weathering and deterioration processes of stones, especially of carbonate rocks (see review by Warscheid & Braams 2000). Carbonate rock substrates in central Europe are colonized almost ubiquitously by biofilms formed by epilithic, crypto-, chasmo- and euendolithic micro-organisms (*sensu* Golubic *et al.* 1980; Fig. 1). Depending on exposure, these lithobiontic communities may form symbiotic associations (lichens) or consist of non-lichenized cyanobacteria, green algae or fungi. This paper deals mainly with the endolithic ecological niche on carbonate rock substrates, commonly occupied by euendolithic micro-organisms, which often form interconnected layers beneath the rock surface. Thus the term 'endolithic biofilms' is used to characterize the principal microbial assemblages on and within carbonate rock surfaces and to discuss their survival strategies. On the microscopic scale, endolithic biofilms create new internal surfaces near the rock surface, which modify the microenvironmental conditions quantitatively as well as qualitatively. Thus the colonized rock is a far more complex system than a simple inorganic rock face. Three morphological and functional surface interfaces can be recognized: (1) the original 'inorganic' surface between carbonate rock and atmosphere; (2) the interface between lithobiontic organisms (lichens, fungi, bacteria, cyanobacteria, green algae) and the atmosphere, where the principal interactive processes between organisms and atmospheric agents take place (water and nutrient uptake, photosynthesis and respiration); (3) the interface between organisms and carbonate substrate, where the interactions between lithobionts and the substrate take place (substrate dissolution, nutrient transport and accumulation and remineralization).

The overall physical and chemical processes on rock surfaces are strongly influenced by microbial presence. Microbial metabolic

From: SIEGESMUND, S., WEISS, T. & VOLLBRECHT, A. 2002. *Natural Stone, Weathering Phenomena, Conservation Strategies and Case Studies*. Geological Society, London, Special Publications, **205**, 177–194.
0305-8719/02/$15.00 © The Geological Society of London 2002.

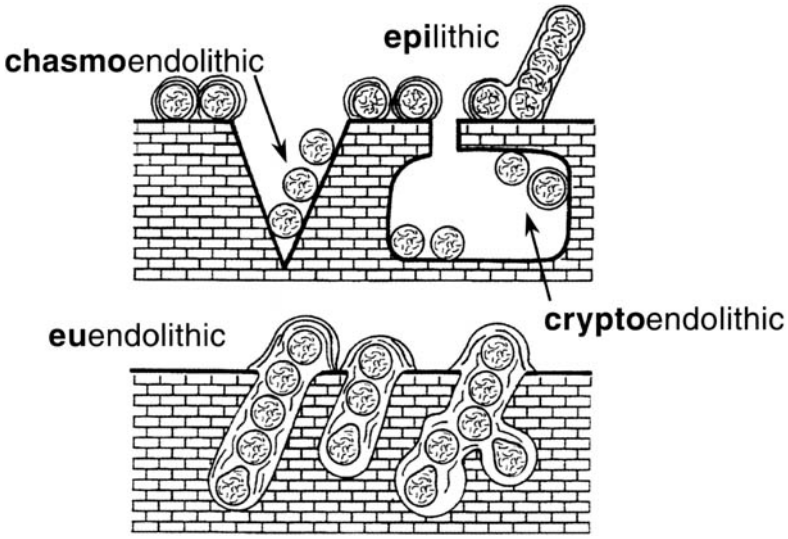

Fig. 1. Classification of ecological niches of lithobiontic micro-organisms: Whereas chasmo- and cryptoendolithic lithobionts colonize pre-existing fissures and cavities, euendoliths actively create their niche by dissolution of the rock substratum (after Golubic *et al.* 1980).

processes as well as their products can have catalytic, stimulating but also repressive effects on surface reactions. The scope of the reactions and their kinetics on inorganic surfaces will differ markedly from those on microbially colonized ones (Banfield *et al.* 1998). The cumulative effect of microbial metabolic activities on globally important biogeochemical changes in the course of the Earth's history has been widely recognized.

Isotopic evidence (Mojzsis *et al.* 1996) and trace fossils (Schopf & Packer 1987; Schopf 1994) indicate the presence of marine microbial life and an interaction between microbes and minerals as early as 3.55–3.85 Ga BP. The microbial colonization of terrestrial systems – and thus the interaction of microbes and soil minerals – might have started between 2.4 and 1.2 Ga BP with cyanobacteria as protagonists (Campbell 1979; Golubic & Campbell 1979; Margulis & Sagan 1999). Despite the rapid evolution of life which created ever more complex and specialized forms, simple but efficient micro-organisms continue to influence and control various, globally relevant ecosystems through biogeochemical actions (Barker *et al.* 1997). Areas where the role of micro-organisms is particularly obvious are: (1) soil formation and plant nutrition; (2) groundwater geochemistry; (3) climatic impact of mineral weathering (on a geological time scale); (4) durability of building materials and stones; and (5) long term stability of geotechnical deposits for radioactive and toxic waste.

Global geochemical cycles are often microbially controlled. The fluxes and distribution of elements such as carbon, sulphur, nitrogen, phosphorus and iron are to a large extent mediated by single-cell organisms (Krumbein 1983). Various effects of micro-organisms on mineral substrates can be observed: (1) physical degradation of materials can cause a drastic enlargement of reactive surfaces; (2) the catalytic effect of microbial metabolic activities can multiply reaction rates enormously, e.g. by a factor of up to 10^6 for the oxidation of Fe^{2+} (Krumbein 1983); (3) changes in pH, e.g. by production of organic acids, can enhance mineral solubilities (Welch & Ullmann 1992); (4) polysaccharides, proteins and organic acids can chemically interact with mineral surfaces (Barker & Banfield 1996; Welch *et al.* 1999); (5) nutritive elements such as K, P and Fe, but also a variety of economically important elements, notably Cu, can be selectively leached from minerals (Pohl 2000). Hinsinger & Jaillard (1993) could demonstrate that micro-organisms often act as a sink for physiologically important elements, thus shifting kinetic equilibria and enhancing mobility for various elements.

The next question to be asked is: in which direction and at what time scale are the rocky substrates affected? Much evidence, and hence extrapolations, is biased towards the conclusion

that lithobiontic organisms and especially euendoliths always exert a negative, i.e. overall destructive, influence on carbonate rocks. This is especially true in the presence of grazing animals (Schneider 1976; Schneider & Le Campion-Alsumard 1999). However, recent work by Silva *et al.* (1999) and Lee & Parsons (1999) suggests that epilithic lichens may exert an overall protective effect on silicate rocks. Le Metayer *et al.* (1999) even propose to slow down the weathering or repair the existing damage by inoculating rock surfaces with carbonate-depositing bacteria.

This paper presents a comparative study of subaerial, microbially colonized carbonate rock surfaces in nature, from climatically, morphologically and geographically different sites. The principal controlling factors affecting the relationship of endoliths to their substrate are reviewed, regionally compared and correlated. Computerized image analysis was applied to detect and quantify endolithic biomass in carbonate rock substrates. Monitored and dated glacial retreat sites provided the opportunity to time the colonization and long-term development of endolithic microbial communities.

Materials and methods

Fieldwork and sample preparation

About 65 specimens were collected from carbonate rock surfaces from localities between the relatively humid Northern Calcareous Alps and the more arid Mediterranean–Maritime Alps. The aim of this widespread sampling was to cover an extensive range of different sites with wide variety of exposures, altitudes, species compositions and climatic conditions. At one locality, the glacial forelands of Schneeloch Glacier and Grosser Gosau Glacier (Dachstein Mountains, Austria), a series of specimens with known time of atmospheric exposure were collected. The timing was deduced from the recorded glacial retreat for the last 100 years. The second set of samples from arid regions was gathered in the Montagne St. Victoire from Provence (southern France).

Samples were taken with hammer and chisel without damaging the endolithic biofilms. They were individually packed in paper bags and stored for several weeks in dry and dark conditions and at room temperature until further treatment.

For optical investigations thin sections slightly more than 30 μm thick were prepared. For investigations by electron microprobe (EMP) the sections were polished. The casting–embedding method (Golubic *et al.* 1970) in combination with staining with OsO_4 (Schneider 1976) for better contrast was applied to achieve an accurate, in situ three-dimensional image of lithobiont morphology free of shrinking.

Imaging methods

Optical microscopy investigations were followed by scanning electron microscopy (SEM), field emission (FE) SEM, transmission electron microscopy (TEM) and the spatial imaging modes of the EMP. Combined and correlated information supplied by these methods was used to characterize various organisms of the biofilm and their interrelations and interactions with the substrate. Images from sections perpendicular to the rock surfaces were digitized and used in image analysis.

The samples were investigated as thin sections (>30 μm), ultra-thin sections (<1 μm), resin-casts and natural rock surfaces. The latter were investigated by FE-SEM which, by means of extremely low beam currents, enables observation of uncoated specimens at high magnifications and resolutions (Schmidt 1994; Jaksch 1996).

Electron imaging was accomplished with the SEM S-2300 from Hitachi, the FE-SEM 1530 from LEO, the EMP JXA 8900 R from Jeol and the TEM EM 301 from Philips. The EMP investigations were carried out at the Department for Geochemistry at Göttingen University, and the TEM images were supplied by the Department of Microbiology and Genetics at Göttingen University. Carbon coating and gold sputtering of SEM specimens was accomplished with a Cressigton Carbon Coater 208 and a Cressigton Auto Sputter Coater 108.

Image analysis

Image analysis is an efficient tool for depicting the distribution of endolithic biomass in the rock substrate with a resolution of a few micrometres. Digital images were generated from optical microscopy of thin sections using polarized light with a Megavision T2 Capture Station. The resolution of the image files was 1200 by 1200 pixels. The raw images show the carbonate rock substrate in light or bright colours whereas the biomass (saturated with resin) has optically isotropic behaviour, thus appearing in dark tones. The image files were fed into the analytical software Zeiss-Vision KS 400 for further processing.

The pictures were binarized, i.e. the greyscales are divided into either black or white

areas after definition of a specific threshold value. The measurement of the biomass to substrate ratio works by counting black and white pixels along successive lines from the rock surface into the pure, non-colonized rock. The resulting files give ratios of black and white pixels and thus the area ratios of biomass and substrate as a function of the distance from the rock surface. The area ratios are proportional to the volume ratios of rock substrate and biomass. For each specimen a characteristic and reproducible curve is obtained which delineates the distribution of biomass (in vol%) in the rock for a pre-selected profile depth (generally about 1000 μm) as a function of distance from the sample surface.

Biodiversity

The purpose of taxonomically characterizing the biofilms is for the comparison and correlation of species composition with geographical, geological and climatic factors specifically affecting the sampling site as well as with geochemical and image-analytical data (Pohl 2000). Specimens with clearly developed lichen thalli were determined by their morphological appearance and spores by R. Türk (Salzburg), B. Weber (Kaiserslautern) and B. Günzel (Göttingen). Cyanobacteria were determined by T. Le Campion-Alsumard (Marseille) with special consideration of their pheno- and ecotype. Fungi and green algae were partially determined by M. Hoppert and C. Flies (Göttingen; Flies 1999) using DNA analysis.

Determination of lichen substances

For determination of acids within the biofilms, high performance liquid chromatography was used according to Mangels (1990), Skoog & Leary (1996) and Huneck & Yoshimura (1996). Instrumentation was as follows: Waters™ 600 S controller; Waters™ 616 pump; ProntoSIL™ 120-3-C18AO column, 250 × 3.1 mm, Bischoff Chromatography; Waters™ 486 tunable absorbance detector with 210 nm, computing with Waters™ Millennium 32 software; eluent was 50 mM phosphoric acid, flow rate 0.5 ml min^{-1}; injection volume 20 μl, run time 15 min. The extraction of 100 mg samples was carried out by shaking the samples for 2 h under 7 Hz with 0.015 M NH_4Cl/NH_3 solution under pH of 9.25.

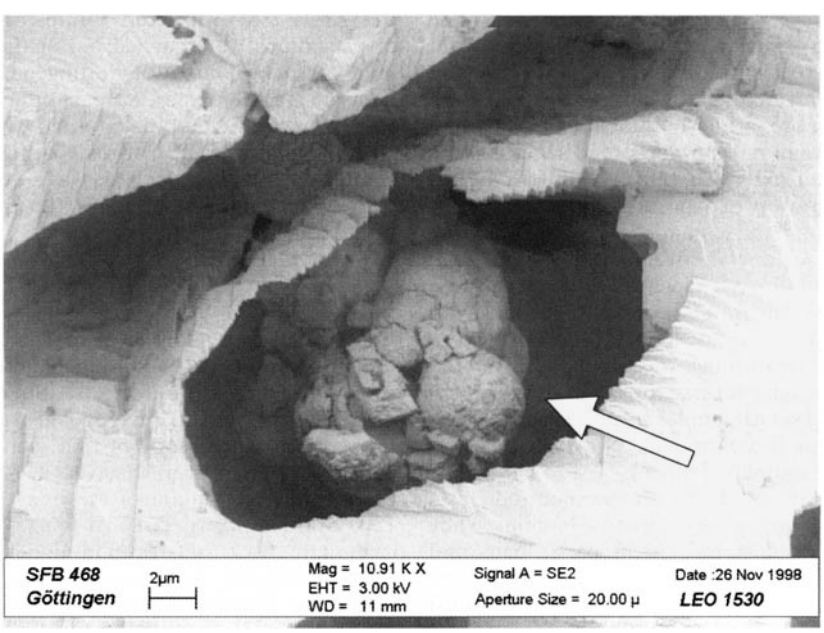

Fig. 2. FE-SEM image of a micropit etched from the carbonate rock substratum by coccoid cyanobacteria. The cells (indicated by arrow) are situated at the bottom of the pit, well protected from harsh environmental conditions. The sample derives from a SE-exposed cliff from an elevation of 1800 m a.s.l. from the Untersberg near Salzburg, Austria.

Results

Colonization and establishment of endolithic biofilms

All investigated natural carbonate rock exposures were found colonized endolithically by lichens, cyanobacteria, green algae and fungi. The density of colonization may vary as well as the maximum penetration depth and biomass per unit area. Even on surfaces which are strongly marked by chemical corrosion (exhibiting a characteristic microkarst relief) euendolithic micro-organisms actively create small cavities (micropits; Danin *et al.* 1982; Sterflinger & Krumbein 1997) where they survive despite the most extreme and adverse environmental conditions (Fig. 2). 'Bare rock', as described frequently in both scientific and belletristic literature, should therefore, at least where carbonate rocks are concerned, be considered a rare exception.

Mesoscopic appearances of endolithically colonized rock surfaces can differ widely: texture, colour, microrelief and roughness of the rock surfaces can be strongly altered. One rarely finds surfaces reflecting the actual colour of the carbonate rock. However, at the microscopic scale, an abundance of common features becomes apparent, which are characteristic of the internal morphology and structure common to nearly all endolithic biofilms observed. Micromorphology is controlled by both ecological factors and the physiological needs of the micro-organisms. The micromorphology of the endolithic biofilms and their adjacent rock substrates thus reflects an adaptation to an optimized endolithic life strategy. Virtually all endolithic biofilms in carbonate rocks show, with minor modifications, a vertical zonation parallel to the rock surface, which develops independently of the presence of particular photo- or mycobionts, lichen species, or the degree and completeness of lichenization (Fig. 3 and Table 1).

Typical alpine lichens forming zoned endolithic biofilms are *Hymenelia coerulea, Hymenelia prevostii, Protoblastenia incrustans* and many *Verrucaria* species. The residual surface layer of the rock has a relatively constant thickness between 50 and 100 μm. The actual thickness is most likely linked to ecological factors such as light intensity, the amplitude of temperature changes and the resulting matrix stress (i.e. water deprivation). We observed that endolithic biofilms from protected (humid and shaded) sites show a residual substrate thickness of only a few micrometres (Fig. 3). Photobionts from intensely insolated, dry sites with high temperature ranges retreat to depths of 150–250 μm below the rock surface. These photobionts can additionally be protected by 'cushions' of extracellular polymeric sustances (EPS), orientated toward the surface, which provide light control (filter) and water retention (Fig. 4). The mean depth of the zone of photobionts in moderate conditions is about 150 μm below the rock surface.

The diameters of cells and cell colonies are highly variable: single cells of coccoid photobionts measured about 5–10 μm in diameter, cell colonies 30–80 μm. The sexual reproductive structures produced by mature lichens, the perithecia, may be as large as 100–300 μm in

Table 1. *Standard zones of endolithically colonized carbonate rock surfaces*

Depth (below rock surface)	Zone of biofilm
c. 0–150 μm	Mostly intact **residual substrate layer** towards the rock surface, partly interlocking with the lichen cortex (stratum of dead/degenerating cell material).
c. 150–300 μm	Zone of **photobiont** (green algae or cyanobacteria), frequently (but not always) associated with hyphal cells of fungi. Green algae and cyanobacteria are capable of actively dissolving the substrate (by means of extracellular polysaccharides (EPS) or excreting organic acids) thus actively creating habitable cavities. Their depth depends on the optimum quantity of light needed for photosynthesis.
several mm	Zone of **mycobiont** (fungi). Hyphally expressed fungal cells penetrate much deeper into the substrate than the photobiont, as they are not dependent on light as a limiting factor. They are also capable of active substrate solution and often forming dense hyphal networks extending into depths of several millimetres (Fig. 3). The profile-base below a zone of gradual thinning of the fungal hyphae is constituted by the biogenically unaltered substrate.

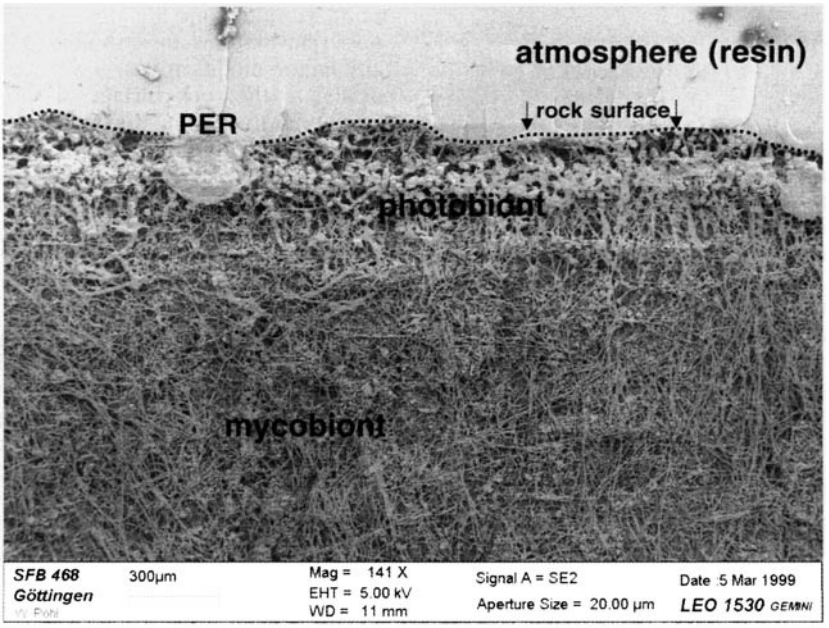

Fig. 3. FE-SEM image of a typically zoned euendolithic lichen biofilm. The image was taken from an epoxy resin cast perpendicular to the original rock surface. The rock substratum was partially removed by etching. Clearly the zone of the mycobiont (bottom and central part of image), the photobiont and the residual substratum 'shield' (near dotted line) can be differentiated. PER = perithecium of the lichen. Specimen GG7, 2300 m a.s.l., Dachstein Mountains, Austria.

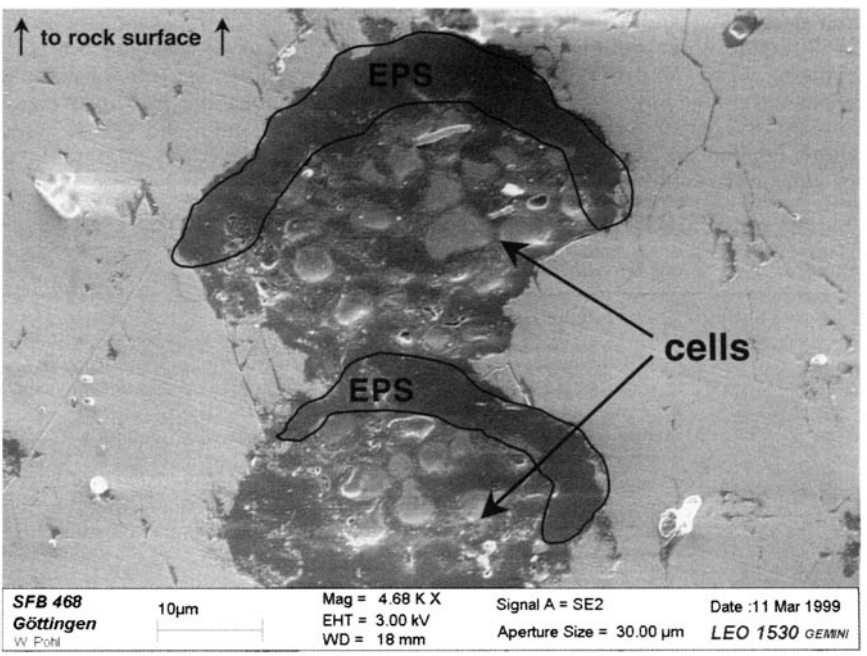

Fig. 4. Colonies of endolithic cyanobacteria with photo-/hydrotactically arranged caps of EPS (extracellular-polymeric substances, highlighted by thin black lines). Thus a highly efficient protection in the direction of the highest water and radiation gradient is achieved. Specimen GG13, 2200 m a.s.l., Dachstein Mountains, Austria.

diameter. They frequently thrust through the residual substrate surface, making direct contact with the atmosphere, into which they discharge their spores. The fungi observed in the endolithic biofilms (probably belonging to ascomycetes) regularly grow hyphae and form dense and complex mycelial networks. They show a remarkable variability in space and time, with respect to their colonization properties. They can be pioneers as in a 13 year old specimen from the foreland of Grosser Gosau Glacier (2250 m a.s.l., Dachstein region, Austria), or the dominant species, or symbiotic partners, or nearly absent in mature biofilms. Microfissures, crystal cleavage planes and/or initial cavities created by pioneering fungi at the rock surfaces may be used by the photobionts as pathways into the interior of the substrate. Colonization depends further on the primary grain size, the type of stratification and porosity of the rock as well as on the orientation of the rock surface. The use of the substrate as a shield against external stress proved to be a decisive evolutionary selection advantage and a successful survival strategy of lithobionts.

Generally, the colonization of the rocks proceeds as follows. The substrate is initially attacked by single cells, which penetrate perpendicular to the rock surface into the substratum by means of chemical dissolution. The colonization is initiated by fungi followed by photobionts, or by photobionts alone. When the depth of the light-optimum is reached, the growth continues laterally, enlarging this cavernous habitat until a distinct cell layer is established. This process clearly results in a loss of mineral substrate. Thus, in the initial colonization phases of an endolithic biofilm, a *destructive* impact on the carbonate rock surface must be assumed. However, as soon as the endolithic biofilm is established, the erosional activities are reduced, so that a stabilized biofilm may act as protection of the rock surfaces from further damage by biogenic or inorganic destructive forces.

The ultrastructure of endolithic biofilms

The ultrastructure of the organisms associated with the endolithic biofilms was investigated in cooperation with microbiologists (Flies 1999) using TEM (Pohl *et al.* 2000). Investigations focused on samples from the forelands of the receding glaciers in the Dachstein Mountains, Austria, collected between 2000 and 2400 m a.s.l. The glacier's retreat was exactly dated by the Austrian Alpine Club. These samples contained relatively young biofilms, which colonized formerly uninhabitable rock faces.

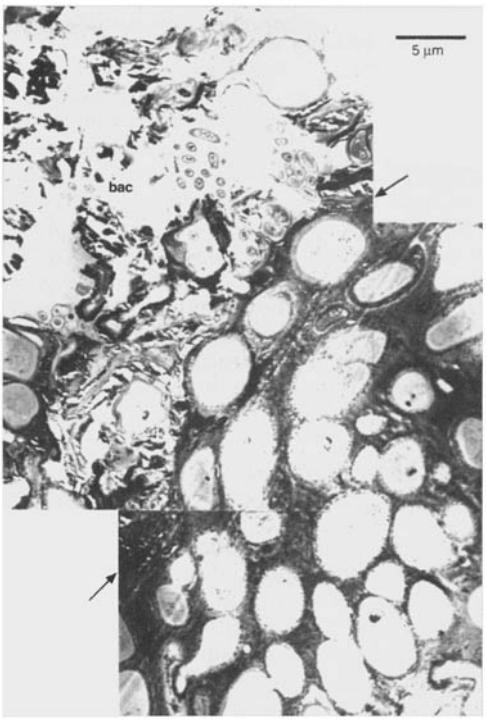

Fig. 5. TEM image depicting zoning within the realm of photobionts in an endolithic biofilm. A distinctive division into two sublayers is observable: one of physically intact vital cells (round, regular, clear shapes at lower right), the other showing dead, degenerating cells in various stages of decomposition with associated bacterial colonies (e.g. one labelled 'bac', upper left). Image after Flies (1999). The vitality of the cells has been confirmed by fluorescence microscopy with analogous samples. Sample from 2300 m a.s.l., Dachstein Mountains, Austria.

Transmission electron microscopy confirmed that endolithic micro-organisms almost always form cell colonies. They are in most cases consortia of photo- and heterotrophic organisms. However, these endolithic cell associations do not show lateral homogeneity but grow discontinuously, leaving intermittent, practically non-colonized substrate areas. Colonies are embedded in thick and dense layers of EPS which fill the intercellular spaces as well as the space between cell walls and the rock substrate.

The photobiontic zone is differentiated into three layers (Fig. 5). The uppermost layer consists mainly of strongly deformed and degenerated cells. The EPS in this layer is frequently colonized by bacteria. The massive occurrence of several morphologically different types of

bacteria was observed on the degenerated cell colonies. The next layer underneath is composed of cells which are physically intact, but show little or no vitality. Their EPS contains many small mineral particles (a few nanometres in diameter) which tend to accumulate preferentially near the walls of conjugated fungal cells. This is followed by a layer of vital cells with intact, apparently functioning chloroplasts, embedded in the EPS, constituting the innermost sublayer. The EPS of these cells (regardless of whether photobiont or mycobiont) showed only the sporadic presence of bacteria. No evidence of any destructive bacterial activities could be observed in this zone.

Image analysis of endolith biomass distribution

Image analysis was applied to quantify the depth of penetration of endolithic microorganisms into substrate, and to assess the volume ratio of endolithic biomass versus substrate as a function of the distance from the rock surface. Statistical parameters such as maximum and average volume ratios, maximum penetration depth, skewness and kurtosis of the biomass distribution were obtained. Image analysis provided highly reproducible data for these parameters.

A simple optical investigation of binarized micrographs of thin sections and the matching histograms of the volume ratios (the latter were programmed to be automatically generated using the software ZeissVision KS 400) already reveals conspicuous differences between various types of biofilms.

Two morphologically different biofilms are compared, both sampled in the Northern Calcareous Alps from similar rock types (Fig. 6). One specimen (71-2) was taken from a westwardly exposed rock face near the summit of Salzburger Hochthron (Salzburg, Austria) at an altitude of 1800 m a.s.l. It consisted mainly of the endolithic lichen *Hymenelia prevostii*. Another specimen (98-2), representing a biofilm made up mainly by non-lichenized cyanobacteria, was collected from the bottom of a westwardly exposed, dry alpine valley near Hochkalter (Berchtesgaden, Germany) at an altitude of 2200 m a.s.l. from the northern face of a freestanding boulder. The surface orientation (determined with a geological compass) for specimen 71-2 was 270/70 and for specimen 98-2 it was 058/65. On both sites the 'hybrid' epi-/endolithic lichen *Rhizocarpon umbilicatum* was also found. The various measured data and their statistical derivatives (see Table 2) show marked differences between the two samples.

Specimen 71-2 was collected at lower altitude from the westward orientated site on Untersberg. Copious precipitation throughout the year supports markedly more biomass and a deeper average substrate penetration. However, the maximum volume ratio (max. *V/V*) as well as the average volume ratio (∅ *V/V*) of biomass versus substrate are clearly lower than in specimen 98-2 from Hochkalter. The kurtosis is similar for both samples, the clear negative values indicating a biomass distribution flatter than a Gaussian distribution. Skewness on the other hand yields differing values for the two specimens. While 98-2 shows an almost symmetrical biomass distribution (indicated by a skewness close to zero), biomass distribution in 71-2 is clearly asymmetrical, whereby a negative skewness points to a distribution peak position at biomass ratios smaller than average. These numerical differences are obviously caused by the filigree fungal network reaching comparatively deep into the rock, but amounting to little biomass. In the volume ratio histogram (Fig. 7) this causes numerous small values over a relatively wide depth range.

In sample 98-2 (Hochkalter, Fig. 6) the biomass of the photobiontic zone is concentrated within a noticeably smaller depth range, but the volume ratios are distinctly higher than in 71-2. The cell colonies lie closer to the rock surface, are larger and grouped more densely than in the sample from Untersberg (71-2). Together with the smaller amount of biomass per unit area this is regarded as a measurable indicator for the adaptation of the endolithic biofilm to the smaller flux of light (one of the essentials of photobiontic life) and the amount of hard radiation (e.g. UV, regarded as a stress factor, from which the biofilm retreats) on the northerly orientated rock face. The higher altitude and the location of the sample site in the valley hollow could also cause longer snow cover and lower average temperature, thus further limiting the productive capacities of the biofilm.

What can be demonstrated with this example is that the data gained from image analysis can in fact be used as characteristic values and parameters for the description, typology and classification of endolithic biofilms. Yet another such parameter is the biomass per unit area. By multiplication of a standard volume with the average of the volume ratios measured over a given depth interval, the endolithic biomass per unit area can be calculated fairly accurately (given the rock substrates are clear, have a low

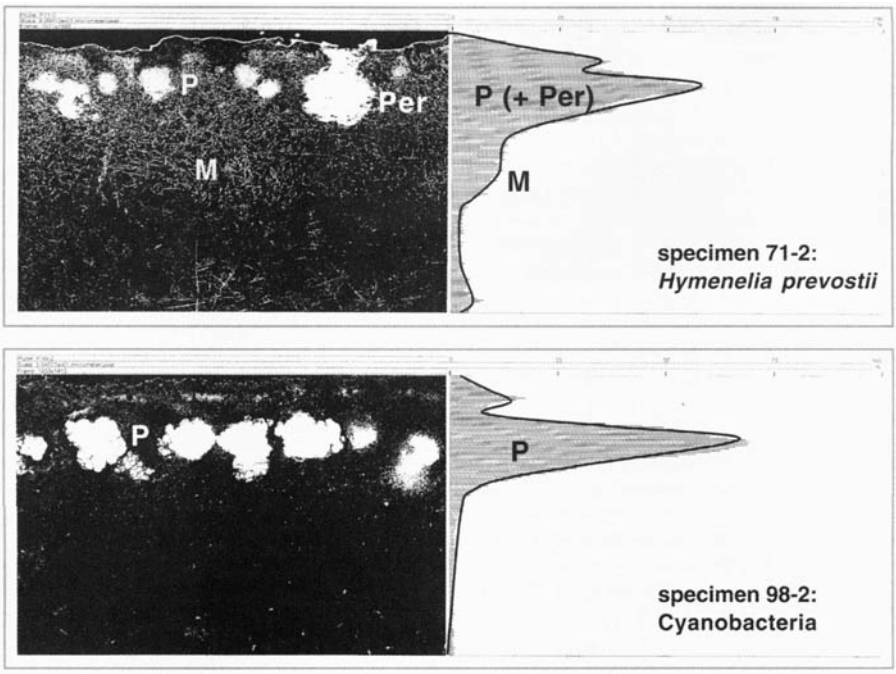

Fig. 6. Example of binary thin section images (left side) for two different types of endolithic biofilms. The corresponding histograms of biomass content and distribution (right side) were determined by computerised image analysis. (Top) *Hymenelia prevostii* (Salzburger Hochthron, Austria, 1800 m a.s.l.) with colonies of photobionts (P), a perithecium (Per) and the hyphal network of the mycobiont (M). The histogram points out the asymmetric distribution of the biomass with a maximum at the photobiontic zone and a smaller submaximum in the realm of the mycobiont. (Bottom) Biofilm consisting of cyanobacteria (*Gloeocapsa* sp.) without symbiontic partner (2200 m a.s.l., Hochkalter, Germany) exhibits one homogeneous layer of photobionts (P), no perithecia and no mycobiont. The colonized zone is distinctly narrower than for *H. prevostii* and does not show a submaximum.

Table 2. *Comparison of image analytical values for two specimen from similar rock substrates in the Northern Calcareous Alps*

Specimen	Biomass ($cm^3\ m^{-2}$)	max. *V/V*	∅ *V/V*	Max. depth (μm)	Skewness	Kurtosis
71-2 Untersberg	169	0.55	0.26	730	−0.17	−1.06
98-2 Hochkalter	44	0.70	0.35	190	0.06	−1.52

max. *V/V*, maximum volume ratio of biomass to rock substrate; ∅ *V/V*, average volume ratio; max. depth, maximum penetration depth

content in opaque particles and bright interference colours under polarized light). The values thus obtained show characteristic differences corresponding to various ecological and taxonomic factors and are reasonably reproducible for analogous samples.

The amount of endolithic biomass per unit area can, therefore, be regarded as an index for the vitality of an endolithic biofilm and correlated with various site-specific parameters and factors, such as altitude, rock surface orientation, surface age and climate. Besides highlighting differences between data obtained from particular specimens, image analysis can also be used to reveal and accentuate common features within sample groups.

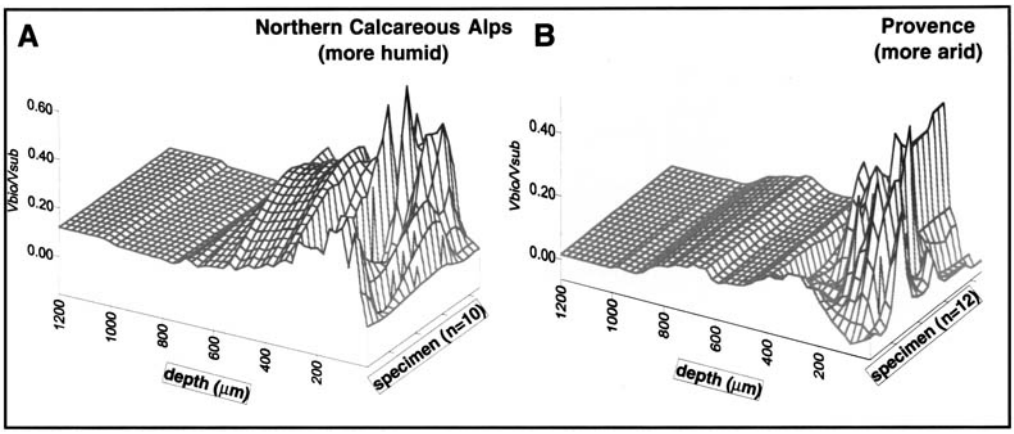

Fig. 7. Results of the determination of the volume ratios of biomass *versus* rock substratum (V_{Bio}/V_{Sub}) from two sample groups: (A) Northern Calcareous Alps (Austria and Germany); (B) Provence (France). The horizontal axes indicate depth below rock surface and the number of specimens; on the vertical axis the V_{Bio}/V_{Sub} ratios are plotted. The distribution pattern of endolithic biomass versus depth shows distinct differences between the two sample groups. The colonization is deeper and more intense in the substrata from the more humid Northern Calcareous Alps, shallower and with lower density in the samples from the more arid Provence.

The three-dimensional graph in Figure 7 shows the biomass distribution as a function of depth for a total of 22 samples from two different sets: one from the relatively humid Northern Calcareous Alps (A), the other (B) from the relatively arid region of Provence (France). It can be clearly demonstrated that in the Provence samples the highest biomass intensity is reached relatively closer under the rock surface and the ratios of $V_{Biomass}/V_{Substrate}$ rapidly decrease towards the substrate interior.

The average colonization intensity and penetration depth are markedly deeper in the more humid substrate in the Northern Calcareous Alps. Caused by the higher abundance of fungi (possibly resulting from the photobiont's higher productivity), a second peak in the $V_{Biomass}/V_{Substrate}$ distribution is developed even deeper into the substrate.

These differences in the graphs are confirmed by median values and statistics with data from image analysis (see Table 3). The smaller skewness for the Provence samples (more arid climate) indicates a more symmetrical distribution. The higher kurtosis in the Provence group points at a high biomass concentration within a small depth range. The striking differences in biomass per unit area, maximum volume ratios and maximum penetration depths are consistent with a higher prosperity of the endoliths in the cooler, more humid Northern Calcareous Alps.

Another relevant factor is the large difference in the average altitude of the sampling sites in the Northern Calcareous Alps compared to Provence. While the average sampling site was at 2000 m a.s.l. in the former, the average altitude in Provence was only 950 m a.s.l. Here the lower intensity of potentially harmful, hard radiation (e.g. UV) could be responsible for the lower depth of the main biomass peak in the sample group from Provence.

Table 3. *Median values of numerical data from image analyses*

Sample group	Biomass ($cm^3\ m^{-2}$)	Skewness	Kurtosis	max. *V/V*	∅ *V/V*	Max. depth (µm)
North. Calc. Alps	55.15	0.4203	−1.1817	0.55	0.18	300
Provence	26.84	0.4104	−0.6617	0.44	0.18	180

Definitions as in Table 2

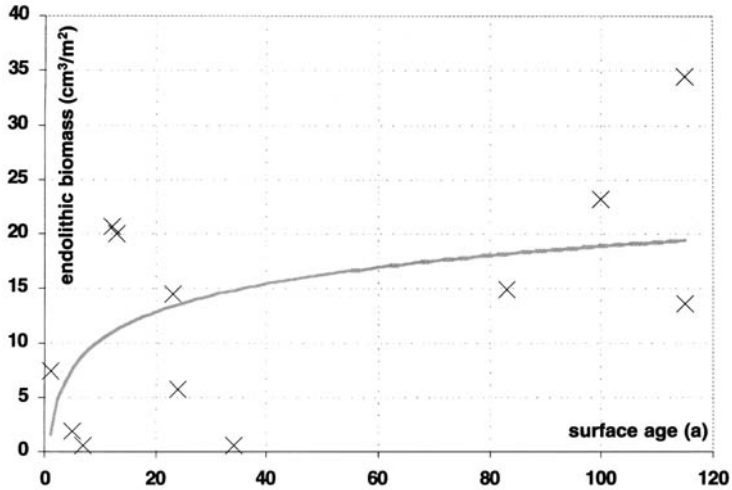

Fig. 8. Age-dependent development of endolithic biomass content as determined by computerized image analysis. The samples derive from immediate glacial foreland in the Dachstein Mountains (Austria). The increase of biomass as a function of time roughly follows a logarithmic path. Owing to the influence of other factors, such as microscale surface porperties, variation is relatively high.

Biofilm development as a function of time

Colonization of subaereal rocks by microbial endolithic biofilms is a slow process. To investigate the biofilm development as a function of the time of rock surface exposure to the atmosphere, measurements of the biomass per unit area were conducted on dated samples from areas of glacial retreat in the Dachstein Mountains (Austria). Although variance of biomass content was high, a general logarithmic trend of time-dependent biomass increase could be detected. The data are given in Figure 8, demonstrating a swift initial increase of biomass, which indicates a thorough endolithic colonization within a few years. The average increase in biomass over a time period of about 120 years was approximately 0.25 cm^3 m^{-2} per year. However, the departures from this value are often considerable in individual samples, reflecting the strong influence of the particular microenvironments.

Figure 9 exemplifies the development of the endolithic colonization of carbonate rock surfaces in four stages as a function of time. Despite the general increase of the biomass per unit area (V_{Bio}) and the volume ratios (V_{Bio}/V_{Sub}) as indicated by the specimens SL5, GG12 and SL9, other factors can have a prevailing influence. Thus very young biofilms can already have a very mature appearance, if the site-specific environmental conditions are favourable, e.g. water storing fissures on the rock surface (as demonstrated by specimen GG7).

The general trend of endolithic biomass increase with the ageing of a rock surface can be deduced from the first three diagrams (samples SL5, GG12 and SL9) in Figure 9, visually as well as from the measurements of the biomass content. The ageing of a carbonate rock surface correlates with an increase in density, depth and intensity of endolithic colonization. However, there is one exception: the specimen GG7 (the bottom diagram in Fig. 9) supports after only 12 years without ice cover a differentiated, mature and fully lichenized endolithic biofilm, consisting of green algae and fungi. Even the reproductive organs (perithecia) are developed.

This unusually mature biofilm demonstrates the importance of local variations of ecological and geological/mineralogical factors (grain size, grain boundary geometry, microcracks augmenting water storage potential, substrate geochemistry). This leads to an important amendment: factors such as the microtopography and, subsequently, the water retention potential at the rock surface are often the dominant ones. The surface colonization is distinctly higher in the vicinity of micro- and mesocracks and fissures than on smooth surfaces with few morphological features. This documents the ecological key advantage from the additional water supply.

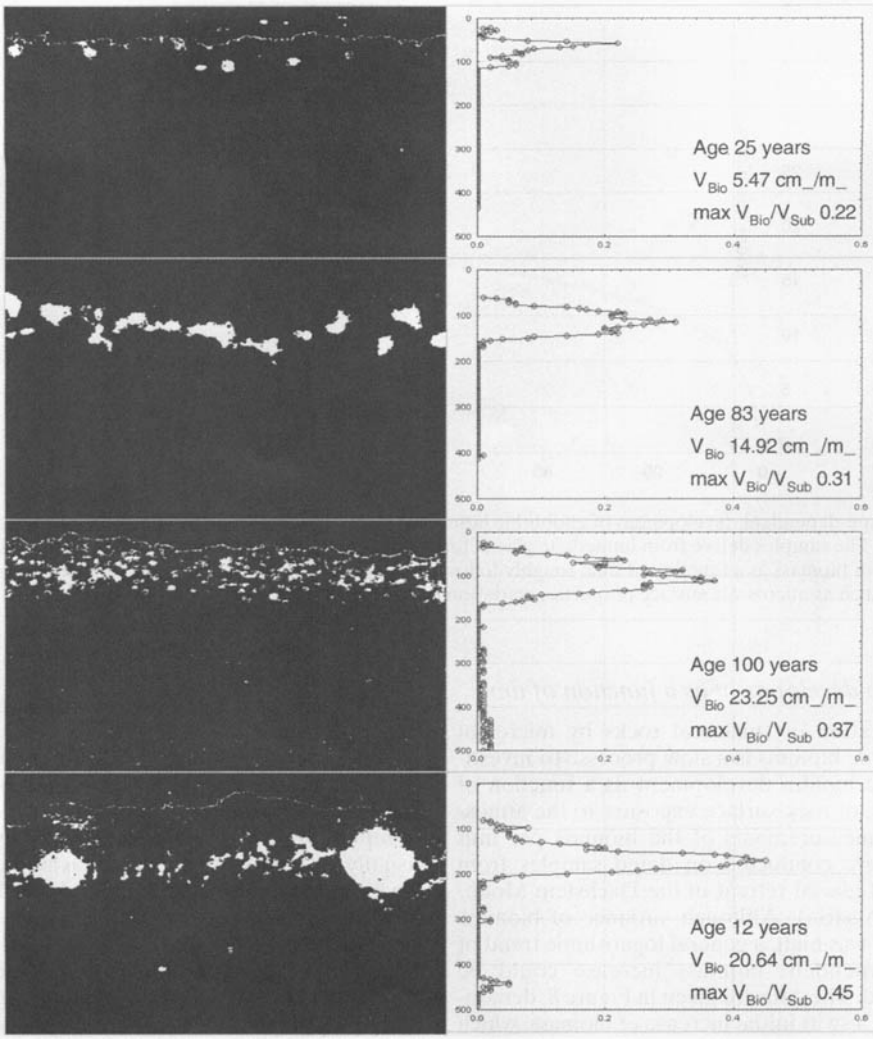

Fig. 9. Four exemplary stages in the development of endolithic biofilms from the Dachstein Mountains (Austria). From top to bottom samples are SL5, GG12, SL9, GG7 (SL = Schneeloch Glacier, GG = Grosser Gosau Glacier). X-axes, V_{Bio}/V_{Sub} volume ratios; Y-axes, depth (in μm); dotted lines, rock surfaces. Despite the general increase of the biomass per unit area (V_{Bio}) and the volume ratios (V_{Bio}/V_{Sub}) as indicated by specimens SL5, GG12 and SL9, other factors also can have a dominant influence. Thus very young biofilms can undergo a very rapid development and maturation if the site-specific environmental conditions (especially humidity) are favourable, as demonstrated by specimen GG7.

Discussion

Colonization and survival strategies of endolithic biofilms

Subaerially exposed rocks are extreme environments, which pose serious obstacles to the establishment of a microbial community. A fungal spore, for example, or a juvenile green alga or cyanobacterium which is accidentally placed on a natural carbonate rock surface in alpine regions, at around 2000 m a.s.l., faces conditions very threatening to its existence: high variations of temperature, with extreme values on both ends of the scale, frequent passes of the freeze point, strong and hard solar radiation, long dry periods and mechanical bombardment by ice crystals during

snowstorms. The logical 'escape route' leads *into* the rock. A few lucky ones find their niche as crypto- or chasmoendoliths (see Golubic *et al.* 1980) but pre-existing fissures and pores are relatively rare in micritic limestone. Thus the substrate has to be actively made accessible, which – by using organic acids – is a moderate task on the easily soluble limestone (Gehrmann-Janssen 1995; Pohl 2000).

Therefore, the initial phenomenon resulting from the colonization of carbonate rocks is 'biopitting' (Danin *et al.* 1982; Sterflinger & Krumbein 1997), i.e. the creation of small pits by the micro-organisms, which serve as first, rudimentary shelters at the substrate surface. In these pits the micro-organisms find at least temporary shelter from the harsh environment and have a base for further proliferation. Depending on the specific ecological situation at the site, they eventually continue their retreat into the substrate and find their ecological optimum at a specific depth, where biomass production and metabolic processes reach their relative maximum.

As soon as the micro-organisms have collectively (i.e. as colonies) started to live euendolithically, numerous advantages become apparent. The residual substrate layer on top of the biofilm and the biofilm's EPS augment water retention and shield from electromagnetic radiation. Life in the subsurface cavities offers additional protection from mechanical stress. The organisms are able to prosper and multiply. However, being photobionts they are restricted to a zone which is confined downwards by the availability of sufficient light, and upwards by excessive radiation intensity, matrix stress and the mechanical stability of the substrate. Consequently, characteristic zones of photobionts, found almost ubiquitously on carbonate rock surfaces, develop 150–300 μm beneath the surface. The substrate not dissolved during the early stages of colonization remains untouched by the micro-organisms and constitutes a mechanical shield against stress factors from above.

The development of endolithic biofilms on initially uninhabited carbonate rock surfaces, culminating eventually in mature biofilms, correlates clearly with an increase in the concentrations of oxalic acid in the biofilms. While on young surfaces (below 20 years) concentrations between 0.1 and 0.4 $\mu g\ g^{-1}$ were measured, samples over 100 years of age yielded between 1.0 and 1.6 $\mu g\ g^{-1}$ of oxalic acid. Obviously the oxalic acids play an especially important role during the colonization phase on carbonate rocks (see also Gehrmann-Janssen 1995; Pohl 2000).

On the other hand, older and eventually 'mature' biofilms (i.e. samples from rock surfaces continuously exposed to atmospheric action for several hundreds) show a correlation of the endolithic biomass per unit area and the concentration ratios of malic and oxalic acid: higher biomass contents cause higher ratios of malic to oxalic acid, pointing to a disproportional abundance of malic acid in more prosperous biofilms. Presumably oxalic and (the livelier the biofilm the more) malic acid fulfil specific physiological functions in the metabolism of mature biofilms. An obvious one would be leaching nutritive elements from externally acquired mineral particles (e.g. aeolian clay minerals) thus making them available to the biofilm (Banfield *et al.* 1999; Pohl 2000).

Fungi also play an important part in the initial colonization of carbonate rocks. They were frequently observed to act as pioneer colonists, just as green algae or cyanobacteria, but with a clear bias towards particularly stressful sites: dry, hot and with intense irradiation. Under these latter conditions, in a few cases (e.g. in the southern walls of the Montagne St. Victoire, Provence, France) fungi were observed to remain the dominant group long after the initial stages of colonization. These findings are consistent with observations of Sterflinger & Krumbein (1997), who, on extremely hot and dry sites additionally afflicted by osmotic stress, found predominantly fungi as endolithic inhabitants. These thrived epilithically, chasmo- and euendolithically in the carbonate rock substrate almost ubiquitously, often without any associated photobiontic organisms. Danin *et al.* (1982) found dense lichen colonization on carbonate sufaces in more humid regions (>550 mm mean annual rainfall) and micropits made by *Gloeocapsa* spp. on surfaces in more arid regions (<300 mm mean annual rainfall). The authors used this observation as a climatic indicator. We observed the same feature on carbonate rocks in the Northern Calcareous Alps (Salzburger Hochthron). On north and NW-exposed and more humid rock faces we observed a dense colonization with endolithic lichens. On south-exposed highly insolated rock faces we found severely restricted species diversity and biomass, preferably of cyanobacteria forming micropits.

The 'joint venture' of photobiontic organisms and fungi can in fact be viewed as a model for an ideal symbiosis. Where the generation of high energy nutrients (above all others, sugars) is concerned, photosynthesis enables distinctly higher productivity than the heterotrophy of fungi (Nash 1996). Therefore, the photobionts

are able to supply a substantially large mycobiontic partner with their excess sugar (Banfield *et al.* 1999). The presence of fungi, in turn, can also constitute an advantage for the photobionts: the dense and complex cell fabric of their hyphal network (including EPS) serves as a large and efficient storage facility for water and nutrients without being confined to the 'photic zone' near the rock surface. Thus the fungal symbiont offers the photobionts an expanded field for nutrient supply and water storage. Without the mycobiont the microbial phototrophs remain in physically narrower confinement of their ecological optimum.

Stability and conservation of rocks and monuments

Questions concerning stability of rocky surfaces are: How does an established biofilm behave in the further course of its existence and in which way does it influence the destruction processes of building stones and stone monuments? The model derived from microbial activities on silicate-sandstone surfaces illustrates perpetual repetition of colonization, destabilization and exfoliation (desquamation) and eventually recolonization of freshly exposed surfaces (Büdel & Wessels 1991; Wessels & Wessels 1995; Friedmann 1982). However, no indications of any of these processes could be observed in the case of endolithic organisms in carbonate rocks. A zone of mechanical destabilization, as described by Wessels & Schoemann (1988), Wessels & Wessels (1995) and Walton (1993), was not observed on carbonate rock surfaces. While actually empty micro- and mesopits were sometimes found as residual traces of former lichen colonization they were interpreted as the result of increased air pollution and/or acid rain, rendering survival for many lichen species impossible and yielding to less sensitive and less differentiated biofilms such as non-lichenized cyanobacteria and/or fungi (R. Türk). Essentially an endolithic biofilm on carbonate rock surfaces seems to behave in a conservative way as soon as it has reached equilibrium with the site-specific ecological conditions: temperature, availability of water and nutrients, intensity of electromagnetic radiation. Perpetual surface colonization with continuing substrate removal would inadvertently result in a loss of the residual substrate between photobionts and the atmosphere, thus depriving the endolithic biofilm of its protective cover. This would very shortly (within weeks or months) do massive damage to the lithobiontic community. It is, therefore, reasonable to assume, that a long-term sustainable *modus vivendi* for endoliths would require refined strategies to accomplish it.

One of these strategies may be recognized in the 'cell recycling' within the photobiontic layer, which could be demonstrated by TEM images (Fig. 5). Within the photobiontic zone constant cell recycling takes place. Cells on the upper fringe of the photobiontic layer eventually die (as they are the ones exposed to the highest stress level). The cells as well as their EPS are subsequently decomposed by bacteria, the final products being, besides organomineral precipitates with low solubility, carbon dioxide and water (Fig. 10). The organomineral phases are often found to be oxalates (Gehrmann-Janssen 1995; Pohl 2000) and accumulated in the uppermost part of the photobiontic zone. Thus constantly new space is freed for vital, growing cells from the lower parts of the photobiontic layer. Additionally this quasi 'cortex' from dead and degenerating cells and cell fragments acts as additional protection of the biofilm against stress factors from the outside.

The crucial advantage of these internal, volume-conserving recycling processes is that despite allowing dynamic growth within the biofilm, the conservation of the residual substrate 'shield' towards the atmosphere is still secured. Thus a continuous vertical growth of the biofilm, which at some point must lead to a catastrophic breakdown such as observed on silicate sandstone, can be efficiently avoided on most carbonate substrates without limiting the overall productivity within the biofilm. Krumbein & Jens (1981) argue convincingly that micro-organisms from the Negev Desert (Israel) actively build a protective cover against the extreme heat and dryness in the form of 'desert varnish'. Only in this 'pseudo-endolithic' niche is survival in the extreme desert environment possible.

An endolithic biofilm model

Because of the relative simplicity of the system microorganism–rock–substrate–atmosphere of endolithic biofilms it is tempting to use it as a model for larger and more complex systems. Such a model was recently developed by Banfield *et al.* (1999) for epilithic lichens on silicate rocks. Here a similar model is presented for euendolithic biofilms on largely monomineralic carbonate rocks.

The participating organisms, the mineral, gaseous and liquid phases, the morphological and ecological setting and the major physical

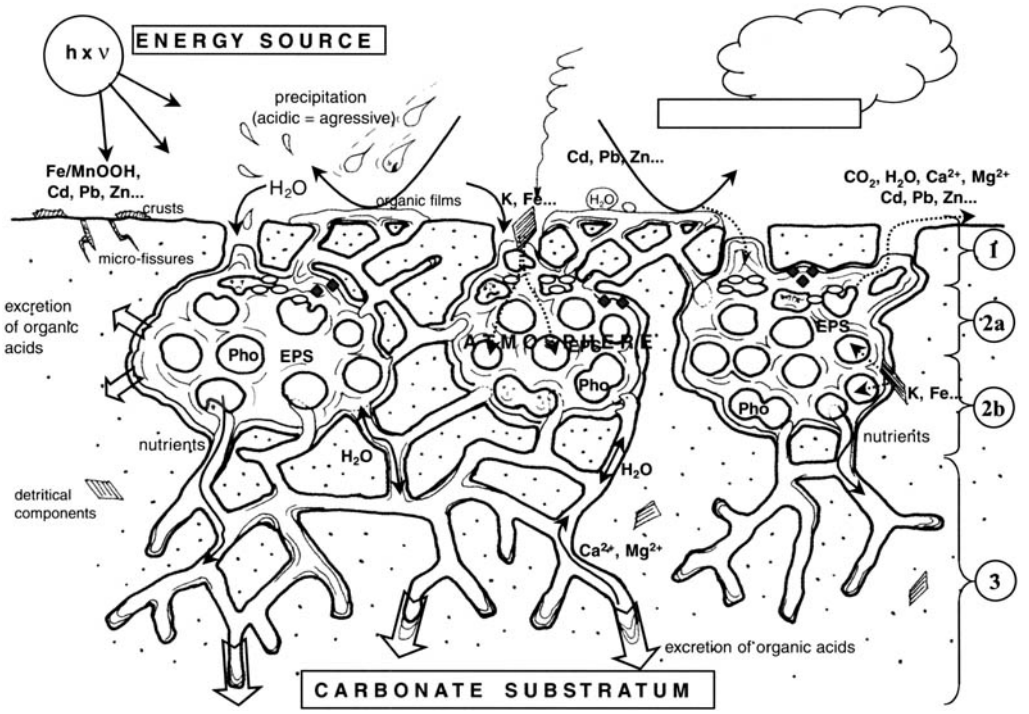

Fig. 10. Schematic model for the *modus vivendi* of endolithic biofilms (lichens) on carbonate rock substrata including participating organisms, mineral, gaseous and liquid phases, morphological and ecological setting and major physical and chemical processes. Ellipses = bacteria; diamonds = mineral precipitates; Pho = photobionts. The model is divided into three distinct zones (I to III). Zone I: residual substrate cover constituting a protective mineral cover. Zone IIa: catabolic zone within the phytobiontic layer. Superannuated or damaged cells die and are decomposed by bacteria. Zone IIb: vital photobiontic zone: ecological optimum, at least occasionally conditions favourable for photosynthesis and other metabolic processes prevail. The photobionts commonly form colonies enveloped with thick EPS layers. Zone III: heterotrophic mycobiont, not limited to the photic zone and thus penetrating the substratum down to a few millimetres or centimetres.

and chemical processes of this model are schematically presented in Figure 10. The model is divided into three distinct zones (strata) numbered (I to III).

Zone I: residual substrate cover. It constitutes a mineral protective layer, shielding the lithobionts from harmful effects of atmospheric agents. It is often sparsely colonized by fungi, occasionally by endolithic cyanobacteria and bacteria. Metabolic processes relevant for the biofilm as a whole do not take place in this layer. In the process of initial colonization this layer is locally perforated while the organism passes into deeper layers below.

Zone IIa: catabolic zone within the photobiontic layer. It is composed largely of damaged cells, which die and are decomposed by bacteria. The cells suffer a lysis process, and are degraded finally to CO_2 and H_2O as well as organomineral phases.

Zone IIb: active photobiontic zone. Here the photobionts encounter their ecological optimum with respect to temperature, water retention potential, and the necessary amount of light. They are protected from damaging radiation and mechanical abrasion stress from the atmosphere. Reproduction (by cell division) is initiated when the conditions approach a relative optimum. Conditions considered favourable for photosynthesis, slow growth and other metabolic processes are described as poikilotrophic (Gorbushina *et al.* 1999). One striking adaptation mechanism is the normalized chlorophyll content, which in lichens from high alpine regions is twice that of lichens in moderate climatic situations (Scherr *et al.* 1998; Pohl 2000). This is probably closely connected with the poikilotrophic way of life.The photobionts commonly form colonies which are enveloped with thick EPS.

Zone III: Mycobiont zone. Due to its heterotrophic metabolism the fungi are not limited to the photic zone in the rock substrate. Thus the fungal mycelium of a lichen can act as a buffer and storage facility for water and nutrients beyond the photic zone, to which the photobionts are limited. This facilitates water and nutrient management for the photobionts, thereby augmenting the success of poikilotrophy in the symbiosis of photo- and mycobionts (Gorbushina *et al.* 1999). The growth of the mycobiont is basically limited by the capacity of the photobiont to assure organic nutrient supply (e.g. sugars; Banfield *et al.* 1999).

Surface protection or accelerated weathering?

Regardless of tackling problems of global element fluxes, geomorphology and karst morphology or heritage and monument conservation, the crucial question for the evaluation of the interactions of epi- and endolithic biofilms and their substrates is their impact on the overall mass balance on the carbonate surface. If compared with purely non-organic factors, do biofilms covering a rock exert a protective or destructive effect? Do they retard weathering or augment the rock or building stone decomposition? Lee & Parsons (1999) and Silva *et al.* (1999) have suggested a protective rather than destructive role of epilithic lichens on silicate rocks.

Based on our results we came to a similar conclusion: endolithic biofilms under natural conditions exert an overall protective effect on carbonate rocks. This hypothesis is supported by the following observations.

1. The colonization by endolithic biofilms and penetration leaves an external protective layer of the rock intact.
2. Although the mass balance on carbonate rock is negative during the initial stages of colonization, the increase of biomass ceases and so does the rock dissolution that generated the endolithic space for it.
3. There are no indications of a continuous loss of material by exfoliation and desquamation, linked to cyclic colonization dynamics as on siliciclastic rocks (Büdel & Wessels 1991; Wessels & Wessels 1995).
4. An established biofilm is maintained by internal recycling, involving death and bacterial degradation of cells, nutrient recycling and regrowth without biomass increase.
5. There is no evidence of progressive loosening and finally dislodging of grains, grain-to-grain aggregates up to whole-rock scales by fungal cell pressure as described for endolithically colonized sandstones (Ortega-Calvo *et al.* 1991) and carbonate rocks under extremely arid conditions (Danin *et al.* 1982; Danin 1993; Sterflinger & Krumbein 1997).
6. Progressive bio-abrasion of endolithically colonized rocks by gastropods and other grazing animals as observed on marine limestone coasts (Schneider 1976) is absent on alpine air-exposed rock surfaces.
7. The process applied on carbonate rocks is a precise etching, forming cavities whose morphology complies with that of the organisms and is totally independent of grain boundaries and other lithological and structural features of the rock (e.g. fossils, secondary fills of pores and fissures, grain shape and crystal axes).

The work presented in this paper was supported by the German Research Foundation (DFG) as subproject A2 within the framework of the Special Research Branch (SFB) No. 468, 'Interactions at Geological Interfaces'.

We kindly thank T. Le Campion-Alsumard (Centre d'Océanologie, Marseille) for help with determination of cyanobacteria, R. Türk (Department for Plant Physiology, University of Salzburg) for lichen determination, A. Kronz and T. Heinrichs (Faculty of Geosciences, Göttingen University) for EMP and SEM operation respectively, and S. Eins (Department for Clinical Anatomy, Göttingen University) for invaluable help with image analysis. Their help was crucial to our work and was highly appreciated throughout the 2.5 year running time of the project. We thank T. Le Campion-Alsumard and especially S. Golubic (Boston University) for the extensive and extremely valuable critical remarks during review of this paper.

References

BANFIELD, J. F., WELCH, S. A. & EDWARDS, K. J. 1998. Microbes as geochemical agents. *The Geochemical News*, **96**, 11–17.

BANFIELD, J. F., BARKER, W. W., WELCH, S. A. & TAUNTON, A. 1999. Biological impact on mineral dissolution: Application of the lichen model to understanding mineral weathering in the rhizosphere. *Proceedings National Academy of Sciences USA*, **96**, 3404–3411.

BARKER, W. W. & BANFIELD, J. F. 1996. Biologically versus inorganically-mediated weathering-

reactions: Relationships between minerals and extracellular polymers in lithobiontic communities. *Chemical Geology*, **132**, 55–69.

BARKER, W. W., WELCH, S. A. & BANFIELD, J. F. 1997. Biochemical weathering of silicate minerals. *In*: BANFIELD, J. F. & NEALSON, K. H. (eds) *Geomicrobiology: Interactions between Microbes and Minerals. Reviews in Mineralogy*, **35**(1) 391–428.

BÜDEL, B. & WESSELS, D. C. 1991. Rock inhabiting blue-green algae/Cyanobacteria from hot arid regions. *Algological Studies*, **64**, 385–398.

CAMPBELL, S. E. 1979. Soil stabilization by a prokaryotic deseert crust: Implications for Precambrian land biota. *Origins of Life*, **9**, 335–348.

DANIN, A. 1993. Pittinig of calcareous rocks by organisms under terrestrial conditions. *Israel Journal of Earth Sciences*, **41**(2–4), 201–207.

DANIN, A., GERSON, R., MARTON, K. & GARTY, J. 1982. Patterns of limestone and dolomite weathering by lichens and blue-green algae and their palaeoclimatic significance. *Palaeogeography, Palaeoclimatology, Palaeoecology*, **37**, 221–233.

FLIES, C. 1999. *Untersuchungen zur Zusammensetzung endo- und epilithischer Biofilme an Oberflächen von Karbonatgesteinen*. Diploma Thesis, Institut für Mikrobiologie und Genetik, University of Göttingen.

FRIEDMANN, E. I. 1982. Endolithic micro-organisms in the Antarctic cold desert. *Science*, **215**, 1045–1052.

GEHRMANN-JANSSEN, C. 1995. *On the biopitting corrosion by epilithic and endolithic lichens on carbonate rocks – biophysical and biochemical weathering aspects*. PhD Thesis, University of Oldenburg.

GOLUBIC, S. & CAMPBELL, S. E. 1979. Analogous microbial forms in recent subaerial habitats and in Precambrian cherts: *Gloeothece coerulea* Geitler and *Eosynechococcus moorei* Hofman. *Precambrian Research*, **8**, 201–217.

GOLUBIC, S., BRENT, G. & LE CAMPION, T. 1970. Scanning electron microscopy of endolithic algae and fungi using a multipurpose casting-embedding technique. *Lethaia*, **3**, 203–217.

GOLUBIC, S., FRIEDMANN, I. & SCHNEIDER, J. 1980. The lithobiontic ecological niche, with special reference to micro-organisms. *Journal of Sedimentary Petrology*, **51**(2), 475–478.

GORBUSHINA, A. A., KRUMBEIN, W. E. & PALINSKA, K. A. 1999. Poikilotrophic growth patterns in rock inhabiting cyanobacteria. *In*: PESCHEK *et al.* (eds) *The Phototrophic Procaryotes*. Kluwer Academic/Plenum Publishers, New York, 657–664.

HINSINGER, P. & JAILLARD, B. 1993. Root induced release of interlayer potassium and vermiculitization of phlogopite as related potassium depletion in the rhizosphere of rye grass. *Journal of Soil Science*, **44**, 525–534.

HUNECK, S. & YOSHIMURA, I. 1996. *Identification of Lichen Substances*. Springer, Berlin.

JAKSCH, H. 1996. Neues Konzept für ein hochauflösendes Niederspannungs-Schottky-SEM. *CLB – Chemie in Labor und Biotechnik*, **47**(10).

KRUMBEIN, W. E. (ed.) 1983. *Microbial Geochemistry*. Blackwell Scientific Publications, Oxford.

KRUMBEIN, W. E. & JENS, K. 1981. Biogenic rock varnishes of the Negev Desert (Israel): an ecological study of iron and manganese transformation by cyanobacteria and fungi. *Oecologica*, **50**(1), 25–38.

LEE, M. R. & PARSONS, I. 1999. Biomechanical and biochemical weathering of lichen-encrusted granite: textural controls on organic-mineral interactions and deposition of silica-rich layers. *Chemical Geology*, **161**, 385–397.

LE METAYER, L. G., CASTANIER, S., ORIAL, G., LOUBIERE, J. F. & PERTHUISOT, J. P. 1999. Applications of bacterial carbonatogenesis to the protection and regeneration of limestones in buildings and historic patrimony. *In*: CAMION, G. F. (ed.) *Microbial Mediation in Carbonate Diagenesis. Sedimentary Geology*, **126**(1–4), 25–34.

MANGELS, J. 1990. *Quantifizierung bio-, geo- und anthropogener Carboxylationen in Werksteinen, deren Ablaufwässern und in Gesamtdepositionen mittels HPLC*. Dissertation, Faculty of Chemistry, University of Hamburg.

MARGULIS, L. & SAGAN, D. 1999. *Leben. Vom Ursprung zur Vielfalt*. Spektrum akademischer Verlag, Heidelberg.

MOJZSIS, S. J., ARRHENIUS, G., MCKEEGAN, K. D., HARRISON, T. M., NUTMAN, A. P. & FRIEND, C. R. L. 1996. Evidence of life before 3800 million years ago. *Nature*, **384**, 55–59.

NASH, T. H. III 1996. *Lichen Biology*. Cambridge University Press, Cambridge.

ORTEGA-CALVO, J. J., HERNANDEZ-MARINE, M. & SEIZ-JIMINEZ, C. 1991. Biodeterioration of building-materials by cyanobacteria and algae. *International Biodeterioration*, **28**, 165–185.

POHL W. 2000. *Wechselwirkungen zwischen endolithischen Biofilmen und Karbonatgesteins-Oberflächen in alpinen Gebieten Mitteleuropas*. PhD Thesis, University of Göttingen (World Wide Web address: http://webdoc.gwdg.de/diss/2000/pohl)

POHL, W., HOPPERT, M., FLIES, C., GÜNZL, B., RUPPERT, H. & SCHNEIDER, J. 2000. Endolithic biofilms: A model for extraterrestrial Ecological Niches? *In*: HOOVER, R. B. (ed.) *Conference on Instruments, Methods and Missions Astrobiology II*, Denver, Colorado. *The International Society for Optical Engeneering, Proceedings*, **3755**, 223–231.

SCHERR, C., WEBER, B. & BÜDEL, B. 1998. *Methoden der CO_2-Gaswechsel und pH-Mesung gesteinsbewohnender Flechten*. Project report, University of Kaiserslautern.

SCHMIDT, P. F. 1994. *Praxis der Rasterelektronenmikroskopie und Mikrobereichsanalyse*. Kontakt und Studium, **444**. Expert Verlag, Renningen Malmsheim.

SCHNEIDER, J. 1976. *Biological and Inorganic Factors in the Destruction of Limestone Coasts*. Contributions to Sedimentology, **6**. Schweizerbart, Stüttgart.

SCHNEIDER, J. & LE CAMPION-ALSUMARD, T. 1999. Construction and destruction of carbonates by marine and freshwater cyanobacteria. *European Journal of Phycology*, **34**, 417–426.

SCHOPF, J. W. 1994. The oldest known records of life: Early Archean stromatolites, microfossils and organic matter. *In*: BENGTSON, S. (ed.) *Early Life on Earth*. Columbia University Press, New York, 193–207.

SCHOPF, J. W. & PACKER, B. M. 1987. Early archean microfossils (2.2 billion to 3.5 billion-year-old) from Warrawoona Group, Australia. *Science*, **237**, 70–73.

SILVA, B., RIVAS, T. & PRIETO, B. 1999. Effects of lichens on the geochemical weathering of rocks. *Chemosphere*, **39**(2), 379–388.

SKOOG, D. A. & LEARY, J. J. 1996. *Instrumentelle Analytik: Grundlagen, Instrumente, Anwendungen*. Springer, Berlin.

STERFLINGER, K. & KRUMBEIN, W. E. 1997. Dematiaceous fungi as a major agent for biopitting on mediterranean marbles and limestones. *Geomicrobiology Journal*, **14**, 219–230.

WALTON, D. W. H. 1993. The effects of cryptogams on mineral substrates. *In*: *Primary Succession on Land*. BES Special Publication, **12**, Blackwell Scientific, Oxford, 33–53.

WARSCHEID, T. & BRAAMS, J. 2000. Biodeterioration of stone: a review. *International Biodeterioration & Biodegradation*, **46**, 343–368.

WELCH S. A. & ULLMANN, W. J. 1992. Dissolution of feldspars in oxalic acid solutions. *In*: KHARAKA, Y. K. & MAEST, A. S. (eds) *Water–Rock Interaction*. AA Balkema, Rotterdam, **7**(1), 127–130.

WELCH, S. A., BARKER, W. W. & BANFIELD, J. F. 1999. Microbial extracellular polysaccharides and plagioclase dissolution. *Geochimica et Cosmochimica Acta*, **63**(9), 1405–1419.

WESSELS, D. & WESSELS, L. 1995. Biogenic weathering and microclimate of Clarens Sandstone in South Africa. *Cryptogamic Botany*, **5**(3), 288–298.

WESSELS, D. C. J. & SCHOEMANN, P. 1988. Mechanism and rate of weathering of Clarens sandstone by an endolithic lichen. *South African Journal of Science*, **84**, 274–277.

Biodeterioration of calcareous and granitic building stones in urban environments

NICK SCHIAVON

Department of Earth Sciences, Downing Street, Cambridge University, Cambridge, CB2 3EQ, UK

Present address: Dipartimento di Chimica 'Ciamician', University of Bologna, via Selmi 2, 40126 Bologna, Italy (e-mail: schiavon@ciam.unibo.it)

Abstract: Scanning electron microscopy in secondary (SEM) and back-scattered (BSEM) mode associated with energy-dispersive X-ray spectroscopy has been used to investigate decay features associated with biological colonization of calcareous and granitic building stones in monuments and rock outcrops in the UK, Portugal and Spain. In combination with physical decay caused by lichen hyphae penetrating the stone substrate, this study reveals how chemical attack by organic acid exudates derived from metabolic activity of lichens and leading to the crystallization and growth of inorganic salt compounds within the stone microfabric is contributing to the destruction and weakening of the building stone surface. BSEM analysis is particularly useful in showing extensive dissolution and corrosion of mineral surfaces underneath biological patinas. Both Ca-sulphate (gypsum) and Ca-oxalate (weddellite) precipitates are clearly associated with the presence of fungal hyphae and bacterial activity particularly in the case of calcareous building stones; the Ca-oxalates present in the example examined are then the result of biomineralization processes and do not derive from past restoration treatments or from air pollution as suggested by many authors. In urban locations, lichenous cover may facilitate the deposition of particulate airborne pollutants on the stone surface. Biological patinas are by no means forming a protective layer on the biocolonized substrate; as is the case with sulphate or non-sulphate soiling patinas from urban air pollution, they act as localized sites of intense desegregation of the stone underneath. Their prompt (but careful) removal and a biocidal treatment of the infested sites in the building is then suggested to avoid permanent loss of detail, particularly harmful in the case of carved surfaces.

Air pollution has been widely recognized as the main factor responsible for decay of building stones in urban areas. High levels of SO_2 in the polluted atmosphere lead to the well-known sulphation mechanisms in a variety of lithological types used as building materials such as limestone, granite and sandstone. It is often assumed that inorganic salt precipitation such as sulphates and nitrates at the surface and/or within the stone fabric comes only as a result of dry and wet deposition processes of urban air pollutants on the stone substrate. Biological colonization by bacteria, algae, fungi and lichens is often regarded as playing a significant role in physical and chemical stone decay only in rural, unpolluted areas. The origin of oxalate patinas in urban monuments, for instance, is at the centre of a scientific debate between researchers who advocate a biologically mediated precipitation mechanism involving the reaction between metabolically produced oxalic acid by lichens and Ca-bearing building materials (DelMonte *et al.* 1987) and others who claim an anthropogenic origin for the oxalic acid either as airborne pollutant (Saiz-Jimenez 1989) and/or as a residue from past conservation treatments applied to stone surfaces (Lazzarini & Salvadori 1989). Back-scattered electron microscopy has proved a useful tool in investigating rock biodeterioration (Wierzchos & Ascaso 1994).

This paper illustrates the use of scanning electron microscopy, both in secondary and back-scattered mode (SEM and BSEM, respectively) interfaced with energy-dispersive spectroscopy (EDS) in investigating decay features and microfabric aspects associated with extensive biological colonization of granitic and calcareous building stones from monuments and buildings across Europe (UK, Spain and Portugal). The main aims of the project were to ascertain whether biodeterioration plays a major role in urban stone decay as it does in the rural environment and to assess whether lithological parameters (mineralogy, porosity) might influence the type of biodeterioration active in monuments built in granite or limestone. The possible presence of common decay forms induced by biological attack on stones of different lithology

From: SIEGESMUND, S., WEISS, T. & VOLLBRECHT, A. 2002. *Natural Stone, Weathering Phenomena, Conservation Strategies and Case Studies*. Geological Society, London, Special Publications, **205**, 195–205.
0305-8719/02/$15.00 © The Geological Society of London 2002.

and in different environmental conditions was also a goal of this research.

Materials and experimental

Surface weathered samples with or without a macroscopically evident biological cover (i.e. lichen colonization; Fig.1) of calcareous and granitic building stones have been collected from the following monuments/buildings and locations.

1. Ely Cathedral, UK: micritic limestone substrate ('clunch') with lichenous cover. Urban environment, low pollution.
2. London Bridge, UK: granitic substrate. Urban environment, high pollution.
3. Monasterio S. Martin Pinario, Santiago de Compostela, Spain: granitic substrate. Urban environment, low pollution.
4. Iglesia Santiago de Vigo, Vigo, Spain: granitic substrate with reddish surficial patinas. Urban environment, medium pollution.
5. Igresia dos Carmo, Oporto, Portugal: granitic substrate with dark surficial patinas. Urban environment, medium pollution.
6. Torre dos Clerigos, Oporto, Portugal: granitic substrate with dark, thin surficial patinas. Urban environment, high pollution.
7. Dartmoor National Park, Merrivale, UK: granitic substrate with lichenous cover. Rural environment, very low pollution.

Fig. 1. Lichen colonization of chalk building limestone. Ely Cathedral, UK.

Rough specimens and thin sections spanning the patina–stone substrate contact were examined by electron microscopy. Thin sections were hand polished down to a thickness of 60–70 μm (thicker than the standard 30 μm used in routine petrographical analyses to account for differences in hardness between rock substrate and weathering patinas). After sputter coating with a thin carbon (thin sections) or gold (rough specimens) layer, samples were examined in a Jeol 820L SEM (with a Robinson back-scatter detector) interfaced with a Link 860 EDS system. Back-scattered electron imaging was used for thin-section work as it provides better image resolution when studying materials with a complex chemical/mineralogical composition such as the weathering patinas under investigation.

Electron microscopy results

Limestone substrate, urban environment

Examination of the outer surface of the weathered stone colonized by epilithic lichens shows a thick and dense network of lichen rhyzines and thalluses, masking the limestone–patina interface (Fig. 2). Associated with algal filaments, amorphous and well crystallized Ca-rich precipitates can be found. Crystals have been identified by BSEM and EDS (C/O ratio and Mg content) and by X-ray diffraction (XRD) as calcite (Ca-carbonate) and weddellite (Ca-oxalate). Clusters of Ca-oxalate crystals with bipyramidal habit and tetragonal symmetry are particularly frequent on the outer portion of the lichenous patinas within the lichen medulla and in an extracellular position (Fig. 3). Ca-sulphate (gypsum) is also present as small crystalline aggregates but is not common. Spherical aluminosilicate particles typical of air pollution from fossil fuel combustion together with quartz and K-feldspar particles from soil dust are present but not abundant. The growth of calcium oxalate crystals does not seem to affect the substrate directly but the contact between the

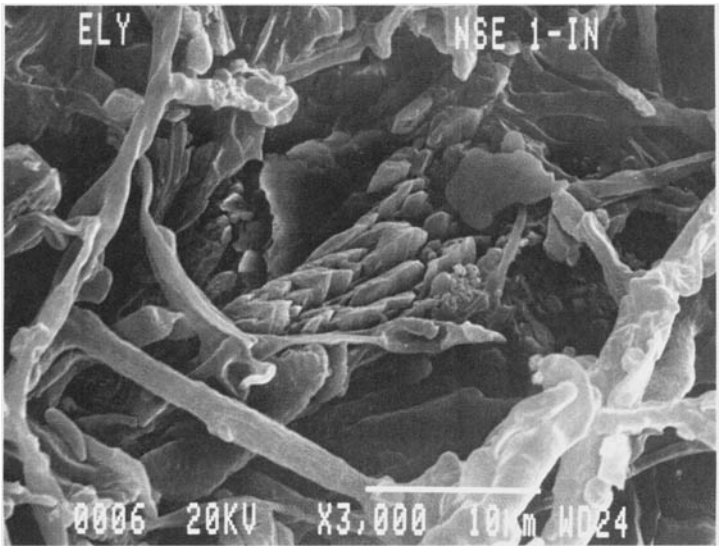

Fig. 2. SEM micrograph view of the exposed surface showing thick and dense network of lichen hyphae and rhyzines on limestone. Ely Cathedral, UK.

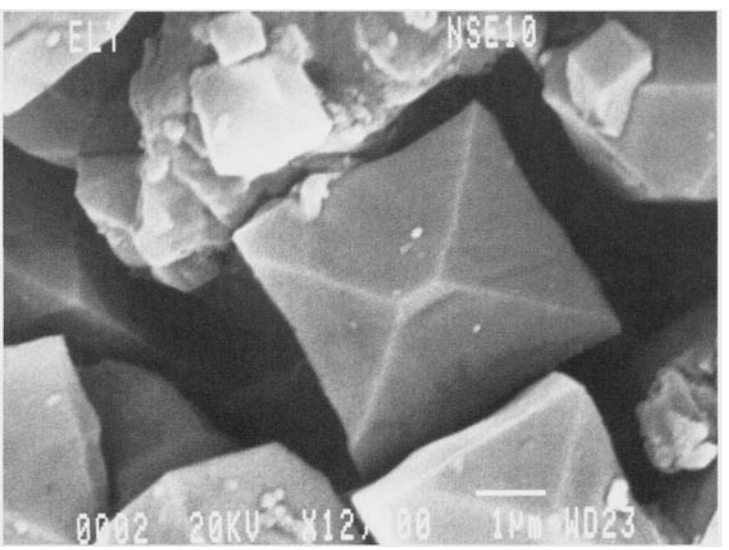

Fig. 3. SEM micrograph view of the exposed surface showing clusters of well formed authigenic Ca-oxalate crystals with bipyramidal habit within lichen biofilm on limestone. Ely Cathedral, UK.

patina and the underlying limestone shows episodes of dissolution and corrosion affecting in particular calcite grains (Fig. 4).

Granitic substrate, urban environment

Whether or not the presence of a biological cover is macroscopically evident on the samples examined, bacterial activity, algal filaments and lichen elements are all clearly detected under SEM examination. All samples show, albeit at different degrees, extensive biocolonization. Lichen hyphae are often penetrating between mineral grains in the granitic substrate enlarging pre-existing weakness points such as cleavage planes in feldspars and micas and/or

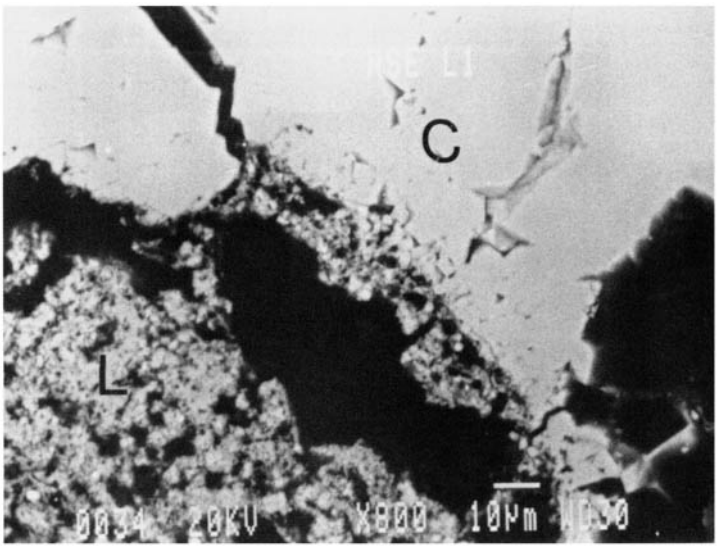

Fig. 4. BSEM micrograph of limestone–lichen patina interface. Calcite of the stone substrate (C) shows evidence of dissolution at the contact with biofilm (L). Ely Cathedral, UK.

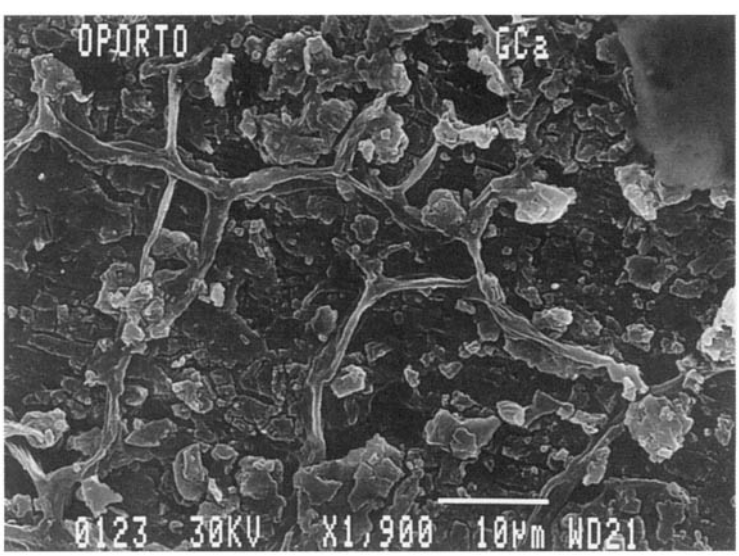

Fig. 5. SEM micrograph view of the exposed surface showing widespread colonization of K-feldspar by algal filaments leading to desegregation of granite superficial microfabric. Igresia dos Carmo, Oporto, Portugal.

intragranular cracks in quartz crystals, and resulting in intense desegregation of the stone fabric (Fig 5). Besides this decay action of a physical nature, episodes of dissolution/etching of mineral grains and precipitation of amorphous and crystalline compounds intimately associated with biological activity are evidence for biochemically derived decay. Etching pits and grooves and dissolution cavities are particularly frequent on feldspars and muscovite micas (Fig. 6) but are common also in more chemically resistant quartz surfaces and on other less soluble accessory granite minerals such as apatite. Chemical weathering fronts do not proceed preferentially along pre-existing mineral weakness points and lines (such as fractures and cleavage planes) but often cut across mineral cleavage planes (Fig. 6). Dissolution

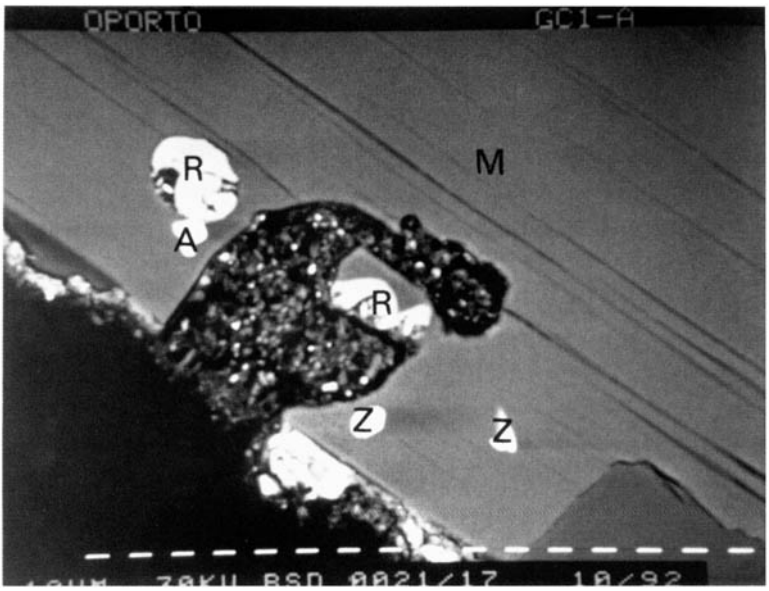

Fig. 6. BSEM micrograph of biological patina–granite interface. Weathering patina on granitic substrate shows selective dissolution of muscovite mica (M) relative to zircon (Z), allanite (A) and rutile (R) inclusions. Note how dissolution front cuts across cleavage planes in muscovite. Torre dos Clerigos, Oporto, Portugal.

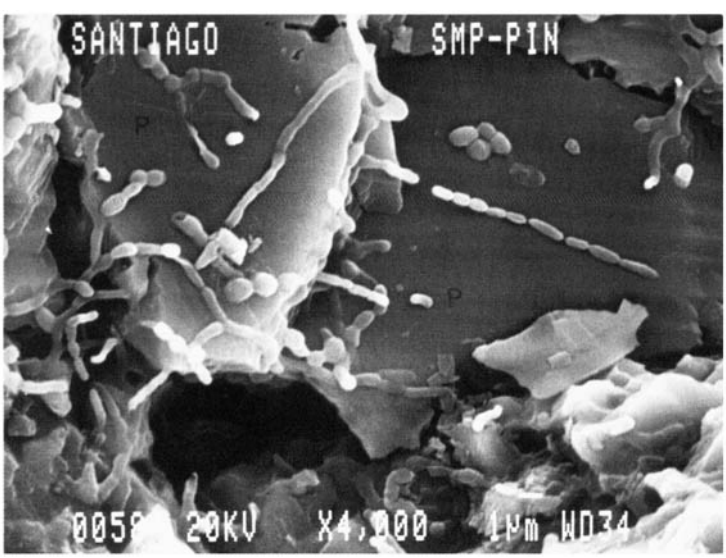

Fig. 7. SEM micrograph view of the exposed surface showing biocolonization by cyanobacteria of biotitic mineral surface leading to the precipitation of biofilm of polysaccharide nature. Monasterio de S. Pinario, Santiago de Compostela, Spain.

episodes on silicate minerals are often coupled with precipitation of amorphous deposits with an Si-rich or Al+Si-rich elemental composition.

Cyanobacterial activity is also responsible for the coating of the stone surface with amorphous P-rich compounds, resembling polysaccharide gels (Fig. 7). The crystallization of gypsum with authigenic crystals displaying the typical monoclinic habit is often localized on algal filaments, suggesting a biologically mediated mechanism

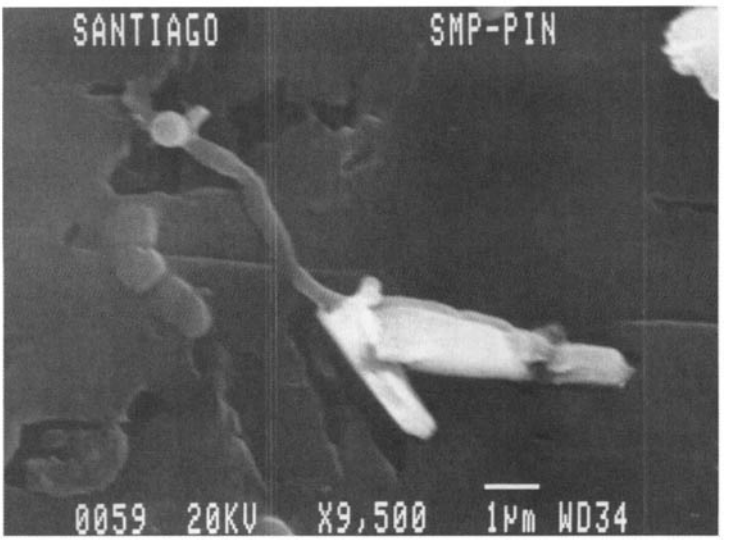

Fig. 8. SEM micrograph view of the exposed surface showing authigenic gypsum crystals nucleating on lichen hyphae on etched albite surface. Monasterio de S. Pinario, Santiago de Compostela, Spain.

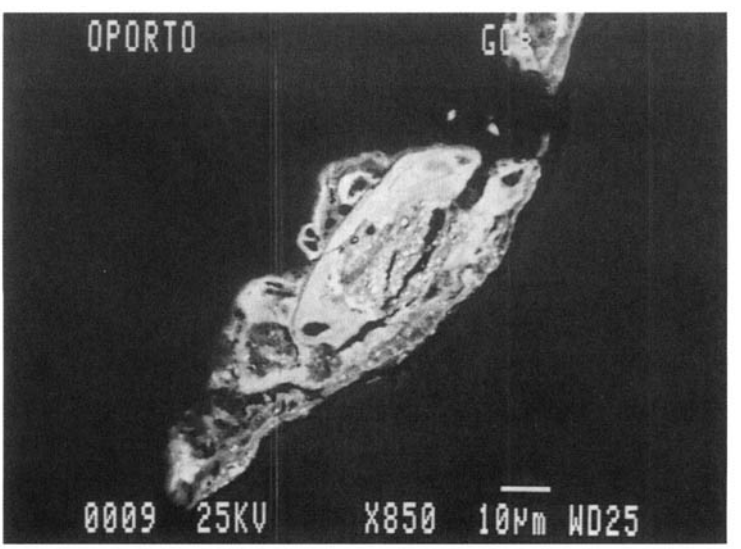

Fig. 9. BSEM micrograph of biological patina–granite interface. Dark, thin iron-rich (brighter areas) patinas on albite surface display faint lamination pattern and chemical attack of granitic substrate. Torre dos Clerigos, Oporto, Portugal.

of growth (Fig. 8). Dark patinas often displaying a reddish colour in field samples, a feature common to many sampling sites, reveal an Fe-rich composition under EDS analysis and a faintly laminated microstructure under BSEM (Fig. 9) resembling that of algal growth; underneath these thin dark patinas an area of intense decay of the granitic substrate is commonly present.

Granitic substrate, rural environment

As a reference for biological decay of granite in a rural, unpolluted location, samples of granitic rocks coated by foliose epilithic lichens in the Dartmoor National Park, UK, have been analysed. The contact between the stone substrate and the lichenous cover shows intense

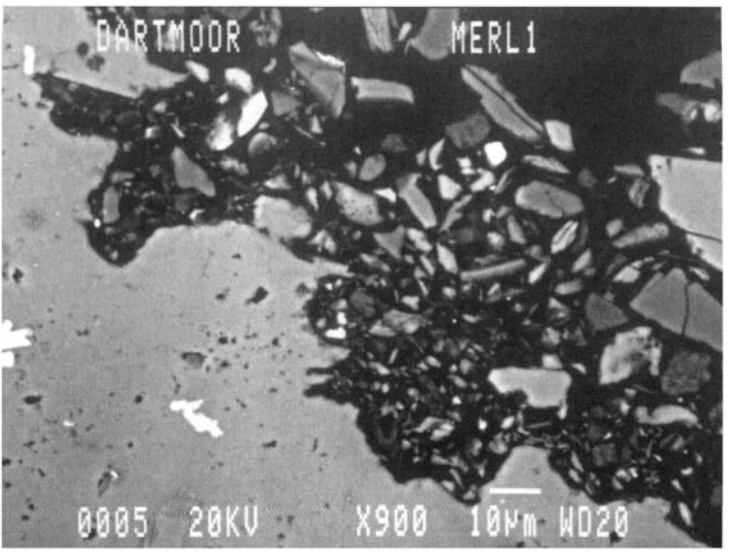

Fig. 10. BSEM micrograph of lichenous patina–granite interface. Note deep chemical corrosion of quartz with incorporation of quartz fragments in growing weathering patina. Dartmoor National Park, UK.

desegregation of the granite surface with incorporation of fragmented material clearly derived from the building stone underneath into the biological patina. In fact, the patina is largely made up of fragments of granitic minerals, i.e. micas, feldspars and quartz (Fig. 10). The depth of the weathered zone from the lichen–stone interface ranges from few micrometres up to 0.5 cm. The EDS chemical analysis of these patinas confirms an elemental composition consistent with that typical of granite apart from higher levels of Ca and Fe. Iron-oxidized outer rims are often visible on weathered granite minerals. Besides physical decay particularly active on biotite crystals where it causes the splitting of biotite flakes along cleavage planes, the electron microscopy investigation shows evidence for etching and chemical attack on quartz (Fig. 10), feldspar and biotite (Fig. 11) surfaces; etch pits are common and the examination of thin sections previously treated with concentrated H_2O_2 to remove the organic fraction, clearly shows the casts of dissolution trenches and pits on mineral surfaces (Fig. 12).

Discussion

Despite high levels of air pollution from both domestic/industrial and motor traffic activities, all the weathering patinas from urban sites display a medium to high degree of biocolonization. This is not unexpected given the fact that cyanobacteria and some lichen species are known to be resistant to relatively high concentrations of air pollutants in the atmosphere and that bacterial activity may metabolize N and S compounds through redox reactions and may also utilize polycyclic aromatic hydrocarbons (PAH) as the sole carbon source (Saiz-Jimenez 1993). Moreover, electron microscopy investigation reveals extensive lichenous and bacterial activity on the stone surface in samples without macroscopic evidence for a biological cover. Penetration of lichen hyphae and rhyzines deep within the substrate causing the destruction of the stone microfabric is common not only on 'soft' lithologies such as limestone but also on 'hard' stones such as granites (Del Monte *et al.* 1996). The mechanism of hyphae penetration is not only of a physical nature, i.e. through hyphae turgor pressures which have been shown to reach values exceeding the compressive strength of most rock substrates (Dornieden & Gorbushina 2000), but also of a chemical nature as the dissolution trenches associated with fungal hyphae on quartz mineral surfaces and the extensive evidence for biocorrosion occurring at the rock substrate–biological patina interface clearly show (Figs 4, 6, 10–12).

The chemical attack by lichens on rock substrates may be explained by the chelating action of the so-called 'lichen substances' (a group of weak organic acids such as oxalic acid) responsible for the formation of complexes with

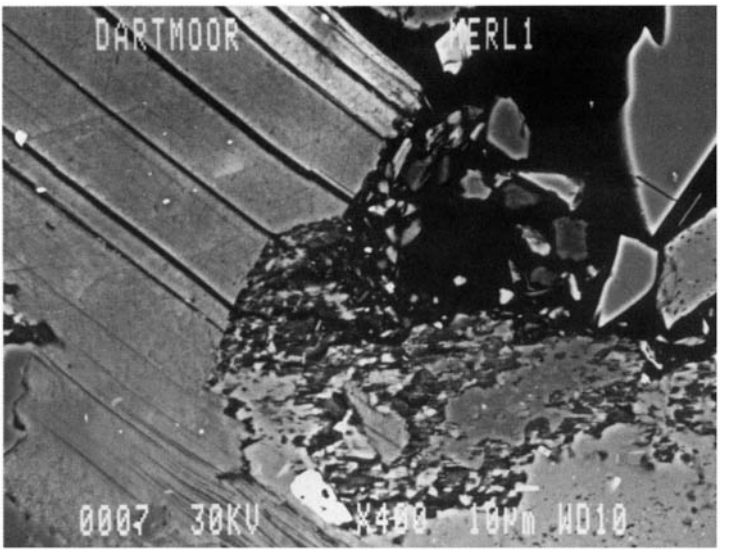

Fig. 11. BSEM micrograph of lichenous patina–granite interface. Physical and chemical decay of biotitic mineral substrate underneath the biological cover leads to the desegregation of the stone fabric. Dartmooor National Park, UK.

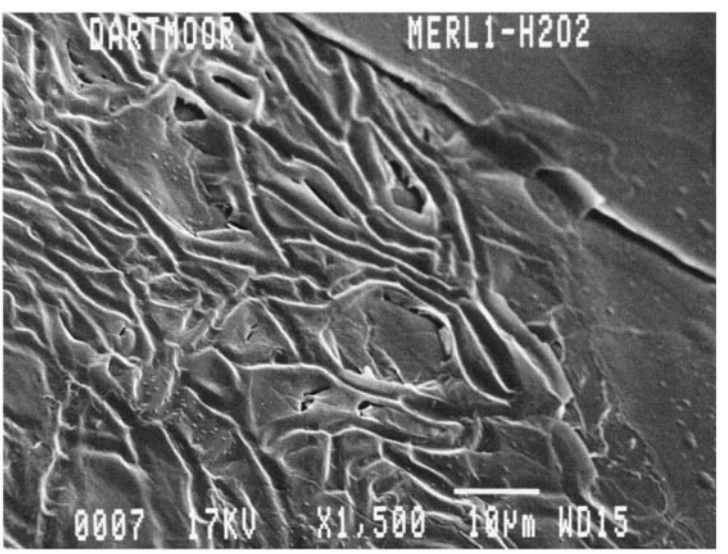

Fig. 12. SEM micrograph view of the surface of the granite after treatment with H_2O_2 to remove the biological patina. Dissolution trenches left on mica surface after removal of the organic cover are clearly visible. Dartmoor National Park, UK.

metallic cations extracted from the stone and used as nutrients (Eckhardt 1985; Robert & Berthelin 1986; Wierzchos & Ascaso 1994; DelMonte *et al.* 1996; Figuereido & DaSilva 1996; Jones & Wakefield 2000). Bio-erosion may also be performed by cyanobacteria which have been shown to extract calcium ions from calcareous stones and precipitate them as calcium carbonate in extracellular polymeric substances (EPS) of a mucopolysaccharide nature (Albertano *et al.* 2000). If these cations were indeed leached from the building stone and not from mineral fragments from soil dust and/or anthropogenic airborne particulate from

air pollution incorporated in the patinas as suggested by some authors (Casal-Porto *et al.* 1989), then one would expect the elemental composition of the patinas to be correlated with the mineralogical composition of the lithic substrate; the latter option seems to better explain the evidence presented in this study according to the following considerations.

Ca-rich precipitates

A Ca-rich substrate such as limestone provides Ca ions leading to the widespread precipitation of Ca-oxalate, Ca-carbonate and amorphous Ca-rich aggregates (Fig. 4). Of particular interest to stone conservators and scientists is the genesis of calcium oxalate films on works of art and monuments with the presence of Ca-oxalate being ascribed either to the degradation of past protective treatments applied to the stone (Lazzarini & Salvadori 1989), or to oxalic acid present as an air pollutant in urban areas (Saiz-Jimenez 1989), or to oxalic acid derived from metabolic activities of lichens and its reaction with Ca-bearing materials (DelMonte *et al.* 1987). The SEM evidence presented in this study showing extracellular precipitation of well formed, authigenic crystals of weddellite within lichen thalli growing on a limestone substrate supports the biological mechanism advocated by the latter authors; furthermore, the dissolution features present at the interface of lichen–Ca-bearing building stone suggests that the oxalate crystals grow at the expense of the limestone substrate. Despite the fact that biologically mediated Ca-oxalate has been found on rocks with low Ca content, the predominantly sodic plagioclasic composition of the granitic rocks investigated in this study does not seem to have favoured the precipitation of well-formed Ca-oxalate crystals which in fact have not been detected. Nevertheless, EDS analysis has shown a certain degree of Ca enrichment in amorphous deposits in the patinas; this Ca may derive from Ca-feldspars (plagioclases) in the granite (DelMonte *et al.* 1996), although, in this case, an external source such as leaching from adjacent mortar joints is more likely (Casal-Porto *et al.* 1989; Schiavon 1993).

Fe-rich patinas and other amorphous deposits

Weathering patinas growing on granitic stone in both urban and rural environments often show areas enriched in Fe relative to the rock substrate (Isherwood & Street 1976; Schiavon 1993). BSEM is particularly useful in showing how this iron enrichment is commonly associated with the presence in the substrate immediately underneath the weathered surficial layer of minerals containing Fe such as biotite. An external source for iron may be postulated for the red patinas from urban areas, i.e. from railings, road chippings or anthropogenic iron-rich airborne particulates (Nord & Ericsson 1993; Schiavon & Zhou 1996) but the ubiquitous presence of iron enrichment in lichenous layers coating outcrops of granite in the unpolluted location of Dartmoor National Park, far away from possible sources of air pollution, suggests leaching from the stone substrate by the chelation mechanism as the most likely cause of Fe enrichment. Leaching of Fe from biotite in granitic rocks by lichen-produced organic acids through the mechanism of chelation with the subsequent precipitation, for example, of Fe-oxalate crystals (humboldtite) has often been reported (Robert & Berthelin 1986; DelMonte *et al.* 1996; Figuereido & DaSilva 1996).

Despite the absence of crystalline Fe-oxalate in the cases examined here, the following lines of evidence confirm a mainly biological origin for the weathered layers examined in this study, not only when an obvious lichen cover is present such as in the case of the Dartmoor patinas but also for the dark and thin Fe-rich patinas found in the Oporto and Santiago urban samples.

(a) Back-scattered electron microscopy detailing the microfabric of the patinas shows the development of a laminated 'stromatolitic' texture (Fig. 9) reminiscent of desert varnish deposits for which a bacterially mediated mechanism of growth is widely assumed (Krumbein & Jens 1981; Nagy *et al.* 1991).
(b) Secondary electron microscopy of rough surfaces of patinas reveals extensive biocolonization with cyanobacteria and lichen elements (hyphae, medulla, rhyzines, fruiting bodies) adhering to the stone substrate (Figs 2, 5, 7).
(c) Decay features such as desegregation of the stone microfabric underneath weathered surficial patinas in urban areas (Figs 5, 6) are very similar to the ones observed in the unpolluted reference location in Dartmoor (Figs 10, 11) where there is no contribution to decay from air pollution.
(d) The ability of bacteria, fungi and lichens to concentrate and precipitate Fe and P (see below) compounds is

indeed well known (Robert & Berthelin 1986; Krumbein & Jens 1981; Nagy *et al.* 1991).

Moreover, iron-rich patinas investigated in this study are often associated with P-rich amorphous patinas developing preferentially where the localized presence of phosphate-rich accessory minerals such as apatite and allanite in the granitic substrate is associated with colonization by lichens and cyanobacteria. Extracellular polymeric substances (EPS) of mucopolysaccharide nature with a P-rich composition found at the surface of building stones have indeed been identified as products of lichens and of cyanobacteria metabolic activities (Gutierrez *et al.* 1995; Pinna & Salvadori 2000).

The Si-rich and Al-Si amorphous deposits are mainly associated with feldspar and quartz mineral surfaces which again show dissolution features and evidence of leaching (Figs 10, 12). Eckhardt (1985) has shown in leaching experiments using 0.1M oxalic acid, substantial extraction of K from micaceous silicate minerals. Microbially produced organic acids and complexing compounds are also known to increase the solubility of silicate and quartz minerals (Bennett & Siegel 1987). Taking into account the widespread occurrence of iron oxides in the investigated patinas, it is interesting to note that redox reactions involving iron have been reported to lead to increased solubility of quartz in laboratory experiments (Morris & Fletcher 1987), probably because of breakdown of an ultra-thin ferrous iron/silica complex formed on the quartz surface with accompanying liberation of silica. On the other hand, quartz solubility is also greatly increased under alkaline conditions (pH > 9) and studies have shown that conditions resulting from the production of alkaline compounds (ammonia and sodium carbonate) by micro-organisms and lichens can promote the solubilization of silica (Robert & Berthelin 1986; Leite-Magalhes & Sequeira-Braga 2000).

Biomineralization chemical processes also lead to the precipitation of crystalline inorganic compounds such as sulphates that are often regarded as products derived exclusively from the interaction of air pollutants (namely SO_2) with building materials (Leite-Magalhes & Sequeira-Braga 2000). SEM evidence showing authigenic gypsum crystals nucleating on algal filaments (Fig. 8) suggests that sulphate deposition may well be enhanced by biological mechanisms. Whether or not gypsum crystallization comes solely as a result of air pollution or is a biologically mediated process, relative to a fresh building surface, biological patinas are sites of increased deposition of both gaseous (SO_2 and NO_x) and particulate (anthropogenic fly-ash and soil dust) pollutants due to their enhanced porosity (either intrinsic to the patinas open fabric or bioinduced on the stone mineral fabric) and moisture retention.

Conclusions

This SEM study confirms previous findings highlighting the important contribution of biologically mediated processes in the decay of building stones in urban as well as in rural areas. Electron microscopy reveals colonization patterns and decay features on building stone surfaces undetected under visual inspection of the building.

Biodeterioration contributes to decay in a twofold manner: (a) by a direct action either physical, i.e. penetration of hyphae within the stone substrate leading to desegregation of the stone into mineral fragments, or chemical by dissolution and precipitation of inorganic compounds within the stone fabric; (b) by an indirect action through the absorption of gaseous and particulate air pollutants (such as SO_2) leading to the sulphation of the stone and decay due to crystallization of sulphate and other salts.

The nature of authigenic mineral and amorphous deposits making up the weathered patinas and their chemical composition largely depends on the mineralogical nature of the stone substrate to which they adhere, inasmuch as the colonizing organisms (bacteria, fungi, algae, lichens) require mineral elements, i.e. Ca, Fe, Si, Al, P, as nutrients.

Biological patinas, in particular lichenous ones, do not play a protective role with respect to the building stone substrate as some authors suggest (Nimis *et al.* 1990; Ariño *et al.* 1995); on the contrary, their prompt removal followed by adequate biocidal protection is needed to avoid and stop important loss of surface material from buildings and monuments.

References

ALBERTANO, P., BRUNO, L., BELLEZZA, S. & PARADOSSI, G. 2000. Polysaccharides as a key to bio-erosion. *In*: FASSINA, V. (ed.) *Proceedings of the 9th International Congress on Deterioration and Conservation of Stone*, Venice, **1**, 425–431.

ARIÑO, X., ORTEGA-CALVO, J. J., GOMEZ-BOLEA, A. & SAIZ-JIMENEZ, C. 1995. Lichen colonization of the Roman pavement at Baelo Claudia (Cadiz,

Spain): biodeterioration vs bioprotection. *Science of the Total Environment*, **167**, 353–363.

BENNETT, P. & SIEGEL, D. I. 1987. Increased solubility of quartz in water due to complexing by organic compounds. *Nature*, **326**, 684–686.

CASAL-PORTO, M., SILVA, B., DELGADO-RODRIGUEZ, J. 1989. Agents and forms of weathering in grantic rocks used in monuments. *In*: BAER, N., SABBIONI, C. & SORS, A. (eds) *Science, Technology and European Cultural Heritage*, Bologna, 439–442.

DELMONTE, M., SABBIONI, C. & ZAPPIA, G. 1987. The origin of calcium oxalates on historical buildings, monuments and natural outcrops. *Science of the Total Environment*, **67**, 17–39.

DELMONTE, M., RATTAZZI, A., ROMÃO, P. & ROSSI, P. 1996. The role of lichens in the weathering of granitic buildings. *In*: VICENTE, M. A., DELGADO-RODRIGUEZ, J. & ACEVEDO, J. (eds) *Degradation and Conservation of Granitic Rocks in Monuments*, EC Research Report 5, 301–306.

DORNIEDEN, T. & GORBUSHINA, A. A. 2000. New methods to study the detrimental effects of poikilotroph microcolonial micromycetes (PMM) on building materials. *In*: FASSINA, V. (ed.) *Proceedings of the 9th International Congress on the Deterioration and Conservation of Stone*, Venice, **1**, 461–468.

ECKHARDT, F. E. W. 1985. Solubilisation, transport and deposition of mineral cations by microorganisms-efficient rock weathering agents. *In*: J. J. DREVER (ed.) *The Chemistry of Weathering*, NATO ASI Series, 161–173.

FIGUEREIDO, O. & DA SILVA, T. P. 1996. Non destructive x-ray fluorescence analysis of heavy metals in lichens using synchroton radiation. *In*: VICENTE, M. A., DELGADO-RODRIGUEZ, J. & ACEVEDO, J. (eds) *Degradation and Conservation of Granitic Rocks in Monuments*, EC Research Report 5, 289–294.

GUTIÉRREZ, A., MARTINEZ, M. J., ALMENDROS, G., GONZALEZ-VILA, A. T. & MARTINEZ, A. T. 1995. Hyphal-sheath polysaccharides in fungal deterioration. *Science of the Total Environment*, **167**, 315–328.

ISHERWOOD, D. & STREET, A. 1976. Biotite induced grussification of the Boulder Creek Granodiorite, Boulder County, Colorado. *Geological Society of America Bulletin*, **87**, 366–370.

JONES, M. S. & WAKEFIELD, R. D. 2000. A study of biologically decayed sandstone with respect to Ca and its distribution. *In*: FASSINA, V. (ed.) *Proceedings of the 9th International Congress on the Deterioration and Conservation of Stone*, Venice, **1**, 473–481.

KRUMBEIN, W. E. & JENS, K. 1981. Biogenic rock varnishes of the Negev desert (Israel): an ecological study of iron and manganese transformation by cyanobacteria and fungi. *Oecologia*, **50**, 25–38.

LAZZARINI, L. & SALVADORI, O. 1989. A reassessment of the patina called 'scialbatura'. *Studies in Conservation*, **34**, 20–26.

LEITE-MAGALHÃES, S. & SEQUEIRA-BRAGA, M. A. 2000. Biological colonization features on a granite monument from Braga (NW Portugal). *In*: FASSINA, V. (ed.) *Proceedings of the 9th International Congress on the Deterioration and Conservation of Stone*, Venice, **1**, 521–529.

MORRIS, R. C. & FLETCHER, A. B. 1987. Increased solubility of quartz following ferrous-ferric iron reactions. *Nature*, **330**, 558–561.

NAGY, B., NAGY, L. A., RIGALI, M. J., KRINSLEY, D. H. & SINCLAIR, N. A. 1991. Rock varnish in the Sonoran desert: microbiologically mediated accumulation of manganiferous sediments. *Sedimentology*, **38**, 1153–1171.

NIMIS, P. L., CASTELLO, M. & PEROTTI, M. 1990. Lichens as biomonitors of sulphur dioxide pollution in La Spezia (N. Italy). *Lichenologist*, **22**(3), 333–344.

NORD, A. G. & ERICSSON, T. 1993. Chemical analysis of thin black layers on building stone. *Studies in Conservation*, **38**, 25–35.

PINNA, D. & SALVADORI, O. 2000. Endolithic lichens and conservation: an underestimated question. *In*: FASSINA, V. (ed.) *Proceedings of the 9th International Congress on the Deterioration and Conservation of Stone*, Venice, **1**, 513–519.

ROBERT, M. & BERTHELIN, J. 1986. Role of biological and biochemical factors in soil mineral weathering. *In*: *Interaction of Soil Minerals with Natural Organics and Microbes*. Soil Science Society of America, Special Publications, **17**, 453–495.

SAIZ-JIMENEZ, C. 1989. Biogenic vs anthropogenic oxalic acid in the environment. *In*: ALESSANDRINI, G. (ed.) *Le pellicole ad ossalati:origine e significato nella conservazione delle opere d'arte*, Milano, 22–34.

SAIZ-JIMENEZ, C. 1993. Deposition of airborne organic pollutants on historic buildings. *Atmospheric Environment*, **27B**, 77–85.

SCHIAVON, N. 1993. Microfabrics of weathered granite in urban monuments. *In*: THIEL, M. J. (ed.) *Conservation of Stone and Other Materials*, E & FN Spon, RILEM, 271–278.

SCHIAVON, N. & ZHOU, L. P. 1996. Magnetic, chemical and microscopical characterization of urban soiling on historical monuments. *Environmental Science & Technology*, **30**, 3264–3269.

WIERZCHOS, J. & ASCASO, C. 1994. Application of back-scattered electron imaging to the study of lichen-rock interface. *Journal of Microscopy*, **175**, 54–59.

This page intentionally left blank

Biofilms and their extracellular environment on geomaterials: methods for investigation down to nanometre scale

M. HOPPERT[1], R. BERKER[1], C. FLIES[1], M. KÄMPER[1], W. POHL[2], J. SCHNEIDER[2] & S. STRÖBEL[1]

[1] *Institut für Mikrobiologie und Genetik, Universität Göttingen, Grisebachstrasse 8, D-37077 Göttingen, Germany (e-mail: mhopper@gwdg.de)*

[2] *Institut für Geologie und Dynamik der Lithosphäre, Universität Göttingen, Goldschmidstrasse 3, D-37077 Göttingen, Germany*

Abstract: On solid surfaces of building material, micro-organisms form a tightly attached layer that may affect the underlying substratum. The biofilm is mainly composed of cells and extracellular polymeric substances (EPS; mostly various polysaccharides). Attachment of the mature biofilm on the substratum is mediated by the EPS. For analysis by transmission electron microscopy, the biofilm structure must be maintained by appropriate methods that stabilize the organisms and especially the EPS. Specially adapted preparation techniques allow detachment of a surface biofilm or dissolution of the substratum without affecting the biofilm structure. The cellular and extracellular structures are retained in such a way that they are detectable by various specific marker systems.

Micro-organisms are ubiquitous and adhere to virtually every material ('substratum'; Beveridge *et al.* 1997; Geesey 2001). Thus, microbial colonization ('biofilm' formation) of natural rocks and building stones is unavoidable. Also the surfaces of processed materials (glass, metal) and synthetic products (plastics, varnishes) are affected (Golubic *et al.* 1980; Gehrmann *et al.* 1992; Danin 1993; May *et al.* 1993; Ariño & Saiz Jimenez 1996; Warscheid 1996, 2000; Mansch & Bock 1998; Brüggerhof *et al.* 1999; Warscheid & Braams 2000). Some organisms may penetrate the material and live as subsurface biofilms inside the material, down to several centimetres beneath the surface. In stone, they are most common and are referred to as endolithic biofilm (Golubic *et al.* 1980).

The chemical composition of the colonized material, the surface relief and moistening regimen determine the growth of micro-organisms on surfaces (Etymezian *et al.* 1998). The colonizers are regularly oligotrophic, i.e. adapted to a low input of organic nutrients. In a mature biofilm, the organisms are embedded in a layer of extracellular polymeric substance (EPS). The EPS is secreted by the organisms and mediates the attachment to the surface. Often, primary producers (green or blue-green algae) provide the organic substrate for other organisms that grow on the organic material (John 1988). The micro-organisms may cause deterioration of the material or are causative agents of dark patina on surfaces. Especially on building stone, the patinas are disturbing for aesthetic reasons or cause associated problems by, for example, excessive warming upon exposure to sunlight. Cleaning of the surface, application of coatings and/or biocides may only temporarily bring about reduction of excessive colonization. In order to avoid excessive biofilm growth, climatic and edaphic factors, direction of rainwater flow on the outside of the building, rising damp, rigidity of the building material against deterioration, and surface structure of the building material have to be taken into account. It has to be noted that biofilms may not be the primary cause of stone deterioration. The stone may be colonized as a result of (non-biogenic) affection of a surface. Biofilms may not cause deterioration of the surface at all or may even protect a surface from other deteriorative effects (Hawksworth 2001).

Presently, numerous techniques are at hand for investigation of the interaction between a micro-organism and its substratum at the structural level. Biofilms may be very well investigated by (fluorescent) light microscopy. The optical resolution of the light microscope allows visualization of the overall biofilm composition, i.e. identification of cell morphotypes, species (with the aid of markers) and extracellular polymers (Bartosch *et al.* 1996). Light microscopy, in spite of a low detection limit of fluorescent targets, does not provide, of course, the resolution of structures smaller than 200 nm. The mechanism of interaction between biofilms

From: SIEGESMUND, S., WEISS, T. & VOLLBRECHT, A. 2002. *Natural Stone, Weathering Phenomena, Conservation Strategies and Case Studies*. Geological Society, London, Special Publications, **205**, 207–215.
0305-8719/02/$15.00 © The Geological Society of London 2002.

and their substrata at submicrometre dimensions is poorly understood. Thus, scanning and transmission electron microscopy as well as scanning force microscopy provide the most straightforward methods for investigation of structure–function relationships between organisms and their substratum (Ray *et al.* 1997; Lower *et al.* 2001). Here, structures involved in adhesion and deterioration of material are directly visible. Specific marker systems locate targets inside or outside ultrathin sections of cells with a resolution down to 20 nm (Rohde *et al.* 1988). However, organisms must be processed in a way to withstand the high vacuum conditions and electron bombardment in the electron microscope. Organisms are regularly not stable in their native state (except in scanning electron microscopes equipped with low vacuum environmental chambers) and have to be chemically fixed or deeply frozen prior to processing for electron microscopy. Stabilizing the highly hydrated EPS is even more difficult.

This chapter presents an overview of electron microscopic methods adapted for the investigation of surface-attached or subsurface biofilms, used for specific detection of extracellular polymers. Special emphasis is given to methods which allow chemical fixation and resin embedding but stabilize the *in vivo* highly hydrated EPS.

Preparative methods

Biofilm samples

Samples of biofilms were collected from various natural habitats or were cultivated on artificial media in defined culture (see also Pohl *et al.* 2000):

(a) biofilm dominated by green algae grown on a periodically moistened polyethylene surface under greenhouse conditions;
(b) artifical biofilm raised on a viscose matrix submerged in culture medium (0.8% w/v nutrient broth medium, pH 7.0; Tada *et al.* 1995), composed of the two bacterial species *Brevibacterium helvolum* and *Acinetobacter lwoffii*; the organisms have been isolated from a biofilm community grown on a ceramics surface;
(c) 'nitrifying' biofilm grown on granulated pumice stone dominated by *Nitrosomonas* sp. cells (Kanning 1997);
(d) endolithic biofilm from limestone rocks in high alpine glacier forelands (Pohl & Schneider 2002);
(e) artificial biofilm raised on a polyethylene matrix composed of a novel isolate (Gram-negative bacterium) from biofilm (a) and the cyanobacterium *Anabaena cylindrica* (strain SAG 1403-2);
(f) biofilm dominated by heterotrophic bacteria and fungi grown on a polyethylene surface (Millsap *et al.* 1997).

Processing of surface-attached biofilms from their substratum

A biofilm attached to a smooth or a moderately sculptured surface (plastics or stone material) is covered with a gelatin layer. After solidification (accelerated by refrigeration for 10 min), the specimen is incubated in 0.7–3% (v/v) glutaraldehyde fixing solution for 1–3 h. Aldehyde concentration and incubation time will depend on the film thickness here varying between 0.5–2.5 mm. After rinsing the specimen three times in 50 mM phosphate buffer (containing 0.9% w/v NaCl), the gelatin layer was carefully peeled off the surface, together with the attached biofilm. The biofilm–gelatin sandwich was then embedded in agar (to protect the exposed side of the biofilm), and subjected to dehydration and resin embedding according to standard protocols, which comprise embedding in epoxy resin (Spurr 1969), low-temperature embedding resin (Carlemalm *et al.* 1982) or freeze substitution of specimens (Robards & Sleytr 1985) and ultrathin sectioning (see Hoppert & Holzenburg (1998) for overview). For subsequent immunolocalization of extracellular polymers, specimens were subjected to low-temperature embedding as described in Carlemalm *et al.* (1982). Before transmission electron microscopy, all sections (mounted on nickel specimen grids) were stained with 10% lead citrate and/or 4% (w/v) uranyl acetate solution for 5 min.

Processing of biofilms that penetrate the substratum

When biofilms have penetrated the substratum, removal with a gelatin layer would not be successful. These biofilms were prepared as follows. A sample of the substratum (e.g. a carbonate stone) was collected from the sampling site. The extension of the biofilm into the depth of the substratum was estimated under a stereomicroscope. A thin sheet of the block containing the biofilm in its whole extension into the depth was then cut with a saw microtome. The whole sample was embedded in

gelatin solution as described above and, after fixation of the gelatin layer and rinsing, subjected to decalcification in a 10% (w/v) EDTA solution (N,N'-1,2-ethanediylbis [N-(carboxymethyl)-glycine], disodium salt, adjusted with NaOH to pH 8.0). Decalcification needed 2–7 days with several changes of the EDTA solution. After decalcification was completed, the remaining biofilm was visible as a thin mat or filamentous network, stabilized by the gelatin layer at the side of the former substratum surface. The film was then embedded in agar and subjected to dehydration and resin embedding according to standard protocols (see above).

Alternatively, a thin sheet of the original sample was chemically fixed and resin embedded according to the standard protocols. After polymerization of the resin, the specimen was sectioned by use of a saw microtome, to get a thin plate of the substratum. The layer of polymerized resin stabilized the substratum surface and the biofilm. The exposed stone was then subjected to decalcification as described above. During decalcification, the biofilm became exposed, still stabilized by the polymerized resin at one side. The biofilm was then dehydrated and embedded for a second time. As a result, the stone substratum was completely replaced by resin. Sectioning was then performed after resin polymerization according to established procedures with a diamond knife; further processing was performed as described above.

Use of marker systems

For production of antibodies specifically directed against the polysaccharide fraction of extracellular polymeric substances produced by a specific organism, the polymers were extracted from a pure culture of this organism according to an established procedure (May & Chakrabarty 1994). To produce polyclonal IgG antibody in rabbits (Harlow & Lane 1988) 600–700 μg polysaccharide were applied as antigen.

Colloidal gold (supplier: British Bio Cell, Oxford, UK) was routinely used as electron-dense marker for electron microscopy. The gold colloid was purchased coupled to protein A, or 'secondary' antibodies that bind to otherwise invisible primary markers (specific for a component of the biofilm). Lectins as specific markers were directly coupled to the gold colloid (Table 1). Coupling of the lectins to gold colloid was performed according to established procedures (Horisberger 1985), whereby Bandeiraea and Concanavalin A were coupled without further pretreatment. Arachis, lentil and wheat-germ agglutinin were pretreated as follows (Horisberger 1985). The lectin was coupled to bovine serum albumin (BSA) with gluradialdehyde as coupling agent. The optimum concentration of both proteins was determined by mixing stock solutions of 10 mg/ml lectin and 40 mg/ml BSA between 2:1 and 0.1:1 BSA:lectin weight ratio. Stock solutions and dilutions were prepared in 10 mM potassium phosphate buffer (pH 7.0). After addition of glutaraldehyde (3%, v/v, final concentration), the solution was incubated for 1 h at room temperature. Large protein precipitates were then removed by filtering the solution with a nitrocellulose filter of 0.2 μm pore size. A serial dilution of the filtrate (1:2, 1:4, 1:8, 1:16 etc.) was used to stabilize colloidal gold solutions by incubation at room temperature for 5 min. Gold particle sizes ranged between 5 and 20 nm in diameter. After addition of 10% (w/v) sodium chloride solution, non-stabilized gold forms large clusters, visible as a colour change of the wine-red colloidal solution to blue-violet. Coupling between protein and colloid was performed with an excess of 10% of the minimum stabilizing protein–gold concentration. The protein–gold conjugate was centrifuged repeatedly at 30 000 × g at room temperature to remove the non-conjugated protein in the supernatant and large gold clusters. The latter are found as small pellets tightly attached to the centrifuge tube. A loose cloudy layer of concentrated colloid is sucked off and used for localization.

Several controls confirmed the specificity between the primary marker and the component of the specimen as well as the specificity of the electron-dense marker system to the primary marker. Incubation of the specimen exclusively with the electron-dense marker produced no signal. Incubation of the primary marker with the free antigen or, for lectins, with a 10 mM solution of the monosaccharide of highest affinity (see Table 1) suppressed the signal.

Results and discussion

Preparation of biofilms for transmission electron microscopy

The microbial biofilms from various natural and synthetic materials have all been subjected, in the end, to ultrathin sectioning, localization procedures and visualization in a transmission electron microscope (TEM, see also Pohl *et al.* 2000). Since transmission electron microscopy requires the preparation of ultrathin-sectioned

Table 1. *Specificity of various lectins (Leatham & Atkins 1983)*

Lectin	Source (plant name)	Highest monosaccharide affinity	Highest affinity to (groups in) oligosaccharides
Arachis	*Arachis hypogaea* (peanut)	galactose	galactosyl (β-1,3) N-acetylgalactosamine
Bandeiraea (five isolectins)	*Griffonia (Bandeiraea) simplicifolia*	N-acetylgalactosamine	α-N-acetylgalactosamine residues, α-galactose residues
Concanavalin A	*Canavalia ensiformis* (jack bean)	mannose, glucose	α-mannose residues
Lentil (three isolectins)	*Lens culinaris* (lentil)	mannose, glucose	α-mannose residues
Wheat-germ agglutinin	*Triticum vulgaris* (wheat)	N-acetylglucosamine	dimers or trimers of N-acetylglucosamine

specimens, either the biofilm must be sectioned together with the underlying substratum, or the substratum must be removed before further processing. Numerous materials may be sectioned together with adhering organisms, especially resin coatings, varnishes and plastic material (such as polyethylene or viscose, see Fig. 1). Here, care has to be taken that the biofilm does not become artificially detached from the substratum surface. Adhesion of the film on the surface may be enhanced by chemical fixation as long as reactive groups (e.g. primary amino groups) are present that allow cross-linking to the biofilm. Generally, gelatin embedding of a small biofilm sample on the substratum before chemical fixation in glutaraldehyde solution is more practical. Sectioning of resin-embedded specimens containing a small number of mineral fragments below the thickness of a single ultrathin section (regularly 0.1 μm) is possible without excessive damage of the (disposable) glass knife. When attached to a gelatin layer and chemically fixed with cross-linking aldehyde fixatives, the tight layer may be peeled off the substratum surface, whereby ideally the complete biofilm is removed. This treatment allows resin embedding and sectioning of the specimen according to standard procedures (Fig. 1a). Figure 1b shows a biofilm dominated by *Acinetobacter lwoffii* on a plastic (here viscose) surface. The film covering the surface of the substratum has been grown in a nutrient solution. Usually only the surface is covered with organisms. Occasionally, single organisms have penetrated the material. The ammonia-oxidizing biofilm as depicted in Figure 1c was originally attached to the surface of pumice stone. Similarly to the biofilm in Figure 1a, the substratum could be removed completely.

For biofilms that are surrounded by a hard substratum (rather than attached to its surface), processing without dissolution of the substratum may be impossible. All materials that are rapidly dissolved by micro-organisms are, of course, also susceptible to a respective chemical treatment. The methods for preparation depend on the chemical nature of the mineral matrix. Regularly, most rigid and chemically inert areas (e.g. quartz grains) are not penetrated or penetrable by organisms. In calcareous sandstone, for instance, organisms penetrate dissolvable cement, whereas rigid (quartz) grains are less affected. The preparation of the biofilm from these materials with decalcifying agents dissolves the calcareous cement whereby grains and matrix components become liberated and may be removed by extensive rinsing. Homogeneous carbonates, which are often actively dissolved by micro-organisms (Golubic *et al.* 1980), may be completely removed with solutions containing EDTA as chelating agent. Similar decalcification protocols are widely used for preparation of calcified tissue form bone or cartilage, but also for coral specimens (Brain, 1966; Priess *et al.* 2000). An appropriately chemically fixed specimen withstands the procedure. Figure 2 shows a cross-section of an endolithic lichen thallus after chemical fixation and dissolution of the substratum. In spite of certain shrinkage of the algal protoplast, the cytological features are maintained. The antigenicity is retained as demonstrated by immunolocalization of a key enzyme (ribulose bisphosphate carboxylase), which is present in high concentration in chloroplasts of the algal symbiont between the thylakoids (Fig. 2c). Of course, not all structures may be conserved in a way that specific marker systems may still be used to detect them. This has to be checked out for every system before starting the experiment.

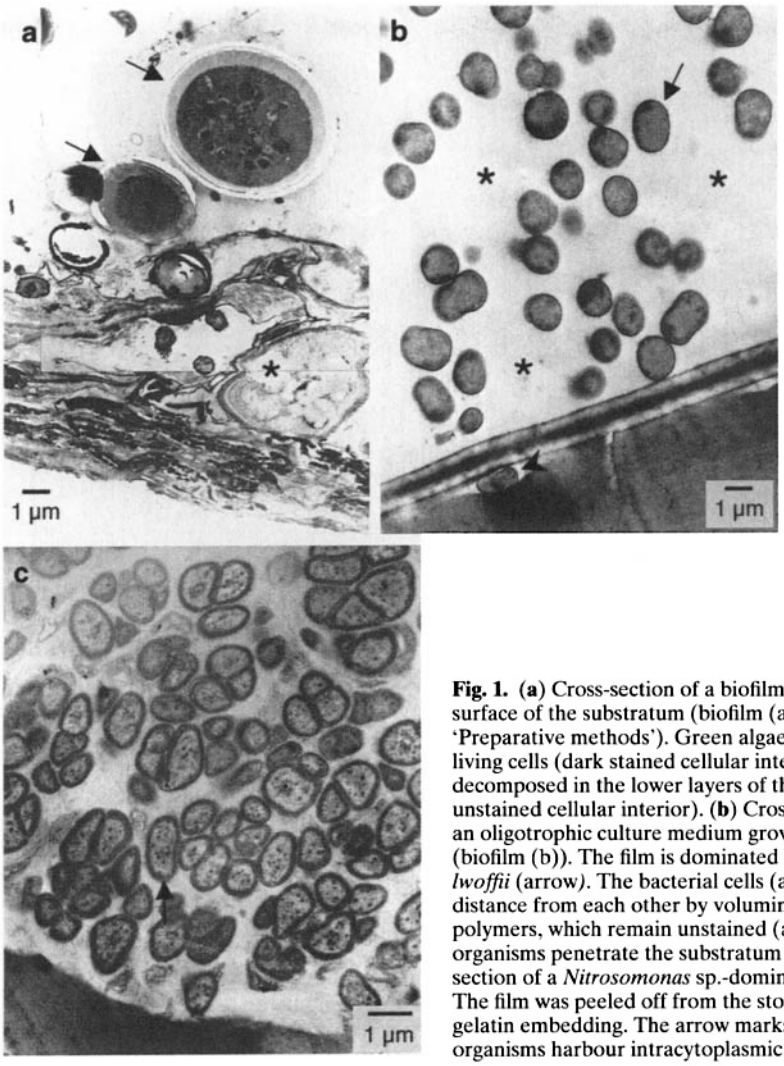

Fig. 1. (**a**) Cross-section of a biofilm detached from the surface of the substratum (biofilm (a) as described in 'Preparative methods'). Green algae form an upper layer of living cells (dark stained cellular interior, arrow) and become decomposed in the lower layers of the film (asterisk, unstained cellular interior). (**b**) Cross-section of a biofilm in an oligotrophic culture medium grown on a viscose surface (biofilm (b)). The film is dominated by cells of *Acinetobacter lwoffii* (arrow). The bacterial cells (arrows) are kept at a distance from each other by voluminous extracellular polymers, which remain unstained (asterisk). Eventually, the organisms penetrate the substratum (arrow head). (**c**) Cross-section of a *Nitrosomonas* sp.-dominated biofilm (biofilm (c)). The film was peeled off from the stone substratum after gelatin embedding. The arrow marks an individual cell. The organisms harbour intracytoplasmic membranes.

Localization of the biofilm extracellular polymers

During the early stages of biofilm development, the organisms are in direct contact with the substratum (Lappin-Scott & Bass 2001). In mature biofilms, the extracellular polymeric substance (EPS) acts as glue between the cells and mediates contact to the substratum. EPS is a reservoir of several enzyme activities as well as a protective barrier against toxic compounds and rapid desiccation. Thus, the organisms in a mature biofilm are regularly not in direct contact with their substratum (Flemming & Wingender 2001). All compounds excreted by the organisms diffuse through the EPS or belong to the polymeric substances themselves (Banfield *et al.* 1999). EPS fills the finest pore spaces, and induces high mechanical stress to the substratum due to swelling upon moistening (Kiessl 1989). Deterioration of the substratum by, for example, excreted organic acids and/or chelating agents takes place at the interface between EPS and substratum. On the other hand, EPS may also replace, to some extent, the extracted cement and keep the non-dissolvable components of the stone in place.

It is difficult to keep the highly hydrated EPS stabilized during the dehydration steps of the embedding procedures. Figure 3 illustrates the differences in the appearance of a conventionally treated biofilm organism surrounded by an irregular layer of collapsed EPS (Fig. 3a) and EPS stabilized by preincubation with a specific

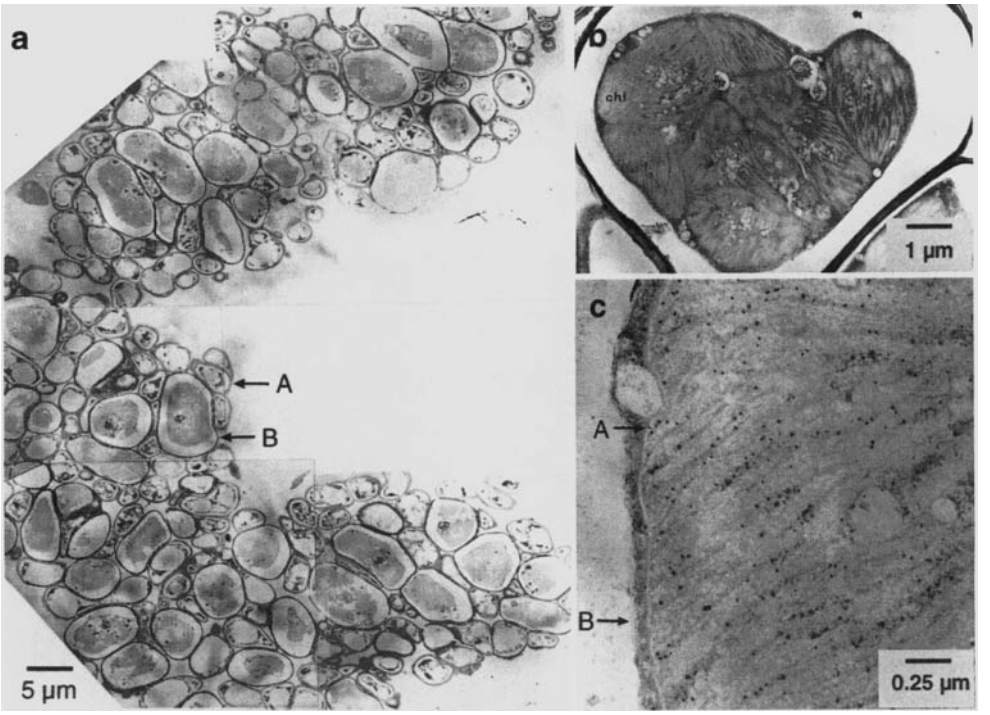

Fig. 2. (**a**) Endolithic lichen after dissolution of the surrounding carbonate rock (biofilm (c) as described in 'Preparative methods'). A, Fungal hypha (mycobiont of the lichen); B, green algal cell (phycobiont). (**b**) A green algal cell with considerable shrinkage of the protoplast after preparation, but generally maintained cytological features, especially the algal chloroplasts (chl). (**c**) Immunolocalization of ribulose bisphosphate carboxylase (black dots) demonstrates that antigenicity is retained. A, Chloroplast membrane; B, cytoplasmic membrane of the algal protoplast.

anti-EPS antibody prior to fixation and embedding (Fig. 3b). The immunoglobulin G protein is chemically cross-linked during the fixation procedure with glutaraldehyde and marks the original extension of the EPS layer surrounding the cell. For subsequent localization procedures, the bound antibodies may interfere with the marker system. Therefore, the biofilms that mainly consist of EPS have been subjected to low temperature embedding or cryofixation and subsequent freeze substitution of the specimen (Fig. 4). Localization of EPS produced by either of the biofilm organisms is possible by application of several marker techniques with colloidal gold as coupled to a specific probe. In Figure 4a, the marker system specific for the EPS of a definite organism (a Gram-negative heterotrophic bacterium isolated from a biofilm as depicted in Fig. 1a) is excluded from the EPS produced by a cyanobacterium, indicating the presence of well-defined, separated regions of extracellular polymers for the biofilm organisms. This technique allows estimation of the contribution of a specific organism to the formation of a biofilm. As depicted in Figure 4a, the EPSs of two organisms are well separated: a clear frontier between the otherwise invisible EPSs of the different organisms is present.

The specific composition of EPS carbohydrates may be used for affinity binding of lectin markers. These proteins bind to specific short carbohydrate sequences (Table 1). When coupled to colloidal gold, they are suitable markers for electron microscopy. Thus, distribution of EPS in the biofilm becomes visible, such as the interconnections between organisms brought about by EPS (Fig. 4b). Lectins with different specificities coupled to gold markers of distinguishable size may be used to discriminate between EPS variants of micro-organisms (Fig. 4c, d).

Conclusions

After stabilization of the organisms and their EPSs, it is possible to use established techniques

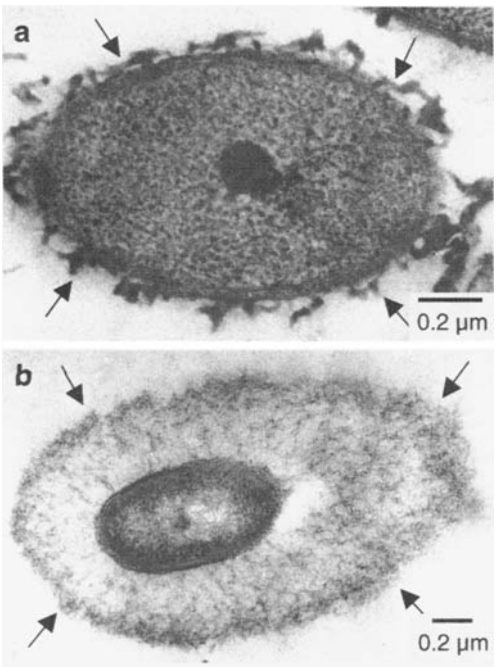

Fig. 3. (**a**) Gram-negative bacterium isolated from the biofilm as depicted in Figure 1a with an extended capsule, consisting of EPS. Conventional chemical fixation, dehydration and embedding (Spurr 1969) lead to an irregularly coagulated layer surround the cell (arrows). (**b**) Incubation with antibodies directed against the polysaccharide component of EPS before fixation and embedding reveal the actual extent of the capsule (arrows).

for localization of macromolecular components by transmission electron microscopy, either inside cells or in the EPS. EPS composition is detectable with the presented techniques at resolution down to the scale of several nanometres. The EPS, as a glue between organisms and substratum and as carrier of all deteriorative agents, chelators, polymers and enzyme proteins, may be viewed as the true causative agent of deterioration. The presented techniques help to determine the role of the EPS in deterioration processes. This opens the way to understanding the deterioration of material at a small scale and in its early stages.

References

ARIÑO, X. & SAIZ-JIMENEZ, C. 1996. Biological diversity and cultural heritage. *Aerobiologia*, **12**, 279–282.

BANFIELD, J. F., BARKER, W. W., WELCH, S. A. & TAUNTON, A. 1999. Biological impact on mineral dissolution: Application of the lichen model to understanding mineral weathering in the rhizosphere. *Proceedings of the National Academy of Sciences of the USA*, **96**, 3404–3411.

BARTOSCH, S., QUADER, H. & BOCK, E. 1996. Confocal Laser Scanning Microscopy: A new method for detecting micro-organisms in natural stone. *In*: *Biodeterioration and Biodegradation.* DECHEMA monographs, **133**, VCH, Frankfurt, 37–43.

BEVERIDGE, T. J., MAKIN, S. A., KADURUGAMUWA, J. L. & LI, Z. 1997. Interactions between biofilms and the environment. *FEMS Microbiological Reviews*, **20**, 291–303.

BRAIN, E. B. 1966. *The Preparation of Decalcified Sections*. Charles C. Thomas, Springfield, IL.

BRÜGGERHOFF, S., CHEBA, S., LEISEN, H. & WARSCHEID, T. 1999. Carbonate crusts on marble fragments at the excavation site in Milet, Turkey: Examination of crust formation and first results of a cleaning concept. *Proceedings of 12th Triennial Meeting Lyon of the ICOM Committee for Conservation*. James & Lames, London, 731–736.

CARLEMALM, E., GARAVITO, R. M. & VILLIGER, W. 1982. Resin development for electron microscopy and an analysis of embedding at low temperature. *Journal of Microscopy*, **126**, 123–143.

DANIN, A. 1993. Pitting of calcareous rocks by organisms under terrestrial conditions. *Israel Journal of Earth Sciences*, **41**, 201–207.

ETYMEZIAN, V., DAVIDSON, C., FINGER, S., STRIEGEL, M. F., BARABAS, N. & CHOW, J. C. 1998. Vertical gradients of pollutant concentrations and deposition fluxes on a tall limestone building. *Journal of the American Institute for Conservation*, **37**, 187–210.

FLEMMING, H. C. & WINGENDER, J. 2001. Relevance of microbial extracellular polymeric substances (EPSs) – Part I: Structural and ecological aspects. *Water Science and Technology*, **43**, 1–8.

GEESEY, G. G. 2001. Bacterial behavior at surfaces. *Current Opinion in Microbiology*, **4**, 296–300.

GEHRMANN, C. K., KRUMBEIN, W. E. & PETERSEN, K. 1992. Endolithic lichens and the corrosion of carbonate rocks – a study of biopitting. *International Journal of Mycology and Lichenology*, **5**, 37–48.

GOLUBIC, S., FRIEDMAN, E. I. & SCHNEIDER, J. 1980. The lithobiontic ecological niche, with special reference to micro-organisms. *Journal of Sedimentology and Petrology*, **51**, 475–478.

HARLOW, E. & LANE, D. 1988. *Antibodies: A Laboratory Manual*. Cold Spring Harbor Laboratory Press, Cold Spring Harbor, NY.

HAWKSWORTH, D. L. 2001. Do lichens protect or damage stonework? *Mycological Research*, **105**, 386.

HOPPERT, M. & HOLZENBURG, A. 1998. *Electron Microscopy in Microbiology*. Bios, Oxford.

HORISBERGER, M. 1985. The gold method as applied to lectin cytochemistry in transmission and scanning electron microscopy. *In*: BULLOCK, G. R. & PETRUSZ, P. (eds) *Techniques in Immunocytochemisty*, Vol. 3. Academic Press, London, 155–178.

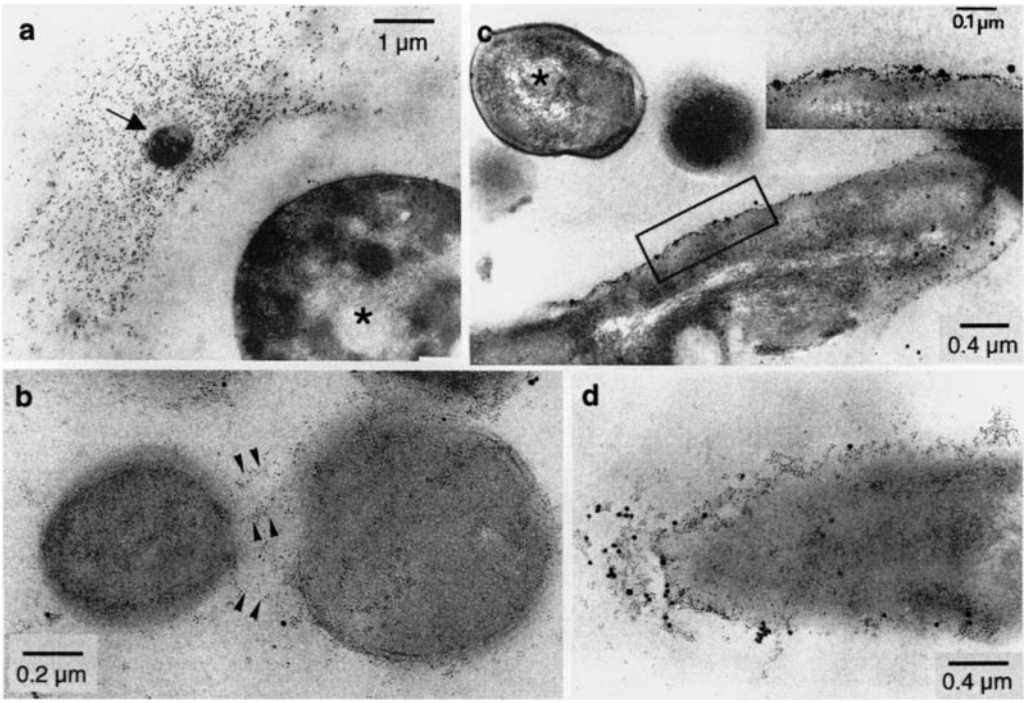

Fig. 4. (**a**) Exclusion of a specific polysaccharide marker (immunoglobulin G antibodies directed against the polysaccharide fraction of EPS produced by the organism marked by an arrow) from the EPS of a filamentous cyanobacterium (*Anabaena cylindrica*, marked by an asterisk) in an artificial biofilm (biofilm (e) as described in 'Preparative methods'). (**b**) Space between two bacterial cells (biofilm (f)) is filled with extracellular polysaccharides as indicated by the binding of Arachis lectin markers (arrow heads). (**c**) Localization of two lectin binding sites (Arachis, large gold particles) and Concanavalin A (small gold particles) on ultrathin sections of a bacterial biofilm organism grown on a polyethylene surface (biofilm (f)). Not all organisms expose binding sites for the lectins. The cross-section of a bacterial cell highlighted by an asterisk is not marked by gold particles. (**d**) Pole of a cell in biofilm (f) with a clear concentration of Aracis lectin binding sites at a cell pole, indicating an uneven distribution of the specific polysaccharide types over the cell surface.

JOHN, D. M. 1988. Algal growth on buildings: a general review and methods of treatment. *Biodeterioration Abstracts*, **2**, 81–102.

KANNING, K. 1997. *Optimierung der unvollständigen Nitrifikation in Hochleistungsbiofilmreaktoren: Verfahrenstechnische, kinetische und mikrobiologische Untersuchungen am Beispiel des Airlift-Schlaufenreaktors*. Cuvillier, Göttingen.

KIESSL, K. 1989. Bauphysikalische Einflüsse bei der Krustenbildung am Gestein alterBauwerke. *Bauphysik*, **11**, 44–49.

LAPPIN-SCOTT, H. M. & BASS, C. 2001. Biofilm formation: attachment, growth, and detachment of microbes from surfaces. *American Journal of Infection Control*, **29**, 250–251.

LEATHAM, A. J. C. & ATKINS, N. J. 1983. Lectin binding to paraffin sections. *In*: BULLOCK, G. R. & PETRUSZ, P. (eds) *Techniques in Immunocytochemisty*, Vol. 2. Academic Press, London, 39–70.

LOWER, S. K., HOCHELLA, M. F. JR. & BEVERIDGE, T. J. 2001. Bacterial recognition of mineral surfaces: nanoscale interactions between *Shewanella* and α-FeOOH. *Science*, **292**, 1360–1363.

MANSCH, R. & BOCK, E. 1998. Biodeterioration of natural stone with special reference to nitrifying bacteria. *Biodegradation*, **9**, 47–64.

MAY, E., LEWIS, F. J., PEREIRA, S., TAYLER, S. SEAWARD, M. R. D. & ALLSOPP, D. 1993. Microbial deterioration of building stone – a review. *Biodeterioration Abstracts*, **7**, 109–123.

MAY, T. B. & CHAKRABARTY, A. M. 1994. Isolation and assay of *Pseudomonas aeruginosa* alginate. *Methods in Enzymology*, **235**, 295–304.

MILLSAP, K. W., REID, G., VAN DER MEI, H. C. & BUSSCHER, H. J. 1997. Adhesion of Lactobacillus species in urine and phosphate buffer to silicone rubber and glass under flow. *Biomaterials*, **18**, 87–91.

POHL, W. & SCHNEIDER, J. 2002. Impact of endolithic biofilms on carbonate rock surfaces. *In*: SIEGESMUND, S., WEISS, T. & VOLLBRECHT, A. (eds)

Natural Stone, Weathering Phenomena, Conservation Strategies and Case Studies. Geological Society, London, Special Publications, **205**, 177–194.

POHL, W., HOPPERT, M., FLIES, C., GÜNZL, B., RUPPERT, H. & SCHNEIDER, J. 2000. Endolithic biofilms: A model for extraterrestrial ecological niches? *Proceedings of SPIE* (The International Society for Optical Engineering, Bellingham, WA), **3755**, 223–231.

PRIESS, K., LE CAMPION-ALSUMARD, T., GOLUBIC, S., GADEL, F., & THOMASSIN, B. A. 2000. Fungi in corals: black bands and density-banding of *Porites lutea* and *P. lobata* skeleton. *Marine Biology*, **136**, 19–27.

RAY, R., LITTLE, B., WAGNER, P. & HART, K. 1997. Environmental scanning electron microscopy investigations of biodeterioration. *Scanning*, **19**, 98–103.

ROBARDS, A. W. & SLEYTR, U. B. 1985. *Low Temperature Methods in Biological Electron Microscopy*. Elsevier, Amsterdam.

ROHDE, M., GERBERDING, H., MUND, T. & KOHRING, G. W. 1988. Immunoelectron microscopic localization of bacterial enzymes: pre- and postembedding labeling techniques on resin-embedded samples. *In*: MAYER, F. (ed.) *Methods in Microbiology*, Vol. 20. Academic Press, London, 175–210.

SPURR, A. R. 1969. A low viscosity epoxy resin embedding medium for electron microscopy. *Journal of Ultrastructural Research*, **26**, 31–43.

TADA, Y., IHMORI, M. &YAMAGUCHI, J. 1995. Oligotrophic bacteria isolated from clinical materials. *Journal of Clinical Microbiology*, **33**, 493–494.

WARSCHEID, T. 1996. Impacts of microbial biofilms in the deterioration of inorganic building materials and their relevance for the conservation practice. *Zeitschrift für Bauinstandsetzungen*, **2**, 493–504.

WARSCHEID, T. 2000. Mikrobieller Befall und Schädigung von Baustoffen. *In*: BAGDA, E. (ed.) *Biozide in Bautenbeschichtungen*. Expert-Verlag, Renningen-Malmsheim, 10–27.

WARSCHEID, T. & BRAAMS, J. 2000. Biodeterioration of stones – a review. *International Biodeterioration and Biodegradation*, **46**, 343–368.

This page intentionally left blank

Limestone weathering of historical monuments in Cairo, Egypt

BERND FITZNER, KURT HEINRICHS & DENNIS LA BOUCHARDIERE
Geological Institute, Aachen University, Working group 'Natural stones and weathering', Wuellnerstrasse 2, D-52062 Aachen, Germany
(e-mail: fitzner@geol.rwth-aachen.de)

Abstract: Since pharaonic times local limestones have been used in Cairo for monument construction. Weathering damage on many historical stone monuments in Cairo is alarming. Studies on properties and weathering behaviour of the limestones were carried out by means of laboratory tests and in situ investigation of many historical monuments. The laboratory studies reveal considerable petrographical variations for the Middle Eocene limestones. The limestone weathering was assessed with respect to weathering forms, weathering products and weathering profiles. A classification scheme of weathering forms and their intensities was tailored to optimal applicability for all Cairo historical monuments constructed from limestones. Monument mapping has been applied for the detailed registration of weathering forms and as a basis for the quantitative rating of stone damage by means of damage categories and damage indices. For the historical monuments in the centre of Cairo the combined evaluation of weathering forms, weathering products and weathering profiles shows clear correlations between the development of weathering damage and salt loading of the limestones as a consequence of air pollution and rising humidity. They demonstrate the need and urgency for monument preservation measures.

In Greater Cairo, Egypt (comprising the governorates of Cairo, Giza and Qalubiyya) are located monuments of outstanding historic and artistic importance, ranging from pharaonic monuments to Roman, Coptic and Islamic monuments (Fig. 1). The pyramids of Giza as part of ancient Memphis, the capital of the Old Kingdom of Egypt, represent the most famous pharaonic monuments. In ancient time, the pyramids were considered one of the Seven Wonders of the World. In 1979 UNESCO inscribed the 'extraordinary funerary monuments of Memphis and its necropolis' into the World Heritage List. Only a few Roman and Coptic monuments have remained in Cairo city, located in the quarter of Old Cairo. The Islamic monuments represent the main group of historical monuments in Cairo. More than six hundred Islamic monuments are concentrated in the centre of Cairo (Fig. 2). The majority of these monuments such as mosques, madrasas, city walls, gates, fortifications, aqueducts, monumental tombs, palaces, minarets, domes, residences, warehouses, hospitals or fountains date back to the periods of the Fatimids, Ayyubids, Mamluks and Ottomans (Behrens-Abouseif 1992; Williams 1993). In 1979 Islamic Cairo was inscribed by UNESCO into the World Heritage List as 'one of the world's oldest Islamic cities, which – founded in the 10th century – became the new centre of the Islamic world, reaching its Golden Age in the 14th century'.

Tertiary porous limestones from local quarries have been used for construction of monuments in Cairo since pharaonic times until today (Fig. 3). In monument preservation practice the limestones are still used for stone replacement or rebuilding works at Cairo

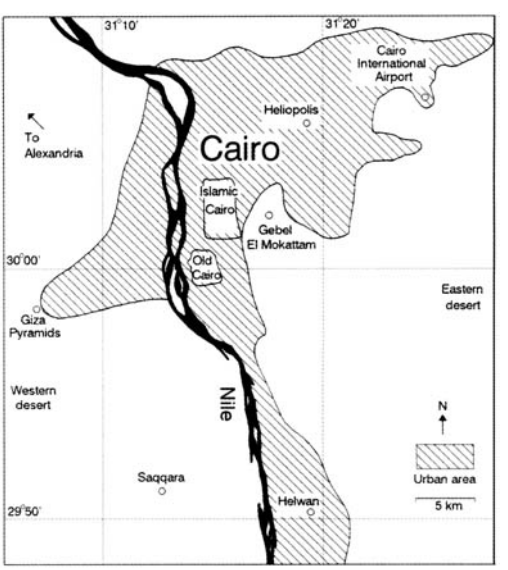

Fig. 1. Greater Cairo.

From: SIEGESMUND, S., WEISS, T. & VOLLBRECHT, A. 2002. *Natural Stone, Weathering Phenomena, Conservation Strategies and Case Studies*. Geological Society, London, Special Publications, **205**, 217–239.
0305-8719/02/$15.00 © The Geological Society of London 2002.

Fig. 2. Islamic centre of Cairo.

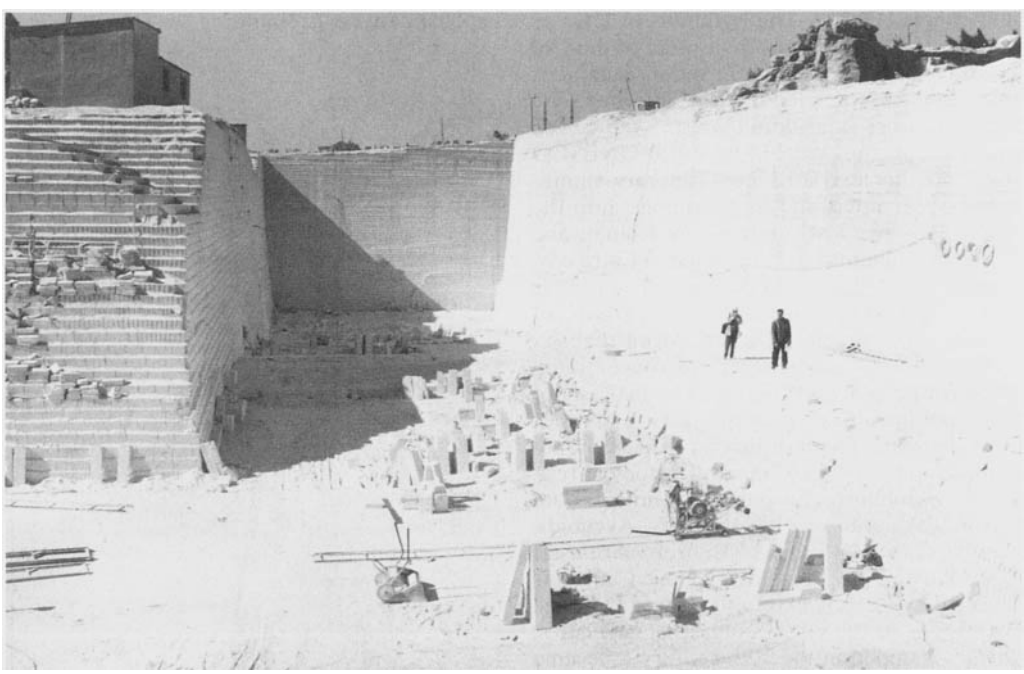

Fig. 3. Limestone quarry, Mokattam mountains west of Cairo city.

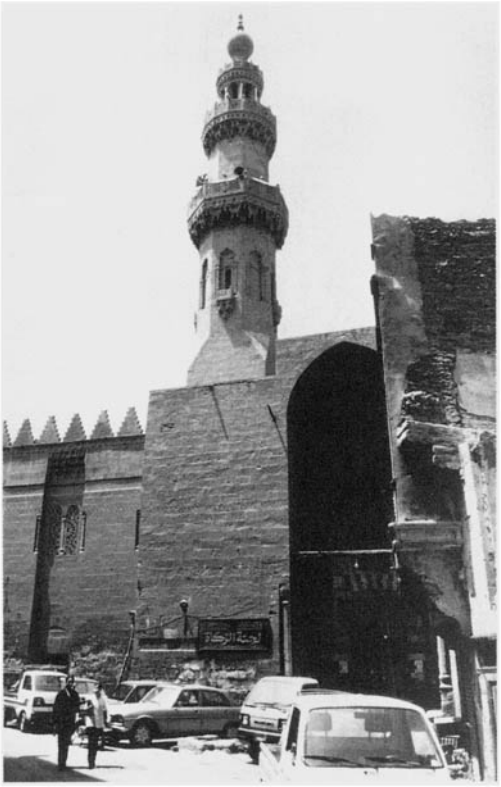

Fig. 4. El-Merdani Mosque.

Fig. 5. Weathering damage on a lower part of El-Merdani Mosque.

historical monuments. Porous limestones represent a stone type that was commonly used for the construction of historical monuments in the whole Mediterranean area.

Many historical limestone monuments in the Cairo area are seriously threatened by damage and are in need of intervention. Stone weathering represents an important cause of damage. Systematic studies were carried out for the petrographical characterization of the limestones and for the analysis of their weathering behaviour. These studies comprised laboratory analyses of the limestones and in situ investigation of quarries and Islamic monuments and, additionally, pilot studies of the Giza pyramids. The in situ investigation included survey, classification and mapping of weathering forms and in situ measurements. Very detailed studies were carried out on the El-Merdani Mosque in the frame of the Concerted Action 'Study, characterization and analysis of degradation phenomena of ancient, traditional and improved building materials of geologic origin used in the construction of historical monuments in the Mediterranean area' (ERB-IC18-CT98-0384), funded by the European Commission. The El-Merdani Mosque in the quarter of Tabbana was built in the fourteenth century as one of the finest examples of Islamic architecture in Cairo (Fig. 4). The mosque was restored a century ago by the Arab Antiquities Conservation Committee (Williams 1993). Preservation measures such as reconstruction, structural reinforcement and renovation of walls were carried out, but today the mosque is again in need of intervention. In particular, the considerable weathering damage to the lower parts of the monument is striking (Fig. 5). This state of damage is very characteristic of many Islamic monuments in the centre of Cairo (Figs 6 and 7). In the following, results are presented on provenance and petrographical properties of the limestones used in the construction of the historical Cairo monuments, on weathering forms, weathering profiles and weathering products, and on causes, development and rating of weathering damage on the monuments.

Fig. 6. Weathering damage on Mausoleum of Sultan Al-Mansur Qalawun.

Provenance, stratigraphy and petrographical properties of the limestones

Eocene outcrops in the area of Greater Cairo predominantly provided the limestones for the construction of the historical stone monuments in this region. In particular, these were the Mokattam limestone plateau east of Cairo city, the Helwan limestone plateau in the SE and the Giza limestone plateau in the western part of Greater Cairo (Fig. 1). The pyramids were mainly constructed from local Giza limestones. Limestones from the Mokattam area were used additionally, as for the facing dimension stones of the Great Pyramid of Cheops (Khufu), only a few of which have remained (Klemm & Klemm 1993). In the Mokattam area and in the Helwan area limestones were quarried for the historical monuments in Cairo city. They are still being used for stone replacement or rebuilding works at these monuments as well as for modern buildings (Figs 8 and 9).

The following information on the geological setting refers to Said (1990). Most of the limestones used on historical monuments in Greater Cairo are related to the Mokattam Group of the Middle Eocene (Fig. 10). The Gebel Mokattam represents the type locality of this group. The Mokattam Group is subdivided into the older Mokattam Subgroup and the younger Observatory Subgroup. The type section of the Observatory Subgroup is the Observatory plateau at Helwan. At Gebel Mokattam the Mokattam Group comprises from bottom to top the two formations of Lower Building Stone and Gizehensis (Mokattam Subgroup) and the two formations of Upper Building Stone and Giushi (Observatory Subgroup). The Mokattam Subgroup does not seem to have an equivalent in the Helwan area. The Observatory Subgroup at Helwan is subdivided into Gebel Hof formation and Observatory formation. The Gebel Hof formation and the lower part of the Observatory formation are correlated with the Upper Building Stone formation at Gebel Mokattam, and the upper part of the Observatory formation with the Giushi formation. The thickness of the beds of the Observatory Subgroup at Helwan is significantly greater than at Gebel Mokattam. At Giza the Mokattam Subgroup comprises the Mokattam formation. The lowermost members of this unit are considered as the oldest section of the entire Cairo area. Beds equivalent to the Observatory Subgroup are very thin at Giza. The Subgroup

Fig. 7. Weathering damage and elevated water table, Mausoleum of Sultan Al-Mansur Qalawun.

Fig. 8. Stone replacement, Hospital of Sultan Al-Mansur Qalawun.

comprises the Observatory formation which correlates with the Upper Building Stone formation at Gebel Mokattam, whereas the presence of beds equivalent to Giushi formation is still questionable.

Laboratory studies were carried out on limestones from quarries at Gebel Mokattam and at Helwan, from outcrops at the Giza plateau and from El-Merdani Mosque in the Islamic centre of Cairo. The limestones from the Helwan area are currently used for the restoration of monuments in the centre of Cairo. Results of mineral composition and classification of the limestones – based on microscopy studies – are presented in Table 1. All limestones can be characterized as almost pure limestones. Calcite $CaCO_3$ represents the predominating carbonate mineral. As X-ray diffraction analysis has shown, dolomite $CaMg(CO_3)_2$ and ankerite $Ca(Mg, Fe)(CO_3)_2$ may occur subordinately as further carbonate minerals. The limestones – except some limestones from Gebel Mokattam – show low contents of quartz. A low content of opaque matter is characteristic of the limestones. Additionally, in most of the limestones small amounts of salt minerals – halite and/or gypsum – were detected by means of X-ray diffraction analysis. This confirms the findings of Elhefnawi (1998), according to which primary salts are very characteristic of the Eocene limestones in Egypt.

Petrographical variations of the limestones concern the proportions of the carbonate components micrite (microcrystalline carbonate), sparite (coarsely crystalline carbonate) and bioclasts (fossil fragments). According to the limestone classification established by Folk (1962), the limestones range from fossiliferous micrite to sparse biomicrite, packed biomicrite and poorly washed biosparite.

Results on porosity properties of the limestones are presented in Table 2. They are based on the joint evaluation of data obtained by mercury porosimetry, nitrogen adsorption (BET method) and transmitted light microscopy with image analysis.

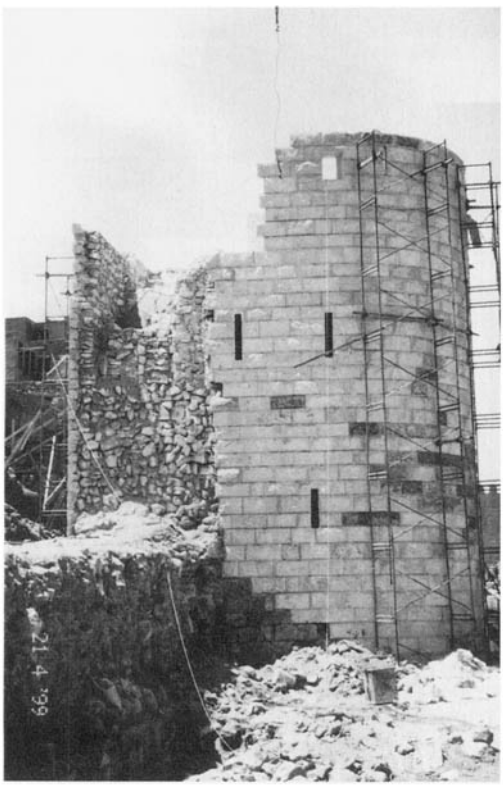

Fig. 9. Restoration works, northern wall of Cairo.

The results reveal remarkable differences between the limestones regarding their porosity characteristics such as total porosity, pore size distribution, pore radius, radius of pore entries and pore surface. Further laboratory tests have shown that considerable differences between the limestones also concern their strength/hardness properties and their water absorption/desorption behaviour. Each region of origin (Mokattam, Helwan, Giza) is characterized by significant petrographical variations of its limestones. The case study of El-Merdani Mosque and the studies on many further monuments in Cairo have shown that different limestone varieties were often used at the same monument. Limestones with considerable petrographical variations are still used for monument restoration.

Weathering forms on the limestone monuments

Weathering forms are the visible result of weathering processes which are initiated and controlled by interacting weathering factors. By means of weathering forms the weathering state of stone surfaces can be described according to phenomenological/geometrical criteria at centimetre to metre scale. Weathering forms represent an important parameter for the characterization, quantification and rating of stone deterioration. The objective and repro-

<table>
<tr><th>GROUP</th><th>SUBGROUP</th><th>GEBEL MOKATTAM</th><th>HELWAN</th><th>GIZA PYRAMIDS PLATEAU</th></tr>
<tr><td rowspan="5">MOKATTAM</td><td rowspan="3">OBSERVATORY</td><td>Giushi
33 m</td><td rowspan="2">Observatory
136 m</td><td>Giushi (?)
Concealed</td></tr>
<tr><td rowspan="2">Upper
Building
Stone
70 m</td><td rowspan="2">Observatory
16 m</td></tr>
<tr><td>Gebel Hof
121 m</td></tr>
<tr><td rowspan="3">MOKATTAM</td><td>Gizehensis
6 m</td><td rowspan="3"></td><td rowspan="3">Mokattam
90 m</td></tr>
<tr><td>Lower
Building
Stone
27 m</td></tr>
<tr><td></td><td></td></tr>
</table>

Fig. 10. Rock units of the Mokattam Group, Middle Eocene (Said 1990).

Table 1. *Mineral composition and classification of limestones used for construction or restoration of monuments in the Cairo area. Transmitted light microscopy*

Lithotype	Mineral composition (%)						Classification (Folk 1962)
	Calcite*			Quartz	Opaque matter	Others†	
	Micrite	Sparite	Bioclasts				
Limestone M1		99		1	<0.1	–	Poorly washed
	54	39	6				biosparite
Limestone M2		84		15	1	<0.1	Poorly washed
	32	17	35			f, h	biosparite
Limestone M3		99		1	<0.1	–	Poorly washed
	14	12	73				biosparite
Limestone M4		92		8	<0.1	–	Poorly washed
	31	34	27				biosparite
Limestone M5		91		8	1	–	Poorly washed
	40	29	22				biosparite
Limestone H1		99		<1	<1	–	Sparse
	70	7	22				biomicrite
Limestone H2		99		<1	<0.1	–	Fossiliferous
	66	32	1				micrite
Limestone E1		99		<1	1	–	Fossiliferous
	73	21	5				micrite
Limestone E2		99		<1	<1	–	Fossiliferous
	72	25	2				micrite
Limestone E3		99		<0.1	1	–	Fossiliferous
	88	10	1				micrite
Limestone E4		98		1	1	–	Poorly washed
	26	46	26				biosparite
Limestone G1		99		1	<1	–	Sparse
	70	5	24				biomicrite
Limestone G2		99		1	<1	–	Sparse
	52	5	42				biomicrite
Limestone G3		99		<1	<1	–	Poorly washed
	23	29	47				biosparite
Limestone G4		99		<1	<1	–	Sparse
	75	6	18				biomicrite
Limestone G5		97		3	<1	–	Packed
	37	8	52				biomicrite
Limestone G6		99		1	<1	–	Poorly washed
	40	27	32				biosparite

* Subordinately dolomite or ankerite may occur
† f, feldspar; h, heavy minerals
Limestones M1–M5: quarries, Mokattam mountains. Limestones H1–H2: quarries, Helwan. Limestones E1–E4: El-Merdani Mosque, Cairo. Limestones G1–G6: outcrops/pyramids, Giza plateau.

ducible survey and evaluation of weathering forms require a standardized classification scheme of weathering forms. Such a classification scheme was developed based on investigation of stone monuments worldwide considering different stone types and environments (Fitzner *et al.* 1995; Fitzner & Heinrichs 2002). Based on a systematic survey of weathering forms on historical monuments in Cairo (e.g. pyramids, tombs and temples at Giza, old wall of Cairo, aqueduct, city gates of Bab Zuwayla, Bab al-Nasr and Bab al-Futuh, citadel, al-Aqmar Mosque, complex of Sultan Al-Mansur Qalawun, al-Azhar Mosque, Sultan Hasan Mosque, Blue Mosque, Sultan Barquq School, dome of Sultan Qansuwa Abu Said, madrasa and dome of Al Salih Nadjmed), this classification scheme of weathering forms was updated and tailored to optimal applicability at all Cairo historical ashlar monuments made of

Table 2. *Porosity properties of limestones used for construction or restoration of monuments in the Cairo area. Joint evaluation of data obtained by mercury porosimetry, nitrogen adsorption (BET) and transmitted light microscopy with image analysis*

Lithotype	Total porosity (vol%)	Porosity in pore radii classes 0.001–0.1 μm (vol%)	0.1–10 μm (vol%)	10–1000 μm (vol%)	Median pore radius (μm)	Median radius of pore entries (μm)	Pore surface ($m^2 g^{-1}$ / $m^2 cm^{-3}$)
Limestone M1	18.6	1.5	14.0	3.1	2.2	0.7	1.8 / 4.0
Limestone M2	20.0	0.8	12.6	6.6	5.3	0.9	1.0 / 2.2
Limestone M3	25.3	0.9	6.4	18.0	39.0	1.1	1.4 / 2.7
Limestone M4	25.3	1.3	18.0	6.0	2.8	0.9	1.8 / 3.7
Limestone M5	26.8	1.8	19.4	5.6	2.7	0.7	2.9 / 5.9
Limestone H1	8.5	1.7	6.5	0.3	0.6	0.1	1.8 / 4.5
Limestone H2	37.4	5.1	28.1	4.2	1.2	0.8	7.2 / 12.3
Limestone E1	10.8	0.8	9.6	0.4	0.8	0.3	0.5 / 1.3
Limestone E2	22.0	1.0	17.5	3.5	2.1	1.0	0.5 / 1.1
Limestone E3	22.9	1.9	18.1	2.9	1.7	1.0	1.4 / 2.9
Limestone E4	24.5	0.5	6.3	17.7	40.0	5.7	0.3 / 0.6
Limestone G1	12.0	1.7	8.9	1.4	1.2	0.3	1.9 / 4.5
Limestone G2	18.6	1.3	11.0	6.3	5.0	0.9	1.4 / 3.2
Limestone G3	19.2	0.8	8.2	10.2	12.5	1.1	0.8 / 1.7
Limestone G4	24.8	2.0	20.8	2.0	1.3	0.5	3.3 / 6.8
Limestone G5	25.6	2.2	13.4	10.0	6.0	0.5	2.4 / 5.0
Limestone G6	34.1	1.2	27.0	5.9	2.4	1.0	2.1 / 3.9

Limestones M1–M5: quarries, Mokattam mountains. Limestones H1–H2: quarries, Helwan. Limestones E1–E4: El-Merdani Mosque, Cairo. Limestones G1–G6: outcrops/pyramids, Giza plateau.

limestone. The optimization of the classification scheme for the Cairo monuments has included an intensity classification of the weathering forms.

A section of the classification scheme summarizing the frequent weathering forms observed on the limestone monuments in Cairo is presented in Table 3. Examples of weathering forms are shown in Figures 11–15. Examples of the intensity classification of weathering forms developed for the Cairo limestone monuments are presented in Table 4. The intensity classification has been differentiated for limestone monuments composed of small- to medium-sized dimension stones (Table 4, intensity classification A) and limestone monuments composed of huge dimension stones (Table 4, intensity classification B) considering the different ranges of intensities.

Based on the classification of weathering forms and their intensities, the monument mapping method was applied for registration, documentation and evaluation of weathering forms. The mapping method represents a non-destructive, well-established procedure, which allows quantitative evaluation of complete stone surfaces according to type, intensity and distribution of weathering forms. It makes an important contribution to rating of weathering damage, weathering prognosis, information on causes and processes of stone weathering and to sustainable monument preservation (Fitzner *et al.* 1995, 1997). As an example of the computer-enhanced illustration of weathering forms registered by monument mapping, the map of all weathering forms of group 1 'loss of stone material' is shown for a lower masonry part of the El-Merdani Mosque (Figs 16 and 17). In the same way maps were prepared for all stone surfaces of monuments that were studied in Cairo showing the weathering forms of group 2 'discoloration/deposits', group 3 'detachment' and group 4 'fissures/deformation'. All weathering forms and their combinations were evaluated quantitatively.

The investigation of weathering forms on limestone monuments in Cairo has shown a wide range of weathering forms and their intensities. Back weathering (W), relief (R) and break out (O) represent very frequent weathering forms characterizing loss of stone material. The depth of back weathering and relief on the

Table 3. *Typical weathering forms on limestone monuments in Cairo*

Groups of weathering forms	Main weathering forms		Individual weathering forms
	Terminology	Definition	
Group 1 – loss of stone material	Back weathering (W)	Uniform loss of stone material parallel to the original stone surface.	Back weathering due to loss of scales (sW), due to loss of crumbs (uW) or due to loss of crusts (cW).
	Relief (R)	Morphological change of the stone surface due to partial or selective weathering.	Rounding/notching (Ro), alveolar weathering (Ra), weathering out dependent on stone structure (tR), weathering out of stone components (Rk), clearing out of stone components (Rh).
	Break out (O)	Loss of compact stone fragments.	Break out due to anthropogenic impact (aO), due to constructional cause (bO) or due to natural cause (nO).
Group 2 – discoloration/ deposits	Discoloration (D)	Alteration of the original stone color.	Coloration (Dc).
	Soiling (I)	Dirt deposits on the stone surface.	Soiling by particles from the atmosphere (pI) or from water (wI).
	Loose salt deposits (E)	Poorly adhesive deposits of salt aggregates.	Efflorescences (Ee), subflorescences (Ef).
	Crust (C)	Strongly adhesive deposits on the stone surface.	Dark-coloured crust tracing or changing the morphology of the stone surface (dkC, diC), light-coloured crust tracing or changing the morphology of the stone surface (hkC, hiC).
Group 3 – detachment	Granular disintegration (G)	Detachment of individual grains or small grain aggregates.	Granular disintegration into sand (Gs).
	Crumbly disintegration (P)	Detachment of larger compact stone pieces of irregular shape.	Crumbling (Pu).
	Flaking (F)	Detachment of small, thin stone pieces (flakes) parallel to the stone surface.	Single flakes (eF) or multiple flakes (mF).
	Contour scaling (S)	Detachment of larger, platy stone pieces (scales) parallel to the stone surface, but not following any stone structure.	Single scales (eS) or multiple scales (mS).
	Detachment of crusts with stone material (K)	Detachment of crusts with stone material sticking to the crust.	Detachment of dark-coloured crusts tracing or changing the morphology of the stone surface (dkK, diK), detachment of light-coloured crusts tracing or changing the morphology of the stone surface (hkK, hiK).
Group 4 – fissures/ deformation	Fissures (L)	Individual fissures or systems of fissures due to natural or constructional causes.	Fissures independent of stone structure (vL) or fissures dependent on stone structure (tL).

Classification of weathering forms based on Fitzner *et al.* (1995) and Fitzner & Heinrichs (2002).

Table 4. *Intensity classification of weathering forms on limestone monuments in Cairo. Examples: weathering forms relief (R), break out (O) and contour scaling (S)*

Weathering form	Parameter for intensity classification	Intensity classification A*		Intensity classification B†	
Relief (R) Morphological change of the stone surface due to partial or selective weathering.	Depth d of relief (cm)	Intensity 1	$d \leq 0.2$	Intensity 1	$d \leq 5$
		Intensity 2	$0.2 < d \leq 0.5$	Intensity 2	$5 < d \leq 15$
		Intensity 3	$0.5 < d \leq 1$	Intensity 3	$15 < d \leq 25$
		Intensity 4	$1 < d \leq 3$	Intensity 4	$25 < d \leq 50$
		Intensity 5	$3 < d \leq 5$	Intensity 5	$50 < d \leq 75$
		Intensity 6	$5 < d \leq 10$	Intensity 6	$75 < d \leq 100$
		Intensity 7	$d > 10$	Intensity 7	$d > 100$
Break out (O) Loss of compact stone fragments.	Volume v of break out (dm^3)	Intensity 1	$v \leq 0.01$	Intensity 1	$v \leq 1$
		Intensity 2	$0.01 < v \leq 0.125$	Intensity 2	$1 < v \leq 10$
		Intensity 3	$0.125 < v \leq 0.5$	Intensity 3	$10 < v \leq 25$
		Intensity 4	$0.5 < v \leq 1$	Intensity 4	$25 < v \leq 50$
		Intensity 5	$v > 1$	Intensity 5	$50 < v \leq 100$
				Intensity 6	$100 < v \leq 250$
				Intensity 7	> 250
Contour scaling (S) Detachment of larger, platy stone pieces parallel to the stone surface, but not following any stone structure.	Thickness t of scales (mm)	Intensity 1	$t \leq 2$	Intensity 1	$t \leq 5$
		Intensity 2	$2 < t \leq 5$	Intensity 2	$5 < t \leq 10$
		Intensity 3	$5 < t \leq 10$	Intensity 3	$10 < t \leq 20$
		Intensity 4	$10 < t \leq 20$	Intensity 4	$20 < t \leq 50$
		Intensity 5	$t > 20$	Intensity 5	$t > 50$

* Intensity classification A: for limestone monuments composed of small to medium-sized dimension stones, e.g. Islamic monuments in the centre of Cairo

† Intensity classification B: for limestone monuments composed of huge dimension stones, e.g. pyramids of Giza

monuments in the centre of Cairo may amount to more than 10 cm. Especially on the lower parts of many of these monuments, very often the depth of relief and back weathering is strikingly high. On the huge dimension stones of the Giza pyramids relief and back weathering can occur with depths of even up to more than 1 m. Break out of compact stone fragments on the Cairo monuments as well as fissures (L) frequently indicate structural instabilities. The impact of earthquakes like that in 1992 should be considered an additional cause of break out and fissures. According to Badawi & Mourad (1994) 140 Islamic monuments in Cairo were severely affected by this earthquake.

Soiling (I), loose salt deposits (E) and crusts (C) are the main weathering forms characterizing deposits on the monuments. Soiling by pollutants from the atmosphere – poorly adhesive, mainly grey to black deposits of dust and soot – and crusts are very characteristic of the monuments in the centre of Cairo; however, they are less significant on the monuments in the outer parts of Greater Cairo like the Giza monuments. Dark grey to black crusts (Fig. 13) often affect especially the middle and upper parts of monuments in Cairo city, whereas compact whitish crusts (Fig. 14) as well as efflorescences mainly prevail on the lower parts of many monuments.

Granular disintegration (G), crumbly disintegration (P), flaking (F) and contour scaling (S) as well as transitional forms between these, like granular disintegration to flaking (G–F), granular disintegration to crumbly disintegration (G–P), flaking to contour scaling (F–S), flaking to crumbly disintegration (F–P) or crumbly disintegration to contour scaling (P–S), represent very frequent weathering forms characterizing current detachment of stone material. Additionally, detachment of crusts with stone material (K) can be observed on many monuments in the centre of Cairo. The studies show some trend that increasing loss of stone material corresponds to decreasing size of detaching stone elements. This indicates an increasing incoherence of the stone components in the course of weathering progression. Considerable loss and detachment of stone material affects

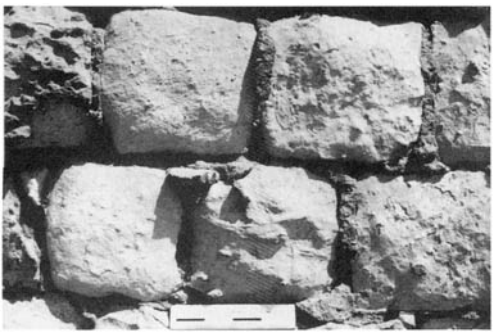

Fig. 11. Weathering form 'relief' (R). Image width *c.* 90 cm.

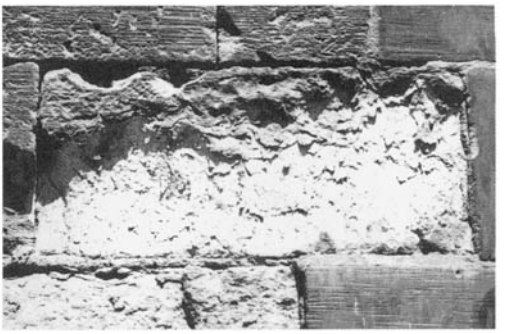

Fig. 12. Weathering forms 'back weathering' (W), 'crust' (C) and 'flaking' (F). Image width *c.* 70 cm.

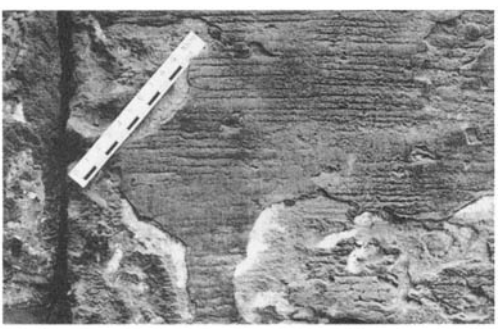

Fig. 13. Weathering forms 'back weathering' (W), 'crust' (C) and 'detachment of crusts with stone material' (K). Image width *c.* 30 cm.

Fig. 14. Weathering forms 'back weathering' (W), 'crust' (C), 'detachment of crusts with stone material' (K) and 'granular disintegration' (G). Image width *c.* 30 cm.

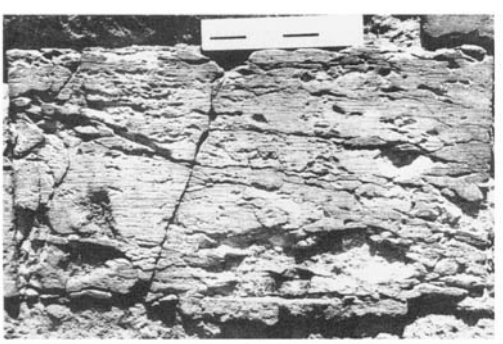

Fig. 15. Weathering forms 'relief' (R), 'break out' (O), 'crumbly disintegration' (P) and 'fissures' (L). Image width *c.* 70 cm.

not only the outer walls, but also the inner walls of many monuments in Cairo city.

Rating of stone damage

While weathering forms allow the detailed, objective and reproducible description and mapping of stone deterioration phenomena, damage categories and damage indices were integrated into the monument mapping method as tools for the rating of stone damage (Heinrichs & Fitzner 1999; Fitzner *et al.* 2002; Fitzner & Heinrichs 2002). For the rating of individual stone damage, six damage categories were defined: 0, no visible damage; 1, very slight damage; 2, slight damage; 3, moderate damage; 4, severe damage; 5, very severe damage. A correlation scheme of weathering forms and damage categories was developed for the limestone monuments in Cairo considering the high historic and artistic value of these monuments. In this correlation scheme, damage categories were proposed for all weathering forms in dependence upon their intensities. A section of this correlation scheme is shown in Table 5. The correlation scheme of weathering forms and damage categories was differentiated for limestone monuments composed of small to medium-sized dimension stones and limestone monuments composed of huge dimension

Fig. 16. El-Merdani Mosque, lower part of the SE facade.

Table 5. *Correlation scheme for weathering forms and damage categories. Example: relating of the weathering form back weathering (W) to damage categories considering different intensity ranges of the weathering form*

Weathering form Back weathering (W)	Damage categories				
	1 very slight damage	2 slight damage	3 moderate damage	4 severe damage	5 very severe damage
Back weathering on small to medium-sized dimension stones (e.g. Islamic monuments)*	$0 < d \leq 0.2$	$0.2 < d \leq 0.5$	$0.5 < d \leq 1$	$1 < d \leq 5$	$d > 5$
Back weathering on huge dimension stones (e.g. pyramids of Giza)*	$0 < d \leq 5$	$5 < d \leq 15$	$15 < d \leq 25$	$25 < d \leq 50$	$d > 50$

* Values for depth d of back weathering (in cm)

stones considering the different intensity ranges of several weathering forms. Based on the correlation scheme, damage categories were derived for all weathering forms and their combinations registered by means of monument mapping. The damage categories were illustrated in maps and were evaluated quantitatively. Maps of damage categories are shown for parts of the El-Merdani Mosque (Fig. 18) and the Great Pyramid of Cheops (Figs 19–21) as examples.

Damage indices – linear damage index DI_{lin} and progressive damage index DI_{prog} – were calculated for conclusive quantification and rating of stone damage. Their calculation is based on the quantitative evaluation of the damage categories (Fig. 22). According to the calculation mode, both damage indices range between 0 and 5. The linear damage index corresponds to average damage category, whereas the progressive damage index emphasizes the proportion of higher damage

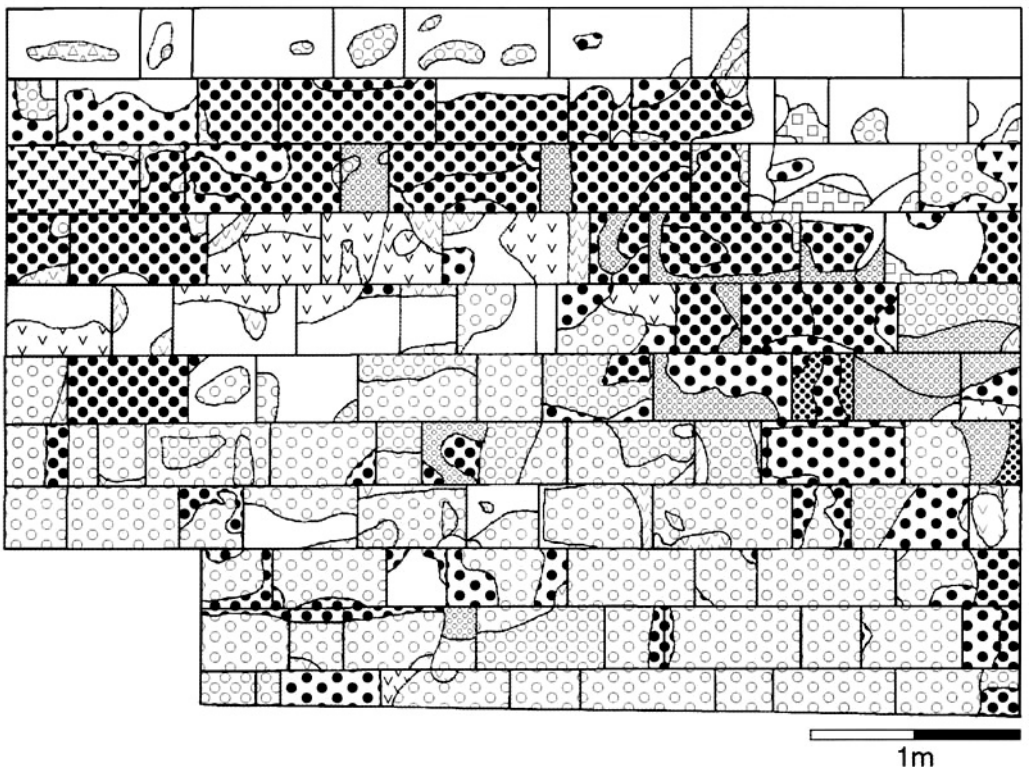

WEATHERING FORMS	INTENSITIES

Back weathering (W)	Intensities according to depth d of back weathering (cm)						
	Intensity 1 $d \leq 0.2$	Intensity 2 $0.2 < d \leq 0.5$	Intensity 3 $0.5 < d \leq 1$	Intensity 4 $1 < d \leq 3$	Intensity 5 $3 < d \leq 5$	Intensity 6 $5 < d \leq 10$	Intensity 7 $d > 10$
sW							
cW							
zW							

Relief (R)	Intensities according to depth d of relief (cm)						
	Intensity 1 $d \leq 0.2$	Intensity 2 $0.2 < d \leq 0.5$	Intensity 3 $0.5 < d \leq 1$	Intensity 4 $1 < d \leq 3$	Intensity 5 $3 < d \leq 5$	Intensity 6 $5 < d \leq 10$	Intensity 7 $d > 10$
Ro							

Break out (O)	Intensities according to volume v of break out (dm^3)				
	Intensity 1 $v \leq 0.01$	Intensity 2 $0.01 < v \leq 0.125$	Intensity 3 $0.125 < v \leq 0.5$	Intensity 4 $0.5 < v \leq 1$	Intensity 5 $v > 1$
oO					

Fig. 17. Map of weathering forms. Group 1 of weathering forms, 'loss of stone material'. El-Merdani Mosque, lower part of the SE facade.

Fig. 18. Map of damage categories. El-Merdani Mosque, lower part of the SE facade.

categories. There is the following relation between the damage indices: progressive damage index ≥ linear damage index (Fitzner & Heinrichs 2002).

With respect to monument preservation, damage categories and damage indices are very suitable indicators for need and urgency of interventions. Maps of damage categories locate those parts of monuments on which interventions have to focus. Examples of results on damage indices in addition to damage categories are presented considering: rating of stone damage for entire parts of monuments; characterization of damage zonation on monuments; and comparison of stone durability.

Visible stone damage was found on all historical limestone monuments in Greater Cairo. Regarding the monuments in Cairo city, considerable amounts of moderate, severe or even very severe stone damage (damage categories 3, 4 and 5) were found especially on the lower parts of the monuments. The linear damage index DI_{lin} calculated for such lower parts ranges between 2.2 and 3.1, and the progressive damage index DI_{prog} between 2.6 and 3.2. Considering the range of the damage indices between 0 and 5.0 per definition, these results indicate a rather alarming state of damage and the need and urgency of preservation measures. Frequently, a zonation of damage was observed at these lower parts of the monuments in Cairo city, very similar to the example shown in Figure 18 for the El-Merdani Mosque: a lower zone with mainly very slight, slight or moderate damage, a middle to upper zone with mainly severe or even very severe

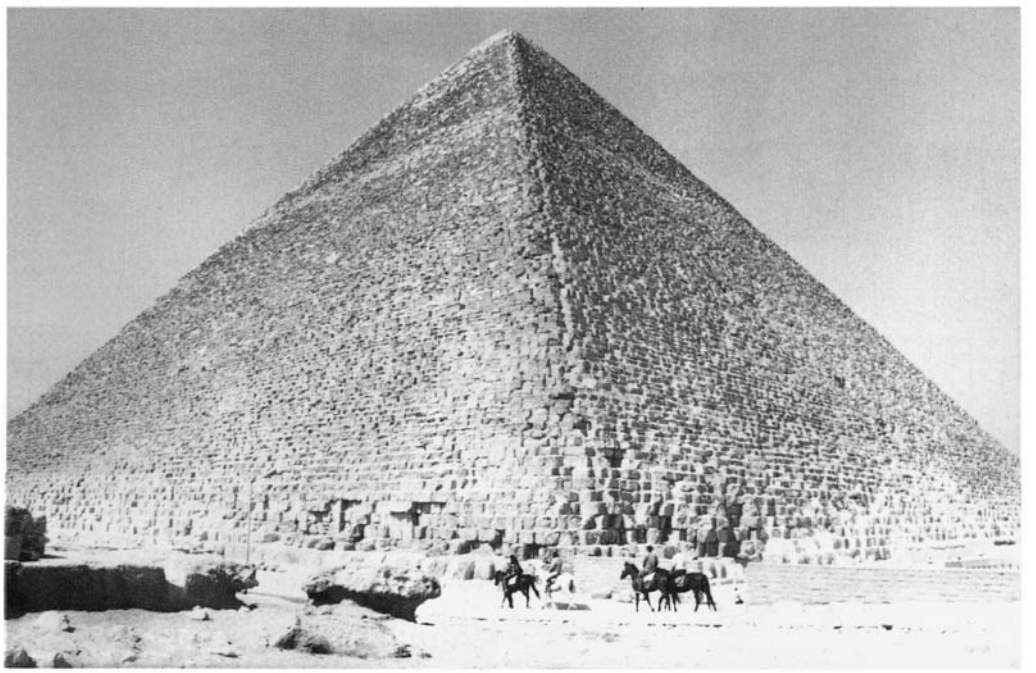

Fig. 19. Great Pyramid of Cheops, Giza.

Fig. 20. Great Pyramid of Cheops, lower part of the southern side (investigation area darker).

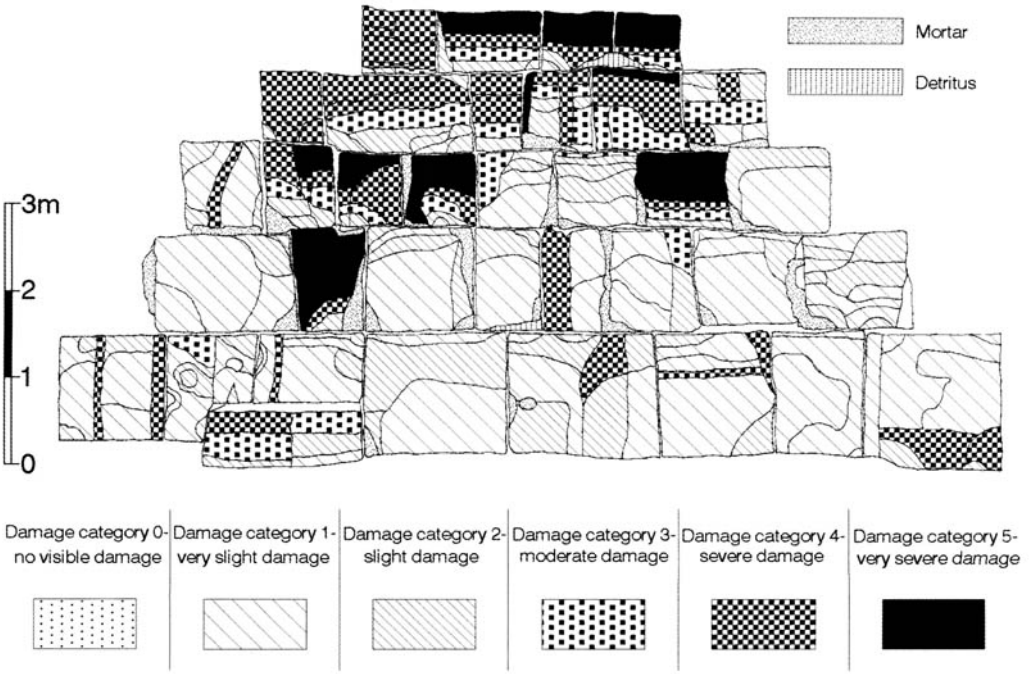

Fig. 21. Map of damage categories. Great Pyramid of Cheops, lower part of the southern side.

LINEAR DAMAGE INDEX	PROGRESSIVE DAMAGE INDEX
$DI_{lin} =$	$DI_{prog} =$
$\frac{(A\cdot 0)+(B\cdot 1)+(C\cdot 2)+(D\cdot 3)+(E\cdot 4)+(F\cdot 5)}{100}$	$\sqrt{\frac{(A\cdot 0^2)+(B\cdot 1^2)+(C\cdot 2^2)+(D\cdot 3^2)+(E\cdot 4^2)+(F\cdot 5^2)}{100}}$
$\downarrow$	$\downarrow$
$\frac{B+(C\cdot 2)+(D\cdot 3)+(E\cdot 4)+(F\cdot 5)}{100}$	$\sqrt{\frac{B+(C\cdot 4)+(D\cdot 9)+(E\cdot 16)+(F\cdot 25)}{100}}$
A = Area (%) – damage category 0 B = Area (%) – damage category 1 C = Area (%) – damage category 2	D = Area (%) – damage category 3 E = Area (%) – damage category 4 F = Area (%) – damage category 5
$\sum_{A}^{F} = 100$	
$0 \leq DI_{lin} \leq 5$	$0 \leq DI_{prog} \leq 5$

Fig. 22. Damage indices.

damage, and an uppermost zone with mainly very slight or slight damage. In order to quantify this zonation of stone damage, damage indices were calculated individually for rows of dimension stones (Fig. 23). Maximum damage indices – DI_{lin} up to 4.2, DI_{prog} up to 4.3 – were found at a height in the range between 2.0 and 2.5 m above ground level. It is striking that at El-Merdani

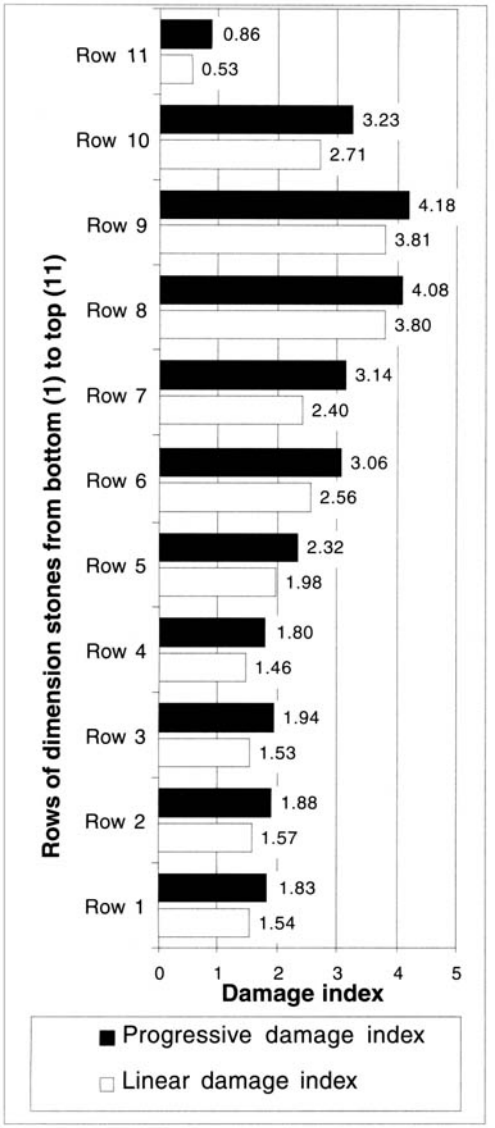

Fig. 23. Damage indices according to rows of dimension stones. El-Merdani Mosque, lower part of the SE facade.

Mosque and many other monuments, this zonation of stone damage can superpose the heterogeneous distribution of different limestone varieties in the walls of the monuments.

In contrast, the distribution of damage categories and the damage indices derived for the pilot investigation area at the Great Pyramid of Cheops clearly trace the four different limestone varieties found there and their different durability:

- compact limestone: mainly very slight or slight damage (damage categories 1 and 2), DI_{lin} = 1.2, DI_{prog} = 1.4, high durability;
- soft limestone: mainly severe or very severe damage (damage categories 4 and 5), DI_{lin} = 4.4, DI_{prog} = 4.5, very low durability;
- two intermediate limestones: mainly very slight to severe damage (damage categories 1–4), DI_{lin} = 2.2–2.5, DI_{prog} = 2.5–2.9, low to moderate durability.

Weathering products and weathering profiles

In addition to weathering forms and their rating by means of damage categories and damage indices, weathering products and weathering profiles characterize the weathering state of natural stones and provide information on factors and processes of stone weathering.

Studies on the lower parts of the El-Merdani Mosque – considered to be very representative for the lower parts of many limestone monuments in the historical centre of Cairo – have shown a considerable salt loading of the limestones by halite (NaCl) and gypsum ($CaSO_4 \cdot 2H_2O$). This concerns the outer walls and walls in the interior of the monument in the same way. Surface samples were analysed by means of X-ray diffraction with respect to salt minerals. Different weathering forms were considered, in particular different types of deposits and detachment. Results on salt minerals related to weathering forms are summarized in Table 6.

In the early phases of stone weathering a higher content of gypsum correlates with the detachment of larger-sized stone elements, whereas in the advanced phases of stone weathering the higher content of halite correlates with decreasing size of detaching stone elements.

Additionally, powder samples collected in the course of drilling resistance measurements on lower parts of the El-Merdani Mosque were studied geochemically. The samples correspond to the outermost 4 cm of the dimension stones. In all samples halite and gypsum were found. The content of halite in the surface zone of the dimension stones (0–4 cm) ranges between 2.5 and 7.0 wt%, the content of gypsum between 0.5 and 4 wt%.

Weathering profiles were studied for information on causes and development of stone damage on the limestone monuments. Depth weathering profiles on dimension stones

Table 6. *Salt minerals related to weathering forms. El-Merdani Mosque*

Groups of weathering forms	Weathering forms		Salt minerals
Deposits	Loose salt deposits	Efflorescences	Halite prevailing, rarely gypsum
		Subflorescences	Halite and frequently gypsum
	Crust	Dark-coloured crust	Gypsum significantly prevailing
		Light-coloured crust	Halite significantly prevailing
Detachment	Contour scaling		Gypsum prevailing (back side of the scales)
	Flaking to contour scaling		Gypsum and halite
	Granular disintegration to crumbly disintegration		Halite, rarely gypsum
	Granular disintegration to flaking		Halite, rarely gypsum
	Granular disintegration		Halite, subordinately gypsum

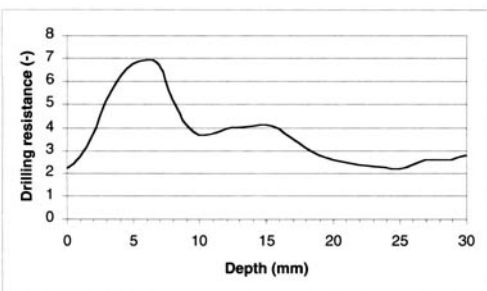

Fig. 24. Weathering profile type 1. Drilling resistance.

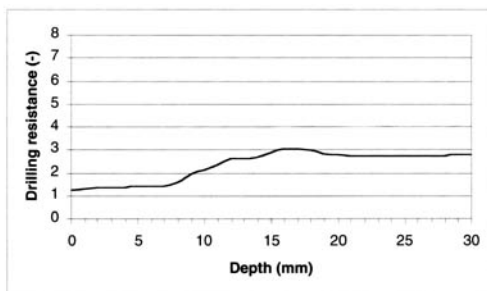

Fig. 25. Weathering profile type 2. Drilling resistance.

obtained by in situ drilling resistance measurements and by laboratory studies on drill cores and vertical weathering profiles on monument walls obtained by laboratory studies on salt load and by mapping and evaluation of weathering forms are presented in the following.

Drilling resistance measurements were carried out in situ considering different states of weathering. By means of this method, drilling with drill bits of 3 mm in diameter is made with constant pressure, energy supply and rotation speed. The drilling depth is monitored versus drilling time. The drilling resistance as a parameter of stone hardness is calculated as a function of depth. Examples of drilling resistance profiles obtained from measurements at the El-Merdani Mosque are presented in Figures 24 and 25. Two main types of profiles were found:

Type 1: profiles with decrease in drilling resistance from the stone surface to the stone interior (Fig. 24);
Type 2: profiles with increase in drilling resistance from the stone surface to the stone interior (Fig. 25).

Profiles of type 1 indicate accumulation of salt in the surface zone of the dimension stones. As an example, the drilling resistance profile in Figure 24 can be characterized as follows:

- the outermost zone with low drilling resistance corresponds to the light-coloured crust of almost pure halite;
- the zone with the first maximum peak of drilling resistance corresponds to a hardening by cementation in the contact zone salt crust – limestone;
- the zone with the first minimum peak of drilling resistance already traces the zone of future detachment of the crust with adherent stone material;
- the zone with the second maximum peak of drilling resistance traces a secondary zone of salt accumulation;
- the backward zone with decreasing drilling resistance corresponds to the transition to the unweathered limestone.

Profiles of type 2 indicate stone disintegration in the surface zone of the dimension stones. As an

Table 7. *Vertical weathering profile (0–3.5 m above ground level). Outer facades, El-Merdani Mosque*

	Lower zone (0–1.2 m)	Middle to upper zone (1.2–2.8 m)	Uppermost zone (2.8–3.5 m)
Loss of stone material*	frequent, mainly low intensities	very frequent, often high intensities	very rare, low intensities
Deposits on the stone surface*	very frequent, low to high intensities	very frequent, low to high intensities	very frequent, low to high intensities
Detachment of stone material*	rare, mainly low intensities	very frequent, often high intensities	very rare, low intensities
Rating of damage*	mainly very slight, slight or moderate	mainly severe or even very severe	mainly very slight or slight
Damage indices*	1.0–2.0	3.0–4.3	0.5–1.5
Salt load (depth: 0–4 cm)	moderate	very high	low to moderate
Halite–gypsum relation (depth: 0–4 cm)	halite ≥ gypsum	halite >> gypsum	halite ≤ gypsum

* Evaluation based on mapping of weathering forms

example, the drilling resistance profile in Figure 25 can be characterized as follows:

- the outer zone with low drilling resistance correlates with considerable stone disintegration, especially granular disintegration;
- the zone with the maximum peak of the drilling resistance traces a zone of salt accumulation;
- the backward zone with almost constant drilling resistance corresponds to the transition to the unweathered limestone.

Ultrasonic studies and porosity studies of the drill cores from El-Merdani Mosque have confirmed these two main types of depth weathering profiles (Fig. 26). With respect to weathering profiles of type 1, increasing ultrasonic velocity, decreasing total porosity and median pore radius and decreasing density – considering the lower density of the salts – from the stone interior towards the stone surface indicate the accumulation of salt in the surface zone of the limestone. Regarding weathering profiles of type 2, decreasing ultrasonic velocity and increasing porosity and median pore radius and the decreasing density from the stone interior towards the stone surface indicate increasing disintegration in the direction of the stone surface in combination with salt loading of the limestone.

With respect to the historical limestone monuments in Cairo city, it was mentioned that considerable stone damage especially affects their lower parts. The results presented for these parts of the monuments have shown that all detachment of stone material and subsequent loss of stone material is linked to salt loading of the limestones. The comparison of results obtained from in situ investigation and laboratory analyses has allowed the evaluation of vertical weathering profiles of these lower parts of the monuments characterizing the interrelation between salt loading and stone deterioration. A characteristic example is shown in Table 7. Three zones of the vertical profile are distinguished. The lower zone is characterized by very slight to moderate stone damage and moderate salt loading by halite and gypsum. Halite is slightly prevailing as the salt mineral. The middle to upper zone shows severe to very severe stone damage and very high salt loading by gypsum and halite. Compared to gypsum, the content of halite is significantly higher. The uppermost zone is characterized by very slight to slight stone damage and low to moderate salt loading by gypsum and halite. The gypsum–halite relation increases upwards. Comparison of quantitative information on salt load and state of stone damage by means of vertical weathering profiles has proved the clear correlation between salt loading of the limestones and their state of damage (Fig. 27). It can be seen that stone damage increases as salt load increases.

The zonation of the stone damage and the type and intensity of salt loading indicates that salt weathering processes in the lower and in the middle to upper zone are mainly induced by

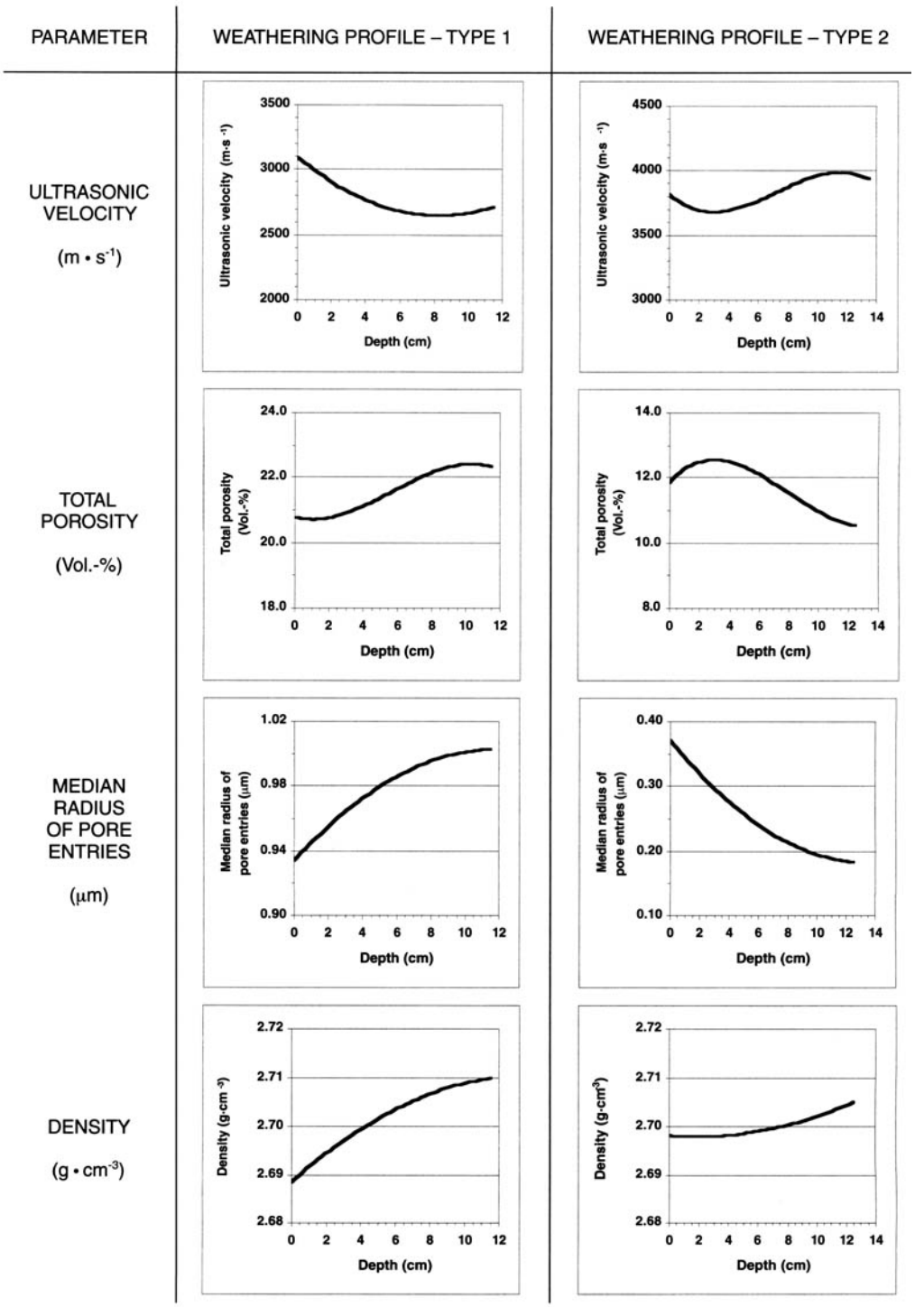

Fig. 26. Weathering profiles type 1 and type 2. Ultrasonic velocity, total porosity, median radius of pore entries, density.

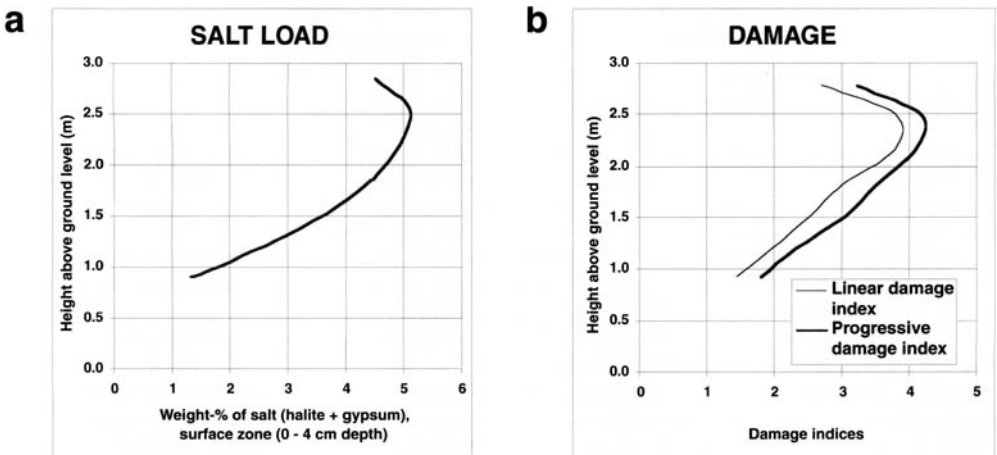

Fig. 27. Correlation between salt load (**a**) and stone damage (**b**) across a vertical profile. El-Merdani Mosque, lower part of the SE facade.

salt-loaded rising humidity, whereas the uppermost zone represents the transitional zone to the upper parts of the monuments mainly affected by gypsum related to air pollution.

Discussion and conclusions

All historical limestone monuments in Cairo are affected by weathering. Studies on the weathering of the limestones were carried out comprising laboratory analysis and in situ investigation, the latter including detailed survey of weathering forms, registration and evaluation of weathering forms by means of monument mapping and in situ measurements. The studies were aimed at the petrographical characterization of the limestones and at the characterization and quantification of weathering forms, weathering products and weathering profiles, which in combination represent the state of weathering and which provide information on factors and processes of stone weathering. The methodological approach has guaranteed information on all scales of stone weathering ranging from nanoscale (<mm), to microscale (mm to cm), mesoscale (cm to m) and macroscale (>m). Rating of stone damage was an additional important objective of the studies.

The laboratory studies of the local Eocene limestones used on the monuments in Cairo since pharaonic times until today have revealed a wide range of different limestone varieties with considerable variation of their petrographical properties.

Based on a systematic survey of historical monuments in Cairo, a detailed classification scheme of weathering forms was worked out, tailored to optimal applicability at all Cairo historical monuments constructed of limestones. The monument mapping method was applied as an established and internationally accepted non-destructive procedure for the precise registration, documentation and quantitative evaluation of weathering forms. Damage categories and damage indices were established as very suitable tools for the quantitative rating of stone damage on the Cairo historical monuments. A correlation scheme of weathering forms and damage categories was developed, applicable to all historical monuments in Cairo. Weathering forms, damage categories and damage indices were applied to Egyptian monuments for the first time. This systematic approach can now be transferred to all historical limestone monuments in Cairo.

A great variety of weathering forms characterizing loss of stone material, deposits, detachment of stone material and structural discontinuities were found on the limestones, as well as a considerable range of intensities.

At the pyramids of Giza east of Cairo city, remarkable recession of the stone surface up to the metre range in combination with intense current detachment of stone material was found on the huge dimension stones.

Weathering forms such as soiling, black crusts and whitish crusts are very characteristic of the limestone monuments in the centre of Cairo. The black crusts – mainly composed of gypsum – very frequently occur on the middle and upper parts of the monuments, whereas the whitish crusts – almost purely composed of halite – are

mainly limited to the lower parts of the monuments. Considerable loss of stone material in combination with intense current detachment of stone material is very characteristic of the lower parts of many monuments in Cairo city. Frequently, this also concerns stone structures in the interior of the monuments. The results obtained from in situ investigation and laboratory tests have shown that all kinds of stone detachment and subsequent loss of stone material are linked predominantly to salt loading of the limestones. The significance of salts has become obvious in all results on weathering forms, weathering products and weathering profiles. Two paths of stone detachment and subsequent loss of stone material can be distinguished as a consequence of salt loading.

(1) Accumulation of salt on the stone surface with formation of salt crusts. Reaching a critical thickness, the crusts begin to blister and then detach with adherent stone material. The texture in the front zone of the remaining stone material is already weakened. Salt accumulation continues causing further detachment of stone material.

(2) Salt deposits in the pore space of the limestones cause disintegration resulting in detachment of stone material. Type, quantity and depth of the salt deposits control intensity and velocity of stone detachment and the size of the detaching stone elements. The velocity of stone detachment increases in the course of weathering progression, whereas the size of the detaching stone elements decreases at the same time. This indicates increasing textural weakness of the limestones in the course of weathering progression.

Two very important sources of the salts can be distinguished, in accordance with the findings of other authors (e.g. Croci 1994; Hawass 1993). (1) The increase of air pollution in Cairo as a consequence of the rapid expansion of the city (industry, traffic etc.) results in increasing deposition of pollutants from the atmosphere on the monuments with subsequent salt formation, especially gypsum, on the stone surface or in the pore space of the limestones close to the surface. (2) The water table (ground water, subsoil water) has risen significantly during the last few decades. It can be observed that in extreme cases the water table has reached the ground floor of monuments (see Fig. 7). Insufficient or leaking sewage systems have caused increasing water pollution. Salt solutions from the subsurface intrude by capillary rise into the walls of the monuments and salts are precipitated – especially halite – on the stone surface or in the pore space of the limestones close to the surface.

Additionally, the natural content of salts in the limestones must be taken into account. Lime mortar and plaster – the latter especially used on the walls in the interior of many monuments – must be considered as further sources of salts. Detailed quantitative information on air pollution, subsurface conditions and quality of subsurface water is required for further improvement of knowledge as well as for suitable environmental management in the context of monument preservation activities.

Regarding the lower parts of monuments in the centre of Cairo, the most severe stone damage was found at those zones of the walls which correspond to the main level of salt precipitation from rising humidity. A clear correlation between extent of salt loading and degree of stone damage – following a vertical profile – was shown for such lower parts of Cairo monuments.

Stone damage on numerous monuments in Cairo is alarming. This demonstrates the need and urgency of preservation measures. Preservation measures like control of capillary rise, desalination, cleaning, stone repair, fixation or consolidation of loose stone material, structural reinforcement and stone replacement are under consideration. Environmental management and rehabilitation aspects will have to be considered additionally.

The authors would like to thank the European Commission for research funds in the frame of the Concerted Action ERB-IC18-CT98-0384, and T. Abdallah and his team from the Engineering Center for Archaeology and Environment, Cairo University, for the support of the field campaigns.

References

BADAWI, H. S. & MOURAD, S. A. 1994. Observations from the 12 October 1992 Dahshour earthquake in Cairo. *In*: *Natural Hazards*, **10**, Kluwer, Dordrecht, 261–274.

BEHRENS-ABOUSEIF, D. 1992. *Islamic Architecture in Cairo – An Introduction*. E. J. Brill, Leiden.

CROCI, G. 1994. Damages and restoration of monuments in Cairo. *In*: FASSINA, V., OTT, H. & ZEZZA, F. (eds) *Proceedings of the 3rd International Symposium on the Conservation of Monuments in the Mediterranean Basin 'Stone and Monuments: Methodologies for the Analysis of Weathering and Conservation'*, 22–25 June 1994, Venice. Soprintendenza ai Beni Artistici e Storici di Venezia, Italy, 425–431.

ELHEFNAWI, M. A. 1998. Sodium chloride in some Egyptian Eocene limestones: paleosalinity and application. *Sedimentology of Egypt, Cairo*, **6**, 103–112.

FITZNER, B. & HEINRICHS, K. 2002. Damage diagnosis on stone monuments – weathering forms, damage categories and damage indices. *In*: PRIKRYL, R. & VILES, H. A. (eds) *Understanding and managing stone decay, Proceedings of the International Conference 'Stone weathering and atmospheric pollution network (SWAPNET)'*, 7–11 May 2001, Prachov Rocks, Czech Republic, Karolinum Press, Charles University, Prague, 11–56.

FITZNER, B., HEINRICHS, K. & KOWNATZKI, R. 1995. Weathering forms – classification and mapping. *Denkmalpflege und Naturwissenschaft, Natursteinkonservierung I*. Verlag Ernst & Sohn, Berlin, 41–88.

FITZNER, B., HEINRICHS, K. & KOWNATZKI, R. 1997. Weathering forms at natural stone monuments – classification, mapping and evaluation. *International Journal for Restoration of Buildings and Monuments*, **3**(2), 105–124.

FITZNER, B., HEINRICHS, K. & LA BOUCHARDIERE, D. 2002. Damage index for stone monuments. *In*: GALAN, E. & ZEZZA, F. (eds) *Protection and conservation of the cultural heritage of the Mediterranean cities, Proceedings of the 5th International Symposium on the Conservation of Monuments in the Mediterranean Basin*, 5–8 April 2000, Seville, Spain, Swets & Zeitlinger, Lisse, The Netherlands, 315–326.

FOLK, R. L. 1962. Spectral subdivision of limestone types. *In*: HAM, W. E. (ed.) *Classification of Carbonate Rocks – A Symposium*. American Association of Petroleum Geologists, Tulsa, Memoir 1, 62–84.

HAWASS, Z. 1993. The Egyptian monuments: problems and solutions. *In*: THIEL, M. J. (ed.) *Proceedings of the International RILEM/UNESCO Congress 'Conservation of Stone and other Materials: Research – Industry – Media*, 29 June–1 July 1993, Paris. E & FN Spon, London, Vol. 1, 19–26.

HEINRICHS, K. & FITZNER, B. 1999. Comprehensive characterization and rating of the weathering state of rock carved monuments in Petra / Jordan – weathering forms, damage categories and damage index. *Annual of the Department of Antiquities of Jordan*, **XLIII**, 321–351.

KLEMM, R. & KLEMM, D. D. 1993. *Steine und Steinbrüche im Alten Ägypten*. Springer, Berlin.

SAID, R. (ed.) 1990. *The Geology of Egypt*. Balkema, Rotterdam.

WILLIAMS, C. 1993. *Islamic Monuments in Cairo – A Practical Guide* (4th edition). American University in Cairo Press, Cairo.

This page intentionally left blank

Characterizing the construction materials of a historic building and evaluating possible preservation treatments for restoration purposes

M. ALVAREZ DE BUERGO BALLESTER & R. FORT GONZÁLEZ
Instituto de Geología Económica (CSIC-UCM), Facultad de Ciencias Geológicas, Universidad Complutense de Madrid, 28040 Madrid, Spain
(e-mail: alvarezm@geo.ucm.es)

Abstract: The palace of Nuevo Baztán is a state-designated historic monument in central Spain built in the early eighteenth century. The main building material used in its facades is limestone. The aim of this investigation was to characterize the limestone, defining deterioration mechanisms contributing to the decay of the stone facades and testing a series of potential preservation treatments. The limestone is a biosparite; two microfacies were identified according to microscopic differences (limestones A and B) with distinct petrophysical characteristics mainly due to their different pore systems. Primary deterioration mechanisms were identified as those related to cycles of thermal and hygric stress, biodeterioration and those associated with structural movements. Main decay forms in the surface of the stone are erosion with material loss, spalling and flaking, chromatic alteration, fissures and biodeterioration. Conservation products possessing water-repellent properties were therefore considered. From an initial selection of ten products, two siloxane-based products were ultimately determined to be the most effective on the basis of chromatic variables, water vapour permeability, water–stone contact angle, scanning electron microscope observations and durability (artificial ageing tests). Both products reduce water absorption rates and are expected to slow the rate of limestone decay. This study also demonstrates the value of advance testing of potential treatment methods before application in the field.

The Madrid region (Spain) occupies the centre of the Iberian Peninsula. Nuevo Baztán is a small village 45 km ESE of the City of Madrid. At an altitude of 830 m above sea level, this village lies on flat terrain (locally named 'Páramo') between the Tajuña and Henares rivers, both tributaries of the Jarama river. The closest mountain ranges (Central System or Sierra de Madrid, altitude 2200 m) are 50 km NW. In an eastward direction, the Mediterranean Sea, as the closest coast, is 350 kilometres away. Nuevo Baztán overlies the Páramo limestone Formation (Upper Miocene), which is the source of the building's limestone. This geological unit consists of compact greyish- and yellowish-coloured limestones of lacustrine origin, which appear as different facies: fossiliferous, onchoid-rich, massive, karstified limestone, etc. The unit is affected by karstic phenomena, lying locally on a doline (a shallow conical depression) filled with residual deposits (clays, silt, sand and pebbles). The aquifers in the project site are of a karstic type, and are supplied by direct infiltration of rainwater. The surrounding vegetation of Nuevo Baztán is composed of oak woods (*Quercus lusitanica*) and arid land crops (olive trees and grape vines).

The palace of Nuevo Baztán, designated an artistic and historic monument in 1941 by the government, belongs to the Nuevo Baztán complex, an industrial/agricultural estate built by the architect Churriguera between 1709 and 1713 at the commission of landowner Juan de Goyeneche. Active operations ceased after 1725.

The complex, an example of Baroque urbanism in a rural environment, is arranged around the palace and the church; the latter are housed in the same building (Fig. 1). The building's ground plan is rectangular and occupies an area of 1910 m^2 (49.24 m long × 38.78 m wide), most of which corresponds to the palace, the church representing only 315 m^2 of the whole area. The monument will therefore hereafter be referred to as 'the palace'. The Palace's four facades face approximately north, east, south and west (main facade with the main doorways to both palace and church).

The palace, designed as the founder's residence, occupies the northern part of the building; the two-storey (6.8 m high, 10 m high roof included) rectangular palace takes the form of two corridors enclosing a central open courtyard, with a central well. Its clear horizontal design is broken only by a square-plan tower

From: SIEGESMUND, S., WEISS, T. & VOLLBRECHT, A. 2002. *Natural Stone, Weathering Phenomena, Conservation Strategies and Case Studies*. Geological Society, London, Special Publications, **205**, 241–254.
0305-8719/02/$15.00 © The Geological Society of London 2002.

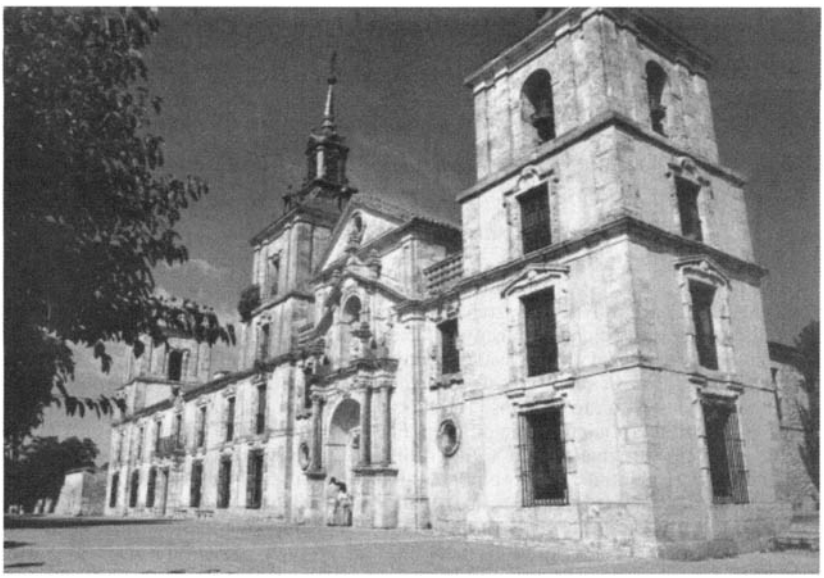

Fig. 1. Main facade of the palace of Nuevo Baztán.

(18.5 m high) in the NW corner with a flat roof, topped with a limestone balustrade.

The church occupies the southern area of the building and is flanked by two four-storey towers (27.5 m high). The slate roofed towers are crowned with broach spires with wind vanes and harbour a bell tower in the interior. The northern tower is common to the church and palace providing a marked vertical feature.

There is one underground storey, which extends from 4.40 m up to 6.70 m in depth to beyond the area of the palace. This room was used as a wine cellar under the palace, and served as a crypt under the church, both built in brickwork vaults. Its foundations are a continuous trench with a rubblework core beneath the walls, and wells under pillars.

Three squares, or plazas, surround the building: the 'spectacle' square faces the eastern facade, to the west lies the church or main square, and to the south the market square. The complex also includes several other structures (workshops, factories and houses), some of which are connected to the palace but for the present purposes will not be described.

The primary building material is limestone. The primary ornamental elements are found on both main doorways to the palace and church, and framing windows and balconies (lintels, jambs and sills). Some of the architectural details are related to water drainage. The facades are equipped with roof gutters and gargoyles, and around the building there is a ditch for ground surface drainage to prevent water infiltration towards the basement's subsoil.

The building was almost continuously inhabited until recently, when ownership was transferred to the regional government. There is no existing information on the original project or building plans, although there is some reference to repair work undertaken during the second half of the twentieth century.

The inside of the palace is currently being rehabilitated. Occasionally, local exhibitions are held in some of the rehabilitated rooms. There is also a project to rebuild the interconnected basements, galleries and storage rooms such that it will be possible to open this area of the palace to the public.

According to the Krakow Charter of 2000:

> 'Maintenance and repairs are a fundamental part of the process of heritage conservation. These actions have to be organised with systematic research, inspection, control, monitoring and testing. Possible decay has to be foreseen and reported on, and appropriate preventive measures have to be taken ... Conservation/ preservation techniques should be strictly tied to interdisciplinary scientific research on materials and technologies used for the construction, repair and/or restoration of the built heritage.'

Before restoration is attempted, the causes of

stone deterioration need to be established to eliminate or mitigate them effectively. It is widely understood that the degradation of materials used in the construction of historic buildings and monuments is caused by both environmental factors (predominantly meteorological conditions and atmospheric pollution) and inherent properties of the materials. During the last two decades, the scientific community has become increasingly aware of the need to undertake preliminary investigation into the causes of stone deterioration; several recently published accounts of such studies can be found (e.g. Price 1996). Poorly conserved monuments may also be the result of previous uncontrolled rehabilitation and restoration attempts, which can actually accelerate degradation (Price 1996). This underscores the importance of understanding the petrophysical properties of the materials, and the changes the stone undergoes when protective treatments are applied (Fort *et al.* 2000b, 2002).

The aim of this project was to characterize the facade limestone and to identify the deterioration mechanisms causing the decay forms observed on the surface of the stone. The ultimate aim was to assess the efficiency and durability of several preservation treatments with a water-repellent effect applied to the rock, to reduce or delay water absorption by the stone and consequently slow stone deterioration.

The use of preservation products must not be considered a substitute for cleaning monument stone. A detailed description of how this should be undertaken, however, falls outside the scope of this project. There are also some other aspects (e.g. biodeterioration, cement mortars), which require further investigation.

Methods

Environmental conditions

Environmental variables affecting the palace were identified to gain insight into the degradation processes the building materials have undergone. Towards this end, temperature and relative humidity sensors were installed on each of the palace's four facades in March 1999, to allow continuous monitoring over the course of a year (HOBO-Onset loggers; Box Car 2.06 Software for Hobo Data Loggers).

As the palace's underground wine cellar and storerooms frequently flood during the winter seasons, the depth of the water table was monitored between September 1999 and July 2000 in two wells: one inside the palace (in the open courtyard) and the other outside the building. Pollution was not monitored since the complex is located in a rural area with no nearby factories or industry, little traffic and no significant winds to transport pollutants from urban areas.

Petrological and petrophysical investigations

Samples of the palace's stone were collected for its petrographical, petrochemical and petrophysical characterization, as well as to assess the efficiency and durability of the limestone impregnated with different water-repellent products. For the petrophysical study, 15 limestone cylindrical specimens, 50 mm in diameter and of variable length (100–400 mm), were used.

Petrographic analysis was performed by means of the study of thin sections under the petrographic microscope. Mineralogical identification was carried out by X-ray diffraction (XRD) and Fourier transform infrared spectroscopy (FTIR, KBr pellets). Scanning electron microscopy (SEM), with secondary and backscattered electron imaging combined with an X-ray dispersive energy microanalyser (EDX), was used mainly to study the limestone treated with the water-repellent products (on both gold-sputtered irregular samples and graphite-sputtered polished sections). The electron microprobe, combined with a microanalyser, was used to analyse a patina on the stone; standards were those described by Jarosevich *et al.* (1980) and provided by the Smithsonian Institute in Washington DC.

Chemical composition of the limestone was determined using atomic emission spectrometry with inductive-coupling plasma (ICP-AES).

Certain petrophysical parameters were measured solely to determine the petrophysical characteristics of the limestone (i.e. capillarity coefficient). Others were analysed to assess treatment efficiency (i.e. stone–water dynamic contact angle, water vapour permeability, chromatic parameters $L^*a^*b^*$ (CIE 1986), open porosity, ultrasound wave transmission velocity, direct measurements, and water absorption and evaporation). Further factors were studied to evaluate treatment durability (i.e. chromatic parameters). The full range of parameters evaluated also included real and bulk densities, dynamic Young's modulus, pore size distribution and porosity accessible to mercury (Hg-intrusion porosimetry).

Artificial ageing tests, performed to assess the durability of the selected products, simulated actual environmental conditions to which the stone is subject, including freezing and thawing

with exposure to ultraviolet radiation (20 cycles), salt crystallization (15 cycles), and wetting–drying (30 cycles). Tests were performed according to NORMAL guidelines (Normativa Manufatti Lapidei, Italian Committee for Normalization of Procedures on Stone Materials) and RILEM recommendations (1980).

Results

Building materials

The stone used to build the palace is limestone, both as ashlars masonry (approximately 75–90 cm long, 40–45 cm wide and 50–60 cm deep) in the main parts of the building (main doorways, bases, corners, window and balcony frames, some tower levels), and as mortared rubblework and rough stones in the walls between openings, windows and balconies. The palace tower was built as composite walls (double-sided rubblework walls with a clay core). The building's roof is made of Arabic tiles. The finishing of the limestone ashlars that form the main facade is of two types – projected with a hammered finish or sunken with a smooth finish – and is most prominent on the main palace and church doorways, and around the windows and balconies of the whole building.

Materials applied in earlier interventions include greyish limestone (probably Colmenar limestone) and cement mortars. The latter were used for repointing and rendering rubblework walls, substituting the original lime mortar (Escuela de Arquitectos Técnicos 1987). Several restoration projects carried out on the building are recorded in the National Record Office (1953, 1955, 1956, 1957, 1961, 1970, 1973, 1974). Some of these records include details of the various interventions. For instance, the church bell-tower was consolidated (originally built in stone rubblework with lime mortar) by strengthening the wall with composite brickwork and stone rubblework; the building's corners were stone dressed and plain walls cement mortar rendered; and limestone ashlars framing the windows were partly replaced. There are also records of replaced limestone elements (balustrades, bases and breast walls) in the north-eastern tower. Reports of strengthening walls by introducing a concrete beam date back to 1970 when the northern wall of the palace tower partially collapsed. The use of cement mortar to repair the slating and tiling of the roofs of both towers flanking the palace is also described. In another intervention rendering described as 'annoying' was removed from the main facade.

Petrology and petrography of the limestone. The stone consists of biosparite with an abundance of algal remains (oncholiths, stromatolite fragments, algal balls). Porosity is mostly interparticle, with some samples showing siliciclastic grains (mainly quartz) and a higher proportion of micrite than sparite. Iron oxide and gypsum cement were detected in some samples. Two characteristic microfacies (the same facies with different microscopic features) were identified by petrographic analysis and are hereafter referred to as limestone A and limestone B (Fig. 2). Petrographic differences between the two microfacies are related to the nature and

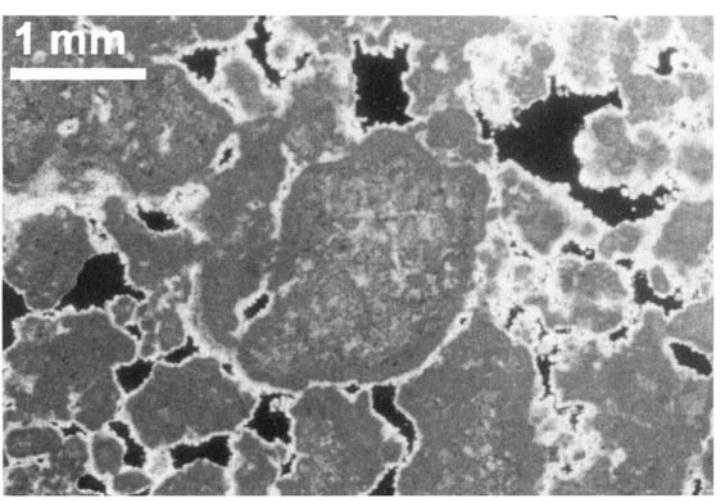

Fig. 2. Petrographic image of the biosparitic limestone of Nuevo Baztán.

Table 1. *Chemical composition of limestones by ICP-AES*

	Limestone A	Limestone B
SiO_2	1.11	0.15*
Al_2O_3	0.319	0.08*
Fe_2O_3	0.06*	0.04*
MnO	t	t
MgO	0.38*	0.34*
CaO	55.07	55.72
Na_2O	t	t
K_2O	0.03*	t
TiO_2	0.01*	0.01*
P_2O_5	t	t
LOI	42.39	42.30
Total	99.28	98.55

* Value below detection limit
t, trace; LOI, loss of ignition

abundance of fossil types (oncholiths, stromatolites, gastropods, ostracods and charophyte remains), porosity, pore size distribution and the degree of fissure cementation.

Both microfacies are mostly calcite-based (Table 1) with a sulphur content ($\%S_{total}$) below 0.02%: 0.019% for limestone A, and 0.010% for limestone B. Assuming that all the sulphur occurs as sulphates, this would only account for a sulphate content under 0.06%, which is considered low for salt crystallization mechanisms causing stone deterioration.

Origin of the limestone. The source of the building's limestone is the Calizas del Páramo Formation (Upper Miocene), petrographically classified as biomicrites. In the project site, these limestones were highly exploited in the past and provided block masonry for building, and aggregates for road construction. Most of the area's quarries are currently inactive or supply only aggregates.

A study of the origin of the limestone used to build the palace was carried out. Since the original quarries, known to be the source of the building stone because of their proximity to the building (2 km), presently underlie houses belonging to the Nuevo Baztán municipal district, built in 1968, sampling was conducted in the limestone quarries of the neighbouring districts of Valdilecha, Pozuelo del Rey and Villar del Olmo. The limestones from the quarries of Valdilecha (7 km SW of Nuevo Baztán, presently exploited for aggregates) and Pozuelo del Rey (7 km west from Nuevo Baztán, presently a landfill) were found to closely resemble the palace stone in terms of their petrography, and are proposed as a source of material for future repair work.

Petrophysics of the limestone. Petrophysically (Tables 2 and 3), limestone A has a higher open porosity, i.e. porosity accessible to water (n_0) than limestone B, and also a higher water

Table 2. *Petrophysical properties of the limestones*

	Limestone A	Limestone B
Real density (kg/m^3)	2700	2600
Bulk density (kg/m^3)	2500	2400
Open porosity (%)	8.38±1.13	6.91±0.93
Water saturation coefficient (%)	3.90±0.51	2.68±0.25
Water absorption coefficient at 48 h (%)	2.48±0.35	1.84±0.28
Porosity accesible to Hg (%)	6.61	4.76
<5 μm (%)	98	85
>5 μm (%)	2	15
Water vapour permeability coef. (g/m^2 24 h mmHg)	0.20±0.16	0.11±0.05
Water–stone contact angle (°)	49±12	42±4
Capillarity coefficient (kg/m^2 h$^{0.5}$)	0.0076±0.0055	0.0035±0.0008
Ultrasound velocity (m/s)	5529±186	5754±135
Dynamic Young's modulus (MPa)	75812±5855	83091±4353

Table 3. *Chromatic parameters of limestones*

	L*	a*	b*	C	YI	WI
Limestone A	81.66±1.26	2.34±0.34	7.61±0.57	8.1±4	13.24±1.06	28.37±3.43
Limestone B	81.87±1.25	2.35±0.18	8.73±0.73	8.3±3	15.03±1.26	24.24±3.54

L*, lightness; a*, red/green hue; b*, yellow/blue hue; C, chroma; YI, yellow index; WI, whiteness index

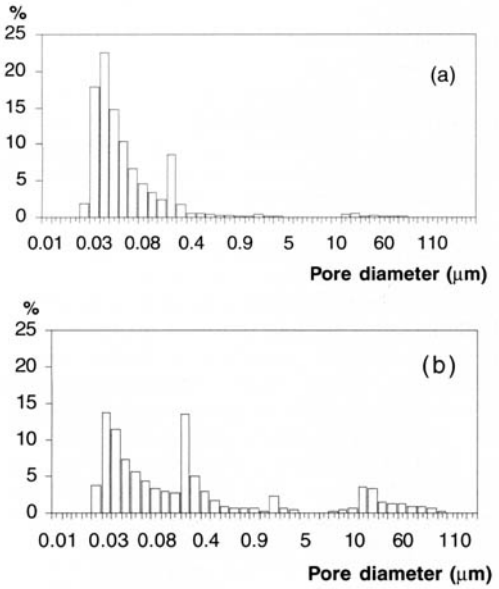

Fig. 3. Pore size distribution of (**a**) limestone A and (**b**) limestone B.

absorption rate, water vapour permeability, proportion of micropores (Fig. 3) and capillarity coefficient, and a lower ultrasound wave transmission velocity and dynamic Young's modulus. The limestones are almost identical in terms of chromatic variables and similar in their stone–water contact angle. Statistical analysis of the data revealed that limestone A was more heterogeneous than B.

The limestones are thus of a moderate–low open porosity (<9%) and comprise mainly (>85%) micropores (of diameter <5 μm according to the definition by Russel 1927). The rock has a maximum water absorption capacity (total immersion at atmospheric pressure) of under 3% (absorption of less than 2.5% weight of water at 48 hours), is permeable to water vapour, has a low capillarity coefficient and is of very high physico-mechanical quality, as confirmed by the ultrasound wave transmission velocity. The stone–water contact angle indicates a low degree of water repellence (Ferreira & Delgado Rodrigues 2000). The differences between the limestone types are sufficient to give rise to different deterioration patterns.

Patina. The limestone surface shows the remains of a well-preserved orange-yellowish film or patina (Alvarez de Buergo *et al.* 2002); its hue is more intense in the palace's lower areas and in zones protected from rainwash and solar radiation. On average, the film is some 80 mm thick, although it exceeds 200 mm in places. The manual application of this surface patina would account for its varying thickness. Through microscopy, the patina was observed to evenly cover the limestone surface and was firmly attached to it, with a distinct film–limestone interface evident. The presence of the patina appears to impede the formation of a biological film.

The patina shows discrete lamination/stratification; three different layers of some 50 μm each in thickness could be discerned by optical microscopy in some areas, distinguished by differing textures and colours. In these areas, it seemed that the patina was fully preserved and presented a thickness of some 150 μm. Generally, the patina's texture is cryptocrystalline towards the limestone interior and slightly more microcrystalline closer to the rock surface; in other areas, the patina is almost completely isotropic. In the patina's surface layer, very fine-grained quartz, feldspar, calcite and gypsum are the only thoroughly crystallized and recognizable mineral phases attributable to the adhesion of atmospheric dust observed. Beneath the patina and across the limestone, a system of fissures running parallel to the rock surface was observed and is probably responsible for the scaling and detachment of the patina, in response to the effects of cyclic wetting and drying.

Mineralogically, the patina is composed of calcite, gypsum, quartz and potassium feldspar, with traces of whewellite, calcium phosphate, and iron oxide and hydroxide. The calcite and gypsum are considered part of the patina itself, although possible contamination from the substratum cannot be completely ruled out. No biological structures or pollutant particles were seen on SEM examination; the patina appeared as a film evenly covering the stone. Using backscattered electrons, it was much easier to distinguish between the patina and the substratum. Electron microprobe analyses indicated a higher phosphorus content in the patina than in the limestone (Fig. 4). This high P content has been linked by some authors (Kouzeli *et al.* 1988; Lazzarini & Salvadori 1989) to the application of milk-derived protective treatments (casein). The use of animal milk would account for the presence of sulphur and phosphorus in the patina (lactoalbumin is sulphur-rich and casein is a phosphorus protein found in milk). The presence of calcium oxalates might be explained by the formation of oxalic acid from this type of intentionally applied compound, without precluding possible bacterial

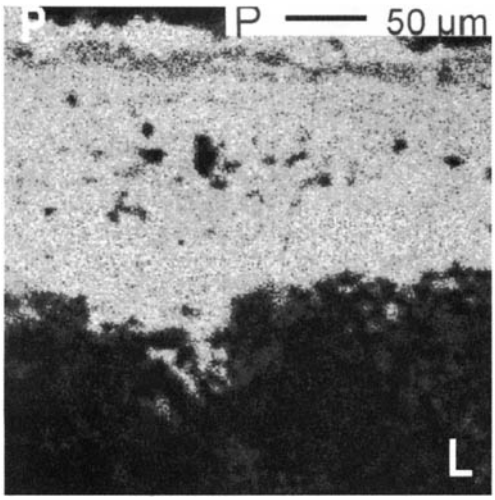

Fig. 4. Phosphorus distribution map in a cross-section of limestone (L, dark) and patina (P, grey).

contribution, and its subsequent combination with existing calcium. The patina owes its colour to the presence of iron associated with the use of ochre colouring pigments.

The characteristics of this patina suggest that it is the remains of a past treatment (Álvarez de Buergo *et al.* 2002), probably applied just after the building's construction, without precluding subsequent reapplications. Its original composition was possibly a mixture of lime, gypsum, ochre pigment, and milk-derived compounds. The purpose of the patina appears to have been to protect the external surface of the stone and render its surface appearance more uniform. Owing to its good condition and the fact that it has become a historical feature of the building, its preservation under any further conservation treatments is recommended.

Environmental conditions

Climatic analysis. The climate of Nuevo Baztán is officially classified as 'semidry to dry temperate Mediterranean' (ITGE 1988). Average temperature and rainfall values for the project site range from 11°C to 14°C and 400 mm to 600 mm, respectively. The annual number of days of rainfall varies from a low of 20 days, in the driest years, to over 100 days. Eighty per cent of the region's precipitation takes the form of rain, with snow, fog and other forms constituting the remainder; on average, the region experiences 50 days of frost (temperature ≤0C°) annually.

Typical daily temperature and relative humidity values monitored at the palace's facades are 0°C to 10°C and 60–90% respectively in winter, and 20–35°C and 20–50% in summer. While the palace is subjected to as much as 32°C and almost 95% variation in temperature and relative humidity over the course of a year, daily temperature and humidity fluctuations have been known to reach 29°C (in summer) and 86% respectively in a given day. The highest temperature changes were monitored in the west facade, and lowest in the north facade. The highest relative humidity variations were recorded in the south wall, and lowest in the north-facing facade.

Changes in the water table. Given the fact that local aquifers acquire their water from rainfall and that the underground area has been flooded in the past, it was considered appropriate to measure the depth of the water table under the project site (floor 4.40–6.70 m from the ground floor). The values obtained ranged from 7.30 m to 6.75 m. This water level variation of 55 cm is sufficient to cause some flooding of the palace's underground level during spring. The consequence of these fluctuations is rising damp in the walls and damage to the foundations. However, this damage does not affect the walls above ground level or the outside of the palace (although no damp-proof courses were built in). Moreover, this dampness dries out during the summer and autumn. To prevent new flooding events, a drainage pump has been recently installed that mostly operates during the rainy periods.

Deterioration of materials

The palace has suffered steady deterioration, due primarily to past abandonment and vandalism, and also to the constant modification, extension and repair it has undergone for almost 300 years. The actions of different owners have resulted in divided or shared inner rooms, which sometimes restricted accessibility and in some cases even modified the facade's recesses. The roof was at one stage partially ruined (the date or cause of collapse is not documented but it was repaired in 1970) and the north facade of the palace tower partly collapsed because of a door opening in the wall, which caused an enormous crack running from the cornice to the ground floor. The wall was repaired by installing a concrete beam (Díaz Alter 1991).

The decay forms on the stone surfaces are fissuring ashlars with material loss (mostly due to structural causes, a third of the void lintels show displacement and fissuring, and, on

occasion, fissures correspond to the action of iron elements), and scaling and flaking of the stone surface, mainly attributable to material fatigue due to thermal and hygric cycling. As mentioned above, the stone facade is subjected to maximum daily fluctuations of up to 29°C in temperature and 86% in relative humidity, as well as to a maximum of 100 days per year of rainfall and an average of 50 days per year of frost. These climatic characteristics, together with the petrophysical properties of the limestone (low stone–water contact angle and low capillarity coefficient) would create a strong temperature gradient and water accumulation focused on an area less than 5 mm deep. Depending on the climatic conditions, freezing–thawing or wetting–drying could lead to spalling of the stone surface, erosion of elements with overall volume reduction, differential deterioration, and water runoff along the facade giving rise to chromatic alterations (Ordaz & Esbert 1988).

There are also signs of biodeterioration on a large proportion of the stone facade surfaces, believed to be related to the activity of both micro-organisms and plants. The growth of plant roots has resulted in the movement and displacement of some ashlar blocks. Microbiological activity gives rise to green or greyish patinas (chromatic alteration) on the surface of the stone ashlar blocks (biological films) that give the stone a soiled appearance and could enhance deterioration processes by generating hydrophilic zones. As mentioned above, when the ochre patina occurs on the surface of an ashlar block, these biological films do not develop. Rust staining, another chromatic alteration due to the oxidation of iron compounds, was also observed, along with graffiti, especially on the renderings, which show material loss, fissures, blisters, bulges and detachments. The use of cement mortars has, in all probability, contributed to the current state of these renderings, mainly due to their low adherence to the rubblework walls, and possibly to the rigidity related to the use of cement. The partial lack of mortar in the stone masonry joints is also a noticeable feature, and at times was repaired by repointing with cement mortars. No efflorescence was observed, suggesting a possible absence of salts or insufficient amounts for salt crystallization processes.

The pathologies and decay forms described occur as isolated points, with the exception of biodeterioration, which is more generalized. The zones presenting the highest degree of material loss are those most exposed to weather (i.e. rain), such as corners and ashlars protruding from the facade plane. Signs of biodeterioration are especially marked in areas protected from rainwash, where moisture can accumulate. The projected and hammered-finished ashlars, which expose a larger surface area to the elements than sunken and smooth-finished ashlars, show correspondingly greater deterioration with more volume reduction and biodeterioration. Measurable deterioration caused by plant growth was observed on the building's facades during the course of this two-year study.

Conservation treatments

Before any conservation treatment, the stone facades need to be cleaned. Due to the decay forms observed and their origin, water-based cleaning and the use of specific biocides might be appropriate. After the cleaning process, which should always involve an in situ pre-test to establish the ideal cleaning conditions and the efficiency of the method (Fort *et al.* 2000*a*), it is advisable to protect the facades, since the stone is always much more sensitive to deterioration and soiling. In general, when removing stone soiling and surface deposits, the original stone roughness is restored, increasing the specific surface area exposed and thus vulnerable to potential deterioration. Protecting the stone should be considered as part of a maintenance programme aimed at impeding or mitigating deterioration as much as possible.

Treatment selection and application

Given the degree of deterioration of the building's limestone, it was considered appropriate to evaluate the use of water-repellent products to reduce water penetration into the material (Alvarez de Buergo & Fort González 2001). As mentioned previously, many of the pathologies affecting the stone surface appear to be related to deterioration mechanisms involving cycles of wetting–drying and heating–cooling.

Ten hydrophobic products, some of which also had a consolidating effect (which restores the stone's lost cohesion), were pre-selected. The criteria followed for the preliminary selection of these ten products were their common use in stone conservation, the fact that they represented a wide composition range (organic, organosilicic and inorganic), and their solubility in water or in organic solvents (Table 4). The products were applied by brushing one side of the stone samples or by total immersion for 3 minutes in the treatment solution (depending on the property to be determined or the test)

Table 4. *Selected water repellent products*

Product (abbreviation)	Manufacturer/ supplier	Composition*	Solvent*
Tegosivin HL 100 (HL100)	Goldschmidt	Methyletoxy-polysiloxane	8% in white spirit
BPS 7700 (7700)	Trion-Tensid AB	Siloxane	White spirit + aromatics
Silo 111 (S-111)	C.T.S. España	Oligosiloxane	12% in Solveso 100 (turpentine)
Parrogum Invisible (PI)	Azco Nobel Coatings	Saturated polyester + polysiloxane + inorganic acid ester	Organic solvents
Tegosivin HE 328 (HE328)	Goldschmidt	Alkyl-alkoxy silane/siloxane/ polymethyl-siloxane	10% in water
Acrisil 201/O.N. (A-201)	C.T.S. España	Acrylic and siliconic resin	1:2 in AC-204 solvent
Graffi Capa 300 (300)	Trion-Tensid AB	Siloxane and microcrystalline wax	1:1 white spirit
Cosmolloid 80 (C-80)	C.T.S. España	Microcrystalline wax	Cover with white spirit and stir
Consistone "C" (C"C")	Azco Nobel Coatings	Soluble lime + siloxane	Water
Radcon #7 (R#7)	Ariadna Enterprise	Sodium silicate (biochemically modified)	Not supplied

* Data supplied by manufacturers

until constant weight (at a temperature of 20°C, and 25% relative humidity). Since two limestone microfacies were used in the building's construction, petrographically and petrophysically distinct although more difficult to visually distinguish (Table 3), the treatments selected were required to be effective on both microfacies. The latter would, in turn, be expected to show different responses to treatment since each type of stone shows a distinct pore system. These systems differ in terms of both pore volume and pore size distribution, properties which control the intake and amount of water-repellent absorbed, the penetration depth of the treatment, the distribution of the product and the type of coating or film provided by treatment.

Efficiency of the treatments

Efficiency of the pre-selected treatments. According to Botteghi *et al.* (1992), hydrophobic products should be water-repellent (liquid state), permeable to water vapour, adhere to the stone, cover the pore system as a transparent film, and not alter the colour of the stone surface over which they are applied. Thus, to assess the efficiency of the selected treatments, the water–stone contact angle, water vapour permeability and chromatic values were determined in the limestone specimens before and after treatment (Table 5). The hydrophobic effect of the treatments was estimated by calculating E_{ca} (Ferreira & Delgado Rodrigues 2000) or efficiency determined by the water–stone contact angle. The latter was defined as the ratio of the contact angle of the treated stone and 90°, which is considered the minimum threshold. The higher this ratio, the higher the efficiency; values below 1 were taken to indicate an ineffective treatment.

These tests were chosen as rapid and reliable performance indicators. Treated stone samples were also subjected to SEM (Figs 5 and 6) to estimate penetration depth, product distribution through the pore system of the rock, degree and type of coating, filming capacity, adherence to material, continuity of treatments, spalling or cracking, etc. (Alvarez de Buergo *et al.* 2001). Based on these tests, the two most efficient treatments were then selected according to the following criteria: (a) least chromatic variation, (b) least reduction in water vapour permeability, (c) highest liquid water-repellence values (as reflected by increased water–stone contact angle), and (d) highest adherence capacity to the substratum and capacity to form an even, uninterrupted film over the material. Penetration depth is not the best indicator of the efficiency of a water-repellent treatment (Alvarez de Buergo & Fort González 2001). The selection process was as follows: first, treatments with an E_{ca} value under 1 (Table 5) were rejected given their poor hydrophobicity, irrespective of the type of limestone (products HL00, S-111, HE328, C-80, A-201 and R#7). The remaining products were rejected on the grounds of achieving a reduction in water

Table 5. *Treatment efficiency assessment*

	Limestone A				Limestone B			
	E_{ca}	ΔPV (%)	ΔE^*	PD (μm)	E_{ca}	ΔPV (%)	ΔE^*	PD (μm)
HL100	0.79	−34.5	0.94	1.3–2.6	0.74	−15.7	10.60	6–7
7700	1.39	−19.4	3.58	6–7	1.34	−18.9	7.98	3–4
S-111	0.88	−57.3	4.46	3–8	1.34	−20.5	1.87	7
PI	1.71	−48.7	6.95	2–4	1.60	−32.0	7.76	7
HE328	0.96	−6.4	3.07	20	1.26	−27.4	0.86	6–10
A-201	1.06	−55.0	2.08	4–8	0.81	−51.5	9.58	3–5
300	1.09	−79.2	6.02	1–2	1.04	−23.1	7.89	1–5
C-80	0.70	−63.2	5.80	3–4	0.77	−32.9	11.17	20
C"C"	1.17	−47.2	11.33	3–8	1.04	−36.7	8.77	20
R#7	0.53	−92.0	4.38	0	0.48	−77.0	7.32	7–8

E_{ca}, efficiency determined by stone–water contact angle; ΔPV, variation of the water vapour permeability; AE*, global colour variation; PD, penetration depth estimated by SEM

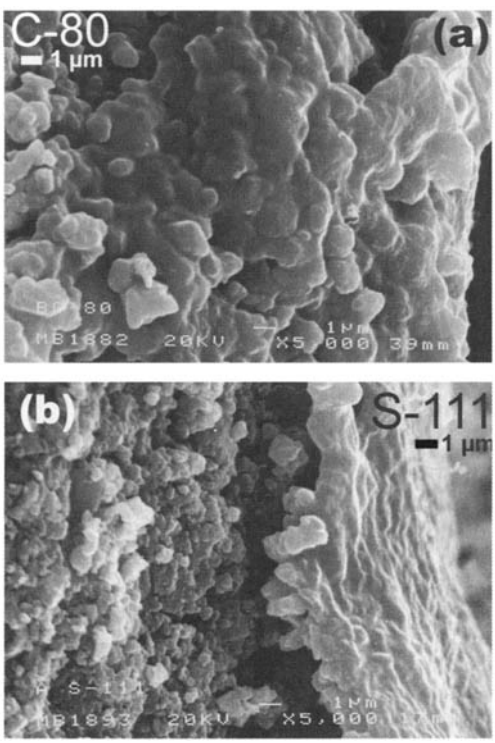

Fig. 5. SEM images (secondary electrons) of cross-section samples, external surface to the right, inside to the left. (**a**) Limestone B impregnated with the C-80 product. (**b**) Limestone A impregnated with the S-111 product.

vapour permeability of over 50% (product 300) or an overall colour change in the stone (ΔE^*) of over 10 units (product C"C"). This left the two products BPS 7700 (7700) and Parrogum Invisible (PI), both siloxane-based compounds (Table 4).

Efficiency of the treatments selected. The variables open porosity, water absorption, chromatic factors and ultrasound wave transmission velocity were determined in stone fragments treated with 7700 and PI and compared with values obtained in untreated samples (Table 6, Fig. 7). Treatment of limestone A with both products led to a drop in open porosity close to 20%, while this variable was reduced by around 5.5% when limestone B was treated. Water absorption curves indicated that, regardless of the type of limestone, both treatments drastically reduced water absorption, at least over the first 3 days of the test. Colour changes were highly variable although values were low, never exceeding a change of 3.5 units. Finally, ultrasound wave transmission velocities were substantially higher for the treated limestones compared to untreated controls, with the exception of limestone A treated with 7700, in which this variable remained practically unchanged. The general behaviour of both treatments was, nevertheless, very similar.

Durability of the selected treatments

The ageing tests (freezing and thawing with exposure to ultraviolet radiation, salt crystallization and wetting–drying cycles, Table 7) were chosen based on the climatic conditions to which the building is subjected (temperatures below 0°C, frequent rain and a wide temperature and relative humidity range even on a daily basis). The salt crystallization test was included because of the stone's S_{total} content, which although low (<0.02%), should not be neglected. The S level is also susceptible to sudden change if the environmental conditions change, for instance when pollutant levels rise. Moreover, since most of the rock pores may be

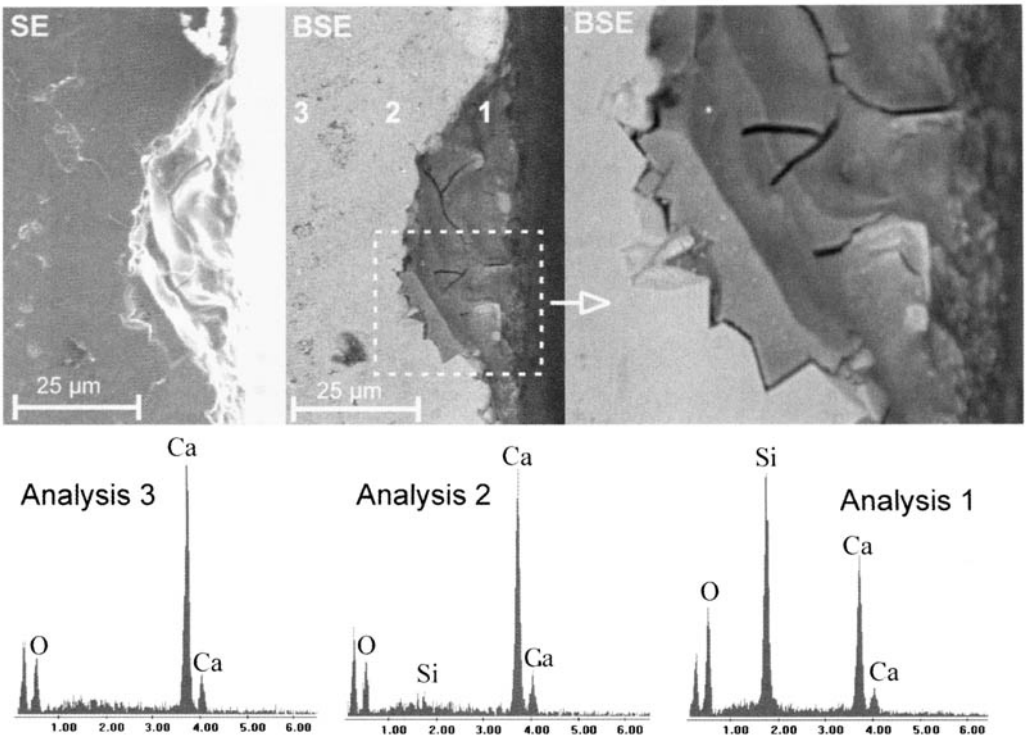

Fig. 6. SEM images (SE and BSE) of a limestone impregnated with the PI product, showing the EDX analyses in three different points.

Table 6. *Modification of porosity, ultrasound propogation velocity and global colour (ΔE^*) of limestone before (UT, untreated) and after the application of the selected treatments*

		Limestone A	Limestone B
Open porosity n_0 (%)	UT	8.04±1.31	6.64±0.53
	7700	6.49±1.28	6.28±0.55
	Δ (%)	−19.28	−5.42
	UT	8.80±1.10	7.09±0.63
	PI	7.13±1.35	6.69±0.61
	Δ (%)	−18.92	−5.64
Ultrasound velocity (m/s)	UT	5608±287	5757±94
	7700	5596±277	5878±89
	Δ (%)	−0.21	+2.06
	UT	5412±140	5747±195
	PI	5502±123	5872±96
	Δ (%)	+1.64	+2.13
Global colour variation (ΔE^*)	UT-7700	1.80±0.97	2.34±0.31
	UT-PI	1.49±0.20	1.20±0.70

classed as micropores (diameter <5 µm), this lithic substrate is *a priori* susceptible to processes of deterioration.

The effects of accelerated ageing were evaluated in terms of changes in appearance (no modifications were observed), weight and chromatic variables. Both treatments showed a very similar effect on limestones A and B, diminishing the degree of deterioration with respect to untreated stone specimens and increasing their

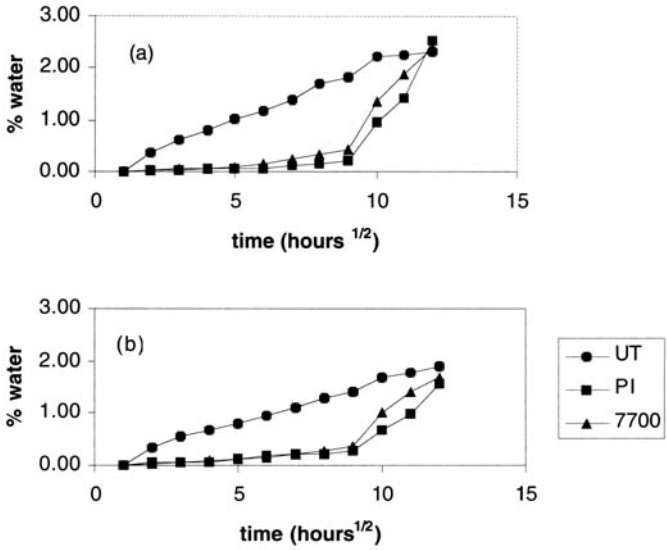

Fig. 7. Water absorption by total immersion at atmospheric pressure of the untreated (UT) and treated limestone test specimens: (**a**) limestone A, (**b**) limestone B.

Table 7. *Results of accelerated artificial ageing tests*

		Limestone	UT	7700	PI
Salt-crystallisation	Δ Weight	A	−1.76	−0.20	−0.04
	(%)	B	−0.73	−0.19	−0.03
Freezing–thawing + UV	Δ Weight	A	−0.042	−0.012	−0.023
	(%)	B	−0.026	−0.014	−0.017
	Δ Weight	A	–	1.79	1.49
	(%)	B	–	2.34	1.20
	ΔE^*				
	ΔE^*				
Wetting–drying	Δ Weight	A	+0.01	+0.01	+0.00
	(%)	B	3	6	6
			+0.00	+0.01	+0.01
			4	3	0

durability. In terms of durability, limestone treated with product PI shows a lower weight loss and a lower global colour variation (ΔE^*) than that treated with product 7700 after the performance of the ageing tests.

Discussion and conclusions

The main conclusions to be drawn from the present findings are as follows.

Where possible, potential preservation products should be tested on appropriate samples before field application to the stone of historic monuments. As observed in this study, a single product may show varying effects on slightly different types of limestone (microfacies). The different porosity of the limestones and their pore size distribution appear to be determining factors in the behaviour of these protective treatments.

Once the stone has been characterized, it is important to select a simple basic methodology to identify products showing most appropriate behaviour. In the present case, products based on siloxane showed the greatest effectiveness.

Patinas can hold clues to past treatment efforts, and, moreover, may play a significant role in the preservation of stone surfaces. Where a patina is present, its origin should be established (i.e. natural or intentionally applied) and its alteration over time as compared to its present composition should be characterized. It should also be noted whether the patina affords protection to the stone

surface. In this study, it was concluded that the patina prevented the development of a biological film and thus acted as a barrier to biodeterioration. Because of its efficiency against deterioration, and its consideration as a historical feature of the building, preservation of the patina is recommended. One approach might be the reproduction of this patina for future application, as suggested in the Krakow Charter of 2000.

The rate of deterioration of the materials that make up the palace's facades is not excessive, being mainly the consequence of abandonment, lack of maintenance work and previous inappropriate repairs. The primary deterioration mechanisms are those related to water erosion and related mechanisms including freeze–thawing and wetting–drying processes, to fatigue from thermal cycling, to biodeterioration and those associated with structural movements.

If it were necessary to replace some of the limestone during a further intervention, the present petrographic study served to identify similar material to the original stone in nearby quarries.

The fact that a product proves to be efficient in the laboratory does not necessarily mean it will be similarly effective in situ, since not all existing variables can be taken into account in vitro. The same is true for the durability assays. These give an idea of how a product will behave but will never faithfully predict behaviour in the real long term. It is thus recommended that before applying any treatment to a facade, an in situ evaluation be conducted, and whenever possible, behaviour should be assessed by tests of real exposure to the environment (Fort *et al.* 2000*b*).

We acknowledge the Madrid regional community for financial support through project 06/0108/98 and for the granting of a postdoctoral scholarship (02/280/1998).

The authors gratefully acknowledge the assistance of S. Siegesmund (Geowissenschaftliches Zentrum der Georg-August-Universität Göttingen) and E. Doehne (The Getty Conservation Institute, Los Angeles), in the final editing of the text.

References

ALVAREZ DE BUERGO, M. & FORT GONZÁLEZ, R. 2001. Basic methodology for the assessment and selection of water repellent treatments applied on carbonatic materials. *Progress in Organic Coatings*, **43**, 258–266.

ALVAREZ DE BUERGO, M., FORT GONZÁLEZ, R. & GÓMEZ HERAS, M. 2001. Efficiency of stone conservation treatments by means of scanning electron microscopy. *Annales Géologiques des Pays Helléniques*. Edition Speciale, **39**, in press.

ALVAREZ DE BUERGO, M., FORT GONZÁLEZ, R., LÓPEZ DE AZCONA, M. C. & MINGARRO MARTÍN, F. 2002. Analysis of the ochre patina on the limestone of Palacio de Nuevo Baztán, Madrid, Spain. *In*: GALÁN, E., ZEZZA, F. (eds) *Protection and Conservation of the Cultural Heritage in the Mediterranean Cities*. Balkema, Lisse, 391–396.

BOTTEGHI, C., MATTEOLI, U., PAGANELLI, S. *et al.* 1992. Polyfluoalkymethacrylates as materials for the protection of stones. *Scientific & Technological Cultural Heritage*, **1**, 111–122.

CIE. 1986. *Colourimetry* (second edition). Publication CIE nordm, 15.2, Central Bureau of the CIE, Vienna.

DÍAZ ALTER, M. E. 1991. La rehabilitación del conjunto monumental de Nuevo Baztán. *In*: *El innovador Juan de Goyeneche*. El Señorío de la Olmeda y el conjunto arquitectónico de Nuevo Baztán, Comunidad de Madrid, 1–25.

ESCUELA DE ARQUITECTOS TÉCNICOS. 1987. El proyecto de Nuevo Baztán, en marcha: la toma de datos, toda una historia. *Bia*, **104**, 45–57.

FERREIRA, A. P. & DELGADO RODRIGUES, J. 2000. Assessment of durability of water repellents by means of exposure tests. *In*: FASSINA, V. (ed.) *Ninth International Congress on Deterioration and Conservation of Stone*, Venice, Italy, 19–24 June 2000. Elsevier, Amsterdam, 273–283.

FORT GONZÁLEZ, R., MINGARRO MARTÍN, F., LÓPEZ DE AZCONA, M. C. & RODRÍGUEZ BLANCO, J. 2000*a*. Chromatic parameters as performance indicators for stone cleaning techniques. *Color Research and Application*, **25**(6), 442–446.

FORT GONZÁLEZ, R., LÓPEZ DE AZCONA, M. C., MINGARRO MARTÍN, F., ALVAREZ DE BUERGO, M. & RODRÍGUEZ BLANCO, J. 2000*b*. A comparative study of the efficiency of siloxanes, methacrylates and microwaxes-based treatments applied to the stone materials of the Royal Palace of Madrid, Spain. *In*: FASSINA, V. (ed.) *Proceedings of the Ninth International Congress on Deterioration and Conservation of Stone*, Venice, Italy, 19–24 June 2000. Elsevier, Amsterdam, **2**, 235–243.

FORT GONZÁLEZ, R., LÓPEZ DE AZCONA, M. C. & MINGARRO MARTÍN, F. 2002. Assessment of protective treatments based on their chromatic evolution: limestone and granite in the Royal Palace of Madrid, Spain. *In*: GALÁN, E. & ZEZZA, F. (eds) *Protection and Conservation of the Cultural Heritage of the Mediterranean Cities*. Balkema, Lisse, 347–442.

INSTITUTO TECNOLÓGICO Y GEOMINERO DE ESPAÑA (ITGE). 1988. *Atlas Geocientífico del Medio Natural de la Comunidad de Madrid*.

JAROSEVICH, E. J., NELEN, J. A. & NORBERG, J. A. 1980. Reference samples for electron microprobe analysis. *Geostandards Newsletters*, **4**, 43–47.

KOUZELI, K., BELOYANNIS, N., TOLIAS, C. & DOGANI, Y. 1988. Ancient and Byzantine conservational treatments on the Parthenon. *In*: *Deterioration and Conservation of Stone*. Institute of

Conservation and Restoration of Cultural Property and Nicholas Copernicus University, Torun, Polonia, 687–694.

KRAKOW CHARTER 2000. Principles for Conservation and Restoration of Built Heritage. *In: The International Conference on Conservation*. World Wide Web address: http://a1.arch.pk.edu.pl/c2000/en/charter.html

LAZZARINI, L. & SALVADORI, O. 1989. A reassessment of the formation of the patina called scialbatura. *Studies in Conservation*, **34**, 20–26.

ORDAZ, J. & ESBERT, R. M. 1988. Glosario de términos relacionados con el deterioro de las piedras de construcción. *Materiales de Construcción*, **38**(209), 39–45.

PRICE, C. A. 1996. *Stone Conservation. An Overview of Current Research*. Research in Conservation reference series, The Getty Conservation Institute.

RUSSEL, S. A. 1927. *Stone Preservation Committee Report* (Appendix I). HM Stationery Office, London.

Thermal behaviour of weathered and consolidated marbles

J. RUEDRICH, T. WEISS & S. SIEGESMUND

Geowissenschaftliches Zentrum der Universität Göttingen, Goldschmidtstrasse 3, 37077 Göttingen, Germany (e-mail: jruedri@gwdg.de)

Abstract: To optimize stone consolidation it is necessary to understand the mechanisms of weathering in marbles, and its control by the mineralogical composition and the rock fabric. A knowledge of how the stone consolidants affect the weathering mechanisms and if they are compatible with the stone is also an important consideration. The weathering of marble can begin with thermal stress whereby cracks are generated. To verify whether consolidation influences the thermal behaviour of marbles, we compared the behaviour of weathered and consolidated marbles. For the investigations four marbles were selected with various fabrics (e.g. texture, grain size, grain boundary geometry, etc.) and different weathering conditions. Three consolidation approaches were adopted: a solved polymethyl-methacrylate ($PMMA_{sol}$) dissolved in xylenes, a polysilicic acid ester (PSAE) and a total impregnation with a monomer methyl-methacrylate ($PMMA_{poly}$). Measurements of the porosity and effective pore size distribution evidenced a strong modification of the pore space by consolidation. Both PMMA approaches show a re-establishment of cohesion which can be determined by ultrasonic velocity measurements. By reaching the respective glass transition temperatures of $PMMA_{sol}$ and $PMMA_{poly}$, a strong modification of thermal behaviour occurs. The PSAE consolidated marbles show only minor changes of dilatation, but due to its low bonding effect no significant cohesion between the crystals occurs.

For over a century stone consolidants have been extensively used for conservation purposes to save deteriorated natural building stones. Although a huge quantity of knowledge exists about consolidation, the selection of an appropriate impregnation material is still largely based on empirical considerations. If a consolidant appears to give acceptable results with one type of stone, it is often applied to other stone types, without properly determining if the consolidant is compatible with them. Some of the factors affecting the performance of consolidants are known, such as penetration depth and moisture transfer through consolidated stone. However, only a few considerations have been given to other important factors, e.g. compatibility of their thermal properties with the rock mineralogy and the rock fabric (cf. Clifton 1980).

Thermal dilatation processes are responsible for the initial degradation of marbles. Kessler (1919) found that repeated heating of marbles may lead to permanent dilatations due to microfracturing and that thermally treated marbles show a remarkable non-reversible change in length especially during the first heating cycle (Sage 1988; Tschegg *et al.* 1999; Siegesmund *et al.* 2000). Even small temperature changes of 20°C to 50°C may result in damage (Battaglia *et al.* 1993). Marble has a very simple mineralogical composition. It consists of calcite and/or dolomite with other accessory phases (e.g. quartz, mica etc.). Calcite and dolomite exhibit a pronounced anisotropy of the thermal expansion coefficient at different crystallographic directions (Kleber 1959) leading to stresses within the sample during heating. When these stresses exceed the threshold of cohesion a thermally induced deterioration is observed (cf. Sage 1988). The rock fabric, which includes grain size, grain aspect ratios, grain shape preferred orientation, lattice preferred orientation (texture) and the microcrack populations, significantly controls the material's behaviour during thermal stress (e.g. Siegesmund *et al.* 1997).

At present little is known concerning the manner or degree of change of thermoelastic properties upon impregnation. Siegesmund *et al.* (1999) observed an increase of directional dependence of the thermal expansion coefficient for samples of Wunsiedel marble impregnated with PMMA. However, this specimen was relatively unweathered which means that the rock's structure was more or less intact (i.e. good cohesion between the grains and low porosity).

In contrast, this paper investigates the influence of impregnation materials on thermal behaviour of weathered marbles with a special regard to the interaction between rock fabric and stone consolidant. Four marbles with different fabrics were selected: Carrara, Lasa, Sterzing (Italy) and Prieborn (Poland). Detailed

From: SIEGESMUND, S., WEISS, T. & VOLLBRECHT, A. 2002. *Natural Stone, Weathering Phenomena, Conservation Strategies and Case Studies*. Geological Society, London, Special Publications, **205**, 255–271.
0305-8719/02/$15.00 © The Geological Society of London 2002.

fabric analyses were performed on each sample. These marbles had been outside for different time spans, and therefore represent very different weathering conditions. The samples from Lasa, Sterzing and Prieborn show an intermediate decay, whereas the Carrara specimen is strongly deteriorated.

Marble samples were impregnated with the following consolidants: polymethyl-methacrylate ($PMMA_{sol}$) dissolved in xylenes, a polysilicic acid ester (PSAE) and methyl-methacrylate ($PMMA_{poly}$) polymerized within the marble. Thermal expansion measurements were carried out on both weathered and consolidated samples and the degradation by heat treatment was determined by ultrasonic velocity measurements. Moreover, porosity and pore size distribution analyses were used to characterize the intruded volume of consolidant and the occupied pore radii classes.

Analytical methods

A reference coordinate system for the investigations, with respect to the macroscopically visible elements of foliation and lineation (Fig. 1a) was chosen. The XY-plane marks a metamorphic foliation while the X-direction is parallel to the lineation. An arbitrary coordinate system was defined, if the specimens did not show any macroscopically visible fabric elements.

Petrographic analyses (in polarized light) on standard thin sections were performed for a qualitative description of different grain parameters (e.g. mineralogical composition, grain boundary geometry, microcrack systems). Quantitative values for different fabric parameters (grain size, grain boundary orientation etc.) were obtained from digital image analyses (Duyster 1991).

Scanning electron microscopy (SEM) on fractured surfaces (fractography) was applied for the identification and characterization of microcracks in stone and to determine the relationship of the deposit of the consolidant to the stone substrate.

The lattice preferred orientation (here referred to as texture) of the marbles was determined by means of neutron diffraction (cf. Leiss & Ullemeyer 1999). Due to the high penetration depth of neutrons, large sample volumes may be investigated and a better approximation of the bulk rock texture is achieved.

For a quantitative determination of porosity and pore size distribution mercury porosimetry was used (cf. Brakel *et al.* 1981).

Ultrasonic velocity measurements were used for the detection of marble degradation by thermal treatment on cubic rock samples (65 × 65 × 65 mm). Transient times of ultrasonic pulses were determined (piezoceramic transducers, resonant frequency 1 MHz) in three orthogonal directions using the pulse transmission technique (Birch 1960, 1961). The measurements were performed with dry, completely water-saturated and experimentally impregnated samples.

The thermal expansion behaviour was measured on cuboids (10 × 10 × 50 mm). The directional dependence of the thermal expansion was determined as a function of temperature using a triple dilatometer (cf. Tschegg *et al.* 1999; Siegesmund *et al.* 2000). The final displacement resolution was better than 1 μm. For a detailed description of the experimental setup refer to Widhalm *et al.* (1996). The thermal expansion coefficient α expresses the expansion of a material as a function of temperature. Calcite shows an extremely anisotropic α (Kleber 1959): $\alpha_{11} = 26 \times 10^{-6}\,K^{-1}$ parallel and $\alpha_{22} = \alpha_{33} = -6 \times 10^{-6}\,K^{-1}$ perpendicular to the

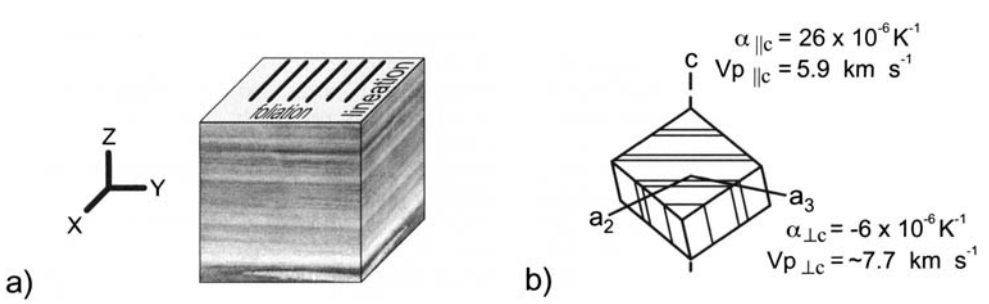

Fig. 1. (**a**) Reference coordinates with respect to foliation and lineation. (**b**) The calcite cleavage rhombohedron together with the values for thermal dilatation (Kleber 1959) and ultrasonic velocities (Dreyer 1974) in the directions of the c- and a-axes of the single crystal.

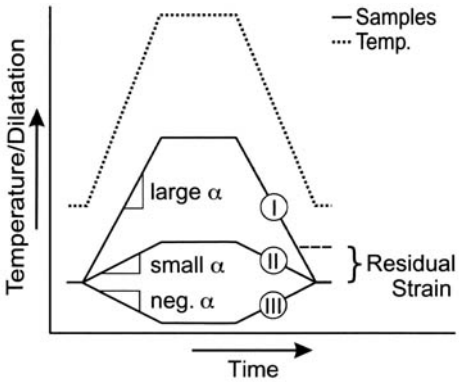

Fig. 2. Curves for different thermal dilatation coefficients α observed in expansion measurements (I = large α, II = small α and III = negative α). Residual strain remains if a sample does not return to its initial length.

crystallographic c-axis (Fig. 1b), i.e. calcite contracts normal to the c-axis and expands parallel to the c-axis during heating. The coefficient of thermal expansion for the investigated marbles was calculated from the experimentally determined temperature and dilatation data ($\alpha = \Delta l(l \times \Delta T)$). In Figure 2, heating/cooling ramps are schematically shown for a strong (small α), a weak (large α) and a negative thermal dilatation coefficient. All investigations were performed on three mutually perpendicular specimens to gain information on the directional dependence of the data.

Consolidation

The $PMMA_{sol}$ is a specially modified polymethyl-methacrylate with a minor portion of polymethyl-butyl copolymer and some acid groups added for better adhesion (cf. Koblischek 1990). The acrylic resin has a molecular size smaller than 24 nm, the density is about 0.95 g cm^{-3}, and the glass transition temperature (T_g) is approximately 60°C. For the purpose of this investigation it is dissolved in xylenes to a concentration of 40%. The polymer becomes effective after evaporation of the solvent by forming films of varying strength.

The PSAE is an ethylsilicate comprising three to five silicic acid ester molecules. The oligomers have a molecular size between 1.2 and 6 nm with the predominant portion about 3 nm (Koblischek 1990). The PSAE is dissolved in ethanol with an active ingredient content of 40%.

For the $PMMA_{poly}$ approach the rock samples are fully impregnated with monomer methyl-methacrylate and polymerized in situ. The $PMMA_{poly}$ generated by this means is a Plexiglas with a T_g at approximately 85°C and a thermal dilatation coefficient (α) of 70×10^{-6} K^{-1}. The impregnation solution also contains an acrylic silane and acrylic acid (Lorenz & Ibach 1999). The volume reduction during the polymerization is approximately 20 vol%.

The first two methods are usually used for on-site consolidation. Both consolidants are normally applied on the rock surface and are incorporated by capillary uptake. To facilitate impregnation, the dissolved consolidants are repeatedly applied with a smaller agent content. In order to gain a complete impregnation of the materials under investigation, the stone consolidants are applied under a vacuum of 0.07 bar followed by a confining pressure up to 6 bar. To provide an interconnecting porosity, the marble samples were thermally preconditioned by heating them up to 200°C. This procedure was not necessary for the sample from Carrara since it was already extremely deteriorated.

The third consolidation method is normally not performed on site. Before impregnation, the rock samples were dried by heating up to approximately 70°C (cf. Lorenz & Ibach 1999). The samples were then placed in a vessel which was introduced in a vacuum/pressure kettle. Under vacuum the vessel was fully filled with monomer methyl-methacrylate. The radical polymerization was initiated at approximately 80°C after some vacuum/pressure stages (0.75/25 bar).

Grain fabrics

Carrara marble

The Carrara marble was taken from the exterior of a strongly weathered window sill from the Marble Palace in Potsdam (Germany). The specimen is of a bright white colour and contains irregular grey veins. The veins are folded and show a streak-like distortion and usually range in width from 0.5 to 2 cm. A preferred orientation of the veins is not clearly detectable. The sample shows a strong decay in the form of granular disintegration.

Microstructurally, the Carrara marble shows a nearly equigranular polygonal grain fabric (Fig. 3a) with straight grain boundaries and 120° triple-point junctions (Fig. 4a). The grain size in the white areas is about 200 μm and the grain size distribution shows a narrow maximum

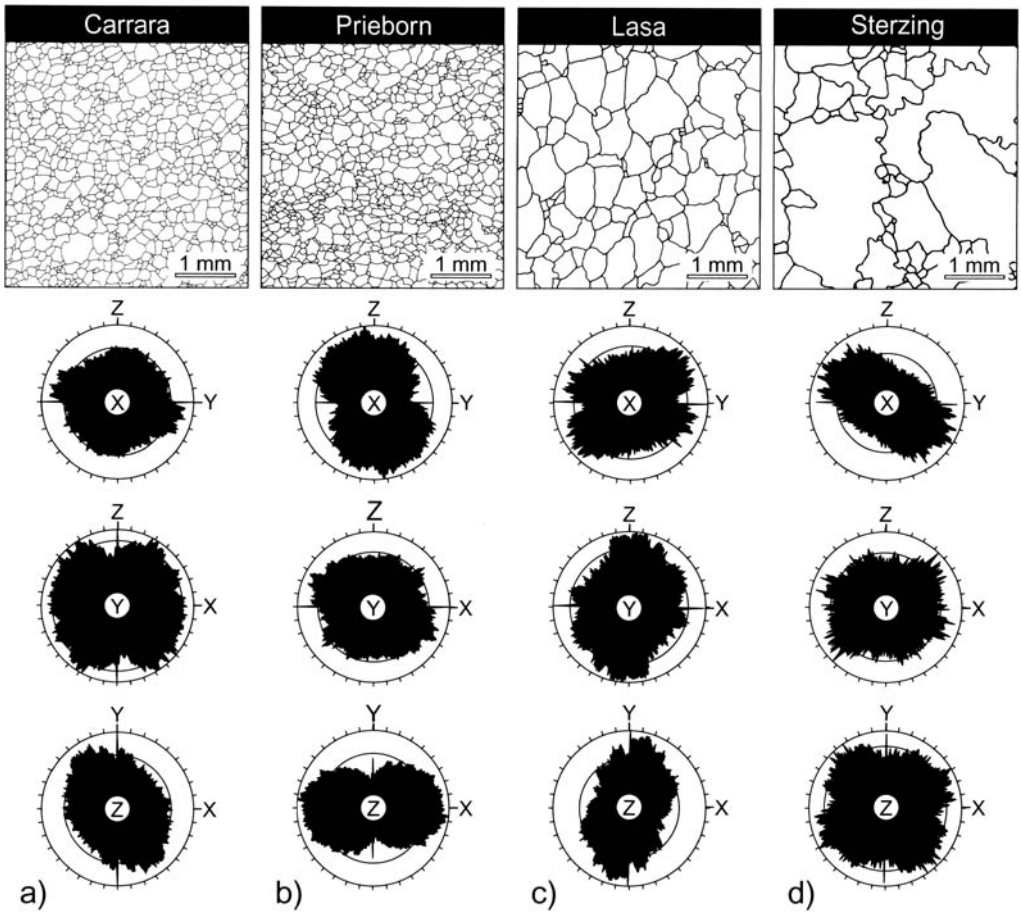

Fig. 3. Results from quantitative image analyses. Top, thin section drawings illustrating the grain fabric and the relative grain size differences (XY-plane). Below, the statistical orientations of grain boundaries are shown in the YZ-, XY-, XZ-plane.

(Fig. 5a). In the XY-plane of the investigated sample a weak preferred grain boundary orientation (subparallel Y-direction) can be observed (Fig. 3a).

The grey veins are fine grained (average grain size = 50 μm) and the grains have a very strong undulose extinction. Grain boundaries are interlobate and a high amount of fluid inclusions or graphite occurs which probably causes the grey colour of the veins.

Prieborn marble

The weathered sample of the Prieborn marble (Poland) was also taken from the Marble Palace and represents an exposed outside staircase. The marble is grey in colour and exhibits a foliation of alternating dark and light grey layers. The start of degradation is observable along the grain boundaries and, in particular, within the superficial layers. However, the state of deterioration is less pronounced than that of the Carrara marble.

The grain fabric is very similar to that of the Carrara marble (Fig. 3b). However, the grain boundaries are slightly more curved or very finely serrated (Fig. 4b). The average grain size is about 200 μm (Fig. 5b) intercalated with fine-grained layers with grain size less than 100 μm. A grain shape preferred orientation of weakly elongated grains can be observed in the YZ-section (||Z-direction) and also in the XY-plane (||X-direction) of the specimen (Fig. 3b).

Twinning rarely occurs, even though a preferred orientation of the lamellae subparallel to the foliation is detectable in the

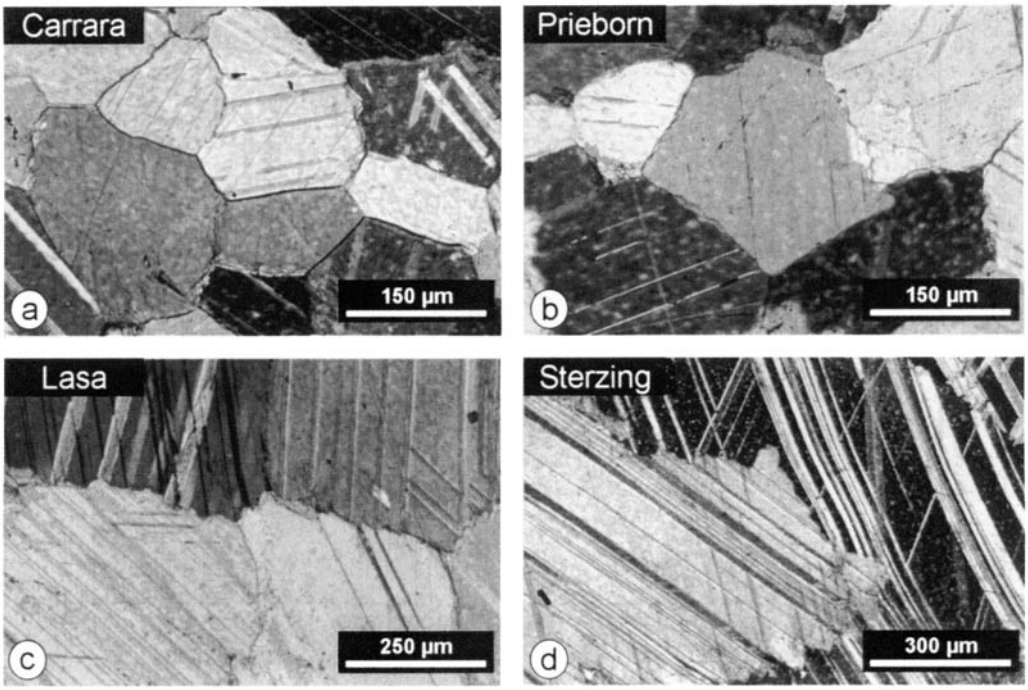

Fig. 4. Photomicrographs (crossed polarizers) showing the grain boundary geometry. The images correspond to the XZ-section.

XZ-section. The grain boundaries are open and decorated with dark material. Together with fluid inclusions, this causes the grey colour of the marble. Small quartz grains and pyrite occur as accessory mineral phases.

Lasa marble

The Lasa sample comes from a replaced grave stone exposed for more than 40 years. Macroscopically the marble shows a bright white colour. Only a few light grey layers about 4 cm wide could be observed marking the foliation. The main weathering feature of this sample is a weak chemical exsolution at the rock surface along grain boundaries and cleavage planes of the calcite crystals.

The grain fabric of the marble is more or less inequigranular (Fig. 3c) and the grain boundary geometry is slightly irregular (Fig. 4c). In contrast to the Carrara and Prieborn marble types, the Lasa sample exhibits a larger average grain size of about 700 µm (Fig. 5c). In all the investigated directions a slight preferred orientation of grain boundaries can be observed which is most evident in the XY-plane (Fig. 3c).

Sterzing marble

This sample was originally used as a grave stone. Macroscopically the marble is characterized by a greyish white colour and a coarser grain size. Superficially, a pronounced chemical exsolution along calcite cleavage planes and grain boundaries is observable.

This marble shows a seriate grain fabric (Fig. 3d). The grains have irregular shapes with strongly curved, interlocking grain boundaries (Fig. 4d). Twinning is more frequent and the grains show undulose extinction, deformation bands, subgrain formation and bent twin lamellae. This fabric is interpreted as the result of a late-stage deformation with the interlocking grain boundaries indicating grain boundary migration (Fig. 3d). Subgrains as well as recrystallized grains along the grain boundaries also reveal a subgrain rotation recrystallization (Passchier & Trouw 1996).

The average grain size is about 1.5 mm (Fig. 5d). The coexistence of large and small grains can only be visualized when the diameters of the grains are shown as a fraction of the total number of grains (Fig. 5d). With respect to the total number of grains, smaller grains show a higher frequency compared with larger ones.

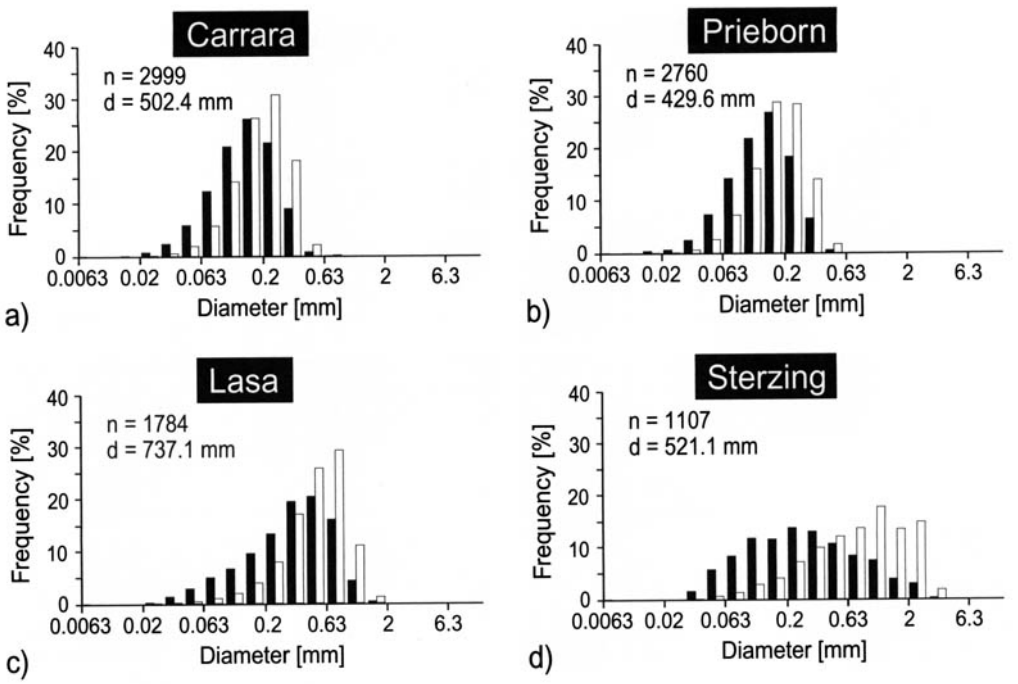

Fig. 5. Grain size distributions determined by quantitative image analysis. The values of the different sections (XY-, YZ-, XZ-plane) have been averaged. The relative frequency of a specific diameter class has been calculated with respect to the total diameter (grey bars; d = total diameter) and to the total number of grains (black bars; n = total number).

A pronounced preferred orientation of grain boundaries is only observable in the YZ-plane and is oblique to the Y-direction (Fig. 3d).

Trails of fluid inclusions are common. Moreover, the sample exhibits biotite flakes on the grain boundaries and within the calcite grains. Quartz is found as an accessory mineral (about 1%), which occurs as small round inclusions in calcite crystals.

Texture

The calcite single crystal has extreme anisotropic properties. Therefore, the texture may have an important influence on the strong directional dependence of physical/mechanical parameters (Widhalm *et al.* 1996; Siegesmund *et al.* 1999).

The marbles in this study show significant differences in their texture. Two general texture types can be defined. The first is observed for the Carrara and the Prieborn marbles and can be described as a c-axis fibre type (Fig. 6a,b). The c-axes form a slightly elongated maximum perpendicular to the foliation, whereas the a-axes show a girdle distribution subparallel to the foliation with a maximum parallel to the X-direction. Although both marbles exhibit similar grain fabrics and also similar texture patterns, the texture strength is different. The Prieborn marble shows a strong c-axis maximum of 3.6 mrd, while the Carrara marble exhibits a maximum of only 2.0 mrd (mrd = multiples of random distribution). The Sterzing marble also shows the characteristics of a c-axis fibre type (Fig. 6d). The Carrara and the Prieborn marbles show a weak girdle distribution of the a-axes, which is more pronounced for the Sterzing marble.

The second texture type can be found in the Lasa marble. The c-axes of this marble show a girdle distribution (Fig. 6c) and the a-axes form a point maximum preferentially orientated parallel to the X-direction. Due to this particular texture type, a different thermal expansion behaviour is expected when compared to the other marbles.

Pore space characteristics of weathered and impregnated samples

Grain boundary cracks and intragranular cracks parallel to cleavage planes and twin lamellae are

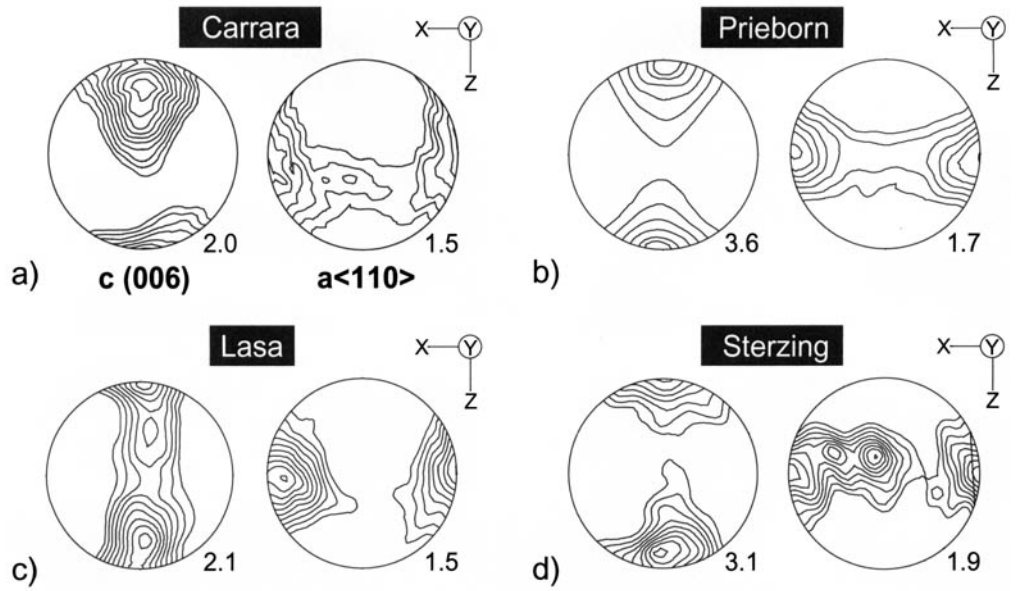

Fig. 6. Texture patterns of the different marbles (lower hemisphere, stereographic projection; lowest contour is equal to 1.0 multiples of random distribution (mrd); the relative maxima are given).

observable in all investigated marble samples. Thus, the pore spaces of the weathered marbles are characterized by a primary crack porosity. The intergranular cracks are found predominantly in the Carrara and Prieborn marbles, and therefore, in fine grained marbles with relatively straight grain boundaries. Intragranular cracks frequently occur in the coarser grained Sterzing marble. The curved, interlocking grain boundary geometry of this marble type leads to an activation of internal planes in the calcite crystals.

Stone consolidants within the pore space

The disposition of stone consolidants within the pore space of the marbles provides important information about the adhesion between calcite and the impregnation material. Evaluations can be made about the modification of the pore space including secondary porosity and its interconnected network.

The $PMMA_{sol}$ consolidated marbles are characterized by locally isolated films in the pore space, detectable by SEM analyses. These isolated films vary in shape and size depending on the marble. In the strongly weathered Carrara marble with its large pore radii these films occur as relatively expanded coatings at grain boundaries (Fig. 7a). These coatings are sporadic and reproduce the relief of the underlying grain boundary topography (Fig. 7b). The $PMMA_{sol}$ films often exhibit holes with irregular shape. The rims of these holes appear rounded and cannot be explained by fracturing, e.g. during sample preparation. They are interpreted as shrinkage phenomena generated during evaporation of the solvent. The size of the films depends on the pore size. The Carrara and Prieborn marbles exhibit large films, while the Lasa and the Sterzing marbles, with relatively small pore sizes, show only isolated small accumulations.

The PSAE occurs as irregular, flat shards, separated by cracks (Fig. 7c). This structure can be attributed to shrinkage after gelation. The individual fragments show a mostly disc-like polygonal shape, and their size varies between approximately 5 and 30 μm. The width of the shrinkage cracks between the shards ranges from 0.5 to 3 μm (Fig. 7d). The fact that all of the PSAE gel remains in place on fractured surfaces, and that there is no negative pattern of cleavage planes and grain boundaries in the gel, indicates little or no cohesion between the gel and the calcite grains.

The $PMMA_{poly}$ appears as relatively dark coatings in the SEM images using the backscattered mode. In contrast to the PSAE consolidant, the negative pattern of cleavage planes on the detached $PMMA_{poly}$ plane is evidence that the cracks were completely filled (Fig. 7e) and

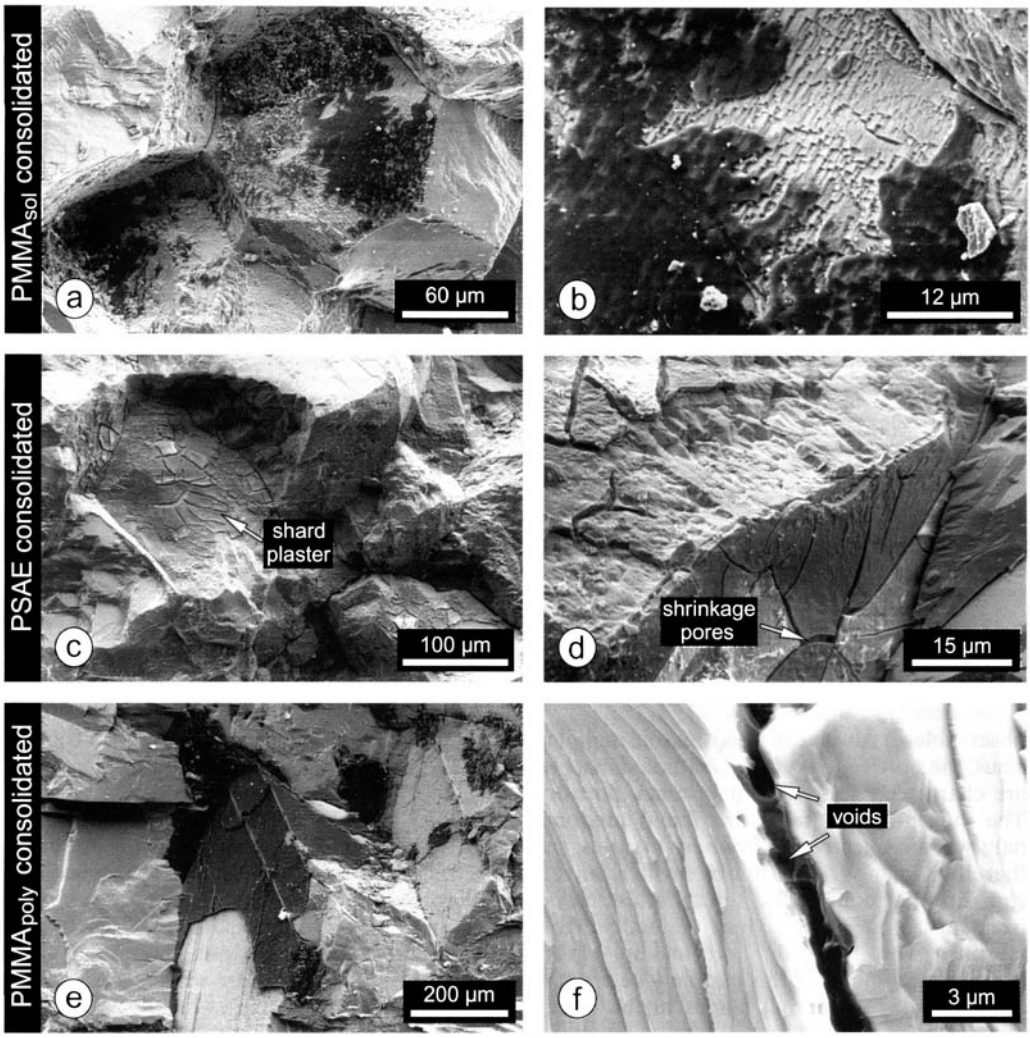

Fig. 7. Backscattered images (SEM) of impregnated specimens (fractography). (**a–d**) Consolidated samples of Carrara marble which show a preferred cracking along grain boundaries. (**e,f**) Sterzing marble with a preferred degradation along intragranular planes.

that a pronounced cohesion was induced by this consolidation process. In sections perpendicular to the filled cracks, small holes with oval shapes about 1 µm in size are observable. They occur in the central parts of the $PMMA_{poly}$ (Fig. 7f). They are interpreted as voids due to volume reduction of the $PMMA_{poly}$ during polymerization (see also Lorenz & Ibach 1999).

Porosity and pore size distribution

The pore size distribution has been determined for all weathered and impregnated marble samples. The comparison between consolidated and unconsolidated samples gives important clues about sizes of pores preferentially invaded by each consolidant.

As an example of the data obtained for $PMMA_{sol}$ impregnation, the pore size distribution measurements of the Lasa marble are given in Figure 8a,b. For this marble type a porosity reduction of about 40% is observable after $PMMA_{sol}$ impregnation which corresponds to the percentage of active ingredient in the treatment solution. Thus the bulk of the pore volume is filled by this solution.

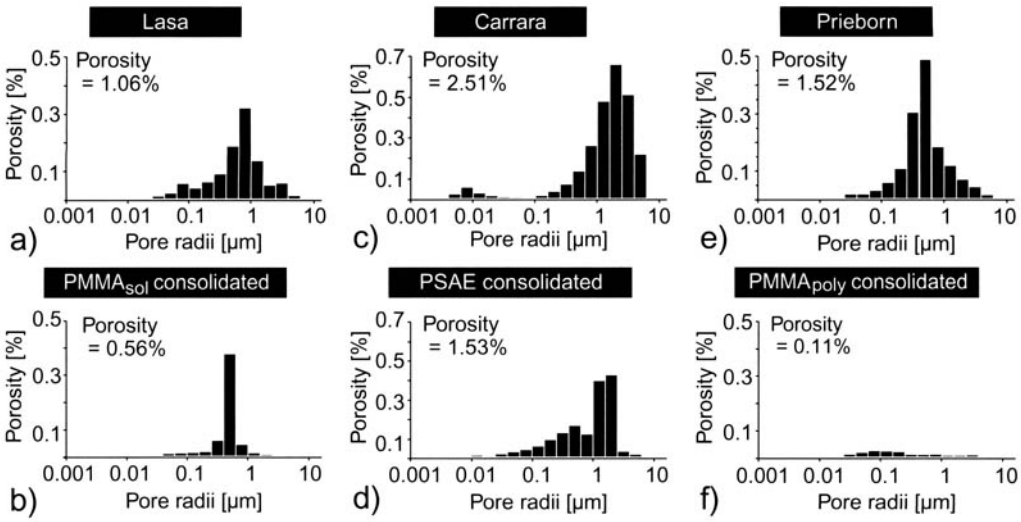

Fig. 8. Modification of the pore size distribution and porosity by consolidation. Data are given for the unconsolidated and consolidated samples of (**a**,**b**) Lasa, (**c**,**d**) Carrara and (**e**,**f**) Prieborn marbles.

The distribution of pore sizes was also clearly modified by impregnation. Whereas the weathered sample shows a broad distribution of pore radii classes around a single maximum from 0.630 μm to 1.000 μm, the majority of the classes of the impregnated sample are strongly reduced. The pore size frequency maximum is shifted by one pore size class downward. This downward shifting of the pore size maximum after impregnation is evident for all samples impregnated with $PMMA_{sol}$.

For the modification of the pore space by PSAE impregnation the Carrara marble will serve as an example (Fig. 8c,d). The weathered sample shows a porosity of 2.51% while the porosity of impregnated specimens is 1.53%. This means a reduction of porosity due to consolidation of approximately 40%. The pore size distribution for the weathered Carrara sample shows a significant maximum in the radius range from 0.630 μm to 6.300 μm and a second, submaximum between 0.004 μm and 0.016 μm (Fig. 8c). The impregnated sample does not exhibit the lower peak (Fig. 8d). This indicates that (i) this pore class was filled by the PSAE (molecular size approximately 3 nm) or (ii) the pores are no longer accessible to mercury. Furthermore, the pore sizes above 1 μm are strongly modified. Pore sizes above 2.512 μm almost completely vanished and a new maximum occurs between 1.000 μm and 2.512 μm. These pore sizes are evident in untreated samples, and therefore become more prominent because other pore sizes are filled. For all samples impregnated with PSAE a comparable behaviour can be observed.

The pore size distributions for the Prieborn marble without and with full impregnation with $PMMA_{poly}$ are shown in Figure 8e,f. The porosity is reduced from 1.52% in the weathered sample to 0.11% in the impregnated specimen. This reduction of approximately 93% is higher than the expected reduction of about 80% by volume reduction due to polymerization. Thus, the majority of the voids created by polymerization are not accessible to mercury.

The pore size distribution of the weathered sample shows a strong maximum in the range from 0.159 μm to 1.585 μm and the distribution for the impregnated sample shows that almost all pores are closed (Fig. 8f). Only a few pores with a size of about 0.100 μm are still present.

Thermal dilatation

The thermal dilatation measurements were performed using four heating cycles up to 42°C, 65°C and 90°C with a heating rate of about 1°C min^{-1}. The third cycle up to 90°C was repeated to verify if the samples show a modified behaviour. The maximum temperature (T_{max}) was held for 60 min permitting thermal equilibration of the specimens. After each cycle the samples were cooled to the initial temperature of about 25°C.

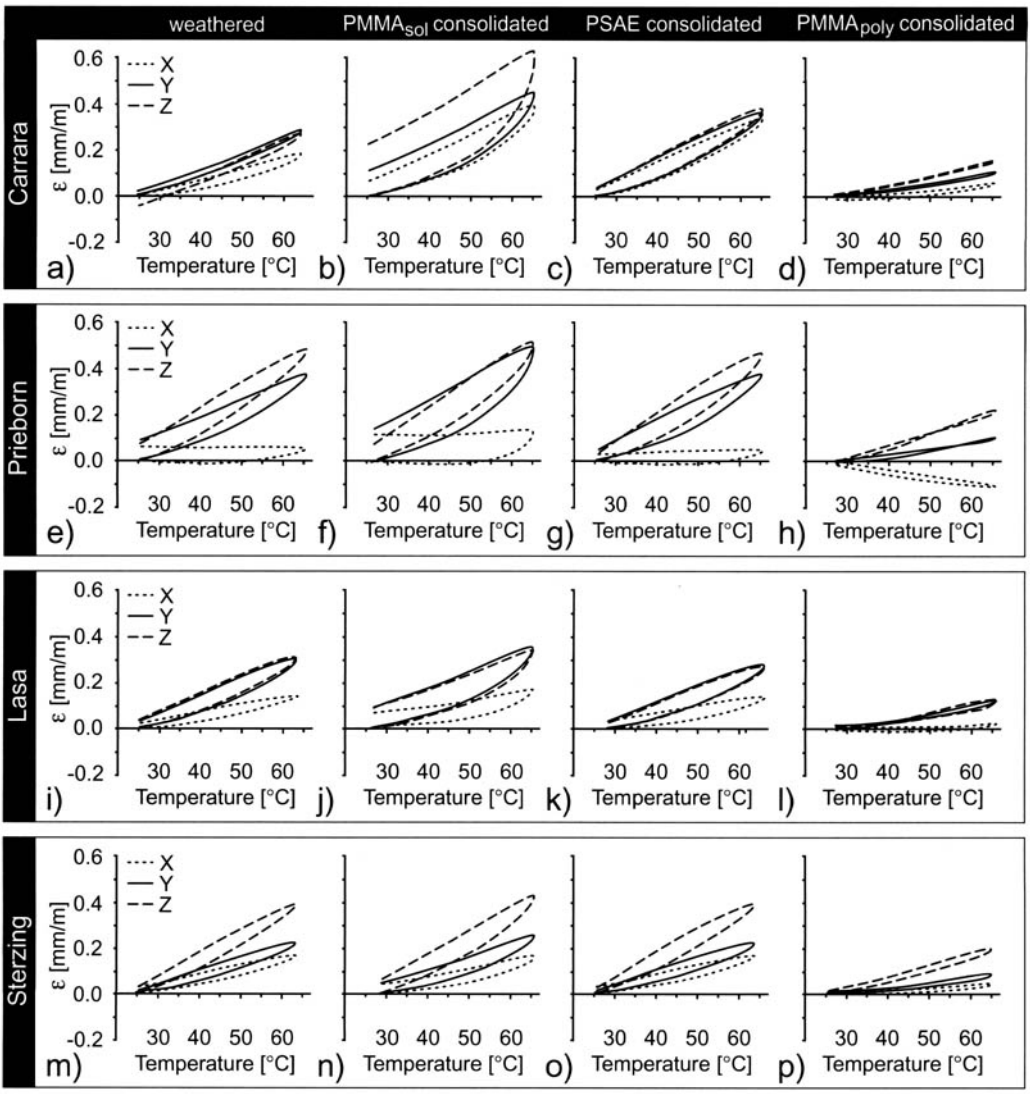

Fig. 9. Experimentally determined thermal dilatation as a function of heating up to 65°C for weathered and consolidated marbles. The dilatation curves are given for the X-, Y- and Z-direction.

The calcite single crystal coefficients of thermal dilatation can be treated as linear because the temperature interval at a maximum $\Delta T = 65°C$ used for the dilatation experiments is insignificant. Thus, the thermal dilatation ε (mm m^{-1}) observed in the experiments should be closely linked to the texture strength of the respective sample.

The different marbles show a more or less pronounced directional dependence of thermal dilatation. This is a well known phenomenon (Widhalm *et al.* 1996; Tschegg *et al.* 1999; Siegesmund *et al.* 2000) and can be attributed to the anisotropic expansion behaviour of the calcite single crystal (see Fig. 1b) in conjunction with a lattice preferred orientation (texture; see Fig. 6a–d). Furthermore, the intensity for directional dependence of consolidated and weathered samples is comparable for the respective marble types.

The anisotropy of thermal dilatation for the Prieborn and Lasa marbles will serve as an example in the discussion on the effect of texture (Fig. 9e,i). The thermal dilatation of the

Table 1. *Residual strains $\Delta\varepsilon$ (mm m^{-1}) for weathered and consolidated Carrara and Prieborn marbles as a result of heat treatment*

	Direction	Cycle 42°C	Cycle 65°C	Cycle 90°C	Cycle 90°C
Carrara marble					
Weathered	X	0.000	0.000	0.000	0.000
	Y	0.000	0.000	0.000	0.000
	Z	−0.071	−0.047	−0.055	−0.032
$PMMA_{sol}$	X	0.000	0.063	0.111	0.000
	Y	0.000	0.108	0.057	0.000
	Z	0.040	0.225	0.181	0.000
PSAE	X	0.021	0.027	0.049	0.000
	Y	0.000	0.039	0.056	0.000
	Z	0.000	0.039	0.059	0.000
$PMMA_{poly}$	X	0.000	0.000	0.150	0.043
	Y	0.000	0.000	0.159	0.034
	Z	0.000	0.000	0.102	0.000
Prieborn marble					
Weathered	X	0.000	0.054	0.099	0.000
	Y	0.027	0.086	0.134	0.000
	Z	0.042	0.066	0.094	0.000
$PMMA_{sol}$	X	0.000	0.116	0.085	0.000
	Y	0.032	0.141	0.095	0.000
	Z	0.000	0.074	0.030	0.000
PSAE	X	0.000	0.027	0.047	0.000
	Y	0.000	0.052	0.055	−0.026
	Z	0.035	0.045	0.042	0.000
$PMMA_{poly}$	X	0.000	0.000	0.141	0.031
	Y	0.000	0.000	0.185	0.026
	Z	0.000	0.000	0.128	0.000

Prieborn sample parallel to the Z-direction (parallel to the c-axis maximum, cf. Fig. 6b) is larger than the expansion parallel to the X-direction (parallel to the a-axis maximum, cf. Fig. 6b). The expansion parallel to the Y-direction represents an intermediate direction. This expansion behaviour is typical for c-axis fibre type marbles (Leiss & Weiss 2000). In contrast, the texture of the Lasa sample represents an a-axis fibre type (Fig. 6c). Thus, the thermal expansion (ε) shows nearly identical values for the Y- and Z-direction controlled by the girdle distribution of the c-axis (see Fig. 6c). The lowest ε is observed parallel to the a-axis maximum (X-direction).

The texture strength is also evidenced in the expansion behaviour of the samples. The Carrara marble with a relatively weak c-axis maximum of 2.0 mrd shows only a small anisotropy, whereas the Prieborn marble with a c-axis maximum of 3.6 mrd has a stronger directional dependence of thermal dilatation ε.

A permanent expansion (residual strain; cf. Battaglia *et al.* 1993; Siegesmund *et al.* 2000) is well documented by the thermal expansion of the X-direction of the Prieborn marble (Fig. 9e). This direction corresponds to the maximum of the a-axis concentration, i.e. the direction of the negative single crystal thermal dilatation coefficient. Due to the strong texture of this specimen, a contraction with increasing temperature can be predicted from the texture, and is demonstrated by the experimental results shown in Figure 9e for the temperature range up to 45°C. Above 45°C the thermal dilatation reaches positive values. After heat treatment the residual strain of the specimen is similar in extent to the observed maximum of dilatation (Fig. 9e).

In the following section the thermal dilatation behaviour is summarized with respect to the ramps. The curves for a maximum temperature of 65°C are shown in Figure 9a–p while residual strains are given in Table 1.

The thermal dilatation behaviour for unconsolidated samples during the first heating cycle up to 42°C shows a more or less linear expansion, whereas no residual strain remains. Only for the Z-direction of the Carrara marble does a contraction occur. This behaviour observed in the Carrara marble holds for all applied cycles (cf. Table 1), and is interpreted as

a fabric collapse due to its advanced decay pattern.

For cycles up to 65°C the Lasa and Sterzing marble (Fig. 9i,m) exhibit a slight increase of thermal dilatation above 40°C resulting in a weak residual strain. The same behaviour occurs for the Prieborn marble, whereas the permanent length change after cooling is more pronounced (Fig. 9e; cf. Table 1).

The heating cycle up to 90°C leads to a stronger non-linearity of the curves and a more or less pronounced residual strain. Again, the Prieborn marble shows the highest values, and therefore the strongest thermal degradation (cf. Table 1).

The largest residual strain for the Prieborn marble occurs parallel to the Y-direction, since many other investigated marble types show the main residual strain parallel to the c-axis maximum (Siegesmund *et al.* 2000). However, image analyses reveal that a preferred orientation of grain boundaries in the XZ-plane exists (see Fig. 3b) causing a preferred crack propagation in this direction. Since this marble shows a thermal degradation along grain boundaries, their preferred orientation could be the cause for the preferred crack propagation in the XZ-plane.

The second heating cycle up to 90°C was performed in order to prove whether the thermal degradation is linked only to the maximum temperature or to the differential temperatures. In the first case, the residual strain should be vanishingly small and in the second case, the residual strain should be as large as that observed for the first 90°C cycle. For all samples, the residual strain observed for the second 90°C cycle is vanishingly small (cf. Table 1). Thus, the main damage takes place between 40°C and 90°C.

Consolidated samples

The $PMMA_{sol}$ impregnated marble samples show a distinct modified thermal behaviour especially for cycles of higher temperatures. By heating the $PMMA_{sol}$ consolidated samples up to 42°C a relatively linear thermal expansion is observed and, correspondingly, no residual strain remains (Fig. 10a). Only the Z-direction of the Carrara marble and the Y-direction of the Prieborn marble show a slight residual strain after heat treatment (Table 1) indicating that the directions of strongest thermal degradation were preferentially activated after consolidation.

By heating the $PMMA_{sol}$ consolidated marbles up to 65°C (especially for the Prieborn and Carrara marbles) the slope of the curves, and thus the thermal expansion coefficients increase when the temperature transcends 50°C (Figs 9b,f and 10b). Both samples exhibit a large residual strain after heat treatment in all directions, which is significantly larger than the residual strain of the respective non-impregnated specimens. This effect can be attributed to a weakening of the resin when approaching its glass transition temperature (T_g = approximately 60°C). The amount of residual strain indicates that (i) new cracks are generated or (ii) the PMMA is stretched. For the Lasa and Sterzing samples a comparable expansion behaviour is observable, whereas a smaller residual strain occurs (Fig. 9h,j), resulting from the small initial degradation.

For the $PMMA_{sol}$ impregnated Carrara marble a large directional dependence of thermal dilatation and of the residual strain is observed (Fig. 9b). The effect of $PMMA_{sol}$ is different in several directions, which can be explained by the preferential orientation of the system of cracks.

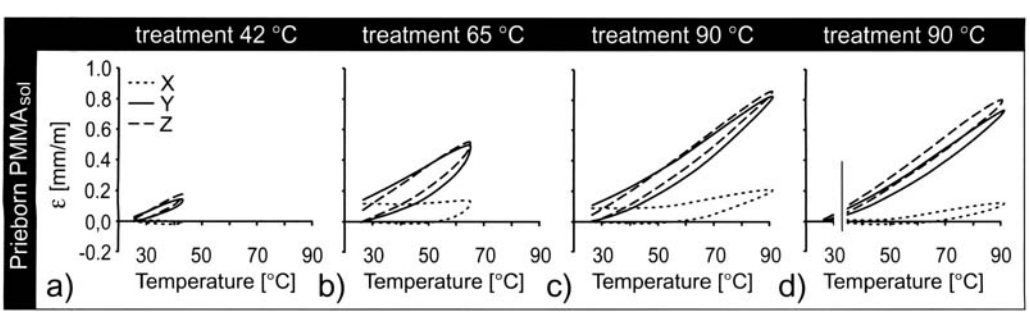

Fig. 10. Thermal dilatation curves of heating cycles up to (**a**) 42°C, (**b**) 65°C (**c**) 90°C and (**d**) 90°C for the Prieborn marble consolidated with $PMMA_{sol}$.

The dilatation behaviour of the samples by the first heating up to 90°C is characterized by a slight increase of the hysteresis loop above approximately 50°C (cf. Fig. 10c). A pronounced residual strain is found only for the Carrara and Prieborn marbles, but it is lower than the observed change in length for the heating cycle up to 65°C. The only exception is represented by the X-direction of the Carrara marble (Table 1) because a larger residual strain remains. For the second heating cycle up to 90°C no further residual strain occurs (cf. Table 1), while the hysteresis follows a more linear trend (see for example the Prieborn marble in Fig. 10d).

The PSAE consolidated samples show only minor changes compared with non-impregnated specimens (Fig. 9c,g,k,o). For the heating cycle up to 42°C the thermal dilatation is more or less linear. Also, no significant residual strain remains after treatment. A slightly increased residual strain is seen only for the X- and Z-direction of the Carrara and the Prieborn marbles, respectively (Table 1).

The dilatation scenario for the second cycle up to 65°C is only slightly modified, except for the Carrara marble (Fig. 9c). In contrast to the unconsolidated Carrara sample, no contraction is observed parallel to the Z-direction and the maximum expansion is slightly increased. The observations indicate that the PSAE in the pore space has stabilized the grain fabric.

For the first heating up to 90°C all PSAE-consolidated samples show a slight increase of dilatation and a weak residual strain (Table 1).

The small modifications induced by PSAE impregnation probably originated by a low thermal expansion coefficient in these materials. Furthermore, no structural changes of the PSAE can be observed such as determined for the PMMA resins (glass transition temperature).

For the $PMMA_{poly}$ consolidated marbles and heating cycles up to 42°C and up to 65°C a very similar behaviour occurs. This consolidation method generates the most conspicuous change of thermal expansion behaviour. All samples show a pronounced reduction of thermal dilatation and a change of the elastic behaviour after impregnation. This is shown by the strong modification of the hysteresis loops (Fig. 9d,h, l,p), i.e. the curves are very linear. For the Prieborn marble parallel to the X-direction a pronounced contraction can be observed (Fig. 9h). The contraction direction is coincident with the preferred orientation of the a-axis. This can be attributed to the adhesion generated by $PMMA_{poly}$ consolidation, which leads to a stronger transfer of the single crystal properties in the whole rock. Furthermore, for all samples of $PMMA_{poly}$ consolidation no residual strain remains for the heating cycles up to 42°C and up to 65°C (Table 1).

Only when the $PMMA_{poly}$ consolidated samples were heated up to 90°C did the thermal dilatation behaviour change significantly. This is characterized by a surge of thermal dilatation around 80°C (Fig. 11). After cooling to the initial temperature a pronounced residual strain also remains. The experimentally determined

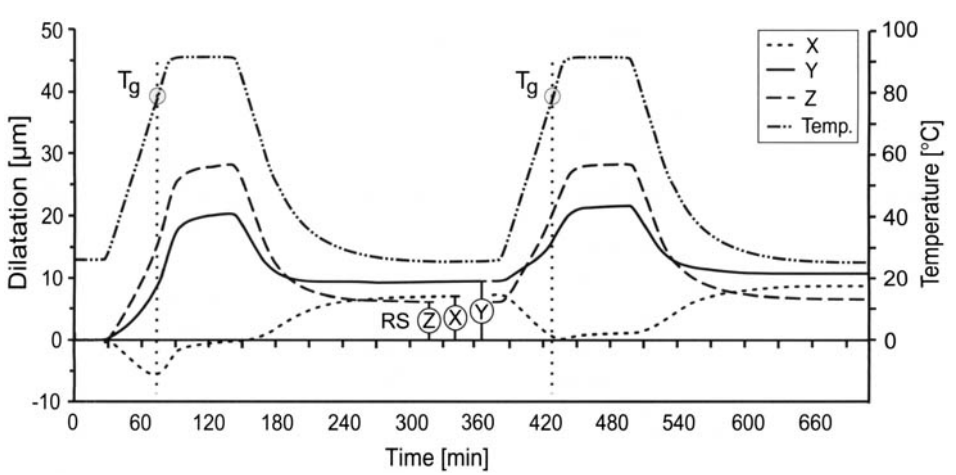

Fig. 11. Dilatation curves of two heating cycles for treatment up to 90°C of a $PMMA_{poly}$ consolidated Prieborn marble. RS = residual strain, as given for all directions after the first heating cycle.

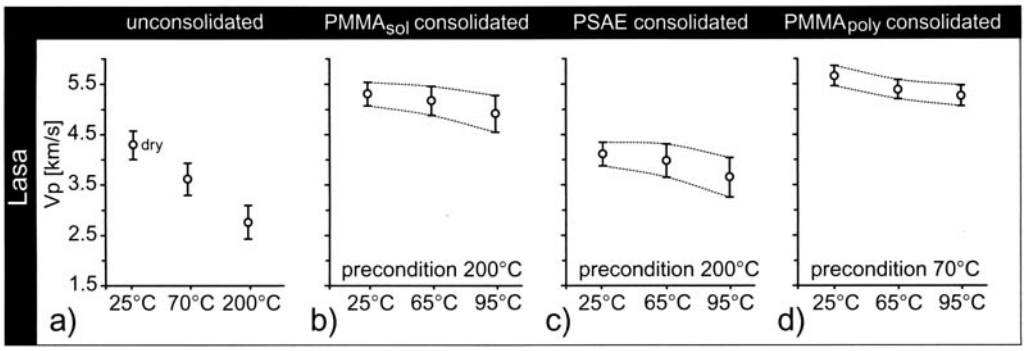

Fig. 12. Experimentally determined ultrasonic velocities (V_p) for the Lasa marble. Values are given for different sample conditions: (**a**) dry and pre-conditioned by heating the samples up to 70°C and 200°C; (**b–d**) consolidated and thermally treated up to 65°C and 90°C.

temperature for a significant change of the material coincides with the glass transition temperature of the $PMMA_{poly}$ used.

For the second heating cycle up to 90°C the transition point is only weakly developed (Fig. 11). Nevertheless a measurable residual change in length can be determined for most samples (cf. Table 1).

Ultrasonic wave velocities

A method for determining the state of deterioration and of the improvement by consolidation is by measuring the velocities of ultrasonic waves through the samples, i.e. of compressional waves (V_p). This method is efficient, quick and non-destructive (Snethlage *et al.* 1999). The basic principle is that the magnitude of the rock degradation is monitored by decreasing V_p (cf. Weiss *et al.* 2000). Inversely, the velocities should increase by cohesion re-establishment (cf. Snethlage *et al.* 1999).

The velocity data observed for weathered and consolidated Lasa marble are shown in Figure 12a–d as an example, but the same relationships apply to the other marbles. For dry samples the velocities range from 4.0 to 4.6 km s^{-1}. Before consolidation, the specimens were heated up to 70°C ($PMMA_{poly}$) or 200°C ($PMMA_{sol}$ and PSAE). The corresponding velocity reduction as a consequence of thermal degradation is about 0.7 km s^{-1} by the 70°C heating and 1.5 km s^{-1} by the 200°C heating (see Fig. 12a). These velocities have to be treated as the initial condition of the specimens before consolidation.

The velocity data in the initial stage after consolidation (25°C) are given in Figure 12b,c,d for the different consolidation approaches. All impregnated samples show an increase of ultrasonic velocities, although significant differences occur for the respective consolidation materials.

PSAE consolidation results in a relatively weak increase of ultrasonic velocities of about 1.4 km s^{-1} (Fig. 12c). In contrast, $PMMA_{sol}$ and $PMMA_{poly}$ exhibit a more pronounced change of velocities (Fig. 12b,d). The velocities increased at approximately 2.5 and 2.1 km s^{-1} respectively. The other marbles show a similar pattern of increases of ultrasonic velocities. After heating cycles up to 65°C and 95°C which are comparable with the cycles applied for the dilatation measurements, the ultrasonic velocities for all samples show a slight reduction (Fig. 12c,d). However, the slight reduction of ultrasonic velocities is in the range of resolution of this method.

Discussion

The porosimetry analyses verified that significant differences exist between the investigated marbles in their initial (weathered) stage. For example, the Carrara marble shows a strong deterioration with a sugar-like crumbling of the rock surface. In contrast, the Prieborn, Lasa and Sterzing marbles are less deteriorated which is evident by an initial porosity of less than 1%. However, their weathering histories are different which makes comparison difficult. Observations from the Marmorpalais in Potsdam (Germany) have shown that the Prieborn marble exhibits similar weathering properties to the Carrara marble (Ruedrich *et al.* 2001*a*). Both marble types are characterized by a sugar-like crumbling, indicating a degradation along the grain boundaries. Thus, the main difference between the marble samples is

essentially the weathering intensity rather than the deterioration mechanism.

Magnitude and directional dependence of thermal behaviour frequently coincide with the texture of a marble, i.e. the residual strain is largest parallel to the preferred orientation of the c-axes (Siegesmund *et al.* 2000). However, marbles can exhibit c-axis maxima as well as girdle distributions (e.g. Lasa marble) and the texture strength may vary. Since grain boundary cracking is the predominant type of degradation in marble, a preferred orientation of grain boundaries also leads to an anisotropic distribution of the thermal degradation. Thus, a certain amount of anisotropy in both the thermal expansion coefficient and the residual strain is a general property of all marbles (e.g. Widhalm *et al.* 1996). Consolidation of a marble with a preferred crack system results in an anisotropic distribution of the consolidant. Since the consolidation material has a more or less pronounced effect on the thermal dilatation behaviour, a directional dependence has to be expected for the consolidation.

The consolidation of a porous material leads inevitably to a modification of the pore space, e.g. reduction of porosity and a shift of effective pore radii. Furthermore, secondary effects by gel segregation or curing generates a new pore geometry, e.g. shrinkage cracks in PSAE and $PMMA_{sol}$, voids in $PMMA_{poly}$. Consequently, the interconnectivity is changed and thus other physical parameters of the impregnated marbles, e.g. the water uptake behaviour, should be significantly changed.

The PSAE approach does not improve the cohesion between the grains significantly (see also Goins *et al.* 1996). This effect is evident in the SEM analyses as well as in the relatively small increase of ultrasonic velocities. Furthermore, the thermal behaviour is only slightly modified due to consolidation. However, a PSAE consolidation can stabilize the microstructure of strongly weathered marbles and subsequent impregnation with a cohesion-reinforcing consolidant is possible.

An improved bonding between the grains was generally observed for both PMMA consolidants. This was verified qualitatively by fractography and quantitatively by a pronounced increase of the ultrasonic wave velocities (Fig. 12b,d). However, the expansion behaviour was strongly modified near the specific glass transition temperatures of the two PMMA consolidants. When the temperature reaches the T_g of the respective PMMA consolidants, a significant residual strain occurs (see Table 1). A small decrease in ultrasonic velocity suggests that this residual strain is not unequivocally linked to thermal degradation, but more evidently to a change of the consolidant behaviour from more elastic to more plastic.

A clear change in the dilatation curves after $PMMA_{poly}$ consolidation proves that a significant change in the material's properties occurs. A pronounced reduction of thermal expansion and a significant increase in ultrasonic velocity indicate a good bonding between the calcite surfaces and the $PMMA_{poly}$. However, the extreme reduction of thermal expansion is difficult to understand. Even if the thermal expansion coefficient of polymerized MMA is about $\alpha = 70 \times 10^{-6}\ K^{-1}$, the volume of $PMMA_{poly}$ which invaded the pore space of the marbles is too small for a measurable decrease of dilatation. Thus, the observed reduction of dilatation is possibly caused by a good bonding between the calcite surfaces and the reduction in pore space.

All natural stones from a quarry contain a certain amount of microcracks as a consequence of their complex geological history. Furthermore, weathering causes an increase in pore space. This pore space obviously accommodates a certain part of sample expansion (buffering) until it is closed (cf. Ruedrich *et al.* 2001*b*). $PMMA_{poly}$ impregnation leads to a strong porosity reduction, and thus the buffering vanishes. The final result is a compound material, while the other consolidants do not show this effect. Since strongly anisotropic marbles can show a contraction even after $PMMA_{poly}$ consolidation, the changed thermal expansion behaviour has to be considered for preservation concepts. Furthermore, a difference in thermal behaviour between consolidated and unconsolidated components has to be expected.

In the field, marbles are subjected to numerous temperature changes (e.g. day–night cycles). From the laboratory experiments it is obvious that the thermal degradation of a marble vanishes once a certain temperature is reached. Subsequent cycles at the same temperature result in a significantly reduced or no residual strain. However, on-site the marbles are generally subjected to water, which may reinforce the dilatation and lead to the steady progress of rock damage (Grimm 1999).

Conclusions

The microstructure, the state of preservation and the type of consolidant used are competing parameters determining the thermoelastic properties of a marble. Based on the present

investigation the following conclusions can be drawn.

Thermal degradation of marble depends not only on the texture, but also on the shape fabric of the respective marble. Thus, a complete three-dimensional fabric characterization is indispensable for a quality assessment of marble and associated preservation purposes.

Consolidation of marble using $PMMA_{sol}$, $PMMA_{poly}$ and PSAE changes its thermoelastic properties, since either a consolidation or a stabilization of weathered marbles is observed. The most drastic change is observed for $PMMA_{poly}$. However, the change in the thermoelastic properties varies. Both PMMA consolidants lead to an increase in cohesion between the grains while PSAE stabilizes the microstructure by simply reducing the porosity.

All consolidants reduce the porosity. $PMMA_{sol}$ and PSAE treated marbles show a decrease in porosity and pore radius size according to their agent content, whereas for $PMMA_{poly}$ the porosity almost completely vanishes. Furthermore, other physical properties important for weathering like water absorption will be changed as well after impregnation.

A reinforced cohesion between the grains due to impregnation can be monitored by ultrasonic wave velocity measurements. Both PMMA consolidants show a significant increase in ultrasonic wave velocities after treatment, whereas this effect is limited for PSAE. Therefore, ultrasonic wave velocities seem to be the proper tool for quantifying the effect of consolidation.

After passing the glass transition temperature, a residual strain is observed in thermal dilatation measurements. This does not necessarily coincide with a deterioration, since ultrasonic wave velocities do not show a drastic decrease in thermally treated consolidated marbles.

We are grateful to H. W. Ibach and P. J. Koblischek for their help with the consolidants. Thanks go to G. Wheeler, R. Snethlage and U. Lindborg for their comments. Our work was supported by the Deutsche Bundesstiftung Umwelt and a Heisenberg fellowship from the Deutsche Forschungsgemeinschaft (Si 438/10-1,2 and Si 438/13-1).

References

BATTAGLIA, S., FRANZINI, M. & MANGO, F. 1993. High sensitivity apparatus for measuring linear thermal expansion: preliminary results on the response of marbles. *Il Nuovo Cimento*, **16**, 453–461.

BIRCH, F. 1960. The velocity of compressional waves in rocks up to 10 kilobars, Part I. *Journal of Geophysical Research*, **65**, 1083–1102.

BIRCH, F. 1961. The velocity of compressional waves in rocks to 10 kilobars, Part 2. *Journal of Geophysical Research*, **66**, 2199–2224.

BRAKEL, J. VAN, MODRY, S. & SVATA, M. 1981. Mercury porosimetry: State of the art. *Powder technology*, **29**, 1–12.

CLIFTON, J. R. 1980. *Stone Consolidating Materials – A Status Report.* US Department of Commerce, National Bureau of Standards, NBS Technical Note 1118:46.

DREYER, W. 1974. *Materialverhalten anisotroper Festkörper: Thermische und elektrische Eigenschaften.* Springer, Wien.

DUYSTER, J. 1991. *Strukturgeologische Untersuchungen im Moldanubikum (Waldviertel, Österreich) und methodische Untersuchungen zur bildanalytischen Gefügequantifizierung von Gneisen.* PhD thesis, Göttingen, Geology.

GOINS, E. S., WHEELER, G. S. & WYPYSKI, M. T. 1996. Alkoxysilane film formation on quartz and calcite crystal surfaces. *Proceedings 8th Internatioal Congress on Deterioration and Conservation of Stone*, Berlin, 1255–1264.

GRIMM, W. D. 1999. Observations and reflections on the deformation of marble objects caused by structural breaking-up. *Zeitschrift Deutsche Geologische Gesellschaft*, **150**, 195–236.

KESSLER, D. W. 1919. *Physical and chemical tests on the commercial marbles of the United States.* Technology papers of the Bureau of Standards, No. 123.

KLEBER, W. 1959. *Einführung in die Kristallographie.* VEB Verlag Technik, Berlin.

KOBLISCHEK, P. J. 1990. Protection of surfaces of natural stone and concrete through polymers. *In*: MEGUID, S. A. (ed.) *Surface Engineering.* Elsevier Applied Science, 62–71.

LEISS, B. & ULLEMEYER, K. 1999. Texture characterisation of carbonate rocks and some implications for the modeling of physical anisotropies, derived from idealized texture types. *Zeitschrift Deutsche Geologische Gesellschaft*, **150**, 259–274.

LEISS, B. & WEISS, T. 2000. Fabric anisotropy and its influence on physical weathering of different type of Carrara marbles. *In*: LEISS, B., ULLEMEYER, K. & WEBER, K. (eds) *Textures and physcial properties of rock. Journal of Structural Geology*, Special Issue, **22**, 1737–1745.

LORENZ, H. G. & IBACH, H. W. 1999. Marble conservation by Ibach-Total-Impregnation Process: Quality control and optimisation by microscopic and petrophysical data. *Zeitschrift Deutsche Geologische Gesellschaft*, **150**, 397–406.

PASSCHIER, C. W. & TROUW, R. A. J. 1996. *Microtectonics.* Springer, Berlin.

RUEDRICH, J., SIEGESMUND, S. & RICHTER, D. 2001*a*. Marble columns and their state of weathering: structural evidences and ultrasonic tomography. *Zeitschrift Deutsche Geologische Gesellschaft*, **152**, 665–680.

RUEDRICH, J., WEISS, T. & SIEGESMUND, S. 2001*b*. Deterioration characteristics of marbles from

the Marmorpalais Potsdam (Germany): a compilation. *Zeitschrift Deutsche Geologische Gesellschaft*, **152**, 637–664.

SAGE, J. D. 1988. Thermal microfracturing of marble. *In*: MARINOS, P. & KOUKIES, G. (eds) *Engineering Geology of Ancient Works*, Balkema, Rotterdam, 1013–1018.

SIEGESMUND, S., VOLLBRECHT, A., ULLEMEYER, K., WEISS, T. & SOBOTT, R. 1997. Application of geological fabric analyses for the characterization of natural building stones – case study Kauffung marble (in German). *International Journal for Restoration of Buildings and Monuments*, **3**, 269–292.

SIEGESMUND, S., WEISS, T., VOLLBRECHT, A. & ULLEMEYER, K. 1999. Marble as a natural building stone: rock fabrics, physical and mechanical properties. *Zeitschrift Deutsche Geologische Gesellschaft*, **150**, 237–257.

SIEGESMUND, S., ULLEMEYER, K., WEISS, T. & TSCHEGG, E. K. 2000. Physical weathering of marbles caused by anisotropic thermal expansion. *International Journal of Earth Science*, **89**, 170–182.

SNETHLAGE, R., ETTL, H. & SATTLER, L. 1999. Ultrasonic measurements on PMMA-impregnated marble sculptures. *Zeitschrift Deutsche Geologische Gesellschaft*, **150**, 387–396.

TSCHEGG, E. K., WIDHALM, C. & EPPENSTEINER, W. 1999. Reasons for insufficient shape stability of marble plates. *Zeitschrift Deutsche Geologische Gesellschaft*, **150**, 283–297.

WEISS T., SIEGESMUND, S. & RASOLOFOSAON, P. N. J. 2000. The relationship between deterioration, fabric, velocity and porosity constraint. *Proceedings 9th International Congress on Deterioration and Conservation of Stone*, Venice, 215–223.

WIDHALM, C., TSCHEGG, E. K. & EPPENSTEINER, W. 1996. Anisotropic thermal expansion causes deformation of marble cladding. *Journal of Performance of Constructed facilities*, **10**, 5–10.

This page intentionally left blank

The influence of petrographic, architectural and environmental factors in decay patterns and durability of granite stones in Braga monuments (NW Portugal)

J. M. S. MATIAS & C. A. S. ALVES
University of Minho, CCA/CT, Gualtar, 4710 Braga, Portugal
(e-mail: juana_matias@hotmail.com)

Abstract: In order to discuss decay patterns and susceptibility of granite types used in architectural works, the decay features of 39 monuments built with granite stones and presenting diverse architectural characteristics, date of construction and environmental characteristics (including exposition conditions, traffic intensity, etc.) are compared. Decay patterns of biotite-rich medium- to fine-grained (frequently porphyritic) granite stones are related to weathering inherited from the quarry (expressed by yellowing), to the presence of heterogeneous elements (enclaves and phenocrysts) and to grain size variations. Fine-grained leucogranitic stone decay is mainly controlled by tectonic foliation. The characteristics of stone application, including how and where stone was used, influence decay patterns by favouring salt pollution concentration, biological colonization and fixation of atmospheric pollutants. Erosive decay features (linked mainly to salt pollution) and stone coatings (linked to biological action and atmospheric and organic pollution) are widespread decay forms that affect granite stones in Braga monuments.

Braga (NW Portugal, Fig. 1) is located in the Central Iberian Zone of the Iberian Peninsula (Julivert *et al.* 1974). From the geological point of view the region is dominated by granitic rocks of Hercynian age. There are also Palaeozoic metasedimentary rocks and sedimentary deposits of Pliocene–Pleistocene age. Granite stone is, therefore, an important element of the built heritage of this town. Several decay features related to anthropogenic and geogenic factors affect the granite stones of these monuments. The decay aspects discussed in this paper concern surface modifications that affect the aesthetic value of stones. Certain authors have considered some natural chromatic alterations of stones as 'finishing' (Mostafavi & Leatherbarrow 1993) but, in the present paper, all alterations that occur after employment of the stones in the monuments will be considered decay features (since the original aspect of the stone is altered).

Fig. 1. Location of the town of Braga.

Although decay processes have been modelled, and several laboratory essays have tried to simulate decay processes, only comparison of decay features of diverse buildings may avail the real time and space scale of these decay processes and the simultaneous effects and interactions of diverse decay agents (Jeannette 1992; Smith 1996; Lewis & McDonal 1997; Nord & Holenyi 1999).

The main goals of this paper are (i) to discuss and identify decay patterns of granite stones in Braga monuments; (ii) to discuss stone susceptibility and durability as result of stone characteristics and application aspects (architectural and environmental characteristics).

From: Siegesmund, S., Weiss, T. & Vollbrecht, A. 2002. *Natural Stone, Weathering Phenomena, Conservation Strategies and Case Studies*. Geological Society, London, Special Publications, **205**, 273–281.
0305-8719/02/$15.00 © The Geological Society of London 2002.

Table 1. *Climatological normals for Braga from the 1961–1990 period (data from the Portuguese National Institute of Meteorology and Geophysics)*

	Air temperature (°C)			Precipitation (mm)		Number of days with		
Month	med.	max.	min.	total	max.	snow	dew	frost
Jan	8.7	13.2	4.3	212.7	92.0	0.2	5.3	9.0
Feb	9.5	13.9	5.1	208.6	90.2	0.1	5.8	5.2
Mar	10.9	16.0	5.8	143.0	95.4	0.0	11.1	2.2
Apr	12.3	17.6	6.9	123.8	99.4	0.0	11.8	0.8
May	14.8	20.4	9.2	108.0	74.2	0.0	10.9	0.0
June	18.4	24.5	12.3	67.4	73.5	0.0	13.5	0.0
July	20.4	27.1	13.7	20.4	24.5	0.0	15.5	0.0
Aug	20.1	27.4	12.8	25.7	44.0	0.0	16.6	0.0
Sep	18.9	25.6	12.2	77.9	123.7	0.0	14.0	0.0
Oct	15.5	21.1	9.9	147.0	162.5	0.0	13.2	0.0
Nov	11.4	16.3	6.5	166.7	81.1	0.0	10.0	3.3
Dec	9.3	13.8	4.8	213.3	103.5	0.0	6.0	8.1
Year	14.2	19.7	8.6	1514.5	162.5	0.3	133.7	28.6

Materials and methods

The decay features of 39 monuments are considered, including results of previous studies regarding the Archiepiscopal and Biscainhos Palace (Alves 1997; Leite Magalhães & Sequeira Braga 2000) and the Idol's Fountain (Aires-Barros *et al.* 1998).

This study includes 19 churches and chapels, 14 civil and military buildings and six fountains. Most of the monuments were built between the sixteenth and twentieth centuries, but there are older monuments and portions of monuments (Costa 1985; Oliveira 1999; DGEMN 2000). This group of monuments allowed the study of decay features of granite used for walls and façade masonry blocks, windows and door frame elements, ornamental details, paving slabs, columns and arches, and subjected to different environmental conditions, e.g. interior/exterior, varied exposition orientation (Fig. 2), diverse surroundings, etc. Table I presents some climatological data of Braga from the period 1961–1990 (Portuguese National Institute of Meteorology and Geophysics). Data concerning air pollution, namely SO_x and NO_x levels, were not available.

A detailed visual survey was performed of all the studied monuments, in order to distinguish the decay features affecting granite stones and their distribution in the monuments. The decay features detected and the characteristics used for their field distinction are presented in Table 2 (partly following nomenclature suggestions of Fitzner *et al.* (1992) and Dorn (1998)). Efflorescence samples were furthermore characterized by optical microscopy (immersion method, using the indications of Arnold (1984)) and by X-ray diffraction, since salt efflorescences could be useful fingerprints of salt pollution (Arnold & Zehnder 1989; Arnold 1996; Alves & Sequeira Braga 2000). Some samples of stone coatings were also studied, using scanning electron microscopy with microanalysis system (SEM/EDS) (LEICA S360).

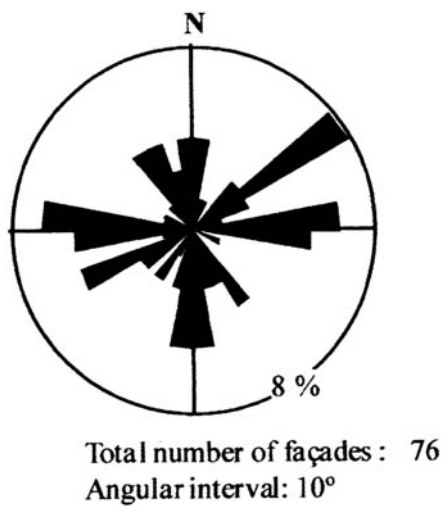

Fig. 2. Rose diagram of azimuth of exposition of surveyed facades (given by the exposition sense of the vector normal to the facade plane).

Granite stone characteristics

The granite stones used in these monuments present varied petrographic characteristics, but two types are dominant and, therefore, will be the object of consideration (allowing

Table 2. *Decay features on the studied monuments and macroscopic characteristics used for distinction*

Designation	Macroscopic characteristics
Fissures	Crack lines at the stone surface
Granular disintegration	Detachment of stone grains
Flakes	Detachment of small, planar elements parallel to the stone surface
Scales	Detachment of large, planar elements parallel to the stone surface
Efflorescences	Salt aggregates on stone surface
Black crusts	Very dark spongy concretions
Biological colonization	Biological related coatings (including diverse organisms and soiling resulting from biological colonization)
Patinas	Generic term for thin stone coatings without clear genetic evidence

comparison of different architectural and environmental situations).

The most frequent stones are similar to Braga granite (Ferreira *et al.* 2000), a late-D_3 (deformation phase of the Hercynian orogeny) monzogranite, biotite-rich, medium- to fine-grained, frequently porphyritic granite, with mafic microgranular xenoliths. The mineralogical composition is (Ferreira *et al.* 2000): quartz (22–28%) + plagioclase (28–36%, Na 19–36%), K-feldspar (22–31%) + biotite (10–19%) + muscovite (<4%) + ilmenite + apatite + zircon + monazite + thorite. The stones in the monuments present variable coloration (from bluish grey to different yellow tints), related to weathering inherited from the quarry (Alves 1997; Alves *et al.* 1996).

Also frequent, namely on facades of some more recent buildings, are fine-grained leucogranitic stones (with colour index <5%, as defined in LeMaitre (1989)) which present evidence of tectonic foliation. The fine-grained leucocratic stones are similar to the fine-grained variety of the Gondizalves granite (Ferreira *et al.* 2000), a syn-D_3 granite, with N40W tectonic foliation and petrographic variability, from two-mica medium-grained granite to muscovitic fine-grained granite. The mineralogical composition is (Ferreira *et al.* 2000): quartz (35–36%) + albite (34–36%, An 1–3%) + microcline (11–14%) + muscovite (14–16%) + biotite (2%) + apatite + zircon + monazite ± rutile ± sillimanite ± ilmenite. However, the origin of the leucogranitic stones is not unequivocal (since there are other occurrences of similar granites near the region) and is presently under research.

Results and discussion

The comparison of decay feature distribution in monuments allows the discussion of decay patterns related, on one hand, to stone characteristics and, on the other hand, to the characteristics of stone application (including architectural characteristics of the monuments and characteristics of the surrounding environment).

Granite stone characteristics

Decay patterns related to petrographic characteristics of the two main granite types are summarized in Table 3. Biotite-rich granite stone decay is clearly dependent on stone coloration (degree of discoloration marked by

Table 3. *Decay patterns related to stone characteristics*

Stone characteristics	Decay patterns
Biotite-rich granite	
Coloration (yellowing)	Yellower stones: more intense and extensive erosive decay; higher frequency of black crust.
Heterogeneity	Surface irregularities by differential erosion:
Phenocrysts	positive relief
Basic xenoliths	positive relief
Micaceous nodules	negative relief.
Grain size	Coarser grained stones present more intense granular disintegration.
Fine-grained leucogranite	Frequent occurrence of patinas.
Tectonic foliation	Flakes along whole block faces parallel to foliation; fissures and erosion along foliation planes; biological colonization along fissures.

Fig. 3. Differential relief in pavement biotite-rich granite stones associated with basic xenoliths.

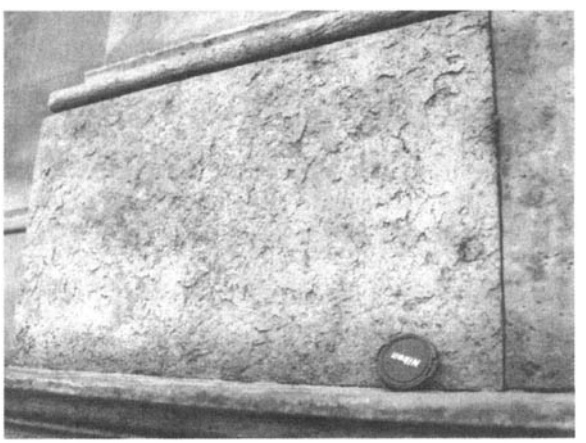

Fig. 4. Flakes along whole leucogranitic stone face.

yellowing), which represents weathering inherited from the quarry, the more yellowed stones being less durable, as previously observed by Alves (1997), Begonha (1997) and Delgado Rodrigues (1979, 1996). This discoloration is related to weathering that granites suffer in natural massifs and that affects the properties of the stones used on monuments, namely through porous media development that favours pollutant absorption and migration (for characterization of these porous media see Alves (1997) and Alves *et al.* (1996)) and through physical weakening. The higher frequency of black crusts on more yellow stones can also be due to the more developed porous media of these stone, a factor already proposed by Aires-Barros (1991) for marble and limestone. The presence of heterogeneous elements like xenoliths and phenocrysts also has a marked effect on the performance of these stones, with development of surface irregularities, resulting from differential erosion (Fig. 3). This decay pattern is more pronounced on pavement stones. Decay by granular disintegration is also more pronounced on coarser grained stones.

On fine-grained leucogranitic stones, tectonic foliation, constituting weakness planes, controls development of flakes or fissures and patinas, according to the orientation of stone faces to foliation (Figs 4, 5). While on biotite-rich granite stones flakes tend to occur near mortar joints and corners, flakes on leucogranitic stones tend to affect the whole stone face. Curiously, the development of scales on leucogranitic stones does not seem to be directly related to the orientation of foliation and tends to concentrate near mortar joints and corners as with biotite-rich granite stones.

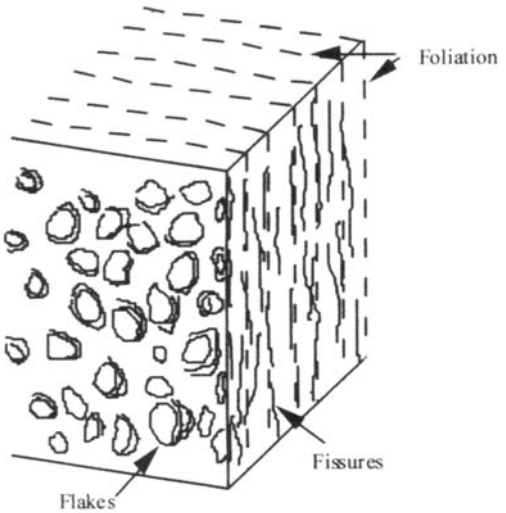

Fig. 5. Effects of foliation on fine-grained leucogranitic stone decay.

It is noticeable that leucogranitic stones are frequently affected by patinas (which are perhaps more noticeable on account of the lighter coloration of these stones). Black crusts are only observed on biotite-rich granite stones, but whether this pattern is related to the stones' characteristics or to the monuments' location (and surrounding environment) is not yet clear.

Granite stone application

Table 4 shows decay patterns related to the influence of exposition, height, mode of application, use given, and the monuments' surrounding environment (including traffic intensity, presence of other buildings and trees, etc).

According to the performed survey, architectural characteristics of facades have a bigger influence on the occurrence and distribution of decay features than orientation, namely by the presence of places that favour moisture and solution accumulation, like balconies, cornices, etc. (Fig. 6); places that have been considered as, potentially, presenting a higher salt regime (Duffy & O'Brien 1996) (Fig. 6). Accentuated decay associated with concentration of moisture and solutions is also observed on the sheltered

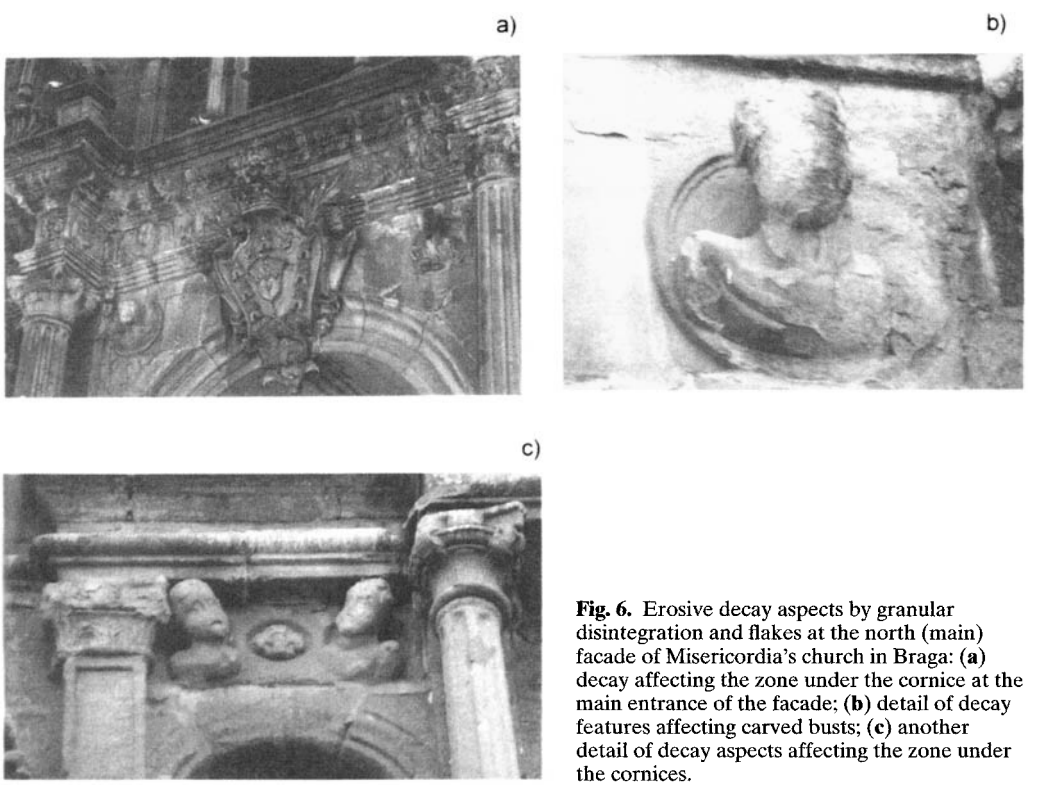

Fig. 6. Erosive decay aspects by granular disintegration and flakes at the north (main) facade of Misericordia's church in Braga: (**a**) decay affecting the zone under the cornice at the main entrance of the facade; (**b**) detail of decay features affecting carved busts; (**c**) another detail of decay aspects affecting the zone under the cornices.

Table 4. *Decay patterns related to the characteristics of stone application (including surroundings)*

Stone applications	Decay pattern
Façades	
Orientation	Frequent and extensive biological colonization in north facades; more intense and frequent flaking in south facades.
Height	Lower zones present more frequent occurrence of erosive decay features and dark patinas. Erosive decay features at higher portions depend on architectural characteristics. Biological colonization and some patinas (leucogranitic stones) occur along the whole height of facades.
Architectural characteristics	Regardless of height, places where moisture and solutions accumulate (balconies, cornices, etc.) present more intense erosion, black crust formation and biological colonization. Scales and flakes tend to concentrate near mortar joints and corners. Projecting and artistic details are more affected by erosion.
Surroundings	Biological colonization is increased by sun sheltering effects of other buildings and trees. Dark patinas and black crusts are associated with narrow streets and intense traffic.
Fountains	Frequent occurrence of patinas with diverse tonalities and biological colonization. Scarce occurrence of erosive aspects.
Pavements and stairs (exterior)	Surface irregularities are linked to differential erosion. Occasionally, erosion occurs near joints (linked to salt and moisture concentration).
Arches and arcades	Erosive decay and biological colonization are more frequent at base of piers. More intense erosive decay occurs at the sheltered portions of arches.
Interior rooms	Erosive decay occurs at the floor and at the base of walls and pillars. Scales and flakes occur more frequently near mortar joints and corners. Projecting corners are more susceptible to erosion. More intense erosive decay is associated with occurrence of efflorescence of diverse soluble salts.

Fig. 7. Decay of borders of pavement stones.

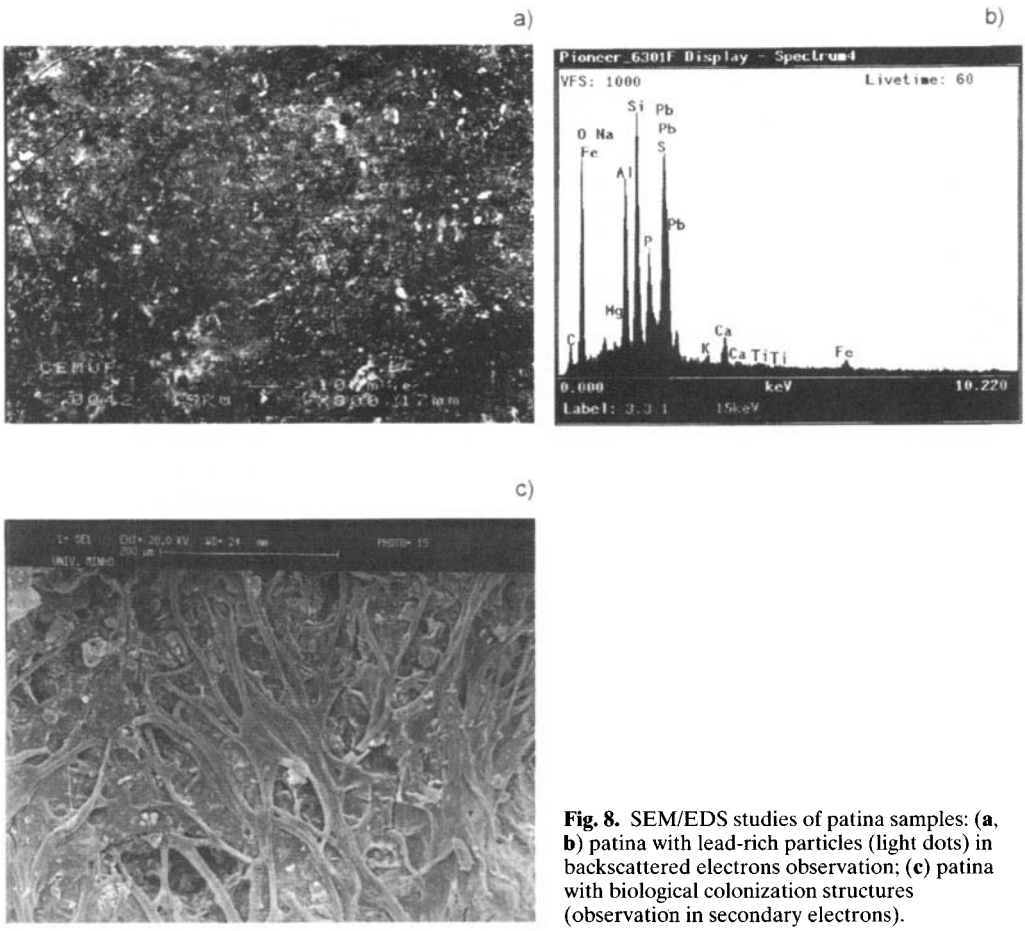

Fig. 8. SEM/EDS studies of patina samples: (**a**, **b**) patina with lead-rich particles (light dots) in backscattered electrons observation; (**c**) patina with biological colonization structures (observation in secondary electrons).

portions of arcades and, occasionally, borders of pavement slabs (Fig. 7). The effect of facade orientation is also countered by the sheltering effect of trees and/or buildings in the surroundings. Nevertheless, it is observed that north facades are more susceptible to soiling by biological colonization and that south facades, which are sunnier and windier, tend to present more intense development of flakes. The intense development of scales and flakes is observed on some west facades.

The base of building walls is frequently the zone most affected both by erosive decay (associated with capillary rise) that affects both interior and exterior elements, and by the development of patinas (affecting facades). However, it must be mentioned that discoloration by patinas affects entire facades made with leucogranitic stones.

Discoloration resulting from the diverse stone coatings is a major problem affecting outside features. Biological colonization distribution is clearly related to moisture and sun exposition balance and black crusts show characteristic elements, namely gypsum aggregates and particles (LeFèvre 1992), in association with atmospheric pollution. The coatings grouped as patinas show evidence of a more complex and varied genesis, related to pollution (atmospheric and organic) (Fig. 8a,b), moisture balance and influence of microbiological activities (Fig. 8c).

In contrast to observations regarding other cities with granite stone monuments (Urquhart *et al.* 1996), biological soiling is a major problem affecting outside granite stone elements, which could result from the high annual rainfall observed in Braga (1514.5 mm/year, mean value for the 1961–1990 series, data from the Portuguese Meteorological Institute).

The distribution of some stone coatings (namely black crusts and some dark patinas)

seems to be related to traffic intensity in the streets surrounding the monument (especially to the proximity of traffic lights).

Inside the monuments, decay is mostly associated with saline pollution and is frequently limited to the portions nearer the ground. The most intense decay is usually associated with salt efflorescence occurrences. The occurrence of salt efflorescences may be an indicator of more intense saline pollution regimes. These salt efflorescences show varied mineralogy, with predominance of sulphates (gypsum is the most frequent sulphate, thenardite is also frequent, and there are minor and localized occurrences of aphthitalite, hexahydrite, epsomite, syngenite, and darapskite) and nitrates (mainly nitre, occasionally nitratine), but also chlorides (halite), carbonates (trona, thermonatrite and one occurrence of calcite).

The study developed by Alves & Sequeira Braga (2000) regarding salt systems of some Braga buildings indicated that gypsum is ubiquitous, being linked to a background salt system related to ground solutions that may result from the combination of several geogenic and anthropogenic sources, since calcium and sulphate are common ions in rainwater, groundwater, mortars, human and animal waste, etc.

The sources of other salts (with more localized distributions) are associated with animal waste (nitre), human waste (nitre, nitratine, halite, epsomite and hexahydrite) and the use of cement mortars (alkaline sulphates and carbonates).

Biological colonization is almost absent inside the monuments, and the rare situations observed seem to be associated with infiltration.

Conclusions

The study of decay features allows identification of the main decay patterns that affect granite monuments of Braga, and the influence of petrographic, architectural and environmental factors on the durability of granite stones as architectural material.

For biotite-rich, medium- to fine-grained, frequently porphyritic granite stones, decay is related to yellowing (with more pronounced and extensive erosive decay and also more frequent black crust formation on more yellowed stones), grain size variation (coarser grained stones show more intense erosive decay) and the presence of heterogeneous elements (differential erosion of phenocrysts and enclaves). Tectonic foliation of fine-grained leucogranitic stones affects the distribution of fissures, flakes and biological colonization on these stones.

Erosive decay is strongly linked to salt pollution, being favoured by features that allow solution accumulation and circulation (architectural details and mortar joints). Intensity of salt pollution resulting from local characteristics also affects erosive decay, as is shown by more intense decay inside buildings associated with salt efflorescences and by more intense decay of pavement slabs associated with places with buried corpses.

Chromatic modifications (related to biological colonization, black crusts and patinas) are a major problem affecting stone applied as exterior elements. Biological colonization shows a widespread occurrence on the stones of these monuments and constitutes the main discoloration factor, being its distribution related to substrate moisture and sun exposure. Distribution of black crusts, whose formation is related to atmospheric pollution, seems related to the specific characteristics of surrounding traffic. The studied patinas show varied characteristics and complex genesis processes related to the action of diverse agents (there being evidence of the important role of biological agents).

This work received financial support from the Portuguese POCTI Program, through the POCTI/1999/CTA35600 Project and through pluriannual funding for the CCA/CT, and also from the Instituto Português do Património Arquitectónico (IPPAR) and from the Misericórdia of Braga.

Acknowledgements are also due to the authorities responsible for each of the studied monuments, for allowing surveying and sampling works, and to two anonymous referees, R. Löfvendahl and S. Siegesmund for their suggestions regarding this paper.

References

AIRES-BARROS, L. 1991. *Alteração e alterabilidade das rochas*. INIC, Lisbon.

AIRES-BARROS, L., SEQUEIRA BRAGA, M. A., PAMPLONA, J., LIMA, A. & ALVES, C. 1998. Fonte do Ídolo (Braga). Diagnóstico do estado de conservação. *Comunicação. do Instituto Geológico e Mineiro, Actas do V Congresso*. Nacional de Geologia, Lisbon, **84**, fasc. 2, 190–193 (in Portuguese).

ALVES, C. A. S. 1997. *Estudo da deterioração de materiais graníticos aplicados em monumentos da cidade de Braga (Norte de Portugal). Implicações na Conservação do Património Construído*. PhD thesis, Universidade of Minho (in Portuguese).

ALVES, C. A. S & SEQUEIRA BRAGA, M. A. 2000. Decay effects associated with soluble salts on granite buildings of Braga (NW Portugal). *Environmental Mineralogy: Microbial Interactions, Anthropogenic Influences, Contaminated Land and Waste Management*. Mineralogical

Society of Great Britain & Ireland, Book Series, **9**, 181–199.

ALVES, C. A. S., HAMMECKER, C. & SEQUEIRA BRAGA, M. A. 1996. Water transfer and decay of granitic stones in monuments. *Comptes Rendus de l'Académie des Sciences, Paris*, **323**(5), 397–402.

ARNOLD, A. 1984. Determination of mineral salts from monuments. *Studies in Conservation*, **29**, 129–138.

ARNOLD, A. 1996. Origin and behaviour of some salts in context of weathering on monuments. *In*: *EC Research Workshop: Origin, Mechanisms and Effects of Salts on Degradation of Monuments in Marine and Continental Environments*, Bari, 133–139.

ARNOLD, A. & ZEHNDER, K. 1989. Salt weathering on monuments. *1st International Symposium: The Conservation of Monuments in the Mediterranean Basin*, Bari, 31–58.

BEGONHA, A. 1997. *Meteorização do granito e deterioração da pedra em monumentos e edifícios da cidade do Porto*. PhD thesis, Braga (in Portuguese).

COSTA, L. 1985. *Braga – Roteiro monumental e Histórico do Centro Cívico*. Câmara Municipal de Braga (in Portuguese).

DELGADO RODRIGUES, J. 1979. *Some problems raised by the study of the weathering of igneous rocks*. Memórias LNEC, **517**.

DELGADO RODRIGUES, J. 1996. A brief introduction to the degradation and conservation of granitic rocks. *In*: RODRIGUES, J. D. & COSTA, D. (eds) *Conservation of Granitic Rocks*, LNEC, Lisbon, 1–12.

DGEMN 2000. *IPA – Inventário do Património Arquitectónico (Concelho de Braga)*. World Wide Web address: http://www.monumentos.pt/dgemn/wgetent?userid=ipa&typ=cc&conc=0303 (in Portuguese).

DORN, R. I. 1998. *Rock Coatings*. Elsevier, Amsterdam.

DUFFY, A. P. & O'BRIEN, P. F. 1996. A basis for evaluating the durability of new building stone. *In*: SMITH, B. J. & WARKE, P. A. (eds) *Process of Urban Stone Decay*, Donhead Publishing, London, 253–260.

FERREIRA, N., DIAS, G., MEIRELES, C. & SEQUEIRA BRAGA, M. A. 2000. *Notícia explicativa da folha 5-D (Braga)*. IGM (in Portuguese).

FITZNER, B, HEINRICHS, K. & KOWNATZKI, R. 1992. Classification and mapping of weathering forms. *7th International Congress on Deterioration and Conservation of Stone*, Lisbon, 957–968.

JEANNETTE, D. 1992. Morphologie et nomenclatures des altérations. *In*: *La Conservation de la pierre monumentale en France*. CNRS, 73–81.

JULIVERT, M., FONTBOTÉ, J., RIBEIRO, A. & CONDE, L. 1974. *Memória explicativa del Mapa tectónico de la Península Ibérica y Baleares, escala 1:1000000*. Instituto Geológico Min. España (in Spanish).

LEFÈVRE, R. A. 1992. Les effets de la pollution atmosphérique. *In*: *La Conservation de la pierre monumentale en France*. CNRS, 82–87.

LEITE MAGALHÃES, S. M. & SEQUEIRA BRAGA, M. A. 2000. Biological colonization features on a granite monument from Braga (NW, Portugal). *Proceedings of 9th International Congress on Deterioration and Conservation of Stone*, Venice, vol. 1, 521–529.

LEMAITRE, R. W. (ed.) 1989. *A Classification of Igneous Rocks and Glossary of Terms. Recommendations of the International Union of Geological Sciences Subcommission on the Systematics of Igneous Rocks*. Blackwell Scientific Publications, Oxford.

LEWIS, M. D. & MCDONAL, W. H. 1997. Assuring the durability of stone facades in new construction. *In*: *Degradation of Natural Building Stones*, ASCE Geotechnical Special Publications, **72**, 116–137.

MOSTAFAVI, M. & LEATHERBARROW, D. 1993. *On Weathering: The life of buildings in Time*. MIT Press, Massachusetts.

NORD, A. G. & HOLENYI, K. 1999. Sulphur deposition and damage on limestone and sandstone in Stockholm city buildings. *Water, Air and Soil Pollution*, **109**, 147–162.

OLIVEIRA, E. P. 1999. *Braga – Percursos e memórias de granito e oiro*. Campo das letras, Editores S. A. (in Portuguese).

SMITH, B. J. 1996. Scale problems in the interpretation of urban stone decay. *In*: SMITH, B. J. & WARKE, P. A. (eds) *Process of Urban Stone Decay*. Donhead Publishing, London, 3–18.

URQUHART, D. C. M., YOUNG, M. E., MACDONALD, J., JONES, M. S. & NICHOLSON, K. A. 1996. Aberdeen granite buildings: a study of soiling of decay. *In*: SMITH, B. J. & WARKE, P. A. (eds) *Process of Urban Stone Decay*. Donhead Publishing, London, 66–77.

This page intentionally left blank

Investigations into provenance and properties of ancient building sandstones of the Zittau/Görlitz region (Upper Lusatia, Eastern Saxony, Germany)

STEFFEN MICHALSKI[1,2], JENS GÖTZE[1], HEINER SIEDEL[2], MICHAEL MAGNUS[3] & ROBERT B. HEIMANN[1]

[1] *Freiberg University of Mining and Technology, Department of Mineralogy, Brennhausgasse 14, D-09596 Freiberg, Germany (e-mail: goetze@mineral.tu-freiberg.de)*

[2] *Dresden University of Technology, Department of Geotechnical Engineering, D-01062 Dresden, Germany*

[3] *Freiberg University of Mining and Technology, Department of Geology, B.-v.-Cotta-Strasse 2, D-09596 Freiberg, Germany*

Abstract: Mineralogical and technical properties were investigated of building sandstones from ancient monuments of the Zittau/Görlitz region (Germany) as well as material from potential source quarries. The complex study included macroscopic rock description and detailed investigations by polarizing microscopy (phase composition, texture, grain size distribution), cathodoluminescence (quartz types, feldspar and kaolinite content), scanning electron microscopy (accessories, pore cement, diagenetic grain surface features) as well as the analysis of open macroporosity (total water uptake) and the pore size distribution function (Hg porosimetry). For the first time, mineralogical and technical data were obtained for building sandstones of the Zittau region. The results not only confirmed earlier conjectures concerning different source areas for the ancient building sandstones of the Zittau and Görlitz area but also allowed the unequivocal assignment of historically used material to specific sandstone occurrences. The data obtained provide a comprehensive basis for the interpretation of weathering damage suffered by the historical monuments and give useful hints for their successful conservation and reconstruction.

Sandstones of the Upper Lusatia region of Germany (Fig. 1) have been used as important building material since the thirteenth (Görlitz) and fourteenth centuries (Zittau). Recently, extensive conservation and reconstruction of historical buildings and cultural monuments in this region have led to an increasing demand for detailed information on the ancient stone material.

Knowledge about provenance and technical properties of building material is required to evaluate weathering processes and successfully preserve and reconstruct historical buildings. Since the weathering and deterioration of natural stone generally depend on phase composition and textural properties, mineralogical investigations play an important role in the characterization of this material. Unfortunately, to date such comprehensive studies are still lacking.

The concept of the present study involved several steps. First, careful evaluation of historical data provided clues concerning the provenance of the ancient building sandstones in the Görlitz and Zittau region. Secondly, samples from the potential source rocks were investigated and compared with selected material of recent reconstruction activities. Based on these results, the mineralogical and technical properties of different sandstone types were compiled and the stone material of historical buildings and monuments assigned to possible source rocks.

Materials and methods

Sample material

Görlitz region. The use of sandstones in the Görlitz region can be dated back to the thirteenth century. The material used consists mainly of Cretaceous sandstones of the North-Sudetic Basin. These sediments were deposited from the Upper Cenomanian to the Lower Santonian in a predominantly marine environment (Milewicz 1959).

Previous investigations of Fitzner *et al.* (1993) indicated that the ancient building sandstones from the Görlitz region differ in their properties from sandstones of the central part of the

From: SIEGESMUND, S., WEISS, T. & VOLLBRECHT, A. 2002. *Natural Stone, Weathering Phenomena, Conservation Strategies and Case Studies.* Geological Society, London, Special Publications, **205**, 283–297.
0305-8719/02/$15.00 © The Geological Society of London 2002.

Table 1. *Mineralogical properties of sandstone samples from historical buildings and natural occurrences of the Görlitz region*

Sample	Occurrence	Stratigraphic position	Colour, (grain size)	Mineral composition	Accessories	Peculiarities
G-ST01	Historical quarry between Hohkirch and Langenau	Coniac	Light-grey fine-grained (60–350 μm) homogeneous	>99% quartz (homogeneous or undulatory extinction)	Ilmenite, rutile, tourmaline, mica, zircon, monazite	Partially pore-filling cement (kaolinite + iron oxides)
G-ST02	Historical quarry Krauschteich near Niederpenzighammer	Santonian	Yellowish-grey medium-grained (150–600 μm) conglomeratic	>99% quartz (<10% poly-crystalline grains)	Ilmenite, rutile, tourmaline, mica, zircon, monazite	No pore-filling cement
G-ST03	Historical quarry Krauschteich near Niederpenzighammer	Santonian	Yellowish-grey coarse-grained (200–1200 μm) conglomeratic	>99% quartz (*c.* 50% poly-crystalline grains)	Tourmaline, rutile, mica, zircon	No pore-filling cement, brittle deformation, mineral inclusions in quartz, chert clasts
G-BW01	Biblisches Haus Neissstrasse 29, Görlitz		Light-grey fine-grained (70–300 μm) homogeneous	>99% quartz (homogeneous or undulatory extinction)	Ilmenite, rutile, tourmaline, mica, zircon	Partially pore-filling cement (kaolinite + iron oxides)
G-BW02	Bürgerhaus Untermarkt 17, Görlitz		Grey fine-grained (80–270 μm) homogeneous	>99% quartz (homogeneous or undulatory extinction)	Ilmenite, tourmaline, rutile, mica	Partially pore-filling cement (kaolinite + iron oxides)
G-BW03	Schönhof Brüderstrasse 8, Görlitz		Yellowish-grey coarse-grained (130–1800 μm)	>99% quartz (*c.* 50% poly-crystalline)	Tourmaline, zircon, mica	No pore-filling cement, brittle deformation, chert clasts, mineral inclusions in quartz
G-BW04	Church Deutsch Ossig, near Görlitz		Yellowish-grey medium-grained (300–650 μm)	>99% quartz (<50% poly-crystalline)	Ilmenite, tourmaline, zircon	No pore-filling cement, mineral inclusions in quartz, chert clasts

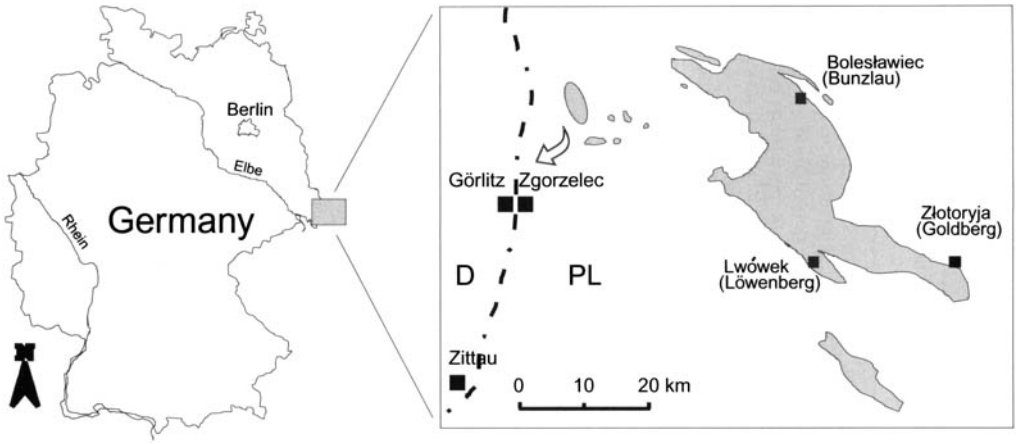

Fig. 1. Schematic map showing the investigated area including a close-up of the distribution of Upper Cretaceous sandstones of the North-Sudetic Basin; the arrow marks the historical supply of sandstone material from the Görlitz 'Kommunalheide'.

North-Sudetic Basin which were mainly used as construction material for buildings and monuments erected in Berlin (Ehling 1998). A thorough enquiry into documents deposited in the Görlitz city archives revealed that sandstones from the so-called 'Kommunalheide', a marginal part of the Cretaceous basin, have been used since the fourteenth century for monuments in this region (Fig. 1). Historical quarries were mentioned for several communities in the region of Hohkirch (Przesieczany), Langenau (Dłuzina), Niederpenzighammer (Stojanow) and Deschka, which all (with the exception of Deschka) now belong to Poland. According to their production from the fourteenth to seventeenth centuries, the occurrences of Ober-Penzighammer and Langenau were the most important quarries of ancient sandstones. Therefore, material from these occurrences was included in the present study (Table 1).

Sandstone samples of historical monuments were taken from buildings recently under reconstruction. The available material consists of a sandstone sample from the inner part of Biblisches Haus (Fig. 2a), a sample from the portal of Bürgerhaus (Fig. 2b), and a sandstone piece from the window sill of the Schönhof (Brüderstrasse 8) in Görlitz (see Table 1). An additional sandstone sample from the church of Deutsch Ossig near Görlitz was included in the present study. The history of the buildings and sample locations are summarized in Michalski (2001).

Zittau region. Sandstones of the Zittau region are in general of Turonian age and are similar to Cretaceous sandstones of the Elbe valley, Germany (Pietzsch 1962; Prescher & Walther 1977). Middle Turonian sediments are distributed in the Oybin–Johnsdorf region, whereas Upper Turonian sandstones are especially found in the Waltersdorf–Hochwald region. Specific features of the sandstones (intense silicification, high porosity) can be related to the overprinting of the sediments by Tertiary volcanism (*c.* 25 Ma). Because of their toughness and compressive strengths these sandstones were predominantly used as millstones.

Although utilization of sandstone as building material can be dated back to the fourteenth century, most of the quarries were abandoned as early as the end of the nineteenth century. Nevertheless, Michalski (2001) proved the existence of at least 40 historical quarries. Natural material from three main areas of sandstone occurrences (Waltersdorf, Oybin, Hochwald) was included in the present study (Table 2). The coarse-grained, conglomeratic sandstones of the Johnsdorf region were not considered because of their predominant use as millstones.

The stone samples from historical monuments of the Zittau region were available exclusively in the form of drill cores. The material derives from the ruin of the Oybin monastery, the Marienkirche in Zittau and a tombstone from the Zittau monastery (Table 2).

Analytical methods

The sample material was split into pieces to obtain material to study the technical properties and prepare thin sections. Two polished thin sections embedded in epoxy resin (Epo-Tek

Table 2. *Mineralogical properties of sandstone samples from buildings and historical quarries of the Zittau region*

Sample	Occurrence	Stratigraphic position	Colour, (grain size)	Mineral composition	Accessories	Peculiarities
Z-ST01	Historical quarry Teufelsmühle, Oybin district	Middle Turonian	Yellowish-grey conglomeratic (100–4000 μm),	>99% quartz (*c.* 50% poly-crystalline)	Tourmaline, mica, rutile, monazite, zircon, xenotime	Almost no pore-filling cement, zircon inclusions in quartz, brittle deformation
Z-ST02	Historical quarry Katzenkerbe, Oybin district	Middle Turonian	Yellowish-grey conglomeratic (80–8000 μm),	>99% quartz (*c.* 50% poly-crystalline)	Tourmaline, mica, rutile, monazite, zircon, xenotime	Almost no pore-filling cement, zircon inclusions in quartz, brittle deformation
Z-ST03	Historical quarry near Krompach, Hochwald	Upper Turonian	Yellow to grey medium-grained (100–700 μm)	>99% quartz (<1% poly-crystalline)	Garnet	Partially pore-filling cement (kaolinite, illite)
Z-ST04	Roter Steinbruch, Sonneberg, Waltersdorf district	Upper Turonian	Yellowish-grey medium-grained (100–400 μm)	>99% quartz (<5% poly-crystalline)	Tourmaline, mica, ilmenite, rutile ≤1% feldspar	No pore-filling cement, chert clasts
Z-ST05	Haselbruch, Sonneberg, Waltersdorf district	Upper Turonian	Light grey fine-grained (60–270 μm)	>99% quartz (homogeneous, undul. extinct.)	Ilmenite, mica, zircon, tourmaline ≤1% feldspar	Partially pore-filling cement (kaolinite, iron oxides)
Z-ST06	Leichensteinbruch, Helleberg, Waltersdorf district	Upper Turonian	Yellowish-grey fine-grained (40–200 μm)	Quartz (monocryst.) *c.* 6% feldspar	Ilmenite, mica, tourmaline, monazite, zircon	Partially pore-filling cement (illite, iron oxides)
Z-ST07	Wändesteinbruch, Helleberg, Waltersdorf district	Upper Turonian	Yellowish-grey fine-grained (60–260 μm)	>99% quartz (homogeneous, undul. extinction)	Ilmenite, mica, tourmaline	Authigenic quartz overgrowths, chert clasts
Z-ST08	Wändesteinbruch, Helleberg, Waltersdorf district	Upper Turonian	Yellowish-grey coarse-grained (60–3000 μm)	>99% quartz (90% homogen., 10% polycryst.)	Tourmaline, rutile	No pore-filling cement, brittle deformation
Z-BW01	Ruin of the Oybin monastery (drill core)		Yellowish-grey conglomeratic (80–8000 μm)	>99% quartz (*c.* 50% poly-crystalline)	Tourmaline, mica, rutile, monazite, zircon, xenotime	Almost no pore-filling cement, zircon inclusions in quartz, brittle deformation
Z-BW02	Marienkirche, Zittau (drill core)		Yellowish-grey fine-grained (60–250 μm)	>99% quartz (homogeneous, 90% und. ext.)	Ilmenite, mica, tourmaline	Almost no pore-filling cement
Z-BW03	Tombstone, Zittau monastery (drill core)		Yellowish-grey fine-grained (50–200 μm)	>99% quartz (homogeneous, undul. extinct.)	Tourmaline, mica, ilmenite, rutile, ≤1% feldspar	Partially pore-filling cement (kaolinite, iron oxides)

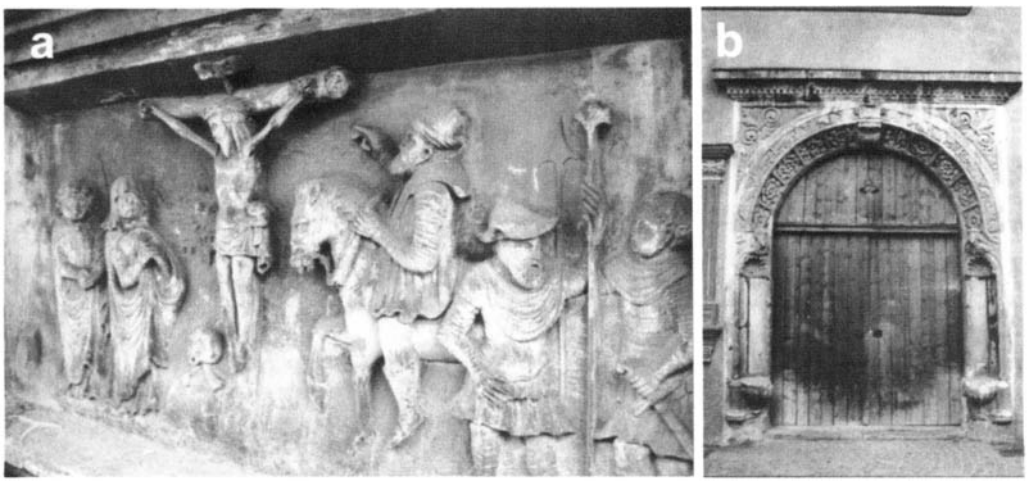

Fig. 2. Details of historical monuments from the Görlitz region: (**a**) sandstone relief on the wall of Biblisches Haus, Görlitz, showing the crucifixion of Jesus Christ; (**b**) portal of Schönhof in Görlitz.

301) were prepared of each sample. One of the thin sections was stained with blue dye to enhance the colour contrast of the pore space. Furthermore, three orthogonally orientated thin sections parallel and perpendicular to the sediment bedding were obtained to study the dependence of mineralogical parameters on the sample orientation (texture).

The macroscopic sample description was complemented by a thorough microscopic investigation using a polarizing microscope (Jenapol, Zeiss Jena). These studies included the determination of the mineralogical composition of the sandstones (modal composition, accessories), granulometric properties (grain size distribution, roundness and sphericity according to Pettijohn *et al.* 1973), texture, pore space, cement material, and diagenetic features. Granulometric properties of the quartz grains were quantified by computer-aided image analysis (KS 300, Kontron) in accordance with Magnus (1998).

Scanning electron microscopy (SEM Jeol JSM 6400) coupled with energy dispersive microanalysis (Noran-Vantage EDX) was performed to reveal details of diagenetic and weathering processes in the sandstones (mineral alteration and neoformation, grain surface textures, etc.) and to confirm results of polarizing microscopy (mineral chemistry, opaque minerals).

Cathodoluminescence (CL) microscopy was used to obtain additional information on possible similarities or differences of the relatively homogeneous quartz sandstones. Analyses were performed on carbon-coated polished thin sections using a HC1-LM hot-cathode luminescence microscope at an acceleration voltage of 14 kV and with a current density of *c.* 10 μA mm^{-2} (Neuser *et al.* 1995). Luminescence images were captured 'on-line' during CL operations by an adapted digital video camera (Kappa 961-1138 CF 20 DXC with cooling stage). The contents of quartz grains with different CL colours were semiquantitatively counted in four CL images of each sample. The standard deviation (2σ) was calculated according to Van der Plas & Tobi (1965).

Technical parameters of the sandstone samples determined included the analysis of total water uptake ($W_{m,a}$) and the pore size distribution function by mercury porosimetry. The total water uptake was analysed according to DIN 52103 (1988) on massive test specimens of 100–400 g mass in triplicate. Porosity and pore size distribution were measured by mercury high-pressure porosimetry (Ritter & Drake 1945) in the pressure range of 0.1–200 MPa.

Results and discussion

Görlitz region

Mineralogical composition and texture of the sandstones. The most relevant mineralogical properties of the investigated sandstone samples of the Görlitz region are summarized in Table 1. In general, the material consists of quartz sandstones with quartz contents >99%.

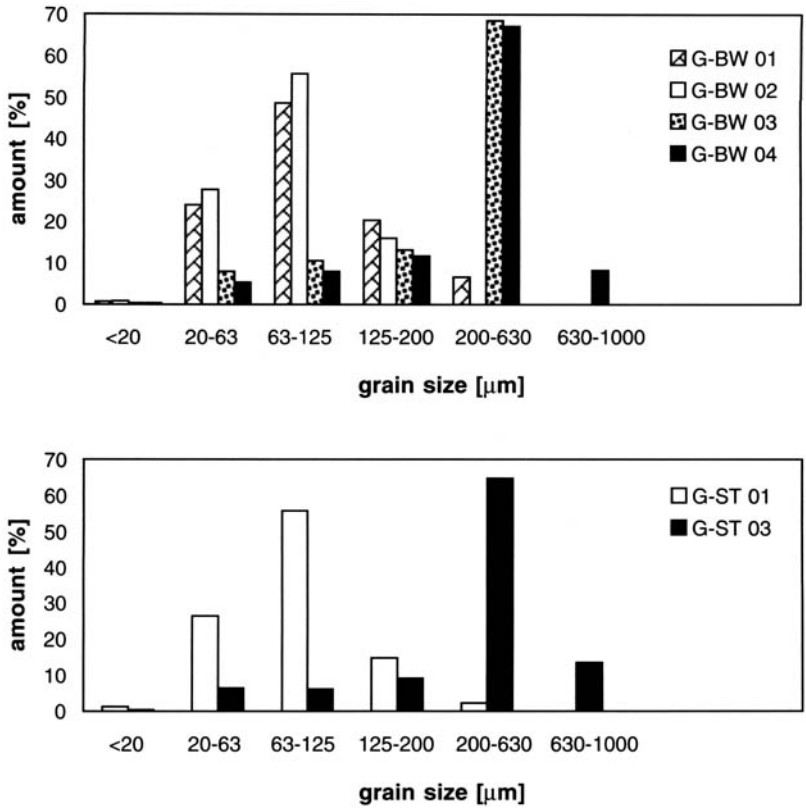

Fig. 3. Grain size distribution of sandstone samples from historical buildings (G-BW01 to 04) and quarries (G-ST01, 03) of the Görlitz region.

The content of accessory minerals is below 1%. The characteristic accessory mineral suites are presented in Table 1.

According to granulometric properties (grain size distribution (see Fig. 3), roundness, sphericity) and porosity, the sandstone samples can be subdivided into two main groups. The samples G-ST01 and G-BW01/02 represent fine-grained (20–200 μm), homogeneous sandstones with pore-filling cements consisting mainly of kaolinite and iron oxides (Fig. 4a,b). In contrast, the samples G-ST02/03 and G-BW03/04 are medium- to coarse-grained (200–630 μm) without pore-filling cement but with authigenic quartz overgrowths (Fig. 4c). Furthermore, the coarse-grained sandstones (G-ST03 and G-BW03) show features of brittle deformation.

Cathodoluminescence (CL) microscopy. CL microscopy provides information about the different luminescence colours of the detrital quartz grains. The diversity of CL colours in quartz depends on its origin and permits the recognition of specific physico-chemical condition of formation. Knowledge of the different CL colours provides the basis for provenance studies assuming that the CL colour of the clastic quartz grains remained unchanged from its original source rock. Zinkernagel (1978) established one of the first classification schemes of quartz CL colours in sandstones. He divided the CL phenomena into three groups: (I) 'violet' or blue luminescing quartz derived from igneous and high-grade metamorphic rocks; (II) 'brown' luminescing quartz from low-grade regional metamorphic rocks; and (III) non-luminescing quartz of authigenic (sedimentary) or hydrothermal origin.

Numerous investigations of a wide spectrum of quartz-bearing rocks showed that such a simple genetic correlation of quartz particles based upon their CL properties is not possible in every case, because quartz grains with similar CL colours and emission spectra may have grown under different genetic conditions. Nevertheless, a general classification is often

used tentatively including the following CL colour shades of quartz (e.g. Ramseyer *et al.* 1988; Götze *et al.* 2001): (i) blue to violet: plutonic quartz as well as quartz phenocrysts in volcanic rocks, and high-grade metamorphic quartz; (ii) red: matrix quartz and quartz phenocrysts in volcanic rocks; (iii) brown: quartz from regional metamorphic rocks; (iv) non- or weakly luminescing: authigenic quartz; (v) short-lived blue-green: hydrothermal and pegmatitic quartz.

The quartz grains of the investigated sandstones were classified according to their luminescence colours using the scheme brown CL, blue-violet CL, red CL. The frequency of the different CL colours was evaluated semiquantitatively. The results confirm the earlier conclusions drawn from the thin section analysis. The two sample groups can also be distinguished by their CL behaviour, i.e. the ratios of differently luminescing quartz grains (Table 3 and Fig. 5).

In samples G-ST01 and G-BW01/02 kaolinite is detectable due to its bright blue CL, randomly distributed within the pore space. In these samples the amounts of brown luminescing quartz grains are relatively high (Fig. 5a,b). In contrast, the samples G-ST02/03 and G-BW03/04 are characterized by high amounts of quartz grains with short-lived bottle green and blue CL which disappears after several seconds of electron irradiation and turns to a stable blue CL. This behaviour indicates an origin from a granitic (and/or pegmatitic) source (Matter & Ramseyer 1985; Götze *et al.* 2001). Another conspicuous feature of this sample group is the occurrence of brittle deformation (Fig. 5). In contrast to previous assumptions (Milliken & Laubach 2000), the fracturing of grains is not only limited to polycrystalline quartz grains of metamorphic origin. The results of the present study also proved the existence of fractured quartz grains of presumably igneous origin (blue CL, see Fig. 5c,d). The grain splinters are generally concentrated in the pore space, and sometimes the cracks are healed by non-luminescing secondary quartz (Fig. 5d).

The amount of detrital quartz grains of volcanic origin is low in all sandstone samples from the Görlitz region. Single grains with red CL and visible growth zoning were observed. Furthermore, no detrital feldspar was detected.

Technical properties. The results of the analyses of total water uptake ($W_{m,a}$) are summarized in Table 4. In general, this property depends

Table 3. *Amounts of differently luminescing quartz grains (in grain%) in sandstone samples from the Görlitz region*

Sample	Brown CL	Blue CL	Red CL
G-ST01	35 ± 4.0	64 ± 4.0	1 ± 0.8
G-ST02	27 ± 5.5	70 ± 5.7	3 ± 2.0
G-ST03	2 ± 4.7	95 ± 6.6	2 ± 4.7
G-BW01	57 ± 6.0	41 ± 5.9	1 ± 1.4
G-BW02	53 ± 5.2	47 ± 5.2	1 ± 1.0
G-BW03	10 ± 6.6	85 ± 7.7	5 ± 4.5
G-BW04	11 ± 8.4	87 ± 9.0	2 ± 3.6

The 2σ standard deviation was calculated according to Van der Plas & Tobi (1965)

Table 4. *Selected technical properties of sandstone samples from the Görlitz region*

Sample	$W_{m,a}$ (%)	Bulk density (g cm^{-3})	Solids density (g cm^{-3})	Total porosity (vol%)	Hg porosity (vol%)	'Closed porosity' (vol%)	r_{50} (μm)	Total pore volume (mm^3 g^{-1})	Micro-pores (<0.1 μm) (%)
G-ST01	6.0±0.4	1.99	2.60	25.20	24.36	0.84	6.2	122.4	1.62
G-ST02	5.0±0.4	2.13	2.66	20.00	17.40	2.60	14.0	81.7	0.65
G-ST03	3.5±0.1	2.24	2.66	15.80	13.61	2.19	11.2	60.8	0.98
G-BW01	n.d.	1.99	2.65	25.00	22.37	2.63	6.1	112.4	2.16
G-BW02	6.4±0.2	2.04	2.66	23.30	22.79	0.51	5.5	111.7	2.08
G-BW03	4.3±0.2	2.19	2.66	17.50	14.97	2.53	5.0	68.4	1.81
G-BW04	6.2±0.3	2.09	2.66	21.40	19.20	2.20	24.6	91.8	0.38

n.d., not determined

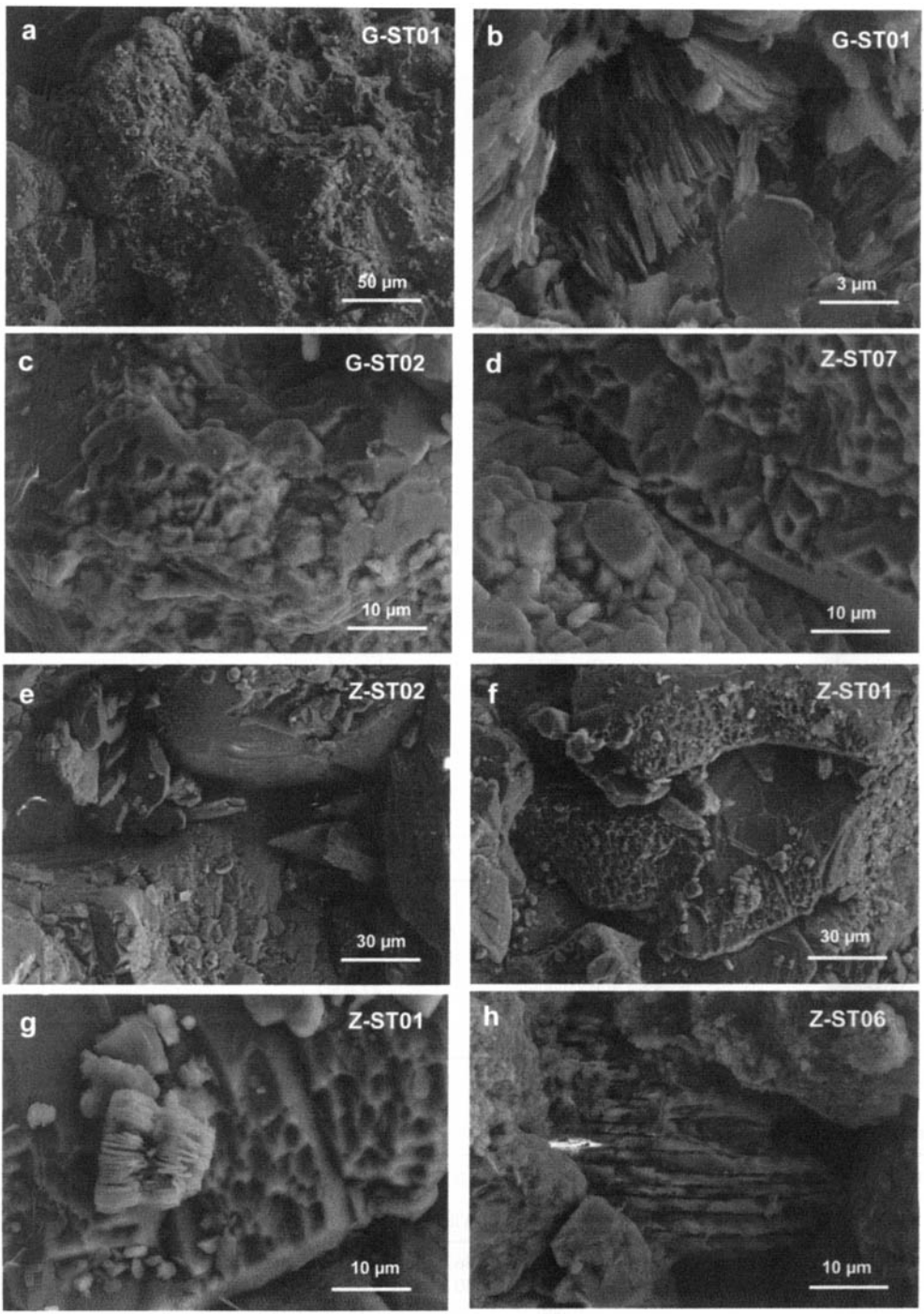

Fig. 4. SEM micrographs of selected sandstone samples from the Görlitz and Zittau region (**a**) Sandstone from the historical quarry between Hohkirch and Langenau (Görlitz region) which is predominantly cemented by kaolinite. (**b**) Detail of (a) showing flakes of kaolinite within a pore space. (**c**) The sandstone sample from the historical quarry Krauschteich near Niederpenzighammer (Görlitz region) is characterized by distinct diagenetic quartz grain overgrowths. (**d**) Secondary quartz growth at grain boundaries within a sandstone

mainly on the open pore space. The data are similar and scatter in the range from 3.5 to 6.6%.

Besides the bulk and solids density, porosity and pore-size distribution are important parameters for the characterization of porous natural stone material. The results shown in Table 4 demonstrate that the parameters fit into the range of typical building sandstones (Winkler 1994). While the bulk density increases with coarsening of grain size, the porosity correlates negatively with the bulk density.

The difference between the calculated total pore space and the pore space measured by Hg porosimetry varies between 0.5 and 2.6%. This value characterizes the closed pore space and pores with a diameter <3.8 nm, which cannot be measured by Hg porosimetry. An important parameter for the weathering resistance of building sandstones is their pore size distribution (Fig. 6). In particular the amount of micropores, i.e. pores with a diameter <0.1 μm, can influence the weathering behaviour and salt crystallization within the pore space of sandstones (Fitzner & Snethlage 1982). The results in Table 4 show variations of this parameter in the range between 0.4 and 2.2 vol%.

The comparison of all technical parameters determined allows the sandstone sample of the Görlitz region to be subdivided into two main groups (compare Table 4 and Fig. 6). Similarities exist between samples G-ST01 and G-BW01/02, and G-ST02/03 and G-BW03/04, respectively. This is in general accordance with the conclusions drawn from the mineralogical investigations.

Provenance of the ancient sandstone building material. The results of the mineralogical and technical investigations on ancient sandstone material of historical buildings in Görlitz as well as natural occurrences of potential source rocks lead to the conclusion that the sample material can be subdivided into two main groups: sandstones from the quarries of Langenau and sandstones from the quarries of Niederpenzighammer. Samples of the historical quarry of Langenau (G-ST01) show similarities with the building sandstones G-BW01/02 whereas the sandstones of the quarry Krauschteich near Niederpenzighammer (G-ST02/03) are similar to those of G-BW03 and G-BW04. This subdivision is based mainly on the results of grain size distribution, pore size distribution and the typical luminescence behaviour of the detrital quartz grains.

Hence assumptions concerning the provenance of historical sandstone material in the Görlitz region could be confirmed, even though no detailed information exists in any archive about the origin of the historically used building materials. It is suggested that the fine-grained sandstone material used for Biblisches Haus (G-BW01) and the Untermarkt 17 building (G-BW02) derives from the historical quarries of Langenau (G-ST01). The ancient medium-grained sandstone material of Schönhof in Görlitz (G-BW03) and the church in Deutsch-Ossig (G-BW04) quite likely derives from the historical quarries of Niederpenzighammer (G-ST03).

Zittau region

Mineralogical composition and texture of the sandstones. Mineralogical properties of sandstones of the Zittau region obtained from investigations of sample pieces as well as thorough thin section analysis are compiled in Table 2. Similarly to the sandstones of the Görlitz region, the material consists mainly of quartz sandstones with quartz contents >99%. Although the content of accessory minerals is below 1%, typical accessory mineral suites enable differentiation between the samples (Table 2). The Upper Turonian sandstones of the Waltersdorf district have accessory mineral assemblages consisting of tourmaline, mica, ilmenite, and rutile, whereas the Middle Turonian sandstones of the Oybin region in addition contain remarkable concentrations of zircon, monazite (and xenotime). In contrast, garnet is the only typical accessory mineral in the sample from Krompach (Hochwald).

Further results on internal quartz structures (polycrystallinity, undulatory extinction) and

sample from the Wändesteinbruch (Waltersdorf district). The authigenic quartz cement resulted in high mechanical strength of the sandstones. (**e**) Sandstone sample from the historical quarry Katzenkerbe (Oybin district) which shows distinct features of brittle deformation. Note the small fractured quartz grains wedged into the former pore space. (**f**) Sandstone sample from the historical quarry Teufelsmühle (Oybin district) showing a grain boundary with features of pressure solution in the contact zones. (**g**) Diagenetic kaolinite crystals on a quartz grain surface within a sandstone sample from the historical quarry Teufelsmühle (Oybin district). (**h**) Detrital feldspar grain (alkali feldspar) showing features of alteration and dissolution in this sandstone sample from the Leichensteinbruch (Waltersdorf district).

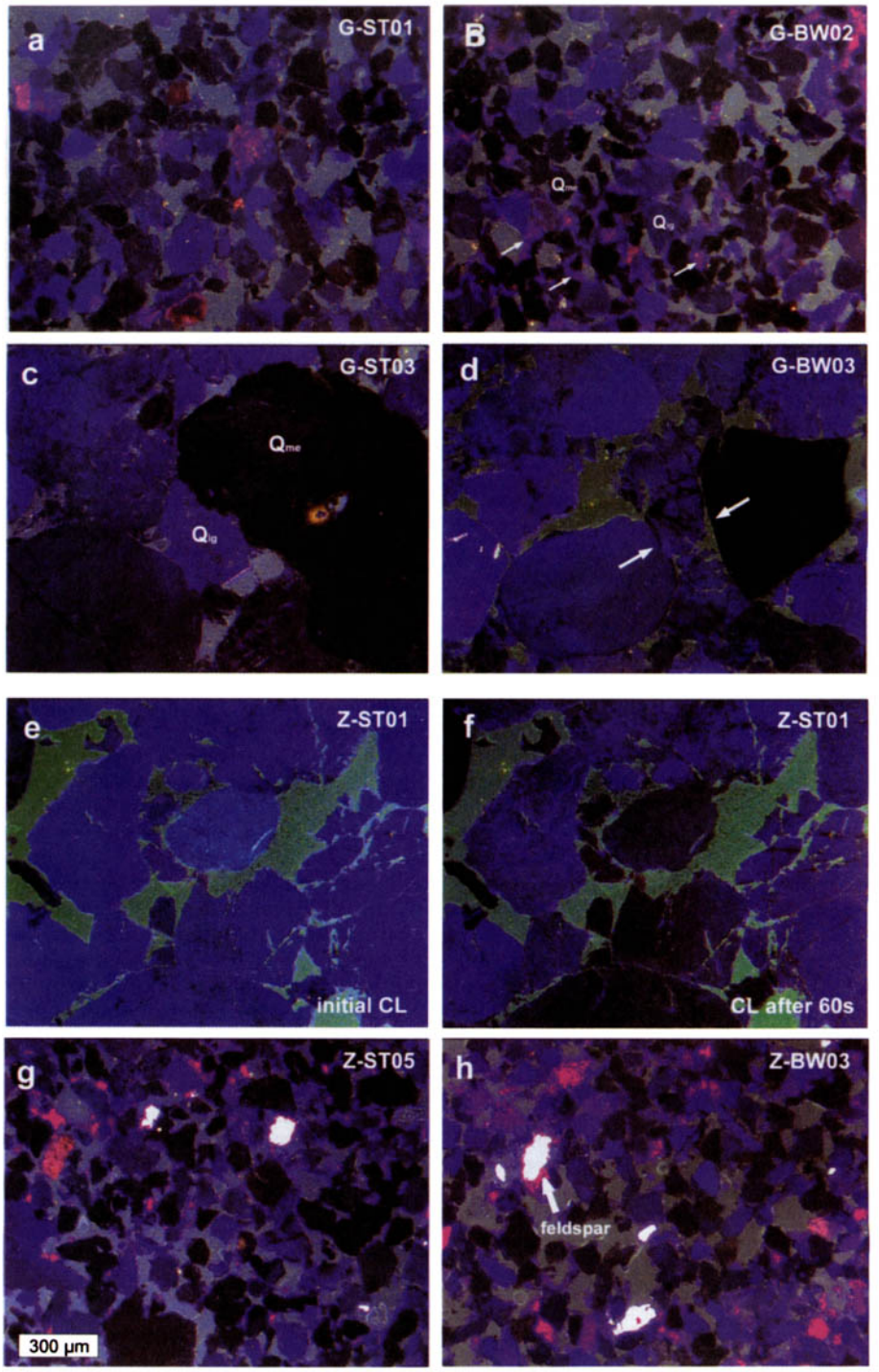

Fig. 5. CL micrographs of selected sandstone samples from the Görlitz and Zittau region (**a**, **b**) Sandstone G-ST01 from a historical quarry between Hohkirch and Langenau and G-BW01 from Biblisches Haus Görlitz. The micrographs illustrate very similar grain size distribution and CL properties of the detrital quartz grains (ratio of brown to blue-violet luminescing grains). The arrows point to kaolinite, which is randomly distributed

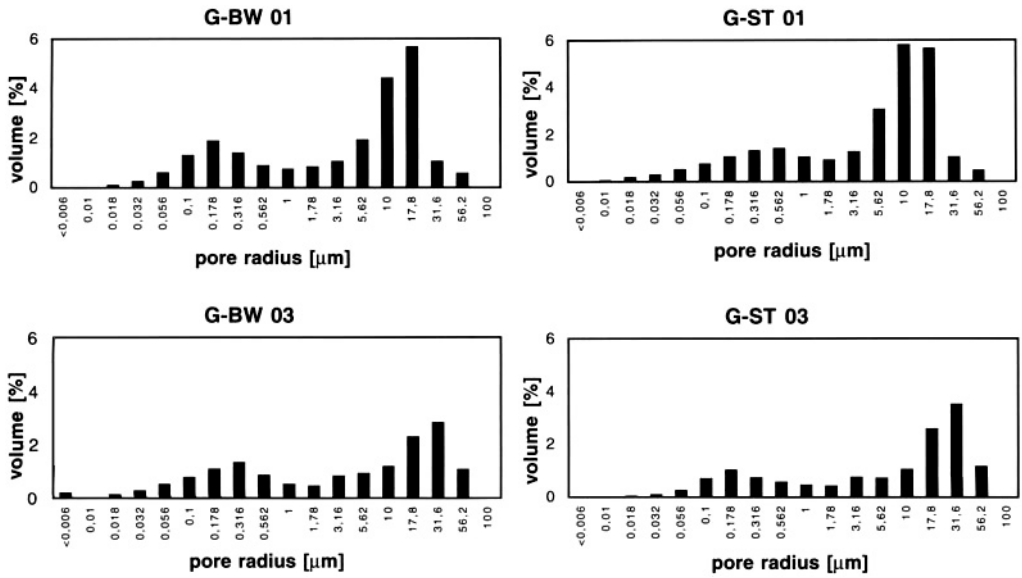

Fig. 6. Pore size distribution of selected building sandstones of the Görlitz region. The sample pairs G-ST01/G-BW01 and G-ST03/G-BW03 show a very similar pore size distribution pattern indicating identical source rock material.

granulometric properties (grain size distribution (see Fig. 7), roundness, sphericity), and porosity emphasize this trend. The samples Z-ST01/02, Z-ST08 and Z-BW01 represent coarse-grained, conglomeratic sandstones with almost no pore-filling cement, which show clear features of brittle deformation (Fig. 4e). The high amount of fractured, angular quartz grains is also reflected in the roundness parameters of these samples (bimodal distribution), which clearly differ from the other samples (Fig. 8). In addition, about 50% of the quartz grains in the samples Z-ST01/02 and Z-BW01 show polycrystalline internal structures.

The samples Z-ST07 and Z-BW02 are fine-grained (50–250 µm) and have in general no pore-filling cement but show features of diagenetic quartz growth (Fig. 4d). The sandstone samples Z-ST05/06 and Z-BW03 have similar grain size distributions to the former, but pore-filling cements consist of clay minerals and iron oxides.

Cathodoluminescence (CL) microscopy. In general, blue luminescing quartz grains prevail in the sandstones of the Zittau region (Fig. 5, Table 5), indicating a dominant igneous source of the clastic material. A characteristic luminescence feature was observed in samples Z-ST01/02 and Z-BW-02. The quartz grains in these samples exhibit a transient blue CL, which

within the pore space (the deep blue CL colour of kaolinite has been modified by overexposure). (**c**, **d**) CL micrographs of sample G-ST03 from the historical quarry Krauschteich near Niederpenzighammer and G-BW03 from Schönhof in Görlitz. The coarse-grained sandstones consist of high amounts of blue-violet luminescing igneous quartz grains (Q_{ig}) and low contents of metamorphic quartz (Q_{me}) with brown CL. The arrows mark features of brittle deformation, where a quartz grain is fractured between two adjacent detrital grains. (**e**, **f**) Sandstone sample Z-ST01 from the historical quarry Teufelsmühle, Oybin district. The coarse-grained, conglomeratic sandstone shows characteristic features of fracturing and brittle deformation, typical of the sandstones of the Oybin district. The comparison of the initial CL (e) and the CL after 60 seconds of electron irradiation reveals the transient blue CL which disappears during electron bombardment. This CL feature can be related to a secondary overprinting of the sandstones by migrationg fluids associated with Tertiary volcanism. (**g**, **h**) Samples Z-ST05 from the Haselbruch (Waltersdorf district) and Z-BW03 from a tombstone, Zittau. The two samples show very similar grain size distribution and CL characteristics of the detrital quartz grains. Remarkable is the occurrence of kaolinite in pore spaces and detrital grains of brightly luminescing feldspar.

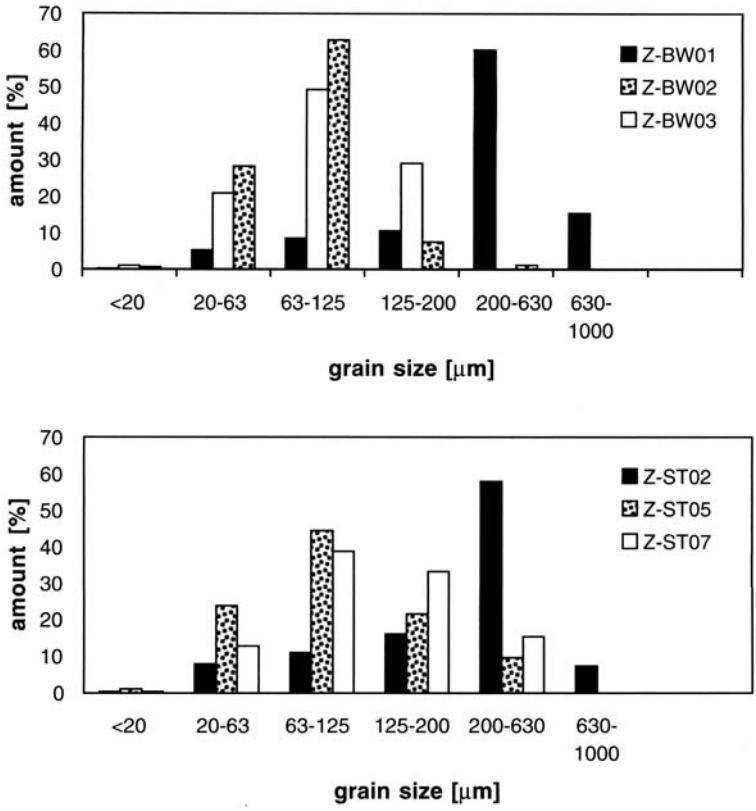

Fig. 7. Grain size distribution of investigated sandstone samples from historical buildings and quarries of the Zittau region.

Table 5. *Amounts of differently luminescing quartz grains (in grain%) in sandstone samples from the Zittau region*

Sample	Brown CL	Blue CL	Red CL
Z-ST01	13 ± 9.9	83 ± 11.2	4 ± 6.0
Z-ST02	3 ± 6.8	94 ± 8.8	3 ± 6.8
Z-ST03	12 ± 6.7	85 ± 7.3	3 ± 3.5
Z-ST04	21 ± 6.7	77 ± 6.9	2 ± 2.3
Z-ST05	39 ± 4.8	61 ± 4.8	0 ± 0.5
Z-ST06	32 ± 3.6	67 ± 3.6	1 ± 0.6
Z-ST07	35± 5.8	65 ± 5.8	0 ± 0.7
Z-ST08	8 ± 5.8	90 ± 6.5	2 ± 3.2
Z-BW01	9 ± 8.0	91 ± 8.0	0 ± 0.0
Z-BW02	26 ± 3.2	73 ± 3.2	1 ± 0.8
Z-BW03	27 ± 2.6	73 ± 2.6	1 ± 0.5

The 2σ standard deviation was calculated according to Van der Plas & Tobi (1965)

disappears after 30–60 s of electron irradiation (Fig. 5e,f). This is remarkable insofar as the short-lived blue CL appears not only on blue (granitic) quartz grains but also on brownish luminescing metamorphic ones. In accordance with results of other studies (Graupner *et al.* 2000), this can be interpreted as caused by secondary hydrothermal overprinting of the sandstones. Since the samples also show strong features of brittle deformation it is assumed that the sandstones were influenced by the Tertiary volcanism in this region. Similarly to the

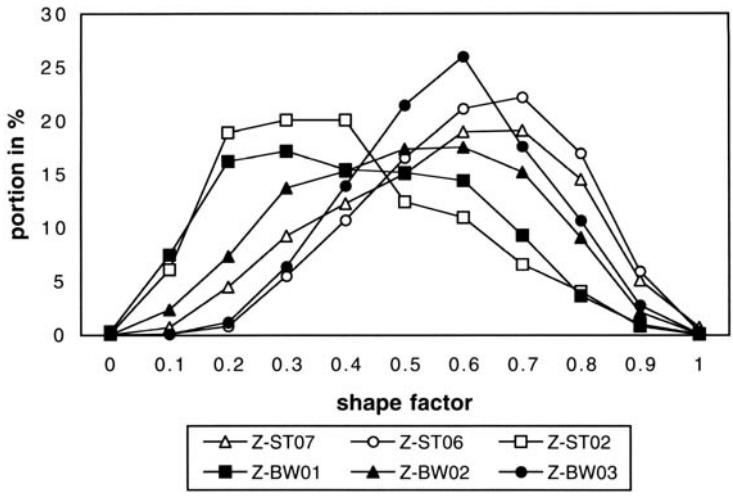

Fig. 8. Distribution of shape factor of detrital quartz grains of sandstones from the Zittau region as obtained by image analysis. The factor is calculated by the ratio of the theoretical smallest convex outline to the real grain outline. Accordingly, the ratio can vary between 0 (angular grains) and 1 (well rounded grains). Brittle deformation in samples Z-ST02 and Z-BW01 resulted in large amounts of small angular quartz grains with low roundness.

samples from the Görlitz region, the fracturing of grains is not limited to polycrystalline quartz grains of metamorphic origin but also occurs in blue luminescing quartz grains of probably igneous origin. Brittle deformation can be interpreted as a result of deformation during tectonic activities which is supported by the existence of features of pressure solution on detrital quartz grains (Fig. 4f). In addition, migrating hydrothermal fluids in the vicinity of volcanic eruptions led to the typical short-lived blue CL and also caused the crystallization of small flakes of authigenic kaolinite (Fig. 4g). This process is also emphasized by the occurrence of diagenetic quartz overgrowths and silica cement in these samples that resulted in increasing compressive strength of the sandstones of the Oybin district.

Another criterion for the differentiation of the sandstone samples of the Zittau region is the frequency of kaolinitic pore cement. In the samples Z-ST03, Z-ST05 and Z-BW03 high concentrations of kaolinite are detectable in the pore space due to their typical bright blue CL. The clay minerals in the pore-filling cement in sample Z-ST06 do not luminesce confirming the presence of illite.

Furthermore, in sample Z-ST06 approximately 6 grain% feldspar were detected by CL (Figs 4h, 5h). Because of the small grain size, the feldspar was not detectable by conventional polarizing microscopy. Residual grains of feldspar (≤1 grain%) were also detected in samples Z-ST04/05 and Z-BW03.

Technical properties. Some relevant technical properties of the sandstone samples of the Zittau region are summarized in Table 6. The total water uptake ($W_{m,a}$) scatters over a broad range between 1.7 and 10%. These values correlate well with the porosity: the more open the pore space of the samples, the higher their total water uptake.

The bulk density of the sandstone samples increases with increasing grain size whereas increasing porosity leads to a decrease of the bulk density. The coarse-grained sandstones have porosities <20% whereas the fine- to medium-grained material has porosities >20%. The difference between the calculated total pore space and the pore space measured by Hg porosimetry varies between 0.3 and 5.0%. Negative values obtained for the samples Z-ST06 and Z-BW03 (Table 6) are probably caused by analytical errors. The amount of micropores <0.1 μm is low and shows variations in the range between 0 and 1.5 vol%.

Provenance of the ancient sandstone building material. The investigation of ancient sandstone material of the Zittau region was a first attempt to characterize important building sandstones of this region. Because of the limited number of samples and the lack of historical data

Table 6. *Selected technical properties of sandstone samples from the Zittau region*

Sample	$W_{m,a}$ (%)	Bulk density (g cm^{-3})	Solids density (g cm^{-3})	Total porosity (vol%)	Hg porosity (vol%)	'closed porosity' (vol%)	r_{50} (mm)	Total pore volume (mm^3 g^{-1})	Micro-pores (<0.1 μm) (%)
Z-ST01	3.1±0.1	2.20	2.65	17.10	12.12	4.98	13.8	55.1	0.40
Z-ST02	2.2±0.4	2.41	2.65	9.10	8.03	1.07	6.0	33.3	0.12
Z-ST03	4.8±0.4	2.16	2.66	18.80	18.48	0.32	10.7	85.5	0.90
Z-ST04	7.3±0.2	2.08	2.66	21.80	20.16	1.64	17.6	96.9	0.17
Z-ST05	7.7±0.1	1.98	2.66	25.70	22.93	2.77	8.1	115.8	1.03
Z-ST06	5.8±0.1	2.09	2.66	21.50	22.54	–	6.0	107.9	1.52
Z-ST07	9.2±0.8	1.86	2.66	30.00	28.56	1.44	17.6	153.6	0.57
Z-ST08	4.7±0.4	2.20	2.65	17.10	15.78	1.32	17.0	71.7	0.16
Z-BW01	6.1±0.1	2.11	2.66	20.60	17.69	2.91	24.4	83.9	0.82
Z-BW02	7.5±0.6	1.92	2.65	27.60	25.95	1.65	13.3	135.1	0.00
Z-BW03	9.9*	1.88	2.65	29.10	29.21	–	12.2	155.4	0.75

* Only one measurement

concerning supply of building sandstones from ancient quarries, the results have a more tentative character. Nevertheless, significant similarities and differences between the different sandstone provinces and the ancient building materials could be drawn by comparison of mineralogical composition (main components and accessories), CL behaviour of the detrital quartz grains, grain size distribution, and porosity.

The sandstones of the Oybin district are coarse-grained and partially conglomeratic, and show typical features of secondary overprinting by volcanic activities (brittle deformation, transient blue CL). The ancient building sandstone of the ruin of the Oybin monastery (Z-BW01) can be assigned to this source rock type (Z-ST02).

The fine- to medium-grained sandstones of the historically important Waltersdorf district can be distinguished in particular by their varying amounts of detrital feldspar grains, characteristic accessory mineral assemblages, and the kaolinite content in the pore space. In these samples, CL microscopy provided the most useful information regarding the typical rock characteristics. The ancient building sandstones Z-BW02/03 can be assigned to the Waltersdorf source rocks. The sandstone from the Marienkirche in Zittau (Z-BW02) is very similar to the material from the historical quarry Helleberg (Z-ST07), whereas the tombstone in the Zittau monastery (Z-BW03) very likely consists of material from the Haselbruch (Z-ST05). Because of the limited number of samples these conclusions are only tentative and must be confirmed by additional studies.

Conclusions

The aim of the present study was to characterize ancient building sandstones as well as sandstones of historical quarries of the Görlitz and Zittau region. The study was designed to obtain mineralogical and technical data useful for characterization and differentiation of the various sandstone types. The results emphasize that the combination of macroscopic rock description, thin section and CL microscopy coupled with image analysis, scanning electron microscopy, and analysis of technical parameters (Hg porosimetry, total water uptake) is very useful for this purpose. In particular, CL has proved a powerful tool for provenance studies of quartz-rich building sandstones.

Based on results of phase composition, grain size distribution, texture, porosity and CL colours of detrital quartz grains, all ancient building sandstones of the Görlitz region investigated could be assigned to historically used source rocks. The material of Biblisches Haus and Bürgerhaus in Görlitz derives from a historical quarry located between Hohkirch and Langenau whereas the Schönhof in Görlitz and the church in Deutsch Ossig were built with sandstones from the Niederpenzighammer district. These results confirm ancient records obtained from documents in the Görlitz city archives.

For the first time, mineralogical and technical data were obtained for building sandstones of the Zittau region. Although few historical data exist about possible source rocks of the building material, the sandstones could be assigned to parent rocks of different districts. The sandstones used for the Oybin monastery derive from the historical quarry Katzenkerbe in the Oybin district. The material of the

Marienkirche in Zittau is very similar to sandstones of the historical Wändesteinbruch, Helleberg (Waltersdorf district). Finally, the sandstone material of a tombstone in a Zittau monastery appears to originate from the Haselbruch (Waltersdorf district).

Because of the limited quantity of sandstone material available of historical Zittau monuments (in most cases only drill cores) and possible petrographic variations of sandstone types within a specific quarry area, the data presented have to be interpreted with caution. More studies are needed to confirm the first conclusions drawn from this study. However, the present results provide a comprehensive basis for the interpretion of weathering damage on historical monuments and also give useful hints towards their successful conservation and reconstruction.

The data used in this publication have been acquired by S. Michalski during preparation of his Masters thesis (Freiberg University of Mining and Technology, 2000). The Hg porosimetry was performed at the Building Materials Laboratory of the Chair of Building Materials (Technical University Dresden). The Institute of Diagnosis and Conservation on monuments (IDK) in Dresden is gratefully acknowledged for financial support.

References

DIN 52103. 1988. *Prüfung von Naturstein und Gesteinskörnungen. Bestimmung von Wasseraufnahme und Sättingungswert.* 08/1988.

EHLING, A. 1998. *Die oberkretazischen Bausteine Schlesiens.* PhD thesis, University of Hannover.

FITZNER, B. & SNELTHAGE, R. 1982. Ein fluss der Porenradienverteilung auf das verwitterungsverhalten ausgewählter sandstein. *Bautenschulz und Bausanierung*, **5**(3), 97–103.

FITZNER, B., HEINRICHS, K., SIEDEL, H. & WENDLER, E. 1993. Herkunft, Materialeigenschaften und Verwitterungszustand des Schlesischen Oberkreide-Sandsteins an der Grabkapelle des Heiligen Grabes in Görlitz. *Jahresbericht des Forschungsprogramms Steinzerfall-Steinkonservierung*, **5**, 261–282.

GÖTZE, J., PLÖTZE, M. & HABERMANN, D. 2001. Origin, spectral characteristics and application of the cathodoluminescence (CL) of quartz: a review. *Mineralogy and Petrology*, **71**, 225–250.

GRAUPNER, T., GÖTZE, J., KEMPE, U. & WOLF, D. 2000. CL for characterizing quartz and trapped fluid inclusions in mesothermal quartz veins: Muruntau Au ore deposit, Uzbekistan. *Mineralogical Magazine*, **64**, 1007–1016.

MAGNUS, M. 1998. *Mikroskopische Phasen- und Kornformanalyse klastischer Sedimente mittels Bildanalyse am Beispiel des Unterturons der Elbezone.* Freiberger Forschungshefte, **C480**, TU Bergakademie Freiberg.

MATTER, A. & RAMSEYER, K. 1985. Cathodoluminescence microscopy as a tool for provenance studies of sandstones. *In*: ZUFFA, G. G. (ed.) *Provenance of Arenites.* Reidel, Dordrecht, 191–211.

MICHALSKI, S. 2001. *Systematisierung und mineralogisch-technische Charakterisierung von Sandsteinen aus der niedersächsischen und sächsischen Oberlausitz.* Masters thesis, TU Bergakademie Freiberg.

MILEWICZ, J. 1959. Die stratigraphische Einteilung der Kreideablagerungen der Nordsudetischen Mulde. *Zeitschrift für angewandte Geologie*, **5**, 261–263.

MILLIKEN, K. L. & LAUBACH, S. E. 2000. Brittle deformation in sandstone diagenesis as revealed by scanned-CL imaging with application to characterization of fractured reservoirs. *In*: PAGEL, M., BARBIN, V., BLANC, P. & OHNENSTETTER, D. (eds) *Cathodoluminescence in Geosciences.* Springer-Verlag, Berlin, 225–243.

NEUSER, R. D., BRUHN, F., GÖTZE, J., HABERMANN, D. & RICHTER, D. K. 1995. Kathodolumineszenz: Methodik und Anwendung. *Zentralblatt für Geologie und Paläontologie, Teil I*, **H. 1/2**, 287–306.

PETTIJOHN, H. F., POTTER, P. E. & SIEVER, R. 1973. *Sand and Sandstone.* Springer-Verlag, Berlin.

PIETZSCH, K. 1962. *Geologie von Sachsen.* Deutscher Verlag für Wissenschaft, Berlin.

PRESCHER, H. & WALTHER, H. 1977. *Museum für Geologie der Südostoberlausitz – Eine Einführung in die Ausstellung.* Städtische Museen Zittau.

RAMSEYER, K., BAUMANN, J., MATTER, A. & MULLIS, J. 1988. Cathodoluminescence colours of alpha-quartz. *Mineralogical Magazine*, **52**, 669–677.

RITTER, H. L. & DRAKE, L. C. 1945. Pore size distribution in porous materials. *Industrial and Engineering Chemistry, Analytical Edition*, **17**, 782–791.

VAN DER PLAS, L. & TOBI, A. C. 1965. A chart for judging the reliability of point counting results. *American Journal of Science*, **263**, 87–90.

WINKLER, E. M. 1994. *Stone in Architecture. Properties, Durability* (third edition). Springer-Verlag, Wien.

ZINKERNAGEL, U. 1978. Cathodoluminescence of quartz and its application to sandstone petrology. *Contributions to Sedimentology*, **8**, 1–69.

This page intentionally left blank

Bowing of marble panels: on-site damage analysis from the Oeconomicum Building at Göttingen (Germany)

A. KOCH & S. SIEGESMUND

Geowissenschaftliches Zentrum der Universität Göttingen, Goldschmidtstrasse 3, D-37077 Göttingen, Germany (e-mail: akoch4@gwdg.de)

Abstract: The use of natural stone panels or cladding material for building facades has led to some durability problems, especially with marble slabs. To examine the effects of intrinsic and extrinsic parameters on bowing, a very detailed study was performed on the Oeconomicum Building at the University of Goettingen. In total 1556 panels from the whole building were measured with respect to bowing using a bow-meter. The variation of bowing ranges from concave (up to 23 mm/m) to convex (up to −11 mm/m). The variation is not controlled by the position with respect to the geographical coordinates, height above ground, shadows, temperature etc. On the north facade the different rock structures visible on the panel surfaces are a result of the marble slabs being cut in different directions. The different degrees of bowing are associated with the structure of the marble since all other influencing factors are relatively constant (position, temperature, moisture content, building physics). Experimental data on the expansion behaviour under dry and/or wet conditions reveal different degrees of bowing with respect to the rock fabric and may help to explain the observed differences in bowing. The effect of the rock fabric, especially of the lattice preferred orientation in this case, clearly controls the deterioration of the marble and the degree of bowing. The bowing is also characterized by an increase in the porosity, decreasing values of ultrasonic wave velocities and flexural strength. The loss of cohesion in the strongly deteriorated panels is clearly visible in the microstructure by the open grain boundaries which are interconnected to intergranular microcracks.

Marbles and limestones exhibit a large variation in the way they weather including back-weathering, micro-karst, breakouts, coloration, formation of crusts, biological colonization, granular desintegration and flaking. In recent times, relatively thin slabs have been used for complete facades on commercial buildings in contrast to the more traditional thick stone facings. New developments in cutting machinery allow the design of slabs up to 15 mm thick. The most spectacular deterioration feature of these marble slabs is their bowing behaviour. Such phenomena, however, are well known from ancient grave stones (Grimm 1994, 1999). The now completely replaced facade cladding of Finlandia Hall in Helsinki (Ritter 1992) or the Amoco Building in Chicago (Trewitt & Tuchmann 1998), both made of Carrara marble, are often cited as examples. Presently, the Grand Arche de la Defense in Paris is under reconstruction due to fixing problems resulting from the bowing of stone panels.

Logan *et al.* (1993) explained the bowing of marble slabs on the Amoco Building as being due to the anomalous expansion–contraction behaviour of calcite combined with the release of locked residual stresses based on laboratory testing. The hypotheses of other researchers have required the presence of moisture or gravity variation (Bucher 1956; Bortz *et al.* 1988; Winkler 1994). However, all the existing explanations can be regarded as being due to intrinsic and extrinsic properties. The extrinsic properties include temperature, moisture, freeze–thaw cycles, environmental factors, conservation or cleaning effects, anchoring or fixing systems, joint widths, dimension and thickness of slabs. The intrinsic properties of the stone are determined by the mineralogical composition and the rock fabric (i.e. grain size, grain boundary configuration, shape and lattice preferred orientation as well as the microcrack fabric). These intrinsic properties control the mechanical and physical properties such as porosity, permeability, Young's modulus, compressive, tensile and flexural strength, thermal expansion and thermal conductivity.

To help in understanding the mechanical weathering of marble, a very detailed study on bowed marble panels was performed at the Oeconomicum Building of the University of Goettingen (Fig. 1). Different approaches were applied for the characterization of the type and degree of bowing. All panels were inspected with a bow-meter (Fig. 2) to determine the intensity of bowing with respect to the geometry

From: SIEGESMUND, S., WEISS, T. & VOLLBRECHT, A. 2002. *Natural Stone, Weathering Phenomena, Conservation Strategies and Case Studies*. Geological Society, London, Special Publications, **205**, 299–314.
0305-8719/02/$15.00 © The Geological Society of London 2002.

Fig. 1. Representative part of the Oeconomicum Building (western part, north facade).

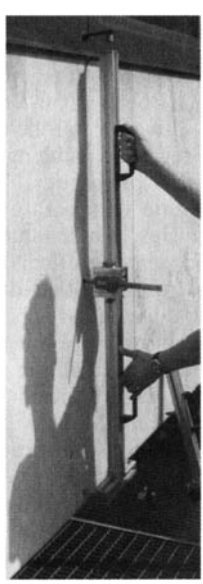

Fig. 2. Aluminium bridge (bow-meter) for measuring the bowing along the vertical centre line of the stone panels.

and physics of the building. Demounted panels were analysed in more detail in the laboratory; tests performed included mineralogical, fabric and petrophysical studies. Field studies suggest that bowing is also controlled by the rock structure, therefore emphasis was placed on the relationship between rock fabric, loss in strength and the type of bowing.

Building characteristics

The Oeconomicum Building at the University of Goettingen was built in 1966. The three-storied rectangular building has a length of 83 m in the north–south direction and a width of 55 m in the east–west direction with a height of 13 m. All facades are clad with panels of a white to dark strongly decorated marble (Peccia; see Fig. 1) of identical dimensions (length 128 cm, width 67 cm and thickness 3 cm). Each elevation has four rows of panels with windows in between (height 180 cm), each with a row of ventilation ducts (height 50 cm) above. Looking from the left to the right all panels were combined into groups of four except the outermost ones. The facades are interrupted only at two doors in the lowermost rows. The number of panels is 312 on the south facade, 308 on the north facade, 472 on the west facade and 464 on the east facade. In total 1556 marble panels were used as ornamentation on the building, corresponding to a total area of 1300 m^2. The open joint width between the panels was

originally 5 mm, but has now decreased to 0–3 mm; the joints were not filled with any kind of sealant.

The slabs are mounted with a kerf on a continuous rail at the bottom and are held by a 'ledge' at the top. There are no other mechanical anchoring or fixing systems. The cladding is ventilated with a cavity gap of 1–2 cm between the panels and the ferroconcrete structure.

Surrounding trees shelter parts of the facade. Some medium to large trees approximately 10 m high shade parts of the lower two rows on the east facade in the early morning. A similar situation is observed on the west facade where the shading of the trees influences the lower rows during the late afternoon in summer. On the south facade approximately half of the lower two rows are shaded by trees as well as parts of the third row. Some areas are permanently sheltered. The shading has occurred only in the recent past since the trees are quite young.

The original honed surface of the panels is still preserved except on parts of the lowermost rows where graffiti has been removed.

Goettingen is situated 167 m above sea level and features a climate typical for central Europe. The minimum monthly average temperature is 0°C in January and the maximum is 17°C in July. The average rainfall is 700 mm/a with a monthly average of at least 40 mm/month.

Experimental

To investigate the bowing phenomena of facade panels, systematic examinations of the cladding were carried out, along with detailed mapping of the cladding. Slabs from the building were demounted for further investigations to understand the mineralogy, rock fabric and important petrophysical properties with respect to the bowing.

The amount of bowing of each single panel was measured by an aluminium measuring bridge (bow-meter) with two supporting mounts, one with two legs, the other with one supporting leg ensuring stability (Fig. 2). The measuring bridge is equipped with a ruler fixed lengthways so that the distance between two supporting points is adjustable and measurable. To measure the bowing of one panel, the bow-meter is placed along the vertical centre line with support points at a distance of 1.20 m from each other and about 4 cm from the margin. A measuring mount including a vernier calliper is fixed concentrically between the support points. Before each measurement the vernier calliper was reset on a plane surface (for example a plate glass window). The bowing (B) of a panel is given as:

$$B = d / L \times 1000 \times a$$

where d (mm) is the measured value, L (mm) is the distance between two support points and a is a correction factor of 1.1. Positive values indicate concave and negative values convex bowing. Since all areas of a panel do not bow equally, the question arises as to how the degree of bowing is to be measured. A direct comparison of the results obtained from 50 panels where both vertical and diagonal measurements were recorded gives an empirically determined correlation factor of 1.1 between these different approaches (Fig. 3). Based on this correlation factor, all data are presented as diagonal measurements.

The character of the bowing was determined on four demounted panels using an orthogonal net with dimensions of 1.1 m × 0.6 m or 1 m × 0.6 m, respectively; measurements were taken every 10 cm to evaluate the small-scale geometry of bowing. The results are given as isolines illustrating lines of equal degree in bowing. In addition, at each of these points the ultrasonic wave velocities (V_p) was also measured.

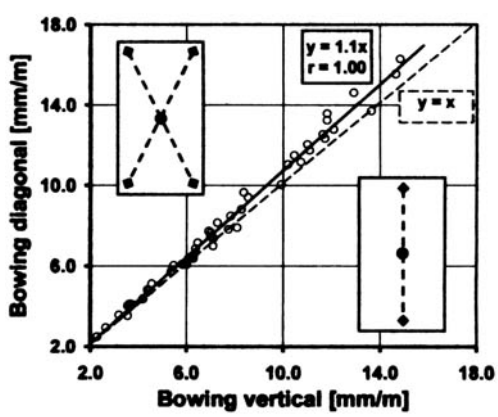

Fig. 3. Correlation between diagonal and vertical measurements, determined on 50 panels with a broad variation in bowing. The solid line represents the regression line, where r equals the correlation coefficient. The dashed line represents the perfect conformity of both measurements and is given for comparison only. The sketches illustrate the two different kinds of measurements and are each related to the corresponding axis. Diagonal bowing is determined as the median of two diagonal measurements per panel.

The temperature data of the panel surfaces were measured with a Raytek® Raynger ST 60 infrared thermometer. The porosity of representative samples from each panel representing different degrees of bowing was determined by a standard weighting method. The permeability of cylindrical samples was measured by the transient method using air as a flow medium. The gas pressure was kept constant at 0.5 MPa on one side of the sample. The determination of the flexural strength has been carried out in accordance with the standard EN 12372 (1999) on rectangular samples of 180 mm × 50 mm × 30 mm in two different directions orthogonal to the panel edges.

The mineralogy and fabric data were evaluated on orthogonal thin sections which were cut parallel to the macroscopic structures. To determine the texture, neutron diffraction was applied. The pole figure measurements were carried out at the time-of-flight neutron diffractometer NSHR, which is located at the pulsed reactor IBR-2 of the Frank Laboratory for Neutron Physics of the Joint Institute of Nuclear Research at Dubna (Russia) (Walther *et al.* 1995; Ullemeyer *et al.* 1998).

Results

The cladding material at the Oeconomicum Building is a coarse-grained Peccia marble ('Cristallino Virginio') from Switzerland. It consists mostly of a dark to white, sometimes light whitish calcitic matrix which is transected by brownish biotite veins or greyish graphite veins. These veins appear in a millimetre to centimetre scale, sometimes in a decimetre scale or they may be completely absent. The panels without any visible structures are homogenous and white in colour. The veins define the foliation as well as light white millimetre to centimetre thick elongated lenses or coarser-grained calcitic veins. The dark veins are sometimes folded, which is often observed at the panels from the north facade (see Fig. 1). All other claddings show a more or less visible foliation.

Most of the panels exhibit a remarkable concave bowing (Fig. 4a). Depending on the amount of bowing, panels may show cracks in the upper corners (Fig. 4b) up to 15 cm long as well as cracks at the junction with the kerf (Fig. 4c). At an advanced stage of deterioration these cracks can become transformed into larger-scale breakouts.

As illustrated in Figure 5 the degree of bowing is different at each facade. Nearly all panels are bent concave except for the east facade where row 2 shows a clear convex bowing of about −6.8 ± 2.3 mm/m. Row 1 of the east facade is also almost totally convex, but much weaker with a mean value of −1.5 ± 1.1 mm/m. The same observation occurs at parts of the east facade (row 3) and at the north facade (row 1). All other panels show a more or less concave bowing with average row values of 1.3 ± 1.0 mm/m (south facade row 1) up to 15.6 ± 2.9 mm/m (east facade row 4). The maximum value for a single panel was also registered in the latter row at 23 mm/m. The east facade holds the maximum of both concave and

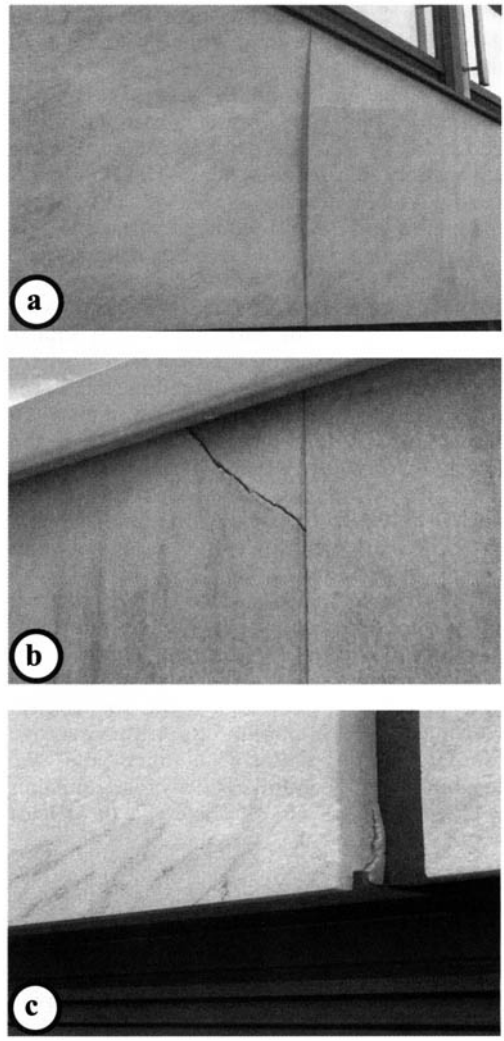

Fig. 4. Observed damage on the investigated marble panels. (**a**) Concave bowing (left panel). (**b**) Crack at the upper corner. (**c**) Crack initiated at the kerf.

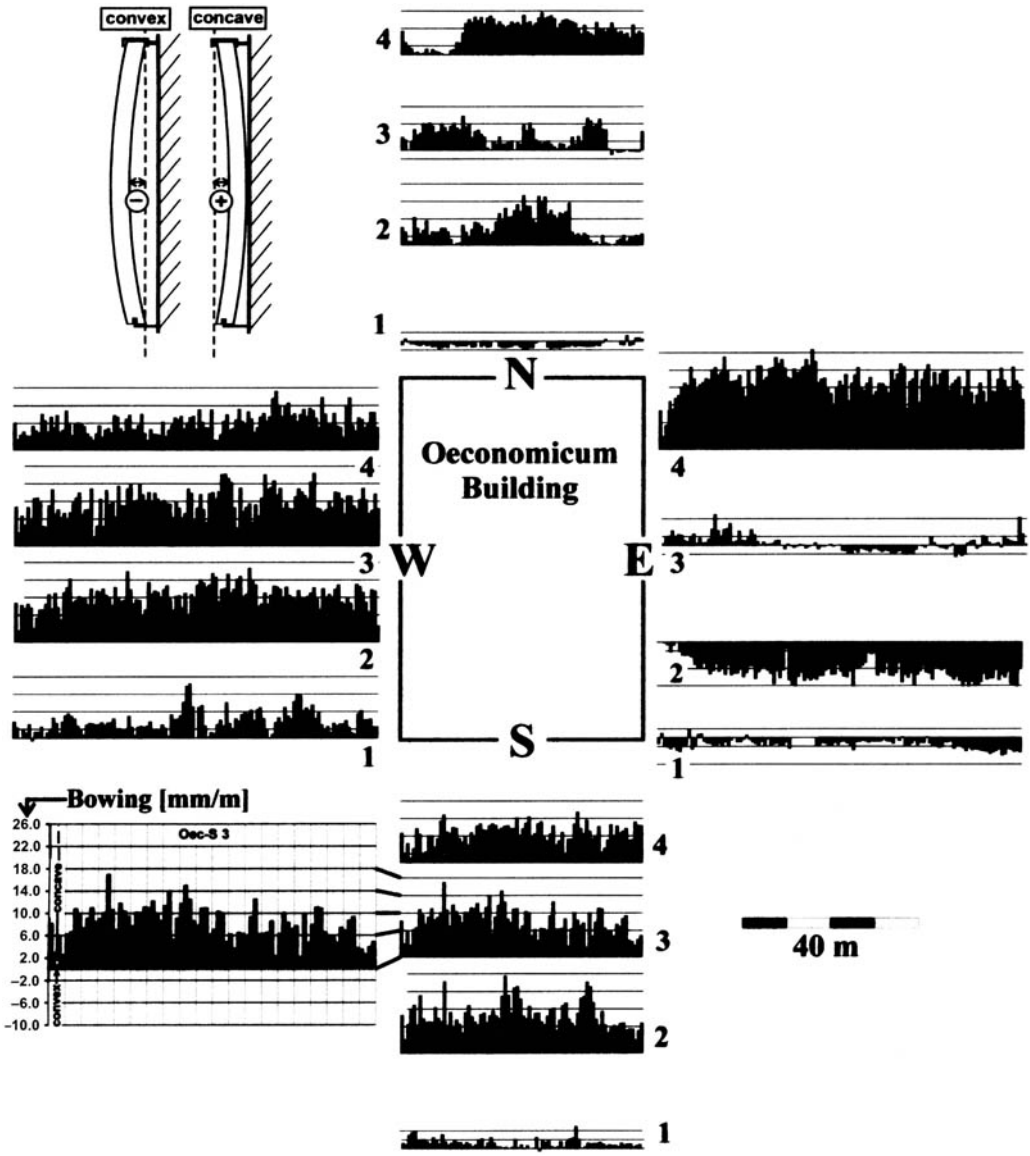

Fig. 5. Quantification of the bowing of all facade panels at the Oeconomicum Building depending on the orientation and the height. The histograms present the degree of bowing in the respective rows. As sketched at the upper left, positive values are equivalent to concave bowing and negative values are equivalent to convex bowing. To identify the amount of bowing by means of the height of the columns a complete diagram of row 3 (south facade) has been enlarged.

convex bowing (Fig. 5). In contrast, the west and south facades exhibit a more homogeneous distribution with a low mean bowing in the lowermost row (west facade: 3.7 ± 2.4 mm/m; south facade: 1.3 ± 1.0 mm/m) and a medium degree of bowing in rows 2–4 with mean values of 6–10 mm/m. The lowermost parts of each facade generally show the lowest values. The north facade exhibits comparable patterns with very weak convex bowing in row 1 and relatively weak concave ones in rows 2–4.

The bowing behaviour at the same height can

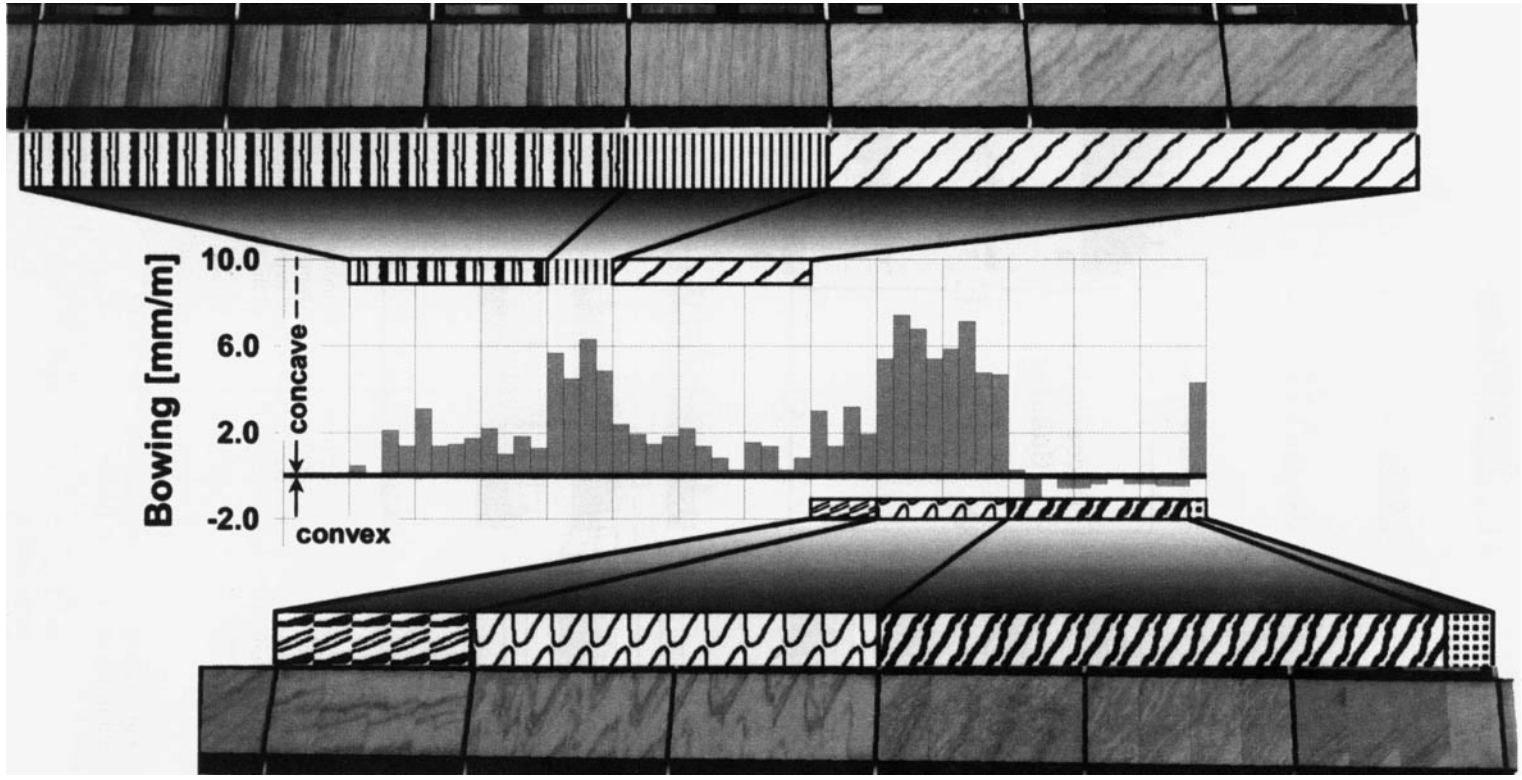

Fig. 6. Correlation between macrostructural fabric elements and bowing. The ornamental pattern of facade panels in the third row of the north facade is due to different block-cut directions and is also connected to different orientations of the foliation.

change from one group of panels to the next one. Very rarely is the bowing different from panel to panel within a single group. The macroscopically observed structure is more or less comparable for each single panel within each row of four panels. This means that the cutting direction, with respect to any metamorphic layering, foliation or macroscopic folds, was different for most of the groups. For aesthetic reasons the panels with identical ornamental or decorative elements, i.e. the same cutting direction, were arranged in such a way that panels with a comparable structure are combined together (Fig. 6; see also Fig. 1). Even if it is not yet known how the rock structure influences bowing, it is obvious from these findings that there is a causal connection between fabric anisotropies and the bowing of panels. Therefore, the close correlation between the fabric and the amount of bowing given in Figure 6 has to be considered without any doubt as a control on the deterioration mechanisms.

In order to illustrate the decay of stone panelling, detailed mapping of the building was found to be the most appropriate method (Fig. 7). Consequently, it is useful and necessary to distinguish different classes of deformation (Fig. 7). Figure 8 gives a first rough correlation between (a) an evaluated deformation class, and (b) the relative frequency of visible damage like cracks (length ≥10 cm) and breakouts (fracture ≥10 cm). From weak convex bowing (class −2: 1%) to strong concave bowing (class 5: 81%) an increase in cracking occurs. Furthermore, the ratio of panels showing both cracks and breakouts increases rapidly from class 3 (1%) to class 5 (31%).

Temperature is one of the main factors which may significantly influence the degree of bowing (Rosenholtz & Smith 1949; Sage 1988; Siegesmund *et al.* 2000). Measurements have been made at the panel surfaces to get an impression of how bowing is affected by temperature. Figure 9 illustrates the bowing surface temperature relationship measured on clear sunny days. Rows 1 and 2 of the south facade were investigated because these were areas where the highest expected temperatures would be influenced by different shadow impacts. The first dataset includes two different time periods (noon and afternoon) which takes into account moving shadows produced by trees. However, no significant difference in the range of temperature between the two rows can be observed. The temperature varies from 14 to 34°C at noon and from 21 to 32°C during the late afternoon, thus the differences in bowing between row 1 (1.3 ± 1.0 mm/m) and row 2 (8.7 ± 3.0 mm/m) cannot be explained exclusively by surface temperature. The temperature maximum in the middle of row 2 is in fact congruent with the bowing maximum.

To examine the effect of bowing on the mechanical and physical properties, as well as on the rock fabric, nine panels from different facades representing a broad variation of bowing were removed (Table 1). The panels were selected for their degree of deterioration: (a) panels with a low degree of bowing from sheltered places like the north facade; (b) panels with a medium degree of bowing exposed to the sun for part of the day and less sheltered places such as the west or east facade; and (c) panels with a high degree of bowing from very exposed locations like the south facade or, in one case, the uppermost row of the east facade (Table 1).

Porosity has been correlated with bowing and is demonstrated in Figure 10. Panels with a low degree of bowing show a porosity of 0.3% up to 0.7%. Strongly bowed panels have a porosity of up to 1.7%. Since the porosity has been measured in the panel centre it is possible that other parts of the panel have a much higher porosity. In conclusion it is obvious that the degree of bowing is correlated with an increase in the porosity.

A large scattering of the flexural strength (R_{tf}) is observed for weakly bowed panels with values 5.3 ± 0.5 MPa up to 13.4 ± 1.3 MPa (Fig. 11). The flexural strength decreases with an increase in bowing. In the medium to strongly bowed panels the strength variation is less pronounced with a range of 5.5 ± 0.2 MPa to 1.6 ± 0.2 MPa. In addition, the standard deviation of single values is significantly lower compared with panels of a high flexural strength (see error bars in Fig. 11).

The anisotropy of the flexural strength (A_{Rtf} (%) = $(R_{tf\,max} - R_{tf\,min})/R_{tf\,max} \times 100$) reaches values of up to 53%. The anisotropy of flexural strength depends on the orientation of the

Table 1. *Summary of the demounted panels*

Sample	Bowing (mm/m)		Facade	Row
L1	low	0.2	north	2
L2	low	0.0	north	2
L3	low	0.6	north	3
M1	medium	7.1	east	3
M2	medium	11.3	west	3
M3	medium	11.9	east	2
H1	high	17.1	south	3
H2	high	23.3	east	4
H3	high	25.6	sount	2

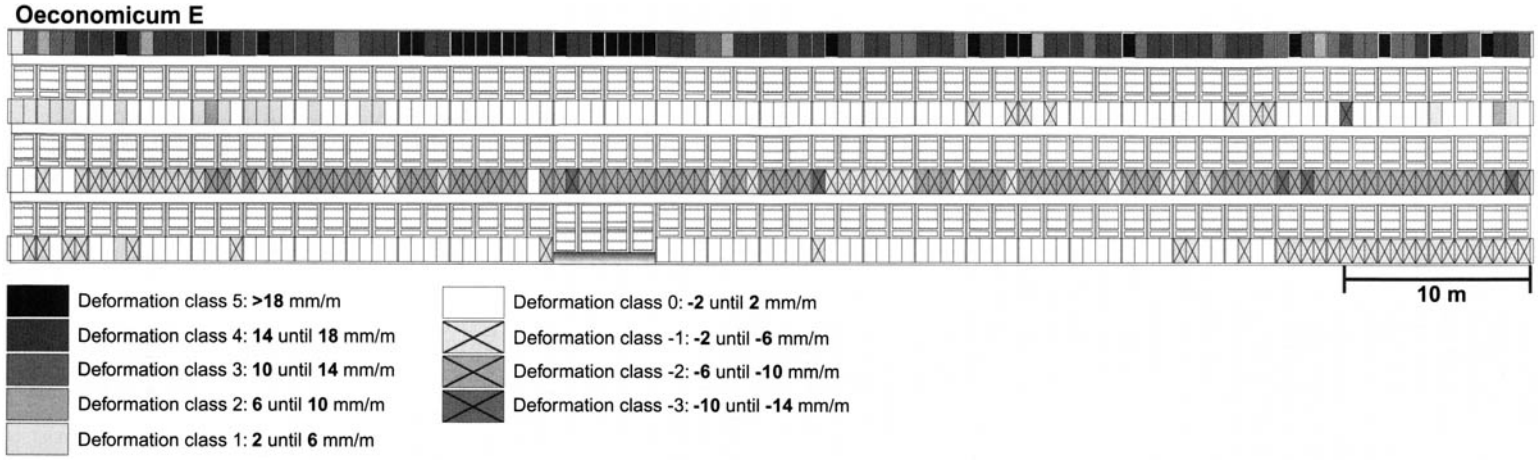

Fig. 7. Building map of the east facade of the Oeconomicum Building (true to scale) indicating the degree of deformation in the panels (compare with Fig. 5).

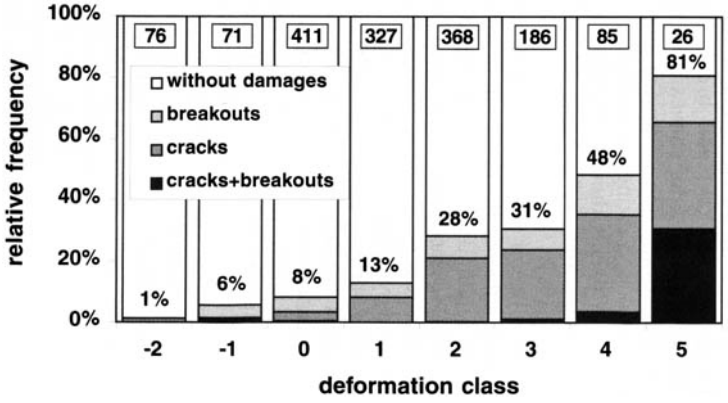

Fig. 8. Relative frequency of damaged panels depending on the deformation class. The absolute number of panels in each class is indicated at the top of the columns.

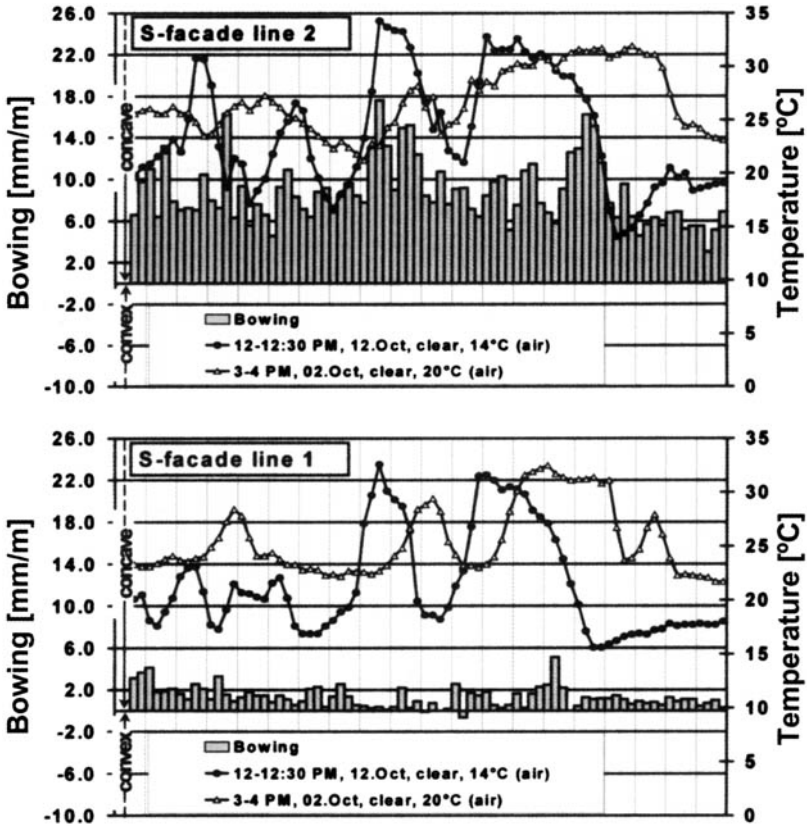

Fig. 9. Bowing surface temperature relationship of the lower two rows at the south facade.

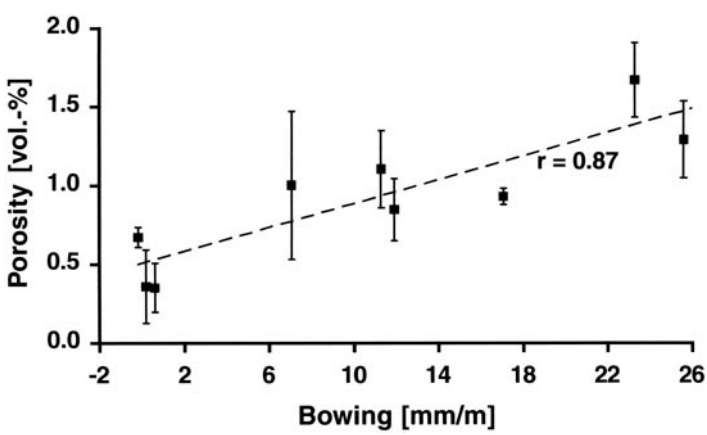

Fig. 10. Porosity of nine demounted panels depending on the degree of deformation (concave bowing). The standard deviations are indicated by error bars. The regression line (dashed) and the correlation coefficient (r) are given.

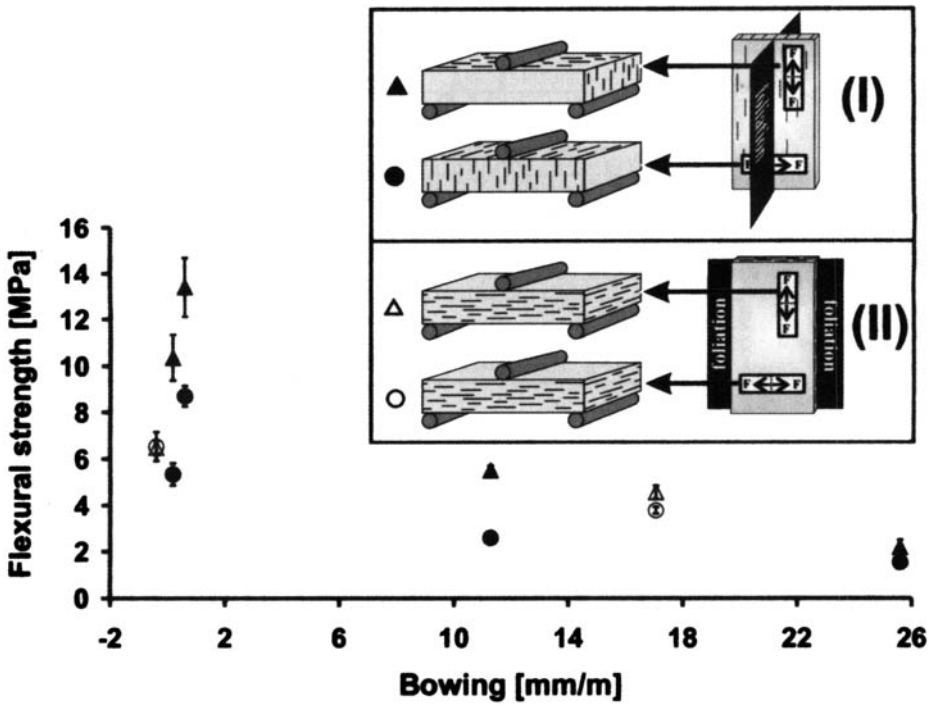

Fig. 11. Flexural strength of demounted panels depending on the degree of deformation (concave bowing). The values of flexural strength are given per panel in two directions of the vectored forces parallel to the panel edges. F equals force. The standard deviations are indicated by error bars.

foliation (see sketches in Fig. 11). The lowest values in strength are always observed where the direction of load is parallel to the foliation plane and where the resultant forces (F) are vectored perpendicular to the foliation (labelled as a solid circle in Fig. 11). In panels where the foliation is orientated as shown in sketch I of Figure 11, the flexural strength is reduced at least 30% in a direction where the resultant forces are vectored parallel to the short edge. In contrast, the panels with the smallest differences in flexural strength between two measured directions (anisotropies of 1% and 17%) show a foliation parallel to the panel surface (Fig. 11, sketch II), so that the resultant forces of the flexural strength are each measured parallel to the foliation plane.

The geometry of bowing for the most strongly deformed panels (H1, H2, H3, M2) is given in Figure 12. The V_p distribution is also illustrated, since ultrasonic measurements were often used as a non-destructive tool to quantify rock deterioration. This fact is based on the observation that the porosity and crack geometry control the reduction in velocity when progressively weathered (Weiss *et al.* 2002). All panels show a more or less symmetrical and homogeneous bowing. The isolines of equal bowing vary from a circular shape (Fig. 12a) to elliptical, where the ellipses can be elongated vertically (Fig. 12b,c) or horizontally (Fig. 12d). The most homogeneous distribution of the isolines in H1 (Fig. 12a) is recognized for panels where the surface is parallel to the foliation plane (compare with Fig. 11, sketch II), while a more elliptical distribution (Fig. 12b,d) is associated with a steeply inclined foliation with respect to the panel surface (compare with Fig. 11, sketch I). Looking at the V_p distributions (Fig. 12) two panels show relatively slow velocities in the range of 2.2–3.2 km/s (H1) and 1.7–3.1 km/s (H2). This is equivalent to a more highly deteriorated marble in the sense of Weiss *et al.* (2002). The distinctly higher velocities for M2 (3.6–4.5 km/s) and H3 (3.0–4.4 km/s) are measured parallel to the foliation (compare with Fig. 11, sketch I). The V_p minima of M2 and H3 are orientated parallel to the bowing maximum, while for H1 and H2 the pattern appears more complex.

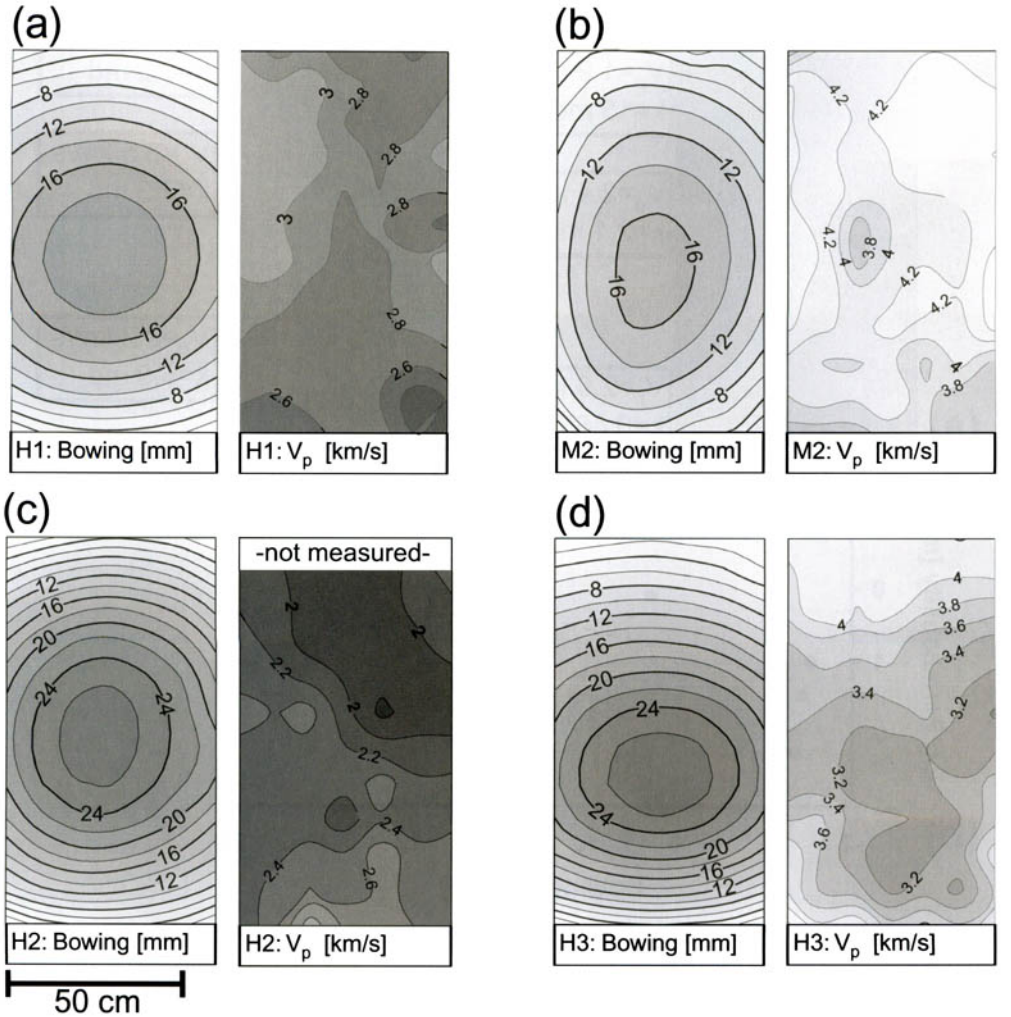

Fig. 12. Isoline pattern: bowing geometry versus V_p pattern. Dark grey indicates a strong bowing and a low V_p.

Two (H2, H3) of the four panels that feature the highest differences in V_p were also investigated with respect to their permeabilities to evaluate the interconnected pore space (Fig. 13a). A V_p minimum correlates with a maximum in air permeability. Comparing both panels it can be observed that H3 tends to higher values in permeability as well as in V_p corresponding to a measured direction parallel to the foliation. The behaviour of permeability across the different degrees of bowing of the panels is shown in Figure 13b. The permeability tends to increase with bowing, so a strong variation of permeability within single panels (H2 and H3) was found.

Discussion and conclusion

It is generally assumed that the deformation and deterioration of marble depends on a combination of intrinsic and extrinsic factors. The magnitude and orientation of bowing differ widely for the same marble type (see Fig. 5). When considering the north facade of the Oeconomicum Building, all extrinsic and most intrinsic factors are comparable. The influence of temperature and moisture, the effect of fixing systems and the building physics are more or less identical. The only difference is the orientation of the macroscopic foliation with respect to the panel surface, which suggests that slabs of

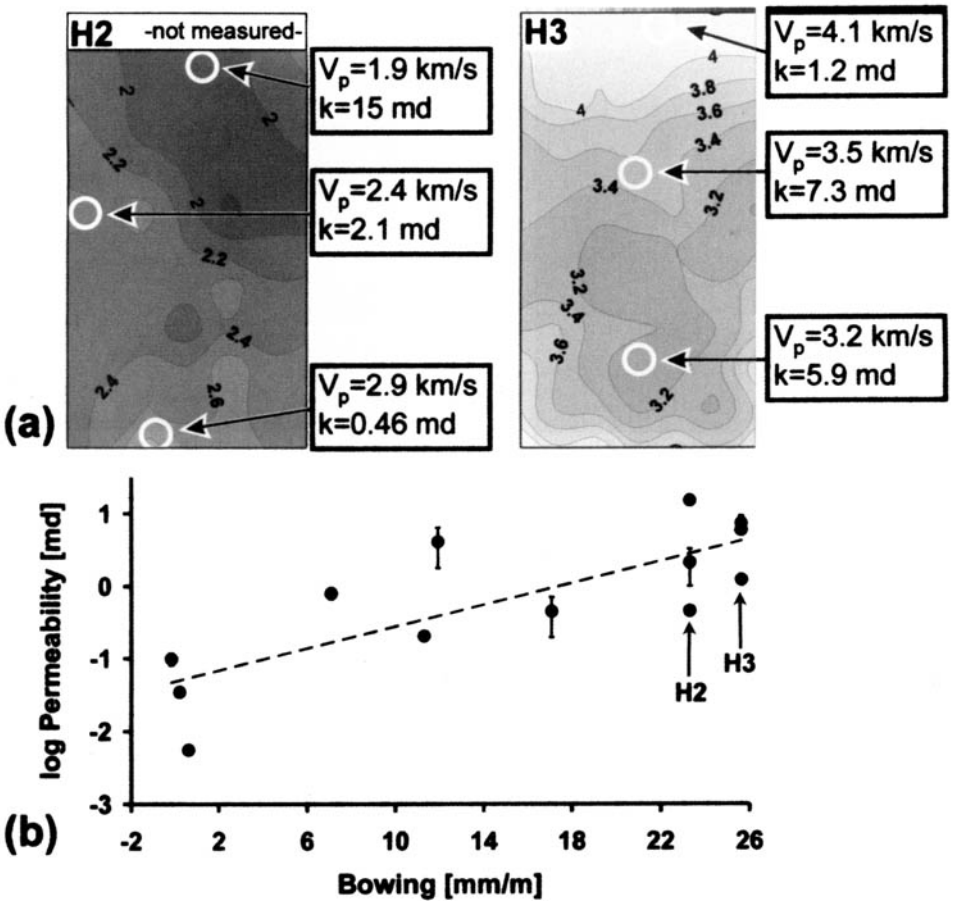

Fig. 13. (**a**) Comparison of ultrasonic velocity (V_p) and permeability (k) for panel H2 and H3. (**b**) Correlation between permeability (logarithmic scale) and deformation (concave bowing). The regression line (dashed) is given. The standard deviations are indicated by error bars. The permeability of panels H2 and H3 is given for three different measuring points (compare with (a)).

marble were cut in various orientations from larger quarry blocks (see Fig. 6). It is assumed that for aesthetic reasons panels with the same decorative elements were combined to form a group of four panels.

To understand the bowing, the microfabric of the strongly deteriorated Peccia marble was examined. The marble is characterized by a large grain size distribution, i.e. from medium to coarser grained (Fig. 14). The medium grain size is between 1 and 2 mm with a maximum of up to 6 mm. Domains with a coarser grain size exhibit a polygonal to interlobate shape, and straight to slightly curved grain boundaries (Fig. 14c). Less coarse grain size domains show an interlobate to sometimes amoeboid grain boundary geometry, where bulging frequently occurs, suggesting grain boundary migration as the predominant mechanism (Fig. 14a,b). More evidence of crystal-plastic deformation is presented by deformation twins and undulous extinction. Furthermore, the fabric is characterized by a preferred grain boundary orientation more or less parallel to the foliation (Fig. 14b,d). In thin sections from strongly bowed panels, open grain boundaries, which are frequently interconnected to intergranular microcracks, can be observed (Fig. 14d). Intracrystalline cracks along twin planes are more rare.

Quantified rock fabrics and their effects on physical properties may contribute significantly to the understanding of rock weathering. Thus, the crystallographic preferred orientation of calcite was measured. The texture was

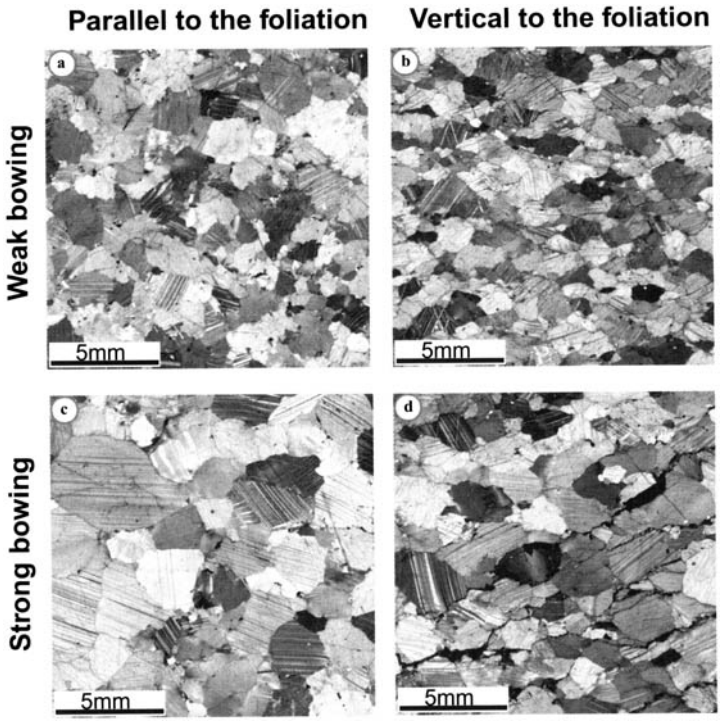

Fig. 14. Representative thin section images (crossed polarizers) from the demounted panels: (**a**) section parallel to foliation, weak bowing; (**b**) section vertical to foliation (horizontal to image plane), weak bowing; (**c**) section parallel to foliation, strong bowing; (**d**) section vertical to foliation (horizontal to image plane), strong bowing.

measured via neutron diffraction and quantified by simple mathematical operations (e.g. Siegesmund & Dahms 1994). The (006) pole figure (Fig. 15a) of calcite shows an intensity maximum normal to the foliation with a weak tendency to form a girdle distribution around the foliation plane, while the (110) poles are arranged on a great circle around the (006) pole density maximum (Fig. 15b). The crystallographic a-axes corresponding to the (110) poles are orientated within the foliation plane. The maximum intensity of 3.6 mrd (multiples of random distribution) of (006) indicates a strong texture (Fig. 15a) and consequently a pronounced anisotropy of the physical rock properties. The importance of calcite textures to the contribution of physical weathering due to thermal treatment has been quantitatively shown by Siegesmund *et al.* (2000) and more extensively by Zeisig *et al.* (2002). A general observation is that the maximum deterioration is closely linked to the c-axis maximum. The coefficient α of calcite is extremely anisotropic (Kleber 1959): $\alpha_{11} = 26 \times 10^{-6}\,K^{-1}$ parallel and $\alpha_{22} = \alpha_{33} = -6 \times 10^{-6}\,K^{-1}$ perpendicular to the crystallographic c-axis, i.e. calcite contracts normal to the c-axis and expands parallel to the c-axes during heating, while the opposite holds true when cooling.

To discuss these effects more quantitatively, preliminary results obtained for Rosa Estremoz marble may be used. Both marbles, Peccia and Rosa Estremoz, are comparable with respect to the lattice and shape preferred orientation (Fig. 15a,c) as well as in their grain boundary geometry. The thermal expansion behaviour was measured on cuboids (10 mm × 10 mm × 50 mm) parallel and normal to the c-axis and a-axis maxima as a function of temperature in the range between 20°C and 80°C (Fig. 15d). The thermal expansion of the samples is extremely anisotropic. As a result of the strong texture (Fig. 15c), a distinct elongation parallel to the c-axis maximum and a more or less constant value parallel to the a-axis concentration can be observed. Systematic measurements on marble reveal that heating and cooling lead to a loss of cohesion along grain boundaries (e.g. Sage

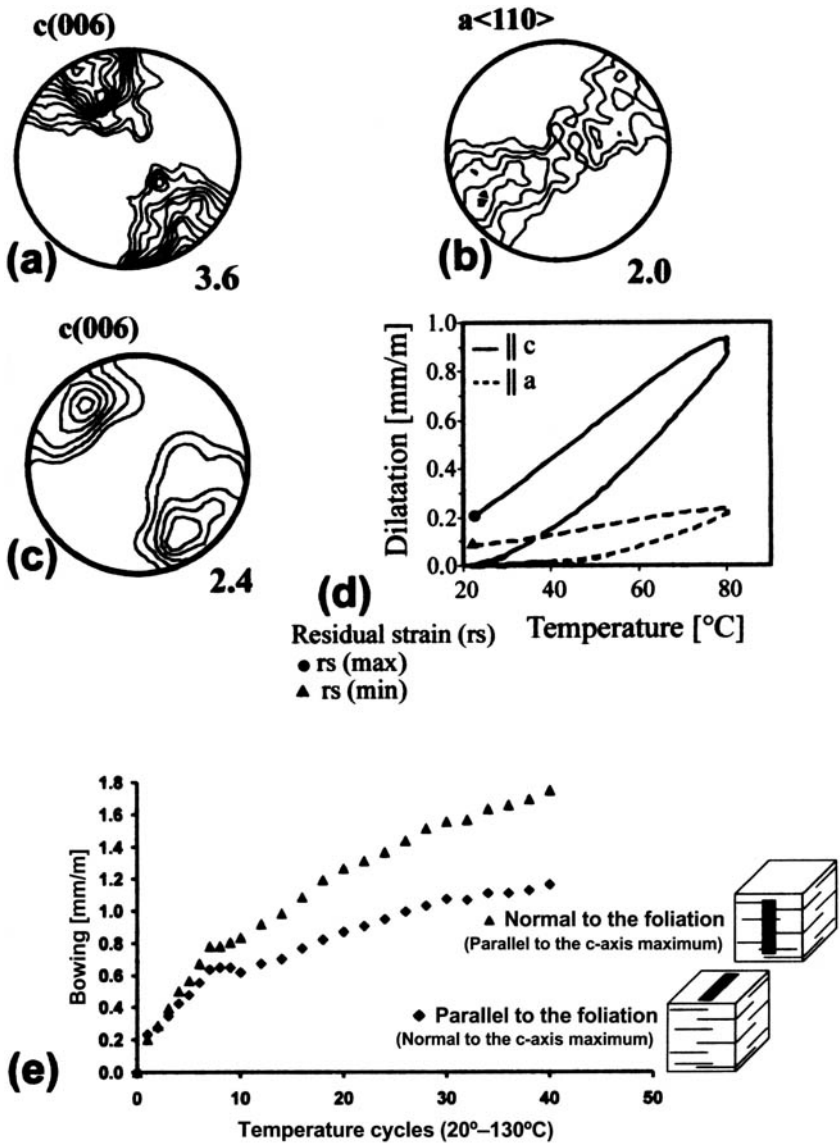

Fig. 15. Correlation between lattice preferred orientation, directional dependence of thermal dilatation and bowing velocity of marble. (**a**) Pole figure of the basal (006) planes of the Peccia marble. (**b**) Pole figure of the a <110> axis of the Peccia marble. (**c**) Pole figure of the basal (006) planes of the Rosa Estremoz marble: lower hemisphere; stereographic projection; lowest contour is equal to 1.0 multiples of random distribution; the relative maxima are given. (**d**) Experimentally determined thermal dilatation as a function of temperature given for Rosa Estremoz marble. (**e**) Bowing of Rosa Estremoz marble versus number of heating cycles (20–130°C). Each curve represents the mean bowing trend of three slabs (400 mm × 100 mm × 30 mm), taken from two different cut-directions with respect to the foliation.

1988; Franzini *et al.* 1984; Zeisig *et al.* 2002). A measurable quantity of the corresponding internal destruction of a marble is the residual strain, i.e. a permanent length change. The residual strain after one heating–cooling cycle of Rosa Estremoz varies between 0.2 mm/m and 0.1 mm/m (Fig. 15d). The effect of the thermal degradation can be easily recognized in the

Peccia marble, since most grain boundaries are open and interconnected to intergranular cracks (Fig. 14d).

The bowing potential of Rosa Estremoz was tested in the laboratory. The test was performed in such a way that the marble specimen (slab of 400 mm × 100 mm × 30 mm) was exposed to moisture on one side and infrared heating on the reverse side. The applied temperature ranged between 20°C and 130°C, and a total of 40 cycles was performed. The difference between both applied approaches was that in the bowing test the effect of moisture is also considered. From dry experiments it is well known (e.g. Battaglia *et al.* 1993) that after some heating cycles (not more than three to five cycles usually) the residual strain will not increase any more, while in the second approach, which includes moisture, the deterioration may increase progressively leading to the bowing effect. The continuous length changes with the applied cycles is clearly documented in Figure 15e. Again, two different samples were used with the same orientation as for the dry thermal treatment (see Fig. 15d). The deterioration rate is different and much faster for samples parallel to the c-axis maximum (1.7 mm/m), whereas perpendicular to these orientations a residual strain of 1.1 mm/m after 40 cycles occurred.

The thermal and/or moisture induced loss of cohesion along grain boundaries or the formation of microcracks is responsible for the increase in porosity with progressive bowing (Fig. 10). Consequently, the increase in permeability clearly indicates that the newly formed pore spaces developed an interconnected network which is supported by the increase in permeability at zones of more pronounced bowing (Fig. 13). Additionally, the reduction in the ultrasonic wave velocities in geometry and magnitude is strongly correlated with the deterioration (Fig. 12). The same observation can be drawn from the decrease in flexural strength (Fig. 11). All vectored physical properties are strongly dependent on direction as a function of the rock fabric.

The detailed observations presented here confirm most of the results that can be found in the literature. Moreover, this study shows that in addition the rock fabric is a very important parameter, when the degree of bowing and the loss in strength are discussed in terms of risk analysis. Caution is needed when trying to correlate the bowing without any fabric considerations. The effect of the rock fabric, especially the lattice preferred orientation, clearly contributes to the deterioration of marbles and finally the degree of bowing. However, this experimental approach cannot explain the processes which determine concave and convex bowing behaviour.

The help of A. Hüpers, C. Müller and G. Maslowski is gratefully acknowledged. We would also like to thank B. Grelk for comments and unreserved discussion. Careful review by T. Yates and G. Ashall is thankfully appreciated. S. Siegesmund thanks the German Science Foundation for a Heisenberg Fellowship.

References

BATTAGLIA, S., FRANZINI, M. & MANGO, F. 1993. High sensitivity apparatus for measuring linear thermal expansion: preliminary results on the response of marbles. *Il Nuovo Cimento*, **16**, 453–461.

BORTZ, S. A., ERLIN, B. & MONK, C. B. 1988. Some field problems with thin veneer building stones. *In: New Stone Technology, Design and Construction for Exterior Wall Systems*. American Society for Testing and Materials, Philadelphia, Special technical publication **996**, 11–31.

BUCHER, W. H. 1956. Role of gravity in orogenesis. *Bulletin of the Geological Society of America*, **67**, 1295–1318.

EN 12372, 1999. *Determination of flexural strength under concentrated load*. Deutsches Institut für Normung e.V., Berlin.

FRANZINI, M., GRATZIU, C. & SPAMPINATO, M. 1984. Degradazione del marmo per effetto di variazioni di temperatura. *Rendi conti della Società Italiana di Mineralogia e Petrologia*, **39**, 47–58.

GRIMM, W.-D. 1994. „... zum Steinerweichen" – Verformung von Marmorplatten auf alten Friedhoefen. *Naturstein*, Ulm, **10/94**, 52–57.

GRIMM, W.-D. 1999. Observations and reflections on the deformation of marble objects caused by structural breaking-up. *Zeitschrift der Deutschen Geologischen Gesellschaft*, Stuttgart, **150**(2), 195–235.

KLEBER, W. 1959. *Einführung in die Kristallographie*. VEB Technik, Berlin.

LOGAN, J. M. , HADEDT, M., LEHNERT, D. & DENTON, M. 1993. A case study of the properties of marble as building veneer. *International Journal of Rock Mechanics, Mining Sciences & Geomechanics*, **30**, 1531–1537.

RITTER, H. 1992. Die Marmorplatten sind falsch dimensioniert. *Stein*, **H.1/1992**: 18/19.

ROSENHOLTZ, J. L. & SMITH, D. T. 1949. Linear thermal expansion of calcite, var. Iceland spar, and Yule Marble. *The American Mineralogist*, **34**, 846–854.

SAGE, J. D. 1988. Thermal microfracturing of marble. *Engineering Geology of Ancient Works and Historical Sites*, 1013–1018.

SIEGESMUND, S. & DAHMS, M. 1994. Fabric-controlled anisotropy of elastic, magnetic and thermal properties of rocks. *In*: BUNGE, H. J., SKROTZKI, W., SIEGESMUND, S. & WEBER, K. (eds) *Textures of Geological Materials*. Oberursel (DGM Informationsgesellschaft), 353–379.

SIEGESMUND, S., ULLEMEYER, K., WEISS, T. & TSCHEGG, E. K. 2000. Physical weathering of marbles caused by anisotropic thermal expansion. *International Journal of Earth Sciences*, **89**, 170–182.

TREWITT, T. J. & TUCHMANN, J. 1988. Amoco may replace marble on Chicago headquarters. *ENR* (March), 11–12.

ULLEMEYER, K., SPALTHOFF, P. L., HEINITZ, J., ISAKOV, N. N., NIKTIN, A. N. & WEBER, K. 1998. The SKAT texture diffractometer at the pulsed reactor IBR-2 at Dubna: experimental layout and first measurements. *Nuclear Instruments & Methods in Physics Research*, **A412**(1), 80–88.

WALTHER, K., HEINITZ, J., ULLEMEYER, K., BETZL, M. & WENK, H. R. 1995. Time-of-flight texture analysis of limestone standard: Dubna results. *Journal of Applied Crystallography*, **28**, 503–507.

WEISS, T., RASOLOFOSAON, P., SIEGESMUND, S. 2002. Ultrasonic wave velocities as a diagnostic tool for the quality assessment of marble. *In*: SIEGESMUND, S., WEISS, T. & VOLLBRECHT, A. (eds) *Natural Stone, Weathering Phenomena, Conservation Strategies and Case Studies*. Geological Society, London, Special Publications. **205**, 149–164.

WINKLER, E. M. 1994. *Stone in Architecture*. Berlin.

ZEISIG, A., SIEGESMUND, S., WEISS, T. 2002. Thermal expansion and its control on the durability of marbles. *In*: SIEGESMUND, S., WEISS, T. & VOLLBRECHT, A. (eds) *Natural Stone, Weathering Phenomena, Conservation Strategies and Case Studies*. Geological Society, London, Special Publications. **205**, 65–80.

Bending strength properties of untreated and impregnated igneous, sedimentary and metamorphic dimension stones of different thickness

T. SAHLIN[1], J. STIGH[1] & B. SCHOUENBORG[2]

[1] *Göteborg University, Earth Sciences Centre; Geology, PO Box 460, SE-405 30 Göteborg, Sweden (e-mail: torgny@gvc.gu.se)*

[2] *SP, Swedish National Testing and Research Institute, PO Box 857, SE-501 15 Borås, Sweden*

Abstract: A production method has been developed that makes it possible to produce dimension stone tiles only 4 mm thick without high amounts of waste material. The tiles are impregnated with a mixture of potassium-based water-glass, water, colloidal silica, and Berol 048 (non-ionic surfactant), using a repeated cycling between vacuum and atmospheric pressure. Mineralogy, fabric, and porosity affect the mechanical properties of rock used as dimension stone in the building industry. Tests for bending strength have been performed on tiles of eight different untreated and impregnated samples of igneous, sedimentary, and metamorphic rocks. Samples of three different thicknesses (4, 7 and 10 mm) were used in the tests. The untreated rock samples that had a fine-grained texture, low crack density, high mafic mineral content or a distinct ductile metamorphic texture showed the highest bending strength values, whereas those that had high amounts of carbonate minerals, and high crack or void density exhibited the lowest values. The stone types that gained the most from impregnation, in general, were those with high crack or void density.

A production method has been developed that makes it possible to produce dimension stone tiles only 4 mm thick without high amounts of waste material. The tiles are impregnated with a mixture of potassium-based water-glass, water, colloidal silica, and Berol 048 (non-ionic surfactant), using a repeated cycling between vacuum and atmospheric pressure. There is no difference in colour or lustre between untreated and impregnated stone. Conventional dimension stone tiles used as building material are normally untreated and are at least 10 mm thick. The purpose of the impregnation treatment is to increase the mechanical strength and durability of stone tiles and to allow production of more tiles from a raw block by making thinner tiles. This is an advantage not only economically but also environmentally. In addition, the product is easier to handle due to its reduced weight.

Rocks differ in physical and chemical properties, depending on mineralogy, grain size, grain shape, porosity, and water content. The mechanical properties are important when using rocks as building materials. This study concerns bending strength, a crucial mechanical property when using dimension stones for flooring and outdoor cladding.

A test programme was set up in order to investigate differences in bending strength properties between impregnated and untreated stone material. The tests for bending strength were performed on eight different rocks under both impregnated and untreated conditions, and with three different sample thicknesses. Altogether four igneous (two granites, one larvikite, and one dolerite), two sedimentary (one sandstone and one limestone), and two metamorphic (one gneiss and one marble) rocks were chosen. The studied rocks exhibit large variations in mineralogical compositions, and in chemical and physical properties.

Previous work and scientific studies have been performed concerning treatment, conservation, consolidation, and to a lesser extent impregnation of already existing buildings, sculptures, and monuments totally or partly made up of stone material. However, most of the earlier investigations have been concentrated on sandstones, limestones, and marbles since these rocks are not as resistant to weathering as crystalline rocks such as granites, and they are the rock types most frequently used in old buildings and cultural artefacts, and the research in general has focused on historic preservation.

Rocks analysed

Eight rock types of different origin and with a wide range in physical and chemical properties

From: SIEGESMUND, S., WEISS, T. & VOLLBRECHT, A. 2002. *Natural Stone, Weathering Phenomena, Conservation Strategies and Case Studies*. Geological Society, London, Special Publications, **205**, 315–328.
0305-8719/02/$15.00 © The Geological Society of London 2002.

Table 1. *Rock types with geological name, international trade name and name in this study used*

Rock type	Geological name	International trade name	Name used in this study
Granite	Växjö granite	Tranås Red	Tranås granite
Granite	Iddefjord granite	Iddefjord Monolith Grey	Iddefjord granite
Syenite to monzonite	Larvikite	Blue Pearl	Blue Pearl larvikite
Dolerite	Manyika-type noritic dolerite	Nero Zimbabwe	Nero Zimbabwe dolerite
Sandstone	Dala sandstone	Älvdal Quartzite	Dala sandstone
Limestone	Holen/Segerstad limestones	Jämtland Limestone	Jämtland limestone
Gneiss	Migmatitic gneiss	Barents Red	Barents gneiss
Marble	Dolomitic marble	Snow White of Thassos	Thassos marble

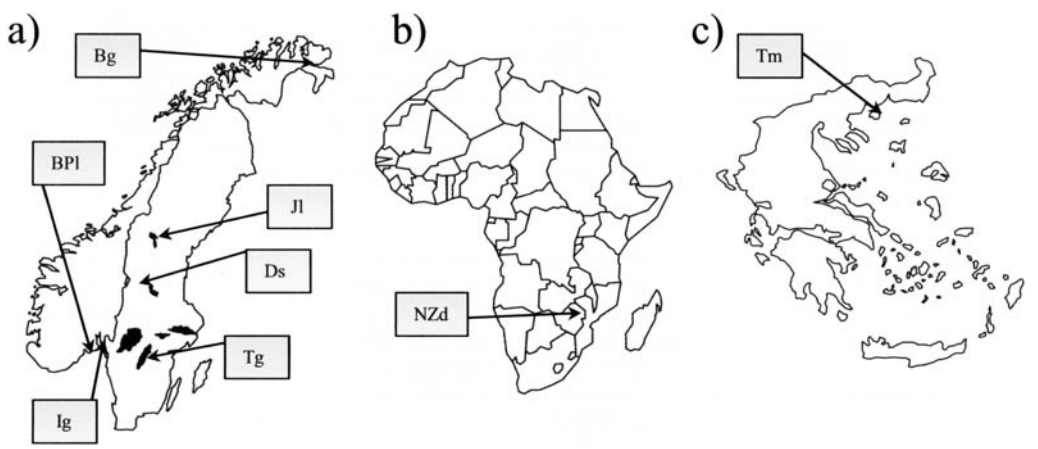

Fig. 1. Geographic localities of the studied rocks. (**a**) Norway and Sweden: Tranås granite (Tg), Iddefjord granite (Ig), Blue Pearl larvikite (BPl), Dala sandstone (Ds), Jämtland limestone (Jl), and Barents gneiss (Bg). (**b**) Africa: Nero Zimbabwe dolerite (NZd). (**c**) Greece: Thassos marble (Tm).

have been studied (Table 1). The geographic localities of the investigated rocks are shown in Figure 1. Mineralogical and textural analyses were performed using untreated rock samples. For determination of the mode of each rock type used, modal analysis was carried out on thin sections using a polarizing microscope.

Tranås granite

The Tranås granite is a variety of the Proterozoic Växjö granite (e.g. Persson *et al.* 1985; Jarl & Johansson 1988) quarried at Kungshult, approximately 7 km NNW of Tranås, Småland, southern Sweden (Fig. 1). The Tranås granite is produced in one quarry only and the annual production is about 600 m^3 (A. Janiak, pers. comm. 2000). Both raw blocks and finished products are produced for export and domestic use.

In hand specimen the Tranås granite displays pale, bluish-grey 5–10 mm quartz grains, 10–15 mm red feldspars, dispersed subordinate green epidote, and some dark minerals. Microcracks are randomly orientated. The texture is coarse-grained, phaneritic, and inequigranular. In thin section (Fig. 2a) the granite consists of undulose quartz (*c.* 40 vol%), slightly perthitic microcline (*c.* 40 vol%), sericitized plagioclase (*c.* 15 vol%), and minor biotite, chlorite, epidote, sphene, zircon, and opaque minerals. The quartz grains occur either as large deformation domains or as

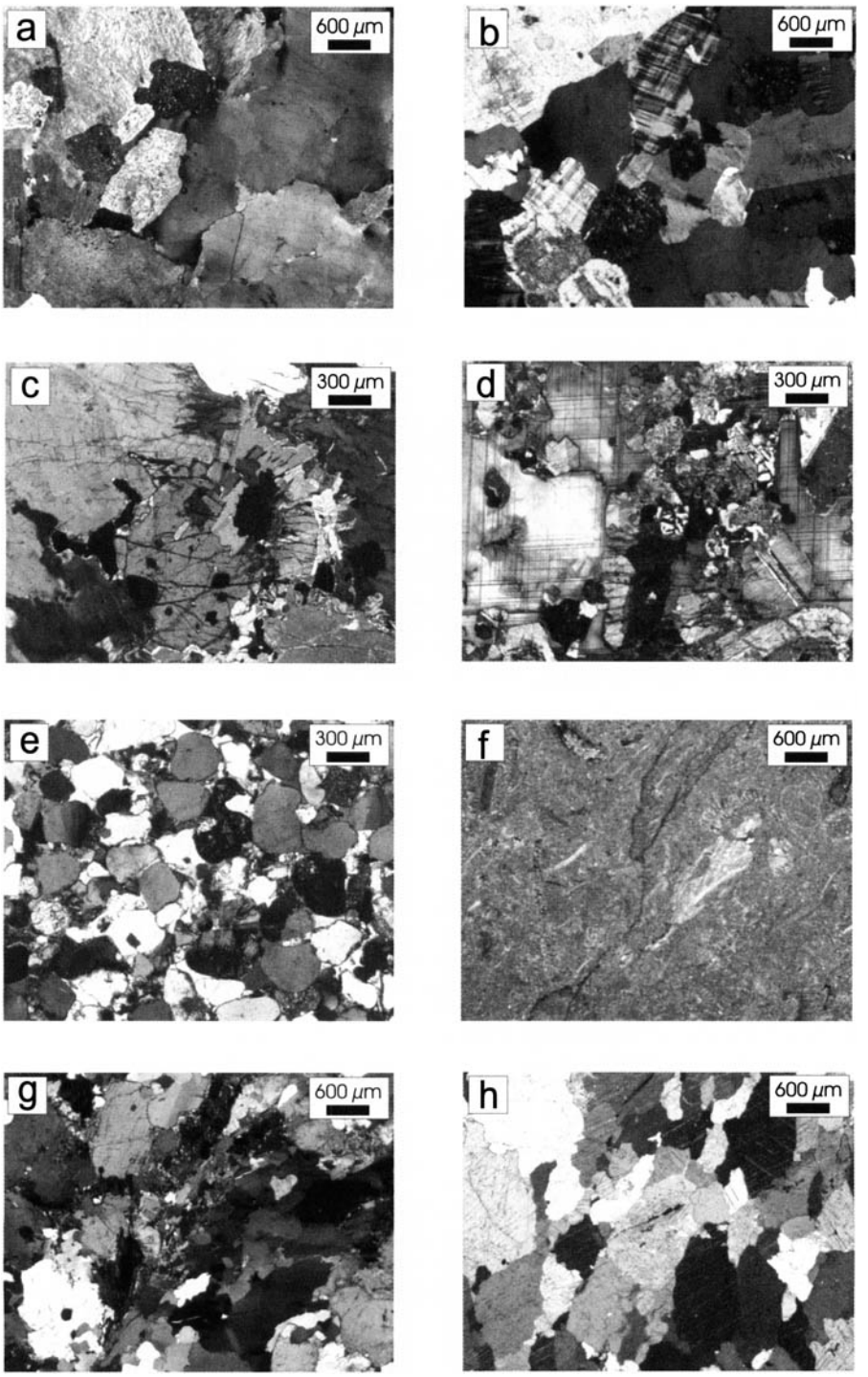

Fig. 2. Microscopic images of the analysed rock samples; polarized light with crossed polars. (**a**) Tranås granite. (**b**) Iddefjord granite. (**c**) Blue Pearl larvikite. (**d**) Nero Zimbabwe dolerite. (**e**) Dala sandstone. (**f**) Jämtland limestone. (**g**) Barents gneiss. (**h**) Thassos marble.

subgrains mixed with epidote. In the microcracks within larger mineral grains, epidote and some of the biotite grains are chloritized.

Iddefjord granite

The international trade name of the grey variety of the Neoproterozoic Norwegian Iddefjord granite is Iddefjord Monolith Grey or simply Iddefjord. This granite is quarried south of Halden, Østfold, south-eastern Norway (Fig. 1). Both raw blocks and processed products are produced for export and domestic use. Reusch (1891) first described the quarrying operations for this rock.

The Iddefjord granite belongs to the Bohus-Iddefjord batholith, which occurs in Sweden and Norway. The batholith is a composite granitic massif formed by multiple magma pulses (Eliasson 1992). Usually the granite is grey or reddish grey, but bluish grey varieties do occur (Pedersen & Maaløe 1990). In general, the granite is evenly grained, but slightly porphyric varieties do exist. The main minerals are plagioclase, microcline, and quartz. The accessory minerals are biotite, hornblende, muscovite, Fe-oxides, chlorite, apatite, sphene, and zircon.

In hand specimen the Iddefjord granite used in this study displays a phaneritic, inequigranular, and coarsely medium-grained texture. The quartz grains are grey and 1–2 mm, the feldspars primarily are grey and 1–10 mm, and the dark mineral grains are about 1 mm. In thin section (Fig. 2b), the granite is composed of strained, undulose quartz (*c.* 30 vol%), microcline with tartan twinning (*c.* 30 vol%), and plagioclase (*c.* 30 vol%). The accessory minerals are biotite (ordinary and chloritized varieties), chlorite, epidote, euhedral allanite, and some opaque minerals. The feldspars are in general poikilitic, enclosing chlorite and biotite. Quartz and feldspar show high microcrack density.

Blue Pearl larvikite

Permian larvikite, first described by Brøgger in 1890, is one of the most commonly used dimension stones in the world. It is produced from approximately 20 quarries in the Larvik district, Vestfold, southern Norway (Berthelsen & Sundvoll 1996) (Fig. 1). Raw blocks of a value corresponding to more than 47 million Euros are exported annually. Depending on qualitative characteristics such as colour, brightness, and lustre, the larvikite is divided into two different international trade names: Blue Pearl and Emerald Pearl. The Blue Pearl is more expensive and well known, showing a bluish, deep, intense, pearly lustre.

According to Brøgger (1890), the larvikite is a variety of augite syenite to monzonite consisting of rhomb-shaped ternary feldspars (with a distinctive schiller texture), barkevikite (Fe-rich hornblende), Ti-augite, and lepidomelane (Fe-rich biotite). Minor nepheline, Fe-rich olivine or quartz may be present. Different varieties of larvikite are to be found in the Larvik district (Berthelsen *et al.* 1996).

The coarse-grained, phaneritic, and inequigranular Blue Pearl larvikite consists almost entirely of feldspar grains, up to 3 cm of various shapes, with subordinate dark minerals. Most of the feldspar grains exhibit a moonstone schiller texture, which is due to an intimate cryptoperthitic lamellar intergrowth, and are microcracked. The variation in end-member composition, anorthite (Ca), albite (Na), and orthoclase (K), in the feldspar of larvikite is $An_{7-15}Ab_{61-67}Or_{8-32}$ (Engvoldsen 1991). In thin section (Fig. 2c), the Blue Pearl larvikite consists of cryptoperthitic feldspar (*c.* 90 vol%) and minor clinopyroxene, barkevikite, biotite, lepidomelane, Fe-rich olivine, augite, quartz or nepheline, sphene, and opaque minerals.

Nero Zimbabwe dolerite

The Proterozoic Nero Zimbabwe dolerite is quarried in northeastern Zimbabwe (Fig. 1). 'Black granite' is the common international trade name for a dark grey to black dolerite (microgabbro or diabase) used for monumental and decorative purposes (Barton *et al.* 1991). The main source of 'black granite' is in northeastern Zimbabwe in the Mutoko region. 'Black granite' of Zimbabwe has the international trade name Nero Zimbabwe, although some other names occur. This dolerite has been quarried from a number of places since the early 1970s from within a large, gently inclined sill between 50 and 100 m thick (Barton *et al.* 1991; Roberts 1992). Nero Zimbabwe is produced and exported mainly as raw blocks.

The Nero Zimbabwe belongs to the Manyika-type noritic dolerite (Barton *et al.* 1991) and is composed of almost equal amounts of pyroxene and plagioclase. The best quality is almost black in colour and has an even medium-grained texture. The plagioclase grains are cloudy due to the presence of numerous minute needle-like inclusions. These inclusions may affect the internal reflectivity of the plagioclase grains, enhancing the dark appearance of the polished stone (Barton *et al.* 1991; Roberts 1992). Some parts of the sill show concentrations of plagio-

clase grains and this phenomenon reduces the 'production quality' and hence the trade value of the rock.

In hand specimen the Nero Zimbabwe dolerite is greyish black, and the plagioclase is characterized by a silver-metallic lustre. The texture is fine- to medium-grained, subophitic, and aphanitic. In thin section (Fig. 2d), the essential minerals are plagioclase (*c.* 35 vol%), clinopyroxene (*c.* 30 vol%), orthopyroxene (*c.* 10 vol%), and a myrmekitic quartzo-alkali-feldspatic residue (*c.* 10 vol%). The accessory minerals consist of quartz, biotite, hornblende, and magnetite. Plagioclase is between 0.25 and 5 mm and is generally poikilitic, enclosing both pyroxenes. The orthopyroxene shows a weak pleochroism and occurs mainly as euhedral (*c.* 3 mm), lath-shaped grains. It also occurs as smaller intergranular grains. The clinopyroxene appear as large (*c.* 5 mm) lath-shaped grains and also as small (*c.* 1 mm) intergranular grains or intergrown aggregates often associated with the myrmekite. Fracture-infills of fine-grained alteration material (biotite and hornblende) are typical. The magnetite exhibits both euhedral and skeletal grains.

Dala sandstone

The Middle Proterozoic Dala sandstone clastic sequence is about 800 m thick and occupies an area of more than 6000 km^2 in west-central Sweden and adjacent parts of Norway (Lindström *et al.* 1991; Pulvertaft 1985). The sandstone is used as a dimension stone, and is produced from only one quarry in Mångsbodarna, the county of Dalarna, central Sweden (Fig. 1). The international trade name is Älvdal Quartzite. Both raw blocks and processed products are produced for export and domestic use. Annual production, in terms of raw blocks, is approximately 1500 m^3 (R. Eriksson, pers. comm. 2000).

The mineralogical composition of the ruddy and fine-grained Dala sandstone comprises the detrital components quartz (*c.* 70 vol%), feldspar (*c.* 15 vol%), and rock fragments (*c.* 10 vol%). The most common diagenetic minerals are quartz, illite, chlorite, hematite, titanium minerals, calcite, and feldspar (Hjelmqvist 1966; AlDahan 1985). The sandstone displays a quartzitic microcrystalline character and the grains are well rounded (Fig. 2e). The matrix consists of quartz.

In thin section (Fig. 2e), the Dala sandstone used in this study shows major undulose quartz, alkali feldspar with tartan twinning, sericitized plagioclase and minor calcite, hematite, and allanite. Hematite occurs between the quartz and the feldspar grains. The major minerals display a saccharoidal texture.

Jämtland limestone

The Jämtland Limestone, which is the common trade name for the Ordovician Holen and Segerstad limestones, is produced in a few quarries situated in the Östersund area in the county of Jämtland, central Sweden (Fig. 1). This limestone has been quarried since the twelfth century. Main products for export and domestic use are wall and floor casings, staircases, and window seats. Limestones of different colours, mainly brownish red and grey, are quarried and processed.

The Jämtland limestone used in this study is brownish red in colour and contains mainly calcite (*c.* 80 vol%), some quartz (*c.* 10 vol%), and hematite, which gives the brownish red colour (Karis & Strömberg 1998). In hand specimen most of the grains cannot be identified, except hematite fracture-infills and dispersed quartz blebs approximately 5 mm in length. In general, the limestone shows high crack density. In thin section (Fig. 2f), the Jämtland limestone contains calcite, some quartz and hematite. Quartz and hematite occur as fracture-infills. The texture is microcrystalline.

Barents gneiss

The reddish and migmatitic Barents gneiss is quarried in the area of Grasbakken in Nesseby, Finnmark, northern Norway (Fig. 1) and its international trade name is Barents Red. A bluish-grey variety, which is named Barents Blue, is quarried in Bugøynes approximately 25 km east of Grasbakken. The total resources of these dimension stones are estimated to be 1.3 $\times$ 10^6 m^3 (E. Lund, pers. comm. 2000) and are produced for export and domestic use as raw blocks and processed products.

The Barents gneiss belongs to the Archean Varanger Gneiss Complex and is characterized by red and dark diffuse banding, which is parallel, folded, and in some cases very irregular. It is generally medium-grained with granoblastic texture. The origin of some of the banded units is not certain although most lithologies are probably of igneous derivation (Dobrzhinetskaya *et al.* 1995). The metamorphic grade corresponds to amphibolite facies.

In thin section (Fig. 2g), the Barents gneiss consists of quartz (*c.* 40 vol%), plagioclase (*c.* 15 vol%), microcline (*c.* 30 vol%), biotite

(*c.* 15 vol%), and minor apatite. The microcline is perthitic and exhibits tartan twinning. Biotite constitutes the planar fabric and some of the grains are chloritized.

Thassos marble

In Greece, nearly 3500 marble producers and manufacturers employed more than 50 000 people in 1995. The most exploited area is Drama–Kavala–Thassos in the northeastern part of the country where more than 100 000 m^3 of white and greyish-white marble is produced and processed for export each year. Marble from the Thassos island (Fig. 1) has been quarried since the seventh century BC and is used in sculptures and buildings all over the world. The dolomitic Thassos marble used in this study is quarried in the northeastern part of the island and is known as Snow White of Thassos.

In hand specimen the Thassos marble is characterized by an extremely bright colour. The texture is fine-grained and saccharoidal. The marble has been dolomitized and dedolomitized periodically (Waelkens *et al.* 1988). Due to these processes voids have been formed. The marble consists of 86 wt% dolomite, 12 wt% calcite, and 2 wt% quartz (Alexandri 1991). However, no quartz has been found in the Thassos marble used in this study. In thin section (Fig. 2h), dolomite and calcite exhibit a bimodal grain size distribution. Larger grains are approximately 1.3 mm and the smaller ones are about 0.2 mm. Deformational twinning as well as sutured to curved planar grain boundaries occur. The texture is a combination of inequigranular, decussate (interlocking grains), and xenotopic (anhedral grains).

Impregnation chemical

The impregnation chemical is composed of four components: potassium-based water-glass, water, colloidal silica, and Berol 048 (Table 2). Potassium-based water-glass, also called potassium silica (SiO_2/K_2O), has a mole ratio within the range 0–4. The ratio of the water-glass used is 3.3 (trade qualities are usually 2.0–3.5). The viscosity of water-glass in general (including sodium-based water-glass) is between 10 and 1000 mPa s. However, it varies with temperature, especially within the range 0–60°C. An increase in the temperature will cause a significant drop in viscosity. pH is generally within the range 11–13.5 (trade quality). The density is generally between 1100 and 1650 kg m^{-3}.

Colloidal silica, or silica sol (SiO_2/Na_2O), has a mole ratio of approximately 100 and consists of 10–50 nm silica particles homogeneously dispersed in water. The silica sol used in this study has been developed by Eka Chemicals, Sweden. The trade name is Bindzil®30/220 with a particle size of 15 nm, a pH of 9.7 and a viscosity of less than 7 mPa s.

Berol 048, developed by Akzo Nobel Surface Chemistry, Sweden, is a non-ionic surfactant based on tridecyl alcohol. It has a hydrophilic character. The density at 20°C is 1020 kg m^{-3}. The viscosity at the same temperature is 140 mPa s. Berol 048 is used as a wetting agent during the impregnation process and 0.786 g is added per litre of impregnation solution.

Methods

Production of thin stone tiles

Rock slabs about 16 mm thick were cut from raw blocks using diamond cut-off wheels and flushing water. A vacuum chamber connected to a vacuum pump via an autoclave was used for the slabs intended to be impregnated. The pump was connected for 20 minutes at a pressure of approximately −1 bar, allowing moisture and dirt to escape from the crack and pore systems within the slabs. Inside the chamber, the slabs were treated with the impregnation chemical using a repeated cycling between vacuum and atmospheric pressure. After the impregnation

Table 2. *Components of the impregnation chemical*

Components	Density (kg m^{-3})*	Concentration (wt%)
Potassium-based water-glass	1200	64.6
Water	1000	8.5
Colloidal silica	1200	26.9
Berol 048	1020	+

*After the hardening/dehydration process the density of the impregnation chemical is approximately 2100 kg m^{-3}.
+0.786 g is added per litre of impregnation solution.

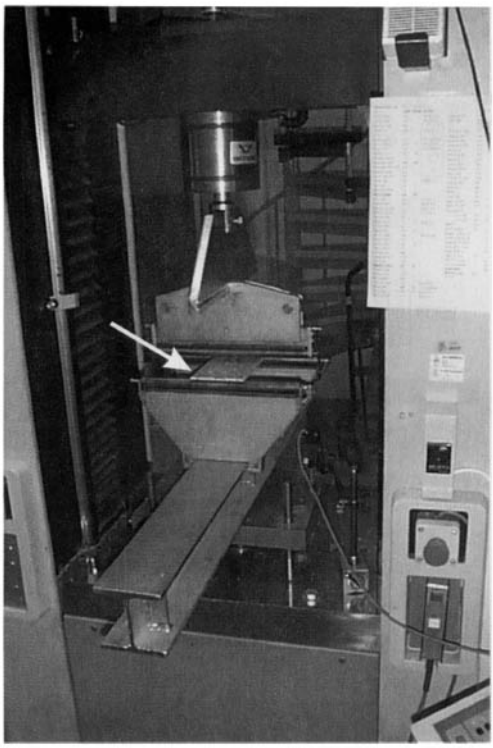

Fig. 3. The Instron 1253/8500 testing machine. The arrow points at a rock sample situated between the knife-edges.

process, the slabs were dried with infrared heating. The impregnated slabs were then further processed to their final thickness (4, 7 or 10 mm).

The rocks used are considered to be isotropic, except the Dala sandstone where the anisotropy, which is weak, is due to diagenesis. Since the rocks do not show preferred mineral orientations due to deformation all sample slabs were cut randomly from the raw block material. The samples (including those intended to be impregnated) were then mixed before further processing.

Bending strength tests

The bending strength tests were performed on impregnated as well as untreated samples. Prior to the tests, the impregnated samples were dried at 70°C for three days. The reason for this was to ensure that the impregnation chemical was completely dried and dehydrated before performing the tests. Five samples of each series of impregnated and untreated rocks were used.

The bending strength was measured according to DIN 52112-A on dry samples by use of an Instron 1253/8500 testing machine with a load cell capacity of 10 kN (Fig. 3). Rectangular prisms 200 × 100 mm in size were used. These were placed on two supporting knife-edges in a three-point load setup (Fig. 3). The sample thicknesses were 4, 7 and 10 mm, in order to be able to correlate the results of the impregnated samples with the corresponding thickness of the untreated ones. The samples were 'calibrated' on both surfaces but honed on the upper surface only. Calibration is used here in the same way as in the natural stone industry, i.e. a final control and finishing to the required dimension tolerances. The applied load rates were 1.18 N s^{-1} for the 4 mm thick samples, 3.63 N s^{-1} for the 7 mm samples, and 7.41 N s^{-1} for the 10 mm ones. The diameter of the supporting knife-edges, situated underneath and perpendicular to the length direction of a sample, was 20 mm. The span length between these supporting knife-edges was 180 mm. The loading knife-edge, situated above a sample, was placed at the centre of the span, parallel to the supporting knife-edges.

Results

The bending strength results are presented according to a subdivision into igneous, sedimentary, and metamorphic rock samples. The relationships between the impregnated and the untreated rock samples, irrespective of thickness, are shown in Figures 4 and 5.

Igneous rocks

The untreated Nero Zimbabwe dolerite showed the highest strength, independent of thickness in relation to the other untreated rocks studied. The untreated Iddefjord granite had the lowest strength.

For the impregnated samples, the dolerite maintained its high strength values. However, the Tranås granite showed both higher and lower strength values for the various thicknesses. The most marked improvement was in the Iddefjord granite. For example, the 4 mm impregnated samples were twice as strong as their untreated counterparts.

Similarly to the Iddefjord granite, the impregnated Blue Pearl larvikite displayed higher strength values than the corresponding untreated samples.

The impregnated 4 and 10 mm Nero Zimbabwe dolerite showed higher strength values relative to the untreated specimens of 4 and 10 mm thickness, respectively. However, the impregnated 7 mm samples showed lower strength than the 7 mm untreated ones.

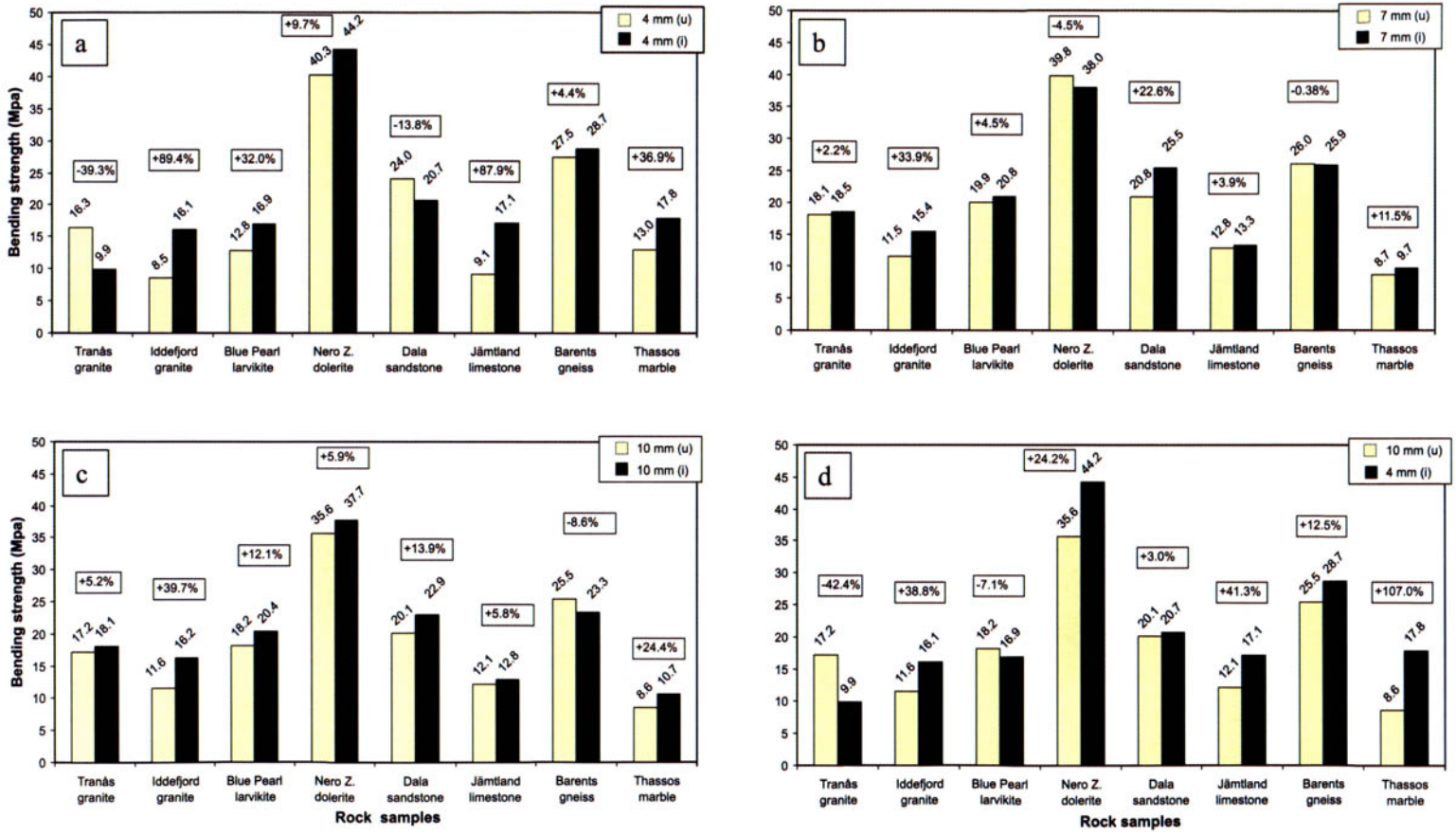

Fig. 4. Bending strength mean values of untreated (u) and impregnated (i) rock samples of different thickness. The value on top of each bar is the mean value of each sample series. The percentages correspond to the difference in strength between untreated and impregnated samples of each rock type of specific thickness. (**a**) 4 mm samples. (**b**) 7 mm samples. (**c**) 10 mm samples. (**d**) 10 mm untreated versus 4 mm impregnated samples.

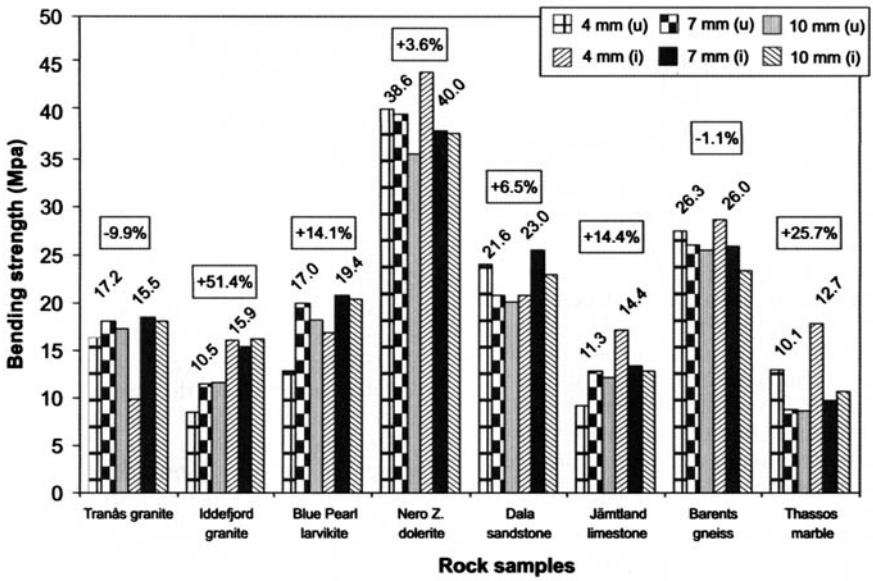

Fig. 5. Compilation of bending strength mean values of all untreated (u) and impregnated (i) samples. The values on top of bars correspond to the mean values of each 4, 7 and 10 mm untreated and impregnated sample series respectively. The percentages correspond to the difference in strength, taking into account all thicknesses, between untreated and impregnated samples of each rock type.

Sedimentary rocks

The Dala sandstone showed higher strength values than the Jämtland limestone, irrespective of thickness and impregnation.

The 7 and the 10 mm impregnated Dala sandstone showed higher strength than corresponding untreated samples of the same thickness. In contrast, the inverse relationship was shown for the 4 mm samples. A slightly higher strength was obtained for the 4 mm impregnated samples compared to the 10 mm untreated ones.

A much higher strength (almost 90%) was shown for the 4 mm impregnated Jämtland limestone compared to the 4 mm untreated samples, whereas only a slightly higher strength was shown for the 7 and 10 mm impregnated samples compared to the corresponding untreated samples. Higher strength was shown for the 4 mm impregnated samples compared to the 10 mm untreated ones.

Metamorphic rocks

The Barents gneiss showed higher strength values than the Thassos marble independent of thickness and impregnation.

Higher strength values were obtained for the 4 mm impregnated Barents gneiss compared to the corresponding untreated 4 and 10 mm samples. Approximately no strength difference was shown between the impregnated and the untreated 7 mm samples. Regarding the 10 mm impregnated versus the 10 mm untreated samples, the impregnated ones showed lower strength. When comparing each thickness separately, irrespectively of thickness, the impregnated Thassos marble showed higher strength compared to the untreated ones. The strength of the 4 mm impregnated samples was more than twice as high compared to the 10 mm untreated samples.

Coefficient of variation

For each sample series, coefficients of variations (CVs) have been calculated from the individual strength values and their corresponding means and standard deviations (Table 3). CVs can be used when comparing the spread of the observations in different sample series and hence information can be obtained about the heterogeneity of a rock. The CV is defined by:

$$\mathrm{CV} = \frac{100 \times S}{\overline{X}}$$

where S is the standard deviation and $\overline{X}$ is the mean value of a sample series.

Discussion

Mineral composition, grain size, grain shape, porosity, permeability, and water content are important factors that affect the physical properties of rock materials. The spatial distribution and the density of these factors can influence the rock in such a way that it will show different physical properties in different directions (anisotropy). These differences are controlled by mineral orientation and distribution, grain size distribution, foliation/stratification, and orientation and distribution of fractures or pore systems. Hence, the size and shape (scale factor) of a sample is important in this context, especially for heterogeneous and anisotropic rocks. This means that the dimension of the test specimen in relation to the setup of the strength machine (distance between supporting knife-edges) is an important influencing parameter.

According to Onodera & Asoka Kumara (1980), the mechanical properties of a rock depend upon its genetic texture including mineral composition and microcracks. Compressive strength and tensile strength show a linear increase with decreasing grain size or increasing grain boundary surface area per unit volume. In general, microcrack dimensions are comparable with grain size. The coarser the grain size the longer and wider are the existing microcracks. Tensile strength increases with decreasing grain size and crack density. Whereas compressive strength does not vary much with decreasing grain size, tensile strength is remarkably higher in the finer grained rocks.

Bending strength is a combination of compressive and tensile strength. During a bending strength test, the forces acting on a sample correspond to a combination of compressive and tensile stresses.

Untreated material

Bending strength mean values based on the three different thicknesses of each rock can be viewed in Figure 5. In this section the untreated rock samples, without considering specific thickness, are discussed in relation to bending strength properties of the rock types, their mineralogy, and fabric, including microcracks.

The granites (Tranås and Iddefjord) show similar mineral composition. The even-grained Tranås granite displays coarser grains but lower microcrack density than the inequigranular Iddefjord granite. The Tranås granite showed higher strengths compared to the Iddefjord granite, which most likely is primarily due to the microcrack density. Mafic (Fe-Mg rich) minerals are less fragile/brittle than felsic minerals. Fracture infills of epidote and biotite in microcracked larger quartz and feldspar grains are common in the Tranås granite, which could be related to the higher strengths. This type of infill cannot be recognized in the Iddefjord granite.

The Nero Zimbabwe dolerite showed the highest strengths. This may be due to its fine-grained texture and generally low crack density in combination with its mafic mineral content (e.g. the high pyroxene content).

The Blue Pearl larvikite showed intermediate bending strength values. This could be due to the fact that the less fragile mafic minerals are situated in between the more fragile microcracked and large-sized feldspar grains.

The Dala sandstone has a higher strength compared to the Jämtland limestone, the Thassos marble, and the igneous rocks except for the dolerite. The rather high strength values obtained by the sandstone may be due to the fine-grained mineral grains and well-cemented matrix.

The Jämtland limestone exhibited low strengths, which may be due to the fact that carbonate minerals are fragile, in combination with the high crack density.

The Barents gneiss showed high strengths; only the Nero Zimbabwe dolerite showed higher values. Gneiss is in general a heterogeneous and anisotropic rock. However, the Barents gneiss did not show high CVs (Table 3). On the other hand, this rock shows a distinct ductile metamorphic texture, almost of anatectic character, which may affect the strength.

The Thassos marble showed low strength values, probably because carbonate minerals are fragile in combination with the presence of voids.

Bending strength and thickness dependence

Bending strength is dependent on sample size including its thickness. A thicker sample may contain larger defects, affecting its strength ('thickness defect risk', TDR). However, if a sample shows larger (or equal) grain size than the corresponding thickness of the sample, the grains are distributed in such a way that no supporting surrounding grains exist in the 'third dimension' ('no supporting grains in the third dimension', NSG). For such samples, the bending strength may be lower compared to samples of the same thickness showing smaller grain size distributed in three dimensions.

The highest bending strength values for the Tranås granite and the Blue Pearl larvikite was obtained for the 7 mm samples. The lower value

Table 3. Bending strength mean values, standard deviations, and CVs for the untreated (u) and the impregnated (i) rock sample series of different thickness

Rock name	Sample series	Mean value (MPa)	Standard deviation	Coefficient of variation (%)
Tranås granite	4 mm u	16.3	1.5	8.9
	4 mm i	9.9	2.8	28.6
	7 mm u	18.1	1.6	9.1
	7 mm i	18.5	0.6	3.0
	10 mm u	17.2	1.4	8.1
	10 mm i	18.1	0.9	4.9
Iddefjord granite	4 mm u	8.5	0.9	10.2
	4 mm i	16.1	0.4	2.2
	7 mm u	11.5	0.3	2.3
	7 mm i	15.4	1.3	8.4
	10 mm u	11.6	0.5	4.5
	10 mm i	16.2	0.5	3.1
Blue Pearl larvikite	4 mm u	12.8	4.1	32.1
	4 mm i	16.9	1.7	10.1
	7 mm u	19.9	1.0	5.0
	7 mm i	20.8	0.7	3.1
	10 mm u	18.2	0.4	2.3
	10 mm i	20.4	1.5	7.5
Nero Zimbabwe dolerite	4 mm u	40.3	3.5	8.7
	4 mm i	44.2	2.5	5.6
	7 mm u	39.8	2.6	6.5
	7 mm i	38.0	1.3	3.5
	10 mm u	35.6	3.6	10.1
	10 mm i	37.7	1.2	3.1
Dala sandstone	4 mm u	24.0	3.9	16.2
	4 mm i	20.7	1.6	7.9
	7 mm u	20.8	2.6	12.5
	7 mm i	25.5	1.6	6.3
	10 mm u	20.1	1.1	5.7
	10 mm i	22.9	2.7	11.8
Jämtland limestone	4 mm u	9.1	2.6	28.7
	4 mm i	17.1	4.9	28.4
	7 mm u	12.8	6.1	47.5
	7 mm i	13.3	3.5	26.0
	10 mm u	12.1	1.6	13.5
	10 mm i	12.8	1.7	13.4
Barents gneiss	4 mm u	27.5	1.2	4.3
	4 mm i	28.7	0.8	2.7
	7 mm u	26.0	0.9	3.5
	7 mm i	25.9	3.7	14.2
	10 mm u	25.5	0.8	3.2
	10 mm i	23.3	2.6	11.2
Thassos marble	4 mm u	13.0	0.6	4.9
	4 mm i	17.8	1.5	8.3
	7 mm u	8.7	0.2	2.5
	7 mm i	9.7	0.5	5.5
	10 mm u	8.6	0.2	2.1
	10 mm i	10.7	0.5	4.7

obtained for the 4 mm samples could be due to the NSG effect, since these rocks are coarse-grained, whereas the lower values for the 10 mm samples could be due to the TDR effect since these two rocks display high density of microcracks.

The 4 mm samples of the Iddefjord granite exhibited the lowest strength. The somewhat stronger 7 and 10 mm samples showed the same values. The lowest value obtained for the 4 mm samples could be due to the NSG effect. The feldspar grains show various sizes (1–10 mm). There is no TDR effect. This could be due to the high microcrack density in the quartz and

feldspar grains that may impair the bending strength even in the thinnest samples.

The highest strength for the Nero Zimbabwe dolerite was obtained for the 4 and 7 mm samples. This could be due to the fact that this rock is very fine-grained and hence did not display any NSG effect for these thin samples. The lower strength for the 10 mm samples could be due to the TDR effect.

The Dala sandstone and the Barents gneiss showed the same thickness trends. The 4 mm samples showed the highest strength followed by the 7 mm ones, and finally the 10 mm ones. For the Dala sandstone this phenomenon could be due to the rock's fine-grained texture and hence there was no NSG effect for the 4 mm samples. The bending strength values for the 4 mm Barents gneiss cannot be explained by the NSG effect since this rock is in general coarse-grained. On the other hand, the gneiss shows a distinct ductile metamorphic texture, which may give strength in two dimensions. The strength of the 7 and 10 mm samples may be due to the TDR effect.

The Jämtland limestone exhibited the same thickness dependence trends as the Tranås granite and the Blue Pearl larvikite. However, the strength results for the 4 mm samples cannot be explained by the NSG effect since this rock is very fine-grained. The limestone exhibited very high coefficients of variations (Table 3), and hence the results from the different thicknesses are hard to interpret.

The 4 mm Thassos marble showed the highest strength values. The values obtained from the 7 and 10 mm samples were approximately the same. The high bending strength result obtained from the 4 mm samples could be due to the absence of the NSG effect since the marble is fine-grained. The Thassos marble exhibits voids, which could be related to the lower strengths for the 7 and 10 mm samples due to the TDR effect.

Impregnated versus untreated material

Not all impregnated rock types showed improved bending strength compared to the corresponding untreated samples. The values vary not only depending on rock type, but also depending on thickness.

It is believed that the impregnation chemical used in this study covers the surface of the impregnated rock samples with a thin layer. However, its penetration ability, penetration depth and transport paths during impregnation are a subject for future investigations. Interpreting the bending strength test results, in general, regarding the different impregnated rock samples (of different thickness) in relation to untreated samples is complicated. The following points are important to bear in mind. (1) The influence of the impregnation process, i.e. the vacuum treatment and stresses induced during penetration of the chemical and stresses induced during the drying process before testing, has not been studied. (2) The dehydration/contraction effect of the impregnation chemical may be smaller in a sample's interior due to less contact with air compared to near-surface areas. (3) The adhesiveness of the impregnation chemical on mineral grains may differ depending on the grains' chemical and physical properties and in turn may differ between different rock types. (4) The size of cracks and/or pore systems may affect not only the penetration depth of the impregnation chemical, but also what the dehydrated products' network will look like. This in turn may influence at least the mechanical properties of impregnated materials. (5) Depending on mineralogy, chemical reactions may take place between certain minerals and the impregnation chemical, which could change the physical properties of impregnated materials. (6) The stability of the impregnation chemical in time (durability).

The impregnated 4 mm Tranås granite showed much lower bending strength compared to corresponding untreated samples. On the other hand the 7 and 10 mm samples exhibited a slight strength improvement for the impregnated samples. This phenomenon could be due to the Tranås granite being sensitive to the impregnation process and further to the processing afterwards (sawing, calibration, polishing). Existing microcracks may be longer and wider and maybe even new cracks will be developed during the processing. The 4 mm samples may then be more sensitive during the further processing than the 7 and 10 mm ones.

The Dala sandstone showed the same trend as the Tranås granite. The difference between the 4 mm samples was not as high as for the granite, whereas the bending strength improvement for the impregnated 7 and 10 mm sandstone samples was slightly higher. This could be due to the fact that the sandstone is also sensitive to microcrack propagation during processing but not as much as the Tranås granite.

Irrespectively of thickness, the impregnated Iddefjord granite, Blue Pearl larvikite, Jämtland limestone, and Thassos marble showed higher strength values compared to corresponding untreated samples. The greatest difference was obtained for the 4 mm samples. This means that these rocks are not sensitive to the processing.

The Iddefjord granite showed the greatest differences between impregnated and corresponding untreated material. This is most likely primarily due to the high microcrack density, which may have a three-dimensional perpendicular network that might act as penetration paths for the impregnation chemical. In addition, the Bohus-Iddefjord granite (Asklund 1947) has a distinctive fracture system with three fracture sets perpendicular to each other. It has been used as a source for paving stone production due to this well developed fracture pattern.

The impregnated 4 and 10 mm Nero Zimbabwe dolerite showed slightly higher strength than the untreated counterparts. On the other hand, the impregnated 7 mm dolerite showed slightly lower bending strength in relation to the corresponding untreated samples. However, even if the dolerite is quite homogeneous compared to the other rocks studied, this phenomenon could be due to heterogeneity differences between sample series (see CVs in Table 3). For example, the impregnated 7 mm sample series could have a somewhat different mineralogy and texture, and may display higher microcrack density than the other series.

The impregnated 4 mm Barents gneiss showed slightly higher strength compared to corresponding untreated samples. No difference in strength was observed between the impregnated and untreated 7 mm samples. The impregnated 10 mm samples displayed slightly lower strength than the 10 mm untreated ones, which could be due to heterogeneity differences between sample series (Table 3).

Conclusions

Of the untreated rocks, the Nero Zimbabwe dolerite showed the highest bending strength values compared to the other rocks studied, due to its fine-grained texture, normally low crack density, and high mafic mineral content. The Barents gneiss showed the second highest strength, probably due to its distinct ductile metamorphic texture. The Jämtland limestone and the Thassos marble exhibited the lowest values, most likely because these rocks have high amounts of carbonate minerals, and high density of cracks and voids, respectively. The Tranås granite showed higher strength values than the Iddefjord granite, and this is probably due to differences in microcrack density and the mafic mineral content.

When comparing the strength differences between impregnated rocks versus their untreated counterparts, we conclude that the Nero Zimbabwe dolerite does not improve with impregnation. This is probably due to a low penetration ability of the impregnation chemical, which in turn is due to the dolerite's fine-grained texture and in general low crack density. The Tranås granite is likewise not suitable for impregnation for production of 4 mm tiles. For production of 7 or 10 mm tiles there is no need for impregnation. This phenomenon may be due to sensitivity to the impregnation process and further processing, where microcrack propagation may take place, especially regarding production of 4 mm tiles. The Thassos marble, the Jämtland limestone, and in particular the Iddefjord granite are the most suitable rocks for impregnation. This is most likely primarily due to the void content for the marble and the high microcrack density for the limestone and the granite that may act as penetration paths for the impregnation chemical.

The geological factor that seems to have most effect on the bending strength properties examined in this study is the fabric of the rock and not the mineralogy (cf. Åkesson *et al.* 2001). However, a relationship also exists between bending strength properties and mafic mineral content.

In order to obtain the highest quality of thin untreated dimension stone products regarding bending strength properties, rocks should have a fine-grained texture, low crack or void density, high mafic mineral content or a distinct ductile metamorphic texture. Rock types that display the highest strength improvement due to impregnation are those with high crack or void density.

For the production of very thin (e.g. 4 mm) and fragile dimension stones, there must not be a high bending strength difference between impregnated and untreated material. During the cutting and sawing processes less waste material will in general be produced for impregnated material.

For an understanding of how the impregnation process differs between rock types, further studies have to be performed on the impregnation chemical itself regarding its penetration ability, adhesiveness, dehydration/contraction properties, potential chemical reactions with minerals, and durability/ageing factors. Different impregnation chemicals with varying physical and chemical properties may have to be developed for rock types with different physical and/or chemical properties. Moreover, different impregnation techniques may have to be developed for rocks with different properties. More fragile rocks should

not be subjected to such high pressure differences and/or so many pressure cycles during the impregnation operation as the less fragile rocks.

Techstone Sweden AB is thanked for initiating the project and for providing the dimension stone material. The personnel at the Building Materials Division at SP Swedish National Testing and Research Institute, especially L. Hagnestål, L. Carlsson, and S. Lindskog, are thanked for technical assistance prior to and during the performance of the tests. This work benefited from financial support by Techstone Sweden AB and Teknikbrostiftelsen i Göteborg, Sweden.

References

ÅKESSON, U., LINDQVIST, J. E., GÖRANSSON, M. & STIGH, J. 2001. Relationship between texture and mechanical properties of granites, central Sweden, by use of image-analysing techniques. *Bulletin of Engineering Geology and the Environment*, **60**, 277–284.

ALDAHAN, A. A. 1985. Mineral diagenesis and petrology of the Dala Sandstone, central Sweden. *Bulletin of the Geological Institutions of the University of Uppsala*, **12**.

ALEXANDRI, I. 1991. *The Greek Marble Index*. Print All Publications, Athens.

ASKLUND, B. 1947. *Svenska stenindustriområden I-II. Gatsten och kantsten*. Sveriges Geologiska Undersökning **C 479**.

BARTON, C. M., CARNEY, J. N., CROW, M. J., DUNKLEY, P. N. & SIMANGO, S. 1991. The geology of the country around Rushinga and Nyamapanda. *Zimbabwe Geological Survey Bulletin*, **92**.

BERTHELSEN, A. & SUNDVOLL, B. 1996. *Beskrivelse til geologisk kart over Norge – 1:250 000 Oslo*. Norges Geologiske Undersøkelse.

BERTHELSEN, A., OLERUD, S. & SIGMOND, E. M. O. 1996. *Geologisk kart over Norge, berggrunnskart Oslo. Scale 1:250 000*. Norges Geologiske Undersøkelse.

BRØGGER, W. C. 1890. Die Mineralien der Syenitpegmatitgänge der Südnorwegischen Augit-und Nephelinsyenite. *Zeitschrift für Kristallographie und Mineralogie*, **16**.

DIN 52112. 1988. *Testing of natural stone; Bending test*.

DOBRZHINETSKAYA, L. F., NORDGULEN, Ø., VETRIN, V. R., COBING, J. AND STURT, B. A. 1995. Correlation of the Archaean rocks between the Sørvaranger area, Norway, and the Kola Peinsula, Russia (Baltic Shield). *In*: ROBERTS, D. & NORDGULEN, Ø. (eds) *Geology of the eastern Finnmark – western Kola Peninsula region*. Norges Geologiske Undersøkelse, Special Publications, **7**, 7–27.

ELIASSON, T. 1992. Magma genesis and emplacement characteristics of the peraluminous Sveconorwegian Bohus granite, SW Sweden. *Geologiska Föreningens i Stockholm Förhandlingar*, **114**, 452–455.

ENGVOLDSEN, T. 1991. Larvik ringkompleks. *Stein*, **18**, 18–21.

HJELMQVIST, S. 1966. *Beskrivning till berggrundskarta över Kopparbergs län*. Sveriges Geologiska Undersökning **Ca 40**.

JARL, L.-G. & JOHANSSON, Å. 1988. U-Pb zircon ages of granitoids from the Småland-Värmland granite-porphyry belt, southern and central Sweden. *Geologiska Föreningens i Stockholm Förhandlingar*, **110**, 21–28.

KARIS, L. & STRÖMBERG, A. 1998. *Beskrivning till berggrundskartan över Jämtlands län. Del 2: Fjälldelen*. Sveriges Geologiska Undersökning **Ca 53**:2.

LINDSTRÖM, M., LUNDQVIST, J. & LUNDQVIST, TH. 1991. *Sveriges geologi från urtid till nutid*. Studentlitteratur, Lund, Sweden.

ONODERA, T. F. & ASOKA KUMARA, H. M. 1980. Relation between texture and mechanical properties of crystalline rocks. *Bulletin of the International Association of Engineering Geology*, **22**, 173–177.

PEDERSEN, S. & MAALØE, S. 1990. The Iddefjord granite: geology and age. *Norges Geologiske Undersøkelse Bulletin*, **417**, 55–64.

PERSSON, L., BRUUN, Å. & VIDAL, G. 1985. *Beskrivning till berggrundskartan HJO SO*. Sveriges Geologiska Undersökning **Af 134**.

PULVERTAFT, T. C. R. 1985. Aeolian dune and wet interdune sedimentation in the Middle Proterozoic Dala sandstone, Sweden. *Sedimentary Geology*, **44**, 93–111.

REUSCH, H. 1891. Granitindustrien ved Idefjorden. *Norges Geologiske Undersøkelse/Aarbok*, **1**, 70–77.

ROBERTS, A. E. 1992. *Black Granite from the Mutoko District*. 23rd Annual Report of the Institute of Mining Research, University of Zimbabwe, No. 136.

WAELKENS, M., DE PAEPE, P. & MOENS, L. 1988. Quarries and marble trade in antiquity. *In*: NORMAN, H. & WAELKENS, M. (eds) *Classical Marble; Geochemistry, Technology, Trade*. Nordhoff International Publishing, 11–28.

Atmospheric pollution and building materials: stone and glass

R. A. LEFÈVRE & P. AUSSET

Laboratoire Interuniversitaire des Systèmes Atmosphériques (LISA), Joint Research Unity CNRS - Universities Paris VII and Paris XII, Faculty of Sciences, 94010 Créteil, France (e-mail: ausset@lisa.univ-paris12.fr)

Abstract: The research carried out by LISA on the decay of stone and glass by atmospheric pollution is presented. On building facades, areas unsheltered from rain are clear and eroded, while those that are sheltered darken due to the development of black crusts containing anthropogenic particles (fly-ash, soot) cemented by a framework of gypsum crystals. On calcareous stones, in-depth sulphation of the stone substrate may also occur at the same time. On porous calcareous stones, the black crusts detach periodically forming black slabs, creating a white, grey and black jigsaw-like pattern on the remaining stone surface. By exposing stone test samples to field and/or laboratory controlled polluted atmospheric conditions, the formation of embryonic black crusts has been observed. Grey crusts developed during pre-industrial times have been found to contain unburnt wood debris as a record of past air pollution. Glass alters by leaching, corrosion, encrusting and soiling. The quantification of the effects of atmospheric pollution can be accomplished either directly on buildings of different ages, or through field and/or laboratory controlled experiments. Modelling of the alteration of materials by atmospheric pollution consists of the determination of dose–response functions, of acceptable levels and thresholds and in risk assessment mapping.

The massive increase in the production and consumption of energy in the past two centuries, due to industrial development, public and private transport and domestic heating, as well as the replacement of wood by coal and oil derivatives as fossil fuels, has led to increased atmospheric emissions of gaseous (SO_2) and particulate (fly-ash, soot) sulphurous compounds.

As a result, significant sulphation of building materials at the material–atmosphere interface ensued with widespread precipitation of dihydrated calcium sulphate crystals (gypsum: $CaSO_4$, $2H_2O$). The sulphation is accompanied by physical and aesthetic alterations, depending on sulphur atmospheric concentrations and on other parameters like the relative humidity of the air, position of building materials with regards to their exposure to rain run-off, their calcium availability, their porosity and their surface state.

The chemical and mineralogical nature, as well as the surface properties of materials undergoing sulphation, have an influence on this phenomenon, determining its modalities which appreciably differ from a calcareous stone to a siliceous one, from compact to porous stone, from stone to glass and other materials.

Knowledge of the mechanisms of interaction between building materials and air pollution is indispensable for the accurate selection of the appropriate maintenance policies and treatment techniques to be applied to damaged building facades, the cost of which is not negligible. Furthermore, it will also be of help in elaborating policies of environmental protection related to the buildings under study, especially when dealing with buildings belonging to our cultural heritage.

This paper deals with the experience of LISA on two materials: stone and glass. It is not intended to provide an exhaustive review of all the work in this field.

The sulphation mechanism: location on facades and statues, and at the material–atmosphere interface

At a detailed level of observation, the facade of a building or the surface of a statue in an urban polluted environment (Fig.1) shows the presence of dark and clear areas, their distribution being directly linked to their mode of exposure to rain (Camuffo *et al.* 1982, 1983; Camuffo 1984).

Dark areas of a facade or of a statue are always located in sheltered parts of the building. In these dark areas the presence of grey or black crusts can be observed; mineralogical and microscopical examination reveals these crusts to be constituted of a framework of gypsum

From: SIEGESMUND, S., WEISS, T. & VOLLBRECHT, A. 2002. *Natural Stone, Weathering Phenomena, Conservation Strategies and Case Studies*. Geological Society, London, Special Publications, **205**, 329–345.
0305-8719/02/$15.00 © The Geological Society of London 2002.

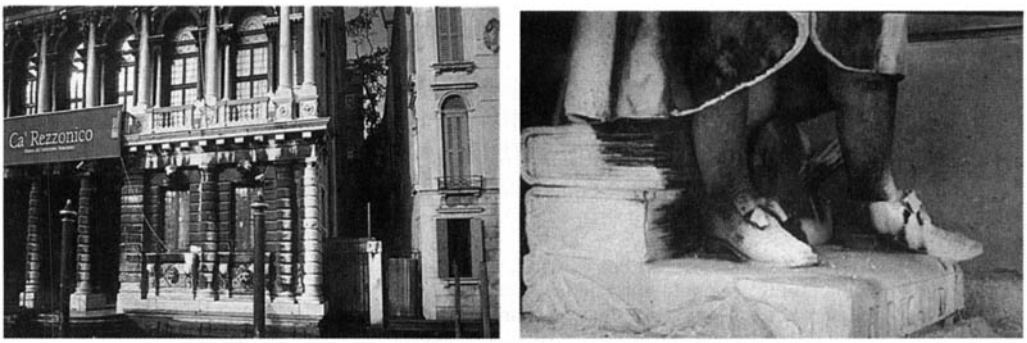

(a) (b)

Fig. 1. (**a**) Facade of the Ca'Rezzonico along the Canal Grande in Venice: the parts unsheltered from rain are washed out and clear, whilst black crusts develop on the sheltered areas. (**b**) Feet of the statue of Rigaud, one of the Hommes Illustres statues, before recent restoration, Carrousel Square, Louvre Palace, Paris. The parts of the statue unsheltered from rain and run-off are clear, whilst the sheltered areas are black.

crystals embedding atmospheric particles. At the start of their growth, the new crusts are grey but blacken progressively through the deposition of black airborne particles. The location of gypsum crusts sheltered from rain is easily explained by the necessity of maintaining the mechanism of particle sedimentation–accretion for their growth: episodes of rain washout can rapidly remove from the surface particles previously deposited and can dissolve the embryonic gypsum cement that had formed, notwithstanding the fact that gypsum, being a hydrated mineral, always needs a certain degree of humidity in the air (through vapour and/or fog droplets) for its growth.

Clear areas of the same facade or statue are those directly washed by rain or by water run-off originating from broken gutters or pipes. This continuous washing with rain or run-off water maintains a fresh cleaned surface which tends to preserve its original colour. Airborne particles which are deposited between rain episodes are washed out by the next ones and any gypsum cement which has started to precipitate is dissolved: in this case, the surface may show evidence of loss of material together with erosion features.

The formation of black crusts on building facades and statues in a polluted urban atmosphere is valid no matter what the constituting materials of the building/monument are. However, only sulphation occurring *above* the surface of materials (i.e. black crusts) or its absence (i.e. washing out, erosion episodes) is macroscopically observable. On the contrary, sulphation occurring *below* the surface can only be detected by detailed microscopical examination in the laboratory of field collected samples.

Glass, especially the type used on facades of tall contemporary buildings, is maintained transparent and more or less clean only when washed out by driving rain or by periodic and often very expensive cleaning sessions. Stained glass windows of churches which are not regularly cleaned, can be affected by leaching and/or corrosion processes (with the possible formation of craters) if exposed to rain of variable pH. They also may become opaque due to the growth of gypsum crusts in areas sheltered from rain (Lefèvre *et al.* 1998). In addition, ancient stained glass often has a chemical composition which makes it particularly prone to weathering due to the high potassium and low sodium content.

As mentioned above, gypsum development tends to be localized at the interface between the material and the atmosphere containing SO_2 in gaseous form or dissolved in rain or fog microdroplets (which often also contain calcium ions; Del Monte and Rossi 1997) and particles (which may contain sulphur and calcium ions).

Gypsum crystallization may occur immediately above or below the surface. In the case of gypsum crystallization immediately *above* the surface, gypsum is present regardless of the presence of calcium-bearing constituents in the original material (in fact, superficial gypsum crusts have been reported on calcareous or siliceous stone, cement, mortar, concrete, ceramics, brick, glass, stained glass, metal, wood, polymer, painting, etc.) This sulphation

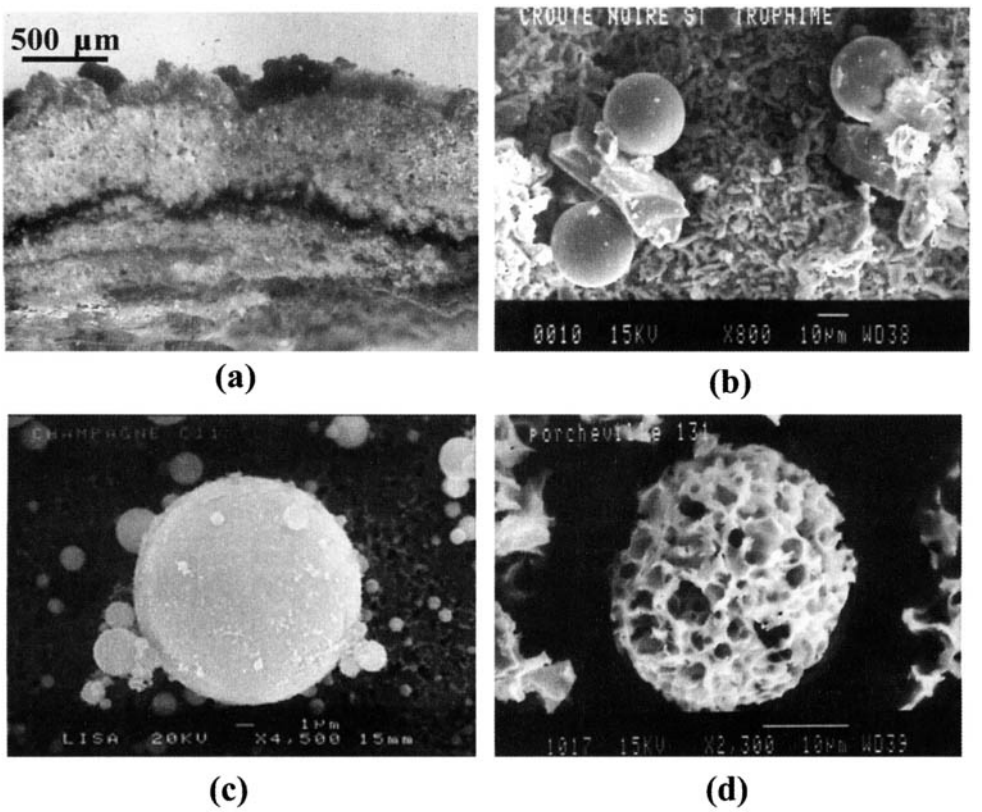

Fig. 2. (**a**) Section of a black crust on limestone, observed by optical microscopy: the stone is visible at the bottom of the microphotograph; the crust is made up by an irregularly stratified mixture of white gypsum associated with black fly-ash (Romanesque Portal of Saint-Trophime Church, Arles, France). (**b**) Scanning electron microphotograph of the surface of the same black crust: acicular crystals of gypsum and smooth fly-ash. (**c**) Alumino-silicated smooth fly-ash sampled in the electrostatic precipitator of a coal-burning power plant. (**d**) Carbonaceous spongy fly-ash sampled in the electrostatic precipitator of a heavy oil-burning power plant.

mechanism proceeds in an outward direction from the stone surface towards the surrounding atmosphere. As a result, a superficial gypsum crust is responsible for blackening of the surface which becomes progressively darker with time, i.e. from grey to black (Fig. 2a and b). Among the deposited atmospheric particles, particular attention has been paid recently to fly-ash emitted mainly by coal and heavy oil combustion processes (Fig. 2c and d; Ausset *et al.* 1994); in fact, it has been shown that these particles contain significant amounts of sulphur together with elements such as V, Ni and Fe which may act as catalysts in the sulphation reaction. By analysing stone samples experimentally exposed to real (in field test site) or simulated (in laboratory atmospheric chamber) polluted atmospheric conditions, the embryonic stage of black crust formation can be observed: fly-ash particles are anchored to the surface of the stone through precipitation of gypsum crystals. These crystals are present on the surface of the fly-ash and on the surface of the surrounding stone (Ausset *et al.* 1999; Figs 3 and 4).

In the case of gypsum crystallization immediately *below* the surface, gypsum develops only if free calcium is available in the substrate, e.g. as calcium carbonate (calcite: $CaCO_3$). The sulphation weathering front advances in an inward direction from the atmosphere–material interface towards the inner part of the material through the porous network of the stone in gaseous (SO_2) or liquid (H_2SO_4) form. Gypsum then precipitates by replacing calcite and this reaction often leads to significant structural damage such as fracturation, blistering and slab

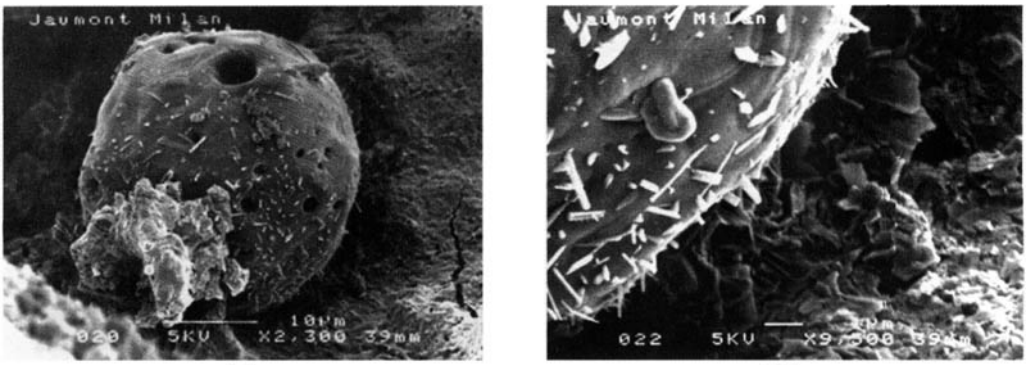

(a) (b)

Fig. 3. Gypsum crystals grown on a fly-ash particle deposited on the surface of Jaumont limestone exposed for one year (1986–1987) to the polluted atmosphere of Milan and at the contact between this fly-ash and the stone: (**a**) general view; (**b**) close-up view of small acicular crystals of gypsum growing on the fly-ash particle and on larger tabular crystals of gypsum anchoring the particle to the surrounding limestone substrate (Ausset *et al.* 1999).

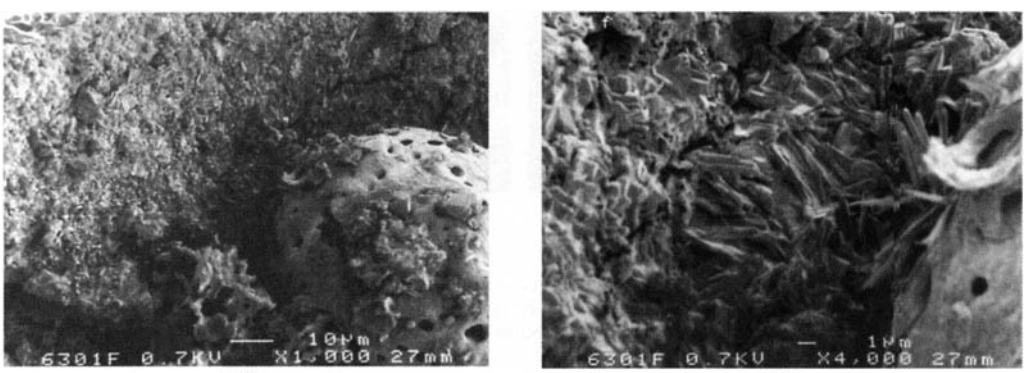

(a) (b)

Fig. 4. Gypsum crystals grown at the contact between a fly-ash particle and the Jaumont limestone substrate after one year in the Lausanne Atmospheric Simulation Chamber: (**a**) general view; (**b**) close-up view of acicular gypsum, attached to the fly-ash particle, anchoring it to the surrounding limestone substrate (Ausset *et al.* 1999).

detachment due to the changes in mineral volume associated with gypsum–calcite transition.

In summary, the mechanism evoked to explain the presence and the growth of gypsum black crusts *above* the surface of materials consists both in the continuous supply of atmospheric particles and in their cementation by gypsum crystals originating from the reaction between atmospheric SO_2 and calcium ions present in fog droplets or in calcium-rich particles present in the air (calcite, gypsum). A supply of calcium by the substrate, even if present in mobilizable form, is not indispensable as demonstrated by the presence of gypsum crusts on metals like bronze (Ausset *et al.* 1991) or on wood (tree trunks; Del Monte & Lefèvre 2001*a*, *b*). On the other hand, the presence of free calcium in the substrate is indispensable for an in-depth sulphation front to be active.

The role of porosity and relative humidity in stone sulphation: black crusts and white, grey and black slabs

The two sulphation mechanisms, i.e. occurring above and below the surface of material, may act at the same time or be independent of one another. For example, Carrara marble may be

covered by surficial gypsum crusts without any significant sulphation acting below its surface when the relative humidity of the air does not exceed the critical value of 80%. Above this value in-depth sulphation of marble takes place rapidly due also to the 100% calcitic composition of the stone (Girardet & Furlan 1983; Vergès-Belmin 1994). Building stones with medium porosity like the lutetian limestone used to construct the main monuments (for example the Louvre and Notre-Dame Cathedral) and the buildings by Haussmann in Paris present several forms of decay related to atmospheric pollution. Areas unsheltered from rain appear washed and show erosion features, but can also present an original form of structural alteration: the development and detachment of white slabs. The thickness of these slabs (a few millimetres) seems to correspond exactly to the depth of penetration of water during rain episodes rapidly saturating the superficial porous network before running off the surface (phenomenon of refuse). At the end of the rain episode, during the drying phase, water evaporating within the rock fabric leads to the crystallization of dissolved salts (mainly calcium sulphates) along a plane just below the stone surface thus facilitating the detachment of the white stone slabs. This phenomenon has been observed in the Cour Carrée of the Louvre Palace and on the Saint Eustache Church in Paris.

When dealing with lithologies characterized by significant porosity and surface roughness and situated in areas with high levels of air pollution and thus high rates of airborne particulate deposition, some deposited particles will withstand washout episodes and remain stuck to the stone surface: in this case, a black crust may be present even in the unsheltered parts of a building facade and evaporation–crystallization cycles may lead to the detachment of a black rather than a white stone slab. When fully grown, a typical cross-section of a black slab from the stone–atmosphere interface in an inward direction is constituted by a black crust, a slice of sound stone more or less impregnated by gypsum, a level of gypsum responsible for the detachment. The detachment mechanism explains the relative thinness of black patinas coating the outer surface of black slabs: there simply was not enough time for the crusts to grow as thick as they would have been in areas sheltered from rain before being detached from the surface. This phenomenon of 'self-cleaning' may also be invoked to explain the presence of a white, grey and black jigsaw-like pattern, often observed on building facades such as on the Saint-Eustache Church in Paris: indeed the process of continuous detachment of small black slabs from a facade leads to the exposure of white stone parts that darken progressively with time, being subjected to airborne particulate deposition.

The Touraine tuffeau, a porous and superficially rough chalk used in the construction of the Cathedral of Tours and of monuments in the Loire Valley, also shows many examples of such multicoloured jigsaw-like patterns. In fact, these monuments would be completely blackened under the effects of air pollution, if they had not been spontaneously self-cleaned by the periodic detachment of black slabs. One may argue that this self-cleaning mechanism, inasmuch as it may provide a somewhat effective and free-of-charge means of building maintenance, has beneficial economical consequences; however, we must take into account that a significant loss of material together with unacceptable surface recession of the building facade is always associated with the above process. Therefore, in this case, replacement of the decayed tuffeau with sound, less porous stone like Richemont limestone is recommended. The white, grey and black jigsaw pattern may also be present even in areas sheltered from rain as is the case in Psalette Cloister at the northern side of the Cathedral of Tours: here, water condensation episodes are so significant under the vaults that the water is able to penetrate through the black crusts and reach the underlying rock substrate where it evaporates at depth following the same mechanism previously described for rain-exposed areas.

Finally, the same white, grey and black pattern may also develop when capillary rise of salt-saturated water combines with air pollution. This phenomenon has been observed, for example, in Venice, at the base of palaces constructed with the white stone of Istria (Fig. 1): black crusts due to accumulation and cementing of atmospheric particles are present in areas sheltered from rain, but tend to detach spontaneously leading to the jigsaw pattern when the salts contained in the capillary rise crystallize.

Ancient stained glass, modern glass and atmospheric pollution

Glass is widely regarded as a non-weatherable material. Indeed many ancient glass artifacts reach us apparently intact. However, modern tools of investigation of material surfaces show that, if at the macroscopic scale the glass might seem to be intact, this is not the case at the microscopic level.

Fig. 5. Saint-John Baptist stained glass window of the Sainte-Chapelle in Paris: (**a**) viewed by transparency from the interior of the Chapel; (**b**) viewed from the exterior: black gypsum crusts develop in the parts sheltered from rain.

The principal factor in the decay of glass is water, that causes, when its pH is below 9, a superficial leaching of alkaline and alkaline earth elements called 'modifiers' in the irregular network of SiO_4 tetrahedra. As a result, a surface layer of hydrated amorphous silica develops acting as a barrier against further propagation of the leaching in the interior of the glass. In fact, it progresses only along fractures parallel or perpendicular to the glass surface (Libourel *et al.* 1994; Sterpenich & Libourel 2001). When the pH of the water is above 9, the network of the tetrahedra is destroyed and glass corrodes. In polluted atmospheric conditions, the pH of water is more often acid than basic and the leaching mechanism predominates. Its intensity depends mainly on the glass chemical composition: ancient glasses, in particular those of stained glass windows, are generally potassium-rich and not highly resistant to weathering whereas modern ones, being sodium-rich, may be relatively durable.

The decay effects of current levels of air pollution on glass samples with a chemical composition similar to ancient stained glass consist of leaching leading to the development of neocrystallizations at the surface. At first, their chemical composition reflects the glass composition and the nature of gaseous pollutants (sulphates and nitrates of calcium, sodium, potassium). But slowly gypsum becomes the predominant phase and a black gypsum crust develops progressively as on stone in areas sheltered from rain (Munier *et al.* 2001). Examples of such gypsum crusts have been observed on ancient stained glass windows of Tours Cathedral (Lefèvre *et al.* 1998) and Sainte-Chapelle in Paris (Fig. 5) (Munier & Lefèvre 2000).

The main damage caused by atmospheric pollution to modern calco-sodic durable glass is mainly aesthetic: it consists of soiling provoked by the deposition of soot particles at the glass surface, including areas which are unsheltered from rain. That is a paradox, which calls for continuous and often expensive cleaning operations. On the other hand, leaching of modern calco-sodic glass is an insignificant phenomenon, without any observable consequence in the short term.

Changes in the nature of atmospheric pollution as recorded on material surfaces

Before the industrial revolution, wood was the most widely used fuel for cooking, heating and handicraft purposes. Atmospheric air pollution originating from wood combustion is reported in the literature (Brimblecombe 1987) and recorded even on paintings dating from before the industrial revolution and the invention of photography. Examples of the effects of pre-industrial wood combustion on building facades which have been preserved by a combination of circumstances (walling-up and/or burial) against

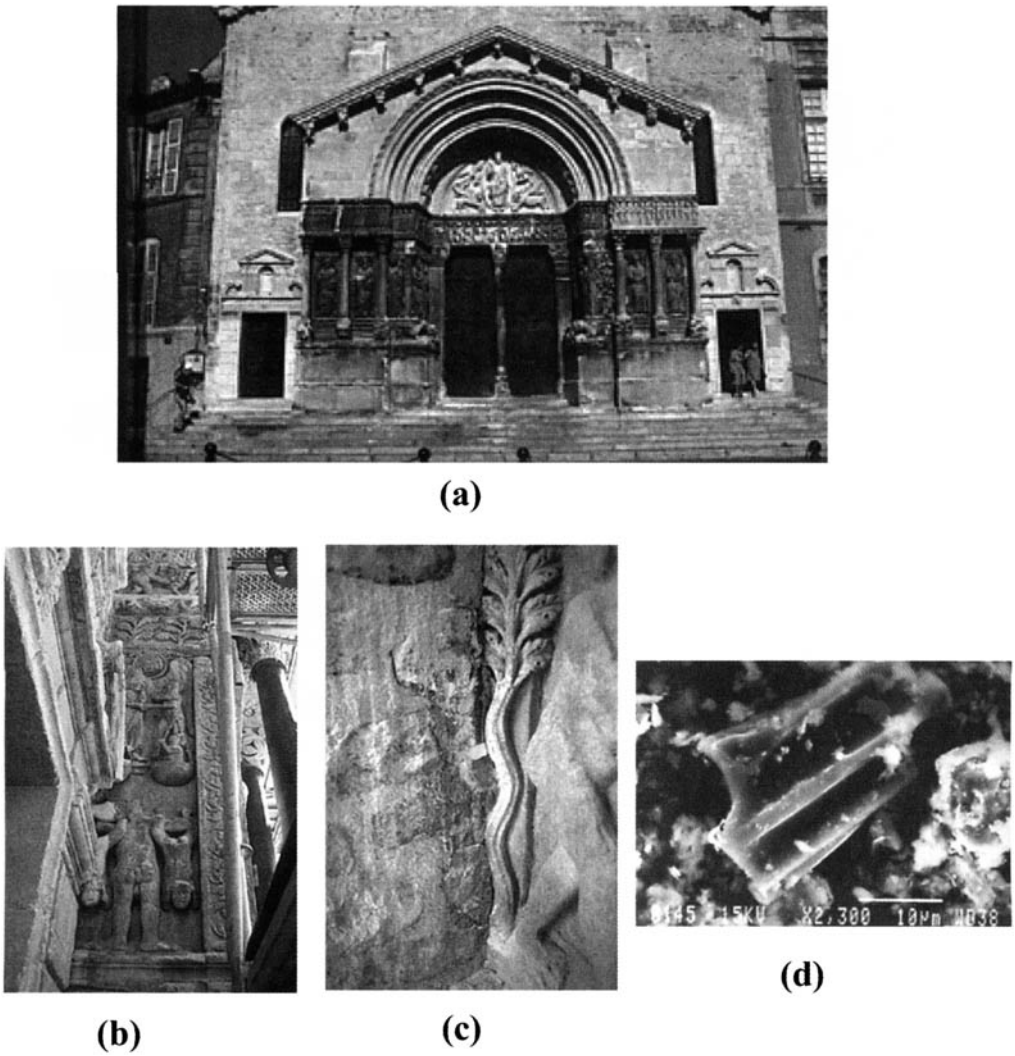

Fig. 6. The Saint-Trophime Church in Arles (France). (**a**) The western facade during recent restoration works: the lower uncleaned part of the Romanesque portal is black, whilst the restored tympanum and two lateral portals appear clear. (**b**) The frieze of the Romanesque portal is enclosed by the masonry of the northern lateral portal. (**c**) Detail of the frieze. (**d**) Wood debris within ancient crusts developed between 1180 and 1646 on the enclosed frieze when exposed to the polluted atmosphere of Arles.

later industrial air pollution have been reported: a demonstrative example is the Romanesque Portal of the Saint-Trophime Church in Arles (southern France; Fig. 6; Ausset *et al.* 1998).

The Primatial Church of Saint-Trophime in Arles dates from the late eleventh and early twelfth centuries. Its Romanesque west portal was constructed in about 1180 and has not been modified since (Fig. 6a). This portal was flanked in 1636 by two lateral doorways, whose masonry encloses small sections of Romanesque frieze to a depth of 10 to 15 cm (Fig. 6b and c). When recent restoration work began (1989) the enclosed part of the frieze was uncovered. A grey, ultra-thin crust (200 μm in thickness) was disclosed, which had developed between 1180 and 1636. The presence of this crust demonstrates that the concentration of airborne dust particles in the atmosphere of Arles even before the industrial revolution was high enough to be

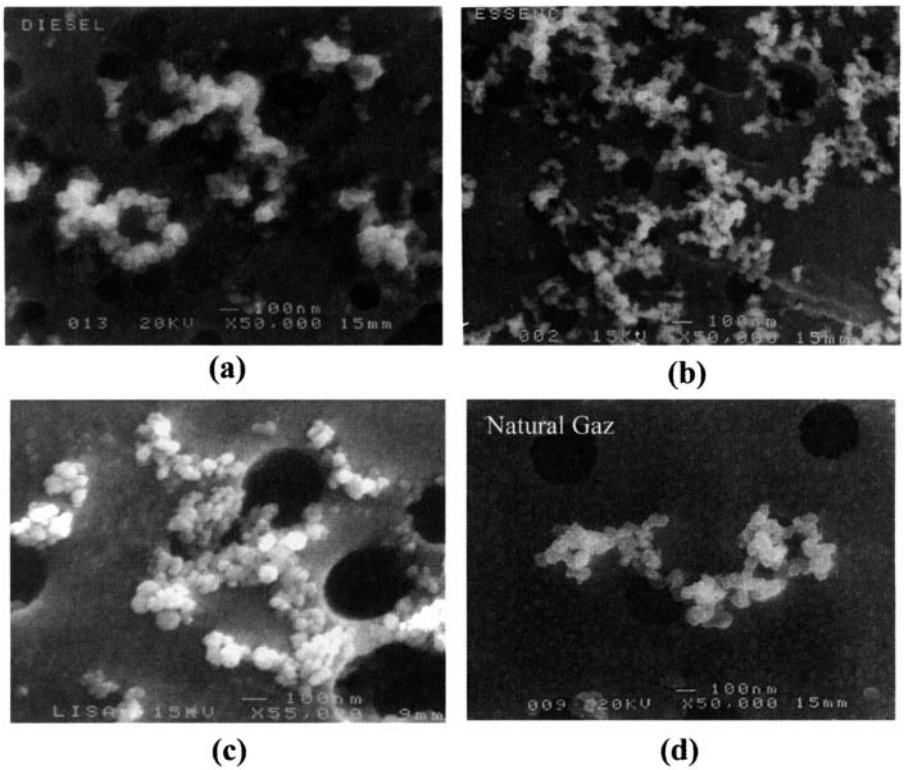

Fig. 7. Ultrafine particles emitted into the atmosphere by the combustion of oil derivatives: (**a**) soot particles from heavy oil combustion in a diesel engine; (**b**) soot particles from gasoline combustion; (**c**) soot particles from kerosene combustion; (**d**) soot particles from natural gas combustion.

responsible for darkening the facade of the church and for the development of a grey crust. The nature of the particles (wood debris; Fig. 6d) and of the cement (mainly calcite with minor gypsum) present in this crust reflects the nature of the predominant fuel (wood) as well as the nature of the dominant gaseous pollutant present in the Arles atmosphere at the time of crust formation (i.e. CO_2 and minor SO_2 originating from wood combustion).

Identical particles of wood have been observed in the grey crusts sampled on the plaque commemorating the coronation of Charles V by Pope Clement VII in 1530, which is located on the facade of the Palazzo d'Accursio overlooking Piazza Maggiore in Bologna (Ausset *et al.* 1998), on the Garisenda Tower in Bologna (Del Monte *et al.* 2001*b*) and on the heads of the Kings of Juda statues which adorned the facade of Notre-Dame in Paris from the thirteenth century until 1792, and are currently displayed in the French National Museum of Middle Age, Hôtel de Cluny, Paris (Ausset *et al.* 2000; Del Monte *et al.* 2001*a*).

Since the industrial revolution, wood has been replaced by coal and more recently by oil derivatives as the most widely used fuel. This change has led to a dramatic increase in SO_2 dominated pollution and in the sulphation rate of superficial materials.

As mentioned in previous paragraphs, sulphated crusts developed after the industrial revolution are composed of a framework of gypsum crystals embedding airborne particulates such as fly-ash from fossil fuel combustion (coal and oil). The granulometric, mineralogical and chemical composition of fly-ash derived from these different pollution sources is quite distinctive; the changing nature of air pollution induced by the transition from wood to coal and from coal to oil can then be seen recorded in the stratigraphical distribution of fly-ash particles derived from each source and embedded within the growing sulphated crusts (Del Monte *et al.* 2001*b*).

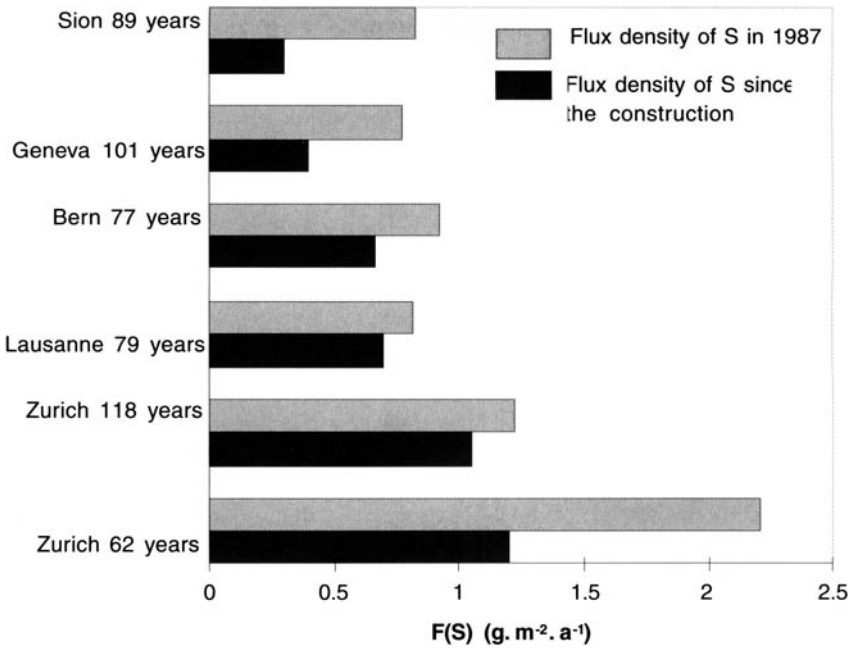

Fig. 8. Mean flux density of sulphur $F(S)$ that passed through the surface and was deposited inside different buildings constructed with Bern sandstone since their construction and during the year 1987 (modified from Furlan & Girardet 1992).

The tightening of regulations concerning SO_2 atmospheric emissions, which imposed the use of low-sulphur fuels, the progressive dismissal of coal, and stricter controls on industrial and vehicular emissions, has led in the last decades to a significant decrease in the concentration of SO_2 and fly-ash in the air. However, the atmospheric concentration of NO_x pollutants originating from nitrogen oxidation during combustion and of ultra-fine particles (soot) originating from the combustion of oil derivatives (gasoline, light oil, kerosene, natural gas; Fig. 7) is on the increase. As opposed to fly-ash derived from coal and oil, the chemical and morphological uniformity typical of soot particles makes the attribution of a specific pollution source altogether more problematical.

Are the thin black coverings which are currently developing on the surface of buildings recently cleaned, embryonic gypsum crust or a new type of smooth and compact crusts linked to the new atmospheric pollution? On the other hand, the replacement of sulphates by nitrates at the surface of materials is scarcely observed, probably because of the high solubility of nitrates in water: it may be inferred that they disappear immediately after formation.

Quantification of the effects of atmospheric pollution on stone

The quantification of effects of atmospheric pollution on stone can be approached in three different ways: (i) by direct measurements on buildings, for which the time of exposure to atmospheric pollution is well known; (ii) by exposure of samples on different field test-sites for a fixed duration with continuous on-site measurement of meteorological and environmental parameters; (iii) by exposure of samples in a laboratory simulating chamber where meteorological and environmental parameters are fixed and controlled.

On different buildings constructed with the same stone, it is possible to measure the mean flux density of sulphur (g m^{-2} a^{-1}) that passed through their surface and accumulated since their construction and to compare with the flux density of sulphur during one chosen year (Fig. 8). The results indicate clearly the evolution of sulphurous atmospheric pollution during the last decades on the different sites where the buildings are located.

By grinding down a known surface of a stone sample (10 cm^2 for example) in subsequent thin

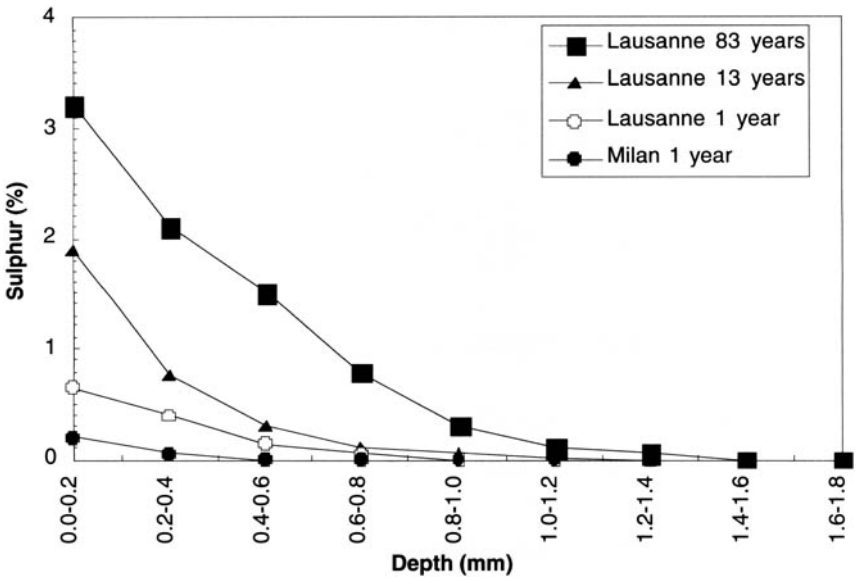

Fig. 9. Sulphur concentration (%) profiles inside Bern sandstone on buildings of different ages in Milan and Lausanne (modified from Connor & Girardet 1992).

steps (0.1 mm for example) until reaching the unsulphated sound substrate (at the depth of 2.5 mm for example), the sulphur concentration profiles according to depth can be obtained for the same stone exposed on different sites during different time periods: the higher the amount of air pollution in the studied site and the longer the exposure time, the higher is the extent of deposition and depth of penetration of sulphur within the stone (Fig. 9).

A direct relationship can be established between the uptake of SO_2 by the same stone in different field test-sites and the SO_2 concentration existing in the surrounding atmosphere. (Girardet & Furlan 1983; Furlan & Girardet 1988, 1991) (Fig. 10).

On the same test-site, different types of natural stone take up sulphur in a different manner depending on their chemicomineralogical composition and petrophysical properties (Fig. 11).

These field experiments have been complemented with laboratory experiments in Lausanne Atmospheric Simulation Chamber (LASC), at the Federal Polytechnic School of Lausanne (Switzerland) (Ausset *et al.* 1996; Girardet *et al.* 1996). The experiment lasted one year with sample withdrawing after 3, 6, 9 and 12 months. In the cells the temperature was maintained at 13°C and the relative humidity at 78%, so that no water condensation could occur, the dew point being never attained. The SO_2 and NO_2 concentrations were 125 and 50 ppb respectively, corresponding to those of a particularly polluted city in the 1970s and 1980s (Milan). Two types of stone were chosen for this experiment: Jaumont limestone and Bern sandstone. These stone samples introduced in LASC were either untreated, or coated with fly-ash from heavy oil combustion or soot from light oil combustion.

A progressive decrease in the uptake of sulphur by the samples was observed according to the exposure time (Fig. 12). This sulphur uptake corresponds to the substitution of calcite by gypsum (Fig. 13). It decreases from the surface to the depth of the samples.

All the results of experiments on field test-sites and in the simulating chamber allow estimation of the sulphur deposition velocity V (m s^{-1}), from the sulphur flux density F (g m^{-2} s^{-1}), measured on the sample, divided by the SO_2 concentration C (g m^{-3}), measured in the atmosphere. Then, it is possible to establish the dose–response function for a stone, for example, the sulphur uptake for a certain SO_2 concentration.

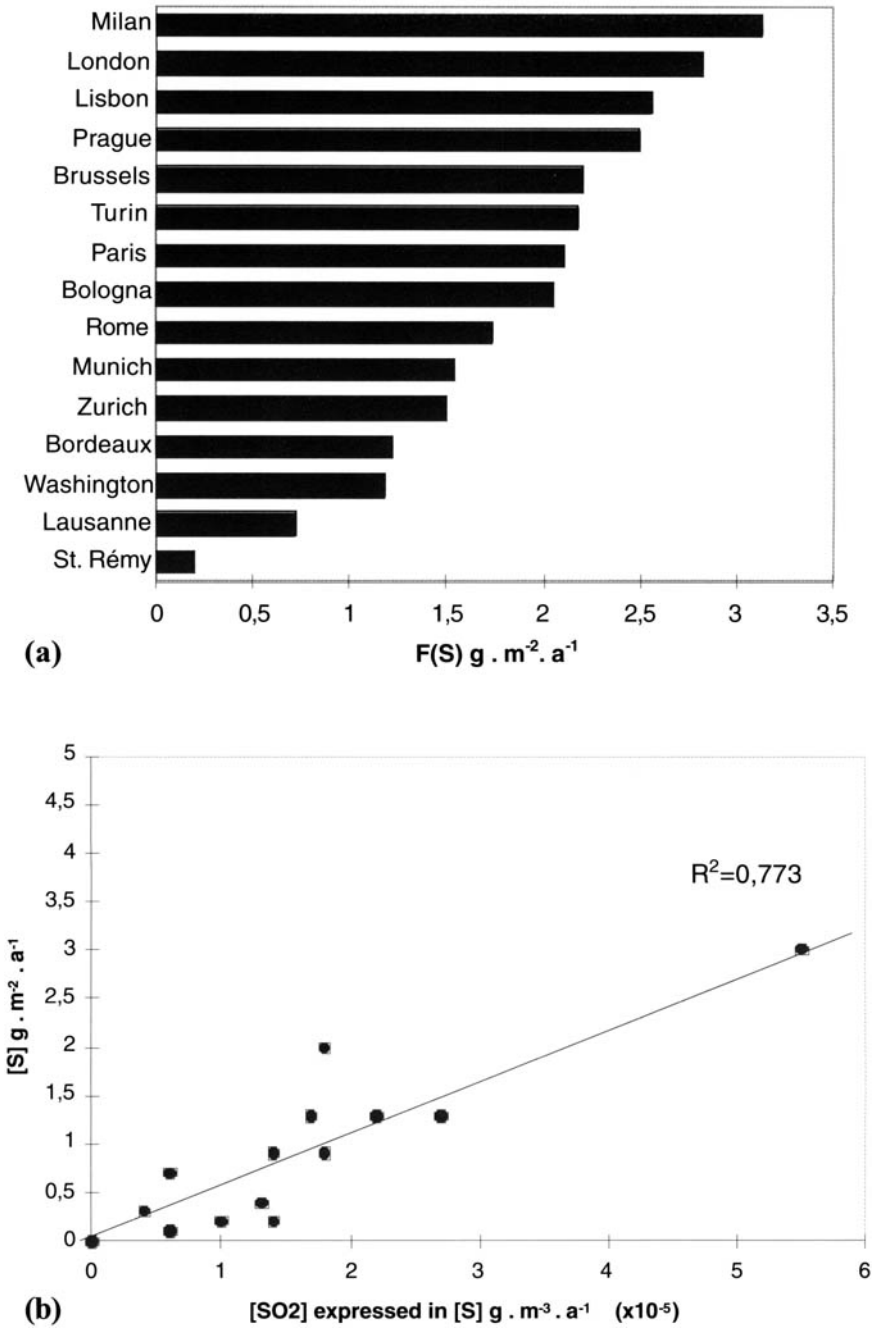

Fig. 10. Villarlod sandstone exposed in 1986–1987 on different field test-sites in Europe and the United States (modified from Furlan & Girardet 1992). (**a**) Flux density of sulphur passing through the surface and accumulating inside the samples; (**b**) correlation between the mean SO_2 concentration in the air (expressed in sulphur concentration) and the mean flux density of sulphur deposited inside the samples.

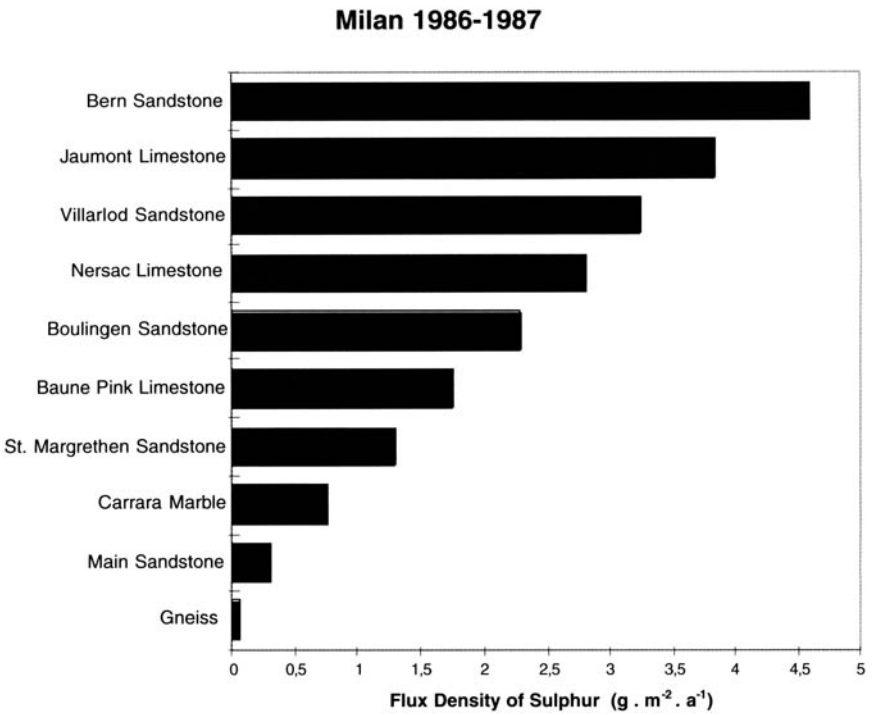

Fig. 11. Flux density of sulphur passing through the surface and accumulating inside different types of natural stone exposed for one year (1986–1987) in Milan (modified from Furlan & Girardet 1992).

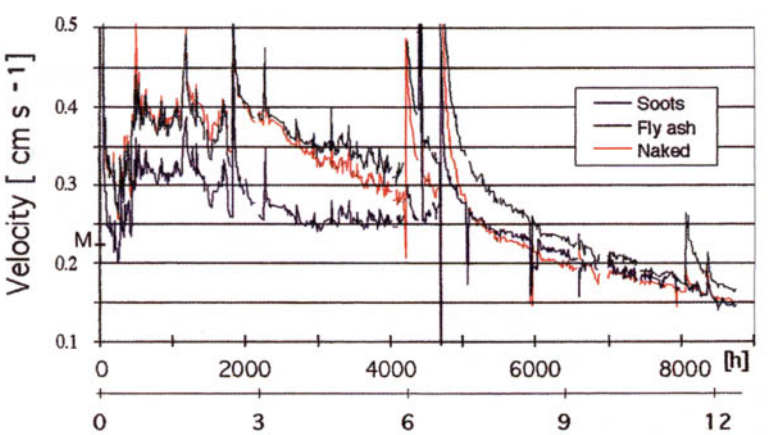

Fig. 12. SO_2 deposition velocity (cm s^{-1}) onto the Jaumont limestone (uncoated and coated by fly-ash or by soot) during 12 months of exposure in the Lausanne Atmospheric Simulation Chamber (Ausset *et al.* 1996).

Modelling the interaction between stone and atmospheric pollution: dose–response functions, critical or acceptable load and risk assessment mapping

An alternative approach with respect to the dose–response function concept was adopted by the International Cooperative Programme of the Economic Commission for Europe of the United Nations 'Alteration of materials by atmospheric pollution, including historical and cultural monuments' (ICP 'Materials'). This function is the expression of the alteration of the weathered material (response) in relation to the atmospheric parameters measured on the exposure site (dose).

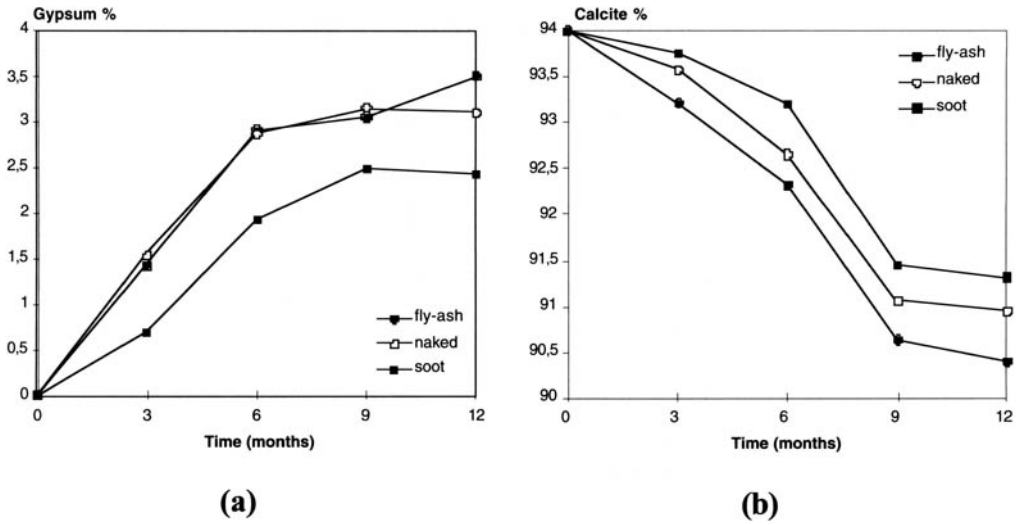

Fig. 13. Time series analyses (% per month) of the evolution of gypsum (**a**) and calcite (**b**) concentrations under the surface of Jaumont limestone exposed for one year in the Lausanne Atmospheric Simulation Chamber.

The atmospheric parameters of concern are the monthly means of temperature (T, °C), of time of wetness (TOW, total time when $RH >$ 80% and $T > 0$°C), of relative humidity (RH, %), of gas concentration in the atmosphere: $[SO_2]$, $[NO_x]$, $[O_3]$ etc. (mg m^{-3}), of height (mm) and pH of rain, and duration (t, years) of sample exposure to the atmosphere (Kucera & Fitz 1995).

A dose–response function is the sum of dry f_{dry} and wet f_{wet} alteration (Tidblad *et al.* 1998) and can be expressed as follows (with K = corrosion rate):

$$K = f_{dry}(T, RH, [SO_2], [NO_2], [O_3], t) + f_{wet}(Rain, [H^+], t)$$

From this general formula an equation can be determined if data regarding doses and responses are available. For stone, K is a lineic recession (mm), for glass, K is the corrosion expressed by the thickness of the leached layer LL (nm). The calculated dose–response functions for two stones and two medieval-like calco-potassic glasses, all unsheltered from rain, are as follows.

Portland limestone:

$$K = t^{0.96} \times (2.7 \times [SO_2]^{0.48} \times e^{(-0.018 \times T)} + 0.019 \times Rain \times [H^+])$$

Mansfield dolomitic sandstone when $T < 10$°C:

$$K = t^{0.91} \times (2.0 \times [SO_2]^{0.52} + 0.028 \times Rain \times [H^+])$$

Mansfield dolomitic sandstone when $T > 10$°C:

$$K = t^{0.91} \times (2.0 \times [SO_2]^{0.52} \times e^{(-0.013 \times (T-10))} + 0.028 \times Rain \times [H^+])$$

Glass M1:

$$LL = 0.013 \times [SO_2]^{0.49} \times RH^{2.75} \times t$$

Glass M3 when $T < 10$°C:

$$\ln(LL) = -0.98 + 0.45 \times \ln(t) + 0.37 \times \ln[NO_2] + 1.36 \times \ln(RH) + 0.041 \times (T - 10)$$

Glass M3 when $T > 10$°C:

$$\ln(LL) = -0.98 + 0.45 \times \ln(t) + 0.37 \times \ln[NO_2] + 1.36 \times \ln(RH) + 0.101 \times (T - 10)$$

To establish a link between dose–response functions and economic considerations a novel notion must be introduced: critical load. This notion has been defined for ecosystems by Nilson (1986) as follows: 'The highest deposition of a compound that will not cause chemical changes leading to long-term harmful effects on ecosystem structure and function'. However, as such this notion is not acceptable for materials because, in this case, even a minimal dose of pollutants may lead to decay (Kucera & Fitz 1995). Thus it is necessary to introduce the modified concept of acceptable load.

This concept of acceptability is based on comparison between the pollution on the studied site and the ' background pollution' of a site containing no specific sources of pollutants. The acceptable corrosion is noted as K_{acc} and the 'background' corrosion as K_b. The values of K_b are determined for each material as $K_b = A \times t^k$, where A and k are two constants for each material and each type of exposition (sheltered and unsheltered).

One defines then $K_{acc} = n \times K_b$. The recommended values for n are between 1.2 and 2, based on economical considerations. The acceptable load is then that for which the corrosion remains below the acceptable corrosion: $K \leq K_{acc}$.

This concept of acceptable load has an interesting property for graphic representation: it is easily illustrated by mapping and allows the zones where the corrosion thresholds are exceeded to be identified.

The mapping of acceptable corrosion needs to have available dose–response functions and acceptable loads for each material concerned and each dose regarding a representative zone. Interpolation calculations are necessary when all the meteorological and environmental parameters are not available for each mesh of the network (50 × 50 km in the EMEP Network). The 'Krigeage method' was used to obtain the map of SO_2 distribution (Fig. 14) and the map of the risk for Portland limestone based on the dose–response function displayed (Fig. 15) for France.

Conclusion: some old questions were answered but many new ones are created

Much progress has been made in the last two decades in the knowledge of the interactions between building materials and atmospheric pollution due essentially to research carried out by the Italian School of Padua and Bologna (Camuffo *et al.* 1982, 1983) showing the paramount role of the position of materials relative to their exposure to rain. After a descriptive and analytical phase, a mechanistic approach was adopted by the scientific community involved in these problems. Nowadays the mechanisms of decay reactions are quite well known for stone, but less so for glass. However, new data have to be collected and new approaches have to be developed along the following lines of research:

- few data are available on the action on building materials of other pollutants besides sulphur, e.g. NO_x, O_3, VOC;
- little is known concerning the decay behaviour of other materials besides stone and glass, e.g. cement, mortar, concrete, ceramics, brick, metal, painting, polymers (Martinez-Ramirez *et al.* 1998; Rendell & Jauberthie 1999; Sabbioni *et al.* 2001; Demirbas *et al.* 2001);
- the determination of critical or acceptable thresholds and loads for materials has still to be completed for Europe;
- the mapping of the risk for materials due to atmospheric pollution, from dose–response functions, remains to be accomplished on a European scale;
- the economical approach expressed in terms of cost–benefit ratio of the abatement of atmospheric pollution and of its action against buildings is not adopted by economists and urbanists on a wide scale;
- the evaluation of the respective advantages of building maintenance policies, either light and continuous preventive conservation or heavy, periodic and expensive interventions, remains to be done.

Knowledge of the degradation of materials in polluted atmospheres constitutes a solid background for these various approaches. But time runs quickly and atmospheric pollution changes its nature and intensity: the risk exists to study fossil phenomena.

These studies benefited from funding by the Regional Council of Ile de France (Programme SESAME, 1995), the European Commission (Contracts 'LASC' EV5V-CT92-0116 and 'ARCHEO' ENV4-CT95-0092), the Franco-German Research Programme for the Conservation of Historic Monuments, the Geomaterials Programme of the CNRS, the Programme PRIMEQUAL of the French Ministry of the Environment, the French Agency for the Environment and Energy Management (ADEME) and the International Co-operative Programme of the United Nations 'Effects of atmospheric pollution on materials, including historic and cultural monuments'. We thank N. Schiavon for help with English.

References

AUSSET, P., LEFÈVRE, R. A. & PHILIPPON, J. 1991. Interactions entre les microsphérules silicatées atmosphériques et les surfaces de monuments en calcaire et en bronze. PACT, *Journal of the European Study Group on Physical, Chemical, Mathematical and Biological Techniques Applied to Archeology*, **33**(II-3), 135–147.

AUSSET, P., LEFÈVRE, R. A., PHILIPPON, J. & VENET, C. 1994. Présence constante de cendres volantes industrielles dans les croûtes noires d'altération

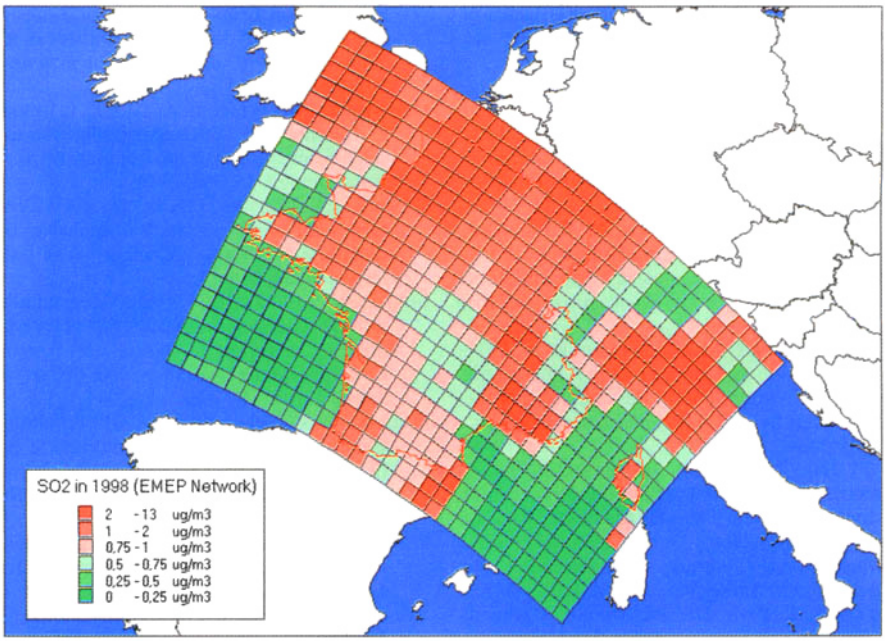

Fig. 14. Map of distribution for France of the SO_2 concentration ($\mu g\ m^{-3}$) in air in 1998, calculated by the EMEP Network.

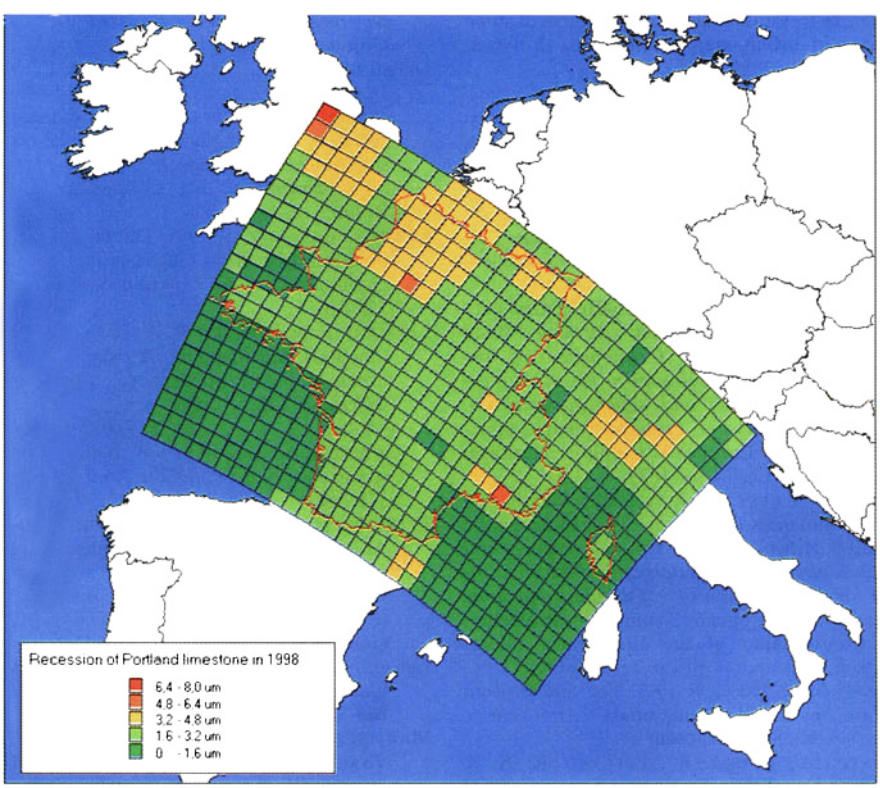

Fig. 15. Map of the risk (lineic recession) for Portland limestone in France calculated from dose-response function by ICP Materials in its first phase (1987–1994) and from the environmental parameters existing in 1998.

superficielle de monuments français en calcaire compact. *Comptes Rendus de l'Académie des Sciences.*, Paris, **318**(II), 493–499.

AUSSET, P., CROVISIER, J. L., DEL MONTE, M., *et al.* 1996. Experimental study of limestone and sandstone sulphation in polluted realistic conditions: the Lausanne Atmospheric Simulation Chamber (LASC). *Atmospheric Environment*, **30**, 3197–3207.

AUSSET, P., BANNERY, F., DEL MONTE, M. & LEFÈVRE, R. A. 1998. Recording of pre-industrial atmospheric environment by ancient crusts on stone monuments. *Atmospheric Environment*, **32**(16), 2859–2863.

AUSSET, P., DEL MONTE, M. & LEFÈVRE, R. A. 1999. Embryonic sulphated black crust in Atmospheric Simulation Chamber and in the field: role of the carbonaceous fly ash. *Atmospheric Environment*, **33**, 1525–1534.

AUSSET, P., DEL MONTE, M., LEFÈVRE, R. A. & THIÉBAULT, S. 2000. Past air pollution recordings on stone monuments: the Heads of the King of Juda statues from Notre-Dame Cathedral (Paris). *9th International Congress on Deterioration and Conservation of Stone*, Venice, Vol. 1, 339–347.

BRIMBLECOMBE, P. 1987. *The Big Smoke*, Methuen, London.

CAMUFFO, D. 1984. The influence of run-off on weathering of monuments. *Atmospheric Environment*, **18**, 2273–2275.

CAMUFFO, D., DEL MONTE, M. & SABBIONI, C. 1982. Wetting deterioration and visual features of stone surfaces in urban area. *Atmospheric Environment*, **16**, 2253–2259.

CAMUFFO, D., DEL MONTE, M. & SABBIONI, C. 1983. Origin and growth mechanisms of the sulfated crusts on urban limestone. *Water, Air and Soil Pollution*, **19**, 351–359.

CONNOR, M. & GIRARDET, F. 1992. Etude du mode de fixation du soufre sur un grès calcareux. *In*: DELGADO, J. (ed.) *7th International Congress on Deterioration and Conservation of Stone*. Lisbon, 407–416.

DEL MONTE, M. & LEFÈVRE, R. A. 2001*a*. Particulate matter in the urban atmosphere. *Advanced Study Course «Sciences and Technologies of the materials and of the environment for the protection of stained glass and stone monuments»*. European Commission, Protection and Conservation of the European Cultural Heritage, Research report n. 14, 99–107.

DEL MONTE, M. & LEFÈVRE, R. A. 2001*b*. Weathering of stone and glass of monuments by atmospheric pollution. *Advanced Study Course «Sciences and Technologies of the materials and of the environment for the protection of stained glass and stone monuments»*. European Commission, Protection and Conservation of the European Cultural Heritage, Research report n. 14, 123–131.

DEL MONTE, M. & ROSSI, P. 1997. Fog and gypsum crystals on building materials. *Atmospheric Environment*, **31**, 1637–1646.

DEL MONTE, M., AUSSET, P. , LEFÈVRE, R. A. & THIÉBAULT, S. 2001*a*. Evidence of pre-industrial air pollution from the Heads of Kings of Juda Statues from Notre-Dame Cathedral in Paris. *The Science of the Total Environment*, **273**, 101–109.

DEL MONTE, M. , FORTI, P., AUSSET, P., LEFÈVRE, R. A. & Tolomelli, M. 2001*b*. Air pollution records on selenite in the urban environment. *Atmospheric Environment*, **35**, 3885–3896.

DEMIRBAS, A., OZTÜRK, T., KARATAS, F. O. 2001. Long-term wear on outside walls of buildings by sulfur dioxide corrosion. *Cement and Concrete Research*, **31**, 3–6.

FURLAN, V. & GIRARDET, F. 1988. Vitesse d'accumulation des composés atmosphériques du soufre sur diverses natures de pierre. *6th International Congress on Deterioration and Conservation of Stone*, Torun, 187–196.

FURLAN, V. & GIRARDET, F. 1991. Pollution atmosphérique et durabilité des pierres de construction. *Collogue International sur la Détérioration des Matériaux de Construction*, La Rochelle, 79–91.

FURLAN, V. & GIRARDET, F. 1992. Pollution atmosphérique et réactivité des pierres. *In*: DELGADO, J. (ed.) *7th International Congress on Deterioration and Conservation of Stone*. Lisbon, 156–161.

GIRARDET, F & FURLAN, V. 1983. Mesure de la vitesse d'accumulation des composés soufrés sur des éprouvettes de pierre exposées en atmosphère rurale et urbaine. *4th International Congress on Detererioration and Preservation of Stone Objects*, Louisville, 159–168.

GIRARDET, F., AUSSET, P., DEL MONTE, M., FURLAN, V., JEANNETTE, D. & LEFÈVRE, R. A. 1996. Etude expérimentale de prise en soufre de deux pierres calcaires dans la chambre de simulation atmosphérique de Lausanne. *8thInternational Congress on Deterioration and Conservation of Stone*. Berlin, vol. 1, 349–358.

KUCERA, V. & FITZ, S. 1995. Direct and indirect air pollution effects on materials including cultural monuments. *Water, Air and Soil Pollution*, **85**, 153–165.

LAURANS, E. & LEFÈVRE, R. A. 2001. Dose-response functions and mapping of risk for materials in urban polluted atmosphere. *Pollution Atmosphérique*, **172**, 557–569.

LEFÈVRE, R. A. & AUSSET, P. 2001. The effects of atmospheric pollution on building materials: stone and glass, *Pollution Atmosphérique*, **172**, 571–588.

LEFÈVRE, R. A., DERBEZ, M., GRÉGOIRE, M. & AUSSET, P. 1998. Origin of sulphated grey crusts on glass in polluted urban atmosphere: the stained-glass windows of Tours Cathedral (France). *Glass Science and Technology, Glastechische Berichte*, **71**, 75–80.

LIBOUREL, G., BARBEY, P.& CHAUSSIDON, M. 1994. L'altération des vitraux. *La Recherche*, **262**, 168–188.

MARTINEZ-RAMIREZ, S., PUERTAS, F., BLANCO-VARELA, M. T. & THOMPSON, G. E. 1998. Effect of dry deposition of pollutants on the degradation of

lime mortars with sepiolite. *Cement and Concrete Research*, **28**, 125–133.

MUNIER, I. & LEFÈVRE, R. A. 2000. Comparison of the particles and cements of sulphated crusts from stained-glass, lead and stone of the Sainte-Chapelle in Paris. *5th International Symposium on the Conservation of Monuments in the Mediterranean Basin*, Seville, 36.

MUNIER, I., LEFÈVRE, R. A. & LOSNO, R. 2001. Atmospheric factors influencing the formation of neocrystallisations on low-durability glass exposed to urban atmosphere, *19th International Congress on Glass*, Edinburgh, July 2–6.

NILSON, J. 1986. Critical loads for nitrogen and sulfur. *Miljørapport 1986*. Nordic Council of Ministers, Copenhagen.

RENDELL, F. & JAUBERTHIE, R. 1999. The deterioration of mortar in sulphate environments. *Construction and Building Materials*, **13**, 321–327.

SABBIONI, C., ZAPPIA, G., RIONTINO, C. *et al.* 2001. Atmospheric deterioration of ancient and modern hydraulic mortars. *Atmospheric Environment*, **35**, 539–548.

STERPENICH, J. & LIBOUREL, G. 2001. Medieval stained glass windows: a physical and chemical characterisation of alteration. *Advanced Study Course « Sciences and technologies of the materials and of the environment for the protection of stained glass and stone monuments»*. European Commission, Protection and Conservation of the European Cultural Heritage, Research report n. 14, 171–180.

TIDBLAD, J., MIKHAILOV, A. & KUCERA, V. 1998. Unified dose-response function after 8 years of exposure. *Multipollutant Effect of Air Pollutants on Materials – Modelling and Verification*. Swedish Corrosion Institute Report C 2000–11.

VERGÈS-BELMIN, V. 1994. Pseudomorphism of gypsum after calcite, a new textural feature accounting for the marble sulphation mechanism. *Atmospheric Environment*, **28**, 295–304.

This page intentionally left blank

Modelling the rapid retreat of building sandstones: a case study from a polluted maritime environment

B. J. SMITH[1], A. V. TURKINGTON[2], P. A. WARKE[1], P. A. M. BASHEER[3], J. J. McALISTER[1], J. MENEELY[1], J. M. CURRAN[1]

[1] *School of Geography, Queen's University Belfast, BT7 1NN, UK*

[2] *Department of Geography, University of Kentucky, Patterson Office Tower, Lexington, KY 40506-0027, USA*

[3] *School of Civil Engineering, Queen's University Belfast, BT7 1NN, UK*

Abstract: Sandstones are widely used as building stones throughout NW Europe. Unlike limestone, sandstones tend to experience episodic and sometimes rapid surface retreat associated with the action of salts and often leading to the development of hollows/caverns in the stone. The unpredictability of these decay dynamics can present significant problems when planning conservation strategies. Consequently, successful conservation requires a better understanding of the factors that trigger decay and determine the subsequent decay pathway. An overview of results from previous studies provided the basis for simulation experiments aimed at identifying the factors that (a) initiate decay and (b) permit the continuance of salt weathering despite rapid loss of surface material. These simulation studies involve investigation of changes in micro-environmental conditions as surface hollows develop and examination of salt weathering dynamics within such hollows. These data combined with knowledge gained from previous work have allowed the refinement of a conceptual model of rapid sandstone retreat. In this model decay is linked to the establishment of positive feedback conditions through interactions between factors such as porosity, permeability, mineralogy and their effect on salt penetration.

The pre-eminent use of limestone in prestigious ecclesiastical and municipal structures has greatly influenced general assumptions regarding the nature of stone decay. This is exemplified by the perception that decay tends to be characterized by a gradual and progressive loss of surface material primarily through the effects of chemical dissolution (Smith in press). However, not all building stones behave in this way. Quartzitic sandstones, in particular, which are widely used across NW Europe, tend to experience episodic and sometimes rapid, catastrophic surface retreat often associated with the disruptive effects of accumulated salts (Bluck 1992; Smith *et al.* 1994). Characteristically, sandstones are immune to all but limited solution, but particularly prone to disruption by granular disintegration, contour scaling and multiple flaking – decay features that are triggered by intrinsic and/or extrinsic factors. Central to successful stone conservation in such cases is a greater understanding of these trigger factors and the intervention required to switch off the feedback mechanisms that maintain and often accelerate decay once it starts.

The salts responsible for decay of non-calcareous sandstones can derive from several sources. Sulphur in the atmosphere can react with mortars or adjacent limestones to produce gypsum which then washes over or through nearby non-calcareous stones (Cooper *et al.* 1991). Alternatively, gaseous pollutants can react with limestone fragments blown on to the stone as dust, or gypsum may be contained within fly-ash particles deposited directly on to buildings. Although gypsum is generally considered to be the principal agent of decay, in reality stone may contain a cocktail of salts derived, for example, from marine aerosols, rising groundwater and locally from road de-icing (Smith *et al.* 1991).

Mechanisms of salt weathering and their effects have been widely examined under both natural and experimental conditions and their impact on the urban environment has been greatly informed by multidisciplinary studies of naturally salt-rich environments such as coasts and deserts (e.g. Bluck & Porter 1991; Butlin 1991; Cooke & Gibbs 1993; Goudie 1985; Price 1996; Viles 1993). These studies have identified salt weathering as a threshold phenomenon that can initiate rapid stone loss through the cumulative effects of crystallization, thermal expansion, hydration/dehydration and enhanced silica dissolution. Such mechanisms characteristically operate where salt concentrates at the surface,

From: SIEGESMUND, S., WEISS, T. & VOLLBRECHT, A. 2002. *Natural Stone, Weathering Phenomena, Conservation Strategies and Case Studies.* Geological Society, London, Special Publications, **205**, 347–362.
0305-8719/02/$15.00 © The Geological Society of London 2002.

to produce granular disaggregation, or at depth to cause scaling. The precise zone of concentration and hence pattern of decay is a complex interaction between the solubility characteristics of individual salts and the porosity and wetting and drying characteristics of the stone and the stone surface.

The behaviour of individual sandstone blocks is thus often characterized by stability after emplacement, followed by rapid decay as diminishing strength is exceeded by an exceptional external stress or a gradual accumulation of internal stresses. In some circumstances, negative feedback mechanisms, such as the loss of salt together with weathered debris or the regrowth of case-hardened surface layers, might operate to re-establish stability until the decay threshold is again breached. Alternatively, under some circumstances or on particular stones, positive feedback mechanisms are triggered that accelerate decay by effects such as multiple flaking. This can lead to the complete destruction of individual blocks over periods measured in years rather than tens or hundreds of years. Rapid decay is manifested as surface recession compared to surrounding stones and the creation of a cavernous hollow (Fig. 1).

Because accelerated surface retreat is such a common decay feature in sandstone, attempts have been made to explain its development with the emphasis on altered microenvironmental conditions. In particular, it is suggested that shaded hollows or caverns could form more humid environments that favour retention and penetration of salts derived directly or indirectly from atmospheric pollutants. However, this does not explain why, with reduced wash-in and near-surface concentration, any salts present are not rapidly lost together with the debris. Neither does such a microenvironmental model explain why only certain stones on an otherwise uniform facade experience rapid, catastrophic failure.

Clearly, the explanation for such significant deterioration reflects the complex interaction between microenvironmental conditions, subtle variations in stone properties, the nature and mix of salts and the dynamics of salt input, output and storage. To control catastrophic, salt-induced decay requires an understanding of the factors that determine establishment of positive feedback mechanisms that perpetuate decay once it is initiated. To achieve this understanding three questions need to be answered.

Fig. 1. Scrabo sandstone block on St. Matthew's Church exhibiting severe surface retreat and material loss through multiple flaking and granular disintegration.

1. Why are certain sandstones susceptible to salt weathering?
2. How do microenvironmental conditions on stonework influence decay?
3. What permits continued salt weathering despite rapid stone loss?

There has been considerable exploration of question 1 (e.g. Goudie *et al.* 1970; Price 1978; Yates & Butlin 1996), some examination of question 2 (e.g. Dragovich 1981; Smith & McAlister 1986), but very little consideration of question 3. It is on these last two aspects that this paper proposes to concentrate through:

- the characterization of stone, salt and construction conditions associated with the onset, continuation and stabilization of rapid retreat on selected buildings;
- the characterization of thermal, moisture and pollution regimes associated with microenvironments created by rapid retreat;
- the reproduction of scaling and flaking features within a climatic cabinet under controlled conditions.

Through investigation of the above, a conceptual model of rapid sandstone retreat will be formulated, which may ultimately increase understanding of conditions that predispose stone to rapid decay and thus help inform choice of conservation strategies and indeed replacement stone.

Assumptions and questions regarding the rapid decay of sandstones

The conceptual framework for rapid retreat outlined above emphasizes strength/stress thresholds as controls on the rate of decay over time. However, acceptance of this model also requires the testing of a number of additional, inherent assumptions. These assumptions include:

- that moisture and salt are cycled through the exposed surfaces of stone blocks with frequent complete drying out, an assumption that is also central to most stone durability tests;
- that cycles of wetting and drying concentrate salt in surface/near-surface zones;
- that in a polluted urban environment, gypsum is the main salt responsible for breakdown and that for non-calcareous stone the reaction between atmospheric sulphur and mortars is a major source of this salt;
- that in addition to pollution-derived salts, stonework accumulates a range of other environmental salts, especially chlorides in maritime and near-maritime locations.

These assumptions can be resolved into a series of questions that have to be addressed before it is possible to refine the initial decay model and to identify factors that influence decay, determine susceptibility to retreat and control the speed of stone response to environmental stresses. These questions are:

- What processes lead to initial surface loss/scaling of a stone?
- What maintains decay while salt-rich debris is rapidly lost from retreating blocks?
- What is the relationship between surface loss and preparatory subsurface weathering and do weathering and surface loss alternate or progress simultaneously?
- What are the pathways by which moisture and salt migrate through and over sandstone blocks in buildings and how are they modified by block retreat?
- What microenvironmental conditions exist within caverns or hollows and how are they modified as blocks retreat?
- What are the moisture conditions within stone blocks as they retreat?

Answers to the above questions were sought through the combination of laboratory-based simulation study, exposure trials and a case study site investigation (St. Matthew's Church) in conjunction with local conservation architects.

Location of the case study

Belfast has a long and ongoing history of atmospheric pollution (especially sulphur and particulates) and because of its cool temperate maritime location (Fig. 2) experiences particularly wet, salt-rich urban environmental conditions (Smith *et al.* 1991). Because of the city's location in a valley between two upland areas it is particularly prone to high concentrations of SO_2 and NO_X during high pressure anticyclonic conditions that give rise to temperature inversions that effectively trap and facilitate the concentration of atmospheric pollutants.

St. Matthew's Church, situated in east-central Belfast, was built between 1881 and 1883

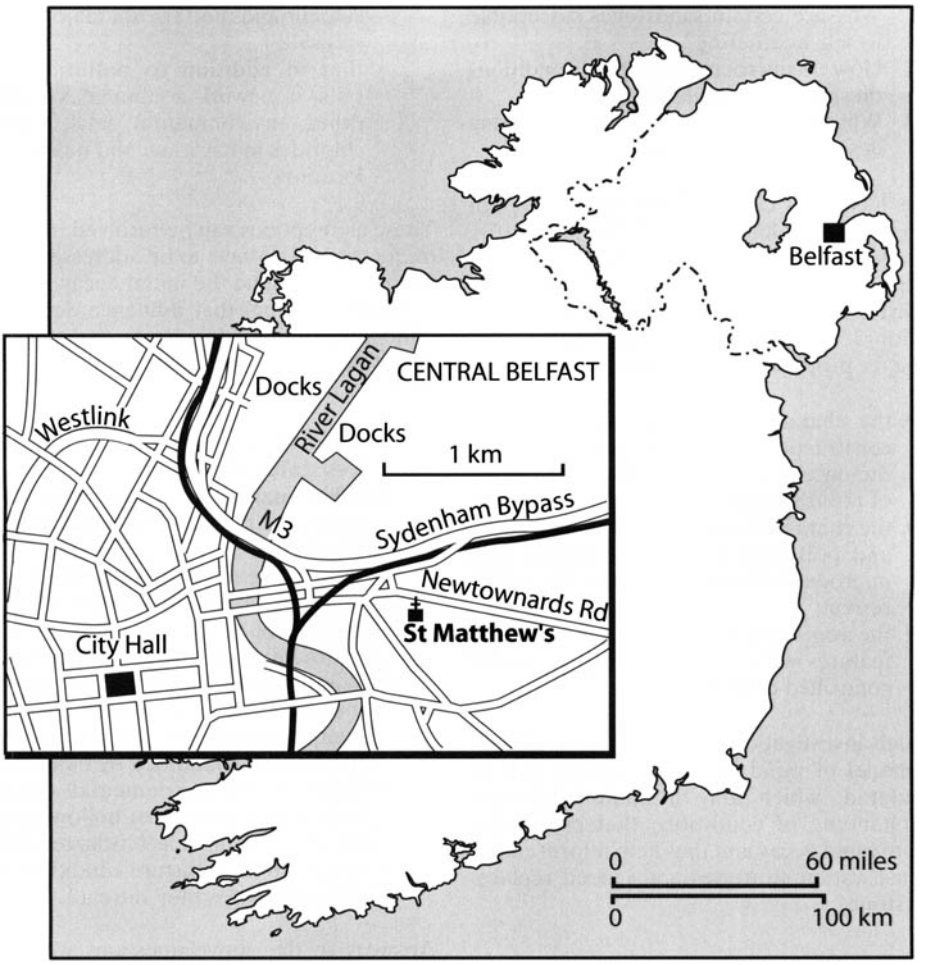

Fig. 2. Map showing location of Belfast and St. Matthew's Church.

primarily from local Triassic Scrabo sandstone, with detailing in Scottish Dumfries sandstone. At the beginning of the study the structure comprised sandstone blocks in varying stages of decay and was scheduled for major renovation thus providing the opportunity for extensive sampling of complete blocks and an input into decisions regarding choice of conservation strategies. Scrabo sandstone is non-calcareous and has highly variable structural and mineralogical properties, which include well-defined bedding planes and lenses of smectite clays. Intrusion of a dolerite sill in the area of the source quarry led to the progessive transformation of pore-filling smectite, quartz and dolomite in the sandstone to grain-coating talc at the lowest contact temperatures. At higher temperatures talc reacted with calcite to produce an actinolite amphibole that occurs as acicular needles protruding into pore spaces (McKinley *et al.* 2001*a*).

In addition to the use of Scrabo sandstone, samples of Dumfries and Dunhouse sandstones were also used in laboratory studies and for exposure trials. Use of a variety of sandstones with different structural and mineralogical properties (Table 1) allowed identification of the variability of response to exposure conditions and thus contributed to a better understanding of some of the factors controlling the nature and rate of deterioration.

Table 1. *Properties of quartz sandstones referred to in the text*

	Rock type and classification (Folk 1974)	Age	Grain size (mm)	Matrix/cement (wt%)	Porosity (vol%)	Permeability (md)	Saturation coefficient	Water absorption (wt%)	Bulk specific gravity (g m^{-3})
Dumfries sandstone	Red sandstone: quartz arenite	Permian	Medium range 0.5–0.2, mean 0.4	Iron oxide occurring as grain coatings and cement (~5%)	18–25	200–1000 (mean 600)	0.67	5.7	2173
Dunhouse sandstone	Yellow sandstone: sub-arkose	Carboniferous	Fine range 0.13–0.4, mean 0.2	Calcite (4%), clay minerals (8%), iron oxide (6%)	16–18	50–150 (mean 80)	0.66	4.7	2167
Scrabo sandstone	Red to white sandstone: arkose	Triassic	Medium range 0.1–0.5, mean 0.3	Clay minerals (smectites), actinolite, talc (~10% in total)	15–25	5–1500 (mean 500)	0.70	6.4	2110

Characterizations of conditions associated with rapid retreat of sandstones

Previous investigations of Scrabo sandstone in natural exposures and on St. Matthew's Church combined with exposure trials and laboratory investigation of the effects of mortars during construction have greatly improved our understanding of the complexity of variables that may significantly contribute to observed decay dynamics of sandstone. As a preliminary to experimental data presented in the following sections, the main points to emerge from these studies are summarized below.

Salt distribution in weathered sandstone

Most studies of building stone decay have been restricted, by necessity, to the sampling of material that falls or can be easily removed from the outer 10–15 mm of block surfaces. The opportunity to sample complete blocks from St. Matthew's allowed analysis by ion chromatography (IC), atomic absorption spectroscopy (AAS) and X-ray diffraction (XRD) of salt distribution through two-dimensional transects of the blocks from the exposed face to the block base. These data showed that while visible disruption in the form of scaling and flaking were confined to the outer 10–15 mm of stone, high concentrations of $CaSO_4$ (gypsum) and NaCl (halite) were detectable some 40–60 mm into the substrate where enlargement and coalescence of some pore spaces as identified by scanning electron microscopy (SEM) indicated the formation of an incipient fracture zone (Warke & Smith 2000). It was suggested that the mobility of $CaSO_4$ may have been enhanced by the presence of NaCl as demonstrated by Price & Brimblecombe (1994).

Three-dimensional salt distribution in sandstone

As a progression from the two-dimensional analysis of salt distribution, whole blocks were analysed to give a three-dimensional image of salt distribution in blocks from St. Matthew's. This added a further layer of complexity by identifying salt 'hotspots' within the substrate particularly of sulphates and chlorides. These 'hotspots' are significant because they provide potential salt reservoirs to fuel decay as the outer surface retreats. The evidence indicates that in addition to the 'hotspots' the widespread distribution of salts within the blocks may reflect migration by ionic diffusion during the

often prolonged periods of block wetness (Turkington & Smith 2000).

Sandstone modification during construction

Experimental evidence indicates that during block emplacement, mortar can alter block edge permeability characteristics and can contribute, in particular, to calcium loading around the block edges (Smith *et al.* 2001). The significance of these findings is twofold. First, the reduction in block edge permeability may restrict moisture movement across the mortar–stone interface. Second, reduced block edge permeability may help to constrain moisture and salt migration through the outer surfaces of the blocks, ultimately contributing to the enhancement of surface retreat.

Gypsum formation in Scrabo sandstone

Natural mineralogical properties of sandstone can have major implications for decay dynamics. Scrabo sandstone, for example, contains diagenetic, pore-filling fibrous actinolite (Ca Mg amphibole). Examination of weathered Scrabo sandstone identified the sulphation of this fibrous actinolite with the resulting formation of gypsum and production of talc, both minerals that are not present in the quarry-fresh stone (McKinley *et al.* 2001*b*). The pore-filling nature of the actinolite means that gypsum is formed precisely where it can achieve maximum disruption.

Surface alteration of sandstone exposed to polluted urban conditions

Exposure trials of Dunhouse sandstone at sites throughout Belfast over a period of six years have shown the extent and spatial variability of stone surface alteration. Sample tablets of sandstone mounted on aluminium racks were either exposed or sheltered from rainwash. The former replicated rainwashed conditions on a building surface while the latter simulated conditions in hollows developed by retreating blocks where the interior surfaces are sheltered from direct rainwash, but remain open to gaseous and particulate deposition. A full description of methodology and results is given in Turkington (in press), but selected data and observations relevant to this discussion are made here and shown in Figure 3.

IC and AAS analysis showed that after six years of exposure the sheltered stone tablets had the highest concentrations of chloride and sulphate. Deposition and accumulation particularly of sulphate increase over time contributing to the formation of gypsum crusts that were readily identifiable by SEM. The highest concentrations of sulphate were generally found on samples located in the city centre. The accumulation of sulphate and development of gypsum crusts on sheltered samples reflect the

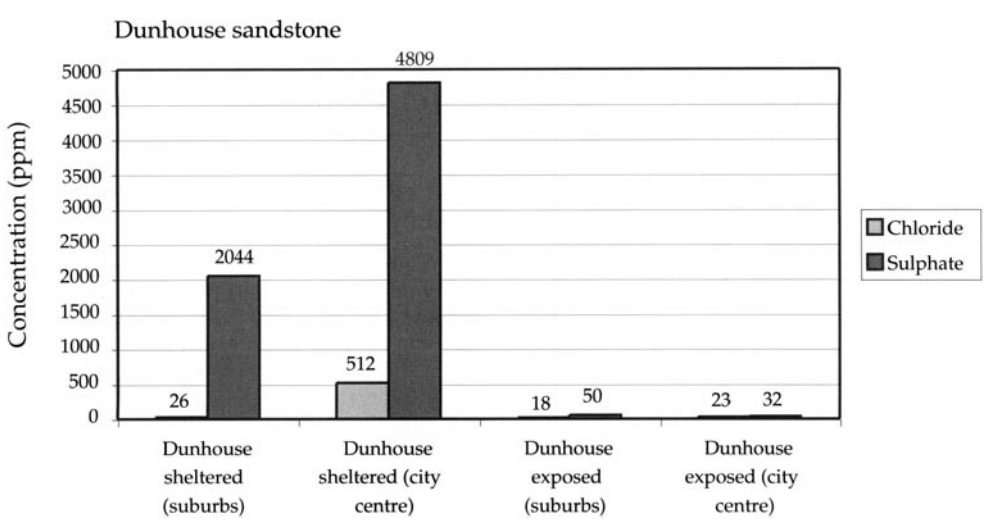

Fig. 3. Differential accumulation of chloride and sulphate on Dunhouse sandstone tablets exposed in sheltered and unsheltered conditions in the city centre and suburbs of Belfast for six years.

effective mobilization of elements in the absence of direct rainwash through the effects of fog and condensation (atmospheric humidity) combined with the occasional action of driven rain.

Deposition of chloride does not exhibit the same consistency in accumulation over time with high levels of chloride recorded after only two years of exposure at a site located close to Belfast docks where the input of marine aerosols is undoubtedly significant. This site is close to St. Matthew's Church where similarly high concentrations of chloride were recorded (Warke & Smith 2000; Turkington & Smith 2000).

The high concentrations of gypsum identified on surface and substrate material of sandstone at St. Matthew's Church (Warke & Smith 2000; Turkington & Smith 2000) indicate a net accumulation of gypsum, much of which is attributed to past pollution conditions. However, exposure trial data highlight the potential significance of continued gypsum accumulation under contemporary conditions.

Microclimatic conditions within cavernous hollows

Better understanding of the microenvironmental conditions created as sandstone blocks retreat is central to identification of the weathering processes that operate, and to the setting of parameters for subsequent simulation and conceptual modelling. Investigation of changing microenvironmental conditions (temperature and block moisture content) within block caverns was undertaken and a detailed description of the experimental procedure and resulting data are reported in Turkington *et al.* (2002). An overview of the methodology and summary of the major findings are presented here.

A test-rig was constructed to replicate conditions in an actively growing cavern. This rig comprised a sandstone block (200 × 100 × 100 mm) embedded in an insulated cabinet wall (Fig. 4). The block was set within a wooden sleeve that allowed it to be progressively pulled back to imitate cavern development as sandstone blocks retreat. The sleeve was also insulated externally with expanded polystyrene in an attempt to reproduce the thermal mass provided by surrounding stone blocks in a wall. Simulated insolation was provided by an infrared lamp placed at an angle of 45° above and to the front of the block. The lamp was automatically switched on and off at pre-set intervals to simulate variable external environmental heating and cooling conditions and a small fan was used to generate airflow within the cavern during some of the experimental runs.

Block and air temperatures were measured using bead thermistors attached to an automatic data logger with thermistors inserted into pre-drilled holes 10, 25, 40 and 55 mm from the block surface. Air temperature at the block surface and within the cavern was also recorded as was relative atmospheric humidity within the test cabinet. Measurement of variations in block moisture content was based on a technique adapted from concrete studies (McCarter *et al.* 2001) whereby changes in electrical resistance between electrodes can be used as indicators of the degree of moisture saturation (Basheer *et al.* 2000). As with the bead thermistors, electrodes were embedded in cement paste in pre-drilled holes 10, 25, 40, 55 and 70 mm from the block surface. The quantitative results of this experiment are presented in Turkington *et al.* (2002), but the main conclusions that are relevant to the modelling of block retreat are summarized below.

- The depth of the subsurface temperature gradient decreases as blocks retreat.
- The steepness of the temperature gradient does not change significantly, especially with only shallow retreat.
- In still air, surface temperatures increase with shallow retreat, but decline significantly once the shadow zone exceeds 30%.
- Maximum surface temperature occurs at 50 mm retreat (50% shade), beyond which surface temperatures decrease.
- Forced airflow markedly reduces surface temperatures and subsurface temperature gradients.
- Evaporation of absorbed moisture reduces surface temperatures and subsurface temperature gradients.
- Drying time much exceeds normal diurnal insolation receipt; thorough wetting by capillary suction is very rapid (*c.* 10 min).
- Wetting does not reduce thermal stress on the stone, but restricts it to the near-surface layer.
- Depth of moisture loss is affected by retreat: as blocks retreat drying becomes only significant in the near-surface zone.
- Blocks with high moisture content display thermal gradients in the near-surface zone that are enhanced by block retreat, as subsurface layers are slower to

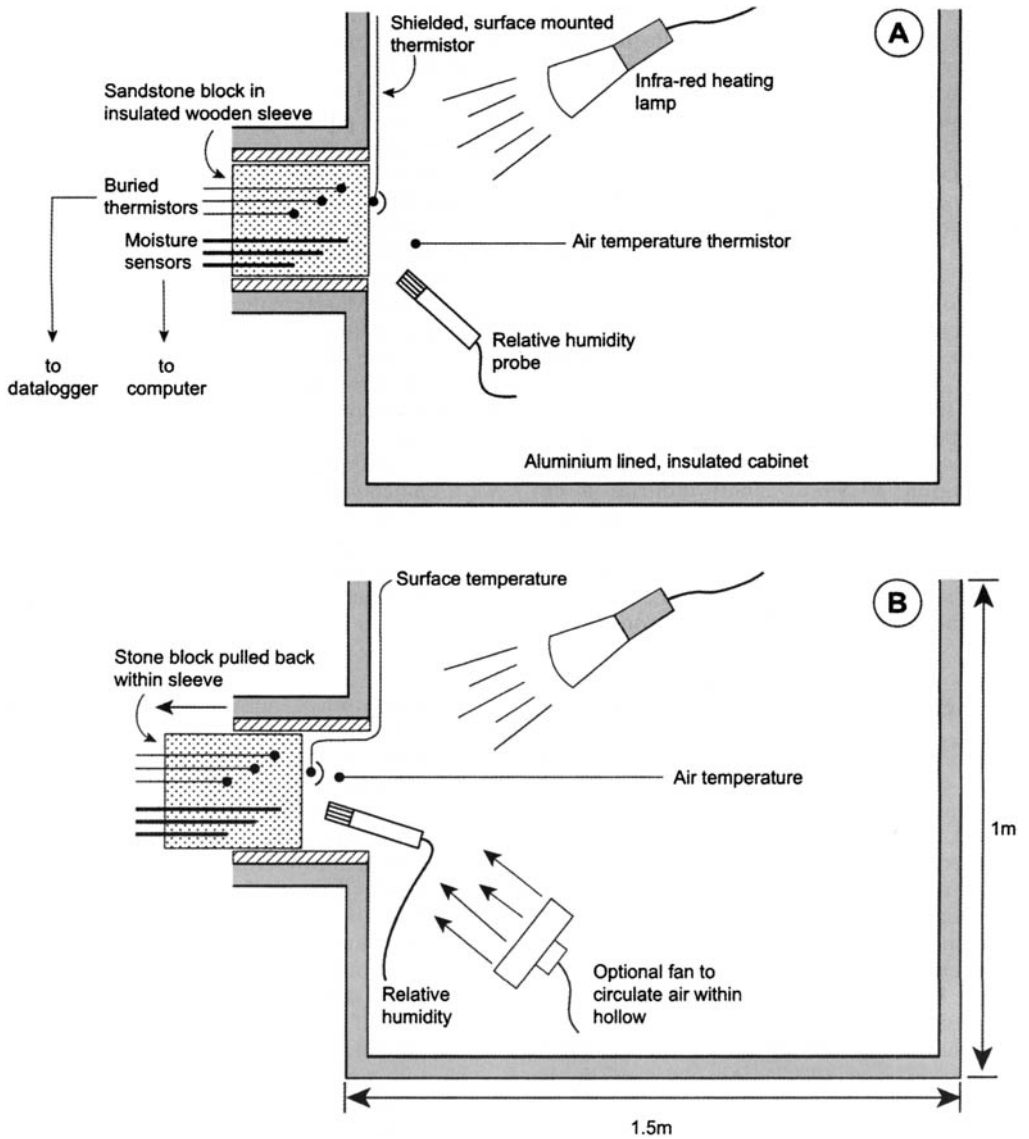

Fig. 4. Schematic diagrams of the environmental cabinet constructed to simulate temperature and moisture conditions associated with rapid retreat of sandstone building blocks. (**A**) Conditions before retreat and (**B**) conditions during retreat.

respond to indirect than to direct heating.

- Moisture cycling is only significant in near-surface layers of retreating stones. Stresses resulting from salt accumulation, and other processes controlled by temperature and moisture cycling, are thus concentrated in a shallow layer.

Effects of block retreat on moisture ingress were not tested. However, because sheltering reduces wetting by rain, this suggests that condensation and water vapour ingress are the principal moisture sources when stone has retreated. Direct precipitation is, however, unlikely to penetrate the stone to any great depth. A summary of potential salt and moisture flows based upon these observations and those in the preceding sections is given in Figure 5. Data from this experiment provided

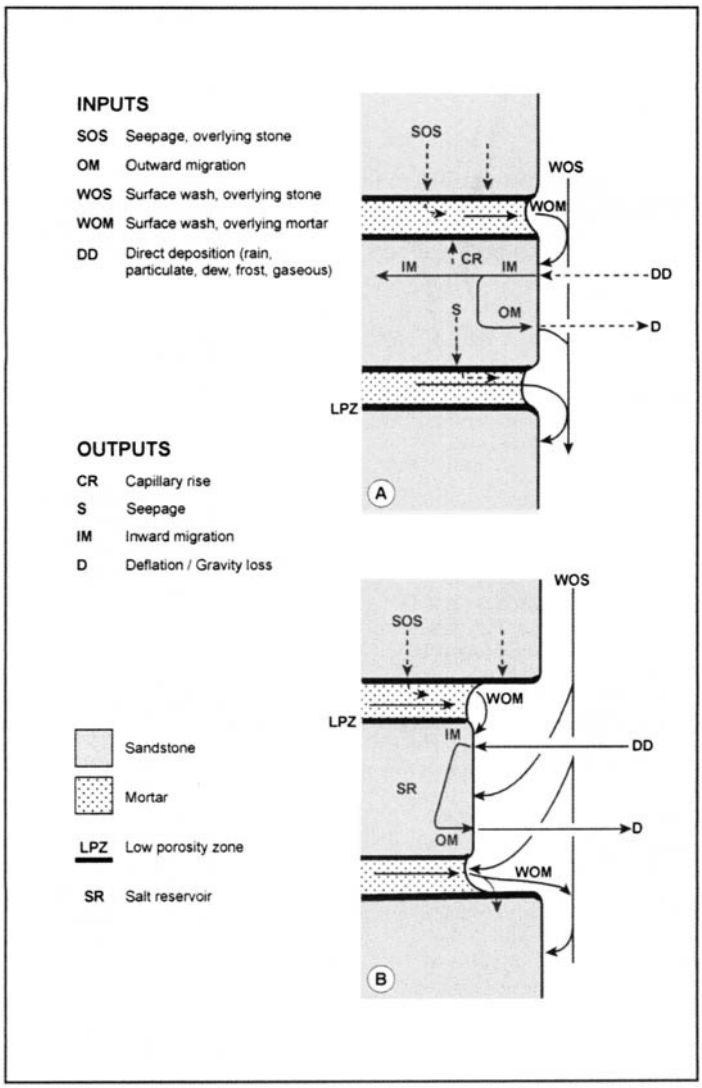

Fig. 5. Moisture and salt pathways on a rainwashed sandstone block (**A**) and on a block experiencing rapid retreat by salt weathering (**B**). The pathways are deduced from salt distributions on sandstone walls and simulated environmental conditions.

the protocols for salt weathering simulations designed to replicate decay observed on rapidly retreating sandstone blocks which are reported in the following section.

Simulation of salt weathering within hollows

The majority of laboratory simulations of salt weathering have applied water/salt solution before each environmental cycle by immersion or by pouring known volumes onto exposed surfaces (e.g. Smith & McGreevy 1988; Goudie & Viles 1997). This closely replicates surfaces subject to rainwash and/or driven rain. However, in this simulation experiment the aim was to reproduce shallow surface wetting of stone by direct deposition of salt-rich moisture similar to that experienced in cavernous hollows. A summary of methodology and results follows.

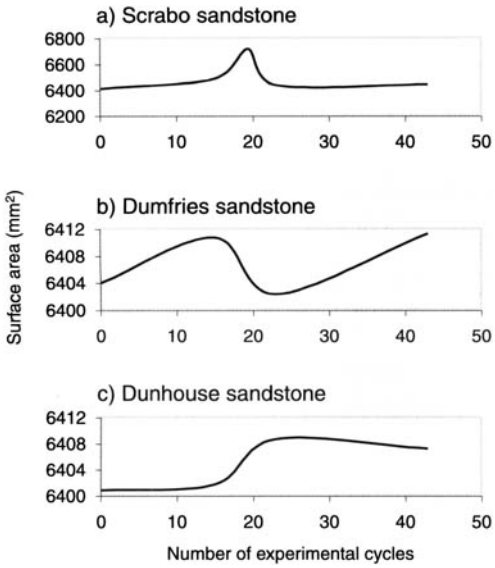

Fig. 6. Changing block surface area values (mm^2) after 43 cycles in the salt spray cabinet. It is important to note that the surface distortion values recorded on both the Dumfries and Dunhouse sandstone blocks were minor when compared to those exhibited by the Scrabo sandstone. Points to note include the peak in Scrabo sandstone values around 20 cycles reflecting surface blistering and flaking and the subsequent loss of this material. Two phases of surface distortion were recorded on the Dumfries sandstone block, possibly related to the gradual development of a deep-seated fracture followed by a period of settling between approximately 15 and 22 cycles before initiation of the second phase of distortion that may have ultimately resulted in surface failure if the experimental run had continued. Finally, after 43 cycles the Dunhouse sandstone block surface had started to show evidence of distortion after which it appeared to settle for the remainder of the experimental run. Although the changes measured on all three blocks are small, they are considered to be real, as each observation is the product of 100 individual measurements over the block surface and observations for each block showed consistent trends over time.

A salt corrosion cabinet was used in which stone samples are wetted by a fine salt spray and dried in a controlled thermal regime. These initial experiments were not designed to unravel the subtleties of environmental and lithological controls, but specifically to ensure condensation and subsequent drying out of the stone, and to this end the so-called 'Negev' temperature regime of Goudie & Viles (1997) was used. This cycled stone from 15°C to 50°C twice within 23 hours, with 3 hours of salt spray (10% $MgSO_4$ solution) towards the end of each low temperature phase. This solution was chosen because of its proven effectiveness in disrupting sandstone (Smith & McGreevy 1988).

Two 100 mm cubes of each of three sandstone types, Scrabo, Dunhouse and Dumfries, were used. Each was embedded in a jacket of expanded polystyrene restricting the movement of moisture to the one exposed horizontal block face. After each 23 hour cycle surface topography was measured by lowering an engineer's dial gauge gently onto the surface in a grid pattern. These data were used to produce digital terrain models from which surface area was calculated. This charted surface distortion as salts crystallized and flakes and scales lifted and collapsed.

After 23 daily cycles one block of each stone type was removed and the surfaces gently brushed to remove loose debris. This was washed to remove the salt and weighed to give weight loss. Only the Scrabo sandstone block showed any measurable weight loss (19 g after 23 cycles) and this was associated with surface distortion as blisters formed and collapsed at around day 20 of the experimental run (Fig. 6a). The three remaining blocks experienced a further 20 cycles after which any loose surface debris was gently removed and weighed. Again, it was only the remaining Scrabo sandstone block that showed any significant weight loss (28.9 g after 43 cycles) as it continued to weather by granular disintegration and isolated flaking – features redolent of the rapidly retreating blocks observed at St. Matthew's Church.

Dumfries sandstone showed two phases of surface distortion that could be associated with incipient scaling, but possibly too deep to be manifested as surface breakdown and material loss (Fig. 6b). A similar distortion was observed on the Dunhouse sandstone block (Fig. 6c) but this developed later than the Dumfries and both signs of disruption were minor compared to that exhibited by the Scrabo sandstone samples.

To examine subsurface conditions vertical cores were dry cut from block centres. These were cut into 10 mm slices, mechanically disaggregated and the conductivity of a water-soluble extract (shaken for 2 hours in deionized water) measured by conductivity probe. These conductivity data are used as a proxy to gauge salt penetration (Fig. 7a–f). These data clearly show that at the end of the experimental run (43 cycles) salt penetration in both the Dunhouse and Dumfries sandstone samples was restricted

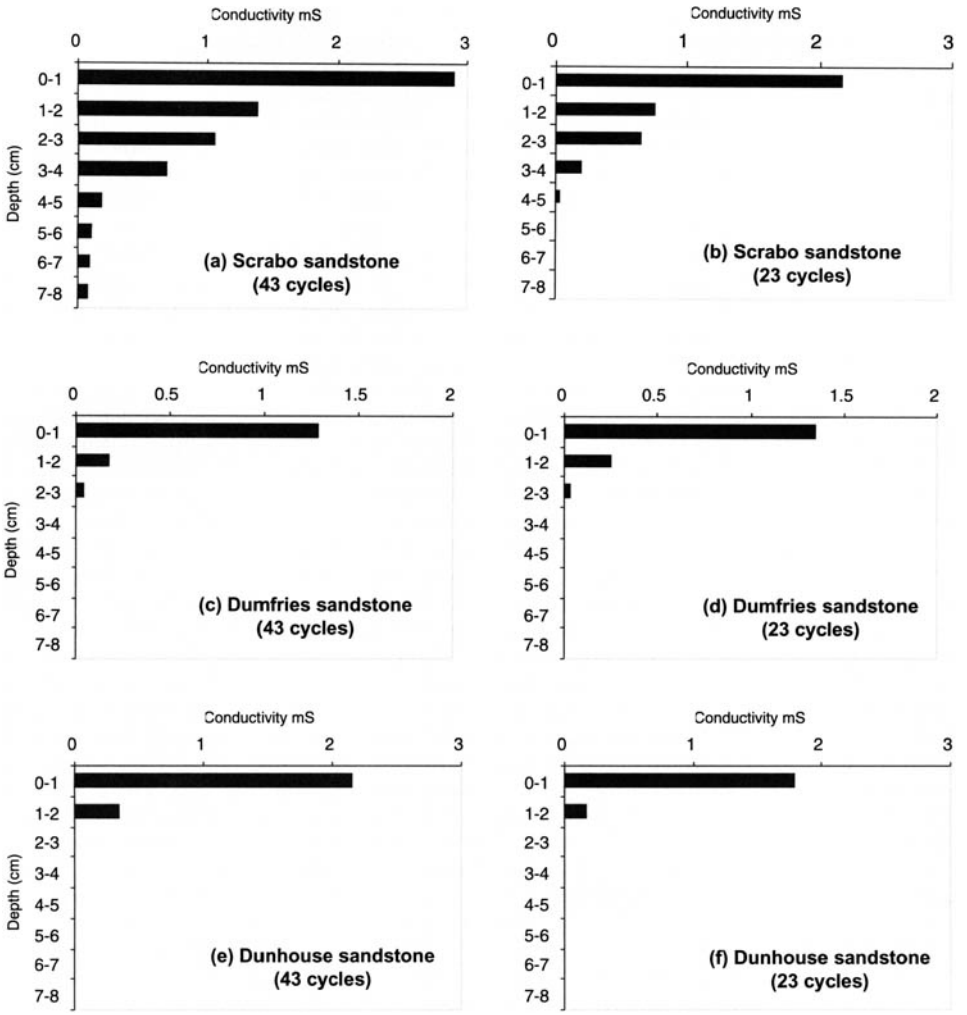

Fig. 7. Conductivity measurements of powdered samples with depth below the exposed surface of blocks used in the salt weathering simulation study. Higher values were recorded for both Scrabo sandstone blocks (**a**, **b**). These values reflect the greater depth of salt penetration in comparison to both the Dumfries (**c**, **d**) and Dunhouse (**e**, **f**) sandstone samples, where salts tended to accumulate in the surface and near-surface layers.

to the outer 20–30 mm of stone with highest conductivity recorded in the surface and near-surface zone (0–10 mm) (Fig. 7c–f). In contrast, conductivity data from the Scrabo sandstone samples indicate much deeper salt penetration extending to a depth ≥50 mm in the substrate material (Fig. 7a, b).

Using data from this simulation experiment and the understanding of decay processes, controlling factors and conditions of exposure gained from previous studies summarized here, it is possible to construct a model describing the dynamics of rapid block retreat in sandstone.

A conceptual model of rapid block retreat

Conductivity measurements (Fig. 7) clearly demonstrate the near-surface accumulation of salts at the end of the drying cycle in the more open textured Dumfries and Dunhouse sandstones. This could reflect greater moisture and salt storage capacity in these stones and/or the very effective return of moisture to the surface

by evaporation. A possible consequence of rapid surface drying is that any further moisture loss has to be by vapour transfer. Under these conditions some salt can be left behind to accumulate close to the wetting front. This could in turn close off pores, inhibit further salt penetration by ponding of moisture during the next wetting phase and encourage yet more salt accumulation. Such positive feedback conditions have previously been suggested as a mechanism for the eventual formation of surface scales that break away from the underlying stone at or near a shallow wetting front (Smith & McGreevy 1988; Smith *et al.* 1988). Evidence for this is seen in the Dumfries samples where after 23 diurnal cycles an incipient scale is observed several millimetres below the stable block surface. After 43 cycles a fully developed scale is observed with marked salt accumulation in the fracture zone (Fig. 8c). The scale itself is intact sandstone and the block surface shows only surface roughening.

This breakdown and salt distribution pattern contrasts with the Scrabo sandstone blocks, where salt penetration is greater. This could reflect the lower porosity of the Scrabo that requires less moisture and salt to completely fill subsurface pores, and higher moisture suction in this finer textured stone. Surface drying is also likely to be slower from the lower porosity, clay-rich Scrabo. This allows salts to migrate in solution and encourages surface efflorescence, complete pore filling and disaggregation. Under conditions of limited moisture availability this pattern cannot continue indefinitely. As salts accumulate and are not fully mobilized during wetting they begin to act as pore fillers. This reduces infiltration and encourages further surface and near-surface salt accumulation (Smith & Kennedy 1999). As surface porosity is reduced, it is possible to envisage that moisture from direct deposition may penetrate only a few millimetres, which could explain the predominance of granular disintegration and shallow flaking (Fig. 8a). However, as grains disaggregate and blisters form, a secondary porosity is created which allows wetting of intact, salt-rich stone beneath surface flakes and salt-cemented debris. In this way multiple flakes may form before loose surface material completely detaches. This pattern of breakdown is seen in the Scrabo blocks, where a complete subsurface layer was structurally disrupted by crystallized salt completely filling pores (Fig. 8b).

On buildings such as St. Matthew's Church surface salt may be added to by deep salts derived either from periods of saturation prior to surface retreat or from neoformation within the block (Turkington *et al.* in press; McKinley *et al.* 2001*b*). This creates a potent environment for self-sustained rapid retreat by flaking and granular disintegration. The presence of incipient scales and flakes on the Dumfries blocks might suggest that, given time, other sandstones might also be prone to similar retreat. However, and assuming similar salt availability, stones with a higher initial porosity may experience delayed onset of retreat and material loss may be more episodic through periodic scaling rather than almost continuous flaking. This was certainly the case on St. Matthew's Church, where widespread rapid retreat was confined to Scrabo sandstone while Dumfries sandstone typically exhibited sporadic decay of individual blocks and a propensity for contour scaling. However, a dogmatic distinction between scales and flakes may be spurious, in that scales can comprise a number of flakes. These may be discontinuous across the surface of a scale and may interconnect to form a larger mass. Alternatively, crystallized salts and/or biological growths may hold flakes together.

Finally, it is interesting to note that Dunhouse sandstone exhibited the least surface damage, although sectioning did identify some limited blistering (Fig. 8d). As with Dumfries, this subsurface fracturing possibly registered as the very slight surface distortion. The performance of the three stone types in the experiment therefore conformed very closely to the observed and assumed durability sequence under conditions of use, where Scrabo sandstone shows little resistance to salt weathering, Dumfries weathers more slowly, but is eventually prone to scaling, and Dunhouse is increasingly used as a replacement stone because of its assumed resistance to salt-induced decay.

The simulation described here is designed to replicate rapid retreat, but observational evidence suggests that this only commences some time after construction following the breaking away of an extensive contour scale. Data in this and previous studies (e.g. Smith *et al.* 1994) suggest that contour scaling of Scrabo sandstone is associated with the slow accumulation of gypsum within 10–20 mm of the surface. Gypsum appears to derive from atmospheric sources and surface wash from lime mortars. Studies by Warke & Smith (2000) and Turkington & Smith (2000) also suggest that gypsum acts in combination with mobile chloride salts from marine aerosols that exploit fractures initiated by the gypsum.

The factors that determine salt weathering susceptibility are known to be complex (Goudie & Viles 1997). However, in the case of Scrabo

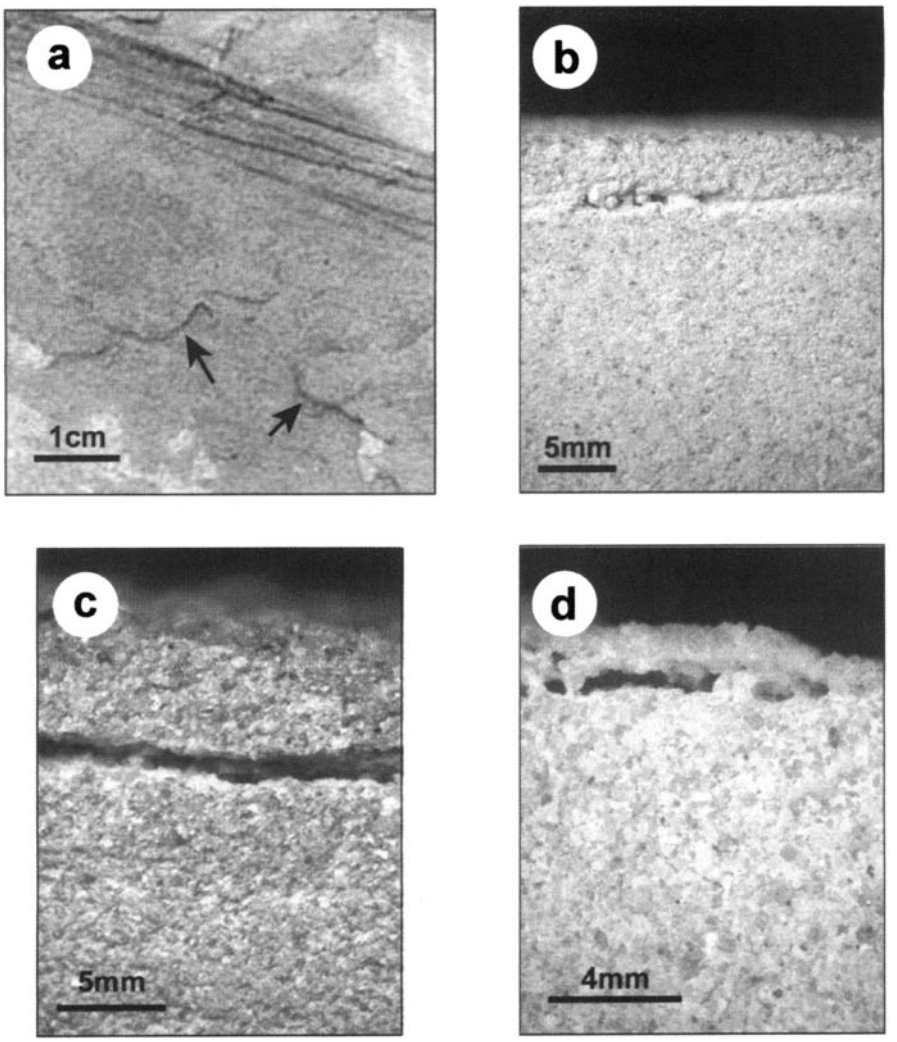

Fig. 8. (**a**) Flaking on the surface of Scrabo sandstone after 23 cycles in the salt spray cabinet. (**b**) Cross-section of Scrabo sandstone block after 43 cycles showing a salt-filled subsurface fracture. (**c**) Well-developed subsurface fracture with substrate separation in Dumfries sandstone after 43 cycles. (**d**) Superficial blistering identified in the cross-section of the Dunhouse sandstone block after 43 cycles.

sandstone, previous experiments (e.g. McGreevy & Smith 1984) have linked salt weathering to the presence of clay bands and lenses, primarily smectite. When wetted with salt solutions, clay-rich surface areas expand and compromise the structure of the surrounding sandstone. This response may reflect increased microporosity associated with clays partially filling pores or swelling of the clay itself. It is difficult to dissociate these two effects and it seems most probable that they combine rather than act separately.

The importance of clays in controlling salt weathering on St. Matthew's Church was further corroborated by the initial architect's survey that identified a close correlation between clay content and delaminated stones identified for complete replacement. Whether delamination/contour scaling is followed by rapid surface retreat will depend upon a number of factors including the depth of any salt-rich, pre-weathered zone below the scale and its exploitation by wetting and drying once the scale breaks away. Whether this triggers rapid retreat appears to depend primarily on the

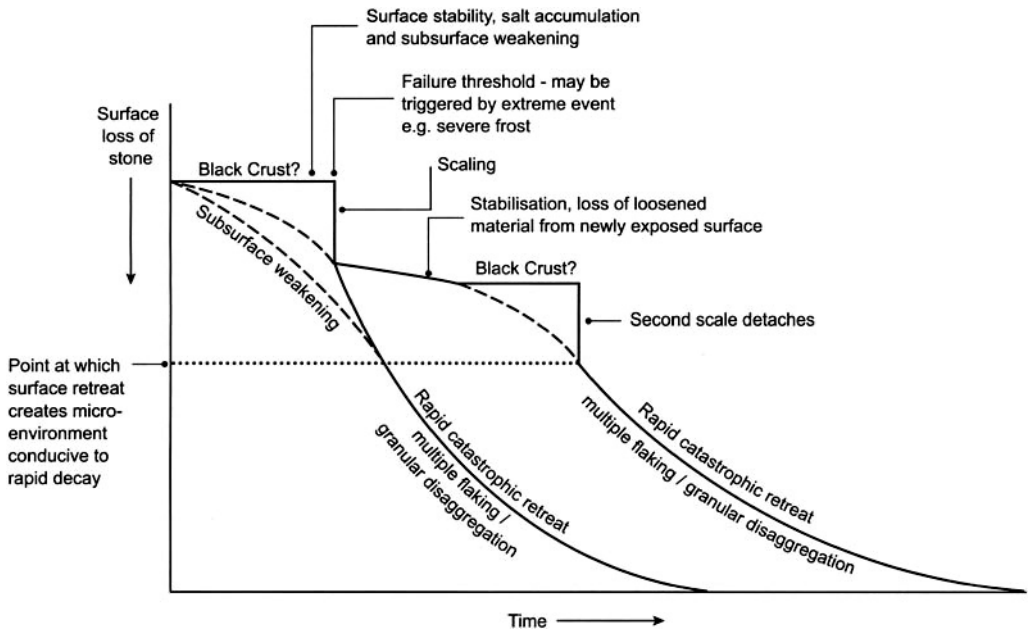

Fig. 9. Schematic diagram illustrating possible decay pathways associated with the rapid retreat of building sandstone blocks through salt weathering.

degree of shelter from rain and rainwash created by delamination. If frequent surface washing persists it is possible that the stone will continue to be deeply wetted and any additional surface salt accumulation will be gradual. Under these conditions scaled surfaces could, after some limited disaggregation, stabilize until sufficient salt has accumulated to trigger more scaling. If, however, sufficient retreat occurs to protect the surface from regular rainwash, conditions amenable to rapid retreat are created. These include direct deposition of atmospheric moisture and salts, limited surface wetting, near-surface salt accumulation and drying – enhanced by turbulent airflow in the hollow. Under this regime gypsum deposition continues, including that from the outflow of adjacent mortars (Fig. 5). However, it is likely that rapid surface breakdown would inhibit surface build up of atmospheric salts. It seems probable therefore that, as illustrated by the exposure trials and analyses of weathered blocks from St. Matthew's, retreat would be linked to the combined deposition of chloride salts and gypsum acting synergistically with chloride salts already stored at depth within the stone. These possible decay routes are indicated in Figure 9 and represent modifications to the original model proposed in the introduction.

Summary and conclusions

This study describes the rapid retreat of building sandstones in a wet, polluted maritime environment. Visible decay is triggered by the delamination of surface layers associated with the near-surface accumulation of chloride and sulphate salts, particularly gypsum. Once retreat is initiated in an individual sandstone block, it becomes partially sheltered from rainwash. Under these conditions the net deposition of pollution-derived salts and marine aerosols increases and further retreat is encouraged as these salts exploit a pre-weathered, structurally weakened zone formed below the original scale. If this allows retreat to continue to the point where more than 50% of the block is in shadow, conditions are created that increasingly concentrate temperature and moisture cycling and salts in the near-surface zone. Concentration of environmental cycling in this shallow zone encourages rapid weathering, despite the constant loss of salt-rich debris from the surface. Retreat is further fuelled in this wet maritime environment by a reservoir of deep salts, especially chlorides, that appear to migrate into blocks, possibly by ionic diffusion following deposition from atmospheric pollution and marine aerosols, under saturated conditions

when unsheltered blocks are exposed to prolonged rainwash and driven rain.

In the particular case of Scrabo sandstone, gypsum may also be formed within blocks by alteration of the accessory mineral actinolite. If the initial phase of rapid retreat does not create conditions amenable to shallow temperature and moisture cycling, the weathered surface may stabilize and the slow accumulation of gypsum is reinstated under conditions of a greater moisture flux, leading eventually to a second phase of delamination.

Conditions found in the hollows caused by block retreat were recreated in a salt spray cabinet where the retreat of Scrabo sandstone blocks, by multiple flaking and granular disintegration, was successfully replicated using a 10% $MgSO_4$ mist. The same experiment did not produce measurable surface loss from blocks of more porous Dumfries sandstone, but sectioning of the blocks revealed incipient contour scaling of an intact surface layer less than 10 mm thick. Conductivity measurements also showed that salt accumulation in the Dumfries sandstone was concentrated on drying in a very narrow subsurface layer coinciding approximately with the scale. Although this salt accumulation would eventually have led to surface loss, it would also have removed most of the accumulated salt. This suggests that loss of material from this particular stone type would be slower and more episodic, depending on the time taken for more salts to accumulate and individual scales to form. This is confirmed by observations on St. Matthew's Church, where Dumfries sanstone showed less severe decay than Scrabo sandstone with a propensity for contour scaling.

The rapid decay of Scrabo sandstone, both under test conditions and on the building, appears to be linked to its lower porosity and the presence of swelling clays, especially montmorillonite, within pores, which encourage rapid pore-filling by absorbed salts, deeper salt penetration and retention of salts at greater depth on drying. A useful means of investigating these relationships would be to measure pore throat characteristics of fresh and salt-loaded stone by, for example, mercury intrusion porisimetry. Unfortunately this was not available during this project, but could form the basis of future research. As a consequence, on drying there is not such a discrete lower boundary to the zone of salt accumulation that appears to favour contour scaling in the Dumfries sandstone. Similarly, as salt-rich debris is lost from the surface, it reveals an equally salt-rich substrate that continues to flake and scale.

Data presented here demonstrate the complex interactions between factors such as porosity, permeability, mineralogy and salt availability and their role in determining the establishment of positive feedback conditions. This improved understanding of decay dynamics has implications for decisions regarding conservation strategies when the application of inappropriate treatments may inadvertently act as a trigger for the decay sequence. However, in the customary call for further research in this area, special emphasis must be placed on testing the conceptual model described here under 'real-world' conditions.

This work could not have been carried out without the support, advice and probing questions of the staff of Consarc Design Group Ltd., especially D. Stelfox and J. Savage, and McConnell Brothers who removed blocks, prepared test walls and advised on mortar preparation. Diagrams were prepared by G. Alexander of the QUB Geography cartographic unit and financial support was provided by EPSRC grants GR/L99500/01 and GR/L57739/01.

References

BASHEER, P. A. M., NOLAN, E., MCCARTER, W. J. & LONG, A. E. 2000. Effectiveness of in-situ preconditioning methods for concrete. ASCE *Journal of Materials in Civil Engineering*, **12**, 131–138.

BLUCK, B. 1992. The composition and weathering of sandstone with relation to cleaning. *In*: WEBSTER, R. G. M. (ed.) *Stone Cleaning and the Nature of Soiling and Decay Mechanisms of Stone*. Donhead, London, 125–127.

BLUCK, B. J. & PORTER, J. 1991. Sandstone buildings and cleaning problems. *Stone Industries*, March, 21–27.

BUTLIN, R. 1991. Effects of air pollution on buildings and materials. *Proceedings of the Royal Society, Edinburgh*, **97B**, 255–272.

COOKE, R. U. & GIBBS, G. B. 1993. *Crumbling Heritage?* National Power & Power Gen, Swindon.

COOPER, T. P. *et al.* 1991. Contribution of calcium from limestone and mortar to the decay of granite walling. *In*: BAER, N. S. *et al.* (eds) *Science, Technology and the European Cultural Heritage*. Butterworth-Heineman, Oxford, 456–459.

DRAGOVICH, D. 1981. Cavern microclimates in relation to preservation of rock art. *Studies in Conservation*, **26**, 143–149.

FOLK, R. L. 1974. *Petrology of Sedimentary Rocks*. Hemphills, Austin, Texas.

GOUDIE, A. S. 1985. *Salt Weathering*. Oxford School of Research, Paper, **8**.

GOUDIE, A. S. & VILES, H. A. 1997. *Salt Weathering Hazards*. Wiley, Chichester.

GOUDIE, A. S., COOKE, R. U. & EVANS, I. S. 1970. Experimental investigation of rock weathering by salts. *Area*, **4**, 42–48.

MCCARTER, W., CHRISP, T., BUTLER, A. & BASHEER, P.

2001. Near-surface sensors for condition monitoring of cover-zone concrete. *Construction and Building Materials*, **15**(2–3), 115–124.

McGreevy, J. P. & Smith, B. J. 1984. The possible role of clay minerals in salt weathering. *Catena*, **11**, 169–175.

McKinley, J., Worden, R. H. & Ruffell, A. H. 2001*a*. Contact diagenesis: the effect of an intrusion on reservoir quality in the Triassic Sherwood sandstone Group, Northern Ireland. *Journal of Sedimentary Research*, **71**, 484–495.

McKinley, J., Curran, J. M. & Turkington, A. V. 2001*b*. Gypsum formation in non-calcareous building sandstone: a case study of Scrabo sandstone. *Earth Surface Processes and Landforms*, **26**, 869–875.

Price, C. A. 1978. The use of the sodium sulphate crystallisation test for determining the weathering resistance of untreated stone. *International Symposium on Deterioration & Protection of Stone Monuments*. UNESCO, Paris, Paper 3.6.

Price, C. A. 1996. *Stone Conservation: an Overview of Current Research*. Getty Conservation Institute, Santa Monica.

Price, C. A. & Brimblecombe, P. 1994. Preventing salt damage in porous materials. *In*: *Preventive Conservation: Practice, Theory and Research*. International Institute for Conservation, London, 90–93.

Smith, B. J. 2002. Background controls on urban stone decay: lessons from natural rock weathering. *In*: Brimblecombe, P. (ed.) *Air Pollution Reviews – Vol. 2: The Effects of Air Pollution on the Built Environment*. Imperial College Press, London, in press.

Smith, B. J. & Kennedy, E. M. 1999. Moisture loss from stone influenced by salt accumulation. *In*: Jones, M. S. and Wakefield, R. D. (eds) *Aspects of Stone Weathering, Decay and Conservation*. Imperial College Press, London, 55–64.

Smith, B. J. & McAlister, J. J. 1986. Observations on the occurrence and origin of salt weathering phenomena near Lake Magadi, Southern Kenya. *Zeitschrift für Geomorphologie*, **30**, 445–460.

Smith, B. J. & McGreevy, J. P. 1988. Contour scaling of a sandstone by salt weathering under simulated hot desert conditions. *Earth Surface Processes and Landforms*, **13**, 697–706.

Smith, B. J., Whalley, W. B. & Fassina, V. 1988. Elusive solution to monumental decay. *New Scientist*, **1615**, 49–53.

Smith, B. J., Whalley, W. B. & Magee, R. W. 1991. Background and local contributions to acidic deposition and their relative impact on building stone decay: a case study of Northern Ireland. *In*: Longhurst, J. W. S. (ed.) *Acid Deposition: Origins, Impacts and Abatement Strategies*. Springer-Verlag, Berlin, 241–266.

Smith, B. J., Magee, R. & Whalley, W. B. 1994. Breakdown patterns of quartz sandstone in a polluted urban environment: Belfast, N. Ireland. *In*: Robinson, D. A. & Williams, R. B. G. (eds) *Rock Weathering and Landform Evolution*. Wiley, Chichester, 131–150.

Smith, B. J., Turkington, A. V. & Curran, J. M. 2001. Calcium loading of non-calcareous building stone during construction. *Earth Science Processes and Landforms*, **26**, 877–883.

Turkington, A. V. (in press). Initial stages of sandstone decay in a polluted urban environment. *Proceedings of SWAPNET meeting*, Wolverhampton, May 1999.

Turkington, A. V. & Smith, B. J. 2000. Observations of three-dimensional salt distribution in building sandstone. *Earth Surface Processes and Landforms*, **25**, 1317–1332.

Turkington, A. V., Smith, B. J. & Basheer, P. A. M. 2002. The effect of block retreat on sub-surface temperature and moisture conditions in sandstone. *In*: Prikryl, R. & Viles, H. A. (eds) *Understanding and managing stone decay*. Karolinum Press, Prague, 113–126.

Viles, H. A. 1993. The environmental sensitivity of blistering of limestone walls in Oxford, England. *In*: Thomas, D. S. G. & Alison, R. J. (eds) *Landscape Sensitivity*. Wiley, Chichester, 309–326.

Warke, P. A. & Smith, B. J. 2000. Salt distribution in clay-rich weathered sandstone. *Earth Surface Processes and Landforms*, **25**, 1333–1342.

Yates, T. & Butlin, R. 1996. Predicting the weathering of Portland limestone buildings. *In*: Smith, B. J. & Warke, P. A. (eds) *Processes of Urban Stone Decay*. Donhead, London, 194–204.

Oolitic limestone in a polluted atmospheric environment in Budapest: weathering phenomena and alterations in physical properties

ÁKOS TÖRÖK

Department of Construction Materials and Engineering Geology, Budapest University of Technology and Economics, H-1111 Budapest, Sztoczek u. 2, Hungary (e-mail: atorok@epito.bme.hu)

Abstract: In Budapest damage due to atmospheric pollution on many public buildings is severe. Black encrustations, white crusts and other decay features of a soft oolitic limestone have been studied in detail by using field measurements and laboratory analyses. Limestone weathering was assessed by description of weathering forms, by on-site petrophysical tests (Duroscope, Schmidt hammer, water absorption) and by laboratory mineralogical assessment and thermoanalysis (X-ray diffraction, Derivatograph). There is a clear correlation between the organic carbon content in stone and location of the site, particularly in the polluted city centre. Gypsum, which is not an indigenous mineral in the limestone, can contribute up to 70% of the crust composition and indicates the importance of air-derived SO_2. This mineralogical change in stone composition leads to changes in physical properties, by strengthening laminar black crusts and white case hardened crusts and weakening the host rock.

Atmospheric pollution has long been recognized as one of the main causes of accelerated deterioration of limestones (Kieslinger 1949; Winkler 1966; Amoroso & Fassina 1983; Camuffo *et al.* 1983). The reaction of airborne sulphuric acid and limestone surfaces leads to the formation of sulphated crusts (Winkler 1970; Amoroso & Fassina 1983; Camuffo *et al.* 1983; Fassina 1991; Camuffo 1995). By the entrapment and by the catalytic effect of dust particles (mostly organic carbon compounds), black crusts are formed (Camuffo 1995; Dolske 1995; Maravelaki-Kalaitzaki & Biscontin 1999; Del Monte *et al.* 2001). Although the mechanism and the chemical reactions of such processes have been described in detail (Ausset *et al.* 1996, 1999; Rodriguez-Navarro & Sebastian 1996; Primerano *et al.* 2000) the mechanical properties of different weathering forms, especially of crusts, have received less attention. It has been demonstrated on granites (Irfan & Dearman 1978; Christaras 1991*a*) and on limestones (Christaras 1991*b*; Bell 1993) that with weathering, there is a decrease in strength. Christaras (1991*c*, 1996) showed that non-destructive tests such as Schmidt hammer tests or ultrasonic sound velocity measurements are applicable in estimating weathering rates of monumental stones. Nevertheless, in these studies only the mechanical properties of severely weathered rock surfaces were analysed and there are no data on the mechanical properties of weathering crusts, such as black crusts or white crusts. These are important parameters since the differences in the mechanical behaviour of crusts and host rock can provide further information toward the understanding of the crust formation mechanism and its subsequent mechanical breakdown, i.e. scaling, blistering or flaking.

Porous, soft oolitic limestone walls of public buildings, in the polluted inner city as well as in less polluted localities in Budapest, were studied. Wind and rain exposure, lithological differences, decay features and physical properties were recorded and small samples were analysed mineralogically. In addition it is also demonstrated that Duroscope is an important non-destructive test method that can be used for measuring mechanical properties of weathered stone surfaces.

Location of sites

Despite air quality improvement in recent years, Budapest still suffers from severe air pollution. The annual average concentration of SO_2 dropped between 1980 and 2000. Other pollutants such as NO_2 have shown a variation in concentration in the past 20 years (Table 1). The concentration of aerosol particles (including sulphate, nitrate, ammonium) decreased by 23% from 1980 (86 $\mu g\ m^{-3}\ a^{-1}$) to 2000 (66 $\mu g\ m^{-3}\ a^{-1}$) due to the decrease in background concentration, but it is still higher than the health limit value of 50 $\mu g\ m^{-3}\ a^{-1}$ (MEP

From: SIEGESMUND, S., WEISS, T. & VOLLBRECHT, A. 2002. *Natural Stone, Weathering Phenomena, Conservation Strategies and Case Studies*. Geological Society, London, Special Publications, **205**, 363–379.
0305-8719/02/$15.00 © The Geological Society of London 2002.

Table 1. *The concentration of most important atmospheric pollutants in Budapest*

Pollutant	1980*	1995*	2000*	2000†
SO_2 (μg m^{-3})	63	25	18	30
NO_2 (μg m^{-3})	46	68	48	154
Flying dust (μg m^{-3})	n.d.	210	246	544
Settling dust (g m^{-2} per 30 days)	9	5	4	14

* Yearly average
† Winter average
The winter maximum is due to heating and atmospheric stability (data from MEP 2001).

2001). The amount of settling dust has decreased slightly in the last two decades, while the flying dust particles still occur in very high concentrations (246 μg m^{-3}), especially in autumn and in winter (MEP 2001; Table 1). The pollution distribution is uneven since the city centre, which is less than 5% of the territory of Budapest, is a veritable trap of pollutant gases and particles yet contains about 50% of the total pollution emissions for the city. In addition, the temporal distribution of pollution is uneven. This is mainly due to transportation emissions. During rush hours emissions are about eight to nine times higher than at any other time of day (Moingl *et al.* 1991). The continental climate of Budapest also favours formation and entrapment of pollution plumes. In autumn and in winter, at times of atmospheric stability, fog develops (18 to 52 days per year; CSO 1986) and often aggravates the pollution, since fog water droplets contain far higher concentrations of pollutants than rain (Del Monte & Rossi 1997). The mean annual temperature is 10.3°C. The winters are characterized by several frost and thaw cycles (73 to 87 frosty days per year; CSO 1986). Winter heating also contributes to high pollution levels during this time of year (Table 1).

The studied buildings are located both in the pollution plume of the city centre and outside it. The Citadella is a fortress on a small elevated hill where constant wind and higher altitude prevent the formation of a pollution plume. This is indicated by the presence of lichens (site 1 on Fig. 1). Mathias Church is located on Castle Hill where vehicle transport is restricted (site 2 on Fig. 1). The House of Parliament sits along the windy Danube riverside and is adjacent to the inner city (site 3 on Fig. 1). The final site, College of Fine Arts, is in the traffic burdened city centre where only very rare and mild winds blow (site 4 on Fig. 1).

Methodology

The placement of different types of oolitic limestones on the selected walls was graphically recorded. This was followed by visual inspection and description of decay features according to Smith *et al.* (1992) and Fitzner *et al.* (1995). On selected blocks, mechanical property testing of stone surfaces and crusts were undertaken using the Schmidt hammer (type L-9) and Duroscope (five readings at each measured point). Test results were compared to values of fresh unaltered stone blocks. Schmidt hammer and Duroscope rebound values denote surface strength. With Duroscope, due to its small spring-loaded mass, it is possible to detect low strength values although the precision of the measurements depends on the smoothness of the surface. Consequently, measurements of irregular surfaces such as framboidal black crusts are not reliable or representative. Reliable Schmidt hammer tests were also not possible on these crusts, since the strong spring-loaded mass would destroy the framboidal structure and thus the measured value would correspond to the host rock and not to the crust. Water adsorption tests by the Karsten-tube method were also performed.

Thirty-two samples (4 to 55 g) were collected by scraping the surfaces and by chiselling: framboidal black crusts (six samples), laminar black crusts (six samples), grey dust layers (two samples), thick white hard crusts (seven samples), thin white blistering and flaking crusts (six samples) and host rock (five samples). Mineralogical composition was determined by X-ray diffraction (XRD) with a Phillips diffractometer (PW 1130 generator, PW 1050 goniometer, Cu anode and monochromator, 40 kV, 20 mA, angle 5–70°, step size 0.02°, time per step 1.0 second). Thermogravimetric and differential thermoanalysis (TGA-DTA) were carried out by a MOM Derivatograph to measure gypsum and organic carbon contents (400–600 mg sample size; heating rate 10°C min^{-1}, 20–1000°C; and thermogravimetric sensitivity 100–200 mg). Thin sections were also prepared by using resin impregnation to visualize textural and mineralogical changes of host rock and altered rock surfaces.

Soft oolitic limestone

Provenance of the limestone

Miocene oolitic limestone was a popular building and ornamental stone in Budapest at the end of the nineteenth century. Several quarries were operated in the suburbs of

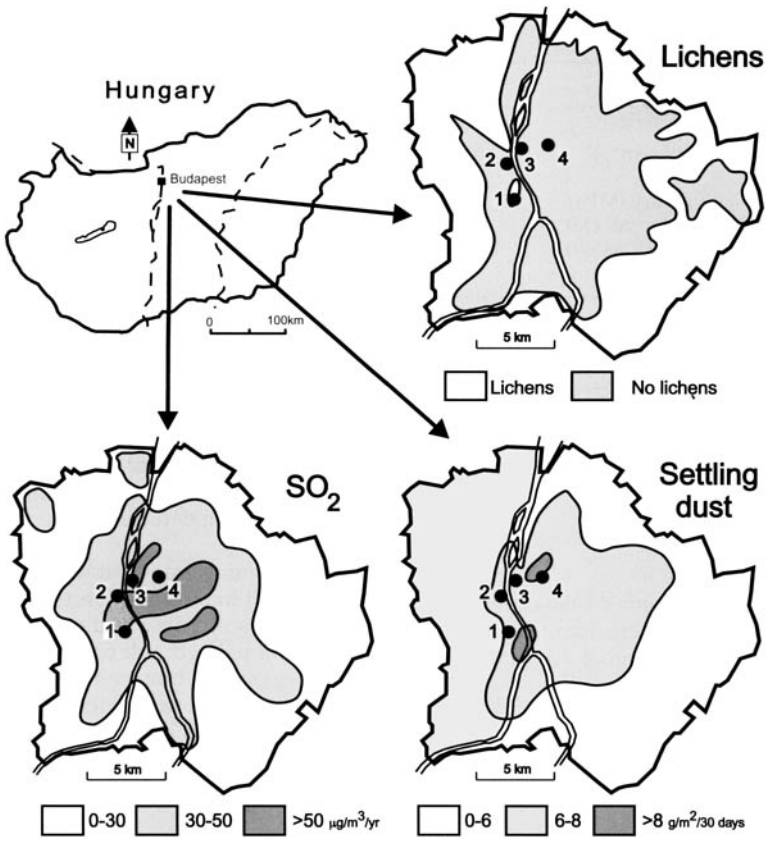

Fig. 1. The location of the studied sites in Budapest, with reference to air pollution controlled distribution of lichens, sulphur dioxide and dust. 1, Citadella fortress; 2, Mathias Church; 3, House of Parliament; 4, College of Fine Arts.

Budapest during that time but are no longer in operation (Tétényi plateau region). Subsurface galleries are known from the Kőbánya and Budafok districts. Presently, one quarry is still in operation in Sóskút village; it is only 30 km from the city centre.

Lithology and physical properties

Freshly quarried Miocene oolitic limestone is light yellow to yellowish white. It consists of small, well to moderately rounded calcitic ooids and micro-oncoids of 0.2–2.0 mm in diameter. Although calcite ($CaCO_3$) is the primary mineral, small quantities of quartz and feldspars are also present and correspond primarily to ooid cores. Gypsum ($CaSO_4.2H_2O$) is not detected in the quarry stones. The ooids, red algae fragments, gastropods, bivalves and foraminfera are surrounded by circumgranular acicular to bladed calcite cement. Grain to grain contact also occurs often associated with thin cement rims. Most pores are intergranularly connected and this ensures a high effective porosity (up to 30%). The pore size of intergranular pores is in the order of 0.1 to 2 mm, while the intragranular pores in the foraminifers or within the ooids are generally smaller. The texture shows some variation in the size of ooids (0.1–2 mm) and in the amount of other particles, but they are primarily ooid grainstones or bioclastic ooid grainstones. It is also possible to differentiate the lithological varieties by visual inspection based on grain size and bioclast content. Fine-grained oolitic (average gain size 1 mm) and medium-grained oolitic (grain size 1 to 2 mm) limestones were commonly used for building although the use of coarser bioclastic oolitic limestones with larger pores also occurs. A common sedimentary feature of this limestone is cross-bedding. Characteristic physical properties are presented in Table 2. Hungarian

Table 2. *Petrophysical properties of the oolitic limestone*

Petrophysical properties	
Density air-dry (g cm^{-3})	1.6–1.8
Density water-saturated (g cm^{-3})	1.9–2.1
Porosity (wt%)	21–31
Compressive strength air-dry (MPa)	3–11
Compressive strength water sat. (MPa)	1–7
Schmidt hammer rebound (R value)	18–23
Duroscope rebound (D value)	13–21

Miocene oolitic limestone is similar to some other oolitic limestones, such as British Great Oolite (Monks Park limestone) (Bell 1993; Viles 1994) or French Jaumont limestone (Ausset *et al.* 1996), but it is much softer, lighter and more porous.

Weathering features

Several forms of mechanical breakdown, alteration and deposition were identified on this oolitic limestone. The most frequent stone decay feature is crust formation. Crusts can be classified according to their colours and morphology (Camuffo *et al.* 1983; Fassina 1991; Smith *et al.* 1992; Fitzner *et al.* 1995; Camuffo 1995, Maravelaki-Kalaitzaki & Biscontin 1999).

White crusts

Light coloured crusts are formed on rain and/or wind exposed surfaces. Two types of white crusts have been identified: thick, hard white crusts and thin white crusts. Thick case hardened crusts are smooth and almost flat and occur on medium-grained oolitic limestones (Figs 2 and 3). These crusts range from a few millimetres to a centimetre in thickness. While calcite is the primary mineral, the gypsum content of these crusts is always more than 20%. It is important to emphasize that organic carbon has been detected in these crusts (0.4%) (Fig. 4).

Thin (1 mm), 'fragile' crusts develop on very fine-grained limestones. On thin crusts, surface irregularities are observed (Fig. 5). Thin crusts can have a pale greyish colour, which is due to their organic carbon content. The measured maximum of 0.8% was detected in greyish white blistering crusts (Fig. 4).

Fig. 2. Exposed wall of Citadella fortress shows different forms of crust formation (mostly thick white case hardened crusts) and removal (scaling, blistering). Arrow marks the close-up view shown in Figure 3.

Fig. 3. Case hardened smooth crust on exposed wall of Citadella; detail of Figure 2 (coin is 1.8 cm).

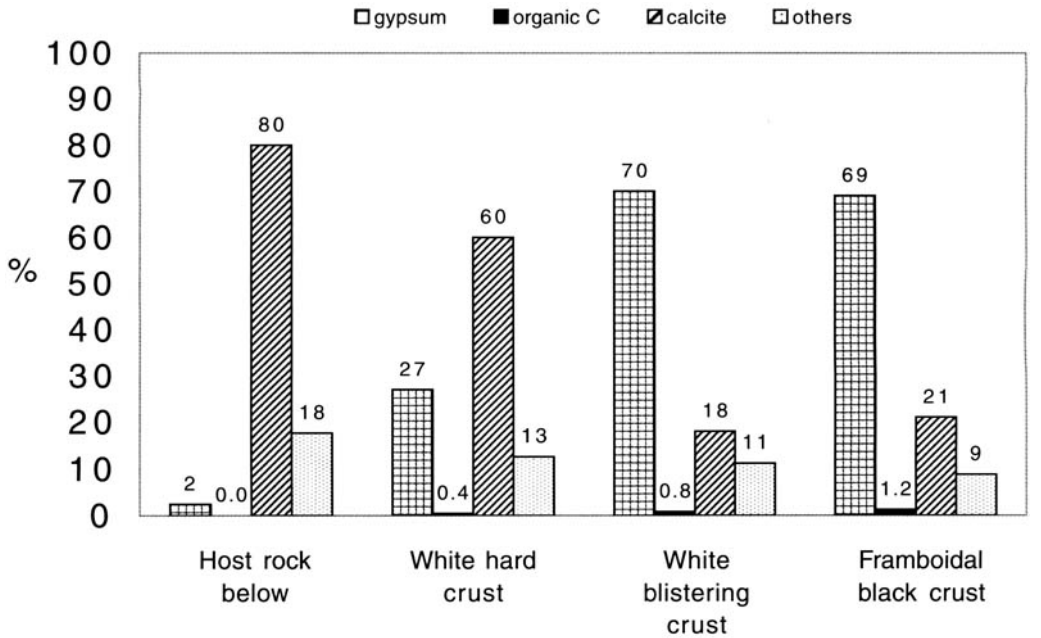

Fig. 4. Mineralogical composition of different crust types and host rock from a less polluted hill site, Citadella fortress.

Fig. 5. Blistering thin white crust and blackening in the joints, Citadella (coin is 2.2 cm).

Thick and thin white crusts do not show mineralogical differences under the petrographic microscope. The surface of white crusts is irregular with signs of chemical dissolution. Primary sedimentary structures of the ooids (concentric laminae) are not visible, and parts of the ooids have been removed by dissolution. Dissolved calcium carbonate is reprecipitated below the surface, and in the pores, as micrometre-sized inclusion-rich calcite crystals. The zone thickness, where pores are subsequently filled with calcite, varies between 1 cm (thick case hardened crusts) and 1 mm (thin crusts). Small percentages of gypsum have been detected in the host rock beneath the white crusts, which are not visible under the microscope.

Schmidt hammer values of thick, hard white crusts are higher than those of the host rock indicating that these crusts form a rigid and hard cover on coarse limestone (Fig. 6). Duroscope rebound values of thick, hard white crusts are more than double those of the host rock (Fig. 7). The altered host rock has the lowest rebound values while white flaking crust show slightly higher Duroscope values (Fig. 8). Water absorption tests have shown that both thin and thick white crusts form an impermeable layer, which prevents water infiltration into the porous limestone via the crust.

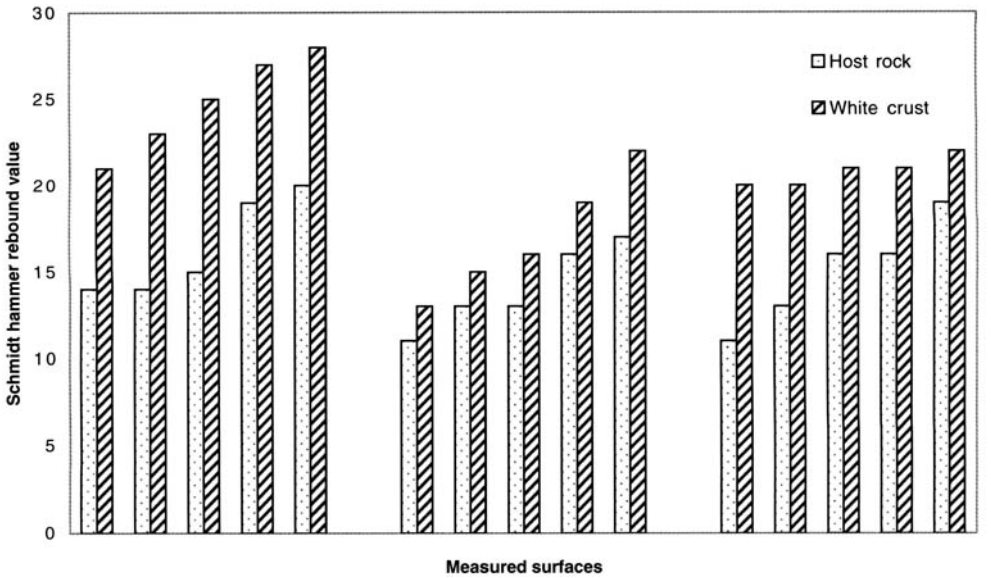

Fig. 6. Schmidt hammer rebound values of three rock blocks, white crust and host limestone.

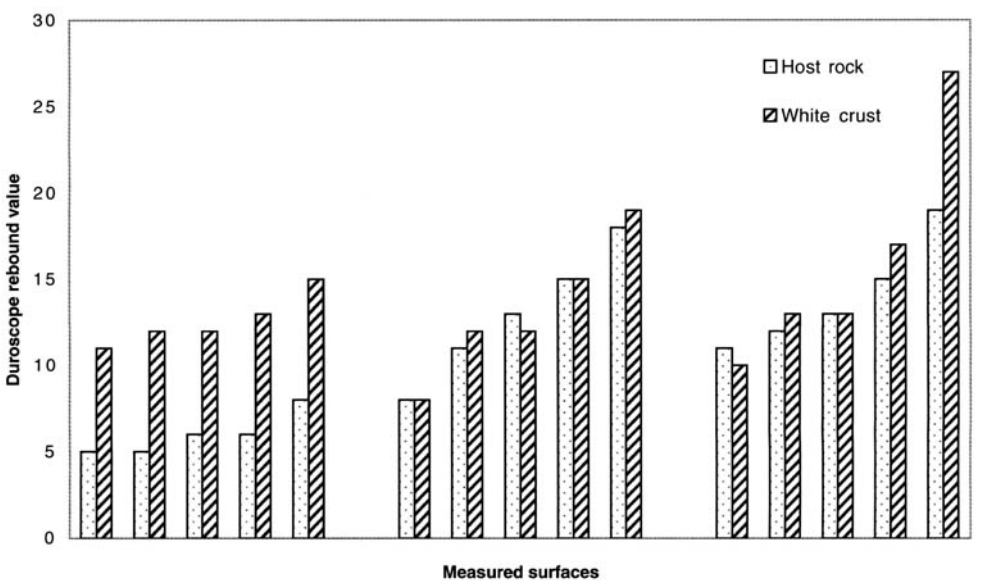

Fig. 7. Duroscope rebound values of three rock blocks, white crust and host limestone.

Black crusts

Two black crust types were documented: thick framboidal black crusts and thin laminar black crusts. Framboidal black crusts evolve on protected parts of walls, generally below cornices or ornaments (Fig. 9). Similar black crust morphology is also known as dendritic black crust (Camuffo 1995; Maravelaki-Kalaitzaki & Biscontin 1999) or as ropey ('bubble-shaped') crust (Antill & Viles 1999). Large surfaces are also covered by framboidal crusts especially on sheltered ashlars which are not exposed to direct rainwash. These crusts form over heavily weathered stones with a maximum thickness of approximately 2 cm. The

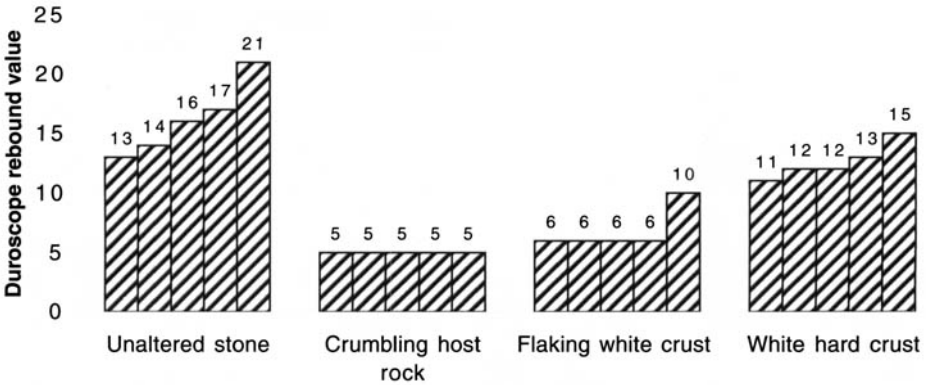

Fig. 8. Differences in Duroscope rebound values of fresh ooidal limestone, altered rock and different crusts (five sets of measurements for each type).

Fig. 9. Framboidal black crust in the sheltered zone, College of Fine Arts.

primary constituents of framboidal black crusts are gypsum (more than 60%), calcite (6 to 21%) and organic carbon (up to 3%). The mean gypsum and organic carbon concentrations show some variation depending on whether the crusts are formed in the city centre (2.8% maximum organic carbon content; Fig. 10) or in less polluted sites (1.2% organic carbon content; Fig. 4). The host rock below the crusts is always calcite-rich but in every case also contained some gypsum.

Laminar crusts form a thin coating on vertical walls and surfaces. In laminar black crusts a mean gypsum concentration of 35% is found alongside calcite with a mean concentration of 46%. The organic carbon content of such crusts is less than 1% (Fig. 10).

Black crusts of coarse limestones are composed of small, scattered angular quartz grains, which float in a fine dark matrix as identified under a polarizing petrological microscope. The matrix is black and contains particles of less than 0.002 mm. Besides these fines, larger gypsum crystals are also observed (up to 0.06 mm). These crystals are black or transparent with a greyish tinge; this differs from the generally clear transparent colour of gypsum. The black and grey colours are related to small, dark, organic-rich inclusions (carbonaceous particles). The irregular contact between the crust and the carbonate rock is dissolutional (Fig. 11). The presence of gypsum crystals is not restricted to the crustal zone, but they are also found more than 1 cm beneath the crust (Fig. 12). Inward from the crust the crystal size of gypsum gradually decreases. Below the crust, greyish and inclusion-rich gypsum crystals are found on the top of circumgranular calcite cement rims of the ooids.

Laminar black crusts have higher Schmidt hammer rebound values than the host rock (Fig. 13). The majority of Duroscope rebound measurements also yielded higher values (Fig. 14). Water absorption tests indicate that black laminar crusts form a low-permeability layer on the surface of the porous limestone, which reduces water infiltration (Fig. 15).

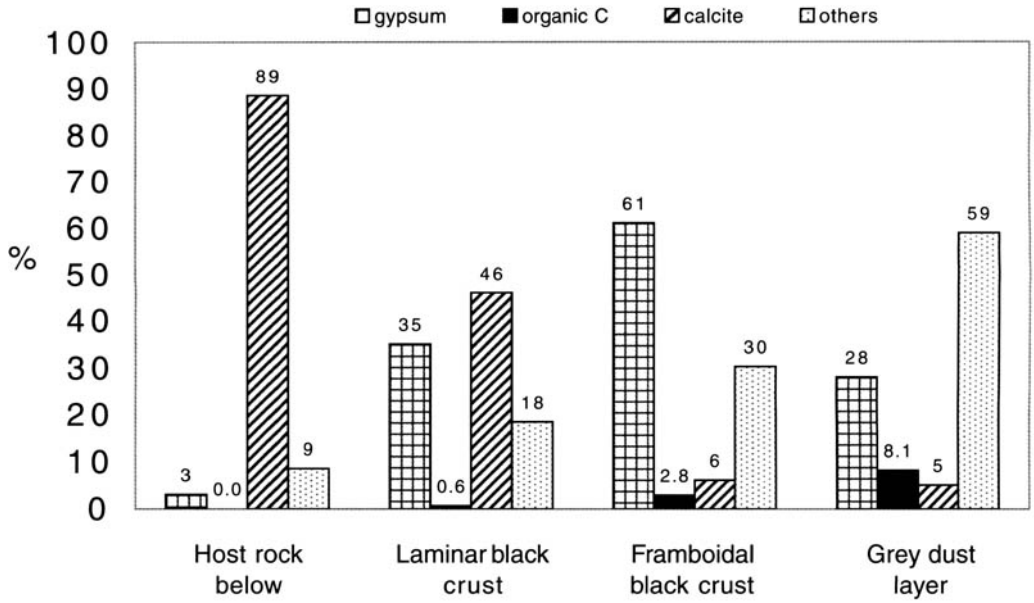

Fig. 10. Mineralogical composition of different crust types and host rock from the polluted city centre, College of Fine Arts.

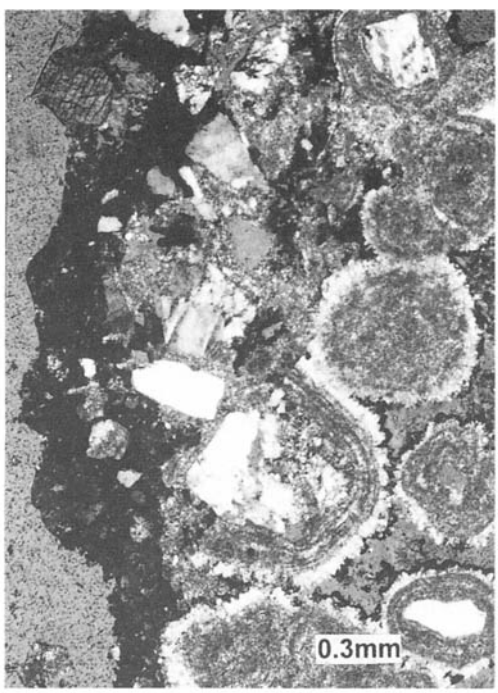

Fig. 11. Thin section photograph of a black crust and host oolitic limestone. Note the irregular dissolutional boundary between the crust and the limestone and the presence of dark gypsum crystals in the pores below.

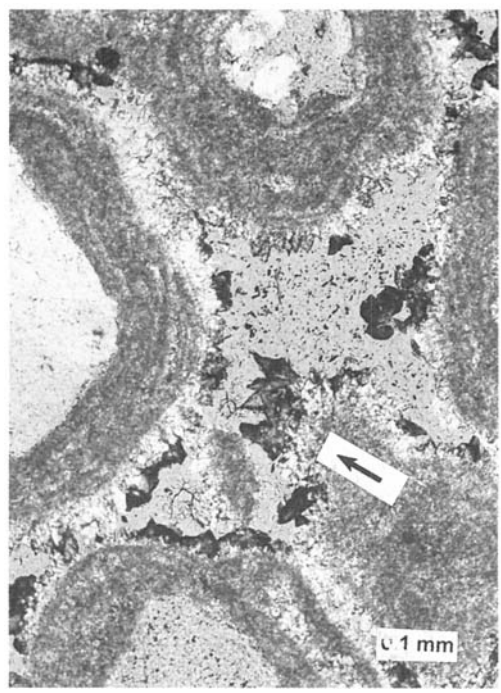

Fig. 12. Thin section photograph. Dark grey idiomorphic gypsum crystals are on the top of calcite cement and within the pores (arrow).

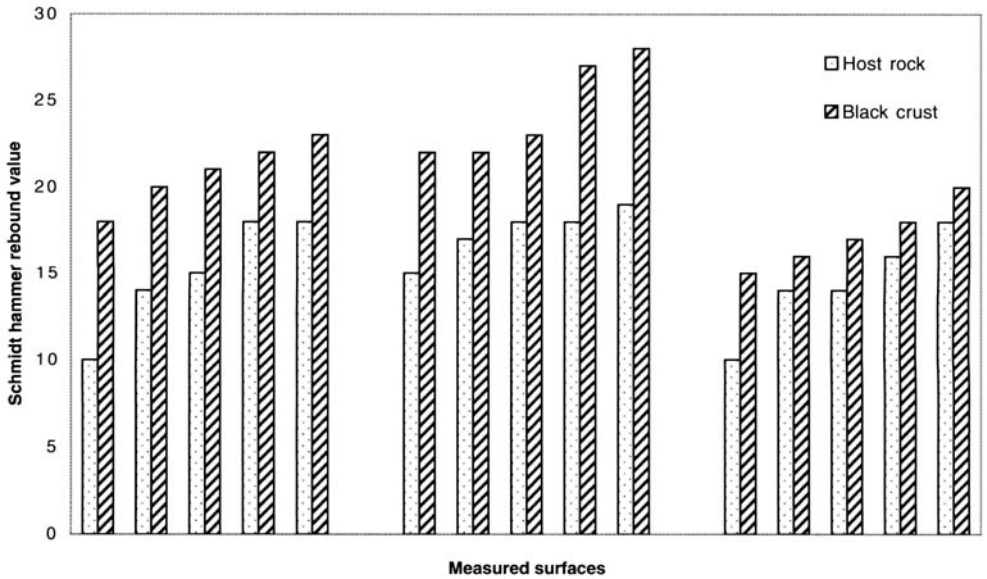

Fig. 13. Schmidt hammer rebound values of three rock blocks, thin black laminar crust and host limestone.

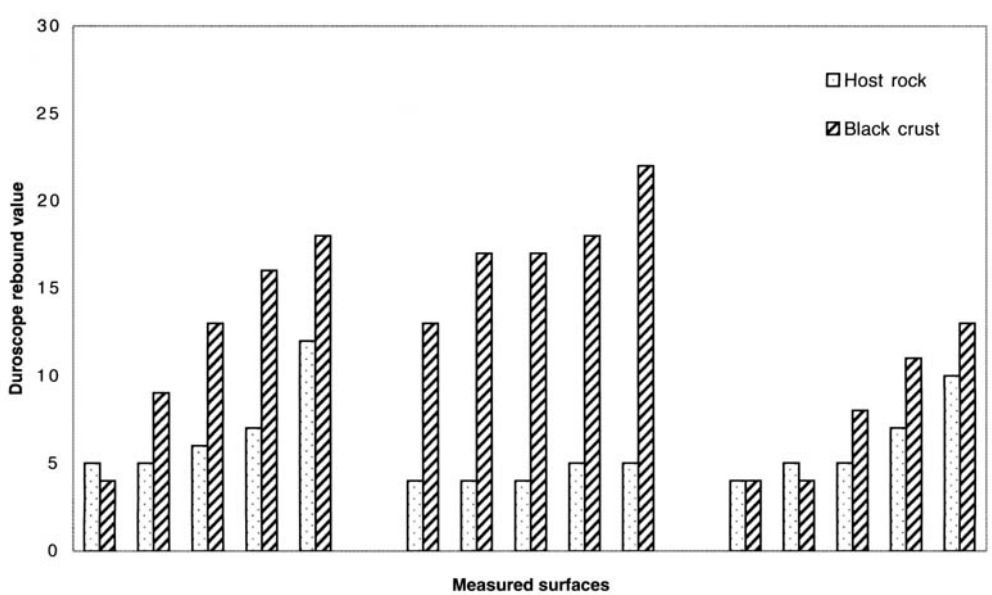

Fig. 14. Duroscope rebound values of three rock blocks, thin black laminar crust and host limestone.

Grey dust layer

Grey dust forms an approximately millimetre-thick, or in some cases a centimetre-thick unconsolidated layer on the stone surface that can be removed without affecting the underlying stone surface. It is found primarily on sheltered and dry stone surfaces in the city centre. The grey dust layer is very rich in organic carbon (8.1%) and in other minerals (59%; mostly quartz). The average gypsum content is also relatively high (28%) (Fig. 10).

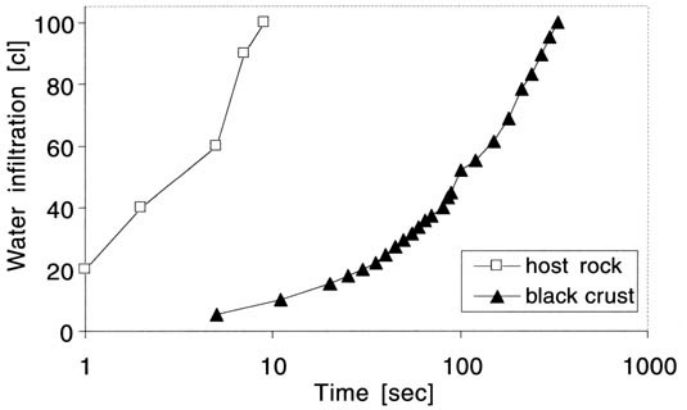

Fig. 15. Water absorption curves for black laminar crust and the limestone below the crust.

Mechanical breakdown

Crust removal features such as contour scaling, blistering and flaking are very common but do not occur equally on all crusts. Thick, white, case hardened crusts show contour scaling (Figs 2 and 3), thinner white crusts are characterized by multiple flaking, while very thin white crusts tend to blister (Fig. 5). Surface-parallel laminar black crusts also form blisters or scales, while thicker framboidal black crusts scale with the detachment of the entire crust, rather than flaking. When there are no crusts, or after crust removal, granular disintegration begins and crumbling is observed (Fig. 16). The result is the rounding of edges and corners as well as significant material loss (up to 4 cm). An extreme case of mechanical breakdown is alveolar weathering (honeycombs). It is observed only on severely weathered wall sections where no crust is preserved. Stone surfaces exposed after crust removal are weak, meaning that they have low Schmidt hammer and Duroscope rebound values (Figs 6, 7, 13 and 14). Small quantities of gypsum were identified in all samples that are prone to granular disintegration, i.e. after crust removal (Figs 4 and 10). Fractures and cracks are formed due to salt crystallization (gypsum), frost action and also as a result of the structural motion of the building.

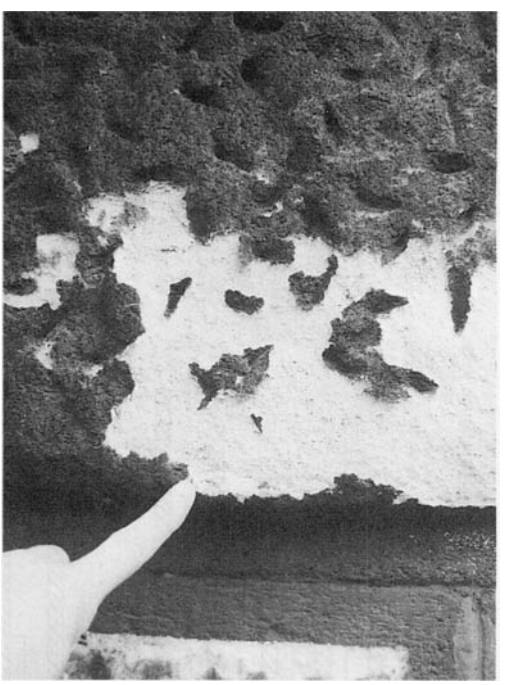

Fig. 16. Crumbling begins when protective black crust is removed, House of Parliament.

Combination of weathering features

The combination of these decay features is also observed on stone blocks, e.g. flaking crusts surround case hardened crusts and blackening occurs in protected microenvironments (Fig. 17). There are blocks where at least three generations of crusts and other decay features have been identified indicating that crust formation can take place in a succeeding order (Fig. 18).

Distribution of weathering features

At the College of Fine Arts, located in Budapest's enclosed city centre where wind and

Fig. 17. Combination of decay features, scaling white hard crust and newly formed crust below, blackened scaling crust at the lower corner, Mathias Church (coin is 2.2 cm).

rain exposure is limited, thick, white, case hardened crusts or white blistering crusts are not found (site 4, Fig. 1). Conversely, black crusts and grey dust layers are frequent. In the city centre it was observed that when black crusts are removed by rainfall, a white-washed surface is formed. At Mathias Church, which is adjacent to the city centre where pollution levels are lower and winds are moderate, the role of wall orientation in the formation of different decay features was documented (site 2, Fig. 1). The northern facade, which is protected from direct rainfall by a nearby building, mostly exhibits black laminar crusts (Fig. 19). The eastern wall, which is directly washed by rain, is characterized by white to pale grey washed stone surfaces (Fig. 20). At this site, black laminar crusts are prone to blistering and scaling. It should also be noted that white crust formation and mechanical breakdown of these crusts are less common. Close to the city centre on the riverside of the Danube, at the House of Parliament (site 3, Fig. 1), wind plays a more important role. North winds sweep away pollution and therefore the distribution of decay forms is mostly controlled by exposure. At this site, white crusts form in exposed areas; black laminar crusts accumulate in vertical zones sheltered from rainwater (Fig. 16); and black framboidal crusts develop in condensation zones. Black crusts are less common than in the city centre and there is no evidence for the accumulation of a grey dust layer. Citadella fortress, which is located in a moderately polluted environment on the top of a small hill (site 4, Fig. 1) and is exposed to wind and rain throughout the year, exhibits the most severe signs of mechanical weathering. The exposed wall sections display intense white crust formation, scaling, blistering, flaking and a variety of granular disintegration (Fig. 2). The blackening is limited to sheltered microenvironments such as joints between blocks (Fig. 5), or beneath edges and cornices. Nevertheless, at the entrance gate where the wall is entirely protected from rain and wind, a uniform laminar black crust has formed, which tends to scale (Figs 21 and 22).

Discussion

The different genesis and wind/rain exposure are reflected in the mineralogical composition of crusts (Amoroso & Fassina 1983; Dolske 1995; Zappia *et al.* 1998). The black colour of crusts of the oolitic limestone is clearly attributed to organic carbon (Ausset *et al.* 1999; Ghedini *et al.* 2000). It is air-borne in origin, since no organic carbon was detected in quarry stone samples. Derivatograph analyses showed that in most of the samples the organic matter shows two thermal peaks indicating that there are at least two different types of organic carbon present (Riontino *et al.* 1998; Ghedini *et al.* 2000). The second peak is at higher temperatures above 250–300°C. This temperature can be correlated with the temperature of diesel engine combustion indicating that a part of the organic carbon is in the form of soot emitted from diesel engines of trucks, buses and cars. This type of organic carbon is found in all sites independent of location. Overall, however, the crusts in the polluted city centre contain more organic carbon than those on the less polluted hill (Figs 4 and 10). The high organic carbon content of the grey dust layer in the city centre and high concentration of other minerals such as quartz are also indicative of a wind-blown origin and dry deposition of settling dust.

Since no type of sulphate or sulphur is found in the quarry stone, the detected gypsum is considered to be exclusively a weathering product. Gypsum formation strongly depends on microclimatic conditions since small deposited particles concentrate on areas which remain moist (Dolske 1995; Zappia *et al.* 1998).

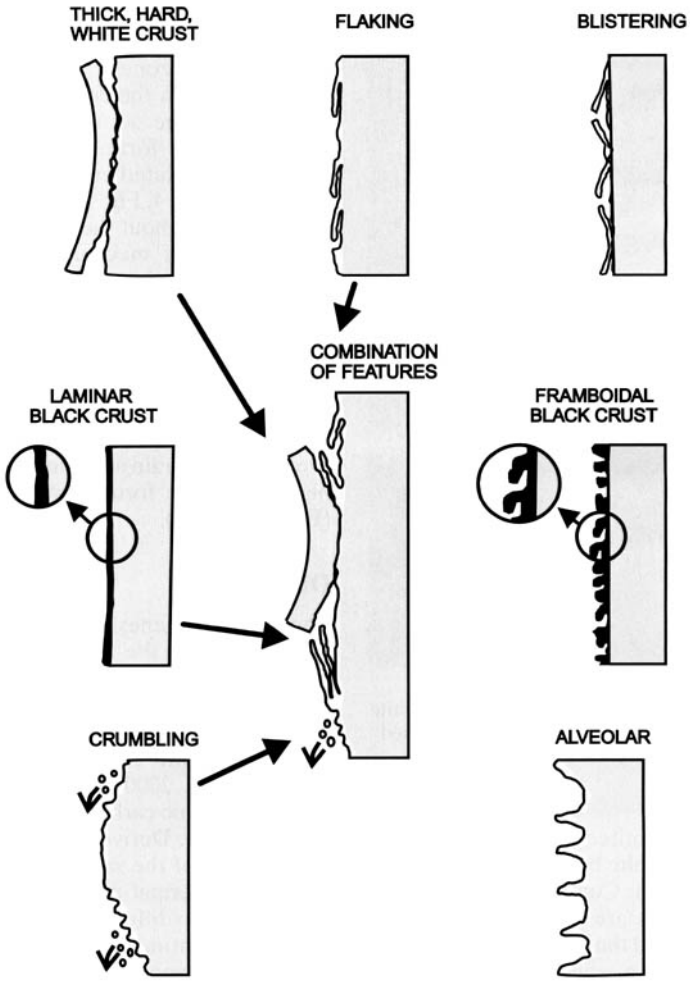

Fig. 18. Most important decay features and their combination in the ooidal limestone of Budapest.

The simulation chamber experiments show that humidity, SO_2 and particulate matter, especially fly-ash, lead to the rapid formation of gypsum on limestone (Ausset *et al.* 1996; Rodriguez-Navarro & Sebastian 1996). Organic carbon particles, which have a high reaction surface, serve as catalysts (Amoroso & Fassina 1983; Del Monte & Rossi 1997) and the high sulphur, V, Ni, and Fe contents of fly-ash particles accelerate the sulphation reaction. The resultant gypsum crystals fix fly-ash particles to the limestone surface (Ausset *et al.* 1999). Consequently, the surface accumulation of gypsum in black framboidal crusts on the oolitic limestone is a reaction product between atmospheric SO_2 and calcium ions present in the fog droplets or calcium-rich particles present in the air (calcite, fly-ash) (Ausset *et al.* 1999).

Nevertheless, the chemical transformation of calcium carbonate into gypsum cannot be entirely excluded (Amoroso & Fassina 1983; Camuffo *et al.* 1983; Camuffo 1995; Maravelaki-Kalaitzaki & Biscontin 1999). Thus the most effective gypsum formation takes place on wet sheltered surfaces, where organic carbon (mostly fly-ash) is present and not washed away by rain (Zappia *et al.* 1998; Primerano *et al.* 2000). The growth of framboidal black crusts proceeds since an increase in surface roughness enhances the fixation process (Ausset *et al.* 1999). As a consequence these crusts are generally thick, have very high gypsum contents (more than 60%) and are very rich in organic carbon (Figs 4 and 10).

The difference in mineralogical composition of the framboidal black crusts in the polluted

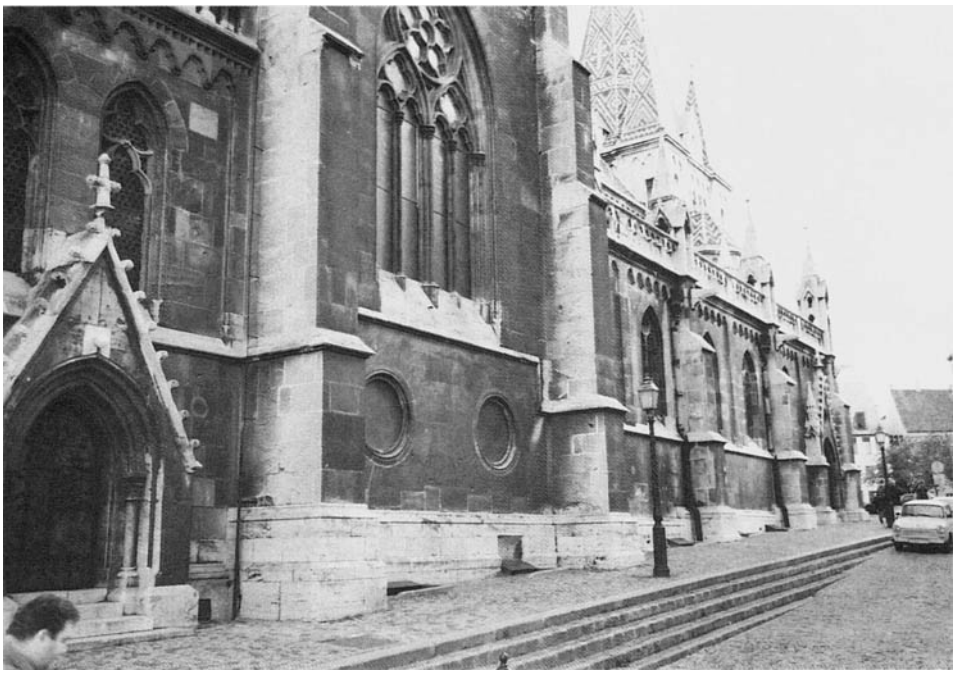

Fig. 19. Black laminar crust on the sheltered wall of Mathias Church (see also Fig. 20).

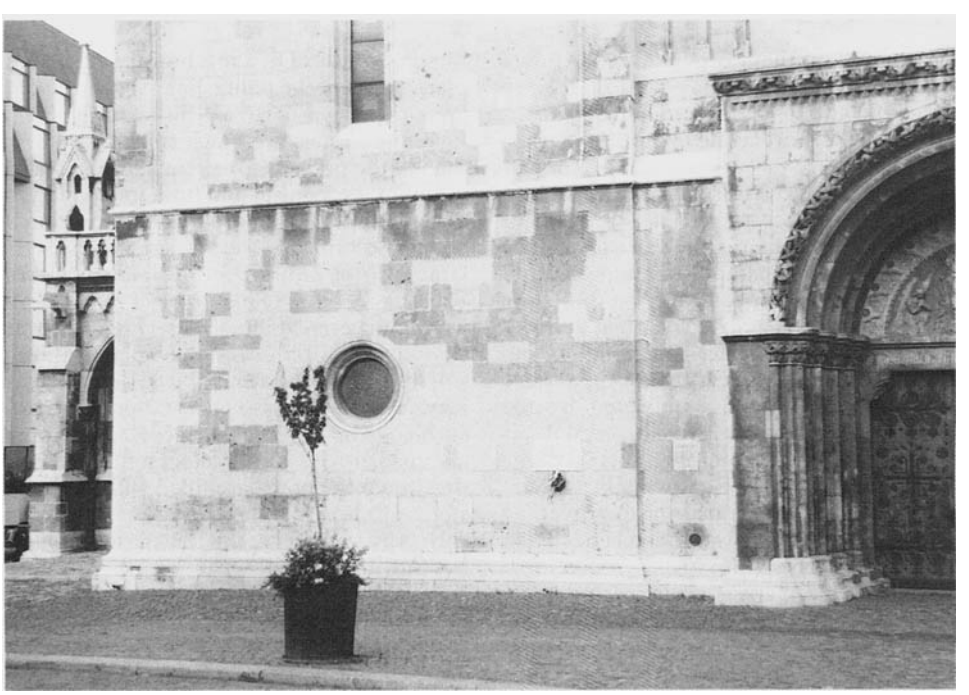

Fig. 20. White-washed surface on exposed wall of Mathias Church.

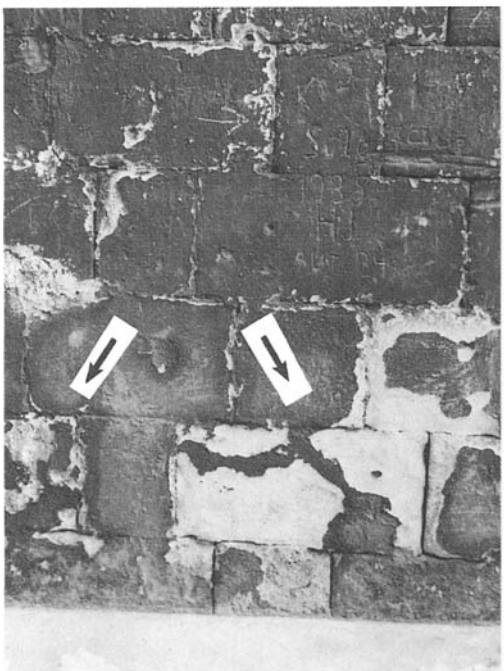

Fig. 21. A sheltered wall is mostly covered by laminar black crusts at Citadella. Photograph was taken in 1993. See the changes (arrows) in crust cover compared to Figure 22.

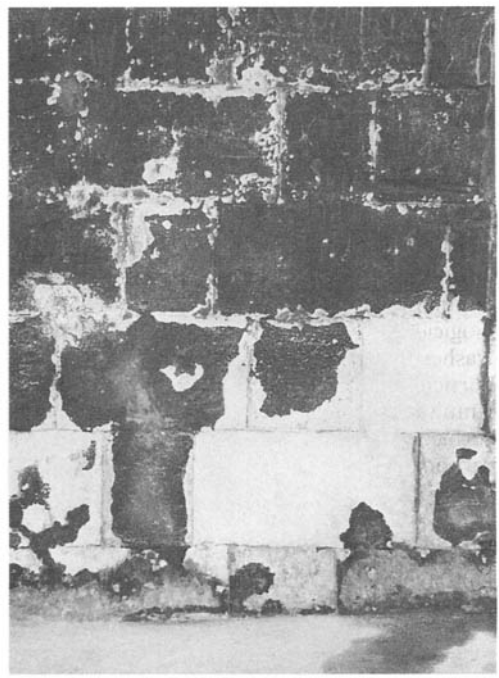

Fig. 22. Removal of parts of the black crust is a rapid process and can take place within years (eight years). Compare this picture, taken in 2001, to Figure 21 (1993).

city centre and on the less polluted hill (Figs 4 and 10) also suggests that air pollution makes a major contribution to crust mineralogy as it provides SO_2 and particulate matter for gypsum formation.

On laminar black crusts of vertical walls, a similar reaction takes place but with a major difference. In this scenario, the vertical or steep walls do not allow for the formation of water droplets. In the initial phase of crust formation the solution containing organic carbon particles penetrates into the rock via pore conduits and the sulphation reaction occurs below the surface (Ausset *et al.* 1996). It is indicated by the presence of idiomorphic gypsum crystals as pore-lining dark grey cement (Fig. 12). The large crystal size indicates free growth of gypsum. XRD analyses also confirmed this observation: more than 3% of gypsum was found beneath the crusts in the host rock (Fig. 10).

By studying black crusts on Istria limestone, Maravelaki-Kalaitzaki & Biscontin (1999) proposed that in compact black crusts gypsum is formed at the expense of micritic substrate after the absorption of SO_2. Decreased quantities of decay products such as gypsum were measured in such crusts. On the contrary, the laminar black crusts of the oolitic limestone in Budapest are rich in gypsum (35% in average; Fig. 10). Gypsum crystals are much smaller in the crust than in the pores below. This suggests a slightly different mechanism and time frame of gypsum formation. It is proposed that both precipitation and dissolution processes act on the surface (Camuffo *et al.* 1983; Rodriguez-Navarro & Sebastian 1996). Laminar black crust forms a very low-permeability layer (Fig. 15), thus it significantly reduces the penetration of sulphate-rich solutions into the stone and gypsum formation is restricted primarily to the surface. On vertical surfaces fewer organic carbon particles are able to settle and attach, thus when the pores are filled and the irregular stone surfaces are levelled the thickening of such crust ceases, i.e. the thickness is controlled by the crust itself. The weathering-related mineralogical changes are also reflected in physical properties of laminar black crusts. These crusts have higher Duroscope rebound and Schmidt hammer rebound values than the host rock (Figs 13 and 14).

Laminar black crusts of the oolitic limestone

in Budapest are not as stable as the compact black crusts of Istria stone (Maravelaki-Kalaitzaki & Biscontin 1999), or as strongly attached as the thin black crusts on marbles (Moropoulou *et al.* 1998; Bugini *et al.* 2000) or the stabile blisters and the very slowly exfoliating black crusts in Oxford (Viles, 1993). The removal of scaling and blistering crusts occurs within few years (Figs 21 and 22).

The formation mechanism of thick, case hardened white crusts is similar to that of laminar black crusts despite differing mineralogical compositions. On exposed walls, rain washes the sulphate-rich solution and air-borne particulate matter into limestone pores as it simultaneously slightly dissolves the stone surface (Camuffo 1995). By dissolution both the carbonate and the free calcium are carried into solution (Maravelaki-Kalaitzaki & Biscontin 1999). Evaporation causes the solution to become increasingly concentrated and both gypsum and calcite precipitate. Accordingly in white crusts, calcite occurs in two forms, first as a dissolved and reprecipitated mineral and second as a substrate mineral. The pores within the crust become cemented and compact, forming an impermeable case hardened crust (Fig. 3). When it rains the water penetrates below the impermeable crust and dissolution and salt crystallization shift to the zone below the crust.

Calcite mobilization from below the crust, gypsum crystallization and frost action lead to the weakening of the host rock relative to the crust (lower Duroscope and Schmidt hammer rebound values) and finally to crust removal by scaling (Fig. 2). Thick case hardened white crusts remain stable for longer periods than thin white crusts, but once scaling commences rapid granular disintegration follows.

Blistering white crusts are formed on exposed walls. They differ from case hardened crusts in their thickness, morphology, mineral composition and strength, which suggests differences in the formation mechanism. These crusts develop only on very fine or fine-grained oolitic limestones. This indicates that in addition to exposure, lithology is also one of the key control factors of crust genesis (Fronteau *et al.* 1999). The thin (less than 1 mm) crust does not form a continuous impermeable layer on the stone surface (Fig. 5), thus rain can penetrate below it. In addition it prevents the rapid evaporation of water and enables gypsum to crystallize below the crust (cf. three-stage model of blister formation of Viles (1993)). Hence blistering crusts enclose more gypsum (70%) than scaling case hardened crusts (27%) since the infiltrating but entrapped solutions provide a continuous sulphate supply. Another important element in the formation of thin gypsum-rich crusts is the pore radius. In the larger pores of coarse-grained oolitic limestones the relative humidity is lower than in the smaller pores (Camuffo 1995) of fine-grained oolitic limestones. Accordingly the latter are more responsive to condensation–evaporation cycles and gypsum precipitation begins earlier from the supersaturated solution of the micropores.

The removal of both black and white crusts is a complex process. The most probable explanation is salt weathering combined with frost action. The crystallization of gypsum can exert a pressure of up to 100 MPa on the pore walls (Winkler 1970) and ice crystallization generates pressure of 200 MPa at −22°C (Bell 1993). These values are much higher than the compressive strength of the oolitic limestone (Table 2). In Budapest both forms of crystallization-related pore pressure occur. Gypsum crystallization occurs from spring to autumn and ice crystallization predominates in winter. It is difficult to differentiate which one has the more significant role in crust removal. The presence of gypsum in the pores beneath the crust (Fig. 12) suggests that mechanical weathering caused by gypsum crystallization is a significant process. Similar mechanisms of salt weathering have been described in detail for many other salts by Goudie & Viles (1997).

Conclusions

Soft oolitic limestone shows severe forms of decay in Budapest. The high atmospheric pollution (SO_2 and soot in dust) combined with a continental climate are responsible for the accelerated weathering. Mineralogical differences in the crusts reflect differences in genesis and different contributions of pollutants in crust formation. Gypsum is the primary mineral formed as a result of air pollution: it is present in all weathering forms, as well as in the host rock below the crust. The highest gypsum content was measured in black framboidal crusts and in white blistering crusts. In the latter, gypsum is the prevailing mineral (up to 70%). In the polluted city centre the organic carbon content of the crusts can be double that in the less polluted sites. Dust crusts are rich in organic carbon and wind-blown particles.

There are different weathering features on wind- and rain-exposed and on sheltered wall sections. On exposed walls, white case hardened crusts, or light coloured blistering and flaking crusts are formed. Acid rain-related dissolution

and reprecipitation of calcite and precipitation of some gypsum lead to the formation of case hardened white crusts. Although particle deposition is limited in these sites, a minor proportion of wind-driven dust is present in the crust in the form of organic carbon. In sheltered vertical to subvertical walls, thin laminar black crusts are developed. The protected, moist condensation zones are characterized by gypsum-dominated thick framboidal black crusts.

Crust formation leads to changes in the mineral composition of the stone surface and an increase in surface strength as indicated by Duroscope and Schmidt hammer rebound values. Both laminar black crusts and white hard crusts are denser and harder than the host rock. Concurrently the host rock beneath the crust becomes weaker and softer and has much lower Duroscope and Schmidt hammer rebound values than the fresh stone due to gypsum crystallization and possible mobilization of calcium.

The help of K. Kocsányi-Kopecskó (XRD, DTA-DTG analyses), G. Hajnal, E. Saskői, E. Horthy, E. L. Árpás and Gy. Emszt is very much appreciated. The reviews and comments of P. Ausset, J. Cassar and E. Bede are very much appreciated and significantly improved the quality of this paper. M. Hajpál finalized some of the graphs. I am also very grateful to J. Lukács, B. Andrássy and J. Herkules who provided access to the construction site and restoration works at the House of Parliament. The guidance of E. Bánóczky and B. Mátéffy at Mathias Church is also acknowledged. This work was partly financed by the Széchenyi Found.

References

AMOROSO, G. G. & FASSINA, V. 1983. *Stone Decay and Conservation*. Elsevier, Amsterdam.

ANTILL, S. J. & VILES, H. A. 1999. Deciphering the impacts of traffic on stone decay in Oxford: some preliminary observations from old limestone walls. *In*: JONES, M. S. & WAKEFIELD, R. D. (eds) *Aspects of Stone Weathering, Decay and Conservation*. Imperial College Press, London, 28–42.

AUSSET, P., CROVISIER, J. L., DEL MONTE, M. *et al.* 1996. Experimental study of limestone and sandstone sulphation in polluted realistic conditions: The Lausanne atmospheric simulation Chamber (Lasc). *Atmospheric Environment*, **30**, 3197–3207.

AUSSET, P., DEL MONTE, M. & LEFÈVRE, R. A. 1999. Embryonic sulphated black crusts on carbonate rocks in atmospheric simulation chamber and in the field: role of carbonaceous fly-ash. *Atmospheric Environment*, **33**, 1525–1534.

BELL, F. G. 1993. Durability of carbonate rock as a building stone with comments on its preservation. *Environmental Geology*, **21**, 187–200.

BUGINI, R., TABASSO, M. L. & REALINI, M. 2000. Rate of formation of black crusts on marble. A case study. *Journal of Cultural Heritage*, **1**, 111–116.

CAMUFFO, D. 1995. Physical weathering of stone. *The Science of the Total Environment*, **167**, 1–14.

CAMUFFO, D., DEL MONTE, M. & SABBIONI, C. 1983. Origin and growth mechanisms of the sulfated crusts on urban limestone. *Water, Air, and Soil Pollution*, **19**, 351–359.

CHRISTARAS, B. 1991*a*. Méthode d'évaluation de l'altération et modification des propriétés mécaniques des granites an Grèce du Nord. *Bulletin of the International Association of Engineering Geology*, **43**, 21–26.

CHRISTARAS, B. 1991*b*. Durability of building stones and weathering of antiquities in Creta/Greece. *Bulletin of the International Association of Engineering Geology*, **44**, 17–25.

CHRISTARAS, B. 1991*c*. Weathering of natural stones and physical properties. *In*: ZEZZA, F. (ed.) *Weathering and Air Pollution*. Community of Mediterranean Universities, Bari, 169–174.

CHRISTARAS, B. 1996. Non destructive methods for investigation of some mechanical properties of natural stones in the protection of monuments. *Bulletin of the International Association of Engineering Geology*, **54**, 59–63.

CSO 1986. *A környezet állapota és védelme* (*State and Protection of Environment*). Central Statistic Office, Budapest (in Hungarian).

DEL MONTE, M. & ROSSI, P. 1997. Fog and gypsum crystals on building materials. *Atmospheric Environment*, **31**, 1637–1646.

DEL MONTE, M., AUSSET, P., FORTI, P., LÈFEVRE, R. A. & TOLOMELLI, M. 2001. Air pollution records on selenite in the urban environment. *Atmospheric Environment*, **35**, 3885–3896.

DOLSKE, D. 1995. Deposition of atmospheric pollutants to monuments, statues, and buildings. *The Science of the Total Environment*, **167**, 15–31.

FASSINA, V. 1991. Atmospheric pollutants responsible for stone decay. Wet and dry surface deposition of air pollutants on stone and the formation of black scabs. *In*: ZEZZA, F. (ed.) *Weathering and Air Pollution*. Community of Mediterranean Universities, Bari, 67–86.

FITZNER, B., HEINRICHS, K. & KOWNATZKI, R. 1995. Weathering forms – classification and mapping. *In*: *Denkmalpflege und Naturwissenschaft, Natursteinkonservierung I*. Ernst and Sohn, Berlin, 41–88.

FRONTEAU, G., BARBIN, V. & PASCAL, A. 1999. Impact du faciès sédimento-diagenétique sur l'altération en œuvre d'un géomatériau calcaire. *Comptes Rendus de l'Académie des Sciences, Series IIA, Earth and Planetary Science*, **328**, 671–677.

GHEDINI, N., GOBBI, G., SABBIONI, C. & ZAPPIA, G. 2000. Determination of elemental and organic carbon on damaged stone monuments. *Atmospheric Environment*, **34**, 4383–4391.

GOUDIE, A. S, & VILES, H. 1997. *Salt Weathering Hazards*. John Wiley and Sons, Chichester.

IRFAN, T. Y. & DEARMAN, W. R. 1978. Engineering classification and index properties of a weathered

granite. *Bulletin of the International Association of Engineering Geology*, **17**, 79–90.

KIESLINGER, A. 1949. *Die Steine von Sankt Stephan*. Verlag Herold, Wien.

MARAVELAKI-KALAITZAKI, P. & BISCONTIN, G. 1999. Origin, characteristics and morphology of weathering crusts on Istria stone in Venice. *Atmospheric Environment*, **33**, 1699–1709.

MEP 2001. *Report on the State of Environment*. Ministry of Environmental Protection, Hungary.

MOINGL, J., STEINER, F., TAJTHY, T. & VÁRKONYI, T. 1991. *Budapest levegőszennyezettsége (Air pollution in Budapest)*. Report, Fővárosi Levegőtisztasági Kft., Budapest (in Hungarian).

MOROPOULOU, A., BISBIKOU, K., TORFS, K., VAN GRIEKEN, R., ZEZZA, F. & MACRI, F. 1998. Origin and growth of weathering crusts on ancient marbles in industrial atmosphere. *Atmospheric Environment*, **32**, 967–982.

PRIMERANO, P., MARINO, G., DI PASQUALE, S., MAVILIA, L. & CORIGLIANO, F. 2000. Possible alteration of monuments caused by particles emitted into the atmosphere carrying strong primary acidity. *Atmospheric Environment*, **34**, 3889–3896.

RIONTINO, C., SABBIONI, C., GHEDINI, N., ZAPPIA, G., GOBBI, G. & FAVONI, O. 1998. Evaluation of atmospheric deposition on historic buildings by combined thermal analysis and combustion techniques. *Themochimica Acta*, **321**, 215–222.

RODRIGUEZ-NAVARRO, C. & SEBASTIAN, E. 1996. Role of particulate matter from vehicle exhaust on porous building stones (limestone) sulfation. *The Science of the Total Environment*, **187**, 79–91.

SMITH, B. J., WHALLEY, W. B. & MAGEE, R. 1992. Assessment of building stone decay: a geomorphological approach. *In*: WEBSTER, R. G. M. (ed.) *Stone Cleaning and the Nature and Decay Mechanism of Stone*. Proceedings of the International Conference, Edinburgh, UK. Donhead, London, 249–257

VILES, H. A. 1993. The environmental sensitivity of blistering of limestones walls in Oxford, England: a preliminary study. *In*: THOMAS, D. S. G. & ALLISON, R. J. (eds) *Landscape Sensitivity*. John Wiley, Chichester, 309–326.

VILES, H. A. 1994. Observations and explanations of stone decay in Oxford, UK. *In*: THIEL, M. J. (ed.) *Conservation of Stone and Other Materials, Vol. I, Causes of Disorders and Diagnosis*. E & FN Spon – RILEM, London, 115–120.

WINKLER, E. M. 1966. Important agents of weathering for building and monument stone. *Engineering Geology*, **1**, 381–400.

WINKLER, E. M. 1970. The importance of air pollution in the corrosion of stone and metals. *Engineering Geology*, **4**, 327–334.

ZAPPIA, G., SABBIONI, C., RIONTINO, C., GOBBI, G. & FAVONI, O. 1998. Exposure tests of building materials in urban atmosphere. *The Science of the Total Environment*, **224**, 235–244.

This page intentionally left blank

Principal decay patterns on Venetian monuments

VASCO FASSINA[1], MONICA FAVARO[2] & ANDREA NACCARI[2]

[1] *Soprintendenza ai Beni Artistici e Storici del Veneto, San Marco 63, 30124 Venice, Italy (e-mail: vasco.fassina@soprintendenzapsadveneto.it)*

[2] *Istituto Veneto per i Beni Culturali, via della Libertà 5-12, 30175 Venice, Italy*

Abstract: In most Venetian monuments studied, the stone decay was ascribed to the transformation of calcium carbonate into calcium sulphate. This phenomenon is commonly observed elsewhere and has been pointed out by many authors. In order to explain why different forms of decay are present on a building facade, samples were taken from different areas of many monuments. Analytical results were related to different forms of decay, defined respectively as white washing, dirt accumulation and dirt wetting. A simplified model of stone decay is presented and its validity tested on several Venetian monuments. Results showed that the features visible on stone surfaces corresponded to different degrees of deterioration. Sulphate formation is greatest in the black dendrite-shaped crusts, which are generally formed at the interface between the white washing areas and the sheltered ones, which were defined as dirt wetting area.

The decay forms of the most common lithotypes used in Venetian monuments were also studied. Results obtained showed that in compact limestone, gypsum formation affects the stone only on the surface. In contrast, on marble a different mechanism of decay takes place: the decohesion of calcite crystals, due to thermal changes, favours the penetration of sulphuric acid solution into intergranular spaces, thus causing the transformation of calcium carbonate into calcium sulphate, not only on the surface, but also inside the marble.

During recent decades many authors have studied the forms of decay of building materials on different Venetian monuments (Fassina *et al.* 1976, 2001; Fassina 1978, 1988*a*, 1994, 1999; Lazzarini 1972, 1979; Marchesini 1970; Torraca 1969).

The attempt to correlate the decay forms observed on buildings with atmospheric agents has been carried out systematically since the UNESCO Venice campaign launched in 1971 for the safeguard of Venetian monuments which were decaying at an increasing rate during that period.

The rapid increase in industrialization and urbanization, which took place in the district of Mestre and Marghera at the beginning of 1950s, sharply increased air pollutant concentration in the atmosphere. Contemporaneously stonework constructed several centuries ago started to deteriorate very quickly as a consequence of increased air pollution.

In most Venetian monuments studied, stone decay is ascribed to the transformation of calcium carbonate into calcium sulphate. To explain the mechanism of stone decay and black crust formation it is important to focus attention on the stone–atmosphere interface in order to estimate qualitatively and quantitatively the new-formation products and try to correlate them with the different decay features commonly observed on the facade of monuments. Characteristic staining patterns, defined in terms of black and white areas, are frequently observed and are generally correlated to different degrees of decay due to the diverse mechanisms of deterioration involved (Amoroso & Fassina 1983; Fassina 1994; Fassina *et al.* 2000).

Our investigation was mainly focused on:

(i) the new-formation products present in areas characterized by different morphologies of decay;
(ii) the mechanism of decay taking place on the most common lithotypes present on Venetian monuments;
(iii) the composition of rain and fog in Venice in relation to the decay of building materials.

Experimental method

To assess the diverse processes of decay, surface samples of decayed stone were taken from several monuments according to the following criteria:

(i) the degree of decay through macroscopic observation;
(ii) the orientation of the individual architectural elements;

From: SIEGESMUND, S., WEISS, T. & VOLLBRECHT, A. 2002. *Natural Stone, Weathering Phenomena, Conservation Strategies and Case Studies*. Geological Society, London, Special Publications, **205**, 381–391.
0305-8719/02/$15.00 © The Geological Society of London 2002.

(iii) the exposure to direct rainfall (white areas);
(iv) the degree of shelter from rainwater (black areas).

The collection of fog water was carried out by using active collectors with a fan attachment, which draws the air laden with fog droplets into the collector. The fog/rain collector comprises three basic parts: the rain collector, the fog collector and the sensor unit. The fog water collector is simply a base holding a bottle with a funnel leading into it. The rain will fall into the funnel and drip into the collection bottle.

To assess the different alteration products the following analytical methods were used: cross-section to identify the different layers on the surface, scanning electron microscopy (SEM) providing morphological information on crystals, X-ray distribution by energy dispersive spectrometry (EDS) of chemical elements which allows determination of their origin in relation to conservation treatments carried out in the past or atmospheric pollution decay, and ion chromatography (IC) to determine qualitatively and quantitatively the water-soluble anions most harmful for stone decay.

Discussion of the results

Fog water composition

The interaction between gaseous and particulate pollutants and the stone surface is strongly influenced by the presence of a liquid phase, which speeds up any reaction. For this reason fog and water events during a five-year period have been investigated. Fog is formed by smaller droplets than rain, consequently since the acid is less diluted, ion concentrations in fog are substantially higher than those found in rain samples and fogs are up to twenty times more acidic than rain. In order to explain these differences we must remember that (Brewer *et al.* 1983): (i) fog occurs closer to the ground level and therefore is exposed to greater concentrations of pollutants; (ii) fog droplets have smaller diameters thereby having a far greater combined surface area, permitting enhanced diffusion of ions or gases and therefore a higher final concentration; (iii) rainstorms are generally accompanied by the addition of fresh air masses, hence raindrops fall through an increasingly clean environment as opposed to fog droplets, which experience a more uniformly polluted environment.

Fog formation in Venice occurs primarily during the late autumn and early winter months of November, December and January. Fog during these months, occurs almost twice as often during the night as it does during the daytime hours. Conversely, summer fog occurs three times as often during the daytime hours as it does during the nightime.

A comparison of the fog and rain sample data from this study finds average concentrations of chlorides and sulphates to be seven to 16 times higher in fog samples while concentrations of nitrates were discovered to be slightly higher than the rain samples (Fig. 1). This finding could be due to the fact that fog samples show the chemistry of the local air while rain tends to be more general in that it can represent air quality due to either long- or short-range transport.

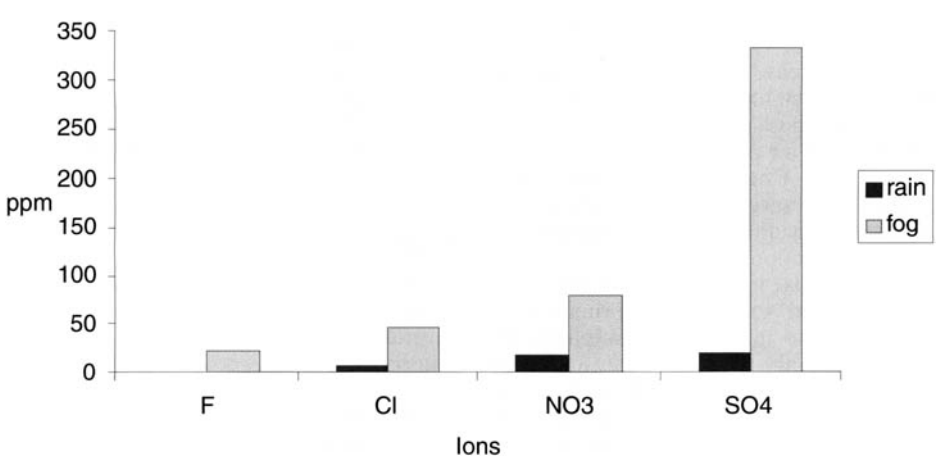

Fig. 1. Comparison of rain and fog samples. Average values for 1990.

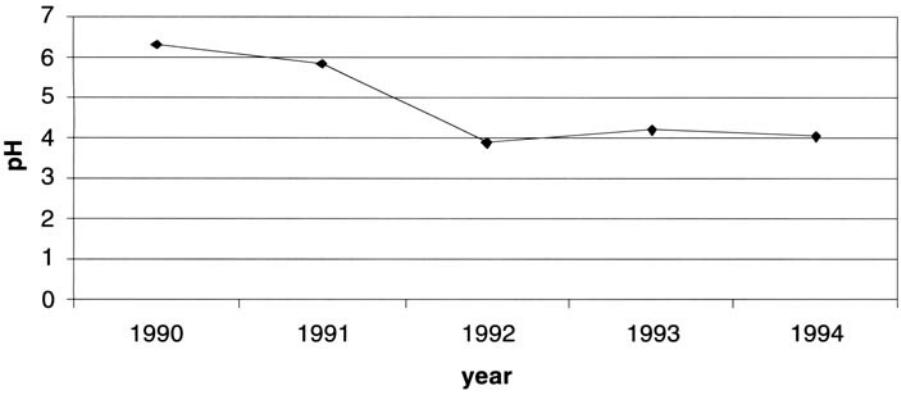

Fig. 2. Average values of pH during a five year period.

As regards the pH of fog samples collected, only 13% of the events have a pH above 6, while the remaining ones showed a pH lower and in particular 65% have a pH between 3 and 5. In Figure 2 the average pH values are reported.

The data show a predominant concentration of sulphates with respect to the other ions. In urban conditions generally nitrate concentrations are similar to the sulphate ones and it is well known automobiles are the primary source of nitrates. In Venice the low amount of nitrates is ascribed to the lack of automobiles, while chlorides become predominant during fog events which are accompanied by wind blowing from the sea. In this condition fog incorporates sea salt aerosols dominated primarily by chlorides (Fassina & Stevan 1992).

Mechanisms of decay in relation to exposure to rainwater: white washing, dirt accumulation, dirt wetting

On limestone building surfaces different situations create a marked contrast between washed and unwashed areas. On the top and sides of an exposed face of a building deposition of rain is usually several times greater than over the remainder of the walls due to deflection of air and rain. This causes a white washing area. Sometimes on vertical surfaces a fairly even accumulation of dirt is observed except where some feature causes a concentration, tending to produce a lighter cleaner streak across the general pattern.

In places sheltered from the rain, dirt can accumulate as incoherent stratification, as an incoherent powder adhering to the stone, or as incrustations strongly bound to the surface. These surfaces are black due to the collection of black carbonaceous particles and other atmospheric particles and represent a growth zone in which the transformation of calcium carbonate into gypsum takes place. A close observation of sheltered areas shows two different morphologies of deterioration which are defined as dirt accumulation and dirt wetting (Robinson & Baker 1975).

Dirt accumulation takes place far from rain washing areas and is characterized by black superficial deposits that grow on the surface due to the collection of atmospheric particles and to the transformation of calcium carbonate into gypsum.

Dirt wetting takes place at the interface between running water and sheltered areas. The thick and hard crust has a rough and spongy appearance and grows upon the original surface. According to our observation dirt accumulation, dirt wetting and white washing are generally present together on any buildings shown in Figure 3.

It is very important to understand if there is any correlation between the macroscopic observations and the formation of alteration products in different areas. For this reason macroscopic observations of decay forms were subsequently correlated with quantitative analytical data in order to build a simple model to explain in a general way the decay phenomena.

This simplified model was tested on several Venetian monuments and the features visible on stone surfaces correspond to different degrees of deterioration. In fact, quantitative analyses carried out on stone samples, taken from diverse areas, stressed that sulphates are present in different amounts according to the degree of sheltering irrespective of differences

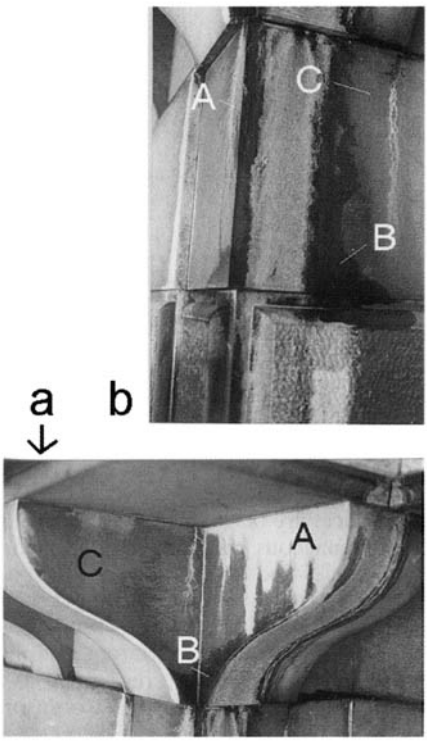

Fig. 3. On any building white washing (A), dirt accumulation (C) and dirt wetting (B) are clearly visible.

in stone texture and structure. An example of application of this model is the survey carried out on the portal of St. Mark's Basilica (Fassina 1988*b*, 1994, 1999). The degree of sulphatation in protected areas was found to depend on the distance from the rain washing areas (Table 1). In the Panel of Bakers the different decay areas – white washing, dirt accumulation and dirt wetting – are clearly visible (Fig. 4): dirt accumulation takes place far from running water and shows a thin deposition of black carbonaceous particles and the extent of sulphatation is generally less than 40%; dirt wetting is located at the interface between washed and unwashed areas and shows a very thick and rough black dendrite-shaped crust and the extent of sulphatation is larger than 40%.

Forms of decay in relation to different rock textures and structures: Istrian limestone and marble

Observations carried out on many Venetian monuments have shown that each lithotype decays differently according to its textural and structural properties. A typical example is represented by Istrian stone and marble, which are the materials most commonly used in monument construction.

Table 1. *Percentages of soluble sulphates from samples taken from the third arch, representing the Arts and Crafts, from the main Portal of Saint Mark's Basilica*

Panel	Sample	Sulphates (%) (black crust, dirt wetting)	Sulphates (%) (black deposit, dirt accumulation)
Bakers	SM1	67.3	
Bakers	SM2		40.3
Bakers	SM3	56.4	
Bakers	SM15	60.9	
Butchers	SM4	56.8	
Butchers	SM5		29.6
Butchers	SM16		30.8
Milkmen	SM6	59.5	
Milkmen	SM7	69.8	
Bricklayers	SM8	62.4	
Shoemaker	SM9	52.7	
Shoemaker	SM14	60.7	
Barbers	SM11	60.7	
Joiners	SM12		37.3
Joiners	SM13		40.5
Sawyers	SM18	69.9	
Blacksmiths	SM19		42.5
Blacksmiths	SM20	52.4	
Fishermen	SM21		31.9
Fishermen	SM22		39.4

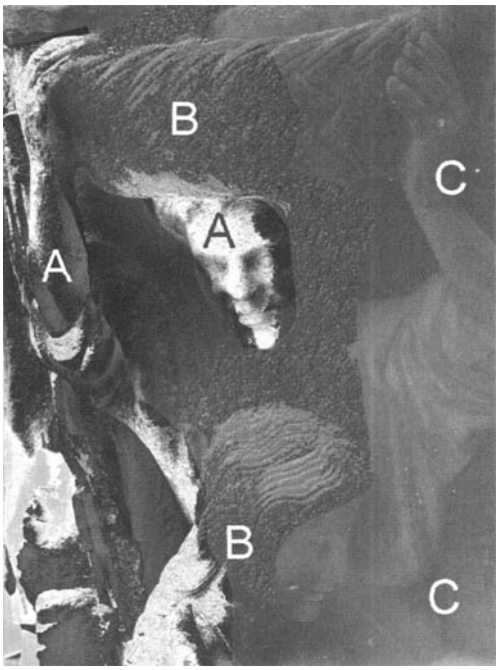

Fig. 4. In the panel of Bakers the dirt accumulation area (C) is grey-black in colour and deposition of carbonaceous particles occurs, whereas the dirt wetting area (B) shows the formation of a thick, rough, black dendrite-shaped crust which grows upon the original surface.

Istrian stone is very compact limestone characterized by a very low porosity (0.25–0.33 $cm^3/100$ g), which presents three types of weathering: white superficial deposits, black superficial deposits, and dendrite-shaped black crusts.

White superficial deposits were classified as white washing. A careful observation of the white areas indicates that these are always associated with running water and the formation of a white thin layer tightly adhering to the stone is due to the continuous reaction between acidic water and the stone surface.

According to many authors the whiteness of limestone surfaces was ascribed for a long time to sulphatation processes. In order to ascertain the mechanism of whitening formation many samples were taken from white areas and were observed under the optical microscope and analysed by X-ray diffraction and ion chromatography.

Optical microscope observation shows that a thin recrystallization white layer is present above the limestone. As the ion chromatography data showed the presence of low amounts of sulphates (less than 1%) and X-ray diffraction analysis showed the absence of gypsum and the presence of calcium carbonate, it can be concluded that this white layer is due to recrystallization of calcite previously dissolved by acidic water according to the well known reaction:

$$CO_2+H_2O \Rightarrow H_2CO_3$$

$$CaCO_3+CO_2+H_2O \Rightarrow Ca(HCO_3)_2$$

$$Ca(HCO_3)_2 \Rightarrow CaCO_3+CO_2+H_2O$$

In this case the high solubility of calcium sulphate does not allow the formation of a thick gypsum layer.

As regards the other anions, chlorides are generally present at a level below 1%. Chlorides are mainly dependent on the deposition of marine aerosols. In the lower parts of buildings, the presence of chlorides can be ascribed to salt migration from the water of the lagoon by means of rising moisture.

Black areas characterized by superficial deposits were classified as dirt accumulation. Black deposits show the presence of carbonaceous particles mixed together with gypsum crystals. If the surface is very compact then gypsum formation affects the stone only in the superficial layer without penetrating to depth, as it is clearly visible in Figure 5a, b.

Black areas characterized by dendrite-shaped crust were classified as dirt wetting. These are generally present on sheltered areas and have a rough and spongy appearance and a thickness of 3–5 mm. Under the optical microscope, a close observation of the crust shows the formation of many gypsum crystals growing perpendicularly to the stone surface. The black crust is forming without any damage to the stone surface beneath, which was originally exposed to the atmosphere (Fig. 6). The very low porosity of the stone does not allow any penetration of pollutants, such as sulphuric acid, but only a superficial interaction, which causes the transformation of the calcium carbonate into gypsum. The increase in roughness of the surface is ascribed to the higher molecular volume of the gypsum, which is double that of the calcium carbonate. When the stone surface presents microcracks or contains abundant clay impurities along the sedimentation beds, penetration of sulphuric acid solution can occur causing the formation of a white gypsum powder in the interstices between scales, provoking the exfoliation of the stone.

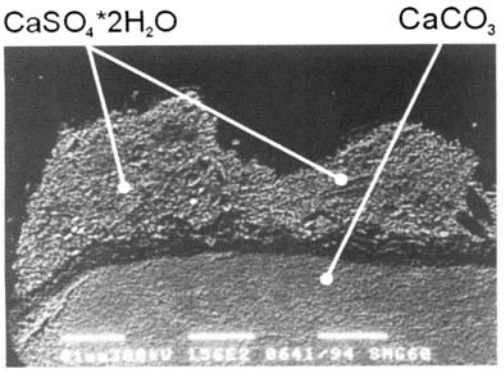

(a)

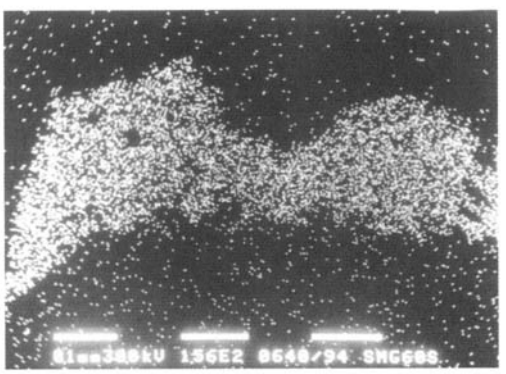

(b)

Fig. 5. Black areas characterized by superficial deposits were classified as dirt accumulation areas. (**a**) Gypsum formation on compact Istrian limestone is forming on the surface without damaging the stone surface beneath. (**b**) X-ray map of sulphur distribution shows the localization of gypsum on the surface.

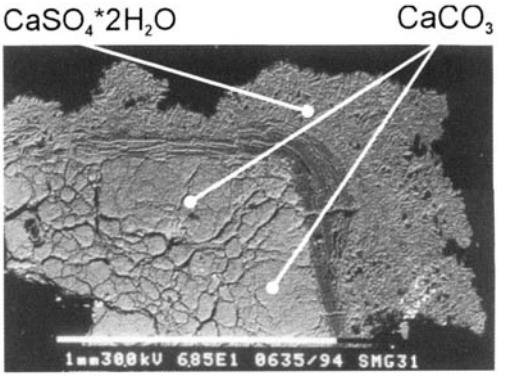

Fig. 6. Black areas characterized by dendrite-shaped crust were classified as dirt wetting areas. Gypsum forms on the compact limestone surface without penetrating inside it. The formation of a massive crust is also favoured by recrystallization of gypsum due to wetting and drying cycles. The thickness of the crust is proportional to the period of exposure and the frequency of wetting and drying cycles.

Saccharoidal marbles are very pure metamorphic limestones, characterized by a crystalloblastic structure and calcite crystals with a density between 0.85 and 1.25 $cm^3/100$ g.

According to Kessler (1919), thermal changes can cause a permanent expansion of marble very probably due to slipping of the individual calcite crystals one on another. According to Marchesini *et al.* (1972) the weathering of marble is at first purely physical, due to the increase in the porosity caused by thermal changes. For instance, in experiments carried out on different types of saccharoidal marbles the porosity increased by up to 40–50% of the original material, when they are subjected to temperature fluctuations of 50°C. The increase of porosity is caused by the marked anisotropy of calcite crystals; this means that when an increase of temperature takes place the crystal expands in one direction and contracts in the transverse direction. Such movements cause an internal cleavage of crystals and detachment of one crystal from another.

Other agents easily attack saccharoidal marbles, which have suffered an increase in porosity; in particular the circulation of water containing soluble salts is favoured by the increase in porosity.

Among the disaggregated crystals the penetration of water containing pollutants from the atmosphere causes a reaction between calcite crystals and the solution (Marchesini *et al.* 1972; Fassina 1993).

A careful examination of Carrara marble from the Basilica of St. Mark (Fassina 1988*b*, 1999), the Portal of SS. Giovanni and Paolo church (Fassina 1992), Pilastri Acritani (Fassina *et al.* 1993), Madonna dell'Orto church (Fassina *et al.* 1994) and Ca' d'Oro facade (Fassina & Rossetti 1994, Fassina 2001) indicates the presence of three different morphologies of deterioration. (i) Superficial granular disaggregation on the surfaces directly exposed to rainwater (white washing) is mainly ascribed to natural agents, such as thermal changes, and is strongly accelerated by the decreasing pH of acid rain of urban polluted environment (Fig. 7). (ii) Black superficial deposits (dirt accumulation) – under the optical microscope thin layers of black deposits appear to be formed by a very dark external layer which progressively becomes less dark moving towards the inner part of the marble.

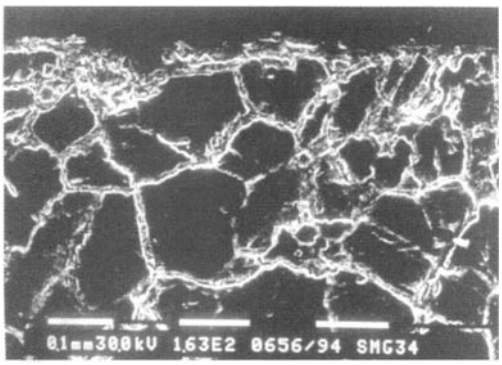

Fig. 7. Marble exposed to weathering agents. Decohesion of calcite crystals due to thermal changes is visible.

(iii) Dendrite shaped-crust mainly located in sheltered areas (dirt wetting) is caused by the transformation of calcium carbonate into gypsum which is more active than in other areas (Fassina 1994*c*). The microcracks generated by thermal changes are easily penetrated by sulphuric acid solutions, which attack the edges of calcite crystals to form calcium sulphate. The final result is a disaggregation of calcite crystals and the crumbling of large pieces of marble exposing the underlying surface to the aggressive action of atmospheric pollutants. The emerging surface is white and lacks cohesion (Fig. 8). The mechanism described above was found on numerous samples taken from sheltered positions and is easily recognizable under the optical microscope and SEM.

Cross-sections of altered layers generally show the presence of an external layer which was in contact with the atmosphere and contains a generous deposition of carbonaceous particles (which are easily recognizable under the optical microscope; Fig. 8) and gypsum crystals (which can be recognized by an X-ray map of sulphur; Fig. 9). Under the dark external layer calcite crystals appears detached (Fig. 10).

SEM observations and X-ray maps show the presence of gypsum crystals, which are formed by reaction of calcite crystals and sulphuric acid that has penetrated in microcracks. In Figure 10 it is possible to observe the penetration of pollutants from the atmosphere, black carbonaceous particles and gypsum crystals. Under SEM the microcracks appear filled with microcrystals with no easily recognizable habit and their sizes are very small in relation to calcite crystals (Fig. 11). Many X-ray maps of sulphur were carried out to test the hypothesis that intergranular spaces are filled with crystals resulting from the chemical transformation of calcite due to sulphuric acid attack (Fig. 9).

The primary gypsum forms on calcite crystal surfaces along the intergranular spaces; it is found at progressively deeper locations below the surface with increasing duration of exposure to the polluted atmosphere. In sheltered areas gypsum formed on marble surfaces builds a massive crust, the thickness of which is proportional to the period of exposure and the frequency of wet-to-dry cycles.

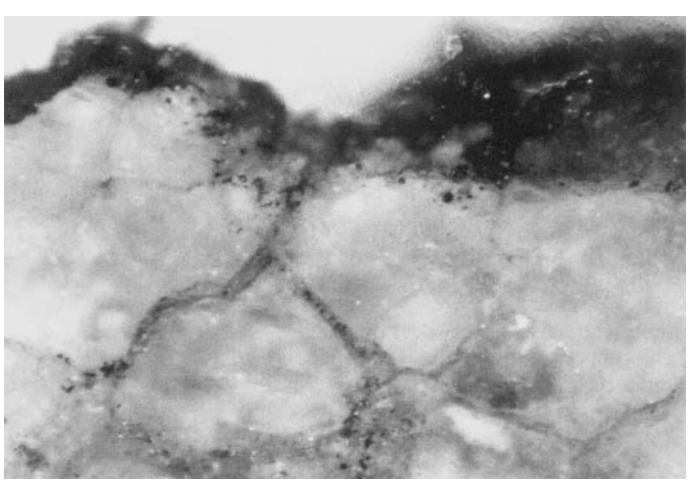

Fig. 8. Carbonaceous particles and other particulate pollutants are visible inside the intergranular space of strongly decayed marble.

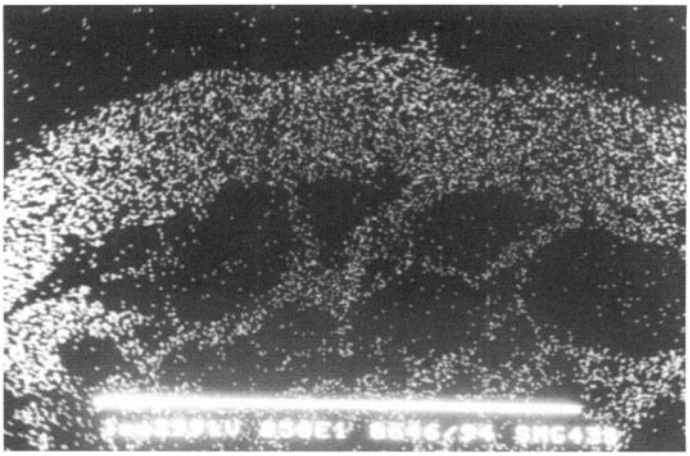

Fig. 9. X-ray map of sulphur distribution shows the presence of gypsum on the surface and between marble grains.

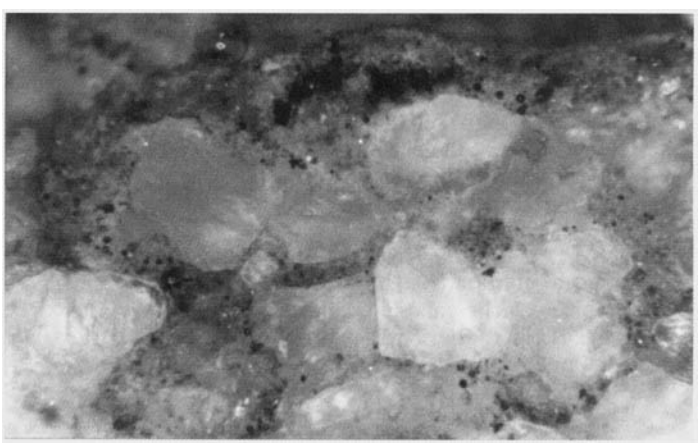

Fig. 10. Beneath the external surface calcite crystals appear detached.

A schematic representation of the mechanism of black crust formation is presented in Figure 12. In dirt wetting areas calcium carbonate is transformed into gypsum which is growing upon the original surface (I stage). Subsequently gypsum penetration inside the pores causes decohesion of calcium grains and detachment of large pieces of marble (II stage). In white washing areas running water causes erosion of the surface due to the transformation of calcium carbonate into calcium bicarbonate (II stage).

Memory effect

In the Basilica of Saint Mark the amount of sulphates found at the beginning of the 1970s has been compared with the analyses made 15

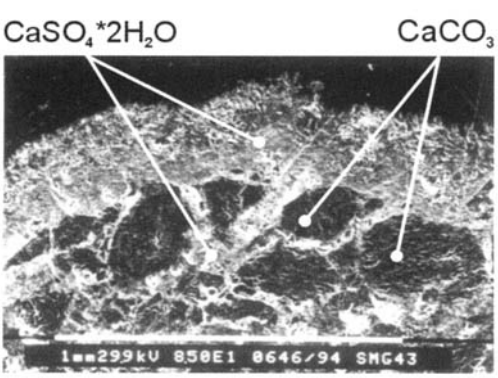

Fig. 11. Small crystals inside the intergranular space left by the decohesion of calcite crystals.

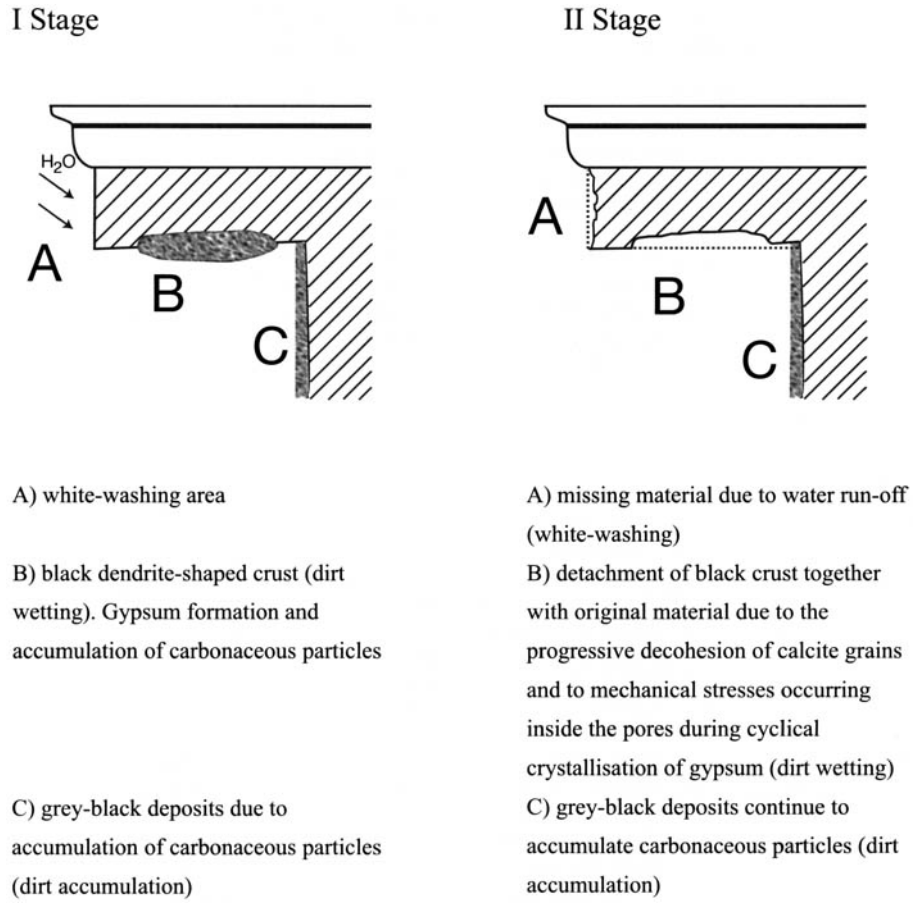

Fig. 12. Schematic representation of the mechanism of black crust formation in sheltered areas.

years later. The increasing amount of sulphates, from 40% to 60%, showed that the sulphation process was still active, notwithstanding that in the same period the sulphur dioxide concentration in the Venetian environment was drastically reduced, due to reduced emission of industrial pollutants and the substitution of oil by methane in domestic heating systems.

This is only an apparent contradiction because the building materials are affected by the so-called 'memory effect', which means that the decay processes are strongly influenced by the cumulative exposure of materials to the environment. Certainly the decrease in environmental pollution represents a positive step in slowing down the decay processes, but there is not a proportional change between the decrease in pollution and the decrease in deterioration processes because the new-formation products are always active in an environment which is characterized by thermal and moisture fluctuations.

Conclusion

From macroscopic observations three types of decay are generally distinguishable on the surface of monuments: white washing, dirt accumulation and dirt wetting. Quantitative data obtained by sampling in different areas according to the degree of blackness and the degree of shelter from rain water has allowed development of a simplified model of the deterioration morphologies.

In white washing areas the formation of a surface skin is prevented because the stone is exposed to the washing action of the rain, which has the effect of removing both the soluble

compounds and the deposited soot. As a consequence skin formation does not occur in rain washed areas.

The whiteness of the stone surface was wrongly ascribed for a long time by many authors to the sulphatation process. Our analyses showed that the white washing areas are due to the recrystallization of calcite.

Dirt accumulation and dirt wetting are confined to black areas and represent two different morphologies of decay, which are dependent on the distance from the rain washed areas. Dirt accumulation takes place in well-sheltered locations away from rain washing areas and it is characterized by black superficial deposits that accumulate on the surface due to the deposition of atmospheric particles. In addition to carbonaceous particles a moderate sulphatation process is also present. Dirt wetting areas are found at the interface between running water and the more sheltered areas. The thick and hard black crust has a rough and spongy appearance and grows upon the original surface. Observations show that the sulphate formation is greater in the black dendrite-shaped crusts, which are generally formed at the interface between the white washing areas and the sheltered ones. The reason why dirt wetting areas show greater concentration of sulphate is that, after every rain event, they remain moist for a longer time than dirt accumulation areas. Wetness time plays an important role favouring the dissolution of gaseous sulphur dioxide and the deposition of carbonaceous particles which, as is well known, speed up the oxidation to sulphuric acid and subsequent gypsum formation.

As regards the morphology of deterioration of marble and Istrian stone the macroscopic observations show that they exhibit different types of decay, notwithstanding they have the same chemical composition and are exposed to the same environment. The factors responsible for this different behaviour are, on the one hand, the intrinsic properties of the stone, that is their texture and structure and, on the other hand, the geometry of the monument, that is the degree of shelter from rainwater.

Istrian stone, after the removal of the black crusts, appears to be in a good state of conservation and indicates that decay is only superficial, probably due to the low porosity of the stone that does not allow the penetration of water and consequently limits any deterioration process.

White marble is severely damaged due to the different texture of calcite grains which, after a certain time, allows water to penetrate into intergranular spaces, and favours the reaction of acid sulphur-bearing solutions which form gypsum around the grains. This is the starting point from which a progressive attack of calcite marble takes place. In contrast to the Istrian stone, there is penetration of gypsum crystals inside the marble, which causes an intimate mixture of original calcite, gypsum, carbonaceous particles, and natural or man-made atmospheric dust. Gypsum crystals found in the intergranular space can be ascribed to different mechanisms: (i) primary formation due to the penetration of sulphuric acid solution coming from the atmosphere and the subsequent reaction with calcite crystals; (ii) secondary formation due to the penetration of gypsum previously formed in the atmosphere; (iii) gypsum, first formed on the surface, can penetrate inside the marble during the wetting phase. The presence of gypsum crystals inside the marble can cause mechanical stresses inside the pores during the drying phase because crystallization causes expansion.

Summarizing, the mechanism of marble decay takes place in different steps: (i) exposure to natural atmospheric thermal changes shows a long-term effect of crystal decohesion (physical alteration); (ii) penetration of sulphur-bearing solution into intergranular spaces (previously formed by thermal changes) and subsequent transformation of calcium carbonate into gypsum (chemical alteration); (iii) gypsum crystallization inside the pores due to drying phase causes expansion and consequently mechanical stresses (mechanical alteration). The first step is very slow and occurs on a time-scale of a hundred years. The second and third steps became important starting from the middle of the last century according to an exponential relationship between time and damage effects. The time-scale of damage is strongly reduced to a few decades.

References

AMOROSO, G. G. & FASSINA, V. 1983. *Stone Decay and Conservation*. Elsevier Science Publishers, Amsterdam.

BREWER, R. L., GORDON, R. J., SHEPARD, L. S. & ELLIS, E. C. 1983. Chemistry of mist and fog from the Los Angeles urban area. *Atmospheric Environment* **17**, 2267–2270.

FASSINA, V. 1978. A survey on air pollution and deterioration of stonework in Venice, *Atmospheric Environment*, **12**, 2205– 2211.

FASSINA, V. 1988*a*. Stone decay of Venetian monuments in relation to air pollution. *In*: MARINOS, P. G. & KOUKIS, G. (eds) *Proceedings of International Symposium on the Engineering*

Geology of Ancient Work, Monuments and Historical Sites. A. A. Balkema, Rotterdam, 787–796.

FASSINA, V. 1988*b*. The stone decay of the main Portal of Saint Mark's Basilica in relation to natural weathering agents and to air pollution. *In*: *Proceedings of the 6th International Congress on Deterioration and Conservation of Stone*, Torun, 12–14 Sept., 276–286.

FASSINA, V. 1992. The stone decay of the Portal of the Basilica of SS. Giovanni e Paolo in Venice. *Proceedings of the 7th International Congress on Deterioration and Conservation of Stone*, Lisbon, June 15–18. 119–128.

FASSINA, V. 1993. The weathering mechanisms of marble and stone of Venetian monuments in relation to the environment. *Proceedings of the 10th Triennial Meeting of ICOM, Committee for Conservation*, Washington, August 22–28. 345–351.

FASSINA, V. 1994. The influence of atmospheric pollution and past treatments on stone weathering mechanisms of Venetian monuments. *European Cultural Heritage Newsletter*, **8**(2), 23–35.

FASSINA, V. 1999. Il degrado delle formelle dell'arcone centrale della Basilica di S. Marco in relazione all'inquinamento atmosferico. *In*: VIO, E. & LEPSCHY, A. (eds) *Scienza e tecnica del restauro della Basilica di S. Marco*. Istituto Veneto di Scienze Lettere e Arti, Venezia, 611–650.

FASSINA V. 2001. *Studio dello stato di conservazione dei materiali della facciata di Ca' d'Oro in relazione al degrado di origine naturale e antropica*. Quaderno 22, Soprintendenza BAS Venezia.

FASSINA, V. & ROSSETTI, M. 1994. Weathering of marble in relation to natural and anthropogenic agents on the Ca' d'Oro facade (Venice). *Proceedings of the III International Symposium on the Conservation of Monuments in the Mediterranean Basin*, Venice, June 22–25. 825–834.

FASSINA, V. & STEVAN, A. 1992. Fogwater composition in Venice in relation to stone decay. *Proceedings of the 7th International Congress on Deterioration and Conservation of Stone*, Lisbon, June 15–18. 365–373.

FASSINA, V., LAZZARINI, L. & BISCONTIN, G. 1976. Effects of atmospheric pollutants on the composition of black crusts deposited on Venetian marbles and stones. *In*: *Proceedings of the 2nd International Symposium on the Deterioration of Building Stones*, Athens, 201–211.

FASSINA, V., FUMO, G., ROSSETTI, M., ZEZZA, F. & MACRÌ, F. 1993. The marble decay of Pilastri Acritani and problems of conservation. *Proceedings of the International RILEM/UNESCO Congress on the Conservation of Stone and other Materials*, Paris, 29 June–1 July. 75–82.

FASSINA, V., BASSO, A. & ROSSETTI, M. 1994. Studies of patinas on the stone surface of Madonna dell'Orto church. *Proceedings of the III International Symposium on the Conservation of Monuments in the Mediterranean Basin*, Venice, June 22–25. 835–842.

FASSINA, V., FAVARO, M., CRIVELLARI, F. & NACCARI, A. 2001. The stone decay of monuments in relation to atmospheric environment. *Annali di Chimica*, **91**, 767–774.

KESSLER, D. W. 1919. *Physical and Chemical tests on the commercial marbles of the United States*. USB Standard, Technical Paper No. 123, Government Printing Office, Washington.

LAZZARINI, L. 1972. Forme e cause di alterazione di alcuni marmi e pietre a Venezia. *Centro di Studio Cause di Deperimento e metodi di Conservazione delle Opere d'arte*. CNR, Roma.

LAZZARINI, L. 1979. Morfologia del degrado dei materiali lapidei a Venezia. *Atti del Convegno Associazione Civica Venezia Serenissima*. 47–57.

MARCHESINI, L. 1970. Effetti dell'inquinamento atmosferico sui materiali lapidei a Venezia. *Aria e Acqua*, **III**, 22.

MARCHESINI, L., BISCONTIN, G. & FRASCATI, S. 1972. Relazione tra porosità ed invecchiamento di marmi saccaroidi. *Centro di Studio Cause di Deperimento e metodi di Conservazione delle Opere d'arte*. CNR, Roma.

ROBINSON, G. & BAKER, M. C. 1975. *Wind-driven rain and buildings*. Technical Paper no. 445, Division of Building Research, National Research Council of Canada, Ottawa.

TORRACA, G. 1969. L'attuale stato delle conoscenze sulle alterazioni delle pietre. cause e metodi di trattamento. *In*: GNUDI, C. (ed.) *Sculture all'Aperto, Degradazione dei Materiali e Problemi Conservativi*. Rapporto della Soprintendenza alle Gallerie di Bologna, No. 3, Edizioni Alfa, Bologna.

This page intentionally left blank

Acid deposition and the deterioration of stone: a brief review of a broad topic

A. ELENA CHAROLA[1] & ROBERT WARE[2]

[1]*3618 Hamilton Street, Philadelphia, PA 19104, USA (e-mail: charola@worldnet.att.net)*

[2]*44 Grand Street, Apt. 1, New York, NY 10013, USA*

Abstract: The causes of stone deterioration due to acid deposition are examined, with specific reference made to important research on this subject from the past thirty years. The major topics covered include: dry deposition of atmospheric pollutants, the primary agent of acid deterioration of stone in urban areas; wet deposition, commonly referred to as acid rain; and major deterioration mechanisms. Key factors are dry deposition of gaseous pollutants such as SO_2 and NOx, the nature of the stone, including texture and porosity, and the presence of moisture on its surface as well as the 'time of wetness'.

Over the past half century, 'acid rain' has gained more and more attention as a cause of stone deterioration. Strictly speaking, acid rain is a misnomer. In fact, acid precipitation originating from air pollution can occur both as wet and dry deposition (see Fig. 1). Several publications have addressed the issue of air pollution and/or acid precipitation. Some of the most important include Camuffo (1998), Brimblecombe (1987, 1996), Laurenzi Tabasso & Marabelli (1992), Zezza (1991), the UK Building Effects Review Group (1989), Rosvall & Aleby (1988), and Baboian (1986). Specific chapters devoted to this topic can be found in other books, including Aires-Barros (2001), Charola (2001), Price (1996), Winkler (1994), Irving (1991*a*, *b*), Lazzarini & Laurenzi Tabasso (1986), Amoroso and Fassina (1983) and the US Committee of Conservation of Historic Stone Buildings and Monuments (1982).

With the increase of published studies concerning the effects of acid rain on stone, compilation and evaluation of this information is becoming more and more difficult. As stated by Price (1996, p. 7): 'There has been very little effort to pull it all together and to produce a clear statement of findings to date'. It is the intent of the present overview to synthesize the material from the most relevant publications and provide a better understanding of the issue's complexity. Despite the large amount of information on the subject, it is extremely difficult to determine how much of the deterioration of stone is due to acid deposition, since decay results from various interacting mechanisms, many of which also occur in natural weathering. Nevertheless, useful correlations between concentration of air pollutants in the atmosphere and damage on stone can be made.

Dry deposition

In highly polluted areas, dry deposition is far more important than wet deposition as a source of building stone decay (Furlan & Girardet 1983*a*). This type of deposition results from the transfer of pollutant gases and/or particles, including aerosols, from the atmosphere to a surface in the absence of rain. In general, dry deposition originates from nearby sources and is therefore called short-range deposition (Torraca 1988). Gases are the most important contributors to dry deposition, and their arrival at the surface in question is governed by molecular diffusion or atmospheric turbulence. Gases can react with both the surface of the stone and with aerosol particles. For the latter, particle size is an important determinant of the manner in which deposition occurs as discussed extensively by Camuffo (1998). While gravitional settling increases with particle diameter, Brownian deposition decreases with particle diameter, hence deposition velocity shows a minimum for particles between 0.1 μm and 1 μm (Hicks 1982). For submicrometre particles (<0.1 μm) Brownian diffusion is most important: the smaller the particle, the faster its deposition rate, since the surface acts as a sink, retaining the particles through the action of Van der Waals forces. These processes are strongly affected by the presence of temperature gradients, leading to thermophoresis, or water vapour gradients, if condensation or evaporation processes are operative (i.e. the Stefan effect) and if the particles and/or the surface in question carry an electrostatic charge (Camuffo *et al.* 1987).

The actual deposition process of gases and larger particles occurs in the boundary layer at

From: SIEGESMUND, S., WEISS, T. & VOLLBRECHT, A. 2002. *Natural Stone, Weathering Phenomena, Conservation Strategies and Case Studies*. Geological Society, London, Special Publications, **205**, 393–406.
0305-8719/02/$15.00 © The Geological Society of London 2002.

Fig. 1. One of the sculptures at the Church of Notre-Dame du Sablon, Brussels, in 1982. The sculpture is carved out of Euville stone, a pure limestone imported from France. Note the thick black gypsum crust formed on areas protected from direct rain (dry deposition), and the white eroded surface of the rain-exposed parts (wet deposition), such as the top of the hands and the far edge of the pier to the left. On the other pier, the detachment of the black surface crust can be observed (photo A. E. Charola).

the surface and is influenced by the nature of the substrate, its surface conditions and its micro-environment. As is to be expected, the concentration of gases and particles affects their rate of deposition. The deposition rate is enhanced by an increase in concentration of the pollutants, air turbulence, roughness and heterogeneity of the receiving surface, chemical affinity of the surface for the pollutants, and surface moisture. The concentration of pollutants found within a few centimetres above the receiving surface, together with microclimatic conditions, is most relevant to an analysis of dry deposition. These conditions may be fairly different from those in the nearby atmosphere, at a distance of some metres from the receiving surface, which in turn vary with daily and seasonal climatic changes.

A good discussion of sources, sinks and abundance of the most important air pollutants relevant to the deterioration of stone is given by Amoroso & Fassina (1983, pp. 54–110). Apart from CO_2, a normal constituent of the atmosphere whose concentration has increased due to the burning of fossil fuels, the key components involved in the deterioration of stone are the oxides of nitrogen and sulphur. Most of the oxides of nitrogen, NO and NO_2, generally referred to as NO_x, are produced by high temperatures in combustion engine sources. In the industrial countries, these make up 70–80% of the total amount in the atmosphere (Fassina 1991, 1988). The resultant nitric acid (HNO_3) can also be found in the gas phase (Fassina 1988; Livingston 1985). Sulphur oxides result from the combustion of sulphur containing materials and sulphur dioxide (SO_2) is the key atmospheric pollutant. Fassina (1991) provides an overview of data on the increase of SO_2 gas emission from the end of the nineteenth century to mid-twentieth century. Table 1 summarizes average concentrations of some of the chemical species relevant to atmospheric corrosion. Natural sources of SO_2 emissions include volcanoes, sea spray, and biogenic processes, while anthropogenic, or 'man-made', sources include combustion of coal, petroleum, and ores. A more detailed review of this topic can be found in Irving (1991*a*).

Camuffo (1991*a*) has discussed the role of climatic factors in the distribution of gaseous and airborne particulates in Europe. The relative importance of airborne particulates and gases depends on various factors such as weather conditions as well as their interaction with the stone surface. The transport of SO_2 and NO_x in the vicinity of the stone surface relies on random kinetic motion (Camuffo 1998). Under dry conditions, SO_2 and NO_2 deposition is low, as proven in many studies (Gauri *et al.* 1973; Serra & Starace 1978). Atmospheric turbulence will evidently increase this rate (Camuffo 1998).

Dry particle aerosols can contain calcium carbonate, or calcite, which will contribute to an increase of SO_2 and sulphate absorption and subsequent sulphur deposition on non-calcareous stones. They can also contain calcium sulphate particles, or gypsum, generally in the 1–2 μm range, generated from sulphur deposition on calcareous stones or from wind erosion of exposed gypsum beds, as is the case in Italy (Amoroso & Fassina 1983, p. 131). Aerosols containing hygroscopic salts, such as ammonium

Table 1. *Average concentrations of some air pollutant species relevant to the deterioration of stone*

Pollutant	Natural background concentration	Concentration in urban areas	Concentration in rural areas (Europe)
SO_2	~0.1 ppbv	≤50 ppbv	~5 ppbv
NO_x	~0.01 ppbv ?	≤50 ppbv	~5 ppbv
CO_2	275 ppmv	350–375 ppmv	345 ppmv
O_3	~10 ppbv	20–40 ppbv	~25 ppbv
Sulphate aerosols	≤1 μg m^{-3}	≤20 μg m^{-3}	~5 μg m^{-3}
Nitrate aerosols	≤1 μg m^{-3}	≤10 μg m^{-3}	~5 μg m^{-3}
Sulphate in rainwater	≤1 mg l^{-1}	≤10 mg l^{-1}	~5 mg l^{-1}
pH of rainwater	4.5–6	4.5–6	4–4.5

Adapted from table 4 of Brimblecombe & Rodhe (1988)

sulphate in areas with an ammonia-enriched atmosphere, magnesium sulphate in maritime areas, or sodium sulphate generated by paper manufacture or the combustion of lignin-sulphur compounds, can serve as condensation nuclei for droplets. The deliquescent nature of these salts, i.e. magnesium or sodium sulphate, will favour their adhesion to the stone surface.

Brimblecombe (1987, 1991*a*, *b*; Brimblecombe & Rodhe 1988) extensively studied changes in air pollution in England. Improved air quality in London during the past century can be attributed to urban expansion and the dispersion of pollutant sources with their consequent dilution. Legislation and improved control methods have subsequently contributed to this as well. The beneficial effect of legislation in decreasing pollution was also observed by Davidson (1979) in Pittsburgh. Improved atmospheric visibility from the mid-nineteenth century to the present clearly shows the impact of the smoke control ordinance introduced in the late 1940s.

There is no doubt that the largest contributors to the deterioration of stone are sulphur pollutants, especially SO_2. One of the fundamental questions is how SO_2 interacts with the stone, that is, whether sulphites are formed first and subsequently oxidized or whether sulphates are the only reaction products. The oxidation of SO_2 can occur in a homogeneous process in the gas phase or heterogeneously in gas–liquid or gas–solid reaction (Amoroso & Fassina 1983, pp. 177–221; Fassina 1988; Laurenzi Tabasso & Marabelli 1992). Of the several mechanisms that can oxidize SO_2 homogeneously in the gas phase, the most relevant involves free radicals in photochemical smog (Amoroso & Fassina 1983, pp. 177–178).

For gas–liquid reaction, the absorption of the gas is more rapid than the desorption reaction. This can occur on moist surfaces of stone, particularly when catalytic particles are present or at water droplet interfaces. Smaller droplets (<100 μm diameter) have a higher absorption rate (less than 1 s) than larger ones. The rate-determining step is the oxidation of the SO_2 (Beilke & Gravenhorst 1978). Several factors influence this oxidation rate. One is the presence of one or more heavy metals that can act as catalysts. Another is the pH of the droplet/solution, which is in turn affected by the presence of alkaline gases such as ammonia (Fassina & Lazzarini 1979) or of calcite particles.

For the gas–solid reaction, two possibilities have been postulated. One corresponds to an initial adsorption of the SO_2 on the surface, neutralization to sulphite and subsequent oxidation to sulphate (Amoroso & Fassina 1983, p. 216). The second corresponds to the oxidation of the adsorbed SO_2 catalysed by surface impurities and subsequent sulphation reaction (Skoulikidis & Papakonstantinou-Ziotis 1981). According to the studies carried out by Gauri and co-workers (Gauri *et al.* 1982/83, Gauri & Gwinn 1982/83) using high SO_2 concentrations, the initial reaction product is always $CaSO_3.\frac{1}{2}H_2O$. Furthermore, their experiments showed that the presence of moisture is crucial for the reaction, confirming previous studies (Serra 1969; Serra & Starace 1972, 1978). Recent studies confirmed all of these results and highlight the importance of nucleation and growth of the reaction products in the sulphation process (Moroni & Poli 2000). Finally, the presence of oxidants, such as NO_2, was found to increase the reaction rates significantly (Johansson *et al.* 1988).

Although sulphur pollutants have contributed much towards stone deterioration, their concentration has been decreasing as mentioned previously. Not so the emissions of nitrogen oxides and volatile organic compounds, especially from automobiles (Brimblecombe 1991*a*; Behlen *et al.* 1996). The oxidation of NO to nitric acid can proceed through

homogeneous oxidation with ozone, which appears to be the most effective process for NO_2 generation. During the day, further oxidation is carried out by OH radicals. During the night, ozone continues the oxidation to an NO_3 radical. This reaction does not contribute significantly in the daytime because of the photolytical destruction with NO. The NO_3 radical leads to the formation of HNO_3 gas. The overall formation of this gas proceeds at about the same rate for either mechanism (Fassina 1988). Nitric acid shows the highest deposition velocity and will result in the eventual formation of highly soluble nitrates (Behlen *et al.* 1996).

Livingston (1991) presents a good discussion on the various methods of estimating deposition rates for both dry and wet deposition. Deposition rate is a function of stone 'susceptibility' or capability of a given stone surface to 'capture' the pollutant in question as confirmed by the interesting studies of Furlan and Girardet discussed below.

Among the most interesting studies involving measurement of depostion rates are those that Furlan and Girardet carried out between 1983 and 1996. Their research was complemented by a similar study using an atmospheric simulation chamber (Ausset *et al.* 1996; Girardet *et al.* 1996) to study Jaumont limestone and Berne molasse, two rock types that had been previously used in outdoor exposure tests (Furlan & Girardet 1988). The stone samples were exposed 'naked' and covered with either fly-ash or soot particles. It was found that after one year of chamber exposure in real-life conditions (125 ppb SO_2, 50 ppb NO_2 at 79% relative humidity (RH) and 13°C) the results obtained are comparable to those observed in site tests. The presence of fly-ash appeared to increase the SO_2 deposition velocity for the Jaumont stone after the first half-year, but not that for the Berne molasse. Soot particles appeared to protect the surface from sulphur deposition. When sulphur does deposit it penetrates into the stone to a depth of about 0.8 mm. Further laboratory studies with a simulation chamber confirmed that the reactivity of stones to SO_2 can increase significantly with increased relative humidity, and to a smaller extent with increased temperature, but that these increases depend on the nature of the stone (Girardet & Furlan 1996).

The deposition of 'dry' sulphur was measured on samples of a calcareous sandstone, Villarlod blue molasse, exposed in various protected areas (Furlan & Girardet 1983*b*, *c*). The amount of sulphur deposited in urban areas was approximately double that found in rural areas, 1.6 to 0.8 gS m^{-2} a^{-1}) respectively. They also confirmed that the flux of 'dry' sulphur was far more important than the flux of 'humid' sulphur. This research was continued for the case of the molasse d'Ostermundigen, another calcareous sandstone, measuring the deposit on buildings of known construction date, ranging from 1869 to 1925 (Furlan & Girardet 1988). For comparison, the current deposition rate was measured on samples of the same stone. For urban centres, such as Zurich, no modifications appear to have occurred in the past 60 years, while in other centres such as Geneva and St. Gallen, significant increases have occurred. Still other centres, such as Lausanne, showed a current deposition rate only slightly above the mean of the past 80 years. Table 2 presents a summary of these data.

Further studies compared atmospheric

Table 2. *Mean deposition rate since construction and current deposition rate of 'dry' sulphur on the molasse d'Ostermundingen from buildings in various Swiss cities*

Building	Location	Construction date	Sulphur deposit (g S m^{-2})	Rate of sulphur deposition (g S m^{-2} a^{-1})	
				Mean	Current
St.François Church	Lausanne centre	1903	55.5	0.70	0.81
Casino de Berne	Berne	1910	52.3	0.67	0.92
Caserne: original	Zurich centre	1869	123.3	1.05	1.22
Caserne: restored	Zurich centre	1925	74.5	1.20	1.22
Ariana Museum	Geneva (suburb)	1886	39.5	0.39	0.77
Natural History Museum	Sion centre	1898	27.2	0.30	0.82
Natural History Museum	St. Gallen centre	1877	27.5	0.25	1.65

Adapted from table I in Furlan & Girardet (1988)

Table 3. *Atmospheric aggressiveness of various cities in Europe and Washington, DC, based on the annual deposition of 'dry' sulphur on a calcareous sandstone, molasse de Villarlod*

City	'Dry' sulphur deposit ($g\ S\ m^{-2}\ a^{-1}$)	City	'Dry' sulphur deposit ($g\ S\ m^{-2}\ a^{-1}$)
Lucerne	0.56	Washington, DC	1.18
Lausanne	0.72	Bordeaux	1.21
Bern	0.78	Munich	1.54
Neuchâtel	0.85	Roma	1. 73
Freiburg	0.91	Paris	2.11
Basel	1.25	Brussels	2.20
Geneva	1.31	Lisboa	2. 57
Lugano	1.32	London	2.83
Zurich	1.50	Milan	3.14

Data from figure 3 in Furlan & Girardet (1992)

aggressivenes of various sites in Europe and Washington, DC, for the molasse de Villarlod after one year of exposure. Aggressiveness was evaluated on the basis of sulphur surface deposit that built up over the year. Table 3 presents a summary of these data. The study also included exposing, at the most aggressive site, Milan, ten different stones ranging from siliceous ones, like gneiss and sandstones, to calcareous sandstones, limestones and marble (Furlan & Girardet 1992). The amount of 'dry sulphur' deposited varied significantly between the stones and three categories of reactivity could be established. The most reactive stones proved to be the molasses, limestones and calcareous sandstones; Carrara marble was found to be less reactive, while the siliceous sandstones and gneiss could be classified as non-reactive.

While the studies of Furlan and Girardet, discussed above, aimed to evaluate the reactivity of different stones as well as to reproduce the observed deterioration in environmental chambers, other studies, such as the National Materials Exposure Program, summarized by the UK Building Effects Review Group (1989), were based on long-term field exposure studies of different materials at different sites, following the weight change procedure used for metal corrosion with the aim of obtaining damage functions. The various approaches that can be used to develop these functions are discussed by Livingston (1997). From these long-term – in some instances ten plus years – exposure studies, it was found that the developed damage functions did show some predictive capabilities (Butlin *et al.* 1992), although the model over-predicted stone loss for a very wet Scottish site (Webb *et al.* 1992). It was found that for the Portland stone used in this study, the natural solubility of the stone in water was the dominant term in the model.

Wet deposition

Wet deposition generally plays a lesser role than dry deposition in the acid deterioration of stone. However, in rural areas with low pollution wet deposition can be just as important as dry deposition (Furlan & Girardet 1983*a*). Wet deposition is concerned with the incorporation of pollutant substances in cloud droplets, i.e. rain-out, and by entrapment during their fall, i.e. wash-out. The combined effect ot rain-out and wash-out is called 'acid rain'. The pollutants incorporated in wet deposition are usually produced by distant sources (Torraca 1988). Although the acidity of rain is often blamed for stone decay, particularly in calcareous stones, it has been found that acidity frequently decreases as rainfall continues. Camuffo has studied this in the particular case of Padua and has summarized the situation for Venice (Camuffo *et al.* 1984, 1988). Wet deposition will affect only the exposed surfaces of a building, while dry deposition can affect all surfaces of a building (Furlan & Girardet 1988).

Rain is more efficient in scavenging airborne pollutants than cloud droplets. Acidity in rainfall, as well as turbulent runoff, will attack the stone surface. But a strong rain will also wash away accumulated dry deposit from the stone surface. This is not the case for a soft drizzle, fog and dew, called 'occult precipitation', which does not remove the deposit but provides sufficient moisture to chemically activate dry deposits, thus turning out to be far more damaging than 'acid rain' (Camuffo 1991*b*). The increased time of wetness also allows more time for the capture

of airborne gaseous and particulate pollutants. Occult precipitation is particularly important in areas with special climatic conditions such as Venice and California. The deposition of moisture droplets on stone surfaces follows the same mechanisms discussed for particles. However, aerosol deposition is less affected by stone nature than SO_2 deposition (Furlan 1991).

The efficiency of 'acid rain' depends on droplet formation and the intensity of precipitation as well as on the vertical distribution of trace substances in the atmosphere. It would appear that the main source of sulphate in rainwater results from the oxidation of anthropogenically generated SO_2 via the entrapment of SO_4^{2-}-containing particles and sulphuric acid-containing aerosols (Amoroso & Fassina 1983, pp. 138–141). Other contributions, such as from seawater sulphate, are much smaller even in coastal areas.

The main mechanisms that will define the final chemical composition of a droplet are: (a) nucleation scavenging, i.e. when suspended hygrophilic particles adsorb water forming embryos that then grow into droplets; (b) scavenging of gas and particles during the evolution of the dispersed system, i.e. when droplets adsorb gases and capture suspended particles; (c) chemical reactions in the dispersed liquid phase, i.e. reactions that occur within the droplet once pollutants have entered them; and (d) microphysical evolution of the system as a function of atmospheric conditions, i.e. Stefan flow, thermophoresis, aerodynamic impaction, Brownian movements, coalescence and other such microphysical mechanisms that alter the chemical composition or the dimension of the droplets (Camuffo 1990).

In northern and central Europe, the great frequency of rainfall makes wet deposition important. Measurements of the acidity of rainwater for Como, northern Italy, gave a yearly average of pH 4.2, which is lower in winter months due to fossil fuel combustion (Rocchi & Mosello 1979). The acidity of rainwater is affected significantly by short-range or microclimatic factors (Camuffo 1990, 1991*a*).

Various studies on the composition of fog water in Venice have been carried out (Fassina & Stevan 1992; Camuffo *et al.* 1997). It was found that fog had higher concentrations of pollutants than rain droplets because the former forms in the lowest layers of the atmosphere, the most polluted one over densely populated areas. Average concentration of chlorides and sulphates can be seven to 16 times higher in fog than in rain. This is attributed to the fact that fog mainly collects local air pollution. Hoffmann (1986) carried out similar studies for California.

Guidobaldi (1981) was among the first to explain the hydrodynamic action of acid rain on monuments and its relation to the deterioration of calcareous stones. His experiments differentiate between corrosion due to neutralization of the acid and mechanical erosion by solution flow over the stone surface. Further studies (Guidobaldi & Mecchi 1985) confirmed that increased rain intensity decreases contact time and thus chemical dissolution of the marble, while additional washing can contribute significantly, although to a lesser degree, to the corrosion of marble. Charola (1988) provides a general discussion of the various factors affecting the acid dissolution rate of calcareous materials: below pH 4, the dissolution is transport-controlled, while between pH 4 and 6, the reaction appears to be controlled by surface kinetics and influenced by other factors such as hydrodynamic flow and the pressure of CO_2. The importance of the resulting gypsum, and its subsequent crystallization, to the overall deterioration is emphasized.

Reddy *et al.* (1985, 1986; Baedecker & Reddy 1993) found a positive linear correlation between the amount of recession of the surface of Vermont marble samples and the rainfall quantity and hydrogen ion deposition. A related field study by Sherwood & Reddy (1988) on Vermont marble and Indiana limestone exposed to a rural as well as urban environment showed that the relative contribution of acidity to the dissolution of the stones was similar; however, the amount of sulphate ion in the run-off from the limestone was three times that of the marble at the same site. Furthermore, pristine rain accounts for most of the calcite dissolution of exposed marble (75–80%) and limestone (50–75%) while about 20–25% of the marble dissolution could be attributed to the urban pollution. This was confirmed in field studies by Steiger *et al.* (1993). The relative contribution of dry SO_2 deposition and acid rain to the total Ca^{2+} loss of various stones shows that acid rain causes approximately 74% of Ca^{2+} loss in rural areas and only 21% in polluted areas. Run-off water analysis of two obelisks, one in Carrara marble and the other in Pennsylvania blue marble, as well as of two similar statues both in Carrara marble, served to determine that the rate of calcium removal depended more on the shape of the monument, i.e. hydrodynamic flow, than on marble type. However, for similar geometry, the coarser grained Pennsylvania blue marble accumulated more sulphur than the finer grained Carrara marble (Sherwood &

Dolske 1992; Dolske 1995). Irving (1991*b*) provides a complete review of these field studies.

An analysis by Livingston (1992) supports the conclusion that dry deposition, rather than acid rain, is the dominant factor for stone deterioration in urban areas. For this purpose, graphical methods were used to resolve the total Ca^{2+} loss into the components originating from acid rain, dry deposition, and karst dissolution by application of electrolyte theory and carbonate equilibria.

Deterioration mechanisms

The deterioration of stone caused by 'acid rain' is difficult to evaluate. Apart from the increased deposition of particulates in urban areas, there is no unique characteristic that differentiates this type of deterioration from others. The stone itself is an active partner in the reaction, and thus different stones behave differently.

The degree of damage due to acid deposition depends on the nature of the stone and the presence of moisture. Generally, calcareous stones are more susceptible to deterioration than purely siliceous ones and both porosity and texture play an important role in determining the type and extent of deterioration. Irving (1991*b*) concludes that acid rain on carbonate rocks accounts for between 5 and 20% of chemical weathering for dry deposition of SO_2, between 7 and 26% for dry deposition of HNO_3, and around 10% for wet deposition. Meteorological and microclimatic factors also play an important role in the deterioration of stone, as discussed by Camuffo (1994). A study on the deterioration of Pinczów limestones illustrates the importance of stone structure and porosity in weathering patterns (Kozlowski *et al.* 1990).

Among the first studies to observe differences in the deterioration of calcareous stones is a paper by Marchesini (1969) in which the effects of air pollution/acid rain on Greek marbles and Istria stone in Venice are compared. Three deterioration layers above the sound marble are described: a dark surface deposit, highly sulphated calcite crystals, and sulphate edges around calcite crystals. The first two layers tend to flake off, and the sulphate edges on the calcite crystals facilitate their decohesion, giving rise to observable 'sugaring'. In the case of the Istria stone, a compact structure and lower surface porosity make the stone less reactive, leading to surface'whitening' but no in-depth deterioration. Nevertheless, this type of stone may have natural veins and inhomogeneities that serve as entries for pollutants. The orientation of these veins in relation to the exterior surface is critical to the stone's long-term durability. Rossi-Manaresi (1991) also discusses the different deterioration patterns observed in Istria limestone as well as other clay-containing calcareous stones like Verona limestone and calcarenites.

Charola & Koestler (1985/86) showed that samples of relatively porous limestones, such as the Leithakalt calcarenite, tended to crust formation with an underlying area of increased porosity and decohesion, when exposed in less polluted areas, as shown in Figure 2. This process is typical of a diffusion mechanism (Cussler & Featherstone 1981; Domaslowski 1982). In contrast, the prevalence of gypsum crystallization between calcite grains and crystal boundaries, as shown in Figures 3 and 4, with accompanying etching of calcite crystal surfaces was noted in more polluted, central areas of Vienna. The preferential dissolution of smaller calcite grains explains in part the sugaring effect and greater susceptibility to deterioration of these types of stones.

The deterioration patterns observed on limestone and marble monuments are summarized by Camuffo (1990) as resulting from the three ways water can wet their surface: (1) run-off associated with 'white areas' where the surface is eroded and covered with reprecipitated spatic calcite crystals; (2) 'black areas' resulted on surfaces without run-off but where percolation and windborne droplet deposition occurred; and (3) 'grey areas' formed in absence of run-off, percolation and/or droplet deposition. These last are not chemically affected but merely covered by a layer of dust and particles.

Mirwald *et al.* (1988) studied the effect of pollution on the main types of stone in Cologne cathedral. The stones include a volcanic trachyte, two sandstones, and a limestone. The trachyte tends to deteriorate through exfoliation, and the neighbouring limestone blocks contribute significantly to this problem. The limestone is affected by a leaching and dissolution process and erodes away where exposed to direct water action. Less exposed parts are covered with a black crust. On the other hand, one of the sandstones, which can contain up to 15% clays and 10% dolomite, was the most affected material. The other sandstone, containing only 10% clays and no calcareous material, was the most resistant material. Another German field study exposed 13 types of stones, ranging from limestones, through calcareous sandstones to silicate and clay-rich sandstones, to different air pollutions levels at two sites in Germany (Steiger *et al.* 1993). The study showed

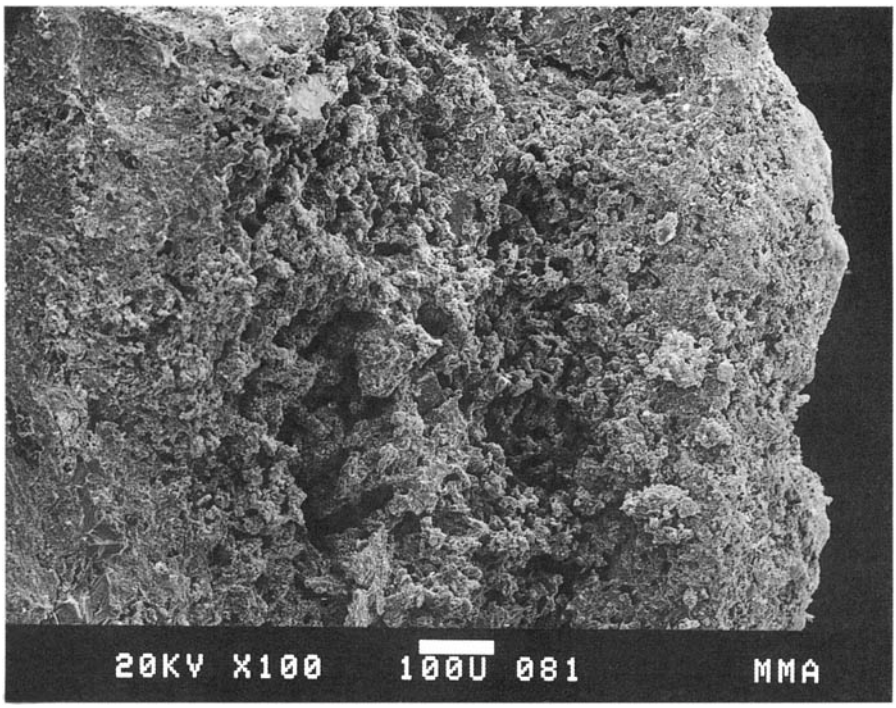

Fig. 2. Crust formation on an exposed surface of calcarenite (Leithakalk) from the town-gate, 'Wiener Tor', at Hainburg, in the outskirts of Vienna. The SEM photomicrograph shows the cross-section from the hardened exterior black crust, through an area with marked loss of cohesion to the interior sound stone, typical of a diffusion mechanism (from Charola & Koestler 1985/86, reproduced with permission).

that dry deposition of Ca-rich aerosol particles is not negligible and that the atmospheric input of SO_2 is important both for material loss of carbonate stone by dissolution and the accumulation of sulphates in the porous system, regardless of the nature of the stone. However, the ratio of sulphates remaining in the stone to that washed out by the driving rain is dependent on the stone's ability to absorb water. Thus the dominant weathering mechanism (chemical dissolution or mechanical stress from gypsum enrichment) will be highly variable.

In an interesting laboratory study by Haneef *et al.* (1992), two stones of a different nature, a granite and a limestone, were stacked over each other and exposed to cycles of artificial acid rain and drying. It was observed that maximum deterioration occurred on the lower stone in the region immediately adjacent to the upper stone regardless of the nature of the stone and compares to the average exposed surface. This was explained by the longer time of wetness coupled with run-off from the overlying stone.

The ubiquitous gypsum-rich black crusts that form in protected areas of stones are one of the most obvious signs and agents of stone deterioration. The formation of black crusts on limestone depends on exposure, porosity, and texture. Camuffo *et al.* (1982, 1983, 1987) suggest that differences in thermal expansion of gypsum crystals on calcite favour the disruption of the stone surface. The relative contributions of chemical agents, microclimate, and surface geometry have been summarized as follows for microporous calcareous marbles and compact limestones: rainwater washing over a surface will have a solubilizing effect which is increased by turbulence and low pH; water also mobilizes any compounds that are found on the surface by dry deposition, thus increasing the initial pH of the resulting solution; and water from fog or night dew is in general insufficient to 'activate' any dry deposit or to dissolve the calcite of the stone surface. However, condensation can be relevant, particularly in spring when warm and humid air masses reach stone surfaces at temperatures below the dew point. For more porous limestones these processes can be significantly different.

Furlan & Girardet (1983*a*) describe alteration phenomena for Swiss sandstone. These

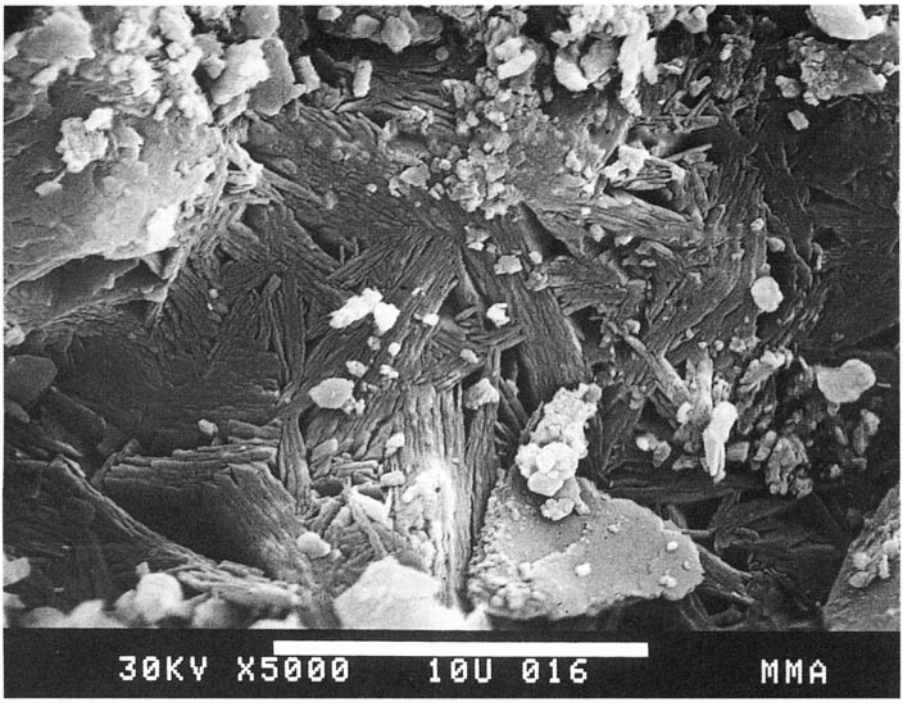

Fig. 3. SEM photomicrograph of platy gypsum crystals that developed against the surface of a calcite crystal which detached, within a calcarenite (Leithakalk) sample taken from the Post Office building (Ungargasse) in Vienna (from Charola & Koestler 1985/86, reproduced with permission).

phenomena can be differentiated depending on whether the stone is exposed to rainwater, resulting in blistering and exfoliation or contour scaling, or protected from rainwater, resulting in surface decohesion to a depth of 1 to 3 mm.

Carbonaceous particles are very active in forming black crusts when they are wet, because they contain both sulphurous compounds and catalysts. They can also absorb SO_2 from the atmosphere and can serve to nucleate gypsum crystals. Thus the gypsum in the crust is partly due to the transformation of the calcareous surface and partly contributed from particle deposition and nucleation (Camuffo 1990; Del Monte 1991). The contribution of carbonaceous particles to the black colour of patinas and crusts on monuments is discussed by Sabbioni *et al.* (1996). The three main sources of carbon outlined are: (a) deposition of atmospheric particles containing elemental and organic carbon compounds; (b) biological weathering resulting in the formation of oxalates; and (c) calcium carbonate from underlying materials such as stone and mortars. Differences between the black crusts currently forming and the grey crusts that formed in Paris between the thirteenth and eighteenth centuries are discussed by Ausset *et al.* (2000*a*) and attributed to the different fuel, i.e. wood, that was used during those centuries.

Gisbert *et al.* (1996) describe black crusts on a porous Spanish sandstone with a high fossil content. The authors distinguish three layers in these crusts describing the morphology and sizes of the gypsum crystals found in them. Five types of particles are described: (a) small spheres (<5 μm) from fuel oil combustion in domestic heating; (b) small smooth spheres composed mainly of iron oxides generated by fuel oil and coal combustion; (c) smooth spheres of aluminosilicate composition resulting from coal combustion; (d) subspherical particles containing lead, zinc, and iron resulting from petroleum combustion; and (e) carbonaceous skeletal particles attributed to the combustion of industrial fuel. The influence of fly-ash on the growth mechanism of black crusts on Jaumont limestones has been addressed by Ausset *et al.* (2000*b*).

While black crusts on calcareous stones are mainly composed of gypsum, as discussed above, for the case of siliceous stones, such as sandstone and granite, two different types of

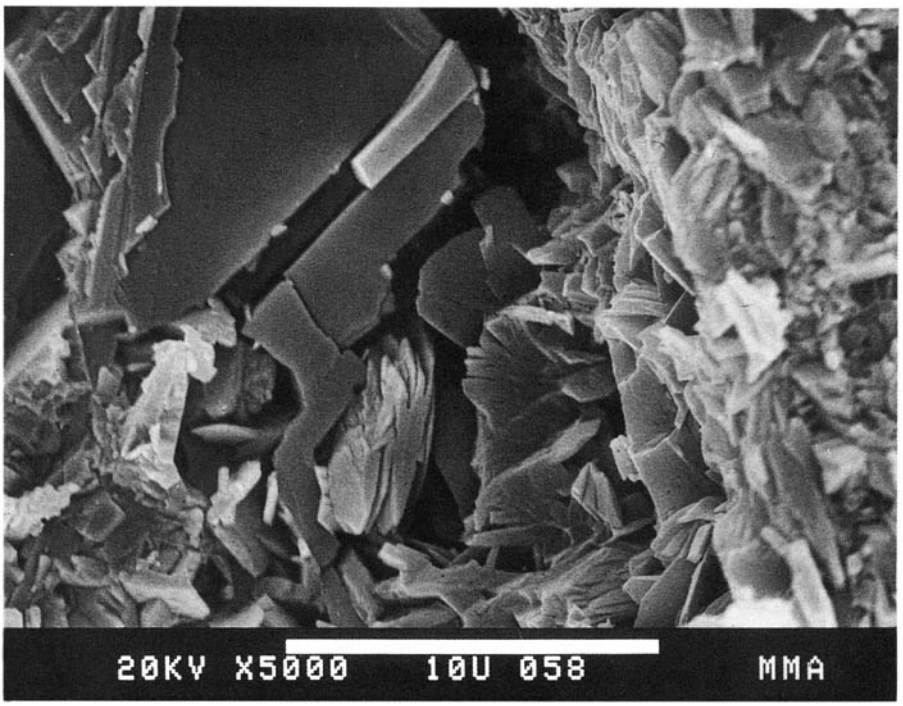

Fig. 4. SEM photomicrograph showing a calcite crystal etched at the lower left side and fractured by the growth of gypsum crystals. The calcarenite (Leithakalk) sample was taken from the St. Stephen's Cathedral, Stefansdom, in Vienna (from Charola & Koestler 1985/86, reproduced with permission).

black deposits can form. In protected areas thin crusts develop, mainly composed of gypsum, resulting from the deposition of gypsum- and calcium-containing aerosols, with the eventual conversion to gypsum of the latter. On the other hand, very thin black layers – veneers – form in exposed areas. On sandstones, these thin glossy layers are mainly constituted by silicate minerals and iron oxides/hydroxides with some gypsum trapping soot and carbon particles according to Nord & Tronner (1992) who identified some hundred other components in them, while Thomachot & Jeannette (2000) elucidated the mechanism of their formation by water absorption and evaporation. On granite, these layers are lustreless, and similarly formed by iron-containing particles that, for the particular Oporto granite studied, originate from traffic and engine wear among other sources (Begonha & Sequeira Braga 1996).

Conclusions

The following key points can be drawn.

- Dry deposition of gaseous pollutants from short-range transport is the key factor in the deterioration of stone, particularly calcareous stones.
- Among gaseous pollutants, SO_2 is the main contributor to deterioration, probably because SO_2 results in the formation of slightly soluble gypsum.
- Each stone has a particular 'reactivity' to SO_2 attack depending on composition, texture, and porosity.
- Gypsum crusts will contribute to deterioration, particularly through dissolution and penetration into the stone matrix, the latter being also dependent on texture and porosity.
- The importance of NO_x should not be underestimated for the future.
- Surface moisture and time-of-wetness are critical for pollutant deposition.
- Wet deposition contributes only in part to deterioration mechanisms, except in rural areas with high rainfalls. In this case, karst dissolution could be more important than wet deposition of acidic components.
- Fog or 'occult' deposition can be particu-

larly important in areas with special climatic conditions, such as Venice or Los Angeles.

- The calcite dissolution mechanism is transport-controlled by the H^+ concentration, i.e. activity, below pH 4; above this pH, surface kinetics starts playing an increasing role and, above pH 6, the reaction rate is surface-controlled.
- Soiling of the stone results from particulate deposition. When emissions are lowered, soiling will decrease and previous soiling will eventually be washed away.

As stated by Camuffo (1995): 'chemical weathering is not directly related to the concentration of pollutants in the air, but to the combined action of the pollutants deposited on the monument surface, when microclimatic or meteorological factors may trigger some deterioration process'.

This paper is a highly abridged version of the Literature Review (Charola 2001) that was carried out through a consulting agreement with US/ICOMOS for the National Center for Preservation Technology and Training of the National Park Service. The authors thank D. Camuffo, Padova, Italy, and H. Ruppert, Göttingen, Germany, for their critical review and helpful comments to improve the manuscript.

References

AIRES-BARROS, L. 2001. *As rochas dos monumentos portugueses. Tipologias e patologias.* Instituto Portugués do Património Arquitectonico, Lisbon.

AMOROSO, G. G. & FASSINA, V. 1983. *Stone Decay and Conservation.* Elsevier, Amsterdam.

AUSSET, P., CROVISIER, J. L., DEL MONTE, M., *et al.* 1996. Experimental study of limestone and sandstone sulphation in polluted realistic conditions: the Lausanne Atmospheric Simulation Chamber (LASC). *Atmospheric Environment*, **30**, 3197–3207.

AUSSET, P., LEFÈVRE, R. A., DEL MONTE, M. & THIÉBAULT, S. 2000*a*. Past air pollution recordings on stone monuments: the heads of the Kings of Juda statues from Notre-Dame Cathedral (Paris). *In*: FASSINA, V. (ed.) *Proceedings of the 9th International Congress on Deterioration and Conservation of Stone.* Elsevier, Amsterdam, Vol. 1, 339–347.

AUSSET, P., LEFÈVRE, R. A. & DEL MONTE, M. 2000*b*. Early mechanisms of development of sulphated black crusts on carbonate stone. *In*: FASSINA, V. (ed.) *Proceedings of the 9th International Congress on Deterioration and Conservation of Stone.* Elsevier, Amsterdam, Vol. 1, 329–337.

BABOIAN, R. (ed.) 1986. *Materials Degradation Caused by Acid Rain.* American Chemical Society, Washington, DC, Symposium Series **318**.

BAEDECKER, PH. A. & REDDY, M. M. 1993. The erosion of carbonate stone by acid rain. *Journal of Chemical Education*, **70**: 104–108.

BEGONHA, A. & SEQUEIRA BRAGA, M. A. 1996. Black crusts and thin black layers in granitic monuments: their characterization and the role of air pollution. *In*: RIEDERER, J. (ed.) *Proceedings of the 8th International Congress on Deterioration and Conservation of Stone.* Möller Druck und Verlag, Berlin, 371–375.

BEHLEN, A., WITTENBURG, C., STEIGER, M. & DANNECKER, W. 1996. Dry deposition of NO, NO2, HONO, HNO3 and PAN on historical building stones. *In*: RIEDERER, J. (ed.) *Proceedings of the 8th International Congress on Deterioration and Conservation of Stone.* Möller Druck und Verlag, Berlin, 377–385.

BEILKE, S. & GRAVENHORST, G. 1978. Heterogeneous SO_2-oxidation in the droplet phase. *Atmospheric Environment*, **12**, 231–241.

BRIMBLECOMBE, P. 1987. *The Big Smoke.* Methuen, London.

BRIMBLECOMBE, P. 1991*a*. History of air pollution and deterioration of heritage. *In*: ZEZZA, F. (ed.) *Weathering and Air Pollution.* First Course, Community of Mediterranean Universities, University School of Monument Conservation. Mario Adda Editore, Bari, 23–32.

BRIMBLECOMBE, P. 1991*b*. History of air pollution and damage to the cultural heritage of European cities. *In*: BAER, N. S., SABBIONI, C. & SORS, A. I. (eds) *Science, Technology and European Cultural Heritage.* Butterworth-Heinemann, Oxford, 51–66.

BRIMBLECOMBE, P. 1996. *Air Composition and Chemistry* (2nd edn). Cambridge University Press, Cambridge.

BRIMBLECOMBE, P. & RODHE, H. 1988. Air pollution – historical trends. *In*: ROSVALL, J. & ALEBY, S. (eds) *Air Pollution and Conservation. Safeguarding our Architectural Heritage.* Elsevier, Amsterdam, 107–124.

BUTLIN, R. N., COOTE, A. T., DEVENISH, M., *et al.* 1992. Preliminary results from the analysis of stone tablets from the National Materials Exposure Programme (NMEP). *Atmospheric Environment*, **26B**, 189–198.

CAMUFFO, D. 1990. Acidic precipitation research in Italy. *In*: BRESSER, A. H. M. & SALOMONS, W. (eds) *Acidic Precipitation. Vol. 5. International Overview and Assessment.* Springer Verlag, New York, 229–265.

CAMUFFO, D. 1991*a*. Environment and microclimate. *In*: BAER, N. S., SABBIONI, C. & SORS, A. I. (eds) *Science, Technology and European Cultural Heritage.* Butterworth-Heinemann, Oxford, 37–50.

CAMUFFO, D. 1991*b*. Physical weathering of monuments. *In*: ZEZZA, F. (ed.) *Weathering and Air Pollution.* First Course, Community of Mediterranean Universities, University School of Monument Conservation. Mario Adda Editore, Bari, 51–66.

CAMUFFO, D. 1994. Aspetti meteorologici e microclimatici nel degrado dei materiali lapidei. *In*: *Conservazione del Patrimonio Culturale*. Accademia Nazionale dei Lincei, Contributi del Centro Linceo Interdisciplinare 'Beniamino Segre', No. **88**, Roma, 9–27.

CAMUFFO, D. 1995. Physical weathering of stones. *The Science of the Total Environment*, **167**, 1–14.

CAMUFFO, D. 1998. *Microlimate for Cultural Heritage*. Elsevier, Amsterdam,.

CAMUFFO, D., DEL MONTE, M., SABBIONI, C. & VITTORI, O. 1982. Wetting, deterioration and visual features of stone surfaces in an urban area. *Atmospheric Environment*, **16**, 2253–2259.

CAMUFFO, D., DEL MONTE, M. & SABBIONI, C. 1983. Origin and growth mechanisms of the sulfated crusts on urban limestone. *Water, Air and Soil Pollution*, **19**, 351–359.

CAMUFFO, D., DEL MONTE, M. & ONGARO, A. 1984. The pH of the Atmospheric precipitation in Venice, related to both the dynamics of precipitation events and the weathering of monuments. *The Science of the Total Environment*, **40**, 125–139.

CAMUFFO, D., DEL MONTE, M. & SABBIONI, C. 1987. Influenza delle precipitazioni e della condensazione sul degrado superficiale dei monumenti in marmo e calcare. *'Materiali Lapidei' Supplemento al Bollettino d'Arte*. Ministero per i Beni Culturali e Ambientali No. **41**, 15–36.

CAMUFFO, D., BERNARDI, A. & ZANETTI, M. 1988. Analysis of the real-time measurement of the pH of rainfall at Padova, Italy: seasonal variation and meteorological aspects. *The Science of the Total Environment*, **71**, 187–200.

CAMUFFO, D., STURARO, G. & VALENTINO, A. 1997. The climate of Venice and its action on monument decay. *In*: MOROPOULOU, A., ZEZZA, F., KOLLIAS, E. & PAPACHRISTODOULOU, I. (eds) *4th International Symposium on the Conservation of Monuments in the Mediterranean Basin*. Technical Chamber of Greece, Athens, 53–65.

CHAROLA, A. E. 1988. Chemical-physical factors in stone deterioration. *In*: ROSVALL, J. & ALEBY, S. (eds) *Air Pollution and Conservation. Safeguarding our Architectural Heritage*. Elsevier, Amsterdam, 125–132.

CHAROLA, A. E. 2001. Review of the literature on the topic of acidic deposition on stone. *US/ICOMOS Scientific Journal*, **3**, 19–58.

CHAROLA, A. E. & KOESTLER, R. J. 1985/86. SEM study of the deterioration of monumental stones in Vienna. *Wiener Berichte über Naturwissenschaft in der Kunst*, **2/3**, 176–185.

CUSSLER, E. L. & FEATHERSTONE, J. D. B. 1981. Demineralization of porous solids. *Science*, **213**, 1013.

DAVIDSON, C. I. 1979. Air pollution in Pittsburgh: a historical perspective. *Journal of the Air Pollution Control Association*, **29**, 1035–1041.

DEL MONTE, M. 1991. Stone monument decay and air pollution. *In*: ZEZZA, F. (ed.) *Weathering and Air Pollution*. First Course, Community of Mediterranean Universities, University School of Monument Conservation. Mario Adda Editore, Bari, 101–110.

DOLSKE, D. A. 1995. Deposition of atmospheric pollutants to monuments, statues and buildings. *The Science of the Total Environment*, **167**, 15–31.

DOMASLOWSKI, W. 1982. La Conservation préventive de la pierre. *Musées et Monuments XVIII*, 15–57.

FASSINA, V. 1988. Environmental pollution in relation to stone decay. *In*: ROSVALL, J. & ALEBY, S. (eds) *Air Pollution and Conservation. Safeguarding our Architectural Heritage*. Elsevier, Amsterdam, 133–174.

FASSINA, V. 1991. Atmospheric pollutants responsible for stone decay. Wet and dry surface deposition of air pollutants on stone and the formation of black scabs. *In*: ZEZZA, F. (ed.) *Weathering and Air Pollution*. First Course, Community of Mediterranean Universities, University School of Monument Conservation, Mario Adda Editore, Bari, 67–86.

FASSINA, V. & LAZZARINI, L. 1979. Sulphur dioxide atmospheric oxidation in the presence of ammonia related to the deterioration of building materials in Venice. *In*: *Proceedings of the 3rd International Congress on Deterioration and Preservation of Stones*, Venice. Università degli Studi di Padova, Padova, 25–33.

FASSINA, V. & STEVAN, A. 1992. Fogwater composition in Venice in relation to stone decay. *In*: DELGADO RODRIGUES, J., HENRIQUES, F. & TELMO JEREMIAS, F. (eds) *Proceedings of the 7th International Congress on Deterioration and Conservation of Stone*. Laboratório Nacional de Engenharia Civil, Lisbon, 365–374.

FURLAN, V. 1991. Mesure du dépôt de soufre 'sec' et rèactivité intrinseque des pierres. *In*: ZEZZA, F. (ed.) *Weathering and Air Pollution*. First Course, Community of Mediterranean Universities, University School of Monument Conservation. Mario Adda Editore, Bari, 131–138.

FURLAN, V. & GIRARDET, F. 1983*a*. Considerations on the rate of accumulation and distribution of sulphurous pollutants in exposed stones. *In*: WITTMANN, F. H. (ed) *Materials Science and Restoration*. Lack und Chemie, Filderstadt, 285–290.

FURLAN, V. & GIRARDET, F. 1983*b*. Pollution atmosphérique et dégradation de la molasse. 1re partie. *Chantiers/Suisse*, **14**, 989–994.

FURLAN, V. & GIRARDET, F. 1983*c*. Pollution atmosphérique et dégradation de la molasse. 2e partie. *Chantiers/Suisse*, **14**, 1081–1084.

FURLAN, V. & GIRARDET, F. 1988. Vitesse d'accumulation des composés atmosphériques du soufre sur diverses nature de pierre. *In*: CIABACH, J. (ed.) *Proceedings of the 6th International Congress on Deterioration and Conservation of Stone*. Nicholas Copernicus University Press, Torun, 187–196.

FURLAN, V. & GIRARDET, F. 1992. Pollution atmosphérique et réactivité de pierres. *In*: DELGADO RODRIGUES, J., HENRIQUES, F. & TELMO JEREMIAS, F. (eds) *Proceedings of the 7th International Congress on Deterioration and*

Conservation of Stone. Laboratório Nacional de Engenharia Civil, Lisbon, 153–161.

GAURI, K. L. & GWINN, J. A. 1982/83. Deterioration of marble in air containing 5–10 ppm SO2 and NO2. *Durability of Building Materials*, **1**, 217–223.

GAURI, K. L., DODERER, G. C., LIPSCOMB, N. T. & SARMA, A. C. 1973. Reactivity of treated and untreated marble specimens in an SO_2 atmosphere. *Studies in Conservation*, **18**, 25–35.

GAURI, K. L., POPLI, R. & SARMA, A. C. 1982/83. Effect of relative humidity and grain size on the reaction rates of marble at high concentrations of SO_2. *Durability of Building Materials*, **1**, 209–216.

GIRARDET, F. & FURLAN, V. 1996. Réactivité des pierres au SO2 atmosphérique, étude en chambre de simulation et corrélation avec les mesures en site réel. *In*: RIEDERER, J. (ed.) *Proceedings of the 8th International Congress on Deterioration and Conservation of Stone*. Möller Druck und Verlag, Berlin, 341–347.

GIRARDET, F., FURLAN, V., AUSSET, E. P., DEL MONTE, M., JEANNETTE, D. & LEFÈVRE, R. A. 1996. Etude expérimentale de la prise en soufre d'un calcarie et d'un grès calcareux dans la chambre de simulation atmosphérique de Lausanne. *In*: RIEDERER, J. (ed.) *Proceedings of the 8th International Congress on Deterioration and Conservation of Stone*. Möller Druck und Verlag, Berlin, 349–358.

GISBERT, J., MARÍN-CHAVES, C. & ANDALUZ, N. 1996. Black crusts from Rueda Cloister: an approximation to fossil effects of pollution in a semi-arid climate. *In*: RIEDERER, J. (ed.) *Proceedings of the 8th International Congress on Deterioration and Conservation of Stone*. Möller Druck und Verlag, Berlin, 387–392.

GUIDOBALDI, F. 1981. Acid rain and corrosion of marble. An experimental approach. *In*: ROSSI-MANARESI, R. (ed.) *The Conservation of Stone II*. Centro per la Conservazione delle Sculture all'Aperto, Bologna, 483–497.

GUIDOBALDI, F. & MECCHI, A. M. 1985. Corrosion of marble by rain. The influence of surface roughness, rain intensity and additional washing. *In*: FÉLIX, G. (ed.) *Proceedings of the 5th International Congress on Deterioration and Conservation of Stone*. Presses Polytechniques Romandes, Lausanne, 467–474.

HANEEF, S. J., DICKINSON, C., JOHNSON, J. B., THOMPSON, G. E. & WOOD, G. C. 1992. Simulation of the degradation of coupled stones by artificial acid rain. *Studies in Conservation*, **37**, 105–112.

HICKS, B. B. 1982. Wet and dry surface deposition of air pollutants and their modeling. *In*: *Conservation of Historic Buildings and Monuments*. National Academy Press, Washington, DC, 183–196.

HOFFMANN, M. R. 1986. Fog and cloud water deposition. *In*: BABOIAN, R. (ed.) *Materials Degradation Caused by Acid Rain*. American Chemical Society, Washington, DC, Symposium Series **318**, 64–91.

IRVING, P. M. 1991*a*. *Acidic Deposition: State of Science and Technology. Vol. I Emissions, Atmospheric Processes and Deposition*. US National Acid Precipitation Assessment Program, Washington, DC, 1–3 – 8–110.

IRVING, P. M. 1991*b*. *Acidic Deposition: State of Science and Technology. Vol. III Terrestrial, Materials, Health and Visibility Effects*. US National Acid Precipitation Assessment Program, Washington, DC, 16–25 – 24–129.

JOHANSSON, L.-G., LINDQVIST, O. & MANGIO, R. E. 1988. Corrosion of calcareous stones in humid air containing SO_2 and NO_2. *In*: ROSVALL, J. & ALEBY, S. (eds) *Air Pollution and Conservation. Safeguarding our Architectural Heritage*. Elsevier, Amsterdam, 255–265.

KOZLOWSKI, R., MAGIERA, J., WEBER, J. & HABER, J. 1990. Decay and conservation of Pinczów porous limestone. I. Lithology and weathering. *Studies in Conservation*, **35**, 205–221.

LAURENZI TABASSO, M. & MARABELLI, M. 1992. *Il Degrado dei Monumenti in Roma in Rapporto all'Inquinamento Atmosferico*. BetaGamma, Viterbo.

LAZZARININI, L. & LAURENZI TABASSO, M. 1986. *Il Restauro della Pietra*. Cedam, Padova.

LIVINGSTON, R. A. 1985. The role of nitrogen oxides in the deterioration of carbonate stone. *In*: Félix, G. (ed.) *Proceedings of the 5th International Congress on Deterioration and Conservation of Stone*. Presses Polytechniques Romandes, Lausanne, 509–516.

LIVINGSTON, R. A. 1991. Atmospheric deposition and its measurement with regard to air pollution legislation to protect monuments. *In*: BAER, N. S., SABBIONI, C. & SORS, A. I. (eds) *Science, Technology and European Cultural Heritage*. Butterworth-Heinemann, Oxford, 67–77.

LIVINGSTON, R. A. 1992. Graphical methods for examining the effects of acid rain and sulfur dioxide on carbonate stones. *In*: DELGADO RODRIGUES, J., HENRIQUES, F. & TELMO JEREMIAS, F. (eds) *Proceedings of the 7th International Congress on Deterioration and Conservation of Stone*. Laboratório Nacional de Engenharia Civil, Lisbon, 375–386.

LIVINGSTON, R. A. 1997. Development of air pollution damage functions. *In*: BAER, N. S. & SNETHLAGE, R. (eds) *Saving Our Architectural Heritage. The Conservation of Historic Stone Structures*. Dahlem Workshop Report, J. Wiley & Sons, Chichester, 37–62.

MARCHESINI, L. 1969. Comportamento dei Marmi e della Pietre a Venezia. *In*: ROSSI-MANARESI, R. & RICCÒMINI, E. (eds) *La Conservazione delle Sculture all'Aperto*. Rapporti della Soprintendenza alle Gallerie di Bologna, Bologna, 78–86.

MIRWALD, P. W., KRAUS, K. & WOLFF, A. 1988. Stone deterioration on the Cathedral of Cologne. *In*: ROSVALL, J. & ALEBY, S. (eds) *Air Pollution and Conservation. Safeguarding our Architectural Heritage*. Elsevier, Amsterdam, 365–386.

MORONI, B. & POLI, G. 2000. Corrosion of limestone in humid air containing sulphur and nitrogen dioxides: a model study. *In*: FASSINA, V. (ed.) *Proceedings of the 9th International Congress on*

Deterioration and Conservation of Stone. Elsevier, Amsterdam, Vol. 1, 367–374.

NORD, A. G. & TRONNER, K. 1992. Characterization of thin black layers. *In*: DELGADO RODRIGUES, J., HENRIQUES, F. & TELMO JEREMIAS, F. (eds) *Proceedings of the 7th International Congress on Deterioration and Conservation of Stone*. Laboratório Nacional de Engenharia Civil, Lisbon, 217–225.

PRICE, C. A. 1996. *Stone Conservation. An Overview of Current Research*. Research in Conservation, Getty Cconservation Institute, Los Angeles.

REDDY, M. M., SHERWOOD, S. & DOE, B. 1985. Limestone and marble dissolution by acid rain. *In*: FÉLIX, G. (ed.) *Proceedings of the 5th International Congress on Deterioration and Conservation of Stone*. Presses Polytechniques Romandes, Lausanne, 517–526.

REDDY, M. M., SHERWOOD, S. I. & DOE, B. R. 1986. Limestone and marble dissolution by acid rain: an onsite weathering experiment. *In*: BABOIAN, R. (ed.) *Materials Degradation Caused by Acid Rain*. American Chemical Society, Washington, DC, Symposium Series **318**, 226–238.

ROCCHI, G. & MOSELLO, R. 1979. Inquinamento dell'aria e caratteristiche dell'acqua piovana in città lacustri dell'Italia settentrionale: il caso di Como. *In*: *Proceedings of the 3rd International Congress on Deterioration and Preservation of Stones*, Venice. Università degli Studi di Padova, Padova, 35–42.

ROSSI-MANARESI, R. 1991. Alterazione chimica e degrado di litotipi carbonatici nei monumenti. *In*: ZEZZA, F. (ed.) *Weathering and Air Pollution*. First Course, Community of Mediterranean Universities, University School of Monument Conservation. Mario Adda Editore, Bari, 139–145.

ROSVALL, J. & ALEBY, S. (eds) 1988. *Safeguarding our Architectural Heritage*. Elsevier, Amsterdam.

SABBIONI, C., ZAPPIA, G., GHEDINI, N. & GOBBI, G. 1996. Carbon due to atmospheric deposition on stone monuments and historical buildings. *In*: RIEDERER, J. (ed.) *Proceedings of the 8th International Congress on Deterioration and Conservation of Stone*. Möller Druck und Verlag, Berlin, 333–340.

SERRA, L. M. 1969. Degradazione del marmo in presenza di anidride solforosa. *In*: ROSSI-MANARESI, R. & RICCÒMINI, E. (eds) *La Conservazione delle Sculture all'Aperto*. Rapporti della Soprintendenza alle Gallerie di Bologna, Bologna, 66–71.

SERRA, M. & STARACE, G. 1972. An isotopic tracer method for studying absorption and oxidation of sulphur dioxide on calcium carbonate. *In*: *1st International Symposium on the Deterioration of Building Stones*. Centre de Recherches et d'Études Océanographiques, La Rochelle, 185–188.

SERRA, M. & STARACE, G. 1978. Study of the reactions between gaseous sulphur dioxide and calcium carbonate. *In*: *UNESCO/RILEM International Symposium on the Deterioration and Protection of Stone Monuments*. UNESCO/RILEM, Paris, 3.7.1–3.7.19.

SHERWOOD, S. I. & DOLSKE, D. A. 1992. Acid depostion impacts on marble monuments at Gettysburg. *In*: DELGADO RODRIGUES, J., HENRIQUES, F. & TELMO JEREMIAS, F. (eds) *Proceedings of the 7th International Congress on Deterioration and Conservation of Stone*. Laboratório Nacional de Engenharia Civil, Lisbon, 247–255.

SHERWOOD, S. I. & REDDY, M. M. 1988. A field study of pollutant effects on carbonate stone dissolution. *In*: MARINOS, P. G. & KOUKIS, G. C. (eds) *Engineering Geology of Ancient Works, Monuments and Historical Sites*. Balkema, Rotterdam, 917–923.

SKOULIKIDIS, TH. & PAPAKONSTANTINOU-ZIOTIS, P. 1981. Mechanism of sulphation by atmospheric SO_2 of limestones and marbles of the ancient monuments and statues. I. Observations in situ (Acropolis) and laboratory measurements. *British Corrosion Journal*, **16**, 63–69.

STEIGER, M., WOLF, F. & DANNECKER, W. 1993. Deposition and enrichment of atmospheric pollutants on building stones as determined by field exposure experiments. *In*: THIEL, M.-J. (ed.) *Conservation of Stone and Other Materials*. E & FN Spon, London, 35–42.

THOMACHOT, C. & JEANNETTE, D. 2000. Petrophysical properties modifications of Strasbourg's cathedral sandstone by black crusts. *In*: FASSINA, V. (ed.) *Proceedings of the 9th International Congress on Deterioration and Conservation of Stone*. Elsevier, Amsterdam, Vol. 1, 265–273.

TORRACA, G. 1988. Air pollution and the conservation of building materials. *In*: ROSVALL, J. & ALEBY, S. (eds) *Air Pollution and Conservation. Safeguarding our Architectural Heritage*. Elsevier, Amsterdam, 199–208.

UK BUILDING EFFECTS REVIEW GROUP. 1989. *The Effects of Acid Deposition on Buildings and Building Materials in the United Kingdom*. HMSO, London.

US COMMITTEE ON CONSERVATION OF HISTORIC STONE BUILDINGS AND MONUMENTS. 1982. *Conservation of Historic Stone Buildings and Monuments*. National Academy Press, Washington, DC.

WEBB, A. H., BAWDEN, R. J., BUSBY, A. K. & HOPKINS, J. N. 1992. Studies on the effects of air pollution on limestone degradation in Great Britain. *Atmospheric Environment*, **26B**, 165–181.

WINKLER, E. M. 1994. *Stone: Properties, Durability in Man's Environment*. Springer, New York.

ZEZZA, F. (ed.) 1991. *Weathering and Air Pollution*. First Course of the Conservation of Monuments University School. Mario Adda Editore, Bari.

Implications of future climate change for stone deterioration

HEATHER A. VILES

School of Geography and the Environment, University of Oxford, Mansfield Road, Oxford, OX1 3TB, UK (e-mail: heather.viles@geog.ox.ac.uk)

Abstract: Climate change over the next 100 years is likely to have a range of direct and indirect impacts on many natural and physical environments, including the built environment. Important influences on the built environment will include alterations in temperature, precipitation, extreme climatic events, soil conditions, groundwater and sea level. Some processes of building stone decay will be accelerated or worsened by climate change, whilst others will be retarded. The impacts on individual processes can be conceptualized, but it is difficult to assess or quantify the overall risk posed by climate change given currently available data. Linking global-scale changes to the response of individual walls or buildings remains a challenge. Overall changes in decay rates could also be related to climatic change. As an example downscaled climate predictions, knowledge of stock at risk and long-term decay rates can be used to assess the future of building stone decay in the UK. Using the UK Climatic Impacts Programme's (UKCIP98) regional climate change projections an increasing NW–SE climatic gradient is predicted, which should enhance chemical weathering of silicate building materials in the NW and increase crystallization damage of limestones in the SE.

The global climate has, over geological time, experienced great change over a range of time spans. For example, during the Quaternary period which covers approximately the last 2.4 million years global climates have oscillated through a series of glacial and interglacial episodes, with shorter term warming and cooling periods recorded in many places (such as the Younger Dryas which affected northern latitudes some 12 000 years ago). Over the past 1000 or so years (and probably stretching back much further; Liu *et al.* 2000) shorter term climatic variability has also been observed within the global system. Phenomena such as El Nino–Southern Oscillation (ENSO) and the North Atlantic Oscillation (NAO) have been shown to cause decadal scale fluctuations in temperature and rainfall over large areas (Changnon 2000; Diaz & Markgraf 2000; McCabe & Dettinger 1999; Wilby *et al.* 1997). Superimposed upon these trends, and perhaps interacting with them, has been the recently acknowledged impact of human-induced global warming over the last century. The third assessment of the Intergovernmental Panel on Climate Change reported that global average surface temperatures increased by about 0.6°C over the twentieth century, and that there is now strong evidence that most of the warming over the last 50 years is attributable to human activities (Houghton *et al.* 2001). The global climate system is highly complex, and untangling the contributions of different factors (including external forcing factors, both human and natural, as well as internal readjustments) to observed change can be very difficult. Although there are still dissenting voices within the scientific community, it is clear that the consensus viewpoint is that human-induced global warming is now occurring and will continue to affect the global climate for at least the next century or two.

Fears about human-induced climate change have spawned a whole series of papers on the likely impacts of global warming on various components of the natural and human environment (e.g. Goudie 1996; Grime *et al.* 2000). The building stone deterioration community has been slow to consider in detail the threats posed by global warming to the decay of cultural heritage, buildings and engineering structures, although agencies such as the UK Engineering and Physical Science Research Council (EPSRC) have addressed issues of climate change and the built environment in a recent funding scheme. This paper provides a first attempt at a qualitative analysis of the likely future impacts of climate change on building stone deterioration to provide a starting point for further discussion and research.

Climate change scenarios for the next 100 years

Several attempts have been made in recent years to model the global climatic future, with

From: SIEGESMUND, S., WEISS, T. & VOLLBRECHT, A. 2002. *Natural Stone, Weathering Phenomena, Conservation Strategies and Case Studies*. Geological Society, London, Special Publications, **205**, 407–418.
0305-8719/02/$15.00 © The Geological Society of London 2002.

Table 1. *Key projections of climate trends and extreme events in the IPCC Third Assessment*

Change	Likelihood*
Rate of increase of global average surface temperature will exceed anything experienced over last 10 000 years	Very likely
Nearly all land areas will warm more than global average, particularly northern high latitudes in cold season	Very likely
Precipitation will increase by end of twenty-first century over northern mid- to high latitudes in winter	Likely
In areas where increase in mean precipitation is predicted, larger year-to-year variations will occur	Very likely
Higher maximum temperatures and more hot days over nearly all land areas	Very likely
Higher minimum temperatures, fewer cold days and frost days over nearly all land areas	Very likely
Reduced diurnal temperature range over most land areas	Very likely
More intense precipitation events over many northern hemisphere mid- to high latitude land areas	Very likely, over many areas
Increased summer continental drying and associated risk of drought	Likely, over most mid-latitude continental interiors
Increase in tropical cyclone peak wind intensities, mean and peak precipitation intensities	Likely, over some areas

Adapted from Houghton *et al.* (2001)
* Very likely = 90–99% chance; likely = 66–90% chance

the Intergovernmental Panel on Climate Change (IPCC) providing a general consensus viewpoint. The IPCC reported in mid-2001, after previous reports in 1990 and 1996, with further refinements to the understanding of the causes, magnitudes and consequences of future climate change (Houghton *et al.* 2001). Based on a range of scenarios of future emissions of greenhouse gases, and on a range of climate models, the IPCC indicate that both global average temperature and sea level are projected to rise over the twenty-first century. Global average surface temperatures are predicted to rise by 1.4 to 5.8°C between 1990 and 2100, which represents a much larger rate of warming than that observed over the twentieth century and one which, based on palaeoclimate data, is very likely to surpass anything experienced over the last 10 000 years. The models also suggest that nearly all land areas will warm more quickly than the global average, and that northern high latitudes in the cold season will experience particularly high warming. For example, northern regions of North America and northern and central Asia are predicted to experience temperature rises of 40% more than the global average. Global water vapour content and precipitation are also predicted to increase, with probable increases in precipitation by the second half of the twenty-first century over northern mid- to high latitudes and Antarctica in winter. Global mean sea level is projected to rise by 0.09 to 0.88 m between 1990 and 2100. Areas that are experiencing subsidence will experience particularly high relative rates of sea level rise. Increases in both surface temperatures and sea level are projected to continue for several hundred years even after greenhouse gas emissions stabilize, because of the long timescales over which deep oceans adjust. Table 1 summarizes the key weather and climate projections made by the IPCC which are likely to impact upon building stone deterioration.

Four aspects of future climate change are likely to have an impact on stone deterioration. Although in reality these are all interconnected and often mutually reinforcing, it is useful to

treat them separately. Firstly, trends in atmospheric composition and basic climatic attributes will have an impact on fundamental processes of stone decay. Increasing concentrations of carbon dioxide and other trace gases in the atmosphere alter air chemistry and influence chemical reactions. Furthermore, in general increasing temperatures will encourage chemical reactions as well as reduce the likelihood of freezing in many environments, and alterations to regional seasonal and annual rainfall totals will provide more or less water to the stone decay system. As Table 1 shows, most land areas are likely to experience reduced diurnal temperature ranges, and fewer cold and frost days. Whilst trace gas concentrations will change in a blanket fashion across the globe, other changes in climatic attributes will vary regionally. Some areas, for example, will experience more serious warming trends than others, with northern hemisphere high latitudes likely to experience particularly rapid warming.

Impacts of future climate change on the variability (on seasonal to decadal scales) of climate will provide a second major influence on stone deterioration. Many processes of stone deterioration do not act in a regular, gradual manner but are concentrated in episodic bursts related to the presence of extreme events such as severe storms. As shown in Table 1 some extremes of weather and climate are projected to increase for many areas (e.g. year-to-year variations in precipitation for those areas seeing an increase in average precipitation, higher maximum temperatures, more intense precipitation events over many mid- to high latitude areas in the northern hemisphere, increased summer drying in mid-latitude continental interiors). However, our knowledge of the future changes in extreme events such as tropical cyclones is much more limited.

Changes in the global atmospheric system are linked with changes in the terrestrial and oceanic systems, and some of these interconnected changes will also have ramifications for building stone deterioration. For example, biotic communities and species will respond to climate change, as will sea levels, soil chemistry and groundwater. Several recent studies have tried to predict the likely response of terrestrial biota to climatic change looking at species and community responses (Sykes *et al.* 1996; Grime *et al.* 2000). Some time lag will be involved in the response of organisms such as trees to climate change, although fast-growing and colonizing organisms such as many micro-organisms are likely to react quickly if at all. Buildings are often colonized by a range of organisms, ranging from opportunistic plants, through slow-growing lichens to highly tolerant micro-organisms and almost nothing is known about the likely response of most of these organisms to climate change. Feedbacks between changed biotic communities and the atmosphere will probably cause further alterations to the climate as a result of alterations in carbon dioxide storage and emissions from vegetated areas.

Impacts of climate change on sea levels are well-known, but complicated, as there are a large number of factors affecting sea level, only some of which relate to climate. Recent IPCC projections of sea level rise associated with global warming over the next century are slightly less than predicted in the 1990s at 0.09 to 0.88 m between 1990 and 2100. Using the central value of 0.48 m over the period 1990–2100 this will give an average rate of 2.2 to 4.4 times the rate of rise experienced during the twentieth century (Houghton *et al.* 2001, p. 642). Some areas will experience much more rapid relative sea level rises than these average figures, because of local alterations in land levels (caused by isostatic processes) and different responses to warming of different oceans. For example, several of the models used by the IPCC predict a maximum sea level rise in the Arctic Ocean, possibly related to declining salinity from increased freshwater and precipitation inputs producing density changes. Low-lying, subsiding areas especially around seas with rapidly rising waters will be particularly at risk.

Terrestrial hydrology will respond to both changed climate and sea levels, as water inputs to the system and base level conditions both change. Of major potential importance to building stone deterioration will be potential alterations in groundwater and soil water levels and chemistry. Soil water and some groundwater will be directly affected by global warming, as some areas will experience greater drying out of soils and others will receive more moisture. In many areas of low-lying coast groundwater levels and salinities will both rise as a consequence of increased intrusion of seawater into the groundwater bodies. Groundwater in many locations is already highly influenced by more local human impacts, however, and thus climate change impacts are likely to be complex and variable from one area to another.

Human activity will itself also be influenced by climate change, and this provides a fourth important factor for stone deterioration in the future. Changed climatic conditions will encourage changing building practices, and also alterations in the use of many buildings and

Table 2. *Major types of stone deterioration process*

Physical	Chemical	Biological
Freeze–thaw (cryoclasty)	Dissolution of calcite and other soluble minerals	Biophysical attack (forces exerted by growing organisms, wetting and drying)
Salt crystallization, hydration and thermal expansion (haloclasty)	Sulphation	Biochemical attack (action of organic acids and other organically produced compounds)
Heating and cooling (thermoclasty)	Hydrolysis of silicate minerals	Bioprotection (production of a protective crust or film)
Loading and unloading	Production of new minerals	

structures. For example, warmer winter temperatures in the temperate northern latitudes would obviate the need for the application of de-icing salts to many roads in winter, thus reducing the threat to building materials from saline compounds. More indirectly, climate change will influence land use and regional economies, permitting increased development in some areas and influencing the 'stock at risk' in terms of buildings and structures.

Impacts of climate change on stone deterioration

Some processes of stone deterioration will be accelerated or worsened by future climate change, whilst others will be retarded. Although it is conceptually quite simple to envisage the impact of climate change on individual processes, the difficulty comes in trying to weigh up the importance of different impacts and compare them with other factors affecting stone decay processes and outcomes (such as air pollution). Also, there are difficulties in quantifying many of the climatic impacts on stone deterioration processes, especially where synergism between processes occurs. Furthermore, for some deterioration processes we still do not have enough information on how climate influences them to make clear predictions. The following discussion separates physical, chemical and biological processes of deterioration following Table 2 for ease of presentation, although a challenge for forthcoming research is to investigate their linked responses to climate change.

Direct impacts of climate change and variability

A range of stone deterioration processes will be affected both by general future trends in atmospheric composition, rainfall and temperature and the likely alterations in the variability of storms etc. Looking first at the physical weathering processes in Table 2, all but loading and unloading are directly influenced by climate and require cycling of temperature to produce decay. Global warming will alter both the magnitude of cycling (notably the diurnal temperature range) and also its temporal distribution (i.e. how many days of the year experience critical diurnal ranges). As shown in Table 1 reduced diurnal temperature ranges are very likely for most land areas over the next 100 years. Thermoclasty should respond simply to changes in temperature cycling, with decreased magnitude and frequency of temperature fluctuations producing less stress. However, it is not just a question of changing temperatures, as some of these physical processes (notably freeze–thaw and haloclasty) require moisture and changes in rainfall may be critical to altering the water supply. Global warming will reduce the impact of freeze–thaw weathering in many parts of the world, by increasing minimum temperatures to above freezing point over large parts of the year. However, other areas which currently experience near-continuous freezing may become more vulnerable to freeze–thaw action as maximum temperatures rise more frequently above zero, thus buildings in some permafrost areas may become more vulnerable to deterioration. Furthermore, currently very dry cold areas may become more prone to frost weathering if rainfall increases bringing more water, as is predicted for northern hemisphere high latitudes by the end of the twenty-first century (see Table 1).

The three main processes of salt weathering (crystallization, hydration and thermal expansion) will each respond to altered temperature cycling in different ways, and the overall net effect may be very hard to predict and quantify.

This is especially true where (as in many environments) mixtures of salts are found. Salts become more soluble at higher temperatures, some remarkably so (e.g. sodium sulphate is only 14% as soluble at 0°C than at 35°C). Thus, warming may discourage crystallization out of solution. On the other hand, increasing temperatures may encourage evaporation which also helps to promote crystallization through the production of supersaturated solutions (Goudie & Viles 1997). Hydration of salts is highly sensitive to temperature and humidity, and thus may be affected by climate change, as will thermal expansion. However, climate change will also have indirect effects on salt weathering as it may increase the presence of salts as well as the presence of moisture and the nature of temperature cycling. Increasing aridity in some vulnerable areas, for example, may encourage evaporation and movement of salts to the near-surface zone, providing more scope for salt weathering.

Chemical weathering processes will be affected by changing atmospheric composition, increased temperatures, and alterations in rainfall amounts. Increasing concentrations of some trace gases will accelerate some weathering reactions, but these increases will probably be minor in comparison with the changes in atmospheric chemistry induced by local air pollution. Most chemical reactions are encouraged by higher temperatures and water acts as an important reagent within which chemical reactions to take place. Some important weathering reactions will be influenced by a range of components of climate change. For example, in terms of the dissolution of limestone in water acidified by carbon dioxide, warmer temperatures will reduce the rate of dissolution of carbon dioxide in water, but conversely will shift the equilibria of the $CO_2 \leftrightarrow H^+ + HCO_3^-$ system. Also, higher concentrations of CO_2 in the future global atmosphere will further encourage dissolution. Higher air temperatures and more rainfall will favour chemical weathering in general (Kump *et al.* 2000), but areas which experience declines in rainfall may not see such change.

The biological component of stone deterioration will undoubtedly experience important alterations as a consequence of climate change, as species and communities react to changing environmental conditions. Micro-organisms and lower plants such as lichens contribute to stone deterioration through biophysical processes (stresses produced by growing, wetting and drying etc.) and biochemical processes (decomposition of minerals through excretion of organic acids and other compounds, and the production of new mineral forms), but can also play a bioprotective role through providing a surface cover which reduces the impact of other decay processes. As Prieto *et al.* (2000) point out from studies of a mixed lichen community on granite monuments, different lichen species can have very different effects on biodeterioration at one site.

The impacts of climate on micro-organism communities (especially the biofilms common on the surface of many building stones) are much less well understood than those on higher plant communities and animal species. As many micro-organisms extract nutrients from atmospheric inputs, the impacts are likely to be great. On the other hand, many micro-organisms are extremely tolerant and grow under a wide range of environmental conditions including some very hostile environments in which they appear to play key roles in mineral transformations (for example, the biodegradation of pollutants on black crusts; Saiz-Jimenez 1997). One hypothesis about the impacts of climate change on biodeterioration is that as rainfall increases, biological growth will also increase, but the growth will be more benign and less damaging than in drier environments where endolithic growth forms are common (Viles 1995). Certainly, there has been a rise in some biodeteriorative lichen species in Britain, such as the recent spread of *Dirina massiliensis* forma *sorediata* reported by Seaward (1997). However, the reasons for this are uncertain, and may relate to both changes in climate and reduction in air pollution. B. J. Smith (pers. comm.) has noted a rise in algal coverage on sandstone walls in Belfast, Northern Ireland, which seems to be correlated with increasing precipitation levels. Further work needs to be done to establish whether changing climates will alter the balance in any one area between biophysical and biochemical attack and bioprotection.

Indirect effects of climate change: sea level, biota and groundwater alterations

Locally, indirect effects of climate change may be particularly crucial to the future of stone deterioration. Near-coastal sites, for example, in areas likely to experience relatively large rises in sea level may experience a shift in dominance of weathering processes related to marine influences (such as salt weathering). Studies in the Mediterranean coastal zone, for example the work of Moropoulou *et al.* (1995) in Rhodes, indicate the important role that the marine

environment plays in conditioning decay. More generally, changes in terrestrial biota as a consequence of global warming may have knock-on effects on stone deterioration, through changing shading, leaf drop and alterations in plant effects on soil moisture and chemistry. Because of time lags in the reaction of vegetation to climate change, and the compounding influences of local human activity on plant communities around most buildings, these impacts are probably going to be generally minor. One possibly widespread and fundamental result of global warming is likely to be alterations in the depth and composition of groundwater which will have several impacts on stone deterioration. Where groundwater levels rise, the 'wick effect' (Goudie 1986) may become a more important component of damage to building stone, especially when soluble salt contents also rise. Several recent studies from low-lying areas with a propensity for salinization indicate potentially severe impacts of future climate change. Thus, Sherif & Singh (1999) suggest that a 50 cm rise in sea level around the Mediterranean will cause saline water to intrude a further 9 km inland in the Nile Delta aquifer. Local subsidence is occurring in the Nile Delta region which compounds relative sea level rise here, and pumping of groundwater and damming upstream are also reducing the supply of fresh water. Similar saltwater intrusion has occurred in the coastal plains of the Lower Mary River, Australia, for a range of reasons, and may occur more widely in other coastal lowland settings in Australia as a result of global warming (Mulrennan & Woodroffe 1998). Already such salinization is having an impact on archaeological sites (e.g. Roman ruins on the Tunisian coast are now in salinized soils; Oueslati 1995) and may affect modern buildings in vulnerable areas around the Mediterranean and in the Middle East.

Indirect effects of climate change: social change

The reaction of human societies to global warming will, in itself, provide some major impacts on stone deterioration. Warming of urban areas will, in cooler parts of the world, reduce the need for extensive heating inside buildings. This will have at least two rather different impacts on stone deterioration. Directly, this will produce less of an obvious temperature gradient in winter between external and internal walls, and indirectly, it will lead to less burning of fossil fuel for generation of heat (with concomitant effects on local air pollution levels, as well as a reduction of global greenhouse gas emissions from fossil fuel burning). Reductions in the need for de-icing salt (or urea) application to freezing-prone roads have also been mentioned, and will reduce the damage caused by such agents to roadside stone. In hotter climates, global warming may increase the need for internal air conditioning, thus causing increased external/internal temperature gradients, and increasing pollution associated with energy generation. Other human responses to climate change are less easy to quantify, and their impacts on stone deterioration are probably varied but of low importance. For example, climate change bringing increased rainfall might encourage different architectural styles and the use of different materials. Worries about human contributions to global warming might also encourage the use of more 'environmentally friendly' techniques of construction, and the revitalized use of locally sourced building materials.

Weighing up competing impacts

A key task which awaits the research community is to provide a balanced assessment of the different levels of risk provided by the various aspects of climate change for the built environment and stone deterioration. Undoubtedly, some of the impacts discussed in the previous section will be more important than others, and the balance between them will vary from area to area. Stone deterioration in reality involves a complex mixture of chemical, physical and biological processes and we need to be able to analyse the impacts of climate change on this nexus of interacting processes. The analysis so far has also only considered stone deterioration, but there is also the whole linked issue of stone soiling, which will also be affected by climate change. For example, increased rainfall may encourage removal of dust and pollution-generated particulates, but on the other hand may encourage micro-organism growths which themselves can produce extensive soiling. The impacts of climate change need to be compared with other threats to building fabric, such as air pollution, natural hazards (such as earthquakes), and management practices. A conceptual framework for looking at the competing, and often interacting, risks facing buildings in the future is presented in Figure 1. Modelling provides a useful way of investigating these competing risks, through simulating the (often synergistic) processes which operate on stone surfaces and investigating the variation of these processes as a result of changes in key climatic parameters

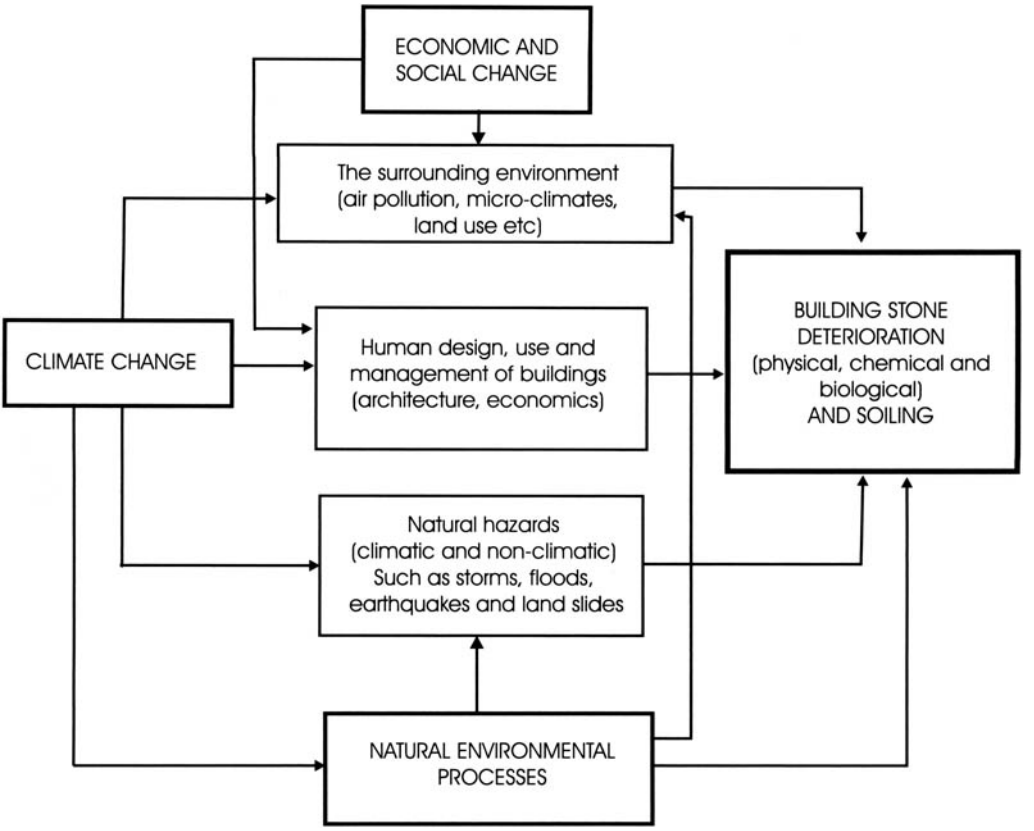

Fig. 1. A conceptual diagram of climate change and other factors affecting future building stone deterioration.

(e.g. temperature and rainfall). Antill & Viles (in press) present details of a numerical model which simulates a range of decay processes on limestone and could be used to investigate the future impacts of climate change. Although climate change will have an impact upon individual deterioration processes as discussed in the review above, perhaps what is of most concern to building managers is the overall effect on rates of weathering and erosion. Studies such as the National Materials Exposure Programme (NMEP) and International Materials Exposure Programme (IMEP) provide a vast data source on rates of decay of exposure tablets in different environmental conditions which could provide useful information.

Scale issues in relating climate change to stone deterioration

An important issue is the difficulty of linking global-scale changes in climate to the deterioration of individual walls, buildings or structures. One aspect of this is the problems involved in meaningful downscaling of global climatic predictions to smaller regions. A second aspect is the difficulty of relating regional climatic data to the microclimates which control most weathering processes (Pope *et al.* 1995; Viles 2001). For example, despite given rainfall amounts recorded for a city at the local meteorological station, the four walls of a building in a city centre street canyon may receive highly variable and contrasting amounts of rainfall. Similarly, average air temperature values from a meteorological station will not reflect the diversity of temperatures experienced on stone surfaces within the complex geometry of buildings, but it is these temperatures which are crucial to the deterioration processes occurring on those surfaces. Some progress has been made in understanding the relationships between regional climate and the microclimates of buildings, but this needs to be consolidated upon if useful predictions are to be made.

Investigating the future of stone deterioration in urban Britain

As an example of the way forward for predicting the impact of climate change on stone deterioration it is helpful to consider the case of the UK where several recent projects have produced (a) downscaling of climate characteristics and predictions which would be used as a basis for analysis and (b) long-term records of overall rates of stone decay which could be continued into the future. Comparison of the two sequences would allow simple quantification of the relations between climate and overall rates of stone decay.

Downscaling climate predictions

Several attempts have been made to produce UK-wide predictions of climate change, based on the global IPCC scenarios. Although there are many flaws with such attempts, given the vast gaps in knowledge about the behaviour of climate within the NW European area, some useful scenarios have been produced by the UK Climatic Impacts Programme (UKCIP) which form the basis of the subsequent discussion (Hulme & Jenkins 1998). The UKCIP98 predictions (which will be updated in 2002) present four scenarios of change (low, medium-low, medium-high and high) for three times (2020s, 2050s and 2080s). According to these scenarios, average temperatures could have risen between 0.9 and 3.2°C by 2080, with rain increasing by as much as 15% in parts of England and Wales and 17% in Scotland by the same time. Seasonal changes are expected also, with autumns and winters becoming wetter. In spring and summer rainfall patterns are likely to alter, giving wetter conditions in the NW and drier in the SE: for example, rainfall decreases by up to –22% in the south for the high scenario in the 2050s. Temperature rises are likely to be more pronounced in the southeastern parts of the UK, with less rapid rises in the NW. Dramatic decreases in the numbers of days with temperatures less than 0°C are also predicted, with up to 45% fewer by the 2020s, with the greatest changes in NW Scotland, NE coast of England and SW England. These trends mirror accentuations of climatic gradients within the UK during the 1980s and 1990s which are related to changes in the vigour of the westerly circulation caused by alterations in the North Atlantic Oscillation (Mayes 2000). Harrison *et al.* (2001) have taken the UKCIP predictions and, using an 'unintelligent' downscaling method coupled with principal component analysis (PCA) and cluster analysis, produced climatic predictions for a series of 21 bioclimatic zones across the whole of the UK and Ireland. Two zones out of these 21 are discussed in more detail here, firstly zone 13 which covers much of central Northern Ireland and central Southern Ireland, and zone 19 which covers the south and SE coast of England. Figure 2 illustrates the changes in summer and winter temperatures and summer and winter precipitation predicted for these areas under the UKCIP98 scenarios.

Stock-at-risk and stone decay rates

There have also been many attempts to characterize the 'stock-at-risk' in terms of the natural stone building fabric in Britain. As a simple first approximation, we can see that the north and west of the UK are characterized by the presence of stone buildings constructed from acid rocks (especially granites and a range of sandstones), whilst the south and east contain a large stock of buildings and monuments made of limestone, with flints and also popular building materials. Clearly, this is a gross simplification, as most areas contain a great diversity of ages and types of building material, within various architectural styles, and with an increasing dominance of concrete and other non-natural stone materials.

Information on long-term stone decay rates of sandstones and limestones across the UK may be obtained from the NMEP (Butlin *et al.* 1992; Viles *et al.* in press) which ran from 1987 to 1995. Analysis of the NMEP data shows there is no simple relation between stone decay rates and any one climatic parameter. A more detailed dataset of climate, air pollution and stone decay rates comes from the long-term monitoring at St Paul's Cathedral, London (Trudgill *et al.* 2001). Erosion rates on the balustrade of this Portland limestone building have been measured since 1980 using a micro-erosion meter. As Figure 3 shows, erosion rates can be related to trends in both air pollution (SO_2 concentrations) and rainfall, and show a decline over the 20 year period, but no clear causal picture emerges.

Results

Putting regional climatic changes, stock-at-risk and erosion rate studies together, we can see that the NW with its concentrations of acidic building stones such as granite and sandstones is likely to face warmer and wetter conditions, whilst the SE where many limestone buildings are located will experience increased temperatures and drier conditions. Table 3 indicates

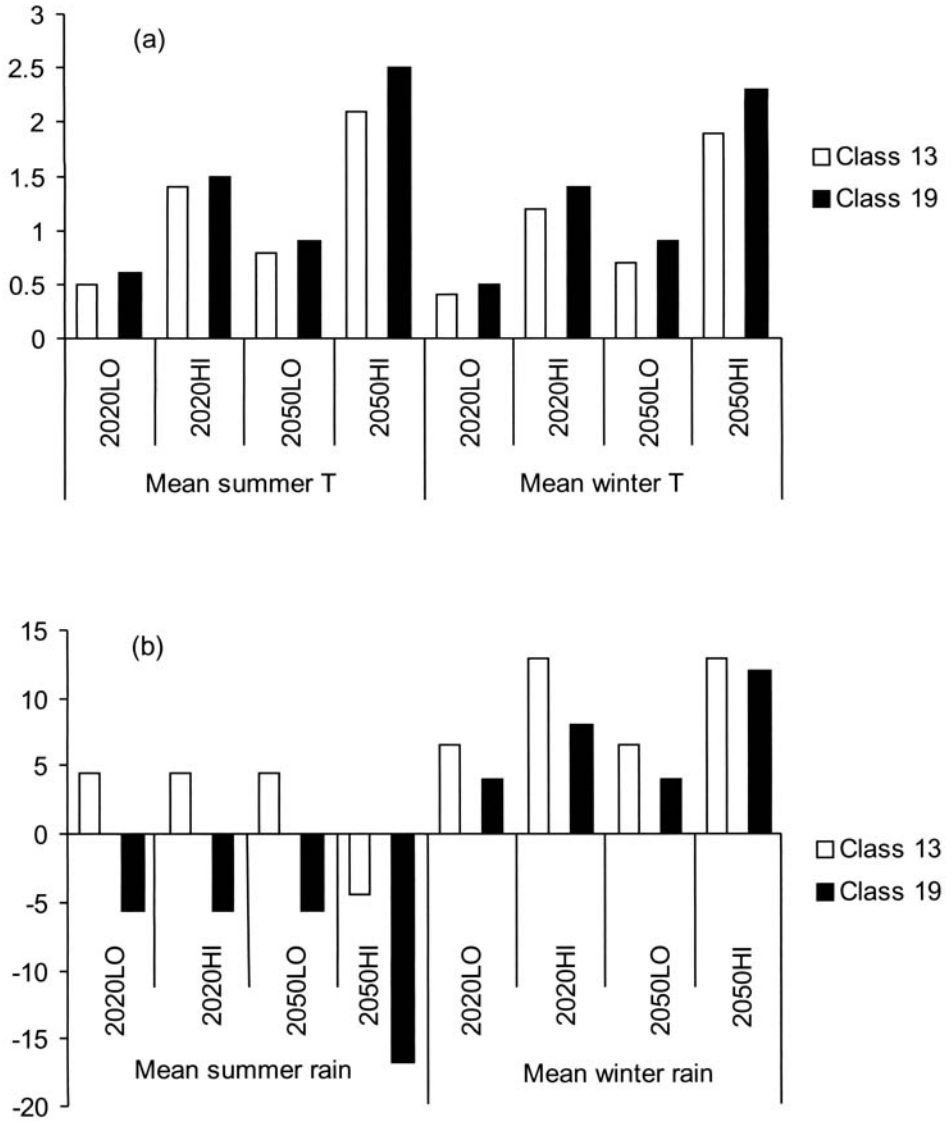

Fig. 2. Predicted increases in (**a**) temperature (°C) and (**b**) rainfall (mm) for winter and summer under a range of UKCIP98 scenarios for bioclimatic class 13 (central and Northern Ireland) and class 19 (coastal south and SE England). Data from Harrison *et al.* (2001).

some possible consequences for the processes of stone decay. In the NW increased biological soiling and chemical weathering are likely, whereas in the SE more salt crystallization and biodeterioration (if drier conditions promote environmental stresses which encourage endolithic growth) should occur. So, the balance of processes operating on different stone types in different areas is likely to change, producing a more pronounced NW–SE gradient (instead of the urban–rural gradients observed in previous decades when urban air pollution was severe). These changes need to be set in the context of generally declining urban pollution levels, which encourages biological growths (such as lichens on acidic stones) and reduces the direct threat of air pollution-enhanced decay to building fabric. However, locally (such as roadside locations) traffic continues to be a major cause of decay and soiling.

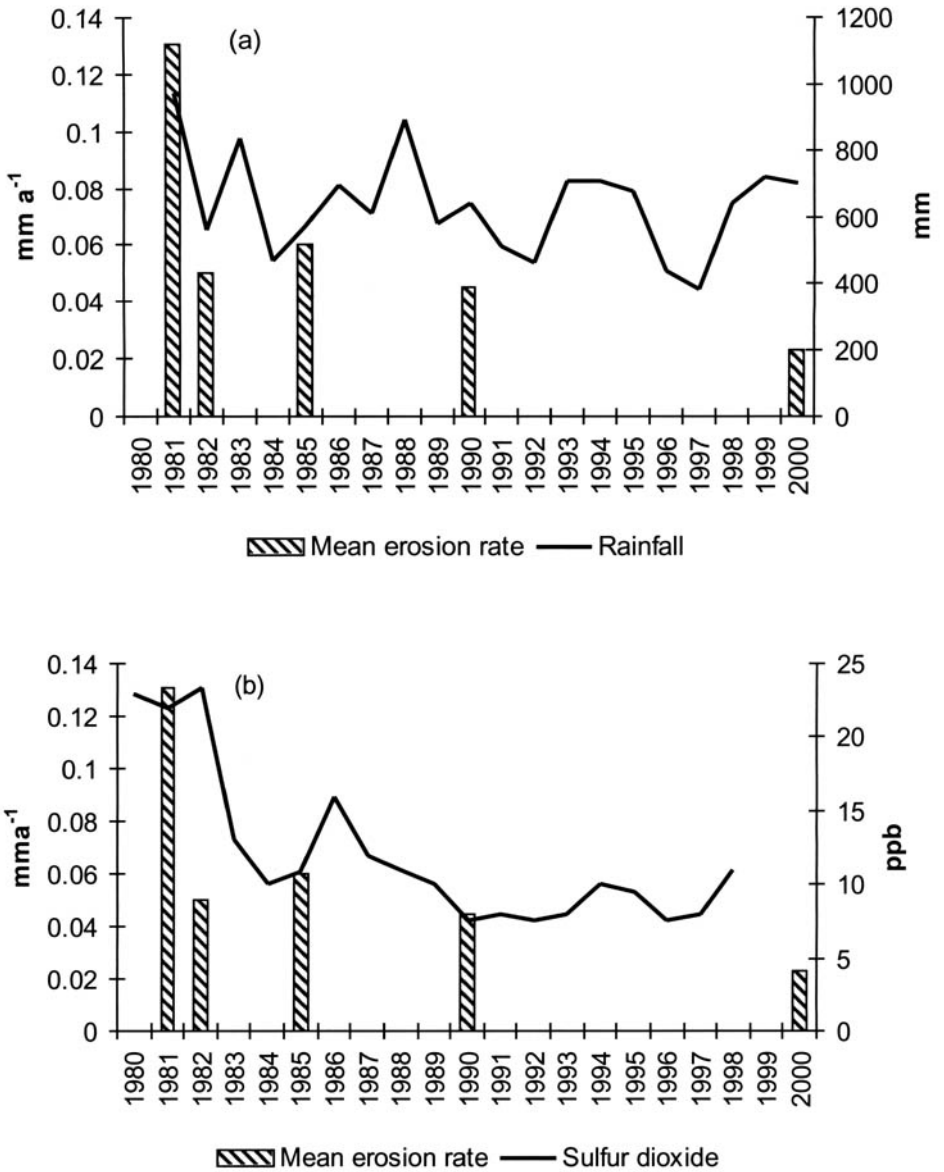

Fig. 3. Erosion rate of Portland limestone balustrade at St Paul's Cathedral, London, plotted with (**a**) rainfall and (**b**) SO_2 concentrations over the period 1980 to 2000. Modified after Trudgill *et al.* (2001).

Whether a 1–2°C temperature rise, and its concomitant effects on precipitation, will have a significant impact on the balance and rate of decay processes needs to be tested further. Taking the information in Figure 2 and applying it to the known climate patterns in key urban areas, such as Belfast (zone 13) and London (zone 19) would enable some predictions of the likely impacts of these climate changes on stone decay rates. Note the increases in both summer and winter rainfall predicted for the Belfast area, and the dramatic decreases in summer rain predicted for the London area. Alternatively, utilizing the information already collected from the NMEP provides some insights into the relations between climatic trends and stone decay, although it is difficult to decouple the impacts of air pollution. Continuing the

Table 3. *Possible consequences of future climate change for building stone decay in the UK*

	Dominant building stone type	Process responses	Other threats	Overall response
NW – warmer, wetter winters	Siliceous sandstones and granites	Increased chemical weathering. Less freeze–thaw weathering. More organic growths contributing to soiling.	Increased storm activity may cause episodic damage. Increased wave heights may encourage faster weathering in coastal areas. Increased flooding may encourage decay.	Enhanced chemical decay processes and biological soiling, reduced physical decay processes
SE – warmer, drier summers	Limestones	Less freeze–thaw weathering. Reduced chemical weathering as a result of less available water. Increased salt crystallization in summer. More deteriorating organic growths.	Increased drying of soils (especially clay-rich soils) will encourage subsidence and building damage. Low-lying coastal areas will be particularly prone to marine encroachment. Increased drought frequency may encourage decay.	Enhanced physical and biological weathering, more dust for soiling, reduced chemical weathering

monitoring at St Paul's Cathedral will also provide invaluable 'real-time' information on changing erosion rates, climate and air pollution over the twenty-first century.

Conclusions

Qualitative assessments of the influence of various aspects (direct and indirect) of climate change on a range of stone deterioration processes can be made using information on the links between climate and decay processes. Numerical modelling offers a way forward to provide more sophisticated analyses and quantitative predictions. It must be borne in mind, however, that our knowledge of climatic change in the future is still not specific enough to make very detailed assessments. Several long-term measurement projects provide a rich data source on overall weathering rates which could also be used to provide correlations with climatic parameters and thus help illustrate the likely trends in stone deterioration in the future. The challenge remains for the building stone deterioration community to provide answers for building managers and planners about how climate change will impact upon stock-at-risk.

References

ANTILL, S. A. & VILES, H. A. (in press). The development and use of computer simulation techniques in the study of weathering processes. *In*: SEARLE, D. (ed.) *Proceedings, SWAPNET 99*. University of Wolverhampton Press.

BUTLIN, R. N., COOTE, A. T., DEVENISH, M. *et al.* 1992. Preliminary results from the analysis of stone tablets from the National Materials Exposure Programme (NMEP). *Atmospheric Environment*, **26B**, 189–198.

CHANGNON, S. A. (ed.) 2000. *El Nino 1997–1998*. Oxford Univerity Press, New York.

DIAZ, H. F. & MARKGRAF, V. (eds) 2000. *El Nino and the Southern Oscillation*. Cambridge University Press, Cambridge.

GOUDIE, A. S. 1986. Laboratory simulation of 'the wick effect' in salt weathering of rock. *Earth Surface Processes and Landforms*, **11**, 275–285.

GOUDIE, A. S. 1996. Geomorphological 'hotspots' and global warming. *Interdisciplinary Science Reviews*, **21**, 253–259.

GOUDIE, A. S. & VILES, H. A. 1997. *Salt Weathering Hazards*. John Wiley, Chichester.

GRIME, J. P., BROWN, V. K., THOMPSON, K. *et al.* 2000. The response of two contrasting limestone grasslands to simulated climate change. *Science*, **289**, 762–765.

HARRISON, P. A., BERRY, P. M., & DAWSON, T. E. (eds) 2001. *Climate Change and Nature Conservation in Britain and Ireland*. UKCIP, Oxford.

HOUGHTON, J. T., DING, Y., GRIGGS, D. J. *et al.* (eds) 2001. *Climate Change 2001: The Scientific Basis*. Cambridge University Press, Cambridge.

HULME, M. & JENKINS, G. J. 1998. *Climate Change Scenarios for the United Kingdom: Scientific Report*. UK Climate Impacts Programme Technical Report No 1. Climate Research Unit, Norwich.

KUMP, L. R., BRANTLEY, S. L. & ARTHUR, M. A. 2000. Chemical weathering, atmospheric CO_2 and climate. *Annual Reviews of Earth and Planetary Science*, **28**, 611–667.

LIU, Z., KUTZBACH, J. & WU, L. 2000. Modelling climate shift of El Nino variability in the

Holocene. *Geophysical Research Letters*, **27**, 2265–2268.

McCabe, G. J. & Dettinger, M. D. 1999. Decadal variations in the strength of ENSO teleconnections with precipitation in the western United States. *International Journal of Climatology*, **19**, 1399–1410.

Mayes, J. 2000. Changing regional climatic gradients in the United Kingdom. *The Geographical Journal*, **166**, 125–138.

Moropoulou, A., Theoulakis, P. & Chrysophakis, T. 1995. Correlation between stone weathering and environmental factors in marine atmosphere. *Atmospheric Environment*, **29**, 895–903.

Mulrennan, M. E. & Woodroffe, C. D. 1998. Saltwater intrusion into the coastal plains of the Lower Mary River, Northern Territory, Australia. *Journal of Environmental Management*, **54**, 169–188.

Oueslati, A. 1995. The evolution of low Tunisian coasts in historical times: from progradation to erosion and salinization. *Quaternary International*, **29/30**, 41–47.

Pope, G. A., Dorn, R. I. & Dixon, J. C. 1995. A new conceptual model for understanding geographical variations in weathering. *Annals, Association of American Geographers*, **85**, 38–64.

Prieto, B, Edwards, H. G.M. & Seaward, M. R. D. 2000. A Fourier transform-Raman spectroscopic study of lichen strategies on granite monuments. *Geomicrobiology Journal*, **17**, 55–60.

Saiz-Jimenez, C. 1997. Biodeterioration vs. biodegradation: The role of microorganisms in the removal of pollutants deposited on historic buildings. *International Biodeterioration and Biodegradation*, **40**, 225–232.

Seaward, M. R. D. 1997. Major impacts made by lichens in biodeterioration processes. *International Biodeterioration and Biodegradation*, **40**, 269–273.

Sherif, M. M. & Singh, V. P. 1999. Effect of climate change on sea water intrusion in coastal aquifers. *Hydrological Processes*, **13**, 1277–1287.

Sykes, M. T., Prentice, I. P. & Cramer, W. 1996. A bioclimatic model for the potential distributions of north European tree species under present and future climates. *Journal of Biogeography*, **23**, 203–223.

Trudgill, S. T., Viles, H. A., Inkpen, R. J. *et al.* 2001. Twenty-year weathering remeasurements at St Paul's Cathedral, London. *Earth Surface Processes and Landforms*, **26**, 1129–1142.

Viles, H. A. 1995. Ecological perspectives on rock surface weathering: Towards a conceptual model. *Geomorphology*, **13**, 21–35.

Viles, H. A. 2001. Scale issues in weathering studies. *Geomorphology*, **41**, 63–72.

Viles, H. A., Taylor, M. P., Yates, T. J. S. & Massey, S. W. 2002. Soiling and decay on N. M.E. P. limestone tablets. *The Science of the Total Environment*, **292**, 215–229.

Wilby, R., O'Hare, G. & Barnsley, N. 1997. The North Atlantic Oscillation and British Isles climate variability, 1865–1996. *Weather*, **52**, 266–276.

Evaluation of the origin of sulphate compounds in building stone by sulphur isotope ratio

WERNER KLEMM[1] & HEINER SIEDEL[2]

[1]*Freiberg University of Mining and Technology, Institute of Mineralogy, Brennhausgasse 14, D-09596 Freiberg, Germany (e-mail: wklemm@mineral.tu-freiberg.de)*

[2]*Dresden University of Technology, Institute of Geotechnical Engineering, Chair of Applied Geology, D-01062 Dresden, Germany*

Abstract: Sulphate salts are a main factor in the deterioration of building materials such as natural stone, mortar, plaster and brick. Although environmental pollution is the main source for the formation of sulphate salts on historical monuments in Central Europe, for more detailed investigations into the reasons for salt formation on specific buildings more precise information about the sources and the transport paths is needed. Sulphur isotope analyses seem to be a useful tool for the characterization of various sources of sulphur in the natural as well as in the anthropogenic environment relevant to salt formation on monuments. Investigations in the southern part of East Germany with extreme environmental pollution until 1990 should demonstrate the advantages and limits of the method. Environmental influences are the main factor for sulphate salt formation at historical monuments in this area. In special cases other sources such as groundwater or building materials are relevant for salt formation. At a regional scale, the $\delta^{34}S$ values for salts and crusts on monuments scatter over a broad range (between +2 and +10‰ in the investigated area). Nevertheless, for special locations or monuments the number of possible sources of sulphur can be minimized if $\delta^{34}S$ values for all relevant influences such as building materials, groundwater and the specific environmental influences (rainwater, dust, SO_2) are available.

Among the salts harmful to building materials, sulphates of cations such as Ca, Mg, Na and K play a dominant role. Potential sources of sulphur include atmospheric pollution (gaseous SO_2 or solid/dissolved SO_4^{2-}), building stones themselves, binder materials and aggregates, the building ground (rising humidity from soil or groundwater) as well as the application of unsuitable repair materials or cleaning and conservation agents. A combination of several of these sources is possible. For the study of deterioration of a specific building all relevant sulphur sources and transport paths have to be taken into consideration and assessed at the beginning of an investigation. Only a good diagnosis can guarantee the right choice of an adequate restoration measure and the sustainability of the intervention. In the case of more complex influences a good diagnosis is rarely possible using classic investigations of salt distribution in a building wall alone. To complement these, the sulphur isotope ratio provides additional information regarding the origin of the sulphate compounds. The basic investigations at a regional scale presented in this study examine if and under which circumstances the sulphur isotope ratio can be applied to fingerprint the different sulphur sources. As the sulphur from air pollution (SO_2, acid rain) is the most frequent source for salt formation on building materials in Central Europe the main target is to distinguish this airborne sulphur from other possible sources.

Environmental pollution by sulphur components and their isotope composition

The global emission of SO_2 is the main source for sulphur compounds in the air and for the higher acidity, i.e. lower pH, of the rainwater.

The high concentrations of sulphate compounds that have accumulated on and in building materials and have resulted in significant material damage are due to long-term exposure. This complicates the reliable identification and quantification of the amount of anthropogenic sulphur involved in the corrosion and salt-forming processes. Exact values for current and past local and regional sulphur emissions are lacking in some areas or are not known completely.

The environmental situation in East Germany has improved remarkably since

From: SIEGESMUND, S., WEISS, T. & VOLLBRECHT, A. 2002. *Natural Stone, Weathering Phenomena, Conservation Strategies and Case Studies*. Geological Society, London, Special Publications, **205**, 419–429.
0305–8719/02/$15.00 © The Geological Society of London 2002.

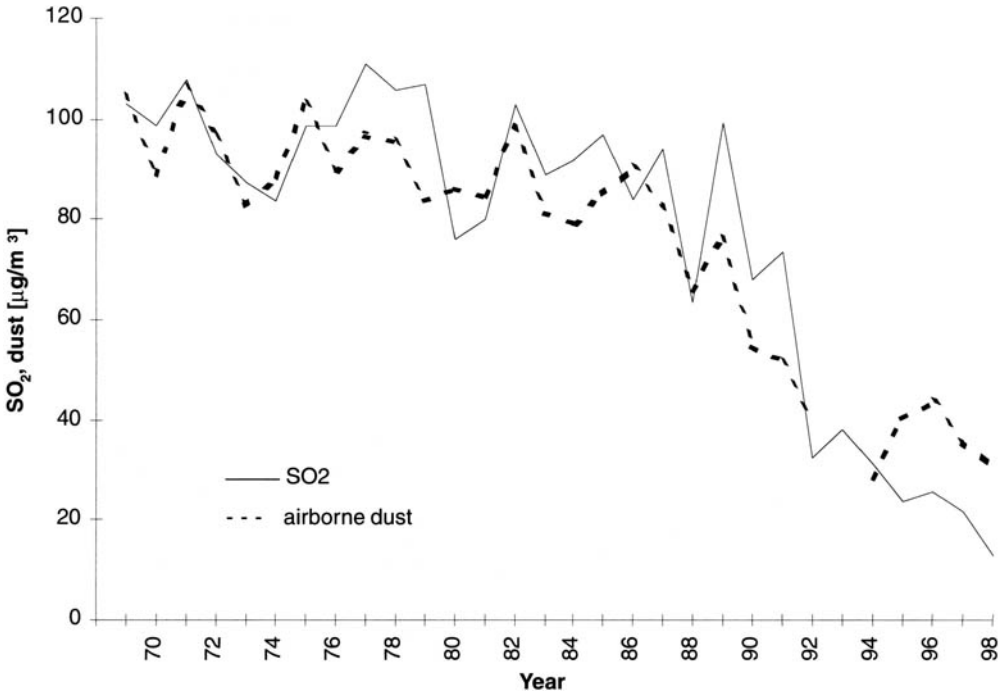

Fig. 1. Mean values of atmospheric SO_2 and dust concentration in Dresden–Radebeul (1969–1998). Data from Sächsisches Landesamt für Umwelt und Geologie.

political reunification in 1990. However, a look into the past shows the extreme long-term pollution of the environment in this area as can be demonstrated by the evolution of average values for SO_2 and dust in the last decades (Fig. 1). The salt accumulations in masonry caused by environmental pollution in the past are now developing their own reaction dynamics even though the actual emission of sulphur has decreased drastically.

The first case studies on buildings (Pye & Schiavon 1989; Rösch & Schwarz 1993; Nord & Tronner 1995) as well as investigations on sources of air pollution and their interactions with the surface of buildings (Dequasie & Grey 1970; Longinelli & Bartelloni 1978; Buzek & Šramek 1985; Torfs *et al.* 1997) show that the analysis of the sulphur isotope composition used as a fingerprint can provide valuable information in this field.

Sulphur consists of the four stable isotopes: ^{32}S (95.02%), ^{33}S (0.75%), ^{34}S (4.21%) and ^{36}S (0.02%). For isotope investigations normally the measured ratios $^{34}S/^{32}S$ are compared to a standard (the Canon Diablo Troilite, CDT) and given as $\delta^{34}S$ value (in ‰):

$$\delta^{34}S = [(^{34}S/^{32}S)_{sample} - (^{34}S/^{32}S)_{standard}{}^{-1}] \times 1000$$

The $\delta^{34}S$ values of sulphur occurring naturally in the atmosphere result from a mixture of sea water spray, volatile biogenic sulphides (e.g. dimethyl sulphide) from inland and sea water, gas emission from the Earth's crust as well as volcanic eruptions in variable quantities.

The anthropogenic pollution of the air with sulphur components is first of all a result of the combustion of coal, mineral oil and natural gas, the smelting of sulphidic ores and the processing of sulphur in industry. Despite the global character of sulphur pollution in the air, the $\delta^{34}S$ values for components such as SO_2 and SO_4^{2-} in a given locality result from the mixture of different local and regional sources and from the natural background. Both the natural and the industrial sources depend on the given specific local conditions. The reaction of the emitted SO_2 to SO_4^{2-} which might lead to an additional change in isotope ratio has as yet not been sufficiently investigated.

The accumulation of sulphate near the surface of stonework or stone sculptures may

Table 1. *$\delta^{34}S$ values for SO_2, rainwater sulphate and crusts on building surfaces measured in USA and several European countries*

Location	SO_2 $\delta^{34}S$ (‰)	Sulphate in rainwater $\delta^{34}S$ (‰)	Crusts on buildings $\delta^{34}S$ (‰)	Reference
Salt Lake City (USA)	−0.68 to +2.96	−1.96 to +6.9	−0.6 to +1.8	Dequasie & Grey (1970)
Antwerp (Belgium)	−11.5 to −0.6	−0.9 to +4.2	−8.3 to +0.8	Torfs *et al.* (1997)
Brunswick (Germany)	−6.5 to −0.5	–	–	Jäger *et al.* (1989)
Cambridge (UK)	–	–	+3.5 to +6.8	Pye & Schiavon (1989)
Prague (Czech Republic)	+2.3	+5.7	+1.8 to +4.5	Buzek & Sramek (1985)
Stockholm (Sweden)	–	–	+6 to +14	Nord & Tronner (1995)
Venice (Italy)	–	−0.2 to +8.3	+4.6 to +5.6	Longinelli & Bartelloni (1978)
Black Forest (Germany)	–	+2.9 to + 4.4	–	Rolland *et al.* (1989)
Fichtelgebirge (Germany)	+1.0 to + 3.3	–	–	Gebauer *et al.* (1994)

result from the direct reaction of SO_2 with the moist material surface as well as from the interaction with acid rainwater and/or from the deposition of dust. The reaction of SO_2 with material surfaces (dry deposition) is thought to be the dominant process (Wittenburg & Dannecker 1992). The formation of gypsum crusts on building surfaces is mainly caused only by atmospheric sulphur components. In various places in Europe and the USA they show different but limited scatter in $\delta^{34}S$ and do not allow a generally applicable assessment of environmental influences on the basis of mean values. Table 1 shows $\delta^{34}S$ values for atmospheric sulphur compounds and gypsum crusts, characterizing the known global scatter as well as local variations.

Apart from the direct influence of the atmospheric sulphur components on building surfaces, the transport of sulphate with rising damp from the ground is another possible way of sulphate accumulation in stonework. Over decades atmospheric sulphur pollution has led to an accumulation of sulphur in soils in various forms via dust and rainwater. From the total sulphur content in soils, the dominating anthropogenic part of the water-soluble sulphate in seeping groundwater as well as the adsorbed sulphate (extractable by phosphate) must be taken into consideration to account for transport from the ground into the masonry with rising humidity. Systematic isotope investigations of the relation between the sulphur in soils and in the zone of rising damp in buildings are still lacking.

Current knowledge of the $\delta^{34}S$ values of natural and anthropogenic sulphate sources is still incomplete and largely based on individual case studies. On the basis of global mean values and variability of the $\delta^{34}S$ values, a differentiation between the various natural sources of atmospheric sulphur, the main source of emission (combustion and industry), the building materials and the soil below the building, is not possible. From the survey of isotope geochemistry of sulphur in the atmosphere, a range of $\delta^{34}S$ values between −10 and +20 can be expected for the environmentally caused sulphate compounds in buildings.

Analytical methods

The isotope ratio $^{34}S/^{32}S$ was measured on SO_2 using a mass spectrometer (Delta VE, Finnigan MAT). For all types of samples, the sulphur was first separated from the matrix as sulphate, precipitated as $BaSO_4$ and subsequently converted to SO_2 using V_2O_5 (Haubrich 2000). The sampling of atmospheric SO_2 was done with surface active monitoring (SAM) filters, impregnated with alkaline solution (Dämmgen *et al.* 1985; Torfs *et al.* 1997). From crusts and mortars the sulphate was separated by classic soda extraction. Salt efflorescences were dissolved in distilled water and filtered. Total sulphur content was determined by elementary analysis using a Heraeus Vario EL system. Water-soluble sulphate contents in rainwater and in water extracts were analysed by ion chromatography (Metrohm IC 690). Phase analysis in salt efflorescences was performed by powder X-ray diffraction. More details can be found in Klemm & Siedel (1999).

Investigations on natural and environmental influences and building materials

Buildings in regions with different environmental situations

At selected historic buildings located in areas with very different air pollution (Fig. 2), the

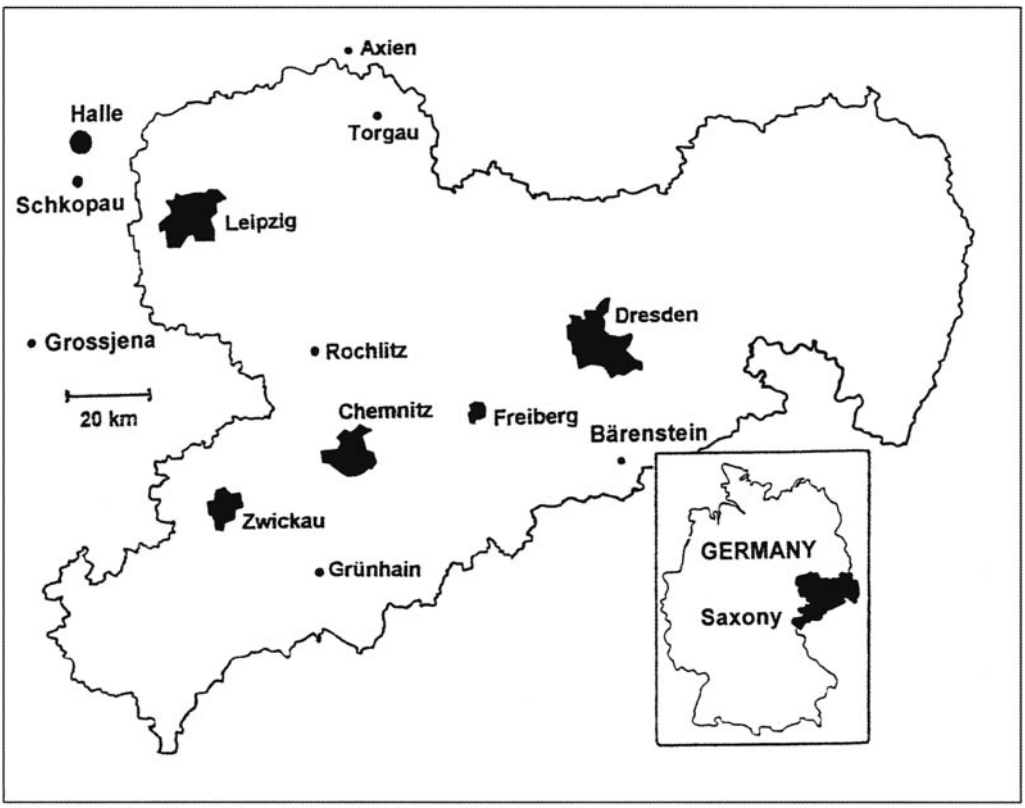

Fig. 2. Sketch map of the investigated area with locations mentioned in the text.

extent to which these complex environmental influences could be deciphered at a regional scale was investigated on the basis of sulphur isotope analyses. In spite of this broad approach, aspects specific to certain buildings were taken into consideration.

Sulphur isotope investigations were performed on salt efflorescences, crusts and building materials from buildings in Axien, Rochlitz and Dresden (Germany) as well as on spot checks of the actual atmospheric sulphur components (SO_2 of the air; SO_4^{2-} in rainfall and dust). Among the sulphate salts that can be found on a building, the black gypsum crusts certainly represent only the environmental influences. Their $\delta^{34}S$ values show limited scatter in specific regions as well as a tendency to more positive values with increasing intensity of environmental pollution (Fig. 3). In Axien, a village in the lowland at least 15 km away from the next small town, no significant local emitters are present. In Rochlitz, a small town lying in a river valley between the industrial centres of Chemnitz and Leipzig, the influences of lignite fuel use in households and local industries must be taken into account as well as the emissions of the industrial centres of the chemical industry and power plants south of Leipzig. The situation of the historic city centre of Dresden, in the Elbe valley, is even worse (annual mean emission values for SO_2 105 μg m^{-3} and dust 77 μg m^{-3} in 1989). Up to the year 1990, the households and industries of the city (population 500 000) mainly received their energy from lignite combustion. A key source of air pollution in the inner city was the lignite-fuelled power plant (currently closed down) only 500 m west of the historic city centre in the most frequent wind direction.

The higher (heavier) $\delta^{34}S$ values of gypsum crusts reflect higher environmental pollution. As the formation of gypsum crusts is a combination of dry and wet deposition processes of sulphur, their $\delta^{34}S$ values are a mixture of various sulphur components of the air (SO_2; SO_4^{2-} from rain, dust particles). The dominance

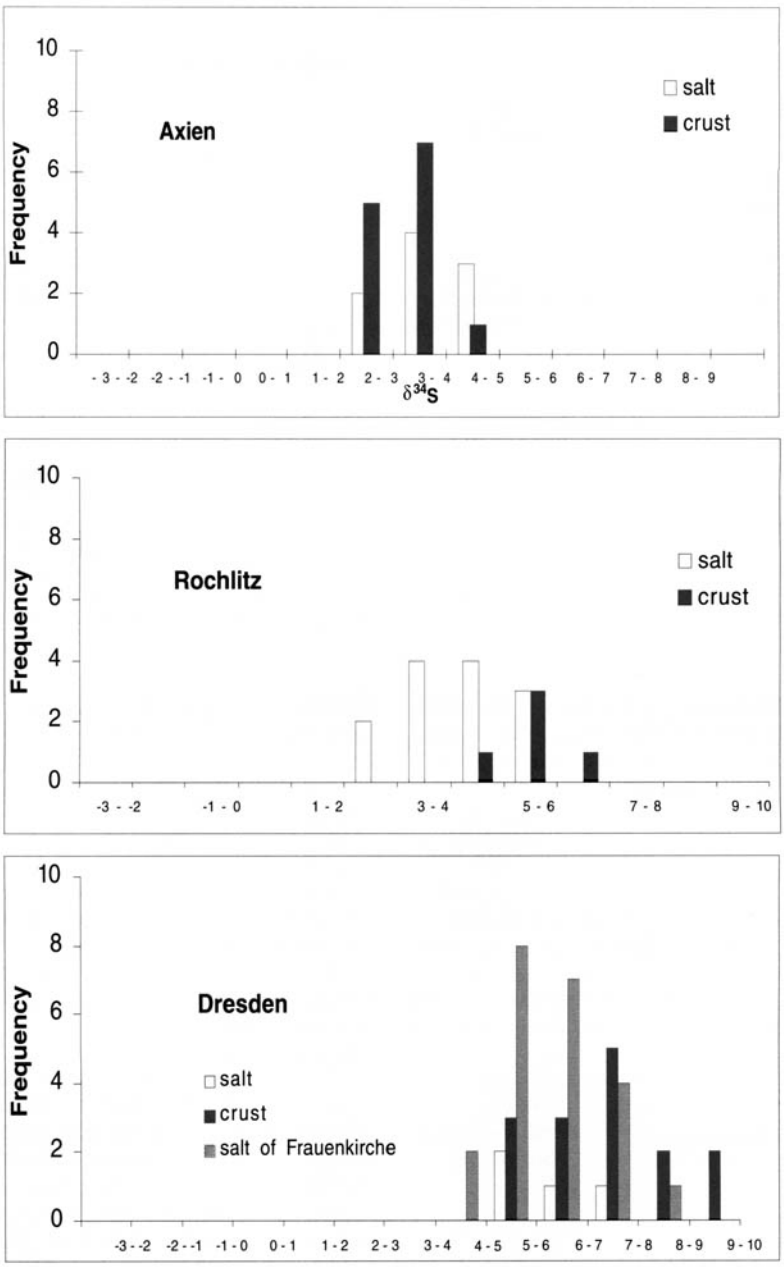

Fig. 3. $\delta^{34}S$ values (in ‰) of crust and efflorescences (salts) in areas of different environmental pollution.

of higher $\delta^{34}S$ in strongly polluted areas and valleys could be interpreted as a higher contribution of SO_4^{2-} from dust particles to crust formation, because they show the highest $\delta^{34}S$ values of all investigated sulphur components from the environment (see below).

The investigations in Axien and Rochlitz showed that magnesium sulphate may also reflect the complex and long-term environmental influences. Magnesium sulphates often occur on buildings with lime mortars produced from dolomitic limestones. Since the magnesium component in the mortar is less stable than the calcium component, intensive and repeated

Table 2. *$\delta^{34}S$ values for efflorescences and building materials at the church of Our Holy Lady in Dresden and for environmental influences*

Material	$\delta^{34}S$ (‰)
Church of Our Holy Lady Dresden, building site	
Efflorescence	
Inside walls	+6.4 to +8.7
Outside walls	+4.8 to +8.4
Mortar	
Joint mortar	+10.4 to +11.8
Grouting mortar	+11.4
Efflorescence test (laboratory) after 10 wet/dry cycles	+9.5 to +9.9
Efflorescence test (laboratory) after 20 wet/dry cycles	+9.3 to +10.3
Tap water	
Used for mortar preparation	+0.9 to +1.0
Original sandstone	
Crusts and thin black layers at the surface	+5.7 to +6.4
Recently quarried sandstone	
Mühlleite quarry	−4.3
City of Dresden	
Crusts at historical buildings	+5.4 to +10.1
Rain water	+4.4 to +7.7
Atmospheric SO_2	+0.3 to +4.5
Atmospheric dust	+11.4

soaking of the mortars by rainfall and the attack of SO_2 lead to the decomposition of the magnesium carbonate and hydroxide compounds and the release of magnesium ions (Hoffmann & Roosz 1978). These ions react with the sulphate, originating from both dry and wet deposition, to form magnesium sulphate efflorescences. For this salt, a narrow range in $\delta^{34}S$ is also found to be typical for local environmental pollution.

In Dresden the efflorescences of other sulphate salts (thenardite, mirabilite, aphtithalite etc.) at several buildings also show an equivalent variation range as the gypsum crusts.

In order to identify additional sources of sulphate with some degree of certainty, these have to be characterized by $\delta^{34}S$ values outside the typical scatter of the local environment.

Differentiation of several sulphur sources

As an example of the type of problems encountered, the investigations carried out on the Church of Our Holy Lady (Frauenkirche) in Dresden and the obtained results will be discussed in more detail. The results of sulphur isotope analyses performed during the rebuilding of the church (destroyed in 1945 at the end of World War II) are summarized in Table 2.

The walls of the church were reconstructed using both old original sandstone and newly quarried sandstone from the Elbe valley. While the newly quarried stones incorporated into the stonework were drying, salt efflorescences started to form on both the inside and the outside walls. On the inside walls, built with only newly quarried sandstone, the salt efflorescence consisted essentially of carbonates. In contrast, on the outside walls, built with both old and new sandstone, mainly sulphates effloresced. The first assumption was that the mortar with pozzolanic additives could be the source of sulphate. However, the $\delta^{34}S$ values of salt efflorescences and the mortar were significantly different. The efflorescences show clearly a lower $\delta^{34}S$ with the lowest values at the outside wall. Efflorescence tests with pure mortar samples in the laboratory atmosphere generated salts with $\delta^{34}S$ values very close to those of the mortar values. Hence, the mortar could be excluded as the originating sulphur source.

The tap water used for mortar preparation had a $\delta^{34}S$ around +1‰ and could also be excluded because systematic wetting of parts of the stonework did not lead to a further decrease of the $\delta^{34}S$ values of the newly formed efflorescence. Very low sulphur concentrations and quite different (negative) $\delta^{34}S$ values for the fresh sandstone from the quarry prove the absence of any 'natural' contribution to the sulphate salt efflorescence. High $\delta^{34}S$ values were found for the sedimenting dust from the air. In contrast, thin black layers on the sandstone surface, some crusts, and sulphate from

Table 3. *Sulphur content and $\delta^{34}S$ values of various binder materials, additives and mortars*

Material	Total sulphur content (wt%)	$\delta^{34}S$ (‰)
Church of Our Holy Lady Dresden building site		
Mortar 450 (for stonework)	0.07	+8.4
Grouting mortar 480	0.06	+11.5
Tubag trass (pozzolanic additive)	0.01	+17.5
Märker trass	0.22	+6.2
Tubag joint mortar	0.1	+10.4 to +11.8
Tubag grouting mortar	0.08	+11.4
Marbos mortar for stonework	0.08	+7.4
Stone repair mortars		
Motema CC	0.27	+5.0
Mineros	0.4	−1.3
Rajasil	0.29	+10.3
Jahn sandstone red	0.30	+5.0
Ledan TB 1	0.7	+7.8

rainwater and especially the SO_2 from the atmosphere show lower $\delta^{34}S$ values.

During the whole building period, the complete building site was totally sheltered from rain and dust by a roof and plastic tarpaulins over the scaffolding. This must be taken into consideration for the interpretation of the data.

The sulphate in the carbonate-dominated efflorescence of the inside walls may only have formed by a reaction of the alkaline pore solution of the mortar with atmospheric SO_2. A small contribution of SO_4^{2-} derived from the mortar cannot be excluded. The few measurements for $\delta^{34}S$ of atmospheric SO_2 in Dresden do not yet allow a certain statement on the long-term mean value, but point towards its influence on salt formation. The efflorescences at original stones of the outside walls are dominated by sulphate compounds and extend also to the neighbouring new sandstone. They were formed preferentially by the reaction of the water-soluble alkaline components from the mortar with the sulphate that is already present in the original sandstone due to its long-term exposure to the environment in the past. The $\delta^{34}S$ values also correspond to the recently measured variation range of environmental influences. Thus, current uptake of SO_2 by the alkaline building materials might also have contributed to salt formation but cannot be precisely differentiated by this method. The salt load of the affected areas is high enough to produce stone damage as can be seen in several places.

Building materials

As shown in the example of the Church of Our Holy Lady in Dresden, the assessment of complex salt formation mechanisms requires that the $\delta^{34}S$ values for the salts, as well as that of the building materials and the environment, be measured. Sulphur isotope data are rare for building stones and for mortar binders. The data presented in Table 3 show that $\delta^{34}S$ values for mortar binders and pozzolanic additives, as well as for stone repair mortars, rarely fall outside the range of environmental sulphur.

Sulphur components of the atmosphere

From the available measurements made on sulphur components, i.e. gaseous SO_2, sulphate in rainwater or in dust from the Dresden atmosphere, the following tendency can be derived:

$$\delta^{34}S\ (SO_2) < \delta^{34}S\ (\text{sulphate rainwater}) < \delta^{34}S\ (\text{sulphate in dust})$$

A larger number of values was measured in the city of Freiberg (Fig. 4). These investigations confirm the tendency shown above. Samples of atmospheric SO_2 and sulphate in rainwater collected at the same time exhibit a nearly constant difference in $\delta^{34}S$ values of about 3‰ (Table 4). Further investigations are required to find out whether the usual sample technique employed for SO_2, i.e. the use of filters saturated with an alkaline solution, may cause the systematic change of the isotope ratio (cf. Torfs *et al.* 1997). This is a question of general interest because the sampling technique is actually a simulation of the SO_2 reaction in the stonework. Initial laboratory tests indicate a fractionation.

The combustion of lignite is thought to be the main anthropogenic source for sulphur pollution of the atmosphere. Analyses of the $\delta^{34}S$ values of gypsum from flue gas desulphurization plants could provide information about the

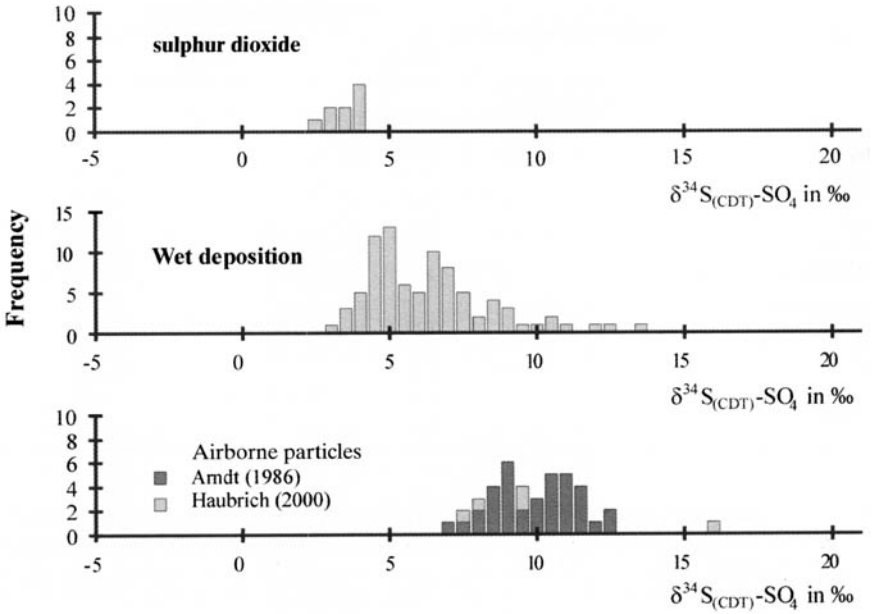

Fig. 4. Distribution of $\delta^{34}S$ values for airborne SO_2 and sulphate in wet deposition and dust (according to Haubrich 2000).

Table 4. *$\delta^{34}S$ in atmospheric SO_2 and in rainwater sulphate and SO_2 deposition rates (determined as SO_4^{2-}) in Freiberg 1997–1998 (from Haubrich 2000)*

Atmospheric SO_2			Sulphate in rainwater	
Period	$\delta^{34}S$ (‰)	SO_4^{2-} (mg/m²d)	Period	$\delta^{34}S$ (‰)
1997			1997	
27.03–24.04	+3.2	8.3	23.03–28.04	+7.0
29.04–12.06	n.d.	7.1	28.04–08.06	+6.0
12.06–24. 07	+4.4	7.7	08.06–26.07	+6.8
24.07–04. 09	+3.3	9.8	26.07–03.09	+6.4
04.09–12.10	+2.4	9.1	03.09–12. 10	+6.6
16.10– 24.11	+2.2	10.3	15.10–22. 11	+5.9
27.11– 06.01	+1.7	9.9	22.11–06. 01	+5.2
1998			1998	
06.01– 16.02	+3.1	10.8	06.01–09. 02	+5.3
16.02– 30.03	+2.3	n.d.	09.02–17. 03	+4.8
30.03– 11.05	+3.4	6.0		
11.05– 22.06	+5.0	6.1		

n.d. = not determined.

sulphur component injected into the atmosphere in the past without desulphurization. Table 5 gives an overview of the first analyses of gypsum from various power plants. The great majority of the $\delta^{34}S$ values ranges between +14 and +17.5‰.

An exception to this is the value for gypsum from the power plant Schkopau (−1.9‰). This appears to be due to the different sulphur isotope pattern of the local lignite. Schkopau lies 50 km south of the city of Halle. The analysis of the patina on a bronze monument of the composer Georg Friedrich Händel in Halle gave a $\delta^{34}S$ value of −4‰ which is remarkably lower than the usual range for environmental influences (+3 to +9‰) in the investigated areas.

Table 5. *$\delta^{34}S$ values for gypsum from flue gas desulphurization plants in Germany*

Flue gas desulphurization plant	Sulphur content (wt%)	$\delta^{34}S$ (‰)
Jentschwalde	14.6 to 19.9	+16. 2 to +17.5
Weisweiler	16.8	+17.2
Frimmelsdorf	20.9	+14.0
Niederausesse	17.2	+16.0
Neurath	21.4	+15.5
Schkopau	19.9	−1.9

Table 6. *$\delta^{34}S$ values of seeping water in comparison to rainwater and atmospheric SO_2 in Oberbärenburg, eastern Erzgebirge Mountains, Saxony*

Sample	Time period	
	14.04–09.05.2000	30.08–25.09.2000
Atmospheric SO_2	+2.4	n.d.
Rainwater	+4.2	+4.0
Seeping water, 30 cm depth	+3.8	+4.0
Seeping water, 60 cm depth	+3.8	+4.1

A further sample of a gypsum crust from the sandstone surface at the Market Church in Halle, showed a $\delta^{34}S$ value of +1‰. It is thus obvious, that compared to the other areas investigated, the Halle region is characterized by significantly lower $\delta^{34}S$ values.

Seeping water in soils

For the transport of sulphur from the ground to the stonework the dissolved sulphur in seeping water must be taken into consideration as a potential source. When compared to rainwater, no clear differences in $\delta^{34}S$ values can be observed (Table 6). This implies that for the sulphate migrating with rising moisture from the ground, the mean $\delta^{34}S$ for rainwater can be used as an approximate value. Therefore, sulphur isotope analysis does not allow differentiation between the sulphur originating from direct rain attack on the stone surface and that coming into the stonework via rising damp.

Application to case studies

Despite the deficiencies in our present knowledge of the natural and anthropogenic sulphur input to the atmosphere and its isotopic composition, sulphur isotope studies allow the identification, to some degree, of the main sulphur sources in suitable cases. The differentiation of the origin of the sulphate present in the newly formed efflorescences during the reconstruction of the Church of Our Holy Lady in Dresden illustrates the usefulness of this technique.

Other examples are the Church in Axien where the groundwater was excluded as a source of sulphate, the Church in Grünhain, where the sulphate could be attributed to the groundwater, and the basement of the Church of Our Holy Lady in Dresden, where again, groundwater provided the main source of sulphate salts (Table 7).

The environmental influences were conclusively demonstrated by isotope analyses for the sulphate salts found on the carvings of the so-called 'Stone Album' in Grossjena (Table 8). The salt efflorescences on the sandstone reliefs with scenes from the Holy Bible carved in the Bunter sandstone bedrock are dominantly magnesium sulphate compounds. The magnesium component may be derived from the dolomitic binder in the sandstone as shown by microscopic investigations (Siedel & Klemm 2001).The sulphur isotope ratio of the efflorescences conclusively excludes any influence of sulphate from strata of the Zechstein subdivision or the Keuper stage (Nielsen & Ricke 1964) exposed nearby that had been considered as possible sources for the efflorescence. The $\delta^{34}S$ values lie within the usual range for environmental influences (+3.4 to +4.4‰ for the city of Leipzig 45 km to the NE). Efflorescences at the surface of applied repair mortars with a quite different isotope ratio were mainly formed by alkali sulphates. The salts show the same $\delta^{34}S$ values as the magnesium sulphates. For their

Table 7. *Correspondence between sulphate salt efflorescence and groundwater according to $\delta^{34}S$ values*

Monument/place	$\delta^{34}S$ efflorescence (‰)	$\delta^{34}S$ groundwater (‰)	Sulphate content in groundwater (mg/l)
Church/Axien	+2.7 to +4.9	+0.1 to +0.4	160–260
Church of Our Holy Lady /Dresden (cellar rooms)	+6.7	+6.1 to +6.4	164–172
Church / Grünhain	+4.9 to +6.6	+5.3 to +5.5	34–35

Table 8. *$\delta^{34}S$ values of efflorescences on the 'Stone Album' (carvings in sandstone bedrock) in Grossjena and possible sources*

Samples	$\delta^{34}S$ (‰)	Sulphate salts
Efflorescences	+2.8 to + 4.3	Hexahydrite, starkeyite, gypsum
Evaporite sulphate*		
from Zechstein	+11.5 (n = 64)	
from Triassic (Muschelkalk)	+20.5 (n = 8)	
from Triassic (Keuper)	+17.5 (n = 9)	
Efflorescence from monuments, city of Leipzig (45 km NE) (environmental influence)	+3.4 to +4.4	Hexahydrite, gypsum
Stone repair mortar	+9.3	
Efflorescence where repair mortar was applied	+4.3	Thenardite, syngenite, aphthitalite, gypsum

* Nielsen & Ricke (1964)

formation, the same mechanism as already discussed at the Church of Our Holy Lady in Dresden is suggested, i.e. the reaction of the alkaline pore solution of the mortars (rich in K^+ and Na^+) with atmospheric SO_2 to alkali sulphate compounds. A trend to somewhat higher $\delta^{34}S$ values, that would indicate the participation of sulphate from the mortar, was not detected.

Conclusions

The study has shown that the sulphur leading to salt formation on monuments is preferentially derived from environmental pollution in the investigated area. This pollution is characterized by a typical range of $\delta^{34}S$ values modified by local emitters. The individual components, i.e. atmospheric SO_2, sulphate in rainwater and sulphate in dust, exhibit distinct ranges in $\delta^{34}S$ values and a systematic difference in the following sequence: $\delta^{34}S$ (SO_2) < $\delta^{34}S$ (sulphate rainwater) < $\delta^{34}S$ (sulphate in dust).

However, further differentiation between individual sulphate sources as well as a quantitative assessment of the portions of atmospheric SO_2 and sulphates from rainwater and/or dust involved in the formation of efflorescences and crusts on a building cannot as yet be achieved with the required degree of certainty. To some extent, this can be attributed to the lack of detailed knowledge of the isotopic composition of potential sulphate sources. Consequently, current investigations require analyses not only of the salt samples from the buildings but also of the environmental components and the relevant building materials. The results prove that the sulphur isotope ratio is suitable as an indicator for complex deterioration processes in laboratory experiments as well as on buildings. Especially for the latter case more investigations on the geochemistry and the isotopic variation of sulphur in the atmosphere and in technical building products are needed for further progress.

The results obtained so far demonstrate the potential of sulphur isotope studies for the improved assessment of the sources of sulphate salts on monuments. While in some cases it may not be possible to achieve a unique identification of the sulphur sources, the method allows the conclusive exclusion of some of the sources thus narrowing down the problem. The

application of this analytical method provides an improved approach for developing well-founded technical measures and restoration decisions that are to be employed in each specific case.

Parts of the investigation were financed by the German Federal Foundation for the Environment (Az 07843). Thanks to E. A. Charola and E. Hansen for helpful comments and for improving the English of the first text version.

References

BUZEK, F. & ŠRAMEK, J. 1985. Sulfur isotopes in the study of stone monument conservation. *Studies in Conservation*, **30**, 171–176.

DÄMMGEN, U., GRÜNHAGE, L. & JÄGER, H.-J. 1985. System zur flächendeckenden Erfassung von luftgetragenen Schadstoffen und ihren Wirkungen auf Pflanzen. *Landschaftsökoklogisches Messen und Auswerten*, **1**(2/3), 95–105.

DEQUASIE, H. & GREY, D. C. 1970. Stable isotpes applied to pollution studies. *American Laboratory*, **2**, 19–27.

GEBAUER, G., GIESEMANN, A., SCHULZE, E.-D. & JÄGER H.-J. 1994. Isotope ratios and concentration of sulfur and nitrogen in needles and soils of Picea abies stands as influenced by atmospheric deposition of sulfur and nitrogen compounds. *Plant and Soil*, **164**, 267–281.

HAUBRICH, F. 2000. *Schwefel- und Sauerstoffisotopen als Tracer für Wechselwirkungen zwischen Atmo-, Pedo-, Hydrosphäre und der Sulfidlagerstätte in der Region Freiberg*. PhD Thesis, TU Bergakademie Freiberg, Institute of Mineralogy.

HOFFMANN, D. & ROOSZ, H. 1977. Interaction between sulfur dioxide and lime plasters. *Second International Symposium on the Deterioration of Building Stones, Athens 1976, Proceedings*. 37–42.

JÄGER, H.-J., GIESEMANN, A., KROUSE, H. R., LEGGE, A. H. & ESSER, J. 1989. Sulphur isotope investigation of atmospheric sulphur input to a terrestrial ecosystem near Braunschweig, FRG. *Angew. Botanik*, **63**, 513–523.

KLEMM, W. & SIEDEL, H. 1999. *Schwefelisotopenanalyse von bauschädlichen Sulfatsalzen an historischen Bauwerken*. Wissenschaftliche Mitteilungen des Instituts für Geologie, TU Bergakademie Freiberg, **8**.

LONGINELLI, A. & BARTELLONI, M. 1978. Atmospheric pollution in Venice, Italy as indication by isotopic analyses. *Water, Air and Soil Pollution*, **10**, 335–341.

NIELSEN, H. & RICKE, W. 1964. Schwefel-Isotopenverhältnise in Evaporiten in Deutschland. Ein Beitrag zur Kenntnis von $\delta^{34}S$ im Meerwassersulfat. *Geochimica Cosmochimica Acta*, **28**, 577–591.

NORD, A. G. & TRONNER, K. 1995. Effect of acid rain on sandstone: The Royal Palace and the Riddarholm Church, Stockholm. *Water, Air and Soil Pollution*, **85**, 2719–2724.

PYE, K. & SCHIAVON, N. 1989. Cause of sulphate attack on concrete, render and stone indicated by sulphur isotope ratios. *Nature*, **342**, 663–664.

ROLLAND, W., GIESEMANN, A., FEGER, K. H. & JÄGER, H.-J. 1991. Use of stable S isotopes in the assessment of S turnover in experimental forested watersheds in the Black Forrest, Southwest Federal Republic of Gemany. *In*: *Stable isotopes in plant nutrition, soil fertility and environmental studies*. International Atomic Energy Agency, Vienna, 593–598.

RÖSCH, H. & SCHWARZ, H. J. 1993. Damage to frescoes caused by sulphate-bearing salts: Where does the sulphur come from? *Studies in Conservation*, **38**, 224–230.

SIEDEL, H. & KLEMM, W. 2001. Sulphate salt efflorescence at the surface of sandstone monuments and at the sandstone bedrock in outcrops – natural or anthropogenic reasons? *Geologica Saxonica*, **46/47**, 203–208.

TORFS, K. M., VAN GRIEKEN, R. E. & BUZEK, F. 1997. Use of stable isotope measurements to evaluate the origin of sulphur in gypsum layers on limestone buildings. *Environmental Science & Technology*, **31**, 2650–2655.

WITTENBURG, CH. & DANNECKER, W. 1992. Dry deposition and deposition velocity of airborne acidic species upon different sandstones. *Journal of Aerosol Science*, **23**, S869–S872.

This page intentionally left blank

A rapid method for the determination of cation exchange capacities of sandstones: preliminary data

MATHIAS SCHÄFER & MICHAEL STEIGER

Institut für Anorganische und Angewandte Chemie, Universität Hamburg, Martin-Luther-King-Platz 6, 20146 Hamburg, Germany (e-mail: steiger@chemie.uni-hamburg.de)

Abstract: A rapid and efficient single-extraction procedure for measuring cation exchange capacities in sandstones has been developed and tested. The method is based on the use of a $SrCl_2$ (0.25 mol l^{-1}) solution to displace the exchangeable cations. The cation exchange capacities (CEC) of three types of natural building stones were analysed, both in freshly quarried material and in weathered samples. Large differences in the sorptive properties of these materials were observed. The measurement of profiles of CEC in weathered sandstones revealed a significant decrease of CEC in the weathered zone close to the exposed surface, most likely reflecting the partial dissolution of clay minerals due to acid attack. CEC measurements appear to be a very sensitive indicator of chemical weathering profiles.

There are quite a large number of different chemical and physical weathering processes that can cause severe damage to natural building stones. Chemical weathering refers to chemical reactions of the mineral constituents of stone. Physical weathering includes all processes generating mechanical stress. Hence, salt weathering which is one of the most common problems in the conservation of stone monuments, is a physical weathering process. The chemical weathering of natural building stones involves the attack of water and associated acidity on the primary and secondary minerals leading to their dissolution, the mobilization of metal cations and, eventually, the formation of clays, e.g. kaolinite (Stumm & Wollast 1990; Drever 1994; Lasaga *et al.* 1994). The mobilization of metal cations from sandstones was observed through analysis of surface run-off water (Steiger & Dannecker 1994).

Typically, the ions released during chemical dissolution from common carbonate and silicate minerals in building stones are Na^+, K^+, Mg^{2+} and Ca^{2+}. The corresponding anions depend on the source of the acidity, but often include sulphate, nitrate and bicarbonate. Hence, soluble salts themselves are the products of chemical weathering reactions and it is not usually possible to clearly separate damage due to chemical reactions and subsequent salt stress. Moreover, the concentration of soluble salts in building stones is also affected by sources other than mineral dissolution, e.g. rising damp and the input of salts from the atmosphere by either wet or dry deposition. Finally, the salts, once enriched in the pore space of building stones, are subject to transport and compositional changes due to fractionated crystallization and ion exchange processes.

The influence of the sorptive properties of mineral surfaces on the composition of pore solutions in building stones has been rarely investigated. It appears that Wendler & Snethlage (1988) were the first to investigate cation exchange capacities (CEC) in weathered building stones. Their measurements revealed significant differences between cation exchange capacities in the weathered zone close to the exposed surface and the unweathered material at greater depth. However, to our knowledge a systematic investigation of ion exchange properties of weathered building stones has not yet been performed. In contrast, measurements of CEC are widely used in soil science and numerous methods for the determination of CEC have been described in the literature (Bache 1976). However, it is well known that results obtained can vary significantly, reflecting differences in how they are measured.

This paper presents an experimental procedure suitable for the investigation of cation exchange capacities in building sandstones. The method allows for a rapid and reproducible determination of the cations adsorbed on mineral surfaces in order to determine profiles in weathered building stones. The study includes three types of natural building stones, the cation exchange capacities of which were analysed both in freshly quarried material and in weathered samples.

From: SIEGESMUND, S., WEISS, T. & VOLLBRECHT, A. 2002. *Natural Stone, Weathering Phenomena, Conservation Strategies and Case Studies*. Geological Society, London, Special Publications, **205**, 431–439.
0305-8719/02/$15.00 © The Geological Society of London 2002.

Methodology

Materials and samples

Three different types of unweathered sandstones were investigated which are commonly used as building stones: (1) Obernkirchen sandstone (Wealden, Lower Cretaceous); (2) Sand sandstone (Middle Keuper, Late Triassic); and (3) Eichenbühl sandstone (Bunter Sandstone, Early Triassic). According to Grimm (1990) these materials represent a broad range of composition. Obernkirchen sandstone (OBK) is a nearly pure quartz sandstone with only minor contributions of muscovite, kaolinite, and some heavy minerals (zircon, rutile, apatite). The major constituents of Sand sandstone (SAN) are quartz, rock fragments (chlorite clasts, hornblende, chert), plagioclase, and alkali feldspars. Considerable amounts of clay minerals (mostly chlorite) are present as cementing material, argillaceous rock fragments, and as coatings filling the pores. No petrographic description of Eichenbühl sandstone (EIC) is available. However, the quarry in Eichenbühl is located very close to one in Ebenheid. The latter sandstone is described in detail by Grimm (1990) and it is assumed that the petrographic characteristics of the two sandstones are very similar. The most abundant constituents in Ebenheid sandstone are quartz, rock fragments (quartz, feldspars), alkali feldspar and argillaceous-ferruginous cements (illite and chlorite). In addition to the sandstone materials pure quartz powder (p.a., Merck, Darmstadt, Germany) was also used in the ion exchange experiments.

Weathered samples of Obernkirchen, Sand, and Ebenheid sandstones were obtained from stone specimens exposed at a field test site located in a highly industrialized urban area in Duisburg (Ruhr area, Germany). The exposure of the stones started in April 1986 (EIC), October 1987 (SAN), and July 1988 (OBK), respectively. The stone samples were exposed to rainfall and, due to local industrial emissions, to a considerably polluted atmosphere with high concentrations of sulphur dioxide and nitrogen oxides (Steiger *et al.* 1993). Stones were retrieved from the exposure site in April 2000 for laboratory analysis. Additional weathered material from two stone monuments was available from sandstone blocks that had been removed in the course of conservation work during the early 1990s from the church of St. Vitus in Iphofen (fifteenth century) and from the castle in Schillingsfürst (eighteenth century). These building stones are similar to Sand sandstone (Middle Keuper), hence, they contain a considerable amount of clay minerals and feldspars. Iphofen and Schillingsfürst are located in rural areas (northern Bavaria) with an extremely low level of local air pollution. Thus, very low concentrations of the major primary air pollutants, i.e. sulphur dioxide, nitrogen oxide etc., are expected.

Sampling and sample preparation

All experiments for the optimization and comparison of procedures for the determination of ion exchange capacities were carried out with the unweathered stone materials and quartz powder. Large amounts of these materials were ground down to <40 μm size fraction by repeated ball-milling and sieving. Samples from weathered stones were taken by drilling in order to determine profiles of salt concentration and cation exchange capacities. Drill-cores were subsequently cut into slices by dry sawing. The thickness of the slices was about 3 mm close to the surface and 10 mm at depth within the substrate. Initial tests with the unweathered materials revealed that there are no differences in CEC measurements for samples prepared by either grinding to <125 μm or by grinding to <40 μm. Therefore, all samples of weathered stone materials were ball-milled to <125 μm size fraction.

When taking samples from monuments, for obvious reasons, the drill diameter must be as small as possible in order to keep the loss of original material to a minimum. Typically, diameters do not exceed 10–20 mm. As a consequence the amount of sample does not usually exceed 500–1000 mg for the desired resolution of the depth profiles. For the extraction of soluble salts 500 mg samples were shaken with 25 ml bidistilled water for 45 min in a polypropylene (PP) vial. After centrifuging, the supernatant liquor was membrane-filtered and directly used for the analysis of cation and anion concentrations.

Ion exchange

All methods used to measure CEC are based on an initial displacement of the exchangeable cations with a saturating salt. A number of preliminary experiments were undertaken with unweathered stone material in order to find an appropriate extraction procedure. Except where otherwise noted, all extractions were carried out by shaking 500 mg of the ground sample with 25 ml of the solution containing the respective adsorbing cation in a PP vial at room temperature. After the desired reaction time

(usually 45 min), the solutions were centrifuged, membrane-filtered and directly used for the analysis of the cations. In order to study the influence of different adsorbing cations, solutions of NH_4OAc, NH_4Cl, NaCl, $SrCl_2$, and $BaCl_2$ were used in the preliminary experiments. The effect of the concentration of the adsorbing cation was investigated in a series of extractions with the following concentrations of these salts: 2, 1, 0.5, 0.25, 0.05, 0.025, 0.0125, 0.00625, 0.003125, 0.001, and 0.0005 mol l^{-1}. The sensitivity of the method to variations in the ratio of the amount of sample and the volume of the solutions used for the extractions was studied in a separate series of measurements, as was the effect of the reaction time. Specified amounts of the different unweathered stone materials (100, 200, 300, 400, 500, 1000, 2000 mg) were extracted in 25 ml of a 0.25 mol l^{-1} $SrCl_2$ solution. Using the same $SrCl_2$ solution and a fixed amount of 500 mg of ground Sand sandstone the extraction time was varied from 30 min to 48 hours.

Building stones are usually contaminated with substantial amounts of soluble salts. Hence, prior to the determination of the adsorbed cations all soluble salts had to be removed by extraction with bidistilled water. To ensure that the samples do not contain even small amounts of soluble species, the aqueous extractions were repeated three times. After centrifuging, the solid residues are then used for the determination of exchange capacities as described before. All extractions including aqueous extracts for the determination of soluble salts and the ion exchange experiments were made in triplicate.

Additional experiments were carried out to investigate the influence of cation mobilization due to the dissolution of mineral constituents of the stone materials. Salt-free samples of the stones were subjected to aqueous elutions using the same procedure as described before. It is assumed that the cation concentrations in these solutions provide an estimate of mobilization due to dissolution. In addition, samples initially saturated with strontium were subsequently extracted by shaking with a 0.25 mol l^{-1} $SrCl_2$ solution again. Hence, the cation concentrations in these solutions directly indicate the influence of mineral dissolution.

Analysis of anions and cations

The concentrations of sulphate, nitrate, and chloride were determined by suppressed ion chromatography with conductometric detection. Ammonium was measured using a photometric technique. The concentrations of the remaining cations were determined by flame atomic absorption (Mg, Ca) and atomic emission spectrometry (Na, K). Significant blank values, i.e. concentrations above the detection limits of the respective method, were observed only in the more concentrated solutions of the saturating salts. Where appropriate, the measured concentrations were blank corrected.

Results and discussion

Measurement of cation exchange capacities

The CEC is taken as equivalent to the sum of the cations Na^+, K^+, Mg^{2+}, Ca^{2+} and NH_4^+ in the extracts. Based on the reproducibility of replicate measurements the overall uncertainty of the CEC determinations was estimated to be ±1.4%, ±2% and ±7% for Sand, Eichenbühl and Obernkirchen sandstones, respectively. A comparison of the measured CEC of unweathered Eichenbühl sandstone obtained with different saturating salts is depicted in Figure 1. There is a significant dependence of CEC on the concentration of the saturating cation. In all cases, however, CEC approaches a constant value at sufficiently large concentrations. In the case of strontium chloride and both ammonium salts, constant CEC values are observed at concentrations ≥0.25 mol l^{-1}, while sodium and barium chlorides require higher concentrations of at least 1 mol l^{-1}. However, differences in the ability of the saturating salts to displace adsorbed cations are obvious.

Clearly, the monovalent cations are less efficient in the displacement of exchangeable cations. The cation exchange capacities obtained with NH_4Cl and NH_4OAc are nearly indistinguishable. Although NH_4Cl solutions are more acidic, there is no obvious significant increase in the measured CEC which would indicate increased mineral dissolution. At sufficiently high concentrations the CEC determined with sodium chloride compares well with the results obtained by using the ammonium salts. However, the use of 1 mol l^{-1} NH_4Cl, which is widely used in soil science (e.g. Meiwes *et al.* 1984), is not sufficient for the complete displacement of all exchangeable cations. Due to their greater selectivity, which is largely an effect of their charge, the bivalent cations are more efficient in the displacement of exchangeable cations. It appears from Figure 1 that the efficiency of strontium is even greater than that of barium. Both cations have been proposed previously for the determination of CEC in soils

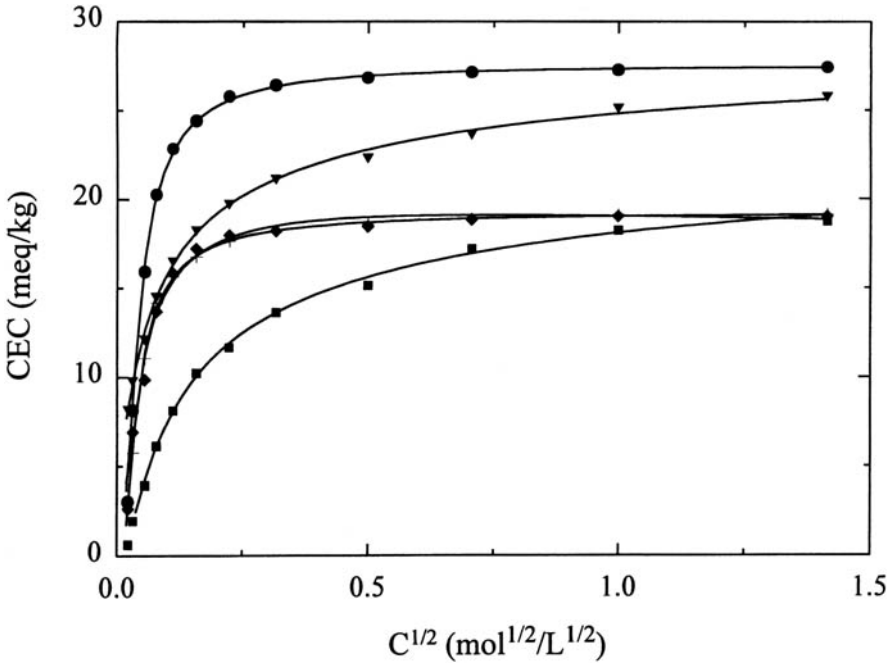

Fig. 1. Comparison of cation exchange capacities measured with different concentrations, *C*, of saturating salts. Symbols have the following meanings: (●) $SrCl_2$; (▼) $BaCl_2$; (◆) NH_4Cl; (+) NH_4OAc; (■) NaCl.

(Mehlich 1948; Bascomb 1964; Edmeades & Clinton 1981; Sänger-von Oepen *et al.* 1993). However, the present results indicate that $BaCl_2$ concentrations of 0.1 and 0.5 mol l^{-1} proposed by Mehlich (1948) and Bascomb (1964), respectively, are not sufficient for the complete displacement of all exchangeable cations. For the same reason, the use of 0.1 mol l^{-1} $SrCl_2$ suggested by Sänger-von Oepen *et al.* (1993) is not recommended.

Nonetheless, for the purpose of this study $SrCl_2$ is still the obvious choice. Even at comparably low concentrations the maximum CEC is obtained with $SrCl_2$. This not only reduces the risk of increased blank values, but particularly diminishes interferences in atomic spectrometric analysis. Moreover, strontium is typically present in building stones in very low concentrations. In contrast, sodium and ammonium are considered to be major cation components of atmospheric aerosols and rain water. It is to be expected that these cations are present in the pore spaces of weathered building stones in soluble and in exchangeable form. Though the CEC values for Obernkirchen, Sand, and Eichenbühl sandstones differ greatly, the relative efficiency of the salts tested and the dependence of CEC on the concentrations of the salt solutions are very similar. Consequently, all further experiments were carried out using a 0.25 mol l^{-1} $SrCl_2$ solution. The experiments with variable reaction times did not reveal any significant trend when prolonging the extractions from 30 min up to 48 h and the final choice made for the time of shaking was 45 min.

The results of the experiments with variable ratios of sample mass and extraction volume are presented in Figures 2 and 3. These experiments were conducted with unweathered Sand sandstone. Figure 2 depicts the influence of sample mass on the sum of the concentrations of the exchangeable cations Na^+, K^+, Mg^{2+} and Ca^{2+}. The regression line shown in Figure 2 provides an excellent representation of the experimental values and the intercept is not significantly different from zero. A comparison of exchangeable Na^+, K^+, Mg^{2+}, and Ca^{2+} and CEC determined with two different amounts of sample, 500 mg and 2000 mg, is shown in Figure 3. Both measurements agree quite well and it is concluded that the method is not sensitive to variations of sample mass in the range studied. For routine measurements a typical sample mass of 500 mg was selected.

Problems often encountered in CEC determinations are due to the dissolution of mineral

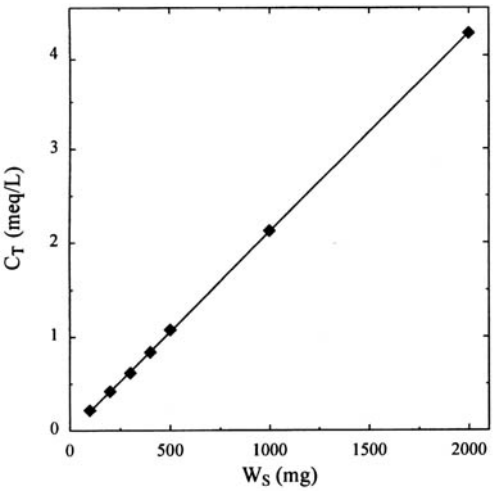

Fig. 2. Influence of sample mass, W_S, of Sand sandstone on the sum of the equivalent concentrations, C_T, of exchangeable cations Na^+, K^+, Mg^{2+} and Ca^{2+}.

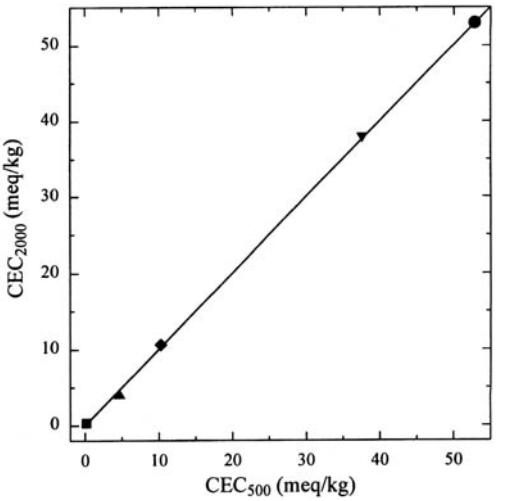

Fig. 3. Comparison of exchangeable Na^+, K^+, Mg^{2+} and Ca^{2+} and CEC in Sand sandstone determined with sample masses of 500 mg and 2000 mg, respectively. Symbols have the following meanings: (●) CEC; (▼) Ca^{2+}; (◆) Mg^{2+}; (▲) K^+; (■) Na^+.

constituents from the sample, hence, an overestimation of exchange capacity. Aqueous extracts and repeated extractions in 0.25 mol l^{-1} $SrCl_2$ were used to assess the effect of mineral dissolution. These experiments were carried out with the unweathered sandstone materials and with quartz powder. Only in the case of the sandstone samples were measurable quantities of Na^+, K^+, Mg^{2+} and Ca^{2+} found in the extracts, thus indicating that mineral dissolution might also affect the concentrations of these cations in the CEC determinations. Depending on the nature of the stone, mineral dissolution might result in an overestimation of CEC in the order of <1–5%. In the case of the experiments with unweathered stones the measured elemental concentrations in pure aqueous extracts were used to correct the concentrations measured in the $SrCl_2$ extracts. In the instance of the CEC determinations in samples of weathered stones, this was usually not possible as the total amount of sample was not sufficient to carry out all the necessary extractions including repeated measurement of CEC, blank values etc. Hence, a slight overestimation of the CEC in weathered stones would appear to be unavoidable.

Cation exchange capacities of unweathered sandstones

The CEC measurements of the unweathered stone samples are summarized in Table 1. CEC is taken as the sum of the exchangeable cations Na^+, K^+, Mg^{2+} and Ca^{2+} as initial experiments revealed no significant amounts of exchangeable ammonium. A CEC of 3.1 meq kg^{-1} was obtained for Obernkirchen sandstone which contains only small amounts of muscovite and kaolinite. The maximum CEC of 53.8 meq kg^{-1} was measured for Sand sandstone. Most likely, this CEC is almost exclusively due to the considerable amount of chlorite present in this sandstone as cementing material and as coatings filling the pores. In the case of Eichenbühl sandstone a CEC of 26.9 meq kg^{-1} was measured which can most likely be attributed to the argillaceous-ferruginous cements containing illite and chlorite. Finally, the results obtained for the three sandstones may be compared to the CEC of the pure quartz powder. In these determinations all exchangeable cations were either below or very close to the detection limit, which is

Table 1. *Cation exchange capacities of unweathered Sand (SAN), Eichenbühl (EIC), and Obernkirchen (OBK) sandstones and equivalent percentages of exchangeable cations*

	SAN	EIC	OBK
CEC (meq kg^{-1})	53.8	26.9	3.1
Na (%)	0.1	0.7	0.0
K (%)	6.5	19.1	12.0
Mg (%)	18.6	32.5	28.0
Ca (%)	74.8	47.7	60.0

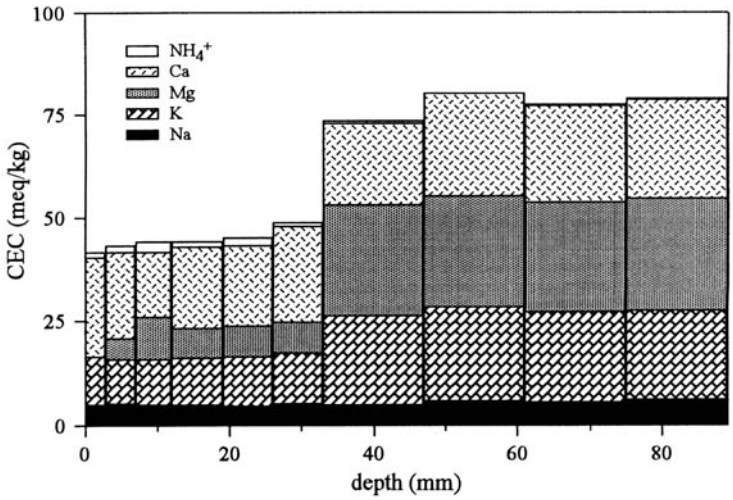

Fig. 4. CEC in weathered Sand sandstone (after 9 years of exposure on field site in Duisburg, Ruhr area).

largely affected by the blank values in the $SrCl_2$ solution. Hence the CEC of 0.02 meq kg^{-1} determined for the quartz powder is only approximate. Nonetheless, this value is so small that it can be concluded that any contribution of quartz and other coarse-grained minerals in the sandstone samples is negligible.

The relative contributions of the different adsorbed cations are expressed as the equivalent percentages making up the exchangeable CEC in Table 1. The bivalent cations, i.e. Mg^{2+} and Ca^{2+}, are clearly dominant in all three sandstones with contributions ranging from at least 80% (EIC) up to 93% (SAN). The contributions of Na^+ are negligible in all stone types.

Profiles of cation exchange capacities in weathered sandstones

The results of the measurements of CEC in a weathered stone specimen are depicted in Figure 4. The drill-core sample was taken in summer 1995 from a Sand sandstone specimen at the exposure site in Duisburg, i.e. roughly nine years after the exposure of the stone. The CEC of 75–80 meq kg^{-1} measured at depth in the substrate (>30 mm) is greater than that determined in the unweathered variety of Sand sandstone. Also, the contributions of the invidual ions are somewhat different with greater contributions of Mg^{2+} and K^+ reflecting the variability of the properties of natural stone even if it comes from the same quarry source. The measured profile shown in Figure 4 reveals a significant decrease in CEC in the first 20–30 mm below the exposed surface to only about half of the original value which is represented by the CEC at greater depth. It can also be seen from Figure 4 that there is a significant fractionation of the equivalent percentage contributions with depth. The decrease in CEC in the weathering zone is to a large extent caused by a decrease in exchangeable Mg^{2+} and K^+.

For comparison, Figure 5 depicts a profile of CEC measured in a drill-core from a historic building (St. Vitus, Iphofen) after an exposure time of about 500 years. Similar results were obtained as for the stone specimen from the test site in Duisburg. A decrease in total CEC near the exposed surface is obvious and, interestingly, the decrease in total CEC is also largely attributed to a selective decrease of exchangeable Mg^{2+} and K^+. Very similar results were obtained for the samples coming from the castle in Schillingsfürst.

There are two possible explanations for the decrease of CEC in the weathering zone. Firstly, it is possible that the exchangeable cations Na^+, K^+, Mg^{2+} and Ca^{2+} that were originally adsorbed to the negative surface charges in the unweathered stone materials are displaced by other ions that have not been measured. Wendler & Snethlage (1988) in their study assumed the displacement of Na^+, K^+, Mg^{2+} and Ca^{2+} by either NH_4^+ or exchangeable hydrogen ions, or both. The second possible explanation for the decrease of CEC in the weathering zone is the partial dissolution of the minerals that are the major contributors to the cation exchange properties of the material due to chemical weathering.

The measured values of exchangeable NH_4^+ in

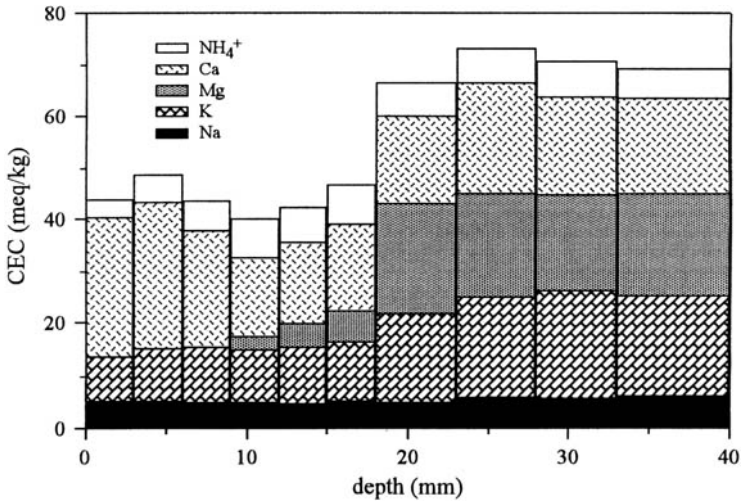

Fig. 5. CEC in weathered sandstone from church of St. Vitus (Iphofen, northern Bavaria).

the present study confirm that the atmospheric input of NH_4^+ to building stones has caused a partial displacement of the original exchangeable cations. The equivalent percentage contribution of NH_4^+ to the total CEC is in the order of 10–20% in the case of the samples from Iphofen, but does not exceed 4% in the samples from Duisburg. Clearly, however, in both cases, NH_4^+ cannot account for the decrease in total CEC.

In order to assess if there is a significant contribution from other cations not measured so far, additional experiments were carried out with weathered samples of Sand and Eichenbühl sandstones. The results of CEC measurements of samples obtained from the Duisburg exposure site after exposure times of 13 (SAN) and 14 years (EIC) are depicted in Figures 6 and 7. The principal features of these CEC determinations are similar to those discussed before. There is a significant decrease in CEC in the weathered zone of both sandstones with exchangeable Mg^{2+} almost completely lost. No significant decrease in the pH values could be determined in the $SrCl_2$ extracts and measurements of aluminium concentrations in the extracts did not reveal any significant contribution of aluminium to the total CEC. Finally, re-exchange experiments using 0.25 mol l^{-1} NH_4Cl were carried out and the results are shown in Figures 6 and 7. It can be seen that there is no excess Sr^{2+} displacement which would indicate the presence of exchangeable cations other than Na^+, K^+, Mg^{2+} and Ca^{2+}. On the contrary, it is not possible to displace all of the Sr^{2+} adsorbed to the mineral surfaces by NH_4^+. However, considering the lower efficiency in the replacement of exchangeable cations of NH_4Cl solutions compared to $SrCl_2$ solution (cf. Fig. 1) this is not surprising.

It is concluded from these experiments that the decrease of CEC close to the surface is most likely the result of chemical weathering, i.e. the partial dissolution of clay minerals. Presumably, very small mineral particles are particularly susceptible to acid attack and dissolution. Due to the strong influence of grain size on the total surface area, the dissolution of a minor fraction of the smallest clay particles might cause a substantial decrease in CEC.

Conclusions

The simple single-extraction procedure using 0.25 mol l^{-1} $SrCl_2$ provides a rapid method for the determination of cation exchange capacities in sandstones. The use of $SrCl_2$ is superior compared to other saturating salts as it is more efficient, at least at moderate concentration, which is desirable to minimize interferences in subsequent analysis of exchangeable cations. Though not extensively studied in the present work, modifications of the method, e.g. buffering or the subsequent displacement of exchangeable strontium (Bache 1976), should be straightforward where appropriate.

The application of the method to the measurement of CEC for three common natural stones revealed large differences in the sorptive properties of these materials yielding a range

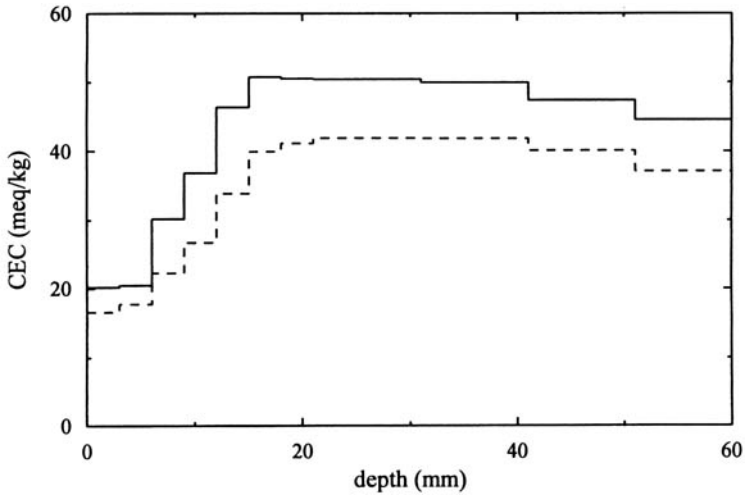

Fig. 6. CEC in weathered Sand sandstone after 13 years of exposure on field site in Duisburg, Ruhr area (—) and amount of exchangeable Sr^{2+} displaced by extraction with 0.25 mol l^{-1} NH_4Cl solution (----).

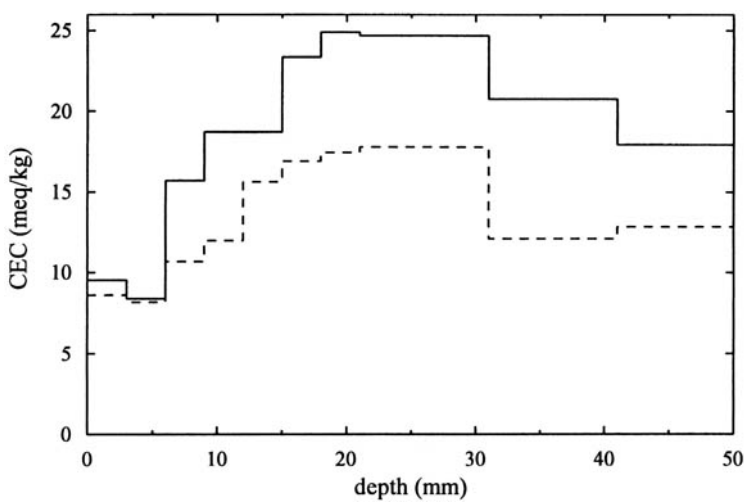

Fig. 7. CEC in weathered Eichenbühl sandstone after 14 years of exposure on field site in Duisburg, Ruhr area (—) and amount of exchangeable Sr^{2+} displaced by extraction with 0.25 mol l^{-1} NH_4Cl solution (----).

of CEC values from 3 to 54 meq kg^{-1}. Qualitatively, these exchange capacities are in good agreement with existing petrographic description of the sandstones (Grimm 1990). Clay minerals occurring as very small particles in sandstones are the most likely single contributor to the cation exchange capacities. The measurement of CEC provides a very simple and rapid method to assess the influence of the presence of clay minerals on the properties of a sandstone material.

The measurement of CEC of weathered sandstones revealed significantly different cation exchange capacities in the weathering zones close the exposed surfaces. Even after relatively short exposure times of 9 to 15 years in a heavily polluted atmosphere, the CEC in the weathering zone is only about half of the value in unweathered samples at greater depth within the substrate. Weathered stones from two monuments located in comparatively unpolluted atmospheres at rural sites yielded similar profiles of CEC. It is concluded from the experiments that CEC profiles reflect the effects of

chemical weathering of clays and other minerals occurring as very small particles. It appears that CEC is a particularly sensitive indicator of the dissolution of colloidal-sized minerals. CEC measurements are also extremely useful in determining actual weathering profiles, i.e. reflecting the penetration of acidity into the interior of the stone. In contrast, profiles of soluble salts do not usually reflect the actual weathering profile, as salts are subject to capillary transport and fractionation due to combined evaporation and crystallization. Nonetheless, the composition of a soluble salt mixture is also affected by both the chemical weathering of mineral constituents and the ion exchange properties of the mineral surfaces. Therefore, a significant influence of ion exchange properties on the composition of a soluble salt mixture is to be expected, indicating that measurements of both soluble salt and CEC profiles might be complementary.

References

BACHE B. W. 1976. The Measurement of cation Exchange Capacities of Soils. *Journal of the Science of Food and Agriculture*, **27**, 273–280.

BASCOMB, C. L. 1964. Rapid method for the determination of the cation exchange capacity of calcareous and non-calcerous Soils. *Journal of the Science of Food and Agriculture*, **15**, 821–823.

DREVER, J. I. 1994. Durability of stone: mineralogical and textural perspectives. *In*: KRUMBEIN, W. E., BRIMBLECOMBE, P., COSGROVE, D. E. & STANIFORTH, S. (eds) *Durability and Change*. John Wiley & Sons, Chichester, 27–39.

EDMEADES, D. C. & CLINTON, O. E. 1981. A simple rapid method for the measurement of exchangeable cations and effective cation exchange capacity. *Communications in Soil Science and Plant Analysis*, **12**, 683–695.

GRIMM, W.-D. 1990. *Bildatlas wichtiger Denkmalgesteine der Bundesrepublik Deutschland*. Karl M. Lipp Verlag, München.

LASAGA, A. C., SOLER, J. M., GANOR, J., BURCH, T. E. & NAGY, K. L. 1994. Chemical weathering rate laws. *Geochimica Cosmochimica Acta*, **58**, 2361–2386.

MEHLICH, A. 1948. Determination of anion and cation exchange properties of soils. *Soil Science*, **66**, 429–445.

MEIWES, K.-J., KÖNIG, N., KHANNA, P. K., PRENZEL, H., ULRICH, B. 1984. Chemische Untersuchungsverfahren für Mineralböden, Auflagehumus und Wurzeln zur Charakterisierung und Bewertung der Versauerung in Waldböden. *Berichte des Forschungszentrums Waldökosysteme/Waldsterben Göttingen*, **7**, 1–67.

SÄNGER-VON OEPEN, P., NACK, T., NIXDORF, J. & MENKE, B. 1993. Vorstellung der $SrCl_2$-Methode nach Bach zur Bestimmung der effektiven Kationenaustauschkapazität und Vergleich mit der NH_4Cl-Methode. *Zeitschrift für Pflanzenernährung und Bodenkunde*, **156**, 311–318.

STEIGER, M. & DANNECKER, W. 1994. Determination of wet and dry deposition of atmospheric pollutants on building stones by field exposure experiments. *In*: ZEZZA, F., OTT, H. & FASSINA, V. (eds) *The Conservation of Monuments in the Mediterranean Basin. Proceedings of the 3rd International Symposium*. Soprintendenza ai beni Artistici e Storici di Venezia, Venice, 171–178.

STEIGER, M., WOLF, F., DANNECKER, W. 1993. Deposition and enrichment of atmospheric pollutants on building stones as determined by field exposure experiments. *In*: THIEL, M.-J. (ed.) *Conservation of Stone and Other Materials, Vol. 11*. F & N Spon, London, 35–42.

STUMM, W. & WOLLAST, R. 1990. Coordination chemistry of weathering: kinetics of the surface-controlled dissolution of oxide minerals. *Journal of Geophysics*, **28**, 53–69.

WENDLER, W. & SNETHLAGE, R. 1988. Die Veränderungen der Kationenaustauschkapazitäten von Sandsteinen im Zuge der Verwitterung an Gebäuden. *In*: *Symposium Umwelteinflüsse auf Oberflächen*. Technische Akademie Esslingen, 11–18.

This page intentionally left blank

Index

Page numbers in *italics* refer to Tables and Figures

abrasion resistance 110, 116, 125–127, *129*
acid deposition
  dry 393–397
  wet 397–399
acid rain 393, 397–399
  effect on stone 399–402
acidity
  of fog water *383*
  and glass behaviour 334
actinolite 352
aerosol pollution 393–397
ageing tests 250–251
air pollution *see* atmospheric pollution
albite texture *120*
algae 180, *211*
Alsace sandstones *see* Meules sandstone; Vosgien sandstone
  Älvdal quartzite *317*, 319
  tile bending strength *322*, 323, 324–327
alveolar weathering 52
ammonium sulphate 394–395
Amoco Building (Chicago) 299
anhydrite in mortar 166
anisotropy *see* under fabric
anthropogenic activity 2, 409–410, 412
Arabella marble thermal expansion study 65–80
atmosphere, effect of climate change on 409
atmospheric aggressiveness 396–397
atmospheric pollution (nitrogen oxides) 337
atmospheric pollution (sulphur oxides and soot) 347
  Budapest study of limestone 363–366
    black crusts 368–370
    breakdown 372
    feature distribution 372–373
    grey dust 371
    origin of features 373–377
    white crusts 366–367
  effects of fog water in Venice
    sampling and analysis 382–383
    stone surface exposure 386–390
Austria marbles *see* Soelk; Wachau
Axien (Germany), sulphur pollution study 422, 423, 427

bacteria 183, *211*, *213*
Barents gneiss *317*, 319–320
  tile bending strength *322*, 323, 324–327
Basel (Switzerland), atmospheric aggressiveness *397*
Baune Pink Limestone *340*
Belfast (Northern Ireland)
  case study of marine-induced sandstone decay 349–350
    effect of actinolite 352
    effect on mortar 352
    salt distribution 351–352
  sulphate/chloride deposits 352–353
bending strength testing of tiles *see* tiles
Bern (Switzerland), atmospheric aggressiveness *397*
Bern Sandstone and atmospheric pollution 338, *340*
Berne molasse 396
biodeterioration/biodegradation
  climate change effects 409, 411
  granite 279
    methods of study 196
    results 197–200
    results discussed 200–201, 203–204
  limestone 241
    methods of study 196
    results 196–197
    results discussed 202–203
biofilms
  methods of study 179–180
    film processing 208–209
    TEM preparation 209–210
  results
    film depth 184–186
    film development 186–187
    film establishment 180–183
    film structure 183
  results discussed
    biofilms and weathering 191–192
    film impact 189–190
    film modelling 190–191
    film survival 187–189
  occurrence 177–179
biological weathering *see* biodeterioration *also* biofilms
Blue Pearl *317*, 318
  tile bending strength 321, *322*, 324–327
Boehme method 116
Bordeaux (France), atmospheric aggressiveness *397*
Boulingen Sandstone *340*
bowing 115, 299
  experiments on panels
    methods 301–302
    results 302–308
    results discussed 309–313
Braga granite 273
  stone decay study 274–275
    methods 274
    results 275–280
Brazil *see* itacolumite studies
Brownian diffusion 393
Brunauer, Emmett, Teller method 83
Brussels (Belgium), atmospheric aggressiveness *397*
Budapest (Hungary), effects of atmospheric pollution 363–364
  Miocene limestone study 364–366
    black crusts 368–370
    breakdown 372

feature distribution 372–373
grey dust 371
origin of features 373–377
white crusts 366–367
Bunter Sandstone
carvings 427, *428*
see also Meules sandstone; Vosgien sandstone; Wesersandstein

Cairo (Egypt)
Mokattam Group as building stone
composition 221, *223*
porosity 221–222, *224*
rate of weathering 227–233
stratigraphy 220–221
weathering forms 222–227
weathering products 233–237
monument legacy 217, *218*
monument weathering 219, *220*, *228*, *231*
calcite
crystallography *151*
thermal expansion 65, 81
calcium oxalate 195, 196, 202
calcium sulphate *see* gypsum
capillary absorption
methods of measurement 21
results for sandstone 26–27
Caraca Group 137
carbon particles 401
carbonate rock surfaces and biofilm formation 177–179
methods of analysis 179–180
results
biofilm depth 184–186
biofilm development 186–187
biofilm establishment 180–183
biofilm structure 183
results discussed
biofilm impact 189–190
biofilm modelling 190–191
biofilm survival 187–189
biofilm and weathering 191–192
see also limestone biodeterioration
Carboniferous stone *see* Dunhouse sandstone
Carrara marble
acid deterioration 398
atmospheric pollution effects *340*, 386, 387
bowing 299
consolidation and thermal testing 265, 266
degradation *150*
fabric 257–258
freeze-thaw properties 14, 16, *17*
grain size *260*
hygric expansion 65
microfabric 10–11
and wave velocity 153, *156*, 158, 159–160
porosity 261
sulphation 332–333
texture 68–70, *71*, 260
thermal expansion study 65–80
cathodoluminescence, Cretaceous sandstones 287, 288–289, 293–295
cation exchange capacity in sandstones
methods 432–433
results 433–435
unweathered sandstone 435–436
weathered sandstone 436–437
results discussed 437–439
chemical weathering *see* weathering
citric acid mortar retarder 171
climate change 407–408
effect on weathering 410–412
microclimate 413
UK case studies 414–417
factors 409–410, 411, 412–413
compressional waves *see* ultrasonic wave velocity
compressive strength
gypsum-based mortar *166*
mylonite 116, 125, *128*
Wesersandstein 110
conservation treatments 248–249
durability of treatments 250–252
efficiency of treatments 249–250
results discussed 252–253
consolidants 255
effect on thermal dilation of marble 263–268, 268–269
appearance of marble 261–262
marble porosity 262–263
ultrasonic wave behaviour 268
types 256, 257
see also water-repellant products
Cretaceous sandstones (Germany) provenance and properties
interpretation of provenance 291, 295–296
mineralogy and petrology testing
methods 285, 287
results 287–291
use in buildings 283–285
crust formation due to atmospheric pollution 330–332, 363, 401–402
Budapest (Hungary) study
black crusts 368–370
feature distribution 372–373
origin of features 373–377
white crusts 366–367
Venice (Italy) study 383, 385, 387, *389*, 390
cryoclasty *see* freeze-thaw
crystal wedging 52
cyanobacteria 180, *182*, 198, 203, *214*

Dala sandstone *317*, 319
tile bending strength *322*, 323, 324–327
darapskite 280
Dartmoor granite biodeterioration 199–200, 202
density 110, 235, *236*
desalination 52, 59
diagenesis in Wesersandstein 105–108
Diamant marble thermal expansion study 65–80
dissolution and climate change 411
dolerite *317*, 318–319
tile bending strength 321, *322*, 324–327
dolomite, thermal expansion 65, 81
dolomitic marble *see* Sivec marble; Swedish marble
Dresden (Germany) sulphur pollution 424, 425, 427
dry deposition 393–397
Dumfries Sandstone 350, *351*, 358, *359*
Dunhouse Sandstone 350, *351*, 358, *359*

efflorescence 53
Egypt *see* Cairo
Eichbühl Sandstone 432
electron microscopy
  techniques for biofilms
    film processing 208–209
    TEM preparation 209–210
  see also SEM images
Ely cathedral limestone biodeterioration *196*, *197*, *198*
epsomite *see* magnesium sulphate

fabric
  anisotropy in mylonite 115–116
    experimental measurement 116–117
    results 117–127
    results discussed 127–133
  itacolumite study 138
  in marble 10–11
    effect on bowing 302–305, 309–311
falling damp 52
Fe (iron) patinas 203
Finlandia Hall (Helsinki) 299
flexibility testing of itacolumite
  method 138
  results 138–144
  results discussed 144–146
flexible quartzite *see* itacolumite
flexural strength 110
fly ash 329, 336–337, 347, 396, 401
fog water 382–383, 398
fracture system analysis 108
France *see* Meules sandstone; Vosgien sandstone
freeze-thaw
  ageing test 250–252
  effect of climate change on 410
  effect on marble 10, 14
  effect on sandstone
    methods of study 21–22
    results 22–28
    results discussed 28–31
  resistance, Wesersandstein 110
Freiberg (Germany), atmospheric aggressiveness *397*
fretting 52
frost and salt weathering 58
fungi and rock colonization 180, 181, 183

gas pollution 393–397
Geneva (Switzerland), atmospheric aggressiveness *397*
geochemistry, Globigerina Limestone Formation 43, 44, 47
Germany *see* Görlitz region; Peccia marble study; Saxony; Zittau region
Gitano marble thermal expansion study 65–80
glacial retreat and biofilm development 183
glass decay 330, 334
global warming *see* climate change
Globigerina Limestone Formation
  research programmes *41*
    church buildings 42
    geochemistry 37–39, 43, 44, 47
    mineralogy 43, 44, 45
    petrology 46–47
    porosity 39, 43, 44–45, 46
    temple buildings 39–40
    weathering 47–49
  stratigraphy *35*, 36–37
    franka 33, *36*
    soll 33, *36*
gneiss *317*, 319–320
  and atmospheric pollution *340*
  tile bending strength *322*, 323, 324–327
Görlitz region sandstones
  interpretation on provenance 291
  mineralogy and petrology testing
    methods 285, 287
    results 287–291
  use in buildings 283–285
Gozo *see* Maltese Islands
Grand Arche de la Defense (Paris) 299
granite
  biodeterioration
    methods of study 196
    results 197–200
    results discussed 200–201, 203–204
  stone decay study, Braga (Portugal) 274–275
    methods 274
    results 275–280
  tile bending strength 316, *317*, 321, *322*, 324–327
Grauer Wesersandstein *see under* Wesersandstein
Greece, marbles
Greece marble thermal expansion study
  methods 67–68
  results 72–78
  results discussed 78–79
  texture 68–70
Grossjena carvings 427, *428*
Grosskunzendorf marble thermal expansion study 65–80
groundwater 280, 412
gypsum formation
  biological mediation of 198, 204
  in crusts 373–374, 376, 377, 394, 400, 401, 422
  effect of salt on 55, 351
  from groundwater 280
  growth 383
    on limestone 385
    on marble *387*, 388
    on sandstone 347
  mechanism for growth 329–332
  reaction with actinolite 352
  S isotope composition 425–427
gypsum-based mortar
  historic uses 165–166
  properties 166–171
  water resistance 171–173

Hagar Qim temple 33, *34*
halite 55, 59
haloclasty *see* salt crystallization
heating and cooling *see* thermoclasty
hexahydrite 280
honeycomb weathering 52
human activity *see* anthropogenic activity
humidity and salt weathering 56
Hungary *see* Budapest
hydrology and climate change 409

hydrolysis and climate change 411
hydrophobic treatment *see* water-repellant products

Iddefjord granite *317*, 318
  tile bending strength 321, *322*, 324–327
Indiana limestone 398
iron (Fe) patinas 203
Istrian stone 385, 399
Itabria Group 137
itacolumite 137
  flexibility testing
    method 138
    results 138–144
    results discussed 144–146
Italian marble
  porosity and temperature analysis
    methods 82–84
    results 84–85
    results discussed 85–87
  see also Carrara; Lasa; Sterzing

Jämtland limestone *317*, 319
  tile bending strength *322*, 323, 324–327
Jaumont limestone 338, *340*, *341*, 396

Kauffung marble, microfabric and wave velocity 153, 154, *156*, 159

larvikite *317*, 318
  tile bending strength 321, *322*, 324–327
Lasa marble
  consolidation and thermal testing 266
  fabric 259
  grain size *260*
  microfabric and wave velocity
    experimental methods 152–153
    results 153–162
  texture 68–70, 260
  thermal expansion study 65–80
  ultrasonic wave velocity 268
Lausanne (Switzerland)
  atmospheric aggressiveness *397*
  atmospheric pollution effects *338*
Leithakalt calcarenite 399, *400*, *401*
leucogranite decay, Portugal 275
  methods of analysis 274
  results 276, *277*
lichen 180, 181, *182*
  in biofilms *212*
  model of growth 190–191
  role in granite biodeterioration 197–200
    mechanisms 200–202, 203–204
  role in limestone biodeterioration 196–197
    mechanisms 202–203
limestone
  atmospheric pollution effects 338, *340*, *341*, *343*
    Istrian stone 385
  biodeterioration
    methods of study 196
    results 196–197
    results discussed 202–203
    see also carbonate rock surfaces
  Miocene oolitic of Hungary 364–366
    black crust 368–370
    breakdown 372
    grey dust 371
    origins of features 373–377
    weathering feature distribution 372–373
    white crust 366–367
  Tertiary Mokattam Group of Cairo
    composition 221, *223*
    monuments and weathering 217, *218*, 219, *220*, *228*, *231*
    porosity 221–222, *224*
    rate of weathering 227–233
    stratigraphy 220–221
    weathering forms 222–227
    weathering products 233–237
  Tertiary Páramo Limestone Formation of Spain
    conservation 248–252
    deterioration 247–248
    patina 246–247
    petrography 243, 244–245
    petrophysics 243, 245–246
  tile bending strength *317*, 319 *322*, 323, 324–327
Lisboa (Portugal), atmospheric aggressiveness *397*
London (UK)
  atmospheric aggressiveness *397*
  micro-erosion study 414, *416*
Lucerne (Switzerland), atmospheric aggressiveness *397*
Lugano (Switzerland), atmospheric aggressiveness *397*

magnesium sulphate (epsomite) 53, 59, 280, 395, 423
magnetic susceptibility 118
Main Sandstone *340*
Maltese Islands (Malta and Gozo)
  building stones 33–35
  geological setting 35–37
  Globigerina Limestone studies
    research programmes 37–40
    results 43–49
marble *317*, 320
  anisotropy 151
  bowing panels, experiments on
    methods 301–302
    results 302–308
    results discussed 309–313
  degradation 149, *150*
  history of study 9
  microfabric and wave velocity
    experimental methods 152–153
    results 153–162
  petrophysical studies
    methods 10
    results 10–14
    results discussed 14–17
    results freeze-thaw 14
  porosity and temperature analysis
    methods 82–84
    results 84–85
    results discussed 85–87
  porosity and wave velocity 151–152
  sulphation 332–333
  thermal behaviour post consolidation 255, 256–257
    effect on dilation 262–268
    effect on marble porosity 262–263

effect on ultrasonic waves 268
overall results discussed 268–269
sample fabric 257–260
sample texture 260
thermal expansion studies
methods 67–68
results 72–78
results discussed 78–79
texture 68–70, *71*
thermal stress degradation 89, *90*
finite element modelling of 90–101
tile bending strength *322*, 323, 324–327
Venetian monument decay 386, 387, 390
weathering *66*
marine-induced decay 58
case study in Belfast 349–350
effect of actinolite 352
effect on mortar 352
salt distribution 351–352
sulphate/chloride deposits 352–353
introduction 347–349
laboratory simulations
microclimate effects 353–355
salt loading effects 355–357
modelling block retreat 357–360
Mars, honeycomb weathering 59
Meules sandstone freeze-thaw response study
methods 21–22
results 22–28
results discussed 28–31
micro-organisms *see* biofilms
microcracking of marble 149
finite element modelling of
methods 90–95
results 95–98
results discussed 99–101
wave velocity study
experimental methods 152–153
results 153–162
microcracking of mylonite 116, 119–122
microfabric, marble 10–11
Milan (Italy) atmospheric pollution *338*, *340*, *397*
Minas Supergroup 137
mineralogy
Cretaceous sandstones 287–288, 291
Globigerina Limestone Formation 43, 44, 45
mylonite 116, 117
Obernkirchen Sandstone 432
mirabilite 424
Moeda Formation 137
Mokattam Group
composition 221, *223*
monuments and weathering 217, *218*, 219, *220*, *228*, *231*
porosity 221–222, *224*
rate of weathering 227–233
stratigraphy 220–221
weathering forms 222–227
weathering products 233–237
molasse d'Ostermundigen 396
mortar
historic uses 165–166
properties 166–171
reaction with sandstone 352
water resistance 171–173
Munich (Germany), atmospheric aggressiveness *397*
muscovite texture *121*
mylonite fabric anisotropy
experimental measurement 116–117
results 117–127
results discussed 127–133

Nero Zimbabwe dolerite *317*, 318–319
tile bending strength 321, *322*, 324–327
Nersac Limestone *340*
Neuchätel (Switzerland), atmospheric aggressiveness *397*
nitratine 280
nitre 280
nitric acid 394, 396
nitrogen oxides (NOx) pollution 337, 394, 395–396
Nuevo Baztán palace (Spain) 241–242
building stone conservation 248–252
building stone deterioration 247–248
building stone patina 246–247
building stone tests
petrography 243, 244–245
petrophysics 243, 245–246
environmental setting 243, 247

Obernkirchen Sandstone
cation exchange capacity 433–435
significance of 437–439
unweathered 435–436
weathered 436–437
mineralogy 432
object-oriented finite (OOF) element modelling of marble degradation
methods 90–95
results 95–98
results discussed 99–101
Oeconomicum Building (Goettingen University, Germany)
bowing marble panels, experiments on
methods 301–302
results 302–308
results discussed 309–313
building characterisation 300–301
climatic setting 301
organic acids and biodeterioration 203
Ouro Preto Stone 137
oxalate patina 195, 196, 202, 246

P wave velocity *see* ultrasonic wave velocity
Palissandro marble
freeze-thaw 14
microfabric 10–11
properties discussed 16
texture 68–70
thermal expansion studies 65–80
Páramo Limestone Formation
properties as building stone
conservation 248–252
deterioration 247–248
patina 246–247
petrography 243, 244–245
petrophysics 243, 245–246
Paris (France) atmospheric pollution *330*, *334*, *397*

particle size distribution, Cretaceous sandstones 288
particulate matter pollution 393–397
patinas 207, 330–332
  granite 276, 279
  limestone 246–247
  see also crust formation
Peccia marble bowing panels
  methods of measurement 301–302
  results 302–308
  results discussed 309–313
penetrating damp 52
Pennsylvania blue marble 398–399
permeability 21, 308
Permian stone *see* Dumfries sandstone
petrography
  itacolumite 138–139
  Meules sandstone 22, *23*
  Páramo Limestone Formation 243, 244–245
  Vosgien sandstone 22, *23*
  Wesersandstein 105
petrology
  Cretaceous sandstones 287–288, 291
  Globigerina Limestone Formation 46–47
petrophysical properties
  marble 10, 14–17
    freeze-thaw 14
    microfabric 10–11
    texture 11–12
    thermal expansion 12–14
  sandstone 21–22, 28–31
    dilation 28
    P wave response 25–26
    petrography 22
    porosity 22–25
    transfer properties 26–27
  Wesersandstein 110–111, *112*
pH
  of fog water *383*
  and glass behaviour 334
physical weathering *see* weathering
Pinczów limestone 399
Piracicaba Group 137
Poland, marbles *see* Grosskunzendorf
pollution *see* atmospheric pollution
polymethyl-methacrylate (PMMA)
  as a consolidant 256, 257
  effect on marble 261–263, 266–269
polysilicic acid ester (PSAE)
  as a consolidant 256, 257
  effect on marble 261–263, 266–269
pore modelling, gypsum-based mortar 167–169, *170*
porosity
  change in weathering profile 235, *236*
  Cretaceous sandstones 287, 289, 291, *293*, 295
  effect on pollution crusts 333
  Globigerina Limestone Formation 43, 44–45, 46
  gypsum-based mortar 167, *169*
  impact of salt crystals 55
  itacolumite study 138, 141
  marble 10, 386
    consolidated 262–263
    effect on wave velocity 151–152
    effect on bowing 305
    experimental measurement 82–84
    experimental results 84–85
    experimental results discussed 85–87
    modelling 161–162
  Mokattam Group 221–222, *224*
  mylonite 116
  Páramo Limestone Formation 246
  sandstone 21, 22–25
  Wesersandstein 110
Portland Limestone and pollution *343*
Portugal
  granite *see* Braga granite
  marble *see* Rosa Estremoz marble
poulticing 59
pressure effect on wave velocity 157–158
Prieborn marble
  consolidation and thermal testing 265, 266, 267
  fabric 258–259
  grain size *260*
  microfabric and wave velocity *156*, 158
  porosity 261
  texture 260
provenance recognition in sandstones 291, 295–296
Pyramids (Egypt) *231*, *232*

quartz texture *120*
  itacolumite study 138, 141–144

rising damp 52
Rochlitz (Germany), sulphur pollution study 422, 423
Rome (Italy), atmospheric aggressiveness *397*
Rosa Estremoz marble
  bowing 311
  thermal expansion study 65–80
Roter Wesersandstein *see under* Wesersandstein

saccharoidal marble 386, 390
St Margrethen Sandstone *340*
St Paul's Cathedral (London) micro-erosion study 414, *416*
Saint-Trophime Church (Arles, France) 335
salt creep 53
salt crystallization (haloclasty) 52
  ageing test 250–252
  effect of climate change on 410
salt damp 52
salt extraction 52
salt hydration distress 52
salt loading on Cairo monuments 233, *234*, *237*
salt pollution
  by capillary action 333
  effect on granite 279–280
salt weathering 431
  experimental observations 55–56
  field observations 56–58
  history of research 52
  interactions 53, *54*
  methods of study 56
  potential 59
  theory 53–55
  treatment 58–59
  see also marine-induced decay
sandstone
  and atmospheric pollution effects 338, *339*, *340*
  cation exchange capacity

methods of measurement 432–433
results 433–437
results discussed 437–439
petrophysical properties
Alsatian sandstone 21–28
Wesersandstein 103–111
salt weathering 347–349
case study in Belfast 349–352
tile bending strength *317*, 319, *322*, 323, 324–327
see also Gorlitz region; Zittau region
Saxony (Germany)
sulphur pollution study 419, 421–424
isotopic source differentiation 424–427
results 427–428
see also Görlitz region *also* Zittau region
Scrabo Sandstone 350, *351*, 358, *359*
sea level, effect of climate change on 409, 411
SEM images
atmospheric pollutants *331*, *332*, *335*, *336*, *387*, *400*, *401*, *402*
biodeterioration *180*, *197*, *198*, *199*, *200*, *201*, *202*, *279*
granite *279*
gypsum-based mortar *167*, *168*, *172*, *173*, *174*
impregnated stone *250*, *251*, *262*
itacolumite *140*
marble *91*, *150*
mylonite *126*, *130*
sandstones *23*, 287, *290*, *292*
Sesia-Lanzo Zone mylonite *see* mylonite
Sivec dolomitic marble
finite element modelling of degradation 90–101
smoke pollution 334–337
sodium sulphate 53, 395
Soelk marble, thermal expansion study 65–80
soil water and pollutants 427
soluble salts and weathering 45
Spain *see* Nuevo Baztán palace
Sterzing marble
consolidation and thermal testing 266
fabric 259–260
freeze-thaw 14
grain size *260*
microfabric 10–11
porosity 261
properties discussed 16
texture 68–70, 260
thermal expansion 65–80
Stone Album carvings 427, *428*
stone lace/lattice 52
storminess, effect of climate change on 409
Strasbourg cathedral study *see* Meules sandstone; Vosgien sandstone
stress-strain curves *128*
sulphates 52, 204
sulphur pollution and sulphation 347, 394, 395, 396, 419
changes with time
coal and oil smoke 336–337
wood smoke 334–336
effect of climate change 411
effect on glass 333–334
effect of humidity 332–333
effect of porosity 333
German case study 421–424
isotope analysis results 427–428
isotope composition 419–421
isotope source differentiation 424–425
atmosphere 425–427
building materials 425
soil 427
mechanism 329–332
modelling dose response 340–342
quantification of effects 337–338
supercooling 19
supersaturation and salt weathering 55
surfactants and salt weathering 58
Swedish marble porosity and temperature
experimental analysis
methods 82–84
results 84–85
results discussed 85–87
syenite *317*, 318
tile bending strength 321, *322*, 324–327
syngenite 280

tafoni 52
temperature
effect of climate change on 409
experimental effects on marble
methods 82–84
results 84–85
results discussed 85–87
tensile strength 21–22
mylonite 116, 122–125
Tertiary stone *see* Globigerina Limestone Formation; Mokattam Group; Páramo Limestone Formation *also under* Budapest
texture
marble 11–12
mylonite 116, 118–119
Thassos marble thermal expansion study 65–80
tile bending strength *322*, 323, 324–327
thenardite 280, 424
thermal dilation of marble 255
effect of consolidant treatment 256, 257, 263–268
appearance 261–262
effect on porosity 262–263
thermal expansion
carbonates 81
marble 10, 12–14
methods of analysis 67–68
results 72–78
results discussed 78–79
thermal stress degradation of marble
finite element modelling of
methods 90–95
results 95–98
results discussed 99–101
thermonatrite 280
tiles, impregnated
bending strength tests
method 321
results 321–323
results discussed 324–327
methods of production 320–321
Touraine tuffeau 333
trace fossils *40*

traffic and patina formation 279
Tranäs granite 316, *317*
  tile bending strength 321, *322*, 324–327
Triassic stone *see* Bunter; Eichbühl Sandstone; Obernkirchen Sandstone; Scrabo Sandstone
trona 280

ultrasonic wave velocity
  change with weathering profile 235, *236*
  marble 149, 268
    methods of measurement 152–153
    results 153–162
    significance in bowing 308
  mylonite 116–117, *131*
  sandstone 21, 25–26

Van der Waals forces 393
Växjö granite 316, *317*
  tile bending strength 321, *322*, 324–327
Venice (Italy)
  atmospheric pollution effects *330*
  fog sampling and analysis 382–383
  stone surface exposure
    Carrara marble 386, 387
    Istrian stone 385
    memory effect 388–389
    saccharoidal marble 386, 390
Vermont marble 398
Villarlod blue molasse 396
Villarlod sandstone and atmospheric pollution *339*, *340*
Volakas marble thermal expansion study 65–80
Vosgien sandstone freeze-thaw response
  methods of analysis 21–22
  results 22–28
  results discussed 28–31

Wachau marble thermal expansion study 65–80
Washington (USA), atmospheric aggressiveness *397*
water
  absorption and uptake
    Cretaceous sandstones 287, 289, 295
    Wesersandstein 110
  resistance in mortar 167, 169, 171–173
  role in weathering 1–2
  saturation and wave velocity 158–161
water-repellant products 248–249
  durability of treatments 250–252
  efficiency of treatments 249–250
  results discussed 252–253
weathering 1–2
  biofilm effects 191–192
  climate effects 410–413
    UK case studies 414–417
  Globigerina Limestone Formation 47–49
  marble 14–15
  processes 1–2
    see also biodeterioration; freeze-thaw; salt weathering; temperature; thermal dilation, thermal expansion, thermal stress
wedellite *see* calcium oxalate
Wesersandstein
  depositional environment 104–105
  diagenesis 105–108
  fractures 108
  geological setting 103–104
  Grauer *104*, *108*, *109*, *110*, *113*
  petrography 105
  petrophysical properties 110–111, *112*
  prospectivity 108–109
  Roter *104*, *108*, *109*, *110*, *113*
  summary of properties 111
wet deposition 397–399
wood smoke pollution 334–336

Young's modulus anisotropy 115

Zittau region sandstones
  interpretation of provenance 295–296
  mineralogy and petrology testing
    methods 285, 287
    results 291–295
  use in buildings 285, *286*
Zurich (Switzerland), atmospheric aggressiveness *397*